DUCTILE FRACTURE UNDER COMBINED TENSION AND SHEAR: THEORY AND APPLICATIONS

A Dissertation

by

MOHAMMAD EBRAHIM TORKI HARCHEGANI

Submitted to the Office of Graduate and Professional Studies of
Texas A&M University
in partial fulfillment of the requirements for the degree of

DOCTOR OF PHILOSOPHY

Chair of Committee,	Amine Benzerga
Committee Members,	Junuthula N. Reddy
	Alan Needleman
	Jay R. Walton
	James Boyd
Head of Department,	Rodney Bowersox

May 2019

Major Subject: Aerospace

ABSTRACT

Fracture causes enormous material and energy waste per annum, with large economical, industrial and environmental impact. In particular, ductile failure under shear-dominated loading pervades in many areas of manufacturing, load-bearing structures and impact protection systems. However, failure in shear remain elusive there being no complete theory of ductile fracture without a physics-based model. A robust micromechanics-based constitutive framework, founded on mechanism-based yield criteria for materials with evolution laws accounting for microstructural evolution, is essential to this end. Experimental observations reveal cell-level plastic deformation as homogeneous or inhomogeneous, the latter being idealized with plasticity confined within intervoid ligaments or occasionally within intervoid plugs. The present thesis is partly targeted to the development of analytical yield functions that predict yielding by either mechanism, attained by limit analysis over a cylindrical cell containing a coaxial void. Nonetheless, existing outcomes indicate the shear-dominated deformation process at early stages as an intermediate state between a homogeneous and an ideally localized one. Correspondingly, a *hybrid* model is adopted consistsing of simple modifications to both an existing homogeneous yield criterion as well as a derived localized yield function. Upon current limitations of a highly complex physical process, a *surrogate* microstructure, tied to a possible *localization plane*, is invoked. The next missing link to the constitutive framework calls for microstructural evolution equations during localized deformation, which sets the second objective of the present work. The body of existing and derived yield criteria supplemented with available and derived evolution equations sets enough grounds for the numerical simulation of ductile fracture, thus the third milestone. The hybrid model predictions are firstly borne out by existing numerical outcomes under combined loading. The parametric studies are then carried through a complete range of loading combinations from uniaxial to pure shear loading. The effects of initial porosity, void shape, relative spacing, void misalignment with the principal loading directions, and matrix plastic anisotropy are accounted for. Furthermore, the strain to failure is evaluated vs. a complete scope of stress triaxialities. The thesis closes with

proposed extensions to 3D voids, void coalescence along columns and other potential prospects for more robust numerical implementation.

Key Words: Ductile fracture; Void coalescence; Combined tension and shear; Homogeneous/ Inhomogeneous Yielding; Strain localization; Simple/Pure shear.

DEDICATION

I feel so obliged as to dedicate this thesis to the Last Savior, to whom the entire mankind is indebted and for whose justice the righteous are avid.

ACKNOWLEDGMENTS

I would like to acknowledge support from the National Science Foundation under Grant Number CMMI-1405226. Further, the finite-element cell-model calculations carried out by Dr. C. Tekoğlu (parts of Chapter 5) and F. A. Medrano (Chapter 8) are sincerely acknowledged.

CONTRIBUTORS AND FUNDING SOURCES

Contributors

This work was supported by a thesis committee consisting of Professor **Amine Benzerga** (chair of the advisory board) from the Departments of Aerospace and Material Science and Engineering, **Alan Needleman** from the Department of Material Science and Engineering, Junuthula N. Reddy from the Department of Mechanical Engineering, Jay Walton from the Department of Mathematics, and James Boyd from the Department of Aerospace Engineering. Further, the student has extensively consulted Prof. Jean-Baptiste Leblond from Sorbonne University and the Institut Jean Le Rond d'Alembert, entitled a special-appointment member, in the analytical part of the present work.

The finite element-based cell-model calculations for parts of Chapter 5 and the entire Chapter 8 were carried out by Dr. C. Tekoğlu from TOBB University of Economics and Technology, and Francisco A. Medrano, respectively. All other work conducted for the thesis was completed by the student independently.

Funding Sources

This graduate study was partly supported by support from the National Science Foundation under Grant Number CMMI-1405226.

TABLE OF CONTENTS

Page

LIST OF FIGURES

FIGURE Page

LIST OF TABLES

TABLE Page

CHAPTER 1 INTRODUCTION

1.1 Overview and Significance

The amount of material and energy waste induced by fracture is among the most remarkable ones per annum, baring large economical, industrial and environmental impacts. Hence, fracture is mostly deemed deleterious, thus to be avoided, as far as the safety in infrastructure or structural integrity is concerned. In fact, the genesis of the knowledge known today as *fracture mechanics* dates back to the catastrophic damages that took place in the American *Liberty ships* due to the ductile-to-brittle transition (DBT) of solids in freezing waters of North Atlantic. In the course of seven years, between 1939 to 1946, 1038 from the 2708 constructed Liberty ships were reported to have damaged, more than 200 of which sank or were damaged beyond repair (including the "Schenectady") [22, 23]. Several other catastrophies have been observed since, including but not limited to the *de Havilland Comet* [24] and *Aloha Airlines Flight 243* [25] crashes in 1954 and 1988, respectively, due to fuselage failure triggered by fatigue and corrosion cracks. Apart from the shipping and air industries, leakage of chemicals from reservoirs has been counted as the source of dramatic fatalities. In the *Ajka alumina sludge* spill in 2010, for instance, the collapse of the northwestern dam corner led to the realease of approximately one million cubic meters (35 million cubic feet) of liquid waste [26].

Just as fracture can be harmful, so too it can be desirable. By virtue of proper engineering of fracture paths, as in metal cutting and/or trimming, material imperfections at the macroscopic level can be avoided or minimized. For instance, *burring* in machined workpieces is a serious cause for fabrication deficiency. Burrs require additional finishing operations, known as *deburring* techniques, and they further complicate the assembly. A careful choice of the machining tool path can minimize burrs within metal pieces [27].

Fracture modes and failure mechanisms are primarily driven by the loading condition. Among the three basic fracture modes (mode I, II, and III), mode I is mainly driven by normal load-

ing whereas modes II and III are triggered by shear [23]. Ductile failure under shear-dominated loading pervades in many areas of manufacturing, load-bearing structures and impact protection systems. The effect of shearing has thus been a prime concern in fracture mechanics and failure prediction from early days. In particular, ductile failure under combined tension and shear has received extensive attention in the past decades for both gaining insight into undesirable failures such as crack propagation under DBT (*e.g.* in welded structures; see [28, 29]), penetration, *etc*. as well as desirable engineering manufacturing processes such as metal forming, cutting, trimming, extrusion, *etc*.

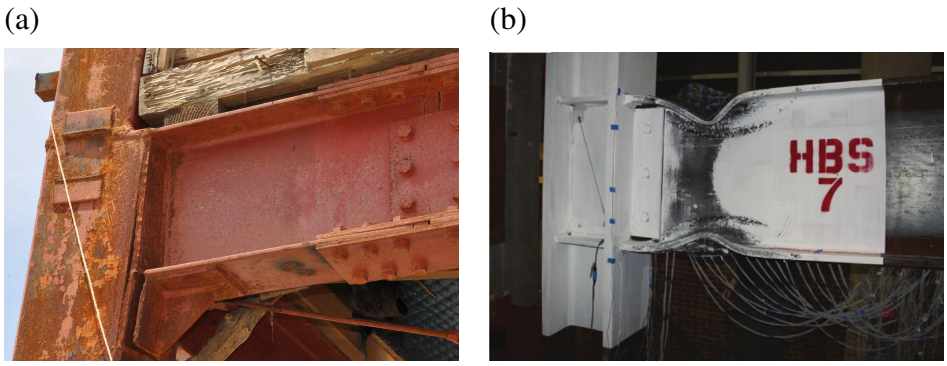

Figure 1.1: (a) Weld failure under combined tension and shear after the 2011 Tohoku Japan Earthquake (reprinted with permission from the *Earthquake Engineering Research Institute* (EERI), Ltd) [1], (b) beam-to-column joint connection failure under combined bending and shear testing [2] (reprinted with permission from *Elsevier*, Ltd).

Figure 1.1a shows failure of a beam-to-column steel connection due to weld tearing under earthquake-induced tensile and shear loads [1]. For design purposes, the cross sections of connecting constituents should be designed based on a predicted ductility behavior germane to earthquake-like lateral loads. A combination of high tensile coupled with significant shear loads can be properly exerted by actuation of the beam from the location of a potential plastic hinge. Figure 1.1b shows an example beam-to-column connection failing under a shear-induced yielding in the web and flange yielding and buckling due to tension and compression, respectively [2].

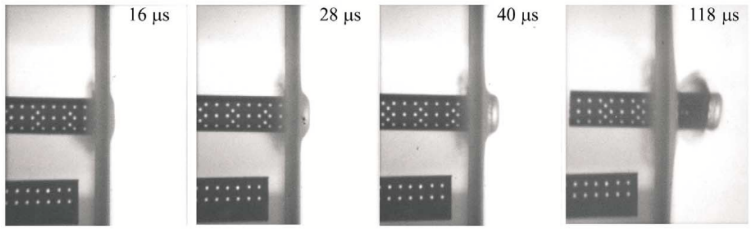

Figure 1.2: Ballistic penetration test carried out by Borvik *et al.* [3] (reprinted with permission from *Elsevier*, Ltd).

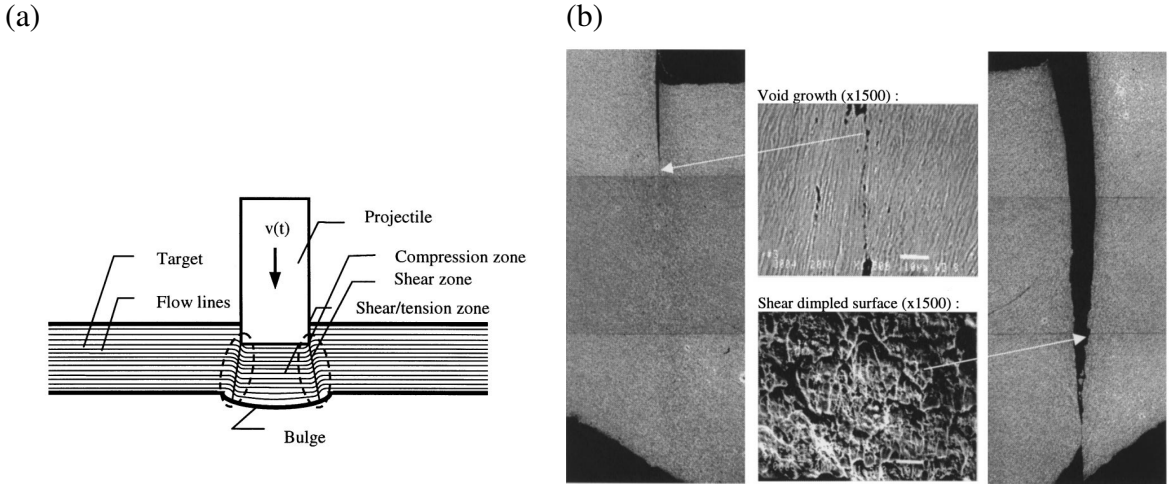

Figure 1.3: (a) Schematic outline of the localized damage zone in a penetration test, (b) tomographical images of localized damage [4] (reprinted with permission from *Elsevier*, Ltd).

Ballistic penetration, as shown in Fig. 1.2, is another practical example triggered by extreme shearing with high shear strains advancing through a small or finite thickness [3, 4]. The overall plug formation process consists of a combination of local *bulging* and global *dishing*. The former dominates at early stages, and the latter becomes prominent towards the end of penetration, as observed in Fig. 1.2a. Further details in this regard can be viewed in Fig. 1.3. The fracture surfaces shown in Fig. 1.3b have been generated from spectral microscopy. They clearly convey the existence of combined tensile and shear loading at the failure stage. The onset of the fracture process corresponds to a plug movement equaling about half of the plate thickness [4].

The target undergoes permanent deformation as increasing function of the projectile velocity, which reaches a maximum at the so-called "ballistic limit" of the velocity. After penetration is

complete, the deformation decreases with velocity until it saturates at a velocity well beyond the ballistic limit. Static and dynamic tests have demonstrated that the maximum deformation within the target towards the onset of fracture is about twice the permanent deformation thereof, indicating remarkable elastic recoil [3, 4].

In forming processes, the boundary conditions corresponding to the existence of rigid zones (such as dies) lead to a build-up of initial shear stresses cutting [6]. The similar phenomenon occurs by introduction of a small sharp notch at the cutting starting point in a cutting experiment or simulation [30, 31].

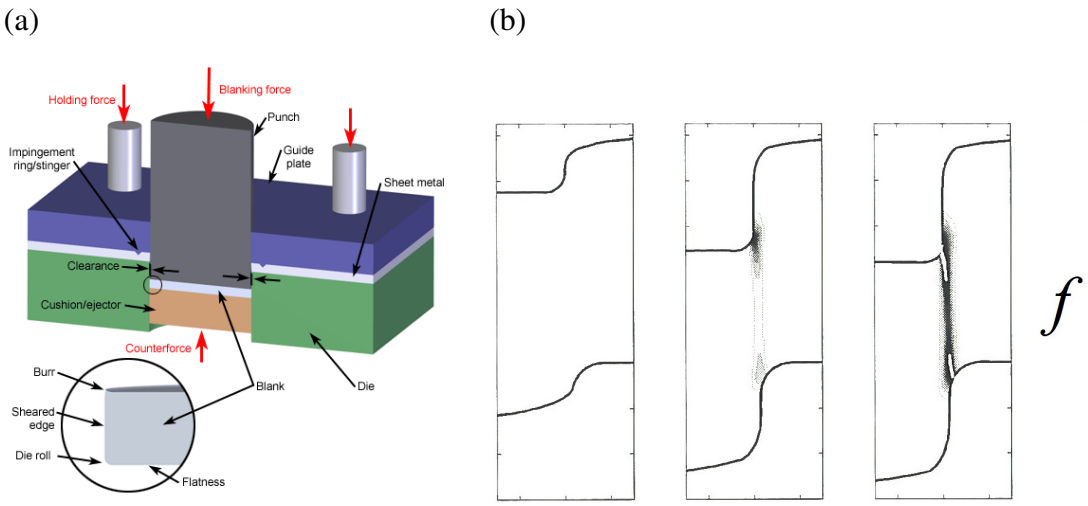

Figure 1.4: (a) Schematic blanking setup (reprinted from [5]), (b) example contours for the void volume fraction f resulting from the simulation of the blanking process by Mediavilla [6] (reprinted with permission from *Elsevier*, Ltd).

Figure 1.4a depicts a schematic setup pertaining to a forming process known as "blanking". A common defect left in a formed specimen is burrs. As stated above, burrs can be minimized with proper engineering of the die and the blanking path. Figure 1.4b presents an example simulation of the blanking process by Mediavilla [6].

The basic failure modes observed in engineering metals at the microscopic level are cleavage, intergranular, and ductile fracture [32]. Ductile fracture occurring by the nucleation, growth, and coalescence of voids is a prime failure mechanism in ductile materials. Fracture can happen

in amorphous, single-crystalline or poly-crystalline materials. More specifically, poly-crystalline metals that do not cleave can fail in a ductile, mostly transgranular manner [13]. In structural materials, voids may nucleate by particle cracking or by decohesion between the particles and matrix. Subsequently, void growth is driven by plastic deformation within the matrix surrounding the voids, and is commonly accompanied by void expansion/contraction, elongation/shortening, and distortion. Void coalescence, which is normally ensued by crack propagation and ultimate failure, is associated with plastic deformation being localized in the intervoid ligaments [13, 33, 34]. The present work is a step forward to the computational modeling of ductile fracture under combined tension and shear, with particular focus on shear-dominated loadings.

1.2 Experimental Facts

Failure in a ductile material can occur by some mechanical instability of a test piece or by damage propagation to cracking. The former can best be exemplified by the formation of a shear band, and the latter stems from plastic flow localizing in microscopic intervoid ligaments, mostly known as "void coalescence" [13, 35]. Experimental characterization of fracture can be reflected partly through macroscopic and partly through microscopic observation of fracture surfaces.

1.2.1 Macroscopic observations

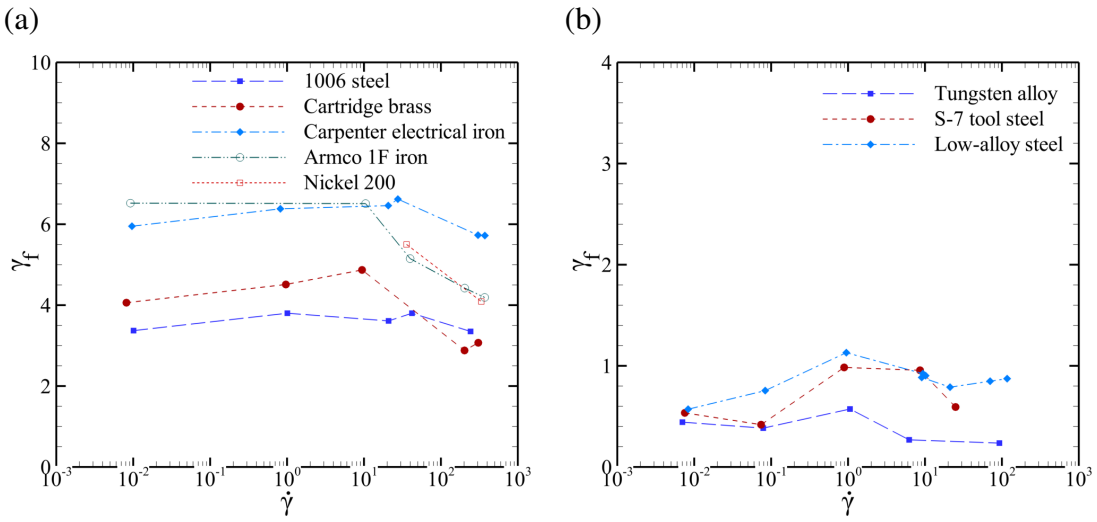

Figure 1.5: Effect of shear strain rate on the average shear strain to fracture for engineering metals: (a) ductile metals [7], (b) less ductile metals [8].

Experimental observation of ductile fracture under shear-dominated loading at the macro scale has been conveyed through bulk or sheet specimens. In the former, combined tensile and shear loads are applied on thin-walled torsion tubes. By virtue of the Saint-Venant principle, the shear strains can be regarded as constant over a large portion of the specimen length.

Among the most comprehensive studies using this method is the reported measurement of ductility for varieties of engineering metal alloys by Johnson *et al.* [7, 8], who came to divide the investigated metals into *ductile* and *less ductile*. Figure 1.5 shows the effect of torsion-induced shear strain rate on the average shear strain to fracture according to [7, 8]. One can observe at least 2 orders of magnitude of difference in γ_f from the lower to the upper limit, keeping mindful that the tensile ductility variation is, by no means, found to be as wide. A compelling explanation regarding these remarkable differences in the measured ductilities still remains elusive.

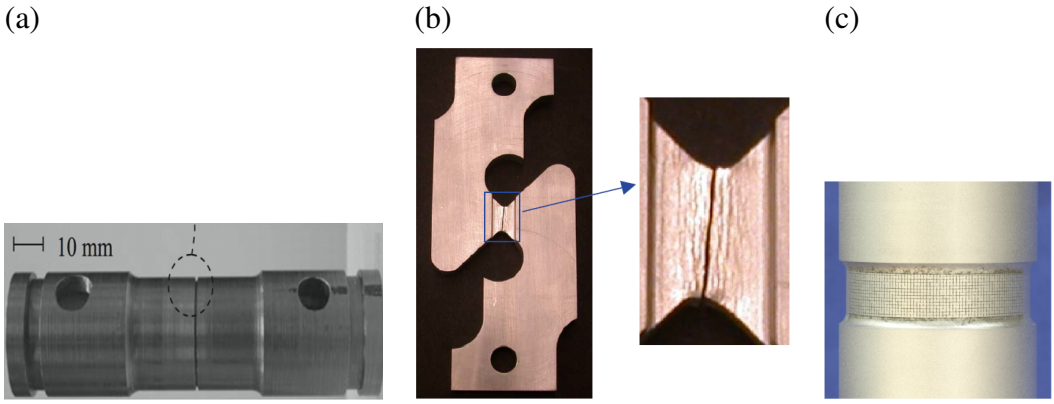

Figure 1.6: Typical combined tensile-shear test specimens: (a) hollow tubes utilized by Barsoum and Faleskog [9, 10], (b) butterfly specimens used by Bao and Wierzbicki [11], (c) hollow tubes employed by Haltom *et al.* [12] (reprinted with permission from *Elsevier*, Ltd).

Later on, Barsoum and Faleskog [36] conducted similar experiments by the introduction of notches to hollow tubes for illustrating the effect of triaxiality. They characterized the stress state in terms of stress triaxiality T and the Lode parameter L by imposing a combined state of tensile and torsion loading at fixed ratio. They employed extensometers and gauge clips (tied to the tube gauge section) to measure tensile displacements and torsion angles, respectively. See Fig. 1.6a. In order to realize straightly oriented fracture surfaces under pure torsion, the ratio between the gauge section length and the notch height was taken as 120. Further, the gauge and notch thicknesses were considered 1.6 and 0.6 (mm), respectively so an almost uniformly distributed shear stress would be witnessed [1]. They further evaluated the stress state inside the notched region from FEM simulations using axisymmetric elements. Notably, their observations from spectral-microscopy fractographs indicated clear distinction among fracture surfaces at low to high triaxialities. They witnessed elliptical dimples at $T < 0.5$, parabolic dimples at $T > 1$, and a transition between the two at $T = 0.85$.

Due to the existing difficulties in the exertion of pure torsion, Arcan sheet specimens were concurrently designed for shearing experimentation on thin sheets [37, 38], and have been both widely employed and modified in the past decades for metals [39], composites [40, 41], polymers [42],

[1] At such small thicknesses, the intervoid distances can come down to be comparable to the void sizes. Therefore, the notion of a representative volume element (RVE) would become questionable.

magnesium [43], *etc*. The main limitation within the Arcan method, however, lies in stress concentration at the vicinity of free surfaces at the sheared cross section, which prompts fracture from the free surface zone, which is not essentially driven by shear. To this challenge, *butterfly* specimens later attracted some researchers for the sake of more uniformity in shear stresses (Fig. 1.6b). Bao and Wierzbicki [11] were among those who explored shear failure in butterfly specimens.

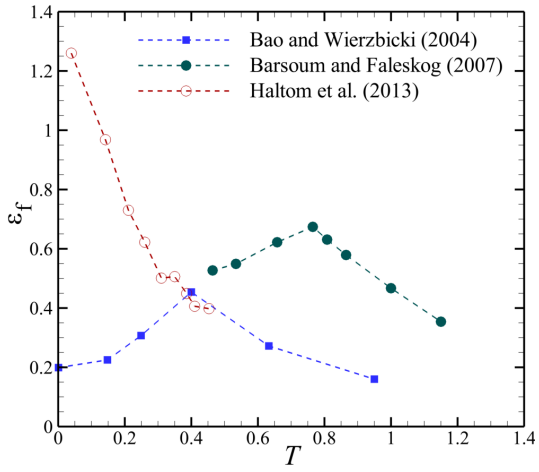

Figure 1.7: Equivalent strain to fracture vs stress triaxiality, resulting from experiments conducted by Bao and Wierzbicki [11], Barsoum and Faleskog [9], and Haltom *et al.* [12].

Yet, butterfly specimens have not duly fulfilled the expected shear uniformity. Hence, Haltom *et al.* [12] have recently conducted torsion experiments with the test specimen revisited (Fig. 1.6c), which unravelled a new finding. See Fig. 1.7.

Fig. 1.7 presents equivalent plastic strain at the failure point, concisely termed "strain to failure" ϵ_f, in terms of stress triaxiality. Earlier torsion experiments on aluminum alloys and steels indicated that the materials were less ductile in shear than under uniaxial tension [9, 11] whereas Haltom *et al.*'s experiments showed the opposite trend [12]. A deep insight into the driving trend can be acquired only with a robust constitutive development of the fracture model. Altogether, experiments, though being revealing, are hard to conduct, especially in presence of shear, and may lead to conflicting results. All the same, numerous studies have striven to incorporate the effect of shear in ductile fracture. Keeping in mind specimen geometry and material variability, the extent to which shear affects ductile fracture remains fairly unsettled.

1.2.2 Microscopic observations

The microscopic texture of fracture surfaces is conventionally examined through spectral electron microscopy (SEM) [44]. Plastic flow at the micro scale can localize due to enlargement or rotation and/or elongation of voids. Void growth emanates from plastic deformation of the material surrounding the void. All the same, void coalescence is governed by plasticity that is localized within a directed intervoid ligament. Therefore, plastic dilatancy, being diffuse or localized, is intertwined with both growth and coalescence. To date, the failure mechanism subsequent to void coalescence that is best understood is by *internal necking* (see [45] and references therein) motivated by the pioneering computational work of Koplik and Needleman [46]. On the other hand, microscale localization by so-called *internal shearing* has also been noticed on the basis of cell model calculations [17, 36, 47, 48]. In a weakly rate-sensitive material, void coalescence by internal necking or shearing manifests by the onset of elastic unloading in layers above and below the void [20,46,48,49]. Occasionally, strains can localize along intervoid plugs forming columns of localized deformation. The latter is termed *coalescence in columns* or *necklace coalescence* [33,50].

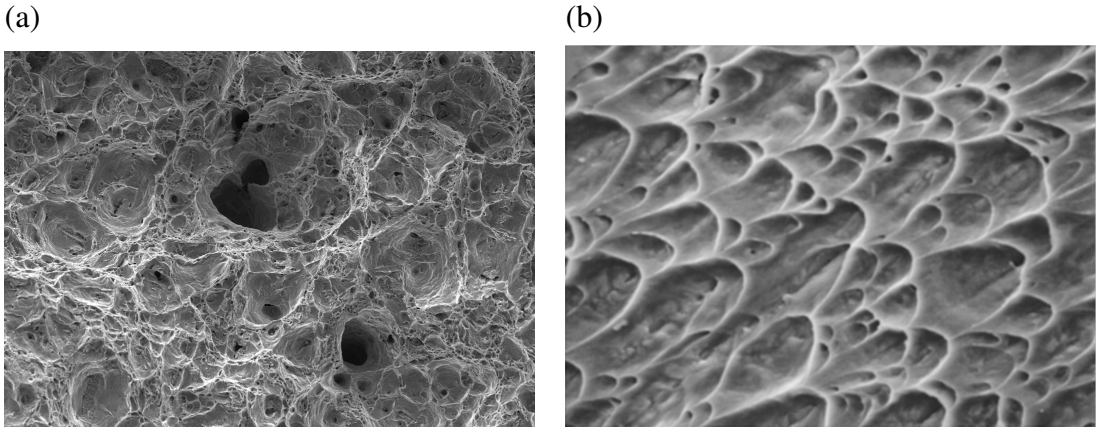

Figure 1.8: Typical fracture surfaces of metals failing in (a) tension, and (b) shear [13] (reprinted with permission from *Elsevier*, Ltd).

The de facto failure mechanism under any loading condition can be envisaged from tomography. Fig. 1.8 compares two typical fracture surfaces exhibiting in the form of dimples. The plastic enlargement of microvoids dominates at moderate to high ratios of tension-to-shear stress

(tension-dominated loading), Fig. 1.8a. Voids are also observed to distort significantly at low tension-to-shear ratios (shear-dominated loading), Fig. 1.8b [13].

Another prominent indication of failure in shear is *shear failure*, *i.e.* failure by shear banding as an instability phenomenon. The latter pervasive in complex fluids [51], granular materials [52,53], rocks [54], polycrystals [55,56], polymers, [57] and amorphous metals (metallic glasses) [58,59]. However, the mechanism of material separation under shear-dominated loadings as well as inside shear bands has remained elusive by far. Understanding it will not only potentially retard failure in shear bands, if desired, but also impact other applications where failure occurs under shear dominated loadings. The stress state in shear bands is generally complex depending on the loading path prior to the onset of strain localization [60]. Correspondingly, shear bands are generally dilational. Hence, upon favorable conditions, void coalescence can also take place inside a shear band. Yet, the arbitrarily small to large tension-to-shear ratios that may be encountered inside shear bands warrants a deeper insight into a physics-based failure mechanism under combined tension and shear.

1.3 Challenges and Objectives

Ductile fracture is a complex phenomenon in the mechanics of materials with both intrinsic and extrinsic effects being involved. Intrinsic effects include induced anisotropies mediated by large plastic deformations, microstructural evolution (void expansions, rotations and distortions), and stress state. Extrinsic effects are relevant to boundary conditions and to the states of incipient plastic instabilities, be it at the material (*e.g.*, shear bands) or structural (*e.g.*, necking) level [61–63].

Void nucleation under predominant shearing involves complex void-particle interactions [64]. Micromechanical void nucleation analyses of the kind pioneered by Needleman [65] are still not available for such loadings. Whether these nucleation conditions fundamentally differ from those under tension with particle locking effects [66, 67] remains to be investigated. Void enlargement at medium to high triaxialities, as well as void shrinking at the limit of low triaxialities are usually accompanied with void shape changes and distortion. Yet, the latter is more prominent at low

stress triaxialities characteristic of remarkable shear stresses. In this regime, void distortion is a key origin to failure. Void distortion can be influenced by several factors, including the presence of shear stresses and void-particle interactions [66, 68]. Void locking and formation of penny-shaped cracks under limited void growth are among the clear examples [67, 69, 70].

A major drawback within the established caliber of work on the effects induced by shear is a missing constitutive framework that takes into account the effective internal state variables that are both measurable and observable. These variables pertain mainly to the rotation and distortion of the microstructure under the effect of shear. Therefore, the major challenges to this task are primarily related to the void-mediated microstructural evolutions mainly associated with void rotation and distortion under the effect of combined tension and shear. Constitutive frameworks merely relying on heurism fail to reveal the physics behind the plastic process, and thus their limitations cannot be revealed unless upon high through-put calculations or heavy experiments [71, 72]. More importantly, the constitutive behavior of porous materials in a state of incipient void coalescence is still at premature stage. Rather than merely on heuristics, plasticity models predicting void growth and coalescence (see Sec. 1.5 for definitions) under combined tension and shear should be derived with a deeper insight into the physics of this process. Apropos of void coalescence, in particular, analytical physics-based models accounting for void coalescence under combined loading from first principles have been lacking. Moreover, a set of equations accounting for the evolution of effective parameters governing the post-coalescence microstructure is far from established. The only way to explore this problem without the present controversies is by adopting a *mechanism-based* approach, which is true to the spirit of the local approach [33, 34]. The present work is thus a step forward to the extraction of a more comprehensive constitutive theory for modeling ductile fracture under combined tension and shear, with particular focus on shear-dominated loadings. Without this step forward, the link between the real failure mechanism and the simulated process would still be missing. The virtues of a mechanism-based constitutive framework abound. In the least, the fracture process can be simulated with measurable and observable state variables. The clear physical demonstration of involved state variables leads to vivid elucidation of the model

limitations at extreme cases. It also eases the calibration of the model by means of adjustable parameters if need be.

In the interest of the foregoing challenges, the following main objectives can be outlined in the following items:

1. Develop and validate a micromechanics-based void coalescence model under combined loading accounting for the effects of stress state and microstructure.

2. Simulate complete fracture processes from micro-void growth to coalescence up to failure, and reconcile failure mechanisms under combined tension and shear with evolving microstructural parameters.

3. Investigate the effects of stress state, strain history, and microstructure on the failure maps of engineering materials representative of structural alloys.

4. Extend the realm of the implemented constitutive framework with some of the more influential underlying assumptions relaxed.

A clearer illustration of the above objectives is demonstrated in Sec. 1.6.

1.4 Approach

In a *global* approach, essentially based on linear elastic (LEFM) and elastic-plastic (EPFM) fracture mechanics, it is generally assumed that fracture can be described by a single, or utmost two, loading parameter, such as K_{Ic} or J_{Ic}, or any equivalent thereof, such as the crack-tip opening displacement (CTOD) [13, 34]. More recent methods based on the global approach have incorporated a second parameter, the T or Q stress [73]. The limitations associated with the global approach, including but not limited to the loss of size effect predictions and inapplicability to non-isothermal loading conditions, have driven the researchers towards adopting a second type of approach, known as the *local* approach, also termed the *top-down* approach [33, 34, 74]. In the latter, fracture parameters are modeled based on local fracture criteria that are established from

tests on bulk specimens (especially notched specimens) or from computational analysis over an elementary cell, usually referred to as a reference volume element (RVE). Within this realm, the key concepts such as *void growth* and *void coalescence*, on the one hand, and matrix plasticity, on the other hand, are inherently coupled. One established way to tackle fracture using a local approach is to calibrate the internal state variables [72, 75]. However, provided that the model is quantitatively robust, the need to the calibration of parameters will be eliminated. Accordingly, the present work aims at *prediction* of critical parameters rather than mere calibration. This sets a paradigm for developing future predictive models and discovering the limitations of existing models.

In the reported literature, a tentative understanding on the effect of stress state on ductile fracture is carried through macroscopic nondimensional descriptors expressed in terms of stress invariants or some equivalent invariant of the stress deviator at the cell level. Among the most widely used are *stress triaxiality* $T = \sigma_{\mathrm{m}}/\sigma_{\mathrm{eq}}$ and the *Lode* parameter $L = -\cos 3\theta$. The former is so defined as the ratio of the mean normal stress to the Mises equivalent stress, and the latter is function of the Lode angle or, equivalently, the third invariant of the stress deviator, J_3. Unless quite lately, isotropic damage models have been expressed exclusively in terms of triaxiality, and have thus failed to capture the essential behaviors in presence of remarkable Lode effects [75–80]. While this class of models have gained in maturity and accuracy, e.g. [14, 81–83], other groups have investigated the tentative effect of J_3 on the stress and microstructural state [36, 71, 84, 85]. However, neither parameter can reveal the essential behaviors in presence of low stress triaxialities. In other terms, this type of work is formulated upon the basic properties of *isotropic* scalar-valued tensor functions. Deformation-induced anisotropies, however, constitute the essence of the damage mechanics of shear-dominated ductile fracture [32, 86]. This anisotropy is of two types: that related to the voids themselves (large plastic strains, changes in void shape and orientation); and that related to their spatial arrangement. Thus, analyses of ductile fracture under shear-dominated loading and interpretation of currently available experiments rely, to a large extent, on accounting for the induced, and eventually initial anisotropies. At this stage, the material response is strictly sensitive towards the loading path, initial microstructure, and void distribution. The reader can

consult [87, 88] for more details. The additional downside within isotropic models is the description of fracture in macroscopic terms, which leaves the fundamental mechanisms underlying such effects elusive. Therefore, the constitutive framework demands a paradigm shift in approaching ductile fracture in combined shear and tension, particularly at low stress triaxialities even if the anisotropy of the material is disregarded.

Interestingly, the micromechanical basis for an understanding of low-triaxiality fracture has been available since the early nineties [89–92] and has been used to model fracture in engineering materials, e.g. [93]. The constitutive model expanded in the present context will be in part supplemented with some of the earlier work [91, 94] and, in part, with more sophisticated models developed in more recent years [14, 95]. The lack of physics-based micromechanical models supplemented with mechanism-based evolution equations of effective state variables, however, calls for more extensive work in this regard. In essence, work on yield criteria and plastic flow potentials accounting for the effects of void shape, volume fraction, and rotation is still scarce. Besides, evolution of state variables affected by shear loading has not been formulated to the adequate extent.

1.5 Potential Impacts

An appropriate constitutive framework, including yield criteria and evolution equations that can quantitatively and qualitatively mimic the physics, would be conducive to an effective way to simulate fracture process up to failure with measurable and observable parameters. The numerical work carried out by Tvergaard and coworkers [16, 17, 21] for combined tension and shear aiming at the cell-level simulation of ductile fracture under combined loading has set a landmark in this field. Nonetheless, it clearly demonstrates that numerical cell-model studies, let alone structural calculations, of porous plasticity under combined loading is not only cumbersome, but also unfeasible at times, *e.g.* in the case of extreme shearing over 3D unit cells [17]. Micromechanics-based modeling would, in effect, eliminate the need for lengthy cell-model calculations and significantly contract voluminous structural calculation thanks to homogenized modeling. Moreover, a constitutive framework developed based on physical parameters would reveal its realm and limitations in conformity with physical processes.

Apart from verifiable simulation of the fracture process under combined tension and shear, another major contribution of the present study is to predict the evolution of strain to failure ϵ_f in terms of stress triaxiality T in a plot known as *fracture locus*, particularly in the $0 \leq T < 1/3$ interval characteristic of shear prevalence. The reported literature lacks a clear dichotomy of important factors such as loading history and microstructural effects at this interval.

The constitutive framework will further allow for a better rationale regarding the significant differences in the ductility of materials subject to shear, as explored by Johnson *et al.* [7, 8], for instance, from torsion experiments. A perspicuous explanation about this wide range of differences lies in the initial microscopic intervoid relative distances. Results in Chapter 7 will further clarify this effect.

Above all, the numerically implemented algorithm can be utilized as a tool for structural calculations. To this end, the numerical framework can be translated into a user-defined subroutine (UMAT) to solve structural boundary-value problems on porous materials. The user-defined subroutine conspicuously eliminates the need to model the microstructure by accounting for the evolution of corresponding microstructural parameters.

1.6 Research Objectives

In this section, the broad objectives stated in Sec. 1.3 are elaborated upon as follows:

1.6.1 Activities under Objective 1

Development of yield criteria encompassing essential microstructural parameters is the first objective. The models are developed from first principles, and are capable of describing the yielding and subsequent flow of a material containing voids in configurations such that microscale localization of plastic flow is possible under combined shear and triaxial tension. Such models would directly be relevant to modeling ductile failure by internal necking, internal shearing or both. Model versions can vary mainly due to uncertainties in the assumptions made on the availability of benchmark solutions. Therefore, inhomogeneous models can be seamlessly juxtaposed to an originally identified unified model accounting for both void growth and coalescence. Meanwhile, assessment

of the models in accordance with finite element-based numerical values is indispensable. Therefore, FEM cell-model limit-analysis calculations are carried out on the same cell geometry in that interest. Chapter 5 collectively presents all the newly derived yield criteria within the present context.

1.6.2 Activities under Objective 2

The numerical implementation of the constitutive framework at hand allows for the apportioning of the inevitably coupled effects of stress state, loading path, and material microstructure on the effective state variables describing ductile fracture of structural materials. To this end, selected inhomogeneous yield criteria along with a judicious choice of the homogeneous yield criterion is the second objective with the aim of simulating the entire process of ductile fracture under combined tension and shear up to ultimate failure. In case the two yeild criteria are derived on the basis of different elementary cell geometries, the resulting multi-surface model is termed *hybrid*. Further clarification on this definition will be provided in Chapters 3 and 6. Alongside, existing evolution equations for internal state variables will be supplemented to the homogeneous model. Yet, since some counterparts for those equations are missing in the reported literature, they need be originally derived for the inhomogeneous process under combined tension and shear. Existing body of equations in this respect is far from established. In particular, the mechanism-based set of post-localized evolution equations should account for the rotation and distortion of voids under combined tension and shear. The model will be assessed with reference to the numerical analyses at the material cell-level carried out by Pardoen and Hutchinson [20] for triaxial loading as well as Tvergaard and coworkers [16, 17] for combined tension and shear. The parametric results will then extend into the states of near-simple and near-pure shearing. Further, example finite-element simulations will be presented to demonstrate the capability of the hybrid model to solve structural boundary-value problems. To this end, the constitutive framework for the porous material is implemented in an ABAQUS user-defined subroutine (UMAT) for the homogenized analysis of boundary-value problems.

1.6.3 Activities under Objective 3

Typical plots known as "fracture loci" present the effective plastic strain to failure ϵ_f in terms of stress triaxiality. Fracture loci are efficacious measures of intrinsic ductile behavior, and are attractive to the industrial sector involved in forming processes. Inasmuch as the low-triaxiality regime is strictly dependent on the loading path, several loading paths with piecewise-constant triaxialities will be adopted in the $0 \leq T < 1/3$ interval, and the constitutive framework is integrated with respect to time along every loading path, whereby the cumulative strain to failure is calculated in each case. Finally, the ϵ_f curve for $0 \leq T < 1/3$ is supplemented to that for $T > 1/3$. There is a singularity at $T = 1/3$ except for a random distribution of voids [88].

1.6.4 Activities under Objective 4

The underlying assumptions employed in the models create limitations in their predictive capabilities. With some of the more influential assumptions relaxed, various extensions can emerge from the same guiding principles. Among all, the following extensions are developed within the confines of the present thesis:

- In conformity with the results of void distortion in a shear field [16], the sheared microstructure can be better represented by introducing a unit cell with non-circular bases. A counterpart of the model accounting for void coalescence under combined tension and shear is thus introduced based on 3D voids. The corresponding microstructure would be represented by cylindrical voids embedded in cylindrical cells, both with elliptical cross sections. The analytical yield loci will be compared to their FEM counterparts emanating from quasi-periodic cell-model calculations with the same cell geometry for selective geometric configurations. The difference between analytical and numerical yield surfaces in some load or microstructure ranges will be suggestive of simple heuristic modifications to the parameters involved in the models.

- The model can further be extended being incorporated with matrix anisotropy (mainly of Hill's identity). Following the model introduced by the present author [15], a micromechanics-

based void coalescence yield function with this capability has been worked out in a recent work by Keralavarma and Chockalingam [96]. Along with the former void growth model presented by Keralavarma *et al.* [14], the present work implements the hybrid model composed of the above two models to investigate the effect of shear in combination with matrix anisotropy.

- In a continuum under arbitrary loading, voids may impinge their lateral or vertical adjacent voids. The failure mechanism in the former is known as *coalescence in layers* and the latter is named *coalescence in columns* or *necklace coalescence* [33]. An analytical criterion describing this mechanism will be developed in terms of the stress and microstructural states based on tentative velocity fields mimicing the plastic deformation concentrated in the plugs connecting voids on top of one another. With every specific microstructure, one of the two coalescence mechanisms has more propensity to occur, depending on which yield criterion is met first. Accordingly, the *effective* failure mechanism will be realized by the innermost yield surface among those emanating from the models accounting for void growth, void coalescence in columns, and void coalescence in layers. The model will be compared to previously predicted values from Gologanu [50] as well as to more exhaustive FEM counterparts from the present study. The present results will investigate the effects induced by all the independent microstructural parameters on the bounds to the yield sufrace.

1.7 Structure of the Thesis

This document is organized in 9 review chapters appended with 11 paper chapters and an additional appendix. The first four chapters introduce backgrounds and fundamental concepts, and the rest provide selective results which are thematically connected to paper chapters (prefixed with "P") elaborating on the summarized results. The additional appendix is provided illustrating a modified cutting-plane algorithm for stress state control in the simulations.

Chapter 1 a general introduction motivating the research carried out, the main goal reflected through objectives, the approach followed in the context of the state of the art, and the existing

challenges in the course of modeling ductile fracture under combined loading.

Chapter 2 reviews the most fundamental plasticity models that function in terms of invariants of the stress tensor and/or its deviator. Especially, the third invariant of the stress deviator J_3 and its effect on failure in shear will be given closer attention. Moreover, the Hill-type plasticity model accounting for matrix anisotropy will be introduced with its underlying assumptions and limitations.

Chapter 3 presents an outline of physics-based models of ductile fracture, that can be coupled with the hardening and microstructural effects or uncoupled from them. The majority of existing models are, however, coupled. The main body of homogeneous and inhomogeneous models and the essence of their different paradigms as well as applicability scopes will be presented therein.

In Chapter 4, the rudiments of the modeling methodology in the present work will be examined in brief. The steps to analytical modeling based on limit analysis, and some numerical strategies for FEM-based limit analysis at the cell level will be elucidated. With the lateral target velocities vanishing, the limit load would pertain to inhomogeneous yielding. It further examines the basic foundations of implementing a hybrid model with specific focus placed on the time integration of constitutive equations. Notions of residuals, Jacobians, the Newton-Raphson method, and the consistent tangent matrix will be overviewed.

Chapter 6 collectively reviews all the analytical models exploited for homogeneous yielding and derived for inhomogeneous yielding within the realm of the present work. Selective yield surfaces will be exhibited for various microstructural variables in comparison with their numerical counterparts. A recent inhomogeneous model accounting for a Hill-type matrix anisotropy [96] will further be introduced in the interest of being utilized as an alternative to that derived by the present author. Moreover, a multi-surface model invoking the effective yield mechanism from a combination of homogeneous and inhomogeneous yieldings will be presented at the limit of an isotropic material characterized by a random distribution of voids with equal void shapes. To this end, the effective yield surface will be showcased on principal and meridian planes. Moreover, fracture loci exhibiting strain to failure in terms of triaxiality will be shown at this limit. The chap-

ter finally introduces a unified model, in extension to that derived by Morin *et al.* [97], derived to incorporate both homogeneous and inhomogeneous processes under combined tension and shear. Example yield surfaces will be shown in the combined stress space with clear indication of smooth transition between homogeneous and inhomogeneous regimes.

Chapter 7 presents the results of micromechanical simulation of ductile fracture under triaxial and combined loadings emanating from the method outlined in Chapter 4 specified into the present constitutive framework. The whole deformation history will be analyzed under several loading and microstructural conditions. Selective state variables comprising equivalent plastic strain, void volume fraction, void aspect ratio and orientation, and relative void spacing will be presented. The effects induced by load combination, initial porosity, elementary cell size, void shape and aspect ratio will be assessed. Furthermore, the strain to failure will be evaluated in terms of stress triaxiality for a wide range of stress triaxialities ranging from zero to 1/3 and from 1/3 to 3. Finally, an example finite-element simulation will be presented to demonstrate the capability of the model for structural boundary-value problems. Alternatively, similar effects coupled with matrix anisotropy with reference to a hybrid model consisting of the models proposed in Ref's [14] and [96] will be investigated.

Chapter 8 extends the realm of the models introduced in Chapter 5 in certain respects. It partly proposes a counterpart of the void coalescence criterion introduced in Chapter 5 for 3D voids, that is founded on limit analysis over a cylindrical cell with an elliptical base containing a void with similar geometry. It further introduces an analytical criterion describing void coalescence in columns based on tentative velocity fields mimicing plastic deformation concentrated in the plugs connecting voids along the vertical direction. For fixed microstructural states, the *effective* failure mechanism will be predicted with reference to the innermost yield surface among those representing void growth, void coalescence in columns, and void coalescence in layers for the same microstructure.

Finally, in Chapter 9, some concluding remarks will be encapsulated, and potential extensions will be projected for consideration in future work.

CHAPTER 2 PLASTIC FLOW THEORIES

The present chapter lists some fundamental concepts constituting the plasticity theory plus some of the most featured yield criteria that can reasonably be employed in deriving effective plasticity models at larger scales. Chapter 3 introduces other yield criteria accounting for plasticity in ductile porous materials.

A typical constitutive framework of plastic deformation consists of four classes of equations: (i) a *yield criterion* by which yielding is evaluated based on the current stress state; (ii) a *flow rule* that describes the increment of plastic strain when yielding occurs or proceeds; (iii) a *strain-hardening* rule to express the material strength in terms of its conjugate plastic strain; (iv) evolution equations of additional state variables upon which the yield criterion may depend. The latter can be scalars, vectors or tensors (as in the case of some kinematic hardening models; see [98] for instance).

2.1 Small Deformation Theory

Plastic flow theories in the small-strain framework are developed on the basis of the following underlying principles:

1. **Elasticity**: The stress and elastic strain tensors in the elastic regime are linearly related by

$$\boldsymbol{\sigma} = \mathbb{L} : \boldsymbol{\epsilon} \tag{2.1}$$

where $\mathbb{L}$ is the elasticity tensor that, assuming the material is isotropic, can be expressed as

$$\mathbb{L} = 2\mu\mathbb{J} + K\boldsymbol{I} \otimes \boldsymbol{I} \tag{2.2}$$

where $\otimes$ denotes the dyadic product which, within a Cartesian coordinate representation, $[\boldsymbol{I} \otimes \boldsymbol{I}]_{ijkl} = \delta_{ij}\delta_{kl}$. Moreover, $K = E/3(1-2\nu)$ is the bulk modulus and $\mu = E/2(1+\nu)$ is the shear modulus, $\boldsymbol{I}$ is the second-order identity tensor, and $\mathbb{J}$ is the fourth-order tensor

transforming a stress tensor into its deviator through a double contraction, *i.e.* $\mathbb{J} : \boldsymbol{\sigma} = \boldsymbol{\sigma}'$, that can be written equivalently as

$$\mathbb{J} \equiv \mathbb{I} - \frac{1}{3}\boldsymbol{I} \otimes \boldsymbol{I} \tag{2.3}$$

where $\mathbb{I}$ is the fourth-order identity tensor transforming any second-order tensor into itself through a double contraction, *i.e.* $\mathbb{I} : \boldsymbol{S} = \boldsymbol{S}$, with $\boldsymbol{S}$ representing any second-order tensor.

2. **Plasticity**: Beyond the elastic limit, the stress components are related through a yield function:

$$\Phi(\boldsymbol{\sigma}; \boldsymbol{\alpha}) = 0 \tag{2.4}$$

with $\boldsymbol{\alpha}$ representing a collection of state variables affecting Φ which, for a hardening material, normally includes but is not limited to the equivalent plastic strain $\bar{\epsilon}$. For an elastic-perfectly plastic isotropic material, (2.4) would simplify into $\Phi(\boldsymbol{\sigma}) = 0$.

3. **Stability**: The stability postulate, addressed first by Drucker [99], entails, for every increment in $\boldsymbol{\sigma}$ and $\boldsymbol{\epsilon}$:

$$d\boldsymbol{\sigma} : d\boldsymbol{\epsilon} \geq 0 \tag{2.5}$$

which is equivalent to Hill's principle of maximum plastic work [100]. In a general thermomechanical framework, both statements follow from the second law of thermodynamics [101].

4. **Loading/Unloading**: The loading and unloading condition is known as the *Kuhn-Tucker* condition [102]. It asserts that, for any admissible stress state $\boldsymbol{\sigma}$, the plastic strain increment (or the plastic rate of deformation accordingly) can be uniquely described as

$$d\boldsymbol{\epsilon}^{\mathrm{p}} = \gamma \mathrm{sgn}(\boldsymbol{\sigma}) \tag{2.6}$$

provided γ and $\boldsymbol{\sigma}$ are constrained by the following *unilateral constraints*:

(a) Admissibility of $\boldsymbol{\sigma}$:

$$\gamma \geq 0 \quad , \quad \Phi(\boldsymbol{\sigma}; \bar{\epsilon}) \leq 0 \tag{2.7}$$

(b) $\gamma = 0$ if $\Phi < 0$, and $\gamma > 0$ only if $\Phi = 0$.

Altogether:

$$\gamma \geq 0 \quad , \quad \Phi(\boldsymbol{\sigma}; \bar{\epsilon}) \leq 0 \quad , \quad \gamma\Phi(\boldsymbol{\sigma}; \bar{\epsilon}) = 0 \tag{2.8}$$

5. **Normality**: Subsequent to Drucker's postulate or Hill's principle of maximum plastic work [100], the plastic part of the strain increment and the normal to the yield surface are co-directional when the effective yield surface $\Phi = 0$ is *smooth*. That is

$$d\boldsymbol{\epsilon}^{\mathrm{p}} = d\Lambda \frac{\partial \Phi}{\partial \boldsymbol{\sigma}} \tag{2.9}$$

where $d\Lambda$ denotes a plastic multiplier. Equation (2.9) is also known as the *associated* flow rule [1]. In case the surface is not smooth, the normal belongs to a hypercone of normals to the yield surface. Koiter [103] proposed the following generalized flow rule:

$$d\boldsymbol{\epsilon}^{\mathrm{p}} = d\Lambda_i \frac{\partial \phi_i}{\partial \boldsymbol{\sigma}} \tag{2.10}$$

with a summation implied on i, where $d\Lambda_i$ are nonnegative and ϕ_i are linearly independent flow potentials.

6. **Additivity**: The total strain increment can be decomposed into elastic and plastic parts:

$$d\boldsymbol{\epsilon} = d\boldsymbol{\epsilon}^{\mathrm{e}} + d\boldsymbol{\epsilon}^{\mathrm{p}} \tag{2.11}$$

where the elastic part stems from elasticity (2.1) such that

$$d\boldsymbol{\epsilon}^{\mathrm{e}} = \mathbb{L}^{-1} : d\boldsymbol{\sigma} \tag{2.12}$$

[1] In the case of a non-associated flow rule, a *flow potential* ϕ enters into (2.9), which is non-identical to the yield function, *i.e.* $\phi \neq \Phi$.

with $\mathbb{L}^{-1}$ denotes the formal inverse of the elasticity tensor, which obeys

$$\mathbb{L}^{-1} = \frac{1}{2\mu}\mathbb{J} + \frac{1}{9K}\boldsymbol{I} \otimes \boldsymbol{I} \tag{2.13}$$

and the plastic part is determined from the flow rule (2.9). Equation (2.13) follows the trace of both sides within $\boldsymbol{\sigma} = \mathbb{L} : \boldsymbol{\epsilon}$, with $\mathbb{L}$ obeying (2.2), and $\mathbb{J}$ has been defined in advance.

7. **Consistency**: The Prager consistency condition [104], is required to close the set of constitutive equations, especially to eliminate the unknown parameter $d\Lambda$ from the system of equations. This condition reads

$$d\phi = \frac{\partial \Phi}{\partial \boldsymbol{\sigma}} : d\boldsymbol{\sigma} + \frac{\partial \Phi}{\partial \boldsymbol{\alpha}} : d\boldsymbol{\alpha} = 0 \tag{2.14}$$

with $\boldsymbol{\alpha}$ defined below (2.4). The consistency condition implies that any strain increment during plastic loading occurs tangential to the yield surface, *i.e.* the subsequent stress state must remain on the subsequent yield surface. Namely, plastic loading over a plastic deformation should result in another plastic deformation.

2.2 Finite Deformation Theory

Within the finite deformation theory, it is typically assumed that the rate of deformation tensor $\boldsymbol{D}$ can be additively decomposed into an elastic and a plastic part. That is

$$\boldsymbol{D} = \boldsymbol{D}^{\mathrm{e}} + \boldsymbol{D}^{\mathrm{p}} \tag{2.15}$$

where the elastic part is given by:

$$\boldsymbol{D}^{\mathrm{e}} = \mathbb{L}^{-1} :\overset{\nabla}{\boldsymbol{\sigma}} \tag{2.16}$$

Further, the loading response of a continuum must be frame-indifferent (objective), *viz.* independent of the observer. Depending on the class of problem, several objective stress rates have been identified [105]. Within the context of ductile fracture models, the Jaumann objective stress

rate $\overset{\triangledown}{\boldsymbol{\sigma}}$ is frequently used. Upon definition:

$$\overset{\triangledown}{\boldsymbol{\sigma}} = \dot{\boldsymbol{\sigma}} + \boldsymbol{\sigma}\boldsymbol{\Omega} - \boldsymbol{\Omega}\boldsymbol{\sigma} \tag{2.17}$$

where $\boldsymbol{\Omega}$ is the skew symmetric part of the velocity gradient.

All the same, it is typically assumed that the plastic strain increment and the normal to the yield surface are co-directional. Accordingly, the plastic part of $\boldsymbol{D}$ originates from the normality condition via the following rule:

$$\boldsymbol{D}^{\mathrm{p}} = \dot{\Lambda}\frac{\partial \Phi}{\partial \boldsymbol{\sigma}} \tag{2.18}$$

where $\dot{\Lambda}$ is a rate-form plastic multiplier associated with the plastic strain tensor, and Φ is termed *flow potential*, taken equal to the yield function at the prevailing case of an *associated flow rule*.

The hybrid model presented in Chapter 6 will be formulated in a corotational framework. That is, the constitutive relations are expressed in a local coordinate tied to the current material configuration, which is rotated from the initial configuration by the rotation tensor $\boldsymbol{R}$ that results from the polar decomposition of the deformation gradient $\boldsymbol{F}$ as

$$\boldsymbol{F} = \boldsymbol{R}\boldsymbol{U} \tag{2.19}$$

where $\boldsymbol{U}$ is a positive-definite symmetric tensor. Correspondingly, constitutive laws need be written in the rotated configuration. The so-derived equations relate merely with the stretch part of deformations, and the rotation part is admitted by rotating quantities to the intermediate configuration. The objective rate of stress $\overset{\triangledown}{\boldsymbol{\sigma}}$ in (2.17) will be then replaced with its time derivative $\dot{\boldsymbol{\sigma}}$ so that the constitutive relation in rate form appears similar to their small-deformation counterparts in the corotational frame.

2.3 Isotropic Models

Every isotropic yield function can be expressed in terms of at least one of the three principal invariants of the stress tensor or, eventually, its deviator. Among all, the invariants typically utilized

in the plasticity theory are the first principal invariant (I_1) of $\boldsymbol{\sigma}$, and the second and third principal invariants of $\boldsymbol{\sigma}'$ (J_2, J_3), defined as [101]:

$$\begin{aligned} I_1 &= \text{tr}\boldsymbol{\sigma} = \sigma_1 + \sigma_2 + \sigma_3 \\ J_2 &= \frac{1}{2}\boldsymbol{\sigma}' : \boldsymbol{\sigma}' = \frac{1}{6}\left[(\sigma_1 - \sigma_2)^2 + (\sigma_2 - \sigma_3)^2 + (\sigma_1 - \sigma_3)^2\right] \\ J_3 &= \det \boldsymbol{\sigma}' = \sigma_1' \sigma_2' \sigma_3' \end{aligned} \tag{2.20}$$

with σ_i and σ_i' denoting the principal values of $\boldsymbol{\sigma}$ and $\boldsymbol{\sigma}'$, respectively. Another relevant set of widely used invariants is (ξ, ρ, θ) which represent a cylindrical coordinate system termed the *Haigh-Westergaard* coordinates. Upon definition:

$$\begin{aligned} \xi &= \frac{1}{\sqrt{3}} I_1 \equiv \sqrt{3} p \\ \rho &= \sqrt{2J_2} \equiv \sqrt{\frac{2}{3}} q \\ \cos 3\theta &= \left(\frac{r}{q}\right)^3 \equiv \frac{3\sqrt{3}}{2} \frac{J_3}{J_2^{3/2}} \end{aligned} \tag{2.21}$$

where $r = 3(\frac{1}{2}J_3)^{1/3}$. The ξ–ρ plane is called the *Rendulic* plane, and θ is called the Lode angle [101]. The above-defined coordinates will be used in Chapter 5 and its corresponding paper, Paper P4 .

2.3.1 Pressure-independent models

An isotropic yield flow theory is generally dependent upon all the three principal stress invariants. For a wide variety of ductile materials, however, the effect of I_1 can be neglected. Amongst the most widely-used models in this category is the J_2 flow theory [101], which expresses the yield condition to be met on the condition of J_2 equaling the material yield stress in pure shear. That is

$$J_2 = \bar{\tau}^2 \tag{2.22}$$

where $\bar{\tau} = \bar{\sigma}/\sqrt{3}$ is the material shear strength, and $\bar{\sigma}$ is the uniaxial yield strength.

In porous plasticity at the cell-level, the plastic deformation for the whole reference volume element (RVE), here denoted with Ω, is generally pressure-dependent due to the presence of voids. The ductile matrix, however, with the void excluded ($\Omega \setminus \omega$, with ω representing the void and its volume), is mostly assumed to obey the von Mises theory with an associative flow rule. Hence, yielding occurs upon with the following condition being met:

(2.23)with the associative flow rule reflected by

$$\begin{aligned} \boldsymbol{d} &= \frac{3}{2}\frac{d_{\mathrm{eq}}}{\bar{\sigma}}\,\boldsymbol{\sigma}' \\ d_{\mathrm{eq}} &\equiv \sqrt{\frac{2}{3}\boldsymbol{d} : \boldsymbol{d}} \end{aligned} \tag{2.24}$$

where σ_{eq} and d_{eq} denote the von Mises equivalent stress and equivalent strain rate, respectively. Criterion (2.3.1) is characteristic of the boundary to the microscopic reversibility domain $\mathcal{C}$, the macroscopic counterpart of which ($\mathcal{C}$) constitutes the effective yield criterion for a porous ductile material [45].

2.3.2 Pressure-dependent models

Pressure independence, though proving efficacious in a wide range of conditions, cannot capture the salient features of plastic deformation in so many materials including porous and granular materials (rocks, soil, *etc.*). Depending on the sensitivity and correlation of the plastic deformation with I_1, several models have been advanced in the literature. From a broad perspective, the dependence of a yield criterion upon pressure can be of two types:

- Some models are *parametrized* based on pressure. That is, the parameters subject to change from material to material are functions of I_1. Examples include, but not limited to, Mohr-Coulomb [106] (see Sec. 2.3.3 for the expression) and Drucker-Prager [107] models mainly for granular materials, the Burzyński-Yagn [108, 109] model for materials with tension-

compression and/or tension-torsion asymmetry, Bresler-Pister [110] and Willam-Warnke [111] models for quasi-brittle and frictional materials as well as concrete, Bigoni-Piccolroaz [112, 113] and Altenbach-Bolchoun-Kolupaev [114] models for quasi-brittle, frictional, and ductile materials, respectively.

The Mohr-Coulomb model, for instance, predicts yielding not based merely on maximum normal or shear stress, rather through a maximized linear combination of normal and shear tractions on the plane that generates this maximum [106]. In another sense, The Mohr-Coulomb criterion represents the linear envelope of the material shear strength vs. the applied normal stress, that reads

$$\tau_{\mathrm{n}} - \sigma_{\mathrm{n}} \tan\phi = c \tag{2.25}$$

where σ_{n} and τ_{n} represent the normal and shear tractions on the plane of maximization, respectively, and c and ϕ are material-specific parameters termed *cohesion* and *internal friction* angle, respectively.

As another instance, the Drucker-Prager model can be expressed, in its basic form, as [107]:

$$\sqrt{J_2} = A + BI_1 \tag{2.26}$$

where constants A and B are determined from experiment.

- Some other models are directly *derived* in correlation with pressure. Likewise, several models exist in this subcategory. Yet two most popular ones are the Gurson [115] and Rousselier [116] models. The algebraic statement of the former can be found in Chapter 3.

2.3.3 J_3 Dependent Models

Apart from being partly representative of macroscopic shearing effects at low-triaxiality stress regimes [36,71,84,85], J_3 is known to influence the hardening effect [117,118]. Yet, a conspicuous explanation on the microscopic effect of J_3 on ductile fracture is still lacking. The effect induced by J_3 is extensively referred to as the *Lode* effect by virtue of the correlation of the Lode parameter.

It was originally introduced by Lode [119], to differentiate between the Tresca and von-Mises yield criteria. Accordingly, the Lode parameter and the corresponding Lode angle can be written as

$$L = -\cos 3\theta \equiv -\frac{27}{2}\det\left(\frac{\boldsymbol{\sigma}'}{\sigma_{\mathrm{eq}}}\right) \tag{2.27}$$

with σ_{eq} denoting the Mises equivalent stress. In an axisymmetric stress state superposed by an axial stress, $L = -1$ in case the major load is the axial, and $L = -1$ if the converse is the case. Indubitably, $L = 0$ at simple shear or pure shear, the latter being equivalent to a biaxial stress state with equal and opposite stresses.

Mohr-Coulomb [106] and Drucker-Prager [107] models, as clear instances, take into account the effect of J_3 in addition to I_1. In a non-associative yielding, the yield function and flow potential in the Mohr-Coulomb model are expressed in terms of the above quantities as [120]:

$$\begin{aligned}\Phi &= I_1 \sin\varphi + \frac{1}{2}\left[3(1-\sin\varphi)\sin\theta + \sqrt{3}(3+\sin\varphi)\cos\theta\right]\sqrt{J_2} - 3c\cos\varphi \\ \phi &= I_1 \sin\psi + \frac{1}{2}\left[3(1-\sin\psi)\sin\theta + \sqrt{3}(3+\sin\psi)\cos\theta\right]\sqrt{J_2} - 3c\cos\psi\end{aligned} \tag{2.28}$$

where φ is the internal friction angle, ψ is the dilation angle, c is the material cohesion, and θ is the Lode angle. In a recent endeavor, Bai and Wierzbicki [121] revisited the Mohr-Coulomb fracture criterion with an objective of *ductile* fracture description in isotropic solids under proportional loading paths.

Alternative to the Drucker-Prager model, Drucker [122] proposed a yield function, suitable to ductile materials, that is directly expressed in terms of J_2 and J_3, by virtue of which the yield surface lies between the von Mises and Tresca yield surfaces:

$$J_2^3 - \alpha J_3^2 = k^2 \tag{2.29}$$

where α is a constant lying between -27/8 and 9/4 for the fulfillment of yield surface convexity, and k is a material constant. Brunig *et al.* [117] proposed the following more general based on

numerical analyses:

$$\sqrt{J_2} - c\left(1 - \alpha I_1 - \beta J_3^{1/3}\right) = 0 \tag{2.30}$$

where α and β are material constants and coefficient c is obtained from the strain state. All the same, Hu and Wang [123] proposed a stress state-based yield criterion for isotropic ductile materials:

$$\alpha I_1 + \sqrt{J_2} + \beta \frac{J_3}{J_2^{3/2}} = c \tag{2.31}$$

where α, β, and c are material constants determined from experiment.

Several extended models have been developed to better predict the correlations among the three stress invariants. For isotropic ductile materials, models such as that of Altenbach-Bolchoun-Kolupaev [114], extended Drucker-Prager model expanded by Subramanya *et al.* [124], the model introduced by Kuroda [125], and Yang *et al.*'s Mises-like yield criterion [126] have been reported in the literature to account for Lode dependence.

2.4 Anisotropic Models

There are several limitations attributive of isotropic plasticity that warrant the advancement of anisotropic models. Due to microstructural effects induced by atomic arrangements, grain morphology and/or texture, wrought engineering materials are often plastically anisotropic even when elastically isotropic. Moreover, large plastic strains, as opposed to infinitesimal deformation, lead to texture development, which itself is a matter of anisotropy. Besides, the formation of intragranular cavities may generate an anisotropic crystalline matrix. The simplest anisotropic plasticity model was developed by Hill [101] in the form of a phenomenological quadratic form expressed as follows:

$$F(\sigma_{11} - \sigma_{22})^2 + G(\sigma_{22} - \sigma_{33})^2 + H(\sigma_{11} - \sigma_{33})^2 + 2(L\sigma_{12}^2 + M\sigma_{23}^2 + N\sigma_{13}^2) = 1 \tag{2.32}$$

where Here F, ..., N are constants to be determined experimentally. Hill's criterion follows simplistic underlying premises. It assumes orthotropy (planar isotropy), tension-compression symme-

try, and pressure independence.

After three decades from this model, Hill proposed the following more general criterion for textured aggregates [127]:

$$H_1|\sigma_1-\sigma_2|^m+H_2|\sigma_2-\sigma_3|^m+H_3|\sigma_1-\sigma_3|^m+K_1|2\sigma_1-(\sigma_2+\sigma_3)|^m+K_2|2\sigma_2-(\sigma_1+\sigma_3)|^m+K_3|2\sigma_3-(\sigma_1+\sigma_2)|^m=\bar{\sigma}^2 \tag{2.33}$$

where Here H_i and K_i are constants to be determined experimentally, and $\bar{\sigma}$ is the material yield strength along one benchmark direction. For plane problems, the value of m is suggested to be taken 6 or 8 for anisotropic metals. Other more general criteria analogous to (2.33) have been proposed in the literature. One widely used counterpart is the Logan-Hosford model [128] expressed as

$$F_1|\sigma_1-\sigma_2|^n+F_2|\sigma_2-\sigma_3|^n+F_3|\sigma_1-\sigma_2|^n=1 \tag{2.34}$$

where F_i are experimentally-determined values, and the exponent n depends on the crystallographic structure. It is mostly considered to be 6 for BCC and 8 for FCC materials. For isotropic materials, this criterion simplifies into the following form, after Hosford [129]:

$$|\sigma_1-\sigma_2|^n+|\sigma_2-\sigma_3|^n+|\sigma_1-\sigma_2|^n=2\bar{\sigma}^2 \tag{2.35}$$

Barlat *et al.* [130] and Karafillis and Boyce [131] proposed a procedure to incorporate anisotropy in pressure-independent models by the application of a fourth order linear transformation operator on the stress or its deviator, *e.g.* $\tilde{\boldsymbol{\sigma}}=\mathbb{Q}:\boldsymbol{\sigma}$ or $\tilde{\boldsymbol{\sigma}}'=\mathbb{Q}:\boldsymbol{\sigma}'$. The corresponding yield function is then obtained from an isotropic function by substituting the principal stress (or stress deviator) values by the principal value for $\tilde{\boldsymbol{\sigma}}$ (or $\tilde{\boldsymbol{\sigma}}'$). Other anisotropic models have also been developed in extension to established models with isotropic basic forms. Among the featured ones are the Caddell-Raghava-Atkins (CRA) model [132] accounting for pressure dependence, the Deshpande-Fleck-Ashby (DFA) model [42] mainly developed for honeycomb structures, and Soare *et al.*'s model [133], mainly employed for sheet metal forming simulations, *etc*.

CHAPTER 3 DUCTILE FRACTURE MODELS

Ductile fracture models are developed to mimic the physical phenomena that trigger fracture, and hence, should be able to capture the salient features of failure mechanisms. The major observed failure mechanisms, subsequent to nucleation of voids by decohesion of the particle-matrix interface or by particle cracking, are void growth and void coalescence, which is ensued by ultimate failure. The credibility of the simulated mechanisms lies in typical fracture surfaces, as those shown in Fig. 1.8.

The present chapter presents an overview of the most prevailing ductile fracture models based on dilatant plasticity reported in the literature to date. It is, however, important to note that these models are mainly developed as means of constitutive modeling rather than fracture modeling per se. Meanwhile, studies such as [134–138] have considered developing or utilizing methods in the simulation of crack growth in solids.

3.1 Homogeneous vs. Inhomogeneous Yielding

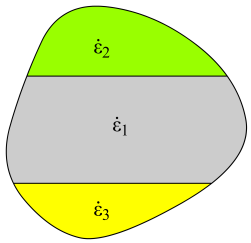

Figure 3.1: Schematic outline of a reference volume element (RVE) with arbitrary geometry undergoing inhomogeneous yielding.

The distinction between homogeneous and inhomogeneous yielding pertains to plastic deformation in the unit cell. If a unit cell of arbitrary geometry, as shown in Fig. 3.1, deforms uniformly over its boundary, the plastic deformation is named "homogeneous", otherwise termed "inhomogeneous". In the exemplified RVE of Fig. 3.1, yielding is considered homogeneous in the case of $\dot{\epsilon}^{(1)} = \dot{\epsilon}^{(2)} = \dot{\epsilon}^{(3)}$, and is inhomogeneous if $\dot{\epsilon}^{(2)} \neq \dot{\epsilon}^{(1)}$ and $\dot{\epsilon}^{(3)} \neq \dot{\epsilon}^{(3)}$.

In particular, $\dot{\epsilon}^{(1)} \neq 0$ and $\dot{\epsilon}^{(2)} = \dot{\epsilon}^{(3)} = 0$ is a special case of inhomogeneous yielding that arises from elastic unloading in regions (2) and (3).

In a solid material, strain rates can localize inside a band with vanishing thickness, the orientation of which can be evaluated from Rice's theory of plastic localization [61]. This must, however, be clearly dissociated from the presently identified concept, with the distinction being of utmost importance in porous materials particularly because voids, when explicitly represented, can act as initial inhomogeneity. In the latter, the plastic strain after elastic unloading becomes localized inside an inner-void ligament with *finite* rather than zero thickness, with the band thickness determined by the void size.

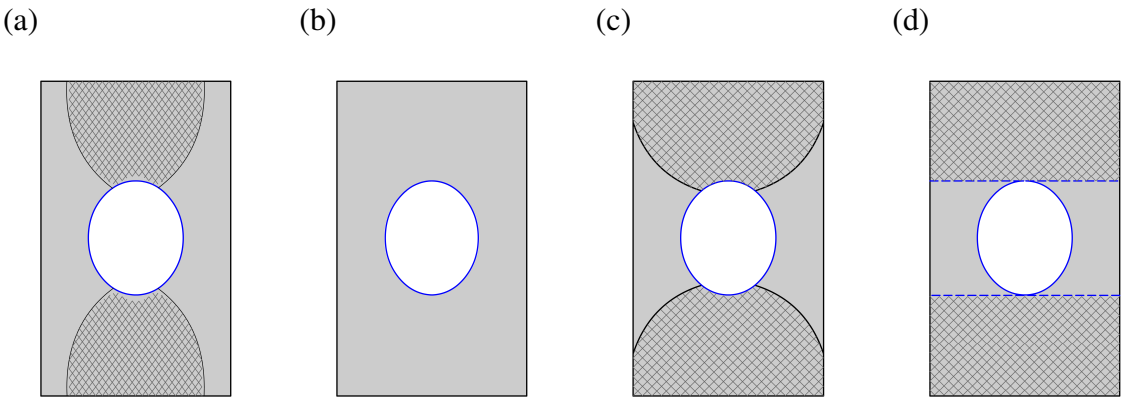

Figure 3.2: Schematic space distribution of plastic deformation at the cell level, with the cross-hatched regions representing elastic unloading: (a) homogeneous yielding, (b) idealized homogeneous yielding, (c) inhomogeneous yielding, (d) idealized inhomogeneous yielding.

Homogeneous yielding is often known to be associated with void growth. Also, among the featured inhomogeneous yielding processes is void coalescence. Nevertheless, the present-invoked terminology is more inclusive than the given examples. Consequent to tension superposed with shear, for instance, voids may grow or shrink down to *void closure* while plastic deformation is homogeneous at the cell level (depending on the ratio between normal and shear stresses). By the same token, yielding is inhomogeneous (almost) from the outset under intense shearing in that plasticity is majorly confined to a close vicinity of the void. Yet, void coalescence and failure might never be realized when the void volume fraction approaches zero. The terms "homogeneous" and

"inhomogeneous" will be thus used throughout the thesis.

A parametric representation of homogeneous or inhomogeneous yielding at the macro scale entails the notion of a reference volume element (RVE), with the equivalent plastic deformation rate homogenized over its whole volume or a subvolume consisting of the intervoid ligament. Both are schematized in Fig. 3.2 (the hatched zones represent elastic unloading). Elastic unloading can be triggered both at early stages, as indicated by Fig. 3.2a, and after significant plastic deformation, as shown in Fig. 3.2c. Nevertheless, mathematical representation of yielding at the macro scale often calls for simplifying assumptions. Therefore, stages such as Fig. 3.2a may be idealized with homogeneous yielding exhibited in Fig. 3.2b so long as considerable lateral plastic deformation is developed above and below the void. Subsequent to further deformation, when elastic unloading spreads further around the void, continued lateral deformation is precluded from part of the zones above and below the void (Fig. 3.2c). Within the realm of the present work, the latter inhomogeneity is taken to be ideally confined to a planar ligament that is intercepted by the void poles, as shown in Fig. 3.2d. The same approach was adopted in numerous previous references [45, 97, 139, 140]. In a recent endeavor, Morin *et al.* [141] investigated the effects on the limit load induced by more general velocity fields, *e.g.* admitting non-planar interfaces (as shown in Fig. 3.2c) or satisfy higher degrees of continuity between the plastically deformable and elastically unloaded (rigid-like) zones.

Mathematically, in case the velocity inside the RVE admits uniform strain-rate boundary conditions, the deformation process can be regarded as homogeneous. In this case, the remotely-applied macroscopic rate of deformation $\boldsymbol{D}$ correlates with the internal velocity field through the position vector:

$$\forall\, \boldsymbol{x} \in \partial\Omega \quad \boldsymbol{v} = \boldsymbol{D}\boldsymbol{x} \tag{3.1}$$

where Ω and $\partial\Omega$ represent the cell domain and boundary, respectively, and $\boldsymbol{x}$ denotes the current position. Equivalently, on account of a constant deformation gradient tensor $\boldsymbol{F}$, one can express (3.1) as

$$\forall\, \boldsymbol{x} \in \partial\Omega \quad \boldsymbol{x} = \boldsymbol{F}\boldsymbol{X} \tag{3.2}$$

where $\boldsymbol{X}$ denotes the initial position.

For inhomogeneous yielding, however, such boundary conditions don't exist (except eventually at the plastically-deformable sub-cell level). The reader is referred to Chapter 4 for more details regarding how to derive plasticity models from tentative velocity fields.

3.2 Void Growth Models

Homogeneous yielding has been described via *void growth* models in the literature. Earlier micromechanical treatment of homogeneous yielding was founded on mere consideration of isolated voids. Of the notable models of this caliber are those proposed by McClintock [76], and Rice and Tracey [77]. Later models were developed based on homogenization over a reference volume element (RVE) in a periodic medium of voids. Gurson's model for spherical and cylindrical voids is among the most extensively known. This model sets a yield criterion for a porous material at the macro scale, and correlates with an evolution law for a single microstructural variable, the void volume fraction f. It assumes a plastically isotropic matrix.

Within the deformation process, however, anisotropies associated with matrix deformation and void shape would emerge. Several extensions of the Gurson model have been developed over the past decades to account for these anisotropies. For homogeneous yielding, Gurson's model and its extensions have set the caliber for decades. The Gurson–Tvergaard–Needleman (GTN) model, for instance, follows Tvergaard's and Needleman's modifications to Gurson's model to encompass the effects due to void interaction and void nucleation [75, 142, 143]. In passing, the Gologanu–Leblond–Devaux (GLD) model [89] extended Gurson for non-spherical voids. This line of models was further extended into incorporation of plastic anisotropy in [14, 95]. Alongside, other micromechanics–based models, mostly in parametric rather than closed form, have been developed for homogeneous yielding driven by shear. This mechanism was investigated in the pioneering work of Fleck and Hutchinson [68] while failure under the same effect was missing in work of the like.

A considerable fraction of work on shear-dominated ductile failure prediction in porous materials addresses supplementing existing Gurson-type yield criteria with damage models. Nahshon

and Hutchinson [71], for instance, proposed a modified damage parameter (denoting porosity in absence of shear) through the addition of a heuristic function of J_3. This damage parameter, while remaining of a heuristic nature, could not preserve the identity of a physical parameter such as porosity. Morgeneyer and Besson [144] introduced a modified strain rate as function of the Lode parameter based on a Gurson-type yield criterion in order to simulate the transition from flat to shear-induced crack propagation. Other efforts in the same respect have been made in [145, 146]. Another class of work, including [16, 17, 147], examine failure mechanisms via cell-model evolution analysis. This class of analyses can be considered as benchmark, but are not well suited for parametric studies due to high computational cost. Micromechanics–based models are thus more extensively sought. Some researchers have striven to introduce such models founded on cell-model calculations. Amongst the featured examples, proposed mainly for triaxial loading, is the model introduced by Thomason [148, 149], later advanced by Benzerga [150] and Tekoglu *et al.* [140], and that of Pardoen and Hutchinson [20], accounting for void growth and coalescence in a wider range of porosities and void shapes.

The following subsections briefly introduce the essence of foregoing models and their limitations.

3.2.1 Rice and Tracey

Rice and Tracey [77] characterized the flow field in an infinite medium made of an rigid–perfectly plastic incompressible non-hardening material containing an isolated spherical void, and subjected the material to remotely uniform tensile with superposed hydrostatic stresses. They adopted a Rayleigh–Ritz procedure to evaluate the enlargement rate of the void. To this end, they assumed a tentative velocity field composed of a remote strain rate, an expansion and a deviatoric isochoric (volume-preserving) field. For the specific case of a triaxial field, the assumed velocity field is of the following form, which consists of an incompressible expansion field superposed by a linear field associated with a uniform deformation rate:

$$\boldsymbol{v} = \boldsymbol{D}\boldsymbol{x} + DD_{\mathrm{eq}} \left(\frac{R_0}{R} \right)^3 \boldsymbol{x} \tag{3.3}$$

with $D_{\mathrm{eq}} = \sqrt{2/3\ \boldsymbol{D} : \boldsymbol{D}}$ denoting the remote equivalent strain rate, and $\boldsymbol{D}$ being the remote rate of deformation tensor. R_0 and R are the initial and current void radii, respectively, and $\boldsymbol{x}$ is the position vector. In both low and high triaxiality ranges, D is found to obey an exponential form. For sufficiently high triaxiality fields, for instance, D is written as

$$D = C \exp\left(\frac{3}{2}\frac{\Sigma_{\mathrm{m}}}{\bar{\sigma}}\right) \tag{3.4}$$

where Σ_{m} and $\bar{\sigma}$ are, respectively, the remote hydrostatic stress and material yield strength, and

$$C = \frac{1}{4}\exp\left\{\int_0^1 \left[A \ln \frac{A + \sqrt{A^2 - B^2}}{2} + A - \sqrt{A^2 - B^2}\right] d\zeta\right\}$$

where

$$A = 1 - \frac{\upsilon}{2}\frac{1 - 3\zeta^2}{\sqrt{3 + \upsilon^2}} \quad , \quad B = \frac{3}{2}\sqrt{\frac{1 - \zeta^2}{3 + \upsilon^2}}$$
$$\upsilon = -\frac{3D_{\mathrm{II}}}{D_{\mathrm{I}} - D_{\mathrm{III}}}$$

where $D_{\mathrm{I}} \geq D_{\mathrm{II}} \geq D_{\mathrm{III}}$ are the principal components of the remote strain rate field. Under axisymmetric tensile loading ($\upsilon = +1$), $C = 0.283$. Based on more accurate dilatation rates, Huang [151] suggested $C = 0.427$ for axisymmetric loading. For more general loading conditions, Rice and Tracey proposed the following heuristic extension:

$$D = 2\left[\alpha' \sinh\left(\frac{3}{2}\frac{\Sigma_{\mathrm{m}}}{\bar{\sigma}}\right) + \beta\upsilon \cosh\left(\frac{3}{2}\frac{\Sigma_{\mathrm{m}}}{\bar{\sigma}}\right)\right] \tag{3.5}$$

only for spherical voids and using Huang's $\alpha' = 0.427$.

Rice and Tracey's model ignores hardening and the interactions between voids. It also overestimates void growth rates in moderate-triaxiality regions. Aside from that, the model is differential, *i.e.* expressed based on remote strain rates rather than merely on stresses. Moreover, this model is not coupled with microstrucrural parameters.

3.2.2 McClintock and coworkers

Among the landmark differential criteria for predicting void growth rate are the models after McClintock *et al.* [152] for the growth and coalescence of voids under combined tension and shear for linearly viscous materials, and McClintock [76] regarding fracture by void growth under generalized plane-strain conditions for linearly viscous and plastically hardening materials with moderate hardening. In the former, the rate of variation in the mean void radius $R = (a + b)/2$ for an elliptical void with major and minor semi-axes a and b for a linearly viscous material was obtained as

$$\frac{\partial R}{\partial \gamma} = \frac{R}{2(1-N)} \sinh{(1-N)\kappa} \tag{3.6}$$

with γ denoting the shear strain, N being the hardening exponent, and $\kappa = \sigma/\tau$ the ratio between the macroscopic normal and shear stresses. In the latter, the current normalized mean radius in a linearly viscous and a plastic material were derived, respectively, as

$$\ln \frac{R}{R_0} = (\sigma_{\mathrm{aa}} + \sigma_{\mathrm{bb}}) \frac{t}{4\mu} \tag{3.7}$$

and

$$\ln \frac{R}{R_0} = \frac{\bar{\epsilon}\sqrt{3}}{2(1-N)} \sinh \left[\frac{\sqrt{3}}{2}(1-N) \frac{\sigma_{\mathrm{aa}} + \sigma_{\mathrm{bb}}}{\bar{\sigma}} + \frac{\epsilon_{\mathrm{aa}} + \epsilon_{\mathrm{bb}}}{2} \right] \tag{3.8}$$

where $(\sigma_{\mathrm{aa}}, \epsilon_{\mathrm{aa}})$ and $(\sigma_{\mathrm{bb}}, \epsilon_{\mathrm{bb}})$ are the normal stresses and their conjugate strains along the major and minor semi-axes, respectively, and $(\bar{\sigma}, \bar{\epsilon})$ are the material yield strength and its conjugate plastic strain. Moreover, μ denotes the viscosity coefficient, and t represents time (scaled in respect to the total time).

3.2.3 Gurson and Extensions

The Gurson model considers three underlying assumptions in the homogenization problem [33]:

(i) The RVE consists of a hollow sphere containing a concentric spherical void, and porosity f is the only effective microstructural variable.

(ii) Plastic flow within the matrix admits the J_2 flow theory with an associated flow rule.

(iii) The trial velocity field consists of an isochoric, isotropic expansion field superposed by a linear field that generates a uniform deformation rate. Having satisfied the boundary conditions, the velocity field can be expressed as

$$\boldsymbol{v} = \frac{b^3 D_{\mathrm{m}}}{r^2}\boldsymbol{e}_r + \boldsymbol{D}'\boldsymbol{x} \tag{3.9}$$

where b is the outer cell radius, $D_{\mathrm{m}} = \frac{1}{3}\mathrm{tr}(\boldsymbol{D})$, and $\boldsymbol{e}_r$ is the unit vector along the radius and directed outward. Accordingly, the microscopic yield criterion and flow rule read

$$\sigma_{\mathrm{eq}} \equiv \sqrt{\frac{3}{2}\boldsymbol{\sigma}' : \boldsymbol{\sigma}'} \leq \bar{\sigma} \quad , \quad \boldsymbol{d} = \frac{3}{2}\frac{d_{\mathrm{eq}}}{\bar{\sigma}}\boldsymbol{\sigma}' \quad , \quad d_{\mathrm{eq}} = \sqrt{\frac{2}{3}\boldsymbol{d} : \boldsymbol{d}} \tag{3.10}$$

where d_{eq} is the microscopic equivalent rate of deformation, and the rest of the notions have been defined in Paper 2. Details aside, the microscopic dissipation function $\pi(\boldsymbol{d}) = \bar{\sigma} d_{\mathrm{eq}}$ (only nonzero inside the matrix volume, and zero in the void) homogenized over the RVE, and subsequent elimination of D_{m} and D_{eq} leads to the following yield function:

$$\Phi = \left(\frac{\Sigma_{\mathrm{eq}}}{\bar{\sigma}}\right)^2 + 2q_1 f \cosh\left(\frac{3}{2}q_2\frac{\Sigma_{\mathrm{m}}}{\bar{\sigma}}\right) - [1 + (q_1 f)^2] \tag{3.11}$$

with $q_1 = q_2 = 1$. The porosity evolution equation corresponding to (3.11) may be written as

$$\frac{\dot{f}}{1-f} = D_{\mathrm{kk}} = \frac{\Phi_{,\Sigma_{\mathrm{m}}}}{\Phi_{,\Sigma_{\mathrm{eq}}}} D_{\mathrm{eq}} \tag{3.12}$$

which emanates basically from incompressibility within the matrix, where , is short-hand notation with a derivative with respect to the underscored variable.

Several heuristic modifications, mainly based on micromechanical cell model calculations, have been exerted onto Gurson's basic model in order that the model be capable of representing limited strain hardening and void interaction effects as well as predicting void nucleation and

coalescence. Tvergaard [143] introduced q_1 and q_2 factors in (3.11) to account for weak interactions among voids. From an analytical solution to a hollow sphere under hydrostatic loadeding, Perrin and Leblond [153] proposed $q_1 = 4/e \approx 1.47$ assuming $q_2 = 1$, close to the value of 1.5 proposed by Tvergaard [143]. Subsequent cell model studies have demonstrated that q_1 and q_2 factors are not all-embracing. In particular, they have been shown to depend heavily on geometry and stress state [46, 154].

As earlier stated in Chapter 1, a tentative understanding of the shear effect has been developed in the literature in terms of the effect of the third invariant of the stress deviator, J_3. Within the existing body of models, this effect is basically of a heuristic nature. A subset of models, as those in [71, 85], in particular, rely on a modification to the Gurson-Tvergaard-Needleman void growth model [75, 78] to account for the effects of shear by virtue of J_3. At the shear-dominated limit, the rate of deformation $\boldsymbol{D}$ is associated with a vanishingly small trace, so that the main damage parameter being the porosity does not evolve. Nahshon and Hutchinson [71], therefore, added a heuristic term, as function of J_3, to the damage evolution equation such that the effect of shear could be incorporated via J_3. Yet, the real physical process behind this heurism remains elusive. Apart from being heuristic, these models tacitly assume that the Lode effect is rooted in the homogeneous deformation process. However, cell model calculations at the micro scale [155–157] have demonstrated that the effect of the Lode parameter on homogeneous yielding is not strong enough to explain the experimental observations. In fact, a complete illustration of void growth in shear cannot be feasible without a clear explanation of the anisotropies induced by intense void elongation and rotation under the effect of shear as well as by the localized plastic deformation realized during inhomogeneous yielding.

3.3 Void Coalescence Models

All models reported as *void coalescence* models describe inhomogeneous yielding processes even though the majority of existing models in this regard are not based on real inhomogeneous mechanisms. On the one hand, since homogeneous yielding is mainly driven by diffuse plastic flow in the matrix, the ductility and/or strain to failure predicted by homogeneous plasticity models

overestimates values measured from experiments. On the other hand, heuristic corrections with the aim of quantitative improvement in this respect would be phenomenological, added to the fact that the physical mechanism of flow localization that gives rise to failure remains elusive. Mechanism–based analytical models derived from first principles would be, therefore, desirable so that the material behavior is simulated with mere integration of a system of constitutive equations based on a robust establishment of the physical process.

Modeling of inhomogeneous yielding in the existing literature is still in early stages. This can be recognized from the majority of existing models pertaining to the growth regime, and considering the complexities and limitations arising when interpreting coalescence as a strain localization phenomenon [141]. Established homogenization methods relying on clear separation of scales will be rather idealistic [150]. Yet, the use of an elementary cell under periodic boundary conditions proves efficacious, and volumetric averaging would remain valid in all deformation processes [33].

A first class of porous plasticity models account for the inhomogeneous process via a critical microstructural parameter. Examples include a critical normalized lateral void size [13] and a critical void volume fraction (porosity) [75]. In the latter approach, the post-localized deformation process is simulated with a heuristic introduction of a porosity acceleration factor, without the physics underlying the process being known [75, 97]. In a second class of models, homogeneous and inhomogeneous yieldings are founded on intrinsic yield criteria. Mathematical models for both processes are carried out through limit analysis. In doing so, homogeneous and inhomogeneous plasticity models, distinguished as being diffuse and localized, respectively, are derived either separately and combined into the so-called hybrid approach or in unification. Each category is briefly introduced in the sequel.

3.3.1 Criticality models

Due to the complexities arising at the modeling of inhomogeneous yielding, earlier models predicted the onset of void impingement in terms of a critical internal state parameter. Depending on the parameter of interest, the corresponding model can be *uncoupled* or *coupled*. The former can be illustrated by void coalescence represented by the normalized lateral void radius $\left(R/R_0\right)_c$, named

void growth ratio. The critical void growth ratio is a constant at the limit of random void distribution, and proves a function of stress triaxiality when the microstructure is periodic or clustered. For an initial void relative spacing of 0.04, for instance, it varies between 4 and 25 as function of triaxiality [13]. In the latter, however, the yield criterion is coupled with the state variable passing through a critical value. In this respect, a critical void volume fraction f_c has been pervasively considered as a criterion for the onset of inhomogeneous yielding [75]. A recent study by Morin *et al.* [72] has introduced a critical combination as $(f+g)_c$, with g denoting a secondary porosity.

3.3.2 Failure in shear

One of the earliest models developed to predict failure under shear-dominated loading was that introduced by McClintock [152] for the void impingement instant in linearly viscous materials. Rather than being a yield function, this model is a micromechanical one that was expanded based on the ability of a distorted void to touch the distorted cell boundaries at the vicinity of the major or minor diagonals. In effect, this model is suggestive of a criticality perspective through an analytical acquisition of the critical state. Following Eq. (3.6) for a constant κ ratio, the condition for voids impinging along the longitudinal direction of the intervoid ligament reads

$$\ln \frac{L}{R_0} = \ln \left(\sqrt{1+\gamma^2} \frac{R}{R_0} \right) \tag{3.13}$$

where $2L$ is the intervoid distance along the shearing direction. All the same, the condition for voids impinging along the vertical direction of the intervoid ligament reads

$$\ln \frac{H}{R_0} = \ln \left(\frac{R}{R_0} \right) \tag{3.14}$$

with $2H$ being the intervoid distance along the direction normal to the plane of shearing. The main downside within the above relations is considering plastic deformation as diffuse while the de facto mechanism is localized around the ligament. Xue [158] introduced a modified heuristic damage parameter D for shear-dominated loadings rooted in the criterion proposed by McClintock *et al.*

in (3.13) as

$$D = K_{\mathrm{D}}(q_1 f + D_{\mathrm{sh}}) \tag{3.15}$$

where

$$K_{\mathrm{D}} = \begin{cases} 1 & \text{for } D \leq D_{\mathrm{c}} \\ \dfrac{1/q_1 - f_{\mathrm{c}}}{f_{\mathrm{f}} - f_{\mathrm{c}}} & \text{for } D > D_{\mathrm{c}} \end{cases} \tag{3.16}$$

and

$$D_{\mathrm{sh}} = \frac{\ln \sqrt{1+\gamma^2}}{\frac{L}{2R}} \tag{3.17}$$

which is further approximated in terms of porosity and $\bar{\epsilon}$ in [158]. In (3.15) and (3.16), q_1 is the Tvergaard parameter, f_{f} and f_{c} are, respectively, the porosity at the onset of inhomogeneous yielding and the critical porosity, and $D_{\mathrm{c}} = q_1 f_{\mathrm{c}}$. The modified damage parameter D thus replaces f in the G–T–N model.

3.3.3 Limit analysis–based models

Another subset of models, heuristic or analytical, relies on the attainment of some plastic limit load over an inter-void ligament within an elementary cell. Thomason [159] was the first to employ this principle to predict the onset of void impingement by internal necking. His first model was two-dimensional, and was later extended by consideration of a square-prismatic cell containing a coaxial square-prismatic void [149]. The sub-volumes above and below the void were considered as rigid, and the axial stress that would create plastic flow in the intervoid ligament was calculated numerically. Thomason used *discontinuous* but kinematically admissible velocity fields to obtain upper-bound estimates of the limit load. He did not provide an analytical solution to the problem. Instead, he obtained numerical solutions and proposed a heuristic formula estimating the limit load at localization as a function of geometric parameters. Subsequent improvements of his model have focused on deriving evolution equations of the microstructural variables [20, 150] with heuristic modifications to Thomason's formula. Nevertheless, none of the above models takes into account combined tension and shear loadings.

Following the work of Thomason, Benzerga [150] extended the applicability of Thomason's model into penny-shaped cracks characterized by void aspect ratios significantly below unity. After a decade-long juncture, work in this field received another headway with the featured micromechanical models proposed by Pardoen and Hutchinson [20] and Nahshon and Hutchinson [71]) for triaxial and shear-dominated loading conditions, respectively. The latter introduced a modified damage parameter (denoting porosity in absence of shear) through the addition of a heuristic function of J_3. This damage parameter, while remaining of a heuristic nature, could not preserve the identity of a physical parameter such as porosity. Meanwhile, Morgeneyer and Besson [144] introduced a modified strain rate as function of the Lode parameter based on a Gurson-type yield criterion in order to simulate the transition from flat to shear-induced crack propagation. In retrospect to the work of Thomason [149] and Benzerga [150], Tekoglu *et al.* [140] extended the realm of those models into combined tension and shear.

More recent studies tend to describe homogeneous and inhomogeneous yieldings under general loading conditions by combining the effects of various independent stress–based parameters in a unit cell. Tekoğlu [160] introduced an effective method to keep track of three independent parameters including the Lode parameter, stress triaxiality, and the normal-to-shear stress ratio. Alternatively, Liu *et al.* [161] developed, based on energy principles in a derivative format, a unified method to establish a consistent criterion accounting for tensile and shear-dominated types of void coalescence.

It remained for Benzerga and Leblond [45], the present author with coworkers, and Morin and coworkers [97, 141] to develop inhomogeneous plasticity models under combined tension and shear from *first principles*, with the cell-level plastic deformation considered localized within the intervoid ligament. Benzerga and Leblond [45] derived a fully analytical expression for the coalescence of voids under triaxial loading from limit analysis over a cylindrical cell embedding a coaxial cylindrical void. Incidentally, their solution revealed some inaccuracy in the fitting procedure proposed by Thomason [148]. More recently, Morin *et al*. [141] developed improved models by considering continuous and generalized discontinuous velocity fields. Their models provide,

in general, tighter upper bounds to the exact yield surface, albeit for different ranges of structural paramaters. The models in [45, 141] are valid under axisymmetric loadings.

Within the present work, the criterion in [45] will be revisited and extended into a state of combined triaxial and shear loading by adding a linear shear-induced velocity field. Thanks to the discontinuous velocity field invoked in [45], a piecewise quadratic yield function will be obtained. See further details in Chapter 5.

The main body of mathematical models of ductile fracture developed from first principles is representative of a periodic or quasi-periodic medium. The effect of void distribution can be dominant when scaling becomes a matter of prominence. A well-motivated discussion on the effect of void distribution can be found in [47, 48, 160, 162–166].

3.4 Evolution Equations of State Variables

The state of the art in ductile fracture modeling relies on a set of yield functions or flow potentials for porous materials. Without supplementing these functions with evolution equations for the state variables, they can be essentially used merely for predicting the onset of inhomogeneous yielding, which is occasionally considered sufficient to estimate strains to failure as a function of loading parameters [88, 167]. For ductile fracture simulations, however, yield functions must be supplemented with evolution laws for effective microstructural parameters. These evolution laws can be presented either as explicit functions of the current state or in time rate form. Evolution equations corresponding to homogeneous deformation have been developed to a remarkable extent in the past decades. In particular, the evolution of void aspect ratio and orientation associated with homogeneous deformation has been represented in mathematical rate form by Gologanu, Ponte Castañeda, and coworkers [91, 92, 94]. In a recent numerics–based study, Madou *et al.* [83] revisited the basic form of evolution equation for void shape and orientation in [91,92,94] utilizing elastic Eshelby tensors, and proposed modified equations that are calibrated in terms of porosity and stress triaxiality.

The current state of the art with regards to post-localized evolution equations is, however, not sophisticated to the expected level. The first endeavors on this task was undertaken by Benzerga

[86, 150] as well as Pardoen and Hutchinson [20]. The former derived evolution equations for the post-localized effective damage state variables reflected through the void relative spacing χ and void aspect ratio w on the basis of boundary conditions and matrix incompressibility. The latter, however, derived phenomenological equations for the post-localized evolution of porosity f and void aspect ratio w based on cell model calculations. Meanwhile, an evolving shape factor γ was introduced by Benzerga [150] along with w in the spirit of void shape changes in the post-localized regime. With a void shape taken to evolve from spheroidal at the onset of inhomogeneous yielding by internal necking to conical at complete failure, the shape factor would evolve from $\gamma = 1/2$ to $\gamma = 1$.

Under a combined effect of tensile and shear loadings, however, homogeneous yielding is coupled with the effects of void elongation and rotation. Hence, the existing equations are not consistent with the post-localized state evolution under the effect of shear. To the best of the author's knowledge, evolution equations of this capacity are still lacking in the literature. Chapter 6 in the present work introduces this set of equations.

3.5 Unified vs. Hybrid Models

Based on analytical limit analysis, homogeneous and inhomogeneous plasticity models can be derived either independently and combined in a hybrid approach or based on the same velocity fields in a unified fashion. There are pros and cons associated with the hybrid perspective, considering different cell-level geometries before and after the onset of inhomogeneous yielding. Among its notable virtues is better coincidence with numerical results in comparison to that in the unified model, esp. at low porosities and/or higher shear stresses. Nevertheless, the hybrid model exhibits corners in its corresponding yield surface, which constitutes some undesirable features from a computational viewpoint.

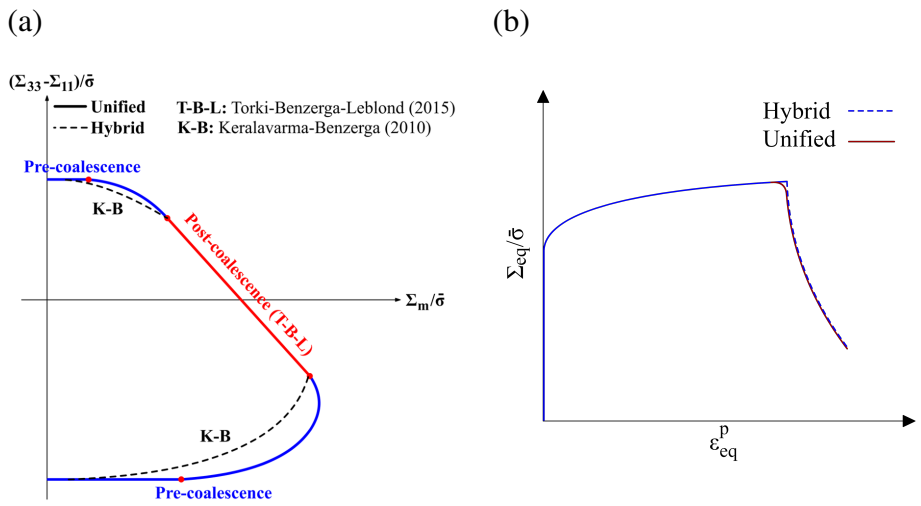

Figure 3.3: (a) Schematic comparison between a unified and a hybrid yield locus (*e.g.* constituted by the Keralavarma–Benzerga homogeneous yield model [14] and the here–derived inhomogeneous criterion. See Chapter 5); (b) schematic stress–strain curves in an arbitrary evolution problem corresponding to a hybrid and a unified model (reprinted with permission from *Elsevier*, Ltd).

Figure 3.3 depicts an example hybrid model invoking the Keralavarma-Benzerga [14] and unified models before and after inhomogeneous yielding occurs. Upon the use of a more general velocity field resembling that utilized by Gurson, Morin *et al.* [97] introduced a unified model accounting for both homogeneous and inhomogeneous yieldings. Within the confines of this research, the same shear velocity field employed in the derivation of the inhomogeneous yield criterion is further superposed to a more universal counterpart of the unified model in [97] under combined axial, lateral, and shear loading (see Paper P3 for derivations). See Chapter 5 for a clearer image on the unified yield criterion derived in the present work.

The plastic framework within the present context is developed based on a hybrid model. A hybrid model may trigger numerical issues resulting from an ill-defined normal to the surface at the point of transition between the two yield surfaces, except when a multi-surface formulation is employed. The latter operates in such a way that the plastic rate of deformation is expressed as a linear combination of all the active surfaces, with the multipliers equaling the plastic multipliers associated with every yield criterion. For the sake of simplicity, however, one can refer to only

one surface at a specific step, and disregard other less effective surfaces. On the other hand, voids at the post-localized process can interconnect only along a discrete set of directions, each possible direction uniquely identified by a unit vector normal to is associated *plane of localization* $\boldsymbol{n}$. Accordingly, there are $k \geq 1$ post-localized yield functions affecting the constitutive framework (a detailed elaboration on the value of k will be given in Chapter 6). The hybrid and/or multi-surface model should then consist of $k + 1$ yield surfaces, with k denoting the selected number of possible localization systems and 1 pertaining to homogeneous yielding.

CHAPTER 4 MODELING METHODOLOGY

Considering the discussed epistemology of ductile fracture modeling in Chapter 1, the present thesis partly aims at developing a micromechanics-based model from first principles that is equipped with measurable and/or observable internal parameters. Not only can such a model predict the critical parameters at failure instants but it can also mimic the active physical fracture processes. The present chapter addresses the principles underlying the analytical modeling and numerical implementation of models in the course of this work. It thus begins with a brief introduction on *homogenization* and *limit analysis*, as the cornerstones of modeling in the present work. The model should further be well predictive. The following sections would then comprise a briefing over a recently developed finite element-based numerical method for the assessment and potential calibration of the derived models. On the other hand, due to the very nature of inhomogeneous deformation, plastic strains can, in general, localize within various possible planes while one plane proves the most effective at every current state. This chapter will, therefore, conceptualize the notion of multiple *localization systems* that can realize the inhomogeneous yielding mechanism that is true to the spirit of the derived models. For complete simulation purposes, however, the model should eventually be supplemented with mechanism-based evolution equations for the internal state variables. This chapter will further present an overview of the numerical path towards the integration of the constitutive framework that encompasses the evolution equations.

4.1 Homogenization Theory

Homogenization is among the most pivotal theories, generally, in all studies related to porous materials, and in pertaining ductile fracture processes in particular. The interest towards homogenization methods stems from the inherent anisotropies in ductile materials at sufficiently small scales. These anisotropies can be attributed to the intrinsic nonlinearities within the constitutive behavior or to the geometric nonlinearities arising in presence of finite strains and rotations. The former is partly rooted in the micro-scale or atomic-scale morphology. Examples in this respect

abound in engineering metals. Homogenization proves efficacious in a range as wide as to include, for instance, steel and aluminum alloys to fiber-reinforced elastomers. The former is representative of poly-crystalline aggregates of randomly oriented single crystals and the latter is a two-phase material system consisting of a second (inclusion) phase distributed randomly or periodically in a surrounding matrix [168].

4.1.1 Characterization of classical homogenization

The basics of classical micromechanics-based homogenization are founded on the Hill-Mandel theorems [169, 170]. Depending on the type of boundary conditions at the cell level, there are basically two approaches possible: the *kinematic* and the *static* approach.

Kinematic boundary conditions are conceived of when the reference volume element (RVE) is subjected to uniform boundary strain rates, as stated in Eq. (3.1) and repeated herein for ease of reference. On this account, there exists a constant tensor $\boldsymbol{D}$ such that

$$\forall\, \boldsymbol{x} \in \partial\Omega \quad \boldsymbol{v} = \boldsymbol{D}\boldsymbol{x} \tag{4.1}$$

where Ω and $\partial\Omega$ represent the cell domain and boundary, respectively, and $\boldsymbol{x}$ is the position vector. All the same, static boundary conditions are considered such that the local tractions at the boundary are equal to those induced by an applied macroscopic stress tensor $\boldsymbol{\Sigma}$ through

$$\forall \boldsymbol{x} \in \partial\Omega \qquad \boldsymbol{\sigma}\boldsymbol{n} = \boldsymbol{\Sigma}\boldsymbol{n} \tag{4.2}$$

with $\boldsymbol{n}$ being the outward boundary unit normal.

Under both circumstances, the *Hill-Mandel Lemma* states that, letting $\boldsymbol{v}$ be a kinematically admissible velocity field and $\boldsymbol{\sigma}$ a statically admissible stress field, it can be deduced that

$$\langle \boldsymbol{\sigma} : \boldsymbol{d} \rangle_\Omega = \boldsymbol{\Sigma} : \boldsymbol{D} \tag{4.3}$$

where $\boldsymbol{\Sigma} = \langle \boldsymbol{\sigma} \rangle_\Omega$ and $\boldsymbol{D} = \langle \boldsymbol{d} \rangle_\Omega$ denote volume averages of micro-scale stress and deformation-

rate tensors, and Ω represents both the RVE domain and its volume. The reader can consult [33] for more details.

Remark 1: The $\boldsymbol{\Sigma} = \langle \boldsymbol{\sigma} \rangle_{\Omega}$ identity is a definition in the kinematic approach whereas it is a theorem in the static approach. The latter can follow from a uniform admissible microscopic rate of deformation $\boldsymbol{d}$ in the Hill-Mandel lemma in (4.3) under static boundary conditions. See [33] for more details.

Remark 2: In the Hill-Mandel lemma, $\boldsymbol{\sigma}$ and $\boldsymbol{d}$ need not relate through a constitutive conjunction.

Remark 3: Under kinematic boundary conditions, $\boldsymbol{v}$ should admit the kinematic relation in (4.1) whereas, with static boundary conditions, $\boldsymbol{v}$ is arbitrary. Moreover, $\boldsymbol{\sigma}$ should be a self-equilibrating stress field (*i.e.* div$\boldsymbol{\sigma} = \mathbf{0}$ in $\Omega \setminus \omega$, with ω denoting the void volume) that obeys the traction-free boundary condition, *i.e.* $\boldsymbol{\sigma n} = \mathbf{0}$ on $\partial\omega$. Alternatively, one can write

$$\boldsymbol{\Sigma} = (1 - f)\langle \boldsymbol{\sigma} \rangle_{\Omega \setminus \omega} \tag{4.4}$$

Besides being self-equilibrating, $\boldsymbol{\sigma}$ is arbitrary under kinematic boundary conditions, whereas it must admit (4.2) under static boundary conditions.

Other homogenization-based methods have been supplied along with those founded on classical homogenization. A brief overview in this regard will be given in Sec. 4.7.1.

4.1.2 Inhomogeneous yielding and homogenization

As earlier pointed out in Chapter 3, inhomogeneous yielding, upon definition, does not correspond to strain localization at the micro scale on the condition of Rice [61]. Rather than infinite concentration, it is represented by the concentration of plastic strains within a layer of a *finite* thickness of the same order as the void size. It may, however, be rational to seek inhomogeneous yielding in terms of a localization mechanism at a larger scale incorporating the effect of voids via a homogenized model. Perrin [171] was amongst those who tried to employ this method to the calculations carried out by Koplik and Needleman [46] upon a mere Gurson-like approach,

where he figured out that the Gurson model was capable of predicting strain localization in layers coincident with invervoid ligaments only for rather large porosity levels [97].

On the other hand, homogenization-based models tacitly rely on the fundamental assumption of *separation of scales* [172]. That is, the average dimension of heterogeneities is way smaller than the dimensions that can influence the macroscopic response. This is generally true for homogeneous yielding. Under inhomogeneous yielding circumstances, however, the void deforms within the confines of a small zone within which the macroscopic response variation, in terms of stresses and strain rates, can be much more considerable. This implies that the notion of a representative volume element (RVE) is questionable in the context of coalescence modeling. Nevertheless, the underlying principles of volumetric averaging correlating local and average material responses are still valid at the unit cell level notwithstanding the presence of rigid-like zones emanating from elastic unloading. Approaches of this kind thus represent the best way possible at present, in absence of a clear-cut homogenization theory of coalescence [97].

4.2 Limit Analysis

As a branch of functional analysis, *limit analysis* is a powerful theory that allows for the attainment of limit loads in structural mechanics problems [173, 174]. The method has been extensively employed in soil mechanics [175, 176], structural mechanics [177–180], as well as in metal forming [181]. One of the most interesting applications of the theory in recent decades has been in the field of mechanics of materials, particularly for porous materials. Its efficacy in this regard makes it applicable in the analytical derivation of micromechanics-based models as well as numerical assessment of the accuracy of existing models.

Classical limit analysis originally applies to ideally plastic materials admitting infinitesimal strains. Plastic deformation is assumed to be incompressible, with the dense matrix considered rigid-ideal plastic admitting a flow theory –such as J_2– along with an associated flow rule [173, 182]. *Sequential* limit analysis, on the other hand, has more recently been proposed, mainly after Yang [183], as a heuristic extension to hardening plastically deformable materials, that incorporates large displacements and strains. Leblond *et al.* [184] demonstrated, in a recent revisiting of the

concept, the conditions to the applicability of sequential limit analysis. Consequent to comparing the general elasto-plastic evolution equations to their counterparts for classical and sequential limit analysis, they deduced that, unlike in classical limit analysis, sequential limit analysis is strictly prohibitive of elasticity.

The classical theory of limit analysis is invoked in both the derivation and assessment of effective yield criteria in the present work. Upon definition, it follows the underlying hypotheses and conditions outlined below [184]:

$$\begin{cases} \dot{\boldsymbol{q}} \neq \mathbf{0} & \text{Stationary plastic deformation} \\ \operatorname{div}\boldsymbol{\sigma} = \mathbf{0} & \text{Equilibrium} \\ \boldsymbol{d} = \boldsymbol{d}^{\mathrm{p}} & \text{Strain rate decomposition} \\ \boldsymbol{d}^{\mathrm{p}} = \dot{\Lambda}\dfrac{\partial \Phi}{\partial \boldsymbol{\sigma}} & \text{Flow rule} \\ \Phi(\boldsymbol{\sigma}) \leq 0\,, \quad \dot{\Lambda} \geq 0\,, \quad \Phi(\boldsymbol{\sigma})\dot{\Lambda} = 0 & \text{Kuhn-Tucker compatibility conditions} \\ \text{B.C.} & \text{Boundary conditions} \end{cases} \tag{4.5}$$

where $\boldsymbol{q}$ denotes the kinematic vector conjugate with the external load vector $\boldsymbol{Q}$. Condition $(4.5)_3$ stems from the underlying premise that, after the attainment of the limit load, plastic deformation becomes *stationary*, *i.e.* $\dot{\boldsymbol{Q}} = \mathbf{0}$. See [184] for proof.

4.3 Effective Dissipation and Yield Criterion

Within the kinematic framework in limit analysis, the effective yield criterion at the macro scale $\Phi(\boldsymbol{\sigma}) = 0$ lies in the identification of a *plastic dissipation* $\pi(\boldsymbol{d})$, defined over the convexity domain $\mathcal{C}$, as [185]:

$$\pi(\boldsymbol{d}) = \operatorname{supp}\{\boldsymbol{\sigma} : \boldsymbol{d} \mid \boldsymbol{\sigma} \in \mathcal{C}\,,\ \forall \boldsymbol{d}\} \tag{4.6}$$

where the *support function*, denoted with $\operatorname{supp}\{f\}$, is defined as the smallest closed set outside which the function f vanishes identically [186]. Note that $\boldsymbol{d}$ must be plastically admissible, admitting Eq. (2.9). On account of the Hill-Mandel lemma in (4.3), $\Pi(\boldsymbol{D})$ can be defined as the effective

plastic dissipation at the macro scale, given by

$$\Pi(\boldsymbol{D}) = \inf_{\boldsymbol{v}\in\mathcal{K}(\boldsymbol{D})} \langle \pi(\boldsymbol{d}) \rangle_{\Omega} \tag{4.7}$$

where Ω refers to the spatial domain over which macroscopic quantities are defined, $\langle\cdot\rangle_{\Omega}$ stands for averaging over Ω, and $\mathcal{C}$ is the microscopic reversibility domain (the boundary of which is the yield surface). The veracity of the *infimum* involved in the definition of Π lies in the fact that the exact assessment of the velocity field that gives rise to a minimum Π is literally impossible for arbitrary stress states, even for relatively simple geometries. However, tentative velocity fields can be adopted such that the evaluated Π is close to minimum. Also, the set of kinematically admissible velocity fields, $\mathcal{K}(\boldsymbol{D})$, is made of incompressible fields ($v_{k,k} = 0$) that are compatible with the overall deformation imposed through $\boldsymbol{D}$. With the dense matrix considered incompressible, the microscopic rate of deformation $\boldsymbol{d}$ must be traceless. Otherwise, Φ will be infinite. By way of analogy, Π can be expressed as the following support function over the macroscopic reversibility domain $\mathcal{C}$:

$$\Pi(\boldsymbol{D}) = \text{supp}\{\boldsymbol{\Sigma} : \boldsymbol{D} \mid \boldsymbol{\Sigma} \in \mathcal{C}\ ,\ \forall \boldsymbol{D}\} \tag{4.8}$$

where

$$\mathcal{C} = \{\boldsymbol{\Sigma} \mid \exists\, \boldsymbol{\sigma} \in \mathcal{C}\}$$

In a material obeying the J_2 flow theory, for instance, the effective dissipation, with reference to (2.3.1) and (2.24), can be expressed as follows [33]:

$$\Pi(\boldsymbol{D}) = \langle \bar{\sigma} d_{\text{eq}} \rangle_{\Omega} = (1-f)\langle \bar{\sigma} d_{\text{eq}} \rangle_{\Omega\setminus\omega} \tag{4.9}$$

Another case that lends itself to a simple expansion of $\Pi(\boldsymbol{D})$ is when the material obeys an associated Hill-type anisotropy. In the latter case, one can utilize the same expansion as in (4.9), but with the following d_{eq} [14, 95]:

$$d_{\text{eq}}^2 = \frac{2}{3}\boldsymbol{d} : \hat{\mathbb{h}} : \boldsymbol{d} \tag{4.10}$$

where $\hat{(.)}$ is representative of a formal inverse for a fourth-order tensor such that, for instance, $\hat{\mathbb{h}} : \mathbb{h} = \hat{\mathbb{h}} : \mathbb{h} = \mathbb{J}$, with $\mathbb{J}$ defined in Chapter 2. Here, $\mathbb{h}$ is the anisotropy tensor in the deviatoric stress space. See [14, 95] for more information.

Following a combination of limit analysis and homogenization theories, the effective yield criterion of a material containing microvoids can be determined using the *inequality of limit analysis* written as [33]

$$\forall\, \boldsymbol{D}, \quad \boldsymbol{\Sigma} : \boldsymbol{D} \leq \Pi(\boldsymbol{D}) \tag{4.11}$$

where $\boldsymbol{\Sigma}$ and $\boldsymbol{D}$ denote the macroscopic stress and rate of deformation tensors, defined as the volume averages of their microscopic counterparts $\boldsymbol{\sigma}$ and $\boldsymbol{d}$ as defined in advance.

If the dissipation function is differentiable, then the effective yield surface is smooth, and (4.11) is equivalent to:

$$\boldsymbol{\Sigma} = \frac{\partial \Pi(\boldsymbol{D})}{\partial(\boldsymbol{D})} \tag{4.12}$$

where $\boldsymbol{D}$ is no longer arbitrary as in (4.11) but represents the rate of deformation corresponding to $\boldsymbol{\Sigma}$ through the macroscopic flow rule. To sum up, if the effective yield surface is smooth, then (4.12) constitutes its parametric equation. Otherwise, inequality (4.11) determines the effective reversibilty domain $\mathcal{C}$ (which is different from the microscopic one $\mathcal{C}$). In order to solve the inequality, one may recourse to graphical methods. See clear indications in Papers P1 –P3 .

Remark 1: There is often a trade-off between the accuracy of the velocity field and the analytical simplicity of the resulting yield criterion. In most cases, a closed-form yield function is not attained except upon the least possible degree of continuity within the velocity field. With a robust numerical implementation of the constitutive framework, however, a parametric representation of the yield function devoid of a closed-form stress-based expression would suffice.

Remark 2: If the velocity field is discontinuous across an interface S then an additional term must be added to (4.9), which writes

$$\frac{1}{\Omega} \int_S \text{supp}_{\boldsymbol{\sigma}^* \in \mathcal{C}} \left\{ \boldsymbol{t}^* \cdot [\![\boldsymbol{v}]\!] \right\} dS \tag{4.13}$$

where $[\![\boldsymbol{v}]\!]$ is the velocity jump across the interface and $\boldsymbol{t}^*$ the traction acting thereon. Accordingly, in the case of a discontinuous velocity field, the above expression can be resolved as the sum of volumetric and surface terms:

$$\Pi = \Pi^{\mathrm{vol}} + \Pi^{\mathrm{surf}} \tag{4.14}$$

where

$$\begin{cases} \Pi^{\mathrm{vol}} & = c\langle \bar{\sigma} d_{\mathrm{eq}} \rangle_{\Omega_{\mathrm{lig}}} = c(1-f_{\mathrm{b}})\langle \bar{\sigma} d_{\mathrm{eq}} \rangle_{\Omega_{\mathrm{lig}} \setminus \omega} \\ \Pi^{\mathrm{surf}} & = \dfrac{1}{\Omega} \displaystyle\int_{S_{\mathrm{int}}} \frac{\bar{\sigma}}{\sqrt{3}} \big| [\![v_{\mathrm{t}}]\!] \big| dS \end{cases} \tag{4.15}$$

with $[\![v_{\mathrm{t}}]\!]$ denoting the discontinuity of tangential velocity, as identified in (4.13), and f_{b} is the porosity within the ligament, here termed *band porosity*. For inhomogeneous yielding occurring by internal necking or shearing, the above-mentioned discontinuity is triggered across the rigid-plastic interfaces S_{int} with a basic Gurson-like velocity field employed. More specific details will be provided in Chapter 6.

Remark 3: In principle, $\boldsymbol{D}$ can be eliminated from the parametric equation (4.12) owing to $\partial\Pi/\partial\boldsymbol{D}$ being positively homogeneous of zero degree. Equation (4.12) may thus be expressed in the form $\Phi(\boldsymbol{\Sigma};\boldsymbol{\alpha}) = 0$, with Φ denoting an effective yield function, expressed in terms of the macroscopic stress tensor $\boldsymbol{\Sigma}$ and a set of other internal state variables denoted with $\boldsymbol{\alpha}$ that, in the realm of ductile fracture, may contain porosity f, $\bar{\sigma}$ or its conjugate $\bar{\epsilon}$, void aspect ratio w, *etc.*. Otherwise, the resulting model could be expressed in parametric form, *i.e.* in terms of the ratios among macro-scale strain rate components. On account of the microscopic plastic flow obeying Drucker's stability postulate –equivalent to Hill's principle of maximum plastic work–, it can be shown (through the application of the Hill-Mandel lemma, see [33] for more details) that the same principle holds at the macro scale. As a consequence, the macroscopic domain of elasticity $\mathcal{C}$ is convex, the plastic rate of deformation $\boldsymbol{D}^{\mathrm{p}}$ belongs to the hypercone of normals to the effective yield surface Φ, and the macroscopic flow rule for a smooth Φ obeys normality.

4.4 Numerical Limit Analysis

The calculation of limit loads using the theory of limit analysis is subject to errors, *e.g.* concerning the quality of the velocity fields adopted in the kinematic approach. Thus, various groups have developed computational frameworks for computing *exact* limit loads. We shall commonly refer to such frameworks as "numerical limit analysis". This method has proven efficacious in the assessment and on-demand calibration of existing ductile fracture models as well as development of enhanced models. It is rooted in mimicking the *current* microstructural state, pertaining to homogeneous yielding or a state of *incipient* inhomogeneous yielding, based on single-step plastic analysis which corresponds to the problem of small-strain plasticity with *no* elastic domain. Until quite recently, the most prevalent method in numerical limit analysis was by developing *special* finite element-based solutions. Since the basic problem is specific to rigid-perfectly plastic materials, finite-element solutions are difficult to formulate properly and are susceptible to various numerical issues [175, 187, 188]. An alternative, rather recent, method consists of using *standard* finite element formulations for numerical limit analysis. This method was devised by Leblond and coworkers [97, 140, 141, 189] and is briefly outlined herein. This method lies in the equivalence between the classical and a modified limit analysis method. This equivalence relies on the finite-element method using an *implicit* algorithm to the plastic correction of elastically predicted stresses through a single large step with no geometry evolution. As a consequence, a one-to-one correspondence can be drawn between $\dot{q}$ and $\boldsymbol{q}^{(1)}$, $\boldsymbol{v}$ and $\boldsymbol{u}^{(1)}$, and between $\boldsymbol{d}$ and $\boldsymbol{\epsilon}^{(1)}$ with $\boldsymbol{q}^{(1)}$, $\boldsymbol{u}^{(1)}$ and $\boldsymbol{\epsilon}^{(1)}$ denoting the *final* kinematic vector, displacements and strains, respectively. Upon a load increment being large enough so that elastic strains can be disregarded compared to their plastic counterparts, the classical limit analysis conditions in (4.5) will become equivalent to the

following [141, 189]:

$$\begin{cases} \boldsymbol{q}^{(1)} = \boldsymbol{q}^{(1)} - \boldsymbol{q}^{(0)} \neq \mathbf{0} & \text{Stationary plastic deformation} \\ \text{div}\boldsymbol{\sigma}^{(1)} = \mathbf{0} & \text{Equilibrium} \\ \boldsymbol{\epsilon}^{(1)} = \boldsymbol{\epsilon}^{(1)} - \boldsymbol{\epsilon}^{(0)} \approx \boldsymbol{\epsilon}^{\mathrm{p}} & \text{Strain decomposition} \\ \boldsymbol{\epsilon}^{\mathrm{p}} = \Delta\Lambda \dfrac{\partial \Phi}{\partial \boldsymbol{\sigma}} & \text{Flow rule} \\ \Phi(\boldsymbol{\sigma}) \leq 0\,, \quad \Delta\Lambda \geq 0\,, \quad \Phi(\boldsymbol{\sigma})\Delta\Lambda = 0 & \text{Kuhn-Tucker compatibility conditions} \\ \text{B.C.} & \text{Boundary conditions} \end{cases} \tag{4.16}$$

with $\boldsymbol{\sigma}^{(1)}$ and $\Delta\Lambda$ denoting the ultimate stresses and plastic multiplier incremented through the whole step, respectively.

A clear consequence of limit analysis with this attitude is that elastic strain rates vanish when the limit load is reached. To this end, the elastic moduli should disappear from the equations and, in turn, plasticity imposes an incompressible velocity field on the material. To this end, the base material of the unit cell should be elastic-perfectly plastic in effect. Accordingly, a high value of Poisson's ratio, close to 0.5, can be enforced so that plastic incompressibility is respected. The value considered in [96, 97, 140] and used herein is $\nu = 0.49$, which maintains a nearly-isochoric velocity field and would not lead to singular solutions. Further, a typical yield strength to Young's modulus ratio of $\bar{\sigma}/E = 0.000225$ has been considered, which correponds to a Young modulus of $E = 4444.5\bar{\sigma}$.

The commercial tool ABAQUS was used in the present work to carry out the numerical calculations. Inasmuch as numerical cell-model calculations in this study are primarily meant to validate the analytical yield criteria, the FEM models were featured to include a unit cell with a geometry identical to that characterized in Chapter 6 admitting quasi-periodic boundary conditions (the term *quasi* denoting the fact that the considered elementary cell is not space-filling). The analysis procedure briefed above allows for any alternative space-filling model with no significant increase in the computational demand. Yet, the least uncertainty lies within the numerical and analytical

cells with identical geometries. Hence, a cylindrical cell containing a cylindrical void has been considered in the present context for the numerical assessment of limit loads at the onset of inhomogeneous yielding. The limit stress value for a frozen microstructure is sought for at each FEM analysis. To this end, the equilibrium equations are to be solved on the basis of initial geometric specifications rather than the deformed state in order that the calculated stress values correspond to a well-defined initial configuration. This can be achieved through switching off geometric nonlinearity in ABAQUS (*NLGEOM=No*; see [190] for more technical details).

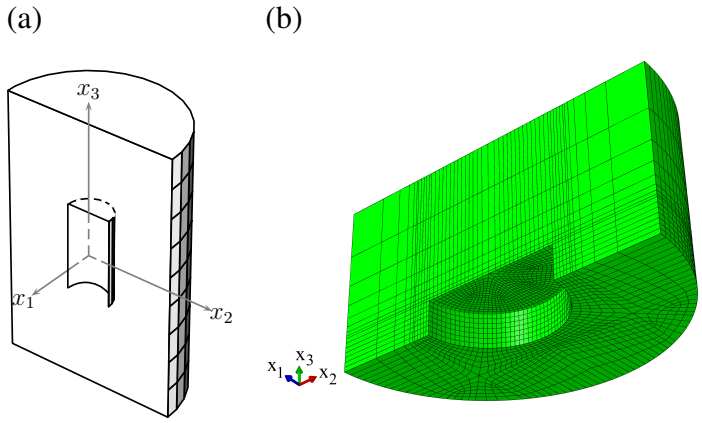

Figure 4.1: (a) One half of a cylindrical cell, (b) a numerically well-conditioned mesh for numerical limit analysis over a cylindrical RVE [15] (reprinted with permission from *Elsevier*, Ltd).

Figure 4.1 depicts a schematic half-cell with symmetry conditions imposed on the meridian plane as well as an example numerically well-conditioned mesh employed in the interest of the assessment of models derived within the realm of this work. Anywhere in a periodic cell, the displacement $\boldsymbol{u}$ at field point $\boldsymbol{x}$ would write:

$$\boldsymbol{u}(\boldsymbol{x}) = (\boldsymbol{E} + \boldsymbol{\Omega}).\boldsymbol{x} + \tilde{\boldsymbol{u}}(\boldsymbol{x}) \tag{4.17}$$

where $\boldsymbol{E}$ is the macroscopic strain tensor, $\boldsymbol{\Omega}$ the (skew-symmetric) macroscopic rotation tensor and $\tilde{\boldsymbol{u}}$ a periodic field. For any two points in periodic correspondence, one would therefore write:

$$\Delta\boldsymbol{u} = (\boldsymbol{E} + \boldsymbol{\Omega}).\Delta\boldsymbol{x} \tag{4.18}$$

where $\Delta\boldsymbol{u}$ is the difference in displacement between the points separated by the vector $\Delta\boldsymbol{x}$. For a cylindrical cell, (4.18) cannot be applied to pairs of points in periodic correspondence since such pairs do not exist. Instead, one ought to impose similar conditions, thus its name *quasi*–periodic. In this respect, the macroscopic strain enforced on the cell is represented by the tensor:

$$\boldsymbol{E} = E_{11}(\boldsymbol{e}_1 \otimes \boldsymbol{e}_1 + \boldsymbol{e}_2 \otimes \boldsymbol{e}_2) + E_{33}\boldsymbol{e}_3 \otimes \boldsymbol{e}_3 + E_{31}(\boldsymbol{e}_1 \otimes \boldsymbol{e}_3 + \boldsymbol{e}_3 \otimes \boldsymbol{e}_1) \tag{4.19}$$

or in matrix form

$$\boldsymbol{E} = \begin{bmatrix} E_{11} & 0 & E_{31} \\ 0 & E_{11} & 0 \\ E_{31} & 0 & E_{33} \end{bmatrix}$$

where

$$\begin{aligned} E_{11} = E_{22} &\equiv \ln\left(\frac{L}{L_0}\right) \approx \frac{U_1}{L_0} \\ E_{33} &\equiv \ln\left(\frac{H}{H_0}\right) \approx \frac{U_3}{H_0} \\ E_{31} &\equiv \frac{U_\mathrm{t}}{2H_0} \end{aligned} \tag{4.20}$$

Here, U_1 denotes a prescribed displacement on the lateral surface (see Papers P2 and P3 for details), whilst U_3 and U_t are, respectively, the normal and tangential displacements prescribed on the top surface.

On the other hand, the macroscopic rotation tensor must be of the form:

$$\boldsymbol{\Omega} = \Omega_{31}(\boldsymbol{e}_3 \otimes \boldsymbol{e}_1 - \boldsymbol{e}_1 \otimes \boldsymbol{e}_3) \tag{4.21}$$

The simplest choice for $\boldsymbol{\Omega}$ in (4.18) would be to take $\boldsymbol{\Omega} = \boldsymbol{0}$. However, this would entail a vertical displacement on the lateral surface. To avoid this, one can choose $\Omega_{13} = -\Omega_{31} = E_{31}$. For the cylindrical cell considered, this choice will considerably simplify the formulation of multi-point

constraint conditions.

In matricial form, the strictly periodic boundary conditions (4.18) would read:

$$\begin{Bmatrix} \Delta u_1 \\ \Delta u_2 \\ \Delta u_3 \end{Bmatrix} = \begin{bmatrix} E_{11} & 0 & 2E_{31} \\ 0 & E_{11} & 0 \\ 0 & 0 & E_{33} \end{bmatrix} \begin{Bmatrix} \Delta x_1 \\ \Delta x_2 \\ \Delta x_3 \end{Bmatrix} \tag{4.22}$$

The above are further replaced by the following quasi-periodic conditions:

- On the top surface, $\Delta \boldsymbol{u} = \boldsymbol{u}(x_1, x_2, H) - \boldsymbol{u}(x_1, x_2, -H)$ and $\Delta \boldsymbol{x}^T = \{0, 0, 2H\}$ so that:

$$\begin{cases} \Delta u_1 = 4E_{31}H \\ \Delta u_2 = 0 \\ \Delta u_3 = 2E_{33}H \end{cases} \tag{4.23}$$

- On the plane Ox_2x_3,

$$u_1(0, x_2, x_3) = 0 \tag{4.24}$$

- On the lateral surface ($x_1^2 + x_2^2 = L^2$, $-H \leq x_3 \leq H$) multi-point constraints are imposed so that the nodes lying on a semi-circle remain on a semi-circle of radius consistent with the prescribed value of E_{11}. Let $\boldsymbol{u}^{\text{ref}}$ be the displacement of some reference node on the semi-circle at some height x_3, say $\boldsymbol{x}^T = \{L, 0, x_3\}$ and $\Delta \boldsymbol{u} = \boldsymbol{u}(x_1, x_2, x_3) - \boldsymbol{u}^{\text{ref}}$, then:

$$\begin{cases} \Delta u_1 = E_{11}(x_1 - L) \\ \Delta u_2 = E_{11}x_2 \\ \Delta u_3 = 0 \end{cases} \tag{4.25}$$

In particular, to simulate coalescence states whereby rigid zones preclude lateral straining, one should take $E_{11} = 0$, hence $U_1 = 0$. Under such circumstances, conditions (4.25) state that the

circles move rigidly.

Since the ultimate load value is not known as such, each stress component for the overall unit cell is calculated in obedience to a simple volume averaging, which can be written as

$$\boldsymbol{\Sigma} = v^{(n)}\boldsymbol{\sigma}^{(n)} \tag{4.26}$$

with summation implied on n, where $v^{(n)} = V^{(n)}/\Omega$ is the volume fraction of the n'th element with respect to the whole unit cell (with Ω being the total cell volume). See Papers P2 and P3 for details.

4.5 Multi-Surface Modeling

Following the *additivity* premise declared in Chapter 2, the total rate of deformation tensor $\boldsymbol{D}$ is decomposed in the following format, with the elastic and the plastic parts stemming from the hyperelastic and hypoelastic laws stated in Eq's (2.16) and (2.18):

$$\boldsymbol{D} = \boldsymbol{D}^{\mathrm{e}} + \boldsymbol{D}^{\mathrm{p}} \tag{4.27}$$

with

$$\boldsymbol{D}^{\mathrm{p}} = \sum_{k=1}^{m} \dot{\Lambda}^k \boldsymbol{N}^k \quad , \quad \boldsymbol{N}^k = \frac{\partial \Phi^k}{\partial \boldsymbol{\sigma}} \tag{4.28}$$

where $D^{\mathrm{p}k}$'s belong to all effective yielding mechanisms, with m denoting the number of all potentially active mechanisms. Within the realm of porous plasticity, active mechanisms can comprise homogeneous yielding as well as inhomogeneous yielding with strains localized inside planes or along columns. See Chapter 8 for concepts. Notably, voids during the inhomogeneous process can interconnect inside various possible *localization planes* accommodating void interactions in different directions. A clear elaboration on this concept will be provided in Chapter 6.

4.6 Time Integration

To the purpose of simulating ductile fracture models, the yield function generally represented by $\Phi([\boldsymbol{V}]) = 0$ would not be beneficial unless supplemented with proper evolution equations for the internal state variables denoted with $[\boldsymbol{V}]$, normally termed $[\dot{\boldsymbol{V}}]$. The constitutive framework then comprises a set of independent state variables (denoted with $[\boldsymbol{V}]$), to be evolved implicitly, and (potentially) another set of dependent state variables that are post-processed and can be expressed in terms of the independent ones. Further illustrations regarding the specific state variables during the homogeneous and inhomogeneous processes will be provided in Section 6.4 as well as Paper P7 . Associated with the vector of independent state variables $[\boldsymbol{V}]$ is a *residual* vector, so defined as the numerical difference between the direct and the differential time rates. That is

$$[\boldsymbol{R}] = \frac{[\boldsymbol{V}] - [\boldsymbol{V}]_0}{\Delta t} - [\dot{\boldsymbol{V}}] \tag{4.29}$$

with $[\boldsymbol{V}]_0$ and $[\boldsymbol{V}]$ denoting the state variables at the beginning and end of every time step, respectively. Within the chosen microstructural simulation, not all of the involved internal state variables are independent. Rather, some are proven to function in terms of one or more parameters within the $(f, w, \boldsymbol{n}^{(3)}, \boldsymbol{n})$ set. The least possible set of independent state variables should then consist of the following elements:

$$\boldsymbol{V} = \left[\boldsymbol{\sigma}', \sigma_m, f, \bar{\epsilon}, s\right]^T \tag{4.30}$$

where $\boldsymbol{\sigma}'$ and σ_m denote, respectively, the deviatoric and mean normal stresses, and $s = \ln w$ is the void aspect ratio in natural logarithmic form. More details in regards to the specific equations will be provided in Chapter 6.

The Newton-Raphson procedure is then employed iteratively to solve the $[\boldsymbol{R}] = \boldsymbol{0}$ equation system at every time step:

$$[\boldsymbol{V}]^{(i+1)} = [\boldsymbol{V}]^{(i)} - \left[\frac{\partial [\boldsymbol{R}]}{\partial [\boldsymbol{V}]^{(i)}}\right]^{-1} [\boldsymbol{R}] \tag{4.31}$$

where the Jacobian matrix $\partial[\boldsymbol{R}]/\partial[\boldsymbol{V}]$ can be evaluated at every iteration within the time step or kept constantly equal to the value at the beginning of the time step, and superscript i denotes the iteration number. Equation (4.31) is repeated until the residual vector $[\boldsymbol{R}]$ lies within a vector of specified tolerances.

Finally, the consistent tangent matrix (mainly developed for global equilibrium, as in a finite element-based analysis), denoted by $\mathbb{L}^{\tan}$ (*e.g.* DDSDDE in ABAQUS) is written as

$$\mathbb{L}^{\tan} = \frac{1}{\Delta t}\left(\frac{\partial \tilde{\boldsymbol{\sigma}}'}{\partial \tilde{\boldsymbol{D}}} + \boldsymbol{I} \otimes \frac{\partial \tilde{\sigma}_{\mathrm{m}}}{\partial \tilde{\boldsymbol{D}}}\right) \tag{4.32}$$

which involves the following constituents:

$$\left[\frac{\partial \boldsymbol{V}}{\partial \tilde{\boldsymbol{D}}}\right] = -\left[\frac{\partial [\boldsymbol{R}]}{\partial [\boldsymbol{V}]}\right]^{-1}\left[\frac{\partial \boldsymbol{R}}{\partial \tilde{\boldsymbol{D}}}\right] \tag{4.33}$$

where use has been made of the same Jacobian as introduced in (4.31).

4.7 Further Notes on Techniques Not Used

4.7.1 Alternative homogenization methods

A distinctive line of work in the classical homogenization field is based on an alternative method in regards to the nonlinear responses of heterogeneous materials. A considerable fraction of work in this field has been built upon the pioneering Hashin-Shtrikman variational method for linearly elastic composites [191] to extract the elastic and overall response of nonlinearly elastic materials, including [192, 193]. Further, based on the use of a "linear comparison composite" (LCC) analytical method, Ponte Castañeda [194, 195] developed more advanced variational principles to improve the bounds to the Hashin-Shtrikman and Beran-Milton (3-point) models for nonlinear composites. Additional research work includes, yet is not limited to, the methods proposed by Suquet [196] concerning power-law or ideally plastic composite materials, the Lurie and Cherkaev method [197], and that of Milton and Serkov [198]. A large cache of work also belongs to Ponte Castañeda and coworkers, who extended the realm of nonlinear homogenization theories

in various respects or for different materials [168, 199–201]. In essence, these models are based on the development of an effective strain-energy density function. As earlier stated in Sec. 4.2, there are serious limitations to the classical homogenization theory apropos of modeling void coalescence. Just as limit analysis based on volumetric averaging can be used to obtain solutions for inhomogeneous yielding processes, so can the class of models developed by Ponte Castañeda and coworkers. Yet, models of this caliber for porous materials remain to be developed. By far, experience with the modeling of homogeneous yielding with, for instance, ellipsoidal voids has it that Ponte Castañeda-type methods are far from being precise except after significant heuristic modifications or tedious analytical enhancements (such as those employing the so-called *second order homogenization*). Therefore, both for the sake of simplicity and until a well-posed theory of homogenization for void coalescence is achieved, we will adhere to limit analysis combined with volumetric averaging.

Along with analytical models, numerical methods have also been proposed to compute the effective mechanical response in multi-phase materials. FFT-based analysis, with FFT standing for "fast Fourier transform", as an example extensively used method, was originally introduced by Suquet and coworkers [202–205] for the effective and local response in heterogeneous media upon a composite image, where heterogeneity relates to some spatial distribution of different phases. The same method was later adapted for the plastic analysis of polycrystals, where the heterogeneity lies in the spatial distribution of crystals with mechanical properties changing with orientation [206–209]. This method can lend itself as a counterpart to the finite-element method for the global (spatial) analysis of boundary-value (BV) problems. In large-scale simulations, *e.g.* with heterogeneities, the FFT method can significantly accelerate the analysis process thanks to the use of stresses and strains in lieu of tractions and displacements, respectively. A recent study has demonstrated a two-order of magnitude improvement in the computational cost in the analysis of phase-transforming (*e.g.* shape-memory) materials [210]. For single-cell calculations, however, FFT bares no perspicuous advantage over FEM. The present work, however, is centered around the constitutive modeling of porous plasticity under combined tension and shear, with a brief portion

to demonstrate the capability of the model in solving BV problems. Considering the extensive use of commercial codes such as ABAQUS, we have opted to write a user-defined subroutine (UMAT) that correlates the constitutive behavior of the porous material with the global equilibrium solved by ABAQUS.

4.7.2 Evolution cell-model calculations

FEM-based calculations carried out at the cell level can serve as benchmark also for the evolution-based phenomenology of void nucleation and growth up to coalescence and failure. Apropos of evolution problems, the pioneering analyses carried out by Needleman [211] and Tvergaard [212] for a periodic array of cylindrical voids, those by Tvergaard [213] and Koplik and Needleman [46] for spherical voids, and that by Besson and Foerch [214], have been followed by several FEM-based evolution studies. Examples in regards to the combination of tensile and shear loadings include the Lode effect investigated via cell-model outcomes by Barsoum and Faleskog [36]. Further studies explored the combined Lode and triaxiality effects with periodic arrays of voids [84, 85, 88, 121, 215, 216] or randomly distributed voids [165, 217].

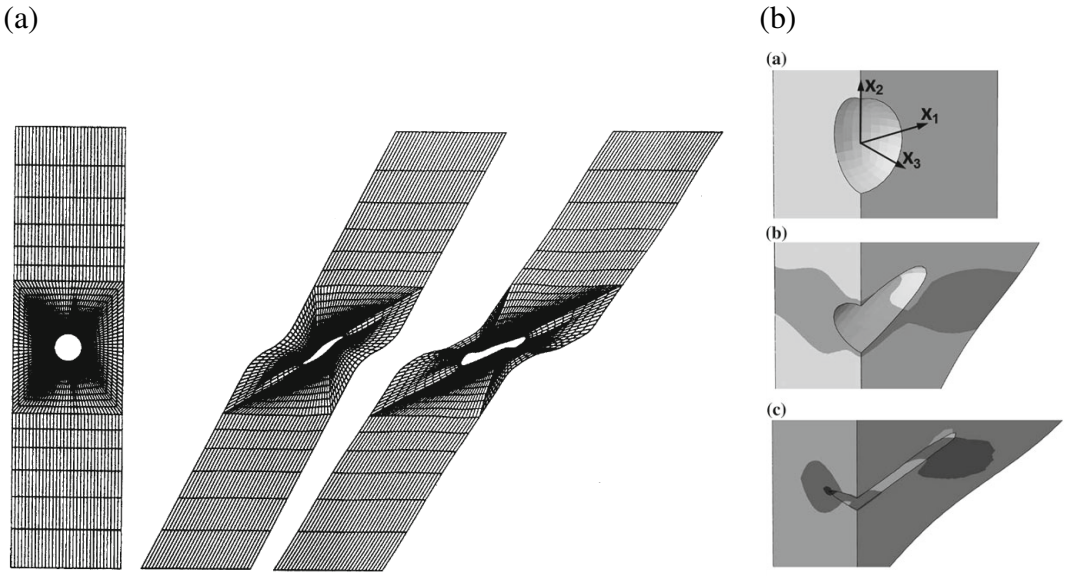

Figure 4.2: (a) Deformation of a unit cell representative of a periodic array of circular voids under simple shearing [16], (b) spherical void elongation under combined tension and shear in a 3D unit cell [17] (reprinted with permission from *Springer*, Ltd).

More recent studies have attempted to describe void growth to coalescence under general loading conditions by combining the effects of various independent stress-based parameters in a unit cell. Tekoğlu [160] introduced an effective method to keep track of three independent parameters including the Lode parameter, stress triaxiality, and shear ratio (defined as the ratio between shear and normal stresses). Alternatively, Liu *et al.* [161] developed, based on energy principles in a derivative format, a unified method to establish a consistent criterion accounting for tensile and shear-dominated types of void coalescence. Such calculations can prove quite useful in the assessment of a complete model that accounts for both homogeneous and inhomogeneous yielding. For the case of combined tension and shear, in particular, the present thesis does not contain any new FEM calculations due to their extreme computational cost. Instead, use has been made of available results, essentially, by Tvergaard and co-workers [16, 17, 21, 218]. Figure 4.2a, for instance, shows a unit cell representing a periodic array of voids under simple shearing. Figure 4.2b, on the other hand, shows void elongation under combined tension and shear in a 3D unit cell.

CHAPTER 5 INHOMOGENEOUS YIELD CRITERIA

This chapter addresses an overview of the inhomogeneous yield functions that are derived from first principles and borne out with numerical results in the course of the present thesis. The models are primarily intended to model inhomogeneous yielding by internal necking, internal shearing or a combination of both. They are obtained by limit analysis and homogenization over a cylindrical elementary cell containing a coaxial cylindrical void of finite height. Plasticity in the deformable matrix is modeled using rate-independent J_2 flow theory admitting kinematically-admissible trial velocity fields, and the effective dissipation function is calculated by exact as well as approximate techniques, the latter generating a simpler function that lies close to the upper bound but loses the upper-bound character. Further, with the constraining conditions for inhomogeneous yielding relaxed, a unified model would follow that accounts for both homogeneous and inhomogeneous yielding. Model predictions are consistently compared with finite-element based estimates of limit loads on unit cells exploiting quasi-periodic boundary conditions. The numerical results are further used to guide a heuristic modification of the models in order to capture the behavior for extremely flat or extremely elongated voids. The approximate inhomogeneous model is finally utilized to predict the effective yield surface as well as strain to failure at the limit of an isotropic material endowed with random void distribution. As such, the effective yield surface will be presented as intersected with principal deviatoric planes (*viz.* the π plane and parallel planes thereof) as well as with principal meridian planes corresponding to purely hydrostatic and purely deviatoric stress states. Detailed discussion on the steps to deriving, assessment, and calibration of models is expounded in Papers P1 –P4 .

5.1 Inhomogeneous Yielding under Combined Tension and Shear

The microstructural geometry is identified in respect to a reference volume element (RVE) that is represented with its corresponding volume Ω for brevity. Herein, the latter is a cylindrical cell embedding a coaxial cylindrical void ω, Fig. 5.1. The inhomogeneous process is characterized

with plastic deformation being localized inside the intervoid ligament, and the rest of the cell admits elastic unloading and can be assumed to be rigid to the first approximation [45]. As such, the microstructure depends on the orientation of the localization band as uniquely defined by a unit normal to the plane transverse to the ligament, as schematically shown in Fig. 5.1.

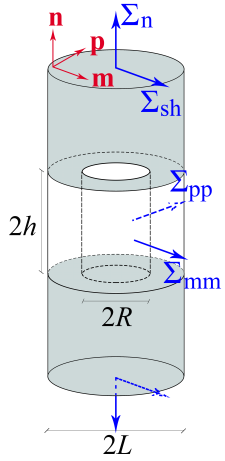

Figure 5.1: Geometry of the cylindrical RVE under combined shear and tension.

Although this RVE is not space filling, it stands as a reasonable approximation of more complex geometries, such as hexagonal-prismatic or square-prismatic cells, which may be considered as unit cells in periodic media. The microstructural geometry is then determined by the following independent dimensionless parameters:

$$w = \frac{h}{R}, \quad \chi = \frac{R}{L}, \quad \lambda = \frac{H}{L} \tag{5.1}$$

defined as the void aspect ratio, the ligament parameter, and the cell aspect ratio, respectively.

The yield function assuming localized yielding of the inter-void ligament is obtained by homogenization of a hollow cylindrical RVE containing a coaxial cylindrical void, as shown in Fig. 5.1. The model derived in Paper P1 (referred to in the sequel as the T-B-L model) is the first analytical criterion that accounts for combined internal necking and shearing in the inter-void ligaments, extending the earlier models of [140, 148, 150]. The effective yield function derived in

Paper P1 can be written in the form

$$\Phi^{\mathrm{I}}(\boldsymbol{\Sigma},\chi,w)=\left(\frac{|\Sigma_{\mathrm{n}}|-t\mathcal{S}(\chi,w)}{b\mathcal{V}(\chi)}\right)^{2}H(|\Sigma_{\mathrm{n}}|-t\mathcal{S})+\left(\frac{\Sigma_{\mathrm{sh}}}{l\mathcal{T}(\chi)}\right)^{2}-1 \tag{5.2}$$

where Φ^{I} denotes the yield criterion representing inhomogeneous deformation. $H(x)$ is the Heaviside step function, equaling 1 if $x>0$ and 0 if $x<0$. Also, $\Sigma_{\mathrm{n}}=\boldsymbol{n}.\boldsymbol{\Sigma}\boldsymbol{n}$, $\Sigma_{\mathrm{sh}}=|\boldsymbol{\Sigma}\boldsymbol{n}-\Sigma_{\mathrm{n}}\boldsymbol{n}|$ are, respectively, the normal and shear tractions on the plane of localization (the latter expressed in magnitude form), and

$$\begin{aligned}\mathcal{V}(\chi)&=\bar{\tau}\left(2-\sqrt{1+3\chi^{4}}+\ln\frac{1+\sqrt{1+3\chi^{4}}}{3\chi^{2}}\right)\\ \mathcal{S}(\chi,w)&=\frac{\bar{\tau}}{3}\frac{\chi^{3}-3\chi+2}{\chi w}\\ \mathcal{T}(\chi)&=(1-\chi^{2})\bar{\tau}\end{aligned} \tag{5.3}$$

are scalar functions that depend on the microstructure variables χ and w, and $\bar{\tau}=\bar{\sigma}/\sqrt{3}$ is the shear yield strength. Note that Φ^{I} depends only on χ and w, *i.e.* λ would not affect the model at a fixed (χ,w) pair. It would, however, indirectly affect the onset of inhomogeneous yielding through the void volume fraction f [46]. The effective stress $\bar{\sigma}$ is the matrix yield strength, taken to depend on its conjugate effective plastic strain $\bar{\epsilon}$, *e.g.* via a power law. The adjustable parameters (t,b,l) are all unit in the basic form of Φ^{I}. The basic model predicts a close upper bound to the limit load for a wide range of χ and w [45]. It, however, overpredicts the stresses associated with the onset of inhomogeneous deformation mainly in the limit of penny-shaped cracks ($w\longrightarrow 0$) and minorly for overly elongated cavities ($w>>1$). The (t,b,l) triplet is adjusted based on exact numerical values. Simple functions have been proposed for (t,b,l) in Paper P1 .

The limit analysis path to the derivation of (5.2) involves *uncontrolled* approximations which would not preserve the upper-bound character of the approach (see [33] for conceptual aspects). In addition, model predictions according to (5.2) were initially assessed modulo existing finite element results of [140] while being mindful of the fact that they pertained to a tetragonal cell

containing a spheroidal void. To overcome this notable discrepancy, the above model was extended in Paper P2 without the simplified evaluation of the dissipation integral. By way of consequence, the following was derived:

$$\Phi(\boldsymbol{\Sigma};\chi,w)=\begin{cases}\dfrac{\mathcal{B}^2}{\bar{\tau}^2}+2f_{\mathrm{b}}\cosh\left[\dfrac{|\Sigma_{\mathrm{n}}|-t\mathcal{S}}{\bar{\tau}}-\sqrt{3\dfrac{\mathcal{B}^2-\left(\Sigma_{\mathrm{sh}}/l\right)^2}{\bar{\tau}^2}}\right]-(1+f_{\mathrm{b}}^2) & \text{for } |\Sigma_{\mathrm{n}}|\geq t\mathcal{S}\\ \left(\dfrac{\Sigma_{\mathrm{sh}}}{l\mathcal{T}}\right)^2-1 & \text{for } |\Sigma_{\mathrm{n}}|\leq t\mathcal{S}\end{cases} \tag{5.4}$$

where

$$\frac{\mathcal{B}^2}{\bar{\tau}^2}=\frac{5}{3}+\chi^4-\frac{2}{3}\sqrt{4+12\chi^4-3\left(\frac{\Sigma_{\mathrm{sh}}}{l\bar{\tau}}\right)^2} \tag{5.5}$$

where $f_{\mathrm{b}}=\chi^2$ is the porosity within the plastically-deformable band.

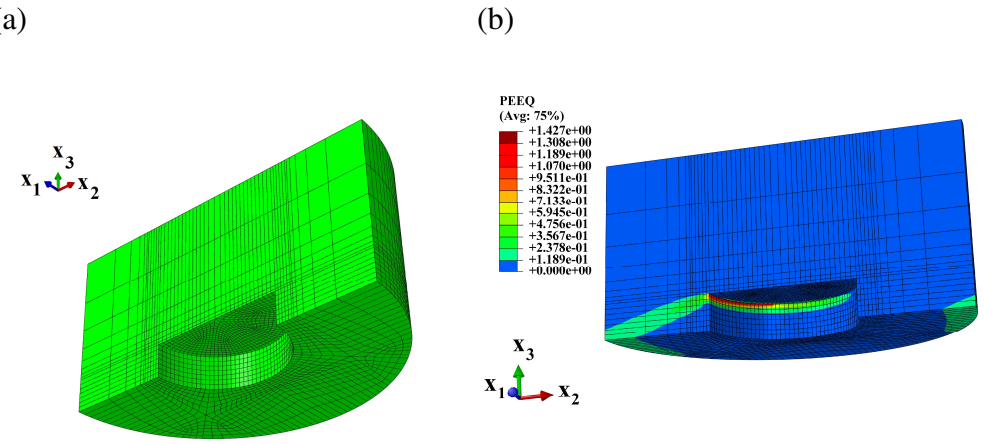

Figure 5.2: (a) Example meshing of a half-cell characterized with $(\chi,w)=(0.4,0.5)$; (b) equivalent plastic strain distribution on initial configuration at the onset of combined internal necking-shearing localization for the same cell [15] (reprinted with permission from *Elsevier*, Ltd).

Based on the principles invoked in Chapter 4, the models have been assessed against numerical results from limit analysis on the same cell geometry. The numerical results were obtained from the single-step small-deformation FEM-based limit analysis (upon the method introduced in Chapter 4) that admit quasi-periodic boundary conditions imposed over the cylindrical cell. See Sec. 4.4

as well as Papers P2 and P3 for more details. Figure 5.2 depicts an example meshing and plastic strain contour resulting from FEM-based limit analysis.

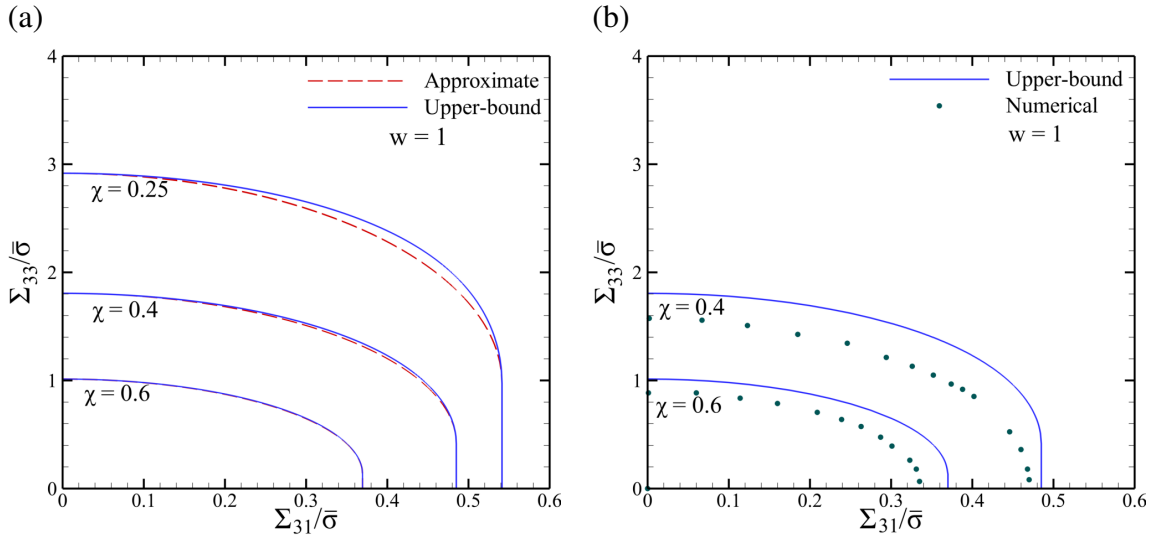

Figure 5.3: Effective yield loci in the Σ_{n}–Σ_{sh} plane: (a) comparison between the upper-bound estimate (5.4) and its approximate counterpart (5.2) for $w = 1$ and several values of χ; (b) comparison between the upper-bound estimate and numerical results emanating from limit analysis on the same cell geometry [15] (reprinted with permission from *Elsevier*, Ltd). See Paper P1 for more details.

Representative yield loci corresponding to the upper-bound criterion (5.4) and its approximate counterpart (5.2) are shown in Fig. 5.3 as solid lines for selective values of the (χ, w) pair. Without loss of generality, one can take, in a single cell, the x_1 and x_3 axes as directed along the shear and normal tractions. Therefore, Σ_{n} and Σ_{sh} can be replaced, respectively, with Σ_{n} and Σ_{sh}. In all plots, the vertical straight parts represent the singular portions of the yield loci. Such parts are not physical inasmuch as they follow from considering discontinuous trial velocity fields. They occupy an increasingly small portion as χ increases so that the criterion resembles more and more an elliptic one in the space of normal and shear stresses. The upper-bound yield loci are also shown in Fig. 5.3b in comparison to their numerical counterparts emanating from limit analysis on the same cell geometry.

Remark: It can be shown that, for $\chi < 0.2$, yield loci given by (5.2) or (5.4) are unlikely to be physical, because strain concentration within the intervoid ligaments does not occur [150]. In such

cases, Gurson-like potentials, that correspond to homogeneous yielding, are more likely to prevail.

5.2 Unified Model for Homogeneous and Inhomogeneous Yielding

Based on limit analysis on the same cylindrical elementary cell as shown in Fig. 5.1, the inhomogeneous criterion (5.4) was further expanded as to incorporate the effect of combined tension and shear on both homogeneous and inhomogeneous processes in a unified fashion. This part was primarily motivated by a simpler model developed by Morin *et al.* [97] with the unit cell subjected to triaxial loading in absence of shear. With the choice of trial velocity fields considered in [97] as basis, so extended as to include shear, the overall model was derived analytically from first principles and is expressed in piece-wise closed form in both upper-bound and quadratic approximate expressions. The model encompasses the stress limits to inhomogeneous yielding, and the transition between subfunctions representing different regimes is cornerless. Following tedious algebraic operations, the model can be expressed in the following form:

$$\Phi(\boldsymbol{\Sigma}, f_{\mathrm{b}}, W, c) = \begin{cases} \sqrt{3}\mathcal{P} - \dfrac{\sqrt{(l\mathcal{T})^2 - (\Sigma_{\mathrm{sh}}^2 + \Sigma_{32}^2)}}{\bar{\tau}} & \\ \text{if } \left| \frac{\Sigma_{\mathrm{ll}}}{\bar{\tau}} + \sqrt{3}(1-c)\left[\dfrac{\sqrt{(l\mathcal{T})^2 - (\Sigma_{\mathrm{sh}}^2 + \Sigma_{32}^2)}}{\bar{\tau}} + \mathrm{sgn}(-\sqrt{3}(1-c) + c\mathcal{P}^{\mathrm{coal}} - \frac{\Sigma_{\mathrm{n}} - \Sigma_{\mathrm{ll}}}{\bar{\tau}}) \right] \right| \leq \frac{t\mathcal{S}}{\bar{\tau}} & \\ \left(\dfrac{\Sigma_{\mathrm{sh}}^2 + \Sigma_{32}^2}{(l\bar{\tau})^2} \right) + \dfrac{\mathcal{P}^2}{3} + 2f_{\mathrm{b}} \cosh\left(\dfrac{\Sigma_{\mathrm{n}} - \mathrm{sgn}(\Sigma_{\mathrm{n}}) t\mathcal{S}}{\bar{\tau}} - \mathcal{P} \right) - (1 + f_{\mathrm{b}}^2) & \text{if } |\mathcal{P}| \geq \mathcal{P}^{\mathrm{coal}} \\ \left(\dfrac{\Sigma_{\mathrm{sh}}^2 + \Sigma_{32}^2}{(l\bar{\tau})^2} \right) + \dfrac{(\mathcal{P}^{\mathrm{coal}})^2}{3} + 2f_{\mathrm{b}} \cosh\left(\dfrac{\Sigma_{\mathrm{n}} - \mathrm{sgn}(\Sigma_{\mathrm{n}}) t\mathcal{S}}{\bar{\tau}} - \mathcal{P}^{\mathrm{coal}} \right) - (1 + f_{\mathrm{b}}^2) & \text{Otherwise} \end{cases} \tag{5.6}$$

where

$$\begin{aligned} \mathcal{P} &= \frac{1}{c}\left(\frac{\Sigma_{\mathrm{n}} - \Sigma_{\mathrm{ll}}}{\bar{\tau}} + \sqrt{3}(1-c)\mathrm{sgn}(-\sqrt{3}(1-c) + c\mathcal{P}^{\mathrm{coal}} - \frac{\Sigma_{\mathrm{n}} - \Sigma_{\mathrm{ll}}}{\bar{\tau}}) \right) \\ (\mathcal{P}^{\mathrm{coal}})^2 &= \frac{5}{3} + f_{\mathrm{b}}^2 - \left(\frac{\Sigma_{\mathrm{sh}}}{\bar{\tau}} \right)^2 - \frac{2}{3}\sqrt{4(1 + 3f_{\mathrm{b}}^2) - 3\left(\frac{\Sigma_{\mathrm{sh}}}{\bar{\tau}} \right)^2} \end{aligned} \tag{5.7}$$

Also, $\Sigma_{\rm ll} = (\Sigma_{\rm mm} + \Sigma_{\rm pp})/2$ is the average lateral stress, and the rest, including the (t, b, l) triad are the same as those introduced for (5.2) and (5.4), taken as unity in the basic form. The reader is referred to Paper P4 for the algebraic details and the approximate counterpart of (5.6).

The numerical assessment of the model was carried out on the same grounds as provided in Sec. 4.4 except for the fact that the zero lateral strain-rate condition (triggering localized plasticity) was relaxed, and thus the inhomogeneous regime emerges as only a portion of the whole yield surface. See Paper P3 on how to impose boundary conditions on the numerical model.

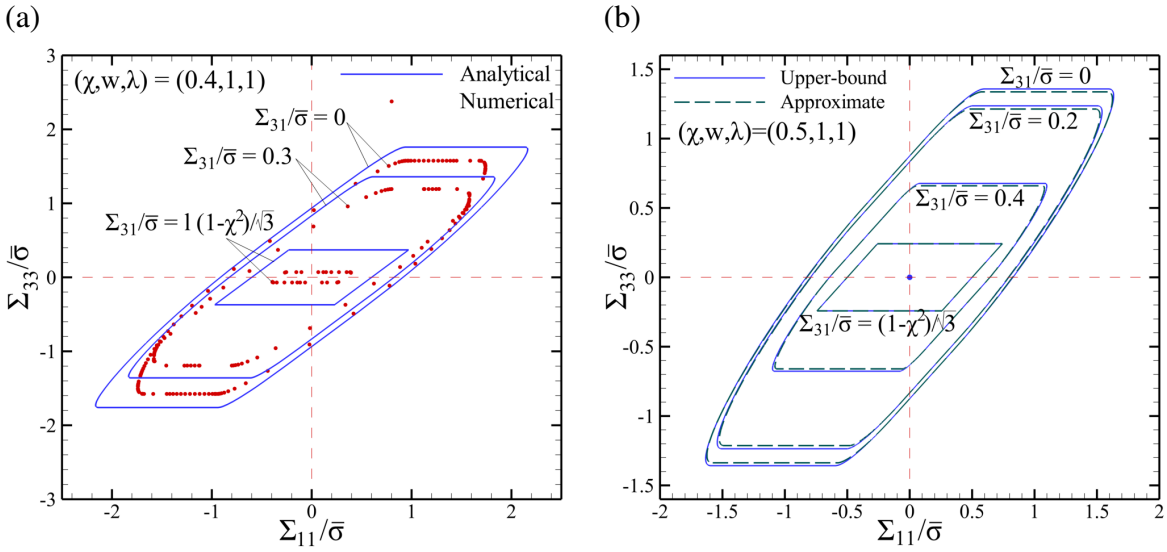

Figure 5.4: (a) Comparison between upper-bound and numerical yield loci in the $\Sigma_{\rm ll}$–$\Sigma_{\rm n}$ stress space for various normalized shear stresses and microstructural parameters $(\chi, w, c) = (0.4, 1, 0.4)$ (corresponding to $\lambda = 1$); (b) predicted yield loci comparing upper-bound and approximate models for various normalized shear stresses and $(\chi, w, c) = (0.5, 1, 0.5)$ (associated with $\lambda = 1$) [18] (reprinted with permission from *Elsevier*, Ltd).

Representative yield loci corresponding to the upper-bound criterion are shown in Fig. 5.4 in comparison to their numerical counterparts for the typical microstructural triple $(\chi, w, \lambda) = (0.4, 1, 1)$, and predicted upper-bound and approximate loci are also compared for different normalized shear stresses for $(\chi, w, \lambda) = (0.5, 1, 1)$. Yielding by the maximum normal stress clearly pertains to the inhomogeneous regime, which proves independent of the lateral stress in this region. Further details in regards to limitations in comparison between analytical and numerical results can

be found in Paper P3 .

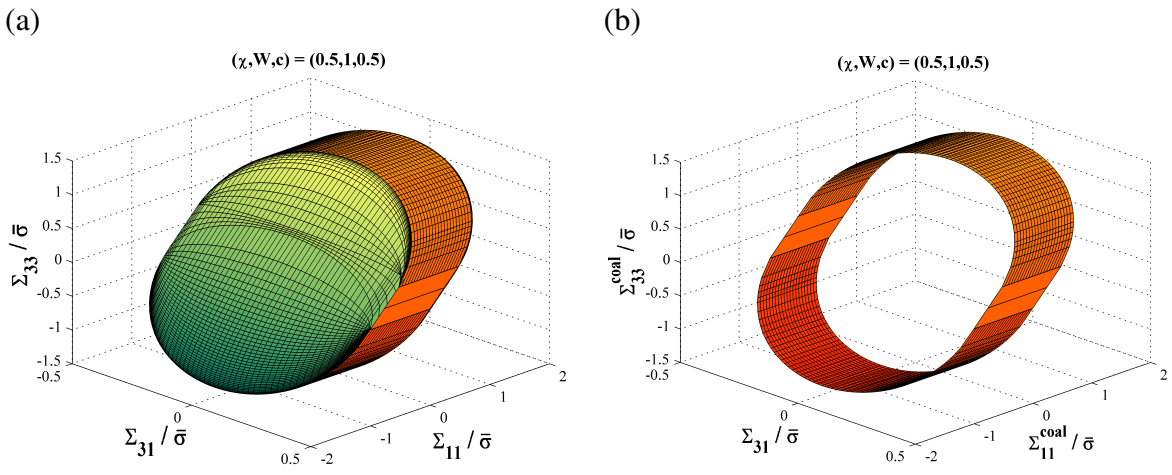

Figure 5.5: (a) 3D yield surface exhibiting axial vs. lateral vs. shear normalized stresses for the representative set of microstructural parameters $(\chi, w, \lambda) = (0.5, 1, 1)$. The sharp-colored sub-surfaces pertain to inhomogeneous yielding [18] (reprinted with permission from *Elsevier*, Ltd).

To gain more insight into the correlation among all three stresses, the complete 3D yield surface for the representative microstructural parameters $(\chi, w, \lambda) = (0.5, 1, 1)$ is shown in Fig. 5.5. The inhomogeneous yield surface is illustrated in orange. For better clarity, the latter is also exclusively shown in Fig. 5.5b. The projection of the cylindroidal inhomogeneous yield surface on the $\Sigma_{\text{ll}} = 0$ plane is nothing but the yield locus exemplified by Fig. 5.3. The lack of uniformity in the lattice lines in Fig. 5.5a pertains to the plotting subroutine developed based on a parametric, rather than closed-form, representation of the yield function Φ. Further improvement of the lattice lines would way darken the surface, and has thus been avoided.

5.3 Isotropic Limit

At the limit of randomly distributed voids, inhomogeneous yielding can be predicted by finding the maximum combination of normal and shear tractions correlating through Eq's (5.2) or (5.4) subjected to a unit normal to the one plane of localization, out of infinite possibilities, that is obtained upon maximization of Φ^{I} as the target function. Under a general stress state, however, effective yielding is governed by a competition of homogeneous and inhomogeneous yield crite-

ria, whichever is met first. Accordingly, the prevailing yield criterion drives the effective yielding mechanism. In extension to a recent effort by Keralavarma [88] investigating through the development of a new tri-surface yield model (the intersection of a homogeneous yield surface and two inhomogeneous surfaces representative of internal necking and combined internal necking with shearing), the present work extends the realm of that investigation into distinctive consideration of two independent microstructural parameters: the ligament parameter χ and the void aspect ratio w (the third parameter being the cell aspect ratio λ can be approximated as unity by virtue of random void distribution).

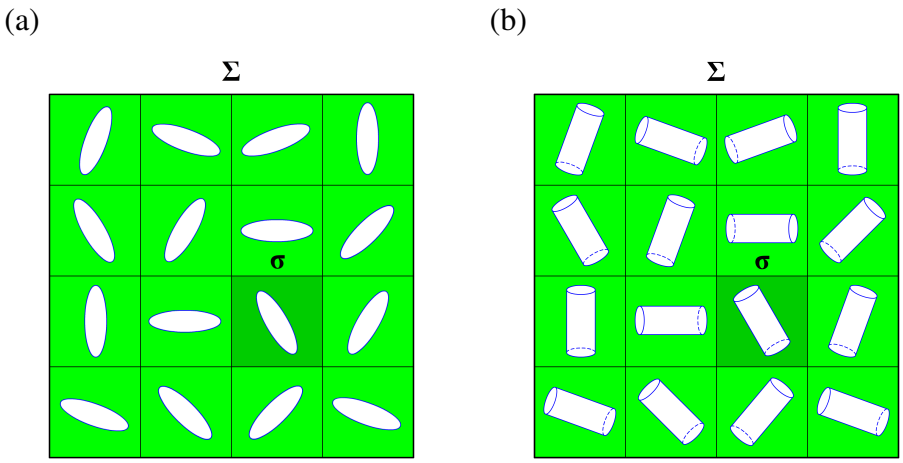

Figure 5.6: (a) Schematic distribution of non-spherical voids with random orientations and their circumscribing cells at early plastic deformation stages, (b) schematic distribution of non-spherical voids (idealized with cylinders) with random orientations.

The voids are taken to have equal shapes while being oriented randomly, as schematically shown in Fig. 5.6, at a macroscopic neighborhood of an arbitrary void. Note, however, that the random dispersion of voids remains feasible only to the extent that plastic deformation is still at early stages, or else some voids would rearrange such that plastic damage continues in a directional manner [89]. To this end, a criterion encompassing the Keralavarma and Benzerga [14] homogeneous model, itself simplified into the GLD model [89] at the limit of isotropic materials, and the inhomogeneous model according to (5.2) was utilized. The homogeneous yield criterion Φ^{H} is a

counterpart of the GLD model revisited for isotropic porous materials following an *ensemble averaging* of effective parameters, originally proposed in [89]. See Paper P4 for details. The effective yield criterion is represented in the Haigh-Westergaard stress space, and the corresponding yield surface is plotted in 3D as well as projected on deviatoric (e.g. the π plane) and meridian planes. The voids are taken to have haphazard orientations but equal shapes. Hence, w generally differs from unity but is common to all voids.

The tri-surface model is firstly authenticated with reference to FEM-based yield loci on deviatoric and meridian planes. This was realized by numerical limit analysis under a normal and two lateral tractions on a cubic unit cell embedding a spherical void admitting periodic boundary conditions, whereby different yield points correspond to different ratios among the three stresses (see Chapter 4 for clarification). The reader can refer to [88] for further details about the employment of this strategy in the present context.

Figure 5.7 compares the tri-surface and numerical yield loci on the deviatoric plane associated with $T = 1$ and $T = 4$ as well as on a meridian plane corresponding to axisymmetric and pure shear with superposed hydrostatic loadings, corresponding to $\theta = 0$ ($L = 1$ accordingly) and $\theta = \pi/6$ ($L = 0$ accordingly), respectively. One can clearly envisage that, unlike with periodic voids, the nonphysical planar parts observed in Fig. 5.3 recede from the model. It is also clear that, at low porosity levels, the FEM yield surface, as well as its effective (tri-surface) counterpart, becomes closer to diffuse yielding whereas, at higher porosities, they tend closer to combined internal necking-shearing. Further details in this respect are explained in [88]. Moreover, the effective analytical surface is not an upper bound. This is due, in part, to the approximation employed in the formulation of the effective yield criterion at the limit of isotropic materials. In particular, the closer-to-real effective yield surface is a combination of both Φ^{H} and Φ^{I}.

The reader should note, according to Fig. 5.7, that the use of (5.2), with or without calibration, loses the upper-bound character at the limit of zero hydrostatic stresses (*i.e.* purely deviatoric loading) under axisymmetric loading, *i.e.* $\theta = n\pi/2, |L| = 1$. This limitation can partly be attributed to the use of different RVE shapes in the analytical and numerical models. This further

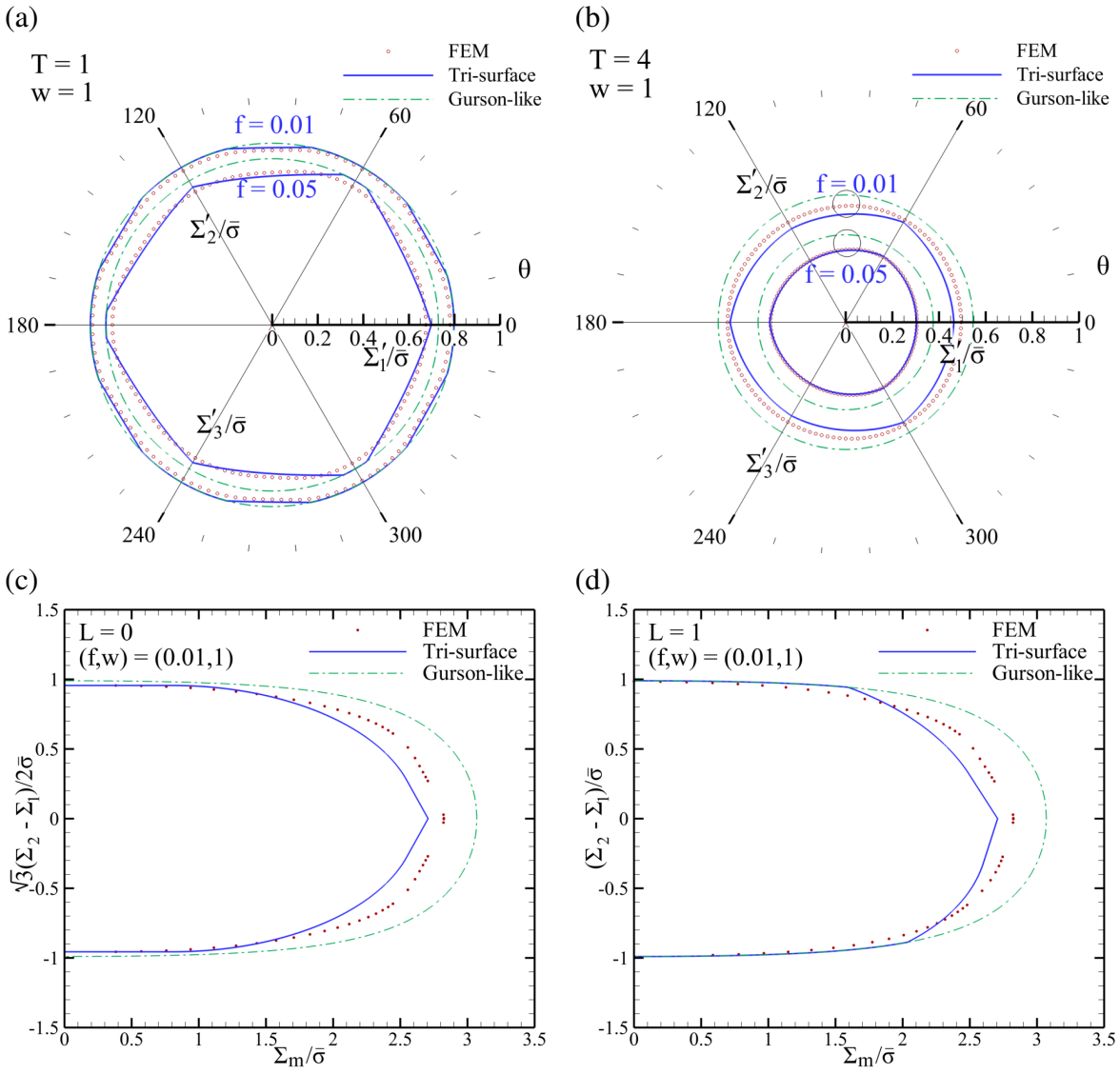

Figure 5.7: Comparison between the tri-surface and numerical yield loci: (a,b) Octahedral plane projections of the yield surface with constant-triaxiality stress states $T = 1$ and $T = 4$ for selective void volume fractions $f = (0.01, 0.05)$; (c,d) cross sections of the yield surface on meridian planes representative of axisymmetric and pure shear with superposed hydrostatic loadings, corresponding to $\theta = 0$ ($L = 1$) and $\theta = \pi/6$ ($L = 0$), respectively.

corroborates the findings of Morin *et al.* [141], who have found the effect of void and cell shape on the yield surface to be minimal for a given microstructural state. The same observation, however, does not necessarily hold in an evolution-based problem, which consists of the entire deformation process from void nucleation to ultimate failure. See [165] for details.

A consequential observation in Fig's 5.7(c) and (d) that can be witnessed at the limit of pure shearing, *i.e.* $\Sigma_{\mathrm{m}} = 0$ at $L = 0$, is the dominance of inhomogeneous yielding, reflected through the effective (tri-surface) locus, over homogeneous yielding. Apart from being an observed fact corroborated by numerical findings [16,17], it can be clearly deduced from the comparison between the shear stresses from Φ^{H} and Φ^{I} at this limit, *i.e.* $\tau = (1 - f)\bar{\tau}$ and $\tau = (1 - f_{\mathrm{b}})\bar{\tau}$, respectively. Nevertheless, the effective mechanism tends towards homogeneous yielding at sufficiently low hydrostatic stresses with sufficiently low-level porosities, when the stress state is axysimmetric, Fig. 5.7c.

The effects induced by χ, as well as the same parametric studies reflected in plots on meridian planes, can be found in Paper P4 . Figure 5.8 depicts the influence induced by the ligament parameter χ and void aspect ratio w on the yield surface projected onto deviatoric planes with constant triaxiality. Figure 5.8 reveals that, with increasing portion of the hydrostatic load (denoted by increasing Σ_{m} or T), the yield surface projection loses its six-fold symmetry, and the surface lies slightly towards the axisymmetric state, *i.e.* $L = 1$ pertaining to $\theta = n\pi/3, n = 0, 1, 2, ...$ (this inclination is more significant when χ varies and w is fixed). Considering the effect of porosity, reflected through the ligament parameter χ, the homogeneous yield surface shrinks whereas the combined necking-shearing surface shrinks faster along with increasing χ. Namely, the effective yielding mechanism tends from diffuse plasticity at $\chi \longrightarrow 0$ towards a combined necking-shearing localized nature with increasing χ. The two surfaces, however, become closer at larger portions of hydrostatic stress, *i.e.* with increasing triaxiality, exemplified with $T = 3$. At this limit, the effective yield mechanism is combined internal necking-shearing at the limit of $L = 0$ admitting $\theta = (2n + 1)\pi/6$, which signifies pure shearing with superposed hydrostatic stress. However, the hydrostatic effect prevails over that of shear, and thus the equivalent stresses would be minimally

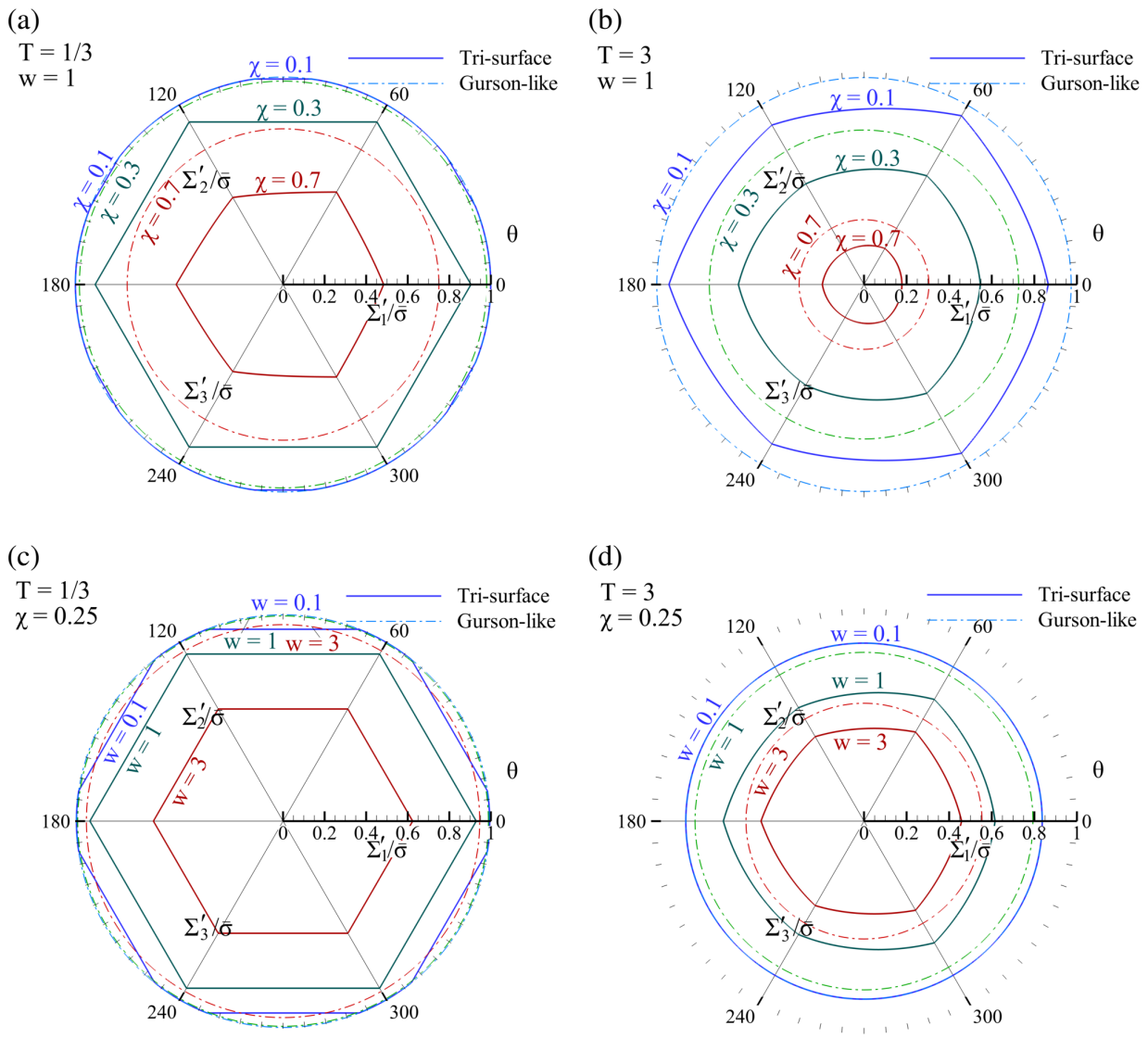

Figure 5.8: (a,b) Effect of the ligament parameter χ (at fixed void aspect ratio $w = 1$), (c,d) effect of the void aspect ratio w (at fixed ligament parameter $\chi = 0.25$), on the effective yield surface projection onto the deviatoric planes with constant triaxialities $T = 1/3$ and $T = 3$.

apart.

Fig's 5.8(c,d) demonstrate combined necking-shearing as the effective yield surface, with a shrinking effective surface for larger values of w, especially for $w > 1$. This has been adduced by former results, as particularly reported in Paper P1 , that the coalescence limit load decreases, even more notably so for $w > 1$, with increasing w. It is also observed that, except at high stress triaxialities (represented by $T = 3$ here) representing large portions of hydrostatic stress, the pure shear limit ($\theta = (2n + 1)\pi/6$) is subdued by the combined internal necking-shearing mechanism. On the other hand, for small to medium triaxialities (see Paper P4 for more illustrations), the effective yielding mechanism for materials with flat voids ($w < 1$) proves to be of a homogeneous type at stress states close to the axisymmetric limit ($\theta = n\pi/3$). For large triaxialities, however, the effective mechanism generally moves towards homogeneous while it still varies from case to case. For flat voids ($w = 0.1$), the effective mechanism is homogeneous under all stress states, just as in the case of axisymmetric loading with smaller triaxialities, whereas it is inhomogeneous for $w \geq 1$ even at this range of large triaxialities. Within periodic void arrays, however, a different trend has been explored wherein the coalescence of flat voids ($w < 1$) could occur at early stages, even so under uniaxial loading ($T = 1/3$) [20]. With randomly distributed voids, both the dilute material limit ($\chi \longrightarrow 0$) and materials containing flat (penny-shaped) cavities yield homogeneously under axisymmetric stress states. See Paper P4 for more information.

Figure 5.9 showcases complete 3D surfaces for a fixed microstructure. For the sake of clarity, the surface corresponding to effective yielding is juxtaposed to the homogeneous yield surface. It is worthy of note that all surfaces are endowed with axis-symmetry and point symmetry at the origin of the stress space. Upon implication, one can deduce that shifting the sign of the Lode parameter, that is realized with a $\pi/3$ rotation on the θ deviatoric plane, equal equivalent stresses will be predicted in accordance with the T-B-L inhomogeneous model.

Finally, the matrix effective plastic strain $\bar{\epsilon}_f$ at a state of incipient inhomogeneous yielding can be regarded as a crude measure of the *strain to failure* $\bar{\epsilon}_f$ at an isotropic limit of the material. In general, there may exist significant plastic deformation after the onset of inhomogeneous yielding.

Yet, the de facto damage mechanism thereafter depends on different extrinsic factors such as the specimen geometry and matrix texture. It is hereby plotted as function of the stress triaxiality. More plots of this type, as well as analogous plots vs. Lode angle θ can be found in Paper P4 .

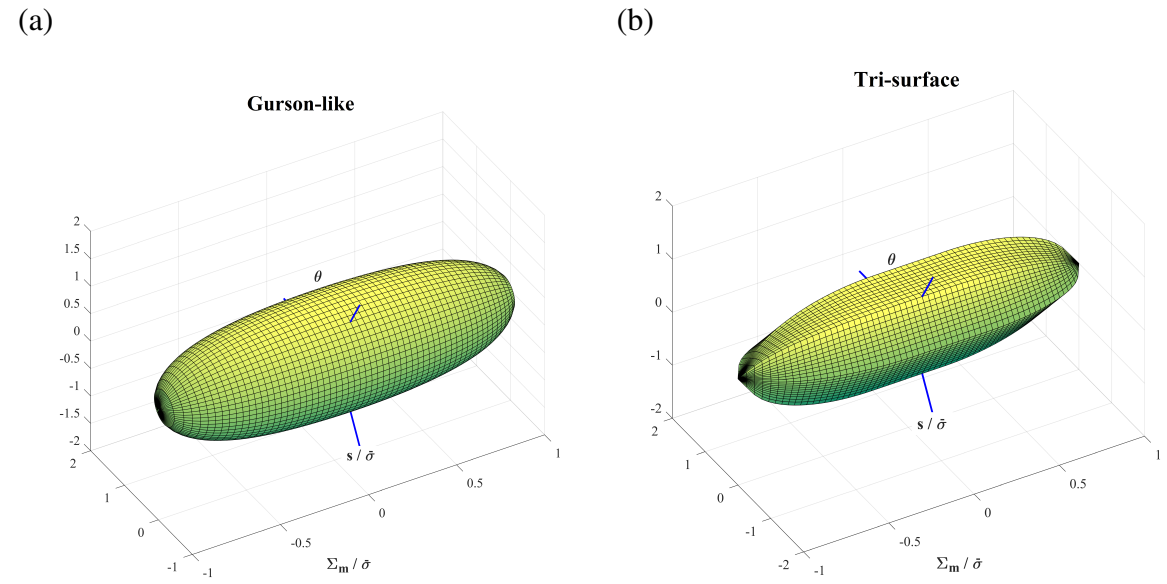

Figure 5.9: Example complete 3D homogeneous and effective surfaces for a frozen microstructure denoted by the $(\chi, w, \lambda) = (0.4, 1, 1)$.

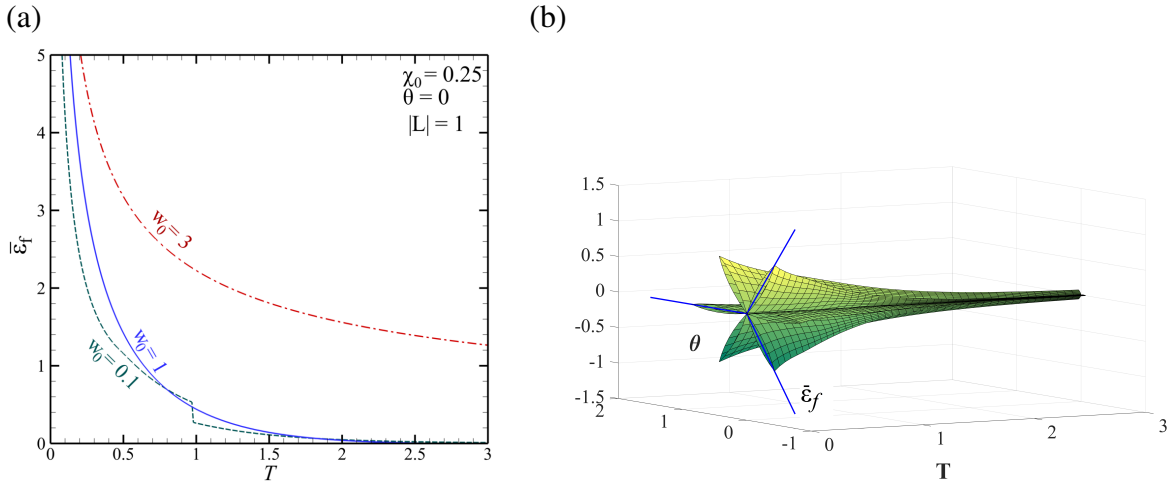

Figure 5.10: (a) Effect of variation in w on the evolution of $\bar{\epsilon}_f$ as function of stress triaxiality T at the example Lode angle of $\theta = 0$; (b) representative 3D surface of $\bar{\epsilon}_f$ evolution as function of Lode angle and stress triaxiality for $(\chi, w) = (0.25, 1)$.

Figure 5.10a illustrates the effects of w alteration on the evolution of $\bar{\epsilon}_f$ as function of stress triaxiality T at the example Lode angle of $\theta = 0$ (corresponding to $L = -1$). The value of $\bar{\epsilon}_f$ is predicted close to zero under stress states close to pure shear ($\theta = (2n+1)\pi/6$) emanating from the inhomogeneous yield criterion $\Phi^{\mathrm{I}} = 0$ happening at early stages of plastic deformation. There are, however, exceptions to this observation. See Paper P4 . The evolution of $\bar{\epsilon}_f$ vs. the Lode angle in simultaneity with stress triaxiality is provided in Fig. 5.10b for $(\chi, w) = (0.25, 1)$. Except at large values of initial w (*i.e.* $w_0 > 1$), the strain to the onset of localization becomes vanishingly small for $T \geq 3$. Also, as earlier revealed by Fig. 5.8 (with more illustrations provided in Paper P4), the effective yielding mechanism is homogeneous for small χ's and w's under small to medium triaxialities, and is inhomogeneous otherwise. This shift in the effective mechanism, indeed, gives rise to slope change in $\bar{\epsilon}_f$ for the case of $w_0 = 0.1$ in Fig. 5.10c.

Remark: The singular limit within $\bar{\epsilon}_f$ at the limit of triaxiality approaching zero (which can be best exemplified by a state of shear-dominated loading) is non-physical inasmuch as failure under shear in a material with *finite porosity* is substantive regardless of void distribution. This calls for more considerate accounting for induced anisotropies emanating from void rotation and/or elongation. By way of consequence, the strain to failure at the $T = 0$ limit would potentially be a large but finite value. This trend has been observed in some recent simple torsion experiments [12]. All the same, a periodic microstructure under *proportional* loading can exhibit varieties of different ductilities under various load combinations. As schematized as in Fig. 5.11, $\bar{\epsilon}_f$ for a state of combined axial and shear loading is shown to be unbounded at the limit of $T = 1/3$, and the shear-dominated low-triaxiality region ($T < 1/3$) is driven by the loading path. A recent investigation by the authors demonstrates the existence of a minimum in the case of a unit cell loaded under combined axial and shear loading. Chapter 7 and Paper P9 elucidate a more thorough discussion on this effect.

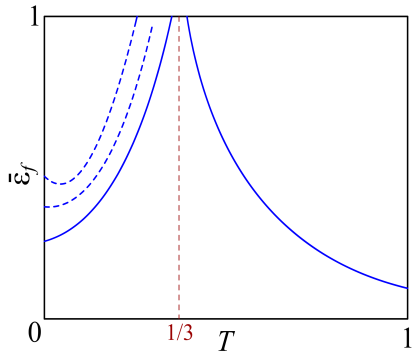

Figure 5.11: Schematic representation of $\bar{\epsilon}_f$ evolution as function of stress triaxiality for a unit cell under arbitrary loading with a periodic void distribution and various loading paths.

CHAPTER 6 HYBRID POROUS PLASTICITY MODEL

The present chapter elucidates the constitutive framework utilized in the present thesis to simulate ductile fracture under combined loading upon numerical implementation. The framework is founded on a multi-surface formulation of porous material plasticity. As such, there are two sorts of multi–surface formulation in the context of micromechanics–based porous material plasticity: *hybrid* and *unified*. In the former, the homogeneous and inhomogeneous models are derived based on different cell geometries, and the cell geometries are united in the latter type. A hybrid micromechanics–based model is developed in this chapter, and numerically implemented to simulate ductile failure under combined tension and shear. The model accounts for the competition of homogeneous and inhomogeneous yield conditions at the fine scale. The constitutive framework comprises existing evolution equations of void elongation and distortion during homogeneous yielding accompanied by original physics–based counterparts for post–localized deformation.

6.1 Hybrid Modeling of Ductile Fracture

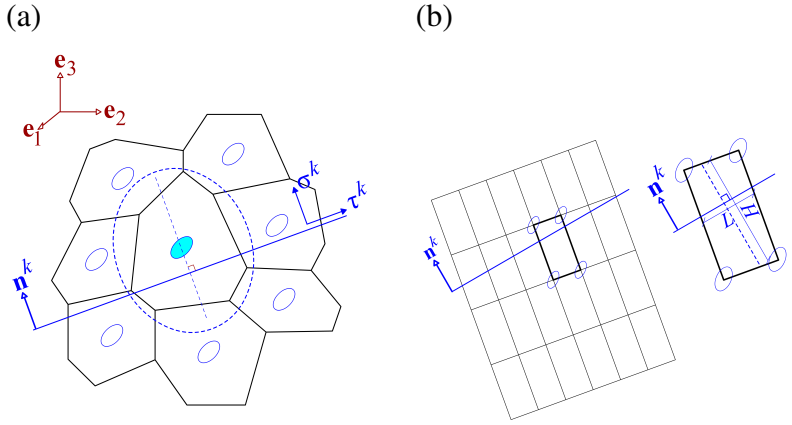

Figure 6.1: (a) Schematic outline of a void aggregate accompanied by a Voronoi tessellation, (b) idealized void cluster admitting an arbitrarily chosen localization plane with normal $\boldsymbol{n}$, together with an excised representative cell.

The voids in a real microscopic domain are distributed neither periodically nor randomly, but through clusters. A statistically robust method for the characterization of clustered void distribution is via Voronoi tessellation [32, 219]. Accordingly, voids during the inhomogeneous process can interconnect along various but a *discrete* number of possible *localization systems* accommodating void interactions in different *localization planes*. Figure 6.1a showcases a schematic void aggregate, and 6.1b shows an idealized equivalent microstructure that can capture the salient features of the circumscribed aggregate. One cannot emphasize enough that, as indicated by Fig. 6.1b, a judiciously chosen localization plane with normal $\boldsymbol{n}$, the underlying microstructure, the average void orientation $\boldsymbol{n}^{(3)}$, and the principal loading directions denoted with $(\boldsymbol{e}_1, \boldsymbol{e}_2, \boldsymbol{e}_3)$ are all independent.

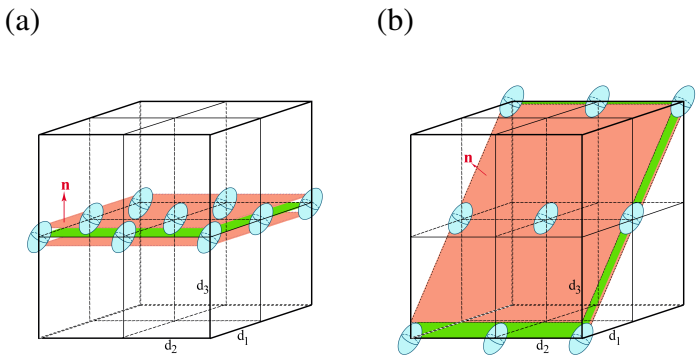

Figure 6.2: Example possible localization systems with their corresponding localization planes and their associated normals.

Figure 6.2 exemplifies two possible localization systems accommodating in-plane void coalescence, *i.e.* coalescence in layers. Nevertheless, normal $\boldsymbol{n}$ can be arbitrarily chosen out of a discrete set of most favorable ones that, in passing, should be evolved according to (6.27) unless otherwise specified. A more complete elaboration on more possible planes, together with their mathematical representations, is provided in Appendix A.

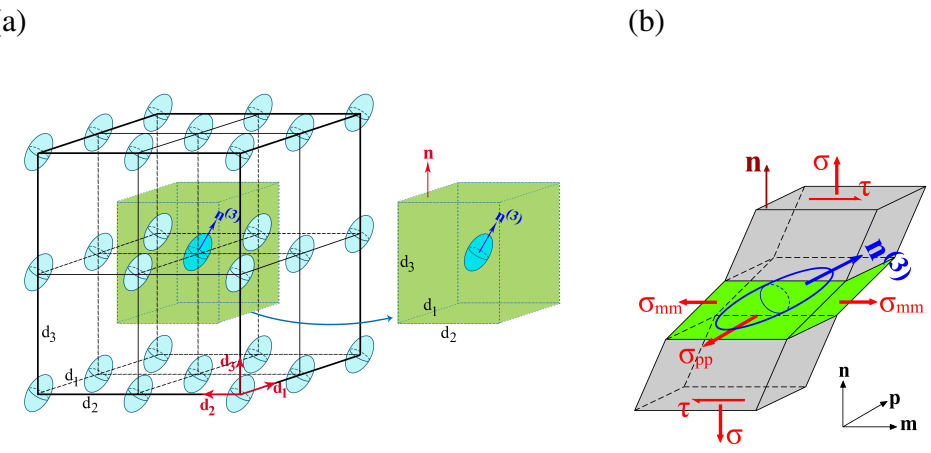

Figure 6.3: (a) Meso–scale positioning of voids in a periodic distribution, accompanied by its equivalent orthorhombic unit cell (RVE) associated with normal $\boldsymbol{n}$ with geometric properties averaged over the tributary volume around the central void; (b) unit cell deformed into monoclinic under the effect of combined tension and shear.

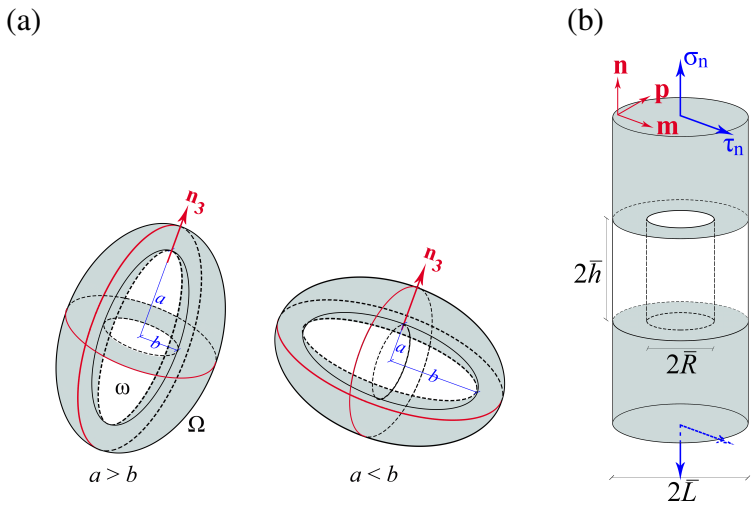

Figure 6.4: Elementary cell identifying the microstructure: (a) during homogeneous plastic deformation, (b) during inhomogeneous plastic deformation.

A more geometrically sound outline of the underlying microstructure is shown in Fig. 6.3a. An effective way to describe the microstructural geometry can then be with the aid of a representative volume element (RVE) constituted from the tributary volume surrounding the central void, as schematized exclusively in Fig. 6.3b having undergone combined tension and shear. Therefore, the

example monoclinic unit cell as shown in Fig. 6.3b can equivalently represent the microstructural domain.

In the simplest case, the cell can be regarded initially orthorhombic which, after shearing, transforms (approximately) into monoclinic. Even upon appreciation of this simplification, the macroscopic response of this cell is not solvable, be the yielding mechanism homogeneous or inhomogeneous. Rather, it is attainable through idealized elementary cells, exemplified by those depicted in Fig's 6.4a and 6.4b, respectively, during homogeneous and inhomogeneous deformation processes. To highlight the distinction between the various RVE's pertaining to different mechanisms, the term "hybrid" is adopted for the proposed model.

In presence of various potentially active mechanisms, a multi-surface formulation is normally employed, commonly with an associated flow rule. Accordingly, the total rate of deformation tensor $\boldsymbol{D}$ is decomposed into the elastic and plastic parts as follows:

$$\boldsymbol{D} = \boldsymbol{D}^{\mathrm{e}} + \boldsymbol{D}^{\mathrm{p}} \tag{6.1}$$

where

$$\boldsymbol{D}^{\mathrm{p}} = \sum_{k=1}^{m} \dot{\Lambda}^k \boldsymbol{N}^k \quad , \quad \boldsymbol{N}^k = \frac{\partial \Phi^k}{\partial \boldsymbol{\sigma}} \tag{6.2}$$

with the $D^{\mathrm{p}k}$'s belong to the m potentially active yielding mechanisms. In the present context, $i = 1$ clearly corresponds to homogeneous yielding, *i.e.* $\boldsymbol{N}^1 = \partial \Phi^{\mathrm{H}} / \partial \boldsymbol{\sigma}$, with 'H' denoting homogeneous yielding. The remaining $\boldsymbol{N}^k$'s are, herein, germane to the various possible localization systems accommodating inhomogeneous yielding, *i.e.* $\boldsymbol{N}^k = \partial \Phi^{k\mathrm{I}} / \partial \boldsymbol{\sigma}$, with 'I' standing for inhomogeneous yielding. Each localization system is then uniquely identified by a unit normal to its associated plane, here denoted with $\boldsymbol{n}$.

Remark 1: At the limit of random void distribution, the number of possible localization modes approaches infinity. Yielding at this limit can be predicted from a maximization problem subjected to a unit normal constraint. See Section 5.3 and Paper P4 for more details.

Remark 2: Upon favorable circumstances, voids can coalesce along plastic plugs formed along

certain directions, thus its name *coalescence in columns* [220] or *necklace coalescence* [221]. The present work presents a model accounting for coalescence in columns (see Chapter 8), but focus will be placed on coalescence in layers. The model will, however, be further predictive by incorporating necklace coalescence, particularly in respect to microstructures with significantly elongated voids or under stress states with a dominant lateral load [33].

Remark 3: Rather than incorporating all yielding mechanisms in a concurrent mood – as stated in (6.2) – the model at the present stage accounts for a successive advancement of mechanisms. That is, the most favorable mechanism deemed possible is triggered at every time step by accounting for the $\Phi = 0$ that is met first. Yet, one should be mindful that more than one mechanism, especially during inhomogeneous yielding, may be active at a time. No possible mechanism should thus be excluded.

The building blocks of the present hybrid model are a homogeneous yield function in the stress space expressed basically as $\Phi^{\mathrm{H}}(\boldsymbol{\sigma}; f, w, \boldsymbol{n}^{(3)}) = 0$ and a discrete set of inhomogeneous yield functions $\Phi^{k\mathrm{I}}(\boldsymbol{\sigma}; f, w, \lambda^k, \boldsymbol{n}^{(3)}, \boldsymbol{n}^k) = 0$, where $k = 1, 2, ..., m$ represents all the localization modes activated by the user. In the present context, Φ^{H} follows the model derived by Keralavarma and Benzerga [14], and Φ^{I} is derived from first principles as earlier pointed out in Chapter 5. The two will be repeated herein for ease of reference.

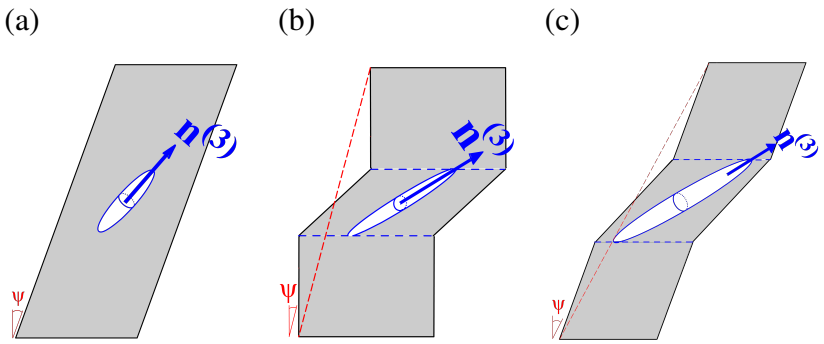

Figure 6.5: Predicted deformation mechanisms under near-simple shearing: (a) totally homogeneous extreme, (b) totally localized extreme (a) de facto inhomogeneous mechanism.

Remark: As schematized in Fig. 6.5 and suggested by direct FEM modeling [16, 21], the

de facto mechanism at the RVE level under combined tension and shear as well as under shear dominance (Fig. 6.5c) is an intermediate mechanism between the fully homogeneous (Fig. 6.5a) and fully localized (Fig. 6.5b) extremes. As such, it is closer to the former at early stages and it approaches the latter end with further advancement of shearing. Therefore, both Φ^{H} and Φ^{I} are subject to some modification in order for the hybrid model be accountable for a thoroughly reliable simulation.

The following sections thus introduce Φ^{H} and Φ^{I} with their proposed modifications.

6.2 Homogeneous Yielding

The underlying microstructure, and thus the lattice transcription in Fig. 6.3, is ineffective during homogeneous yielding in that the corresponding constitutive framework is expressed in terms of porosity f, void aspect ratio w, and void orientation $\boldsymbol{n}^{(3)}$, which are common among all tributary cells. Yet, it would affect the inhomogeneous process at the incipient and continued stages.

6.2.1 Yield criterion

The yield criterion accounting for homogeneous deformation is the model developed by Keralavarma and Benzerga [14]. This model incorporates the combined effects of void shape and interaction as well as matrix anisotropy of Hill type. It can be written in the following form:

$$\Phi^{\mathrm{H}}(\boldsymbol{\sigma}; f, w, \boldsymbol{n}^{(3)}) = C\frac{\sigma_{\mathrm{eq}}^2}{\bar{\sigma}^2} + 2(g+1)(g+qf)\cosh\left(\kappa\frac{\boldsymbol{\sigma}:\boldsymbol{X}}{\bar{\sigma}}\right) - (g+1)^2 - (g+qf)^2 \quad (6.3)$$

where $f = \omega/\Omega$ and $w = a/b$ denote void volume fraction (porosity) and aspect ratio, respectively. Within this framework, the voids are taken as spheroidal, with two equal lateral radii (denoted with b) and a third mismatching radius (known as a), that identifies the void orientation $\boldsymbol{n}^{(3)}$ as schematized in Fig. 6.4a. $w > 1$, $w < 1$ and $w = 1$ would then signify, respectively, a prolate, and oblate, and a spherical void. The porosity f within Φ^{H} is multiplied by a q factor which enables Φ^{H} to capture stress states near simple shearing, which should be above 4/3 [194, 222]. In

the present context, the value introduced by Perrin and Leblond [153], $q = 4/e \approx 1.47$ is proposed. $w > 1$, $w < 1$ and $w = 1$ would then signify, respectively, a prolate, an oblate, and a spherical void.

Also, σ_{eq} is the von–Mises equivalent stress as function of a Hill–type anisotropy tensor [14, 223] stated as

$$\sigma_{\mathrm{eq}}^2 = \frac{3}{2}\boldsymbol{\sigma} : \mathbb{H} : \boldsymbol{\sigma} \tag{6.4}$$

where $\mathbb{H}$ is related to Hill's anisotropy tensor $\mathbb{p}$ through

$$\mathbb{H} \equiv \mathbb{p} + \eta(\boldsymbol{X} \otimes \boldsymbol{Q} + \boldsymbol{Q} \otimes \boldsymbol{X}), \quad \mathbb{p} \equiv \mathbb{J} : \mathbb{h} : \mathbb{J} \tag{6.5}$$

$\boldsymbol{Q}$ and $\boldsymbol{X}$ are functions of void shape and orientation, defined in (6.10), and $\mathbb{J}$ has been defined in Eq. (2.3). The expressions of C, g, κ, η, and α_2 are provided in Paper P7 . $\mathbb{J}$ denotes the deviatoric projection operator, as earlier defined in Chapter 2. The matrix effective stress $\bar{\sigma}$ is taken to depend on its conjugate, briefly termed "plastic strain" $\bar{\epsilon}$, through a hardening law of any arbitrary form . The presently considered hardening rule is the popular power law (see Chapter 7 for details).

6.2.2 Evolution of state

Apart from the all–embracing differential equations describing the evolution of void volume fraction and equivalent plastic strain [33], the evolution of void aspect ratio and orientation associated with Φ^{H} is deduced from [92] and [91, 94], respectively. It is highlighted once again that the successive approach entails only one effective yield function at a time. The following equations are thus developed in terms of one effective Φ.

6.2.2.1 Evolution of porosity

Throughout the plastic deformation process, f is governed by the plastic incompressibility law such that:

$$\dot{f} = (1-f)D_{kk}^{\mathrm{p}} = (1-f)\,\dot{\Lambda}\boldsymbol{I} : \boldsymbol{N} \tag{6.6}$$

with $\dot{\Lambda}$ being the plastic multiplier in rate form, and $\boldsymbol{N} = \partial\Phi/\partial\boldsymbol{\sigma}$ with $\Phi = \Phi^{\mathrm{H}}$.

6.2.2.2 *Evolution of equivalent plastic strain*

Likewise, the evolution of equivalent plastic strain $\bar{\epsilon}$ is obtained through the formation of plastic work equivalence between the macroscopic homogeneous material and the matrix, which reads

$$\boldsymbol{\sigma} : \boldsymbol{D}^{\mathrm{p}} = (1-f)\bar{\sigma}\dot{\bar{\epsilon}} \tag{6.7}$$

where $\bar{\sigma}$ is the conjugate to $\bar{\epsilon}$ through Eq. (7.1). Note that Eq. (6.7 can be exploited for the explicit evaluation of the plastic multiplier $\dot{\Lambda}$ by rearranging in the following equivalent form:

$$\dot{\Lambda} = (1-f)\frac{\bar{\sigma}\dot{\bar{\epsilon}}}{\boldsymbol{\sigma} : \boldsymbol{N}} \tag{6.8}$$

The equations evaluating the evolution of void aspect ratio and orientation conform to different mechanisms. During the homogeneous process, voids can elongate and distort in accordance with plasticity advancing throughout the matrix. In the inhomogeneous process, however, each void is intercepted near its poles by the elastically unloaded rigid–like zones. The existing equations for void shape and orientation evolution should, therefore, be revisited apropos of inhomogeneous yielding. Paper P7 presents the algebraic details to the derivation of these equations. A synopsis of the equations are also enlisted herein.

6.2.2.3 *Evolution of void aspect ratio*

The evolution of the void aspect ratio during homogeneous deformation follows Gologanu *et al.* [92], also employed in [224]:

$$\begin{aligned} \dot{S} &= \boldsymbol{Q} : \boldsymbol{D}^{v} \\ \boldsymbol{Q} &= -\frac{1}{2}(\boldsymbol{n}^{(1)} \otimes \boldsymbol{n}^{(1)} + \boldsymbol{n}^{(2)} \otimes \boldsymbol{n}^{(2)}) + \boldsymbol{n}^{(3)} \otimes \boldsymbol{n}^{(3)} \end{aligned} \tag{6.9}$$

where

$$
\begin{aligned}
\boldsymbol{D}^v &= k\boldsymbol{D}^{\mathrm{p}} + 3\left(\frac{1}{f}\boldsymbol{X}^v - \boldsymbol{X}\right) D^{\mathrm{p}}_{\mathrm{m}} \\
\boldsymbol{X}^v &= \alpha_1(\boldsymbol{n}^{(1)}\otimes\boldsymbol{n}^{(1)} + \boldsymbol{n}^{(2)}\otimes\boldsymbol{n}^{(2)}) + (1-2\alpha_1)\boldsymbol{n}^{(3)}\otimes\boldsymbol{n}^{(3)} \quad , \quad \alpha_1 = \hat{\alpha}_1(w) \\
\boldsymbol{X} &= \alpha_2(\boldsymbol{n}^{(1)}\otimes\boldsymbol{n}^{(1)} + \boldsymbol{n}^{(2)}\otimes\boldsymbol{n}^{(2)}) + (1-2\alpha_2)\boldsymbol{n}^{(3)}\otimes\boldsymbol{n}^{(3)} \quad , \quad \alpha_2 = \hat{\alpha}_2(f) \\
k &= 1 + k_w k_f k_T
\end{aligned}
\tag{6.10}
$$

with the provision of the heuristic factor k (following [92]), calibrated in terms of the void aspect ratio w, porosity f, and stress triaxiality T. See Paper P7 for k_w, k_f, and k_T expressions.

6.2.2.4 Evolution of void orientation

The rate of rotation of the (immaterial) principal axes of the void may be directly obtained from the (material) rotation and strain rates of the void [83, 225], denoted by $\boldsymbol{\Omega}^v$ and $\boldsymbol{D}^v$, respectively. Thus, one can write the total rate of void axis as

$$
\dot{\boldsymbol{n}}^{(3)} = \boldsymbol{\omega}\boldsymbol{n}^{(3)}, \qquad \boldsymbol{\omega} = \boldsymbol{\Omega}^v + \boldsymbol{\Omega}^l \tag{6.11}
$$

where the rotation tensor $\boldsymbol{\omega}$ is the total spin tensor that consists of the void spin, $\boldsymbol{\Omega}^v$, superposed by the void rotation with respect to the material, $\boldsymbol{\Omega}^l$. Here, we exploit $\boldsymbol{\Omega}^v$ as derived in [83, 225] during the homogeneous deformation, and confine it to the plastic ligament at the post–localized inhomogeneous deformation. During the homogeneous process:

$$
\boldsymbol{\Omega}^v = \boldsymbol{\Omega} - \mathbb{C} : \boldsymbol{D}^{\mathrm{p}} \tag{6.12}
$$

where $\mathbb{C}$ is the fourth order spin concentration tensor given by

$$
\mathbb{C} = -(1-f)\mathbb{P} : \mathbb{A}, \qquad \mathbb{A} = [\mathbb{I} - (1-f)\mathbb{S}]^{-1} \tag{6.13}
$$

with $\mathbb{A}$ the strain concentration tensor and $\mathbb{P}$ and $\mathbb{S}$ the Eshelby tensors [226] for a spheroidal inclusion of zero stiffness in an incompressible linear viscous matrix. Further,

$$\boldsymbol{\Omega}^l = \frac{1}{2} \sum_{i \neq j,\, w_i \neq w_j} \frac{w_i^2 + w_j^2}{w_i^2 - w_j^2} \left[(\boldsymbol{n}_i \otimes \boldsymbol{n}_j + \boldsymbol{n}_j \otimes \boldsymbol{n}_i) : \mathbb{A} : \boldsymbol{D}^{\mathrm{p}} \right] \boldsymbol{n}_i \otimes \boldsymbol{n}_j \tag{6.14}$$

where the convention $w_1 = w_2 = w$ and $w_3 = 1$ should be adopted. The case of a spherical void $w = 1$, however, requires a careful treatment; see [14].

6.3 Inhomogeneous Yielding

6.3.1 Yield criterion

The assumptions underlying the mathematical modeling of homogeneous yielding allow for arbitrary orientation of voids whereas inhomogeneous yielding is only warranted in planes. Admittedly, the presently derived inhomogeneous yield conditions have been developed with the void being codirectional with the normal to the localization plane $\boldsymbol{n}$. This lies in the equality of shear-induced responses, based on a Gurson-like velocity field, for an upright and a slanted cylindrical void inside a cylindrical cell. This would inhibit failure under shear–dominated loading (see Paper P6). To bypass this constraint, the real microstructure is mapped into a *surrogate* one, identified with a surrogate void aligned with $\boldsymbol{n}$, as shown in Fig. 6.4b. Accordingly, $\Phi^{k\mathrm{I}}$ for every localization system is parametrized in terms of *effective* microstructural parameters, here denoted with $\bar{\chi}(\boldsymbol{n})$ and $\bar{w}(\boldsymbol{n})$, that correspond to a surrogate cylindrical void aligned with $\boldsymbol{n}$. See Section 6.3.2 for details. With reference to the surrogate RVE shown in Fig. 6.4b, the surrogate parameters read

$$\begin{aligned} \bar{\chi}(\boldsymbol{n}) &= \frac{\bar{R}(\boldsymbol{n})}{\bar{L}(\boldsymbol{n})} \\ \bar{w}(\boldsymbol{n}) &= \frac{h(\boldsymbol{n})}{\bar{R}(\boldsymbol{n})} \\ \bar{\lambda}(\boldsymbol{n}) &= \frac{H(\boldsymbol{n})}{\bar{L}(\boldsymbol{n})} \end{aligned} \tag{6.15}$$

where the third parameter does not enter into Φ^{I} though being indirectly influential (see Section 6.3.4).

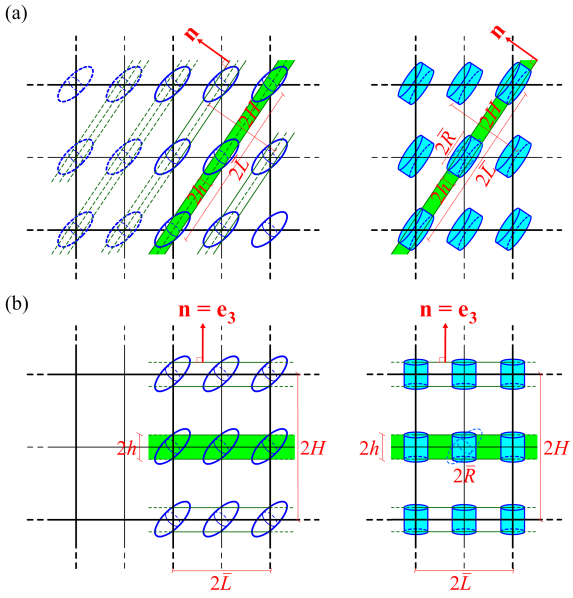

Figure 6.6: 2D idealization of the microstructure with two example localization modes and their associated surrogate microstructures. The figure schematizes the plastically-deformable band as separated from the rigid zones using solid lines and colored regions. Periodicity is denoted with the dashed details.

With reference to Fig. 6.4b, the surrogate microstructures corresponding to two example localization systems are schematized in Fig. 6.6. It is worthy of note that, upon the simple use of χ and w in the basic form of Φ^{I}, failure could never be predicted under shear–dominated loading conditions in that χ would decrease (for a spheroidal void) or, at least, would stay constant (for a cylindrical void), and the void elongation could never trigger internal shearing within the intervoid ligament.

The inhomongeneous yield criterion basically follows Eq. (5.2), but is recast in modified form herein for every localization system according to:

$$\Phi^{k\mathrm{I}}(\boldsymbol{\sigma},\bar{\chi}^k,\bar{w}^k)=\left(\frac{|\sigma^k|-t^k\mathcal{S}(\bar{\chi}^k,\bar{w}^k)}{b^k\mathcal{V}(\bar{\chi}^k)}\right)^2 H(|\sigma^k|-t^k\mathcal{S})+\left(\frac{\tau^k}{\mathcal{T}(\bar{\chi}^k)}\right)^2-1=0 \qquad (6.16)$$

where $\Phi^{k\mathrm{I}}$ denotes the yield function representing inhomogeneous deformation by combined internal necking and shearing in the k'th localization system, and $H(x)$ is the Heaviside step function. Also, $\sigma^k = \boldsymbol{n}^k.\boldsymbol{\sigma}\boldsymbol{n}^k$, $\tau^k = |\boldsymbol{\sigma}\boldsymbol{n}^k - \sigma^k\boldsymbol{n}^k|$ are, respectively, the normal and shear tractions on the k'th plane of localization (the latter expressed in magnitude form), and

$$\begin{aligned}
\mathcal{V}(\bar{\chi}) &= \bar{\tau}\left(2 - \sqrt{1+3\bar{\chi}^4} + \ln\frac{1+\sqrt{1+3\bar{\chi}^4}}{3\bar{\chi}^2}\right) \\
\mathcal{S}(\bar{\chi},\bar{w}) &= \frac{\bar{\tau}}{3}\frac{\bar{\chi}^3 - 3\bar{\chi} + 2}{\bar{\chi}\bar{w}} \\
\mathcal{T}(\bar{\chi}) &= (1 - q_\chi\bar{\chi}^2)\bar{\tau}
\end{aligned} \tag{6.17}$$

are scalar functions that depend on the microstructural variables $\bar{\chi}$ and $\bar{w}$, and $\bar{\tau} = \bar{\sigma}/\sqrt{3}$ is the shear yield strength (the k superscripts have been removed for brevity).

Also, $q_\chi = 1$ in the basic form of the equation but is hereby introduced since the shear stress response based on the present Φ^{I} is overconstrained despite being physically descriptive (see Section 7.1). This overconstraint is partly due to plasticity ideally confined to the inter-void ligament and partly to the notion of $\bar{\chi}$ via the surrogate cell. The latter is revealed by recent cell-level calculations [16] where, at a state of shear domination, plastic deformation is inhomogeneous throughout, yet initially more diffuse than being confined inside the ligament, though it being more significant at the vicinity of the ligament (see Section 7.1 for more details). This overconstraint is strongly suggestive of a calibration to Φ^{I} whereby the effect of $\bar{\chi}$ in the shear term $\mathcal{T}$ or the corresponding evolution of void orientation is retarded based on physics. The following simple form is proposed for q_χ in the present context:

$$q_\chi = \left(q_0 + \frac{q_\infty - q_0}{q_0/\kappa^2 + 1}\right)(1+\psi) \tag{6.18}$$

with $q_\infty = 1$ (pertaining to the absence of shear) and q_0 being function of the void geometry. To the best of the authors' knowledge, $q_0 = 1/3$ and $q_0 = 1/4$ can deliver the most reasonable conformity with numerics for spheroidal and cylindrical voids, respectively. Also, $\kappa \equiv \sigma/\tau$ is the

ratio between the normal and shear tractions on the plane of localization, and $\psi = \tan^{-1}\gamma_{\mathrm{mn}}$ is the shear angle in the $\boldsymbol{m}$–$\boldsymbol{n}$ plane.

6.3.2 *Surrogate parameters*

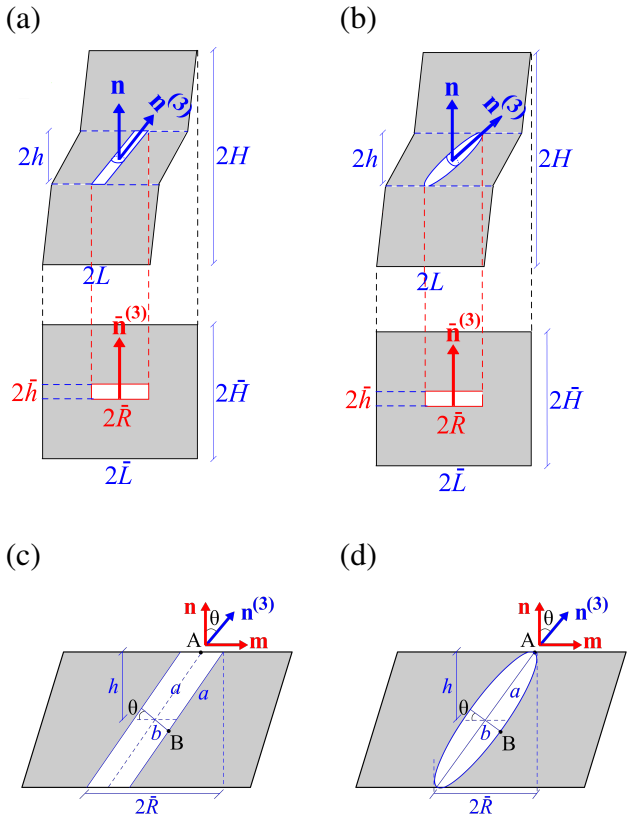

Figure 6.7: Surrogate configuration of a cylindrical cell under combined tension and shear, accompanied by the magnified view of the plastic ligament: (a,c) with a cylindrical void, (b,d) with a spheroidal void.

The notion of surrogate cells implies introducing an effective void aspect ratio $\bar{w}$ and an effective ligament parameter $\bar{\chi}$. Note that the barred notation stands for the average within the plane of localization. Note also that, in addition to $\boldsymbol{n}$, there is an implicit dependence of the above parameters on the void orientation $\boldsymbol{n}^{(3)}$ through $\bar{R}$ and $\bar{h}$.

For formulation purposes, the connection between the void poles and the rigid–like matrix is the underlying principle under combined loading. For cylindrical voids, the void poles are connected to the matrix over the entire upper and lower circular cross sections, as depicted in

Fig. 6.7a. Therefore, the distortion of voids under the effect of shearing will be all alike. The inhomogeneous microstructural evolution would then admit simple geometric relations. See Paper P6 for details.

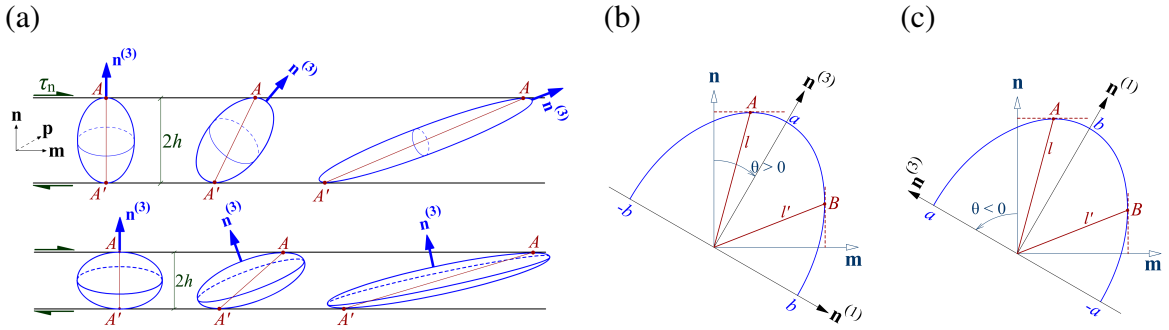

Figure 6.8: (a) Schematized post–localized deformation mechanism, and (b,c) the angles driving the evolved geometry for a spheroidal void under a shear field: (b) a prolate void ($w > 1$), (c) an oblate void ($w < 1$).

All the same, a spheroidal void intercepts with the matrix at two single points of tangency, denoted with A and A' in Fig. 6.8. Correspondingly, prolate ($w > 1$) and oblate ($w < 1$) voids would deform in different manners. That is, prolate voids rotate along with shearing while oblate voids rotate backwards. Both voids, however, deform such that their larger axes incline towards the direction of principal stretch, which proves close to 45° under near–simple shearing. Both deformation modes are schematized in Fig. 6.8a. Altogether, the inhomogeneous microstructural evolution in presence of spheroidal voids can be described by means of the normal and tangential motions of the generatrix AA', as separately schematized for prolate and oblate voids in Fig's 6.8 (a,c), with a magnified void view shown in Fig's 6.8 (b,d). The directional angles identified according to Fig. 6.8b follow the derivations provided in Paper P7 . It should be noted, however, that not all of the angles are independent.

The surrogate cell is obtained by mapping the rotated void with an upright cylinder of axis $\boldsymbol{n}$ with the same volume and porosity, as shown in Fig. 6.7. It implies introducing an effective void aspect ratio, $\bar{w} \equiv \bar{h}/\bar{R}$, and an effective ligament parameter, $\bar{\chi} \equiv \bar{R}/\bar{L}$, related to the internal parameters of the actual microstructure through the following relations:

– Cylinrical voids:

$$\begin{aligned}
\bar{w}(\boldsymbol{n},\boldsymbol{n}^{(3)}) &= w\left(wS+\frac{1}{C}\right)^{-3}\\
\bar{\lambda}(\boldsymbol{n}) &= \frac{\lambda(\boldsymbol{n})}{(1+\gamma_{\mathrm{mn}})^{3}}\\
\bar{\chi}(\boldsymbol{n},\boldsymbol{n}^{(3)}) &= \left(\frac{f\bar{\lambda}}{\bar{w}}\right)^{\frac{1}{3}}
\end{aligned} \tag{6.19}$$

where C and S are short-hand notation for $C=\boldsymbol{n}^{(3)}\cdot\boldsymbol{n}\equiv\cos\theta$ and $S=\boldsymbol{n}^{(3)}\cdot\boldsymbol{m}\equiv\sin\theta$, with θ denoted by the (clockwise positive) angle between the current normal $\boldsymbol{n}$ and void axis $\boldsymbol{n}^{(3)}$, as shown in Fig's 6.7(c,d). Also, $\gamma_{\mathrm{mn}}=2\boldsymbol{m}\cdot\boldsymbol{E}\boldsymbol{n}$ is the shear strain in the m–n plane, and $\boldsymbol{E}=\int\boldsymbol{D}dt$ is the total strain tensor at the current state. See Paper P6 for more details.

– Spheroidal voids:

$$\begin{aligned}
\bar{w}(\boldsymbol{n},\boldsymbol{n}^{(3)}) &= \frac{w}{3\gamma}\left(\frac{1+\mathcal{T}^{2}}{1+\mathcal{T}^{2}w^{2}}\right)^{\frac{3}{2}}\\
\bar{\lambda}(\boldsymbol{n}) &= \frac{\lambda(\boldsymbol{n})}{(1+\eta\gamma_{\mathrm{mn}})^{3}}\\
\bar{\chi}(\boldsymbol{n},\boldsymbol{n}^{(3)}) &= \left(\frac{f\bar{\lambda}}{\bar{w}}\right)^{\frac{1}{3}}
\end{aligned} \tag{6.20}$$

where $0.9\leq\eta<1$ is a heuristic factor introduced so $\bar{\chi}$ can reach unity when the void poles approach the cell corners, and the remaining parameters have been defined in advance. See Paper P7 for more details.

In both $(6.19)_2$ and $(6.20)_2$, $\lambda(\boldsymbol{n})$ is identified at its corresponding localization system, and can be expressed in terms of the basic initial lattice aspect ratios defined as

$$\lambda_1=\frac{d_3}{d_1}\quad,\quad\lambda_2=\frac{d_3}{d_2} \tag{6.21}$$

where d_i have been indicated in Fig. 6.3. In general, the void lattice, and its directors $\boldsymbol{d}_i$ accordingly, need not be aligned with the principal loading directions. Upon convention, however, $\boldsymbol{d}_3$ can

be taken as that with the smallest absolute angle with the major normal load.

In order to derive $\lambda_0(\boldsymbol{n})$ –with the 0 superscript denoting initial state– in terms of λ_1 and λ_2 as well as an arbitrarily-oriented normal $\boldsymbol{n}$, one should evaluate the average inter-void distance inside the plane with normal $\boldsymbol{n}$, here termed L as well as the inter-void distance H, defined as the distance between the inter-plane distance parallel to $\boldsymbol{n}$, as shown in Fig. 6.1b. Having skipped the algebraic details provided in Appendix B, one can write

$$\lambda_0(\boldsymbol{n}_0) = \sqrt{\frac{\lambda_1 \lambda_2}{|\boldsymbol{n}_0 \cdot \boldsymbol{d}_{30}|}} \tag{6.22}$$

which retrieves $\lambda_0 = \sqrt{\lambda_1 \lambda_2}$ when $\boldsymbol{n}_0 = d_{30}$, and λ_1 and λ_2 refer to (6.21). The above-mentioned $\lambda_0(\boldsymbol{n})$ can evolve through the following relation:

$$\lambda(\boldsymbol{n}) = \frac{\lambda_0(\boldsymbol{n}_0)}{\sqrt{\mathcal{J}}} \left(\boldsymbol{n}.(\boldsymbol{F}\boldsymbol{F}^{\mathrm{T}}).\boldsymbol{n} \right)^{\frac{3}{4}} \tag{6.23}$$

with $\boldsymbol{n}$ convected through (6.27). Here, $\boldsymbol{F}$ is the total deformation gradient, with its associated determinant $\mathcal{J} := \det \boldsymbol{F}$. See Appendix B for proof.

6.3.3 Model inputs

In contrast to random dispersion of voids, a periodic domain of voids can accommodate a discrete number of possible localization systems. The possible systems can emanate from the underlying microstructure or arbitrated by the user. Regardless of the origin, a known plane of localization corresponds to a specific inhomogeneous yield criterion, here denoted with $\Phi^{k\mathrm{I}}$, with k representative of the k'th localization mode invoked in the model. Correspondingly, the following inputs should be provided at the initial state:

$$w_0, f_0, \boldsymbol{n}_0^{(3)}, \boldsymbol{n}_0^k, \boldsymbol{d}_{10}, \boldsymbol{d}_{20}, \boldsymbol{d}_{30}, \lambda_1, \lambda_2 \tag{6.24}$$

with the 0 subscript and k superscript denoting the initial state and the k'th active localization system, respectively. Among all, the first two are evolved implicitly (see Sections 6.2.2 and 6.3.4),

and the rest are evolved explicitly in terms of their initial values.

6.3.4 Evolution of state

The equations accounting for the evolution of porosity f and equivalent plastic strain $\bar{\epsilon}$, stated in (6.6) and (6.8), are inclusive of the whole process. So is the general rate stated in (6.11). However, the counterparts to the evolution of void aspect ratio as well as the spin tensors $\boldsymbol{\Omega}^v$ and $\boldsymbol{\Omega}^l$ in (6.9) and (6.12) corresponding to inhomogeneous yielding have not been developed except for $\dot{s}$ under triaxial loading in [20, 150]. In the present study, these equations have been proposed for both cylindrical and spheroidal voids. Papers P6 and P7 , respectively, report the journey to these equations. The equations are restated herein for ease of reference.

6.3.4.1 Orthotropy and localization planes

During the plastic deformation, the principal orthotropy $(\boldsymbol{e}_L, \boldsymbol{e}_T, \boldsymbol{e}_S)$ as well as the void lattice directors $(\boldsymbol{d}_1, \boldsymbol{d}_2, \boldsymbol{d}_3)$ rotate along with the material. Therefore

$$\begin{aligned} &\boldsymbol{e}_m = \boldsymbol{R}\boldsymbol{e}_m^{(0)} \ , \ \boldsymbol{d}_n = \boldsymbol{R}\boldsymbol{d}_n^{(0)} \\ &\boldsymbol{F} = \boldsymbol{R}\boldsymbol{U} \end{aligned} \tag{6.25}$$

where $\boldsymbol{R}$ and $\boldsymbol{U}$ emanate from the polar decomposition of the deformation gradient tensor $\boldsymbol{F}$ at every step of the process, with $\boldsymbol{R}$ being the rotation part. $m =$ (L,T,S) stands for the principal orthotropy axes, and $n = 1, 2, 3$ constitutes the void lattice directors. $\boldsymbol{F}$ can be the directly–imposed or post-processed deformation gradient. Due to the incremental nature of numerical implementation, one can write

$$\boldsymbol{F}^{(i)} = \prod_{j=0}^{i} \boldsymbol{F}^{(j)} \tag{6.26}$$

where $\boldsymbol{F}^{(j)}$ is the deformation gradient between the $j-1$'st and j'th time steps constituted by the incremental displacements at the j'th step, where $j = 1, 2, ..., i$.

Note that the present constitutive framework is expanded based on a corotational formulation, *i.e.* the equations are expanded within the rotated material configuration. Therefore, Eq. (6.25) is

implicit in the formulation.

The normal vector $\boldsymbol{n}$, however, should be evolved through an area vector transformation law [227]. That is

$$\boldsymbol{n} = \frac{\boldsymbol{F}^{-T}\boldsymbol{n}_0}{|\boldsymbol{F}^{-T}\boldsymbol{n}_0|} \tag{6.27}$$

with $|.|$ denoting a vector magnitude.

Having updated the normal $\boldsymbol{n}$, the direction of the resolved shear traction onto the plane with normal $\boldsymbol{n}$ would become

$$\begin{aligned} \boldsymbol{m} &= \frac{\tau}{|\tau|} \\ \boldsymbol{p} &= \boldsymbol{n} \times \boldsymbol{m} \end{aligned} \tag{6.28}$$

where the shear traction τ has been defined below Eq. (5.2), and $\boldsymbol{p}$ is the third base vector completing the orthonormal basis tied to the localization plane corresponding to normal $\boldsymbol{n}$. In case, however, the shear traction vanishes, as in the case of triaxial loading, Eq. (6.28) would be ill–defined. In this case, $\boldsymbol{m}$ and $\boldsymbol{p}$ would stay constant, equal to their previous values (or to their initial values in case the loading is shearless throughout).

One cannot emphasize enough that the foregoing equations of microstructural evolution, as well as the current surrogate state, are valid throughout the process notwithstanding they are mainly invoked in the constitutive framework from the onset of inhomogeneous deformation onwards. Prior to that, they should be updated for use in the evaluation of Φ^{I}.

6.3.4.2 Evolution of void aspect ratio

Upon definition, the void aspect ratio for both cylindrical and spheroidal voids is expressed as $w = a/b$, with the difference lying in a and b, as better clarified in Fig's 6.7(a) and (b). Details aside, one can write, having defined $s = \ln w$:

– Cylindrical voids:

$$\dot{s} = \frac{1}{2}\left(\frac{3C^2}{c} - \frac{1}{f}\right)\boldsymbol{n}\cdot\boldsymbol{D}^{\mathrm{p}}\boldsymbol{n} + \frac{3CS}{c}\boldsymbol{m}\cdot\boldsymbol{D}^{\mathrm{p}}\boldsymbol{n} \tag{6.29}$$

where the ligament volume fraction, c, is given by

$$c^3 = C^3\frac{fw^2}{\lambda^2} \tag{6.30}$$

– Spheroidal voids:

To obtain the post–localized differential equation for the spheroidal void aspect ratio w, the time rate of ℓ (shown in Fig. 6.8) should be developed on the account that the top and bottom void boundaries are attached to the rigid zones. The details provided in Paper P7 are set aside here. In essence:

$$\dot{s} = \frac{(w^2+\mathcal{T}^2)^2}{(w^4+\mathcal{T}^2)(1+\mathcal{T}^2)\left[2-3\frac{\mathcal{T}^2(2w^2-w^4+\mathcal{T}^2)}{(w^4+\mathcal{T}^2)(w^2+\mathcal{T}^2)}\right]}\left[\left(\frac{3}{c} - \frac{(w^4+\mathcal{T}^2)(1+\mathcal{T}^2)}{f(w^2+\mathcal{T}^2)^2}\right)D_{\mathrm{nn}} + \frac{6}{c}\frac{(w^2-1)\mathcal{T}}{w^2+\mathcal{T}^2}D_{\mathrm{nm}}\right] \tag{6.31}$$

for a prolate void with $w > 1$, and

$$\dot{s} = \frac{(w^2+\mathcal{T}^2)^2}{(w^4+\mathcal{T}^2)(1+\mathcal{T}^2)\left[1-\frac{\mathcal{T}^2(-2w^2+w^4-\mathcal{T}^2)}{(w^4+\mathcal{T}^2)(w^2+\mathcal{T}^2)}\right]}\left[\left(-\frac{3}{c} + \frac{(w^4+\mathcal{T}^2)(1+\mathcal{T}^2)}{f(w^2+\mathcal{T}^2)^2}\right)D_{\mathrm{nn}} - \frac{6}{c}\frac{(w^2-1)\mathcal{T}}{w^2+\mathcal{T}^2}D_{\mathrm{nm}}\right] \tag{6.32}$$

for an oblate void with $w < 1$. In the above equations, $\mathcal{T} = S/C = \tan\theta$, where C and S are short–hand notation for $C = \boldsymbol{n}^{(3)}\cdot\boldsymbol{n} \equiv \cos\theta$ and $S = \boldsymbol{n}^{(3)}\cdot\boldsymbol{m}$. Also

$$D_{\mathrm{nn}} = \boldsymbol{n}\cdot\boldsymbol{D}^{\mathrm{p}}\boldsymbol{n}$$

$$D_{\mathrm{mn}} = \boldsymbol{m}\cdot\boldsymbol{D}^{\mathrm{p}}\boldsymbol{n}$$

with elastic strain rates neglected. The ligament volume fraction can be expressed in correlation with (f, w, λ, θ) as

$$c = \left(\frac{3\gamma f}{w\lambda^2}\right)^{1/3}\sqrt{\frac{\mathcal{T}^2+w^2}{\mathcal{T}^2+1}} \tag{6.33}$$

where $\gamma = 1/2$ is the shape factor for a spheroidal void.

Note that Eq. (6.31) retrieves Eq. (12) of [150] at the limit of an upright void under a triaxial stress space. See Paper P7 for details.

6.3.4.3 Evolution of void orientation

During inhomogeneous deformation, one can write, due to plasticity concentrated in the ligament:

$$\boldsymbol{\Omega}^v = \boldsymbol{\Omega} - \frac{1}{c}\mathbb{C} : \boldsymbol{D}^{\mathrm{p}} \tag{6.34}$$

with $1/c$ appearing to represent the plastic rate of deformation inside the ligament.

The post–localized $\boldsymbol{\Omega}^l$, however, should be rederived from first principles. Madou and Leblond [83] have shown that the general form initiated in [91, 225] requires significant amendments due to strong nonlinear effects. They did so by introducing heuristic coefficients calibrated using a large number of finite–element based limit analyses. Here we obtain simpler, parameter–free and probably more accurate equations by considering the constrained kinematics pertaining to post–localization. This involves plastic incompressibility of the intervoid ligament and the fact that the top and bottom boundaries of the void move rigidly with the above and bottom material layers. Details aside, $\boldsymbol{\Omega}^l$ can be written as

$$\Omega^l = \frac{\dot{S}}{S}\boldsymbol{m}\otimes\boldsymbol{m} + \frac{\dot{C}}{C}\boldsymbol{n}\otimes\boldsymbol{n} = \frac{\dot{\mathcal{T}}}{\mathcal{T}}\left(C^2\boldsymbol{m}\otimes\boldsymbol{m} - S^2\boldsymbol{n}\otimes\boldsymbol{n}\right) \tag{6.35}$$

where

$$\dot{\mathcal{T}} = \frac{(\mathcal{T}^2+w^2)(1+\mathcal{T}^2)}{\mathcal{T}(1-w^2)}\left[\frac{\dot{c}}{c} - \frac{1}{3}\left(\frac{\dot{f}}{f} - 2\frac{\dot{\lambda}}{\lambda}\right) + \left(\frac{1}{3} - \frac{w^2}{\mathcal{T}^2+w^2}\right)\dot{s}\right] \tag{6.36}$$

The rates of internal parameters entering the right–hand side of this equation are all established relations. $\dot{c}/c$ can be determined by neglecting the volume change of the elastically–unloaded zones. Thus,

$$\frac{\dot{c}}{c} = \frac{\dot{h}}{h} - \frac{\dot{H}}{H} = \frac{D_{33}}{c} - D_{33} = \frac{1-c}{c}\boldsymbol{n}\cdot\boldsymbol{D}^{\mathrm{p}}\boldsymbol{n} \tag{6.37}$$

Also,

$$\begin{aligned}\frac{\dot{f}}{f} &= \left(\frac{1}{f}-1\right) D^{\mathrm{p}}_{kk} \\ \frac{\dot{\lambda}}{\lambda} &= \frac{\dot{H}}{H} - \frac{\dot{L}}{L} = D_{\mathrm{nn}} - \frac{1}{2}\left(D_{\mathrm{mm}} + D_{\mathrm{pp}}\right)\end{aligned} \tag{6.38}$$

and

$$D_{\mathrm{nn}} = \boldsymbol{n}\cdot\boldsymbol{D}^{\mathrm{p}}\boldsymbol{n} \quad , \quad D_{\mathrm{mm}} = \boldsymbol{m}\cdot\boldsymbol{D}^{\mathrm{p}}\boldsymbol{m} \quad , \quad D_{\mathrm{pp}} = \boldsymbol{p}\cdot\boldsymbol{D}^{\mathrm{p}}\boldsymbol{p}$$

6.3.5 Plastically anisotropic matrix materials

The inhomogeneous yield functions derived in the present work are, though well–sophisticated, limited in certain respects. Among the limitations is disregarding matrix anisotropy whereas the use of Φ^{H} after Keralavarma ane Benzerga [14] is strongly suggestive of its consideration. This was, in turn, embodied by other researchers after the presently developed models were published. The present thesis is, hence, partly aimed at making use of the ensuing models for numerical implementation purposes. This will furnish the constitutive framework to account for the effect of matrix anisotropy throughout the deformation process thanks to both Φ^{H} and Φ^{I} incorporating that effect.

In the case of an orthotropic matrix material, plastic anisotropy idealized as Hill–like was incorporated by Keralavarma and Chockalingam [96]. Following a similar procedure and from the same principles as in Papers P1 and P2 , the following inhomogeneous model was developed therein:

$$\Phi^{\mathrm{I}} = \frac{1}{2}\frac{\boldsymbol{\sigma}_{\mathrm{sh}} : \mathbb{p} : \boldsymbol{\sigma}_{\mathrm{sh}}}{\bar{\tau}^2} + 2q_\chi f_{\mathrm{b}} \cosh\left(\frac{\sigma}{\sigma_{\mathrm{c}}}\ln\frac{1}{q_\chi f_{\mathrm{b}}}\right) - \left[1+(q_\chi f_{\mathrm{b}})^2\right] \tag{6.39}$$

where $\boldsymbol{\sigma}_{\rm sh} = \tau(\boldsymbol{n}\otimes\boldsymbol{m} + \boldsymbol{m}\otimes\boldsymbol{n})$ is the auxiliary shear stress tensor, and

$$\begin{aligned}
&\frac{\sigma_{\rm c}}{\bar{\tau}} = 3b\sqrt{\frac{2}{5}\hat{h}_q}\left[\ln bu\left(1+\sqrt{1+\frac{1}{(bu)^2}}\right) - \sqrt{1+\frac{1}{(bu)^2}}\right]_{u=1}^{1/f_{\rm b}} \\
&3b^2 = \frac{\hat{h}_t}{\hat{h}_q} + \frac{5\alpha}{8\mathcal{W}^2}\frac{\hat{h}_a}{3\hat{h}_q} \quad , \quad \alpha = \frac{1}{12}\left[1 + q_\chi f_{\rm b} - 5(q_\chi f_{\rm b})^2 + 3(q_\chi f_{\rm b})^3\right]
\end{aligned} \tag{6.40}$$

with $q_\chi = 1$ in the basic form. The parameters $\hat{h}_q$, $\hat{h}_t$, and $\hat{h}_a$ are scalar anisotropy factors as functions of $\hat{h}_{ij}$, with $\hat{\mathbb{h}}$ denoting a formal inverse for $\mathbb{h}$, admitting $\hat{\mathbb{h}} : \mathbb{h} = \mathbb{h} : \hat{\mathbb{h}} = \mathbb{J}$. Note also that, unlike those associated with $\Phi^{\rm H}$ (where $\hat{h}_{ij}$ components are expressed in the void-tied basis), $\hat{h}_{ij}$'s corresponding to $\Phi^{\rm I}$ are expressed in the basis tied to the *surrogate* void. See [14, 96] for equations. It is, also, noteworthy that $\mathbb{p}$ is to be calculated within the principal loading frame, that is initially taken coincident with the global coordinate system herein. See Paper P9 for more details. The concept of introducing q_χ into (6.40) follows the same rationale as put forward for (6.16), and q_χ can be taken identical to (6.18) for combined tension and shear, and 1 in absence of shear.

Finally, $\mathcal{W}$ is a function of $f_b = \bar{\chi}^2$ and $\bar{w}$ that is calibrated modulo numerical results, that reads

$$\mathcal{W} = \begin{cases} \dfrac{q_\chi f_b \bar{w}^2}{4\mathcal{W}_0} + \mathcal{W}_0 & \text{for } \sqrt{q_\chi f_b}\bar{w} < 2\mathcal{W}_0 \\ \bar{\chi}\bar{w} & \text{for } \sqrt{q_\chi f_b}\bar{w} \geq \mathcal{W}_0 \end{cases} \tag{6.41}$$

where $\mathcal{W}_0$ is an adjustable parameter (see [96] for the value).

Upon convention, $\bar{\sigma}$ for an orthotropic matrix material is adopted as the yield strength in one principal direction of orthotropy, and the components of the anisotropy tensor $\mathbb{p}$ are scaled accordingly.

6.4 Time Integration of Constitutive Equations

Based on the foregoing discussion in Chapter 4, the constitutive framework of the present hybrid model, following the governing equations stipulated in Sec. 4.6, is formulated within a

corotational framework. Constitutive laws, therefore, need be written in the rotated configuration, with quantities indicated by the tilde ($\sim$) symbol. The objective rate of stress $\overset{\triangledown}{\boldsymbol{\sigma}}$ in (2.17) will be then replaced with $\dot{\boldsymbol{\sigma}}$, and the spin tensor $\boldsymbol{\Omega}$ will vanish from the void orientation evolution in (6.11). Further details can be observed in [224] in this regard.

Due to the existence of high geometric nonlinearity within the problems of porous plasticity, the implicit method of plasticity has been adopted to solve for state variables. Accordingly, the following state variables are updated via the implicit method during the homogeneous and post–localized deformation processes:

– During homogeneous deformation:

$$\boldsymbol{V} = \left[\boldsymbol{\sigma}', \sigma_m, f, \bar{\epsilon}, d\Lambda, S\right]^T \tag{6.42}$$

– During inhomogeneous deformation:

$$\boldsymbol{V} = \begin{cases} \left[\boldsymbol{\sigma}', \sigma_m, f, \bar{\epsilon}, s\right]^T & \text{for } |\sigma| \geq \mathcal{S} \\ \\ \left[\boldsymbol{\sigma}', \bar{\epsilon}, s\right]^T & \text{for } |\sigma| \leq \mathcal{S} \end{cases} \tag{6.43}$$

with $\mathcal{S}$ defined after Eq. (5.2).

$d\Lambda$ is the increment in plastic multiplier, and the rest of variables have been defined in the context. In the singular portion of the yield surface associated with $|\sigma| \leq t\mathcal{S}$, $\boldsymbol{D}^p$ and $\boldsymbol{N} \equiv \partial\Phi/\partial\boldsymbol{\sigma}$ will be traceless, and thus (σ_m, f) would stay constant.

The main portion within the flow rule in Eq. (4.12) to derive the evolution equations of porosity f, void aspect ratio w, and equivalent plastic strain $\bar{\epsilon}$, is the first derivative of the flow potential Φ with respect to stress. To this end

$$\tilde{\boldsymbol{N}}^{\mathrm{H}} \equiv \frac{\partial \Phi^{\mathrm{H}}}{\partial \tilde{\boldsymbol{\sigma}}} = 3C\frac{\tilde{\mathbb{H}} : \tilde{\boldsymbol{\sigma}}}{\bar{\sigma}^2} + 2(g+1)(g+qf)\kappa \sinh\left(\kappa\frac{\tilde{\boldsymbol{\sigma}} : \tilde{\boldsymbol{X}}}{\bar{\sigma}}\right)\frac{\tilde{\boldsymbol{X}}}{\bar{\sigma}} \tag{6.44}$$

and, for Φ^{I} obeying (6.16), for instance:

$$\tilde{\boldsymbol{N}}^{\mathrm{I}} \equiv \frac{\partial \Phi^{\mathrm{I}}}{\partial \tilde{\boldsymbol{\sigma}}} = \frac{2}{\mathcal{V}^2}\left(\sigma_n - t\mathrm{sgn}(\sigma_n)\mathcal{S}\right)\tilde{\boldsymbol{n}} \otimes \tilde{\boldsymbol{n}}\, \mathcal{H}(|\sigma_n| - \mathcal{S}) + 2\frac{\tilde{\boldsymbol{\tau}}_{\boldsymbol{n}} \otimes \tilde{\boldsymbol{n}}}{\mathcal{T}^2} \tag{6.45}$$

with $\mathcal{H}(x)$ has been formerly defined. Accordingly:

$$\begin{aligned} &\frac{\partial \Phi}{\partial \tilde{\boldsymbol{\sigma}}'} = \mathbb{J} : \frac{\partial \Phi}{\partial \tilde{\boldsymbol{\sigma}}} \quad \therefore \quad \frac{\partial \Phi}{\partial \sigma_{kk}} \equiv \frac{1}{3}\frac{\partial \Phi}{\partial \sigma_{\mathrm{m}}} = \boldsymbol{I} : \frac{\partial \Phi}{\partial \tilde{\boldsymbol{\sigma}}} \\ &\tilde{\boldsymbol{D}}^{\mathrm{p}} = \dot{\Lambda}\frac{\partial \Phi}{\partial \tilde{\boldsymbol{\sigma}}} \quad \therefore \quad D^{\mathrm{p}}_{kk} \equiv 3D^{\mathrm{p}}_{m} = \dot{\Lambda}\frac{\partial \Phi}{\partial \sigma_{kk}} \end{aligned} \tag{6.46}$$

Note that, within the confines of the present work, the constitutive derivations are only given for the post–localization regime in Paper P7 . The reader will be well–advised to follow [224] for steps to implementation of the K–B model in (6.3).

6.4.1 Newton–Raphson method

Via a similar procedure as that described in [224], a semi–implicit integration algorithm is employed herein to integrate the post–localized constitutive equations, with the state variables as assembled in (6.43). To this end, one should define a residual with respect to every state variable. At the post–localized process, for instance:

$$[\boldsymbol{R}] = \left[\boldsymbol{R}_{\tilde{\boldsymbol{\sigma}}'},\ R_{\tilde{\sigma}_{\mathrm{m}}},\ R_f,\ R_{\bar{\epsilon}},\ R_s\right]^T \tag{6.47}$$

with their expressions written, in expanded form, as follows:

$$\begin{aligned} \boldsymbol{R}_{\tilde{\boldsymbol{\sigma}}'} &= \frac{1}{2\mu}\left(\frac{\tilde{\boldsymbol{\sigma}}' - \tilde{\boldsymbol{\sigma}}'_0}{\Delta t}\right) + \dot{\Lambda}\frac{\partial \Phi}{\partial \tilde{\boldsymbol{\sigma}}'} - \tilde{\boldsymbol{D}}' \\ R_{\tilde{\sigma}_{\mathrm{m}}} &= \frac{1}{K\Delta t}\left(\sigma_{\mathrm{m}} - \sigma_{\mathrm{m}\ (0)}\right) + \dot{\Lambda}\frac{1}{3}\frac{\partial \Phi}{\partial \sigma_{\mathrm{m}}} - \tilde{D}_{kk} \\ R_f &= \frac{f - f_0}{\Delta t} - (1-f)\dot{\Lambda}\frac{\partial \Phi}{\partial \sigma_{kk}} \\ R_{\bar{\epsilon}} &= \frac{\bar{\epsilon} - \bar{\epsilon}_0}{\Delta t} - \frac{\dot{\Lambda}}{(1-f)}\left(\frac{\boldsymbol{\sigma}}{\bar{\sigma}} : \frac{\partial \Phi}{\partial \tilde{\boldsymbol{\sigma}}}\right) \end{aligned} \tag{6.48}$$

where K and μ are the shear and bulk moduli, respectively. The derivatives of the post–localization flow potential Φ^{I} refer to (6.45). $\boldsymbol{V}_0$ and $\boldsymbol{V}$, respectively, denote the state variables at the beginning and the end of the time increment. The residual associated with $s \equiv \ln w$ is explicated distinctively in that it demands original derivation at the post–localized process.

– During homogeneous deformation:

Following [92], the time rate of the logarithmic void aspect ratio reads:

$$R_s = \frac{s - s_0}{\Delta t} - \dot{\Lambda}\tilde{\boldsymbol{Q}} : \left[k\boldsymbol{N}^{\mathrm{H}} + \left(\frac{1}{f}\tilde{\boldsymbol{X}}^v - \tilde{\boldsymbol{X}} \right) \frac{\partial \Phi^{\mathrm{H}}}{\partial \sigma_{\mathrm{m}}} \right] \tag{6.49}$$

with the parameters identified in (6.10).

– During inhomogeneous deformation:

We can firstly define intermediate parameters q_1 and q_2, following Eq. (6.29) or, alternatively, Eq's (6.31) and (6.32), with the normal and shear parts of $\dot{s}$ secluded. Namely:

$$\begin{cases} q_1 = \dfrac{3S}{2c} \\ \\ q_2 = \dfrac{1}{2}\left(\dfrac{3C^2}{2c} - \dfrac{1}{f} \right) \end{cases} \tag{6.50}$$

for cylindrical voids, and

$$q_1 = \begin{cases} \dfrac{\frac{6}{c}\frac{\mathcal{T}(w^2-1)(\mathcal{T}^2+w^2)}{(\mathcal{T}^2+w^4)(\mathcal{T}^2+1)}}{2 - 3\frac{\mathcal{T}^2(2w^2-w^4+\mathcal{T}^2)}{(\mathcal{T}^2+w^4)(\mathcal{T}^2+w^2)}} & \text{for } w \geq 1 \\ \\ \dfrac{-\frac{6}{c}\frac{\mathcal{T}(w^2-1)(\mathcal{T}^2+w^2)}{(\mathcal{T}^2+w^4)(\mathcal{T}^2+1)}}{1 - \frac{\mathcal{T}^2(-2w^2+w^4-\mathcal{T}^2)}{(\mathcal{T}^2+w^4)(\mathcal{T}^2+w^2)}} & \text{for } w < 1 \end{cases} \tag{6.51}$$

and

$$q_2 = \begin{cases} \dfrac{\frac{(\mathcal{I}^2+w^2)^2}{(\mathcal{I}^2+w^4)(\mathcal{I}^2+1)}\left[\frac{3}{c} - \frac{(\mathcal{I}^2+w^4)(\mathcal{I}^2+1)}{f(\mathcal{I}^2+w^2)^2}\right]}{2 - 3\frac{\mathcal{I}^2(2w^2-w^4+\mathcal{I}^2)}{(\mathcal{I}^2+w^4)(\mathcal{I}^2+w^2)}} & \text{for } w \geq 1 \\ \dfrac{\frac{(\mathcal{I}^2+w^2)^2}{(\mathcal{I}^2+w^4)(\mathcal{I}^2+1)}\left[-\frac{3}{c} + \frac{(\mathcal{I}^2+w^4)(\mathcal{I}^2+1)}{f(\mathcal{I}^2+w^2)^2}\right]}{1 - \frac{\mathcal{I}^2(-2w^2+w^4-\mathcal{I}^2)}{(\mathcal{I}^2+w^4)(\mathcal{I}^2+w^2)}} & \text{for } w < 1 \end{cases} \tag{6.52}$$

for spheroidal voids.

One can further define

$$\begin{aligned} \boldsymbol{q} &= q_1 \boldsymbol{m} + q_2 \boldsymbol{n} \\ \mathcal{M} &= \boldsymbol{n} \otimes \boldsymbol{q} \end{aligned} \tag{6.53}$$

which can supply the residual associated with s as follows:

$$R_s = \frac{s - s_0}{\Delta t} - \dot{\Lambda} \mathcal{M} : \boldsymbol{N}^{\mathrm{I}} \tag{6.54}$$

The Newton–Raphson procedure is then employed iteratively to solve the $[\boldsymbol{R}]^T = \boldsymbol{0}$ equation system at every time step:

$$[\boldsymbol{V}]^{(i+1)} = [\boldsymbol{V}]^{(i)} - \left[\frac{\partial [\boldsymbol{R}]}{\partial [\boldsymbol{V}]^{(i)}}\right]^{-1} [\boldsymbol{R}] \tag{6.55}$$

where the Jacobian matrix $\partial[\boldsymbol{R}]/\partial[\boldsymbol{V}]$ can be evaluated at every iteration within the time step or kept constantly equal to the value at the beginning of the time step, and subscript i denotes the iteration number. Since, however, the number of iterations to convergence is more or less the same whether the initial or updated Jacobian is utilized. Therefore, $\partial[\boldsymbol{R}]/\partial[\boldsymbol{V}]_{(0)}$, *i.e.* the Jacobian at the beginning of every time step, has been used throughout the iteration process due to the fact that convergence is better guaranteed with the initial Jacobian.

Finally, the consistent tangent matrix (mainly developed for global equilibrium, as in a finite

element–based analysis), denoted by $\mathbb{L}^{\tan}$ (*e.g.* DDSDDE in ABAQUS) is written as

$$\mathbb{L}^{\tan} = \frac{1}{\Delta t}\left(\frac{\partial \tilde{\boldsymbol{\sigma}}'}{\partial \tilde{\boldsymbol{D}}} + \boldsymbol{I} \otimes \frac{\partial \tilde{\sigma}_{\mathrm{m}}}{\partial \tilde{\boldsymbol{D}}}\right) \tag{6.56}$$

which involves the following constituents:

$$\left[\frac{\partial \boldsymbol{V}}{\partial \tilde{\boldsymbol{D}}}\right] = -\left[\frac{\partial [\boldsymbol{R}]}{\partial [\boldsymbol{V}]}\right]^{-1}\left[\frac{\partial \boldsymbol{R}}{\partial \tilde{\boldsymbol{D}}}\right] \tag{6.57}$$

where use has been made of the same Jacobian as introduced in (6.55), and

$$\begin{aligned}\left[\frac{\partial \boldsymbol{V}}{\partial \tilde{\boldsymbol{D}}}\right] &= \left[\frac{\partial \tilde{\boldsymbol{\sigma}}'}{\partial \tilde{\boldsymbol{D}}}, \frac{\partial \tilde{\sigma}_{\mathrm{m}}}{\partial \tilde{\boldsymbol{D}}}, \frac{\partial f}{\partial \tilde{\boldsymbol{D}}}, \frac{\partial \bar{\epsilon}}{\partial \tilde{\boldsymbol{D}}}, \frac{\partial s}{\partial \tilde{\boldsymbol{D}}}\right]^T \\ \left[\frac{\partial \boldsymbol{R}}{\partial \tilde{\boldsymbol{D}}}\right] &= \left[\frac{\partial \boldsymbol{R}_{\tilde{\boldsymbol{\sigma}}'}}{\partial \tilde{\boldsymbol{D}}}, \frac{\partial R_{\tilde{\sigma}_{\mathrm{m}}}}{\partial \tilde{\boldsymbol{D}}}, \frac{\partial R_f}{\partial \tilde{\boldsymbol{D}}}, \frac{\partial R_{\bar{\epsilon}}}{\partial \tilde{\boldsymbol{D}}}, \frac{\partial R_s}{\partial \tilde{\boldsymbol{D}}}\right]^T\end{aligned} \tag{6.58}$$

To the reader's insight, the Jacobian components corresponding to the post–localized deformation process have been provided in Paper P7 . For the homogeneous deformation regime, the reader can consult [224].

CHAPTER 7 APPLICATIONS

The present chapter addresses a selective collection of results that simulate the Fracture process under combined tensile and shear loading with the internal state variables that represent the stress, strain, and microstructural state. The results are generated by integration of constitutive equations for one spatial point representing a unit cell based on the hybrid plasticity model propounded in Chapter 6. Contrary to the heavy numerical simulations carried out in [16, 17, 21], the void need not be modeled explicitly, but through the notion of an elementary cell.

The matrix effective stress $\bar{\sigma}$ is taken to depend on its conjugate $\bar{\epsilon}$ through a power law of the form:

$$\bar{\sigma} = \sigma_0(1 + \frac{\bar{\epsilon}}{\epsilon_0})^N \tag{7.1}$$

with σ_0 the initial yield strength and N the hardening exponent.

Furthermore, the imposed deformation gradient is derived on the basis of its value at every time step, that is

$$\boldsymbol{F}^{(i)} = \prod_{j=0}^{i} \boldsymbol{F}^{(j)} \tag{7.2}$$

where $\boldsymbol{F}^{(j)}$ is the deformation gradient between the $j-1$'st and j'th time steps constituted by the incremental displacements at the j'th step, where $j = 1, 2, ..., i$. Note that many commercial codes, such as ABAQUS, calculate $\boldsymbol{F}$ internally, and it thus need not be programmed when the constitutive model is coded in conjunction with those commercial software. For the single cell undergoing normal and lateral as well as shear displacement, $\boldsymbol{F}^{(j)}$ reads:

$$\boldsymbol{F}^{(j)} = \left(1 + \frac{\delta u_m^{(j)}}{L}\right) \boldsymbol{m} \otimes \boldsymbol{m} + \left(1 + \frac{\delta u_p^{(j)}}{L}\right) \boldsymbol{p} \otimes \boldsymbol{p} + \left(1 + \frac{\delta u_n^{(j)}}{H}\right) \boldsymbol{n} \otimes \boldsymbol{n} + \frac{\delta u_t^{(j)}}{H} \boldsymbol{m} \otimes \boldsymbol{n} \tag{7.3}$$

where the constituents $\left(\delta u_m^{(j)}, \delta u_p^{(j)}, \delta u_n^{(j)}, \delta u_t^{(j)}\right)$ are the incremental displacements at the j'th step, where $j = 1, 2, ..., i$. Here, $\delta u_m^{(j)}$, $\delta u_p^{(j)}$, and $\delta u_n^{(j)}$ are the tensile displacement increments along directions $\boldsymbol{m}$, $\boldsymbol{p}$, and $\boldsymbol{n}$, respectively, and $\delta u_t^{(j)}$ is the tangential displacement increment over the

top chord of the cell. Note that all these displacement increments are modified so as to preserve the ratios among the stresses. Moreover,

$$L = L_0 \exp\left(\frac{\epsilon_{mm} + \epsilon_{pp}}{2}\right) \quad , \quad H = H_0 \exp \epsilon_{nn} \tag{7.4}$$

with ϵ_{mm}, ϵ_{pp}, and ϵ_{nn} are the normal strains resolved along the $\boldsymbol{m}$, $\boldsymbol{p}$ and $\boldsymbol{n}$ directions, respectively. Upon consideration of the single cell, $\boldsymbol{n}$ (denoting normal to the invoked localization plane) initially directed along $\boldsymbol{e}_3$ would stay constant thanks to the imposed deformation gradient $\boldsymbol{F}$. Upon consideration of a single cell in the present context, $\boldsymbol{m}$, $\boldsymbol{p}$ and $\boldsymbol{n}$ coincide with the global base vectors $\boldsymbol{e}_1$, $\boldsymbol{e}_2$ and $\boldsymbol{e}_3$, respectively.

The model will be first borne out by existing numerical data through some benchmark response curves under triaxial as well as combined loading. The parametric results are presented in two main sets accordingly, under triaxial and combined loading conditions. Each set of results is extended into further subsets to demonstrate the evolution of various microstructural variables throughout the process. The ratios among the remote normal, lateral, and shear stresses remain constant throughout. Accordingly, stress triaxiality T and the Lode parameter L are constant. A complete guide through the employed algorithm for preservation of stress ratios is illustrated in Appendix C.

The outcomes examined include the effect of initial porosity reflected through the initial effective ligament parameter χ_0. Further, the effect of elementary cell size was expressed in terms of the cell aspect ratio λ. The effect of void shape was also assessed from distinct effects observed for elongated and flat voids. Furthermore, the strain to failure was evaluated in terms of stress triaxiality for a complete scope of stress triaxialities. Finally, an example axisymmetric notched bar FEM simulation was carried out to demonstrate the capability of the model for structural boundary–value problems. To that end, the constitutive framework was implemented in an a user–defined subroutine, and the microstructural effects were evaluated based on homogenized incorporation of the effective microstructural parameters.

7.1 Failure Mechanism in Shear

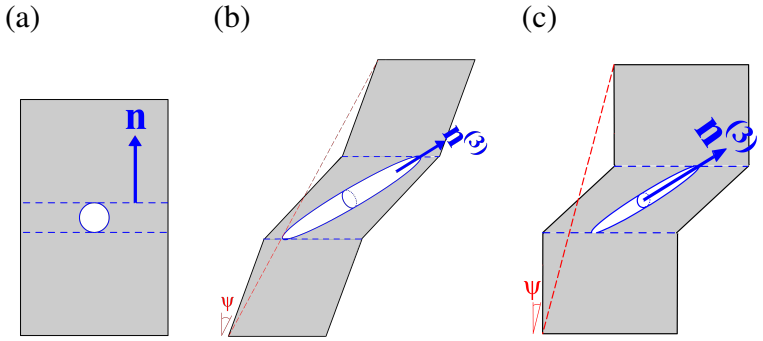

Figure 7.1: Essential features of ductile fracture under combined loading captured by the unit cell model: (a) intial state, (b) inhomogeneous deformation, (c) localized deformation.

The preparatory step to quantitative simulation of ductile fracture processes is a qualitatively proper emulation of the *failure mechanism*. To investigate failure under combined tension and shear, the continuum micromechanics–based framework must be capable of capturing the salient features of sub–cell deformation sketched in Fig. 7.1.

The present section is thus aimed at illustration of the mechanism by which failure occurs under shear–dominated loading which is realized by sufficiently low values of $\kappa = \sigma_{\mathrm{n}}/\tau_{\mathrm{n}}$. In this region, the *basic form* of the inhomogeneous yield criterion computationally dominates from the outset, and all the subsequent deformation mechanism can be described by Φ^{I} along with the supplemented evolution equations. Nevertheless, as seen in the sequel, this deformation mechanism is quantitatively erroneous. This error can be attributed to the underlying premises within Φ^{I} which ideally confines plastic deformation within the ligament intercepting void poles [228]. Recent cell–level calculations, however, have it that, even at a state of shear domination, plastic deformation is more diffuse than ideally within the ligament, at least at early stages of deformation [16, 21]. The following section, therefore, proposes a modification to both Φ^{H} and Φ^{I} so as for the hybrid model to be quantitatively robust.

The results are hereby presented for spheroidal voids, in comparison with their counterparts for cylindrical voids for a unit cell under $\kappa = 0.02$ with the initial simulation parameters given in the

caption. The constitutive formulation exclusive to cylindrical voids is skipped herein, but the reader can find sufficient algebraic details and a more self–contained discussion on the corresponding simulation results in Papers P5 and P6 . It should be remarked, however, that, since a cylindrical void is tied to the upper and lower matrix materials over a whole surface rather than a single point, the whole range of void aspect ratios (below or above 1) behave similarly as far as void rotation is concerned. Nevertheless, a spheroidal void under the effect of shear rotates antithetically when it is prolate ($w \geq 1$) and oblate ($w < 1$).

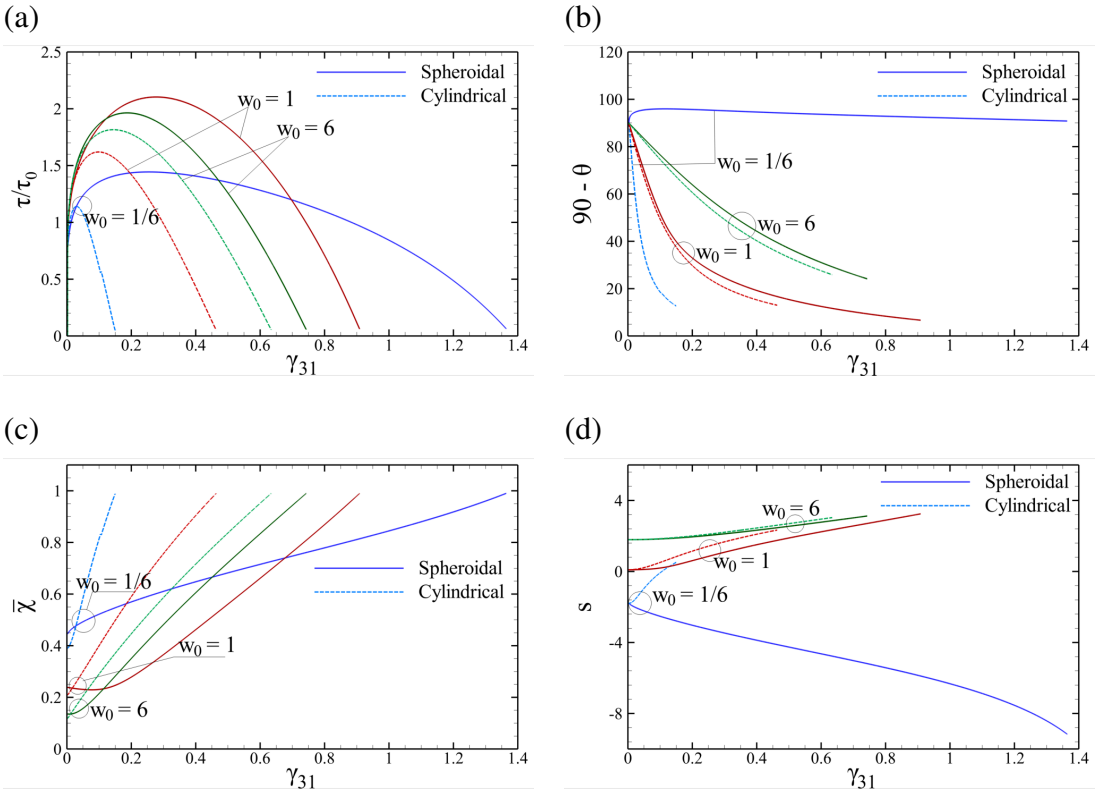

Figure 7.2: Comparison of the predicted failure mechanisms based on the TBL criterion according to Eq. (5.2), for a cell under $\kappa = 0.02$, between a spheroidal and a cylindrical void of the same porosity level with the simulation parameters identified as $f_0 = 0.0005$, $w_0 = 1.1$, $\lambda_0 = 2$, $N = 0.2$, $\sqrt{3}\tau_0/E = 0.002$: (a) normalized shear stress, (b) void angle with the horizontal direction, (c) effective ligament parameter, (d) logarithmic void aspect ratio $s = \ln w$ [19] (reprinted with permission from *Elsevier*, Ltd).

Figure 7.2 shows the comparison between microstructural parameters for spheroidal and cylindrical voids embedded in the same cell. All parameters are presented against the shear strain γ_{31}.

Note that the current framework exhibits a singular behavior rooted in the ill–defined void axis for the case of a spherical void. The latter is, therefore, represented with a void aspect ratio slightly above unity, *i.e.* $w_0 = 1.1$. The largest distinction between the results pertaining to spheroidal and cylindrical voids can be envisaged for $w_0 < 1$ due to an opposite orientation evolution as plotted in Fig. 7.2b, and the difference diminishes with increasing $w_0 > 1$ owing to the synergistic behavior of elongated cylindrical and spheroidal voids. The orientation evolution schematized in Fig. 6.8 can be realized for both prolate and oblate voids by examining Fig. 7.2 b. It can be clearly seen that, soon after the beginning of the deformation process, the oblate void would stop rotating opposite to the shearing direction and begins to rotate along with shearing. Altogether, the overall rotation of an oblate void under shear is small in comparison to its prolate counterpart of the same porosity level.

The void aspect ratio w, as plotted in logarithmic form in Fig. 7.2d, would decrease in an oblate void under shear and it increases for its prolate counterpart. In effect, an elongated upright void elongates more, and an upright flattened void flattens further under shear such that, in both cases, the larger of the two void dimensions tends to align with the direction of the largest principal stretch. For a cylindrical void, however, w increases regardless of it being below or above 1.

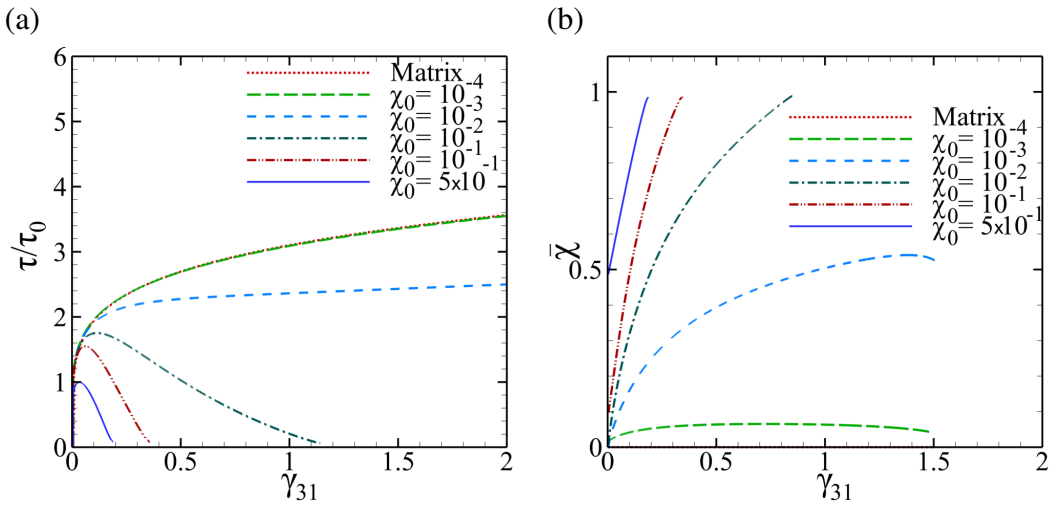

Figure 7.3: (a) Shear response and (b) evolution of ligament parameter for various values of the initial ligament parameter $\bar{\chi}_0$ using $w_0 = 1.1$, $\lambda_0 = 2$, $N = 0.2$, and $\sqrt{3}\tau_0/E = 0.002$.

In all cases, failure is triggered by $\bar{\chi}$ reaching its maximum, which is 1 in its basic form. Yet, $\bar{\chi}$ exhibits different trends with different void shapes. With a cylindrical void, the trend for $\bar{\chi}$ is convex, and thus, the material may not experience failure if the initial void volume fraction is smaller than a certain value (see Fig. 7.3). This situation physically corresponds to asymptotic void closure. Indeed, with extremely elongated void shapes, the surrogate void aspect ratio vanishes ($\bar{w} \to 0$) as shown in Paper P6 . The closed void, which is in the limit a microcrack, deforms as a material line.

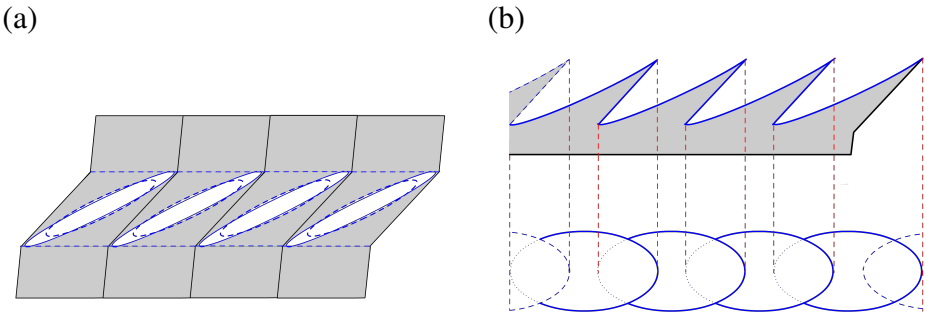

Figure 7.4: Predicted failure mechanism in shear and its connection to the fracture surface of Fig. 1.8b: (a) few neighboring cells near the ultimate state $\bar{\chi} = 1$, (b) side and top views of the cut–out from (a) after material separation.

The above–predicted mechanism can be correlated with the salient features of sheared fracture surfaces as depicted in Fig. 1.8 through the schematic neighborhood as shown in Fig. 7.4. An intermediate and the ultimate states ($\bar{\chi} = 1$) are shown in Fig. 7.4a with dashed and solid lines, respectively. A top view of the so–simulated fracture surface, Fig. 7.4b, provides a rationale for three key experimental observations: (i) parabolic dimples; (ii) low surface roughness; and (iii) low local porosity, relative to tensile fracture surfaces, Fig. 1.8a.

7.2 Model Assessment

This section provides selective outcomes for cell–level predicted internal state variables under triaxial loading as well as combined normal and shear loading in comparison to the existing FEM cell-model calculations.

7.2.1 *Triaxial loading*

The micromechanics–based and FEM–based results of Pardoen and Hutchinson [20] are used to assess the authenticity of the hybrid model with respect to triaxial loading. The following parameters are common among all analyses:

$$f_0 = 10^{-2} \quad , \quad \lambda_0 = 1 \quad , \quad N = 0.1 \quad , \quad \frac{\sigma_0}{E} = 0.002 \quad , \quad E = 210\ GPa \quad , \quad \epsilon_0 = 0.002 \tag{7.5}$$

where σ_0 is the initial matrix yield strength and ϵ_0 is its conjugate strain. E is the Young modulus, N is the hardening exponent, and f_0 denotes the initial porosity. The values of initial void aspect ratio w_0, however, is varied.

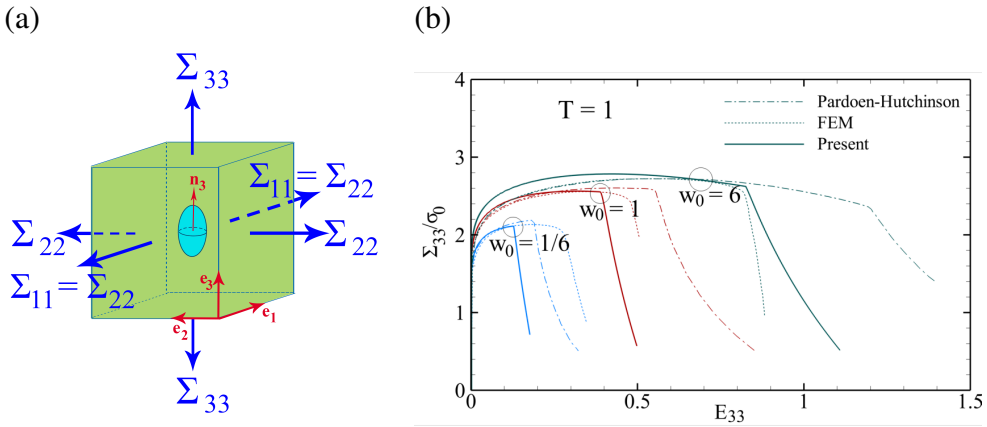

Figure 7.5: Comparison of the present model predictions in absence of shear (solid curves), with the results extracted from Pardoen and Hutchinson's extended model (dashed curves), as well with those obtained from cell–model calculations (dotted curves) in [20] for several values of initial void aspect ratios and a stress triaxiality of $T = 1$.

Figure 7.5 shows a schematic unit cell as well as the comparison among the stress–strain results corresponding to $T = 1$. The stress–bearing capacity in absence of shear is taken to drop to zero when $\bar{\chi}$ exceeds $\sqrt{2}/2 \approx 0.707$ [150].

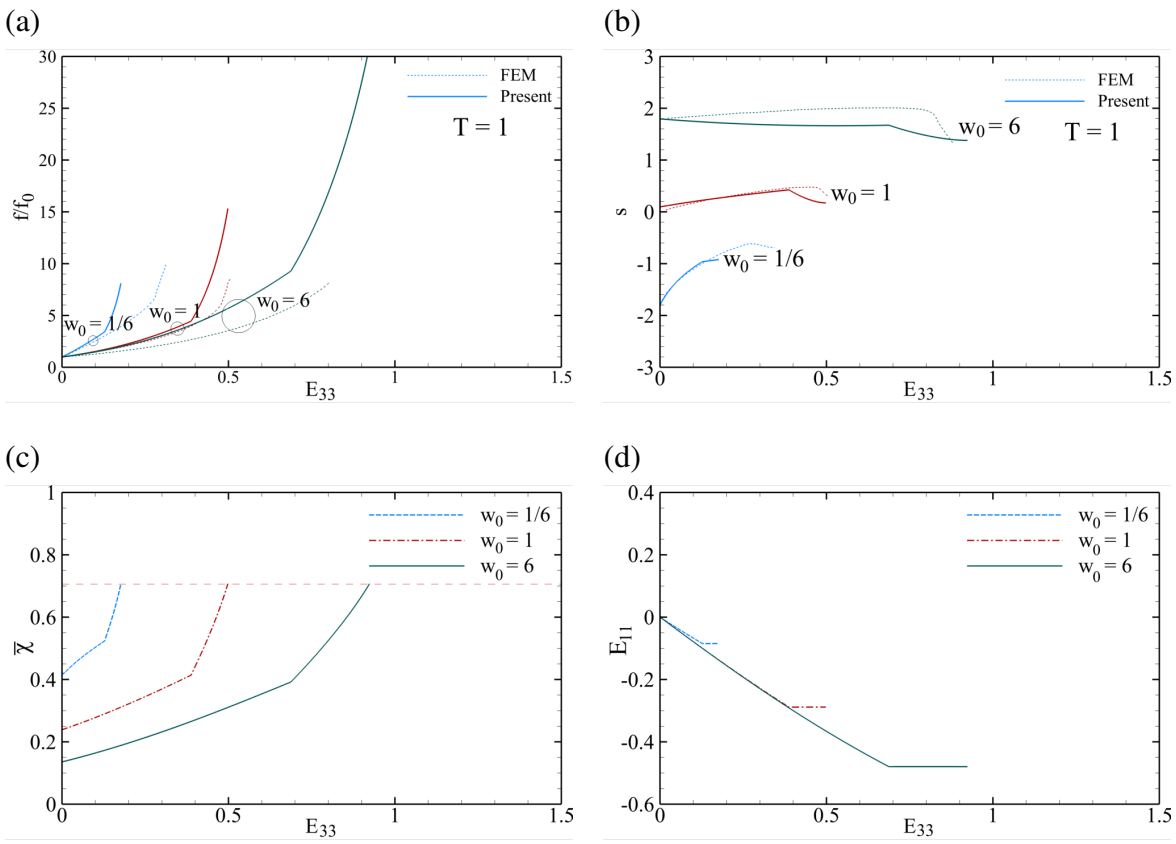

Figure 7.6: Present model predictions under triaxial loading with a $T = 1$ stress triaxiality: (a,b) normalized porosity and logarithmic void aspect ratio, compared to FEM results in [20], (c,d) effective ligament parameter and lateral strains, respectively.

The difference between present predictions and numerical and/or micromechanical results is seen to be more pronounced for larger void aspect ratios. This can be attributed to the rather exaggerated porosity growth predicted from the K–B model (as shown in Fig. 7.6b) as well as the decreasing trend within $s = \ln w$, which would increase the stress level but reduce the strain to coalescence. Other selective microstructural variables are shown in Fig. 7.6. The predicted logarithmic void aspect ratio s is closely tied to its FEM counterpart during void growth except for large w_0's, where both analytical and numerical curves tend towards level but the former predicts a decreasing w. Next, Fig. 7.6c shows that the slope of increasing $\bar{\chi}$ ranges from convex to concave from an initially oblate ($w_0 < 1$) to an initially prolate ($w_0 > 1$) void. Accordingly, an initially flat void at a very low porosity level would be likely to never experience coalescence inasmuch as $\bar{\chi}$

could reach a maximum before coalescence could occur. Further, the zero lateral strain rate at the post–coalescence process is corroborated by Fig. 7.6d.

7.2.2 Combined loading

The coincidence between the analytical and numerical results will not be fulfilled unless by invoking the simple calibration to both Φ^{H} and Φ^{I} identified via (6.18). Accordingly, the analyses carried out by Tvergaard and coworkers for plane–strain and 3D cells under combined and near–simple shear loadings [16, 17] are regarded as comparator. The initial microstructure in both [16, 17] is introduced based on the ($\chi_0 = R_0/L_0, w_0 = h_0/R_0, \lambda_0 = H_0/L_0$) triad (see Fig. 7.7), with χ_0 varying between 0.2 and 0.5, and $(w_0, \lambda_0) = (1, 4)$ remaining fixed.

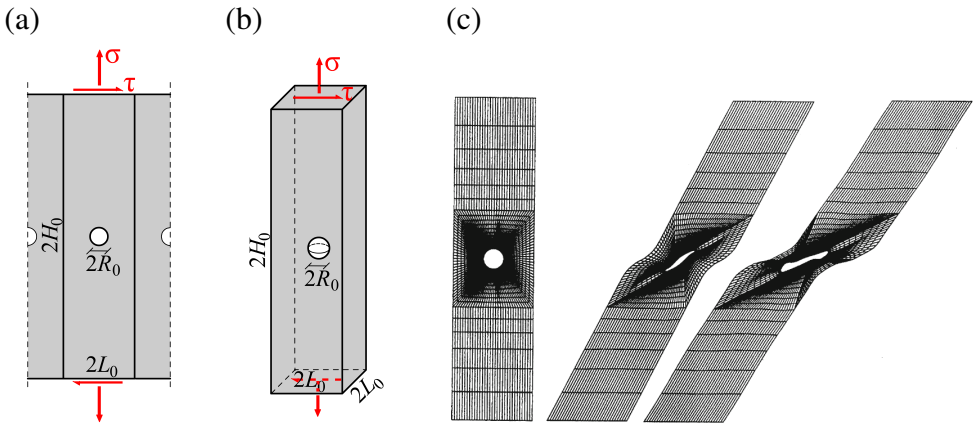

Figure 7.7: Schematic outline of periodic cells under combined tension and shear considered by Tvergaard and coworkers: (a) plane–strain [16,21], (b) 3D [17], (c) staged deformed configurations of the plane-strain cell in [16] under simple shear, *i.e.* $\kappa = 0$ (reprinted with permission from *Springer*, Ltd).

Figure 7.7 shows the schematic outline of the plane-strain [16, 21] and 3D [17] periodic cells as well as the deformed configuration of the plane–strain cell according to the numerical analyses carried out in [16]. In the plane–strain cell, the out–of–plane dimension in both the void and the cell is considered unit and, hence, χ_0, w_0, λ_0 are all defined within the x_1–x_3 plane. In the 3D cell,

however, the lateral dimensions are considered equal. Correspondingly, the initial porosity reads

$$\begin{aligned} \text{Plane strain:} \quad f_0 &= \frac{\pi}{4}\frac{w_0\chi_0^2}{\lambda_0} \\ \text{3D:} \quad f_0 &= \frac{\pi}{6}\frac{w_0\chi_0^3}{\lambda_0} \end{aligned} \tag{7.6}$$

For the sake of better coincidence between analytical and numerical results, the calibrated model predictions are firstly compared to their FEM counterparts for the same initial porosity [72], with the initial microstructure and hardening identified by $(\chi_0, w_0, \lambda_0) = (0.25, 1, 4), N = 0.1$ for the plane-strain cell and $(\chi_0, w_0, \lambda_0) = (0.3, 1, 4), N = 0.2$ for the 3D cell, both shown in Fig. 7.7.

In all FEM-based studies, the analyses have been carried out by considering a maximum void aspect ratio, beyond which the loading is applied onto the void faces rather than onto the cell upper and lower boundaries. Herein, the results pertaining to a maximum void aspect ratio of $w_{\max} = 10$ are considered as comparator.

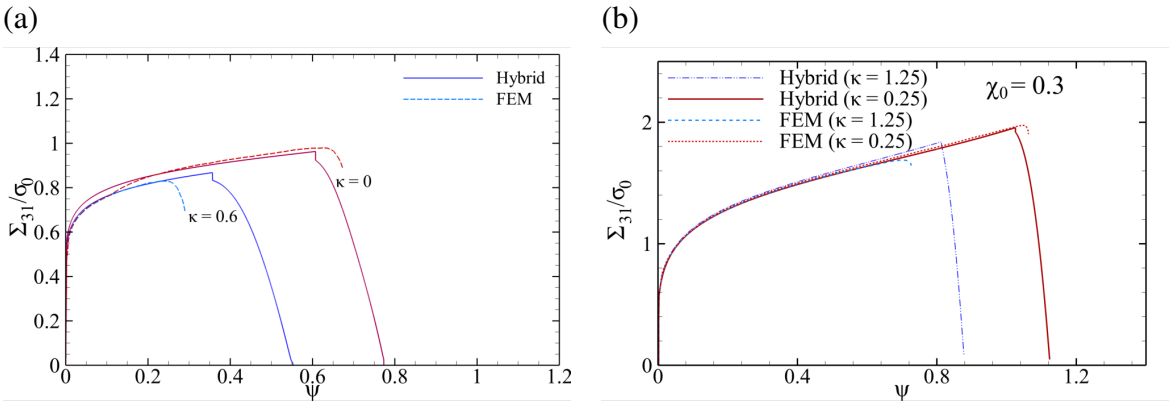

Figure 7.8: Comparison between the present model predicted shear responses vs. cell overall shear angle ψ with FEM cell-model outcomes of Tvergaard and coworkers: (a) for an initially circular void inside a plane-strain unit cell under $\kappa = 0.6$ as well as simple shearing ($\kappa = 0$) [16, 21]; (b) comparison with FEM outcomes of Nielsen *et al.* [17] for an initially spherical void inside a square-prismatic cell under combined axial and shear loading (with the ratio denoted with κ) and $\chi_0 = 0.3$.

Figure 7.8 shows the comparison between the hybrid model predicted response and numerical outcomes for the plane-strain and 3D cells (see Paper P7 for more comparisons).

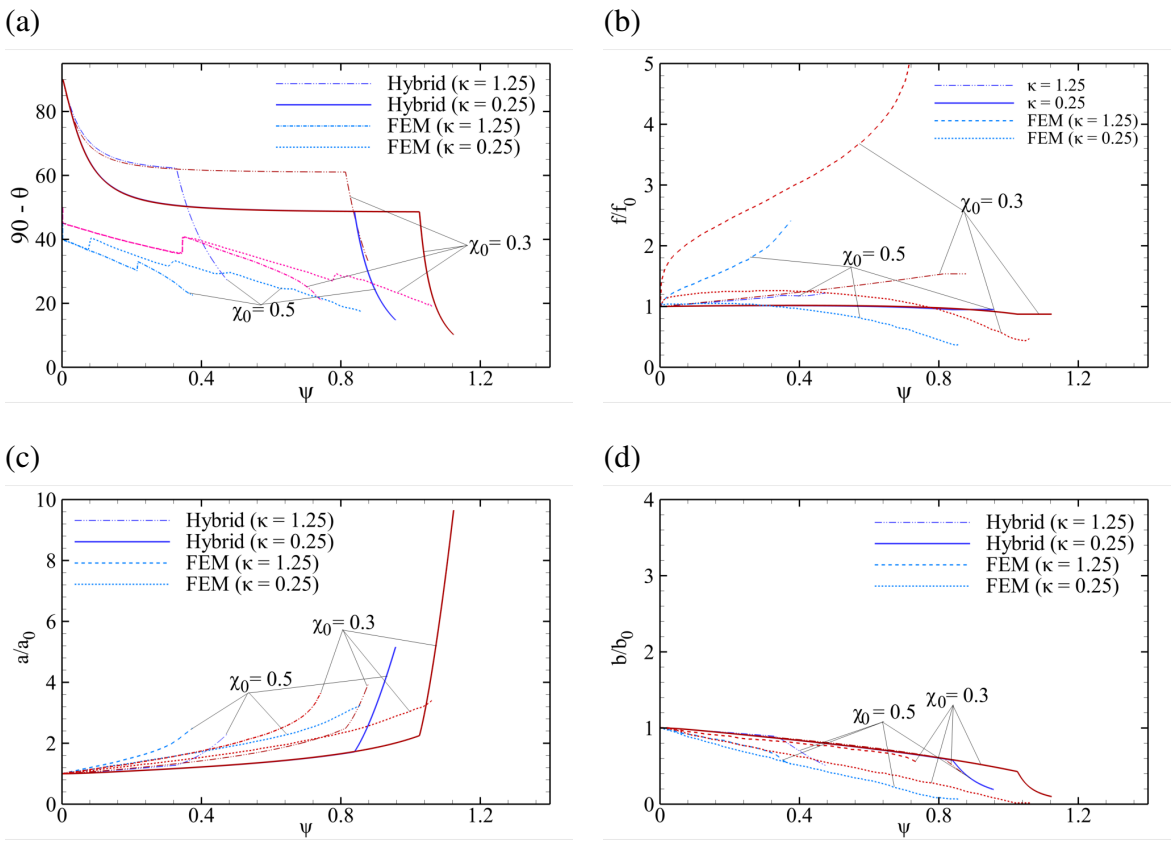

Figure 7.9: Comparison between the present model predicted variables with FEM outcomes of Nielsen *et al.* [17] for an initially spherical void inside a square-prismatic cell under combined axial and shear loading (with the ratio denoted with κ) and $\chi_0 = \{0.3, 0.5\}$: (a) void angle with respect to the horizontal direction, (b) normalized porosity, (c,d) normalized major and minor void semi-axes.

Further comparisons, pertaining to the 3D cell with initial ligament parameters $\chi_0 = \{0.3, 0.5\}$ and $N = 0.2$, are showcased in Fig. 7.9 for selective state variables including the void angle with respect to the $\boldsymbol{m}$–$\boldsymbol{p}$ plane, equaling $90 - \theta$ (with θ identified in Fig. 6.8), porosity f, and the void major and minor semi-axes. The latter is shown only for the in-plane semi-axis b_1.

Fig. 7.9d demonstrates that the overall trend of porosity evolution, inclining or declining, is common between analytical and numerical results with the difference lying in the dilatancy level in FEM values reflected by the more remarkable slope of evolution, especially at larger normal stress portions, *i.e.* larger κ's. Yet, the observed clear distinction between the FEM and analytical porosity values does not bare significant changes in the stress response (as shown in Fig. 7.9a)

inasmuch as the failure mechanism is mainly influenced by $\bar{\chi}$ rather than porosity.

Note that the analytical evolution of $90 - \theta$ is founded on the initial void orientation directed towards $\boldsymbol{e}_3$ since $w_0 = 1.1$ has been taken slightly above unity to forestall the singular behavior of void orientation laws at the limit of a spherical void, and therefore, the initial orientation is well–defined. Within the numerical model, however, the orientation of a strictly spherical void is ill–defined. Upon convention, the void orientation in this case is considered along the principal stretch, which is close to that considered in [16, 17]. Accordingly, the jumps in the numerical evolution of orientation is an artifact employed to extract the major void axis [17].

7.3 Parametric Studies

A more extensive investigation on the various state variables under combined axial and shear stresses, upon the calibrated hybrid model, is addressed next for spheroidal voids. The results are briefly reflected by the following subsections. Further details in this regard are provided in Paper P7 .

7.3.1 Effect of loading

The effect of loading is quantified via the $\kappa \equiv \sigma_{\rm n}/\tau_{\rm n}$ ratio. This section addresses this effect through Fig. 7.10 on the microstructural state variables with the same cell as considered in Sec. 7.2.2 and $\chi_0 = 0.3$. A complete scope of κ ranging from infinity (uniaxial loading) down to (near) zero (simple shearing) can best be exhibited in terms of $\bar{\epsilon}$ since the axial or shear strain each becomes vanishingly small at either of the two extremes. It can be seen, through Fig's 7.10(a,b), that the strain to the onset of localization ϵ_c, as well as strain to failure ϵ_f, from infinity at $\kappa \longrightarrow \infty$ (corresponding to $T = 1/3$), decreases and then increases again with decreasing κ (increasing shear). As farther observed in Fig. 7.11, the minimum strain to failure occurs approximately at $\kappa = \mathcal{S}/\mathcal{T}$, which is nothing but the point of transition between the curved and planar parts of $\Phi^{\rm I}$ according to (5.2). Furthermore, the difference between ϵ_c and ϵ_f becomes smaller with larger κ's noting that a larger portion of the normal stress superposed by shear accelerates rotation, as revealed by Fig. 7.10d, and thus hastens the increase of $\bar{\chi}$, as demonstrated by Fig. 7.10b. The

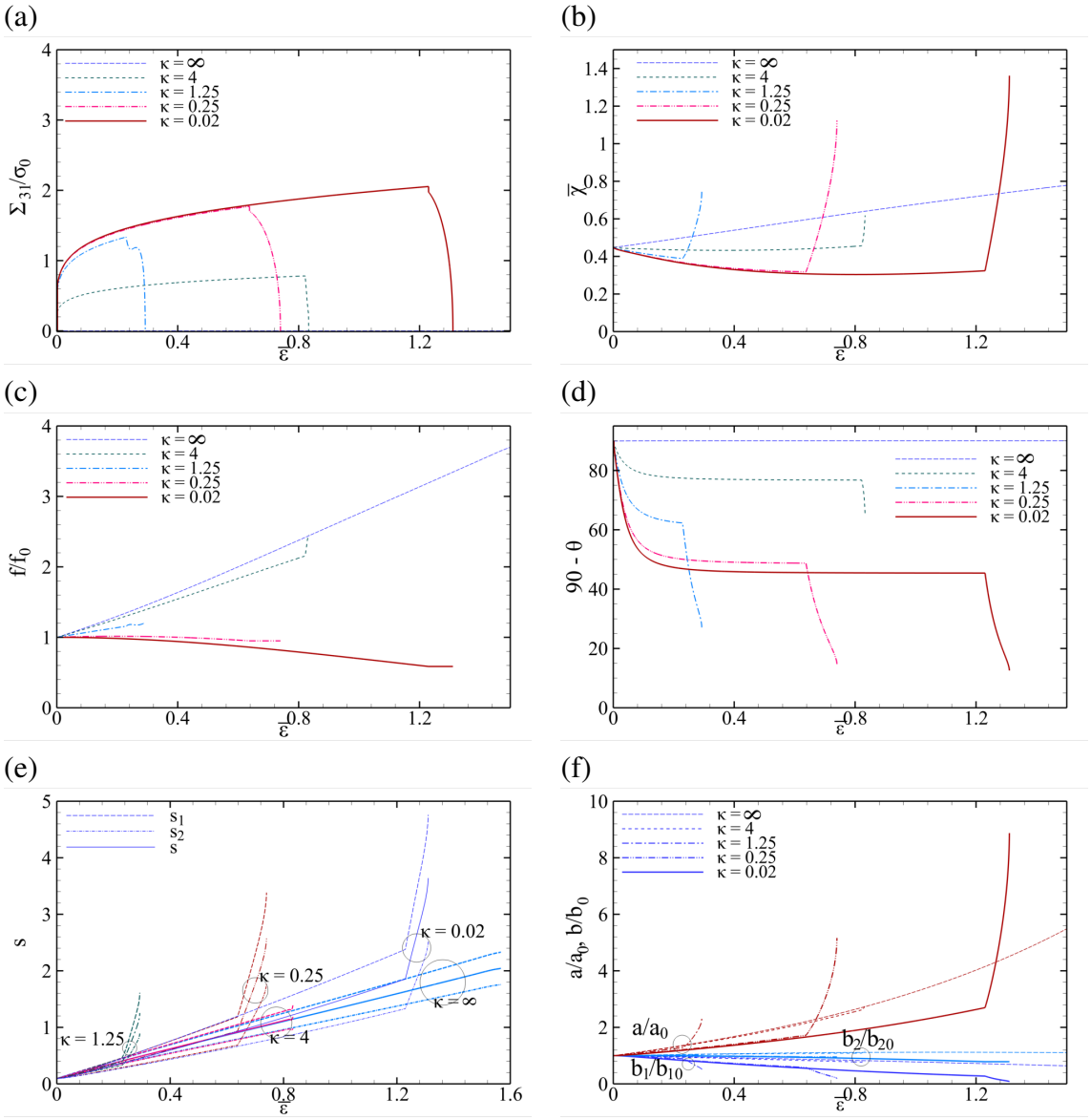

Figure 7.10: Predicted microstructural parameters upon the calibrated hybrid model, plotted against equivalent plastic strain $\bar{\epsilon}$ for the same initial microstructure as considered in Sec. 7.2.2 and $\chi_0 = 0.3$, under a full range of κ: (a) shear response, (b) effective ligament parameter, (c) normalized porosity, (d) void angle with the horizontal direction, (e) logarithmic void aspect ratio, (f) void semi-axes.

latter also shows that, for sufficiently large κ's (*i.e.* $\kappa >> \mathcal{S}/\mathcal{T}$), $\bar{\chi}$ increases during both nearly-homogeneous and localized processes whereas, for smaller κ's, it decreases during the nearly-homogeneous process. This alludes to the fact that, with larger normal stress portions, the void can rotate faster than the cell during the nearly-homogeneous process whilst, at shear-dominated processes, the cell moves faster during this process. During the localized process, however, the void always rotates faster since plastic deformation is (ideally) confined to the ligament intercepted by void poles.

Moreover, one can assert, from Fig. 7.10c, that porosity increases, with its increase accelerated after the onset of localization, for $\kappa > \mathcal{S}/\mathcal{T}$, *i.e.* normally-dominated fields. All the same, for $\kappa < \mathcal{S}/\mathcal{T}$, *i.e.* shear-dominated fields, porosity decreases during the nearly-homogeneous process and stays constant after localized deformation begins. This lies in the traceless nature of $\boldsymbol{D}^{\mathrm{p}}$ according to Φ^{I} for this range of κ.

The s_1 and s_2 void aspect ratios shown in Fig. 7.10e denote, respectively, a/b_1 and a/b_2. Under all combinations of (tensile) axial and shear stresses, in absence of sufficient lateral loads, s as well as s_1 and s_2 increase, with their increase accelerated after localization begins. Throughout the process, $s_1 > s_2$ and the difference between the two increases with deformation advancement. At the end of the localized process, the void aspect ratio increases with its slope approaching infinity. This stage signifies the vertical movement of void poles after extreme shearing, as shown in Fig. 7.7c. Correspondingly, as depicted in Fig. 7.10f, the major and minor void semi-axes increase and decrease, respectively, with shearing, and the trend slope accelerates after the onset of localization. The out-of-plane axis also decreases slightly but stays almost constant throughout the process due to the loading being devoid of lateral stresses.

As earlier remarked, 7.10a was suggestive of a local minimum within ϵ_c and ϵ_f with varying κ. Figure 7.11 gives more insight into this effect by presenting ϵ_c and ϵ_f as function of stress triaxiality T, and provides the physical reason for this local minimum.

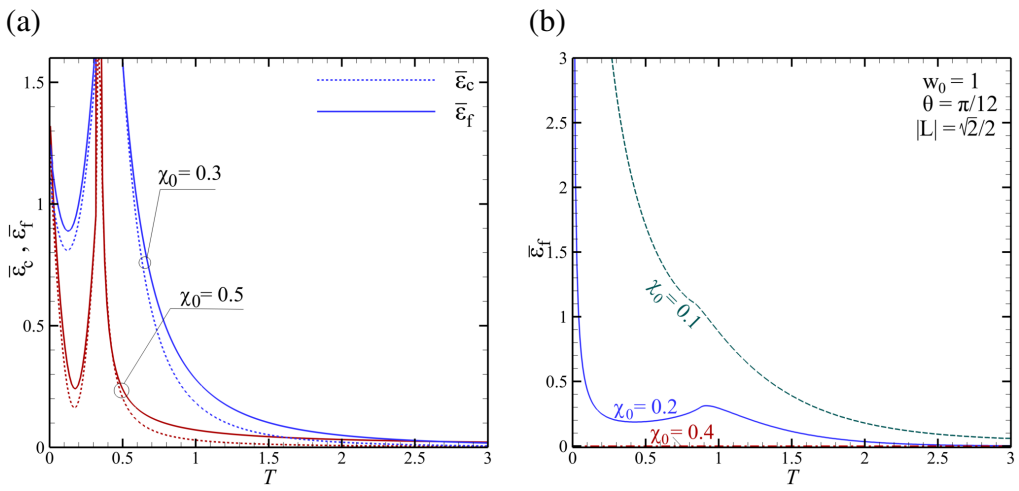

Figure 7.11: (a) Predicted strain to onset of localization ϵ_c as well as strain to failure ϵ_f as function of stress triaxiality T for the same cell as shown in Fig. 7.7a, with $(w_0, \lambda_0) = (1.1, 4)$, hardening exponent $N = 0.2$ and various initial ligament parameters χ_0; (b) evolution of ϵ_c as function of stress triaxiality at the example Lode angle of $\theta = \pi/12$ at the isotropic material limit for several values of $\bar{\chi}$.

In some references, including [88], ϵ_c is normally regarded as equal to ϵ_f for the material since the plastic deformation prior to this point is considerably larger than that after this onset. Figure 7.11, however, reports both strains as function of triaxiality. The underlying microstructure for this evolution is reflected by the same unit cell as shown in Fig. 7.7a, with $(w_0, \lambda_0) = (1.1, 4)$, hardening exponent $N = 0.2$ and various initial ligament parameters χ_0, under combined normal and shear stresses. The two parameters of interest are consequences of the Runge–Kutta integration of equations stating the time rate of $(f, w, \boldsymbol{n}^{(3)})$ as function of $\bar{\epsilon}$. See Paper P7 for more details.

One can notice, through Fig. 7.11a, that ϵ_c is close to ϵ_f at the shear–dominant range of triaxialities. Yet, the difference therein cannot be neglected in a significant range of triaxial loads, *esp.* in an interval of $0.5 < T < 2$ where void coalescence is accelerated due to the existence of lateral loads but significant stress–bearing capacity still remains after the onset of void coalescence. More importantly, in the shear–dominated region ($0 < T < 1/3$), both ϵ_c and ϵ_f admit their minimum values not at the simple–shear limit but somewhere between the two limits. Within a reasonable accuracy, it can be deduced that the minimum to ϵ_c and ϵ_f occurs almost at $\kappa = \mathcal{S}/\mathcal{T}$,

which corresponds to

$$T(\epsilon_{f\min}) = \frac{1}{3}\frac{\mathcal{S}}{\sqrt{\mathcal{S}^2 + 3\mathcal{T}^2}} \tag{7.7}$$

for a combined normal–shear loading, with $\mathcal{S}$ and $\mathcal{T}$ defined in (5.3).

It is, however, noteworthy that, at the limit of isotropic yielding shown in Fig. 7.11b, which stems from random distribution of voids, the ϵ_f vs. T curve is absolutely declining even for the $T < 1/3$ range. Yet, as earlier pointed out in Chapter 5, the value at the $T = 0$ limit should be finite though being admittedly large. The reader is referred to Paper P4 for more explanation.

In the forthcoming subsections, the results are limited to near–simple shearing, here characterized by $\kappa = 0.02$.

7.3.2 Effect of void spacing

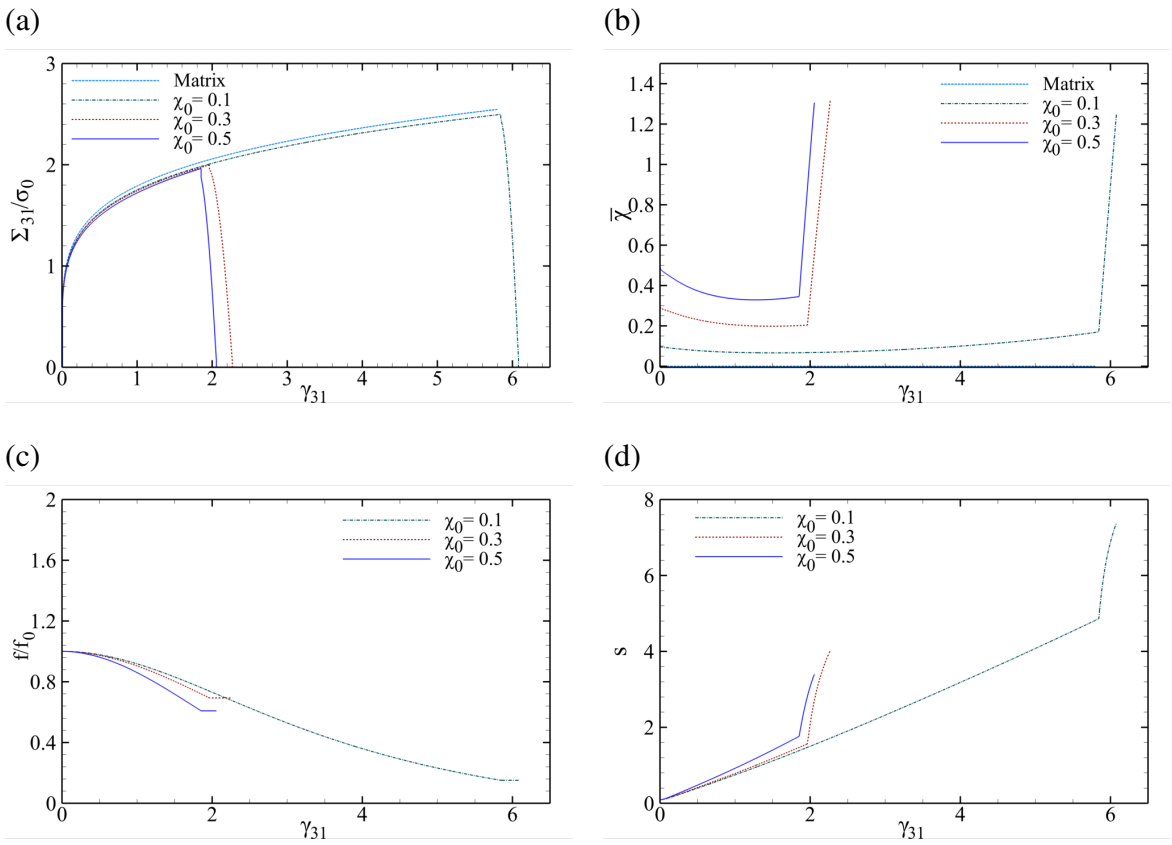

Figure 7.12: Predicted microstructural parameters for the same cell subjected to $\kappa = 0.02$ for various values of χ_0.

The effect of void spacing can be reflected through the notion of initial ligament parameter χ_0. Figure 7.12 presents selective state variables under near-simple shearing ($\kappa = 0.02$) with various values of χ_0, ranging from zero (pertaining to the limit of a dilute matrix) up to rather large values, *e.g.* 0.5. Figure 7.12a reveals that the stress curve (and the tangential stiffness accordingly) up to the point of transition (ϵ_c) is almost insensitive to void spacing provided the other (initial) microstructural parameters stay constant. However, ϵ_c and ϵ_f are closely related to χ_0. In particular, for very small values of χ_0, towards the limit of a dilute material, the onset of localized deformation, as well as failure, gets significantly delayed.

During nearly-homogeneous yielding, as shown in Fig. 7.12b, $\bar{\chi}$ decreases at the early stages of deformation, but it admits a minimum which sets the precursor for the onset of localized deformation. The void aspect ratio, according to Fig. 7.12d, increases with a decreasing inclination slope. The largest slope of increasing s corresponds to the onset of localization, and void elongation slows down further towards failure.

7.3.3 *Effect of cell aspect ratio*

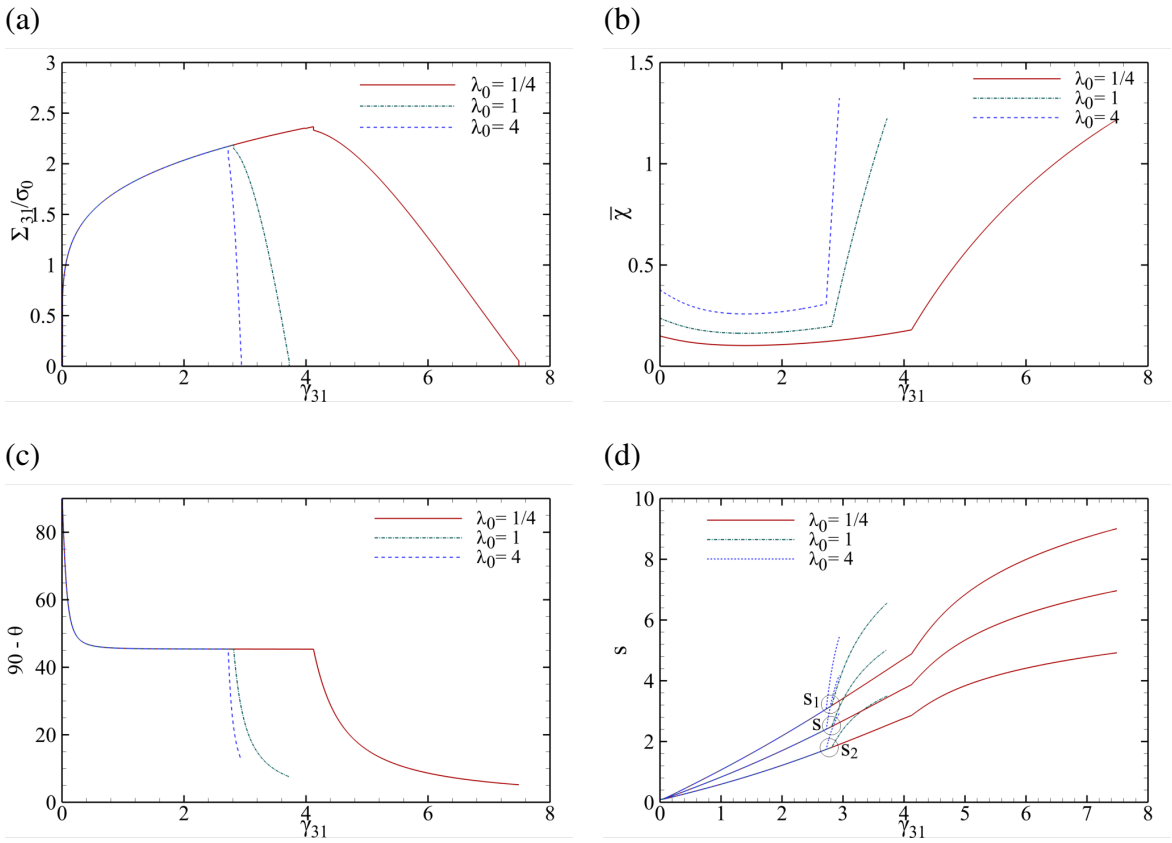

Figure 7.13: Predicted microstructural parameters for the same cell with $(f_0, w_0) = (0.01, 1.1)$ subjected to $\kappa = 0.02$ for various values of λ_0: (a) normalized shear response, (b) effective ligament parameter, (c) void angle with the horizontal direction, (d) logarithmic void aspect ratio.

The effect of initial cell aspect ratio is considered for investigation next. Other parameters, including initial porosity f_0 and void aspect ratio w_0, as well as the hardening exponent $N = 0.2$, are kept fixed upon selective values of $(f_0, w_0) = (0.01, 1.1)$. Figure 7.13 illustrates this effect. Due to the load representing simple shear ($\kappa = 0.02$), λ remains almost constant throughout, and thus is not shown.

At a fixed porosity level, the void spacing χ_0 is smaller in a shorter cell, and thus the void, even after deformation turns localized, has to elongate and rotate more to reach the cell boundaries. The strains to localization and failure are hence larger with shorter cells, as seen in Fig. 7.13a.

Correspondingly, the projection of a rotating-elongating void on a shorter intervoid distance (at a larger λ) evolves faster than that on a longer distance (at a smaller λ). The slope of $\bar{\chi}$ evolution, therefore, is smaller for a shorter cell, and vice versa (see Fig. 7.13b). The void would, accordingly, rotate (Fig. 7.13c) and elongate (Fig. 7.13d) more slowly at the post-localized deformation process, in a shorter cell and vice versa.

7.3.4 Effect of void shape

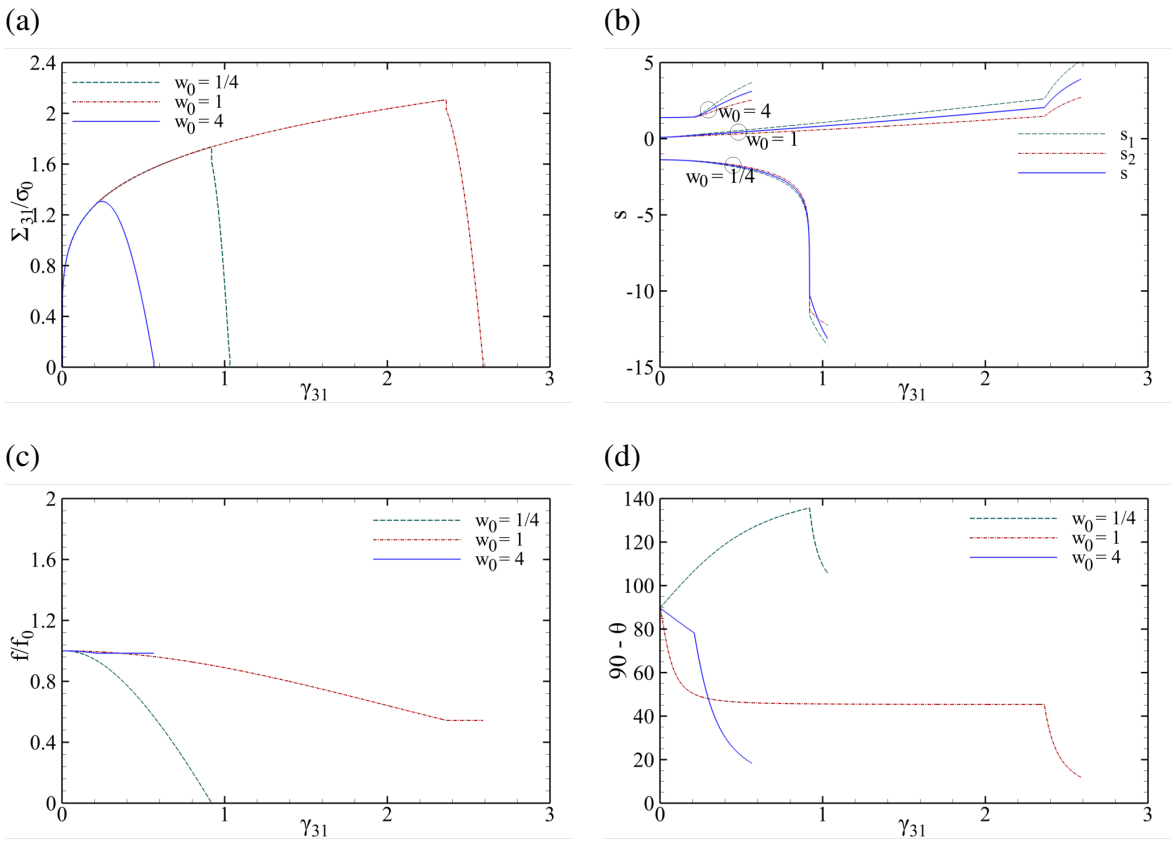

Figure 7.14: Predicted microstructural parameters for the same cell geometry with $(f_0, \lambda_0) = (0.01, 4)$ subjected to near-simple shearing ($\kappa = 0.02$) for various initially upright voids ($\theta_0 = 0$) with aspect ratios w_0 ranging from 1/4 to 4: (a) normalized shear response, (b) logarithmic void aspect ratio, (c) normalized porosity, (d) void angle with the horizontal direction.

The effect of void shape is studied via the variation of the initial void aspect ratio w_0. The latter effect, with w_0 ranging from 1/4 to 4, on the microstructural behavior under simple shearing is shown in Fig. 7.14 at fixed porosity level $f_0 = 0.01$ and cell aspect ratio $\lambda_0 = 4$, with the

same hardening exponent $N = 0.2$. Figure 7.14f substantiates the mechanism shown in Fig. 7.2 and schematized in Fig. 6.8a. Prolate and oblate voids rotate in opposite directions so that the larger axis moves towards aligning with the principal stretch direction, here initially lying close to 45° from the vertical direction and lying further down during the deformation process. Therefore, a prolate void rotates along with shearing and an oblate rotates opposite thereto. There exists, however, a maximum point within the angle curve pertaining to the oblate void which corresponds to a back-turn in rotation. The latter was also observed earlier with the difference being that, within the modified hybrid model, this instant takes place at the onset of localized deformation. This point further corresponds to the instant when the void closes, *i.e.* $a \longrightarrow 0$, $w \longrightarrow 0$ and $f \longrightarrow 0$ as indicated by Fig. 7.14c. At this point, deformation abruptly turns localized where and failure occurs soon afterwards. This observation signifies crack propagation for flat voids under limited void growth. Further, Fig. 7.14a shows the highest ductility as well as limit load for an initially spherical void. Meanwhile, an oblate void with $w = 1/x$ is more ductile than its prolate counterpart with $w = x$ ($x > 1$ implied) under a shear field.

The reader can gain a deeper insight into the behavior of oblate voids in shear fields by considering the behavior of an oblate void under various load combinations (denoted with different κ's). Moreover, a non-spherical void can exhibit widely different conducts under shearing when its initial orientation departs negatively or positively from the upright position. The reader is well-advised to refer to Sections 5.5 and 5.6 of Paper P7 to illustrate these effects. They are skipped herein in the interest of brevity.

7.4 Example Finite Element Simulation

An example FEM–based simulation is presented to demonstrate the capability of the proposed hybrid model to solve boundary–value problems. To this end, the local analysis is realized by the time integration of the material constitutive framework implemented in a user–defined subroutine (UMAT), and the global analysis is carried through discretization of the domain in ABAQUS standard. The example comprises an axisymmetric notched bar under an axial target displacement, which admits triaxial loading towards the center and combined triaxial and intermediate shearing

towards the notch corners [1].

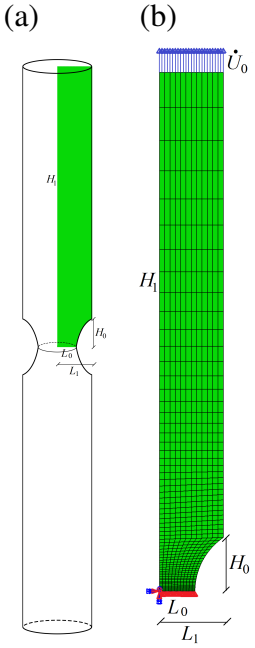

Figure 7.15: (a) Geometry of an axisymmetric bar under axial remote loading, (b) geometry of an equivalent tensile specimen with axisymmetric elements.

To reduce the computational cost, only a quarter of the assemblage is modeled with relative dimensions $(L_0, L_1) = (1.95, 3.5)$, $(H_0, H_1) = (2.9734, 28.75)$, and $\dot{U}_0$ is a prescribed displacement rate exerted at the top chord, as shown in Fig. 7.15. The prescribed relative value at the current study is 10. A uniform grid is used in the gauge section, Fig. 7.15a and, altogether, 756 eight–noded axisymmetric (CAX8R) elements with reduced integration are used. The global boundary conditions are stated in more detail in Paper P7 . The matrix material is endowed with the same constants as listed in Eq. (7.5). A stabilizing factor of 0.1 was considered in the global analysis. Further, a line–search algorithm (with the parameters declared in Paper P7) was acquired to capture the substantial change in the stress slope at the onset of inhomogeneous yielding.

[1]Models with more intense shearing encounter more serious global convergence problems. So for the model to be capable of simulating those models, a multi–surface model should be implemented in terms of a linear combination of Φ^{H} and Φ^{I}. Alternatively, an artificial damping can be incorporated within the constitutive framework and, accordingly, into the exported consistent tangent matrix

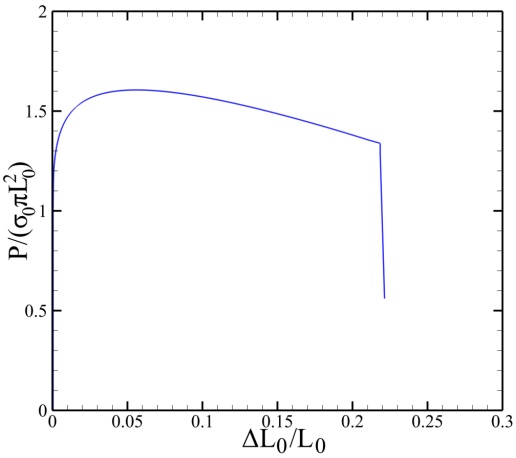

Figure 7.16: Normalized vertical stress emanating from the vertical reaction force divided by the initial cross sectional area at the notched section.

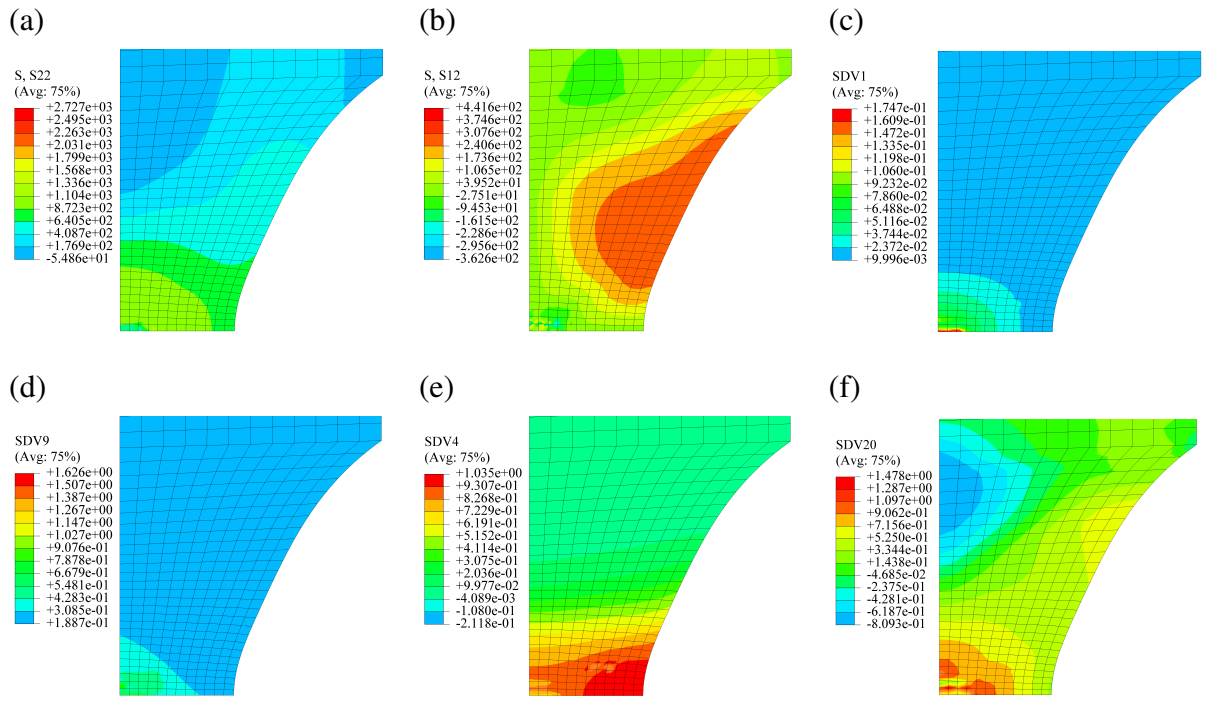

Figure 7.17: Spacial contours of selective internal state variables for the notched bar shown in Fig. 7.15, including: (a,b) axial and shear stresses, respectively, (c) porosity, (d) ligament parameter $\bar{\chi}$, (e) logarithmic void aspect ratio $s = \ln w$, (f) stress triaxiality T.

Figure 7.16 shows the global response given in terms of the bottom face vertical reacting traction vs. relative radius reduction. The analysis has stopped prior to utter failure due to global convergence issues. One can envisage significant softening prior to inhomogeneous deformation

due to damage accumulation, which results in a more than six–fold increase in porosity, as further observed in Fig. 7.17.

To gain better insight into the space distribution of the internal state variables, some selective state variables are shown in Fig. 7.17. Plastic strains are mainly confined within the notched zone, and the gauge zone remains (approximately) elastic. This is totally commensurate with experimental observations in notched bar uniaxial testing. Figure 7.17 demonstrate that the normal stress σ_{22}, along with porosity f, effective void spacing $\bar{\chi}$, and stress triaxiality T are maximum at the specimen center and decrease to their initial values moving towards the gauge section. A closer probe into Fig. 7.17a reveals a dropping stress approaching the bar center, which is characteristic of void coalescence, as further observed in Fig. 7.18b. Among all, $\bar{\chi}$ reduces precipitously with increasing distance from the center towards the notch surfaces. This will be further observed in Fig. 7.18c. All the same, shear stresses are maximum at the notch surface vicinity away from the base. Accordingly, the shear–dominant part of Eq. (5.2) would take over very soon without plasticity being localized at this region. Therefore, the transition to inhomogeneous yielding should be realized merely upon the normal portion of Eq. (5.2) at the vicinity of the notch surface.

The void aspect ratio, however, as shown in Fig. 7.17e, enlarges towards the notch surface near the bottom end. The reason for the void aspect ratio being maximum at this region is the existence of a dominant normal stress superposed by an intermediate shear stress, which corresponds to a maximal void elongation, also stipulated in Ref. [17]. The parts above this zone are either moderately sheared or uniaxially loaded, both triggering less elongation.

The internal state behavior is significantly versatile upon moving away from the reduced cross section. To perceive that, selective state variables are plotted for three different zones starting from the center of the specimen and moving towards the curved surface (shown in Fig. 7.18a), where the shear stress ranges from zero to a finite value.

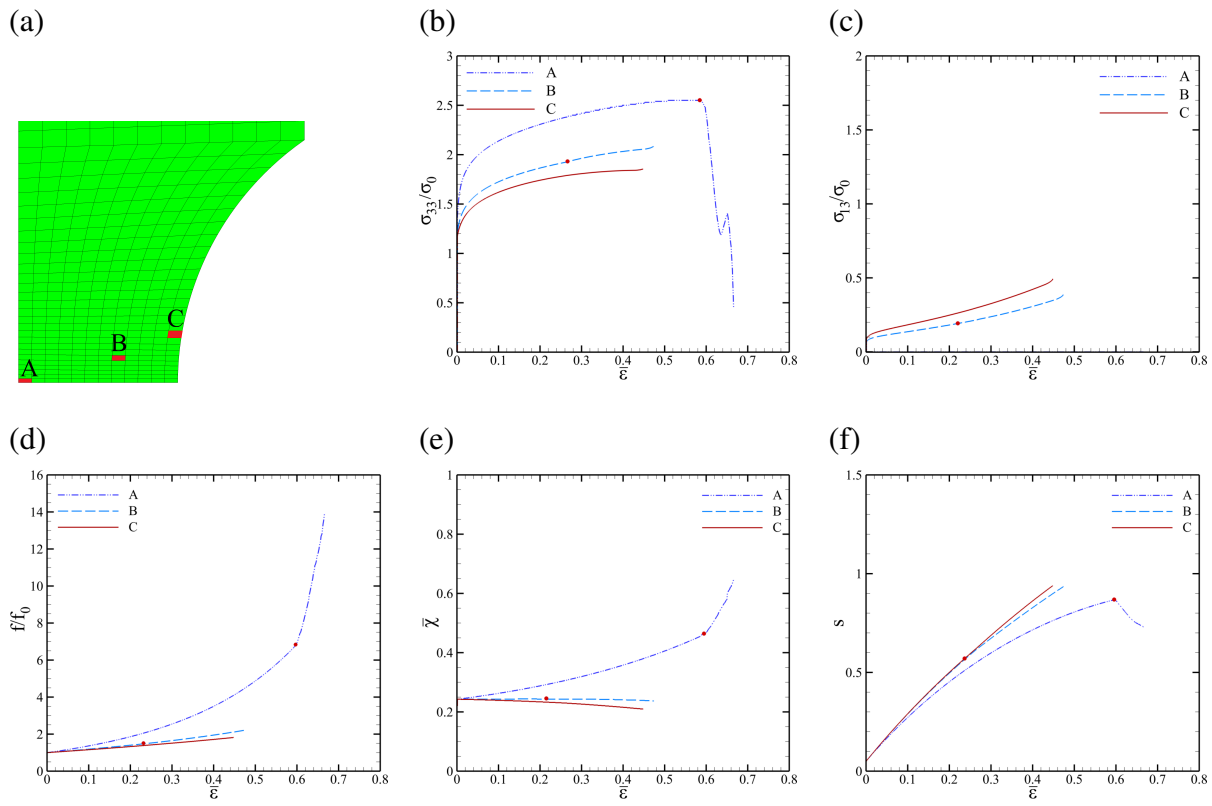

Figure 7.18: Selective microstrucrural parameters for zones A–C, as shown in part (a), with shear stresses ranging from zero to finite values: (b,c) normalized axial and shear stresses, respectively, (d) normalized porosity, (e) effective ligament parameter, and (f) logarithmic void aspect ratio.

Note that inhomogeneous deformation and/or void coalescence occurs in zones (A) and (B), with the transition points shown in red dots. The inhomogeneous yielding, however, is not reminiscent of void coalescence at zone (B) due to the progressive increase in the stress bearing capacity, according to Fig. 7.18b. The average stress response, however (as represented by Fig. 7.16), is declined after the inhomogeneous yielding onset. The shear stress, as depicted in Fig. 7.18c, increases in a more retarded manner at zone (B) due to inhomogeneous deformation being confined to intervoid ligaments, whereas it continues to grow faster at the notch surface (C). More importantly, the effective ligament parameter $\bar{\chi}$ increases at the center, with accelerated increase after coalescence, whereas it decreases at zones (B) and (C). This occurs due to the lateral stresses literally annihilated at these two zones. The inhomogeneous yielding mechanism, however, diminishes the decrease rate of $\bar{\chi}$, as shown after the dotted spot in Fig. 7.18e while it continues decreasing

with an even larger slope at zone (C). Moreover, Fig. 7.18f reaffirms the observation in Fig. 7.17e that the rate of increase in the void aspect ratio enlarges when some shear stress is superimposed to a normal dominant stress. Moreover, the post–localized trend of $s = \ln w$ ranges from declining at the center (with maximum lateral stresses) to increasing at zones (B) and (C) with lateral stresses vanishing and shear stresses coming into play.

7.5 Effect of Matrix Anisotropy

This subsection adumbrates on the fracture process to failure under combined tension and shear with anisotropic matrix materials with the matrix anisotropy idealized as Hill–type orthotropy. The results under triaxial loading, as well as the constitutive model assessment against numerical outcomes, are skipped herein, yet can be found in Paper P8 .

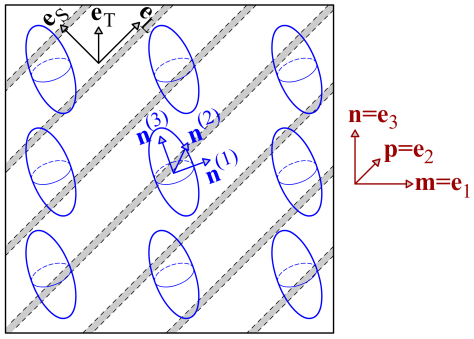

Figure 7.19: Schematic outline of a microstructure consisting of an aggregate of aligned spheroidal voids surrounded by an anisotropic matrix.

To this end, the constitutive framework is governed by the intersection of nearly-homogeneous and localized yield criteria obeying Eq's (6.3) and (6.39) as Φ^{H} and Φ^{I}, respectively, which are both endowed with the effect of matrix anisotropy of a Hill type. The predictive capability of the latter two-surface hybrid model was successfully assessed from comparison to the same benchmark calculations from Pardoen and Hutchinson [20] and Nielsen *et al.* [17] in absence and in presence of shear loads, respectively. See Paper P8 in this regard.

The principal axes of orthotropy are initially oriented along the base vectors $\boldsymbol{e}_{\mathrm{L}}$, $\boldsymbol{e}_{\mathrm{T}}$ and $\boldsymbol{e}_{\mathrm{S}}$, as indicated by Fig. 7.19, and are taken to rotate with the material, in accordance with Eq. (6.25).

Note that the matrix orthotropy basis $(\boldsymbol{e}_{\mathrm{L}}, \boldsymbol{e}_{\mathrm{T}}, \boldsymbol{e}_{\mathrm{S}})$, that tied to the voids $(\boldsymbol{n}^{(1)}, \boldsymbol{n}^{(2)}, \boldsymbol{n}^{(3)})$, and the principal loading directions $(\boldsymbol{e}_1, \boldsymbol{e}_2, \boldsymbol{e}_3)$ do not necessarily coincide, even when they do initially.

Here considered are situations where the principal loading axes are misaligned with the principal directions of matrix orthotropy. The latter was investigated by Kweon *et al.* [224] under triaxial loading, with the whole fracture process considered homogeneous with Φ^{H} obeying Eq (6.3). Yet, the effect induced by shearing, in conjugation with matrix anisotropy, remains to be evaluated. For the sake of brevity, only the results under near-simple shearing are chosen for the present chapter. Similar parametric studies under triaxial loading can be found in Paper P8 .

The rationale underlying the strong effect of matrix anisotropy on void growth has been explicated by Benzerga and Besson [95] and further expanded in [229]. Note that the idealization of a spheroidal void shape is an approximation. Within an anisotropic matrix, the void can develop into a 3D void even under axisymmetric loading.

7.5.1 Effect of shear Hill coefficients

The effect of matrix plastic anisotropy is firstly studied with a spherical void embedded therein. Focus is placed on near–simple shearing with $\kappa = 0.02$, and the cell is considered the same as that shown in Fig. 7.7a, with $(w_0, \chi_0, \lambda_0) = (1.1, 0.5, 4)$ with a hardening exponent of $N = 0.2$. Among the principal directions of orthotropy, the axis of transverse isotropy $\boldsymbol{e}_S$ is taken parallel to the main loading plane normal $\boldsymbol{n} \equiv \boldsymbol{e}_3$.

Table 7.1: Matrix anisotropy coefficients, h_i expressed in the basis of material orthotropy $(\boldsymbol{e}_{\mathrm{L}}, \boldsymbol{e}_{\mathrm{T}}, \boldsymbol{e}_{\mathrm{S}})$.

Matrix	h_{L}	h_{T}	h_{S}	h_{TS}	h_{SL}	h_{LT}
Isotropic	1.000	1.000	1.000	1.000	1.000	1.000
MAT1	1.000	1.000	1.000	2.333	2.333	1.000
MAT2	1.000	1.000	1.000	0.500	0.500	1.000

The anisotropy coefficients in the local coordinate system tied to the orthotropy directors are

tabulated in Table 7.1, with the material notation taken from [14]. All the three matrices have the same Hill coefficients along the three principal directions, *i.e.* h_{L}, h_{T} and h_{S}. Note that a large Hill coefficient in a given direction signifies the weakness/softness of the material in that direction. MAT1 and MAT2 are, therefore, softer and stiffer under shear in comparison to the isotropic material, respectively.

As earlier demonstrated in [224], and further corroborated by the present work, materials with different orthotropy coefficients exhibit different responses even in absence of shear. The latter occurs due to the presence of voids, which develops microscopically nonzero shear stresses at the cell level. This line of results can be found in Paper P8 .

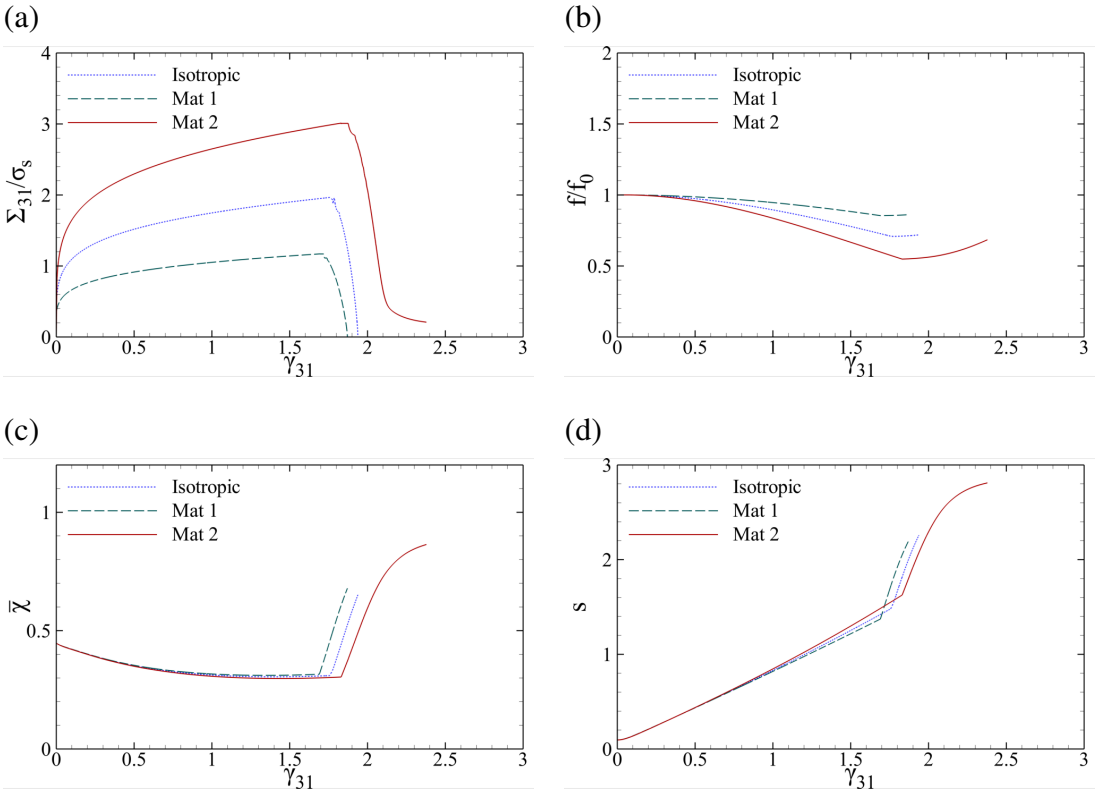

Figure 7.20: Selective microstrucrural parameters with the selected materials of Table 7.1 under near–simple shearing characterized with $\kappa = 0.02$ for the same cell considered in Sec. 7.3 with $(w_0, \chi_0, \lambda_0) = (1.1, 0.5, 4)$: (a) normalized shear stress, (b) void angle with respect to the horizontal axis, (c) normalized porosity, (d) natural logarithmic void aspect ratio.

During the nearly-homogeneous deformation, the correlation between plastic anisotropy and

porosity is taken into account by the κ parameter, with its full expression provided in Paper P7 . The analogous correlation during localized yielding, described by Φ^{I} obeying (6.39), can be envisaged through the notion of σ_{c} in Eq. (6.40).

Figure 7.20 illustrates this effect on various internal state variables for the selected materials of Table 7.1 under near–simple shearing characterized with $\kappa = 0.02$. Figure 7.20a reaffirms the stronger and weaker nature of MAT2 and MAT1 in comparison to the isotropic material, respectively. More appealingly, MAT2 is more ductile against shearing albeit stiffer. Accordingly, ductility and strength can coincide upon regular orthotropy against shear while the same feature cannot be acquired under triaxial loading. See Paper P8 for more details. It can also be observed, through Fig. 7.20(b,d), that the *rate* of void elongation (and rotation) is only slightly affected by matrix anisotropy when the material orthotropy directors are aligned with the main loading directions. Nevertheless, the *values* of these parameters become more distinctively apart with matrix shear anisotropy during localized deformation.

Note that, porosity evolution in general, be the void growing or shrinking, is faster for the material stronger in shear [224]. The latter may itself be attributed to the faster void elongation depicted in Fig. 7.20d, which takes place on account of faster squeezing of the rotating void by the stronger matrix owing to its stronger shear strength (h_{TS} and h_{SL}), that withstands material slippage along the shearing direction. The increased stress level for MAT2 (Fig. 7.20a) can then be ascribed to the sharper decrease in porosity f during nearly-homogeneous yielding. A similar comparison has earlier been observed under triaxial loading [224].

On the other hand, transformation of the $(\boldsymbol{e}_{\mathrm{L}}, \boldsymbol{e}_{\mathrm{T}}, \boldsymbol{e}_{\mathrm{S}})$ basis with respect to $(\boldsymbol{e}_1, \boldsymbol{e}_2, \boldsymbol{e}_3)$ can induce minimal to significant changes in the rotation rate. The following subsection adduces this effect.

7.5.2 *Effect of orthotropy axis change*

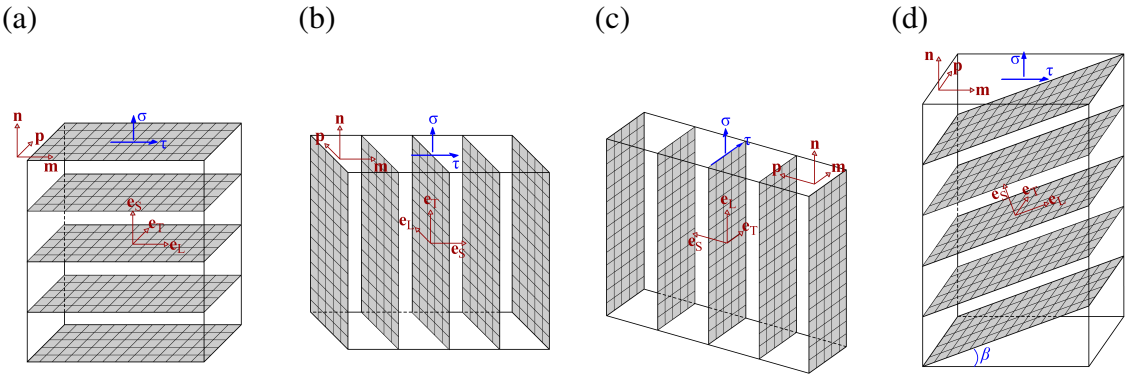

Figure 7.21: Flipped and rotated planes of transverse isotropy at the cell level, with the shear and normal tractions applied along $\boldsymbol{m}$ and $\boldsymbol{n}$, respectively: (a) $\boldsymbol{e}_{\mathrm{L}} = \boldsymbol{m}$, *i.e.* $L = 1$, (b) $\boldsymbol{e}_{\mathrm{L}} = \boldsymbol{p}$, *i.e.* $L = 2$, (c) $\boldsymbol{e}_{\mathrm{L}} = \boldsymbol{n}$, *i.e.* $L = 3$, (d) $\boldsymbol{e}_{\mathrm{L}} = \cos\beta\boldsymbol{m} + \sin\beta\boldsymbol{n}$.

This subsection addresses the internal state variation with a flip or rotation over the material orthotropy directors with respect to the principal loading plane. To this end, the plane of transverse isotropy is subjected to flip or rotation, as sketched schematically in Fig. 7.21, with the planes of transverse isotropy denoted with grated lattices. Note that the right permutation rule holds for all transformation scenarios. For the case of $L = 2$, for instance, $\boldsymbol{e}_{\mathrm{T}} = \boldsymbol{n}$ and $\boldsymbol{e}_{\mathrm{S}} = \boldsymbol{m}$, *i.e.* $(T, S) = (3, 1)$. The corresponding transformation tensor between the Cartesian and orthotropy frames, $\boldsymbol{R}^{*}$, obeys the following forms, as tabulated in Table 7.2, for the above–mentioned cases:

Table 7.2: $\boldsymbol{R}^{*}$ transformation tensors for the transverse isotropy planes schematized in Fig. 7.21.

Case	$\boldsymbol{e}_{\mathrm{L}} = \boldsymbol{m}$	$\boldsymbol{e}_{\mathrm{L}} = \boldsymbol{p}$	$\boldsymbol{e}_{\mathrm{L}} = \boldsymbol{n}$	$\boldsymbol{e}_{\mathrm{L}} = \cos\beta\boldsymbol{m} + \sin\beta\boldsymbol{n}$
$\boldsymbol{R}^{*}$	$\begin{bmatrix} 1 & 0 & 0 \\ 0 & 1 & 0 \\ 0 & 0 & 1 \end{bmatrix}$	$\begin{bmatrix} 0 & 0 & 1 \\ 1 & 0 & 0 \\ 0 & 1 & 0 \end{bmatrix}$	$\begin{bmatrix} 0 & 1 & 0 \\ 0 & 0 & 1 \\ 1 & 0 & 0 \end{bmatrix}$	$\begin{bmatrix} \cos\beta & 0 & -\sin\beta \\ 0 & 1 & 0 \\ \sin\beta & 0 & \cos\beta \end{bmatrix}$

$\boldsymbol{R}^*$ is exploited in the calculation of $\mathbb{h}$ and $\mathbb{p}$ in the global coordinate system. See Paper P8 for more details on the transformation.

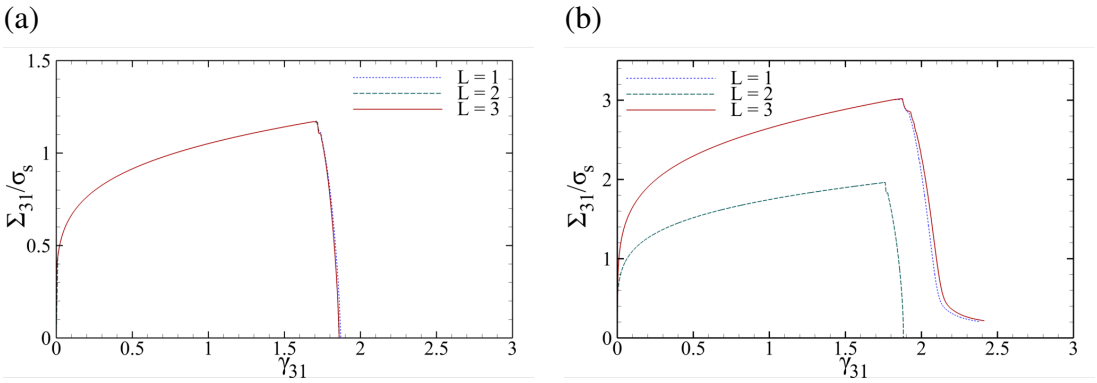

Figure 7.22: Normalized shear stress evolution for MAT1 and MAT2 under near–simple shearing characterized with $\kappa = 0.02$ for the same cell considered in Sec. 7.3 with $(w_0, \chi_0, \lambda_0) = (1.1, 0.5, 4)$, with $\mathrm{L} = 1, 2, 3$, denoting $\boldsymbol{e}_\mathrm{L}$ directed along $\boldsymbol{e}_1$, $\boldsymbol{e}_2$, and $\boldsymbol{e}_3$, respectively.

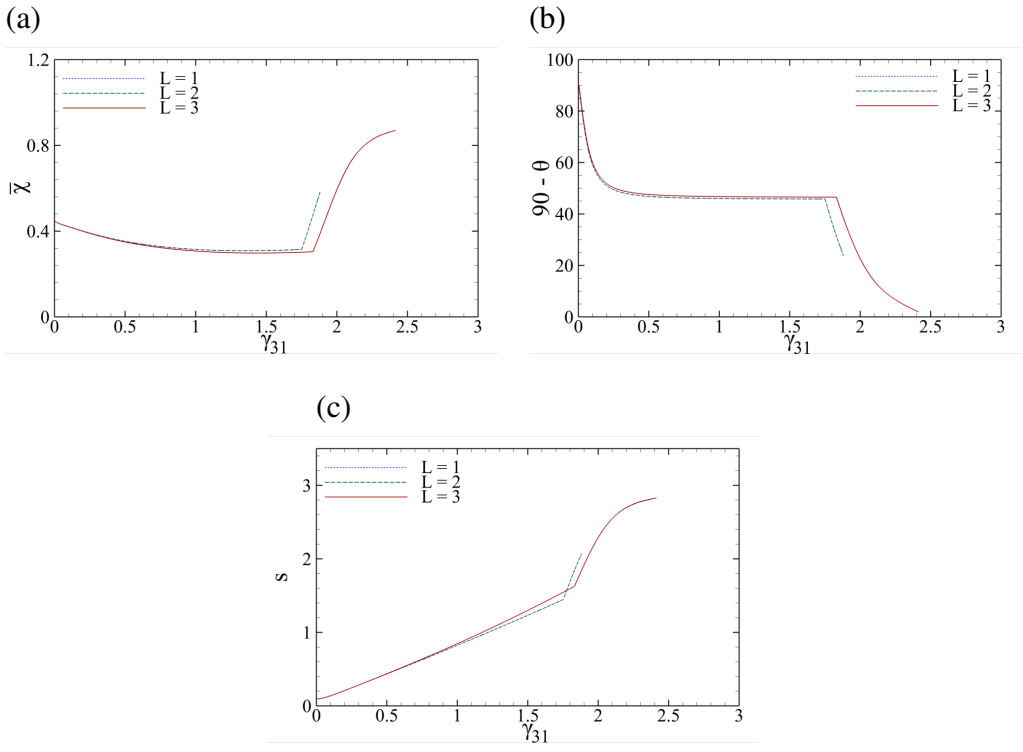

Figure 7.23: Additional selective state variables provided for MAT2 with the stress response shown in Fig. 7.22b: (a) effective ligament parameter, (b) void angle with respect to the horizontal axis, and (c) natural logarithmic void aspect ratio.

Figure 7.22 shows the shear stress evolution for MAT1 and MAT2 with $\boldsymbol{e}_{\mathrm{L}}$ directed along $\boldsymbol{e}_1$, $\boldsymbol{e}_2$, and $\boldsymbol{e}_3$, briefly noted with the "L" index taking on values of 1, 2, and 3, respectively. See Fig. 7.19. In order to gain more insight into this effect, other influential state variables are collected in Fig. 7.23 for MAT2. Figure 7.22a implies negligible difference in the softer material response under shear with flipping the weak macro–scale slip planes horizontally or vertically, with the ductility slightly higher for $\boldsymbol{e}_{\mathrm{L}} = \boldsymbol{e}_1$. This happens due to the perspicuous coupling between shearing in the $x_1 - x_3$ and $x_2 - x_3$ by which one weak/strong plane enfeebles/stiffens the other response vs. shear, and vice versa, whereby $\boldsymbol{e}_{\mathrm{L}} = \boldsymbol{e}_1$ and $\boldsymbol{e}_{\mathrm{L}} = \boldsymbol{e}_3$ exhibit close behaviors.

Note that, for both materials with varying shear Hill coefficients, the responses for $L = 1$ and $L = 3$ lie close to one other. This can be vindicated by the negligible Poisson effect under near-simple shearing such that both material configurations would constitute smaller parallel cross sections with the effective subcell heights remaining equal. In both scenarios, reflected by Fig's 7.21 (a) and (c), parallel planes operate almost independently under shearing for the weak material MAT1, and they would both act parallel plus an additional constraint caused by the strong orthotropy planes in MAT2. This observation is antithetical to that under triaxial loading, where there is clear distinction between the outcomes upon variation of $\boldsymbol{e}_{\mathrm{L}}$ (see [224] for details).

Nevertheless, within the $L = 2$ case, reflected by Fig. 7.21b, subcells function almost consecutively, *i.e.* in series, as being subjected to the shown shear traction τ. On this further occasion, the weak material MAT1 responds close to the other two cases due to being almost devoid of additional inter-planar shear constraints whereby the shear stress is distributed over smaller subcell cross sections. For the stronger material MAT2, however, $L = 1$ and $L = 3$ exhibit clear difference from $L = 2$. A closer examination of Fig. 7.21 can be indicative of this difference. That is, in the (a) and (c) subfigures, the inter-planar shear constraint is induced by the entire orthotropy planes being sheared whereas, in subfigure (b), this constraint is caused by mere rotation of these planes against shear deformation. The former would clearly bare higher stress-bearing capacity and ductility, as demonstrated by Fig. 7.22b.

In view of Fig. 7.23 for MAT2, the shear constraint within the rotating orthotropy planes,

characterized by the $L = 2$ case and as schematized in Fig. 7.22b, fairly impedes void elongation, thereby the corresponding void aspect ratio being smaller at the same shear strain level (Fig. 7.23c). Higher stresses are, however, demanded for the same strain level at the $L = 1$ and $L = 3$ cases considering the foregoing discussion.

The effect of rotating the plane of orthotropy on the state evolution under simple shearing comes next. The results will be presented for the weaker material in shear, MAT1 due to the targeted effect being more significant therefor.

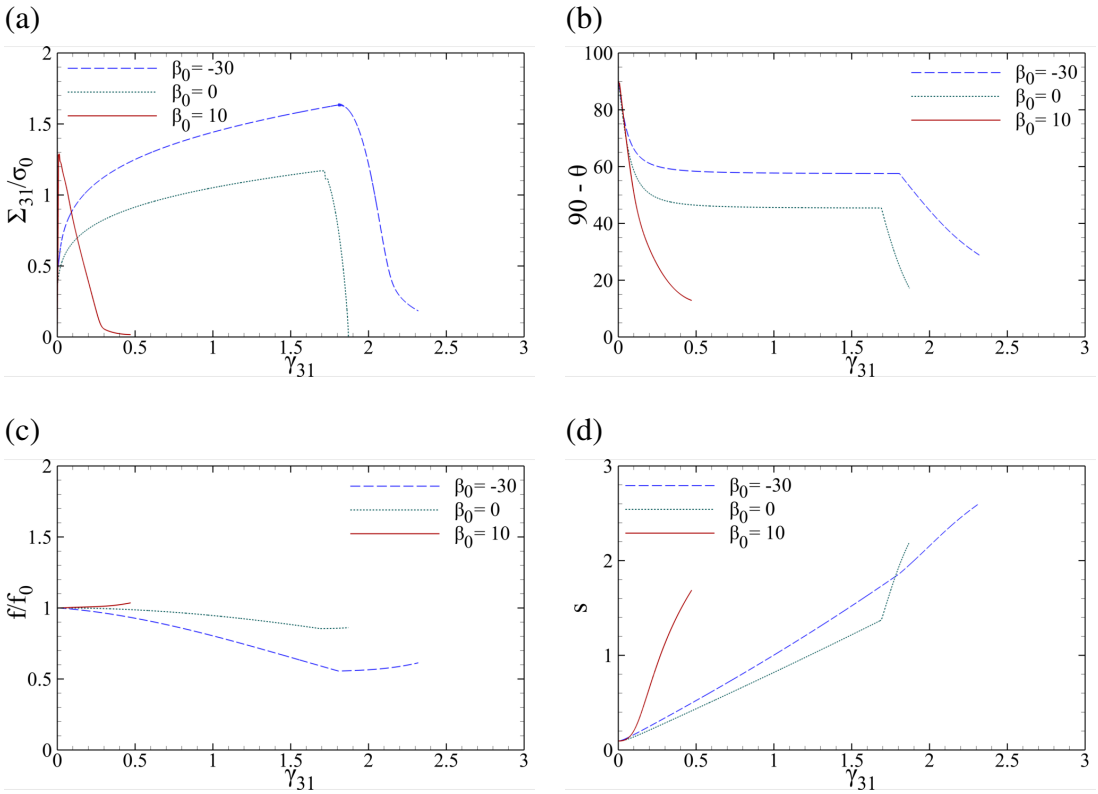

Figure 7.24: Selective internal state variables subjected to a rotated plane of transverse isotropy around the $\boldsymbol{e}_{\mathrm{T}}$ axis for MAT1 (upon properties given in Table 7.1) under near–simple shearing characterized with $\kappa = 0.02$ for the same cell considered in Sec. 7.3 with $(w_0, \chi_0, \lambda_0) = (1.1, 0.5, 4)$: (a) normalized shear stress, (b) void angle with respect to the horizontal axis, (c) normalized porosity, (d) natural logarithmic void aspect ratio.

Further, Fig. 7.24 illustrates the effect of rotating the plane of transverse isotropy around the $\boldsymbol{e}_{\mathrm{T}}$ axis on the internal state evolution for MAT1 upon properties provided in Table 7.1. The corresponding initial rotation angle β_0 (as shown in Fig. 7.21d) assumes negative, zero, and positive

values. A remarkable difference happens to the material conduct with β_0 changing sign. This large difference can be accredited to the equivalent stress state in the orthotropy frame. That is, $\beta_0 < 0$ imparts a pressure on the void, and thus delays failure in shear whereas $\beta_0 > 0$ increases tension which, in conjunction with shear, accelerates rotation and elongation, as demonstrated in Fig's 7.24 (b) and (d), respectively. As such, the porosity increase, indicated by Fig. 7.24c, would further expedite failure. There being, as seen in Fig. 7.24a, failure triggered soon after the elastic limit, a weak plane of transverse isotropy (with respect to shear), rotated positively relative to the plane of loading, is reminiscent of a crack. Note that the predicted stress response is based on the heuristic modification employed in accordance with Eq. (6.18), and is thus amenable to further modification in prospect. More precise results may exhibit larger ductility for the $\beta_0 > 0$ case. See Paper P8 for more explanation.

CHAPTER 8 EXTENSIONS

This chapter presents some extended versions of inhomogeneous yield criteria in respect to those presented in Chapter 5. The demand behind these extensions lies in the physical characteristics of ductile fracture under combined tension and shear that are not well captured by the simpler models. The limitations accompanying the models derived within the confines of this work are due, in part, to the circular cross section considered at the surrogate cell base. In fact, initially 3D voids under shear may have to undergo significant deformation before the voids can transform into spheroids that could be more realistically considered equivalent to cylindrical surrogate voids. In the existing literature, the model introduced by Madou and Leblond [230] accounts for inhomogeneous yielding in microstructures with 3D voids represented with ellipsoids. A well–suited counterpart thereof concerning inhomogeneous yielding is an extension to Eq. (5.2) that is developed over an RVE with elliptical cross sections. The other limitation within the present models is germane to the specific failure mechanism, *i.e.* combined internal necking and shearing, which may not invariably hold in all loading conditions, esp. with the prevalence of lateral to normal stresses or upon variations in the microstructural geometry. Void coalescence in columns (*necklace* coalescence), counter to coalescence in layers, is a newly uncovered ductile fracture mechanism [221] that has not been exhaustively investigated in the literature. A partly-revealing macroscopic stress parameter indicative of the distinction between void coalescence in layers and columns is the Lode parameter L, earlier introduced in Chapter 1. Under triaxial loading, void coalescence in columns is known to prevail for a Lode parameter $L = +1$ (which represents predominant lateral stress) as well as for $L = -1$ (which implies the converse) and elongated voids. The latter was explored by Benzerga [221] in the peculiar distribution of voids in laminated plates, where the extremely prolate (elongated) voids were generated through decohesion of the metallic matrix circumscribing inclusions elongated by the rolling process. Nevertheless, the potentially significant effect of microstructure on this mechanism has remained elusive by far. Gologanu *et al.* were the first and only ones who strove to develop a micromechanics–based model that could describe coalescence

in columns [50, 220]. Their model was derived on the basis of re–homogenization on the homogenized plastic plugs surrounded by a solid torus. The only microstructural parameter deemed effective in their model was porosity. Moreover, they could not derive a closed–form yield criterion. What we opt to do in the present context is to derive a closed-form yield criterion accounting for necklace localization that incorporates the effects of all the three independent microstructural parameters. Meanwhile, more sophisticated models will be introduced, in parametric rather than closed form, based on higher-order tentative velocity fields at the cell level. Since strain localization along columns prevails under the domination of normal loads, the latter is modeled with the effect of shear stresses disregarded.

The extensions of interest are, therefore, derivation of a model accounting for plane-localized yielding with 3D voids, and a series of models predicting column-localized yielding. Farther in the sequel, the *effective* failure mechanism will be drawn from the innermost yield surface between those corresponding to plasticity localized in layers and columns.

8.1 Coalescence of 3D Voids

8.1.1 Microstructural geometry

The outline of a general porous microstructure under remotely applied loading is schematized in Fig. 8.1a. The exact treatment of such a problem is complex if not impossible. The least level of complexity can be ascribed to the localization limit load not being worked out analytically for an orthorhombic cell containing an ellipsoidal void. Therefore, a surrogate cell is considered, as shown in Fig. 8.1b, which may not be space filling but is amenable to mathematical treatment.

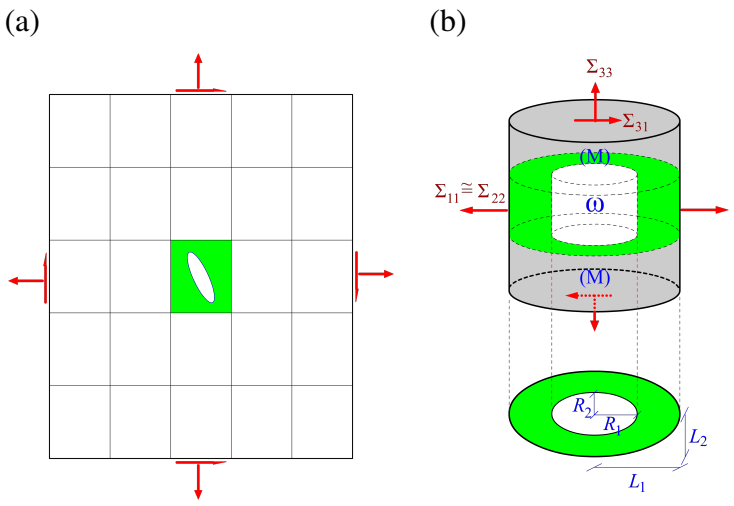

Figure 8.1: (a) Schematic outline of a porous microstructure under remotely applied loading; (b) geometry of a representative cylindrical cell with elliptical base and void under combined tension and shear.

The imposed displacement boundary conditions, as shown in Fig. 8.1b, give rise to a macroscopic stress state with a dominant axial stress, $\Sigma_{33} > \Sigma_{11}$, $\Sigma_{33} > \Sigma_{22}$, as well as shear stresses, Σ_{31} and Σ_{32}. The local cylindrical basis $(\boldsymbol{e}_r, \boldsymbol{e}_\theta, \boldsymbol{e}_z)$ and its global Cartesian counterpart $(\boldsymbol{e}_1, \boldsymbol{e}_2, \boldsymbol{e}_3)$ are utilized in the derivations. Upon the same method advised in Chapter 5 and expounded in Appendices P1 and P2 , the cell is subdivided into a central porous layer identifying a ligament domain, Ω_{lig}, attached to two dense matrices above and below.

The microstructural geometry can be uniquely identified by means of the following dimensionless parameters, only five of which are independent.

$$
\begin{aligned}
\alpha_{\text{v}} &= \frac{R_1}{R_2} \quad , \quad \alpha_{\text{c}} = \frac{L_1}{L_2} \\
\chi_1 &= \frac{R_1}{L_1} \quad , \quad \chi_2 = \frac{R_2}{L_2} \\
w_1 &= \frac{h}{R_1} \quad , \quad w_2 = \frac{h}{R_2} \\
\lambda_1 &= \frac{H}{L_1} \quad , \quad \lambda_2 = \frac{H}{L_2}
\end{aligned}
\tag{8.1}
$$

where α_v and α_c are, respectively, the void and cell in–plane aspect ratios. χ_i is the ligament parameters along the cell axis x_i (with $i = 1, 2$), and w_1 and w_2 are, respectively, the out–of–plane void aspect ratios in the $x_1 - x_3$ and $x_2 - x_3$ planes. Finally, λ_1 and λ_2 are the cell aspect ratios in the corresponding planes. Note that, in principle, α_v and α_c can take any positive value below or above 1. Without loss of generality, however, one can consider the cell major axis along x_1, *i.e.* $\alpha_c \geq 1$ while $0 < \alpha_v < \infty$. For the sake of convenience, the parameters adopted for presenting results are $\alpha_c, \chi_1, \chi_2, w_1, \lambda_1$. λ_1 and λ_2 are ineffective in the yield condition for localization while they can influence the onset of localization through the notion of porosity f [97].

8.1.2 Tentative velocity field

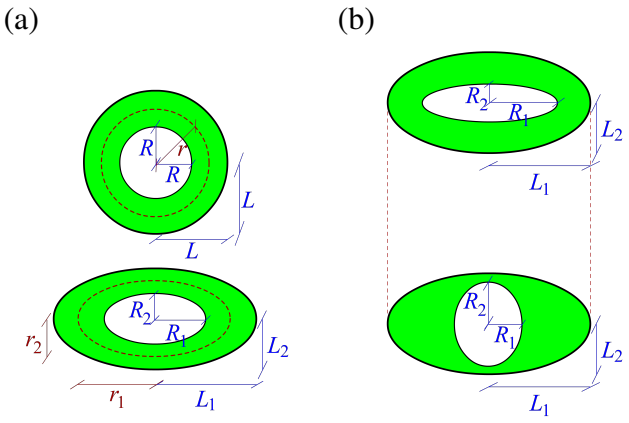

Figure 8.2: (a) Reference circular cross section and its homothetic elliptical counterpart, (b) schematic cross sections of a cylindrical cell with arbitrary inner (void) ellipses coaxial with the same outer (boundary) ellipse.

In order that the extended velocity field can deliver a closed–form solution, the cell cross section should be *homothetic* with the void, *i.e.* $\chi_1 = \chi_2$, as shown in Fig. 8.2a. This renders the values of α constant throughout the cell domain. To this end, the reference cell, characterized with a circular cross section, can be mapped into the cell with a homothetic cross section through a contravariant coordinate transformation [231]. Following rather cumbersome algebraic manipulations, the volume–preserving velocity field employed for the reference cell is transformed, in absence of

shear, into the following mapped field:

$$\boldsymbol{v}(\boldsymbol{x}) = \frac{D_{33}}{c}\left[\frac{1}{4}\left(\frac{L^2}{r} - r\right)\left[(\mathcal{A} + \mathcal{B}\cos 2\theta)\boldsymbol{e}_r - \mathcal{B}\sin 2\theta \boldsymbol{e}_\theta\right] + z\boldsymbol{e}_z\right] \tag{8.2}$$

where $\mathcal{A} = \sqrt{\alpha} + 1/\sqrt{\alpha}$ and $\mathcal{B} = \sqrt{\alpha} - 1/\sqrt{\alpha}$ on account of $\alpha \geq 1$. Moreover, α follows the coordinate transformation from (r, θ, z) into (x_1, x_2, x_3), with $x_3 \equiv z$, which remains constant $\alpha = \alpha_{\mathrm{c}} = \alpha_{\mathrm{v}}$ for a homothetic cross section. Under the same simplistic approach adopted in Chapter 5, the velocity field under combined tension and shear follows the same superposition as exploited in Appendices P1 and P2 .

The steps to derive the localization criterion for coaxial cylindrical cells having elliptical bases with arbitrary χ_1 and χ_2 are similar to those for homothetic cells, except for α varying with r which renders the volumetric integral not analytically calculable. Out of the infinite number of ellipses passing through every point lying in the cell domain, one can pick that emanating from a known $\mathcal{A}$ and $\mathcal{B}$ profile. As later demonstrated in the results, an upper bound to the dissipation for this case can be evaluated by neglecting the r–derivative of α and considering a simplified linear profile for the variation of $\mathcal{A}$ and $\mathcal{B}$ with r. To this end, let the subscripts 'v' and 'c' pertain to the inner ellipse (void boundary) and the outer ellipse (cell boundary), respectively. Correspondingly, the outer ellipse can be identified with α_{c}, which can be prescribed by the user and is generally different from that of the void ellipse α_{v}, the latter uniquely determined from known values of χ_1 and χ_2. It can be easily verified that

$$\alpha_{\mathrm{v}} = \frac{\chi_1}{\chi_2}\alpha_{\mathrm{c}} \tag{8.3}$$

Therefore, the corresponding values of $\mathcal{A}$ and $\mathcal{B}$ obey the following relations:

$$\begin{aligned} \mathcal{A}_{\mathrm{v}} &= \sqrt{\frac{\alpha_{\mathrm{v}}\chi_1}{\chi_2}} + \sqrt{\frac{\chi_2}{\alpha_{\mathrm{v}}\chi_1}} \quad , \quad \mathcal{B}_{\mathrm{v}} = \left|\sqrt{\frac{\alpha_{\mathrm{v}}\chi_1}{\chi_2}} - \sqrt{\frac{\chi_2}{\alpha_{\mathrm{v}}\chi_1}}\right| \\ \mathcal{A}_{\mathrm{c}} &= \sqrt{\alpha_{\mathrm{c}}} + \frac{1}{\sqrt{\alpha_{\mathrm{c}}}} \quad , \quad \mathcal{B}_{\mathrm{c}} = \sqrt{\alpha_{\mathrm{c}}} - \frac{1}{\sqrt{\alpha_{\mathrm{c}}}} \end{aligned} \tag{8.4}$$

where $\alpha_{\mathrm{c}} \geq 1$ is implied in the definition of $\mathcal{B}_{\mathrm{c}}$.

Remark: The yield load corresponding to the localization limit is majorly affected by the minimum void spacing and minorly affected by its maximum value. Hence, as henceforth seen in Fig. 8.3, the yield load in a non–homothetic cell proves smaller in comparison to its homothetic counterpart. Correspondingly, an upper bound to the yield load will be obtained from $\chi_{\max}$ taken as the effective ligament parameter, and a lower bound thereof will be a function of $\chi_{\min}$ involved in the equations. However, a more rigorous upper bound to the yield load can be estimated via the following relation

$$\alpha_{\rm v} = \frac{\chi_{\min}}{\chi_{\max}} \alpha_{\rm c}$$

which gives rise to the following modified counterpart of (8.4):

$$\begin{aligned} \mathcal{A}_{\rm v} &= \sqrt{\frac{\alpha_{\rm v}\chi_{\min}}{\chi_{\max}}} + \sqrt{\frac{\chi_{\max}}{\alpha_{\rm v}\chi_{\min}}} \quad , \quad \mathcal{B}_{\rm v} = \left| \sqrt{\frac{\alpha_{\rm v}\chi_{\min}}{\chi_{\max}}} - \sqrt{\frac{\chi_{\max}}{\alpha_{\rm v}\chi_{\min}}} \right| \\ \mathcal{A}_{\rm c} &= \sqrt{\alpha_{\rm c}} + \frac{1}{\sqrt{\alpha_{\rm c}}} \quad , \quad \mathcal{B}_{\rm c} = \sqrt{\alpha_{\rm c}} - \frac{1}{\sqrt{\alpha_{\rm c}}} \end{aligned} \tag{8.5}$$

where $\alpha_{\rm c} \geq 1$ is implied. The simplest profile that can be conceived is a linear function of dimensionless variable r/L, which preserves the upper–bound character. Let

$$\begin{aligned} \mathcal{A}(r) &= \mathcal{A}_{\rm v} + (\mathcal{A}_{\rm c} - \mathcal{A}_{\rm v}) \frac{\frac{r}{L} - \chi}{1 - \chi} \\ \mathcal{B}(r) &= \mathcal{B}_{\rm v} + (\mathcal{B}_{\rm c} - \mathcal{B}_{\rm v}) \frac{\frac{r}{L} - \chi}{1 - \chi} \end{aligned} \tag{8.6}$$

which, even upon this simplification, the effective dissipation Π cannot be determined analytically. However, the $\mathcal{A}$ and $\mathcal{B}$ can be replaced with their volumetric averages, here denoted with $\bar{\mathcal{A}}$ and $\bar{\mathcal{B}}$, so that Π is analytically calculable. Details aside, $\bar{\mathcal{A}}$ and $\bar{\mathcal{B}}$ can be expressed as

$$\begin{aligned} \bar{\mathcal{A}} &= \frac{\mathcal{A}_{\rm v} + \chi \mathcal{A}_{\rm c}}{1 + \chi} \\ \bar{\mathcal{B}} &= \frac{\mathcal{B}_{\rm v} + \chi \mathcal{B}_{\rm c}}{1 + \chi} \end{aligned} \tag{8.7}$$

which clearly simplifies into $\bar{\mathcal{A}} = \mathcal{A}$ and $\bar{\mathcal{B}} = \mathcal{B}$ in the case of a homothetic cell, identified by

$\mathcal{A}_{\rm v} = \mathcal{A}_{\rm c} = \mathcal{A}$ and $\mathcal{B}_{\rm v} = \mathcal{B}_{\rm c} = \mathcal{B}$. Here, $\chi = \sqrt{\chi_1 \chi_2}$ is the geometric average of the major and minor ligament parameters.

8.1.3 Effective yield criterion

The effective yield criterion accounting for localized deformation under combined tension and shear would then read

$$\Phi(\boldsymbol{\Sigma}, \chi_1, \chi_2, w_1, w_2, \alpha_{\rm v}, \alpha_{\rm c}) = \left(\frac{|\Sigma_{33}| - \mathcal{S}}{\mathcal{V}} \right)^2 \mathcal{H}(|\Sigma_{33}| - \mathcal{S}) + \frac{\Sigma_{31}^2 + \Sigma_{32}^2}{\mathcal{T}^2} - 1 \tag{8.8}$$

with $\mathcal{H}(x)$ being the Heaviside step function (with $\mathcal{H}(x) = 1$ for $x > 1$, $\mathcal{H}(x) = 0$ for $x < 0$, and $\mathcal{H}(0) = 1/2$), and

$$\begin{aligned} \chi_i &= \frac{R_i}{L_i} \quad , \quad w_i = \frac{h}{R_i} \\ \alpha_{\rm v} &= \frac{R_1}{R_2} \quad , \quad \alpha_{\rm c} = \frac{L_1}{L_2} \end{aligned} \tag{8.9}$$

with i taking in the values of 1 and 2. Among the geometric arguments, only four of them are independent and need be prescribed. They are adopted to be $(\chi_1, \chi_2, w_1, \alpha_{\rm c})$ in the present context. The rest follow from these independent parameters as

$$\begin{aligned} w_2 &= \frac{\chi_1}{\chi_2} \alpha_{\rm c} w_1 \\ \alpha_{\rm v} &= \frac{\chi_{\min}}{\chi_{\max}} \alpha_{\rm c} \end{aligned} \tag{8.10}$$

and

$$\begin{aligned} w^2 &= \frac{\chi_1}{\chi_2} \alpha_{\rm c} w_1^2 \\ \chi^2 &= \chi_1 \chi_2 \end{aligned} \tag{8.11}$$

are the geometric average values that are inserted into the following microstructural functions:

$$\frac{\mathcal{V}}{\bar{\sigma}} = \frac{1}{2\sqrt{3}} \left[\sqrt{\mathcal{C}_1} \ln \left(4u\sqrt{\mathcal{C}_1} \left[\sqrt{\mathcal{C}_1} + \sqrt{\mathcal{C}_1 + \frac{\mathcal{C}_2}{u^2}} \right] \right) - \sqrt{\mathcal{C}_1 + \frac{\mathcal{C}_2}{u^2}} \right]_1^{1/\chi^2}$$

$$\frac{\mathcal{S}}{\bar{\sigma}} = \frac{1}{24\sqrt{3}\,\chi(1-\chi)w} \left[3(1+\chi-2\chi^2)(\mathcal{A}_\mathrm{c}-\mathcal{A}_\mathrm{v}) + 4(\chi^3-3\chi+2)(\mathcal{A}_\mathrm{v}-\mathcal{A}_\mathrm{c}\chi) \right]$$

$$\frac{\mathcal{T}}{\bar{\sigma}} = \frac{1-\chi^2}{\sqrt{3}}$$

where

$$\mathcal{A}_\mathrm{v} = \sqrt{\frac{\alpha_\mathrm{v}\chi_\mathrm{min}}{\chi_\mathrm{max}}} + \sqrt{\frac{\chi_\mathrm{max}}{\alpha_\mathrm{v}\chi_\mathrm{min}}} \quad , \quad \mathcal{B}_\mathrm{v} = \left| \sqrt{\frac{\alpha_\mathrm{v}\chi_\mathrm{min}}{\chi_\mathrm{max}}} - \sqrt{\frac{\chi_\mathrm{max}}{\alpha_\mathrm{v}\chi_\mathrm{min}}} \right|$$

$$\mathcal{A}_\mathrm{c} = \sqrt{\alpha_\mathrm{c}} + \frac{1}{\sqrt{\alpha_\mathrm{c}}} \quad , \quad \mathcal{B}_\mathrm{c} = \sqrt{\alpha_\mathrm{c}} - \frac{1}{\sqrt{\alpha_\mathrm{c}}}$$

$$\bar{\mathcal{A}} = \frac{\mathcal{A}_\mathrm{v} + \chi\mathcal{A}_\mathrm{c}}{1+\chi} \quad , \quad \bar{\mathcal{B}} = \frac{\mathcal{B}_\mathrm{v} + \chi\mathcal{B}_\mathrm{c}}{1+\chi}$$

$$\mathcal{C}_1 = \bar{\mathcal{A}}^2 + \frac{\bar{\mathcal{B}}^2}{2} \quad , \quad \mathcal{C}_2 = \bar{\mathcal{A}}^2 + \bar{\mathcal{B}}^2 + 8$$

and, upon convention, $\chi_\mathrm{min} = \min(\chi_1, \chi_2)$ and $\chi_\mathrm{max} = \max(\chi_1, \chi_2)$. The $\alpha_\mathrm{c} \geq 1$ is implied in the definition of $\mathcal{B}_\mathrm{c}$. See Paper P9 for more details and algebraic proofs.

Selective results are hereby presented under stress states in absence of shear as well as under combined tension and shear. Figure 8.3 depicts the variation of the axial limit load for a unit cell with both homothetic and arbitrary elliptical bases vs. the α_c ratio as formerly defined. In the former case, $\alpha_\mathrm{v} = \alpha_\mathrm{c} = \alpha$ constitutes the abscissa, whereby $\chi_1 = \chi_2 = \chi$ can be varied. Subfigure (b) shows the same variation upon arbitrary values of χ_1 and χ_2 and, correspondingly, arbitrary α_v and α_c. For convenience, χ_1 and χ_2 are chosen such that the effective spacing χ, according to (8.11), stays constant, equaling 0.4 at present.

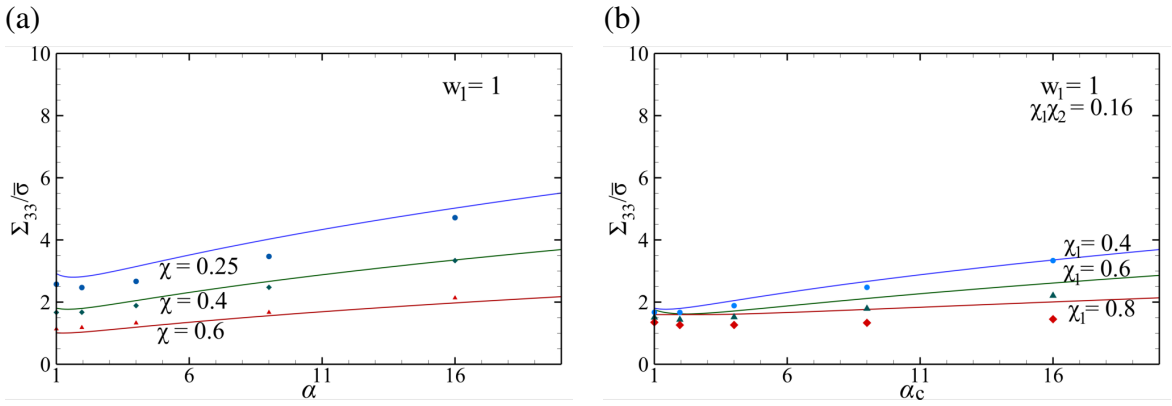

Figure 8.3: Evolution of axial yield load vs. the α_c ratio in comparison to its numerical counterparts: (a) for a homothetic cell, with $\alpha_c = \alpha_v = \alpha$, considering several $\chi_1 = \chi_2 = \chi$'s with $w_1 = 1$; (b) effect of different χ_1 values, ranging from 0.4 to 0.8 with $\chi = \sqrt{\chi_1\chi_2} = 0.4$ fixed, and $w_1 = 1$. The solid lines stand for analytical values, and the dots show numerical ones from cell-model calculations.

The predicted analytical limit loads are seen to be in sensible agreement with their FEM-based counterparts, being mindful of the fact that the model does not incorporate any adjustable parameter nor does it preserve the upper-bound character.

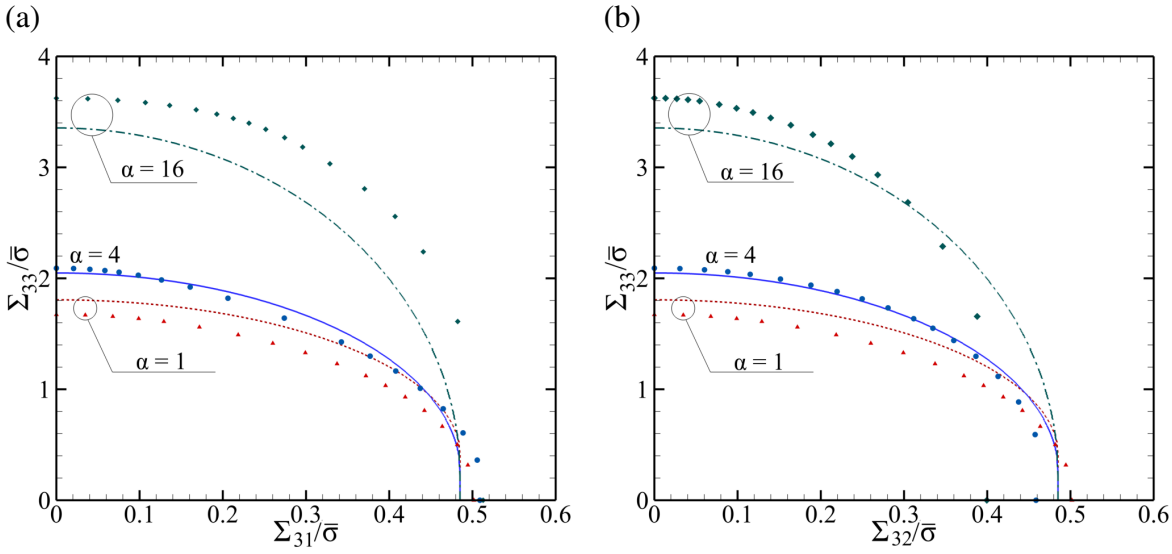

Figure 8.4: Correlation between normal and shear stresses for a homothetic cell with $\chi = 0.4$ and $w_1 = 1$ with several values of α: (a) under shearing applied along x_1 (major axis); (b) under shearing applied along x_2 (major axis). The solid lines stand for analytical values, and the dots show numerical ones from cell-model calculations.

Remark: In accordance with both analytical and numerical results, the minimum limit load, in almost all geometric configurations, corresponds to $\alpha_c = 2$ rather than the circular cross section denoted by $\alpha_c = 1$. Beyond this point, for $\alpha_c \geq 2$, the axial limit load increases with increasing α_c which increases the overall stiffness of the cross section and makes void impingement harder. See Paper P9 for observations.

For the state of combined tension and shear, the results are presented for homothetic cells (for arbitrary cells, they will be similar). The shear stress is once applied along x_1 and once along x_2, one being the semi-major and the other being the semi-minor axis. Figure 8.4 shows the correlation of normal and shear stresses for the aforesaid conditions and several values of the α ratio.

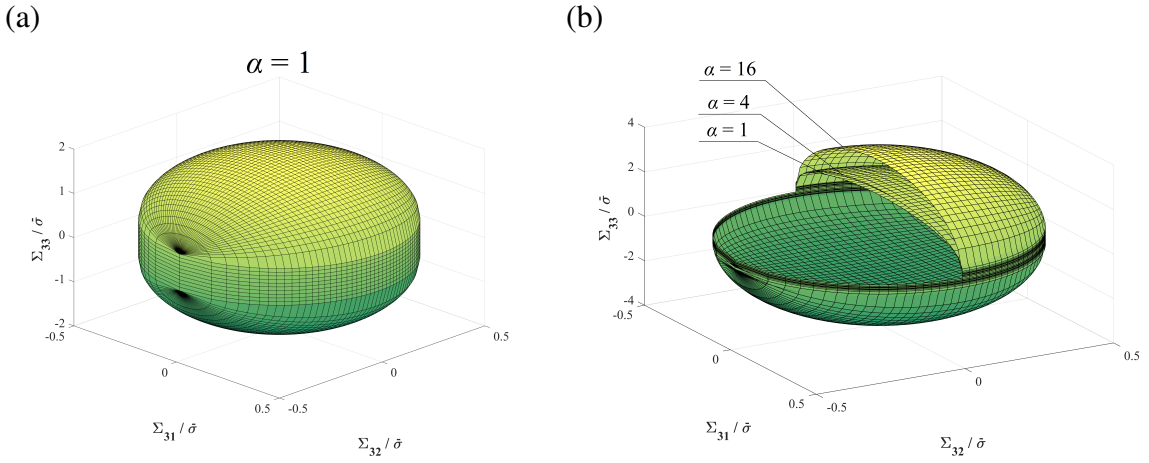

Figure 8.5: Correlation among Σ_{33}, Σ_{31}, and Σ_{32} for a homothetic cell with $\chi = 0.4$ and $w_1 = 1$: (a) reference cell with a circular cross section; (b) effect of the α ratio selected below, equal, and above 1. The latter surfaces are shown partially for better clarity of the effect.

In order to acquire a deeper insight into the yield surface, the yield surface can be presented in the Σ_{33}–Σ_{31}–Σ_{32} stress space, as shown in Fig. 8.5 for the homothetic cell with frozen microstructure denoted with $\chi = 0.4$ and $w_1 = 1$ and several values of α. Symmetry with respect to the Σ_{31} and Σ_{32} is envisaged.

Fig. 8.4 demonstrates that, for a shear stress applied along the major axis, the de facto maximum shear stress $\mathcal{T}$, *i.e.* the shear limit load at zero axial stress, stays almost constant with varying ellipticity. This lies in the rather even distribution of shear strains/velocities. For shearing along

the minor axis, however, some normal strain (and stress) is developed in the form of local vortices around the void (see Paper P9 for observations). As a consequence, $\mathcal{T}$, especially for larger values of α_c, decreases with increasing α_c. Nevertheless, $\mathcal{T}$ in the analytical model is agnostic to the shearing direction. This reveals the limitation of the simplistic Gurson-like shear field developed based on a linear shear velocity profile along the vertical direction in both directions. This constraint warrants a more realistic shear velocity profile that can take into account the effects induced by the cell shape as well as the void shape.

8.2 Void Coalescence in Columns

8.2.1 Microstructural geometry

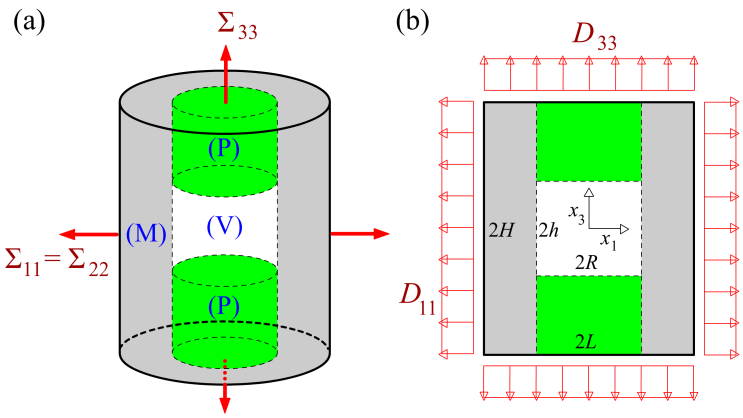

Figure 8.6: (a) Geometry of a cylindrical RVE representing column-like localization under a triaxial loading scheme; (b) lateral projection of the RVE with the induced geometry and macroscopic rate-of-deformation components belonging to each subpart.

Consider the RVE subdivision as shown in Fig. 8.6a. The overall volume can be then decomposed into the following constituents:

$$\Omega = V(\Omega) = \Omega^{(\mathrm{P})} + \Omega^{(\mathrm{V})} + \Omega^{(\mathrm{M})} \tag{8.12}$$

where the subparts (V), (P), and (M) stand for the void, the porous part (excluding the void), and the matrix tori, respectively. The overall geometry of the RVE is then determined by the same independent dimensionless parameters targeted throughout this thesis: χ, w, and λ.

8.2.2 Kinematic relations

The continuity from the macroscopic perspective, along with the isochoric nature of the solid, *i.e.* the (P) and (M) zones, entails that the following relationships hold among the macroscopic rates of deformation (see Paper P10 for details):

$$\begin{aligned} &D_{33}^{(\mathrm{P+V})} = D_{33}^{(\mathrm{M})} = D_{33} \\ &D_{11}^{(\mathrm{P+V})} = \frac{D_{11}}{\chi^2} + \frac{1}{2}\left(\frac{1}{\chi^2} - 1\right) D_{33} \\ &D_{kk}^{(\mathrm{M})} = 0 \quad \therefore \quad D_{11}^{(\mathrm{M})} = -\frac{D_{33}}{2} \end{aligned} \tag{8.13}$$

8.2.3 Tentative velocity field

The isochoric nature of plasticity entails that $\Omega^{(\mathrm{P})}$ and $\Omega^{(\mathrm{M})}$ stay constant. Therefore

$$d_{kk}^{(\mathrm{P})} = \mathrm{div}\boldsymbol{v}^{(\mathrm{P})} = 0 \quad , \quad d_{kk}^{(\mathrm{M})} = \mathrm{div}\boldsymbol{v}^{(\mathrm{M})} = 0 \tag{8.14}$$

The tori obey a Gurson-like velocity field, which reads:

$$\begin{aligned} &v_r^{(\mathrm{M})} = \frac{A}{r} - \frac{B}{2}r \quad , \quad v_z^{(\mathrm{M})} = Bz \\ &v_z^{(\mathrm{M})}(H) = BD_{33} \ \therefore \ B = D_{33} \quad , \quad v_r^{(\mathrm{M})}(L) = D_{11}L \ \therefore \ A = \frac{D_{kk}L^2}{2} \end{aligned} \tag{8.15}$$

The plugs, in the simplest-case scenario, admit the following form of v_r:

$$v_r^{(\mathrm{P})} = D_{11}^{(\mathrm{P+V})} r = \frac{1}{2\chi^2}\left(D_{kk} - \chi^2 D_{33}\right) r \tag{8.16}$$

Therefore, satisfying $v_r^{(\mathrm{P})}(R) = v_r^{(\mathrm{M})}(R)$ reassures a C^0-order continuity along the r direction. The z-wise velocity function should then be derived from a zero-divergence condition, which yields

$$v_z^{(\mathrm{P})} = \frac{1}{\chi^2}[D_{kk}(H - z) + \chi^2 D_{33} z] \tag{8.17}$$

(see Paper P10 for details).

One can easily observe that the derived $v_z^{(\mathrm{P})}$ is discontinuous with respect to z. While this distribution is contrary to reality, it proves feasible in the macroscopic scale provided the macroscopic dissipation induced by this discontinuity is affixed to the total dissipation function. This will be further clarified in Sec. 8.2.4.

A more realistic velocity field is created upon higher continuity induced by a higher-order choice of $v_z^{(\mathrm{P})}$. To this end, one can arbitrate the following field for $v_z^{(\mathrm{P})}$:

$$v_z^{(\mathrm{P})} = D_{33}z + 2\frac{D_{kk}}{\chi^2}(H-z)\left[1-\left(\frac{r}{R}\right)^2\right] \tag{8.18}$$

which, upon satisfaction of div$\boldsymbol{v} = 0$, delivers the following r component:

$$v_r^{(\mathrm{P})} = \frac{-r}{2}\left(D_{33} + \frac{D_{kk}}{\chi^2}\left[-2+\left(\frac{r}{R}\right)^2\right]\right) \tag{8.19}$$

8.2.4 Effective dissipation

Following the same discussion as addressed in Section 4.3, the layer-wise effective dissipations will turn out as

– Minimum continuity:

$$\Pi^{(\mathrm{P})} = \frac{1}{\Omega^{(\mathrm{P})}}\int_{\Omega^{(\mathrm{P})}} d_{\mathrm{eq}}^{(\mathrm{P})} d\Omega = 2\left|D_{11}^{(\mathrm{P+V})}\right|\bar{\sigma} \tag{8.20}$$

Besides, the discontinuity between $v_z^{(\mathrm{P})}$ and $v_z^{(\mathrm{M})}$ promotes an additional term as stated parametrically in (4.15), rewritten herein as follows:

$$\Pi^{\mathrm{surf}} = \frac{1}{\Omega^{(\mathrm{P})}}\int_{S_{\mathrm{int}}} \bar{\tau}[\![\boldsymbol{v}]\!]dS = \frac{w}{\chi^2}\frac{1-c}{c}|D_{kk}|\,\bar{\tau} \tag{8.21}$$

where $\bar{\tau} = \bar{\sigma}/\sqrt{3}$ is the matrix shear strength in terms of the uniaxial yield strength, and S_{int}

is the area of the interface connecting (P) and (M) at $r = R$ (see Paper P10 for details).

– Higher continuity:

$$\Pi^{(\mathrm{P})} = \frac{|D_{33}|\,\bar{\sigma}}{1-c}\int_{v=c}^{1}\mathcal{I}dv \quad , \quad \mathcal{I} = \int_{u=0}^{1}\sqrt{\mathcal{R}(u)}du \tag{8.22}$$

with $u = (r/L)^2$, and

$$\begin{aligned}
&\mathcal{U}_0 = (\xi_1 - 1)^2 \\
&\mathcal{U}_1 = \xi_1 + \xi_1^2(\delta - 1) \\
&\mathcal{U}_2 = \frac{13}{12}\xi_1^2 \\
&\xi = \frac{D_{kk}}{D_{33}} \quad , \quad \xi_1 = 2\frac{\xi}{\chi^2} \\
&\delta = \frac{2}{3}\left(\frac{\lambda(1-v)}{\chi}\right)^2
\end{aligned} \tag{8.23}$$

Note that $\mathcal{I}$ is fortunately calculable analytically. Since $\mathcal{U}_2 \geq 0$, the following integral will be admitted provided the following discriminant is positive [232]:

$$\Delta = \mathcal{U}_0\mathcal{U}_2 - \mathcal{U}_1^2 > 0 \tag{8.24}$$

Then, the integral is expressible as follows:

$$\mathcal{I} = \frac{1}{2}\left[(u+\mathcal{B})\sqrt{\mathcal{R}(u)} + \mathcal{P}\ln|\mathcal{L}|\right]_{u=0}^{1} \tag{8.25}$$

where

$$\begin{aligned}
&\mathcal{B} = \frac{\mathcal{U}_1}{\mathcal{U}_2} = \frac{12}{13}\left(\frac{1}{\xi_1} + \delta - 1\right) \\
&\mathcal{P} = \frac{\mathcal{U}_0 - \frac{\mathcal{U}_1^2}{\mathcal{U}_2}}{\sqrt{\mathcal{U}_2}} = \sqrt{\frac{12}{13}}\frac{1}{|\xi_1|}\left[(\xi_1-1)^2 - \frac{12}{13}\left(1 + \xi_1(\delta-1)\right)^2\right] \\
&\mathcal{L} = \sqrt{\mathcal{U}_2\mathcal{R}(u)} + \mathcal{U}_2 u + \mathcal{U}_1
\end{aligned} \tag{8.26}$$

Note that the discriminant in (8.24) is absolutely positive on account of $u > 0$.

The overall integral in (8.22), however, is not solvable analytically. With the existing mathematical tools, one can numerically estimate the integral. Alternatively, one can approximate the integral by expressing $\mathcal{I}$ in terms of its volumetric average value. See Paper P10 for details.

Note also that continuity between $v_z^{(\mathrm{P})}$ and $v_z^{(\mathrm{M})}$ is satisfied, thereby eliminating the additional surface dissipation.

Moreover,

$$\Pi^{(\mathrm{M})} = \frac{1}{\Omega^{(\mathrm{M})}} \int_{\Omega^{(\mathrm{M})}} d_{\mathrm{eq}}^{(\mathrm{M})} d\Omega \equiv \frac{1}{1-\chi^2} \int_{v=0}^{1} \int_{u=\chi^2}^{1} \bar{\sigma} d_{\mathrm{eq}}^{*(\mathrm{M})}(u,v) du dv = \frac{\bar{\sigma}}{1-\chi^2} \int_{\chi^2}^{1} d_{\mathrm{eq}}^{*(\mathrm{M})} du \tag{8.27}$$

The integral in $\Pi^{(\mathrm{M})}$ can be evaluated in exact or approximate form. The exact form is expressible as

$$\begin{aligned} \Pi^{(\mathrm{M})} = \frac{\bar{\sigma}|D_{33}|}{1-\chi^2} \int_{\chi^2}^{1} \sqrt{\left(\frac{\xi_2}{u}\right)^2 + 1}\, du &= |\xi_2| \left[\sqrt{1 + \left(\frac{u}{\xi_2}\right)^2} - \sinh^{-1}\left(\frac{|\xi_2|}{u}\right) \right]_{u=\chi^2}^{1} \\ &= \frac{|D_{kk}|}{\sqrt{3}(1-\chi^2)} \left[\sinh^{-1}\left(\mathcal{Y}|\xi_2|\right) - \sqrt{1 + \frac{1}{(\mathcal{Y}\xi_2)^2}} \right]_{\mathcal{Y}=1}^{1/\chi^2} \end{aligned} \tag{8.28}$$

where $\xi_2 = \xi/\sqrt{3}$, with ξ defined in (8.23). The counterpart to (8.28) is reported in Paper P10 .

Altogether, the total dissipation is the volumetric average of Π functions over the whole volume. With c_P and c_T denoting the volume fractions of the (P) and (M) subvolumes, the following can be written:

$$\Pi = c_P \left(\Pi^{(\mathrm{P})} + \Pi^{\mathrm{surf}} \right) + c_T \Pi^{(\mathrm{M})} \quad , \quad c_P = \chi^2(1-c)\,,\ c_T = 1 - \chi^2 \tag{8.29}$$

where Π^{surf} obeys (8.21) in the minimum continuity and $\Pi^{\mathrm{surf}} = 0$ in the higher continuity fields.

8.2.5 *Effective yield criterion*

The dissipation function expanded based on the minimum-continuity velocity field is not differentiable, and thus the primitive form of the principal inequality of limit analysis underlies the following piecewise-continuous effective yield criterion. The latter, here termed $\Phi^{\mathrm{col}}=0$, can be written as (see Paper P10 for algebraic details):

$$\Phi^{\mathrm{col}}=\begin{cases}\dfrac{\Sigma_{33}-\Sigma_{11}}{\bar{\sigma}}-(1-c\chi^2)\mathrm{sgn}(\Sigma_{33}) & \text{for } \left|\dfrac{\Sigma_{11}}{\bar{\sigma}}\mathrm{sgn}(\Sigma_{33})+(1-c)\right|\leq\dfrac{w}{\sqrt{3}}\dfrac{(1-c)^2}{c}\\[2ex] \dfrac{\Sigma_{33}-(1-\chi^2)\Sigma_{11}}{\bar{\sigma}}-\dfrac{\chi^2}{\sqrt{3}}\mathrm{sgn}(\Sigma_{33})\left(\dfrac{(1-c)^2}{c}+\left[\sinh^{-1}\left(\mathcal{Y}\dfrac{\chi^2}{3}\right)-\sqrt{1+\dfrac{1}{\left(\mathcal{Y}\frac{\chi^2}{3}\right)^2}}\right]_{\mathcal{Y}=1}^{1/\chi^2}\right) & \\ \text{for } \left|\dfrac{\Sigma_{11}}{\bar{\sigma}}\mathrm{sgn}(\Sigma_{33})-\frac{1}{\sqrt{3}}\left(w\frac{(1-c)^2}{c}+\left[\sinh^{-1}\left(\mathcal{Y}\frac{\chi^2}{3}\right)\right]_{\mathcal{Y}=1}^{1/\chi^2}\right)\right|\leq 1-c & \\[2ex] \left[\dfrac{\Sigma_{33}-\Sigma_{11}}{\bar{\sigma}}+(1-c)\chi^2\mathrm{sgn}(\Sigma_{11})\right]^2+2\chi^2\cosh\left(\sqrt{3}\left[\dfrac{\Sigma_{11}}{\bar{\sigma}}-(1-c)\left(1+\dfrac{w}{\sqrt{3}}\dfrac{1-c}{c}\right)\mathrm{sgn}(\Sigma_{11})\right]\right)-(1+\chi^2) & \text{Otherwise}\end{cases} \tag{8.30}$$

Inasmuch as Π upon the higher-continuity field is everywhere differentiable, the corresponding yield surface is everywhere smooth, thereby expressible in derivative form. Yet, the latter is not attainable in closed form, but in parametric form, *i.e.* in terms of the ξ ratio, upon its definition in (8.23), or any other related ratio.

To this end, the following fundamental derivative must be determined first:

$$\mathcal{I}_{,\xi_1}=\frac{1}{2}\left[\mathcal{B}'\sqrt{\mathcal{R}}+(u+\mathcal{B})\mathcal{R}^*+\mathcal{P}'\ln|\mathcal{L}|+\mathcal{P}\frac{\mathcal{L}'}{\mathcal{L}}\right]_{u=0}^{1} \tag{8.31}$$

where, with reference to the definitions in (8.23), we have:

$$\begin{aligned}
\mathcal{B}' &= \frac{\partial \mathcal{B}}{\partial \xi_1} = \frac{-12}{13\xi_1^2} \\
\mathcal{P}' &= \frac{\partial \mathcal{P}}{\partial \xi_1} = \frac{\sqrt{12}}{13^{3/2}} \text{sgn}(\xi_1) \left[-2(\delta-1)^2 + 3 - \frac{1}{\xi_1^2} \right] \\
\mathcal{R}^* &= \frac{1}{2\sqrt{\mathcal{R}}} \frac{\partial \mathcal{R}}{\partial \xi_1} = \frac{\frac{13}{12}\xi_1 u^2 + [1 + 2(\delta-1)\xi_1]u + (\xi_1 - 1)}{\sqrt{\frac{13}{12}\xi_1^2 u^2 + 2\xi_1[1 + (\delta-1)\xi_1]u + (\xi_1-1)^2}} \\
\mathcal{L}' &= \frac{\partial \mathcal{L}}{\partial \xi_1} = \sqrt{\frac{13}{12}} |\xi_1| \, \mathcal{R}^* + \frac{13}{6}\xi_1 u + [1 + 2(\delta-1)\xi_1]
\end{aligned} \tag{8.32}$$

Then, according to (8.29), the total stress subspace pertaining to localization along void columns can be expressed as

$$\begin{aligned}
\frac{\Sigma_{11}}{\bar{\sigma}} &= \frac{\Sigma_{11}^{(1)}}{\bar{\sigma}} + \frac{\Sigma_{11}^{(2)}}{\bar{\sigma}} \\
\frac{\Sigma_{33}}{\bar{\sigma}} &= \frac{\Sigma_{33}^{(1)}}{\bar{\sigma}} + \frac{\Sigma_{33}^{(2)}}{\bar{\sigma}}
\end{aligned} \tag{8.33}$$

where

$$\begin{aligned}
\frac{\Sigma_{11}^{(1)}}{\bar{\sigma}} \text{sgn}(\Sigma_{33}) &= 2 \int_{v=c}^{1} \mathcal{I} dv \\
\frac{\Sigma_{33}^{(1)}}{\bar{\sigma}} \text{sgn}(\Sigma_{33}) &= -2(\xi - 1) \int_{v=c}^{1} \mathcal{I}_{,\xi_1} dv + \chi^2 \int_{v=c}^{1} \mathcal{I} dv \\
\frac{\Sigma_{11}^{(2)}}{\bar{\sigma}} \text{sgn}(\Sigma_{11}) &= \alpha_1 - \alpha_2 \\
\frac{\Sigma_{33}^{(2)}}{\bar{\sigma}} \text{sgn}(\Sigma_{11}) &= \beta_1 - \beta_2
\end{aligned} \tag{8.34}$$

where

$$\begin{aligned}
\sqrt{3}\alpha_1 = \sinh^{-1}|\xi_2| \quad &, \quad \sqrt{3}\alpha_2 = \sinh^{-1}\frac{|\xi_2|}{\chi^2} \\
\sqrt{3}\beta_1 = \sqrt{1+\xi_2^2} \quad &, \quad \sqrt{3}\beta_2 = \sqrt{\xi_2^2 + \chi^4}
\end{aligned} \tag{8.35}$$

and $\xi_2 = \xi/\sqrt{3}$ as mentioned in advance.

There exist simpler approximate counterparts to both (8.30) or (8.33). The reader can refer to Paper P10 in this regard.

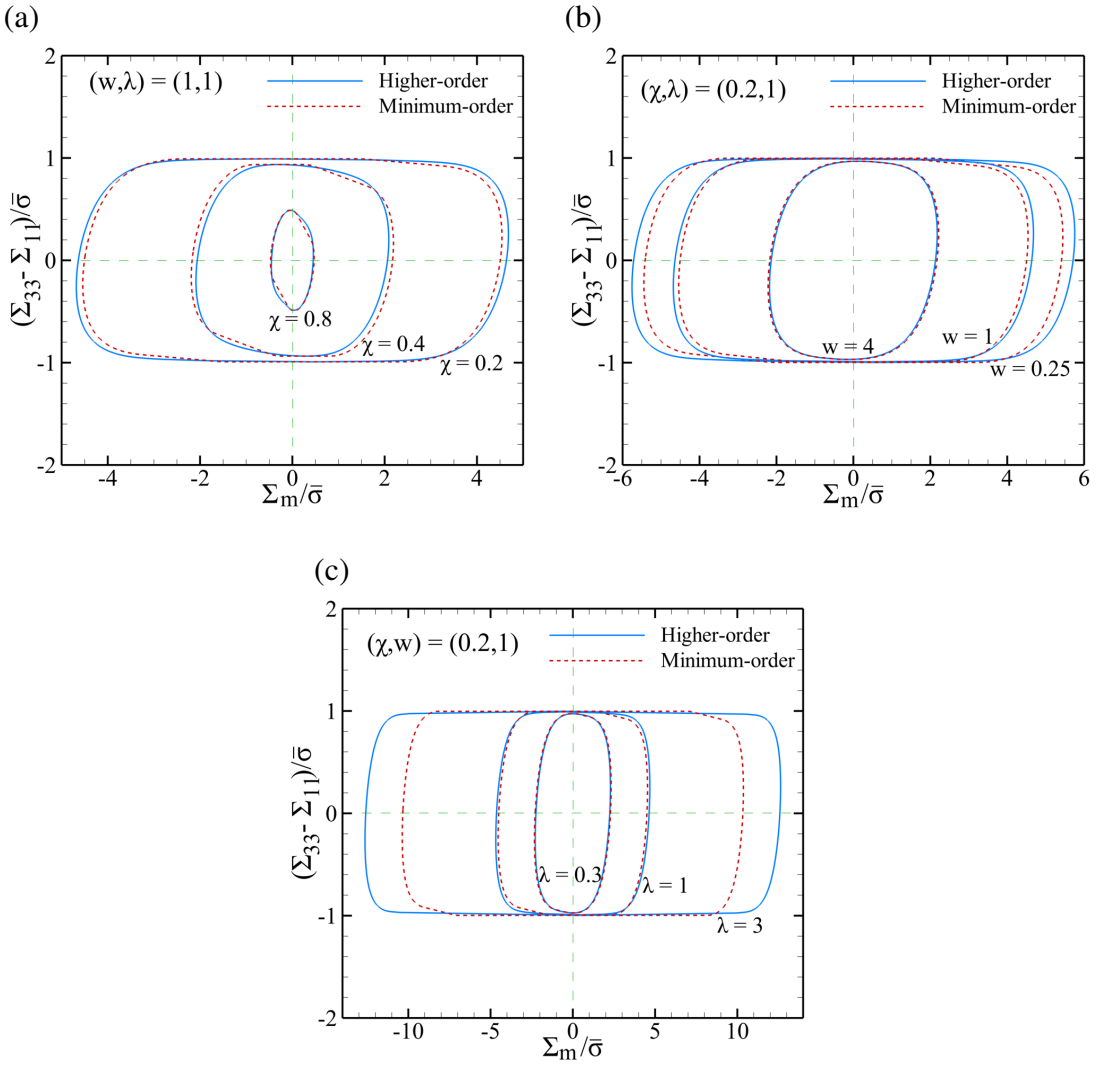

Figure 8.7: Comparison between yield surfaces based on minimum and higher-continuity fields: (a) for fixed (w, λ) and various ligament parameters χ, (b) for fixed (χ, λ) and various void aspect ratios w, (c) for fixed (χ, w) and various cell aspect ratios λ.

Figure 8.7 exhibits the difference between the yield surfaces based on minimum and higher-continuity fields for various void aspect ratios, ligament parameters, and cell aspect ratios. At low hydrostatic stresses, characteristic of mainly deviatoric loads, the predicted limit load is the least sensitive to the velocity profile. This limit corresponds to minimal relative axial velocity between

the plugs and the torus, with the whole cell admitting minimal, albeit nonzero, expansion. All the same, higher continuity within the axial velocity would trigger a higher limit load at larger hydrostatic stresses representative of higher lateral stresses superposed by axial loading. This entails a larger Poisson effect when the torus and plugs are clamped than when they act in parallel modulo minimum continuity. By the same token, the difference between the two surfaces proves inconsequential at large χ's and w's as well as small λ's due to the Poisson effect being limited. Accordingly, the higher-continuity yield surface is a tight lower bound to its minimum-continuity counterpart at large χ's and w's as well as small λ's, and is an upper bound thereof at smaller χ's and w's as well as higher λ's. This upper bound becomes rather spuriously large with increasingly large hydrostatic stresses in that the higher-continuity field exerts overconstraint on the point-wise velocity gradients. As explored in the sequel, the minimum-continuity model stands closer to numerical values, and will be thus favored over the other for assessment purposes.

Note also that the spuriously large hydrostatic stresses pertaining to $\chi = 0.2$, $w = 0.25$, and $\lambda = 3$ is indicative of localization in columns as an erroneous yielding mechanism. The effective mechanism corresponding to these parameters is localization in layers.

The yield surface devised by Eq's (8.30) and (8.33) has a large portion in proximity with the surface accounting for homogeneous yielding which are, more specifically, the planar subsurfaces of (8.30) and the zones with nearly horizontal slopes in (8.33). However, the highly-curved subsurface is the main matter of difference. In the minimum-continuity model, $(8.30)_3$ is counterpart to the planar part signifying localization in layers, *i.e.* with internal necking. The localization mechanism involves a zero increase in the lateral strain, *i.e.* a zero lateral rate of deformation $D_{11} = 0$, which prompts a rigid behavior in the matrix (M) subparts. In order to predict the effective yield surface at every microstructural state, (8.30) or (8.33) should be compared to the whole surface containing homogeneous yielding ensued by localization in layers. Thereupon, the *unified* criterion in absence of shear, according to (5.6) can be compared to its counterparts derived herein, (8.30) or (8.33). An upper bound to the net yield surface for a specified microstructure will be then close to the interior surface between the two surfaces. It would be more convenient to compare the

two surfaces at the same ξ value. The parametric form of (5.6) is thus proposed for comparison in Paper P10 .

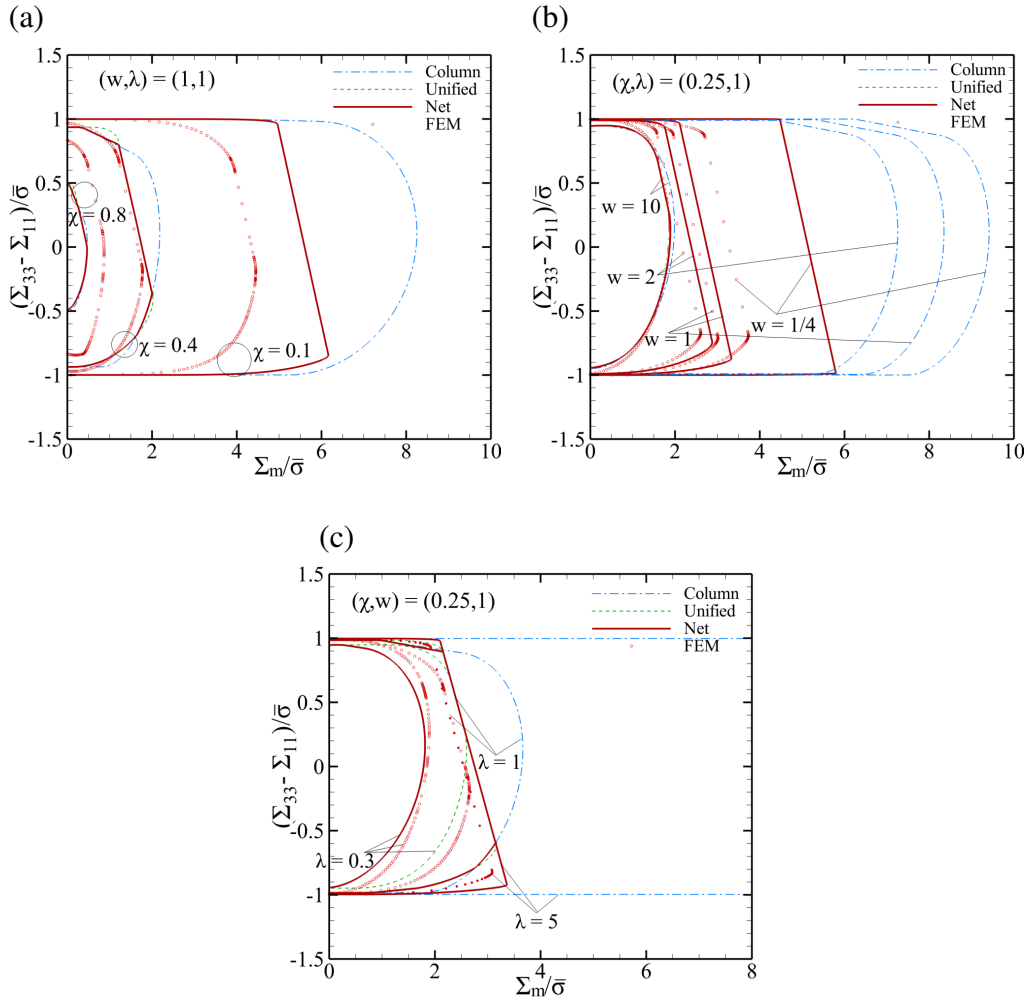

Figure 8.8: Effects of microstructural parameters on the yield loci representing the *unified* model as well as plasticity localized in columns: (a) effect of ligament parameter χ; (b) effect of void aspect ratio w; (c) effect of cell aspect ratio λ.

The effective yield surfaces are further compared to their FEM counterparts obtained from single-step limit analysis over the same-cell geometry. Follwing the technique introduced in Section 4.4, the theoretical grounds for the FEM-based calculation of the limit load at the onset of localization in columns are extensively provided in Paper P10 . In brief, the numerical limit load can be obtained via the imposition of normal and lateral target velocities, represented by target

displacements U_3 and U_1, respectively. Every U_1/U_3 ratio then corresponds to a specific set of lateral and normal limit loads (see Paper P10 on how to access the limit loads).

It suffices to emphasize herein that, in the present context, no restriction will be enacted on the microstructural parameters nor on the U_1/U_3 ratio. Therefore, the localization mechanism will be driven by both the microstructural state and the U_1/U_3 ratio. The only constraint exerted on the geometry is then to assure that, with the adopted (χ, w, λ) set, the void fully fits into the unit cell. That is, the condition $c < 1$ should be satisfied.

Figure 8.8 demonstrates the effects induced by every microstructural parameter on the effective yield surface. While the figures entail attentive examination, it can be conveniently observed that changing the χ or w variable from small to large values (while the rest are kept fixed) would transfer the driving yielding mechanism from layered into column coalescence. Incidentally, for large values of χ and w, the two yielding mechanisms occur almost synonymously while coalescence in layers is triggered slightly sooner, and vice versa. For cell aspect ratios well below unity ($\lambda < 1$), however, coalescence in columns is clearly preferred with significant distance between the two predicted mechanisms. Moreover, the present model accounting for column coalescence violates the upper-bound character [33] at very large values of χ and w as well as for small values of λ. In particular, with χ approaching unity, both (8.30) and (5.6) violate this character. This is rooted in the idealized choice of velocity fields that predict yielding at lower stress states. However, the predicted driving mechanism is both qualitatively and quantitatively (except for $\chi \longrightarrow 1$) well commensurate with the FEM outcomes. Above all, λ induces an opposite effect on the driving yielding mechanism compared to χ and w being varied. That is, changing λ from small to large values (while the rest are constant) would transfer the driving yielding mechanism from column into layered coalescence. Further, the effect of the cell aspect ratio λ is more remarkable when plasticity is localized in columns whereas it bares almost no effect on void coalescence occurring in layers. Thereupon, the points exhibiting FEM results for $\lambda = 5$ have been identified with solid circles in order to be more easily distinguishable from those pertaining to $\lambda = 1$ since they stand on the same slanted line denoting coalescence in layers.

CHAPTER 9 SUMMARY AND OUTLOOK

9.1 Concluding Remarks

The grounds to a robust micromechanics-based constitutive framework to simulate ductile fracture under combined tension and shear phenomenon in porous materials were addressed. The building blocks to the expected framework are mechanism-based yield criteria and evolution laws accounting for microstructural evolution in rated form, especially apropos of void rotation and elongation under shearing. A key feature to the development of such frameworks is to adopt measurable and/or observable parameters as descriptors, that could best be achieved through the notion of a reference volume element (RVE), alias *unit cell*. Experimental observations reveal plastic deformation at the unit cell level as homogeneous or inhomogeneous. The latter can be idealized with plasticity ideally confined within intervoid ligaments (under combined loading), exemplified by void coalescence in layers, and occasionally with coalescence in columns (under the dominance of normal loads) with plasticity more concentrated within intervoid plugs. The first objective was thus to develop a set of analytical yield functions that could mimic localized yielding by either mechanism. The latter was attained by limit analysis over a cylindrical cell containing a coaxial void of finite height. The effective yield surface is bounded by the innermost surface signifying the two mechanisms. Existing numerical analyses [16, 21] indicate that the shear-dominated deformation process is closer to being homogeneous at early stages and would approach the ideal localized state towards the end. Admittedly, a *hybrid* bi-surface model was adopted that consisted of simple modifications to both an existing criterion representing homogeneous yielding [14] as well as a derived criterion denoting fully localized yielding. By its very nature, the latter acts upon a *surrogate* microstructure aligned with a possible *localization plane*, that can emanate from voronoi tessellation upon an underlying microstructure. The constitutive framework was closed by a system of evolution equations pertaining to microstructural state variables during the nearly-localized deformation state derived from first principles. The body of existing and derived yield

criteria supplemented to existing and derived evolution equations were exploited in an implicit numerical integration based on the Newton-Raphson iterative scheme. The latter sets the third objective of the present work. The hybrid model predictions were firstly subjected to assessment in conformity with existing numerical outcomes under triaxial [20] as well as combined normal and shear loading [16, 17, 21]. The parametric studies were then carried out under a complete range of loading combinations from uniaxial to *near-simple* as well as *near-pure* shear loading, with the loading combination characterized by κ denoting the ratio between a normal and a shear traction on a possible localization plane. The effects of initial porosity, void and cell aspect ratios, void misalignment with the principal loading directions, and matrix plastic anisotropy are accounted for. The latter effect was investigated with reference to a counterpart of the here-derived inhomogeneous yield criterion recently introduced in [96]. The strain to failure was further evaluated in terms of stress triaxiality for a complete scope of stress triaxialities upon the loading path constituted by combined normal and shear stresses. An axisymmetric notched bar was finally presented as an example finite-element simulation demonstrating the capability of the hybrid model to solve structural boundary-value problems. To this end, the constitutive framework for the porous material was implemented in an ABAQUS user-defined subroutine (UMAT), and the material was modeled using dilute material elements without need for modeling the microstructure.

Some of the featured findings are enumerated in the following items:

- The effective ligament parameter $\bar{\chi}$, representative of the relative void spacing in the surrogate cell, is the main factor of influence that accounts for failure under combined tension and shear. It is itself a function in direct proportion to the current porosity as well as the cell aspect ratio, and scales inversely with the surrogate void aspect ratio. The latter, under a shear-dominated stress state, starts with a finite value and evolves towards zero until failure. More specifically, the onset of localized deformation as well as ultimate failure were delayed with a smaller χ_0. The limit of a dilute material ($\chi_0 \longrightarrow 0$) would exhibit no failure under shear.

- A shorter cell, characterized by a smaller cell aspect ratio λ, would have a larger strain to

the onset of localization ϵ_c, as well as a larger strain to failure ϵ_f under near-simple shearing. The latter is rooted in the fact that unlike a larger-than-cubic cell (with $\lambda > 1$), a shorter-than-cubic cell ($\lambda < 1$) initially rotates faster than the void does. Besides, at a fixed porosity, a void within a shorter cell is more distant from the cell boundaries than its counterpart in a taller cell.

- Under near-simple shearing ($\kappa \approx 0$), an oblate void ($w < 1$), contrary to a prolate void ($w > 1$), rotates transiently opposite to the shearing direction. Yet, there is a turning point in the middle of the process, which normally occurs at the point of transition into the localized deformation mode, where the void starts moving back towards the shearing direction. Failure for an oblate void occurs in the form of penny-shaped crack propagation that is realized after void closure (characterized by the porosity f approaching zero). Altogether, for both prolate and oblate voids, the larger void axis tends to align with the direction of the principal stretch.

- The strain to the onset of localization ϵ_c, as well as strain to failure ϵ_f was plotted in terms of stress triaxiality for the whole scope of stress triaxialities ranging from zero to 1/3 (shear-dominated interval) and from 1/3 to 3 (normal-dominated interval) by numerical integration of the differential equations expressing porosity, void aspect ratio, and void orientation in terms of the equivalent plastic strain $\bar{\epsilon}$. Within the shear-dominant interval, ϵ_f admits a minimum that can be roughly expressed in terms of the microstructural parameters within the inhomogeneous yield criterion.

- A void was found to be distorted, *i.e.* squeeze (via f decrease), elongate (via w increase), and rotate faster inside a stronger matrix against shear (with $h_{\mathrm{SL}} < 1$ and $h_{\mathrm{TS}} < 1$). Such a matrix would withstand material slippage along the shearing direction. Hence, the void ought to distort more and close sooner at the same shear strain level.

- Higher ductility could not be achieved in simultaneity with larger strength in absence of shear (here denoted with triaxial loading). Yet, the two could coexist under shear-dominated loading. To this end, the plane of transverse isotropy can be placed either parallel or perpen-

dicular to the plane of possible strain localization or normal, the latter such that the shear traction is parallel to the plane. The plane of transverse isotropy can alternatively be rotated clockwise with respect to shearing.

- Below a certain limit of shear-related Hill coefficients h_{SL} or h_{TS} (with S denoting the direction of the normal to the principal loading plane as well as the direction of transverse isotropy), or beyond a certain rotation angle within the plane of transverse isotropy, failure was never predicted under near-simple shearing. Thereupon, shear Hill coefficients, or the placement of orthotropy planes, can be engineered such that, at a specific initial porosity level, failure under shear never occurs.

9.2 Prospective Extensions

The simplifying assumptions as well as the predictive limitations within the introduced models warrant future amendments or extensions to the present work. The suggested prospective work can fall into two main categories that prompt two major lines of future work in extension to this thesis:

9.2.1 Analytical extension

- A major drawback by which the authors were driven to the use of a surrogate microstructure was the crude Gurson-like shear velocity field that would predict no failure within a rotating cylindrical void under simple shearing. A more sophisticated shear field is thus recommended that is commensurate with real void distortion under shear fields. To this end, evolution-based direct cell-model FEM calculations would definitely prove efficacious in the sense of being suggestive of tentative higher-order shear velocity fields. The effect of void orientation should definitely be taken into account.

- The body of analytical models derived in the present context invoked an elastic-perfectly plastic matrix admitting the J_2 flow theory. The effect of hardening would thus be underrated in the corresponding predictions, particularly at the post-localized regime. A proper extension to the series of analytically-derived models is then to incorporate the effect of strain hardening, preferably of a power type.

- Void coalescence in columns is mainly known to prevail under normal load dominance, and thus the effect of shear stresses has been neglected in its corresponding model. Yet, shear can bare a potentially remarkable effect at least in regards to the ranges of shear loads under which necklace coalescence can still be effective. Extensions to the present models accompanied by shear stresses are thus worthwhile attempts.

- The effect due to plastic anisotropy into the *unified* homogeneous-to-localized model, stated in Eq. (5.6), was uncalled for. Introduction of this effect would be a significant contribution for the numerous numerical virtues associated with this model, mainly thanks to the slope continuity within the resulting yield surface.

9.2.2 Numerical extension

- The effective flow rule was expressed in terms of a *consecutive* satisfaction of the yield surfaces describing nearly-homogeneous (Φ^{H}) and fully localized (Φ^{I}) deformation modes. That is, only one flow potential was deemed effective at a time. A *concurrent* use of the yield surfaces would be favored from numerous perspectives. Not only will the resulting solution on this basis be less sensitive to the time step, but also it would generate a smoother transition from Φ^{H} to Φ^{I}. This would allow for easier global convergence, *i.e.* convergence within the equilibrium equations in the discretized space. The latter has been observed as a major downside within the user-defined subroutine (UMAT).

- The above-mentioned lack of global analysis convergence within the UMAT was seen to be more pronounced under significant shear loads, even when superposed by normal loading. Aside from invoking a concurrent multi-surface model, one may need to introduce an artificial damping into the framework, that can make the transition from Φ^{H} to Φ^{I} even smoother and let the solution progress further until failure, *viz.* total loss of stress-bearing capacity. The latter method has been formerly employed by Benzerga [221].

- The example FEM simulation was a minuscule case study presented mainly to demonstrate the potential capability of the proposed model in structural boundary-value analysis. The

UMAT written by the author is still at an elementary stage and is yet to be subjected to remarkable advancement until becoming full-fledged and ready for a vast variety of case studies. The strategies proposed in the above two bullets seem indispensable steps towards global convergence. Among the suggested case studies is the simulation of Arcan tests under combined remote normal and shear loading, pure torsion tests on hollow tubes, and notched bar simulation with plastic anisotropy that triggers the formation of shear bands inside the notch zone. In particular, Arcan tests can be simulated to assess the model in accordance with the experimental outcomes acquired by Basu [43] on magnesium alloys. Moreover, the micromechanical process taking place inside the shear band would be a major consequence of our model. The latter was recently studied [233] merely based on homogeneous yielding according to Φ^{H} equaling the KB model [14]. In a general continuum with arbitrary geometry, more than one possible localization system should be accounted for. A judicious choice of possible systems, however, is dependent upon the underlying microstructure as well as the geometry and boundary conditions.

- The propensity of localization by necklace coalescence was overlooked throughout. Just as strains can localize inside possible planes (here via the notion of a surrogate microstructure), so too could they localize along the direction normal to the plane or along other directions neither in line with the plane normal nor inside the plane. Counting the corresponding yield surfaces in the multi-surface model would deliver a closer-to-real response within the material at hand. A particular example in this regard is porous media with initially elongated voids or that with voids closely spaced apart along the principal loading plane, *i.e.* $w_0 > 1$ or $\lambda_0 < 1$, respectively.

- The use of elliptical-base cells in the post-localized deformation process, along with the counterpart to the KB model introduced by Madou and Leblond [230] for ellipsoidal rather than spheroidal voids, would better portray the multi-axial distortion of voids under shear fields. The model according to Eq. (8.8) is ready for numerical implementation.

- There is significant numerical advantage in the *unified* model with seamless transition from homogeneous to localized yielding. Thanks to it being endowed with slope (C^1) continuity, no abrupt change in stress responses is anticipated. This will potentially eliminate the need for the introduction of artificial damping or any other fictitious stratagem. The model was derived, according to Eq. (5.6), in the present work, and is ready for numerical implementation.

REFERENCES

[1] D. Lingos, "Effects of the 2011 tohoku japan earthquake on steel structures," *EERI Team Field Blog*, 2011.

[2] M. Morrison, D. Schweizer, and T. Hassan, "An innovative seismic performance enhancement technique for steel building moment resisting connections," *Journal of Constructional Steel Research*, vol. 109, pp. 34–46, 2015.

[3] T. Borvik, O. Hopperstad, T. Berstad, and M. Langseth, "A computational model of viscoplasticity and ductile damage for impact and penetration," *European Journal of Mechanics*, vol. 20, pp. 685–712, 2001.

[4] T. Børvik, O. Hopperstad, T. Berstad, and M. Langseth, "Numerical simulation of plugging failure in ballistic penetration," *International Journal of Solids and Structures*, vol. 38, no. 34-35, pp. 6241–6264, 2001.

[5] available online, "Sheet metal cutting (shearing)," *https://www.custompartnet.com/wu/sheet-metal-shearing*, 2009.

[6] V. J. Mediavilla, *Continuous and discontinuous modelling of ductile fracture*. PhD thesis, Technische Universiteit Eindhoven, Eindhoven, 2005.

[7] G. R. Johnson, J. M. Hoegfeldt, U. S. Lindholm, and A. Nagy, "Response of various metals to large torsional strains over a large range of strain rates – Part 1: Ductile metals," *Journal of Engineering Materials and Technology*, vol. 105, pp. 42–47, 1983.

[8] G. Johnson, J. Hoegfeldt, U. Lindholm, and A. Nagy, "Response of various metals to large torsional strains over a large range of strain rates – Part 2: Less ductile metals," *Journal of Engineering Materials and Technology*, vol. 105, pp. 48–53, 1983.

[9] I. Barsoum and J. Faleskog, "Rupture mechanisms in combined tension and shear—-Experiments," *International Journal of Solids and Structures*, vol. 44, pp. 1768–1786, 2007.

[10] I. Barsoum, *The effect of stress state in ductile failure*. PhD thesis, KTH, 2008.

[11] Y. Bao and T. Wierzbicki, "On fracture locus in the equivalent strain and stress triaxiality space," *International Journal of Mechanical Sciences*, vol. 46, pp. 81–98, 2004.

[12] S. Haltom, S. Kyriakides, and K. Ravi-Chandar, "Ductile failure under combined shear and tension," *International Journal of Solids and Structures*, vol. 50, pp. 1507–1522, 2013.

[13] A. Pineau, A. A. Benzerga, and T. Pardoen, "Failure of metals I. Brittle and Ductile Fracture," *Acta Materialia*, vol. 107, pp. 424–483, 2016.

[14] S. M. Keralavarma and A. A. Benzerga, "A constitutive model for plastically anisotropic solids with non-spherical voids," *Journal of the Mechanics and Physics of Solids*, vol. 58, pp. 874–901, 2010.

[15] M. Torki, C. Tekoglu, J.-B. Leblond, and A. Benzerga, "Theoretical and numerical analysis of void coalescence in porous ductile solids under arbitrary loadings," *International Journal of Plasticity*, vol. 91, pp. 160–181, 2017.

[16] V. Tvergaard, "Behaviour of voids in a shear field," *International Journal of Fracture*, vol. 158, pp. 41–49, 2009.

[17] K. L. Nielsen, J. Dahl, and V. Tvergaard, "Collapse and coalescence of spherical voids subject to intense shearing: studied in full 3D," *International Journal of Fracture*, vol. 177, pp. 97–108, 2012.

[18] M. E. Torki, "A unified criterion for void growth and coalescence under combined tension and shear," *International Journal of Plasticity*, 2019.

[19] M. E. Torki and A. A. Benzerga, "A mechanism of failure in shear bands," *Extreme Mechanics Letters*, vol. 23, pp. 67–71, 2018.

[20] T. Pardoen and J. W. Hutchinson, "An extended model for void growth and coalescence," *Journal of the Mechanics and Physics of Solids*, vol. 48, pp. 2467–2512, 2000.

[21] V. Tvergaard, "Shear deformation of voids with contact modeled by internal pressure," *International Journal of Mechanical Sciences*, vol. 50, pp. 1459–1465, 2008.

[22] H. Kobayashi and H. Onoue, "Brittle fracture of liberty ships," *Failure Knowledge Database*, vol. 100, p. 67, 1943.

[23] T. L. Anderson, *Fracture mechanics: fundamentals and applications*. CRC press, 2017.

[24] C. M. Sharp, *DH An Outline of de Havilland History.[With Plates, Including Portraits.]*. Faber & Faber, 1960.

[25] W. R. Hendricks, "The aloha airlines accident—a new era for aging aircraft," in *Structural integrity of aging airplanes*, pp. 153–165, Springer, 1991.

[26] A. Gelencser, N. Kovats, B. Turoczi, A. Rostasi, A. Hoffer, K. Imre, I. Nyiro-Kosa, D. Csakberenyi-Malasics, A. Toth, A. Czitrovszky, *et al.*, "The red mud accident in ajka (hungary): characterization and potential health effects of fugitive dust," *Environmental science & technology*, vol. 45, no. 4, pp. 1608–1615, 2011.

[27] D. Dornfeld, "Strategies for preventing and minimizing burr formation," 2004.

[28] K. L. Nielsen, "3d modelling of plug failure in resistance spot welded shear-lab specimens (dp600-steel)," *International Journal of Fracture*, vol. 153, no. 2, pp. 125–139, 2008.

[29] K. L. Nielsen and V. Tvergaard, "Ductile shear failure or plug failure of spot welds modelled by modified gurson model," *Engineering Fracture Mechanics*, vol. 77, no. 7, pp. 1031–1047, 2010.

[30] J. Mediavilla, R. H. J. Peerlings, and M. G. D. Geers, "Discrete crack modelling of ductile fracture driven by non-local softening plasticity," *Int J Numer Meth Engr*, vol. 66, pp. 661–688, 2006.

[31] J. Mediavilla, R. Peerlings, and M. Geers, "A robust and consistent remeshing-transfer operator for ductile fracture simulations," *Computers & structures*, vol. 84, no. 8-9, pp. 604–623, 2006.

[32] A. A. Benzerga, J. Besson, and A. Pineau, "Anisotropic ductile fracture. Part I: experiments," *Acta Materialia*, vol. 52, pp. 4623–4638, 2004.

[33] A. A. Benzerga and J.-B. Leblond, "Ductile fracture by void growth to coalescence," *Advances in Applied Mechanics*, vol. 44, pp. 169–305, 2010.

[34] A. Pineau, "Development of the local approach to fracture over the past 25 years: theory and applications," *International Journal of Fracture*, vol. 138, pp. 139–166, 2006.

[35] K. Anand and W. A. Spitzig, "Initiation of localized shear bands in plane strain," *Journal of the Mechanics and Physics of Solids*, vol. 28, pp. 113–128, 1980.

[36] I. Barsoum and J. Faleskog, "Rupture mechanisms in combined tension and shear—-Micromechanics," *International Journal of Solids and Structures*, vol. 44, pp. 5481–5498, 2007.

[37] N. Goldenberg, M. Arcan, and E. Nicolau, "On the most suitable specimen shape for testing shear strength of plastics," in *International Symposium on Plastics Testing and Standardization, ASTM STP*, vol. 247, pp. 115–121, 1958.

[38] M. Arcan, Z. Hashin, , and A. Voloshin, "A method to produce uniform plane-stress states with applications to fiber-reinforced materials," *Experimental mechanics*, vol. 18, no. 4, pp. 141–146, 1978.

[39] S.-C. Yen, J. Craddock, and K. Teh, "Evaluation of a modified arcan fixture for the in-plane shear test of materials," *Experimental techniques*, vol. 12, no. 12, pp. 22–25, 1988.

[40] M. Arcan, "The iosipescu shear test as applied to composite materials," *Experimental mechanics*, vol. 24, no. 1, pp. 66–67, 1984.

[41] R. El-Hajjar and R. Haj-Ali, "In-plane shear testing of thick-section pultruded frp composites using a modified arcan fixture," *Composites Part B: Engineering*, vol. 35, no. 5, pp. 421–428, 2004.

[42] V. S. Deshpande, A. Needleman, and E. Van der Giessen, "A discrete dislocation analysis of near-threshold fatigue crack growth," *Acta Materialia*, vol. 49, p. 3189, 2001.

[43] S. Basu, *On the effects of texture and strain-path changes on the ductile fracture of Mg alloys*. PhD thesis, Texas A&M University, College Station, TX, 2016.

[44] D. McMullan, "Scanning electron microscopy 1928–1965," *Scanning*, vol. 17, no. 3, pp. 175–185, 1995.

[45] A. A. Benzerga and J.-B. Leblond, "Effective Yield Criterion Accounting for Microvoid Coalescence," *Journal of Applied Mechanics*, vol. 81, p. 031009, 2014.

[46] J. Koplik and A. Needleman, "Void growth and coalescence in porous plastic solids," *International Journal of Solids and Structures*, vol. 24, no. 8, pp. 835–853, 1988.

[47] F. Scheyvaerts, P. R. Onck, C. Tekoğlu, and T. Pardoen, "The growth and coalescence of ellipsoidal voids in plane strain under combined shear and tension," *Journal of the Mechanics and Physics of Solids*, vol. 59, pp. 373–397, 2011.

[48] M. Dunand and D. Mohr, "Effect of Lode parameter on plastic flow localization after proportional loading at low stress triaxialities," *Journal of the Mechanics and Physics of Solids*, vol. 66, pp. 133–153, 2014.

[49] A. B. Richelsen and V. Tvergaard, "Dilatant plasticity or upper bound estimates for porous ductile solids," *Acta Metallurgica et Materialia*, vol. 42, no. 8, pp. 2561–2577, 1994.

[50] M. Gologanu, *Etude de quelques problèmes de rupture ductile des métaux*. PhD thesis, Université Paris 6, 1997.

[51] P. Schall and M. van Hecke, "Shear Bands in Matter with Granularity," *Annual Review of Fluid Mechanics*, vol. 42, pp. 67–88, 2010.

[52] K. A. Alshibli and S. Sture, "Shear band formation in plane strain experiments of sand," *J. Geotech. Geoenviron. Eng.*, vol. 126, pp. 495–503, 2000.

[53] C. M. Gourlay and A. K. Dahle, "Dilatant shear bands in solidifying metals," *Nature*, vol. 445, pp. 70–73, 2007.

[54] E. Gomez-Rivas and A. Griera, "Shear fractures in anisotropic ductile materials: An experimental approach," *J. Struct. Geol.*, vol. 34, pp. 61–76, 2012.

[55] Q. Wei, D. Jia, K. T. Ramesh, and E. Ma, "Evolution and microstructure of shear bands in nanostructured Fe," *Applied Physics Letters*, vol. 81, pp. 1240–1242, 2002.

[56] T. F. Morgeneyer and J. Besson, "Flat to slant ductile fracture transition: Tomography examination and simulations using shear-controlled void nucleation," *Scripta Materialia*, vol. 65, pp. 1002–1005, 2011.

[57] K. Friedrich, "Crazes and shear bands in semi-crystalline thermoplastics," *Adv. Pol. Sci.*, vol. 52-3, pp. 225–274, 1983.

[58] A. L. Greer, Y. Q. Cheng, and E. Ma, "Shear bands in metallic glasses," vol. 74, pp. 71–132, 2013.

[59] D. C. Hofmann, J.-Y. Suh, A. Wiest, G. Duan, M.-L. Lind, M. D. Demetriou, and W. L. Johnson, "Designing metallic glass matrix composites with high toughness and tensile ductility," *Nature*, vol. 451, pp. 1085–1090, 2008.

[60] T. F. Morgeneyer, T. Taillandier-Thomas, A. Buljac, L. Helfen, and F. Hild, "On strain and damage interactions during tearing: 3D in situ measurements and simulations for a ductile alloy (AA2139-T3)," *Journal of the Mechanics and Physics of Solids*, vol. 96, pp. 550–571, 2016.

[61] J. Rice, "The localization of plastic deformation," in *14th int. cong. Theoretical and Applied Mechanics* (W. Koiter, ed.), pp. 207–220, North–Holland, Amsterdam, 1976.

[62] J. W. Hutchinson and V. Tvergaard, "Shear band formation in plane strain," *International Journal of Solids and Structures*, vol. 17, pp. 451–470, 1981.

[63] Y. Huang, J. W. Hutchinson, and V. Tvergaard, "Cavitation instabilities in elastic–plastic solids," *Journal of the Mechanics and Physics of Solids*, vol. 39, pp. 223–241, 1991.

[64] M. Achouri, G. Germain, P. Dal Santo, and D. Saidane, "Experimental characterization and numerical modeling of micromechanical damage under different stress states," *Materials & Design*, vol. 50, pp. 207–222, 2013.

[65] A. Needleman, "A continuum model for void nucleation by inclusion debonding," *Journal of Applied Mechanics*, vol. 54, p. 525, 1987.

[66] N. A. Fleck, J. W. Hutchinson, and V. Tvergaard, "Softening by void nucleation and growth in tension and shear," *Journal of the Mechanics and Physics of Solids*, vol. 37, pp. 515–540, 1989.

[67] K. Siruguet and J.-B. Leblond, "Effect of void locking by inclusions upon the plastic behavior of porous ductile solids—I: theoretical modeling and numerical study of void growth," *International Journal of Plasticity*, vol. 20, pp. 225–254, 2004.

[68] N. A. Fleck and J. W. Hutchinson, "Void growth in shear," *Proceedings of the Royal Society of London A*, vol. 407, pp. 435–458, 1986.

[69] L. Babout, Y. Bréchet, E. Maire, and R. Fougères, "On the competition between particle fracture and particle decohesion in metal matrix composites," *Acta Materialia*, vol. 52, pp. 4517–4525, 2004.

[70] L. Babout, E. Maire, and R. Fougeres, "Damage initiation in model metallic materials: X-ray tomography and modelling," *Acta Materialia*, vol. 52, no. 8, pp. 2475–2487, 2004.

[71] K. Nahshon and J. W. Hutchinson, "Modification of the Gurson Model for shear failure," *European Journal of Mechanics*, vol. 27, pp. 1–17, 2008.

[72] L. Morin, J.-B. Leblond, and V. Tvergaard, "Application of a model of plastic porous materials including void shape effects to the prediction of ductile failure under shear-dominated loadings," *Journal of the Mechanics and Physics of Solids*, vol. 94, pp. 148–166, 2016.

[73] N. O'Dowd and C. Shih, "Family of crack-tip fields characterized by a triaxiality parameter—i. structure of fields," *J. Mech. Phys. Solids*, vol. 39, no. 8, pp. 989–1015, 1991.

[74] J. W. Hutchinson and A. G. Evans, "Mechanics of materials: Top-down approaches to fracture," *Acta Materialia*, vol. 48, pp. 125–135, 2000.

[75] V. Tvergaard and A. Needleman, "Analysis of the cup–cone fracture in a round tensile bar," *Acta Metallurgica*, vol. 32, pp. 157–169, 1984.

[76] F. A. McClintock, "A criterion for ductile fracture by the growth of holes," *Journal of Applied Mechanics*, vol. 35, pp. 363–371, 1968.

[77] J. R. Rice and D. M. Tracey, "On the enlargement of voids in triaxial stress fields," *Journal of the Mechanics and Physics of Solids*, vol. 17, pp. 201–217, 1969.

[78] A. L. Gurson, "Continuum Theory of Ductile Rupture by Void Nucleation and Growth: Part I– Yield Criteria and Flow Rules for Porous Ductile Media," *Journal of Engineering Materials and Technology*, vol. 99, pp. 2–15, 1977.

[79] G. Rousselier, "Ductile fracture models and their potential in local approach of fracture," *Nucl. Eng. Design*, vol. 105, pp. 97–111, 1987.

[80] J. Lemaitre, "A Continuous Damage Mechanics Model for Ductile Fracture," *Journal of Engineering Materials and Technology*, vol. 107, pp. 83–89, 1985.

[81] K. Danas and P. Ponte Castañeda, "A finite-strain model for anisotropic viscoplastic porous media: I–Theory," *European Journal of Mechanics*, vol. 28, pp. 387–401, 2009.

[82] K. Madou and J.-B. Leblond, "A Gurson-type criterion for porous ductile solids containing arbitrary ellipsoidal voids – I: Limit-analysis of some representative cell," *Journal of the Mechanics and Physics of Solids*, vol. 60, pp. 1020–1036, 2012.

[83] K. Madou, J.-B. Leblond, and L. Morin, "Numerical studies of porous ductile materials containing arbitrary ellipsoidal voids —II: Evolution of the length and orientation of the void axes," *European Journal of Mechanics*, vol. 42, pp. 490–507, 2013.

[84] Y. Bai and T. Wierzbicki, "A new model of metal plasticity and fracture with pressure and Lode dependence," *International Journal of Plasticity*, vol. 24, pp. 1071–1096, 2008.

[85] V. Tvergaard and K. L. Nielsen, "Relations between a micro-mechanical model and a damage model for ductile failure in shear," *Journal of the Mechanics and Physics of Solids*, vol. 58, pp. 1243–1252, 2010.

[86] A. A. Benzerga, J. Besson, and A. Pineau, "Anisotropic ductile fracture. Part II: theory," *Acta Materialia*, vol. 52, pp. 4639–4650, 2004.

[87] N. Thomas and A. A. Benzerga, "On fracture loci of ductile materials under nonproportional loading," *International Journal of Mechanical Sciences*, 2013. . In preparation.

[88] S. M. Keralavarma, "A multi-surface plasticity model for ductile fracture simulations," *Journal of the Mechanics and Physics of Solids*, vol. 103, pp. 100–120, 2017.

[89] M. Gologanu, J.-B. Leblond, and J. Devaux, "Approximate models for ductile metals containing non-spherical voids – case of axisymmetric prolate ellipsoidal cavities," *Journal of the Mechanics and Physics of Solids*, vol. 41, no. 11, pp. 1723–1754, 1993.

[90] M. Gologanu, J.-B. Leblond, and J. Devaux, "Approximate Models for Ductile Metals Containing Non–spherical Voids — Case of Axisymmetric Oblate Ellipsoidal Cavities," *Journal of Engineering Materials and Technology*, vol. 116, pp. 290–297, 1994.

[91] P. Ponte Castañeda and M. Zaidman, "Constitutive models for porous materials with evolving microstructure," *Journal of the Mechanics and Physics of Solids*, vol. 42, pp. 1459–1495, 1994.

[92] M. Gologanu, J.-B. Leblond, G. Perrin, and J. Devaux, "Recent extensions of Gurson's model for porous ductile metals," in *Continuum Micromechanics, CISM Lectures Series* (P. Suquet, ed.), pp. 61–130, New York: Springer, 1997.

[93] A. A. Benzerga, J. Besson, and A. Pineau, "Coalescence–Controlled Anisotropic Ductile Fracture," *Journal of Engineering Materials and Technology*, vol. 121, pp. 221–229, 1999.

[94] M. Kailasam and P. Ponte Castaneda, "Constitutive relations for porous materials : the effect of changing void shape and orientation," in *Micromechanics of Plasticity and Damage of Multiphase Materials, Proc. IUTAM symposium* (A. Pineau and A. Zaoui, eds.), (Sèvres, Paris, France), pp. 215–222, Kluwer Academic Publishers, the Netherlands, 29 August–1 September 1995 1996.

[95] A. A. Benzerga and J. Besson, "Plastic potentials for anisotropic porous solids," *European Journal of Mechanics*, vol. 20A, pp. 397–434, 2001.

[96] S. M. Keralavarma and S. Chockalingam, "A Criterion for Void Coalescence in Anisotropic Ductile Materials," *International Journal of Plasticity*, vol. 82, pp. 159–176, 2016.

[97] L. Morin, J.-B. Leblond, A. A. Benzerga, and D. Kondo, "A unified criterion for the growth and coalescence of microvoids," *Journal of the Mechanics and Physics of Solids*, vol. 97, pp. 19–36, 2016.

[98] D. L. McDowell, E. Marin, and C. Bertoncelli, "A combined kinematic-isotropic hardening theory for porous inelasticity of ductile metals," *International Journal of Damage Mechanics*, vol. 2, pp. 137–161, 1993.

[99] D. C. Drucker, "A definition of stable inelastic material," tech. rep., Brown Univ. Providence RI, 1957.

[100] R. Hill, "A variational principle of maximum plastic work in classical plasticity," *The Quarterly Journal of Mechanics and Applied Mathematics*, vol. 1, no. 1, pp. 18–28, 1948.

[101] R. Hill, *The Mathematical Theory of Plasticity*. Clarendon Press, Oxford, 1950.

[102] J. C. Simo and T. J. Hughes, *Computational inelasticity*, vol. 7. Springer Science & Business Media, 2006.

[103] W. T. Koiter, "Stress-strain relations, uniqueness and variational theorems for elastic-plastic materials with a singular yield surface," *Quarterly of Applied Mathematics*, vol. 11, pp. 350–354, 1953.

[104] W. Prager, "Recent developments in the mathematical theory of plasticity," *Journal of applied physics*, vol. 20, no. 3, pp. 235–241, 1949.

[105] R. Brannon, "Caveats concerning conjugate stress and strain measures for frame indifferent anisotropic elasticity," *Acta mechanica*, vol. 129, no. 1-2, pp. 107–116, 1998.

[106] C. A. Coulomb, "Essai sur une application des regles de maximis et minimis a quelques problemes de statique relatifs a l'architecture (essay on maximums and minimums of rules to some static problems relating to architecture)," 1973.

[107] D. C. Drucker and W. Prager, "Soil mechanics and plastic analysis or limit design," *Quarterly of applied mathematics*, vol. 10, no. 2, pp. 157–165, 1952.

[108] W. v. Burzyński, "Über die anstrengungshypothesen," *Schweizerische Bauzeitung*, vol. 94, no. 21, pp. 259–262, 1929.

[109] Y. I. Yagn, "New methods of strength prediction (in russ.: Novye metody pascheta na prochnost')," *Vestnik inzhenerov i tekhnikov*, vol. 6, pp. 237–244, 1931.

[110] B. Bresler and K. S. Pister, "Strength of concrete under combined stresses," in *Journal Proceedings*, vol. 55, pp. 321–345, 1958.

[111] K. J. Willam, "Constitutive model for the triaxial behaviour of concrete," *Proc. Intl. Assoc. Bridge Structl. Engrs*, vol. 19, pp. 1–30, 1975.

[112] D. Bigoni, *Nonlinear solid mechanics: bifurcation theory and material instability*. Cambridge University Press, 2012.

[113] D. Bigoni and A. Piccolroaz, "Yield criteria for quasibrittle and frictional materials," *International journal of solids and structures*, vol. 41, no. 11-12, pp. 2855–2878, 2004.

[114] H. Altenbach, A. Bolchoun, and V. A. Kolupaev, "Phenomenological yield and failure criteria," in *Plasticity of pressure-sensitive materials*, pp. 49–152, Springer, 2014.

[115] A. L. Gurson, *Plastic flow and fracture behavior of ductile materials incorporating void nucleation, growth and interaction*. PhD thesis, Brown University, Providence, 1975.

[116] G. Rousselier, "Finite deformation constitutive relations including ductile fracture damage," in *Three-Dimensional Constitutive equations of Damage and Fracture* (Nemat–Nasser, ed.), pp. 331–355, Pergamon press, North Holland, 1981.

[117] M. Brünig, S. Berger, and H. Obrecht, "Numerical simulation of the localization behavior of hydrostatic-stress-sensitive metals," *International Journal of Mechanical Sciences*, vol. 42, no. 11, pp. 2147–2166, 2000.

[118] C. Ouyang, Z. Li, M. Huang, L. Hu, and C. Hou, "Combined influences of micro-pillar geometry and substrate constraint on microplastic behavior of compressed single-crystal micro-pillar: Two-dimensional discrete dislocation dynamics modeling," *Materials Science and Engineering*, vol. 526, pp. 235–243, 2009.

[119] W. Lode, "Versuche über den einfluß der mittleren hauptspannung auf das fließen der metalle eisen, kupfer und nickel," *Zeitschrift für Physik*, vol. 36, no. 11-12, pp. 913–939, 1926.

[120] C. S. Desai and H. J. Siriwardane, *Constitutive laws for engineering materials with emphasis on geologic materials*. No. BOOK, Prentice-Hall, 1984.

[121] Y. Bai and T. Wierzbicki, "Application of extended Mohr-Coulomb criterion to ductile fracture," *International Journal of Fracture*, vol. 161, pp. 1–20, 2010.

[122] D. C. Drucker, "Relation of experiments to mathematical theories of plasticity," *Journal of Applied Mechanics*, vol. 16, no. 4, pp. 349–357, 1949.

[123] W. Hu and Z. R. Wang, "Multiple-factor dependence of the yielding behavior to isotropic ductile materials," *Computational materials science*, vol. 32, no. 1, pp. 31–46, 2005.

[124] H. Y. Subramanya, S. Viswanath, and R. Narasimhan, "Influence of crack tip constraint on void growth in pressure sensitive plastic solids–i: 2d analysis," *Engineering fracture mechanics*, vol. 75, no. 5, pp. 1045–1063, 2008.

[125] M. Kuroda, "A phenomenological plasticity model accounting for hydrostatic stress-sensitivity and vertex-type of effect," *Mechanics of materials*, vol. 36, no. 3, pp. 285–297, 2004.

[126] Y. Fengping, S. Qin, and H. Wei, "Yield criterions of metal plasticity in diffierent stress states," *Acta Metallurgica Sinica (English Letters)*, vol. 22, no. 2, pp. 123–130, 2009.

[127] R. Hill, "Theoretical plasticity of textured aggregates," *Math. Proc. Cambridge Phil. Soc.*, vol. 85, pp. 179–191, 1979.

[128] R. W. Logan and W. F. Hosford, "Upper-bound anisotropic yield locus calculations assuming-pencil glide," 1980.

[129] W. F. Hosford, "A generalized isotropic yield criterion," *Journal of Applied Mechanics*, vol. 39, no. 2, pp. 607–609, 1972.

[130] F. Barlat, D. Lege, and J. Brem, "A six-component yield function for anisotropic materials," *International Journal of Plasticity*, vol. 7, no. 7, pp. 693–712, 1991.

[131] A. Karafillis and M. Boyce, "A general anisotropic yield criterion using bounds and a transformation weighting tensor," *Journal of the Mechanics and Physics of Solids*, vol. 41, no. 12, pp. 1859–1886, 1993.

[132] R. M. Caddell, R. S. Raghava, and A. G. Atkins, "A yield criterion for anisotropic and pressure dependent solids such as oriented polymers," *Journal of Materials Science*, vol. 8, no. 11, pp. 1641–1646, 1973.

[133] S. Soare, J. W. Yoon, O. Cazacu, and F. Barlat, "Applications of a recently proposed anisotropic yield function to sheet forming," in *Advanced Methods in Material Forming*, pp. 131–149, Springer, 2007.

[134] X.-P. Xu and A. Needleman, "Numerical simulations of fast crack growth in brittle solids," *Journal of the Mechanics and Physics of Solids*, vol. 42, no. 9, pp. 1397–1434, 1994.

[135] X.-P. Xu and A. Needleman, "Numerical simulations of dynamic crack growth along an interface," *International Journal of Fracture*, vol. 74, no. 4, pp. 289–324, 1996.

[136] J. Remmers, R. de Borst, and A. Needleman, "A cohesive segments method for the simulation of crack growth," *Computational mechanics*, vol. 31, no. 1-2, pp. 69–77, 2003.

[137] S. Osovski, A. Srivastava, J. Williams, and A. Needleman, "Grain boundary crack growth in metastable titanium β alloys," *Acta Materialia*, vol. 82, pp. 167–178, 2015.

[138] A. Srivastava, S. Osovski, and A. Needleman, "Engineering the crack path by controlling the microstructure," *Journal of the Mechanics and Physics of Solids*, vol. 100, pp. 1–20, 2017.

[139] M. Gologanu, J.-B. Leblond, G. Perrin, and J. Devaux, "Theoretical models for void coalescence in porous ductile solids – I: Coalescence in "layers"," *International Journal of Solids and Structures*, vol. 38, pp. 5581–5594, 2001.

[140] C. Tekoğlu, J.-B. Leblond, and T. Pardoen, "A criterion for the onset of void coalescence under combined tension and shear," *Journal of the Mechanics and Physics of Solids*, vol. 60, pp. 1363–1381, 2012.

[141] L. Morin, J.-B. Leblond, and A. A. Benzerga, "Coalescence of voids by internal necking: theoretical estimates and numerical results," *Journal of the Mechanics and Physics of Solids*, vol. 75, pp. 140–158, 2015.

[142] V. Tvergaard, A. Needleman, and K. K. Lo, "Flow localization in the plane strain tensile test," *Journal of the Mechanics and Physics of Solids*, vol. 29, pp. 115–142, 1981.

[143] V. Tvergaard, "On localization in ductile materials containing spherical voids," *International Journal of Fracture*, vol. 18, pp. 237–252, 1982.

[144] T. F. Morgeneyer and J. Besson, "Flat to slant ductile fracture transition: Tomography examination and simulations using shear-controlled void nucleation," *Scripta Materialia*, vol. 65, pp. 1002–1005, 2011.

[145] J. Kadkhodapour, B. Anbarlooie, H. Hosseini-Toudeshky, and S. Schmauder, "Simulation of shear failure in dual phase steels using localization criteria and experimental observation," *Computational Materials Science*, vol. 94, pp. 106–113, 2014.

[146] T.-S. Cao, M. Mazière, K. Danas, and J. Besson, "A model for ductile damage prediction at low stress triaxialities incorporating void shape change and void rotation," *International Journal of Solids and Structures*, vol. 63, pp. 240–263, 2015.

[147] T. Luo and X. Gao, "On the prediction of ductile fracture by void coalescence and strain localization," *Journal of the Mechanics and Physics of Solids*, vol. 113, pp. 82–104, 2018.

[148] P. F. Thomason, "Three–dimensional models for the plastic limit–loads at incipient failure of the intervoid matrix in ductile porous solids," *Acta Metallurgica*, vol. 33, pp. 1079–1085, 1985.

[149] P. F. Thomason, "A three–dimensional model for ductile fracture by the growth and coalescence of microvoids," *Acta Metallurgica*, vol. 33, no. 6, pp. 1087–1095, 1985.

[150] A. A. Benzerga, "Micromechanics of Coalescence in Ductile Fracture," *Journal of the Mechanics and Physics of Solids*, vol. 50, pp. 1331–1362, 2002.

[151] Y. Huang, "Accurate Dilatation Rates for Spherical Voids in Triaxial Stress Fields," *Journal of Applied Mechanics*, vol. 58, pp. 1084–1085, 1991.

[152] F. A. McClintock, S. M. Kaplan, and C. A. Berg, "Ductile fracture by hole growth in shear bands," *International Journal of Fracture*, vol. 2, no. 4, pp. 614–627, 1966.

[153] G. Perrin and J.-B. Leblond, "Analytical study of a hollow sphere made of plastic porous material and subjected to hydrostatic tension— application to some problems in ductile fracture of metals," *Int. J. Plasticity*, vol. 6, no. 6, pp. 677–699, 1990.

[154] X. Gao, J. Faleskog, and C. F. Shih, "Cell model for nonlinear fracture analysis - II. Fracture-process calibration and verification," *International Journal of Fracture*, vol. 89, pp. 375–398, 1998.

[155] X. Gao and J. Kim, "Modeling of ductile fracture: Significance of void coalescence," *International Journal of Solids and Structures*, vol. 43, pp. 6277–6293, 2006.

[156] K. S. Zhang, J. B. Bai, and D. Francois, "Numerical analysis of the influence of the Lode parameter on void growth," *International Journal of Solids and Structures*, vol. 38, pp. 5847–5856, 2001.

[157] A. Srivastava and A. Needleman, "Porosity evolution in a creeping single crystal," *Modelling and Simulation in Materials Science and Engineering*, vol. 20, p. 035010, 2012.

[158] L. Xue, "Constitutive modeling of void shearing effect in ductile fracture of porous materials," *Engineering Fracture Mechanics*, vol. 75, pp. 3343–3366, 2008.

[159] P. F. Thomason, "A theory for ductile fracture by internal necking of cavities," *J. Inst. Metals*, vol. 96, p. 360, 1968.

[160] C. Tekoğlu, "Representative volume element calculations under constant stress triaxiality, lode parameter, and shear ratio," *International Journal of Solids and Structures*, vol. 51, pp. 4544–4553, 2014.

[161] Z. G. Liu, W. H. Wong, and T. F. Guo, "Void behaviors from low to high triaxialities: Transition from void collapse to void coalescence," *International Journal of Plasticity*, vol. 84, pp. 183–202, 2016.

[162] E. Dubensky and D. Koss, "Void/pore distributions and ductile fracture," *D.A. MTA*, vol. 18, no. 11, pp. 1887–1895, 1987.

[163] P. E. Magnusen, E. M. Dubensky, and D. A. Koss, "The effect of void arrays on void linking during ductile fracture," *Acta Metallurgica*, vol. 36, no. 6, pp. 1503–1509, 1988.

[164] V. Tvergaard, "Effect of void cluster on ductile failure evolution," *Meccanica*, vol. 51, pp. 3097–3105, 2016.

[165] K. Kuna and D. Z. Sun, "Three-dimensional cell model analyses of void growth in ductile materials," *International Journal of Fracture*, vol. 81, pp. 235–258, 1996.

[166] C. Tekoglu, "Void coalescence in ductile solids containing two populations of voids," *Engineering Fracture Mechanics*, vol. 147, pp. 418–430, 2015.

[167] D. Lassance, D. Fabrègue, F. Delannay, and T. Pardoen, "Micromechanics of room and high temperature fracture in 6xxx Al alloys," *Progress in Materials Science*, vol. 52, pp. 62–129, 2007.

[168] J. Furer and P. Ponte Castañeda, "A symmetric fully optimized second-order method for nonlinear homogenization," *ZAMM-Journal of Applied Mathematics and Mechanics/Zeitschrift für Angewandte Mathematik und Mechanik*, vol. 98, no. 2, pp. 222–254, 2018.

[169] R. Hill, "The essential structure of constitutive laws for metal composites and polycrystals," *Journal of the Mechanics and Physics of Solids*, vol. 15, pp. 79–95, 1967.

[170] J. Mandel, "Contribution théorique à l'étude de l'écrouissage et des lois d'écoulement plastique," in 11^{th} *International Congress on Applied Mechanics*, pp. 502–509, Springer, Berlin, 1964.

[171] G. Perrin, *Contribution à l'étude théorique et numérique de la rupture ductile des métaux*. PhD thesis, Ecole Polytechnique, 1992.

[172] M. G. Geers, V. Kouznetsova, and W. Brekelmans, "Multi-scale computational homogenization: Trends and challenges," *Journal of computational and applied mathematics*, vol. 234, no. 7, pp. 2175–2182, 2010.

[173] J. Salençon *et al.*, *Application of the theory of plasticity in soil mechanics*. John Wiley & Sons., 1977.

[174] A. R. Ponter, P. Fuschi, and M. Engelhardt, "Limit analysis for a general class of yield conditions," *European Journal of Mechanics*, vol. 19, no. 3, pp. 401–421, 2000.

[175] A. Bottero, R. Negre, J. Pastor, and S. Turgeman, "Finite element method and limit analysis theory for soil mechanics problems," *Computer Methods in Applied Mechanics and Engineering*, vol. 22, no. 1, pp. 131–149, 1980.

[176] W.-F. Chen and X. Liu, *Limit analysis in soil mechanics*, vol. 52. 2012.

[177] P. Hodge, *Limit analysis of rotationally symmetric plates and shells*. Prentice-Hall, 1963.

[178] L. Hao, P. Ke, and W. June, "An anisotropic damage criterion for deformation instability and its application to forming limit analysis of metal plates," *Engineering Fracture Mechanics*, vol. 21, no. 5, pp. 1031–1054, 1985.

[179] S. Sloan, "Lower bound limit analysis using finite elements and linear programming," *International Journal for Numerical and Analytical Methods in Geomechanics*, vol. 12, no. 1, pp. 61–77, 1988.

[180] M. P. Nielsen and L. C. Hoang, *Limit analysis and concrete plasticity*. CRC press, 2016.

[181] W. Johnson and H. Kudō, *The mechanics of metal extrusion*. Manchester University Press, 1962.

[182] W. Prager and P. G. Hodge, "Theory of perfectly plastic solids," 1951.

[183] W. H. Yang, "Large deformation of structures by sequential limit analysis," 1993.

[184] J.-B. Leblond, D. Kondo, L. Morin, and A. Remmal, "Classical and sequential limit analysis revisited," *Comptes Rendus Mécanique*, vol. 346, no. 4, pp. 336–349, 2018.

[185] K. Anoukou, F. Pastor, P. Dufrenoy, and D. Kondo, "Limit analysis and homogenization of porous materials with mohr–coulomb matrix. part i: Theoretical formulation," *Journal of the Mechanics and Physics of Solids*, vol. 91, pp. 145–171, 2016.

[186] W. Rudin *et al.*, *Principles of mathematical analysis*, vol. 3. McGraw-hill New York, 1976.

[187] K. Krabbenhoft, A. V. Lyamin, M. Hjiaj, and S. W. Sloan, "A new discontinuous upper–bound limit analysis formulation," *International Journal for Numerical Methods in Engineering*, vol. 63, no. 7, pp. 1069–1088, 2005.

[188] M. Hjiaj, A. Lyamin, and S. Sloan, "Numerical limit analysis solutions for the bearing capacity factor nγ," *International Journal of Solids and Structures*, vol. 42, no. 5-6, pp. 1681–1704, 2005.

[189] K. Madou and J.-B. Leblond, "Numerical studies of porous ductile materials containing arbitrary ellipsoidal voids — I: Yield surfaces of representative cells," *European Journal of Mechanics*, vol. 42, pp. 480–489, 2013.

[190] A. Documentation, "Version 2018," *Dassault Systèmes*, 2010.

[191] Z. Hashin and S. Shtrikman, "A variational approach to the theory of the elastic behaviour of multiphase materials," *Journal of the Mechanics and Physics of Solids*, vol. 11, no. 2, pp. 127–140, 1963.

[192] J. Willis, "The overall elastic response of composite materials," *Journal of Applied Mechanics*, vol. 50, no. 4b, pp. 1202–1209, 1983.

[193] P. Ponte Castaneda and J. R. Willis, "On the overall properties of nonlinearly viscous composites," *Proceedings of the Royal Society of London A*, vol. A 438, pp. 419–431, 1988.

[194] P. Ponte Castaneda, "The effective mechanical properties of nonlinear composites," *Journal of the Mechanics and Physics of Solids*, vol. 39, pp. 45–71, 1991.

[195] P. Suquet, "Bounds and estimates for the overall properties of nonlinear composites," in *Mecamat'93, Int. seminar on micromechanics of materials, Moret–sur–Loing, France, 6–8 July*, pp. 361–382, 1993.

[196] P. Suquet, "Overall potentials and extremal surfaces of power law or ideally plastic composites," *J. Mech. Phys. Solids*, vol. 41, no. 6, pp. 981–1002, 1993.

[197] K. Lurie and A. Cherkaev, "Exact estimates of conductivity of composites formed by two isotropically conducting media taken in prescribed proportion," *Proceedings of the Royal Society of Edinburgh Section A: Mathematics*, vol. 99, no. 1-2, pp. 71–87, 1984.

[198] G. Milton and S. Serkov, "Bounding the current in nonlinear conducting composites," *Journal of the Mechanics and Physics of Solids*, vol. 48, no. 6-7, pp. 1295–1324, 2000.

[199] P. Ponte Castaneda, "Second-order homogenization estimates for nonlinear composites incorporating field fluctuations: I - theory," *Journal of the Mechanics and Physics of Solids*, vol. 50, pp. 737–757, 2002.

[200] Y. Liu and P. Ponte Castañeda, "Homogenization-based predictions for texture evolution," in *IUTAM Symposium on Computational Mechanics of Solid Materials at Large Strains: Proceedings of the IUTAM Symposium held in Stuttgart, Germany, 20–24 August 2001*, vol. 108, p. 269, Springer Science & Business Media, 2013.

[201] D. Song and P. Ponte Castañeda, "A finite-strain homogenization model for viscoplastic porous single crystals: I–theory," *Journal of the Mechanics and Physics of Solids*, vol. 107, pp. 560–579, 2017.

[202] H. Moulinec and P. Suquet, "A fft-based numerical method for computing the mechanical properties of composites from images of their microstructures," in *IUTAM symposium on microstructure-property interactions in composite materials*, pp. 235–246, Springer, 1995.

[203] H. Moulinec and P. Suquet, "A numerical method for computing the overall response of nonlinear composites with complex microstructure," *Computer Methods in Applied Mechanics and Engineering*, vol. 157, no. 1-2, pp. 69–94, 1998.

[204] J. Michel, H. Moulinec, and P. Suquet, "A computational method based on augmented lagrangians and fast fourier transforms for composites with high contrast," *CMES(Computer Modelling in Engineering & Sciences)*, vol. 1, no. 2, pp. 79–88, 2000.

[205] J. Michel, H. Moulinec, and P. Suquet, "A computational scheme for linear and non-linear composites with arbitrary phase contrast," *International Journal for Numerical Methods in Engineering*, vol. 52, no. 1-2, pp. 139–160, 2001.

[206] R. Lebensohn, "N-site modeling of a 3d viscoplastic polycrystal using fast fourier transform," *Acta Materialia*, vol. 49, no. 14, pp. 2723–2737, 2001.

[207] R. Lebensohn, Y. Liu, and P. Ponte Castañeda, "On the accuracy of the self-consistent approximation for polycrystals: comparison with full-field numerical simulations," *Acta Materialia*, vol. 52, no. 18, pp. 5347–5361, 2004.

[208] R. Lebensohn, R. Brenner, O. Castelnau, and A. Rollett, "Orientation image-based micromechanical modelling of subgrain texture evolution in polycrystalline copper," *Acta Materialia*, vol. 56, no. 15, pp. 3914–3926, 2008.

[209] R. Lebensohn, A. Rollett, and P. Suquet, "Fast fourier transform-based modeling for the determination of micromechanical fields in polycrystals," *Jom*, vol. 63, no. 3, pp. 13–18, 2011.

[210] C. A., J. Segurado, D. Hartl, and A. A. Benzerga, "A variational fast fourier transform method for phase-transforming materials," *(under preparation)*.

[211] A. Needleman, "A numerical study of necking in circular cylindrical bars," *Journal of the Mechanics and Physics of Solids*, vol. 20, pp. 111–127, 1972.

[212] V. Tvergaard, "Influence of voids on shear band instabilities under plane strain conditions," *International Journal of Fracture*, vol. 17, pp. 389–407, 1981.

[213] V. Tvergaard, "Influence of void nucleation on ductile shear fracture at a free surface," *Journal of the Mechanics and Physics of Solids*, vol. 30, pp. 399–425, 1982.

[214] J. Besson and R. Foerch, "Large scale object oriented finite element code design," *Computer Methods in Applied Mechanics and Engineering*, vol. 142, pp. 165–187, 1997.

[215] M. Dunand and D. Mohr, "On the predictive capabilities of the shear modified gurson and the modified mohr-coulomb fracture models over a wide range of stress triaxialities and lode angles," *Journal of the Mechanics and Physics of Solids*, vol. 59, pp. 1374–1394, 2011.

[216] K. Danas and P. Ponte Castañeda, "Influence of the Lode parameter and the stress triaxiality on the failure of elasto-plastic porous materials," *International Journal of Solids and Structures*, vol. 49, pp. 1325–1342, 2012.

[217] F. Fritzen, S. Forest, T. Böhlke, D. Kondo, and T. Kanit, "Computational homogenization of elasto-plastic porous metals," *International Journal of Plasticity*, vol. 29, pp. 102–119, 2012.

[218] V. Tvergaard, "Study of localization in a void-sheet under stress states near pure shear," *International Journal of Solids and Structures*, vol. 75, pp. 134–142, 2015.

[219] Q. Du, V. Faber, and M. Gunzburger, "Centroidal voronoi tessellations: Applications and algorithms," *SIAM review*, vol. 41, no. 4, pp. 637–676, 1999.

[220] M. Gologanu, J.-B. Leblond, G. Perrin, and J. Devaux, "Theoretical models for void coalescence in porous ductile solids – II: Coalescence in "columns"," *International Journal of Solids and Structures*, vol. 38, pp. 5595–5604, 2001.

[221] A. A. Benzerga, *Rupture ductile des tôles anisotropes*. PhD thesis, Ecole Nationale Supérieure des Mines de Paris, 2000.

[222] J.-B. Leblond, G. Perrin, and P. Suquet, "Exact results and approximate models for porous viscoplastic solids," *International Journal of Plasticity*, vol. 10, pp. 213–225, 1994.

[223] R. Hill, "A theory of yielding and plastic flow of anisotropic solids," *Proceedings of the Royal Society of London A*, vol. 193, pp. 281–297, 1948.

[224] S. Kweon, B. Sagsoy, and A. A. Benzerga, "Constitutive relations and their time integration for anisotropic elasto-plastic porous materials," *Computer Methods in Applied Mechanics and Engineering*, vol. 310, pp. 495–534, 2016.

[225] M. Kailasam and P. Ponte Castaneda, "A general constitutive theory for linear and nonlinear particulate media with microstructure evolution," *Journal of the Mechanics and Physics of Solids*, vol. 46, no. 3, pp. 427–465, 1998.

[226] J. Eshelby, "The determination of the elastic field of an ellipsoidal inclusion, and related problems," *Proc. Roy. Soc*, vol. A241, pp. 357–396, 1957.

[227] M. E. Gurtin, E. Fried, and L. Anand, *The mechanics and thermodynamics of continua*. Cambridge University Press, 2010.

[228] M. E. Torki, A. A. Benzerga, and J.-B. Leblond, "On Void Coalescence under Combined Tension and Shear," *Journal of Applied Mechanics*, vol. 82, no. 7, p. 071005, 2015.

[229] S. M. Keralavarma, S. Hoelscher, and A. A. Benzerga, "Void growth and coalescence in anisotropic plastic solids," *International Journal of Solids and Structures*, vol. 48, pp. 1696–1710, 2011.

[230] K. Madou and J.-B. Leblond, "A Gurson-type criterion for porous ductile solids containing arbitrary ellipsoidal voids – II: Determination of yield criterion parameters," *Journal of the Mechanics and Physics of Solids*, vol. 60, pp. 1037–1058, 2012.

[231] R. M. Bowen and C. Wang, *Introduction to vectors and tensors*, vol. 2. Courier Corporation, 2008.

[232] I. S. Gradshtein and I. M. Ryzhik, "Tables of integrals, sums, series and products," 1971.

[233] N. Thomas, *On the path dependence of ductile fracture in anisotropic materials*. PhD thesis, Texas A&M University, College Station, TX, 2016.

[234] T. M. Apostol, *Calculus: Mlulti-Variable Calculus and Linear Algebra, with Applications to Differential Equations and Probability*. John Wiley & Sons, 2007.

[235] J.-B. Leblond and G. Mottet, "A theoretical approach of strain localization within thin planar bands in porous ductile materials," *Comptes Rendus Mecanique*, vol. 336, pp. 176–189, 2008.

APPENDIX A

SOME FEASIBLE LOCALIZATION SYSTEMS

This section describes a consistent and convenient method that allows for a clear identification of the initial microstructure within a voided material. These initial values can then be utilized to evaluate the current values with proper evolution laws. See Eq's (6.23), (6.25), and (6.27).

A.1 Planar Geometry

In a state of arbitrary loading, plastic strain localization among a clustered array of voids can occur according to various patterns. Each pattern is uniquely determined by resolving the stress tensor as well as calculating the microstructural parameters on a plane of localization associated with normal $\boldsymbol{n}$.

In general, any arbitrary plane that can connect an array of voids can be conceived. Not every plane, however, can prove efficacious unless at the limit of randomly distributed voids. Among the feasible ones, we can consider the planar bands connecting up to the first (orthogonal) or second (diagonal) nearest neighboring voids. Therefore, there can exist 3 generic classes of planes which take after the (100), (110), and (111) indices by scaling the dimensions. Each class embraces more than one specific plane. For instance, (100) generalizes into $(\{100\}, \{\bar{1}00\})$, $(\{010\}, \{0\bar{1}0\})$, and $(\{001\}, \{00\bar{1}\})$, constituting the normals to all localization planes as being sub-classes of (100) ($\bar{(.)}$ denoting the negative sign). See Fig. A.1.

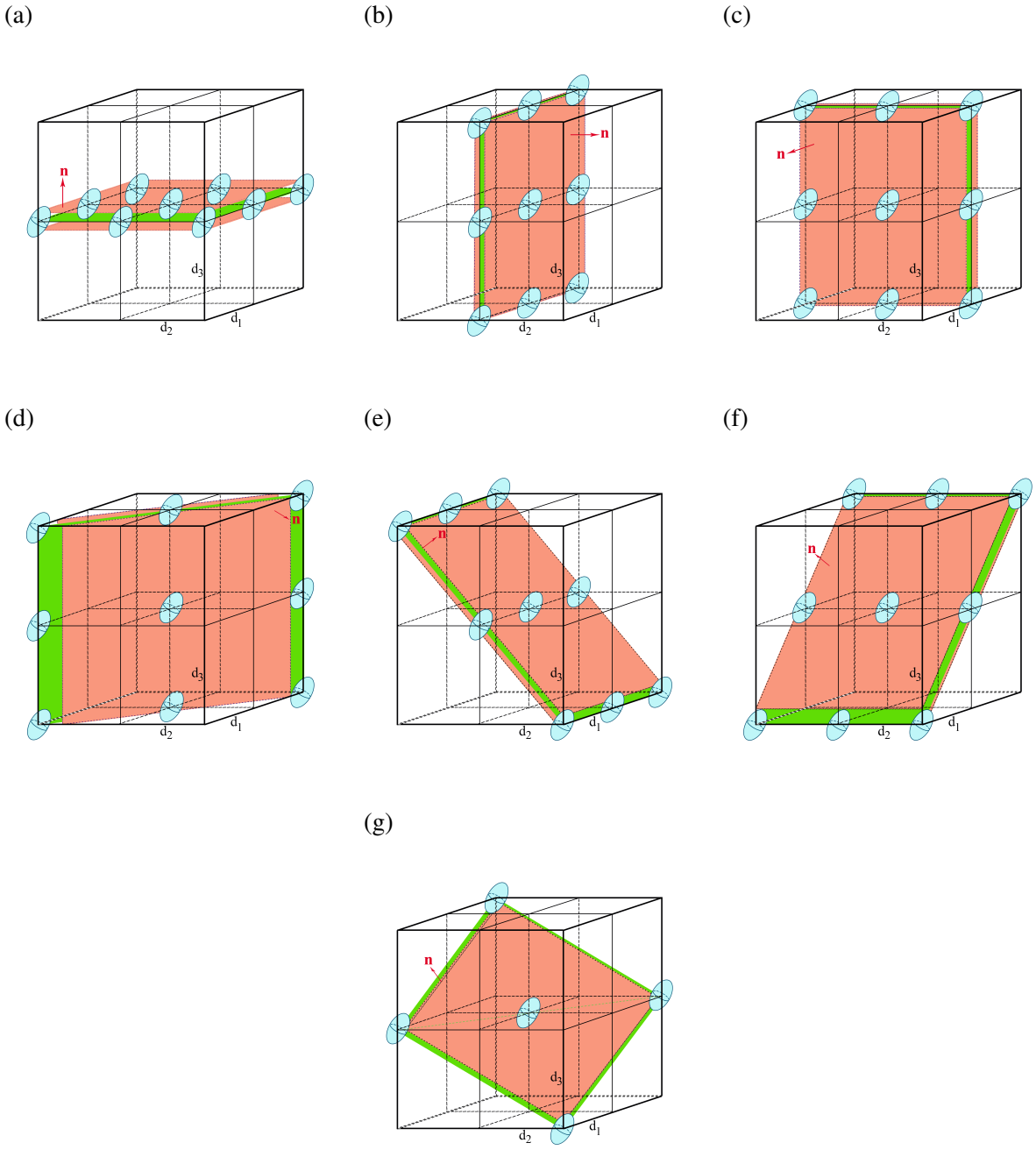

Figure A.1: Geometric outline of the possible localization planes connecting up to the first (orthogonal) or second (diagonal) nearest neighboring voids: (a-c) sub-classes of a vertical system, (d-g) sub-classes of a diagonal system.

With the provided background, voids can be deployed in a lattice as illustrated in Fig. A.1. Each plane of localization can be uniquely defined with a normal $\boldsymbol{n}$ and is also endowed with two

in-plane main directors ($\boldsymbol{m}, \boldsymbol{p}$), as being perpendicular to one another and perpendicular to $\boldsymbol{n}$.

A.2 Initial Microstructure

Within the identified cubic lattice, each localization system can be uniquely identified via its normal $\boldsymbol{n}$. In the considered set of feasible systems, the initial $\boldsymbol{n}$ within every system can be constructed with the initial lateral vectors $\boldsymbol{m}_0$ and $\boldsymbol{p}_0$ that can directly emanate from the initial lattice geometry, as discussed below. Nevertheless, the evolved normal $\boldsymbol{n}$, that can uniquely identify the evolved lattice geometry, need not be expressed in terms of the evolved lateral vectors $\boldsymbol{m}$ and $\boldsymbol{p}$ and can solely depend on $\boldsymbol{n}_0$ and the current deformation gradient $\boldsymbol{F}$. The evolved $\boldsymbol{m}$ can then be expressed in terms of the resolved shear traction onto the plane with normal $\boldsymbol{n}$, and $\boldsymbol{p}$ would result from the cross product of $\boldsymbol{n}$ and $\boldsymbol{m}$ (see Section 6.3.4.1 for further illustration). The initial triad $\boldsymbol{n}_0, \boldsymbol{m}_0, \boldsymbol{p}_0$ can be evaluated, on every localization plane, as function of the initial lattice orientation denoted by its tied basis ($\boldsymbol{d}_{10}, \boldsymbol{d}_{20}, \boldsymbol{d}_{30}$). With reference to Fig. A.1 one can consider the following cases, where localization systems are denoted with Roman numbers:

– Systems (I – III) (Fig's A.1 (a – c)):

$$\begin{aligned} (\mathrm{I}): &\quad \boldsymbol{n}_0 = \boldsymbol{d}_{10}\ ,\ \boldsymbol{m}_0 = \boldsymbol{d}_{30},\ \boldsymbol{p}_0 = \boldsymbol{d}_{20} \\ (\mathrm{II}): &\quad \boldsymbol{n}_0 = \boldsymbol{d}_{20}\ ,\ \boldsymbol{m}_0 = \boldsymbol{d}_{10},\ \boldsymbol{p}_0 = \boldsymbol{d}_{30} \\ (\mathrm{III}): &\quad \boldsymbol{n}_0 = \boldsymbol{d}_{30}\ ,\ \boldsymbol{m}_0 = \boldsymbol{d}_{10},\ \boldsymbol{p}_0 = \boldsymbol{d}_{20} \end{aligned} \tag{A.1}$$

In the next two plane classes, $\boldsymbol{n}$ is obtained from the cross product of its two generators L_1 and L_2. For the sake of more brevity in what follows, the following relative distances are defined:

$$\lambda_{12} = \frac{d_2}{d_1} \quad , \quad \lambda_{23} = \frac{d_3}{d_2} \quad , \quad \lambda_{13} = \frac{d_3}{d_1} \tag{A.2}$$

– Systems (IV – VI) (Fig's A.1 (d – f)):

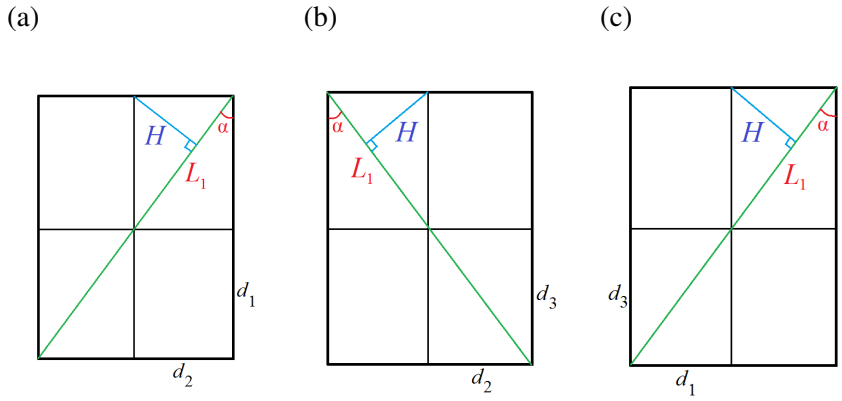

Figure A.2: Constituents of the effective cell aspect ratio $\bar{\lambda}$ at systems (IV – VI). Note that L_2 is perpendicular to the plane, and that $\bar{L} = \sqrt{L_1 L_2}$ emanates from geometric averaging.

$$
\begin{aligned}
&\text{(IV)}: \quad \boldsymbol{m}_0 = \frac{1}{\sqrt{1+\lambda_{12}^2}}(\boldsymbol{d}_{10} - \lambda_{12}\boldsymbol{d}_{20}) \;,\; \boldsymbol{p}_0 = \boldsymbol{d}_{30} \;,\; \boldsymbol{n}_0 = \boldsymbol{m}_0 \times \boldsymbol{p}_0 \\
&\text{(V)}: \quad \boldsymbol{m}_0 = \boldsymbol{d}_{10} \;,\; \boldsymbol{p}_0 = \frac{1}{\sqrt{1+\lambda_{23}^2}}(\boldsymbol{d}_{20} + \lambda_{23}\boldsymbol{d}_{30}) \;,\; \boldsymbol{n}_0 = \boldsymbol{m}_0 \times \boldsymbol{p}_0 \\
&\text{(VI)}: \quad \boldsymbol{m}_0 = \frac{1}{\sqrt{1+\lambda_{13}^2}}(\boldsymbol{d}_{10} + \lambda_{13}\boldsymbol{d}_{30}) \;,\; \boldsymbol{p}_0 = \boldsymbol{d}_{20} \;,\; \boldsymbol{n}_0 = \boldsymbol{m}_0 \times \boldsymbol{p}_0
\end{aligned}
\tag{A.3}
$$

where $|.|$ stands for vector magnitude and $\times$ denotes cross product between two vectors.

– System (VII) (Fig. A.1(g)):

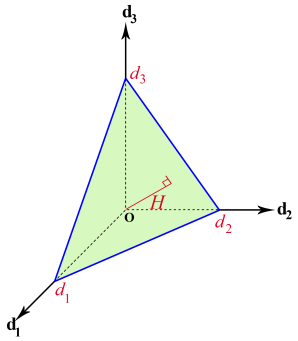

Figure A.3: Effective cell height in system (VII) emanating from the distance between the origin and the plane passing through the intercepts $(d_1, 0, 0)$, $(0, d_2, 0)$, and $(0, 0, d_3)$.

$$\boldsymbol{m}_0 = \frac{1}{\sqrt{1+\left(\frac{\lambda_{13}}{2}\right)^2}}(\boldsymbol{d}_{10} + \tfrac{\lambda_{13}}{2}\boldsymbol{d}_{30})\ ,\ \boldsymbol{p}_0 = \frac{1}{\sqrt{1+\left(\frac{\lambda_{23}}{2}\right)^2}}(\boldsymbol{d}_{20} + \tfrac{\lambda_{23}}{2}\boldsymbol{d}_{30})\ ,\ \boldsymbol{n}_0 = \boldsymbol{m}_0 \times \boldsymbol{p}_0 \tag{A.4}$$

Remark: The resolved traction magnitudes are insensitive towards the sings of components in $\boldsymbol{n}_0, \boldsymbol{m}_0, \boldsymbol{p}_0$. Only one representative component has thus been considered in every localization system. In other terms, among all imaginable systems, only seven of them are independent as explicated above. Any other system is analogous to one of the above.

The initial surrogate cell aspect ratio $\bar{\lambda}_0$ at every system originates from the ratio of the intervoid distance perpendicular to the corresponding plane over the *average* intervoid distance within the plane. Therefore:

– Systems (I – III):

$$\begin{aligned}
\bar{\lambda}_{0\mathrm{I}} &= \frac{d_1}{\sqrt{d_2 d_3}} = \frac{1}{\sqrt{\lambda_{12}\lambda_{13}}} \\
\bar{\lambda}_{0\mathrm{II}} &= \frac{d_2}{\sqrt{d_1 d_3}} = \sqrt{\frac{\lambda_{12}}{\lambda_{23}}} \\
\bar{\lambda}_{0\mathrm{III}} &= \frac{d_3}{\sqrt{d_1 d_2}} = \sqrt{\lambda_{13}\lambda_{23}}
\end{aligned} \tag{A.5}$$

– Systems (IV – VI):

With reference to Fig. A.2:

$$\begin{aligned}
&\bar{\lambda}_{0\mathrm{IV}} = \frac{H_{110}}{\sqrt{L_1 L_2}}\ ,\ L_1 = \sqrt{d_1^2 + d_2^2}\ ,\ L_2 = d_3\ ,\ H_{110} = d_1 \sin\alpha = \frac{d_1 d_2}{L_1}\ \therefore\ \bar{\lambda}_{0\mathrm{IV}} = \frac{1}{(\lambda_{12} + 1/\lambda_{12})^{\frac{3}{4}}(\lambda_{13}\lambda_{23})^{\frac{1}{4}}} \\
&\bar{\lambda}_{0\mathrm{V}} = \frac{H_{011}}{\sqrt{L_1 L_2}}\ ,\ L_1 = \sqrt{d_2^2 + d_3^2}\ ,\ L_2 = d_1\ ,\ H_{011} = d_3 \sin\alpha = \frac{d_2 d_3}{L_1}\ \therefore\ \bar{\lambda}_{0\mathrm{V}} = \frac{(\lambda_{12}\lambda_{13})^{\frac{1}{4}}}{(\lambda_{23} + 1/\lambda_{23})^{\frac{3}{4}}} \\
&\bar{\lambda}_{0\mathrm{VI}} = \frac{H_{101}}{\sqrt{L_1 L_2}}\ ,\ L_1 = \sqrt{d_1^2 + d_3^2}\ ,\ L_2 = d_2\ ,\ H_{101} = d_3 \sin\alpha = \frac{d_1 d_3}{L_1}\ \therefore\ \bar{\lambda}_{0\mathrm{VI}} = \frac{(\lambda_{23}/\lambda_{12})^{\frac{1}{4}}}{(\lambda_{13} + 1/\lambda_{13})^{\frac{3}{4}}}
\end{aligned} \tag{A.6}$$

– System (VII):

With reference to Fig. A.3, the slanted plane has the following equation:

$$\frac{x_1}{d_1} + \frac{x_2}{d_2} + \frac{x_3}{d_3} = 1$$

Herein, H is the distance between the origin $\boldsymbol{O}$ and the slanted plane, which follows from the equation below:

$$H_{\mathrm{VII}} = \frac{1}{\sqrt{\frac{1}{d_1^2} + \frac{1}{d_2^2} + \frac{1}{d_3^2}}}$$

and the area of the parallelogram, as being twice that of the confined triangle, is calculated from the magnitude of the cross product of the generating vectors, that is:

$$A = |(-d_1, d_2, 0) \times (0, -d_2, d_3)| = \sqrt{(d_1 d_2)^2 + (d_2 d_3)^2 + (d_1 d_3)^2} \tag{A.7}$$

Therefore, the equivalent cell aspect ratio in this system reads:

$$\bar{\lambda}_{\mathrm{VII}} = \frac{H_{\mathrm{VII}}}{\sqrt{A}} = \frac{1}{\left[(\lambda_{12}\lambda_{13} + \lambda_{23} + \frac{1}{\lambda_{23}})^2 + (\lambda_{13} + \frac{\lambda_{23}}{\lambda_{12}} + \frac{1}{\lambda_{13}})^2 + (\lambda_{12} + \frac{1}{\lambda_{12}} + \frac{1}{\lambda_{13}\lambda_{23}})^2\right]^{1/4}} \tag{A.8}$$

APPENDIX B

INITIAL AND CURRENT CELL ASPECT RATIOS

In order to derive $\lambda_0(\boldsymbol{n})$ –with the 0 superscript denoting initial state– in terms of λ_1 and λ_2 as well as an arbitrarily-oriented normal $\boldsymbol{n}$, one should evaluate the average inter-void distance inside the plane with normal $\boldsymbol{n}$, here termed L as well as the inter-void distance H, defined as the distance between the inter-plane distance parallel to $\boldsymbol{n}$. See Fig. B.1 first.

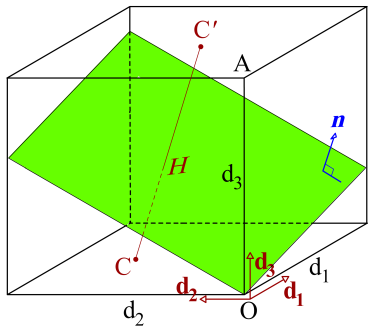

Figure B.1: Arbitrary localization plane relative to an octant of the void lattice.

Without loss of generality, one can assume that the plane passes through the lattice origin (O). With a prescribed initial normal orientation $\boldsymbol{n}_0$ and known initial lattice directors $\boldsymbol{d}_{i0}$, one can write the plane equation within the $\boldsymbol{d}_{i0}$ local basis as

$$n_1 x_1 + n_2 x_2 + n_3 x_3 = D_{\mathrm{O}} \tag{B.1}$$

where $n_i = \boldsymbol{n} \cdot \boldsymbol{d}_i$ and $D_{\mathrm{O}} = n_1 x_{1\mathrm{O}} + n_2 x_{2\mathrm{O}} + n_3 x_{3\mathrm{O}} = 0$, with the 0 subscripts removed for brevity. x_i are identified within the $\boldsymbol{d}_{i0}$ basis.

Upon recasting (B.1) as $x_3 = \phi(x_1, x_2)$, one can determine the area A of the plane within the confines of the lattice octant based on the domain emanating from its projection onto the $\boldsymbol{d}_1$–$\boldsymbol{d}_2$

plane, here denoted with S. To this end, one can write [234]:

$$A = \iint_S \sqrt{1 + \phi_{,1}^2 + \phi_{,2}^2}\, dx_1\, dx_2 \tag{B.2}$$

which, with

$$\phi(x_1, x_2) = -\left(\frac{n_1}{n_3}x_1 + \frac{n_2}{n_3}x_2\right)$$

would simplify, noting $n_1^2 + n_2^2 + n_3^2 = 1$, into

$$A = \frac{d_1 d_2}{n_3} \tag{B.3}$$

Moreover, H can be expressed as the distance between two parallel planes $x_3 = 0$ and $x_3 = d_3$ along the direction $\boldsymbol{n}$ between the intercepts denoted with points C and C'. Without loss of generality, point C can be taken to pass through the origin (O). Accordingly, the line passing through intercepts O and C' can be expressed via the following equation:

$$\frac{x_1}{n_1} = \frac{x_2}{n_2} = \frac{x_3}{n_3} \tag{B.4}$$

With the above equation known, the C' intercept can be obtained by letting $x_3 = d_3$ which, with reference to (B.4) gives

$$x_{iC'} = \frac{n_i}{n_3} d_3 \tag{B.5}$$

with $i = 1, 2, 3$. Therefore, H, identified by the distance between C and C' intercepts, reads

$$H = \mathrm{C\bar{C}}' = \sqrt{\left(\frac{n_1}{n_3}\right)^2 + \left(\frac{n_2}{n_3}\right)^2 + 1} = \frac{d_3}{|n_3|} \tag{B.6}$$

Then, $\lambda_0(\boldsymbol{n})$ will be written as the following ratio:

$$\lambda_0(\boldsymbol{n}_0) = \frac{H(\boldsymbol{n}_0)}{\sqrt{A}} = \frac{d_{30}}{|n_3|}\sqrt{\frac{|n_3|}{d_{10} d_{20}}} = \sqrt{\frac{\lambda_1 \lambda_2}{|\boldsymbol{n}_0 \cdot \boldsymbol{d}_{30}|}} \tag{B.7}$$

which retrieves $\lambda_0 = \sqrt{\lambda_1 \lambda_2}$ when $\boldsymbol{n}_0 = \boldsymbol{d}_{30}$, and λ_1 and λ_2 refer to (6.21).

With the initial cell aspect ratio at hand, one can explicitly evolve it according to the algebraic steps below, that follow Eq. (21) of Ref. [235] for initially cubic cells. To this end, one could firstly write:

$$\lambda(\boldsymbol{n}) = \frac{H(\boldsymbol{n})}{L(\boldsymbol{n})} = \frac{H_0(\boldsymbol{n})}{L_0(\boldsymbol{n})} \frac{H(\boldsymbol{n})/H_0(\boldsymbol{n})}{L(\boldsymbol{n})/L_0(\boldsymbol{n})} \tag{B.8}$$

where the 0 subscripts denote the initial state, and

$$\frac{H_0(\boldsymbol{n})}{L_0(\boldsymbol{n})} = \lambda_0(\boldsymbol{n})$$

Moreover, V_0 and V (initial and current cell volumes) are related via

$$V = \mathcal{J} V_0$$

which implies

$$\frac{H(\boldsymbol{n})}{H_0(\boldsymbol{n})} = \mathcal{J} \frac{A_0(\boldsymbol{n})}{A(\boldsymbol{n})} \tag{B.9}$$

The average cell length L and ligament area A correlate through

$$\frac{L(\boldsymbol{n})}{L_0(\boldsymbol{n})} = \sqrt{\frac{A(\boldsymbol{n})}{A_0(\boldsymbol{n})}} \tag{B.10}$$

On the other hand, a continuum relationship between A_0 and A reads

$$A\boldsymbol{n} = \mathcal{J} \boldsymbol{F}^{-T} A_0 \boldsymbol{n}_0$$

which can be recast, by exploiting a dot product, into the following

$$(A_0 \boldsymbol{n}_0) \cdot (A_0 \boldsymbol{n}_0) = \frac{1}{\mathcal{J}^2} (\boldsymbol{F}^T A \boldsymbol{n}) \cdot (\boldsymbol{F}^T A \boldsymbol{n}) = \frac{1}{\mathcal{J}^2} A^2 \boldsymbol{n} \cdot \boldsymbol{F}\boldsymbol{F}^T \boldsymbol{n} \;\; \therefore \;\; \frac{A_0}{A} = \frac{1}{\mathcal{J}} \sqrt{\boldsymbol{n} \cdot \boldsymbol{F}\boldsymbol{F}^T \boldsymbol{n}} \tag{B.11}$$

Finally, the combination of (B.9 – B.11) yields

$$\lambda(\boldsymbol{n}) = \lambda_0(\boldsymbol{n})\mathcal{J}\left(\frac{A_0(\boldsymbol{n})}{A(\boldsymbol{n})}\right)^{\frac{3}{2}} = \frac{\lambda_0(\boldsymbol{n})}{\sqrt{\mathcal{J}}}\left(\boldsymbol{n}.(\boldsymbol{F}\boldsymbol{F}^{\mathrm{T}}).\boldsymbol{n}\right)^{\frac{3}{4}} \tag{B.12}$$

APPENDIX C

CONSERVATION OF STRESS RATIOS

The ratios among the normal, lateral, and shear stresses ought to be kept constant throughout the analysis. These ratios are defined as $\kappa_n := \Sigma_{ll}/\Sigma_{nn}$ and $\kappa_{\rm sh} := \Sigma_{nl}/\Sigma_{nn}$ in the present context. In other terms, the dimensionless stress parameters named as *stress triaxiality* (T) and *Lode parameter* (L) should be constant throughout. To this end, if the discretization with respect to time and space is done through ABAQUS (whilst the time integration is worked out in a user-defined subroutine (UMAT)), one can make use of the ***Rik's*** algorithm (known alternatively as *arc-length* in ANSYS), which performs analyses upon a load-controlled basis with constant ratios amongst the loads. However, in case the user would like to use an in-house code for time integration of the constitutive laws, then one should include additional subroutines to control the values of T and L. With $(\Sigma_{ll}, \Sigma_{nn}, \Sigma_{nl})$ being the nonzero stress components, the values of T and L obey the following formulas:

$$\begin{aligned} T &= \frac{1}{3}\frac{2\kappa_n + 1}{\sqrt{(1-\kappa_n)^2 + 3\kappa_{\rm sh}^2}} \\ L &= -(1-\kappa_n)\frac{\frac{9}{2}\kappa_{\rm sh}^2 + (1-\kappa_n)^2}{[(1-\kappa_n)^2 + 3\kappa_{\rm sh}^2]^{3/2}} \end{aligned} \tag{C.1}$$

In the present program, a rather simple cutting-plane algorithm has been utilized to do this. The following items describe this procedure in the cases of small and large shear-to-normal stress ratios.

– At small to medium shear-to-normal stress ratios ($0 \leq \kappa_{\rm sh} \leq 1$):

  Each analysis step is associated with a prescribed normal strain increment $d\epsilon_{nn}$, which is a fraction of a total normal strain calculated from a prescribed normal displacement U_n:

$$\epsilon_{nn} = \ln\left(1 + \frac{U_n}{H}\right) \quad , \quad d\epsilon_{nn} = \frac{\Delta t}{\mathcal{T}}\epsilon_{nn} \quad , \quad \epsilon_{nn}^{(i)} = \frac{i}{N_s}\epsilon_{nn} \tag{C.2}$$

where $\mathcal{T}$ is the total time duration, and N_s is the total number of steps. The initial values of normal and shear strain increments come from elasticity:

$$\begin{aligned}
&\mathcal{R}_n = \frac{\epsilon_{ll}}{\epsilon_{nn}} = \frac{(1-\nu)\kappa_n - \nu}{1-2\nu\kappa_n} \quad , \quad \mathcal{R}_{\rm sh} = \frac{\epsilon_{nl}}{\epsilon_{nn}} = \frac{(1+\nu)\kappa_{\rm sh}}{1-2\nu\kappa_n} \\
&\epsilon_{ll} = \mathcal{R}_n \epsilon_{nn} \quad , \quad \epsilon_{nl} = \mathcal{R}_{\rm sh}\epsilon_{nn} \\
&\epsilon_{ll}^{(i)} = \frac{i}{N_s}\epsilon_{ll} \quad , \quad \epsilon_{nl}^{(i)} = \frac{i}{N_s}\epsilon_{nl} \\
&d\epsilon_{ll}^{(i)} = \frac{\Delta t}{\mathcal{T}}\epsilon_{ll}^{(i)} \quad , \quad d\epsilon_{nl}^{(i)} = \frac{\Delta t}{\mathcal{T}}\epsilon_{nl}^{(i)}
\end{aligned} \tag{C.3}$$

Then, the elastic values of $\mathcal{R}_n$ and $\mathcal{R}_{\rm sh}$ should be manipulated in such a way that the desired values of T and L are preserved. The following differential values can be added to the current lateral and shear strains to produce new incremental strains ($d\epsilon_{ll}^{(i)}, d\epsilon_{nl}^{(i)}$).

$$\begin{aligned}
&d\kappa_n = \kappa_n - \frac{\Sigma_{ll}}{\Sigma_{nn}} \quad , \quad d\epsilon_{ll} = \left(\left| \frac{\Sigma_{ll}}{2\lambda\Sigma_{ll} - 2(\lambda+\mu)\Sigma_{nn}} \right| \right)^{p_1} d\kappa_n \\
&d\kappa_{\rm sh} = \kappa_{\rm sh} - \frac{\Sigma_{nl}}{\Sigma_{nn}} \quad , \quad d\epsilon_{nl} = \left(\left| \frac{\Sigma_{nl}}{2\mu\Sigma_{nl} - 2(\lambda+\mu)\Sigma_{nn}} \right| \right)^{p_2} d\kappa_{\rm sh}
\end{aligned} \tag{C.4}$$

The powers (p_1, p_2) depend on the values of T and L, and on the dynamic process (growth or coalescence). The best convergence rate is found to occur if (p_1, p_2) are taken as follows:

$$-0.1 \leq (p_1, p_2) \leq 0.25 \tag{C.5}$$

With these new incremental strains, the Newton-Raphson method solves for the microstructural variables, and with the calculated stresses the new stress values are used to calculate the new values of $T^{(i)}$ and $L^{(i)}$. This procedure is reiterated until the desired values of T and L are retrieved. If the number of iterations for a specific time step tends to be large (e.g. > 20), then one can choose the lower bound of p_1 for triaxiality control and the lower bound of p_2 for control of the Lode parameter. Otherwise, the upper bound 0.25 can be considered.

Remark: If the number of steps is very large, e.g. $N_s = 20000$, then a fraction of N_s, here

termed n_s, should be considered in the calculation of $(d\epsilon_{ll}^{(i)}, d\epsilon_{nl}^{(i)})$. The rate of convergence was proven to be best if $1000 \leq n_s \leq 2000$.

– At large values of shear-to-normal stress ratios (for $\kappa_{\rm sh} > 1$):

With large values of shear-to-normal stress ratios, it would be best that the shear strain be prescribed instead of the normal strain. Otherwise, the declining curve of stress vs equivalent strain will not be captured by the model. That is, the total shear strain is calculated from a prescribed tangential displacement U_t:

$$\epsilon_{nl} = \frac{1}{2}\frac{U_t}{\sqrt{U_t^2 + H^2}} \quad , \quad d\epsilon_{nl} = \frac{\Delta t}{\mathcal{T}}\epsilon_{nl} \quad , \quad \epsilon_{nl}^{(i)} = \frac{i}{N_s}\epsilon_{nl} \tag{C.6}$$

Then, the initial values of normal and lateral strain increments come from elasticity:

$$\begin{aligned} &\mathcal{S}_n = \frac{\mathcal{R}_n}{\mathcal{R}_{\rm sh}} \quad , \quad \mathcal{S}_{\rm sh} = \frac{1}{\mathcal{R}_{\rm sh}} \\ &\epsilon_{ll} = \mathcal{S}_n \epsilon_{nl} \quad , \quad \epsilon_{nn} = \mathcal{S}_{\rm sh}\epsilon_{nl} \\ &\epsilon_{ll}^{(i)} = \frac{i}{N_s}\epsilon_{ll} \quad , \quad \epsilon_{nn}^{(i)} = \frac{i}{N_s}\epsilon_{nn} \\ &d\epsilon_{ll}^{(i)} = \frac{\Delta t}{\mathcal{T}}\epsilon_{ll}^{(i)} \quad , \quad d\epsilon_{nn}^{(i)} = \frac{\Delta t}{\mathcal{T}}\epsilon_{nn}^{(i)} \end{aligned} \tag{C.7}$$

Then, the elastic values of $\mathcal{S}_n$ and $\mathcal{S}_{\rm sh}$ should be manipulated in such a way that the desired values of T and L are preserved. The following differential values can be added to the current normal and lateral strains to produce new incremental strains $(d\epsilon_{nn}^{(i)}, d\epsilon_{ll}^{(i)})$.

$$\begin{aligned} &d\mathcal{K}_n = \frac{\kappa_n}{\kappa_{\rm sh}} - \frac{\Sigma_{ll}}{\Sigma_{nl}} \quad , \quad d\epsilon_{ll} = \left(\left|\frac{\Sigma_{ll}}{2\lambda\Sigma_{ll} - 2\mu\Sigma_{nl}}\right|\right)^{q_1} d\mathcal{K}_n \\ &d\mathcal{K}_{\rm sh} = \frac{1}{\kappa_{\rm sh}} - \frac{\Sigma_{nn}}{\Sigma_{nl}} \quad , \quad d\epsilon_{nn} = \left(\left|\frac{\Sigma_{nn}}{2\mu\Sigma_{nl} - 2(\lambda+\mu)\Sigma_{nn}}\right|\right)^{q_2} d\mathcal{K}_{\rm sh} \end{aligned} \tag{C.8}$$

The powers (p_1, p_2) depend on the values of T and L, and on the dynamic process (growth

or coalescence). The best convergence rate is found to occur if (q_1, q_2) are taken as follows:

$$0.1 \leq (q_1, q_2) \leq 0.25 \tag{C.9}$$

P1 ON VOID COALESCENCE UNDER COMBINED TENSION AND SHEAR

On Void Coalescence under Combined Tension and Shear

M. E. Torki[1], A. A. Benzerga[1,2], J.-B. Leblond[3]

[1] *Department of Aerospace Engineering, Texas A&M University, College Station, TX 77843, USA*

[2] *Department of Materials Science and Engineering, Texas A&M University, College Station, TX 77843, USA*

[3] *Sorbonne Universites, UPMC Univ Paris 06, CNRS, UMR 7190*

Institut Jean Le Rond d'Alembert, F-75005, Paris, France

Abstract

A micromechanics-based yield criterion is developed for a porous ductile material deforming by localized plasticity in combined tension and shear. The new criterion is primarily intended to model void coalescence by internal necking or internal shearing. The model is obtained by limit analysis and homogenization of a cylindrical cell containing a coaxial cylindrical void of finite height. Plasticity in parts of the matrix is modeled using rate-independent J_2 flow theory. It is shown that for the discontinuous, yet kinematically admissible trial velocity fields used in the limit analysis procedure, the overall yield domain exhibits curved parts and flat parts with no vertices. Model predictions are compared with available finite-element based estimates of limit loads on cubic cells. In addition, a heuristic modification to the model is proposed in the limit case of penny-shape cracks to enable its application to materials failing after limited void growth as well as to situations of shear-induced void closure.

Key Words: Ductile fracture; Low triaxiality; Internal necking; Internal shearing; Homogenization; Penny-shaped cracks.

1 Introduction

Ductile fracture under combined tension and shear has seen increasing interest in recent years. Earlier experiments on aluminum alloys and steels indicated that the materials were less ductile in shear than under uniaxial tension [1, 2]. However, more recent experiments show the opposite trend [3]. Keeping in mind specimen geometry and material variability, the extent to which shear affects ductile fracture remains fairly unsettled. Meanwhile, tentative understanding of such effects has been developed by considering the potential effect of the third invariant of the stress deviator, J_3, e.g., [4–6]. However, the fundamental mechanisms underlying such effects remain elusive. In addition, a paradigm shift seems necessary in approaching ductile fracture in combined shear and tension, particularly at low stress triaxiality because models based on stress invariants limit the scope to isotropic behavior. What is peculiar to low triaxiality fracture is that the large plastic strains induce strong microstructural evolutions in terms of void shape, orientation and arrangement, even if the anisotropy of the embedding matrix is disregarded. Thus, analyses of ductile fracture under shear-dominated loading and interpretation of currently available experiments rely, to a great extent, on accounting for the induced, and eventually initial anisotropies.

Void nucleation under predominately shear loading involves complex void–particle interactions [7]. Micromechanical void nucleation analyses of the kind pioneered by Needleman [8] are still not available for such loadings. Whether these nucleation conditions fundamentally differ from those under tension with

particle locking effects [9, 10] remains to be investigated. On the other hand, the behavior of a void, free of particle constraints, in a shear field has been observed [11] and simulated [12, 13]. In a shear field, the initially spherical void would rotate and eventually close into a penny-shape crack [14, 15], unless localization in the ligament takes place before closure [6, 13, 16, 17]. This behavior is in contrast with that prevailing in a triaxial tensile field. In the latter case, Gurson's void growth model [18, 19] and its extensions by Needleman and Tvergaard, e.g., [20, 21] have set the standard for decades. A particularly important, generally neglected aspect of ductile fracture is failure with a limited amount of void growth, even in the absence of a shear component. The linkup of crack-like voids in aluminum alloys [22] and magnesium alloys [23], as recently revealed in tomography, provides such examples.

In general, whether the loading comprises a predominant tensile field or consists of combined tension and shear, fracture ultimately takes place because of plastic flow localization in the intervoid ligament, unless failure occurs by some mechanical instability of the specimen itself. This micro-scale localization is a precursor to void coalescence and must be modeled in order to predict quantitatively ductile fracture. It is generally reported that void coalescence occurs by internal necking [24] or by void-sheeting; see [25] for more details on micromechanisms. In the latter, a shear band typically forms between the voids, and secondary voids may nucleate therein due to intense strains. To date, the void coalescence mechanism that is best understood is by internal necking (see [26] and references therein) motivated by the pioneering computational work of Koplik and Needleman [27]. On the other hand, microscale localization by so-called internal shearing also begins to be understood on the basis of cell model calculations [6, 16, 17, 28]. In a weakly rate-sensitive material, void coalescence by internal necking or shearing manifests by the onset of elastic unloading in layers above and below the void [17, 27, 29, 30].

Interestingly, the micromechanics basis for understanding and analyzing low triaxiality fracture has been available since the early nineties [31–33] and has been used to model fracture in engineering materials, e.g. [24]. Over time, the models have gained in maturity and accuracy, e.g., [34–37]. Deformation-induced anisotropies constitute the essence of the damage mechanics of low triaxiality ductile fracture [38, 39]. This anisotropy is of two kinds: that related to the voids themselves (changes in void shape and orientation); and that related to their spatial arrangement. With this in mind, this paper is a step toward elucidating the effects of shear on ductile fracture. More specifically, the objective is to develop a mathematical model able to describe the yielding and subsequent flow of a material containing voids in configurations such that microscale localization of plastic flow is possible under combined shear and triaxial tension. Such a model would directly be relevant to modeling void coalescence by internal necking, internal shearing or both. The voids are not necessarily equiaxed thus allowing in principle to deal with void configurations that may be produced by evolution from an eventually isotropic initial state.

Mathematical modeling of void coalescence, as a microscale strain localization problem, goes back to the work of Thomason [40] who considered square-prismatic as well as cylindrical voids embedded in a finite cell and subjected to some remote triaxial tensile field. Thomason used *discontinuous* but kinematically admissible velocity fields to obtain upper-bound estimates of the limit load. He did not provide an analytical solution to the problem. Instead, he obtained numerical solutions and proposed a heuristic formula estimating the limit load at localization as a function of geometric parameters. Subsequent improvements of his model have focused on deriving evolution equations of the microstructural variables [30, 41] with heuristic modifications to Thomason's formula. None of the above models takes into account combined tension and shear loadings. Leblond and Mottet [42] tackled this problem by means of 3D finite-element calculations and developed an analytical model based on limit analysis in the spirit of earlier models by Gologanu and co-workers [43,44]. Instead of defining some localized velocity field in full 3D detail, it was assumed in [42] that the limit-load for such a field could be estimated by replacing the central void-rich region of the RVE by some "equivalent" homogeneous porous layer obeying Gurson's homogenized criterion or some variant. Tekoglu et al. [45] have improved upon this model through some suitable extension of Thomason's treatment of coalescence to non-axisymmetric loadings. In doing so, they accounted for both the extensional

and shear components of the microscopic velocity field. However, only that corresponding to shear was expressed in explicit, analytical form. No analytical solution was available then for void coalescence under axisymmetric loadings.

Quite recently, Benzerga and Leblond [26] developed a closed-form solution to the axisymmetric problem of void coalescence. Incidentally, their solution revealed some inaccuracy in the fitting procedure proposed by Thomason [40]. Even more recently, Morin et al. [46] developed improved models by considering either continuous velocity fields or generalized discontinuous fields. Their models provide, in general, tighter upper bounds, albeit for different ranges of structural paramaters. The models in [26, 46] are valid under axisymmetric loadings. The main objective of this paper is to extend the coalescence criterion of Benzerga and Leblond [26] to non-axisymmetric loadings. In a sense, the sought model is an elaboration of that previously developed by Tekoglu et al. [45]. Explicit consideration of the microscopic velocity field around the void in fully analytical form constitutes indeed a more coherent approach to the problem at hand. A secondary objective of this work is to develop a heuristic modification to the criterion of Benzerga and Leblond enabling its application to penny-shape cracks. The proposed modification is motivated by the prescription for the model to pick up the coalescence of flat voids, as would arise for example under shear dominated loadings or in materials failing after limited void growth [22, 23].

The paper is organized in three main sections and three appendices. In Section 2 we develop from first principles the mathematical model of void coalescence, including a graphical method for obtaining the effective yield surface in closed form. In Section 3 we motivate and introduce a heuristic model for flat voids or penny-shaped cracks. The results are presented in Section 4 and discussed in light of available micromechanical finite-element analyses. Details pertaining to the calculation of the effective dissipation and construction of the yield locus are provided in Appendices A and B, respectively. A variant of the homographic function used in the heuristic modification is presented in Appendix C.

2 Mathematical Model

2.1 Variational Principle

The effective yield criterion of a material containing microvoids can be determined using the following inequality of limit analysis [25]:

$$\forall\, \mathbf{D}, \quad \boldsymbol{\Sigma} : \mathbf{D} \leq \Pi(\mathbf{D}) \tag{1}$$

where $\boldsymbol{\Sigma}$ and $\mathbf{D}$ denote the macroscopic stress and rate of deformation tensors, defined as the volume averages of their microscopic counterparts $\boldsymbol{\sigma}$ and $\mathbf{d}$, and $\Pi(\mathbf{D})$ is the effective plastic dissipation given by

$$\Pi(\mathbf{D}) = \inf_{\mathbf{v}\in\mathcal{K}(\mathbf{D})} \langle \sup_{\boldsymbol{\sigma}^*\in\mathcal{C}} \sigma^*_{ij}\, d_{ij} \rangle_\Omega \tag{2}$$

Here, Ω refers to the spatial domain over which macroscopic quantities are defined, $\langle\cdot\rangle_\Omega$ stands for averaging over Ω, $\inf$ and $\sup$ respectively stand for the infimum (greatest lower bound) and supremum (least upper bound) of a set, and $\mathcal{C}$ is the microscopic reversibility domain (the boundary of which is the yield surface). Also, the set of kinematically admissible velocity fields, $\mathcal{K}(\mathbf{D})$, is made of incompressible fields ($v_{k,k} = 0$) that are compatible with the overall deformation imposed through $\mathbf{D}$. If the velocity field is discontinuous across an interface S then a surface term must be added which writes

$$\frac{1}{\Omega}\int_S \sup_{\boldsymbol{\sigma}^*\in\mathcal{C}} t^*_i\, [\![v_i]\!]\, \mathrm{d}S \tag{3}$$

where $[\![\mathbf{v}]\!]$ is the velocity jump across the interface and $\mathbf{t}^*$ the traction acting on it. If the dissipation function is differentiable then the effective yield surface is smooth and (1) is equivalent to:

$$\Sigma_{ij} = \frac{\partial \Pi}{\partial D_{ij}}(\mathbf{D}) \tag{4}$$

where $\mathbf{D}$ is no longer arbitrary as in (1) but represents the rate of deformation corresponding to $\boldsymbol{\Sigma}$ through the macroscopic flow rule. To sum up, if the effective yield surface is smooth then (4) constitutes its parametric equation; if not inequalities (1) define the effective reversibility domain $\mathscr{C}$ (which is different from the microscopic one C). The reader is referred to [25] for further background on this variational definition of the effective yield locus.

2.2 Representative Volume Element

Here, the elementary volume Ω is a cylindrical cell embedding a coaxial cylindrical void ω, Fig. 1a. Although this RVE is not space filling, it stands as a reasonable approximation of more complex geometries, such as hexagonal-prismatic or square-prismatic cells, which may be considered as unit cells in periodic media. This geometry is determined by the following independent dimensionless parameters:

$$W = \frac{h}{R}, \quad \chi = \frac{R}{L}, \quad \lambda = \frac{H}{L} \tag{5}$$

i.e., the void aspect ratio, the ligament parameter, and the cell aspect ratio, respectively. When parameter λ is different from unity it represents the anisotropy in void spacing. The local orthonormal basis associated with cylindrical coordinates r, θ, z is denoted $(\mathbf{e}_r, \mathbf{e}_\theta, \mathbf{e}_z)$ and the global one associated with Cartesian coordinates x_1, x_2, x_3 is denoted $(\mathbf{e}_1, \mathbf{e}_2, \mathbf{e}_3)$, with $\mathbf{e}_3 = \mathbf{e}_z$.

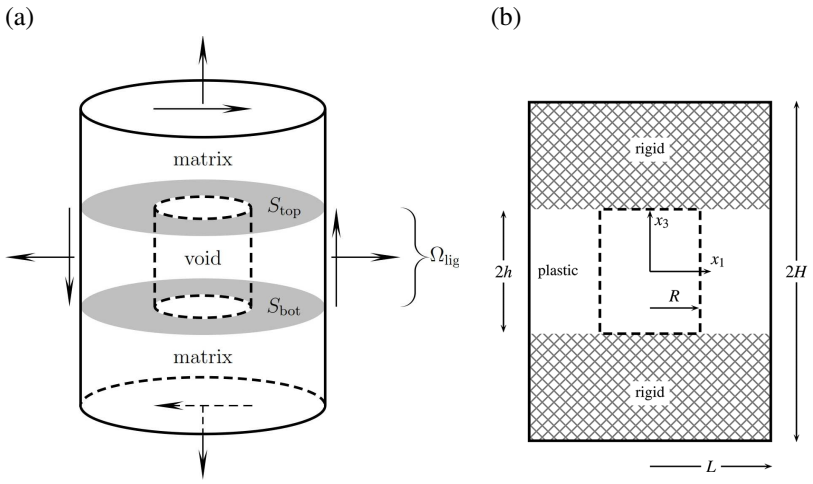

Figure 1: (a) Geometry of the cylindrical RVE under combined shear and tension; (b) Cell parameters.

The same geometry was considered by Benzerga and Leblond [26] and by Morin et al. [46]. The finite element calculations in [46] suggest that the limit analysis results are weakly sensitive to the exact shape of the void (cylindrical versus spheroidal) at fixed aspect ratio. On the other hand, comparison of their results with those of Tekoglu et al. [45] shows that the effect of the shape of the cell (cylindrical versus cubic) is small, but not negligible. This issue will be addressed in more detail when discussing the results. For Ω to be representative of a material in a coalescence state, plastic flow within it is assumed to be confined to the ligaments, Fig. 1b. Hence, the RVE consists of a central porous layer, Ω_{lig}, with plastically deforming ligaments, sandwiched between two rigid zones. The interfaces between these two zones and the central one are denoted S_{top} and S_{bot} (Fig. 2a) and their union S_{int}. The rigid zones represent regions where elastic unloading would take place after strain localization in the full evolution problem studied by cell model

analyses [6, 17, 27]. In what follows, it proves useful to introduce auxilliary geometric parameters:

$$\begin{aligned} f_{\rm b} &\equiv \frac{\omega}{\Omega_{\rm lig}} = \frac{R^2}{L^2} = \chi^2 \\ c &\equiv \frac{\Omega_{\rm lig}}{\Omega} = \frac{h}{H} = \frac{W\chi}{\lambda} \\ f &\equiv \frac{\omega}{\Omega} = c f_{\rm b} \end{aligned} \tag{6}$$

where the domain and its volume are identified for convenience. In (6), $f_{\rm b}$ is the porosity in the central porous band, c is the volume fraction of the band and f is the overall porosity, which does not play an essential role, unlike in void growth models.

2.3 Matrix Plasticity Model

Plastic flow in the matrix (in fact in $\Omega_{\rm lig} \setminus \omega$) is assumed to obey the von Mises yield criterion:

$$\begin{aligned} &\phi(\boldsymbol{\sigma}) = \sigma_{\rm eq}^2 - \bar{\sigma}^2 = 0 \\ &\sigma_{\rm eq} \equiv \sqrt{\frac{3}{2}\sigma'_{ij}\sigma'_{ij}}\,; \quad \sigma'_{ij} \equiv \sigma_{ij} - \frac{1}{3}\sigma_{kk}\delta_{ij} \end{aligned} \tag{7}$$

with the associated flow rule:

$$\begin{aligned} d_{ij} &= \frac{3}{2}\frac{d_{\rm eq}}{\bar{\sigma}}\,\sigma'_{ij} \\ d_{\rm eq} &\equiv \sqrt{\frac{2}{3}d_{ij}d_{ij}} \end{aligned} \tag{8}$$

where $\sigma_{\rm eq}$ and $d_{\rm eq}$ denote the von Mises equivalent stress and equivalent strain rate, respecively. Criterion (7) defines the boundary of the microscopic reversibility domain $\mathcal{C}$ involved in (2).

2.4 Boundary and Admissibility Conditions

Solving variational problem (1)–(2) for a given RVE and the J_2 matrix flow model would deliver the minimum involved in (2) as well as the velocity fields that realize the minimum. Focussing on symmetric solutions, the exact velocity fields can be of two types. One type is consistent with uniform strain-rate boundary conditions (of the Hill–Mandel kind), the other is consistent with nonuniform boundary conditions, such as those resulting from the presence of rigid zones in the RVE. These two types correspond to plasticity being diffuse in the matrix or localized in the ligaments, respectively. For the considered RVE, due to the presence of rigid zones above and below the central void, the cell cannot deform along the x_1 and x_2 directions nor can it shear in the x_1–x_2 plane, i.e., $D_{11} = D_{22} = D_{12} = 0$. Thus, the boundary velocity must be consistent with the following constraints:

$$\left\{ \begin{array}{lll} v_r(L,\theta,z)\mathbf{e}_r + v_\theta(L,\theta,z)\mathbf{e}_\theta & = \dfrac{2z}{c}\,(D_{31}\mathbf{e}_1 + D_{32}\mathbf{e}_2) & (-h \le z \le h; 0 \le \theta \le 2\pi) \\ v_z(r,\theta,\pm H) & = \pm D_{33} H & (0 \le r \le L; 0 \le \theta \le 2\pi). \end{array} \right. \tag{9}$$

where D_{31} and D_{32} are the imposed shearing rates and D_{33} is the imposed axial rate of deformation. Condition $(9)_1$ is completed by requiring that the tangential shear velocity be continuous across the rigid–plastic interfaces and obviously constant in the rigid zones ($h \le |z| \le H$). Boundary conditions (9) stand as an

appproximation of periodic boundary conditions and are consistent with the onset of a localization as in cell model studies [6, 17, 27].

In addition, at the interface between the plastic and rigid parts, the velocity jump, if any, must be purely tangential:

$$[\![\mathbf{v}]\!].\mathbf{n} = 0 \quad \forall \mathbf{x} \in S_{\text{int}} \tag{10}$$

where $\mathbf{n}$ is the interface normal. Also, matrix incompressibility in the intervoid ligament demands that

$$\text{tr}\,\mathbf{d} = \text{div}\,\mathbf{v} = 0 \quad \forall \mathbf{x} \in \Omega_{\text{lig}} \setminus \omega \tag{11}$$

The corresponding stress state is one in which $\Sigma_{11} = \Sigma_{22} < \Sigma_{33}$, $\Sigma_{31} \neq 0$ and $\Sigma_{32} \neq 0$. Note that Σ_{11}, Σ_{22} and Σ_{12} do not affect the yield condition since by the normality flow rule:

$$D_{11} = \frac{\partial \Phi}{\partial \Sigma_{11}} = 0 \quad D_{22} = \frac{\partial \Phi}{\partial \Sigma_{22}} = 0 \quad D_{12} = \frac{\partial \Phi}{\partial \Sigma_{12}} = 0 \tag{12}$$

where Φ is the sought macroscopic yield function. Having assumed normality at the microscopic scale, equation (8), macroscopic normality is a rigorous consequence of the combination of homogenization and limit-analysis [25].

2.5 Admissible Trial Velocity Fields

In general, the exact solution to problem (1)–(2) can only be obtained numerically, e.g., using the finite element method [45]. In analytical treatments, however, trial velocity fields are used in (2) so that upper-bound estimates of the yield locus are obtained from (1) or (4). Any two admissible velocity fields can be compared, the best being that which results in the lowest effective dissipation [25]. Here, we only consider velocity fields that are consistent with localized plasticity, i.e., obeying the boundary conditions expounded in Section 2.4 above. The trial velocity field in the central zone ($-h \leq z \leq h$) is decomposed in two parts

$$\mathbf{v} = \mathbf{v}^{\text{E}} + \mathbf{v}^{\text{S}} \tag{13}$$

with $\mathbf{v}^{\text{E}}$ induced by tension and $\mathbf{v}^{\text{S}}$ by shear:

$$\begin{aligned} \mathbf{v}^{\text{E}}(\mathbf{x}) &= \left(\frac{A}{r} - B\frac{r}{2}\right)\mathbf{e}_r + Bz\mathbf{e}_z \\ \mathbf{v}^{\text{S}}(\mathbf{x}) &= \boldsymbol{\beta}\mathbf{x} \end{aligned} \tag{14}$$

where all parameters (A, B and the constant traceless tensor $\boldsymbol{\beta}$) are set by the boundary conditions. The extensional field $\mathbf{v}^{\text{E}}$ is that used by Benzerga and Leblond [26]. Since it already includes a deviatoric component, the additional field need only be of the form:

$$\mathbf{v}^{\text{S}} = \frac{2z}{c}\left(D_{31}\mathbf{e}_1 + D_{32}\mathbf{e}_2\right) \tag{15}$$

where c is given by $(6)_2$ so that $\boldsymbol{\beta}$ reads in component form:

$$[\boldsymbol{\beta}] = \frac{2}{c}\begin{bmatrix} 0 & 0 & D_{31} \\ 0 & 0 & D_{32} \\ 0 & 0 & 0 \end{bmatrix} \tag{16}$$

In cylindrical coordinates, the components of the velocity of a material point in the ligament are:

$$\begin{aligned} v_r &= \frac{D_{33}}{2c}\left(\frac{L^2}{r} - r\right) + \frac{2z}{c}\left(D_{31}\cos\theta + D_{32}\sin\theta\right) \\ v_\theta &= \frac{2z}{c}\left(-D_{31}\sin\theta + D_{32}\cos\theta\right) \\ v_z &= \frac{D_{33}}{c}z \end{aligned} \tag{17}$$

The corresponding microscopic rate-of-deformation components are obtained as

$$\begin{aligned} d_{rr} &= \frac{\partial v_r}{\partial r} = -\frac{D_{33}}{2c}\left(\frac{L^2}{r^2} + 1\right) \\ d_{\theta\theta} &= \frac{1}{r}\left(v_r + \frac{\partial v_\theta}{\partial \theta}\right) = \frac{D_{33}}{2c}\left(\frac{L^2}{r^2} - 1\right) \\ d_{zz} &= \frac{\partial v_z}{\partial z} = \frac{D_{33}}{c} \\ d_{r\theta} &= d_{\theta r} = \frac{1}{2r}\left(\frac{\partial v_r}{\partial \theta} + \frac{\partial v_\theta}{\partial r} - v_\theta\right) = 0 \\ d_{rz} &= d_{zr} = \frac{1}{2}\left(\frac{\partial v_r}{\partial z} + \frac{\partial v_z}{\partial r}\right) = \frac{1}{c}\left(D_{31}\cos\theta + D_{32}\sin\theta\right) \\ d_{z\theta} &= d_{\theta z} = \frac{1}{2}\left(\frac{\partial v_\theta}{\partial z} + \frac{1}{r}\frac{\partial v_z}{\partial \theta}\right) = \frac{1}{c}\left(-D_{31}\sin\theta + D_{32}\cos\theta\right) \end{aligned} \tag{18}$$

2.6 Effective Dissipation

For convenience, the dissipation function associated with the above velocity field is denoted $\Pi(\mathbf{D})$ although one should bear in mind that it is in fact an upper bound estimate of the exact dissipation. Using (7) and (8) a classical calculation [25] leads to:

$$\Pi(\mathbf{D}) = \langle \bar{\sigma} d_{\mathrm{eq}} \rangle_\Omega \tag{19}$$

where it should be noted that, since the velocity field (17) is discontinuous across the rigid–plastic interfaces S_{int}, the above expression must be taken in the sense of distributions with a strain rate concentrated on a surface. This is equivalent to writing $\Pi(\mathbf{D})$ as the sum of volumetric and surface terms:

$$\Pi = \Pi^{\mathrm{vol}} + \Pi^{\mathrm{surf}} \tag{20}$$

where

$$\begin{cases} \Pi^{\mathrm{vol}} & = c\langle \bar{\sigma} d_{\mathrm{eq}} \rangle_{\Omega_{\mathrm{lig}}} = c(1 - f_{\mathrm{b}})\langle \bar{\sigma} d_{\mathrm{eq}} \rangle_{\Omega_{\mathrm{lig}} \setminus \omega} \\ \Pi^{\mathrm{surf}} & = \dfrac{1}{\Omega}\displaystyle\int_{S_{\mathrm{int}}} \frac{\bar{\sigma}}{\sqrt{3}} \left| [\![v_{\mathrm{t}}]\!] \right| \mathrm{d}S \end{cases} \tag{21}$$

$[\![v_{\mathrm{t}}]\!]$ denoting the discontinuity of tangential velocity. Because the latter only arises from the extensional field $\mathbf{v}^{\mathrm{E}}$, the calculation of the surface term leads to [26]

$$\Pi^{\mathrm{surf}} = |D_{33}| \Sigma^{\mathrm{surf}}(\chi, W), \tag{22}$$

with

$$\frac{\Sigma^{\mathrm{surf}}}{\bar{\sigma}} = \frac{1}{3\sqrt{3}} \frac{\chi^3 - 3\chi + 2}{\chi W} \tag{23}$$

The volumetric term requires careful treatment. Instead of calculating d_{eq} directly based on (18) we first begin by decomposing the total rate of deformation $\mathbf{d} = \mathbf{d}^{\mathrm{E}} + \mathbf{d}^{\mathrm{S}}$ based on (13) to make use of the orthogonality condition $\mathbf{d}^{\mathrm{E}} : \mathbf{d}^{\mathrm{S}} = 0$ so that

$$d_{\mathrm{eq}}^2 = \frac{2}{3}\left(\mathbf{d}^{\mathrm{E}} : \mathbf{d}^{\mathrm{E}} + \mathbf{d}^{\mathrm{S}} : \mathbf{d}^{\mathrm{S}}\right) = \frac{2}{3}\mathbf{d}^{\mathrm{E}} : \mathbf{d}^{\mathrm{E}} + \frac{1}{3}\boldsymbol{\beta} : \boldsymbol{\beta} \tag{24}$$

where use has been made of the relation $\mathbf{d}^{\mathrm{S}} = (\boldsymbol{\beta} + \boldsymbol{\beta}^{\mathrm{T}})/2$ and the components of $\mathbf{d}^{\mathrm{E}}$ are given by:

$$[\mathbf{d}^{\mathrm{E}}] = \frac{D_{33}}{2c} \begin{bmatrix} -\left(\dfrac{L^2}{r^2} + 1\right) & 0 & 0 \\ 0 & \left(\dfrac{L^2}{r^2} - 1\right) & 0 \\ 0 & 0 & 2 \end{bmatrix}. \tag{25}$$

Using (25) and (16) we thus obtain the expression of d_{eq}:

$$d_{\mathrm{eq}}^2 = \frac{D_{33}^2}{3c^2}\left[3 + \frac{L^4}{r^4}\right] + \frac{4}{3c^2}\left(D_{31}^2 + D_{32}^2\right), \tag{26}$$

then that of Π^{vol} from (21) as:

$$\Pi^{\mathrm{vol}} = (1 - \chi^2)\frac{\bar{\sigma}}{\sqrt{3}}\left\langle \sqrt{\delta_{\mathrm{E}}^2 + \delta_{\mathrm{S}}^2} \right\rangle_{\Omega_{\mathrm{lig}} \setminus \omega} \tag{27}$$

where c cancels out; also δ_{E} and δ_{S} are shorthand notations for:

$$\begin{aligned} \delta_{\mathrm{E}}(r) &= |D_{33}|\sqrt{3 + \frac{L^4}{r^4}} \\ \delta_{\mathrm{S}} &= 2\sqrt{D_{31}^2 + D_{32}^2} \end{aligned} \tag{28}$$

Next, the integral in (27) is evaluated approximately as

$$\Pi^{\mathrm{vol}} \approx (1 - \chi^2)\frac{\bar{\sigma}}{\sqrt{3}}\sqrt{\langle \delta_{\mathrm{E}} \rangle_{\Omega_{\mathrm{lig}} \setminus \omega}^2 + \delta_{\mathrm{S}}^2} \tag{29}$$

This approximation, which was initially introduced in [45], is not upper-bound preserving and therefore warrants some assessment against numerical estimates. The calculation is given in Appendix A and yields

$$\Pi^{\mathrm{vol}} = \sqrt{{\Sigma^{\mathrm{vol}}}^2 D_{33}^2 + \mathcal{T}^2\left(D_{31}^2 + D_{32}^2\right)} \tag{30}$$

where Σ^{vol} and $\mathcal{T}$ are functions of the ligament parameter given by:

$$\begin{aligned} \Sigma^{\mathrm{vol}}(\chi) &= \frac{\bar{\sigma}}{\sqrt{3}}\left[2 - \sqrt{1 + 3\chi^4} + \ln\frac{1 + \sqrt{1 + 3\chi^4}}{3\chi^2}\right] \\ \mathcal{T}(\chi) &= \frac{2\bar{\sigma}}{\sqrt{3}}(1 - \chi^2) \end{aligned} \tag{31}$$

Finally, the total dissipation is given by

$$\Pi(\mathbf{D}) = \sqrt{{\Sigma^{\mathrm{vol}}}^2 D_{33}^2 + \mathcal{T}^2\left(D_{31}^2 + D_{32}^2\right)} + \Sigma^{\mathrm{surf}}|D_{33}| \tag{32}$$

where the function $\Sigma^{\mathrm{surf}}(\chi, W)$ is given by (23).

2.7 Void Coalescence Criterion

The effective yield criterion $\Phi(\boldsymbol{\Sigma}) = 0$ corresponding to the effective dissipation (32) is the criterion for void coalescence under combined tension and shear. As it turns out, the dissipation function calculated in (32) is not differentiable because of the term involving $|D_{33}|$. For this reason, one cannot directly obtain the expression of Φ from Eq. (4). Instead, one must resort to the primitive definition of the reversibility domain $\mathscr{C}$ in (1), which writes:

$$\boldsymbol{\Sigma} \in \mathscr{C} \Leftrightarrow \forall\, \mathbf{D}, \quad \boldsymbol{\Sigma} : \mathbf{D} = \Sigma_{33} D_{33} + 2(\Sigma_{31} D_{31} + \Sigma_{32} D_{32}) \leq \Pi \tag{33}$$

With this definition, the yield criterion $\Phi(\boldsymbol{\Sigma}) = 0$ is the equation of $\partial\mathscr{C}$ (boundary of $\mathscr{C}$) which is the yield surface. Note that the transverse stresses Σ_{11}, Σ_{22}, and Σ_{12} do not appear here, in agreement with Eq. (12).

2.7.1 General Solution to Inequality (33)

With no loss of generality, assume $D_{32} = 0$. This amounts to defining the transverse axes x_1 and x_2 in a judicious manner. Let $\Pi^*(D_{33}, D_{31})$ stand for the corresponding dissipation function. Then inequality (33) may be written considering (32):

$$\forall D_{33}, D_{31}, \quad \Sigma_{33} D_{33} + 2\Sigma_{31} D_{31} \leq \sqrt{{\Sigma^{\mathrm{vol}}}^2 D_{33}^2 + \mathcal{T}^2 D_{31}^2} + \Sigma^{\mathrm{surf}} |D_{33}| \equiv \Pi^*(D_{33}, D_{31}) \tag{34}$$

The right-hand side of (34) is fully determined since Σ^{surf}, Σ^{vol} and $\mathcal{T}$ are given by (23) and (31). In order to focus on non-negative values of D_{31} only, we re-write (34) as:

$$\forall D_{33}, \forall D_{31} \geq 0, \quad -\Pi^*(D_{33}, D_{31}) \leq \Sigma_{33} D_{33} + 2\Sigma_{31} D_{31} \leq \Pi^*(D_{33}, D_{31}) \tag{35}$$

where use has been made of (34) for the pair $(-D_{33}, -D_{31})$ considering that Π^* is an even function. The set of inequalities (35) is equivalent to some condition $\Phi(\Sigma_{33}, \Sigma_{31}) \leq 0$ where Φ is the sought yield function. Since Π^* is homogeneous of degree 1 in its arguments, (35) may be recast in the form:

$$\forall p \in \mathbb{R}, \quad -g(p) \leq f(p) \leq g(p) \tag{36}$$

where the ratio

$$p = D_{33}/D_{31} \tag{37}$$

plays the role of a parameter, and functions f and g are defined on $\mathbb{R}$ by:

$$\begin{aligned} f(p) &= \Sigma_{33} p + 2\Sigma_{31} \\ g(p) &= \sqrt{{\Sigma^{\mathrm{vol}}}^2 p^2 + \mathcal{T}^2} + \Sigma^{\mathrm{surf}} |p| \equiv \Pi^*(p, 1) \end{aligned} \tag{38}$$

Next, we implement a graphical solution to constructing the yield surface. The reversibility domain corresponds to straight lines $q = f(p)$ lying between the graphs of the functions $q = -g(p)$ and $q = g(p)$. The yield locus, on the other hand, corresponds to straight lines lying between these graphs but meeting one of them at some point. We study in Appendix B some basic properties of function g to show that (i) g is convex; (ii) it admits a minimum $g(0) = \mathcal{T}$; (iii) it has an angular point at its minimum, i.e., at $p = 0$; and (iv) g admits straight asymptotes of slope $\pm(\Sigma^{\mathrm{vol}} + \Sigma^{\mathrm{surf}})$ for $p \to \pm\infty$. We then proceed as follows to construct the yield locus in three essential steps:

1. Consider the case of shear loading only ($\Sigma_{33} = 0$, $\Sigma_{31} \neq 0$). The yield condition (36) becomes

$$\{\forall p \in \mathbb{R}, \quad -g(p) \leq 2\Sigma_{31} \leq g(p)\} \Leftrightarrow |2\Sigma_{31}| \leq \min_p g(p) = \mathcal{T} \tag{39}$$

   Thus, the points ($\Sigma_{33} = 0$, $\Sigma_{31} = \pm\mathcal{T}/2$) lie on the yield surface, as illustrated in Fig. 2. In the following, we focus on loadings with $\Sigma_{31} \geq 0$ taking advantage of the point symmetry of the yield locus, i.e., $\Phi(-\boldsymbol{\Sigma}) = \Phi(\boldsymbol{\Sigma})$.

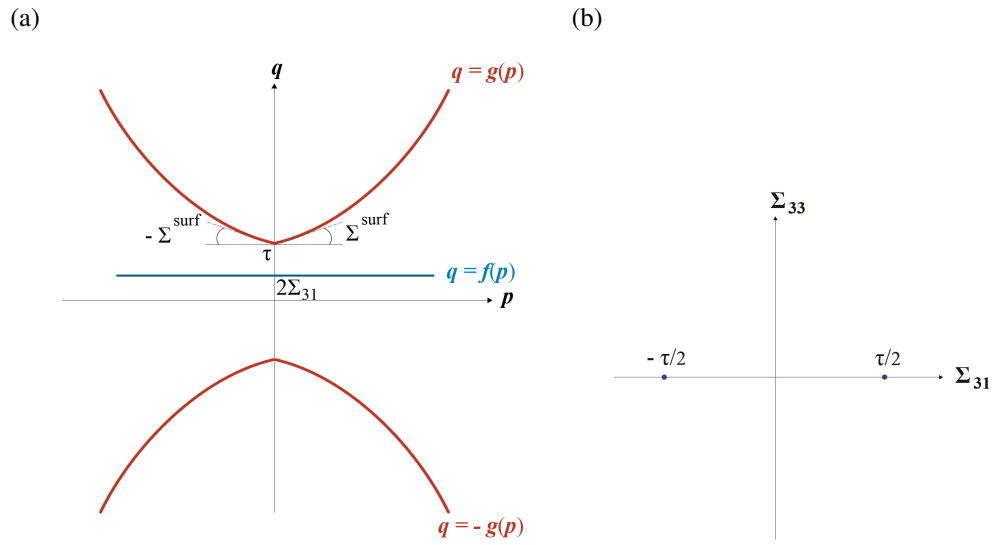

Figure 2: Step 1 of graphical solution to (36): case of shear loading only. (a) The curve $q = f(p) = 2\Sigma_{31}$ is a horizontal line that lies between the curves $q = g(p)$ and $q = -g(p)$ for all values of p provided that $2\Sigma_{31}$ is greater than $-\mathcal{T}$ without exceeding $\mathcal{T}$. (b) Corresponding yield points in the Σ_{33}–Σ_{31} plane.

2. Next, in addition to the shear stress, consider increasing the magnitude of the normal stress subjected to $|\Sigma_{33}| \leq g'(0^+) = \Sigma^{\text{surf}}$. Fig. 3a illustrates the case $\Sigma_{33} > 0$. Since $q = f(p)$ is the equation of a line whose slope is precisely Σ_{33}, it is clear that the condition $|\Sigma_{33}| \leq g'(0^+)$ entails that $f(p) \leq g(p), \forall p$, provided that $f(0) \leq g(0)$. The converse is true. In other terms, the yield condition when $\Sigma_{33} \leq \Sigma^{\text{surf}}$ is that $\Sigma_{31} = \mathcal{T}/2$. The same condition holds for $g'(0^-) < \Sigma_{33} < 0$ by considering the intersections of lines $q = f(p)$ having negative slopes with the appropriate branches of $g(p)$ and $-g(p)$. This step establishes the existence of straight parts in the yield locus, as illustrated in Fig. 3b.

3. Upon increasing further the magnitude of the normal stress, that is beyond Σ^{surf}, the fact that f lies below g and above $-g$ at the origin no longer guarantees the same for all values of p (Fig. 4a). There must me a condition on the shear stress in terms of Σ_{33} for the stress state $(\Sigma_{33}, \Sigma_{31})$ to lie on $\partial\mathscr{C}$. Given Σ_{33}, the value of Σ_{31} must be smaller than that which would make the line $q = f(p)$ tangent to the curve $q = g(p)$ (Fig. 4b). Only when this tangency holds or the line $q = f(p)$ falls below the tangent would the reversibility condition $f(p) \leq g(p), \forall p$ be ensured (recall that we have focused on $\Sigma_{31} > 0$ so that tangency with $q = -g(p)$ is not an issue). Finding the yield point $(\Sigma_{33}, \Sigma_{31})$ amounts then to determining the value of p, say p_0, for which there is tangency. The derivation of p_0 is straightforward (see Appendix B). Upon elimination of p_0 from the tangency condition (also shown in Appendix B) the following relationship is obtained between the shear and normal stresses:

$$\frac{\left(\Sigma_{33} - \text{sgn}(\Sigma_{33})\Sigma^{\text{surf}}\right)^2}{\Sigma^{\text{vol}2}} + 4\frac{\Sigma_{31}^2}{\mathcal{T}^2} = 1 \tag{40}$$

which is the yield condition for $|\Sigma_{33}| > \Sigma^{\text{surf}}$. The corresponding part on the yield locus is illustrated in Fig. 4c. It is shown in Appendix B that (40) represents the regular part of the yield surface, i.e., that which could be obtained by mere differentiation of the dissipation function.

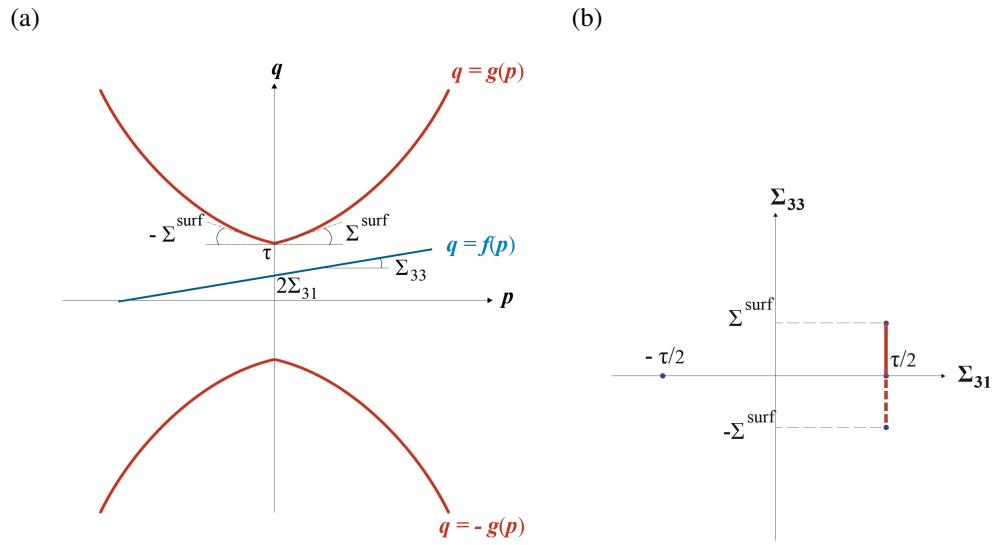

Figure 3: Step 2 of graphical solution to (36): case of combined shear and tension subject to $|\Sigma_{33}| \leq \Sigma^{\text{surf}}$. (a) Illustration for $\Sigma_{33} > 0$ and $\Sigma_{31} > 0$. The slope of the line $q = f(p)$ is smaller than that of $q = g(p)$ at the origin so that the two curves do not cross each other provided that $f(0) \leq g(0)$, i.e. that $\Sigma_{31} \leq \mathcal{T}/2$. (b) Corresponding straight portion of the yield locus appears as solid line. For completeness, the portion corresponding to negative slopes of $q = f(p)$ is shown dashed. As depicted, the asymptotic behavior of function g is exaggerated for clarity purposes.

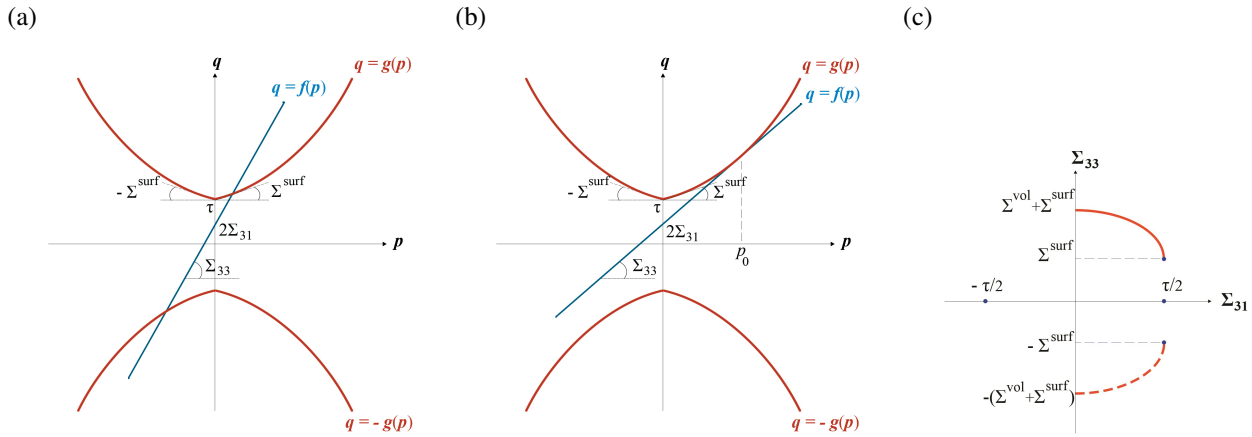

Figure 4: Step 3 of graphical solution to (36): case of combined shear and tension subject to $|\Sigma_{33}| \geq \Sigma^{\text{surf}}$. (a) For an arbitrarily large value of the slope of $q = f(p)$ the inequality cannot be guaranteed for all values of p. (b) Limit case when the slope of $q = f(p)$ is greater than that of $q = g(p)$ at the origin but small enough so as to be tangent to the curve $q = g(p)$ at some point p_0. This point defines the sought yield condition. (c) Corresponding curved portion of the yield locus appears as solid line. For completeness, the portion corresponding to negative slopes of $q = f(p)$ is shown dashed.

2.7.2 Absence of corners in the yield locus

The existence of straight (singular) parts and curved (regular) parts on the yield locus raises the issue of whether there are corners on the yield surface. It is apparent from the above derivation that there are none.

Indeed, the curved parts defined by (40) are semi-ellipses which meet the points $(\Sigma_{33} = \pm\Sigma^{\mathrm{surf}}, \Sigma_{31} = \pm\mathcal{T}/2)$ with vertical tangents. The complete yield surface is shown schematically in Fig. 5 where Σ_{sh} is the signed length of the shear traction, i.e, $\Sigma_{\mathrm{sh}}\mathbf{s} = \Sigma_{31}\mathbf{e}_1 + \Sigma_{32}\mathbf{e}_2$ with $\mathbf{s}$ a unit vector in the direction of shear.

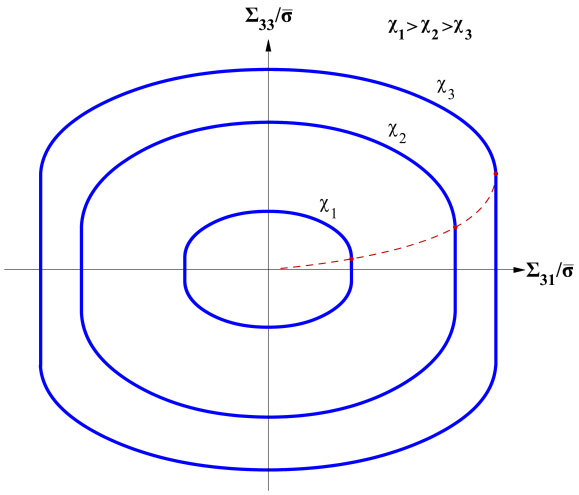

Figure 5: Schematic outline of the complete yield surface.

It is worth noting that in their development of a model unifying void growth and void coalescence, Morin et al. [47] have also obtained a smooth effective yield surface with curved and straight parts. This is traceable to the nondifferentiability of the plastic dissipation function in their model as well. They also offered a graphical construction of the reversibility domain, which is qualitatively similar to that of Section 2.7.1.

In crystal plasticity, as well as some hybrid theories of ductile fracture [39, 48], the presence of corners on the effective yield surface follows from the *ad hoc* assumption of independent activation criteria for slip, or deformation mode for the porous material, respectively. The absence of corners in the present theory is, however, not so intuitive. Inspecting the geometrical arguments, one concludes that the origin of the absence of corners is found in the *nonlinear* expression of the effective plastic dissipation over the intervals where it is differentiable.

2.7.3 Synopsis of Model

The void coalescence criterion, viewed as the effective yield criterion of the porous solid with localized plastic flow within the RVE, is defined as follows:

$$\Phi(\boldsymbol{\Sigma};\chi,W) = \begin{cases} \dfrac{(|\Sigma_{33}| - \Sigma^{\mathrm{surf}})^2}{\Sigma^{\mathrm{vol}\,2}} + 4\dfrac{\Sigma_{31}^2 + \Sigma_{32}^2}{\mathcal{T}^2} - 1 & \text{for } |\Sigma_{33}| \geq \Sigma^{\mathrm{surf}} \\ \\ 4\dfrac{\Sigma_{31}^2 + \Sigma_{32}^2}{\mathcal{T}^2} - 1 & \text{for } |\Sigma_{33}| \leq \Sigma^{\mathrm{surf}} \end{cases} \tag{41}$$

where $\Sigma^{\rm vol}(\chi)$, $\Sigma^{\rm surf}(\chi, W)$ and $\mathcal{T}(\chi)$ are functions of the microstructural parameters χ and W given by (23) and (31) and repeated here for ease of reference:

$$\begin{aligned}
\Sigma^{\rm vol}(\chi) &= \frac{\bar{\sigma}}{\sqrt{3}}\left[2 - \sqrt{1+3\chi^4} + \ln\frac{1+\sqrt{1+3\chi^4}}{3\chi^2}\right] \\
\Sigma^{\rm surf}(\chi, W) &= \frac{\bar{\sigma}}{3\sqrt{3}}\frac{\chi^3 - 3\chi + 2}{\chi W} \\
\mathcal{T}(\chi) &= \frac{2\bar{\sigma}}{\sqrt{3}}(1-\chi^2)
\end{aligned} \tag{42}$$

3 Heuristic Model for Penny-Shaped Cracks

At the material point level, failure may occur by the coalescence of blunted micro-cracks. This phenomenon is common in steels containing elongated inclusions and loaded transverse to the latter [38]. It begins to be documented in various other metallic alloys of technological significance [22, 49]. The above works were mainly concerned with predominately tensile loadings. In presence of shear, even initially equiaxed voids would rotate while closing into micro-cracks and when linkage eventually occurs the voids are quite flat. Furthermore, under compressive loading, microvoids would tend to close by evolving toward microcracks for which the propensity for intervoid ligament localization may increase due to the increase in the ligament parameter χ. Thus, it appears that the phenomenon of microcrack coalescence is of immense practical importance; yet it eludes currently available models of ductile fracture. The objective of this section is to motivate a heuristic modification of the above coalescence criterion to address the limit case of penny-shape cracks.

By examination of the limit $W \to 0$ it is evident that criterion (41) can never be met because of the $1/W$ singularity of the $\Sigma^{\rm surf}$ function. Clearly, this singular behavior is inherited from the model in the absence of shear. In this case, (41) reduces to

$$|\Sigma_{33}| = \Sigma^{\rm vol} + \Sigma^{\rm surf} = \frac{\bar{\sigma}}{\sqrt{3}}\left[2 - \sqrt{1+3\chi^4} + \ln\frac{1+\sqrt{1+3\chi^4}}{3\chi^2}\right] + \frac{\bar{\sigma}}{3\sqrt{3}}\frac{\chi^3 - 3\chi + 2}{\chi W} \tag{43}$$

which is the criterion of Benzerga and Leblond [26]. The reason for this singular behavior is illustrated in the sketch of Fig. 6.

In the currently available models, the height of the localization zone scales with the void height h. This is shown schematically in Fig. 6a (also see Fig. 1a). Therefore, when $W \to 0$ the localization zone vanishes and the purely extensional deformation mode cannot be accommodated. Recently, Morin et al. [46] have assessed criterion (43) against finite-element based limit analysis calculations for the exact same cylindrical geometry. The lowest value of W they considered was 0.2. Their results showed that the model in [26] was quite accurate for a range of microstructural parameters but revealed significant deviations from the finite-element predictions for $W < 0.5$. To remedy this aspect of the model among other potential improvements, Morin et al. [46] developed two new analytical models: one in which the extensional velocity field was continuous across the rigid–plastic interface and one in which this interface was no longer planar but with a discontinuity of the tangential velocity across it. Details aside, the model with the nonplanar interface provided the best improvement to criterion (43) for $W < 0.5$. However, their model has two shortcomings: (i) the coalescence criterion could not be obtained in closed form; and (ii) it still suffers from the $1/W$ singularity. The reason for this is that the nonplanar interface degenerates into a planar one in the limit $W \to 0$. As discussed by Morin et al. [46], the height of the plastic localization zone in the finite-element

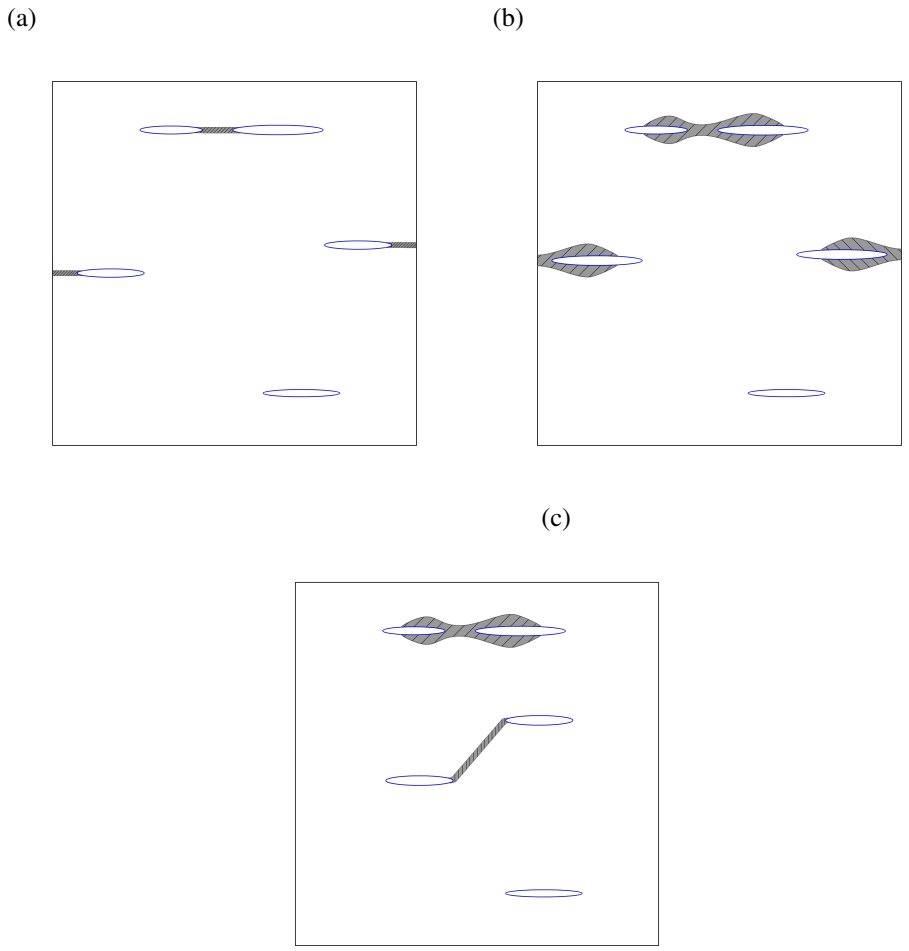

Figure 6: Sketch motivating the need for model calibration in the case of penny-shaped cracks. (a) Localization zone height limited by microcrack height (situation considered in analytical model). (b) More realistic localization zones based on finite-element simulations [46] (situation picked up by heuristic model). (c) Alternative possible localization for random arrangement of voids.

calculations extends above and below the void when this one is very flat (see their Fig. 13b)[1]. In actuality, the interaction plastic zones between neighboring microcracks are closer to the sketch of Fig. 6b. At present, a model based on such RVE is not available and even if it were, the criterion would not be simple, let alone in closed form.

With the above motivation in mind, criterion (41) is modified as follows:

$$\Phi(\boldsymbol{\Sigma};\chi,W)=\begin{cases}\dfrac{(|\Sigma_{33}|-t\Sigma^{\mathrm{surf}})^2}{b^2{\Sigma^{\mathrm{vol}}}^2}+4\dfrac{\Sigma_{31}^2+\Sigma_{32}^2}{l^2\mathcal{T}^2}-1 & \text{for } |\Sigma_{33}|\geq\Sigma^{\mathrm{surf}}\\[2ex] 4\dfrac{\Sigma_{31}^2+\Sigma_{32}^2}{l^2\mathcal{T}^2}-1 & \text{for } |\Sigma_{33}|\leq\Sigma^{\mathrm{surf}}\end{cases} \tag{44}$$

[1]Benzerga's [41] conjecture stating that the rigid zones intercept the void at the poles seems to be falsified for extremely flat voids.

where t, b and l are to be adjusted on the basis of available numerical solutions or experiments. In fact, b and l are constants close to unity whereas $t(W,\chi)$ must be taken as a function of geometric parameters to remedy the $1/W$ singular behavior, which manifests only through the Σ^{surf} term. In the absence of shear, criterion (44) reads:

$$|\Sigma_{33}| = t(\chi,W)\Sigma^{\text{surf}} + b\Sigma^{\text{vol}} \tag{45}$$

Since the original criterion (43) performs very well for $W > 1$ [46] we only require that function t be endowed with the following asymptotic behavior:

$$\begin{aligned} t &\underset{W\to 0}{\sim} a\,W \\ t &\underset{W\to\infty}{\sim} 1 \end{aligned} \tag{46}$$

with a some constant, hence the choice of the homographic function:

$$t(\chi,W) = \frac{(t_0 + t_1\chi)W}{1 + (t_0 + t_1\chi)W} \tag{47}$$

where t_0 and t_1 are parameters to be determined.

4 Results and Discussion

4.1 Model calibrated for penny-shaped cracks

The calibration of the modified model (44) is based on available limit analysis calculations using the finite element method [45,46]. Tekoglu et al. [45] obtained such solutions for spheroidal voids in an orthorombic cell whereas Morin et al. [46] mainly considered cylindrical voids in a cylindrical cell. Detailed comparison between the two sets of FE results at fixed pair (χ, W) and in absence of shear loads shows small, but not negligible differences.

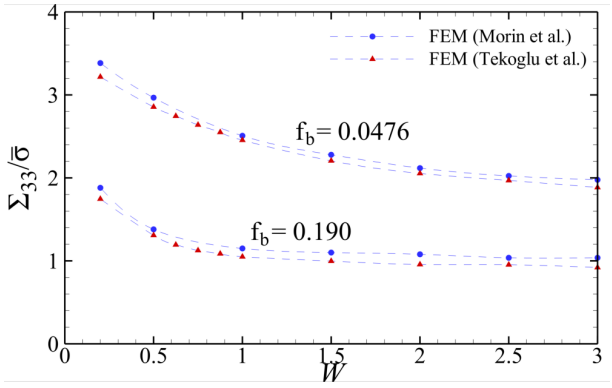

Figure 7: Coalescence stress in absence of shear, Σ_{33}, normalized by the matrix yield stress, $\bar{\sigma}$, versus the void aspect ratio, W, according to the FEM results for a cylindrical cell [46] and a cubic cell [45] for two values of the porosity in the band f_{b}.

Part of the difference is rationalized by invoking the porosity in the band (f_{b} in equation (6)), which takes on different values at fixed χ depending on the assumed shapes of the void and the cell. When the computed limit loads are plotted as a function of f_{b} instead of χ (W being fixed) the difference between the values calculated in Refs. [45] and [46] significantly decreases, as shown in Fig. 7. For reference, the

porosity in the band f_b corresponding to the cell geometry used in [45] is given by $f_b = \frac{\pi}{6}\chi^2$ whereas $f_b = \chi^2$ for the cell used in [46]. Even with this normalization, some differences remain between the two data sets, as depicted in Fig. 7. These differences must therefore be related to the effect of cell shape itself.

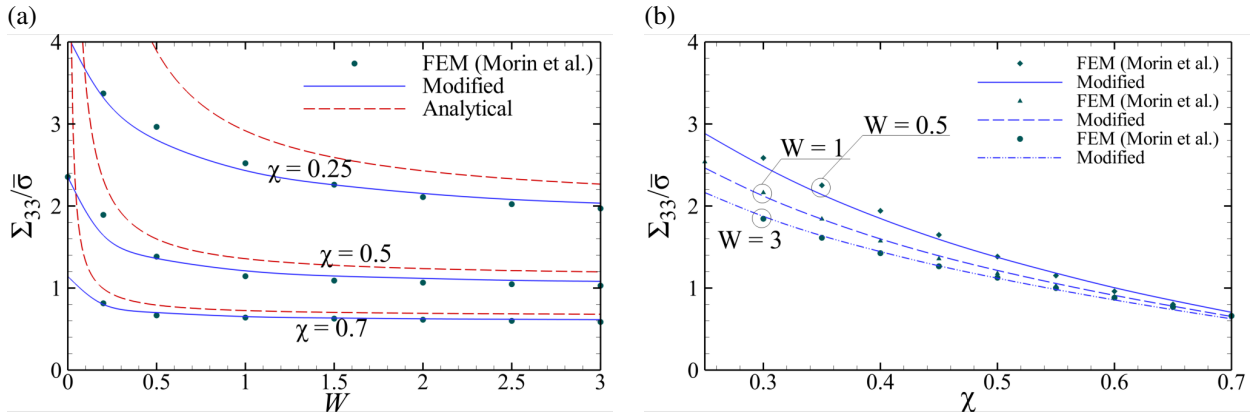

Figure 8: (a) Coalescence stress in absence of shear, Σ_{33}, normalized by the matrix yield stress, $\bar{\sigma}$, versus the void aspect ratio, W, according to the FEM results (points from [46]), the analytical model (dashed lines) and the modified model (solid lines) using $t_0 = -0.84$, $t_1 = 12.9$ and $b = 0.9$ for three values of the ligament parameter χ. (b) $\Sigma_{33}/\bar{\sigma}$ versus χ according to the FEM results and modified model for three values of W.

For the reasons above, the calculations of Morin et al. [46] are used here as a basis for calibrating criterion (44) given that these authors considered the exact same geometry we have used to derive the analytical model. In fact, parameters t_0 and t_1 can be found by confining attention to the value of the limit load corresponding to the limit $W \to 0$, which can be extracted from the estimates made by [50] and used in [41]. Then parameter b is obtained using the numerical results in [46]. It is worth noting that the values of t_0 and t_1 are affected by the choice of b. Using Gologanu's estimates in the limit $W \to 0$: $\Sigma_{33}^{\text{coal}}/\bar{\sigma} = 4.336$ for $\chi = 0.2$ and $\Sigma_{33}^{\text{coal}}/\bar{\sigma} = 2.355$ for $\chi = 0.5$, the values of t_0 and t_1 follow a linear relation with b as $t_0 = 0.4b - 1.2$, $t_1 = -10b + 21.9$. The best fit is thus obtained using $t_0 = -0.84$, $t_1 = 12.9$ and $b = 0.9$. Fig. 8 illustrates the outcome of this calibration procedure. The solid lines correspond to the modified criterion using the above parameters whereas the dashed lines correspond to the criterion, as derived by Benzerga and Leblond [26]. The main correction is introduced for very flat voids. One may notice that the rigorous upper-bound character of the model is lost with the heuristic correction. It is possible to remedy this to some extent by using an alternative form for the $t(\chi, W)$ function (see Appendix C). Finally, parameter l, which does not affect the results in the absence of shear as in Fig. 8, is taken to be unity in the following.

4.2 Coalescence Surfaces

Some example yield surfaces corresponding to the original criterion (41) as well as the modified one (44) are depicted in Fig. 9 for selected values of the microstructural parameters W and χ. The surfaces are shown in a Σ_{33}–Σ_{sh} plane as they are insensitive to normal stresses Σ_{11} and Σ_{22} and to shear stress Σ_{12}. As above, $\Sigma_{\text{sh}}^2 = \Sigma_{31}^2 + \Sigma_{32}^2$ represents the shear stress magnitude.

The length of the straight parts is set by Σ^{surf}. As expected, the effect of the modification manifests mainly for flat cavities. Also, observe that the axial stress required for coalescence decreases with a superposed shear stress. This may have important implications under combined loadings. In all cases, the

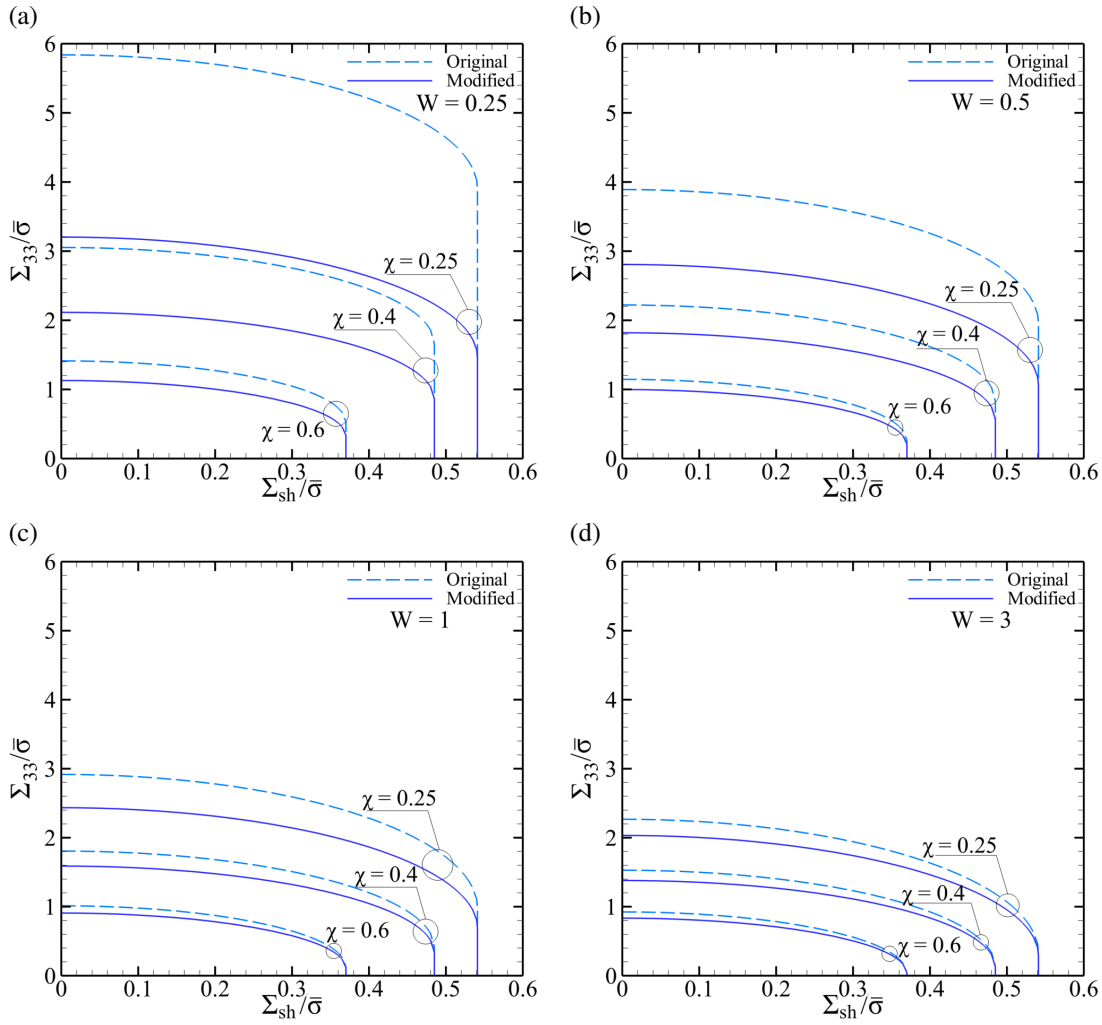

Figure 9: Effective yield loci in the Σ_{33}–$\Sigma_{\rm sh}$ plane (one quadrant shown) using the original analytical criterion (41) (dashed) and the modified criterion (44) (solid) for various values of the ligament parameter χ and four values of the void aspect ratio: (a) $W = 0.25$; (b) $W = 0.5$; (c) $W = 1.0$; (d) $W = 3.0$.

effective yield stress in shear is given by:

$$\Sigma_{\rm sh} = \frac{\bar{\sigma}}{\sqrt{3}}(1 - \chi^2) \tag{48}$$

i.e., a factor of $1-\chi^2$ smaller than without the void, compare with a factor of $1-\chi^3$ predicted by the Gurson model. This type of reduction is consistent with the values obtained in cell model calculations [6, 17].

The yield surfaces in Fig. 9 may be thought of as coalescence surfaces since the rate of change of the ligament size χ is directly related to the normal to these surfaces. Incidentally, the rate of χ is predicted to be nil under pure shear.

4.3 Comparison with finite-element calculations

The only comparison that is presently possible in the case of combined loading is with the analyses carried out by Tekoglu et al. [45]. Figure 10 portrays a comparison of yield surfaces, as predicted using the modified

criterion, with the finite element results of Ref. [45]. In doing so, it is worth emphasizing that the two sets of results correspond to different geometries. To minimize geometry effects, we compare again at fixed doublet $(W, f_{\rm b})$. As discussed above in the context of Fig. 7, there are some expected differences in the absence of shear.

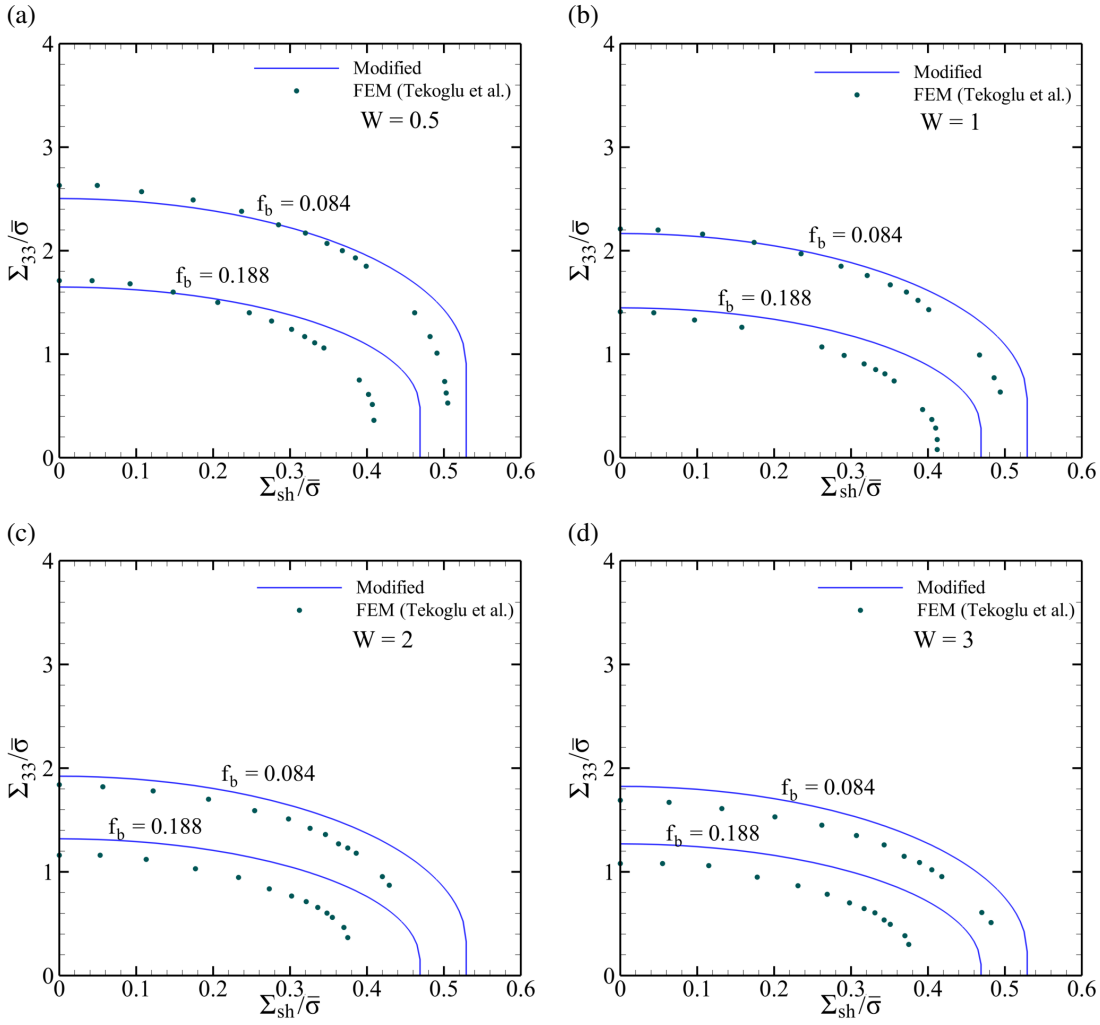

Figure 10: Effective yield loci in the Σ_{33}–$\Sigma_{\rm sh}$ plane using the modified criterion (44) (solid lines) and available FE results [45] (points) for two values of the porosity in the band $f_{\rm b}$ and four values of the void aspect ratio: (a) $W = 0.5$; (b) $W = 1.0$; (c) $W = 2.0$; (d) $W = 3.0$.

Figure 10 reveals several points:

1. There is good qualitative and, in most cases, quantitative correspondence between model and FE results.

2. In some cases with predominant tension, the model predictions lie interior to the FE results. This behavior, which manifests mostly for $W \leq 0.5$, is due to imperfections in the calibration function t and may be remedied using the improved function of Appendix C.

3. In all cases with predominant shear, the model predicts an upper bound of the FE data. The predictions could be further improved by adjusting parameter l. However, we refrain from doing so here because

of uncertainties related to cell shape effects. A more conclusive comparison requires (i) an improved analytical model that is upper-bound preserving (recall that approximation (29) deprives the final criterion from this property); and (ii) a set of FE calculations on the same cylindrical cell subjected to combined loadings. Such efforts are underway and results will be reported elsewhere.

4.4 Application of the Model

The chief concern here has been to develop an effective yield function that seamlessly describes void coalescence by internal necking or shearing. For practical use, the model needs to be supplemented with evolution equations for the internal parameters. For tension dominated loadings, such evolution equations are available [39, 41]. For shear-dominated loadings, the void morphology at the onset of coalescence is heavily distorted. It remains to be seen whether the cylindrical geometry adopted here or the more general ones considered in [39, 41] can represent actual, sheared peanuts shapes [13] even in some average sense.

As it stands, the void coalescence model assumes a doubly periodic distribution of voids whereas real distributions are inhomogeneous. As discussed by Benzerga [41], whether the regular distribution provides a lower or upper bound to ductility is far from settled. This is especially the case when considering random loadings with a finite wavelength comparable with the average void spacing.

5 Concluding Remarks

A void coalescence model accounting for a general loading scheme was developed based on homogenization and limit analysis. The model offers an extension of that recently derived by Benzerga and Leblond [26] to more general stress states. It improves upon the model proposed by Tekoglu et al. [45] in two ways: (i) it is based on a detailed analysis of the microscopic velocity field around the void; (ii) it offers a simpler, yet more robust calibration in the limit of penny-shaped cracks. Salient features of the new model include the following:

- The model captures seamless transitions between so-called internal necking and internal shearing in solids with voids. The effective yield surface (or coalescence surface) exhibits planar (singular) parts and curved (regular) parts and is devoid of any corners. The parameters of the yield surface are functions of the microstructural parameters χ (ligament parameter) and W (void aspect ratio).

- The effective dissipation function arrived at by homogenization is strikingly similar to that used in geophysics for granular materials [51, 52]. The function derived here is, however, non-differentiable and this leads to the presence of planar parts in the coalescence surface.

- A heuristic modification to the analytical model was rationalized on the basis of comparisons with finite-element based limit analysis results from the literature. The modification is mostly relevant to relatively flat cavities, particularly penny-shaped cracks. With the calibration being carried out in the absence of any shear loading, subsequent comparisons were made with available FE results for combined loadings. The model performs quite well.

- Further improvement of the model requires removal of uncertainties associated with two aspects: (i) a small, but non-negligible effect of the cell shape on the coalescence surface; (ii) the loss of the upper-bound character due to approximations in the calculation of the effective dissipation.

Acknowledgments

MT and AAB acknowledge support from the National Science Foundation under Grant Number CMMI-1405226. JBL acknowledges financial support from Institut Universitaire de France (IUF). Support from the NSF International Materials Institute established at Texas A&M, Grant # DMR-0844082 is also acknowledged.

Appendix A Derivation of (30) giving Π^{vol}

Approximate evaluation of Π^{vol} in (29) involves calculating the integral:

$$\langle \delta_{\mathrm{E}} \rangle_{\Omega_{\mathrm{lig}} \setminus \omega} = \frac{1}{\Omega_{\mathrm{lig}} - \omega} \int_R^L \int_0^{2\pi} \int_{-h}^{h} |D_{33}| \left[3 + \frac{L^4}{r^4} \right]^{1/2} r \, \mathrm{d}r \, \mathrm{d}\theta \, \mathrm{d}z \tag{49}$$

Integrating over θ and z and simplifying gives:

$$\langle \delta_{\mathrm{E}} \rangle_{\Omega_{\mathrm{lig}} \setminus \omega} = \frac{1}{1-\chi^2} \frac{2|D_{33}|}{L^2} \int_R^L \left[3 + \frac{L^4}{r^4} \right]^{1/2} r \, \mathrm{d}r \tag{50}$$

Using the change of variable $u \equiv L^2/r^2$ and rearranging leads to:

$$\langle \delta_{\mathrm{E}} \rangle_{\Omega_{\mathrm{lig}} \setminus \omega} = \frac{|D_{33}|}{1-\chi^2} \left[\operatorname{arg\,sinh}\left(\frac{u}{\sqrt{3}} \right) - \sqrt{\frac{3}{u^2} + 1} \right]_1^{1/\chi^2} \tag{51}$$

$$= \frac{|D_{33}|}{1-\chi^2} \left(2 - \sqrt{1+3\chi^4} + \ln \frac{1 + \sqrt{1+3\chi^4}}{3\chi^2} \right) \tag{52}$$

where the identity $\operatorname{arg\,sinh} u = \ln\left(u + \sqrt{1+u^2}\right)$ was used to arrive at the final expression. Finally, inserting (52) into (29) yields the desired relation (30) granted definitions (31).

Appendix B Details Pertaining to Section 2.7

B.1 Properties of function g in Eq. (36)

The functions f and g involved in inequality (36) are defined on $\mathbb{R}$ by:

$$\begin{aligned} f(p) &= 2\Sigma_{31} + p\Sigma_{33} \\ g(p) &= \sqrt{{\Sigma^{\mathrm{vol}}}^2 p^2 + \mathcal{T}^2} + \Sigma^{\mathrm{surf}} |p| \end{aligned} \tag{53}$$

Since g has a term proportional to $|p|$ it has an angular point at $p = 0$. The first and second derivatives of g in $\mathbb{R} \setminus \{0\}$ are:

$$\begin{aligned} g'(p) &= \frac{{\Sigma^{\mathrm{vol}}}^2 p}{\sqrt{{\Sigma^{\mathrm{vol}}}^2 p^2 + \mathcal{T}^2}} + \mathrm{sgn}(p)\Sigma^{\mathrm{surf}} \\ g"(p) &= \frac{{\Sigma^{\mathrm{vol}}}^2 \mathcal{T}^2}{({\Sigma^{\mathrm{vol}}}^2 p^2 + \mathcal{T}^2)^{\frac{3}{2}}} \end{aligned} \tag{54}$$

Since $g"(p) > 0 \, \forall p$, g is strictly convex. Therefore, it admits a unique minimum, which is attained at $p = 0$, i.e. the location of the angular point. The minimum is $g(0) = \mathcal{T}$ and the slopes on either side are: $g'(0^+) = \Sigma^{\mathrm{surf}}$ and $g'(0^-) = -\Sigma^{\mathrm{surf}}$. Finally, the following limits hold:

$$\lim_{p \to \pm\infty} \frac{g(p)}{p} = \pm(\Sigma^{\mathrm{vol}} + \Sigma^{\mathrm{surf}}) \tag{55}$$

This establishes the existence of straight asymptotes at $\pm\infty$. It is important to note that these asymptotes are common to the concave function $-g(p)$, which is also involved in inequality (36).

B.2 Derivation of Eq. (40)

Referring to Fig. 4b, the point p_0 is defined such that the line $q = f(p)$ is tangent to the curve $q = g(p)$. As in the main text, we focus on $\Sigma_{31} > 0$ so that the issue of tangency with the concave curve $q = -g(p)$ does not arise. However, no assumption is made on the sign of Σ_{33}. Find p such that simultaneously:

$$\begin{cases} f'(p) = g'(p) & \Longrightarrow \Sigma_{33} = \dfrac{{\Sigma^{\text{vol}}}^2 p}{\sqrt{{\Sigma^{\text{vol}}}^2 p^2 + \mathcal{T}^2}} + \Sigma^{\text{surf}}\text{sgn}(p) \\ \\ f(p) = g(p) & \Longrightarrow \Sigma_{33} p + 2\Sigma_{31} = \sqrt{{\Sigma^{\text{vol}}}^2 p^2 + \mathcal{T}^2} + \Sigma^{\text{surf}}|p| \end{cases} \tag{56}$$

Obtaining the square root term from the second of these equations and inserting it back into the first leads to

$${\Sigma^{\text{vol}}}^2 p = (\Sigma_{33} - \text{sgn}(p)\Sigma^{\text{surf}})^2 p + 2\Sigma_{31}(\Sigma_{33} - \text{sgn}(p)\Sigma^{\text{surf}}),$$

which is a simple linear equation in p considering that the sign of p is determined. Indeed, having focused on non-negative values of D_{31} and Σ_{31} the positivity of the product $\boldsymbol{\Sigma} : \mathbf{D}$ dictates that $\text{sgn}(p) = \text{sgn}(\Sigma_{33})$. By way of consequence, the point p_0 is given by:

$$p_0 = \text{sgn}(\Sigma_{33}) \frac{2\Sigma_{31}(|\Sigma_{33}| - \Sigma^{\text{surf}})}{{\Sigma^{\text{vol}}}^2 - (|\Sigma_{33}| - \Sigma^{\text{surf}})^2} \tag{57}$$

To eliminate p_0 from (56) insert its expression (57) back into either equation in (56), say the first; this yields:

$${\Sigma^{\text{vol}}}^2 \frac{2\Sigma_{31}(|\Sigma_{33}| - \Sigma^{\text{surf}})}{{\Sigma^{\text{vol}}}^2 - (|\Sigma_{33}| - \Sigma^{\text{surf}})^2} = (|\Sigma_{33}| - \Sigma^{\text{surf}}) \sqrt{{\Sigma^{\text{vol}}}^2 p_0^2 + \mathcal{T}^2}$$

Upon squaring the right hand side and using (57) again one gets successively:

$$\left[\frac{2{\Sigma^{\text{vol}}}^2 \Sigma_{31}}{{\Sigma^{\text{vol}}}^2 - (|\Sigma_{33}| - \Sigma^{\text{surf}})^2}\right]^2 = {\Sigma^{\text{vol}}}^2 \left[\frac{2\Sigma_{31}(|\Sigma_{33}| - \Sigma^{\text{surf}})}{{\Sigma^{\text{vol}}}^2 - (|\Sigma_{33}| - \Sigma^{\text{surf}})^2}\right]^2 + \mathcal{T}^2$$

$$\frac{4\Sigma_{31}^2}{\left[{\Sigma^{\text{vol}}}^2 - (|\Sigma_{33}| - \Sigma^{\text{surf}})^2\right]^2} \left[{\Sigma^{\text{vol}}}^2 - (|\Sigma_{33}| - \Sigma^{\text{surf}})^2\right] = \mathcal{T}^2$$

$$\frac{4\Sigma_{31}^2 {\Sigma^{\text{vol}}}^2}{{\Sigma^{\text{vol}}}^2 - (|\Sigma_{33}| - \Sigma^{\text{surf}})^2} = \mathcal{T}^2,$$

which upon rearranging leads to the desired equation (40).

B.3 Regular vs. Singular Parts of the Yield Surface

The straight parts of the yield surface (Fig. 5) are singular in that they result from the non-differentiability of the dissipation function at $D_{33} = 0$ for all values of the shearing rates. On the other hand, the curved parts are regular. One can show that their equation (40), and more generally $(41)_1$, may be obtained by direct differentiation of $\Pi(\mathbf{D})$. Consider for instance the case $D_{33} \geq 0$; from parametric definition (4) of the yield

locus one gets:

$$\Sigma_{33} = \frac{\partial \Pi}{\partial D_{33}} = \frac{\partial (\Pi^{\mathrm{vol}} + \Pi^{\mathrm{surf}})}{\partial D_{33}} \tag{58}$$

$$\Sigma_{31} = \frac{1}{2}\frac{\partial \Pi}{\partial D_{31}} = \frac{1}{2}\frac{\partial \Pi^{\mathrm{vol}}}{\partial D_{31}} \tag{59}$$

$$\Sigma_{32} = \frac{1}{2}\frac{\partial \Pi}{\partial D_{32}} = \frac{1}{2}\frac{\partial \Pi^{\mathrm{vol}}}{\partial D_{32}} \tag{60}$$

from which one obtains using the expressions (30) and (22) for Π^{vol} and Π^{surf}:

$$\Sigma_{33} = {\Sigma^{\mathrm{vol}}}^2 \frac{D_{33}}{\Pi^{\mathrm{vol}}} + \Sigma^{\mathrm{surf}} \tag{61}$$

$$\Sigma_{31} = \frac{1}{2}\mathcal{T}^2 \frac{D_{31}}{\Pi^{\mathrm{vol}}} \tag{62}$$

$$\Sigma_{32} = \frac{1}{2}\mathcal{T}^2 \frac{D_{32}}{\Pi^{\mathrm{vol}}} \tag{63}$$

In order to eliminate the components of $\mathbf{D}$, which play the role of parameters, rearrange into:

$$\begin{cases} \dfrac{\Sigma_{33} - \Sigma^{\mathrm{surf}}}{\Sigma^{\mathrm{vol}}} & = \dfrac{\Sigma^{\mathrm{vol}} D_{33}}{\Pi^{\mathrm{vol}}} \\ \dfrac{2\Sigma_{3i}}{\mathcal{T}} & = \dfrac{\mathcal{T} D_{3i}}{\Pi^{\mathrm{vol}}} \qquad \text{for } i = 1, 2 \end{cases} \tag{64}$$

then sum the squares of the left hand sides to obtain:

$$\left[\frac{\Sigma_{33} - \Sigma^{\mathrm{surf}}}{\Sigma^{\mathrm{vol}}}\right]^2 + \frac{4(\Sigma_{31}^2 + \Sigma_{31}^2)}{\mathcal{T}^2} = \frac{{\Sigma^{\mathrm{vol}}}^2 D_{33}^2 + \mathcal{T}^2 (D_{31}^2 + D_{32}^2)}{{\Pi^{\mathrm{vol}}}^2} = 1 \tag{65}$$

the right hand side of which is equal to unity by virtue of (30). Eq. (65) is identical to $(41)_1$ in the case $\Sigma_{33} > \Sigma^{\mathrm{surf}}$.

Appendix C Alternative $t(W, \chi)$ Function

Inspection of Fig. 8 reveals that most cases where the upper-bound character is lost belong to the set for which $W < 0.5$. An alternative homographic function that addresses this is one which has the following asymptotic behavior

$$\begin{aligned} t &\underset{W \to 0}{\sim} a\, W \\ t &\underset{W \to \infty}{\sim} 0 \end{aligned} \tag{66}$$

The first of these conditions is identical to that of the t function proposed in the text, as this is required for removing the singular character of the Σ^{surf} function. The second is different but has no major consequence because Σ^{surf} itself vanishes for very elongated voids. One possible function that would not change too much the strength of the decay at $W \to \infty$ is:

$$t(\chi, W) = \frac{(t_0 + t_1 \chi) W}{1 + (t_0 + t_1 \chi) W^{4/3}} \tag{67}$$

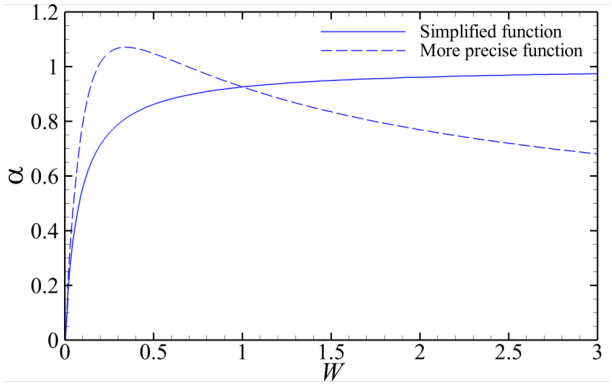

Figure 11: Distinction between the simple and more precise t functions.

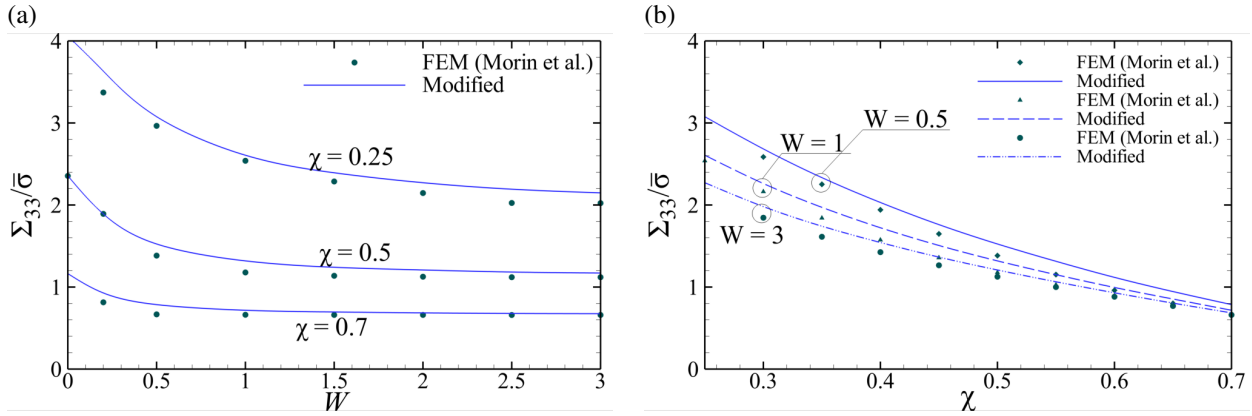

Figure 12: (a) $\Sigma_{33}/\bar{\sigma}$ versus W according to the FEM results (points from [46]) and the modified model (solid lines) using $t_0 = -0.84$, $t_1 = 12.9$ and $b = 1$ for three values of the ligament parameter χ. (b) $\Sigma_{33}/\bar{\sigma}$ versus χ according to the FEM results and modified model for three values of W.

This function is plotted in Fig. 11 along with the simpler function given by equation (47). By interposing a slight "jump" in the t function for $W < 0.5$, the precision of the calibration is augmented. The values of t_0 and t_1 are the same as those in the simpler function. However, the optimum value of b proves to be unity here. This alternative function represents a good compromise between accuracy and simplicity, and it corresponds to complete preservation of the upper-bound character of the model (Fig. 12), at least for the wide range of parameters considered here.

References

[1] Y. Bao and T. Wierzbicki. On fracture locus in the equivalent strain and stress triaxiality space. *International Journal of Mechanical Sciences*, 46:81–98, 2004.

[2] I. Barsoum and J. Faleskog. Rupture mechanisms in combined tension and shear—-Experiments. *International Journal of Solids and Structures*, 44:1768–1786, 2007.

[3] S.S. Haltom, S. Kyriakides, and K. Ravi-Chandar. Ductile failure under combined shear and tension. *International Journal of Solids and Structures*, 50:1507–1522, 2013.

[4] Y. Bai and T. Wierzbicki. A new model of metal plasticity and fracture with pressure and Lode dependence. *International Journal of Plasticity*, 24:1071–1096, 2008.

[5] K. Nahshon and J. W. Hutchinson. Modification of the Gurson Model for shear failure. *European Journal of Mechanics*, 27:1–17, 2008.

[6] I. Barsoum and J. Faleskog. Rupture mechanisms in combined tension and shear—-Micromechanics. *International Journal of Solids and Structures*, 44:5481–5498, 2007.

[7] M. Achouri, G. Germain, P. Dal Santo, and D. Saidane. Experimental characterization and numerical modeling of micromechanical damage under different stress states. *Materials & Design*, 50:207–222, 2013.

[8] A. Needleman. A continuum model for void nucleation by inclusion debonding. *Journal of Applied Mechanics*, 54:525, 1987.

[9] N. A. Fleck, J. W. Hutchinson, and V. Tvergaard. Softening by void nucleation and growth in tension and shear. *Journal of the Mechanics and Physics of Solids*, 37:515–540, 1989.

[10] K. Siruguet and J.-B. Leblond. Effect of void locking by inclusions upon the plastic behavior of porous ductile solids—I: theoretical modeling and numerical study of void growth. *International Journal of Plasticity*, 20:225–254, 2004.

[11] A. Weck and D. S. Wilkinson. Experimental investigation of void coalescence in metallic sheets containing laser drilled holes. *Acta Materialia*, 56:1774–1784, 2008.

[12] V. Tvergaard. Shear deformation of voids with contact modeled by internal pressure. *International Journal of Mechanical Sciences*, 50:1459–1465, 2008.

[13] V. Tvergaard. Effect of stress-state and spacing on voids in a shear-field. *International Journal of Solids and Structures*, 49:3047–3054, 2012.

[14] F. A. Mc Clintock. Ductile fracture by hole growth in shear bands. *Int. J. Frac. Mech.*, 2(4):614–627, 1966.

[15] N. A. Fleck and J. W. Hutchinson. Void growth in shear. *Proceedings of the Royal Society of London A*, 407:435–458, 1986.

[16] K. L. Nielsen, J. Dahl, and V. Tvergaard. Collapse and coalescence of spherical voids subject to intense shearing: studied in full 3D. *International Journal of Fracture*, 177:97–108, 2012.

[17] M. Dunand and D. Mohr. Effect of Lode parameter on plastic flow localization after proportional loading at low stress triaxialities. *Journal of the Mechanics and Physics of Solids*, 66:133–153, 2014.

[18] J. R. Rice and D. M. Tracey. On the enlargement of voids in triaxial stress fields. *Journal of the Mechanics and Physics of Solids*, 17:201–217, 1969.

[19] A. L. Gurson. Continuum Theory of Ductile Rupture by Void Nucleation and Growth: Part I– Yield Criteria and Flow Rules for Porous Ductile Media. *Journal of Engineering Materials and Technology*, 99:2–15, 1977.

[20] C. Chu and A. Needleman. Void nucleation effects in biaxially stretched sheets. *Journal of Engineering Materials and Technology*, 102:249–256, 1980.

[21] V. Tvergaard and A. Needleman. Analysis of the cup–cone fracture in a round tensile bar. *Acta Metallurgica*, 32:157–169, 1984.

[22] Y. Shen, T. F. Morgeneyer, J. Garnier, L. Allais, L. Helfen, and J. Crepin. Three-dimensional quantitative in situ study of crack initiation and propagation in AA6061 aluminum alloy sheets via synchrotron laminography and finite-element simulations. *Acta Materialia*, 61:2571–2582, 2013.

[23] B. Kondori. *DUCTILE FRACTURE OF MAGNESIUM ALLOYS: CHARACTERIZATION AND MODELING*. PhD thesis, Texas A&M University, USA, 2015.

[24] A. A. Benzerga, J. Besson, and A. Pineau. Coalescence–Controlled Anisotropic Ductile Fracture. *Journal of Engineering Materials and Technology*, 121:221–229, 1999.

[25] A. A. Benzerga and J.-B. Leblond. Ductile fracture by void growth to coalescence. *Advances in Applied Mechanics*, 44:169–305, 2010.

[26] A. A. Benzerga and J.-B. Leblond. Effective Yield Criterion Accounting for Microvoid Coalescence. *Journal of Applied Mechanics*, 81:031009, 2014.

[27] J. Koplik and A. Needleman. Void growth and coalescence in porous plastic solids. *International Journal of Solids and Structures*, 24(8):835–853, 1988.

[28] F. Scheyvaerts, P. R. Onck, C. Tekoglu, and T. Pardoen. The growth and coalescence of ellipsoidal voids in plane strain under combined shear and tension. *Journal of the Mechanics and Physics of Solids*, 59:373–397, 2011.

[29] A. B. Richelsen and V. Tvergaard. Dilatant plasticity or upper bound estimates for porous ductile solids. *Acta Metallurgica et Materialia*, 42(8):2561–2577, 1994.

[30] T. Pardoen and J. W. Hutchinson. An extended model for void growth and coalescence. *Journal of the Mechanics and Physics of Solids*, 48:2467–2512, 2000.

[31] M. Gologanu, J.-B. Leblond, and J. Devaux. Approximate models for ductile metals containing non-spherical voids – case of axisymmetric prolate ellipsoidal cavities. *Journal of the Mechanics and Physics of Solids*, 41(11):1723–1754, 1993.

[32] M. Gologanu, J.-B. Leblond, and J. Devaux. Approximate Models for Ductile Metals Containing Non–spherical Voids — Case of Axisymmetric Oblate Ellipsoidal Cavities. *Journal of Engineering Materials and Technology*, 116:290–297, 1994.

[33] P. Ponte Castañeda and M. Zaidman. Constitutive models for porous materials with evolving microstructure. *Journal of the Mechanics and Physics of Solids*, 42:1459–1495, 1994.

[34] K. Danas and P. Ponte Castañeda. A finite-strain model for anisotropic viscoplastic porous media: I–Theory. *European Journal of Mechanics*, 28:387–401, 2009.

[35] S. M. Keralavarma and A. A. Benzerga. A constitutive model for plastically anisotropic solids with non-spherical voids. *Journal of the Mechanics and Physics of Solids*, 58:874–901, 2010.

[36] K. Madou and J.-B. Leblond. A Gurson-type criterion for porous ductile solids containing arbitrary ellipsoidal voids – I: Limit-analysis of some representative cell. *Journal of the Mechanics and Physics of Solids*, 60:1020–1036, 2012.

[37] K. Madou, J.-B. Leblond, and L. Morin. Numerical studies of porous ductile materials containing arbitrary ellipsoidal voids —II: Evolution of the length and orientation of the void axes. *European Journal of Mechanics*, 42:490–507, 2013.

[38] A. A. Benzerga, J. Besson, and A. Pineau. Anisotropic ductile fracture. Part I: experiments. *Acta Materialia*, 52:4623–4638, 2004.

[39] A. A. Benzerga, J. Besson, and A. Pineau. Anisotropic ductile fracture. Part II: theory. *Acta Materialia*, 52:4639–4650, 2004.

[40] P. F. Thomason. Three–dimensional models for the plastic limit–loads at incipient failure of the inter-void matrix in ductile porous solids. *Acta Metallurgica*, 33:1079–1085, 1985.

[41] A. A. Benzerga. Micromechanics of Coalescence in Ductile Fracture. *Journal of the Mechanics and Physics of Solids*, 50:1331–1362, 2002.

[42] J.-B. Leblond and G. Mottet. A theoretical approach of strain localization within thin planar bands in porous ductile materials. *Comptes Rendus Mecanique*, 336:176–189, 2008.

[43] M. Gologanu, J.-B. Leblond, G. Perrin, and J. Devaux. Theoretical models for void coalescence in porous ductile solids – I: Coalescence in "layers". *International Journal of Solids and Structures*, 38:5581–5594, 2001.

[44] M. Gologanu, J.-B. Leblond, G. Perrin, and J. Devaux. Theoretical models for void coalescence in porous ductile solids – II: Coalescence in "columns". *International Journal of Solids and Structures*, 38:5595–5604, 2001.

[45] C. Tekoglu, J.-B. Leblond, and T. Pardoen. A criterion for the onset of void coalescence under combined tension and shear. *Journal of the Mechanics and Physics of Solids*, 60:1363–1381, 2012.

[46] L. Morin, J.-B. Leblond, and A. A. Benzerga. Coalescence of voids by internal necking: theoretical estimates and numerical results. *Journal of the Mechanics and Physics of Solids*, 75:140–158, 2015.

[47] L. Morin, J.-B. Leblond, and A. A. Benzerga. A unified criterion for the growth and coalescence of microvoids. *Journal of the Mechanics and Physics of Solids*, 2015. Submitted.

[48] A. A. Benzerga, J. Besson, R. Batisse, and A. Pineau. Synergistic effects of plastic anisotropy and void coalescence on fracture mode in plane strain. *Modelling and Simulation in Materials Science and Engineering*, 10:73–102, 2002.

[49] B. Kondori and A. A. Benzerga. Effect of Stress Triaxiality on the Flow and Fracture of Mg Alloy AZ31. *Metallurgical and Materials Transactions A.*, 45:3292–3307, 2014.

[50] M. Gologanu. *Etude de quelques problèmes de rupture ductile des métaux*. PhD thesis, Université Paris 6, 1997.

[51] I. F. Collins and G. T. Houlsby. Application of thermomechanical principles to the modelling of geotechnical materials. *Proceedings of the Royal Society of London A*, 453:1975–2001, 1997.

[52] I. Einav and J.P. Carter. On convexity, normality, pre-consolidation pressure, and singularities in modelling of granular materials. *Granular Matter*, 9:87–96, 2007.

P2 THEORETICAL AND NUMERICAL ANALYSIS OF VOID COALESCENCE IN POROUS DUCTILE SOLIDS UNDER ARBITRARY LOADINGS

Theoretical and Numerical Analysis of Void Coalescence in Porous Ductile Solids under Arbitrary Loadings

M. E. Torki[1], C. Tekoğlu[2], J.-B. Leblond[3], A. A. Benzerga[1,4]

[1] *Department of Aerospace Engineering, Texas A&M University, College Station, TX 77843, USA*

[2] *Department of Mechanical Engineering, TOBB University of Economics and Technology, Söğütözü, Ankara, 06560, Turkey*

[3] *Sorbonne Universites, UPMC Univ Paris 06, CNRS, UMR 7190 Institut Jean Le Rond d'Alembert, F-75005, Paris, France*

[4] *Department of Materials Science and Engineering, Texas A&M University, College Station, TX 77843, USA*

Abstract

Micromechanics-based constitutive relations are developed to model plasticity in solids with relatively high levels of porosity. They are especially appropriate to model void coalescence in ductile materials. The model is obtained by limit analysis of a cylindrical cell containing a coaxial void of finite height with plastic flow confined to the ligaments, and loaded under combined tension and shear. Previously obtained analytical estimates were not upper-bound preserving when shear was present and, in addition, were assessed against numerical results obtained for different cell geometries. Here, a rigorous upper-bound model is developed and its predictions are consistently compared with finite-element based estimates of limit loads on the same cylindrical unit cell exploiting quasi-periodic boundary conditions. The numerical results are used to guide a heuristic modification of the model in order to capture the behavior for extremely flat or extremely elongated voids.

Key Words: Ductile fracture; Low triaxiality; Internal necking; Internal shearing; Homogenization; Upper-bound.

1 Introduction

Void coalescence is known to be the last elementary stage of ductile failure [1]. That is, as soon as the first few largest voids approach each other within a fraction ($\sim$0.3–0.5) of the intervoid distance, yet long before they link up, the stress carrying capacity *abruptly* drops, and this upheaval continues to failure at the material point level [2, 3]. This sudden change is associated with strain concentration in the intervoid ligament (a form of micro-scale strain localization). Prior to this, void deformation occurs by diffuse plasticity, the distorsion being due to void enlargement, change of shape, rotation or all [4, 5]. Ultimate failure of a test piece can thus occur if plastic flow successively localizes in intervoid ligaments thereby leading to macroscopic ductile crack growth. This mechanism prevails unless failure occurs by some plastic instability at the scale of many-void populations.

As a precursor to void coalescence, the process of micro-scale strain concentration should thus be modeled for predicting ductile fracture. This involves developing constitutive relations for voided solids in a "coalescence state", to be further defined below. When put together with available models for voided solids

in "pre-coalescence states", e.g., [6] the transition between the two states will correspond to the abrupt change in deformation mechanism.

It is noted that the developed constitutive relations are relevant to describe the plastic response of materials with relatively high levels of porosity, as for example considered by [7]. However, the resulting models are different from pre-coalescence, Gurson-like models, because of fundamental differences in the boundary conditions assumed in developing the said constitutive relations. What is of particular importance is that the porosity levels of interest can be quite low by comparison with those prevailing in engineered porous materials. Typical figures would be on the order of 0.01, perhaps even smaller.

It is also emphasized that this type of models is different from those where void coalescence is viewed as an instability that can be predicted in terms of the pre-coalescence constitutive relations, e.g. [8]; also see [5]. The fundamental premise of the line of models to be developed here is that the pre-coalescence constitutive relations cease to be valid at the critical point, and thus provide no basis for predicting localization; as explained by [9], "An alternative hypothesis would be that some essentially new physical deformation mechanism comes into play, abruptly, and rapidly degrades the strength of the material. In such cases the pre-localization constitutive relations cannot be continued analytically at the critical point, and they provide no basis for prediction of localization."

Internal necking of the intervoid ligaments, as the most prevalent mechanism for void coalescence [1], has been inferred from the pioneering computational work of [2], approximately modeled by [10], [11], [12], [13] and [3], and recently tackled on more rigorous grounds by [14] and [15]. A "coalescence state" is defined in this context as any state after a neck has initiated in the intervoid ligaments, with the deformation mode shifting to purely uniaxial, and elastic unloading taking place outside of these ligaments.

The void coalescence models listed above strictly apply to predominately tensile loadings even if approximate extensions have been attempted so as to incorporate more general loadings [3, 16]. In recent years, there has been revived interest in ductile fracture under combined tension and shear e.g. [17, 18]. More generally, one needs to consider not only the normal stress acting on the localization plane but also the shear stress. When available and fully developed, such models can be utilized to analyze ductile fracture under more general loading schemes, as investigated in some recent works using micromechanical cell analyses [19, 20, 21, 22, 23, 24, 25, 26]. The motivation in accounting for a shear component in the remote loading is two-fold. First, it is of interest to quantify how the internal necking condition is affected by the shear stress. Second, if loading is shear-dominated a seamless transition from internal necking to "internal shearing" may occur, that is with all shear deformation taken up within the intervoid ligament.

Any constitutive relations for a porous material involve dilatant plasticity, at least for associative plastic flow as envisaged here. The chief concern of this paper is to develop such relations for a porous material in which voids are in a state of incipient coalescence (by internal necking or shearing) and consider the effects of normal as well as shear stresses. It is assumed that the presence of a remote shear stress would not change the basic mechanism of strain concentration. There have been quite a few modeling efforts in this direction. [19] and later [27] developed such equations using a "sandwich model" whereby the void is smeared out in the central layer of the sandwich. Later, [28] developed a closed-form solution to the problem of void coalescence under combined tension and shear by considering explicit expressions of the velocity field around the void. Recently, [29] extended the analysis of [14] to plastically anisotropic matrices by considering a sub-family of velocity fields introduced by [15]. Their analysis also accounted for combined tension and shear loadings. However, the limit analysis procedures in both [28] and [29] involved "uncontrolled" approximations which did not preserve the upper-bound character of the approach; see [4] for background. In addition, [28] offered some comparisons of their model predictions with the finite element results of [27]. The model was derived on the basis of a cylindrical cell containing a cylindrical void whereas the calculations in [27] were for a tetragonal cell with a spheroidal void. Notable discrepancies were observed between the finite element results and the model predictions. These discrepancies could be attributed a priori to three possible causes: (i) the choice of trial velocity fields in the analytical approach; (ii)

the uncontrolled approximation made in the analytical approach; (iii) the difference between the geometries of the elementary cells considered in the analytical and numerical approaches. The aim of the present paper is to examine possible causes (ii) and (iii). To this end we develop an improved model preserving the rigorous upper-bound character and carry out cell model calculations using exactly the same cell geometry as that considered in the analytical model.

The paper is organized as follows. Section 2 is devoted to the derivation of the upper-bound model, with details deferred to Appendices A and B. Section 3 presents the principle of the finite element calculations that use the same cylindrical cell, with details about boundary conditions gathered in Appendix C. Finally, Section 4 reports our results, showing comparisons between the upper-bound and approximate models as well as between the new model and unit cell calculations.

2 Analytical Model

2.1 Geometry and Loading

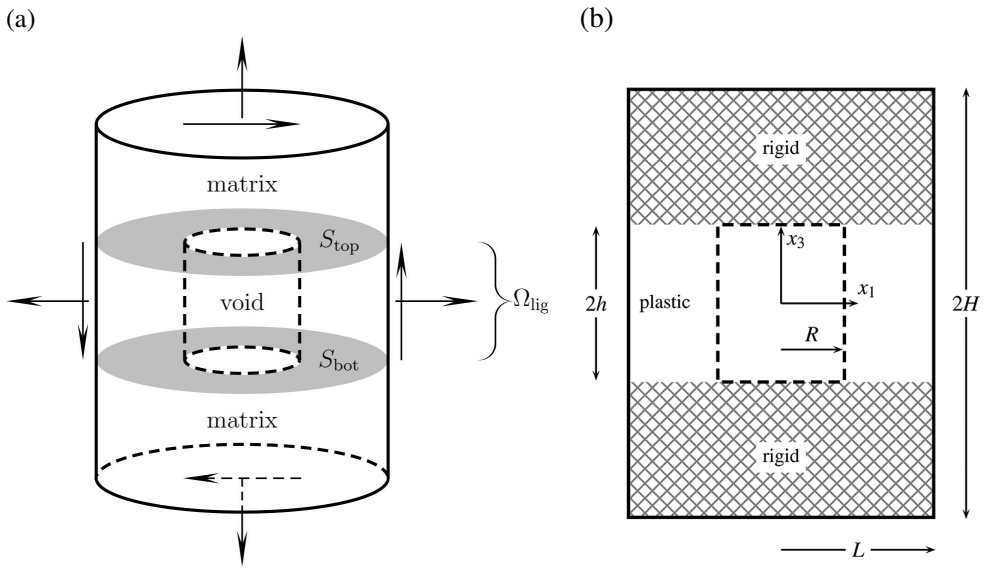

Figure 1: (a) Geometry of a cylindrical cell under combined tension and shear; (b) cell parameters.

As in [28], the elementary volume Ω is a cylindrical cell of height $2H$ and radius L containing a coaxial cylindrical void ω of height $2h$ and radius R, Fig. 1. Use is made of both a local cylindrical basis $(\mathbf{e}_r, \mathbf{e}_\theta, \mathbf{e}_z)$ and a global Cartesian one $(\mathbf{e}_1, \mathbf{e}_2, \mathbf{e}_3)$. The displacement boundary conditions imposed on the unit cell lead to a macroscopic stress state with a predominant axial stress, $\Sigma_{33} > \Sigma_{11}$, $\Sigma_{33} > \Sigma_{22}$, as well as shear stresses, Σ_{12} and Σ_{31}. With no loss of generality, the base vector $\mathbf{e}_1$ is taken parallel to the applied shear force. While not space filling, the analyzed geometry stands as a reasonable approximation of a unit cell in a periodic medium.

To represent "coalescence states" the cell is further divided into a central porous layer that defines the ligament domain, Ω_{lig}, and fully dense regions above and below it. The interfaces between these two regions and the ligament are denoted S_{top} and S_{bot} (Fig. 1a) and their union S_{int}. The height of the ligament domain is set by the void height $2h$; see [28] for background. This geometry is uniquely determined by the independent dimensionless parameters identified in the first row of equation (1), respectively termed the

void aspect ratio, the ligament parameter, and the cell aspect ratio.

$$
\begin{aligned}
&W = \frac{h}{R} \quad , \quad \chi = \frac{R}{L} \quad , \quad \lambda = \frac{H}{L} \\
&f_{\mathrm{b}} \equiv \frac{\omega}{\Omega_{\mathrm{lig}}} = \chi^2 \\
&c \equiv \frac{\Omega_{\mathrm{lig}}}{\Omega} = \frac{h}{H} = \frac{W\chi}{\lambda} \\
&f \equiv \frac{\omega}{\Omega} = c f_{\mathrm{b}}
\end{aligned}
\tag{1}
$$

For convenience, Eq. (1) also introduces other auxiliary parameters which will be used in the derivations: f_{b} is the porosity within the ligament band, c is the volume fraction of the band, and f is the overall porosity.

2.2 Structure of Constitutive Relations

To mimic coalescence states, the regions above and below Ω_{lig} are modeled as rigid (Fig. 1b). In actual evolution problems using the cell model [2, 30, 24], these regions would correspond to elastically unloaded ones. The mechanism of void growth *abruptly* changes due to the unloading that occurs above and below the cavity. Hence, plastic flow is assumed to be confined to the ligament and obey the von Mises yield criterion with the associated flow rule:

$$
\begin{aligned}
&\phi(\boldsymbol{\sigma}) = \sigma_{\mathrm{eq}}^2 - \bar{\sigma}^2 = 0 \qquad \sigma_{\mathrm{eq}} \equiv \sqrt{\frac{3}{2}\sigma'_{ij}\sigma'_{ij}} \\
&d_{ij} = \frac{3}{2}\frac{d_{\mathrm{eq}}}{\bar{\sigma}}\sigma'_{ij} \qquad d_{\mathrm{eq}} \equiv \sqrt{\frac{2}{3}d_{ij}d_{ij}}
\end{aligned}
\tag{2}
$$

where $\boldsymbol{\sigma}'$ is the stress deviator, and σ_{eq} and d_{eq} denote the von Mises equivalent stress and equivalent strain rate, respectively. Also, $\bar{\sigma}$ is the yield stress in simple tension.

The fundamental inequality of limit analysis gives rise to a variational definition of the effective yield criterion of a porous material as follows:

$$
\forall\, \mathbf{D}, \quad \boldsymbol{\Sigma} : \mathbf{D} \leq \Pi(\mathbf{D}), \qquad \Pi(\mathbf{D}) = \inf_{\mathbf{v}\in\mathcal{K}(\mathbf{D})} \langle \sup_{\boldsymbol{\sigma}^*\in\mathcal{C}} \sigma^*_{ij}\, d_{ij} \rangle_{\Omega}; \tag{3}
$$

if the velocity field is discontinuous across an interface S then a surface term must be added to $\Pi(\mathbf{D})$ as

$$
\frac{1}{\Omega}\int_S \sup_{\boldsymbol{\sigma}^*\in\mathcal{C}} t_i^*\, [\![v_i]\!]\, \mathrm{d}S \tag{4}
$$

In (3) $\boldsymbol{\Sigma}$ and $\mathbf{D}$ denote the effective stress and strain rate tensors, defined as volume averages of their microscopic counterparts $\boldsymbol{\sigma}$ and $\mathbf{d}$, and $\Pi(\mathbf{D})$ is the effective plastic dissipation. Also, $\langle\cdot\rangle_{\Omega}$ stands for averaging over Ω, $\mathcal{K}(\mathbf{D})$ is the set of kinematically admissible velocity fields $\mathbf{v}$ compatible with $\mathbf{D}$, $\inf$ and $\sup$, respectively, represent the infimum and supremum over a set, and $\mathcal{C}$ is the microscopic reversibility domain, the boundary of which is the yield surface of the matrix, here given by $(2)_1$. In (4) $\mathbf{t}^*$ denotes the traction acting on the interface and $[\![\mathbf{v}]\!]$ the velocity jump across it.

Thus, stress states that lie within the *effective* reversibility domain, here denoted $\mathscr{C}$, are given by (3), possibly augmented by (4), and the effective yield surface is the boundary of that domain, $\partial\mathscr{C}$. The reader is referred to [4] and [28] for further details. When the effective dissipation function is differentiable the yield surface is smooth. In such cases, the yield surface is defined by the parametric equation:

$$
\Sigma_{ij} = \frac{\partial \Pi}{\partial D_{ij}}(\mathbf{D}) \tag{5}
$$

where $\mathbf{D}$ is no longer arbitrary as in $(3)_1$ but represents the rate of deformation corresponding to $\boldsymbol{\Sigma}$ through the macroscopic flow rule.

2.3 *Trial Velocity Fields*

For general loadings, the exact velocity fields that minimize the integrals in $(3)_2$ cannot be obtained analytically. Nevertheless, use of trial ones leads to an upper bound to the yield surface [4]. Here, the trial velocity fields are taken from [28] and are briefly recalled for completeness. On account of the existing rigid zones above and below the central void, the unit cell considered cannot deform along the x_1 and x_2 directions nor can it shear in the x_1–x_2 plane, i.e., $D_{11} = D_{22} = D_{12} = 0$. In addition, the velocity jump across $S_{\rm int}$, if any, must be purely tangential. Thus, the velocity ought to be consistent with the following constraints:

$$\begin{cases} v_r(L,\theta,z)\mathbf{e}_r + v_\theta(L,\theta,z)\mathbf{e}_\theta &= \frac{2z}{c} D_{31}\mathbf{e}_1 \qquad (-h \le z \le h; 0 \le \theta \le 2\pi) \\ v_z(r,\theta,\pm h) &= \pm D_{33} H \qquad (0 \le r \le L; 0 \le \theta \le 2\pi) \\ [\![\mathbf{v}]\!].\mathbf{n} &= 0 \qquad \forall \mathbf{x} \in S_{\rm int} \end{cases} \tag{6}$$

where D_{31} and D_{33} are the prescribed shear and axial strain rates, and $\mathbf{n}$ is the normal vector to the interface. Condition $(6)_1$ is supplemented by a constant velocity in the rigid zones ($h \le |z| \le H$). Boundary conditions (6) stand as an appproximation of periodic boundary conditions and are consistent with the coalescence states defined above as in cell model studies [2, 30, 24]. It should be noted that owing to the presence of rigid zones in the cell, the velocity field cannot be consistent with uniform strain-rate boundary conditions (of the Hill–Mandel kind).

Details aside, the simplest trial velocity field that fulfills (6) along with the incompressibility condition (tr $\mathbf{d}$ = div $\mathbf{v} = 0$) is given by (in the ligaments only):

$$\mathbf{v}(\mathbf{x}) = \left(\frac{A}{r} - B\frac{r}{2}\right)\mathbf{e}_r + Bz\mathbf{e}_z + \frac{2z}{c} D_{31}\mathbf{e}_1 \tag{7}$$

where c is defined in $(1)_3$, and parameters A and B are determined by boundary conditions as follows:

$$A = \frac{D_{33}L^2}{2c} \quad , \quad B = \frac{D_{33}}{c}$$

The corresponding components of the microscopic rate of deformation tensor $\mathbf{d}$ were reported in [28]. Because of its relative simplicity, velocity field (7) is not continuous across $S_{\rm int}$.

2.4 *Effective Dissipation*

Following [28] an upper bound of the effective dissipation may be expressed as:

$$\Pi = \Pi^{\rm vol} + \Pi^{\rm surf} \tag{8}$$

with

$$\begin{cases} \Pi^{\rm vol} &= c(1-\chi^2)\langle \bar{\sigma} d_{\rm eq} \rangle_{\Omega_{\rm lig}-\omega} \\ \Pi^{\rm surf} &= \dfrac{1}{\Omega}\displaystyle\int_{S_{\rm int}} \frac{\bar{\sigma}}{\sqrt{3}} \left|[\![v_{\rm t}]\!]\right| {\rm d}S \end{cases} \tag{9}$$

where the surface term $\Pi^{\rm surf}$ emerges as a result of the discontinuity of tangential velocity $[\![v_{\rm t}]\!]$ and is thus a direct consequence of (4). The calculation of $\Pi^{\rm surf}$ was carried out by [14] to yield:

$$\Pi^{\rm surf} = |D_{33}|\Sigma^{\rm surf}, \quad \Sigma^{\rm surf}(\chi, W) = \frac{\bar{\sigma}}{3\sqrt{3}} \frac{\chi^3 - 3\chi + 2}{\chi W} \tag{10}$$

It is in the calculation of the volumetric term Π^{vol} that the present work differs from [28]. Indeed, to simplify their treatment Torki et al. made an approximation in evaluating $(9)_1$ which did not preserve the upper-bound character. Here, careful treatment of this term is developed. In accordance with the calculations reported by [28], the expression of d_{eq} as stated in (2) reads

$$d_{\text{eq}}^2 = \frac{D_{33}^2}{3c^2}\left(3 + \frac{L^4}{r^4}\right) + \frac{4D_{31}^2}{3c^2} \tag{11}$$

Then the volumetric portion of the effective dissipation Π^{vol} of $(9)_1$ becomes:

$$\Pi^{\text{vol}} \equiv \Pi^{\text{vol}}(D_{33}, D_{31}) = (1-\chi^2)\frac{\bar{\sigma}}{\sqrt{3}}\left\langle \sqrt{D_{33}^2\left(3 + \frac{L^4}{r^4}\right) + 4D_{31}^2} \right\rangle_{\Omega_{\text{lig}}-\omega} \tag{12}$$

where the parameter c has canceled out. The following approximation was exploited in [28] to reach a simplified volumetric average in (12):

$$\Pi^{\text{vol}} \approx (1-\chi^2)\frac{\bar{\sigma}}{\sqrt{3}}\sqrt{\left\langle D_{33}^2\sqrt{\left(3 + \frac{L^4}{r^4}\right)}\right\rangle_{\Omega_{\text{lig}}-\omega}^2 + 4D_{31}^2} \tag{13}$$

However, this approximation, which was initially introduced by [27], destroys the rigorous upper-bound character, and therefore warrants some assessment against numerical estimates.

Unlike in [28, 27], no approximation is introduced herein. Introducing the change of variable $(D_{33}, D_{31}) \to (D_{33}, \bar{D})$ with

$$\bar{D}^2 = 3D_{33}^2 + 4D_{31}^2, \tag{14}$$

with the constraint $\bar{D}D_{33} \geq 0$, Π^{vol} can be written more concisely as

$$\Pi^{\text{vol}} \equiv \Pi^{*\text{vol}}(D_{33}, \bar{D}) = \frac{2\bar{\sigma}}{\sqrt{3}L^2}\int_R^L \sqrt{\left(D_{33}\frac{L^2}{r^2}\right)^2 + \bar{D}^2}\; r\,\mathrm{d}r \tag{15}$$

which can be evaluated conveniently using the change of variable $u \equiv L^2/r^2$:

$$\Pi^{\text{vol}} = \frac{\bar{\sigma}|\bar{D}|}{\sqrt{3}}\int_1^{1/\chi^2} \sqrt{1+\zeta^2u^2}\;\frac{\mathrm{d}u}{u^2} \quad , \quad \zeta \equiv \frac{D_{33}}{|\bar{D}|} \tag{16}$$

(Note that $|\zeta| \leq 1/\sqrt{3}$). The above integral emerges in various related problems, beginning with the Gurson model as revisited by [4] and its extensions, for example [31][1]. Thus, combining the volume term in (16) with the surface term in (10) one finally obtains:

$$\Pi = \frac{\bar{\sigma}|\bar{D}|}{\sqrt{3}}\left[\zeta\sinh^{-1}(\zeta u) - \sqrt{\frac{1}{u^2}+\zeta^2}\right]_1^{1/\chi^2} + |D_{33}|\Sigma^{\text{surf}} \tag{17}$$

with Σ^{surf} given by $(10)_2$. The dissipation function in (17) is not differentiable, just like the corresponding estimate from [28], see their equation (32). However, unlike the estimate in [28], the above equation provides a strict upper bound to the plastic dissipation.

[1] In equation (49) of [31] the term σ_1/b^2 appears as a typo and should be replaced with $h\sigma_1 D_m$. Also, the bound of the integral should read ξ/f. The same typos slipped in equation (6.11) of [4].

2.5 *Upper-Bound Criterion*

Using the fundamental inequality of limit analysis (3) it can be shown that the upper-bound effective yield surface associated with (17) contains singular parts and regular ones with no vertices. The general procedure for determining the various regions in stress space follows that of [28].

First, since the dissipation function Π depends only on D_{33} and D_{31} the effective yield condition according to (3) or (5) will not depend on Σ_{11}, Σ_{22} and Σ_{12}. Indeed by the normality flow rule[2] $D_{ij} = \dot{\Lambda}\partial\Phi/\partial\Sigma_{ij}$ where Φ is the sought effective yield function and $\dot{\Lambda} \geq 0$ the plastic multiplier; thus, the coalescence conditions $D_{11} = D_{22} = D_{12} = 0$ entail independence of the yield condition vis-a-vis the above-mentioned stress components.

Next, to obtain the singular parts one ought to resort to the primitive definition of the reversibility domain $\mathscr{C}$ in (3). The reasoning for doing so is intricate (see Appendix A) and is based on a graphical method. The result, however, is quite simple. Indeed, the yield locus is defined by:

$$|\Sigma_{31}| = (1-\chi^2)\bar{\tau}; \quad |\Sigma_{33}| \leq \Sigma^{\mathrm{surf}} \tag{18}$$

where $\bar{\tau} = \bar{\sigma}/\sqrt{3}$ is the shear yield strength of the matrix. This equation means that for the indicated range of normal stresses Σ_{33}, the effective yield function is independent of the normal stress and the shear yield stress is obtained by a simple rule of mixture between the yield stresses in the matrix and the void, since χ^2 is exactly the porosity in the band. In what follows, we shall denote $\mathcal{T} = (1-\chi^2)\bar{\tau}$.

On the other hand, the regular parts require a totally different treatment, which is streamlined in Appendix B. The technical part involves eliminating parameter ζ defined by $(16)_2$ to obtain an explicit expression of the effective yield function, which is given by equation (B-13).

The equations of the upper-bound model are recapitulated herein for ease of reference:

$$\Phi(\boldsymbol{\Sigma};\chi,W) = \begin{cases} \dfrac{\mathcal{B}^2}{\bar{\tau}^2} + 2f_{\mathrm{b}}\cosh\left(\dfrac{|\Sigma_{33}| - \Sigma^{\mathrm{surf}}}{\bar{\tau}} - \sqrt{3\dfrac{\mathcal{B}^2 - \Sigma_{31}^2}{\bar{\tau}^2}}\right) - (1+f_{\mathrm{b}}^2) & \text{for } |\Sigma_{33}| \geq \Sigma^{\mathrm{surf}} \\ \dfrac{\Sigma_{31}^2}{\mathcal{T}^2} - 1 & \text{for } |\Sigma_{33}| \leq \Sigma^{\mathrm{surf}} \end{cases} \tag{19}$$

where $\bar{\tau} = \bar{\sigma}/\sqrt{3}$ is the shear yield strength, $f_{\mathrm{b}} = \chi^2$ is the porosity within the plastically-deformable band, and

$$\begin{aligned} \Sigma^{\mathrm{surf}}(\chi,W) &= \frac{\chi^3 - 3\chi + 2}{3\chi W}\,\bar{\tau} \\ \mathcal{T} &= (1-\chi^2)\bar{\tau} \\ \frac{\mathcal{B}^2}{\bar{\tau}^2} &= \frac{5}{3} + \chi^4 - \frac{2}{3}\sqrt{4 + 12\chi^4 - 3\frac{\Sigma_{31}^2}{\bar{\tau}^2}} \end{aligned} \tag{20}$$

In general, the shear stress can be resolved into two components so that Σ_{31}^2 should be replaced with $\Sigma_{31}^2 + \Sigma_{32}^2$ everywhere in the above expressions.

By way of comparison, the equations of the approximate (not bound-preserving) criterion derived by

[2]Having assumed normality at the microscopic scale, equation (2), macroscopic normality is a rigorous consequence of the combination of effective properties and limit-analysis [4].

[28] are:

$$\Phi(\mathbf{\Sigma};\chi,W)=\begin{cases}\left(\dfrac{|\Sigma_{33}|-\Sigma^{\rm surf}}{\Sigma^{\rm vol}}\right)^2+\dfrac{\Sigma_{31}^2+\Sigma_{32}^2}{\mathcal{T}^2}-1 & \text{for } |\Sigma_{33}|\geq\Sigma^{\rm surf}\\[2ex] \dfrac{\Sigma_{31}^2+\Sigma_{32}^2}{\mathcal{T}^2}-1 & \text{for } |\Sigma_{33}|\leq\Sigma^{\rm surf}\end{cases} \tag{21}$$

where

$$\Sigma^{\rm vol}(\chi)=\left(2-\sqrt{1+3\chi^4}+\ln\frac{1+\sqrt{1+3\chi^4}}{3\chi^2}\right)\bar{\tau} \tag{22}$$

In both models (upper-bound and approximate) the yield surface is smooth, i.e., the transition between the two parts is vertex-free; see Appendix A. Also, note that the effective yield stress in shear is much smaller than that predicted by a Gurson-like model given that $\chi^2\equiv f_{\rm b}>f$.

3 Cell-Model Calculations

Previously, [28] presented comparisons between their approximate model and the micromechanical calculations of [27], which were carried out for tetragonal cells containing spheroidal voids. In order to assess the predictive capabilities of the upper-bound model, calculations have now been carried out for the very same unit cell used in the development of the model, Fig. 1. Thereupon, a special small-strain finite element framework is employed which is intended to be the numerical equivalent of the theory of limit analysis; see also [32]. A classical consequence of limit-analysis is that elastic strain rates vanish when the limit load is reached. Therefore, the elastic moduli disappear from the equations and may be chosen arbitrarily, and in turn plasticity imposes an incompressible velocity field on the material. In this study, in order to mimic such a velocity field, a high value of Poisson's ratio is enforced ($\nu=0.49$). Thus the matrix material is modeled as nearly isochoric-elastic ideal-plastic. Also, the yield strength to Young's modulus ratio is taken to be $\bar{\sigma}/E=0.0002$. All calculations were carried out using ABAQUS (Version 6.12) with the option of geometric nonlinearity switched off.

Inasmuch as the calculations are meant to validate the analytical model, it is emphasized that the same cylindrical geometry of Fig. 1 is used to avoid any ambiguity in the comparisons. One difficulty in making this choice is that strictly periodic boundary-conditions cannot be imposed on the cylindrical cell, since it does not truly represent a unit cell in a periodic medium but only "mimics" such a cell. Instead, "quasi-periodic" boundary conditions are prescribed drawing inspiration from rigorous periodicity. Consider one half of the cell (Fig. 2) with symmetry conditions imposed on the meridian plane. Anywhere in a *periodic* cell, the displacement $\mathbf{u}$ at field point $\mathbf{x}$ would write:

$$\mathbf{u}(\mathbf{x})=(\mathbf{E}+\mathbf{\Omega}).\mathbf{x}+\tilde{\mathbf{u}}(\mathbf{x}) \tag{23}$$

where $\mathbf{E}$ is the macroscopic strain tensor, $\mathbf{\Omega}$ the (skew-symmetric) macroscopic rotation tensor and $\tilde{\mathbf{u}}$ a periodic field. For any two points in periodic correspondence one would therefore have:

$$\Delta\mathbf{u}=(\mathbf{E}+\mathbf{\Omega}).\Delta\mathbf{x} \tag{24}$$

where $\Delta\mathbf{u}$ is the difference in displacement between the points separated by the vector $\Delta\mathbf{x}$. For a cylindrical cell equation (24) cannot be applied to pairs of points in periodic correspondence since such pairs do not exist. We shall impose instead conditions similar to (24) to specific, carefully selected pairs of surface points. It is in that sense that such conditions are termed "quasi-periodic".

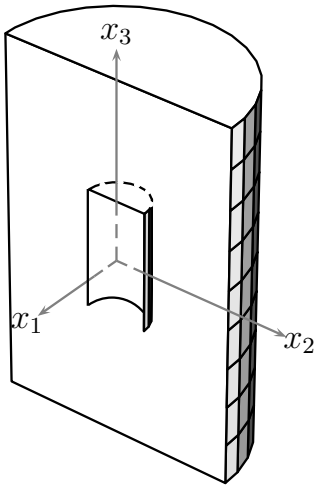

Figure 2: One half of a cylindrical cell.

Specifically, the macroscopic strain enforced on the cell is represented by the tensor:

$$\mathbf{E} = E_{11}(\mathbf{e}_1 \otimes \mathbf{e}_1 + \mathbf{e}_2 \otimes \mathbf{e}_2) + E_{33}\mathbf{e}_3 \otimes \mathbf{e}_3 + E_{31}(\mathbf{e}_1 \otimes \mathbf{e}_3 + \mathbf{e}_3 \otimes \mathbf{e}_1) \tag{25}$$

or in matrix form

$$\mathbf{E} = \begin{bmatrix} E_{11} & 0 & E_{31} \\ 0 & E_{11} & 0 \\ E_{31} & 0 & E_{33} \end{bmatrix}$$

where

$$\begin{aligned} E_{11} &= E_{22} \equiv \ln\left(\frac{L}{L_0}\right) \approx \frac{U_1}{L_0} \\ E_{33} &\equiv \ln\left(\frac{H}{H_0}\right) \approx \frac{U_3}{H_0} \\ E_{31} &\equiv \frac{U_\mathrm{t}}{2H_0} \end{aligned} \tag{26}$$

Here, U_1 denotes a prescribed displacement on the lateral surface (see Appendix C for details), whilst U_3 and U_t are, respectively, the normal and tangential displacements prescribed on the top surface.

On the other hand, the macroscopic rotation tensor must be of the form:

$$\mathbf{\Omega} = \Omega_{31}(\mathbf{e}_3 \otimes \mathbf{e}_1 - \mathbf{e}_1 \otimes \mathbf{e}_3) \tag{27}$$

The simplest choice for $\mathbf{\Omega}$ in (24) would be to take $\mathbf{\Omega} = \mathbf{0}$. However, this would entail a vertical displacement on the lateral surface. To avoid this, one can choose $\Omega_{13} = -\Omega_{31} = E_{31}$. For the cylindrical cell considered, this choice will considerably simplify the formulation of multi-point constraint conditions.

In matrix form, the strictly periodic boundary conditions (24) now read:

$$\begin{Bmatrix} \Delta u_1 \\ \Delta u_2 \\ \Delta u_3 \end{Bmatrix} = \begin{bmatrix} E_{11} & 0 & 2E_{31} \\ 0 & E_{11} & 0 \\ 0 & 0 & E_{33} \end{bmatrix} \begin{Bmatrix} \Delta x_1 \\ \Delta x_2 \\ \Delta x_3 \end{Bmatrix} \tag{28}$$

They are replaced by the following quasi-periodic conditions:

- On the top surface, $\Delta\mathbf{u} = \mathbf{u}(x_1, x_2, H) - \mathbf{u}(x_1, x_2, -H)$ and $\Delta\mathbf{x}^T = \{0, 0, 2H\}$ so that:

$$\begin{cases} \Delta u_1 = 4E_{31}H \\ \Delta u_2 = 0 \\ \Delta u_3 = 2E_{33}H \end{cases} \tag{29}$$

- On the plane Ox_2x_3,

$$u_1(0, x_2, x_3) = 0 \tag{30}$$

- On the lateral surface ($x_1^2 + x_2^2 = L^2$, $-H \leq x_3 \leq H$) multi-point constraints are imposed so that the nodes lying on a semi-circle remain on a semi-circle of radius consistent with the prescribed value of E_{11}. Let $\mathbf{u}^{\text{ref}}$ be the displacement of some reference node on the semi-circle at some height x_3, say $\mathbf{x}^T = \{L, 0, x_3\}$ and $\Delta\mathbf{u} = \mathbf{u}(x_1, x_2, x_3) - \mathbf{u}^{\text{ref}}$, then:

$$\begin{cases} \Delta u_1 = E_{11}(x_1 - L) \\ \Delta u_2 = E_{11}x_2 \\ \Delta u_3 = 0 \end{cases} \tag{31}$$

To simulate coalescence states whereby rigid zones preclude lateral straining we take $E_{11} = 0$, hence $U_1 = 0$. Under such circumstances, conditions (31) state that the circles move rigidly.

In theory, the quasi-periodic boundary conditions are most simply defined by (29)–(31). In practice, however, it is of interest to employ only a quarter of the cell to further reduce the computation time. The corresponding boundary conditions have been worked out by [25] for an tetragonal cell and have been adapted to the cylindrical cell as detailed in Appendix C. In a given calculation the displacements U_3 and U_{t} are imposed and assigned values to cause plastic strains that are large enough compared with elastic strains (see [27, 32] for further details). The ratio between the shear and normal stresses is governed by the U_{t}/U_3 ratio.

For each choice of the pair $(\chi,\ W)$ the critical stress values are, in principle, determined in a *single-step* calculation. The time step needs to be large enough to ensure that the limit load is reached. In practice, this is achieved within the first few increments (5 to 10) of the loading step. The absolute values of U_3 and U_{t} have no effect on the critical stress values.

The critical conditions on the stresses for attainment of the limit load are insensitive to the height H of the cell, hence to λ. For this reason, H is adjusted so as to reduce computational cost. On the other hand, the height H must be large enough to guarantee the possible presence of rigid zones above and below the void[3]. In most cases, the void fully fits into the unit cell when the cell aspect ratio λ is taken as unity. Yet, for some (χ, W) pairs, the void would protrude, and thus λ ought to take other values. Different λ ratios were thus adopted for varying (χ, W) pairs, as shown in Table 1. For each (χ, W) pair, 18 different displacement ratios were imposed, obeying the relation $U_{\text{t}}/U_3 = k/2$, where $k = 0, 2, 3, ..., 10, 20, 30, 40, 80, 120, 160, 200$. A larger U_{t}/U_3 ratio induces a smaller ratio $\Sigma_{33}^{\text{coal}}/\Sigma_{31}^{\text{coal}}$ of the stresses at coalescence and vice versa (note that $\Sigma_{31} = 0$ for $U_{\text{t}}/U_3 = 0$).

Figure 3 shows two typical meshes, used for a void aspect ratio $W = 0.5$ and two values of the ligament parameter $\chi = (0.4, 0.6)$. Each mesh consists of 20-node quadratic brick elements with reduced integration

[3]Also noteworthy is that the rigid zones above and below the void ought to be large enough to set grounds for localization to occur in the x_1 – x_2 plane, referred to as "internal necking", as assumed in the present work. If the void is very close to the top (and bottom) surfaces of the unit cell, coalescence occurs in the x_2 – x_3 plane (primarily named as a "necklace-type" coalescence by [33]), which is out of the scope of this investigation.

W	χ	λ
0.1	0.4	0.5
0.1	0.6	0.5
1.5	0.4	1.2
1.5	0.6	1.5
2.0	0.4	1.6
2.0	0.6	2.0
2.5	0.4	2.0
2.5	0.6	2.5
3.0	0.4	2.4
3.0	0.6	3.0

Table 1: $W - \chi$ values used in the cell model calculations having $\lambda \neq 1$.

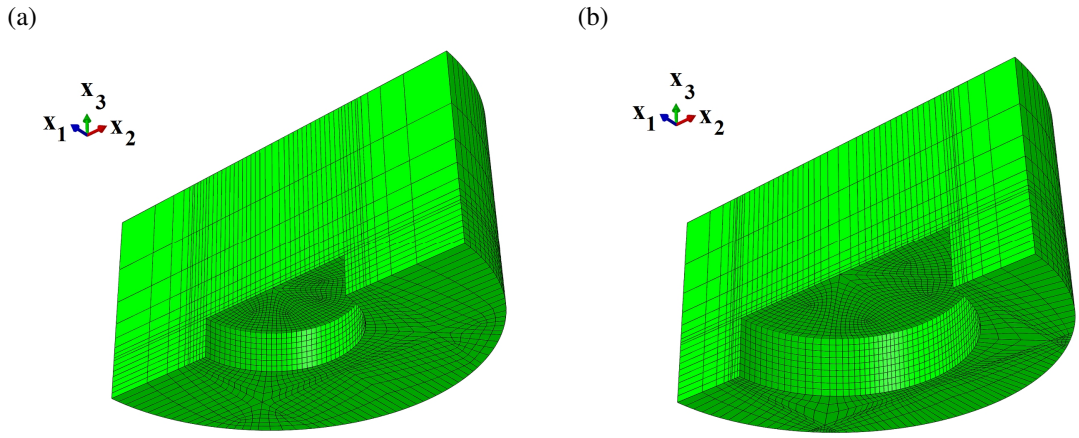

Figure 3: Typical meshes used for $W = 0.5$ and: (a) $\chi = 0.4$, (b) $\chi = 0.6$.

(C3D20R in the ABAQUS element library). A coarser mesh is utilized outside the ligament where the behavior is quasi-rigid. Some calculations have been performed with both C3D8, as in [27], and C3D20R elements types. Differences were small, but C3D20R elements were found to provide more accurate results with fewer elements.

Average stresses over the cell are defined as usual, $\Sigma_{ij} = (1/\Omega) \int_{\Omega-\omega} \sigma_{ij} \, \mathrm{d}V$ with Ω and ω denoting the volumes of the cell and the void, respectively, as before. These average stresses are computed using the discretized formula:

$$\Sigma_{ij} = \sum_{n=1}^{N} \sum_{m=1}^{M} (\sigma_{ij})_n^m v_n^m \tag{32}$$

where N is the total number of elements, M the number of Gauss points per element (here $M = 8$), and $v_n^m = V_n^m/\Omega$ the volume fraction assigned to integration point m within element n. The components of interest are Σ_{33} and Σ_{31}, all others either are zero or do not affect the limit load in the coalescence regime.

4 Results and Discussion

4.1 Upper-Bound versus Approximate Yield Loci

Representative yield loci corresponding to the upper-bound criterion (19) are shown in Fig. 4 as solid lines for several values of the (χ, W) pair. The porosity in the band takes on values between $f_{\rm b} = 0.0625$ and 0.36

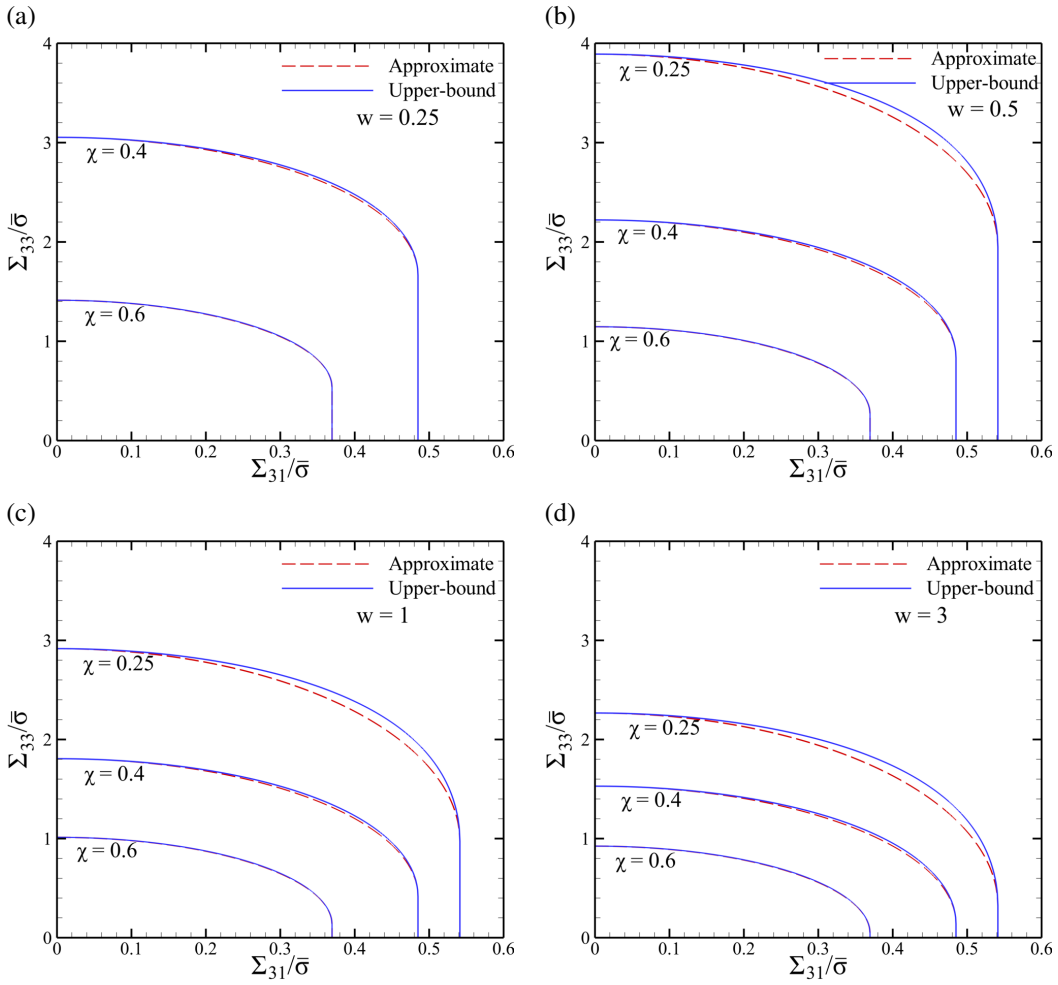

Figure 4: Effective yield loci in the Σ_{33}–Σ_{31} plane – comparison between the upper-bound estimate and its approximate counterpart (as derived in [28]) for several microstructural parameters (χ, W).

for the extreme cases shown of $\chi = 0.25$ and 0.6, respectively. Corresponding values of the total porosity fall between $f \approx 0.004$ and ≈ 0.2 depending on the void aspect ratio and taking $\lambda = 1$ where appropriate. Previous work in the literature shows that for $\chi < 0.2$, yield loci given by (19) are unlikely to be physical, because strain concentration within the intervoid ligaments does not occur [3]. In such cases, Gurson-like potentials are more likely to prevail. The case $\chi = 0.25$ is not shown in Figs.4a,b because for flat voids and $\chi < 0.3$ coalescence is unlikely (see Table 1 in [3]). In all, the vertical straight parts represent the singular portions of the yield loci. Such parts are not physical, as they follow from considering discontinuous trial velocity fields. They occupy an increasingly small portion as χ increases so that the criterion resembles more and more an elliptic one in the space of normal and shear stresses.

For comparison, the approximate yield loci of [28] defined by (21) are also shown dashed in Fig. 4. The singular parts are common to both models. The predictions differ only on the regular curved parts. While

the upper-bound preserving curve is invariably exterior to the elliptic approximation, the two evaluations are always close to each other, especially for larger values of χ. The key observation, therefore, is that the elliptic approximation is quite good over a wide range of internal parameters.

The fact that both models lead to very close predictions can be rationalized as follows. As mentioned above, the two models share the same singular parts; in particular the end points (for $\Sigma_{33} = \Sigma^{\rm surf}$) are the same in the two models; also see Appendix B. Furthermore, the two criteria meet on the Σ_{33} axis, that is in the absence of shear. (Although not obvious, this property is demonstrated in Appendix A; its basic explanation lies in the fact that approximation (13) becomes exact for $D_{31} = 0$). In short, because both loci must meet at the intersections as well as on the Σ_{33} axis, and because they are both convex, they must lie quite close to each other.

4.2 Comparison with Numerical Results

Figure 5 depicts contours of equivalent plastic strain at the onset of localization obtained in the finite element simulations, for two (χ, W) pairs and various values of shear- to normal-strain ratios. The figure illustrates that plastic deformation is diffuse in the plastically-deformable ligament, and it spreads over part of the ligament (a–d) or its entirety (e,f). In the mathematical model, however, it has been presumed that the whole ligament yields, which leads to an overestimation of the limit load. Hence, the analytical model preserves the upper-bound character. Moreover, plastic strains are negligible in the region above the void for all tension-shear combinations. This supports the underlying assumption of rigidity within the parts located above and below the ligament in developing the model (see Fig. 1).

Figure 6 shows the comparison between the cell-model calculations (points) and the upper-bound yield criterion (19) for various combinations of χ and W. Other numerical results were obtained but they are not shown for brevity. It is thus verified that the yield locus predicted by the model is always exterior to that determined numerically. In addition, the predicted locus is reasonably close to the exact one considering the fact that the model does not involve any adjustable parameter. This is especially true for void aspect ratios about unity or larger. However, differences may be noted in the some cases. For instance, in the limit $W \to 0$ of a penny-shape crack, the predicted coalescence stress in the absence of shear wrongly diverges, although not shown in Fig. 6 The singular behavior of the model in this limit has been discussed previously. The corresponding coalescence mechanism is arguably not by internal necking. In this case, modeling the localization would require adopting a thickness of the localization band larger than that of the void, which is nil in this case [34]. Also, for small shear to normal stress ratios, differences are larger for smaller values of χ. For large shear to normal stress ratios, differences are larger for larger values of W, irrespective of χ. It is also worth noting that the predictions could hardly be improved in the pure shear case with ($W = 0.5$, $\chi = 0.4$) or the pure tension case with ($W = 3$, $\chi = 0.6$) without using overly sophisticated velocity fields.

We emphasize that the presence of flat parts in the yield loci near the horizontal axis is a direct consequence of considering discontinuous trial velocity fields in the limit-analysis. Hence, they are not physical. This does not prevent the analytical and numerical criteria to be close to each other in this region. Note that in the absence of shear the improved model of [15], which was based on continuous velocity fields, provides tighter upper bounds for several combinations of the internal parameters.

4.3 Modified Model

The discrepancies with respect to numerical results motivate a heuristic modification of the original model. The main discrepancies occur in two distinct cases, both of some practical importance: (i) very flat voids under conditions of dominant tension; (ii) very elongated voids under conditions of dominant shear. Some improvements have been proposed to remedy these aspects in the context of an approximate model [28]. The same is attempted here for the upper-bound model. Such a heuristic modification unavoidably destroys the

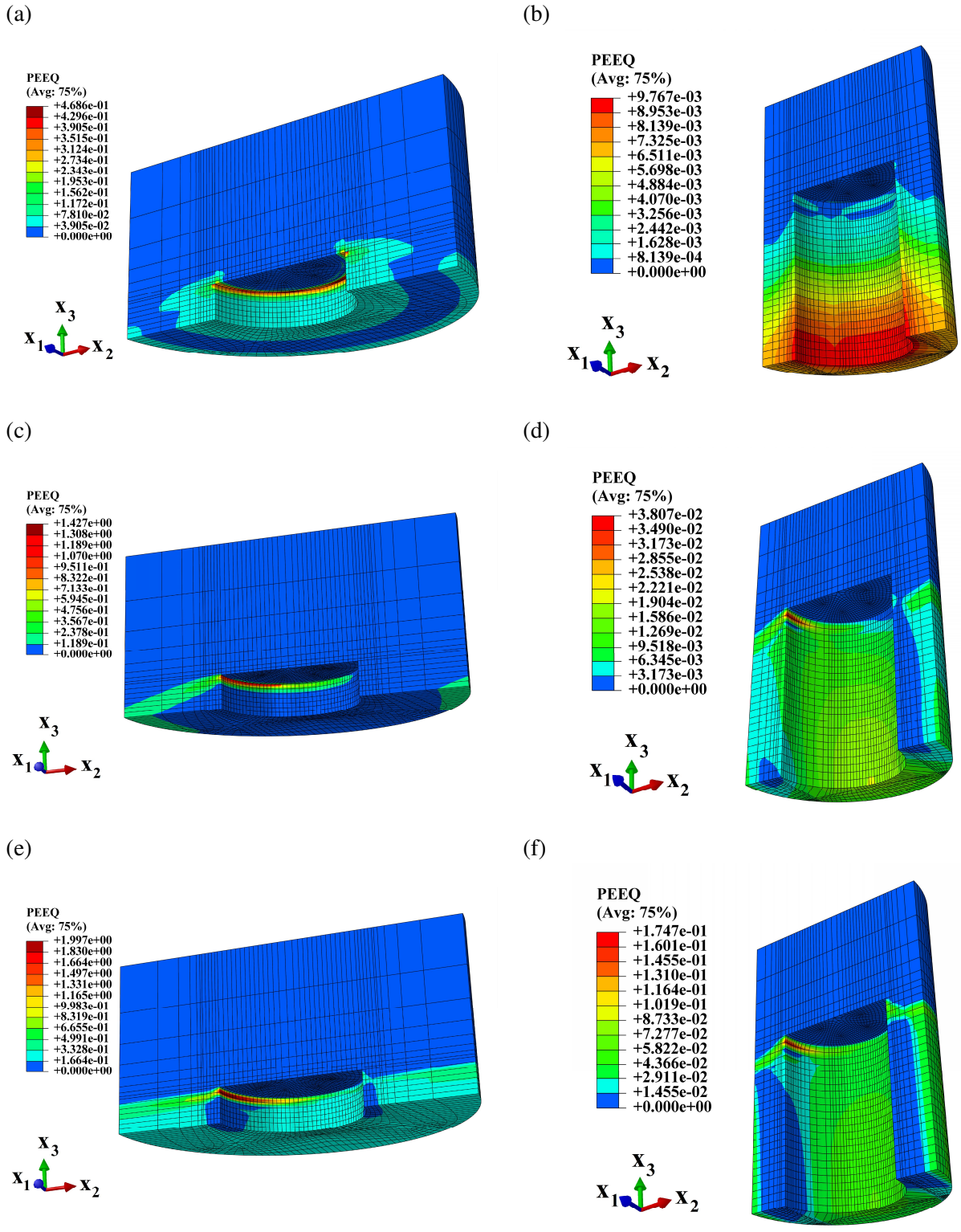

Figure 5: Examples of equivalent plastic strain distributions on initial configurations at the onset of internal necking localization, for: (a,b) $U_t/U_3 = 0$ (zero shear) and $(\chi, W) = \{(0.4, 0.5), (0.6, 3.0)\}$, (c,d) $U_t/U_3 = 5$ (intermediate shear) and $(\chi, W) = \{(0.4, 0.5), (0.6, 3.0)\}$, (e,f) $U_t/U_3 = 20$ (near-extremum shear) and $(\chi, W) = \{(0.4, 0.5), (0.6, 3.0)\}$.

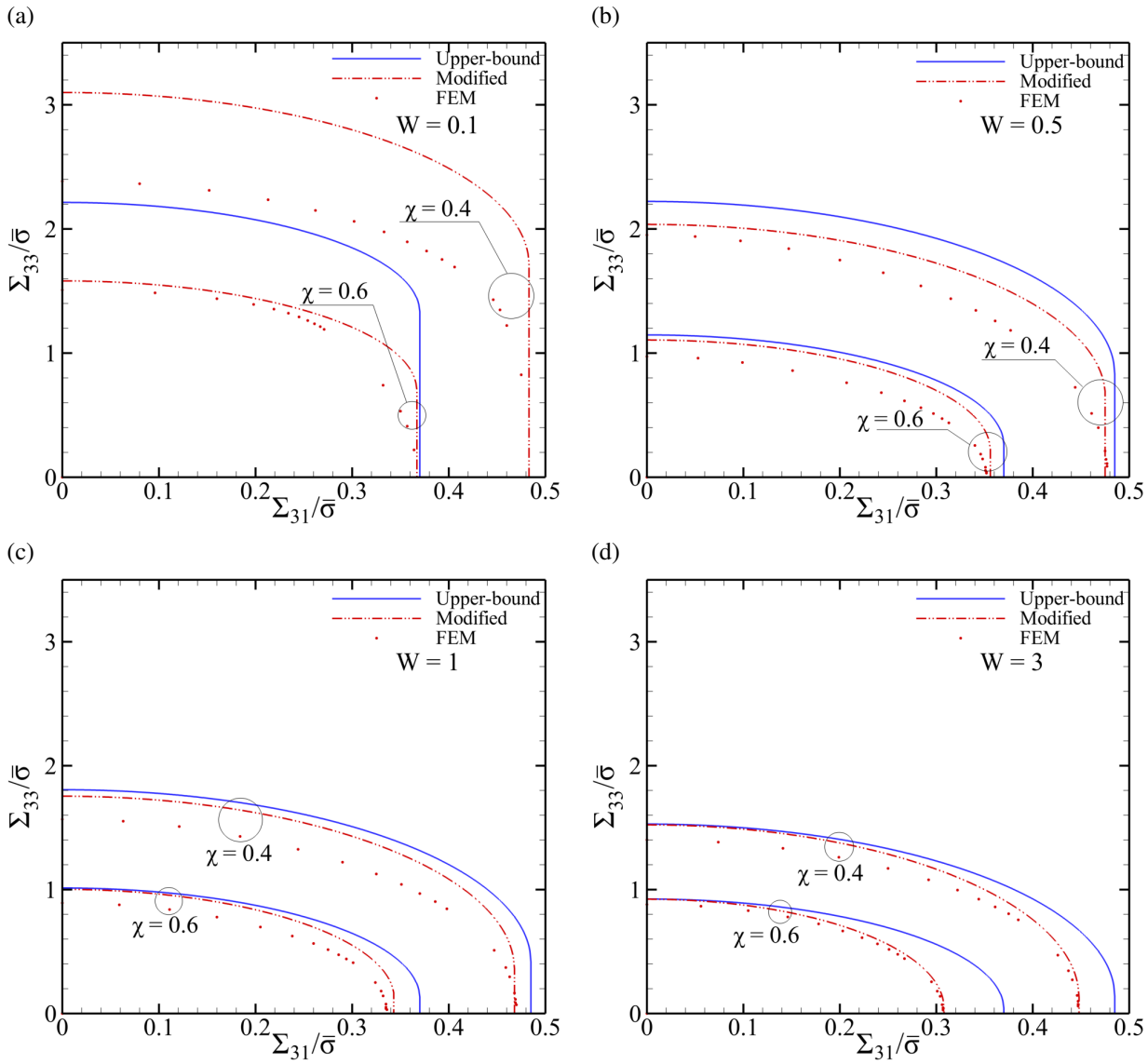

Figure 6: Comparison between the upper bound model (solid lines), modified model (dashed) and numerical yield loci (points) for void coalescence under combined tension and shear, for various values of microstructural parameters W and χ. The modification (described in Section 4.3) is made to improve the results for very oblate ($W \longrightarrow 0$) and very prolate ($W \longrightarrow \infty$) cavities.

rigorous upper-bound character of the model. Again, however, the main implications of this modification are only for extremely flat voids in tension and elongated voids in shear.

Following the procedure explained in Appendix D, the derived criterion is modified as follows:

$$\Phi(\boldsymbol{\Sigma};\chi,W)=\begin{cases}\dfrac{\mathcal{B}^2}{\bar{\tau}^2}+2f_{\mathrm{b}}\cosh\left[\dfrac{|\Sigma_{33}|-t\Sigma^{\mathrm{surf}}}{\bar{\tau}}-\sqrt{3\dfrac{\mathcal{B}^2-\left(\Sigma_{31}/l\right)^2}{\bar{\tau}^2}}\right]-(1+f_{\mathrm{b}}^2) & \text{for } |\Sigma_{33}|\geq t\Sigma^{\mathrm{surf}}\\ \left(\dfrac{\Sigma_{31}}{l\mathcal{T}}\right)^2-1 & \text{for } |\Sigma_{33}|\leq t\Sigma^{\mathrm{surf}}\end{cases} \tag{33}$$

where

$$\frac{\mathcal{B}^2}{\bar{\tau}^2}=\frac{5}{3}+\chi^4-\frac{2}{3}\sqrt{4+12\chi^4-3\left(\frac{\Sigma_{31}}{l\bar{\tau}}\right)^2} \tag{34}$$

and t and l are parameters that can be adjusted on the basis of the cell model calculations of Section 3. Formulae for these quantities, as functions of the internal parameters, are presented in Appendix D. The basic idea is to employ a homographic function of W for t so as to eliminate the singular behavior in the limit of penny-shaped cracks, and a corrective bilinear function for l to improve the prediction for shear loading of elongated voids.

The example yield loci shown below are intended to compare the modified yield criterion with FEM results, as well as assess its putative upper-bound character. Figure 6 illustrates this comparison for various values of χ and W. The calibrated loci for Figs. 6c and 6d may be compared to Figs. 4c and 4d, respectively, to assess the effect of large values of W on the maximum shear stress at coalescence. The largest difference between the modified model and the numerical results is obtained for very flat voids ($W=0.1$) but only for $\chi=0.4$, Fig. 6a. The proposed heuristic correction performs much better for larger values of χ. More elaborate choices for the correction functions are possible, albeit at the expense of simplicity.

5 Concluding Remarks

An upper-bound model of dilatant plasticity has been developed based on limit analysis of a cylindrical elementary cell. The model consists of an effective yield criterion that is appropriate to the regime of void coalescence in materials failing by ductile damage accumulation. Incidentally, the model is also applicable to porous media with periodic distribution of pores, as in some cellular structures. In all applications, the model would represent certain portions of the yield locus and should be supplemented with a model that appropriately represents other portions where plasticity cannot be confined to intervoid ligaments. This results in a hybrid multi-surface approach [35]. Alternatively, [36] have recently developed a unified upper-bound model that describes both void growth and coalescence in the absence of shear. Their approach can be extended to account for shear effects.

In practice, the model can be used in two ways. If there is a finite set of localization planes, such as for periodic or clustered void distributions, then the coalescence criterion (19) may be checked, as is, on as many localization planes as dictated by the underlying void distribution. In this case, an anisotropic void growth model must be used prior to coalescence, e.g. [37, 38]. In such a hybrid multi-surface approach, some approximations would be necessary to account for the different elementary cells used prior to and after coalescence. To this end, the model should also be extended to include evolution equations of the state variables, notably to describe void rotation under shear-dominated loadings. Such work is underway and will be reported elsewhere. On the other hand, if the void distribution is considered as random then an isotropic version of the model may be developed by probing all possible angles in the orientation space [19]. In this case, an isotropic void growth model, such as Gurson's, may be used prior to void coalescence.

The trial velocity fields used in the limit analysis are not as sophisticated as those recently considered by [15] or [29]. However, they present the considerable advantage of enabling an upper-bound result to be derived in closed form.

To further assess the model, cell-model calculations of a new type have been carried out using special boundary conditions, termed quasi-periodic as they simulate rigorous periodicity. The availability of such computational results made it possible to unequivocally validate the model as well as an earlier version that did not preserve the upper-bound character. The major conclusions are as follows:

- The present findings remedy for the uncertainties associated with the model recently derived by [28] from two perspectives: (i) the mathematical approximation involved in the homogenization procedure is relaxed, so that the new model now preserves the rigorous upper-bound character; (ii) the numerical results used for validation of the model are carried out for a cell identical to that considered in its derivation. Although the new model is more complex than the previous one, it remains fully explicit (the yield criterion is still expressed in explicit, not parametric form).

- Salient features of the new model include the following: (i) The planar (singular and non-physical) parts apparent in the approximate effective yield locus of [28] are identically retrieved in the new model. The curved (regular) parts, however, are exterior to their approximate counterparts; (ii) The transition between the two planar and curved zones is devoid of any corners; (iii) All parameters defining the yield surface are functions of the microstructural variables χ (ligament parameter) and W (void aspect ratio).

- The availability of the upper-bound solution allows to check that the approximation previously introduced by [28] did not introduce important errors.

- The discrepancies that were noted in the previous work between the approximate model and numerical results cannot be attributed to the uncontrolled approximation used, nor to the difference between the elementary cells used. Instead, the gap between analytical and numerical results can only follow from the choice of trial velocity fields. The quality of the estimate derived with the velocity fields chosen here may be improved using the kind of heuristic fit described in the paper.

- A heuristic modification to the model was proposed on the basis of the numerical results in order to better predict the onset of coalescence in practical applications. The modifications are two-fold. First, a correction is proposed in the limit of penny-shaped cracks, which reduces to the correction proposed by [28] in the absence of shear loading. Second, a correction is introduced in the case of elongated voids under shear-dominated loading.

Acknowledgments

MT and AAB acknowledge support from the National Science Foundation under Grant Number CMMI-1405226. JBL acknowledges financial support from Institut Universitaire de France (IUF).

Appendix A Singular parts of the yield surface

The primitive definition of the reversibility domain $\mathscr{C}$ in (3) writes:

$$\boldsymbol{\Sigma} \in \mathscr{C} \Leftrightarrow \forall\, \mathbf{D}, \quad \boldsymbol{\Sigma} : \mathbf{D} \leq \Pi \tag{A-1}$$

Considering (17) and the non-zero components of $\mathbf{D}$, it may be recast as:

$$\forall D_{33}, D_{31}, \quad \Sigma_{33}D_{33} + 2\Sigma_{31}D_{31} \leq \frac{\bar{\sigma}|\bar{D}|}{\sqrt{3}} \left[\zeta \sinh^{-1}(\zeta u) - \sqrt{\frac{1}{u^2} + \zeta^2} \right]_1^{1/\chi^2} + \Sigma^{\text{surf}}|D_{33}| \qquad \text{(A-2)}$$

with $\bar{D}$ defined by (14) and $\zeta = D_{33}/|\bar{D}|$. Focussing on non-negative values of D_{31} only, (A-2) is rewritten as:

$$\forall D_{33}, \forall D_{31} \geq 0, \quad -\Pi(D_{33}, D_{31}) \leq \Sigma_{33}D_{33} + 2\Sigma_{31}D_{31} \leq \Pi(D_{33}, D_{31}) \qquad \text{(A-3)}$$

where use has been made of (A-2) for the pair $(-D_{33}, -D_{31})$ and of the fact that Π is an even function. Inequalities (A-3) are equivalent to some condition $\Phi(\Sigma_{33}, \Sigma_{31}) \leq 0$ where Φ is the sought yield function. Since Π is positively homogeneous of degree 1, (A-3) may be written in terms of the ratio $p = D_{33}/D_{31}$ as:

$$\forall p \in \mathbb{R}, \quad -g(p) \leq f(p) \leq g(p) \qquad \text{(A-4)}$$

where the functions f and g are defined on $\mathbb{R}$ by:

$$f(p) = \Sigma_{33}p + 2\Sigma_{31}$$

$$g(p) \equiv \Pi(p, 1) = \bar{\sigma}\sqrt{\frac{3p^2+4}{3}} \left[\frac{p}{\sqrt{3p^2+4}} \sinh^{-1}\left(\frac{pu}{\sqrt{3p^2+4}} \right) - \sqrt{\frac{1}{u^2} + \frac{p^2}{3p^2+4}} \right]_1^{1/\chi^2} + \Sigma^{\text{surf}}|p| \qquad \text{(A-5)}$$

In writing (A-5) use has been made of the relationship:

$$p = \frac{2\zeta}{\sqrt{1-3\zeta^2}} \qquad \text{(A-6)}$$

The function g is convex, admits a minimum $g(0) = 2\mathcal{T}$, its graph has an angular point at its minimum, and admits straight asymptotes of slope $\pm\bar{\sigma}\left[\frac{1}{\sqrt{3}} \sinh^{-1}\left(\frac{u}{\sqrt{3}} \right) - \sqrt{\frac{1}{u^2} + \frac{1}{3}} \right]_1^{1/\chi^2} + \text{sgn}(D_{33})\Sigma^{\text{surf}}$ for $p \to \pm\infty$; see Fig. A-1a.

The yield surface is the boundary of the reversibility domain, now defined by (A-4). As such, the yield locus is the envelope of the straight lines $q = f(p)$ lying between the graphs of the functions $q = -g(p)$ and $q = g(p)$ and meeting one of them at some point, Fig. A-1c. To construct this locus, we only consider loadings with $\Sigma_{31} \geq 0$ due to point symmetry about the origin, and implement a graphical solution as follows.

Two cases are analyzed separately depending on the magnitude of the normal stress. Consider first the case $|\Sigma_{33}| \leq g'(0^+) = \Sigma^{\text{surf}}$. As illustrated in Fig. A-1a, the slope of the straight line $q = f(p)$ is smaller than that of the curve $q = g(p)$ at the origin so that the two curves do not cross each other provided that $f(0) \leq g(0)$, i.e. that $\Sigma_{31} \leq \mathcal{T}$. In this case, therefore, the yield condition is that $\Sigma_{31} = \mathcal{T}$, which is a constant (Fig. A-1b). The same condition holds for $g'(0^-) < \Sigma_{33} < 0$ by considering the intersections of lines $q = f(p)$ having negative slopes with the appropriate branches of the representative curves of the functions $g(p)$ and $-g(p)$.

Next, for $|\Sigma_{33}| \geq \Sigma^{\text{surf}}$ there must be a condition on the shear stress Σ_{31} in terms of Σ_{33} for the stress state to lie on the yield surface. Given Σ_{33}, the value of Σ_{31} must be smaller than that which makes the line $q = f(p)$ tangent to the curve $q = g(p)$ (Fig. A-1c). Only in this case would the condition $f(p) \leq g(p)$ be ensured for every p. Finding the yield point $(\Sigma_{33}, \Sigma_{31})$ then amounts to determining the value of p for which there is tangency. The derivation is quite involved and was illustrated by [28] in the case of the approximate dissipation $g(p)$. It is emphasized that in this case the dissipation function is differentiable and the procedure

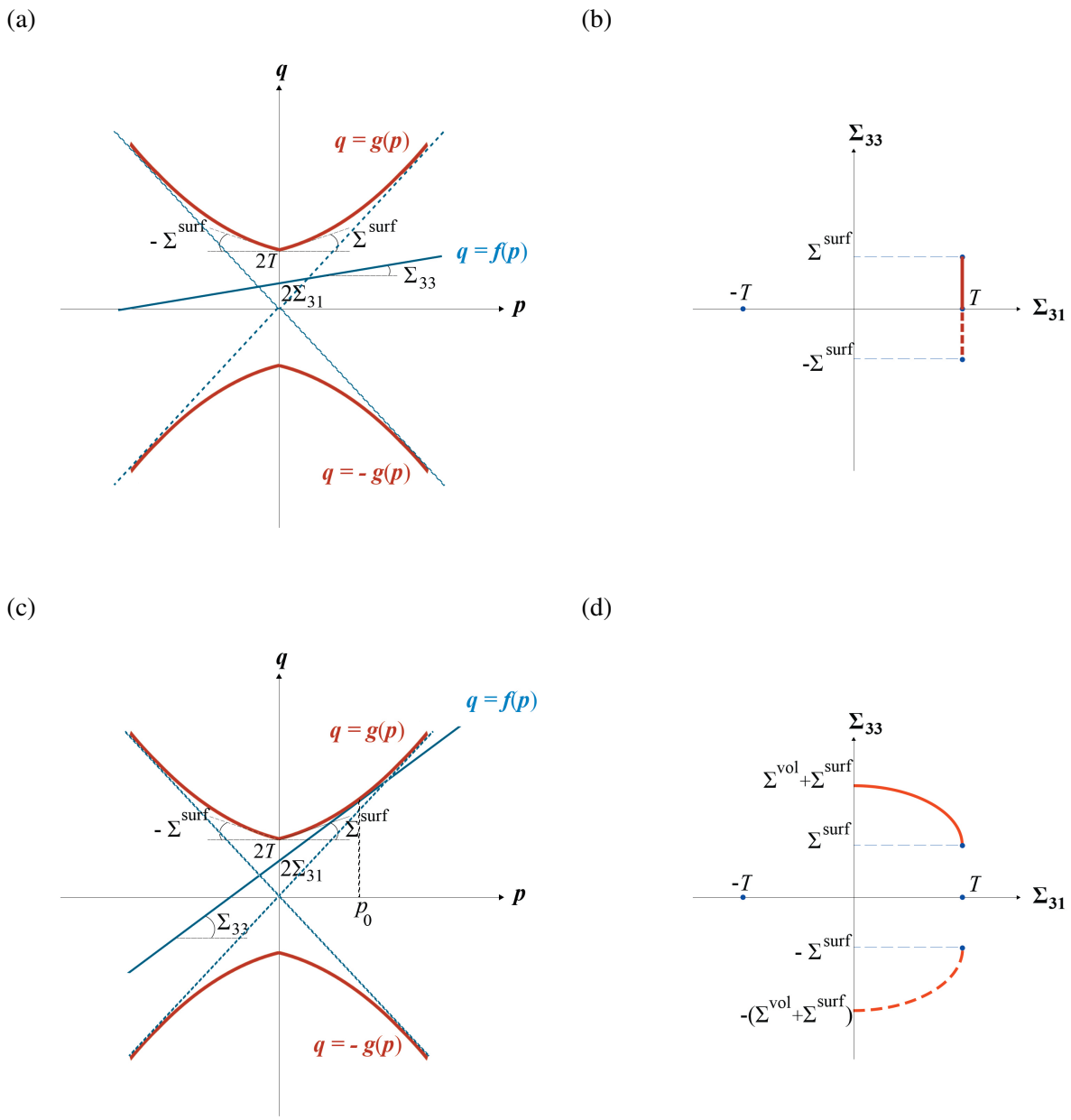

Figure A-1: Construction of the yield locus by a graphical method. (a) Illustration of inequalities (A-4) for $|\Sigma_{33}| \leq \Sigma^{\text{surf}}$; (b) corresponding (singular) part of yield locus. (c) Illustration for $|\Sigma_{33}| \geq \Sigma^{\text{surf}}$; (d) corresponding (regular) part of yield locus.

leads to a locus exactly given by (B-13). Fig. A-1d depicts the corresponding (regular) curved portion of the yield locus. For completeness, the portion corresponding to negative slopes of the line $q = f(p)$ is shown dashed in the figure.

Remark 1: In absence of shear Eq. (B-13), or equivalently Eq. $(19)_1$, predicts a limit load equal to

$\Sigma^{\rm surf}+\Sigma^{\rm vol}$, which is the same value as that obtained by [14]. Indeed, setting $\Sigma_{31}=0$ in $(19)_1$ one gets:

$$\frac{\mathcal{B}^2}{\bar{\tau}^2}=\frac{5}{3}+f_{\rm b}^2-\frac{4}{3}\sqrt{1+3f_{\rm b}^2}=\frac{1}{3}(\sqrt{1+3f_{\rm b}^2}-2)^2 \tag{A-7}$$

which, after plugging in the yield function gives:

$$\begin{aligned}
&\cosh\left(\frac{|\Sigma_{33}|-\Sigma^{\rm surf}}{\bar{\tau}}-\sqrt{3}\frac{\mathcal{B}}{\bar{\tau}}\right)=\mathcal{C}\quad,\quad \mathcal{C}=\frac{1+f_{\rm b}^2-(\mathcal{B}/\bar{\tau})^2}{2f_{\rm b}}=\frac{2\sqrt{1+3f_{\rm b}^2}-1}{3f_{\rm b}}\\
&\text{hence } \mathcal{C}^2-1=\frac{1}{3}\left(\frac{2-\sqrt{1+3f_{\rm b}^2}}{f_{\rm b}}\right)^2\\
&\frac{|\Sigma_{33}|-\Sigma^{\rm surf}}{\bar{\tau}}-\sqrt{3}\frac{\mathcal{B}}{\bar{\tau}}=\cosh^{-1}\mathcal{C}=\ln\left(\mathcal{C}+\sqrt{\mathcal{C}^2-1}\right)=\ln\frac{1+\sqrt{1+3f_{\rm b}^2}}{3f_{\rm b}}\\
&\Longrightarrow \frac{|\Sigma_{33}|}{\bar{\tau}}=\frac{\Sigma^{\rm surf}}{\bar{\tau}}+2-\sqrt{1+3f_{\rm b}^2}+\ln\frac{1+\sqrt{1+3f_{\rm b}^2}}{3f_{\rm b}}\equiv\frac{\Sigma^{\rm surf}}{\bar{\tau}}+\frac{\Sigma^{\rm vol}}{\bar{\tau}}
\end{aligned} \tag{A-8}$$

Remark 2: The upper-bound and approximate yield criteria given by Eqs (19) and (21), respectively, give the same yield condition in the absence of shear. In other words the loci meet on the Σ_{33} axis. This property follows from the fact that approximation (13) is exact for $D_{31}=0$. Upon examination of the two criteria, Eqs (19) and (21), this seems strikingly surprising. Nevertheless, it was shown above that (19) does lead to $\Sigma_{33}=\Sigma^{\rm surf}+\Sigma^{\rm vol}$ when $\Sigma_{31}=0$ although $\Sigma^{\rm vol}$ does not appear explicitly in (19). Obviously, this result is easier to establish by starting from the expression of the total dissipation. Indeed, if one sets $D_{31}=0$ or equivalently $\zeta=1/\sqrt{3}$ in equation (17) then one gets:

$$\begin{aligned}
\frac{\Sigma_{33}-\Sigma^{\rm surf}}{\bar{\sigma}}&=\left[\frac{1}{\sqrt{3}}\sinh^{-1}\left(\frac{u}{\sqrt{3}}\right)-\sqrt{\frac{1}{u^2}+\frac{1}{3}}\right]_1^{1/\chi^2}=\frac{1}{\sqrt{3}}\left[2-\sqrt{1+3\chi^4}+\ln\frac{1+\sqrt{1+3\chi^4}}{3\chi^2}\right]\\
&=\frac{\Sigma^{\rm vol}}{\bar{\sigma}}
\end{aligned} \tag{A-9}$$

where use has been made of the identity: $\sinh^{-1}(x)=\ln\left(x+\sqrt{x^2+1}\right)$ and that the left-hand side of the above equation is nothing but $\Pi^{*\rm vol}/D_{33}$ in the absence of shear.

Remark 3: The transition from the regular (curved) part to the singular (straight) part occurs without any vertex as shown by [28]. A geometric proof of this property was provided by [36]. So is the case because the first derivative of Φ with respect to Σ_{31} from Eq. $(19)_1$ would become unbounded at $\Sigma_{31}=\mathcal{T}$ or, equivalently, its derivative with respect to Σ_{33} would vanish as follows. Letting $(|\Sigma_{33}|,|\Sigma_{31}|)=(\Sigma^{\rm surf},\mathcal{T})$ would give:

$$\begin{aligned}
&\frac{\mathcal{B}^2}{\bar{\tau}^2}=\frac{5}{3}+f_{\rm b}^2-\frac{2}{3}\sqrt{4+12f_{\rm b}^2-3(1-f_{\rm b})^2}=f_{\rm b}^2-2f_{\rm b}+1=(1-f_{\rm b})^2\\
&\text{hence } 3\frac{\mathcal{B}^2-\Sigma_{31}^2}{\bar{\tau}^2}=(1-f_{\rm b})^2-(1-f_{\rm b})^2=0 \text{ and } \frac{|\Sigma_{33}|-\Sigma^{\rm surf}}{\bar{\tau}}-\sqrt{3\frac{\mathcal{B}^2-\Sigma_{31}^2}{\bar{\tau}^2}}=0\\
&\Longrightarrow \frac{\partial\Phi}{\partial\Sigma_{33}}=\frac{\partial}{\partial\Sigma_{33}}\left(\frac{\mathcal{B}^2}{\bar{\tau}^2}\right)+2f_{\rm b}\frac{\rm sgn(\Sigma_{33})}{\bar{\tau}}\sinh\left(\frac{|\Sigma_{33}|-\Sigma^{\rm surf}}{\bar{\tau}}-\sqrt{3\frac{\mathcal{B}^2-\Sigma_{31}^2}{\bar{\tau}^2}}\right)=0
\end{aligned} \tag{A-10}$$

This demonstrates that the yield locus is devoid of any corners.

Appendix B Regular parts of the yield surface

On these, the dissipation function is differentiable so that equation (5) may be used. Since Π is positively homogeneous of degree 1, $\partial\Pi/\partial\mathbf{D}$ is positively homogeneous of degree 0, i.e. $(\partial\Pi/\partial\mathbf{D})(\alpha\mathbf{D}) = (\partial\Pi/\partial\mathbf{D})(\mathbf{D})$, where α is an arbitrary positive real number. By way of consequence, $\partial\Pi/\partial\mathbf{D}$ depends only on the ratio D_{31}/D_{33} of the two independent components of $\mathbf{D}$. This ratio can then, in principle, be eliminated between the two parametric equations of the yield locus; see [4] for generalities.

In practice, however, there arises the difficulty that the obtained expression (17) involves a different ratio, ζ, of D_{33} to the composite strain-rate measure $\bar{D}$. Hence, proceed as follows. From (5) and using the variables $(D_{33}, \bar{D})$ in lieu of (D_{33}, D_{31}) obtain the nonzero stress components as:

$$\begin{aligned}\Sigma_{33} &= \frac{\partial\Pi}{\partial D_{33}} = \frac{\partial\Pi^{*\mathrm{vol}}}{\partial D_{33}} + \frac{\partial\Pi^{*\mathrm{vol}}}{\partial\bar{D}}\frac{\partial\bar{D}}{\partial D_{33}} + \mathrm{sgn}(D_{33})\,\Sigma^{\mathrm{surf}} \\ \Sigma_{31} &= \frac{1}{2}\frac{\partial\Pi}{\partial D_{31}} = \frac{1}{2}\frac{\partial\Pi^{*\mathrm{vol}}}{\partial\bar{D}}\frac{\partial\bar{D}}{\partial D_{31}}\end{aligned} \tag{B-1}$$

where the factor 1/2 in the second equation is due to the fact that D_{31} appears in fact twice in the actual dissipation function, as D_{31} and D_{13}. In (B-1) appear stress-like auxiliary variables $\mathcal{A}$ and $\mathcal{B}$:

$$\begin{aligned}\mathcal{A} &\equiv \frac{\partial\Pi^{*\mathrm{vol}}}{\partial D_{33}} = \frac{\bar{\sigma}}{\sqrt{3}}\left[\sinh^{-1}(\zeta u)\right]_1^{1/\chi^2} \\ \mathcal{B} &\equiv \frac{\partial\Pi^{*\mathrm{vol}}}{\partial\bar{D}} = -\mathrm{sgn}(\bar{D})\frac{\bar{\sigma}}{\sqrt{3}}\left[\sqrt{\frac{1}{u^2}+\zeta^2}\right]_1^{1/\chi^2}\end{aligned} \tag{B-2}$$

which have just been evaluated using the volume term of (17). Hence (B-1) may be rewritten as:

$$\begin{aligned}\Sigma_{33} &= \mathcal{A} + 3\,\mathrm{sgn}(\bar{D})\zeta\mathcal{B} + \mathrm{sgn}(D_{33})\,\Sigma^{\mathrm{surf}} \\ \Sigma_{31} &= \mathrm{sgn}(\bar{D}D_{31})\sqrt{1-3\zeta^2}\,\mathcal{B}\end{aligned} \tag{B-3}$$

Relations (B-3) represent parametric equations of the yield surface. Elimination of ζ leading to an explicit relationship between stress components Σ_{33} and Σ_{31} is somewhat tedious. Its three main steps are summarized below.

First, the definitions of $\mathcal{A}$ and $\mathcal{B}$ are, in fact, a short-cut towards such an elimination process. Indeed, expanding (B-2)$_1$ and (B-2)$_2$, taking the cosh of both sides of (B-2)$_1$, then simplifying leads to:

$$\begin{aligned}\chi^2\cosh\left(\sqrt{3}\,\frac{\mathcal{A}}{\bar{\sigma}}\right) &= \sqrt{1+\zeta^2}\sqrt{\chi^4+\zeta^2} - \zeta^2 \\ \sqrt{3}\,\frac{|\mathcal{B}|}{\bar{\sigma}} &= \sqrt{1+\zeta^2} - \sqrt{\chi^4+\zeta^2}\end{aligned} \tag{B-4}$$

Taking the square in (B-4)$_2$ then permits to eliminate ζ; the following relationship is then obtained in terms of the auxiliary variables $\mathcal{A}$ and $\mathcal{B}$:[4]

$$\left(\sqrt{3}\frac{\mathcal{B}}{\bar{\sigma}}\right)^2 + 2\chi^2\cosh\left(\sqrt{3}\,\frac{\mathcal{A}}{\bar{\sigma}}\right) - (1+\chi^4) = 0 \tag{B-5}$$

Second, to obtain the explicit yield criterion, the quantities $\mathcal{A}$ and $\mathcal{B}$ need to be replaced with Σ_{33} and Σ_{31} in (B-5). A useful intermediate result obtained from (B-4) is

$$1-\chi^2\cosh\left(\sqrt{3}\,\frac{\mathcal{A}}{\bar{\sigma}}\right) = 1+\zeta^2-\sqrt{1+\zeta^2}\sqrt{\chi^4+\zeta^2} = \sqrt{3}\,\frac{|\mathcal{B}|}{\bar{\sigma}}\sqrt{1+\zeta^2} \tag{B-6}$$

[4]These steps are similar to those followed in a "modern" derivation of the Gurson model, e.g. [4].

Taking the squares of (B-3)$_2$ and (B-6), one gets

$$\left(\frac{\Sigma_{31}}{\bar{\sigma}}\right)^2 = 4\left(\frac{\mathcal{B}}{\bar{\sigma}}\right)^2 - \left[1-\chi^2\cosh\left(\sqrt{3}\frac{\mathcal{A}}{\bar{\sigma}}\right)\right]^2 \tag{B-7}$$

where ζ is no longer present. Using then equation (B-5) one obtains:

$$\left(\frac{\Sigma_{31}}{\bar{\sigma}}\right)^2 = 4\left(\frac{\mathcal{B}}{\bar{\sigma}}\right)^2 - \frac{1}{4}\left[1-\chi^4+\left(\sqrt{3}\frac{\mathcal{B}}{\bar{\sigma}}\right)^2\right]^2, \tag{B-8}$$

which is a quadratic equation in $(\mathcal{B}/\bar{\sigma})^2$. Discarding the largest root by noting that $(\sqrt{3}\mathcal{B}/\bar{\sigma})^2 \leq (1-\chi^2)^2 < 1$ from (B-5), we retain the solution:

$$\left(\sqrt{3}\frac{\mathcal{B}}{\bar{\sigma}}\right)^2 = \frac{5}{3}+\chi^4-\frac{2}{3}\sqrt{4+12\chi^4-3\left(\sqrt{3}\frac{\Sigma_{31}}{\bar{\sigma}}\right)^2} \tag{B-9}$$

where the $\sqrt{3}$ factors are introduced to evidence the yield stress in shear $\bar{\tau} \equiv \bar{\sigma}/\sqrt{3}$.

Third, to obtain $\mathcal{A}$ note that by (B-3)$_2$,

$$(\zeta\mathcal{B})^2 = \frac{1}{3}(\mathcal{B}^2-\Sigma_{31}^2) \tag{B-10}$$

Hence (B-3)$_1$ yields:

$$\mathcal{A} = \Sigma_{33} - \mathrm{sgn}(D_{33})\,\Sigma^{\mathrm{surf}} - \mathrm{sgn}(\zeta\mathcal{B}\bar{D})\sqrt{3(\mathcal{B}^2-\Sigma_{31}^2)} \tag{B-11}$$

Now $\mathrm{sgn}(\zeta) = \mathrm{sgn}(D_{33}) = \mathrm{sgn}(\bar{D})$ by definition; hence $\mathrm{sgn}(\zeta\mathcal{B}\bar{D}) = \mathrm{sgn}(\mathcal{B})$. Furthermore it follows from (B-2)$_2$ that $\mathrm{sgn}(\mathcal{B}) = \mathrm{sgn}(\bar{D}) = \mathrm{sgn}(D_{33})$. Finally $\mathrm{sgn}(D_{33}) = \mathrm{sgn}(\Sigma_{33})$ since all three terms in the right-hand side of (B-3)$_1$ have the sign of $\bar{D}$ or D_{33}. Hence (B-11) may be rewritten as

$$\begin{aligned}\mathcal{A} &= \Sigma_{33} - \mathrm{sgn}(\Sigma_{33})\,\Sigma^{\mathrm{surf}} - \mathrm{sgn}(\Sigma_{33})\sqrt{3(\mathcal{B}^2-\Sigma_{31}^2)} \\ &= \mathrm{sgn}(\Sigma_{33})\left[|\Sigma_{33}| - \Sigma^{\mathrm{surf}} - \sqrt{3(\mathcal{B}^2-\Sigma_{31}^2)}\right]\end{aligned} \tag{B-12}$$

Using (B-5), one thus gets the equation of the regular parts of the yield surface in the form:

$$\Phi = \left(\sqrt{3}\,\frac{\mathcal{B}}{\bar{\sigma}}\right)^2 + 2\chi^2\cosh\left[\sqrt{3}\left(\frac{|\Sigma_{33}|-\Sigma^{\mathrm{surf}}}{\bar{\sigma}} - \sqrt{\left(\sqrt{3}\,\frac{\mathcal{B}}{\bar{\sigma}}\right)^2 - \left(\sqrt{3}\,\frac{\Sigma_{31}}{\bar{\sigma}}\right)^2}\right)\right] - (1+\chi^4) = 0 \tag{B-13}$$

where the quantity $\mathcal{B}^2$ is related to Σ_{31} by (B-9).

In the limit $\chi \to 1$, $\Sigma_{33} = \Sigma_{31} = 0$; indeed $\mathcal{A}$ and $\mathcal{B}$ must be zero by (B-5); then $\Sigma_{31} = 0$ by (B-9), so that by (B-12), $\Sigma_{33} = \mathrm{sgn}(\Sigma_{33})\,\Sigma^{\mathrm{surf}} = 0$ by (10). Also, it can be checked that the points $(\Sigma_{31} = \pm\mathcal{T}, \Sigma_{33} = \pm\Sigma^{\mathrm{surf}})$, which lie at the intersections of the straight singular parts and curved regular parts, do satisfy criterion (B-13). Indeed, in such cases $\sqrt{3}|\mathcal{B}|/\bar{\sigma} = \sqrt{3}|\Sigma_{31}|/\bar{\sigma} = 1-\chi^2$.

Appendix C Quasi-Periodic Boundary Conditions on the Unit Cell

The boundary conditions imposed on a quarter of the unit cell are expounded here. The normal and tangential displacements are the two independent degrees of freedom at each center-line. Fig. C-1 shows the various

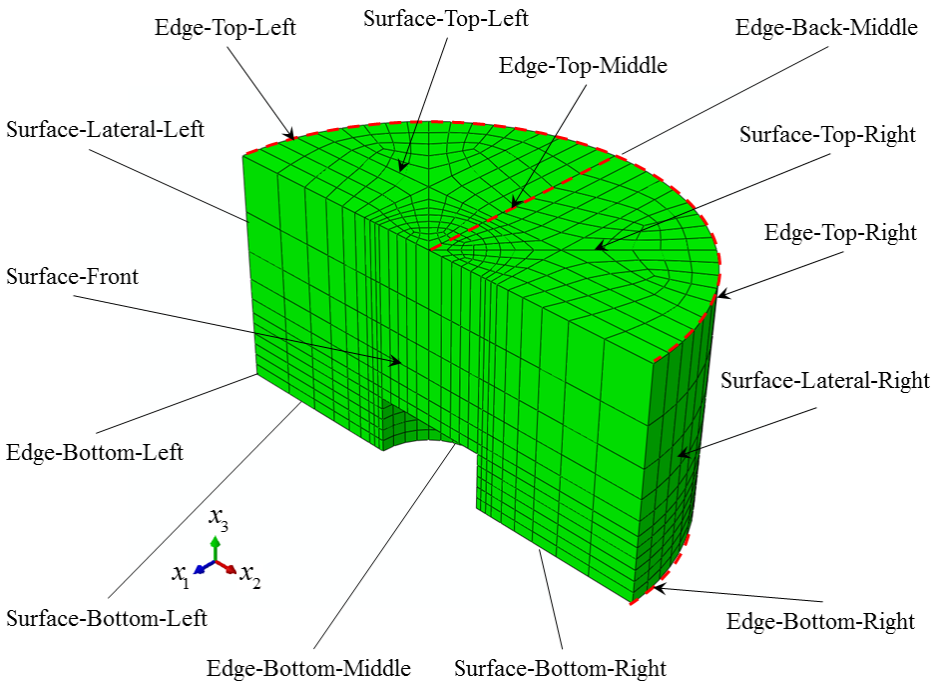

Figure C-1: Finite element mesh for one quarter of an example unit cell with microstructural parameters given as $(\chi, W) = (0.25, 1.0)$, accompanied by the nomenclature used to define various surfaces and edges to which the boundary conditions are imposed. The origin of the reference coordinate system stands at the void center in the undeformed configuration.

surfaces and edges of the computational domain, together with an example mesh as well as the nomenclature used.

Edge-Top-Middle

$$\begin{aligned} u_2(x_1, 0, H) &= \frac{1}{2}U_t, \\ u_3(x_1, 0, H) &= \frac{1}{2}U_3. \end{aligned} \tag{C-1}$$

Surface-Top-Left/Surface-Top-Right

$$\begin{aligned} u_1(x_1, -x_2, H) - u_1(x_1, x_2, H) &= 0, \\ u_2(x_1, -x_2, H) + u_2(x_1, x_2, H) &= U_t, \\ u_3(x_1, -x_2, H) + u_3(x_1, x_2, H) &= U_3. \end{aligned} \tag{C-2}$$

Edge-Top-Left/Edge-Top-Right

$$\begin{aligned} u_1(x_1, -\sqrt{L^2 - x_1^2}, H) &= u_1(x_1, \sqrt{L^2 - x_1^2}, H) = \frac{x_1}{2L}U_1, \\ u_2(x_1, \pm\sqrt{L^2 - x_1^2}, H) &= \frac{1}{2}(U_t \pm \frac{\pm\sqrt{L^2 - x_1^2}}{L}\, U_2), \\ u_3(x_1, \pm\sqrt{L^2 - x_1^2}, H) &= \frac{1}{2}U_3. \end{aligned} \tag{C-3}$$

Surface-Lateral-Left/Surface-Lateral-Right

$$\begin{aligned} u_1(x_1,-\sqrt{L^2-x_1^2},x_3)=u_1(x_1,\sqrt{L^2-x_1^2},x_3) &= \frac{x_1}{2L}U_1, \\ u_2(x_1,-\sqrt{L^2-x_1^2},x_3)-u_2(x_1,\sqrt{L^2-x_1^2},x_3) &= -\frac{\sqrt{L^2-x_1^2}}{L}\,U_2, \\ u_3(x_1,-\sqrt{L^2-x_1^2},x_3)-u_3(x_1,\sqrt{L^2-x_1^2},x_3) &= 0. \end{aligned} \tag{C-4}$$

Edge-Bottom-Left/Edge-Bottom-Right

$$\begin{aligned} u_1(x_1,-\sqrt{L^2-x_1^2},0) &= u_1(x_1,\sqrt{L^2-x_1^2},0)=\frac{x_1}{2L}U_1, \\ u_2(x_1,\pm\sqrt{L^2-x_1^2},0) &= \pm\frac{\sqrt{L^2-x_1^2}}{2L}\,U_2, \\ u_3(x_1,\pm\sqrt{L^2-x_1^2},0) &= 0. \end{aligned} \tag{C-5}$$

Edge-Bottom-Middle

$$\begin{aligned} u_2(x_1,0,0) &= 0, \\ u_3(x_1,0,0) &= 0. \end{aligned} \tag{C-6}$$

Surface-Bottom-Left/Surface-Bottom-Right

$$\begin{aligned} u_1(x_1,-x_2,0)-u_1(x_1,x_2,0) &= 0, \\ u_2(x_1,-x_2,0)+u_2(x_1,x_2,0) &= 0, \\ u_3(x_1,-x_2,0)+u_3(x_1,x_2,0) &= 0. \end{aligned} \tag{C-7}$$

Edge-Back-Middle

$$u_1(-L,0,x_3) = -\frac{1}{2}U_1. \tag{C-8}$$

Surface-Front

$$u_1(0,x_2,x_3) = 0. \tag{C-9}$$

Appendix D Rationale for Heuristic Modification

Criterion $(19)_1$ is modified as follows:

$$\frac{\mathcal{B}^2}{b\bar{\tau}^2}+2f_{\mathrm{b}}\cosh\left[\frac{|\Sigma_{33}|-t\Sigma^{\mathrm{surf}}}{\bar{\tau}}-\sqrt{3\frac{\mathcal{B}^2-\left(\Sigma_{31}/l\right)^2}{\bar{\tau}^2}}\right]-(1+f_{\mathrm{b}}^2)=0 \tag{D-1}$$

where t, b and l are parameters. It is unlikely that constant parameters will fit all purposes. Therefore, t, b and l are considered a priori functions of the internal parameters χ and W. The idea is to obtain the simplest functions that reduce the error between the numerical results and model predictions shown in Fig. 6.

Firstly, parameters t and b are introduced in such a way that the same heuristic modification of [28] is arrived at. There it was shown that a constant value of $b \sim 1$ is appropriate. Also, a homographic function of W was necessary for t in order to remove the singular behavior for $W \to 0$. This behavior manifests in the absence of any shear. The criterion in this case reduces to:

$$\left.\frac{\Sigma_{33}}{\bar{\sigma}}\right|_{\Sigma_{31}=0} = t\Sigma^{\mathrm{surf}} + b\Sigma^{\mathrm{vol}} \tag{D-2}$$

following the same procedure as for obtaining (A-8). The simplest choice for function t is:

$$t(\chi, W) = \frac{(t_0 + t_1\chi)W}{1 + (t_0 + t_1\chi)W} \tag{D-3}$$

where t_0 and t_1 are parameters to be determined on the basis of the numerical results. In doing so, we improve upon the proposal of [28] by limiting the heuristic modification to the range $\chi \geq 0.2$ and taking $t(\chi, W) = t(0.2, W)$ for $\chi < 0.2$ so that the exact limit $\Sigma_{33} \to \infty$ is retained for $\chi \to 0$. The choice of parameters $t_0 = -1.3$, $t_1 = 20.6$ and $b = 1.0$ proves quite good.

Secondly, parameter l aims at reducing the error in the case of prolate voids under shear-dominated loadings. Indeed, the modified criterion (D-1) reduces to $\Sigma_{31} = l(W, \chi)\mathcal{T}$ in pure shear. The fact that l should depend on W is easily inferred from the computational results. The simplest possible form for $l(W, \chi)$ is a bi-linear function (again for $\chi \geq 0.2$ only):

$$l(\chi, W) = \left[1 + (l_1\chi + l_0)W\right]\mathcal{T} \tag{D-4}$$

The results shown in Fig. 6 were obtained using the choice $(l_0, l_1) = (0.035, -0.15)$.

References

[1] A. Pineau, A. A. Benzerga, and T. Pardoen. Failure of metals I. Brittle and Ductile Fracture. *Acta Materialia*, 107:424–483, 2016.

[2] J. Koplik and A. Needleman. Void growth and coalescence in porous plastic solids. *International Journal of Solids and Structures*, 24(8):835–853, 1988.

[3] A. A. Benzerga. Micromechanics of Coalescence in Ductile Fracture. *Journal of the Mechanics and Physics of Solids*, 50:1331–1362, 2002.

[4] A. A. Benzerga and J.-B. Leblond. Ductile fracture by void growth to coalescence. *Advances in Applied Mechanics*, 44:169–305, 2010.

[5] A. A. Benzerga, J.-B. Leblond, A. Needleman, and V. Tvergaard. Ductile Failure Modeling. *International Journal of Fracture*, 201:29–80, 2016.

[6] A. L. Gurson. Continuum Theory of Ductile Rupture by Void Nucleation and Growth: Part I– Yield Criteria and Flow Rules for Porous Ductile Media. *Journal of Engineering Materials and Technology*, 99:2–15, 1977.

[7] F. Fritzen, S. Forest, T. Böhlke, D. Kondo, and T. Kanit. Computational homogenization of elasto-plastic porous metals. *International Journal of Plasticity*, 29:102–119, 2012.

[8] K. Danas and P. Ponte Castañeda. Influence of the Lode parameter and the stress triaxiality on the failure of elasto-plastic porous materials. *International Journal of Solids and Structures*, 49:1325–1342, 2012.

[9] J.R. Rice. The localization of plastic deformation. In W.T. Koiter, editor, *14th int. cong. Theoretical and Applied Mechanics*, pages 207–220. North–Holland, Amsterdam, 1976.

[10] P. F. Thomason. Three–dimensional models for the plastic limit–loads at incipient failure of the inter-void matrix in ductile porous solids. *Acta Metallurgica*, 33:1079–1085, 1985.

[11] A. A. Benzerga, J. Besson, and A. Pineau. Coalescence–Controlled Anisotropic Ductile Fracture. *Journal of Engineering Materials and Technology*, 121:221–229, 1999.

[12] T. Pardoen and J. W. Hutchinson. An extended model for void growth and coalescence. *Journal of the Mechanics and Physics of Solids*, 48:2467–2512, 2000.

[13] M. Gologanu, J.-B. Leblond, G. Perrin, and J. Devaux. Theoretical models for void coalescence in porous ductile solids – I: Coalescence in "layers". *International Journal of Solids and Structures*, 38:5581–5594, 2001.

[14] A. A. Benzerga and J.-B. Leblond. Effective Yield Criterion Accounting for Microvoid Coalescence. *Journal of Applied Mechanics*, 81:031009, 2014.

[15] L. Morin, J.-B. Leblond, and A. A. Benzerga. Coalescence of voids by internal necking: theoretical estimates and numerical results. *Journal of the Mechanics and Physics of Solids*, 75:140–158, 2015.

[16] A. A. Benzerga, J. Besson, and A. Pineau. Anisotropic ductile fracture. Part II: theory. *Acta Materialia*, 52:4639–4650, 2004.

[17] I. Barsoum and J. Faleskog. Rupture mechanisms in combined tension and shear—-Experiments. *International Journal of Solids and Structures*, 44:1768–1786, 2007.

[18] M. Dunand and D. Mohr. Optimized butterfly specimen for the fracture testing of sheet materials under combined normal and shear loading. *Engineering Fracture Mechanics*, 78:2919–2934, 2011.

[19] J.-B. Leblond and G. Mottet. A theoretical approach of strain localization within thin planar bands in porous ductile materials. *Comptes Rendus Mecanique*, 336:176–189, 2008.

[20] I. Barsoum and J. Faleskog. Micromechanical analysis on the influence of the Lode parameter on void growth and coalescence. *International Journal of Solids and Structures*, 48:925–938, 2011.

[21] F. Scheyvaerts, P. R. Onck, C. Tekoğlu, and T. Pardoen. The growth and coalescence of ellipsoidal voids in plane strain under combined shear and tension. *Journal of the Mechanics and Physics of Solids*, 59:373–397, 2011.

[22] V. Tvergaard. Effect of stress-state and spacing on voids in a shear-field. *International Journal of Solids and Structures*, 49:3047–3054, 2012.

[23] K. L. Nielsen, J. Dahl, and V. Tvergaard. Collapse and coalescence of spherical voids subject to intense shearing: studied in full 3D. *International Journal of Fracture*, 177:97–108, 2012.

[24] M. Dunand and D. Mohr. Effect of Lode parameter on plastic flow localization after proportional loading at low stress triaxialities. *Journal of the Mechanics and Physics of Solids*, 66:133–153, 2014.

[25] C. Tekoğlu. Representative volume element calculations under constant stress triaxiality, lode parameter, and shear ratio. *International Journal of Solids and Structures*, 51:4544–4553, 2014.

[26] Z. G. Liu, W. H. Wong, and T. F. Guo. Void behaviors from low to high triaxialities: Transition from void collapse to void coalescence. *International Journal of Plasticity*, 84:183–202, 2016.

[27] C. Tekoğlu, J.-B. Leblond, and T. Pardoen. A criterion for the onset of void coalescence under combined tension and shear. *Journal of the Mechanics and Physics of Solids*, 60:1363–1381, 2012.

[28] M. E. Torki, A. A. Benzerga, and J.-B. Leblond. On Void Coalescence under Combined Tension and Shear. *Journal of Applied Mechanics*, 82(7):071005, 2015.

[29] S. M. Keralavarma and S. Chockalingam. A Criterion for Void Coalescence in Anisotropic Ductile Materials. *International Journal of Plasticity*, 82:159–176, 2016.

[30] I. Barsoum and J. Faleskog. Rupture mechanisms in combined tension and shear—-Micromechanics. *International Journal of Solids and Structures*, 44:5481–5498, 2007.

[31] A. A. Benzerga and J. Besson. Plastic potentials for anisotropic porous solids. *European Journal of Mechanics*, 20A:397–434, 2001.

[32] K. Madou and J.-B. Leblond. Numerical studies of porous ductile materials containing arbitrary ellipsoidal voids — I: Yield surfaces of representative cells. *European Journal of Mechanics*, 42:480–489, 2013.

[33] A. A. Benzerga. *Rupture ductile des tôles anisotropes*. PhD thesis, Ecole Nationale Supérieure des Mines de Paris, 2000.

[34] J. Hure and P. O. Barrioz. Theoretical estimates for flat voids coalescence by internal necking. *European Journal of Mechanics*, 60:217–226, 2016.

[35] A. A. Benzerga, J. Besson, R. Batisse, and A. Pineau. Synergistic effects of plastic anisotropy and void coalescence on fracture mode in plane strain. *Modelling and Simulation in Materials Science and Engineering*, 10:73–102, 2002.

[36] L. Morin, J.-B. Leblond, A. A. Benzerga, and D. Kondo. A unified criterion for the growth and coalescence of microvoids. *Journal of the Mechanics and Physics of Solids*, 97:19–36, 2016.

[37] S. M. Keralavarma and A. A. Benzerga. A constitutive model for plastically anisotropic solids with non-spherical voids. *Journal of the Mechanics and Physics of Solids*, 58:874–901, 2010.

[38] K. Madou and J.-B. Leblond. A Gurson-type criterion for porous ductile solids containing arbitrary ellipsoidal voids – I: Limit-analysis of some representative cell. *Journal of the Mechanics and Physics of Solids*, 60:1020–1036, 2012.

P3 A UNIFIED CRITERION FOR VOID GROWTH AND COALESCENCE UNDER COMBINED TENSION AND SHEAR

A Unified Criterion for Void Growth and Coalescence under Combined Tension and Shear

M. E. Torki
Department of Aerospace Engineering, Texas A&M University, College Station, TX 77843, USA

Abstract

An analytical micromechanics-based yield criterion is developed to describe both void growth and coalescence under combined tension and shear, with smooth transition between growth and coalescence, thus its name *unified*. The model is obtained by limit analysis over a cylindrical elementary cell embedding a coaxial cylindrical void of finite height. The velocity field employed is an extended counterpart of the discontinuous, yet kinematically admissible trial field utilized in a recent work. Plasticity in the deformable matrix is modeled using rate-independent J_2 flow theory, and the effective dissipation function is calculated by exact as well as approximate integration techniques, the latter generating a simpler flow potential. The model is aimed to predict void growth as well as coalescence by internal necking or shearing. The complete yield surface , being function of normal as well as shear stresses, exhibits curved and planar parts signifying void coalescence. The transition between the curved and planar parts is cornerless. The analytical predictions are compared to results of FEM single-step cell-model calculations of limit analysis executed on an identical geometry exposed to quasi-periodic boundary conditions.

Keywords: Ductile fracture; Void growth; Void coalescence; Internal necking; Internal shearing; Rigorous upper-bound character.

1 Introduction

Having been recognized as a driving challenge in solid mechanics, research work on ductile fracture under combined tension and shear has recently received seminal advancement. The paradigm shift in the effective failure mechanism correlates with the prevalence of stress triaxiality or Lode parameter vis-a‘-vis the other. Both experimental results and existing model predictions demonstrate that, from the low-triaxiality (high-ductility) to the high-triaxiality (low-ductility) regime, the failure mechanism switches from void collapse to void growth [1]. Upon favorable conditions, damage in an initially spherical void under a shear-dominated field proceeds up to rotation and eventually closure into a flattened ovalized crack [2, 3, 4, 5]. In a triaxial stress field, however, voids will remain near-spherical. For the latter case, extensions after the seminal work of Gurson (1977) for void growth in plastic solids with finite porosity [6] have established the caliber for decades [7, 8, 9, 10, 11, 12, 13, 14].

The mechanism of void growth in shear was investigated in the pioneering work of Fleck and Hutchinson [15] while failure under the same effect was missing in work of the like. A tentative understanding of the effect of shear on failure of materials has been examined through the third invariant of stress deviator J_3. More exhaustive studies, however, demonstrate that mere consideration of J_3 cannot fully describe the fundamental mechanisms underlying fracture under a combined loading scheme [16, 17]. Failure under the effect of shear should be distinguished from the formation of shear bands. That is, failure in shear is triggered by shear-induced localized deformation, i.e. coalescence in shear, whereas a shear band is a

bifurcation (instability) phenomenon that can happen even in absence of shear [18, 19]. Yet, shear coalescence can happen inside a shear band if there is significant amount of shear acting onto the voids. A considerable fraction of work on ductile failure prediction in porous materials addresses supplementing existing yield criteria, mainly of a Gurson-type identity, with damage models. Amongst the featured models proposed mainly for triaxial and shear-dominated loading conditions are the models proposed by Pardoen and Hutchinson [20] and Nahshon and Hutchinson [21]), respectively. The latter introduced a modified damage parameter (denoting porosity in absence of shear) through the addition of a heuristic function of J_3. This damage parameter, while remaining of a heuristic nature, could not preserve the identity of a physical parameter such as porosity. Morgeneyer and Besson [22] introduced a modified strain rate as function of the Lode parameter based on a Gurson-type yield criterion in order to simulate the transition from flat to shear-induced crack propagation. Other efforts in the same respect have been made by Kadkhodapour *et al.* [23] and Cao *et al.* [24]. Another class of work, including [25], examine failure mechanisms via cell-model evolution analysis. This class of analyses can be considered as benchmark, but are not well suited for parametric studies due to high computational cost. Micro-mechanics-based models are thus more extensively sought. The main body of mathematical models of ductile fracture developed from first principles is representative of a periodic or quasi-periodic medium. The effect of void distribution can be dominant when scaling becomes a matter of prominence. A well-motivated discussion on the effect of void distribution can be found in [26, 27, 5, 28, 29, 30, 31, 32].

In essence, modeling of void coalescence in the existing literature is still in early stages. This can be recognized from the very fact that the majority of existing models pertain to the growth regime, and that the complexities and limitations arising when interpreting coalescence as a strain localization phenomenon [33] would further complicate the modeling technique in that established homogenization methods relying on clear separation of scales will be rather idealistic [34]. Yet, the use of an elementary cell, by no means representative of the whole domain, proves efficacious in that volumetric averaging and the Hill–Mandell lemma remain valid in all deformation processes [35]. While void growth correlates with plastic flow being diffuse in the matrix, ultimate failure subsequent to the onset of coalescence can occur only if plastic flow localizes in the inter-void ligament. [1]

Existing mathematical models accounting for void growth are both well-established and sophisticated. Rather, void coalescence models lie in a hue of empiricism. Following the pioneering work of Thomason [36], it was only Benzerga [34] who extended the applicability of Thomason's model into penny-shaped cracks characterized by aspect ratios close to nil. Then, without any more advanced models introduced from first principles, Pardoen and Hutchinson [20] proposed a better heuristic micro-mechanics-based void coalescence model to mimic ductile fracture under triaxial loading. Over a decade past, Tekoglu *et al.* [37] extended the realm of Thomason's and Benzerga's models into combined tension and shear. It remained for Benzerga and Leblond [38], Torki *et al.* [39, 40], and also Morin *et al.* to develop void coalescence models from first principles until [14] introduced a model for void growth accompanied by void coalescence in a unified perspective.

Altogether, the first class of porous plasticity models account for the post-coalescence process via the heuristic introduction of a porosity acceleration factor, without the physics underlying the process being known [7, 14]. In a second class of models, void growth and coalescence are founded on intrinsic yield criteria. Mathematical models for both processes are carried out through limit analysis. In doing so, void growth and coalescence models, distinguished as being diffuse and localized, can be derived either independently and combined in a hybrid approach or based on the same velocity fields in a unified fashion. There are pros and cons associated with the hybrid perspective, considering different cell-level geometries before

[1] So is the case when void distorsion occurs due to void growth or rotation, and even for other sources of failure such as mechanical instability or the like. In the latter, coalescence may not directly be triggered at local failure, but is mainly characteristic of ultimate failure.

and after the onset of coalescence. Among its notable virtues is better coincidence with numerical results. Nevertheless, a hybrid model exhibits corners on its corresponding yield surface, as schematized in Fig. 1a, which constitutes some undesirable features from a computational viewpoint. See [11, 12, 13] for further illustrations. Fig. 1 depicts an example hybrid model invoking the Keralavarma-Benzerga and Torki *et al.* [11, 39] models before and after coalescence, respectively, in comparison to a unified model with seamless transition between void growth and coalescence. Corresponding stress-strain behavior curves have also been schematized in Fig. 1b highlighting the smooth progression into the post-coalescence deformation process.

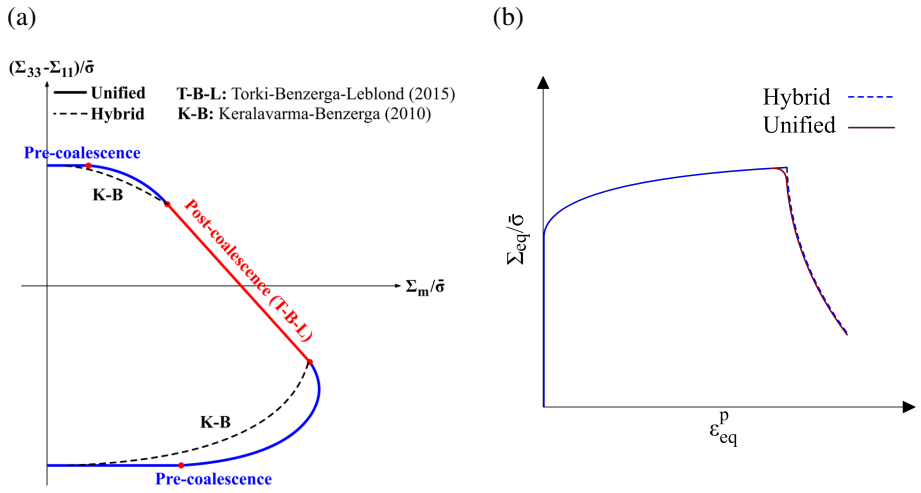

Figure 1: (a) Schematic unified yield locus (as developed for zero shear stress by Morin *et al.* [14]) as compared with a hybrid locus (exemplified by the Keralavarma-Benzerga model [11] for void growth and the T-B-L model [39] for coalescence) for specific microstructural parameters as defined in 2.1; (b) schematic stress-strain curves in an arbitrary evolution problem corresponding to a hybrid and a unified model.

Morin *et al.* [14] were the first to propose a unified model, who extended the work of Benzerga and Leblond [38] to derive the first analytical model accounting for both the growth (among weakly interacting voids) and coalescence of voids (among strongly interacting voids) but only under triaxial loading. Following [14], the aim of the present work is to extend that model into combined triaxial and shear loadings from the same unified perspective. Neglecting the effect of shear would not only lose one remarkable ingredient within the consitutive framework in presence of significant shear stresses but also dramatically overestimate strain to failure even at the limit of randomly distributed voids [41]. The present work, therefore, tends to develop a model that can describe the whole process from void growth to coalescence under *arbitrary* loading conditions. The effect of shearing might sound trifling at first sight. However, as adduced by algebraic details in Sec. 2.7, it adds significant complexities to the model both in its parametric form and in the final closed-form solution. The effect of shear stress manifests in elaborate coupled form within all subfunctions of the yield surface that cannot be attained by mere addition or multiplication to the model in absence of a shear-induced term. Moreover, it leads to an extra singularity within the model that cannot be realized by simply appending Morin *et al.*'s model with the coalescence function in [40]. This singular part constitutes a plane, rather than a line, that signifies the stresses' correlation within the flow potential under shear-dominated loads. The model explicitly involves the normal, lateral, and shear stresses rather than implicitly through nondimensional loading indicators (as within the work of Keralavarma [41]). Last but not least, the model accounts for the effects induced by all independent parameters that uniquely define the microstructural geometry, including void and cell shape effects. Within the present modeling framework, the applications would pertain to the ductile failure of metals (where the microstructure continuously

evolves while the average porosity will remain small to moderate [42]) and even in polymers (where the microstructure can remain fixed but the porosity may increase drastically [43]).

Meanwhile, steps to and results of limit analysis cell-model calculations with quasi-periodic boundary conditions representing axisymmetric superimposed by shear loading, corresponding to a cell with the same geometry, are presented. More details on imposition of periodic boundary conditions on the unit cell are explained in Appendix C. The results of this section are utilized for assessment of the as-derived model with numerical results. Of particular consequence is that FEM unit cell calculations — with no direct recourse to trial velocity fields — would exhibit curved and flat zones [33, 14]. These distinct parts correspond, respectively, to plastic flow occurring either filling across the matrix or localized through the intervoid ligaments, the latter representing coalescence of internal necking/shearing. Hence, normality plays a crucial role in determining the orientation of the parts corresponding to coalescence. Nevertheless, this attribute is disregarded in Gurson's extensions in a sense that uniform boundary conditions are assumed regardless of the stress and microstructural state.

2 Problem Statement

2.1 Elementary (unit) cell

Earlier models of failure in ductile metals were developed for voids isolated in an infinite medium ([44, 45, 46], which would render the so-called *porosity* zero. All later studies, however, have incorporated the effect of a finite porosity by identifying a reference (elementary) cell containing (normally) one or (generally) several voids. This approach would enable scale transitions from micro scale to macro scale whereby the macroscopic response can be explicitly expressed in terms of some (nondimensional) microstructural parameters related to the relative arrangement of voids.

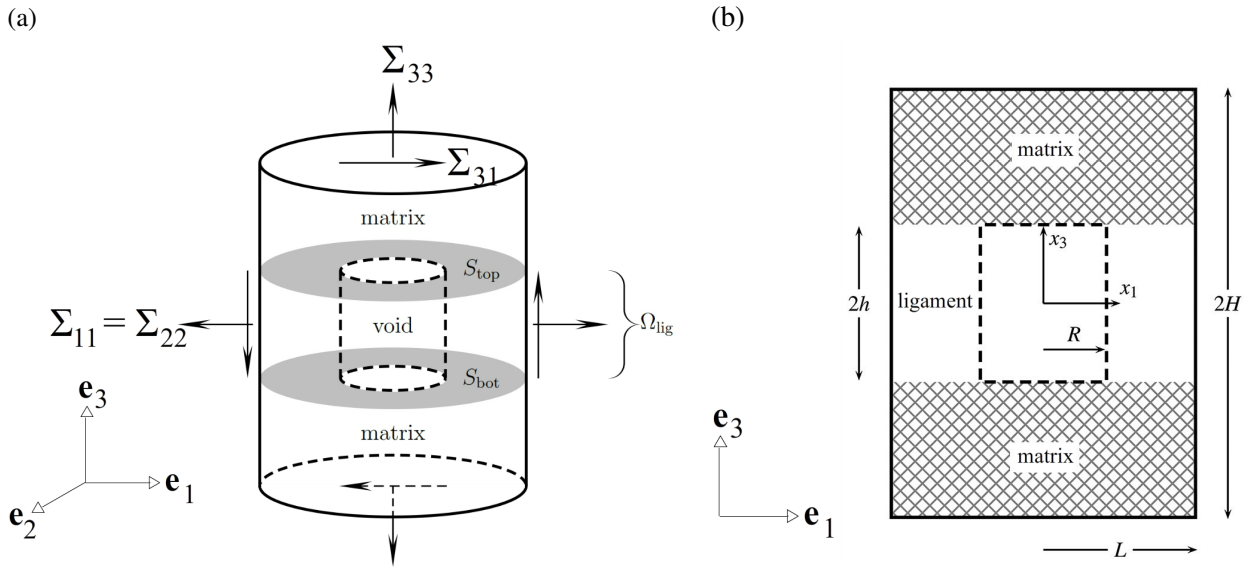

Figure 2: (a) Geometry of a cylindrical cell under a combined loading scheme. (b) Cell parameters.

The microstructural geometry is identified through the definition of an elementary cell, also known as *unit cell*, chosen as schematically shown in Fig. 2 [39, 14]. The latter was first propounded by Benzerga and Leblond [38] which, by its very nature, has supplied a totally analytical upper-bound coalescence model

for the first time with the given velocity field. The elementary volume Ω is a cylindrical cell embedding a coaxial cylindrical void ω, acted upon by macroscopic axial and lateral tensions as well as a macroscopic shear stress as outlined in Fig. 2a. Despite its being not space filling, the given cell stands as a reasonable approximation of more complex geometries in periodic media, *e.g.* a circumscribing hexagonal-prismatic or a square-prismatic cell [2]. Apart from that, Morin *et al.* [33] have found the effect of void shape on the yield surface to be minimal for a given void aspect ratio.

The overall geometry of the cell is determined by the following independent dimensionless parameters:

$$W = \frac{h}{R}, \quad \chi = \frac{R}{L}, \quad \lambda = \frac{H}{L}, \tag{1}$$

defined as the void aspect ratio, the ligament parameter, and the cell aspect ratio, respectively. The local orthonormal basis associated with cylindrical coordinates r, θ, z is denoted as $(\mathbf{e}_r, \mathbf{e}_\theta, \mathbf{e}_z)$, with its global counterpart associated with Cartesian coordinates x_1, x_2, x_3 denoted as $(\mathbf{e}_1, \mathbf{e}_2, \mathbf{e}_3)$, with $\mathbf{e}_3 \equiv \mathbf{e}_z$. Without loss of generality, $\mathbf{e}_r$ and $\mathbf{e}_1$ are directed along the applied shear stress at will. As such, the applied tensile stresses will be represented by Σ_{33} and Σ_{11}, and the only nonzero shear component will be Σ_{31}. Note that, in presence of shear, the $\Sigma_{11} = \Sigma_{22}$ assumption does not hold. This would bare no consequence in the coalescence regime (since the coalescence criterion, as seen in Sec. 2.7.3, is independent of Σ_{11} and Σ_{22}). In the void growth regime, however, this premise is an approximation that warrants assessment against FEM results (Sec. 3.1).

Recent studies demonstrate that geometry can induce a significant effect on the limit load value [47] [3]. Yet, regardless of the employed cell geometry, the effective yield surface derived based on homogenization over a unit cell will be exterior to its FEM counterpart unless the employed approximations are way erroneous or the analytical velocity fields are too simplistic [33, 37, 39].

As discussed more thoroughly in Section 2.4, due to void growth being allowed along the radial and axial directions, the matrix materials (circumscribing above and below the void) and the ligament are both plastically deformable, admitting the J_2 flow theory. However, as soon as *void coalescence* initiates, the matrix layers will turn into rigid due to an elastic unloading running through them (see 2.4) as the strains localize within the central ligament [48, 2, 5]. The interfaces between the matrix layers and ligament are denoted $S_{\rm top}$ and $S_{\rm bot}$ (Fig. 2a) and their union $S_{\rm int}$.
The following auxiliary parameters will be used in the sequel:

$$\begin{aligned} f_{\rm b} &\equiv \frac{\omega}{\Omega_{\rm lig}} = \frac{R^2}{L^2} = \chi^2 \\ c &\equiv \frac{\Omega_{\rm lig}}{\Omega} = \frac{h}{H} = \frac{W\chi}{\lambda} \\ f &\equiv \frac{\omega}{\Omega} = c f_{\rm b} \end{aligned} \tag{2}$$

where the domain and its volume are identified for convenience. $f_{\rm b}$ is the porosity in the central porous ligament, c is the volume fraction of the ligament, and f is the overall porosity, which will not directly enter into the yield criterion due to the existence of matrix layers, underlying that the *ligament porosity* is the effective porosity in our formulation.

[2] Apropos of being truly representative of voids in various orientations, however, the unit cell obviously cannot be representative of the real medium as is. However, the predictive capability of the cell can be well extended to slanted and/or elongated voids by identifying an equivalent microstructure where the slanted void is taken equivalent to a coaxial cylinder with its radius being the projection of the slanted void onto the plane of localization. The promising capability of this scheme has been successfully envisaged in the research work that has been carried out after this work.

[3] In particular, Mbiakop *et al.* [47] have observed that the hydrostatic stress is overestimated, esp. at larger porosities, with a cylindrical unit cell utilized.

2.2 Matrix Plasticity Model

Plastic flow in the matrix (in fact in $\Omega \setminus \omega$) is assumed to obey the J_2 flow theory. Hence, yielding occurs along with the following condition being met at every possible point of the material:

$$\begin{aligned} &\phi(\boldsymbol{\sigma}) = \sigma_{\mathrm{eq}}^2 - \bar{\sigma}^2 = 0 \\ &\sigma_{\mathrm{eq}} \equiv \sqrt{\frac{3}{2}\sigma'_{ij}\sigma'_{ij}}\,; \quad \sigma'_{ij} \equiv \sigma_{ij} - \frac{1}{3}\sigma_{kk}\delta_{ij} \end{aligned} \tag{3}$$

with the associated flow rule

$$\begin{aligned} &d_{ij} = \frac{3}{2}\frac{d_{\mathrm{eq}}}{\bar{\sigma}}\,\sigma'_{ij} \\ &d_{\mathrm{eq}} \equiv \sqrt{\frac{2}{3}d_{ij}d_{ij}} \end{aligned} \tag{4}$$

where σ_{eq} and d_{eq} denote the von Mises equivalent stress and equivalent strain rate, respectively. Criterion (3) is characteristic of the boundary of the microscopic reversibility domain $\mathcal{C}$ involved in (7) [38].

2.3 Limit analysis

The first and foremost feature of the so-called unified model is a generally nonzero value of $D_{11} = D_{22}$, the equality being due to the axial symmetry in the geometry of the unit cell. Therefore, the rate of work associated with the plastic rate of deformation under the macroscopically-applied stress field takes the following form:

$$\begin{aligned} \boldsymbol{\Sigma} : \mathbf{D} &= 2\Sigma_{11}D_{11} + \Sigma_{33}D_{33} + 2\Sigma_{31}D_{31} \\ &\equiv (\Sigma_{11})(3D_m) + (\Sigma_{33} - \Sigma_{11})(D_{33}) + (\Sigma_{31})(2D_{31}) \\ &\equiv \bar{\Sigma}_1\bar{D}_1 + \bar{\Sigma}_2\bar{D}_2 + \bar{\Sigma}_3\bar{D}_3 \end{aligned} \tag{5}$$

The absence of Σ_{21} (as the out-of-plane shear stress) is mainly because the shearing process is taken to happen in the $\mathbf{e}_1$–$\mathbf{e}_3$ plane, and thus Σ_{21} is ineffective on this process (see [39] for more explicit explanations). More specifically, for a known possible localization plane (with normal $\mathbf{n}$) Σ_{31} is replaced by τ_n as being the resolved shear traction on that plane. This has been truly corroborated by FEM outcomes demonstrating that, once plastic deformation localizes somewhere on the plane, it spreads in all directions without necessarily being directed. Therefore, the direction of shear becomes naturally insubstantial when localization is picked to occur at one plane or one among a discrete set of planes.

As illustrated in [39], the fundamental inequality of limit analysis gives rise to the effective yield criterion of a porous material containing microvoids:

$$\forall\, \mathbf{D}, \quad \boldsymbol{\Sigma} : \mathbf{D} \leq \Pi(\mathbf{D}) \tag{6}$$

with $\boldsymbol{\Sigma}$ and $\mathbf{D}$ denoting the macroscopic stress and rate of deformation tensors, defined as the volume averages of their microscopic counterparts $\boldsymbol{\sigma}$ and $\mathbf{d}$, and $\Pi(\mathbf{D})$ is the effective plastic dissipation given by

$$\Pi(\mathbf{D}) = \inf_{\mathbf{v}\in\mathcal{K}(\mathbf{D})} \langle \sup_{\boldsymbol{\sigma}^*\in\mathcal{C}} \sigma^*_{ij}\, d_{ij} \rangle_\Omega \tag{7}$$

Ω refers to the spatial domain over which macroscopic quantities are defined, $\langle\cdot\rangle_\Omega$ stands for averaging over Ω, $\inf$ and $\sup$, respectively, represent the infimum (greatest lower bound) and supremum (least upper bound) of the set, and $\mathcal{C}$ is the microscopic reversibility domain, with the boundary known as *yield surface*. The reader is referred to [35] for further details.

Solving the variational problem represented by (6)–(7) for a given cell and the J_2 matrix flow rule would deliver the minimum involved in (7) as well as the velocity fields realizing the minimum. Owing to the presence of matrix layers in the cell, the exact velocity field is of the type consistent with uniform traction boundary conditions, antithetical to that consistent with uniform strain-rate boundary conditions. The former corresponds to plasticity being localized in the ligaments while the latter accounts for plasticity diffuse in the matrix. Also, the set of kinematically admissible velocity fields, $\mathcal{K}(\mathbf{D})$, is made of expansion fields superimposed by purely deviatoric incompressible fields ($v_{k,k} = 0$) that are compatible with the overall deformation imposed through $\mathbf{D}$.

If the velocity field is discontinuous across an interface S, then a surface term must be added which writes

$$\frac{1}{\Omega}\int_S \sup_{\sigma^*\in\mathcal{C}} t_i^* \,[\![v_i]\!]\,\mathrm{d}S \tag{8}$$

where $[\![\mathbf{v}]\!]$ is the velocity jump across the interface and $\mathbf{t}^*$ the exerted traction. Upon the condition of differentiability, the stress tensor corresponding to the boundary of the domain of reversibility — associated with the effective yield surface — can be derived as the first derivative of the effective dissipation with respect to the rate-of-deformation tensor. In this case, the effective yield surface is smooth and (6) constitutes the following parametric equation:

$$\Sigma_{ij} = \frac{\partial \Pi}{\partial D_{ij}}(\mathbf{D}) \tag{9}$$

where $\mathbf{D}$ is no longer arbitrary as in (6) but represents the rate of deformation corresponding to $\mathbf{\Sigma}$ through the macroscopic flow rule. By way of contrast, if the effective yield surface is not smooth, the primitive inequalities (6) define the effective reversibility domain $\mathscr{C}$, generally differing from its microscopic counterpart $\mathcal{C}$. The reader is well-advised to refer to [35] and [39] for further details.

Hence, by rephrasing Π as $\bar{\Pi}(\bar{\mathbf{D}}) \equiv \Pi(\mathbf{D})$ in the problem at hand, one can define, in the macroscopic level, the following stress state, with its nonzero components stated as corollary:

$$\bar{\mathbf{\Sigma}}(\bar{\mathbf{D}}) = \frac{\partial \bar{\Pi}(\bar{\mathbf{D}})}{\partial \bar{\mathbf{D}}} \therefore \bar{\Sigma}_i = \frac{\partial \bar{\Pi}}{\partial \bar{D}_i} \quad i = 1,2,3 \tag{10}$$

2.4 Kinematics

The reference volume element at hand, being identical to that designed in Fig. 2, can be conceived of as including a plastically deformable ligament (l) and matrix (m) part, as well as a surface of discontinuity ('surf') in between. The inherent kinematic specifications of the problem entail the following properties:

$$\begin{aligned} D_{11} &= D_{11}^{(\mathrm{l})} = D_{11}^{(\mathrm{m})} \\ D_{33} &= cD_{33}^{(\mathrm{l})} + (1-c)D_{33}^{(\mathrm{m})} \\ D_{31} &= cD_{31}^{(\mathrm{l})} + (1-c)D_{31}^{(\mathrm{m})} = cD_{31}^{(\mathrm{l})} \end{aligned} \tag{11}$$

the first induced by the axisymmetric nature of the problem, and the rest derived from a simple volumetric mixture rule, adding to the fact that void growth is only accounted for in the lateral (radial) and axial directions. The factor c has been defined in advance. The third relation attributes shear deformation only to the ligament, and the matrix is only subject to expansion/contraction (this is well in conformity with FEM cell-model calculations). On the other hand, incompressibility of the matrix invokes a traceless rate-of-deformation tensor, whence the following can be written:

$$\mathrm{tr}(\mathbf{D}^{(\mathrm{m})}) = 0 \therefore D_{33}^{(\mathrm{m})} = -2D_{11}^{(\mathrm{m})} = -2D_{11} \tag{12}$$

Therefore, the following relation can be drawn among the porous-zone and average components:

$$\begin{aligned}
\bar{D}_1^{(\mathrm{l})} &\equiv 3D_m^{(\mathrm{l})} = \frac{\bar{D}_1}{c} \\
\bar{D}_2^{(\mathrm{l})} &\equiv D_{33}^{(\mathrm{l})} = \left(\frac{1}{c} - 1\right)\bar{D}_1 + \bar{D}_2 \\
\bar{D}_3^{(\mathrm{l})} &\equiv 2D_{31}^{(\mathrm{l})} = \frac{\bar{D}_3}{c}
\end{aligned} \tag{13}$$

Remark It can be easily inferred, with reference to (12) and (13), that subsequent to the *void coalescence* onset, the zero lateral growth condition $D_{11} = 0$ would demand $D_{11}^{(\mathrm{m})} = D_{22}^{(\mathrm{m})} = 0$ and $D_{11}^{(\mathrm{l})} = D_{22}^{(\mathrm{l})} = 0$. Hence, the matrix layers would freeze into totally rigid zones at coalescence.

2.5 Kinematically Admissible Velocity Fields

A Gurson-like velocity field can be utilized in the ligament zone. That is, for a cylindrical unit cell with a coaxial cylindrical void, the admissible velocity field for $|z| \leq h$ reads:

$$\mathbf{v}^{(\mathrm{l})} = \left(\frac{A^{(\mathrm{l})}}{r} - \frac{B^{(\mathrm{l})}}{2}r\right)\mathbf{e}_r + B^{(\mathrm{l})}z\mathbf{e}_3 + \frac{D_{31}}{c}z\mathbf{e}_1 \tag{14}$$

with the admissibility condition for the velocity field to represent an isochoric process, *i.e.* div$\mathbf{v} = 0$, which is obviously satisfied by adopting the above form. The parameters $A^{(\mathrm{l})}$ and $B^{(\mathrm{l})}$ emanate from condition $(11)_2$ and that requiring $v_r^{(\mathrm{l})}(L) = D_{11}L$. Moreover, the shear-induced velocity field has been nominated upon a simple linear shear strain along the ligament height with the shear stress being applied along x_1, which admits the presence of volume fraction c in its denominator due to the shear strain being confined within the ligament. With the above conditions satisfied, as well as $\mathbf{e}_1$ expanded in polar form, Eq. (14) become equivalent to

$$\begin{aligned}
v_r^{(\mathrm{l})} &= \frac{1}{2}\left[\bar{D}_1^{(\mathrm{l})}\frac{L^2}{r} - \bar{D}_2^{(\mathrm{l})}r\right] + \bar{D}_3^{(\mathrm{l})}z\cos\theta \\
v_\theta^{(\mathrm{l})} &= \bar{D}_3^{(\mathrm{l})}z\sin\theta \\
v_z^{(\mathrm{l})} &= \bar{D}_2^{(\mathrm{l})}z
\end{aligned} \tag{15}$$

And the velocity field in the matrix layers, where $h < |z| \leq H$, should produce a uniform deviatoric strain rate. Hence, in its simplest form, it can be written as:

$$\begin{aligned}
v_r^{(\mathrm{m})} &= \frac{1}{2}(\bar{D}_1 - \bar{D}_2)r \pm \bar{D}_3^{(\mathrm{l})}h\cos\theta \\
v_\theta^{(\mathrm{m})} &= -(\pm\bar{D}_3^{(\mathrm{l})}h\sin\theta) \\
v_z^{(\mathrm{m})} &= (\bar{D}_2 - \bar{D}_1)z
\end{aligned} \tag{16}$$

where the plus and minus signs pertain to $h < z \leq H$ and $-H \leq z < -h$, respectively.

2.6 Effective Dissipation Function

The effective dissipation function Π is reminiscent of an equivalent rate of deformation, d_{eq}, as elucidated in Eq. (4). On the other hand, since, with the J_2 flow theory admitted for the matrix, Π is linear in d_{eq} [35],

each volumetric portion of the cell contributes to Π in proportion to its volume fraction. The total dissipation function can therefore be written as decomposed into three terms:

$$\Pi = c\Pi^{(\mathrm{l})} + (1-c)\Pi^{(\mathrm{m})} + \Pi^{\mathrm{surf}} \tag{17}$$

whence the $\bar{\Sigma}_i$ stresses can be obtained from the first derivative of Π as follows:

$$\bar{\Sigma}_i = c\frac{\partial \Pi^{(\mathrm{l})}}{\partial \bar{D}_i} + (1-c)\frac{\partial \Pi^{(\mathrm{m})}}{\partial \bar{D}_i} + \frac{\partial \Pi^{\mathrm{surf}}}{\partial \bar{D}_i} \quad i = 1,2,3 \tag{18}$$

With infinitesimal straining taken for granted, the strain-rate tensor components can be written in the following well-known cylindrical form component-wise:

$$\begin{aligned}
d_{rr} &= \frac{\partial v_r}{\partial r} \\
d_{\theta\theta} &= \frac{1}{r}\left(v_r + \frac{\partial v_\theta}{\partial \theta}\right) \\
d_{zz} &= \frac{\partial v_z}{\partial z} \\
d_{r\theta} = d_{\theta r} &= \frac{1}{2}\left(\frac{1}{r}\frac{\partial v_r}{\partial \theta} + \frac{\partial v_\theta}{\partial r} - \frac{v_\theta}{r}\right) \\
d_{rz} = d_{zr} &= \frac{1}{2}\left(\frac{\partial v_r}{\partial z} + \frac{\partial v_z}{\partial r}\right) \\
d_{z\theta} = d_{\theta z} &= \frac{1}{2}\left(\frac{\partial v_\theta}{\partial z} + \frac{1}{r}\frac{\partial v_z}{\partial \theta}\right)
\end{aligned} \tag{19}$$

Calculation and simplification of the above strain rate components is conducive to the following equivalent strain rates for the ligament and matrix layers:

$$\begin{aligned}
\left[d_{\mathrm{eq}}^{(\mathrm{l})}\right]^2 &= \frac{2}{3}\mathbf{d}^{(\mathrm{l})} : \mathbf{d}^{(\mathrm{l})} = (D_1^*)^2\frac{L^4}{r^4} + (D_2^*)^2 \\
\left[d_{\mathrm{eq}}^{(\mathrm{m})}\right]^2 &= \frac{2}{3}\mathbf{d}^{(\mathrm{m})} : \mathbf{d}^{(\mathrm{m})} = (\bar{D}_1 - \bar{D}_2)^2
\end{aligned} \tag{20}$$

where

$$(D_1^*)^2 = \frac{\left(\bar{D}_1^{(\mathrm{l})}\right)^2}{3} \tag{21}$$

$$(D_2^*)^2 = \left(\bar{D}_2^{(\mathrm{l})}\right)^2 + \frac{1}{3}\left(\bar{D}_3^{(\mathrm{l})}\right)^2 \tag{22}$$

D_1^* and D_2^* have been defined in the interest of brevity for what follows in calculation of the volumetric integral. With Eq. (20) as repository, the effective dissipation functions corresponding to the ligament and matrix layers can be expressed as reads:

$$\begin{aligned}
\Pi^{(\mathrm{l})} &= (1-f_b)\langle \bar{\sigma} d_{\mathrm{eq}}\rangle_{\Omega\setminus\Omega^{(\mathrm{m})}} = \frac{1}{\Omega_{\mathrm{lig}}}\int_{\Omega\setminus\Omega^{(\mathrm{m})}} \bar{\sigma} d_{\mathrm{eq}}^{(\mathrm{l})}\,\mathrm{d}\Omega\setminus\Omega^{(\mathrm{m})} \\
&= \frac{\bar{\sigma}}{2\pi L^2 h}\int_R^L\int_{-h}^{h} d_{\mathrm{eq}}^{(\mathrm{l})}(2\pi r\,\mathrm{d}r\,\mathrm{d}z) = \frac{2\bar{\sigma}}{L^2}\int_R^L \sqrt{(D_1^*)^2\frac{L^4}{r^4} + (D_2^*)^2}(r\,\mathrm{d}r) \\
\Pi^{(\mathrm{m})} &= \frac{1}{\Omega_{\mathrm{r}}}\int_{\Omega_{\mathrm{r}}} \bar{\sigma} d_{\mathrm{eq}}^{(\mathrm{m})}\,\mathrm{d}\Omega_{\mathrm{r}} = \bar{\sigma}\left|\bar{D}_1 - \bar{D}_2\right|
\end{aligned} \tag{23}$$

on account of $\Omega\backslash\Omega^{(\mathrm{m})}$ being equal to $(1-f_b)\Omega_{\mathrm{lig}}$, (m) representing the matrix, and $\backslash$ denoting exclusion. The dissipation integral can be evaluated either in an algebraically precise or approximate manner, the difference residing in the square root in (23) being part of the integrand or circumscribing the whole integral. The exact integration has been applied, in absence of shear stress, by Morin *et al*. [14] and the approximate method was primarily proposed in [37] and further employed by Torki *et al*. [39] to identify their model describing void coalescence under combined tension and shear.

In order to evaluate the integral in (23) precisely, the simple change of variable $u \equiv L^2/r^2$ (also exploited in [38]) can be exerted, rendering it in the following equivalent form for $\Pi^{(\mathrm{l})}$:

$$\Pi^{(\mathrm{l})} = \bar{\sigma}|D_2^*| \left[\zeta \sinh^{-1}(\zeta u) - \sqrt{\frac{1}{u^2} + \zeta^2} \right]_1^{1/f_b} \tag{24}$$

with $\zeta = D_1^*/|D_2^*|$. By the same token, approximation allows for the passing of the averaging integral through the square root. That is, defining $\langle . \rangle_{\Omega\backslash\Omega^{(\mathrm{m})}}$ as volumetric average over the whole region excluding matrix layers, the approximation at hand has it that the average can be evaluated using

$$\left\langle \sqrt{\mathcal{F}^2 + a^2} \right\rangle_{\Omega\backslash\Omega^{(\mathrm{m})}} \approx \sqrt{\langle \mathcal{F} \rangle^2_{\Omega\backslash\Omega^{(\mathrm{m})}} + a^2} \tag{25}$$

where $\mathcal{F}$ is function of the independent variable (u herein) and a is constant in that terms (even though it may be a function by nature). Consequently, $\Pi^{(\mathrm{l})}$ evaluated in approximate form reads:

$$\Pi^{(\mathrm{l})} = (1-f_{\mathrm{b}}) \left\langle \bar{\sigma} \sqrt{(D_1^*)^2 \frac{L^4}{r^4} + (D_2^*)^2} \right\rangle_{\Omega\backslash\Omega^{(\mathrm{m})}} \approx \bar{\sigma}(1-f_{\mathrm{b}}) \sqrt{\left\langle D_1^* \frac{L^2}{r^2} \right\rangle^2_{\Omega\backslash\Omega^{(\mathrm{m})}} + (D_2^*)^2} \tag{26}$$

The virtue within this approximation is the ease of calculating the volumetric average of a simple rational function in lieu of an improper function embedding another rational function. To this end, we have:

$$\begin{aligned} \left\langle D_1^* \frac{L^2}{r^2} \right\rangle_{\Omega\backslash\Omega^{(\mathrm{m})}} &= \frac{1}{(1-f_{\mathrm{b}})\Omega_{\mathrm{lig}}} \int_{\Omega\backslash\Omega^{(\mathrm{m})}} D_1^* \frac{L^2}{r^2} \, \mathrm{d}\Omega \\ &= \frac{1}{(1-f_{\mathrm{b}})(\pi R^2 L)} \int_R^L \int_{-h}^h D_1^* \frac{L^2}{r^2} (2\pi r \, \mathrm{d}r \, \mathrm{d}z) = \frac{D_1^*}{1-f_{\mathrm{b}}} \ln \frac{1}{f_{\mathrm{b}}} \end{aligned} \tag{27}$$

Furthermore, Π^{surf} can be recast, without any mutation, with reference to its original derivation in [38], as reading:

$$\Pi^{\mathrm{surf}} = |\bar{D}_1| \Sigma^{\mathrm{surf}}(\chi, W) \tag{28}$$

with Σ^{surf} defined as

$$\frac{\Sigma^{\mathrm{surf}}}{\bar{\sigma}} = \frac{1}{3\sqrt{3}} \frac{\chi^3 - 3\chi + 2}{\chi W} \tag{29}$$

Nevertheless, due to the piece-wise nature of absolute functions within the Π constituents, it should be admitted that Π is, in general, not differentiable. Therefore, derivation of the whole yield surface amounts to solving the primitive inequality of limit analysis [35] in Eq. (6). Upon reflection, the complete yield criterion is a pentapartite function embracing the following subsections at each stress half-space: (i) pre-coalescence straight part, (ii) pre-coalescence curved part, (iii) coalescence straight part, the latter demonstrating a slanted negative-slope line in the $\Sigma_{33} - \Sigma_{11}$ vs Σ_{m} curve and a horizontal line in the normal vs radial stress diagram. Implicit here is the fact that the curved parts are derived by means of a closed-form implicit function among the stress components. This closed-form relation will be formulated in its exact as well as an approximate method.

2.7 Subsections of the Unified Yield Surface

An alternative form of (6) can be established by defining:

$$p_1 = \frac{\bar{D}_1}{\bar{D}_3} \quad p_2 = \frac{\bar{D}_2}{\bar{D}_3} \tag{30}$$

which can vary as two independent variables in the nondimensional functions $\mathscr{F}$ and $\mathscr{G}$ defined as follows:

$$\begin{aligned}
\mathscr{F}(p_1,p_2) &= \frac{\mathbf{\Sigma}:\mathbf{D}}{\bar{\sigma}\bar{D}_3} = p_1\frac{\bar{\Sigma}_1}{\bar{\sigma}} + p_2\frac{\bar{\Sigma}_2}{\bar{\sigma}} + \frac{\bar{\Sigma}_3}{\bar{\sigma}} \\
\mathscr{G}(p_1,p_2) &= \frac{\Pi(p_1,p_2,1)}{\bar{\sigma}} = c\frac{\Pi^{(\mathrm{l})}}{\bar{\sigma}\bar{D}_3} + (1-c)\frac{\Pi^{(\mathrm{m})}}{\bar{\sigma}\bar{D}_3} + \frac{\Pi^{\mathrm{surf}}}{\bar{\sigma}\bar{D}_3} \\
&= \sqrt{[(1-c)p_1+cp_2]^2+\frac{1}{3}}\left[\zeta\sinh^{-1}(\zeta u) - \sqrt{\frac{1}{u^2}+\zeta^2}\right]_1^{1/f_{\mathrm{b}}} \\
&+ (1-c)|p_1-p_2| + |p_1|\,\mathrm{sgn}(D_{\mathrm{m}})\frac{\Sigma^{\mathrm{surf}}}{\bar{\sigma}}
\end{aligned} \tag{31}$$

where ζ is identified as the following ratio:

$$\zeta^2 = \left(\frac{D_1^*}{D_2^*}\right)^2 = \frac{p_1^2}{1+3[(1-c)p_1+cp_2]^2} \tag{32}$$

Hence, the following will be counterpart to the inequality in (6):

$$\forall\, p_1, p_2 \quad |\mathscr{F}| \le \mathscr{G} \Longleftrightarrow -\mathscr{G} \le \mathscr{F} \le \mathscr{G} \tag{33}$$

Depending on the value of Σ_{31} (mainly influencing parameter p_2), $\mathscr{F}$ and $\mathscr{G}$ functions can take various forms, leaving the p_1 parameter as axis variable. p_2, however, later expressed as function of $\Sigma_{31}/\bar{\sigma}$, emanates from (45). Due to D_{31} posited without any loss of generality, Π is differentiable with respect to D_{31} except when the latter approaches infinity. The p_2 ratio can, therefore, be directly obtained from Σ_{31} as follows. By defining

$$\xi = \bar{D}_2^{(\mathrm{l})}/D_2^* = \frac{1}{1+\frac{1}{3[(1-c)p_1+cp_2]^2}} \tag{34}$$

as an auxiliary nondimensionalized ratio, Σ_{31} can be expressed, according to (18), by the following

$$\Sigma_{31} = \Sigma_2^*\sqrt{\frac{1-\xi^2}{3}} \tag{35}$$

which delivers p_2 in terms of Σ_{31} as follows:

$$p_2 = c\sqrt{\frac{3}{\frac{(1-f_b)^2}{3(\Sigma_{31}/\bar{\sigma})^2}-1}} \tag{36}$$

Herein, p_2 is a monotonically descending function of Σ_{31}, approaching 0 and infinity when Σ_{31} becomes close to $\mathcal{T}$ and 0, respectively. Figure 3 exhibits a schematic evolution of $\mathscr{F}$ and $\mathscr{G}$ as function of p_1 for varying values of p_2, each p_2 being attributed to a specific magnitude of $\Sigma_{31}/\bar{\sigma}$.

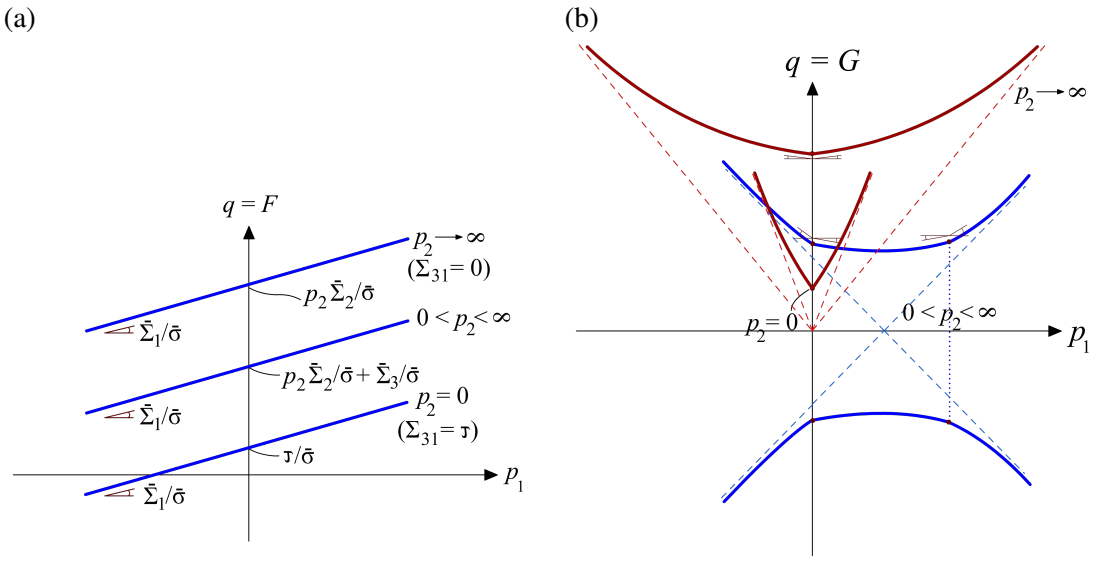

Figure 3: Schematic outline of $\mathscr{F}$ and $\mathscr{G}$ functions vs p_1 with varying values of p_2 as function of $\Sigma_{31}/\bar{\sigma}$. The curve corresponding to $-\mathscr{G}$ has been exhibited only for the general case $0 < p_2 < \infty$. The distinction between left and right slopes at $p_1 = 0$ and $p_1 = p_2$ neighborhoods is illustrated by unequal angles.

Remark 1 Indubitably, $\mathscr{F}$ is a line while $\mathscr{G}$ represents a more elaborate curve entitled to having singular corners at $p_1 = 0$ and $p_1 = p_2$ due to the existence of absolute functions. At the limit cases of $p_2 = 0$ ($\Sigma_{31} = \mathcal{T}$) and $p_2 \longrightarrow \infty$ ($\Sigma_{31} \longrightarrow 0$), $\mathscr{G}$ admits only one singular (angular) point that corresponds to $p_1 = 0$. For the general case of $0 < p_2 < \infty$ ($0 < \Sigma_{31} < \mathcal{T}$), however, $\mathscr{G}$ is a tripartite curve consisting of three smooth sub-curves pertaining to $-\infty < p_1 \leq 0$, $0 < p_1 \leq p_2$, and $p_2 < p_1 < \infty$.

Remark 2 The intermediary smooth curve ranging between singular corners at $p_1 = 0$ and $p_1 = p_2$ expands with increasing p_2, i.e. decreasing $\Sigma_{31}/\bar{\sigma}$. Namely, it extends throughout the whole halfspace, and thus coalescence occurs at $p_2 \longrightarrow \infty$ when $\Sigma_{31} = 0$. Looking into the other extreme $p_2 \longrightarrow 0$, however, the middle curved part would vanish, and coalescence would take place when $\Sigma_{31} = \mathcal{T}$.

Remark 3 It can be proven that the $\mathscr{G}$ curve is always convex. All the same, the $-\mathscr{G}$ curve is concave [33].

Remark 4 The $\mathscr{G}$ and $-\mathscr{G}$ curves admit straight asymptotes at $p_1 \longrightarrow \infty$. The asymptotes to the $-\mathscr{G}$ curve coincide with those pertaining to the $\mathscr{G}$ curve [33]. Agreeing with intuition, the asymptotes should thus intersect somewhere on the p_1 axis. In the interest of simplicity, the mathematical discussion in the following will be given for the positive half-space.

Remark 5 As p_2 approaches 0 and infinity, $\mathscr{G}$ becomes symmetric with respect to the vertical axis. Consequently, the asymptotes intersect at the origin.

By satisfying the primitive inequality (6) considering various critical values of p_1 and p_2, the complete yield surface comprises pre-coalescence planar part, pre-coalescence curved parts, and post-coalescence planar parts. The yield surface is built up through a comprehensive discussion in the following.

2.7.1 Pre-coalescence straight parts

The pre-coalescence straight parts are delivered by the model due to the simple choice of the velocity field. Yet, they are not physical even though they remain close to their curved numerical counterparts. These parts can be represented by the specific case of $p_1 \longrightarrow 0$, where $\bar{\Sigma}_2/\bar{\sigma}$ remains constant and $\bar{\Sigma}_1/\bar{\sigma}$ varies between the two bounds stemming from (37), where the auxiliary stresses Σ_1^* and Σ_2^* would simplify into 0 and

$1 - f_b$, respectively and $\bar{\Sigma}_1/\bar{\sigma}$ stays below its value in the curved part. As Fig. 4a clarifies, at a given p_2, $\mathscr{F}$ has a constant vertical intercept (equaling $p_2\bar{\Sigma}_2/\bar{\sigma} + \bar{\Sigma}_3/\bar{\sigma}$) but a varying slope ($\bar{\Sigma}_1/\bar{\sigma}$) ranging between the left and right-neighborhood slopes at $p_1 = 0$.

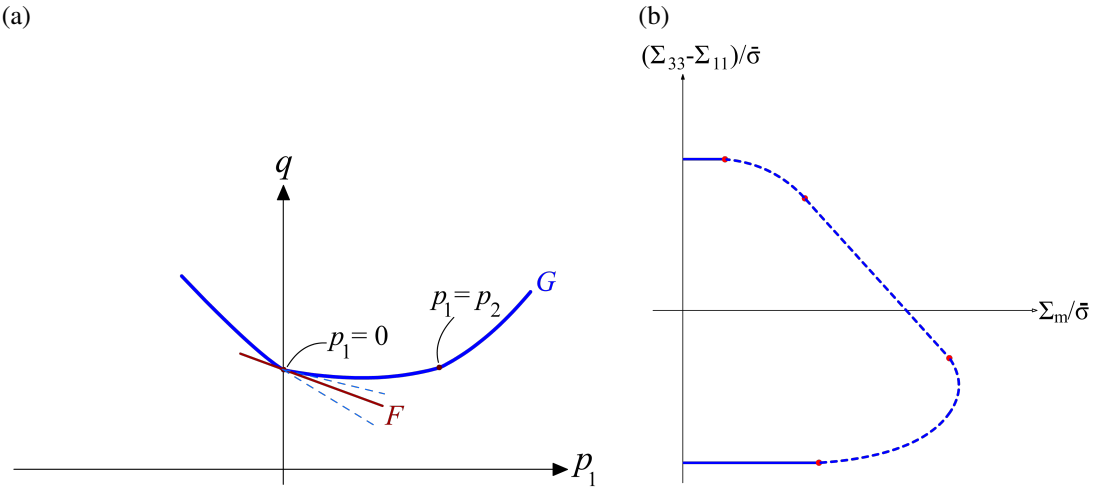

Figure 4: (a) Relative status of $\mathscr{F}$ and $\mathscr{G}$ functions satisfying the $|\mathscr{F}| \leq \mathscr{G}$ inequality justifying the pre-coalescence singular (straight) parts, (b) corresponding zones on a representative yield locus at a given $\Sigma_{31}/\bar{\sigma}$.

The line $\mathscr{F}$ at a specific p_2 (or Σ_{31} accordingly) ranging between the dashed tangential lines gives rise to a range for $\bar{\Sigma}_1$ while the point of tangency stays fixed, *i.e.* at fixed $\bar{\Sigma}_2$. At this point, for yielding to occur:

$$\begin{aligned} \mathscr{F} = \mathscr{G} \implies & \frac{\bar{\Sigma}_2}{\bar{\sigma}} = -(1-c)\mathrm{sgn}(D_{11}) + c\sqrt{(1-f_b)^2 - \left(\frac{\Sigma_{31}}{\bar{\tau}}\right)^2} \\ \mathscr{F}' \leq \mathscr{G}' \implies & \left| \frac{\bar{\Sigma}_1}{\bar{\sigma}} + (1-c)\left[\frac{1}{\sqrt{1+\frac{1}{3(cp_2)^2}}}(1-f_b) + \mathrm{sgn}(D_{11}) \right] \right| \leq \mathrm{sgn}(D_m)\frac{\Sigma^{surf}}{\bar{\sigma}} \end{aligned} \tag{37}$$

where $\bar{\tau} = \bar{\sigma}/\sqrt{3}$ is the matrix shear strength. Equation $(37)_1$ demonstrates that yielding is independent of Σ_m for a given value of f_b and Σ_{31}, and thus is represented by horizontal lines admitting constant $\bar{\Sigma}_2$ (which can lie below or above the Σ_m axis depending on $\mathrm{sgn}(D_{11})$) at the corresponding range of Σ_m, which emanates from $(37)_2$. With reference to p_2 from (36) and, since the right-hand side of $(37)_2$ ought to be always positive, the pre-coalescence straight portion of the yield surface can be expressed in the following simpler style:

$$\begin{aligned} & \sqrt{3}\mathscr{T} - \sqrt{\left(\frac{\mathcal{T}}{\bar{\tau}}\right)^2 - \left(\frac{\Sigma_{31}}{\bar{\tau}}\right)^2} = 0 \\ & \left| \frac{\bar{\Sigma}_1}{\bar{\sigma}} + (1-c)\left[(1-f_b)\sqrt{1-\left(\frac{\Sigma_{31}}{\mathcal{T}}\right)^2} + \mathrm{sgn}(D_{11}) \right] \right| \leq \frac{\Sigma^{surf}}{\bar{\sigma}} \\ & \text{where} \quad \mathscr{T} = \frac{1}{c}\left(\frac{\Sigma_{33} - \Sigma_{11}}{\bar{\tau}} + \sqrt{3}(1-c)\mathrm{sgn}(D_{11}) \right) \end{aligned} \tag{38}$$

where the parameter $\mathscr{T}$ is so defined as it will be used extensively in the sequel.

Remark 1 The signs associated with the pre-coalescence straight part are $\text{sgn}(D_{11}) = -1$ and $\text{sgn}(D_{\text{m}}) = +1$ (for $\Sigma_{33} \geq 0$) or $\text{sgn}(D_{\text{m}}) = -1$ (for $\Sigma_{33} < 0$).

Remark 2 Equation (37) simplifies into Eq. (37) of [14] when $p_2 \longrightarrow 0$, which is representative of $\Sigma_{31} = 0$.

Remark 3 The distinction between $\text{sgn}(D_{11})$ being $+1$ or -1 can be associated with the two extrema of $(\Sigma_{33} - \Sigma_{11})/\bar{\sigma}$ at coalescence. This will be better clarified in subsection 2.7.3.

2.7.2 Pre-coalescence curved parts

Fig. 5a illustrates, at a given p_2, a point of tangency (equality of values and slopes) between $\mathscr{F}$ and $\mathscr{G}$ at an arbitrary point ranging between the two singular points ($p_1 = 0$ and $p_1 = p_2$) on the $\mathscr{G}$ curve. For a microstructure, $\Sigma_{33} - \Sigma_{11}$ and Σ_{m} correlate through the $\bar{D}_1/\bar{D}_2$ ratio (see Eq. (45) for the derivations). The corresponding yield locus then represents a curve intermediating between the pre-coalescence and coalescence straight zones (lying below or above the Σ_{m} axis depending on $\text{sgn}(D_{11})$), as illustrated in Fig. 5b.

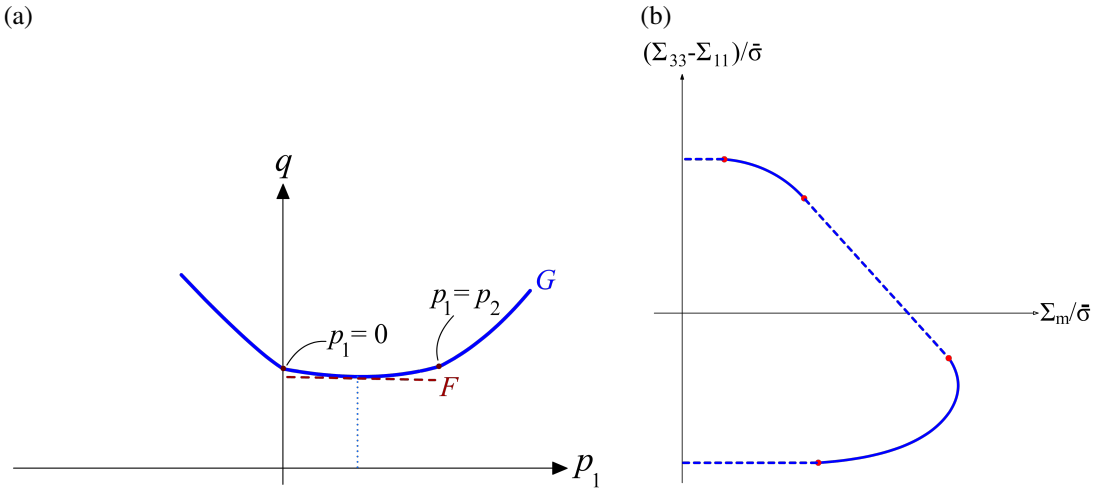

Figure 5: (a) Relative status of $\mathscr{F}$ and $\mathscr{G}$ functions satisfying the $|\mathscr{F}| \leq \mathscr{G}$ inequality justifying the pre-coalescence regular (curved) parts, (b) corresponding zones on a representative yield locus at a given $\Sigma_{31}/\bar{\sigma}$.

Recollecting the technique set forth in [40], one can fabricate, by letting $\Pi^{*(\text{l})} \equiv \Pi^{(\text{l})}(D_1^*, D_2^*)$, auxiliary stresses Σ_1^* and Σ_2^* as defined below:

$$\begin{aligned} \Sigma_1^* &= \frac{\partial \Pi^{*(\text{l})}}{\partial D_1^*} \\ \Sigma_2^* &= \frac{\partial \Pi^{*(\text{l})}}{\partial D_2^*} \end{aligned} \tag{39}$$

which will take the below-mentioned forms:

$$\begin{aligned} \Sigma_1^* &= \bar{\sigma}\left[\sinh^{-1}\left(\frac{\zeta}{f_{\text{b}}}\right) - \sinh^{-1}(\zeta)\right] \\ \Sigma_2^* &= \text{sgn}(D_2^*)\bar{\sigma}\left(\sqrt{1+\zeta^2} - \sqrt{f_{\text{b}}^2+\zeta^2}\right) \end{aligned} \tag{40}$$

and

$$\begin{aligned}\Sigma_1^* &= \left(\bar{\sigma}\ln\frac{1}{f_\mathrm{b}}\right)^2\frac{D_1^*}{\Pi^{(\mathrm{l})}}\\ \Sigma_2^* &= \left[\bar{\sigma}(1-f_\mathrm{b})\right]^2\frac{D_2^*}{\Pi^{(\mathrm{l})}}\end{aligned} \tag{41}$$

using the exact and approximate integration methods, respectively.
In the former, Σ_1^* and Σ_2^* are not explicit functions of $\Pi^{(\mathrm{l})}$, and thus elimination of ζ between Σ_1^* and Σ_2^* demands some intermediary manipulation utilizing trigonometric algebra which would, at furthest, lead to the following relation:

$$\left(\frac{\Sigma_2^*}{\bar{\sigma}}\right)^2 + 2f_\mathrm{b}\cosh\left(\frac{\Sigma_1^*}{\bar{\sigma}}\right) - (1+f_\mathrm{b}^2) = 0 \tag{42}$$

See Appendix A for a detailed proof.

In the latter, however, both Σ_1^* and Σ_2^* are multiples of $\Pi^{(\mathrm{l})}$. Herein, one can easily write, with referral to (27):

$$\begin{aligned}&\left(\frac{1-f_\mathrm{b}}{\ln\frac{1}{f_\mathrm{b}}}\right)^2(\Sigma_1^*)^2 + (\Sigma_2^*)^2 = \bar{\sigma}(1-f_\mathrm{b})^4\frac{\left(\frac{D_1^*\ln\frac{1}{f_\mathrm{b}}}{1-f_\mathrm{b}}\right)^2 + (D_2^*)^2}{\left(\Pi^{(\mathrm{l})}\right)^2} = \bar{\sigma}(1-f_\mathrm{b})^2\\ &\therefore\ \left[\frac{1}{\ln\frac{1}{f_\mathrm{b}}}\left(\frac{\Sigma_1^*}{\bar{\sigma}}\right)\right]^2 + \left[\frac{1}{1-f_\mathrm{b}}\left(\frac{\Sigma_2^*}{\bar{\sigma}}\right)\right]^2 = 1\end{aligned} \tag{43}$$

Henceforth comes the calculation of the $\bar{\boldsymbol{\Sigma}}$ tensor constituents, as defined in (10). Primarily, the following derivatives should be evaluated:

$$\frac{\partial\Pi^{*(\mathrm{l})}}{\partial\bar{D}_i} = \frac{\partial\Pi^{*(\mathrm{l})}}{\partial D_1^*}\frac{\partial D_1^*}{\partial\bar{D}_i} + \frac{\partial\Pi^{*(\mathrm{l})}}{\partial D_2^*}\frac{\partial D_2^*}{\partial\bar{D}_i} = \Sigma_1^*\frac{\partial D_1^*}{\partial\bar{D}_i} + \Sigma_2^*\frac{\partial D_2^*}{\partial\bar{D}_i}\quad i=1,2,3 \tag{44}$$

Meanwhile, back to the definition of ξ in (34), the components of $\bar{\boldsymbol{\Sigma}}$ will become simplified, according to (18), into the following:

$$\begin{aligned}\bar{\Sigma}_1 &\equiv \Sigma_{11} = \frac{\Sigma_1^*}{\sqrt{3}} + (1-c)\left[\xi\Sigma_2^* + \bar{\sigma}\mathrm{sgn}(D_{11})\right] + \mathrm{sgn}(D_\mathrm{m})\Sigma^{\mathrm{surf}}\\ \bar{\Sigma}_2 &\equiv \Sigma_{33} - \Sigma_{11} = c\xi\Sigma_2^* - (1-c)\bar{\sigma}\mathrm{sgn}(D_{11})\\ \bar{\Sigma}_3 &\equiv \Sigma_{31} = \Sigma_2^*\sqrt{\frac{1-\xi^2}{3}}\end{aligned} \tag{45}$$

Elimination of ξ ratio between the first and the third, then plugging the eliminated value in the second and third equations would allow for expressing Σ_1^* and Σ_2^* in terms of the major stress components Σ_{11}, Σ_{33}, and Σ_{31}. To this end, from $(45)_2$ and $(45)_3$, we have

$$\begin{aligned}&\left(\frac{\Sigma_{33}-\Sigma_{11}+(1-c)\bar{\sigma}\mathrm{sgn}(D_{11})}{c\Sigma_2^*}\right)^2 = 1 - 3\left(\frac{\Sigma_{31}}{\Sigma_2^*}\right)^2\\ &\therefore\quad (\Sigma_2^*)^2 = 3\Sigma_{31}^2 + \frac{1}{c^2}\left[\Sigma_{33}-\Sigma_{11}+(1-c)\bar{\sigma}\mathrm{sgn}(D_{11})\right]^2\end{aligned}$$

whence Σ_1^* can be derived from plugging the above Σ_2^* and and $(45)_3$ in $(45)_1$. Consequently, the implicit relation amongst the existing stress components will become:

$$\Phi(\boldsymbol{\Sigma}, f_{\rm b}, W, c) = \left(\frac{\Sigma_{31}}{\bar{\tau}}\right)^2 + \frac{1}{c^2}\left(\frac{\Sigma_{33}-\Sigma_{11}}{\bar{\sigma}} + (1-c)\text{sgn}(D_{11})\right)^2 + 2f_{\rm b}\cosh\left(\sqrt{3}\left[\frac{\Sigma_{33}-\text{sgn}(D_{\rm m})\Sigma^{\rm surf}}{\bar{\sigma}} - \frac{1}{c}\left(\frac{\Sigma_{33}-\Sigma_{11}}{\bar{\sigma}} + (1-c)\text{sgn}(D_{11})\right)\right]\right) - (1+f_{\rm b}^2) = 0 \tag{46}$$

using the exact method and

$$\Phi(\boldsymbol{\Sigma}, f_{\rm b}, W, c) = \frac{1}{(1-f_{\rm b})^2}\left[\left(\frac{\Sigma_{31}}{\bar{\tau}}\right)^2 + \frac{1}{c^2}\left(\frac{\Sigma_{33}-\Sigma_{11}}{\bar{\sigma}} + (1-c)\text{sgn}(D_{11})\right)^2\right] + \frac{\sqrt{3}}{\ln\frac{1}{f_{\rm b}}}\left[\frac{\Sigma_{33}-\text{sgn}(D_{\rm m})\Sigma^{\rm surf}}{\bar{\sigma}} - \frac{1}{c}\left(\frac{\Sigma_{33}-\Sigma_{11}}{\bar{\sigma}} + (1-c)\text{sgn}(D_{11})\right)\right]^2 - 1 = 0 \tag{47}$$

based on the approximate method.

Remark 1 The combination $\Sigma_{33} - \Sigma_{11}$ has been termed *quasi-equivalent* throughout the text in that it can be interpreted as a measure of $\Sigma_{\rm eq}$, the equivalent macroscopic stress for the given cell, as being equal to that only in case of zero shear stress (consult [14]).

Remark 2 Equation (46) specifies into Eq. (32) of Ref. [14] by Morin *et al*. in absence of shear stress ($\Sigma_{31} = 0$).

Remark 3 With fixed microstructural parameters (χ, W, c), changing the signs of $\mathbf{D}$ and $\boldsymbol{\Sigma}$ tensors would produce an identical Φ. Namely, $\Phi(-\boldsymbol{\Sigma}, \chi, W, c) = \Phi(\boldsymbol{\Sigma}, \chi, W, c)$, and thus Φ has point symmetry with respect to the stress space origin.

Remark 4 Gurson's notion included a cylindrical hollow tube (being devoid of circumscribing matrix layers), subjected to tensile loads only. This would entail that $\Sigma^{\rm surf}$ and Σ_{31} vanish. Furthermore, the dissipation integral is evaluated over the ligament only. Hence, $c = 1$ and $f_{\rm b} = f = f_{\rm b}$. Then, Eq. (46) simplifies into the following, which is nothing but Gurson's yield model for a cylindrical void in a cylindrical matrix:

$$\left(\frac{\Sigma_{\rm eq}}{\bar{\sigma}}\right)^2 + 2f\cosh\left(\sqrt{3}\frac{\Sigma_{11}}{\bar{\sigma}}\right) - (1+f^2) = 0 \tag{48}$$

2.7.3 Coalescence limits

The coalescence regime is associated with zero radial strain rate, $D_{11} = 0$. This condition will be met if and only if $\bar{D}_1 = \bar{D}_2$, or equivalently $|p_1 - p_2| = 0$. On the other hand, Π is differentiable at the coalescence bounds. Therefore, the primitive inequality $\mathscr{F} \leq \mathscr{G}$ will hold if and only if the following derivative vanishes:

$$D_{\rm ij} \propto \frac{\partial\Phi}{\partial\Sigma_{\rm ij}} \therefore \frac{\partial\Phi}{\partial\Sigma_{11}} = 0 \tag{49}$$

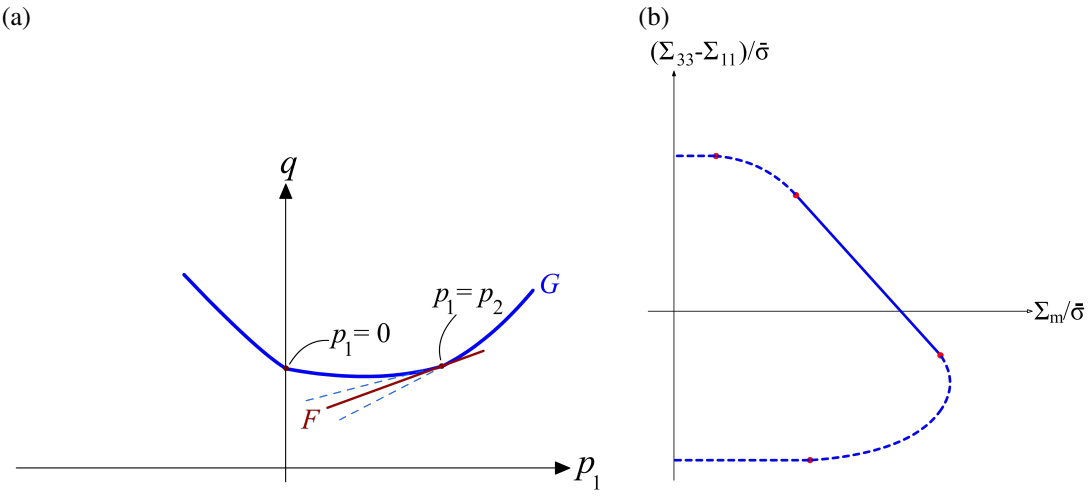

Figure 6: (a) Relative status of $\mathscr{F}$ and $\mathscr{G}$ functions satisfying the $|\mathscr{F}| \leq \mathscr{G}$ inequality justifying the coalescence straight parts, (b) corresponding coalescence zones on a representative yield locus at a given $\Sigma_{31}/\bar{\sigma}$.

The graphical representation of coalescence can be described as demonstrated in Fig. 6, where $\mathscr{F}$ touches $\mathscr{G}$ at $p_1 = p_2$ with its ordinate $(p_2\Sigma_{33}/\bar{\sigma} + \bar{\Sigma}_3/\bar{\sigma})$ being constant (at a given p_2) and its slope $(\bar{\Sigma}_1/\bar{\sigma})$ varying between the adjacent neighborhood slopes. The limit values of $\mathscr{F}$ and $\mathscr{G}$ at this vicinity are:

$$\begin{aligned}
&\lim_{p_1\to p_2} \mathscr{G} = \sqrt{p_2^2+\frac{1}{3}}\left[\zeta \sinh^{-}1\left(\zeta u\right) - \sqrt{\frac{1}{u^2}+\zeta^2}\right]_1^{1/f_\mathrm{b}} + |p_2|\mathrm{sgn}(D_\mathrm{m})\frac{\Sigma^\mathrm{surf}}{\bar{\sigma}} \\
&\zeta = \frac{|p_2|}{\sqrt{1+3p_2^2}} \\
&\lim_{p_1\to p_2} \mathscr{F} = p_2\frac{\Sigma_{33}}{\bar{\sigma}} + \frac{\bar{\Sigma}_3}{\bar{\sigma}}
\end{aligned} \tag{50}$$

With frozen microstructural parameters, the normal stress at a given applied shear stress is constant throughout the coalescence region. That is, Σ_{33} is only function of Σ_{31} and the microstructural parameters χ and W (c will cancel from the equations) at coalescence. Hence, by naming $\Sigma_{33}^\mathrm{coal} = f(\Sigma_{31})$, the mean and quasi-equivalent stresses will be coupled according to the following:

$$g = \frac{\Sigma_\mathrm{m}^\mathrm{coal}}{\bar{\sigma}} + \frac{2}{3}\frac{(\Sigma_{33}-\Sigma_{11})^\mathrm{coal}}{\bar{\sigma}} - f\left(\frac{\Sigma_{31}}{\bar{\sigma}}\right) = 0 \tag{51}$$

which represents a linear relation between $\Sigma_{33}-\Sigma_{11}$ and Σ_m, as shown in Fig. 6b. In the interest of brevity, (46) and (47) can be rephrased as

$$\Phi(\boldsymbol{\Sigma}, f_\mathrm{b}, W, c) = \left(\frac{\Sigma_{31}}{\bar{\tau}}\right)^2 + \frac{\mathscr{T}^2}{3} + 2f_\mathrm{b}\cosh\left(\frac{\Sigma_{33}-\mathrm{sgn}(D_\mathrm{m})\Sigma^\mathrm{surf}}{\bar{\tau}} - \mathscr{T}\right) - (1+f_\mathrm{b}^2) = 0 \tag{52}$$

and

$$\Phi(\boldsymbol{\Sigma}, f_\mathrm{b}, W, c) = \left(\frac{\Sigma_{31}}{\mathcal{T}}\right)^2 + \frac{1}{3}\left(\frac{\mathscr{T}}{\mathcal{T}/\bar{\tau}}\right)^2 + \frac{1}{\sqrt{3}\ln\frac{1}{f_\mathrm{b}}}\left[\frac{\Sigma_{33}-\mathrm{sgn}(D_\mathrm{m})\Sigma^\mathrm{surf}}{\bar{\tau}} - \mathscr{T}\right]^2 - 1 = 0 \tag{53}$$

where the common term $\frac{1}{c}\left(\frac{\Sigma_{33}-\Sigma_{11}}{\bar{\tau}}+\sqrt{3}(1-c)\mathrm{sgn}(D_{11})\right)$ has been replaced by $\mathscr{T}$. Setting, for instance, the derivative in (49) to zero will generate the following intervals for variation of $\Sigma_{33}-\Sigma_{11}$ in the coalescence regime:

$$\frac{\partial\Phi}{\partial(\Sigma_{11}/\bar{\sigma})}=\frac{-2}{c^2}\left[\frac{\Sigma_{33}-\Sigma_{11}}{\bar{\sigma}}+(1-c)\mathrm{sgn}(D_{11})\right]+2f_b\sqrt{3}\sinh\sqrt{3}\left(-\mathscr{T}+\frac{\Sigma_{33}-\mathrm{sgn}(D_{\mathrm{m}})\Sigma^{\mathrm{surf}}}{\bar{\sigma}}\right)=0$$

$$\therefore\quad f_b\sinh\sqrt{3}\left(-\mathscr{T}+\frac{\Sigma_{33}-\mathrm{sgn}(D_{\mathrm{m}})\Sigma^{\mathrm{surf}}}{\bar{\sigma}}\right)=\frac{1}{c\sqrt{3}}\left[\frac{\Sigma_{33}-\Sigma_{11}}{\bar{\sigma}}+(1-c)\mathrm{sgn}(D_{11})\right]=\frac{\mathscr{T}}{\sqrt{3}}$$

$$\therefore\quad f_b\cosh\sqrt{3}\left(-\mathscr{T}+\frac{\Sigma_{33}-\mathrm{sgn}(D_{\mathrm{m}})\Sigma^{\mathrm{surf}}}{\bar{\sigma}}\right)=\sqrt{f_b^2+\frac{\mathscr{T}}{\sqrt{3}}}$$

which, along with the $\cosh$ term extracted from Eq. (52), yields

$$\frac{\mathscr{T}^4}{4}-(\mathscr{M}+\frac{1}{3})\mathscr{T}^2+(\mathscr{M}^2-f_b^2)=0$$

where $2\mathscr{M}=1+f_b^2-3(\Sigma_{31}/\bar{\sigma})^2$. A similar, rather simpler procedure can be adopted in the approximate criterion (53). Altogether, the $\mathscr{T}$ extracted from solution to the above equation, here labeled $\mathscr{T}^{\mathrm{coal}}$, can be written as

$$\begin{aligned}\left(\mathscr{T}^{\mathrm{coal}}\right)^2&\equiv\frac{1}{c^2}\left(\frac{(\Sigma_{33}-\Sigma_{11})^{\mathrm{coal}}}{\bar{\tau}}+\sqrt{3}(1-c)\mathrm{sgn}(D_{11})\right)^2\\&=\frac{5}{3}+f_{\mathrm{b}}^2-\left(\frac{\Sigma_{31}}{\bar{\tau}}\right)^2-\frac{2}{3}\sqrt{4(1+3f_{\mathrm{b}}^2)-3\left(\frac{\Sigma_{31}}{\bar{\tau}}\right)^2}\end{aligned}\tag{54}$$

and

$$\begin{aligned}\mathscr{T}^{\mathrm{coal}}&\equiv\frac{1}{c}\left(\frac{(\Sigma_{33}-\Sigma_{11})^{\mathrm{coal}}}{\bar{\tau}}+\sqrt{3}(1-c)\mathrm{sgn}(D_{11})\right)\\&=\kappa(f_{\mathrm{b}})\,c\frac{\Sigma_{33}-\mathrm{sgn}(D_{\mathrm{m}})\Sigma^{\mathrm{surf}}}{\bar{\tau}}-\sqrt{3}(1-c)\mathrm{sgn}(D_{11})\ ,\ \kappa(f_{\mathrm{b}})=\frac{1}{1+\frac{1}{3}\left(\frac{\ln 1/f_{\mathrm{b}}}{1-f_{\mathrm{b}}}\right)^2}\end{aligned}\tag{55}$$

in the exact and approximate formulations, respectively, where $0<\kappa(f_{\mathrm{b}})<1$ is a bounded function of the ligament parameter. In either form, the plus and minus signs introduced upon taking the square root of the two sides will correspond to the upper and lower values of $\Sigma_{33}-\Sigma_{11}$ representing the bounds of coalescence. Consequently, the yield criterion, expressed in a modified form in the coalescence region, writes:

$$\begin{aligned}&\Phi^{\mathrm{coal}}(\boldsymbol{\Sigma},f_{\mathrm{b}},W)=\frac{1}{\mathcal{L}(f_{\mathrm{b}})}\left(\frac{\Sigma_{33}-\mathrm{sgn}(D_{\mathrm{m}})\Sigma^{\mathrm{surf}}}{\bar{\tau}}\right)^2+\left(\frac{\Sigma_{31}}{\mathcal{T}}\right)^2=0\\&\mathcal{L}(f_{\mathrm{b}})=9\left(\frac{1-\kappa(f_{\mathrm{b}})}{\ln 1/f_{\mathrm{b}}}\right)^2+\frac{\kappa(f_{\mathrm{b}})}{(\mathcal{T}/\bar{\tau})^2}\end{aligned}\tag{56}$$

in its approximate formulation, where $\kappa(f_{\mathrm{b}})$ has been derived in (55).

Remark 1 The coalescence portion, viewed separately, is built upon volumetric averaging within the plastically deformable ligament. The main difference between the diffuse (growth) and localized (coalescence) mechanisms is that the latter is entitled with directionality. That is, plastic deformation becomes

localized in a plane to be specified. In a sense, the post-localized deformation can be expressed as a special case of the diffuse deformation mechanism in case the same microstructural parameters are utilized in both regimes (where, in the present work, the localization plane direction is implicitly assumed). The only difference would then be that the diffuse plastic deformation can be mainly expressed in terms of the (f, w) pair rather than the (χ, w, λ) triad, with f being the void volume fraction.

Remark 2 Equation (54) produces the same function as stated in Eq. $(19)_1$ of [40] as the flow potential for $\Sigma_{33} \geq \Sigma^{\text{surf}}$. Correspondingly, Eq. (56) resembles Eq. (41) of [39] (with a few percent of difference). By the same reasoning as illustrated in Appendix A [40], the transition from the regular (curved) part into the singular (straight) part of the coalescence yield locus occurs in a cornerless mode. The reason lies in the first derivative of Σ_{33} with respect to Σ_{31} being unbounded at $\Sigma_{31\max}$ due to vanishing of the denominator.

Remark 3: The signs attributed to D_{11} and D_m can come directly from the derivations. With reference to Eq. (54), $\text{sgn}(D_{11})$, appearing only during the growth regime, acts as function of the minimum positive value of $(\Sigma_{33} - \Sigma_{11})/\bar{\sigma}$ during void growth, which is fulfilled at the onset of coalescence. Since the post-coalescence regime supposedly progresses down into the negative half-space of $(\Sigma_{33} - \Sigma_{11})/\bar{\sigma}$, $\mathscr{T}^{\text{coal}}$ sets as the distinctive value for determining $\text{sgn}(D_{11})$. Namely:

$$\text{sgn}(D_{11}) = \text{sgn}(-(1-c) + c\mathscr{T}^{\text{coal}} - \frac{\Sigma_{33} - \Sigma_{11}}{\bar{\sigma}}) \tag{57}$$

Remark 4: Following the rationale given in [40], the value of $\text{sgn}(D_{\text{m}})$ at coalescence can be attributed to the sign of Σ_{33}. Since the process correlating void growth and coalescence is a *monotonic* one, a positive Σ_{33} during void growth is followed by a positive Σ_{33} at coalescence, and vice versa. Namely:

$$\text{sgn}(D_{\text{m}}) = \text{sgn}(\Sigma_{33}) \tag{58}$$

2.8 Synopsis of the Model

The unified yield criterion is hereby summarized as to facilitate readership:

$$\Phi(\boldsymbol{\Sigma}, f_{\text{b}}, W, c) = \begin{cases} \sqrt{3}\mathscr{T} - \dfrac{\sqrt{\mathcal{T}^2 - (\Sigma_{31}^2 + \Sigma_{32}^2)}}{\bar{\tau}} & \\ \text{if } \left| \frac{\Sigma_{11}}{\bar{\tau}} + \sqrt{3}(1-c)\left[\dfrac{\sqrt{\mathcal{T}^2 - (\Sigma_{31}^2 + \Sigma_{32}^2)}}{\bar{\tau}} + \text{sgn}(-\sqrt{3}(1-c) + c\mathscr{T}^{\text{coal}} - \frac{\Sigma_{33}-\Sigma_{11}}{\bar{\tau}}) \right] \right| \leq \frac{\Sigma^{\text{surf}}}{\bar{\tau}} & \\ \left(\dfrac{\Sigma_{31}^2 + \Sigma_{32}^2}{\bar{\tau}^2} \right) + \dfrac{\mathscr{T}^2}{3} + 2f_{\text{b}} \cosh\left(\dfrac{\Sigma_{33} - \text{sgn}(\Sigma_{33})\Sigma^{\text{surf}}}{\bar{\tau}} - \mathscr{T} \right) - (1 + f_{\text{b}}^2) & \text{if } |\mathscr{T}| \geq \mathscr{T}^{\text{coal}} \\ \left(\dfrac{\Sigma_{31}^2 + \Sigma_{32}^2}{\bar{\tau}^2} \right) + \dfrac{(\mathscr{T}^{\text{coal}})^2}{3} + 2f_{\text{b}} \cosh\left(\dfrac{\Sigma_{33} - \text{sgn}(\Sigma_{33})\Sigma^{\text{surf}}}{\bar{\tau}} - \mathscr{T}^{\text{coal}} \right) - (1 + f_{\text{b}}^2) & \text{Otherwise} \end{cases} \tag{59}$$

where

$$\begin{aligned} \mathscr{T} &= \frac{1}{c}\left(\frac{\Sigma_{33} - \Sigma_{11}}{\bar{\tau}} + \sqrt{3}(1-c)\text{sgn}(-\sqrt{3}(1-c) + c\mathscr{T}^{\text{coal}} - \frac{\Sigma_{33} - \Sigma_{11}}{\bar{\tau}}) \right) \\ (\mathscr{T}^{\text{coal}})^2 &= \frac{5}{3} + f_{\text{b}}^2 - \left(\frac{\Sigma_{31}}{\bar{\tau}} \right)^2 - \frac{2}{3}\sqrt{4(1+3f_{\text{b}}^2) - 3\left(\frac{\Sigma_{31}}{\bar{\tau}} \right)^2} \end{aligned} \tag{60}$$

in its exact form and

$$\Phi(\boldsymbol{\Sigma}; f_{\mathrm{b}}, W, c) = \begin{cases} \sqrt{3}\mathscr{T} - \dfrac{\sqrt{\mathcal{T}^2 - (\Sigma_{31}^2 + \Sigma_{32}^2)}}{\bar{\tau}} \\ \text{if} \left| \frac{\Sigma_{11}}{\bar{\tau}} + \sqrt{3}(1-c) \left[\dfrac{\sqrt{\mathcal{T}^2 - (\Sigma_{31}^2 + \Sigma_{32}^2)}}{\bar{\tau}} + \mathrm{sgn}(-\sqrt{3}(1-c) + c\mathscr{T}^{\mathrm{coal}} - \frac{\Sigma_{33} - \Sigma_{11}}{\bar{\tau}}) \right] \right| \leq \frac{\Sigma^{\mathrm{surf}}}{\bar{\tau}} \\ \left(\dfrac{\Sigma_{31}^2 + \Sigma_{32}^2}{\bar{\tau}^2} \right) + \dfrac{\mathscr{T}^2}{3} + \dfrac{(\mathcal{T}/\bar{\tau})^2}{\sqrt{3} \ln 1/f_{\mathrm{b}}} \left(\dfrac{\Sigma_{33} - \mathrm{sgn}(\Sigma_{33})\Sigma^{\mathrm{surf}}}{\bar{\tau}} - \dfrac{\mathscr{T}}{3} \right)^2 - (1 - f_{\mathrm{b}})^2 & \text{if } |\mathscr{T}| \geq \mathscr{T}^{\mathrm{coal}} \\ \left(\dfrac{\Sigma_{31}^2 + \Sigma_{32}^2}{\bar{\tau}^2} \right) + \dfrac{(\mathscr{T}^{\mathrm{coal}})^2}{3} + \dfrac{(\mathcal{T}/\bar{\tau})^2}{\sqrt{3} \ln 1/f_{\mathrm{b}}} \left(\dfrac{\Sigma_{33} - \mathrm{sgn}(\Sigma_{33})\Sigma^{\mathrm{surf}}}{\bar{\tau}} - \dfrac{\mathscr{T}^{\mathrm{coal}}}{3} \right)^2 - (1 - f_{\mathrm{b}})^2 & \text{Otherwise} \end{cases} \tag{61}$$

where

$$\begin{aligned} \mathscr{T}^{\mathrm{coal}} &= \kappa(f_{\mathrm{b}})\, c \frac{\Sigma_{33} - \mathrm{sgn}(D_{\mathrm{m}})\Sigma^{\mathrm{surf}}}{\bar{\tau}} - \sqrt{3}(1-c)\mathrm{sgn}(D_{11}) \\ \kappa(f_{\mathrm{b}}) &= \frac{1}{1 + \frac{1}{3}\left(\frac{\ln 1/f_{\mathrm{b}}}{1 - f_{\mathrm{b}}} \right)^2} \end{aligned} \tag{62}$$

in its simpler approximate counterpart. In either form, the first line represents the pre-coalescence singular (straight) part, the second line signifies the pre-coalescence regular (curved) zone, and the third line accounts for the coalescence straight line. As pointed out in advance, the transition from pre-coalescence to coalescence occurs without any slope singularity (sharp corners) except for the maximum shear stress equaling $\mathcal{T}$. A complete description over the extrema of stress components using the properties of $\mathscr{F}$ and $\mathscr{G}$ (or their equivalents $\mathscr{H}$ and $\mathscr{L}$) is covered in Appendix B. Finally, the model predictions will be validated with numerical outcomes in Section 3.1.

Remark: The difference between the regular portions of upper-bound and approximate functions is small. However, the approximate model's prediction of coalescence bounds is not as close as expected to that of the upper-bound model. Therefore, $\mathscr{T}^{\mathrm{coal}}$ had better be evaluated from (60) if one wants to adhere to the approximate model.

Notwithstanding the robust nature of the above model in predicting failure under combined tension and shear, its capability is entitled to its own limitations at extreme circumstances. The word *extreme* alludes to when the induced failure mechanism stays far from the real mechanism. Reference to [39, 40] declares that the extreme cases mainly takes place at very flat ($w << 1$) or much elongated ($w >> 1$) voids under predominantly tensile and shear loading schemes, respectively. The former refers to when the predicted mechanism is internal necking (which entails more work with increasing rigid zones) while the adjacent flattened voids can interconnect with plastic zones extending due to normal plastic deformation. All the same, the latter occurs since, with a long void, internal shearing (extending diagonally) does not occupy the entire ligament whereas the model presumes that plasticity is diffuse within the ligament. A flattened void mainly overpredicts Σ^{surf} and an elongated void tends to enlarge the maximum shear stress $\mathcal{T}$. The discussion pointed out in [39, 40] is suggestive of the following modification:

$$\Phi(\boldsymbol{\Sigma}, f_\mathrm{b}, W, c) = \begin{cases} \sqrt{3}\mathscr{T} - \dfrac{\sqrt{(l\mathcal{T})^2 - (\Sigma_{31}^2 + \Sigma_{32}^2)}}{\bar{\tau}} \\ \text{if } \left| \frac{\Sigma_{11}}{\bar{\tau}} + \sqrt{3}(1-c) \left[\dfrac{\sqrt{(l\mathcal{T})^2 - (\Sigma_{31}^2 + \Sigma_{32}^2)}}{\bar{\tau}} + \mathrm{sgn}(-\sqrt{3}(1-c) + c\mathscr{T}^\mathrm{coal} - \frac{\Sigma_{33}-\Sigma_{11}}{\bar{\tau}}) \right] \right| \leq \frac{t\Sigma^\mathrm{surf}}{\bar{\tau}} \\ \left(\dfrac{\Sigma_{31}^2 + \Sigma_{32}^2}{(l\bar{\tau})^2} \right) + \dfrac{\mathscr{T}^2}{3} + 2f_\mathrm{b} \cosh \left(\dfrac{\Sigma_{33} - \mathrm{sgn}(\Sigma_{33}) t\Sigma^\mathrm{surf}}{\bar{\tau}} - \mathscr{T} \right) - (1 + f_\mathrm{b}^2) & \text{if } |\mathscr{T}| \geq \mathscr{T}^\mathrm{coal} \\ \left(\dfrac{\Sigma_{31}^2 + \Sigma_{32}^2}{(l\bar{\tau})^2} \right) + \dfrac{(\mathscr{T}^\mathrm{coal})^2}{3} + 2f_\mathrm{b} \cosh \left(\dfrac{\Sigma_{33} - \mathrm{sgn}(\Sigma_{33}) t\Sigma^\mathrm{surf}}{\bar{\tau}} - \mathscr{T}^\mathrm{coal} \right) - (1 + f_\mathrm{b}^2) & \text{Otherwise} \end{cases} \tag{63}$$

based on exact integration and

$$\Phi(\boldsymbol{\Sigma}; f_\mathrm{b}, W, c) = \begin{cases} \sqrt{3}\mathscr{T} - \dfrac{\sqrt{(l\mathcal{T})^2 - (\Sigma_{31}^2 + \Sigma_{32}^2)}}{\bar{\tau}} \\ \text{if } \left| \frac{\Sigma_{11}}{\bar{\tau}} + \sqrt{3}(1-c) \left[\dfrac{\sqrt{(l\mathcal{T})^2 - (\Sigma_{31}^2 + \Sigma_{32}^2)}}{\bar{\tau}} + \mathrm{sgn}(-\sqrt{3}(1-c) + c\mathscr{T}^\mathrm{coal} - \frac{\Sigma_{33}-\Sigma_{11}}{\bar{\tau}}) \right] \right| \leq \frac{t\Sigma^\mathrm{surf}}{\bar{\tau}} \\ \left(\dfrac{\Sigma_{31}^2 + \Sigma_{32}^2}{(l\bar{\tau})^2} \right) + \dfrac{\mathscr{T}^2}{3} + \dfrac{(l\mathcal{T}/\bar{\tau})^2}{\sqrt{3}\ln 1/f_\mathrm{b}} \left(\dfrac{\Sigma_{33} - \mathrm{sgn}(\Sigma_{33}) t\Sigma^\mathrm{surf}}{\bar{\tau}} - \dfrac{\mathscr{T}}{3} \right)^2 - (1 - f_\mathrm{b})^2 & \text{if } |\mathscr{T}| \geq \mathscr{T}^\mathrm{coal} \\ \left(\dfrac{\Sigma_{31}^2 + \Sigma_{32}^2}{(l\bar{\tau})^2} \right) + \dfrac{(\mathscr{T}^\mathrm{coal})^2}{3} + \dfrac{(l\mathcal{T}/\bar{\tau})^2}{\sqrt{3}\ln 1/f_\mathrm{b}} \left(\dfrac{\Sigma_{33} - \mathrm{sgn}(\Sigma_{33}) t\Sigma^\mathrm{surf}}{\bar{\tau}} - \dfrac{\mathscr{T}^\mathrm{coal}}{3} \right)^2 - (1 - f_\mathrm{b})^2 & \text{Otherwise} \end{cases} \tag{64}$$

as its approximate counterpart. The recommended calibration functions read:

$$t(\chi, W) = \frac{(t_0 + t_1\chi)W}{1 + (t_0 + t_1\chi)W} \tag{65}$$

where t_0 and t_1 are parameters to be determined from numerical results (the choice of $t_0 = -0.84$, $t_1 = 20.6$ recommended in [39] is a proper one). To prevent an ill-behaved evaluation at $\chi \longrightarrow 0$, $t(\chi, W) = t(0.2, W)$ for $\chi < 0.2$. Secondly, l reads (again for $\chi \geq 0.2$ only):

$$l(\chi, W) = \left[1 + (l_1\chi + l_0)W\right] \mathcal{T} \tag{66}$$

with $(l_0, l_1) = (0.035, -0.15)$ proposed in [40].

The above scheme is heuristic. With regards to oblate voids, a recent work by Hure and Barrioz [49] proposed to consider a plastic flow extending above/below the void. It seems at first sight that, upon a similar approach, parameter c could be varied for the effective porous zone, which might eliminate the call for the use of calibrated functions as multiple of Σ^surf. However, such an effort is beyond the scope and is not along with the driving purpose behind this work, and is therefore left as an outlook for future investigation.

3 Model Assessment and Predictions

3.1 Cell-Model Calculations

The capability of the derived model should be observed by comparison to numerical results. The objective of this section is to elaborate on the steps to calculate the ultimate radial, normal, and shear stress values required to yield under volumetric void growth or lateral void coalescence using FEM analysis. In effect,

the FEM framework employed in this study is intended to be the numerical equivalent of the theoretical plastic limit load analysis of a structure, which corresponds to the problem of small-strain plasticity with *no* elastic domain (see [37]). A classical consequence of limit-analysis with this attitude is that elastic strain rates vanish when the limit load is reached. Therefore, the elastic moduli should disappear from the equations and, in turn, plasticity imposes an incompressible velocity field on the material. In this study, the base material of the unit cell is taken to be elastic-perfectly plastic. Yet, in order to mimic a de-facto limit analysis, a high value of Poisson's ratio, close to 0.5, should be enforced (the value used herein was $\nu = 0.49$, which maintains a quasi-incompressible velocity field and will not lead to singular solutions). Following the yield strength to Young's modulus ratio of $\bar{\sigma}/E = 0.000225$, the Young modulus is taken $E = 4444.5\bar{\sigma}$.

The commercial tool ABAQUS is used to carry out the numerical calculations. Inasmuch as this part of the research is meant to validate the analytical model, the FE model is featured as to include a unit cell (with the geometric properties characterized in Section 2.1) admitting quasi-periodic boundary conditions (the term *quasi-* denoting the fact that the cylindrical cell is not space-filling per se). The analysis procedure allows for any alternative space-filling model with no significant increase in the computational demand. Yet, the least uncertainty lies within the numerical and analytical cells with identical geometries. See [40].

The critical stress value for a specific void configuration (as dictated by a specific $(\chi,\ W)$ pair) is sought for at each FE analysis. To this end, the equilibrium equations are to be solved on the basis of initial geometric specifications rather than the deformed state in order that the calculated stress values correspond to a well-defined initial configuration with a perfectly circular cylindrical void shape. This can be achieved through switching off geometric nonlinearity in ABAQUS (*NLGEOM=No*; for more technical details, consult ABAQUS Documentation [50]). All the geometric parameters would then refer to the initial geometry.

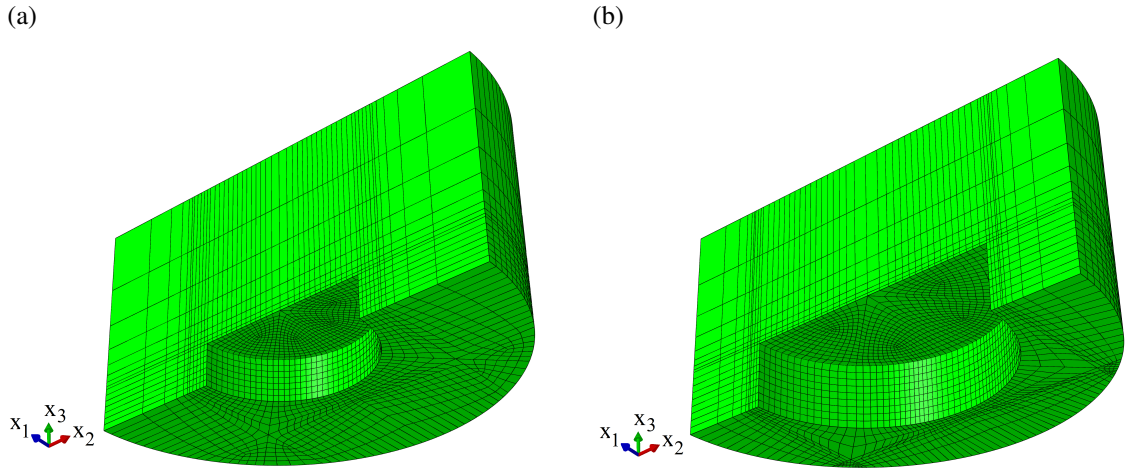

Figure 7: A numerically well–conditioned mesh illustrated for $W = 0.5$ and: (a) $\chi = 0.4$, (b) $\chi = 0.6$.

Figure 7 depicts a numerically well–conditioned mesh illustrated for $\chi = (0.4, 0.6)$ and $W = 0.5$. Due to their quasi-rigid conduct, a coarse mesh can be utilized for the parts away from the voided region.

As stated above, a circular cylindrical cell is not space-filling at first sight. To overcome this apparent shortcoming, the modeled cell figures a periodic void distribution where each void center corresponds to the lattice point of a hexagonal crystal. In most configurations, the void fully fits into the unit cell when the cell aspect ratio λ is considered as unity. Yet, for some (χ, W) pairs, the void will protrude, and thus λ ought to take other values. The reader, however, should be appreciative of the fact that λ bears no influence on the critical stress values at the onset of coalescence so long as the height H is taken large enough to guarantee

the possible presence of rigid zones above and below the void [4]. On the other hand, a larger H value leads to a greater number of elements, and the computational cost will be increased accordingly. Different λ ratios were thus chosen for varying (χ, W) sets, as shown in Table 1.

Table 1: $W - \chi$ sets for which $\lambda \neq 1$

W	χ	λ
0.1	0.4	0.5
0.1	0.6	0.5
1.5	0.4	1.2
1.5	0.6	1.5
2.0	0.4	1.6
2.0	0.6	2.0
2.5	0.4	2.0
2.5	0.6	2.5
3.0	0.4	2.4
3.0	0.6	3.0

The FEM analysis proceeds as controlled by three target displacements $U_1 = U_2$, U_3, and U_t, denoting the lateral, axial, and tangential (shear) displacements, respectively. The target displacements are applied onto the main vertical chords on the lateral surface, and onto the upper surface, respectively. The radial displacement is then distributed over the lateral surface elements through the periodicity equations expanded in Appendix C. The stress distribution and resultant stress components are completely calculable as function of the $R_r = U_1/U_3 = U_2/U_3$ and $R_{\text{sh}} = U_t/U_3$ independent ratios. Since the ultimate load value is not known as such, each stress component for the overall unit cell is calculated in obedience to a simple volume averaging, which can be written as

$$\Sigma_{\text{ij}} = \sum_{n=1}^{N} \sum_{m=1}^{M} (\sigma_{\text{ij}})_n^m v_n \tag{67}$$

where $v_k = V_k/\Omega$ is the volume fraction of each integration point with respect to the whole unit cell (with $\Omega = V_{\text{cell}}$ being the total cell volume). In other terms, macroscopic stress components are calculated by looping over all elements and all Gauss points for each and every element, where N is the total number of elements and M is the number of Gauss points in an element ($n = 8$ for the 20-node quadratic brick element with reduced integration, named as *C3D20R* in the ABAQUS element library [50]). Hence, σ_{ij} is the local stress value at the corresponding integration point.

[4] Also noteworthy is that the zones above and below the void ought to be large enough to set grounds for localization to occur in the x_1 – x_2 plane at coalescence, referred to as *internal necking* the basis of coalescence derivations. If the void is very close to the top (and bottom) surfaces of the unit cell, coalescence occurs in the x_2 – x_3 plane (primarily named as a *necklace*-type coalescence by Benzerga [51], which is beyond the scope of this study. Prior to coalescence, during void growth, localization occurs perpendicular to the ligament.

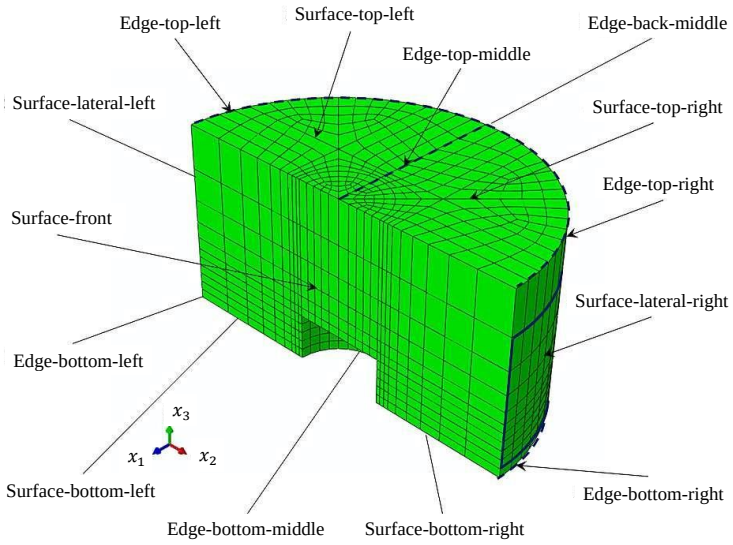

Figure 8: Finite element mesh for one quarter of an example unit cell with microstructural parameters given as $(\chi, W) = (0.25, 1.0)$, accompanied by the nomenclature used to define various surfaces and edges to which the boundary conditions are imposed. The origin of the reference coordinate system stands at the void center in the undeformed configuration.

The FEM analyses are of a single-step strain-controlled identity. The rationale behind this is that the initial configuration should also pertain to the ultimate state without large expansions and/or distortions taking over the process. Moreover, the remote traction values at the onset of localization are not known a priori. Therefore, the radial-to-normal and shear-to-normal stress ratios at the onset of coalescence are mainly influenced by the radial-to-normal (R_r) and tangent-to-normal (R_{sh}) displacement ratios prescribed for the lateral surface and top-face middle chord of the unit cell $(0,\ x_2,\ H)$, respectively (the latter is shown with a dashed line in Fig. 8). A complete explanation on the imposition of periodic boundary conditions on the unit cell is covered in Appendix C.

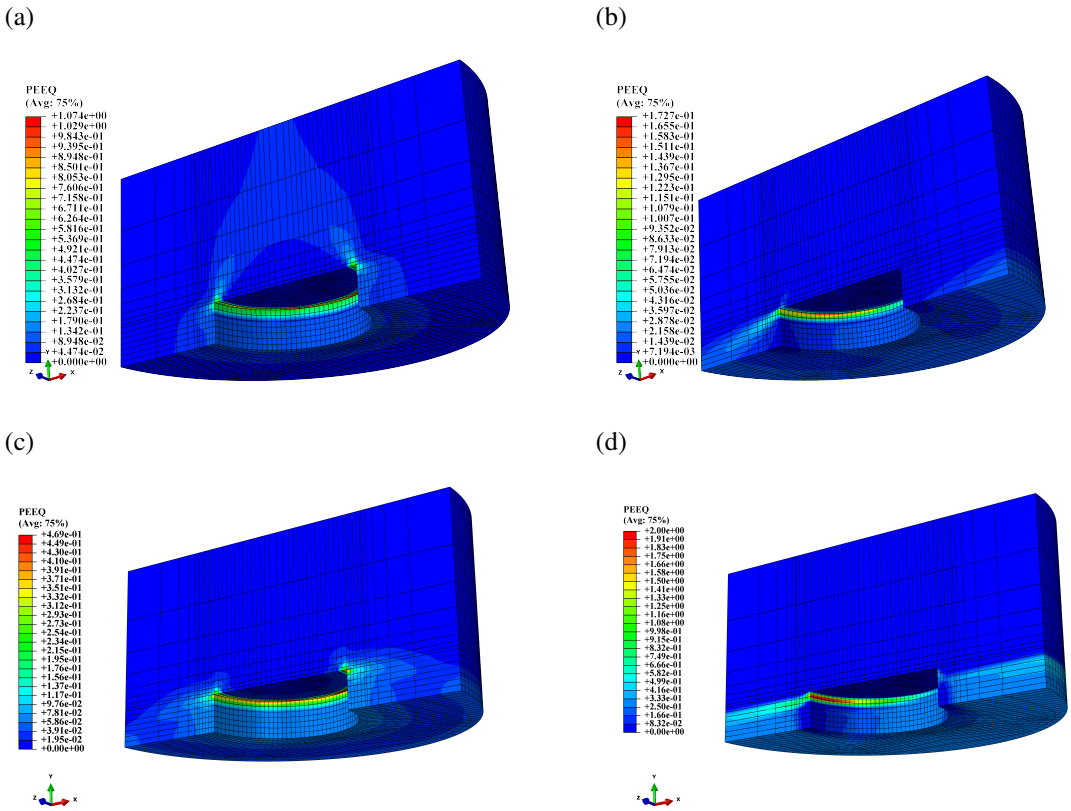

Figure 9: Examples of equivalent plastic strain (PEEQ) contours for fixed microstructural parameters $(\chi, W) = (0.4, 0.5)$ and varying R_r and R_{sh} ratios: (a,b) during void growth prior to coalescence, with (a) $(R_r, R_{\text{sh}}) = (100, 0)$, (b) $(R_r, R_{\text{sh}}) = (1, 20)$, exhibiting diffuse plasticity; (c,d) at the onset of coalescence (with $R_r = 0$), exhibiting an internal necking localization, (c) $R_{\text{sh}} = 0$ (denoting zero shear), (d) $R_{\text{sh}} = 20$ (denoting intense shear).

Figure 9 demonstrates examples of equivalent plastic strain (PEEQ) contours during void growth as well as at the onset of void coalescence for a given geometry and different R_{sh} ratios. In the former, plasticity extends into the solid zone bounding the void whereas, in the latter, it stays within the confines of the ligament, clearly revealing the *internal necking or shearing* mechanism.

3.2 Model predictions vs. numerical results

Enough grounds are now provided for validation of the model. Figure 10a and 10b illustrate representative yield loci in absence of shear ($\Sigma_{31} = 0$) as well as for various values of shear stresses, respectively, shown as compared to FEM results. Similar analysis, only in absence of shear, were carried out by Morin *et al.* [14] for the same unit cell geometry. Note that, due to the uncoupled nature of shear tractions from the triaxial ones, all the points that constitute a curvilinear locus correspond to a single value of U_t.

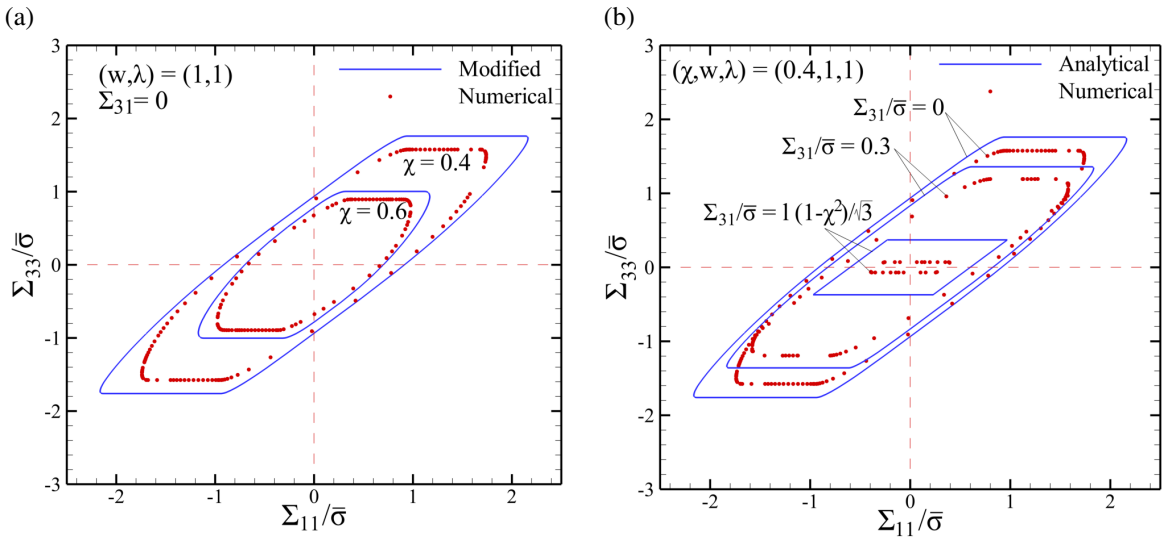

Figure 10: Comparison between analytical and numerical yield loci for microstructural parameters $(W, \lambda) = (1.0, 1.0)$ and $\chi = 0.4, 0.6$: (a) in absence of shear ($\Sigma_{31} = 0$); (b) for $\Sigma_{31} = \{0, 0.3\bar{\sigma}, \mathcal{T}\}$. Note that the modified and analytical maximum shear stresses are almost equally $\mathcal{T} = 0.419\bar{\sigma}$ after modification is applied.

It can be obviously observed that the numerical yield surface subtends its analytical counterpart, admitting the rigorous upper-bound character. That is, the analytical surfaces would invariably stand exterior to its numerical counterpart [35]. The model, at best, should be both upper-bound and rigorous. As clearly seen in Fig. 10, the present model proves close to rigorous for a wide range of shear stresses, and the only case where it keeps being an upper bound but ceases to be rigorous is under extreme shearing, denoted by $\Sigma_{31} = \mathcal{T}$.

Also revealed is the point symmetry of the yield locus with respect to the stress space origin. Above all, the points pertaining to near-maximum shearing all correspond to $U_t \geq 50U_3$. Such an intense shear would trigger a constant axial stress Σ_{33} being equal to the case with $U_1 = 0$, and the lateral stress Σ_{11} range stems from U_1 varying between $-U_3$ and U_3. It can be realized that, in a state of extreme shearing ($\Sigma_{31} \longrightarrow \mathcal{T}$), the only mode of failure is internal shearing as there are no FEM data between the two parallel sets. That is, the inclined linear parts for $\Sigma_{31} = \mathcal{T}$ in Fig. 10b are not physical.

3.3 Representative Yield Surfaces

This subsection reflects the analytical yield surfaces predicted by the model without relying on their FEM counterparts. To this end, the typical well-behaved microstructural triple $(\chi, W, c) = (0.5, 1.0, 0.5)$ has been adopted herein. Figure 11 shows various yield loci upon quasi-equivalent vs mean as well as normal vs radial stress expressions, for shear stress values ranging from 0 to the maximum magnitude $\mathcal{T}$. The approximate loci can be seen to stand interior to the exact counterparts.

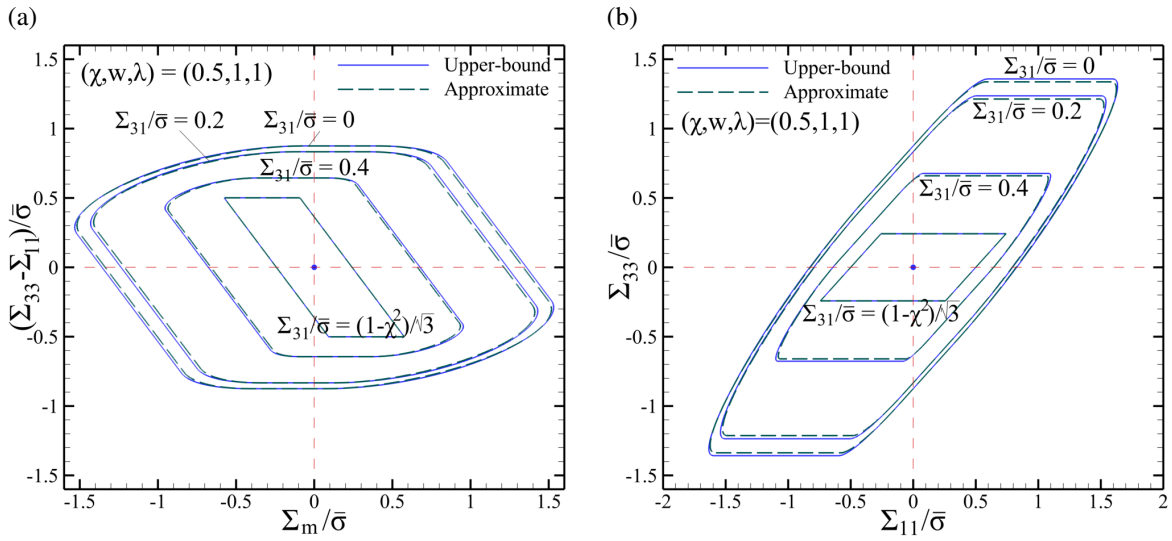

Figure 11: (a) Quasi-equivalent vs mean, and (b) normal vs radial stress yield loci for a representative set of microstructural parameters $(\chi, W, c) = (0.5, 1.0, 0.5)$ with several values of shear stress.

The complete yield surface will be generated upon considering shear stress as a third axis. The 3D yield surfaces for the representative microstructural values $(\chi, W, c) = (0.5, 1.0, 0.5)$ are shown in Fig. 12. The coalescence surfaces are illustrated with a sharper color. For more clarity, they are also exclusively shown in Fig. 13. The projection of the cylindroidal coalescence surface on the $\Sigma_{11} = 0$ plane is nothing but the coalescence yield locus, as showcased in Fig. 13c.

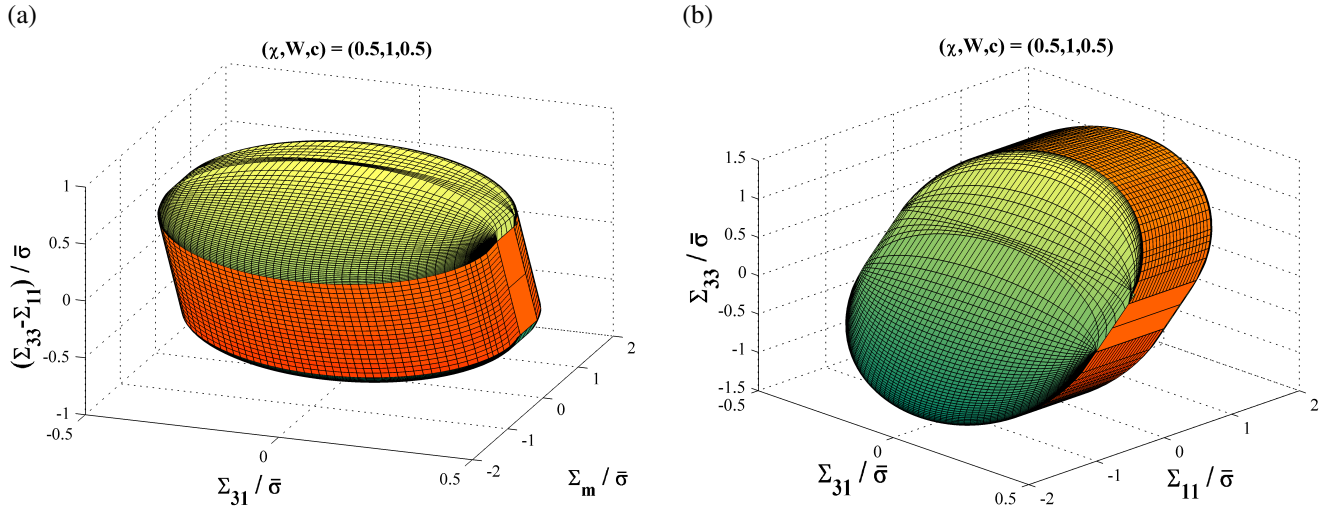

Figure 12: (a) Quasi-equivalent vs mean, and (b) normal vs radial stress 3D yield surfaces for the representative set of microstructural parameters $(\chi, W, c) = (0.5, 1.0, 0.5)$ with shear stress as the third axis. The sharp-colored subsurfaces pertain to the coalescence regime.

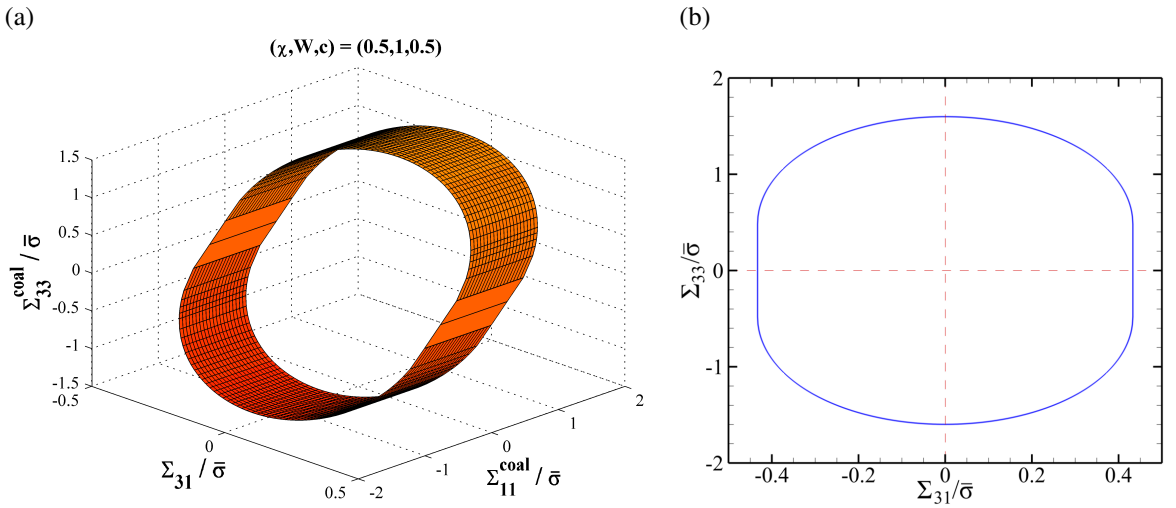

Figure 13: (a) normal vs radial stress 3D yield surface only representing void coalescence for the same set of microstructural parameters $(\chi, W, c) = (0.5, 1.0, 0.5)$; (b) 2D surface projection onto the Σ_{31}–Σ_{33} plane, retrieving the yield locus introduced in [40].

The yield surfaces/loci shown in Fig's are all associated with frozen microstructures. The effects due to varying microstructural parameters are then illustrated in Appendix 3.4.

3.4 Effects of microstructure on yield surface bounds

The representative yield surfaces were given for a single triad of microstructural parameters. The reader, however, may be avid to know how each parameter tends to affect the yield criterion independently, i.e. when the rest of parameters are kept constant. The only independent microstructural parameters in the model derived herein are the void aspect ratio (W), the ligament parameter (χ), and the cell aspect ratio (λ) or, alternatively, the ligament volume fraction (c). In the following comes discussion on the effect of each microstructural parameter at varying values of shear stress.

3.4.1 Effect of cell ligament parameter

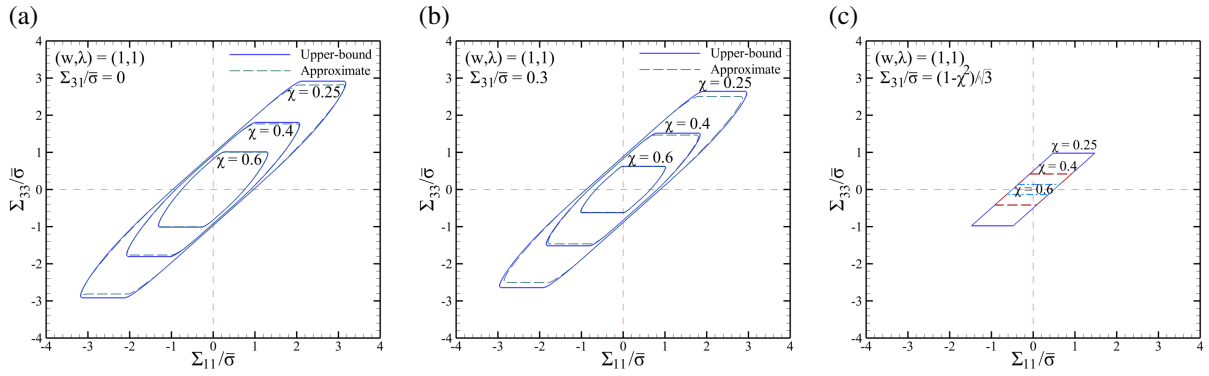

Figure 14: Effect of the ligament parameter χ on the bounds of the normal vs radial stress yield surface, the other microstructural parameters kept constant at $(W, c) = (1.0, 0.5)$: (a) $\Sigma_{31} = 0$, (b) $\Sigma_{31} = 0.3\bar{\sigma}$, and (c) $\Sigma_{31} = \mathcal{T}$.

Figure 14 demonstrates the effect of the ligament parameter χ on the bounds of the yield surface in the corresponding stress space. Increasing χ would shrink the yield surface along both axes, the so-called effect being more remarkable on the axial (Σ_{33}) stress bounds. Moreover, the shrinking effect of χ diminishes with increasing shear.

3.4.2 Effect of void aspect ratio

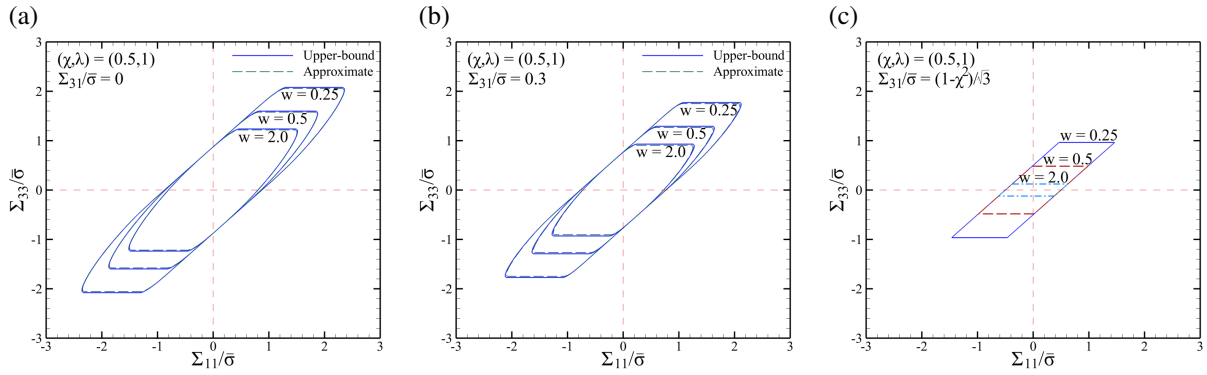

Figure 15: Effect of the void aspect ratio W on the bounds of the normal vs radial stress yield surface, the other microstructural parameters kept constant at $(\chi, c) = (0.5, 0.5)$: (a) $\Sigma_{31} = 0$, (b) $\Sigma_{31} = 0.3\bar{\sigma}$, and (c) $\Sigma_{31} = \mathcal{T}$.

The effect induced by variation of W is depicted in Fig. 15. Increasing W would, for the most part, decrease the bounds of Σ_{33} while the influence on Σ_{11} may not be neglected. Altogether, the pre-coalescence zone, accounting for volumetric void growth, is not significantly affected by the void aspect ratio.

3.4.3 Effect of cell aspect ratio

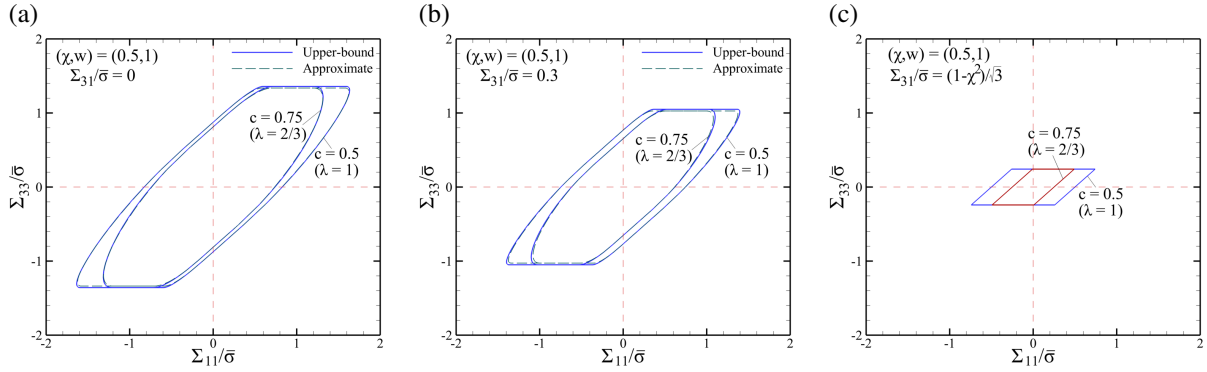

Figure 16: Effect of the cell aspect ratio λ, represented by the ligament volume fraction c in the formulation, on the bounds of the normal vs radial stress yield surface, the other microstructural parameters kept constant at $(\chi, W) = (0.5, 1.0)$: (a) $\Sigma_{31} = 0$, (b) $\Sigma_{31} = 0.3\bar{\sigma}$, and (c) $\Sigma_{31} = \mathcal{T}$. The values of λ associated with $c = (0.5, 0.75)$ are $\lambda = (1.0, 2/3)$.

The cell aspect ratio λ is in inverse proportion with the ligament volume fraction c. However, since the yield functions are directly expressed in terms of c rather than λ, the effect imposed by the former parameter

will be discussed. Figure 16 illustrates this effect. Interesting is the fact that, with other parameters fixed c (or λ), will not affect the axial coalescence stress bounds, whereas it alters the lateral stress bounds at coalescence. Mathematically explained, the c factor is canceled from the equations after setting $\partial\Phi/\partial\Sigma_{11}$ to zero. Physically interpreted, plasticity at internal necking coalescence is mainly dictated by the plastic deformation triggered in the *ligament* circumscribing the void, rather than the whole volumetric domain. Disregarding coalescence, however, decreasing λ (increasing c) has a shrinking effect on the yield surface bounds.

4 Discussion

The results represent a first analytically-derived micromechanics-based model describing void growth and coalescence under combined tension and shear in unified form. The model was derived on the basis of limit analysis over a cylindrical elementary cell embedding a coaxial cylindrical void. It can be clearly evidenced that, unlike that in hybrid models, the transition between the pre-coalescence and coalescence zones occurs in a cornerless mode. Hence, the overall surface, comprising straight and curved portions, admits a C^1-degree continuity. Comparison between analytical and numerical limit loads confirms that the model is preservative of the upper-bound character. The difference between the upper-bound and approximate yield loci is clearly negligible (or zero at maximum shear) even though the approximate model is significantly simpler than the upper-bound counterpart.

Further observed from Fig. 11 is that the yield surface has point symmetry with respect to both space origins. Moreover, the transition between the pre-coalescence and coalescence zones occurs in a cornerless mode (except for the maximum shear stress magnitude, which is more of a theoretical value rather than being practical).

Among all subsurfaces within the yield surface, the horizontal portions in Fig. 11a, equivalent to slanted linear parts in 11b, are non-physical due to the simplistic choice of the velocity field, which satisfies a first-degree continuity within the radial component between the ligament and matrix. Higher degrees of continuity would create a more precise model (with curved parts taking place of the linear parts) but not in closed form.

Upon a deeper scrutiny, the yield surface is found to have singularity in the whole area beneath the locus corresponding to the maximum shear stress $\Sigma_{31} = \mathcal{T}$, and the values of axial and radial stresses (and consequently $\Sigma_{33} - \Sigma_{11}$ and Σ_{m}) can take any value –including zero– inside the circumscribing parallelogram. This represents a planar part on the yield surface, can be more clearly observed in Fig. 12.

One could also see, by looking into the coalescence subsurface in 13, that the coalescence yield locus introduced in [40] appears by viewing the subsurface along the Σ_{11} axis. Correspondingly, the same yield criterion as in [40] will be retrieved by setting $D_{11} = D_{22} = 0$. See (59_3). This would reflect as an elliptical function in $(61)_3$, which resembles that proposed in [39].

The increased difference between analytical and numerical yield loci in Fig. 10 with increased shear is due to the simplistic velocity field, which could have been extended into a more precise one but would no more deliver a closed-form expression of the yield function. Moreover, unlike the onset of coalescence identified in [48] and the like, the present model is devoid of adjustable parameters such as f_c or heuristic factors that could calibrate the function during void growth. However, the main concern regarding a yield function upon derivation is to preserve the upper-bound character, which is fully satisfied herein. On the other hand, the analytical and numerical counterparts cannot be too far, and hence, the model, at best, should be both *upper-bound* and *rigorous*. The present model proves close to rigorous for a wide range of shear stresses, and the only case where it keeps being an upper bound but ceases to be rigorous is under extreme shearing, denoted by $\Sigma_{31} = \mathcal{T}$.

In order for the model to set the benchmark for modeling ductile fracture, it should be numerically

implemented in a plasticity analysis framework. A key feature is then to supplement the model with proper constitutive equations to solve boundary-value problems.

Furthermore, the post-localization constitutive equations are meager in the literature. The evolved values of χ and w has been proposed in [34] in absence of shear. However, void rotation triggers the microstructural evolution, particularly for χ, w, and $\mathbf{n}_3$ (the latter denoting void orientation) more intricate. The simplest corresponding challenge is to develop evolution equations on a localized basis. Moreover, in order for the model to predict failure, a notion of *surrogate* microstructure comes into play, which maps the main cell into an equivalent upright one that warrants the use of the mathematical model. This will be ground for future investigation.

Among all microstructural parameters, the effect of the cell aspect ratio is more intricate. That is, in a microstructural evolution boundary-value problem, the initial cell shape, through λ_0, while f_0 and w_0 are kept constant, would affect the *onset* of void coalescence due to changing the initial void spacing, through χ_0. It, therefore, bares an indirect effect at fixed f_0 and w_0. If, on the other hand, χ_0 and w_0 are fixed instead, then λ_0 would influence void growth as well as the *lateral* stress at the onset of coalescence via affecting the value of porosity f (see Appendix 3.4 for better clarity on this effect). The effect of cell shape has been elucidated through evolution analyses in [48, 16, 34].

Another implication of the methodology discussed herein is how representative the elementary cell can be considered. In a sense, the cell shape could possibly affect the response. An extension of the present work analogous to [29] would therefore be an appealing subject of future work.

5 Conclusions

An upper-bound model of dilatant plasticity was developed, in extension to a simpler model developed in [14] as to incorporate the effect of shear, based on limit analysis of a cylindrical elementary cell. The natural framework of analysis was set by rate-independent J_2 (Mises) plastic flow rule, idealizing the material behavior as rigid-ideally plastic. The model consists of an effective yield criterion that unifies diffuse and localized modes of deformation, mainly designated by void growth and coalescence, in materials failing by ductile damage accumulation. With the choice of trial velocity fields considered in [14] as basis, so extended as to include shear, the overall model was derived all analytically from first principles based on limit analysis and expressed in piece-wise closed form in both upper-bound and quadratic approximate representations. The model encompasses the stress limits to void coalescence, and the transition between subfunctions representing growth and coalescence regimes is cornerless. With reference to a method introduced in [40], the numerical equivalent results with the same cell geometry were obtained from single-step finite-deformation FEM analysis, and the model was assessed therein. To extend the predictive capability of the model into cases with flattened or elongated voids, the as-derived model was modified, with reference to its numerical counterpart, with simple algebraic functions of the microstructural parameters. The model is yet to be numerically implemented to exhibit all its pros and cons. Once implemented, along with essential evolution equations for internal state variables, a complete failure procedure for porous materials from void growth to coalescence ensued by failure can be simulated in a homogenized manner. The constitutive framework can also be implemented in a user-defined subroutine (UMAT) for boundary-value problem simulation purposes. Further, notwithstanding the model is a well-grounded one, more extensive models, as to incorporate the void orientation and/or matrix anisotropy, would be appealing.

Acknowledgments

The author truly acknowledges all the technical and inspirational advice from his PhD advisor, Prof. A. A. Benzerga. Support from the National Science Foundation under grant number CMMI-1405226 is also

acknowledged. The author would also like to thank Prof. A. Needleman for his illuminating discussion about this work.

Appendix A Proof of Eq. (42)

Equation (40) is firstly repeated here for ease of reference.

$$\begin{aligned}\Sigma_1^* &= \bar{\sigma}\left[\sinh^{-1}\left(\frac{\zeta}{f_\mathrm{b}}\right) - \sinh^{-1}(\zeta)\right] \\ \Sigma_2^* &= \mathrm{sgn}(D_2^*)\bar{\sigma}\left(\sqrt{1+\zeta^2} - \sqrt{f_\mathrm{b}^2+\zeta^2}\right)\end{aligned} \tag{A-1}$$

Consider the following identities

$$\begin{aligned}\cosh(a-b) &= \cosh a\cosh b - \sinh a\sinh b \\ \sinh(a-b) &= \sinh a\cosh b - \cosh a\sinh b\end{aligned} \tag{A-2}$$

with $(a,b)\in\mathbb{R}$ are any two real numbers. With (A-2)$_1$ applied on (A-1)$_1$, one can write

$$f_b\cosh\left(\frac{\Sigma_1^*}{\bar{\sigma}}\right) = \sqrt{f_b^2+\zeta^2}\,\sqrt{1+\zeta^2} - \zeta^2 \tag{A-3}$$

which, along with (A-1)$_2$, leads to ζ eliminated in terms of the auxiliary stresses as

$$\zeta^2 = \left[\frac{1-f_b\cosh\left(\Sigma_1^*/\bar{\sigma}\right)}{\Sigma_2^*/\bar{\sigma}}\right]^2 - 1 \tag{A-4}$$

Next, (A-2)$_2$ can be applied on (A-1)$_1$ and, together with (A-1)$_2$, yield

$$f_b\sinh\left(\frac{\Sigma_1^*}{\bar{\sigma}}\right) = \zeta\frac{\Sigma_2^*}{\bar{\sigma}} \tag{A-5}$$

Then, exploiting the correlation between $\cosh^2 a$ and $\sinh^2 a$, one can write

$$\cosh^2\left(\frac{\Sigma_1^*}{\bar{\sigma}}\right) - \sinh^2\left(\frac{\Sigma_1^*}{\bar{\sigma}}\right) = 1 \quad \therefore \quad 1+\left(\frac{\Sigma_2^*}{\bar{\sigma}}\right)^2 - 2\sqrt{1+\zeta^2}\,\frac{\Sigma_2^*}{\bar{\sigma}} = f_b^2$$

which, with ζ plugged in from (A-4), generates the desired relation reading

$$\left(\frac{\Sigma_2^*}{\bar{\sigma}}\right)^2 + 2f_b\cosh\left(\frac{\Sigma_1^*}{\bar{\sigma}}\right) - (1+f_b^2) = 0 \tag{A-6}$$

Appendix B Bounds to the Yield Surface

It is advantageous to know the extrema of each applied stress in absence of the other stresses. This section aims at deriving the applied stress bounds upon expressing the yield criterion in terms of the quasi-equivalent vs mean or normal vs radial stresses, in presence of a nonzero shear stress. Since the absolute extrema for every stress component is sought for, the procedure is, as formerly illustrated, resorting back to the primitive inequality of limit analysis, i.e. Eq. (6). The first and foremost stage to this end is to express the plastic rate of work as well as the dissipation function in an equivalent form that is nondimensional with respect to the deformation rate components $\bar{D}_i$ (or D_{ij}), by dividing both functions by one arbitrary component of $\mathbf{D}$ (or $\bar{\mathbf{D}}$). Like so we will have two functions with nondimensional stress coefficients as

variables, as in (31) for instance. In general, the absolute evolution interval of each stress component can be evaluated with two different attitudes, both resting on the primitive inequality of limit analysis (6): by establishing the inequality condition either on the nondimensional factor (as for p variables) or on the relative status of nondimensionalized functions in whole (as in $\mathscr{F}$ and $\mathscr{G}$ (31)). In the former, the condition is met by setting the non-dimensional coefficient of the considered stress (p_1 and p_2 for instance, in section 2.7) to infinity (except for Σ_{31} as the one component free of multiples), and in the latter, it is satisfied by enforcing the inequality for all values of variables ($\forall\ p$ for instance). Extra care, however, should be taken regarding the first procedure. That is, in order to evaluate the entire stress space bounds, all critical values of nondimensional parameters (p_1 and p_2 for instance).

B.1 Quasi-equivalent vs mean stress, function of shear

Eq. (33) is the equivalent form of the primitive inequality in this case. By exploiting (32) and (42) or (41), one can express the entire stress space, plastic rate of work, and the dissipation function in terms of the (p_1, p_2) ratios, be it in exact or approximate form.

- Range of $\bar{\Sigma}_1$:

As formerly clarified in subsection (2.7), $p_1 \longrightarrow 0$ would give the interval of Σ_{11} in the pre-coalescence singular (straight) part. All the same, setting $p_1 \longrightarrow \infty$ gives rise to the (absolute) maximum value of Σ_{11}. Consequently:

$$\begin{aligned}
&\lim_{p_1\to\infty}(\zeta^2,\xi^2)=\left(\frac{1}{3(1-c)^2},1\right)\\
&|\mathscr{F}|\le\mathscr{G}\Longrightarrow\left|\frac{\bar{\Sigma}_1}{\bar{\tau}}\right|\le\left[\sinh^{-1}\left(\frac{u}{\sqrt{3}(1-c)}\right)-\sqrt{1+\frac{3(1-c)^2}{u^2}}\right]_1^{1/f_{\rm b}}\\
&+\sqrt{3}(1-c)\text{sgn}(D_{11})+\text{sgn}(D_{\rm m})\frac{\Sigma^{\rm surf}}{\bar{\tau}}
\end{aligned}\tag{A-7}$$

in the exact formulation, and

$$\left|\frac{\bar{\Sigma}_1}{\bar{\tau}}\right|\le(1-f_{\rm b})\sqrt{\left(\ln 1/f_{\rm b}\right)^2+3(1-c)^2(\frac{\mathcal{T}}{\bar{\tau}})^2}+\sqrt{3}(1-c)\text{sgn}(D_{11})+\text{sgn}(D_{\rm m})\frac{\Sigma^{\rm surf}}{\bar{\tau}}\tag{A-8}$$

in its approximate form. For the microstructural paramters $(\chi, W, c) = (0.5, 1.0, 0.5)$, for instance, the exact and approximate values will turn out to be 2.83 and 2.81, respectively.

- Range of $\bar{\Sigma}_2$:

Regarding the range of $\Sigma_{33} - \Sigma_{11}$, it can be obtained either from the $|\mathscr{F}| \le \mathscr{G}$ inequality or directly from the implicit relations, (47) or (46), the reason lying in the fact that $\Sigma_{33} - \Sigma_{11}$ stands constant in the pre-coalescence singular region (see subsection 2.7.1). The former approach entails evaluation of $\mathscr{F}$ and $\mathscr{G}$ at $p_2 \longrightarrow \infty$. The latter, however, demands that the inside of $\cosh$ be not smaller than 1 or, in the approximate formulation, the inside of the square root giving solution for $\Sigma_{33} - \text{sgn}(D_{\rm m})\Sigma^{\rm surf}$ be positive. Stated in

mathematical terms:

$$
\begin{aligned}
&|\mathscr{F}| \leq \mathscr{G}, \quad \lim_{p_2 \to \infty} (\zeta^2, \xi^2) = (0, 1.0) \\
&\text{or} \quad 1 - \frac{1}{(1-\mathrm{f_b})^2} \left[\frac{\mathscr{T}^2}{3} + \left(\frac{\Sigma_{31}}{\bar{\tau}} \right)^2 \right] \geq 0 \\
&\Longrightarrow \left| \frac{\bar{\Sigma}_2}{\bar{\tau}} + \sqrt{3}(1-c)\mathrm{sgn}(D_{11}) \right| \leq \sqrt{3} c \sqrt{(\frac{\mathcal{T}}{\bar{\tau}})^2 - \left(\frac{\Sigma_{31}}{\bar{\tau}} \right)^2} \\
&\therefore -\sqrt{3}[(1-c)\mathrm{sgn}(D_{11}) - c\sqrt{(\frac{\mathcal{T}}{\bar{\tau}})^2 - \left(\frac{\Sigma_{31}}{\bar{\tau}} \right)^2}] \leq \frac{\Sigma_{33} - \Sigma_{11}}{\bar{\tau}} \leq -\sqrt{3}[(1-c)\mathrm{sgn}(D_{11}) + c\sqrt{(\frac{\mathcal{T}}{\bar{\tau}})^2 - \left(\frac{\Sigma_{31}}{\bar{\tau}} \right)^2}]
\end{aligned}
\tag{A-9}
$$

- Range of $\bar{\Sigma}_3$:

The range of Σ_{31} can be observed by letting $(p_1, p_2) \longrightarrow 0$. This would generate the following interval:

$$\Sigma_{31} \leq \frac{1 - f_\mathrm{b}}{\sqrt{3}} \bar{\sigma} = \mathcal{T} \tag{A-10}$$

Remark 1: For the sake of more clarity, the yield locus associated with the maximum absolute shear stress constitutes only of the pre-coalescence singular part and the coalescence part, the transition in between occuring with a sharp vertex due to lack of the intermediate curved region, serving as a smoothing agent (see Fig. 11).

Remark 2: The same interval can be derived from the (exact and approximate) formulas describing the curved parts.

B.2 Normal vs Radial stress, function of shear

The components of the stress space herein are $(\Sigma_{11}, \Sigma_{33}, \Sigma_{31})$, with the associated deformation rate components being (D_{11}, D_{22}, D_{33}). Following a similar procedure as elucidated in section 2.7, one can fabricate an alternative form of (6) by defining:

$$q_1 = \frac{D_{11}}{D_{31}} \quad q_2 = \frac{D_{33}}{D_{31}} \tag{A-11}$$

By the same account, the following functions of (q_1, q_2) can be defined:

$$
\begin{aligned}
\mathscr{H} =& \frac{\mathbf{\Sigma} : \mathbf{D}}{\bar{\sigma} D_{31}} \equiv 2q_1 \frac{\Sigma_{11}}{\bar{\sigma}} + q_2 \frac{\Sigma_{33}}{\bar{\sigma}} + 2\frac{\Sigma_{31}}{\bar{\sigma}} \\
\mathscr{L} =& \frac{\Pi(\mathbf{D})}{\bar{\sigma} D_{31}} \equiv \sqrt{\frac{4}{3} + \left[2(1-c)q_1 + q_2\right]^2} \left[\zeta \sinh^{-1}(\zeta u) - \sqrt{\frac{1}{u^2} + \zeta^2} \right]_1^{1/f_\mathrm{b}} \\
&+ 2(1-c)|q_1| + |2q_1 + q_2| \, \mathrm{sgn}(D_\mathrm{m}) \frac{\Sigma^{\mathrm{surf}}}{\bar{\sigma}} \\
\forall \quad & q_1, q_2 : \quad |\mathscr{H}| \leq \mathscr{L}
\end{aligned}
\tag{A-12}
$$

where ζ is expressed in its transformed state as follows:

$$\zeta^2 = \left(\frac{D_1^* / D_{31}}{D_2^* / D_{31}} \right)^2 = \frac{(2q_1 + q_2)^2}{3[2(1-c)q_1 + q_2]^2 + 4} \tag{A-13}$$

Now the tools are at hand to calculate the bounds to the stress components. As formerly pointed out, the absolute evolution interval of each stress component can be evaluated by setting the multiplied ratio to infinity, except for the one component free of multiples, i.e. Σ_{31}.

- Range of Σ_{11}: $q_1 \longrightarrow \infty$

$$\begin{aligned}
&\lim_{q_1\to\infty}\zeta^2 = \frac{1}{3(1-c)^2}\\
&|\mathscr{H}| \le \mathscr{L} \Longrightarrow \left|\frac{\Sigma_{11}}{\bar{\tau}}\right| \le \left[\sinh^{-1}\left(\frac{u}{\sqrt{3}(1-c)}\right) - \sqrt{1+\frac{3(1-c)^2}{u^2}}\right]_1^{1/f_{\rm b}}\\
&+\sqrt{3}(1-c)\text{sgn}(D_{11}) + \text{sgn}(D_{\rm m})\frac{\Sigma^{\rm surf}}{\bar{\tau}}
\end{aligned} \tag{A-14}$$

in the exact formulation and

$$\left|\frac{\Sigma_{11}}{\bar{\sigma}}\right| \le (1-f_{\rm b})\sqrt{\left(\ln 1/f_{\rm b}\right)^2 + 3(1-c)^2(\frac{\mathcal{T}}{\bar{\tau}})^2} + \sqrt{3}(1-c)\text{sgn}(D_{11}) + \text{sgn}(D_{\rm m})\frac{\Sigma^{\rm surf}}{\bar{\tau}} \tag{A-15}$$

in its approximate peer. Equations (A-14) and (A-15) are easily observed to be identical to (A-7) and (A-8), respectively.

- Range of Σ_{33}: $q_2 \longrightarrow \infty$

$$\begin{aligned}
&\lim_{q_2\to\infty}\zeta^2 = \frac{1}{3}\\
&|\mathscr{H}| \le \mathscr{L} \Longrightarrow \left|\frac{\Sigma_{33}}{\bar{\tau}}\right| \le \left[\sinh^{-1}\left(\frac{u}{\sqrt{3}}\right) - \sqrt{\frac{3}{u^2}+1}\right]_1^{1/f_{\rm b}} + \frac{\text{sgn}(D_{33})\,\Sigma^{\rm surf}}{\bar{\tau}}
\end{aligned} \tag{A-16}$$

in the exact formulation and

$$\left|\frac{\Sigma_{33}}{\bar{\tau}}\right| \le \sqrt{\left(\ln 1/f_{\rm b}\right)^2 + 3(\frac{\mathcal{T}}{\bar{\tau}})} + \text{sgn}(D_{\rm m})\frac{\Sigma^{\rm surf}}{\bar{\tau}} \tag{A-17}$$

in its approximate counterpart. For the microstructural paramters $(\chi, W, c) = (0.5, 1.0, 0.5)$, for instance, the exact and approximate values will turn out to be 2.35 and 2.31, respectively.

Remark 1: As clearly observed in Fig. 11, the extreme values of Σ_{33} occur at the coalescence regime, signifying a saturation limit for axial remote stress consequent to the onset of coalescence. This, as illustrated in Fig. 10, has been substantiated by numerical outcomes.

- Range of Σ_{31}: $q_1, q_2 \longrightarrow 0$

$$\begin{aligned}
&\lim_{(q_1,q_2)\to 0}\zeta^2 = 0\\
&|\mathscr{H}| \le \mathscr{L} \Longrightarrow\ \Sigma_{31} \le \frac{1-f_{\rm b}}{\sqrt{3}}\bar{\sigma} = \mathcal{T}
\end{aligned} \tag{A-18}$$

which is identical to the expression stated in (A-10).

Remark 2: The same interval can be derived from (52) (as stated in terms of the coalescence-based $\mathscr{T}^{\mathrm{coal}}$) or (56) in its approximate counterpart. However, the stress state associated with the extreme value of Σ_{31} would not stand limited to coalescence. In fact, in accordance with the rationale given regarding the bounds of $\bar{\Sigma}_3$, the stress state may stand within a pre-coalescence regime represented by a straight part, or within the coalescence trend exhibiting a slant line in the quasi-equivalent vs mean stress expression (see Fig. 11).

Appendix C Quasi-Periodic Cell Boundary Conditions

The periodic boundary conditions imposed on the unit cell are expounded on. Thanks to its geometry, the problem can be completely represented by modeling one quarter of the whole cell. The normal and tangential displacements are then the two independent degrees of freedom at each center-line. Fig. 8 shows the various surfaces and edges of the reduced cell, together with an example meshing of the domain as well as the nomenclature used throughout this section.

For any two points in a periodic array of cells one could write [40]:

$$\Delta\mathbf{u} = (\mathbf{E} + \mathbf{\Omega}).\Delta\mathbf{x} \tag{A-19}$$

where $\Delta\mathbf{u}$ is the difference in displacement between the points separated by the vector $\Delta\mathbf{x}$. For a cylindrical cell, however, (A-19) cannot be applied since paired points with periodic correspondence do not exist. We should then impose conditions similar to (A-19) onto selected pairs of surface points instead, thus its name "quasi-periodic". See [40] for more details.

A complete case-by-case definition of the boundary conditions is written below in accordance with the nomenclature clarified beforehand.

Edge-Top-Middle

$$\begin{aligned} u_2(x_1, 0, H) &= \frac{1}{2}U_t, \\ u_3(x_1, 0, H) &= \frac{1}{2}U_3. \end{aligned} \tag{A-20}$$

Surface-Top-Left/Surface-Top-Right

$$\begin{aligned} u_1(x_1, -x_2, H) - u_1(x_1, x_2, H) &= 0, \\ u_2(x_1, -x_2, H) + u_2(x_1, x_2, H) &= U_t, \\ u_3(x_1, -x_2, H) + u_3(x_1, x_2, H) &= U_3. \end{aligned} \tag{A-21}$$

Edge-Top-Left/Edge-Top-Right

$$\begin{aligned} u_1(x_1, -\sqrt{L^2 - x_1^2}, H) &= u_1(x_1, \sqrt{L^2 - x_1^2}, H) = \frac{x_1}{2L}U_1, \\ u_2(x_1, \pm\sqrt{L^2 - x_1^2}, H) &= \frac{1}{2}(U_t \pm \frac{\pm\sqrt{L^2 - x_1^2}}{L}\, U_2), \\ u_3(x_1, \pm\sqrt{L^2 - x_1^2}, H) &= \frac{1}{2}U_3. \end{aligned} \tag{A-22}$$

Surface-Lateral-Left/Surface-Lateral-Right

$$\begin{aligned} u_1(x_1, -\sqrt{L^2 - x_1^2}, x_3) = u_1(x_1, \sqrt{L^2 - x_1^2}, x_3) &= \frac{x_1}{2L}U_1, \\ u_2(x_1, -\sqrt{L^2 - x_1^2}, x_3) - u_2(x_1, \sqrt{L^2 - x_1^2}, x_3) &= -\frac{\sqrt{L^2 - x_1^2}}{L}\, U_2, \\ u_3(x_1, -\sqrt{L^2 - x_1^2}, x_3) - u_3(x_1, \sqrt{L^2 - x_1^2}, x_3) &= 0. \end{aligned} \tag{A-23}$$

Edge-Bottom-Left/Edge-Bottom-Right

$$\begin{aligned} u_1(x_1, -\sqrt{L^2 - x_1^2}, 0) &= u_1(x_1, \sqrt{L^2 - x_1^2}, 0) = \frac{x_1}{2L} U_1, \\ u_2(x_1, \pm\sqrt{L^2 - x_1^2}, 0) &= \pm\frac{\sqrt{L^2 - x_1^2}}{2L}\, U_2, \\ u_3(x_1, \pm\sqrt{L^2 - x_1^2}, 0) &= 0. \end{aligned} \tag{A-24}$$

Edge-Bottom-Middle

$$\begin{aligned} u_2(x_1, 0, 0) &= 0, \\ u_3(x_1, 0, 0) &= 0. \end{aligned} \tag{A-25}$$

Surface-Bottom-Left/Surface-Bottom-Right

$$\begin{aligned} u_1(x_1, -x_2, 0) - u_1(x_1, x_2, 0) &= 0, \\ u_2(x_1, -x_2, 0) + u_2(x_1, x_2, 0) &= 0, \\ u_3(x_1, -x_2, 0) + u_3(x_1, x_2, 0) &= 0. \end{aligned} \tag{A-26}$$

Edge-Back-Middle

$$u_1(-L, 0, x_3) = -\frac{1}{2} U_1. \tag{A-27}$$

Surface-Front

$$u_1(0, x_2, x_3) = 0. \tag{A-28}$$

Remark 1: The absolute values of $U_1 = U_2$, U_t, and U_3 have no effect on ultimate stress components insofar as the corresponding plastic strains in the unit cell are significantly larger than the elastic strains (see [37] for further details). Stated other way, the value of all displacement components can be taken arbitrarily but enough care has to be taken in that none of the $U_1 = U_2$, U_t, and U_3 values should be comparable to the cell dimensions or the analysis will diverge (since nonlinear geometry has been turned off). A proper choice will then be to take, at every time, the maximum of all three as 0.01, i.e. $\max\{U_1 = U_2, U_t, U_3\} = 0.01$.

Remark 2: As regards the sole objective to define the critical stresses at the onset of void coalescence, U_1 and U_2 are taken to be zero in all the calculations. Therefore, stress distribution at coalescence is governed by the R_{sh} input.

Remark 3: For each (χ, W) pair, 18 different displacement ratios were imposed, obeying the relation R_r or $R_{\text{sh}} = k/2$, where $k = 0, 2, 3, ..., 10, 20, 30, 40, 80, 120, 160, 200$. A larger ratio induces a smaller Σ_{33} value in comparison to the other two stress components, and vice versa (Note: $\Sigma_{31} = 0$ for $U_t/U_3 = 0$).

References

[1] K. Danas and P. Ponte Castañeda. Influence of the Lode parameter and the stress triaxiality on the failure of elasto-plastic porous materials. *International Journal of Solids and Structures*, 49:1325–1342, 2012.

[2] I. Barsoum and J. Faleskog. Rupture mechanisms in combined tension and shear—-Micromechanics. *International Journal of Solids and Structures*, 44:5481–5498, 2007.

[3] V. Tvergaard. Effect of stress-state and spacing on voids in a shear-field. *International Journal of Solids and Structures*, 49:3047–3054, 2012.

[4] K. L. Nielsen, J. Dahl, and V. Tvergaard. Collapse and coalescence of spherical voids subject to intense shearing: studied in full 3D. *International Journal of Fracture*, 177:97–108, 2012.

[5] M. Dunand and D. Mohr. Effect of Lode parameter on plastic flow localization after proportional loading at low stress triaxialities. *Journal of the Mechanics and Physics of Solids*, 66:133–153, 2014.

[6] A. L. Gurson. Continuum Theory of Ductile Rupture by Void Nucleation and Growth: Part I– Yield Criteria and Flow Rules for Porous Ductile Media. *Journal of Engineering Materials and Technology*, 99:2–15, 1977.

[7] V. Tvergaard and A. Needleman. Analysis of the cup–cone fracture in a round tensile bar. *Acta Metallurgica*, 32:157–169, 1984.

[8] M. Gologanu, J.-B. Leblond, and J. Devaux. Approximate models for ductile metals containing non-spherical voids – case of axisymmetric prolate ellipsoidal cavities. *Journal of the Mechanics and Physics of Solids*, 41(11):1723–1754, 1993.

[9] M. Gologanu, J.-B. Leblond, G. Perrin, and J. Devaux. Recent extensions of Gurson's model for porous ductile metals. In P. Suquet, editor, *Continuum Micromechanics, CISM Lectures Series*, pages 61–130. Springer, New York, 1997.

[10] A. A. Benzerga and J. Besson. Plastic potentials for anisotropic porous solids. *European Journal of Mechanics*, 20A:397–434, 2001.

[11] S. M. Keralavarma and A. A. Benzerga. A constitutive model for plastically anisotropic solids with non-spherical voids. *Journal of the Mechanics and Physics of Solids*, 58:874–901, 2010.

[12] K. Madou and J.-B. Leblond. A Gurson-type criterion for porous ductile solids containing arbitrary ellipsoidal voids – I: Limit-analysis of some representative cell. *Journal of the Mechanics and Physics of Solids*, 60:1020–1036, 2012.

[13] K. Madou and J.-B. Leblond. Numerical studies of porous ductile materials containing arbitrary ellipsoidal voids — I: Yield surfaces of representative cells. *European Journal of Mechanics*, 42:480–489, 2013.

[14] L. Morin, J.-B. Leblond, A. A. Benzerga, and D. Kondo. A unified criterion for the growth and coalescence of microvoids. *Journal of the Mechanics and Physics of Solids*, 97:19–36, 2016.

[15] N. A. Fleck and J. W. Hutchinson. Void growth in shear. *Proceedings of the Royal Society of London A*, 407:435–458, 1986.

[16] S. M. Keralavarma, S. Hoelscher, and A. A. Benzerga. Void growth and coalescence in anisotropic plastic solids. *International Journal of Solids and Structures*, 48:1696–1710, 2011.

[17] Z. G. Liu, W. H. Wong, and T. F. Guo. Void behaviors from low to high triaxialities: Transition from void collapse to void coalescence. *International Journal of Plasticity*, 84:183–202, 2016.

[18] V. Tvergaard. Influence of voids on shear band instabilities under plane strain conditions. *International Journal of Fracture*, 17:389–407, 1981.

[19] R. J. Clifton, J. Duffy, K. A. Hartley, and T. G. Shawki. On Critical Conditions for Shear Band Formation at High Rates. *Scrip. Metall.*, 18:443–448, 1984.

[20] T. Pardoen and J. W. Hutchinson. An extended model for void growth and coalescence. *Journal of the Mechanics and Physics of Solids*, 48:2467–2512, 2000.

[21] K. Nahshon and J. W. Hutchinson. Modification of the Gurson Model for shear failure. *European Journal of Mechanics*, 27:1–17, 2008.

[22] T. F. Morgeneyer and J. Besson. Flat to slant ductile fracture transition: Tomography examination and simulations using shear-controlled void nucleation. *Scripta Materialia*, 65:1002–1005, 2011.

[23] J. Kadkhodapour, B. Anbarlooie, H. Hosseini-Toudeshky, and S. Schmauder. Simulation of shear failure in dual phase steels using localization criteria and experimental observation. *Computational Materials Science*, 94:106–113, 2014.

[24] T-S. Cao, M. Mazière, K. Danas, and J. Besson. A model for ductile damage prediction at low stress triaxialities incorporating void shape change and void rotation. *International Journal of Solids and Structures*, 63:240–263, 2015.

[25] T. Luo and X. Gao. On the prediction of ductile fracture by void coalescence and strain localization. *Journal of the Mechanics and Physics of Solids*, 113:82–104, 2018.

[26] E.M. Dubensky and D.A. Koss. Void/pore distributions and ductile fracture. *D.A. MTA*, 18(11):1887–1895, 1987.

[27] P. E. Magnusen, E. M. Dubensky, and D. A. Koss. The effect of void arrays on void linking during ductile fracture. *Acta Metallurgica*, 36(6):1503–1509, 1988.

[28] V. Tvergaard. Effect of void cluster on ductile failure evolution. *Meccanica*, 51:3097–3105, 2016.

[29] K. Kuna and D. Z. Sun. Three-dimensional cell model analyses of void growth in ductile materials. *International Journal of Fracture*, 81:235–258, 1996.

[30] F. Scheyvaerts, P. R. Onck, C. Tekoğlu, and T. Pardoen. The growth and coalescence of ellipsoidal voids in plane strain under combined shear and tension. *Journal of the Mechanics and Physics of Solids*, 59:373–397, 2011.

[31] C. Tekoğlu. Representative volume element calculations under constant stress triaxiality, lode parameter, and shear ratio. *International Journal of Solids and Structures*, 51:4544–4553, 2014.

[32] C. Tekoglu. Void coalescence in ductile solids containing two populations of voids. *Engineering Fracture Mechanics*, 147:418–430, 2015.

[33] L. Morin, J.-B. Leblond, and A. A. Benzerga. Coalescence of voids by internal necking: theoretical estimates and numerical results. *Journal of the Mechanics and Physics of Solids*, 75:140–158, 2015.

[34] A. A. Benzerga. Micromechanics of Coalescence in Ductile Fracture. *Journal of the Mechanics and Physics of Solids*, 50:1331–1362, 2002.

[35] A. A. Benzerga and J.-B. Leblond. Ductile fracture by void growth to coalescence. *Advances in Applied Mechanics*, 44:169–305, 2010.

[36] P. F. Thomason. Three–dimensional models for the plastic limit–loads at incipient failure of the inter-void matrix in ductile porous solids. *Acta Metallurgica*, 33:1079–1085, 1985.

[37] C. Tekoğlu, J.-B. Leblond, and T. Pardoen. A criterion for the onset of void coalescence under combined tension and shear. *Journal of the Mechanics and Physics of Solids*, 60:1363–1381, 2012.

[38] A. A. Benzerga and J.-B. Leblond. Effective Yield Criterion Accounting for Microvoid Coalescence. *Journal of Applied Mechanics*, 81:031009, 2014.

[39] M. E. Torki, A. A. Benzerga, and J.-B. Leblond. On Void Coalescence under Combined Tension and Shear. *Journal of Applied Mechanics*, 82(7):071005, 2015.

[40] ME Torki, C. Tekoglu, J-B Leblond, and AA Benzerga. Theoretical and numerical analysis of void coalescence in porous ductile solids under arbitrary loadings. *International Journal of Plasticity*, 91:160–181, 2017.

[41] S. M. Keralavarma. A multi-surface plasticity model for ductile fracture simulations. *Journal of the Mechanics and Physics of Solids*, 103:100–120, 2017.

[42] V. S. Deshpande, A. Needleman, and E. Van der Giessen. A discrete dislocation analysis of near-threshold fatigue crack growth. *Acta Materialia*, 49:3189, 2001.

[43] A.C. Steenbrink, E. Van der Giessen, and P.D. Wu. Void growth in glassy polymers. *J. Mech. Phys. Solids*, 45(3):405–437, 1997.

[44] F. A. McClintock. A criterion for ductile fracture by the growth of holes. *Journal of Applied Mechanics*, 35:363–371, 1968.

[45] J. R. Rice and D. M. Tracey. On the enlargement of voids in triaxial stress fields. *Journal of the Mechanics and Physics of Solids*, 17:201–217, 1969.

[46] U. F. Kocks, A. S. Argon, and M. F. Ashby. Thermodynamics and kinetics of slip. In B. Chalmers, editor, *Progress in Materials Science*, volume 19, pages 1–289. Pergamon, Oxford, 1975.

[47] A. Mbiakop, K. Danas, and A. Constantinescu. A homogenization based yield criterion for a porous tresca material with ellipsoidal voids. *International Journal of Fracture*, 200:209–225, 2015.

[48] J. Koplik and A. Needleman. Void growth and coalescence in porous plastic solids. *International Journal of Solids and Structures*, 24(8):835–853, 1988.

[49] J. Hure and P. O. Barrioz. Theoretical estimates for flat voids coalescence by internal necking. *European Journal of Mechanics*, 60:217–226, 2016.

[50] ABAQUS Documentation. Version 2018. *Dassault Systèmes*, 2010.

[51] A. A. Benzerga. *Rupture ductile des tôles anisotropes*. PhD thesis, Ecole Nationale Supérieure des Mines de Paris, 2000.

P4 A MULTI-SURFACE MODEL ACCOUNTING FOR MICROSTRUCTURAL SHAPE EFFECTS IN DUCTILE FRACTURE

A Multi-Surface Model Accounting for Microstructural Shape Effects in Ductile Fracture

M. E. Torki[1], S. M. Keralavarma[2], A. A. Benzerga[1]

[1] *Department of Aerospace Engineering, Texas A&M University, College Station, TX 77843, USA.*

[2] *Department of Aerospace Engineering, Indian Institute of Technology Madras, Chennai 600036, India.*

Abstract

A new multi-surface model incorporating diffuse and localized plasticity is developed as a yield criterion for path-dependent failure of porous ductile materials with random distribution of voids. In extension to a recent work where the only effective microstructural entity was porosity, the present work broadens the scope of a similar model into examination of intervoid distance as well as void shape effects via the two independent microstructural parameters: the ligament parameter $\bar{\chi}$ and the void aspect ratio w. Through a random distribution of voids in a plastically isotropic matrix, the multi-surface model hinges on an *isotropic behavior* of the material with respect to all possible directions where yielding can occur. The effective surface represents an extension to the GLD model accounting for intervoid distance (via the introduction of porosity f) and void-shape (w) effects in diffuse plasticity, in conjunction with a recent model for post-localization plasticity under combined tension and shear. Projections of the effective yield surface (representing equivalent Mises stress) were plotted on the deviatoric and meridian planes, compared to existing FEM results, where close coincidence was found. Similar plots then depicted comparison between the surfaces described by the void growth and coalescence models under internal necking with/without conjunction with internal shearing. Finally, the effective plastic strain at the onset of coalescence was expressed in terms of the Lode angle as well as stress triaxiality as a simplistic measure of failure. This function begins with a maximum value and exhibits an asymptotic behavior after the triaxiality of about 2.

Key Words: Ductile fracture; Porous plasticity; Path dependence; Stress triaxiality; Lode parameter.

1 Introduction

Failure of ductile materials is often preceded by the localization of plastic flow, such as diffuse necking or shear banding, followed by crack nucleation and growth in the region of localized plastic flow [1]. In metallic alloys, ductile cracks nucleate and propagate by the growth and coalescence of voids originating from material defects at the micro scale, such as second-phase particles and inclusions, as inferred from fractography and *in situ* X-ray tomography studies [1–3]. The onset of plastic instability and the nucleation of localization bands follow the loss of ellipticity within the rate-form equilibrium equations, the criterion that functions dependent on the material's tangent stiffness [4, 5]. Therefore, predictive modeling of ductile fracture requires accurate plasticity models with the capability of capturing the commonly complicated flow behavior of materials under large deformation mechanisms, as well as damage models that can predict the nucleation and growth of voids throughout the failure process. The two are essentially coupled inasmuch as individual voids grow due to plastic deformation of the surrounding matrix which, in turn, is affected by the presence of voids in the material.

It has long been established that the strain to failure in ductile materials is strongly dependent upon the loading path [6,7]. In a stress space, the loading path can be characterized by two parameters that depend on the ratios amongst the stress tensor invariants for a statistically isotropic material: *stress triaxiality* T, which denotes the ratio of the mean to von Mises effective stress, and the *Lode parameter*, L, proportional to the third invariant of the deviatoric stress, J_3. Under proportional stressing, characterized by constant values of T and L throughout the loading history, ductility (as mainly denoted by equivalent plastic strain $\epsilon^p_{\rm eq}$) is known to decrease exponentially with increasing stress triaxiality, as determined experimentally [7] and from theoretical analyses [8, 9] under predominantly axisymmetric loading conditions. This fundamental observation underpins several widely used models of ductile failure, such as those introduced in [8, 10] and the Gurson-Tvergaard-Needleman (GTN) model [11, 12]. However, the limitation of the foregoing models in predicting failure under shearing has been apparent all along, as they predict zero damage growth and infinite ductility under pure shear loading.

The issue has been brought into focus by more recent experimental studies [13, 14] aimed specifically at understanding ductile failure under shear-dominated loadings characterized with low triaxiality, typical of metal forming operations in the automotive industry. These studies demonstrate a non-monotonic trend of ductility as a function of T, with a bifurcation in strain to failure at small triaxialities that *lower*s strain to failure under low triaxialities (typically $T < 1/3$) that signify shear dominated loadings (as compared to axisymmetric loadings at higher triaxialities). However, these reported trends are not universal and possibly also material dependent, as revealed by more recent experiments that do not exhibit similar trends [7, 15]. The issue gets further complicated by the very fact that truly proportional loading is difficult to achieve experimentally, and non-radial loading paths could bear more elaborate effects on the observed experimental trends. Nevertheless, these studies all implicate an important role of the Lode parameter L, or its counterpart J_3, which had been neglected in most existing models.

Cell model analysis of a quasi-periodic two-dimensional porous unit cell subjected to axisymmetric proportional loading has previously been used to analyze the effect of stress triaxiality on failure of voided materials at the meso scale [9, 16], and the results have been invoked to calibrate theoretical models such as [11]. Remarkably, these studies helped elucidate the yielding mechanism of void growth followed by void *coalescence*, where adjacent voids link up by plastic collapse of their interconnecting ligament. Under axisymmetric loadings, however, negligible void growth occurs at low triaxialities, *i.e.* $T \leq 1/3$, and failure by void coalescence (most prominently by internal necking) is never captured in the simulations. Hence, alternative yielding mechanisms such as the formation of micro shear bands between voids has been hypothesized to justify the low ductility of metals under shear dominated loadings.

Motivated by most recent experimental findings, extensive research work has been conducted on cell model analysis of porous unit cells under general three-dimensional proportional stress histories to investigate the effect of the Lode parameter on ductile failure [17–22]. By definition, the Lode parameter falls in the $[-1, +1]$ interval, with it close to zero denoting shear-dominated loading, as opposed to axisymmetric loadings for which $L = \pm 1$. These studies, which tend to simulate the above *void-sheeting* mode of coalescence, indicate that the strain to the onset of coalescence has a clear dependence on L, being maximum for axisymmetric loadings ($|L| = 1$) and minimum for intense shearing states neighboring $L = 0$. Further, the simulations also evince strong deformation-induced anisotropy due to void-shape evolution at low triaxialities. For instance, under simple shear loading, initially spherical voids evolve into penny-shaped cracks and rotate to align with the major stress direction [19].

Homogenized constitutive models that extend the isotropic [11] model to capture the effects of void-shape evolution have been developed to increasing levels of sophistication, from the early 90's to date [23–29]. By way of contrast, rigorous micromechanics-based models for void coalescence have only been derived quite recently [30–32], extending Thomason's [33] pioneering heuristic model of void coalescence via internal necking. In particular, Torki *et al.* were the first to propound an analytical yield criterion [31], later on developed into a more rigorous upper-bound [34], for void coalescence under combined internal

necking and void-sheeting modes, following early approximate models of [35] and [20]. Recently, Keralavarma and Chockalingam [32] have enhanced the coalescence model of [31] to account for more realistic microscopic deformation fields as well as a Hill-type plastic anisotropy within the matrix [36], though the resulting analysis would not preserve the rigorous upper bound character [37].

Multi-surface plasticity models that independently account for the various possible modes of deformation observed in cell-model simulations at the scale of the voids (*i.e.* void growth by diffuse plasticity vs. void coalescence by strain localization dispersed through the inter-void ligaments), have been proposed as a possible approach to mimic ductile fracture by void growth to coalescence [35, 38, 39]. Recently, such a multi-surface approach has been exploited by [40] to develop an isotropic plasticity model by combining the [11] criterion with the coalescence model of [32]. Isotropic yield loci predicted by the resulting model were shown to be in much better coincidence with numerically determined quasi-exact yield loci than the Gurson model, esp. for large values of the porosity ($\sim \mathcal{O}(0.01)$ and larger) typical of highly damaged materials at zones close to a ductile crack tip. However, the isotropic multi-surface model of [40] did not retain any information related to the void shape. The impending need for the above effect becomes potentially remarkable for fracture at low triaxialities due to void shape evolution as well in materials where initial void shapes are non-spherical due to the elongated shape of the void-nucleating inclusions.

The objective of the present paper is then to develop a hybrid plasticity model and associated state evolution equations for a nominally isotropic material containing a random distribution of non-spherical voids. To this end, the void growth model developed by Keralavarma *et al.* [27] was combined with the void coalescence model derived by Torki *et al.* [31], by means of a similar multi-surface scheme as in the above-referenced works. Effective isotropic peers of the individual yield criteria in [27] and [31], that preserve information about a void shape common to all voids at a macro scale, yet averaged over all possible void orientations, are developed using a two-level homogenization procedure proposed by Gologanu *et al.* [23]. The resulting yield criterion will be assessed by comparison with quasi-exact yield loci predicted by numerical limit analysis of porous unit cells at the meso scale, using the same perspective as in [28, 29]. The state evolution equations will be then integrated under proportional loading paths to obtain the predicted evolution of strain to failure as a function of normalized loading parameters (triaxiality T and the Lode parameter L). It will be deduced that the Lode parameter has a significant influence on the predicted strain to failure under low triaxialities, being consistent with the most recent cell model simulation outcomes. Further, the effect of the average void shape on ductility will as well be illustrated using the new model.

2 Problem Statement

The underlying assumption for the forthcoming formulation is that the material is isotropic and voids are distributed randomly at least at a vicinity around a specific point in space, within a distance which is about of the same order as the voids' spacing range [1]. The relative positioning of a void and its surrounding matrix can be described with the aid of a representative volume element (RVE), that tends to mimic the geometric as well as the loading conditions in meso scale. In the interest of convenience in the derivation of a closed-form yield function, a RVE may be, in general, intrinsic to the model and not space-filling. In effect, a multi-surface yield criterion for a porous plasticity problem takes in a competition between a model accounting for void growth and the one predicting void coalescence, whichever occurs sooner. The former is derived on the basis of diffuse plasticity disbursed throughout the material, and the latter considers plastic deformation as confined within an intervoid ligament. The following subsections expound on the models utilized to describe void growth and coalescence within the context of this work.

[1] In general, voids at a meso-scale distance are neither periodically nor randomly distributed, but rather distributed in clustered form. That is, one can find a vicinity at a point in space where voids are placed quasi-periodically distributed within a small distance

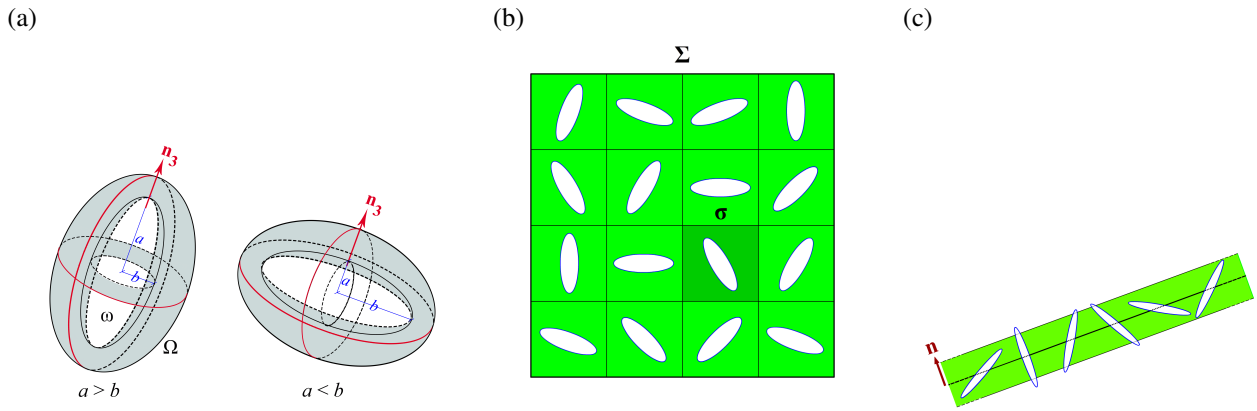

Figure 1: (a) RVE utilized in the model developed by Keralavarma *et al.* [27], (b) schematic distribution of non-spherical voids with random orientations and their circumscribing cells at early plastic deformation stages, (c) schematic random void distribution at a given orientation denoted with normal $\mathbf{n}$.

2.1 Diffuse plasticity

2.1.1 Meso-scale model

Void growth is described with the model developed by Keralavarma *et al.* [27] (referred to henceforth as the K–B model) assuming a microstructure consisting of a plastically anisotropic matrix containing aligned spheroidal voids. A unit vector along the axis of the spheroidal void is denoted by $\mathbf{n}_3$, as shown in Fig. 1a for both prolate and oblate voids. The model reduces to the Gologanu-Leblond-Devaux (GLD) model [23, 41] for the special case of spheroidal voids in an isotropic matrix.

The yield function developed by Keralavarma *et al.* (2010) for the special case of an isotropic matrix can be written in the form [27]:

$$\mathcal{F}^{\mathrm{H}}(\boldsymbol{\sigma},\mathbf{n},f,w)=\frac{3}{2}C\frac{\boldsymbol{\sigma}:\mathbb{H}:\boldsymbol{\sigma}}{\bar{\sigma}^2}+2(g+1)(g+f)\cosh\left(\kappa\frac{\boldsymbol{\sigma}:\mathbf{X}}{\bar{\sigma}}\right)-(g+1)^2-(g+f)^2 \tag{1}$$

where $\bar{\sigma}$ is the yield stress of the matrix material and the fourth order tensor $\mathbb{H}$ is an effective anisotropy tensor for the porous material. f and w are the two microstructural scalar variables denoting the void volume fraction (*i.e.* porosity) and the void aspect ratio $w=a/b$, defined as the ratio of the axial and transverse radii of the spheroidal void. For the case of aligned spheroidal voids in a Von Mises matrix, $\mathbb{H}$ can be written in the form

$$\mathbb{H}=\mathbb{J}+\eta\left(\mathbf{X}\otimes\mathbf{Q}+\mathbf{Q}\otimes\mathbf{X}\right) \tag{2}$$

where $\mathbf{X}$ and $\mathbf{Q}$ are second order tensors coaxial with the void, given by

$$\mathbf{X}=(1-3\alpha_2)\mathbf{n}\otimes\mathbf{n}+\alpha_2\mathbf{I},\qquad \mathbf{Q}=\frac{3}{2}\mathbf{n}\otimes\mathbf{n}-\frac{1}{2}\mathbf{I} \tag{3}$$

$\mathbb{J}=\mathbb{I}-\frac{1}{3}\mathbf{I}\otimes\mathbf{I}$ denotes the deviatoric projection tensor and $\mathbf{I}$ and $\mathbb{I}$ are, respectively, the second and fourth order identity tensors. The parameters in the model, such as C, η, α_2 and g above are functions of f and w. Detailed expressions for all the parameters in the above criterion are provided in Appendix A.

2.1.2 Macro-scale model

With reference to the rationale provided in [23], one can assume that, at a meso (cell) level, all the randomly-distributed voids have approximately equal volume fractions f and shapes w, but random orientations.

This premise can only hold up to intermediate values of plastic strains in that, at very large strains, plastic deformation is usually biased locally and thus the voids at a macro scale are oriented towards a certain direction. That is, a complete theory of porous materials tending to simulate void-shape effects due to non-spherical voids with initially random orientations should be equipped with the progressive development of a so-called *damage texture*. The distribution of non-spherical voids at the meso and macro scales at early stages of plastic deformation is schematized in Fig. 1b. A schematic section of a subset of voids being passed through by a plane with given normal $\mathbf{n}$ is shown in Fig. 1c.

According to the K–B yield criterion, Eq.(1), the domain of admissible stresses at the meso-scale of a unit cell satisfies the following inequality

$$\frac{3}{2}C\frac{\boldsymbol{\sigma}:\mathbb{H}:\boldsymbol{\sigma}}{\bar{\sigma}^2} \leq (g+1)^2+(g+f)^2-2(g+1)(g+f)\cosh\left(\kappa\frac{\boldsymbol{\sigma}:\mathbf{X}}{\bar{\sigma}}\right) \tag{4}$$

where the void orientation $\mathbf{n}$ and therefore the tensors $\mathbf{X}$, $\mathbf{Q}$ and $\mathbb{H}$ vary from cell to cell in a random fashion. Performing an average over all constituent unit cells in the macro-scale RVE depicted in Fig. 1b leads to an approximate macroscopic yield criterion for the RVE. Assuming that meso-scale voids (and therefore unit cells) have equal volumes, the volume average can be replaced with an ensemble average over all possible void orientations, yielding

$$\left\langle\frac{3}{2}C\frac{\boldsymbol{\sigma}:\mathbb{H}:\boldsymbol{\sigma}}{\bar{\sigma}^2}\right\rangle \leq \left\langle(g+1)^2+(g+f)^2-2(g+1)(g+f)\cosh\left(\kappa\frac{\boldsymbol{\sigma}:\mathbf{X}}{\bar{\sigma}}\right)\right\rangle \tag{5}$$

where the notation $\langle\cdot\rangle$ denotes average over all possible void orientations $\mathbf{n}$. Since the scalar parameters in the model such as C, η, α_2 and g depend only on the void volume fraction and shape and are independent of the void orientation, the above further simplified to

$$\frac{3}{2}C\frac{\langle\boldsymbol{\sigma}:\mathbb{H}:\boldsymbol{\sigma}\rangle}{\bar{\sigma}^2} \leq (g+1)^2+(g+f)^2-2(g+1)(g+f)\left\langle\cosh\left(\kappa\frac{\boldsymbol{\sigma}:\mathbf{X}}{\bar{\sigma}}\right)\right\rangle \tag{6}$$

Since the hyperbolic cosine is a convex function function: $<\cosh x> \geq \cosh <x>$, which leads further to:

$$\frac{3}{2}C\frac{\langle\boldsymbol{\sigma}:\mathbb{H}:\boldsymbol{\sigma}\rangle}{\bar{\sigma}^2} \leq (g+1)^2+(g+f)^2-2(g+1)(g+f)\cosh\left(\kappa\frac{\langle\boldsymbol{\sigma}:\mathbf{X}\rangle}{\bar{\sigma}}\right) \tag{7}$$

Unfortunately, the above averaged quantities can only be determined in an approximate sense, since the variation of the mesoscopic stress tensor $\boldsymbol{\sigma}$ from cell to cell as a function of the change in local void orientation cannot be estimated analytically. Instead, we resort to the same Reuss-type approximation employed in [23] by neglecting the above dependence of $\boldsymbol{\sigma}$ on $\mathbf{n}$ and equate the meso- and macro-scale stress tensors; i.e. $\boldsymbol{\sigma}=\boldsymbol{\Sigma}$. With this admittedly crude approximation, the previous inequality simplifies to

$$\frac{3}{2}C\frac{\boldsymbol{\Sigma}:\langle\mathbb{H}\rangle:\boldsymbol{\Sigma}}{\bar{\sigma}^2} \leq (g+1)^2+(g+f)^2-2(g+1)(g+f)\cosh\left(\kappa\frac{\boldsymbol{\Sigma}:\langle\mathbf{X}\rangle}{\bar{\sigma}}\right) \tag{8}$$

It is shown in appendix B that orientation averages of the tensors $\mathbf{X}$ and $\mathbb{H}$ evaluate to

$$\langle\mathbf{X}\rangle=\frac{1}{3}\mathbf{I}, \qquad \langle\mathbb{H}\rangle=\left[1+\frac{2}{5}\eta(1-3\alpha_2)\right]\mathbb{J} \tag{9}$$

Substituting the above in inequality (8) and rearranging, we obtain the following approximate macro-scale yield criterion accounting for void growth in presence of a random distribution of voids:

$$\bar{\mathcal{F}}^{\mathrm{H}}(\boldsymbol{\Sigma},f,w)=\bar{C}\left(\frac{\Sigma_{\mathrm{eq}}}{\bar{\sigma}}\right)^2+2(g+1)(g+f)\cosh\left(\kappa\frac{\Sigma_{\mathrm{m}}}{\bar{\sigma}}\right)-(g+1)^2-(g+f)^2\leq 0 \tag{10}$$

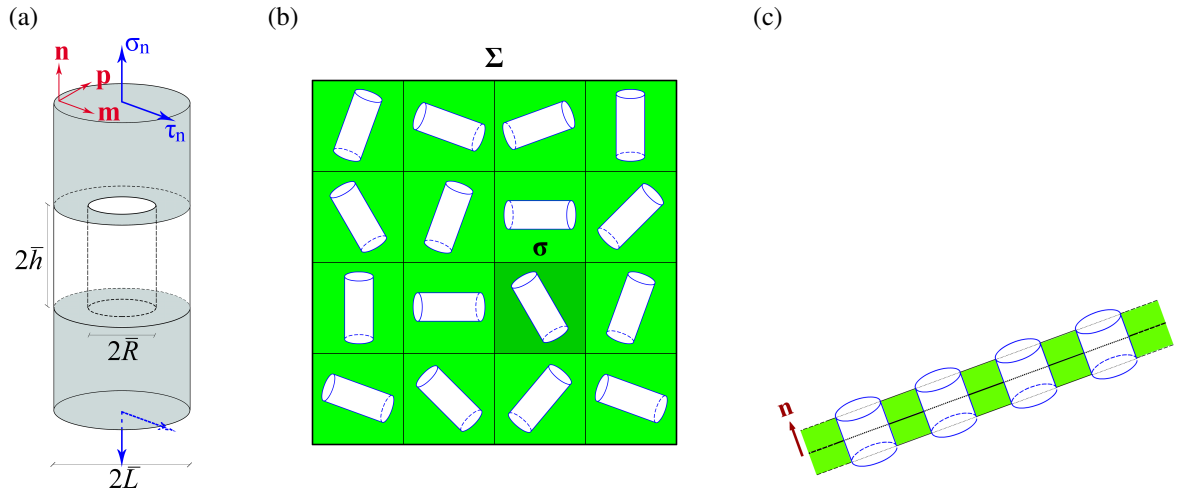

Figure 2: (a) RVE utilized in the model proposed for post-localized plasticity regime by Torki *et al.* [31], (b) schematic distribution of non-spherical voids (idealized with cylinders) with random orientations and their circumscribing cells at early plastic deformation stages, (c) idealized subset of equivalent cylindrical voids being passed through by the same plane with normal $\mathbf{n}$ wherein strains are taken to be localized up to a finite height.

where $\Sigma_{\mathrm{m}} = \frac{1}{3}\Sigma_{kk}$ and $\Sigma_{\mathrm{eq}} = \sqrt{\frac{3}{2}\boldsymbol{\Sigma}' : \boldsymbol{\Sigma}'}$ are the macroscopic mean and Mises equivalent stresses respectively, and $\bar{C} = C\left[1 + \frac{2}{5}\eta(1 - 3\alpha_2)\right]$. Note that the ensemble averaging process described in appendix B leads to an isotropic yield criterion, due to the random distribution of the void orientations.

2.2 Localized plasticity

2.2.1 Meso-scale model

After the onset of void coalescence, plastic deformation inside a meso-scale unit cell is assumed to localize into a ligament separating two neighboring voids, and the rest of the cell undergoes elastic unloading and can be assumed to be rigid to the first approximation [30]. The orientation of the localization band is uniquely defined by a unit normal to the plane transverse to the ligament, as schematically shown in Fig. 2a. The latter is here termed a possible *plane of localization*.

Remark: In presence of randomly-distributed voids, voids can interconnect in any direction, and thus the localization plane can be any arbitrary plane within the Euclidean space. Upon periodic or clustered void distribution, however, this interconnection can occur only along certain directions. This makes the planes of localization only a discrete set. The post-localization microstructure would then be generally affected by the normal $\mathbf{n}$ to the localization plane.

The yield function assuming localized yielding of the inter-void ligament is obtained by homogenization of a hollow cylindrical RVE containing a coaxial cylindrical void, as shown in Fig. 2a. The model derived by [31] (referred to in the following as the T-B-L model) is the first analytical criterion that accounts for combined internal necking and shear strain localization in the inter-void ligaments, extending the earlier models of [20, 33, 38]. The effective yield function derived by [31] can be written in the form

$$\mathcal{F}^{\mathrm{I}}(\boldsymbol{\sigma}, \chi, w) = \left(\frac{|\sigma_{\mathrm{n}}| - \sigma^{\mathrm{surf}}(\chi, w)}{\sigma^{\mathrm{vol}}(\chi)}\right)^2 \mathcal{H}(|\sigma_{\mathrm{n}}| - \sigma^{\mathrm{surf}}) + \left(\frac{\tau_{\mathrm{n}}}{\tau(\chi)}\right)^2 - 1 \tag{11}$$

where $\mathcal{F}^{\mathrm{I}}$ denotes the yield criterion representing inhomogeneous (localized) deformation, which depends

on the void aspect ratio $w = h/R$ and the so called ligament size ratio $\chi = R/L$ (see Fig. 2a) in addition to the stress $\boldsymbol{\sigma}$. $\mathcal{H}(x)$ is the Heaviside step function, equaling 1 if $x > 0$ and 0 if $x < 0$. $\sigma_{\rm n} = \mathbf{n}.\boldsymbol{\sigma}\mathbf{n}$, $\tau_{\rm n} = |\boldsymbol{\sigma}\mathbf{n} - \sigma_{\rm n}\mathbf{n}|$ are, respectively, the normal and shear tractions on the plane of localization, and

$$\begin{aligned}
\sigma^{\rm vol}(\chi) &= \frac{\bar{\sigma}}{\sqrt{3}}\left[2 - \sqrt{1+3\chi^4} + \ln\frac{1+\sqrt{1+3\chi^4}}{3\chi^2}\right] \\
\sigma^{\rm surf}(\chi, w) &= \frac{\bar{\sigma}}{3\sqrt{3}}\frac{\chi^3 - 3\chi + 2}{\chi w} \\
\tau(\chi) &= \frac{1-\chi^2}{\sqrt{3}}\bar{\sigma}
\end{aligned} \tag{12}$$

are scalar parameters that depend on the microstructure variables χ and w. Note that the geometry of the RVE in Fig. 2a may be completely defined by three non-dimensional parameters; χ, w and the aspect ratio of the unit cell $\lambda = h/H$. However, the void coalescence criterion depends only on χ and w and is independent of λ. The model, as is, predicts a close upper bound to the limit load for a wide range of χ and w. It, however, overpredicts the stresses associated with the onset of coalescence mainly in the limit of penny-shaped cracks ($w \longrightarrow 0$) and minorly for overly elongated cavities ($w >> 1$). Therefore, a calibrated counterpart of (12), as introduced in [34], has been exploited in the present context.

2.2.2 Macro-scale model

At the macroscopic scale of an RVE containing a large number of identical randomly oriented voids, shown in Fig. 1b, void coalescence would correspond to the localization of plasticity to a ligament interconnecting voids, whose width may be expected to scale with the size of the voids. The coalescence mechanism can be perceived only by virtue of the normal and shear tractions resolved on the same plane of localization of normal $\mathbf{n}$. This plane, however, is subject to variation in space, plus the fact that the subset of voids being passed through by this plane are themselves randomly oriented. This creates a controversy in the applicability of Eq. (11) in the present context. Nevertheless, one can assume the voids are sufficiently far apart such that the void aspect ratio w can affect the localization band thickness $2h$. In this case, one can roughly estimate the ligament thickness $2h$ as determined by a void oriented along normal $\mathbf{n}$, which implies that the effective void aspect ratio can be taken equal to the main one, *i.e.* $\bar{w} \approx w$ in (11). Note that, in principle, $\bar{w}$ should scale with w with a factor of 2/3 to keep the void volumes equal. It was, however, figured through comparison to numerical results presented in Sec. 4.1, that a better coincidence with benchmark results would be envisaged by considering $\bar{w} \approx w$. The 2/3 coefficient will, therefore, be skipped throughout. One can further exploit the approximate unity of all equivalent cell aspect ratios $\bar{\lambda} = 1$, which is characteristic of random void distribution. The above-mentioned effective parameters are related to the overall porosity via the following relation:

$$f = \frac{\bar{\chi}^3 \bar{w}}{\bar{\lambda}} \tag{13}$$

where we have $\bar{\chi}$ is the effective relative void spacing, that can be appreciated as a measure of porosity at fixed other parameters $\bar{w}$ and $\bar{\lambda}$. After large plastic deformation at high triaxialities (representing near-hydrostatic stress states), however, the average center-to-center spacing between neighboring voids would be the same in all directions, so that one can simply consider $\bar{w} \approx 1$

Recall the meso-scale yield criterion for each equivalent cylindrical RVE inside the localization band as

$$\mathcal{F}^{\rm I}(\boldsymbol{\sigma}, \bar{\chi}, \bar{w}) = \left(\frac{|\sigma_{\rm n}| - \Sigma^{\rm surf}}{\Sigma^{\rm vol}}\right)^2 \mathcal{H}(|\sigma_{\rm n}| - \Sigma^{\rm surf}) + \left(\frac{\tau_{\rm n}}{\mathcal{T}}\right)^2 - 1 \tag{14}$$

where $\Sigma^{\text{vol}} = \sigma^{\text{vol}}(\bar{\chi})$, $\Sigma^{\text{surf}} = \sigma^{\text{surf}}(\bar{\chi}, \bar{w})$ and $\mathcal{T} = \tau(\bar{\chi})$. In order for $\boldsymbol{\sigma}$ to belong to a meso-scale domain of reversibility [37], the following condition should be satisfied,

$$\left(\frac{|\sigma_{\text{n}}| - \Sigma^{\text{surf}}}{\Sigma^{\text{vol}}}\right) \mathcal{H}(|\sigma_{\text{n}}| - \Sigma^{\text{surf}}) \leq \sqrt{1 - \left(\frac{\tau_{\text{n}}}{\mathcal{T}}\right)^2} \tag{15}$$

where σ_{n} and τ_{n} are the normal and shear stresses on the transverse plane of the RVE with normal $\mathbf{n}$, given by $\sigma_{\text{n}} = \mathbf{n} \cdot \boldsymbol{\sigma}\mathbf{n}$ and $\tau_{\text{n}} = |\boldsymbol{\sigma}\mathbf{n} - \sigma_{\text{n}}\mathbf{n}|$ respectively. The macroscopic yield criterion is obtained from (15) by averaging both sides of the inequality over all cylindrical RVEs contained in the coalescence band, which will be denoted by $\langle\cdot\rangle$. Note that this averaging procedure is different from the one used to derive the effective pre-coalescence yield function in section 2.1, since the orientations of the voids and all the equivalent cylindrical voids are assumed to be aligned normal to $\mathbf{n}$.

Let $\boldsymbol{\Sigma} = \langle\boldsymbol{\sigma}\rangle$ denote the average stress in the coalescence band, whose normal and shear components on the band are given by $\Sigma_{\text{n}} = \mathbf{n} \cdot \boldsymbol{\Sigma}\mathbf{n}$ and $\Sigma_{\text{sh}} = |\boldsymbol{\Sigma}\mathbf{n} - \Sigma_{\text{n}}\mathbf{n}|$ respectively. Using the properties of the Heaviside function, it is straightforward to verify the following inequality

$$(|\sigma_{\text{n}}| - \Sigma^{\text{surf}})\mathcal{H}(|\Sigma_{\text{n}}| - \Sigma^{\text{surf}}) \leq (|\sigma_{\text{n}}| - \Sigma^{\text{surf}})\mathcal{H}(|\sigma_{\text{n}}| - \Sigma^{\text{surf}}) \tag{16}$$

Combining (15) and (16), we have

$$\left(\frac{|\sigma_{\text{n}}| - \Sigma^{\text{surf}}}{\Sigma^{\text{vol}}}\right) \mathcal{H}(|\Sigma_{\text{n}}| - \Sigma^{\text{surf}}) \leq \sqrt{1 - \left(\frac{\tau_{\text{n}}}{\mathcal{T}}\right)^2} \tag{17}$$

Averaging both sides of the above inequality over all meso-scale RVEs contained in the localization band, we get

$$\left(\frac{\langle|\sigma_{\text{n}}|\rangle - \Sigma^{\text{surf}}}{\Sigma^{\text{vol}}}\right) \mathcal{H}(|\Sigma_{\text{n}}| - \Sigma^{\text{surf}}) \leq \left\langle\sqrt{1 - \left(\frac{\tau_{\text{n}}}{\mathcal{T}}\right)^2}\right\rangle \tag{18}$$

Since $\sqrt{1-x^2}$ is a concave function of x, we have $\langle\sqrt{1-x^2}\rangle \leq \sqrt{1-\langle x\rangle^2}$. Also, we have $\langle|x|\rangle \geq |\langle x\rangle|$. Using the above two results in (18), we get

$$\left(\frac{|\langle\sigma_{\text{n}}\rangle| - \Sigma^{\text{surf}}}{\Sigma^{\text{vol}}}\right) \mathcal{H}(|\Sigma_{\text{n}}| - \Sigma^{\text{surf}}) \leq \sqrt{1 - \left(\frac{\langle\tau_{\text{n}}\rangle}{\mathcal{T}}\right)^2} \tag{19}$$

Using the definition of $\boldsymbol{\Sigma}$, we can show that $\langle\sigma_{\text{n}}\rangle = \Sigma_{\text{n}}$ while $\langle\tau_{\text{n}}\rangle \geq \Sigma_{\text{sh}}$. Substituting in (19) yields

$$\left(\frac{|\Sigma_{\text{n}}| - \Sigma^{\text{surf}}}{\Sigma^{\text{vol}}}\right) \mathcal{H}(|\Sigma_{\text{n}}| - \Sigma^{\text{surf}}) \leq \sqrt{1 - \left(\frac{\Sigma_{\text{sh}}}{\mathcal{T}}\right)^2} \tag{20}$$

The macroscopic yield criterion for localized plasticity in an arbitrarily oriented coalescence band of voids is obtained by rearranging (20) to write

$$\bar{\mathcal{F}}^{\text{I}}(\boldsymbol{\Sigma}, \bar{\chi}, \bar{w}) = \left(\frac{|\Sigma_{\text{n}}| - \Sigma^{\text{surf}}}{\Sigma^{\text{vol}}}\right)^2 \mathcal{H}(|\Sigma_{\text{n}}| - \Sigma^{\text{surf}}) + \left(\frac{\Sigma_{\text{sh}}}{\mathcal{T}}\right)^2 - 1 \leq 0 \tag{21}$$

In case the modified T-B-L model is used, the corresponding macroscopic version will be of the following form

$$\bar{\mathcal{F}}^{\text{I}}(\boldsymbol{\Sigma}, \bar{\chi}, \bar{w}) = \left(\frac{|\Sigma_{\text{n}}| - t(\bar{\chi}, \bar{w})\Sigma^{\text{surf}}}{b\Sigma^{\text{vol}}}\right)^2 \mathcal{H}(|\Sigma_{\text{n}}| - \Sigma^{\text{surf}}) + \left(\frac{\Sigma_{\text{sh}}}{l(\bar{\chi}, \bar{w})\mathcal{T}}\right)^2 - 1 \leq 0 \tag{22}$$

where the expressions for the parameters t, b and l are given in [34].

2.3 *Tri-surface model*

The effective macroscopic yield criterion derived in section 2.1, assuming diffuse plastic flow in the matrix, is isotropic due to the random orientations of the spheroidal voids at the meso-scale; see Fig. 1b. In contrast, the coalescence criterion derived in section 2.2 is anisotropic, since it is a function of the orientation of the coalescence band defined by the unit vector $\mathbf{n}$. In a statistically isotropic microstructure, where the average void spacing is equal in all spatial directions, the orientation of the coalescence band is determined solely by the applies state of stress. In this case, an effective isotropic coalescence criterion can be obtained using a multi-surface approach by assuming that the effective yield domain is the region in stress space that lies at the intersection of all the yield domains corresponding to all possible orientations of the localization band $\mathbf{n}$ [35, 40]. For the sake of simplicity, the effective parameters $\bar{\chi}$ and $\bar{w}$ will be represented by χ and w in the sequel.

The effective isotropic coalescence function, $\mathcal{F}^{\mathrm{I}^{\mathrm{iso}}}(\mathbf{\Sigma})$, is then the maximum of $\bar{\mathcal{F}}^{\mathrm{I}}(\Sigma_{\mathrm{n}}, \Sigma_{\mathrm{sh}})$ over all possible orientations of the unit vector $\mathbf{n}$; i.e.

$$\mathcal{F}^{\mathrm{I}^{\mathrm{iso}}}(\mathbf{\Sigma}) = \max_{\mathbf{n}} \{\mathcal{F}^{\mathrm{I}}(\Sigma_{\mathrm{n}}, \Sigma_{\mathrm{sh}})\} \qquad \text{s.t.} \qquad g(\mathbf{n}) = n_i n_i - 1 = 0 \quad \text{sum on} \quad i \tag{23}$$

where Σ_{n} and Σ_{sh} are functions of $\mathbf{\Sigma}$ and $\mathbf{n}$ via

$$\Sigma_{\mathrm{n}}(\mathbf{\Sigma}, \mathbf{n}) = \mathbf{n} \cdot \mathbf{\Sigma}\mathbf{n}, \qquad \Sigma_{\mathrm{sh}}(\mathbf{\Sigma}, \mathbf{n}) = \sqrt{\mathbf{n} \cdot \mathbf{\Sigma}^2\mathbf{n} - (\mathbf{n} \cdot \mathbf{\Sigma}\mathbf{n})^2}, \qquad \mathbf{\Sigma}^2 = \mathbf{\Sigma} \cdot \mathbf{\Sigma} \tag{24}$$

Performing the maximization in Eq.(23) over the space of all possible unit vectors $\mathbf{n}$, at fixed $\mathbf{\Sigma}$, leads to the following optimality condition

$$\frac{\partial \mathcal{F}^{\mathrm{I}}}{\partial \mathbf{n}} = (\mathbf{\Sigma}^2 - \tilde{\Sigma}\mathbf{\Sigma})\mathbf{n} = 2\beta\mathbf{n} \tag{25}$$

where the scalar $\tilde{\Sigma}$ is given by

$$\tilde{\Sigma}(\mathbf{\Sigma}, \mathbf{n}) = 2\Sigma_{\mathrm{n}} - 2\eta(\Sigma_{\mathrm{n}} - \mathrm{sgn}(\Sigma_{\mathrm{n}})\Sigma^{\mathrm{surf}})\mathcal{H}(|\Sigma_{\mathrm{n}}| - \Sigma^{\mathrm{surf}}), \quad \eta \equiv \frac{\mathcal{T}^2}{\Sigma^{\mathrm{vol}^2}} \tag{26}$$

and β is a Lagrange multiplier. In other words, the normal to the localization plane $\mathbf{n}$ that maximizes the value of the coalescence function must be an eigenvector of the tensor $\mathbf{\Sigma}^2 - \tilde{\Sigma}\mathbf{\Sigma}$. Since tensors $\mathbf{\Sigma}^2$ and $\mathbf{\Sigma}$ are coaxial, the above condition is satisfied if $\mathbf{n}$ is an eigenvector of $\mathbf{\Sigma}$. In this case, the shear stress Σ_{sh} vanishes, and coalescence occurs by internal necking of the ligaments connecting an array of voids transverse to a principal direction of $\mathbf{\Sigma}$. Assuming $\Sigma_1 \leq \Sigma_2 \leq \Sigma_3$ to be the principal stresses corresponding to principal directions $\mathbf{n}_1, \mathbf{n}_2, \mathbf{n}_3$, the resulting three yield functions can be written in the form

$$\mathcal{F}^{\mathrm{I}^{\mathrm{n}}}(\Sigma_i) = \frac{(|\Sigma_i| - \Sigma^{\mathrm{surf}})^2}{\Sigma^{\mathrm{vol}^2}} \mathcal{H}(|\Sigma_i| - \Sigma^{\mathrm{surf}}) - 1 \tag{27}$$

where Σ_i ($i = 1..3$) are the principal stresses. The above result in fact generalizes the criteria proposed by Benzerga and Leblond [30] and Thomason [33] to the case of a random array of voids inside a coalescence band.

In addition to the above criteria for coalescence by pure internal necking, Keralavarma [40] had shown that the optimality condition of Eq.(25) can also be satisfied if $\mathbf{n}$ is a linear combination of two eigenvectors (say $\mathbf{n}_1$ and $\mathbf{n}_2$) corresponding to unequal values of the principal stresses ($\Sigma_1 < \Sigma_2$), provided that the corresponding $\mathbf{n}$ satisfies the following condition

$$\tilde{\Sigma}(\mathbf{\Sigma}, \mathbf{n}) = \Sigma_1 + \Sigma_2 \tag{28}$$

In this case, void coalescence occurs inside the localization band under a combination of normal and shear stresses on the localization plane. Given the form (26) for $\tilde{\Sigma}$, the above represents a linear equation in $\Sigma_{\rm n}$, which has either no solution or a unique solution in the domain (Σ_1, Σ_2) of admissible values of $\Sigma_{\rm n}$. The solution for $\Sigma_{\rm n}$ reads

$$\Sigma_{\rm n} = \begin{cases} \dfrac{|\Sigma_1 + \Sigma_2| - 2\eta\Sigma^{\rm surf}}{2(1-\eta)} \operatorname{sgn}(\Sigma_1 + \Sigma_2) & \text{if } |\Sigma_1 + \Sigma_2| > 2\Sigma^{\rm surf} \\ \dfrac{\Sigma_1 + \Sigma_2}{2} & \text{if } |\Sigma_1 + \Sigma_2| \leq 2\Sigma^{\rm surf} \end{cases} \tag{29}$$

Note that $\Sigma_{\rm n}$ has the same sign as $\Sigma_1 + \Sigma_2$, since the parameter η defined in $(26)_2$ is smaller than unity for any value of χ. It is emphasized that the above solution for $\Sigma_{\rm n}$ is only valid under the condition that $\Sigma_1 < \Sigma_{\rm n} < \Sigma_2$. Substituting (29) in the above inequality and further simplification leads to the condition

$$\mathcal{D}(\Sigma_1, \Sigma_2) \equiv \frac{\eta}{(1-\eta)} \frac{|\Sigma_1 + \Sigma_2| - 2\Sigma^{\rm surf}}{|\Sigma_2 - \Sigma_1|} < 1 \tag{30}$$

Hence, coalescence under combined tension and shear on a plane with normal $\mathbf{n}$ falling on the $\mathbf{n}_1$–$\mathbf{n}_2$ plane is possible only if the discriminant $\mathcal{D}(\Sigma_1, \Sigma_2)$ defined in (30) is smaller than unity.

The shear stress on the optimal plane $\mathbf{n}$ corresponding to the normal stress $\Sigma_{\rm n}$ can be found from the equation

$$\left[\Sigma_{\rm n} - \left(\frac{\Sigma_1 + \Sigma_2}{2}\right)\right]^2 + \Sigma_{\rm sh}^2 = \left(\frac{\Sigma_1 - \Sigma_2}{2}\right)^2 \tag{31}$$

Substituting $\Sigma_{\rm n}$ and $\Sigma_{\rm sh}$ from (29) and (31) in Eq.(21) and simplifying leads to the following criterion for coalescence within a band of normal $\mathbf{n}$ lying on the $\mathbf{n}_1$–$\mathbf{n}_2$ plane.

$$\mathcal{F}^{\rm I^{sh}}(\Sigma_1, \Sigma_2) = \frac{\left(|\Sigma_1 + \Sigma_2| - 2\Sigma^{\rm surf}\right)^2}{4(\Sigma^{\rm vol^2} - \mathcal{T}^2)} \mathcal{H}(|\Sigma_1 + \Sigma_2| - 2\Sigma^{\rm surf}) + \left(\frac{\Sigma_1 - \Sigma_2}{2\mathcal{T}}\right)^2 - 1, \quad \text{if } \mathcal{D}(\Sigma_1, \Sigma_2) < 1 \tag{32}$$

Two similar criteria for the vector $\mathbf{n}$ lying on the remaining two principal planes can be obtained by cyclic permutation of the indices $(1, 2, 3)$ in Eq.(32).

It has been shown by Keralavarma [40] that the optimality condition of Eq.(23) can only be satisfied if the vector $\mathbf{n}$ lies on one of the principal planes of $\boldsymbol{\Sigma}$, and therefore the six criteria defined by Eqs.(27) and (32) represent the general solution for the optimization problem. The effective isotropic coalescence function $\mathcal{F}^{\rm I^{iso}}(\boldsymbol{\Sigma})$ in (23) then becomes

$$\mathcal{F}^{\rm I^{iso}}(\boldsymbol{\Sigma}) = \max\left\{\mathcal{F}^{\rm I^n}(\Sigma_1), \mathcal{F}^{\rm I^n}(\Sigma_2), \mathcal{F}^{\rm I^n}(\Sigma_3), \mathcal{F}^{\rm I^{sh}}(\Sigma_1, \Sigma_2), \mathcal{F}^{\rm I^{sh}}(\Sigma_2, \Sigma_3), \mathcal{F}^{\rm I^{sh}}(\Sigma_1, \Sigma_3)\right\} \tag{33}$$

In addition to the isotropic coalescence criterion (33), yielding is also possible by diffuse plastic flow, the criterion for which is given by Eq.(10). Combining the two criteria using the multi-surface approach, the effective yield criterion for a statistically isotropic material, accounting for both diffuse and localized plastic flow within a meso-scale RVE, can be written in the following explicit form

$$\mathcal{F}^{\rm iso} = \max\left\{\bar{\mathcal{F}}^{\rm H}(\boldsymbol{\Sigma}), \mathcal{F}^{\rm I^{iso}}(\boldsymbol{\Sigma})\right\} \tag{34}$$

where the individual yield surfaces in (34) are given by equations (10) and (33).

In essence, the effective yield surface comes by way of comparison among the surfaces corresponding to homogeneous yielding, internal necking, and combined internal necking–shearing, thus its name *tri-surface*. Among the latter two, however, the second is always met first and is, hence, prevalent. Yet, juxtaposing the yield surfaces with and without shear would be a proper exposition on the large differences between the two sets of surfaces that, per se, warrants the incorporation of shear stresses in the formulation.

3 Evolution of Porosity and Void Shape

With the elastic deformations being infinitesimal and use of the Jaumann objective rate of stress, the overall deformation rate can be decomposed into an elastic and a plastic part reading

$$\mathbf{D} = \mathbf{D}^e + \mathbf{D}^p, \qquad \mathbf{D}^e = \mathbb{C}^{-1} : \overset{\nabla}{\boldsymbol{\Sigma}} \tag{35}$$

with $\mathbf{D}^e$ and $\mathbf{D}^p$ being, respectively, the elastic and plastic rates of deformation, $\mathbb{C}$ the fourth-order elastic stiffness tensor, and $\overset{\nabla}{\boldsymbol{\Sigma}}$ denotes the Jaumann stress rate. The plastic deformation rate $\mathbf{D}^p$ stems from the yield function through the normality rule which, following the fundamental Hill-Mandel lemma [42, 43], has proven valid at the macro-scale for a porous material provided it holds for the matrix at the micro-scale. Hence,

$$\mathbf{D}^p = \dot{\Lambda}\mathbf{N}, \qquad \mathbf{N} = \frac{\partial \mathcal{F}}{\partial \boldsymbol{\Sigma}} \tag{36}$$

where $\dot{\Lambda}$ is the plastic multiplier and $\mathbf{N}$ is the plastic flow direction tensor normal to the yield surface in stress space. For the present yield functions, one can write:

$$\mathbf{N} = \begin{cases} 3\bar{C}\dfrac{\boldsymbol{\Sigma}'}{\bar{\sigma}^2} + \dfrac{2}{3}(g+1)(g+f)\dfrac{\kappa}{\bar{\sigma}}\sinh\left(\kappa\dfrac{\Sigma_{\mathrm{m}}}{\bar{\sigma}}\right)\mathbf{I}, & \mathcal{F} = \mathcal{F}^{\mathrm{H}} \\ \dfrac{2}{(\Sigma^{\mathrm{vol}})^2}(\Sigma_n - \mathrm{sgn}\,(\Sigma_n)\,\Sigma^{\mathrm{surf}})\mathcal{H}\mathbf{n}\otimes\mathbf{n} + \dfrac{1}{\mathcal{T}^2}[\mathbf{n}\otimes\boldsymbol{\Sigma}\mathbf{n} + \boldsymbol{\Sigma}\mathbf{n}\otimes\mathbf{n} - 2\Sigma_{\mathrm{n}}\mathbf{n}\otimes\mathbf{n}], & \mathcal{F} = \mathcal{F}^{\mathrm{I}}(\mathbf{n}) \end{cases} \tag{37}$$

where $\mathcal{H}$ has been defined in advance. For the growth yield locus, the direction of plastic flow $\mathbf{N}$ depends only on the stress $\boldsymbol{\Sigma}$, while $\mathbf{N}$ for the coalescence locus depends also on the normal to the localization plane $\mathbf{n}$. Hence, if non-unique solutions exist for $\mathbf{n}$, the direction of plastic flow is ill-defined and the corresponding stress state corresponds to a vertex on the yield surface. Reference to Eq's (27) and (29) delivers the following solutions for $\mathbf{n}$:

- One set of $\mathbf{n}$ comprises unit vectors along the principal directions of $\boldsymbol{\Sigma}$; i.e. $\mathbf{n} = \hat{\mathbf{e}}_i$, where the unit vector $\hat{\mathbf{e}}_i$ $(i = 1..3)$ is an eigenvector of $\boldsymbol{\Sigma}$.
- Another set of solutions to $\mathbf{n}$ comprises linear combinations of any two of the three eigenvectors of $\boldsymbol{\Sigma}$, say $\hat{\mathbf{e}}_1$ and $\hat{\mathbf{e}}_2$. I.e. $\mathbf{n} = n_1\hat{\mathbf{e}}_1 + n_2\hat{\mathbf{e}}_2$, where

$$n_1^2 = 1 - n_2^2 = \begin{cases} \dfrac{1}{2(\Sigma_1 - \Sigma_2)(1-\eta)}\left[\Sigma_1 + (2\eta-1)\Sigma_2 - 2\eta\Sigma^{\mathrm{surf}}\mathrm{sgn}\,(\Sigma_1+\Sigma_2)\right] & \text{if } |\Sigma_1+\Sigma_2| > 2\Sigma^{\mathrm{surf}} \\ \dfrac{1}{2} & \text{if } |\Sigma_1+\Sigma_2| \le 2\Sigma^{\mathrm{surf}} \end{cases} \tag{38}$$

  Two more possible solutions can be obtained by considering other pairs of principal stresses and directions in the above.

The effective surface would be determined from the innermost of all coalescence surfaces obtained using the above normals. Using the corresponding solution for $\mathbf{n}$ in $(37)_2$ yields the flow direction tensor $\mathbf{N}$.

In the isotropic representation of the present yield functions at the macroscopic scale, the main microstructural parameters varying as function of the matrix equivalent plastic strain, $\bar{\epsilon}$, are the porosity f and the void aspect ratio w. To this end, the unknown plastic multiplier $\dot{\Lambda}$ need be eliminated in some manner. Using the equality of the plastic work rate at the macro and micro-scales leads to the following condition:

$$\boldsymbol{\Sigma} : \mathbf{D}^p = (1-f)\bar{\sigma}\dot{\bar{\epsilon}} \tag{39}$$

which yields

$$\dot{\Lambda} = (1-f)\frac{\bar{\sigma}\dot{\bar{\epsilon}}}{\boldsymbol{\Sigma} : \mathbf{N}} \tag{40}$$

The evolution equation for porosity is a consequence of the hydrostatic part of the plastic deformation rate $\mathbf{D}^p$, since matrix plastic deformation is isochoric; that is

$$\frac{\dot{f}}{1-f} = \mathrm{tr}(\mathbf{D}^p) = \dot{\Lambda} N_{kk} \tag{41}$$

Note that, due to the presence of the effect of $\mathbf{n}$ in the coalescence criterion, the porosity rate in practice depends only on the normal stress on the localization plane. This implies that, unlike the growth model, damage growth is possible even at zero triaxiality in the multi-surface model.

Further, the average evolution rate of $S = \ln w$ in early stages of plastic deformation (that conforms with the ensemble averaging scheme) is function of the dilatant part of plastic rate of deformation [23]:

$$\dot{S} = \left(\frac{1-3\alpha_1}{f} + 3\alpha_2 - 1\right) D^p_{kk} \tag{42}$$

The above result is consistent with the observed fact that both elongated and flattened voids evolve towards spheres in the early stages of plastic deformation. The effective stress $\bar{\sigma}$ is taken to depend on the effective plastic strain $\bar{\epsilon}$ through a power law of the form

$$\bar{\sigma} = \sigma_0 (1 + \bar{\epsilon}/\epsilon_0)^N \tag{43}$$

is used.

The set of equations (35)–(42) can be integrated in simultaneity until the onset of void coalescence to obtain the evolution of $\bar{\epsilon}$ vs. the Lode angle θ at a specified triaxiality T or vs. triaxiality for a specified Lode angle. The corresponding rate of change in porosity and void shape with respect to $\bar{\epsilon}$ will then be expressible as

$$\begin{aligned} \frac{\partial f}{\partial \bar{\epsilon}} &= (1-f)^2 \frac{N_{kk}}{\frac{\boldsymbol{\Sigma}}{\bar{\sigma}} : \mathbf{N}} \\ \frac{\partial S}{\partial \bar{\epsilon}} &= (1-f)\left(\frac{1-3\alpha_1}{f} + 3\alpha_2 - 1\right) \frac{N_{kk}}{\frac{\boldsymbol{\Sigma}}{\bar{\sigma}} : \mathbf{N}} \end{aligned} \tag{44}$$

4 Results and Discussion

Cross-sections of the multi-surface yield locus in Haigh-Westergaard stress space are examined in this section. This space can be characterized by three variables $(\Sigma_\mathrm{m}, \rho, \theta)$ via the following relations:

$$\begin{aligned} \Sigma_1 &= \Sigma_\mathrm{m} + \sqrt{\frac{2}{3}}\rho\cos(\theta) \\ \Sigma_2 &= \Sigma_\mathrm{m} + \sqrt{\frac{2}{3}}\rho\cos\left(\theta - \frac{2\pi}{3}\right) \\ \Sigma_3 &= \Sigma_\mathrm{m} + \sqrt{\frac{2}{3}}\rho\cos\left(\theta + \frac{2\pi}{3}\right) \end{aligned} \tag{45}$$

where Σ_m is the mean normal stress, θ is the well-known *Lode angle*, and ρ is proportional to the equivalent stress, *i.e.* $\rho = \sqrt{\frac{2}{3}}\Sigma_\mathrm{eq}$. Planes perpendicular to the hydrostatic axis (identified with a perpendicular distance

from the origin equal to $\Sigma_{\rm m}$) are known as *octahedral* planes, while planes cutting through the surface at a specified Lode angle ($\theta = $ cste) are called *meridian* planes. The octahedral plane with $\Sigma_{\rm m} = 0$ is termed the π plane.

Alternatively, the hydrostatic stress can be replaced with stress triaxiality $T = \Sigma_{\rm m}/\Sigma_{\rm eq}$. That is, in lieu of $\Sigma_{\rm m}$, stress triaxiality $T = \Sigma_{\rm m}/\Sigma_{\rm eq}$ can be the parameter to be prescribed; in which case $\Sigma_{\rm m} = T\Sigma_{\rm eq}$. Correspondingly, (45) is recast as follows:

$$\begin{aligned}
\Sigma_1 &= \sqrt{\frac{3}{2}}\rho\left[T + \cos\left(\theta\right)\right] \\
\Sigma_2 &= \sqrt{\frac{3}{2}}\rho\left[T + \cos\left(\theta - \frac{2\pi}{3}\right)\right] \\
\Sigma_3 &= \sqrt{\frac{3}{2}}\rho\left[T + \cos\left(\theta + \frac{2\pi}{3}\right)\right]
\end{aligned} \tag{46}$$

4.1 Model assessment

The accuracy of the present model is first examined by comparison between the predicted yield loci and numerically computed yield loci using a finite elements based limit analysis approach. A periodically voided material is subjected to stress controlled loading with specified values of the triaxiality and the Lode parameter, by loading a unit cell along its principal directions. The values of T and L are controlled by altering the ratios of the three normal remote stresses. In order to facilitate the imposition of periodic boundary conditions as well as have well-behaved meshing, cubic cells embedding coaxial cubic voids have been adopted. The homogeneous model would then reduce to Gurson. See [40] for further discussion upon results for equiaxed voids. Clearly, the only effective microstructural parameter in this respect is porosity f or, alternatively, χ. The FEM results are outcomes to single-step limit analysis calculations, originally introduced by [28, 29] [2]. This method involves the application of large axial and lateral displacements over a porous RVE, with the matrix material admitting an elastic-perfectly plastic von Mises behavior, such that each ratio between the axial and lateral displacements delivers a specific stress state and, correspondingly, a specific pair of triaxiality T and Lode parameter L, *i.e.* a specific $(\Sigma_{\rm m}, \theta)$. The Lode angle θ and the Lode parameter L are related by:

$$L = -\frac{27}{2}\frac{\det(\boldsymbol{\Sigma}^{'})}{\Sigma_{\rm eq}^3} = -\cos 3\theta \tag{47}$$

Since every calculation is carried out in one single step, with the geometric nonlinearity deactivated, the initial and ultimate microstructural variables are the same. The reader is referred to [20, 34, 40] for more explanation regarding this class of FEM calculations.

The curves in Fig. 3 show the yield loci for materials with moderate to large values of the porosity: $f = 0.01$ and $f = 0.05$. The loading path is represented with intermediate ($T = 1$) as well as large ($T = 4$) triaxiality, the former denoting the zone inside a diffuse neck or a notched bar and the latter representative of the plastic zone ahead of a blunt crack tip [7]. Note that the plotted radii equal $\rho = \sqrt{2/3}\Sigma_{\rm eq}/\bar{\sigma}$.

Next, Fig. 4 shows comparison of meridian cross sections for the same porosities on meridian planes corresponding to axisymmetric loading ($L = \pm 1$) and pure shear with superposed hydrostatic stress ($L = 0$).

[2] The same strategy was applied in [34] for comparison between the inhomogeneous model predictions and FEM results.

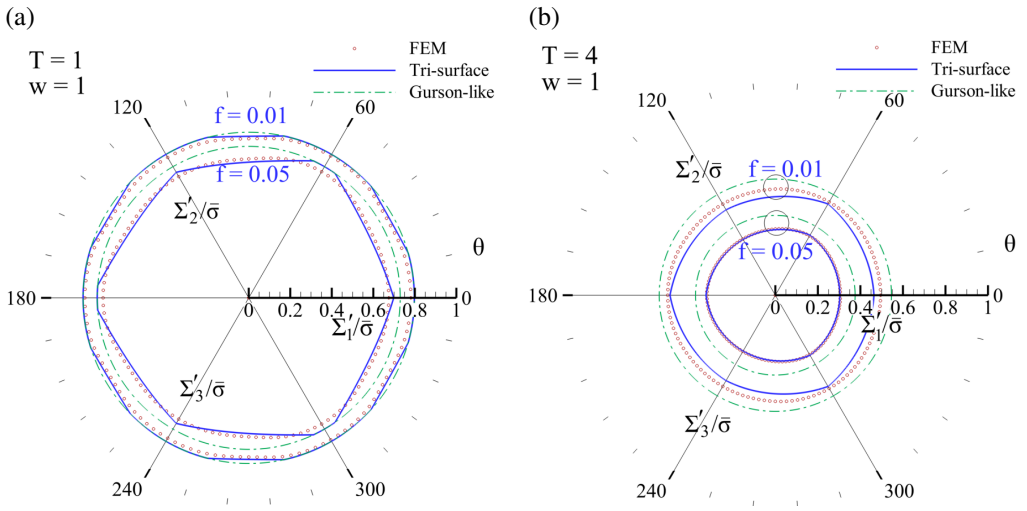

Figure 3: Octahedral plane projections of the yield surface (with the plotted radii being $\rho = \sqrt{2/3}\Sigma_{\text{eq}}/\bar{\sigma}$) with constant-triaxiality stress states for $f = (0.01, 0.05)$ and (a) $T = 1$, (b) $T = 4$.

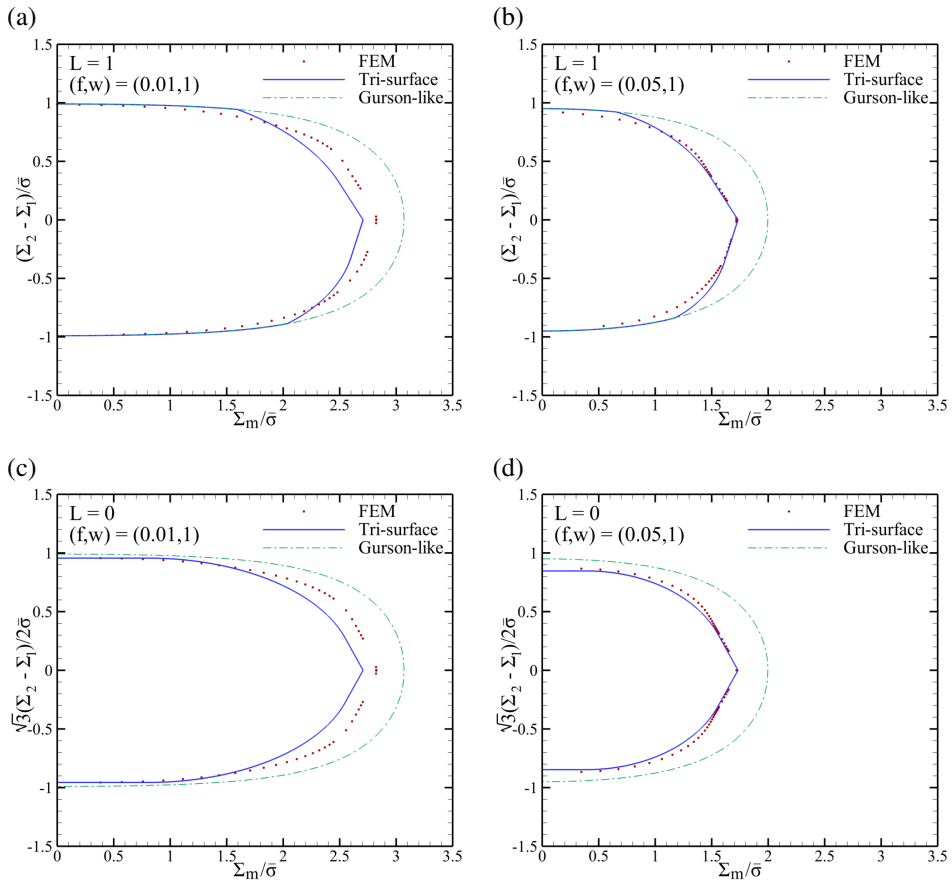

Figure 4: Meridian cross sections of the effective yield surface representing: (a,b) axisymmetric and (c,d) purely deviatoric loading for various porosities, compared with numerical limit analysis results.

The reader should note, according to Fig's 3a and 4, that the use of the T-B-L model, with or without calibration (see [31,34]), loses the upper-bound character at the limit of zero hydrostatic stresses (*i.e.* purely deviatoric loading) under axisymmetric loading, *i.e.* $\theta = n\pi/2, |L| = 1$. This limitation can partly be attributed to the use of different RVE shapes in the analytical and numerical models. This further corroborates the findings of Morin *et al.* [44], who have found the effect of void and cell shape on the yield surface to be minimal for a given microstructural state. The same observation, however, does not necessarily hold in an evolution-based problem, which consists of the entire deformation process from void nucleation to ultimate failure. See [45] for details.

It is also clear that, at low porosities, the FEM yield surface, as well as its effective (tri-surface) counterpart, becomes closer to diffuse yielding whereas, at higher porosities, they tend closer to combined internal necking–shearing. Further details in this respect are explained in [40]. Moreover, the effective analytical surface is not an upper bound. This is due, in part, to the approximation employed in the formulation of the effective yield criterion at the limit of isotropic materials. In particular, the closer-to-real effective yield surface is a combination of both $\mathcal{F}^{\mathrm{H}}$ and $\mathcal{F}^{\mathrm{I}}$.

The comparisons exhibited in Fig. 4 are promising in the sense that the numerical values are closer to the tri-surface curve than to the homogeneous yield surface. More importantly, due to the additional heuristic parameters in the T-B-L model, the yield stress under purely hydrostatic loading is not overestimated unlike in Fig. 7 of [40]. Yet, the heuristic calibration, though not significant, loses the upper-bound character for small porosities. A more consequential observation that can be made in the other limit case of pure shearing, *i.e.* $\Sigma_{\mathrm{m}} = 0$ at $L = 0$, is the dominance of inhomogeneous yielding, reflected through the effective (tri-surface) locus, over homogeneous yielding. Apart from being an observed fact corroborated by numerical findings [17, 19], it can be clearly deduced from the comparison between the shear stresses from $\mathcal{F}^{\mathrm{H}}$ and $\mathcal{F}^{\mathrm{I}}$ at this limit, *i.e.* $\tau = (1-f)\bar{\tau}$ and $\tau = (1-f_{\mathrm{b}})\bar{\tau}$, respectively. Here, $\bar{\tau} = \bar{\sigma}/\sqrt{3}$ is the matrix shear strength and $f_{\mathrm{b}} = \chi^2$ is the porosity within the band, which is always larger than the overall porosity f. For other loading combinations, there exist ranges of mean stress with homogeneous yielding being dominant.

The sequel exhibits the effects induced by each one of the two independent microstructural parameters (χ, w) (while λ is ideally 1 when the voids are randomly distributed) on the yield surface projection onto the deviatoric planes (with constant Σ_{m} or T) and onto the meridian planes (representing either axisymmetric loading $L = \pm 1$ or pure shear with superposed hydrostatic stress $L = 0$). $\bar{\chi}$ and $\bar{w}$ have been denoted with χ and w, respectively, for the sake of simplicity. The same type of effects is examined concerning the strain at the onset of coalescence evolving in terms of the Lode angle as well as triaxiality, each with the other kept constant. Since, at coalescence, two localization mechanisms, *i.e.* internal necking and combined necking-shearing, can be conceived of for plastic deformation, the surfaces resulting from each induced mechanism will be compared in Appendix C.

4.2 Projection onto deviatoric planes

Figure 5 depicts the influence of χ on the yield surface projection onto the deviatoric planes with constant T (with $T = 0$ denoting $\Sigma_{\mathrm{m}} = 0$ or, equivalently, the π plane). Figure 6 depicts the same kind of influence induced by the void aspect ratio w.

Note that, with varying values of χ, w and λ are both kept equal to 1, thereby the porosity equaling $f = \chi^3$. The ligament parameters of 0.1, 0.3, and 0.7 would then correspond to porosity values of 0.1, 2.7, and 34.3 %, respectively. In practice, the real porosities within engineering materials are normally much smaller than the upper bound considered herein. Yet, a rather wide range of porosities well serves the purpose of elucidating the potential effect induced by porosity.

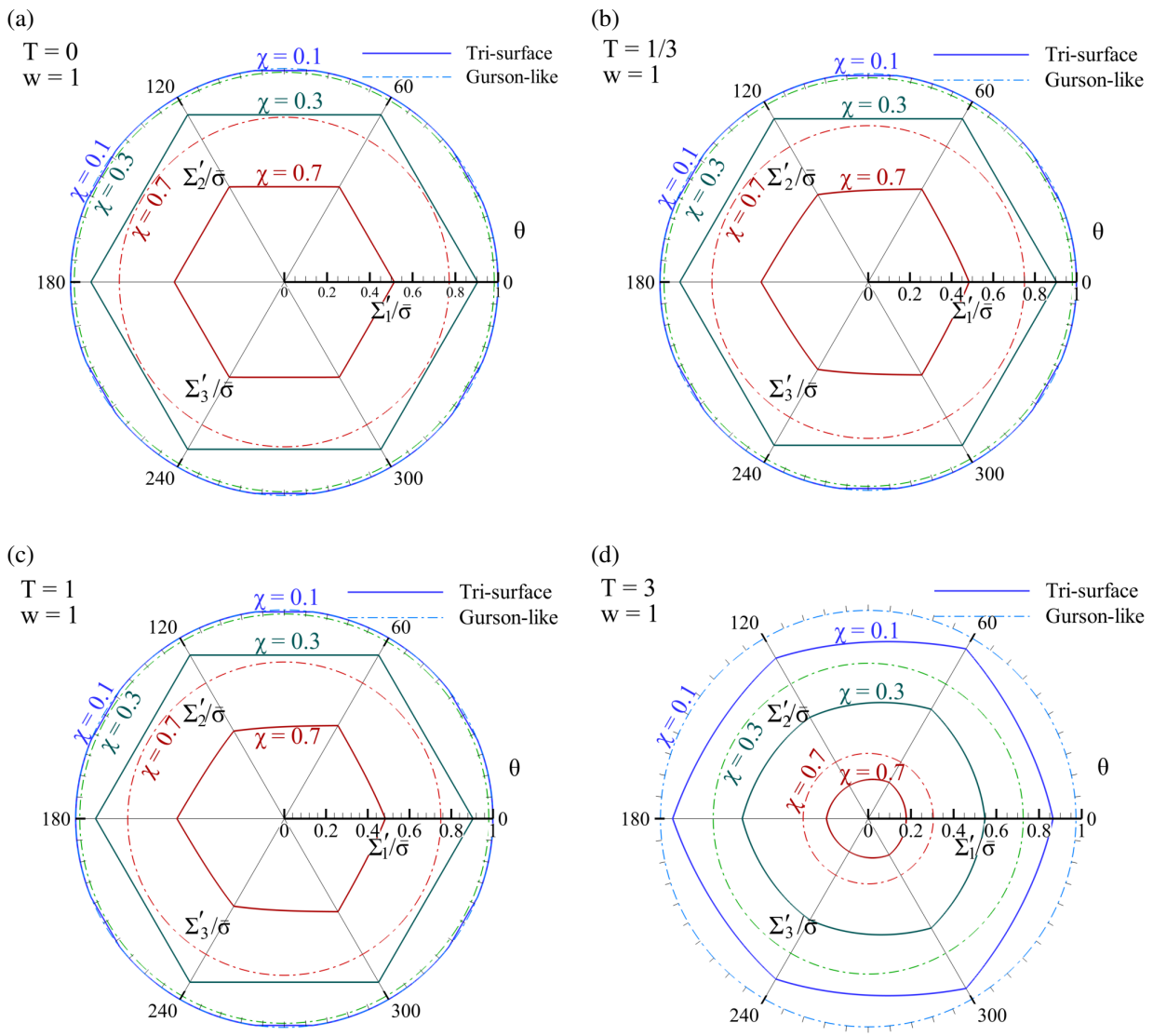

Figure 5: Effect of the ligament parameter χ on the effective yield surface projection onto the deviatoric planes with constant triaxiality.

Considering the effect of porosity, reflected through the ligament parameter χ, the homogeneous yield surface shrinks whereas the combined necking-shearing surface shrinks faster along with increasing χ. Namely, the effective yielding mechanism tends from diffuse plasticity at $\chi \longrightarrow 0$ towards a combined necking-shearing localized nature with increasing χ. The two surfaces, however, become closer at larger portions of hydrostatic stress, *i.e.* with increasing triaxiality, exemplified with $T = 3$. At this limit, the effective yield mechanism is combined internal necking–shearing at the limit of $L = 0$ admitting $\theta = (2n + 1)\pi/6$, which signifies pure shearing with superposed hydrostatic stress. However, the hydrostatic effect prevails over that of shear, and thus the equivalent stresses would be minimally apart. This further corroborates the discussion below Fig. 3, and occurs regardless of the porosity level. More specifically, so long as there is nonzero porosity, be it small or large, plastic deformation is localized under pure shear.

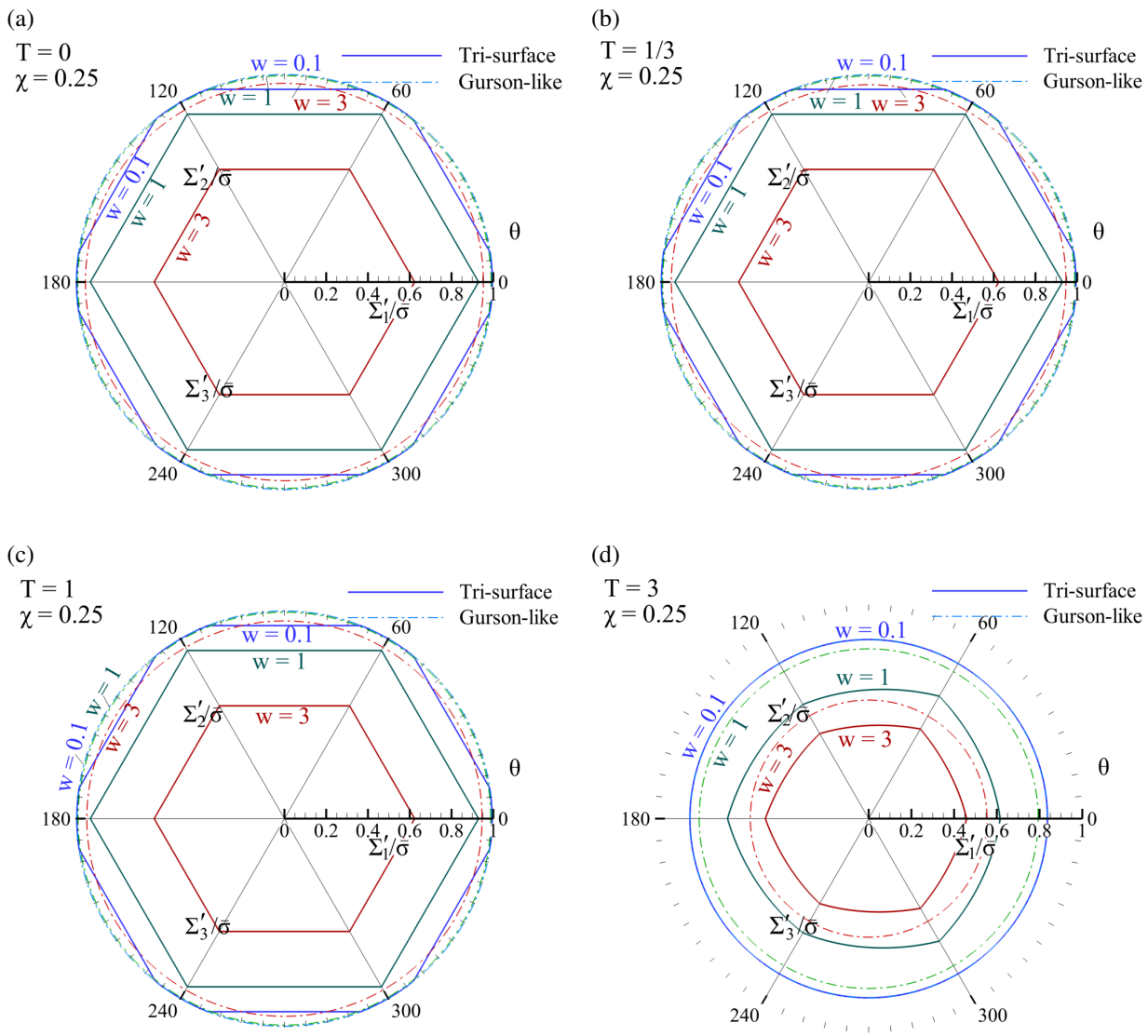

Figure 6: Effect of the void aspect ratio w on the effective yield surface projection onto the deviatoric planes with constant triaxiality.

Apropos of the effect of w, Fig. 6 demonstrates combined necking–shearing as the effective yield surface, with a shrinking effective surface for larger values of w, especially for $w > 1$. This has been adduced by former results, as reported in [31] for instance, that the coalescence limit load decreases, even more notably so for $w > 1$, with increasing w. It is also observed in consonance with Fig. 5 that, except at high stress triaxialities (represented by $T = 3$ here) representing large portions of hydrostatic stress, the pure shear limit ($\theta = (2n + 1)\pi/6$) is subdued by the combined internal necking–shearing mechanism. On the other hand, for small to medium triaxialities, the effective yielding mechanism for materials with flat voids ($w < 1$) proves to be of a homogeneous yielding type at stress states close to the axisymmetric limit ($\theta = n\pi/3$). For large triaxialities, however, the effective mechanism generally moves towards homogeneous while it still varies from case to case. For flat voids ($w = 0.1$), the effective mechanism is homogeneous under all stress states, just as in the case of axisymmetric loading with smaller triaxialities, whereas it is

inhomogeneous for $w \geq 1$ even at this range of large triaxialities. Within periodic void arrays, however, a different trend has been explored wherein the coalescence of flat voids ($w < 1$) could occur at early stages, even so under uniaxial loading ($T = 1/3$) [46]. With randomly distributed voids, both the dilute material limit ($\chi \longrightarrow 0$) and materials containing flat (penny-shaped) cavities yield homogeneously under axisymmetric stress states.

4.3 Projection onto meridian planes

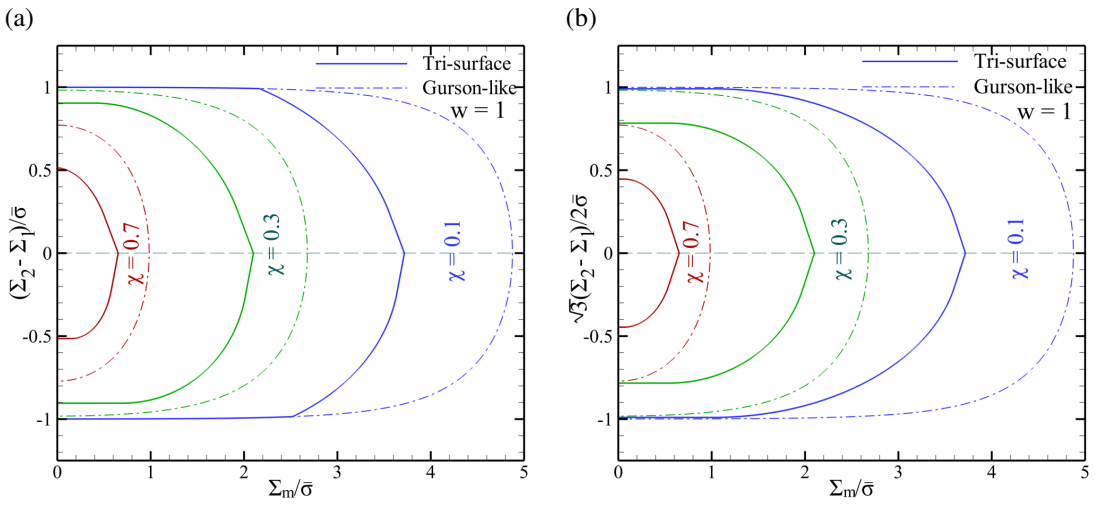

Figure 7: Effect of the ligament parameter χ on the effective and homogeneous (Gurson-like) yield surface projections onto meridian planes denoting (a) axisymmetric loading and (b) pure shear with superposed hydrostatic stress.

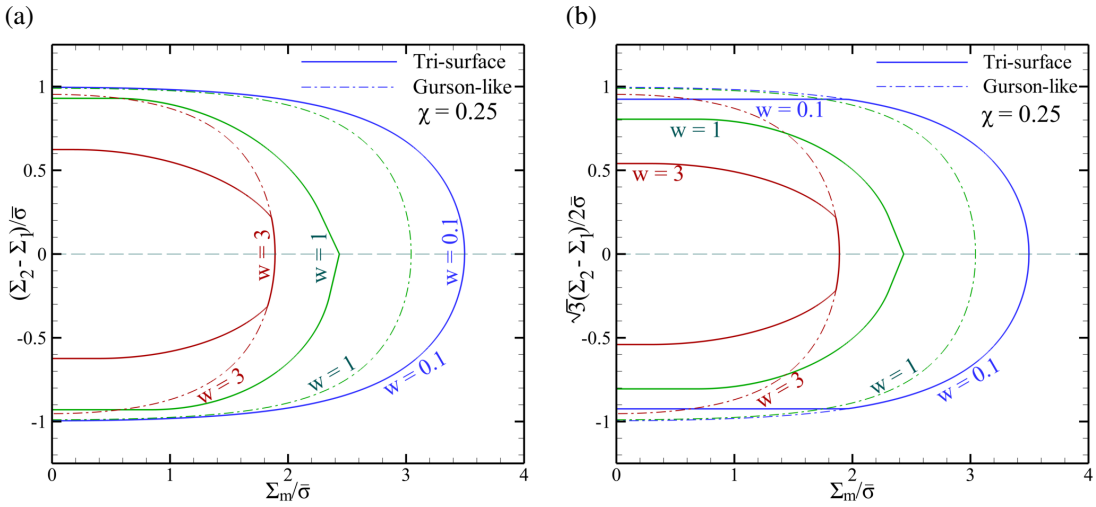

Figure 8: Effect of the void aspect ratio w on the effective and homogeneous (Gurson-like) yield surface projections onto meridian planes denoting (a) axisymmetric loading and (b) pure shear with superposed hydrostatic stress.

The continuing set of figures illustrate the same kind of trends but in the yield surface projection onto the meridian planes denoting axisymmetric loading ($L = \pm 1$) and pure shear with superposed hydrostatic stress ($L = 0$). First, Fig. 7 depicts the influence of χ on the yield surface projection of interest. Figure 8 depicts the same kind of influence induced by the void aspect ratio w.

Upon a similar trend to that observed with the variation of porosity in Sec. 4.1, the inhomogeneous yield surface prevails over the homogeneous at the vicinity of $\Sigma_{\rm m} \longrightarrow 0$ under pure shearing superposed with hydrostatic loading, say $L = 0$, as shown in Fig. 7b. With increasing χ, further difference between the effective and homogeneous surfaces is detected at higher hydrostatic stresses. Thereupon, the difference becomes more pronounced when χ decreases. Nevertheless, the effective mechanism tends towards homogeneous yielding at sufficiently low hydrostatic stresses and low–level porosities approaching the dilute limit, here represented by $\chi = 0.1$, when the stress state is axysimmetric, Fig. 7a. Yet, larger hydrostatic stresses or, equivalently, larger triaxialities, would turn the mechanism towards inhomogeneous yielding as indicated by the large difference between the effective and homogeneous yield surfaces.

Figure 8a demonstrates that the effective yielding mechanism for materials with flat voids is homogeneous for almost the whole range of hydrostatic stresses under axisymmetric loading conditions whereas it is inhomogeneous for all medium to large void aspect ratios. In contrast, under pure shearing with superposed hydrostatic loading (Fig. 8a), the effective mechanism is homogeneous only for sufficiently large hydrostatic stresses (or triaxialities). In particular, the small temper associated with axisymmetric loading (at $\theta = n\pi/3$) shown in Fig. 6c can be envisaged more clearly in Fig. 8 implicating combined internal necking–shearing as the effective mechanism. Throughout the range of Lode parameters, especially under both unit and zero values, the effective yield mechanism for *prolate* voids ($w > 1$) is homogeneous plasticity in the maximal hydrostatic stress zone (or highest triaxiality levels) whereas the localized mode is dominant for (nearly) spherical ($w \approx 1$) voids throughout the hydrostatic range, and for oblate ($w < 1$) voids provided the hydrostatic stress is not significantly large.

Altogether, an isotropic porous material characterized by random dispersion of voids can yield (almost) homogeneously under high triaxialities, *i.e.* dominant hydrostatic stresses, when either porosity f or the void aspect ratio w becomes vanishingly small [47, 48]. The former is representative of the dilute limit of the material, and the latter is reminiscent of penny-shaped cracks.

Incidentally, the effective yield surface, unlike its homogeneous counterpart, admits symmetry with respect to the $\Sigma_2 - \Sigma_1$ only at $L = \pm 1$ (denoting axisymmetric loading) inasmuch as the principal stresses have equal absolute values on the two principal planes regardless of the hydrostatic portion. This generally not the case, however, under shear dominance in that the hydrostatic stress level alters both the plane and magnitude of principal stresses.

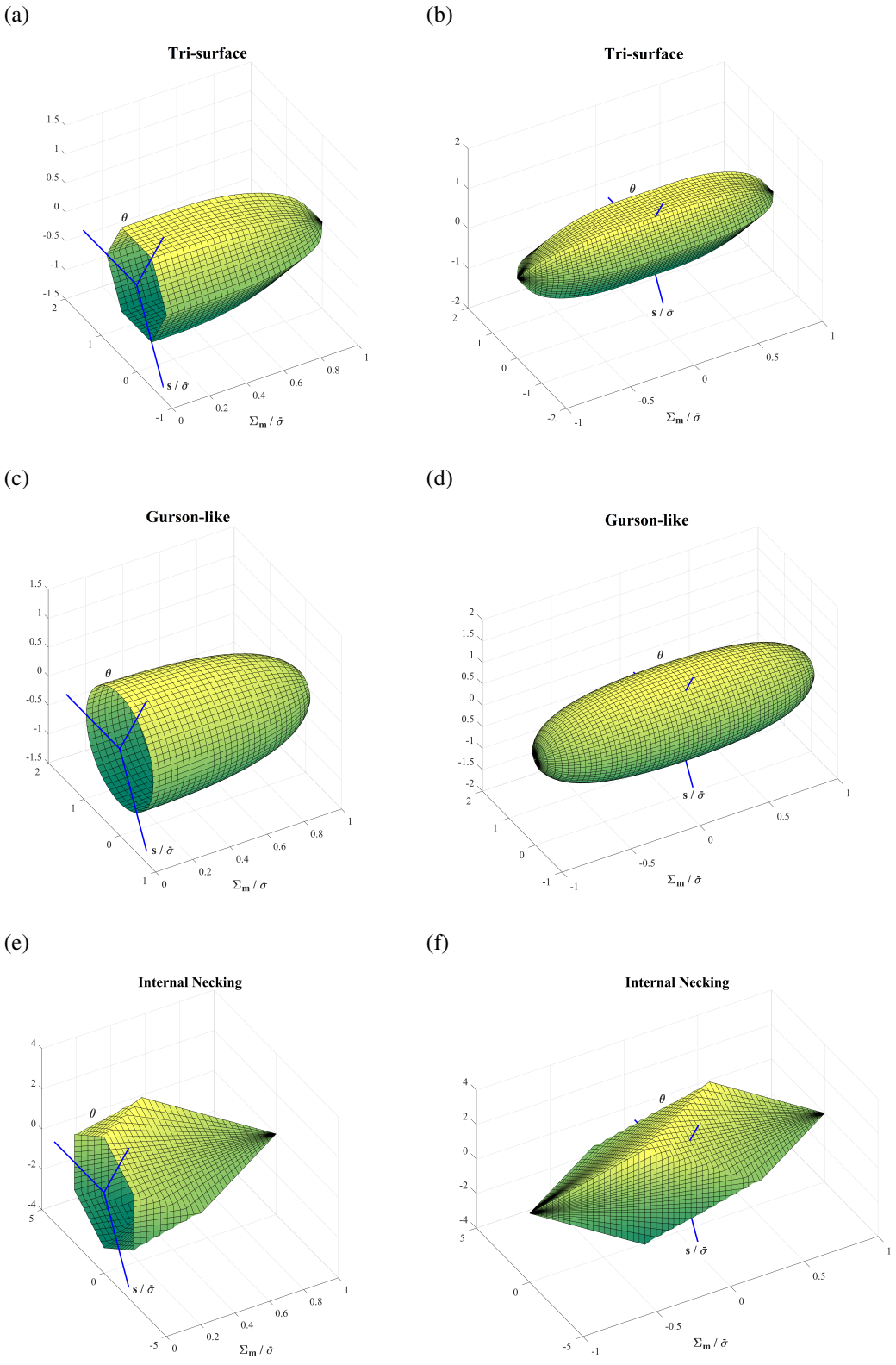

Figure 9: Example half and complete 3D surfaces for a frozen microstructure denoted by the $(\chi, w, \lambda) = (0.4, 1, 1)$ trio exhibiting the surfaces corresponding to: (a,b) the effective criterion, (c,d) the homogeneous model, and (e,f) the inhomogeneous model under the internal necking (note that the surface corresponding to combined necking-shearing is itself the effective surface).

4.4 Sample 3D surface

It may be appealing to observe a complete yield surface in the Haigh-Westergaard stress space incorporating the effect of the Lode parameter/angle. Examples of a half and complete 3D surfaces for a frozen microstructure are shown here, including the surfaces corresponding to the effective criterion, the homogeneous model, and the inhomogeneous model under the internal necking or combined necking-shearing mechanism. Figure 9 depicts this example. Note that all surfaces are endowed with point symmetry at the origin of the stress space. Among all, the homogeneous and combined inhomogeneous yield surfaces admit planar symmetry whereas the internal-necking yield surface is merely point-symmetric (with respect to the origin). Upon implication, one can deduce that shifting the sign of the Lode parameter, realized with a $\pi/3$ rotation on the θ deviatoric plane, equal equivalent stresses will be predicted in accordance with the inhomogeneous model. This observation can be true only at the isotropic limit, *i.e.* with randomly distributed voids. Under periodic void arrays, however, where changing the places of the major and minor normal stresses negates the Lode parameter, plastic deformation would localize in two different planes perpendicular to each other.

4.5 Strain to failure vs. Lode parameter/triaxiality

It is worthy of note that an effective ligament parameter of $\chi = 0.7$ corresponds to a porosity level around 30 $\%$, which is seldom observed in engineering materials. The foregoing results were shown for such a wide variety of χ's for the sake of better illustrative capability. The study of strain to failure, as per this subsection, will be presented for a tighter range of χ. The maximum porosity would then pertain to $\chi = 0.4$, equaling 6.4 $\%$.

Notwithstanding the existence of significant plastic deformation at the post-coalescence regime, the matrix effective plastic strain $\bar{\epsilon}$ at the onset of coalescence is normally regarded as the *strain to failure* $\bar{\epsilon}_f$ for the material. Apart from being intrinsically indicative of failure, this measure proves efficacious since the de facto damage mechanism after the onset of coalescence depends on different extrinsic factors such as the specimen geometry and matrix texture.

This subsection addresses the evolution of $\bar{\epsilon}_f$ as implicit function of the Lode parameter L, so as stress triaxiality T, which is consequence of explicit integration of (44) exploiting the single-step Runge-Kutta solution scheme. To set the reference more globally, the following auxiliary parameter is defined as function of θ when $-\pi/6 \leq \theta \leq \pi/6$:

$$\bar{\theta} = 1 - \frac{\theta}{\pi/6} \quad \therefore \quad -1 \leq \bar{\theta} \leq 1 \tag{48}$$

Figure 10 demonstrates the effect induced by the ligament parameter $\bar{\chi}$ on the evolution of $\bar{\epsilon}$ in terms of the Lode angle θ or its normalized equivalent $\bar{\theta}$ at various triaxialities ranging from a uniaxial $T = 1/3$ to a near-hydrostatic $T = 3$ stress state. Similarly, Figure 11 illustrates the effect induced by the void aspect ratio w.

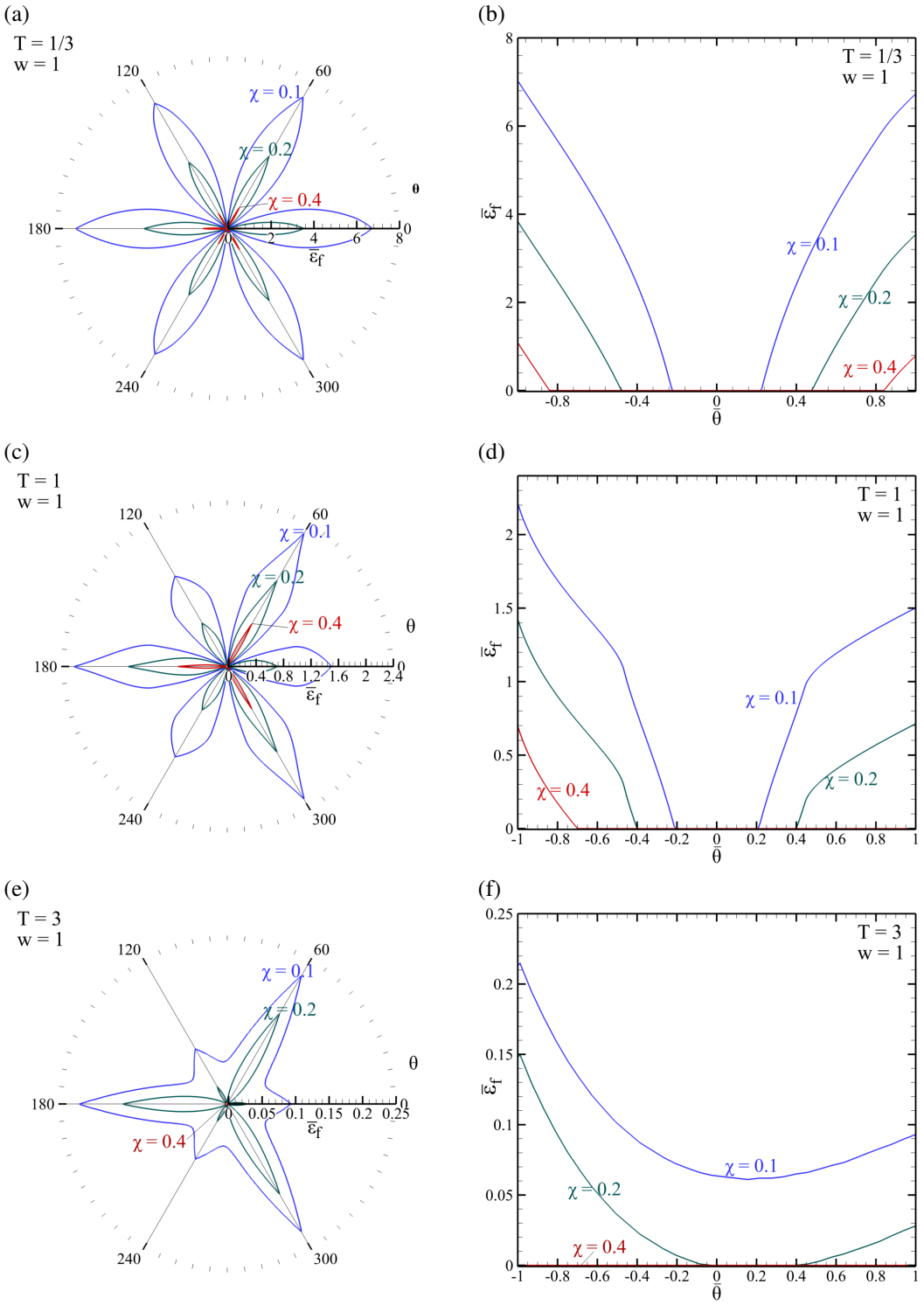

Figure 10: Effect of the ligament parameter $\bar{\chi}$ on the evolution of $\bar{\epsilon}_f$ as function of the Lode angle θ (a,c,e) or its normalized equivalent $\bar{\theta}$ (b,d,f) (noting that $-1 \leq \bar{\theta} \leq 1$) at various triaxialities.

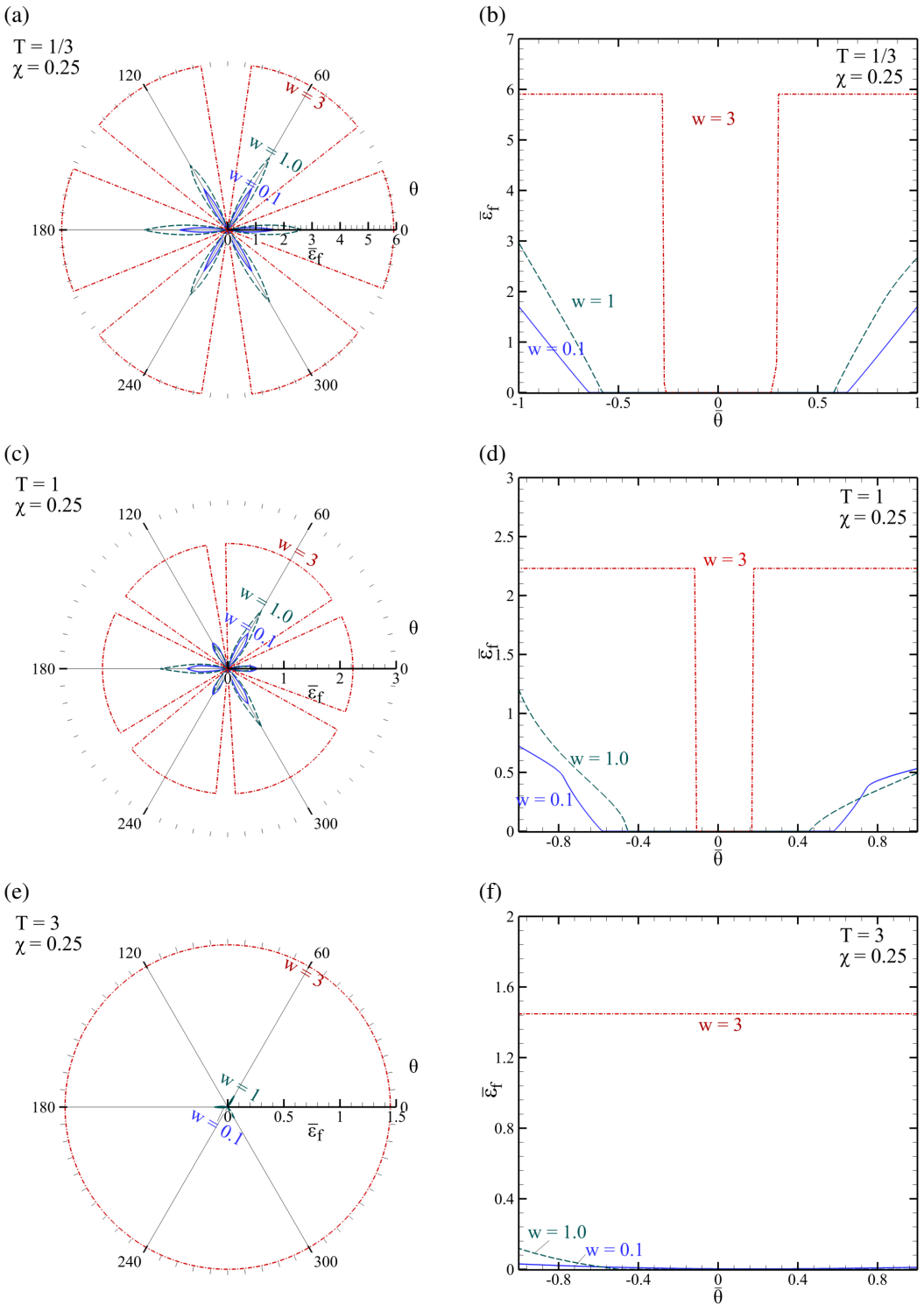

Figure 11: Effect of the void aspect ratio w on the evolution of $\bar{\epsilon}_f$ as function of the Lode angle θ (a,c,e) or its normalized equivalent $\bar{\theta}$ (b,d,f) (noting that $-1 \leq \bar{\theta} \leq 1$) at various triaxialities.

Upon examination of Fig's 10 and 11, $\bar{\epsilon}_f$ is predicted close to zero under stress states close to pure shear ($\theta = (2n+1)\pi/6$) emanating from the inhomogeneous yield criterion $\mathcal{F}^{\mathrm{I}} = 0$ happening at early

stages of plastic deformation. Accordingly, the Lode angles resulting in $L \longrightarrow 0$ in this neighborhood are excluded from the plots. In extension to Ref. [40], which has investigated this effect only for small to moderate porosities, the present study goes so far as to incorporate both χ and w from small to large values, demonstrating that the above-mentioned observation is refuted at very small porosities (*e.g.* with $\chi = 0.1$) as well as large void aspect ratios ($w > 1$) under highly triaxial loadings (*e.g.* $T = 3$). In the former special case, the large hydrostatic portion of loading deters void coalescence in small porosities from happening from the outset, whence $\bar{\epsilon}_f$ is clearly nonzero. With increasing χ, however, $\mathcal{F}^{\mathrm{I}} = 0$ soon predominates almost from the outset, and thus $\bar{\epsilon}_f$ drops close to zero under pure shearing with superposed hydrostatic loading. All the same, one can notice that, for $\chi > 0.2$ under high triaxiality values (here $T = 3$), $\bar{\epsilon}_f$ literally vanishes for $\theta = 2n\pi/3$ (with n inclusive of 0) which declares axisymmetric loading with the *axial* loading prevalent. Existing work in the literature ratifies this finding in that void coalescence takes place soon after plastic deformation begins [46]. At $\theta = (2n+1)\pi/3$, however, indicative of axisymmetric loading with the *lateral* loading dominant, coalescence in layers normal to $\mathbf{n}$ is delayed due to the axial stress being moderate. In actual fact, the voids tend to coalesce in *columns*, *i.e.* along plastic plugs parallel to $\mathbf{n}$ [49], which is not accommodated by the presently invoked $\mathcal{F}^{\mathrm{I}}$.

The latter special case ($w > 1$), on the other hand, corresponds to the case where an elongated void undergoes highly triaxial loading. As such, the plastically deformable intervoid ligament traverses towards the whole unit cell, and thus the effective yielding mechanism at early stages is homogeneous whereby the strains to failure predicted at equivalent stress states inducing equal principal stresses ($\theta = (n\pi/3, (2n+1)\pi/6)$) become almost non-distinguishable. However, the predicted $\bar{\epsilon}_f$ for $w > 1$ is prohibitively large in that the void is obliged to tend towards a sphere so that χ can increase up to the level whereby $\mathcal{F}^{\mathrm{I}} = 0$ can be realized. In practice, however, the overall material response would cease to remain isotropic if, at all, such immense strains are attainable. The more realistic mechanism of coalescence in columns would then deliver a much smaller strain to failure.

Next, Fig. 12 illustrates the effects of alteration in microstructural parameters on the evolution of $\bar{\epsilon}_f$ as function of stress triaxiality T at the example Lode parameters equaling $L = \pm 1$ (corresponding to axisymmetric loading) and $L = \pm\sqrt{2}/2$ (denoting some intermediate combined axisymmetric and shear loading). The value of $\bar{\epsilon}_f$ at $\theta = \pi/6$ (corresponding to $L = 0$) is mostly near-zero (except for large w's or small χ's under large triaxialities). To the reader's better insight into the evolution of $\bar{\epsilon}_f$ vs. the Lode angle in simultaneity with stress triaxiality, Fig. 13 is provided for $(\chi_0, w_0, \lambda_0) = (0.3, 1, 1)$.

Besides with small values of χ_0 or large values of w_0 (*i.e.* $\chi_0 < 0.2$ or $w_0 > 1$), the strain to failure almost vanishes for $T > 2$. Namely, under axisymmetric loading with normal dominance, the strain to failure becomes diminutive under large lateral stresses since voids under large lateral loads can easily impinge laterally by internal necking. Likewise, under axisymmetric loading with lateral load dominance, the strain to failure reduces with increasing the normal stress. Both of these response changes are reflected via the same subfigures, Fig's 12(a) and (c). All the same, under combined axisymmetric and shear stress states, as exemplified by $L = \pm\sqrt{2}/2$ in Fig's 12(b) and (d), $\bar{\epsilon}_f$ for $\chi << 1$ and $w > 1$ are orders of magnitude larger than those for other ranges of χ and w. Note that such large values of $\bar{\epsilon}_f$ for $w > 1$ are non-physical. This further affirms that the real yielding mechanism for elongated voids under such high triaxialities deviates from internal necking or shearing, and warrants accounting for other mechanisms such as coalescence in columns [49].

Moreover, as earlier revealed by Fig's 5 and 6, the effective yielding mechanism is homogeneous for small χ's and w's under triaxialities ranging up to around $T = 1$, and is inhomogeneous for the rest of χ's and w's as well as under higher triaxialities. This shift in the effective mechanism, indeed, gives rise to slope changes within $\bar{\epsilon}_f$ for the cases of $w_0 = 0.1$ in Fig. 12c and $\chi_0 = 0.1$ in Fig. 12b. Similar slope changes can be envisaged also under other loading combinations. The reader can consult [40] for more example cases.

Remark 1: Note that, for intermediate to large porosities, here represented by $\chi_0 > 0.1$, ductility is underestimated in the shear-dominant regime, *i.e.* $T < 1$ and $|L| < 1$, which results in the local maximum

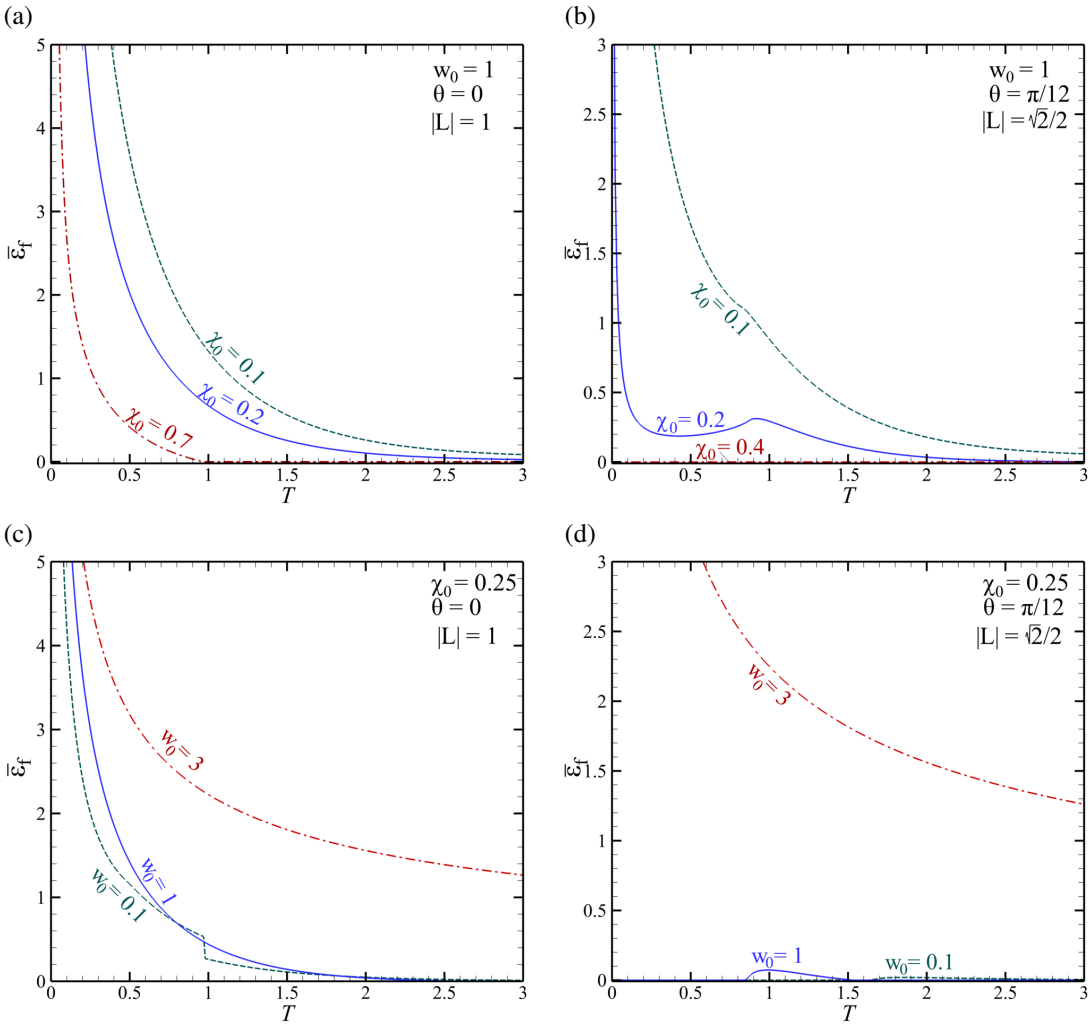

Figure 12: Effect of alteration in microstructural parameters on the evolution of $\bar{\epsilon}_f$ as function of stress triaxiality T under load combinations represented by example Lode parameters $L = \pm 1$ and $L = \pm\sqrt{2}/2$: (a,b) effect of χ_0, (c,d) effect of w_0.

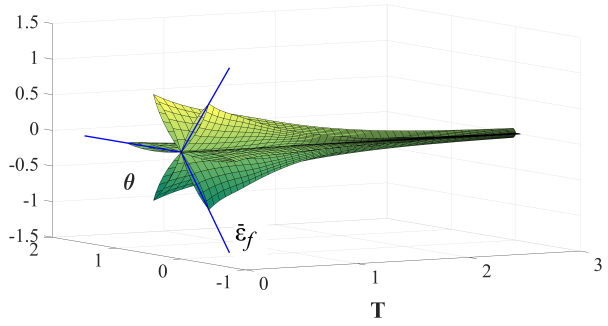

Figure 13: Representative 3D surface of $\bar{\epsilon}$ evolution as function of Lode angle and stress triaxiality for $(\chi_0, w_0, \lambda_0) = (0.3, 1, 1)$.

envisaged in the curve belonging to $\chi_0 = 0.2$ in Fig. 12b. So is the case due to the limitation of equating ϵ_f to ϵ_c, which disregards the significant plastic deformation undergone past the onset of localized deformation. On the other hand, there being a Gurson-like criterion as $\mathcal{F}^{\mathrm{H}}$ effects the propensity of overestimating the ductility corresponding to axisymmetric loading paths, *viz.* $|L| = 1$. It so occurs due to the observed underestimation of damage growth rates with the use of originally-derived Gurson-like models. The latter is normally resolved by the introduction of heuristic parameters [9, 16].

Remark 2: The singular limit within $\bar{\epsilon}_f$ at the limit of triaxiality approaching zero (which can be best exemplified by a state of shear-dominated loading) is non-physical inasmuch as failure under shear in a material with *finite porosity* is substantive regardless of void distribution. This calls for more considerate accounting for induced anisotropies emanating from void rotation and/or elongation. By way of consequence, the strain to failure at the $T = 0$ limit would potentially be a large but finite value. This trend has been observed in some recent simple torsion experiments [15]. All the same, a periodic microstructure under *proportional* loading can exhibit varieties of different ductilities under various load combinations. As schematized as in Fig. 14, $\bar{\epsilon}_f$ for a state of combined axial and shear loading is shown to be unbounded at the limit of $T = 1/3$, and the shear-dominated low-triaxiality region ($T < 1/3$) is driven by the loading path. A recent investigation by the authors demonstrates the existence of a minimum in the case of a unit cell loaded under combined axial and shear loading.

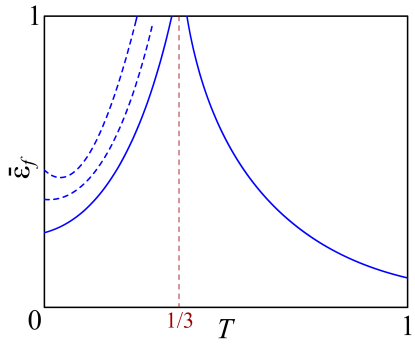

Figure 14: Schematic representation of $\bar{\epsilon}_f$ evolution as function of stress triaxiality for a unit cell under arbitrary loading with a periodic void distribution and various loading paths.

5 Concluding Remarks

This paper addresses an extension to a recent effort [40] investigating through the development of a new multi-surface failure model, incorporating void growth (homogeneous yielding) and coalescence (inhomogeneous yielding), in porous ductile materials with isotropic response on account of random distribution of voids. The present work extends the realm of that investigation by accounting for two distinctive parameters that dictate the microstructural geometry: the ligament parameter χ (indicative of porosity) and the void aspect ratios w (while admitting the existence of a third parameter being the cell aspect ratio, approximated as unity by virtue of random void distribution) upon similar homogeneous and inhomogeneous yield criteria that incorporate the aforementioned parameters. To this end, a hybrid criterion encompassing the intersection of one homogeneous and two inhomogeneous yield surfaces, after Ref's [27] and [31], respectively. The homogeneous yield criterion accounts for diffuse plasticity at the cell level, and the inhomogeneous criterion is a combination of two terms functioning based on normal and shear tractions over an arbitrary plane, representative of internal necking or combined internal necking and shearing.

The effective yield surface, in comparison to the homogeneous and inhomogeneous (internal necking

alone or combined internal necking and shearing), was plotted 3D as well as projected on deviatoric and meridian planes in the Haigh–Westergaard stress space. On an arbitrary deviatoric plane (e.g. the π plane or any parallel plane thereof), the difference between the effective and homogeneous yield surfaces enlarged along with decreasing χ (or decreasing porosity accordingly) or increasing w. Nevertheless, this difference diminishes at higher triaxialities. Under such circumstances, as opposed to that upon periodic void positioning, both the dilute material limit ($\chi \longrightarrow 0$) and a material containing flat (penny-shaped) cavities ($w \longrightarrow 0$) encounter homogeneous yielding under axisymmetric stress states. Otherwise, the effective mechanism is inhomogeneous, by combined internal necking and shearing, which itself tends towards homogeneous yielding with increasing stress triaxiality or, equivalently, with increasing hydrostatic stress.

Acknowledging the effective plastic strain at the onset of coalescence as a crude measure of strain to failure $\bar{\epsilon}_f$, the former was plotted as function of the Lode angle as well as stress triaxiality T, encompassing a complete range of stress states from axisymmetric loading ($L = \pm 1$) to pure shear superposed by hydrostatic loadings $L = 0$ and from pure shearing ($T = 0$) up to nearly hydrostatic loading ($T = 3$). Under large triaxialities as well as for materials with $\chi > 0.2$ or $w \leq 1$ would deliver vanishingly small $\bar{\epsilon}_f$ in the whole range of triaxialities. For materials with elongated (needle-like) voids, however, $\bar{\epsilon}_f$ is significantly overestimated since coalescence in layers (by internal necking or shearing) is the only failure mechanism taken into account in the present context. The more factual failure mechanism for the latter case that can be incorporated in future investigations is void coalescence along plugs of material normal to the plane on which stresses are resolved (also termed coalescence in columns). Meanwhile, $\bar{\epsilon}_f$ resembles a declining exponential function with respect to T, that admits an asymptotic value at large triaxialities ($T > 2$) and grows dramatically at the limit of $T = 0$. Yet, the latter is characteristic of isotropic material behavior as the underlying premise within the present context, which does not generally hold for non-random distribution of voids.

Acknowledgments

The authors earnestly acknowledge financial support from the National Science Foundation under Grant Number CMMI-1405226.

Appendix A K–B/GLD Model Parameters

The parameters embedded in (1) are the building blocks of the void shape effect. They are mainly functions of porosity f and void aspect ratio w (as well as a Hill-type anisotropy tensor $\mathbb{H}$ in the case of anisotropy within the matrix). Note that w in the equations below is the spheroidal aspect ratio w_s, written w for brevity. g, known as *secondary porosity* is defined as:

$$g = 0 \quad \text{(p)}; \qquad g = \frac{e_2^3}{\sqrt{1-e_2^2}} = f\frac{e_1^3}{\sqrt{1-e_1^2}} = f\frac{(1-w^2)^{\frac{3}{2}}}{w} \quad \text{(o)} \tag{A-1}$$

where (p) and (o) stand for "prolate" $(w > 1)$ and "oblate" $(w < 1)$, respectively. By definition, g is non-zero for oblate voids only. e_1 and e_2 are, respectively, the eccentricities of the void and the outer boundary of the spheroidal RVE (shown in Fig. 1a). The latter is an implicit function of f and w.

$$e_1^2 = \begin{cases} 1-\dfrac{1}{w^2} & \text{(p)} \\ 1-w^2 & \text{(o)} \end{cases}, \qquad \frac{(1-e_2^2)^n}{e_2^3} = \frac{1}{f}\frac{(1-e_1^2)^n}{e_1^3}, \qquad n = \begin{cases} 1 & \text{(p)} \\ 1/2 & \text{(o)} \end{cases} \tag{A-2}$$

In addition,

$$\kappa = \begin{cases} \dfrac{3}{h}\left\{1+\dfrac{h_t}{h^2\ln f}\ln\dfrac{1-e_2^2}{1-e_1^2}\right\}^{-1/2} & \text{(p)} \\ \dfrac{3}{h}\left\{1+\dfrac{(g_f-g_1)+\frac{4}{5}(g_f^{5/2}-g_1^{5/2})-\frac{3}{5}(g_f^5-g_1^5)}{\ln\frac{g_f}{g_1}}\right\}^{-1} & \text{(o)} \end{cases} \tag{A-3}$$

where

$$g_f \equiv \frac{g}{g+f}, \quad g_1 \equiv \frac{g}{g+1} \tag{A-4}$$

Next,

$$\alpha_2 = \begin{cases} \dfrac{(1+e_2^2)}{(1+e_2^2)^2+2(1-e_2^2)} & \text{(p)} \\ \dfrac{(1-e_2^2)(1-2e_2^2)}{(1-2e_2^2)^2+2(1-e_2^2)} & \text{(o)} \end{cases} \tag{A-5}$$

$$\begin{aligned} \eta &= -\frac{2}{3h_q}\frac{\kappa Q^*(g+1)(g+f)\text{sh}}{(g+1)^2+(g+f)^2+(g+1)(g+f)[\kappa H^*\text{sh}-2\text{ch}]}, \\ C &= -\frac{2}{3}\frac{\kappa(g+1)(g+f)\text{sh}}{(Q^*+\frac{3}{2}h_q\eta H^*)\eta}, \quad \text{sh} \equiv \sinh(\kappa H^*), \quad \text{ch} \equiv \cosh(\kappa H^*) \end{aligned} \tag{A-6}$$

where $H^* \equiv 2\sqrt{h_q}(\alpha_1-\alpha_2)$, $Q^* \equiv \sqrt{h_q}(1-f)$ and h_q is 1 for an isotropic matrix (see [27] for h_q corresponding to anisotropic matrices). α_1 is itself given by

$$\alpha_1 = \begin{cases} \left[e_1-(1-e_1^2)\tanh^{-1}e_1\right]/(2e_1^3) & \text{(p)} \\ \left[-e_1(1-e_1^2)+\sqrt{1-e_1^2}\sin^{-1}e_1\right]/(2e_1^3) & \text{(o)} \end{cases} \tag{A-7}$$

Note that α_2 and α_1 are identical to those introduced in [24] for isotropic materials. Finally:

$$\alpha_1^{\text{Gar}} = \begin{cases} \dfrac{1}{3-e_1^2} & \text{(p)} \\ \dfrac{1-e_1^2}{3-2e_1^2} & \text{(o)} \end{cases} \tag{A-8}$$

Appendix B Rationale for Eq. (9)

In order to establish the results of Eq.(9), consider the second order tensor

$$\mathbf{A} = \mathbf{n} \otimes \mathbf{n} \tag{A-9}$$

where $\mathbf{n}$ is the void orientation vector. For the random distribution of void orientations in Fig. 1b, it is straightforward to show that

$$\langle \mathbf{A} \rangle = \frac{1}{3}\mathbf{I} \tag{A-10}$$

Considering ensemble averages of the tensors $\mathbf{X}$ and $\mathbf{Q}$ over all void orientations, and using the above result in (3), we have

$$\langle \mathbf{X} \rangle = \frac{1}{3}\mathbf{I}, \qquad \langle \mathbf{Q} \rangle = \mathbf{0} \tag{A-11}$$

Hence, the term $\mathbf{\Sigma} : \langle \mathbf{X} \rangle$ reduced to the mean macroscopic stress Σ_{m}.

Next, consider the orientation average of the tensor $\mathbb{H}$ in Eq.(2)

$$\langle \mathbb{H} \rangle = \mathbb{J} + \eta \langle \mathbf{X} \otimes \mathbf{Q} + \mathbf{Q} \otimes \mathbf{X} \rangle \tag{A-12}$$

Using the second order tensor $\mathbf{A}$ defined in (A-9) and the results of Eq.(A-11), the second term in the above equation evaluates to

$$\langle \mathbf{X} \otimes \mathbf{Q} + \mathbf{Q} \otimes \mathbf{X} \rangle = (1 - 3\alpha_2) \left[3\langle \mathbf{A} \otimes \mathbf{A} \rangle - \frac{1}{3}\mathbf{I} \otimes \mathbf{I} \right] \tag{A-13}$$

It can be shown that the fourth order tensor $\langle \mathbf{A} \otimes \mathbf{A} \rangle$ evaluates to

$$\langle \mathbf{A} \otimes \mathbf{A} \rangle = \frac{2}{15}\mathbb{J} + \frac{1}{9}\mathbf{I} \otimes \mathbf{I} \tag{A-14}$$

Substituting (A-13) and (A-14) in (A-12) leads to the final result $(9)_2$.

Appendix C Comparison of Localization Mechanisms

The appendix reveals the effect of the induced localization mechanism, either internal necking or combined internal necking and shearing. The former always predicts much larger stresses at the yield instance. On the other hand, the effective yield surface is mostly coincident with that resulting from combined necking-shearing. Figure A-1 depicts the influence of χ and w on the yield surface projection onto the π plane.

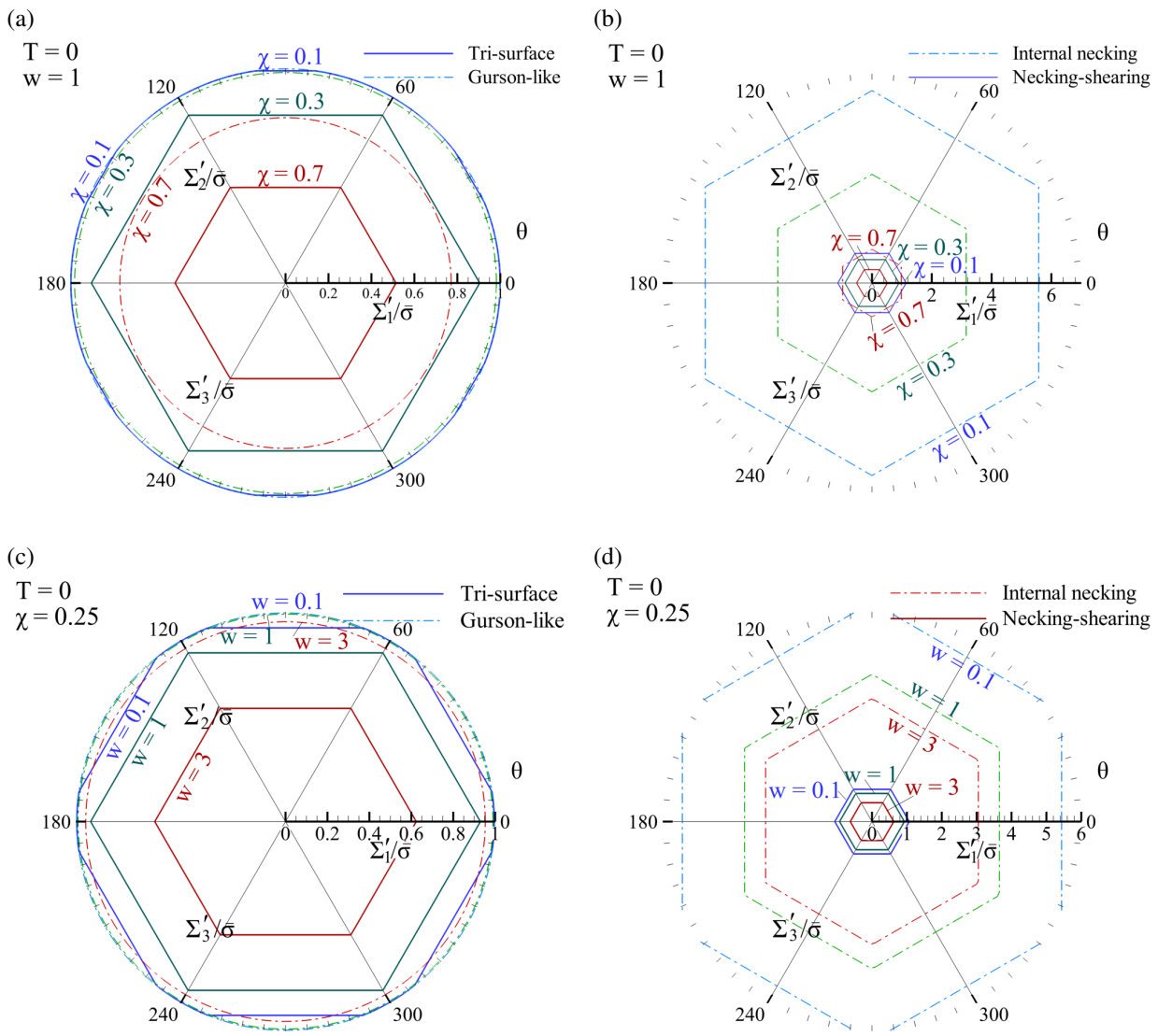

Figure A-1: (a,b) Effect of the ligament parameter χ, (c,d) effect of the void aspect ratio w, on the yield surface projection induced by internal necking or combined necking-shearing onto the deviatoric plane with $T = 0$, *i.e.* π plane.

Next, Fig. A-2 depicts the influence of χ on the yield surface projection onto the meridian planes with constant Lode parameters $L = (\pm 1, 0)$.

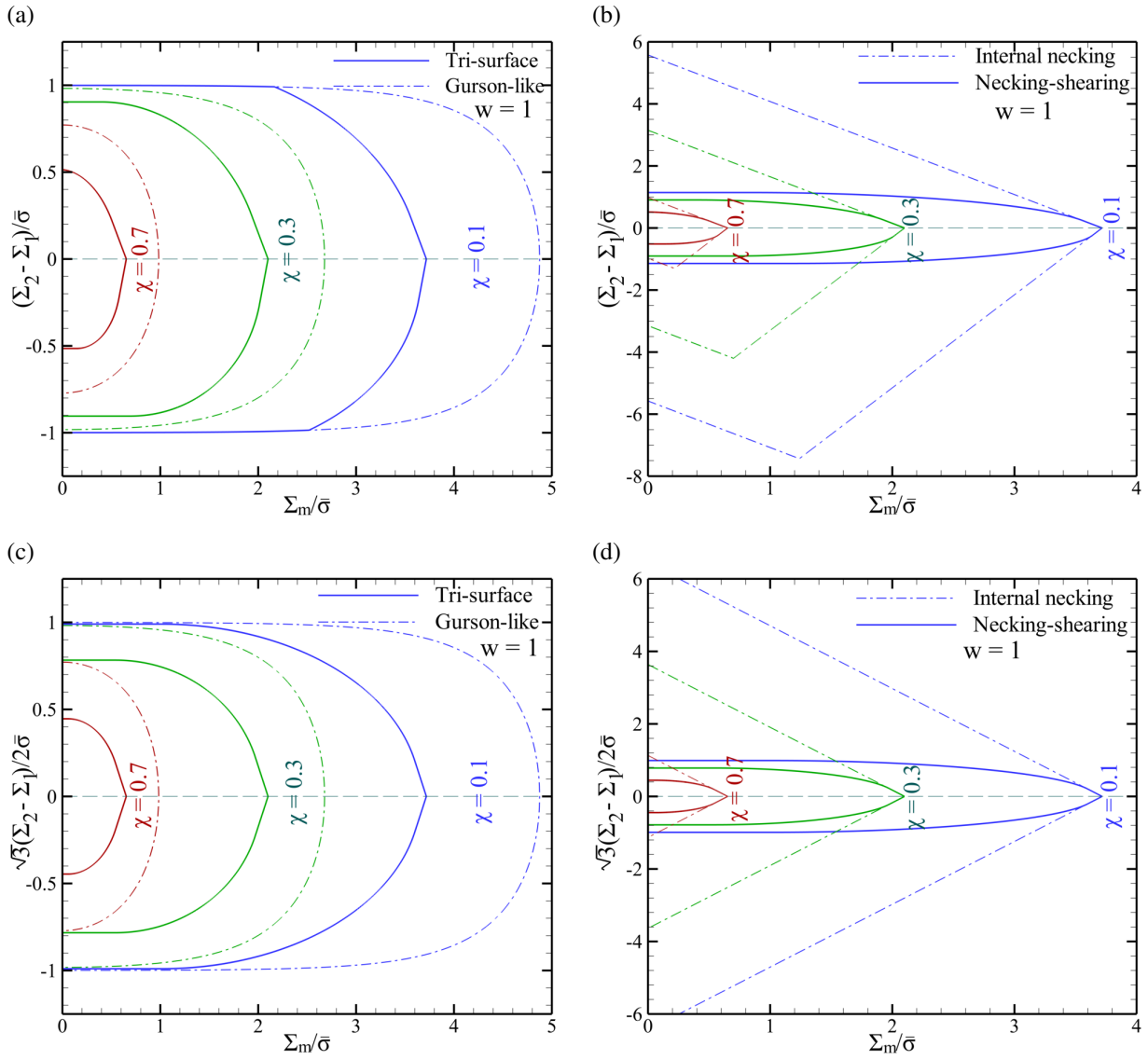

Figure A-2: Effect of the ligament parameter χ on the yield surface projection induced by internal necking or combined necking-shearing onto the meridian planes: (a,b) $L = \pm 1$, (c,d) $L = 0$.

Figure A-3 depicts the same type of influence induced by w.

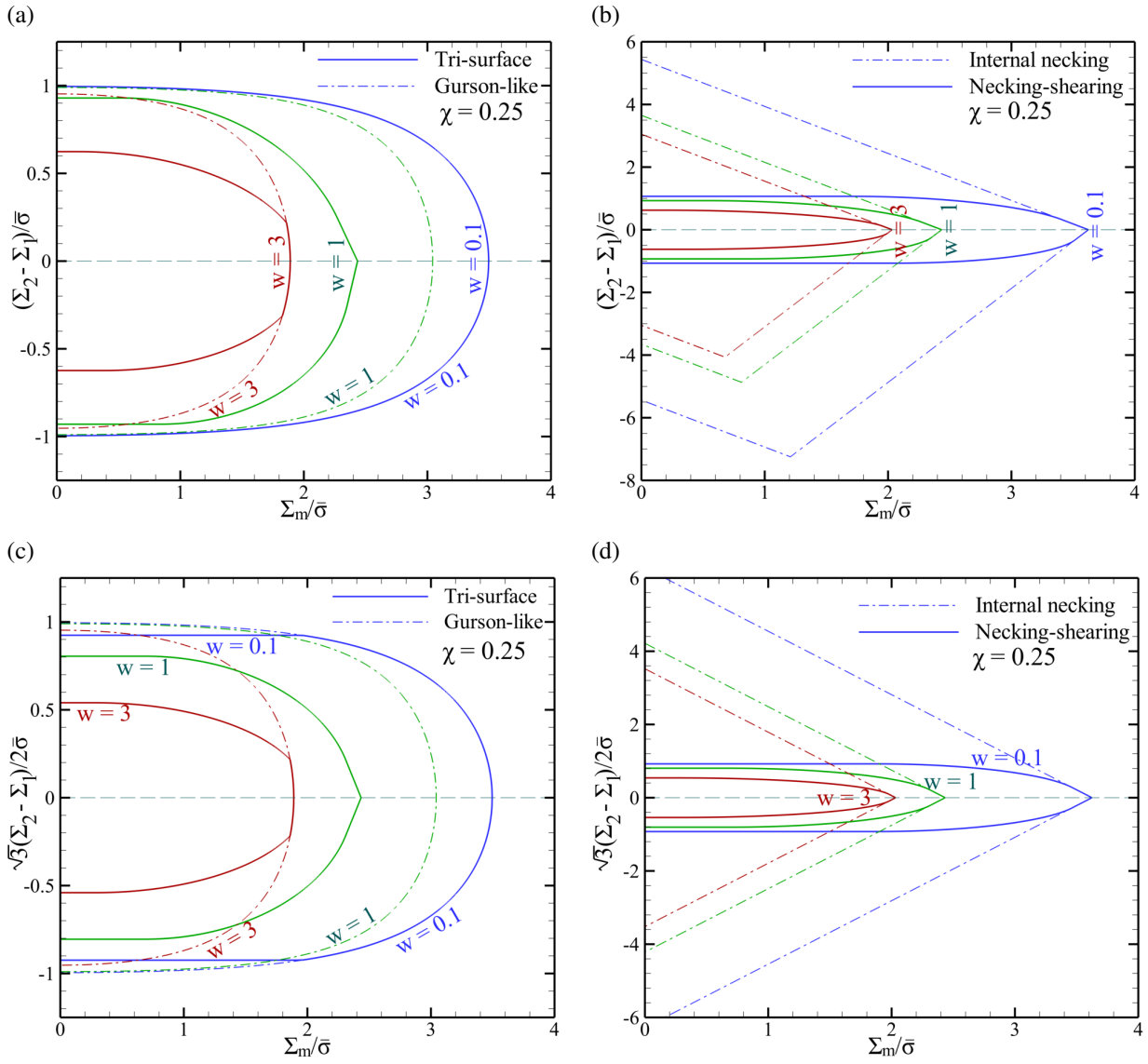

Figure A-3: Effect of the void aspect ratio w on the yield surface projection induced by internal necking or combined necking-shearing onto the meridian planes: (a,b) $L = \pm 1$, (c,d) $L = 0$.

References

[1] A. Pineau, A. A. Benzerga, and T. Pardoen. Failure of metals I. Brittle and Ductile Fracture. *Acta Materialia*, 107:424–483, 2016.

[2] C. F. Tipper. The fracture of metals. *Metallurgia*, 39:133–137, 1949.

[3] J. Gurland and J. Plateau. The mechanism of ductile rupture of metals containing inclusions. *Trans. Quartely of ASM*, 56:442–454, 1963.

[4] J. W. Rudnicki and J. R. Rice. Conditions for the localization of deformation in pressure–sensitive dilatant materials. *Journal of the Mechanics and Physics of Solids*, 23:371–394, 1975.

[5] J.R. Rice. The localization of plastic deformation. In W.T. Koiter, editor, *14th int. cong. Theoretical and Applied Mechanics*, pages 207–220. North–Holland, Amsterdam, 1976.

[6] J. W. Hancock and A. C. MacKenzie. On the mechanisms of ductile failure in high–strength steels subjected to multi–axial stress states. *Journal of the Mechanics and Physics of Solids*, 24:147–169, 1976.

[7] J. W. Hancock and D. K. Brown. On the role of strain and stress state in ductile failure. *Journal of the Mechanics and Physics of Solids*, 31:1–24, 1983.

[8] J. R. Rice and D. M. Tracey. On the enlargement of voids in triaxial stress fields. *Journal of the Mechanics and Physics of Solids*, 17:201–217, 1969.

[9] J. Koplik and A. Needleman. Void growth and coalescence in porous plastic solids. *International Journal of Solids and Structures*, 24(8):835–853, 1988.

[10] G. R. Johnson and W. H. Cook. Fracture characteristics of three metals subjected to various strains, strain rates, temperatures and pressures. *Engineering Fracture Mechanics*, 21:31–48, 1985.

[11] A. L. Gurson. Continuum Theory of Ductile Rupture by Void Nucleation and Growth: Part I– Yield Criteria and Flow Rules for Porous Ductile Media. *Journal of Engineering Materials and Technology*, 99:2–15, 1977.

[12] V. Tvergaard and A. Needleman. Analysis of the cup–cone fracture in a round tensile bar. *Acta Metallurgica*, 32:157–169, 1984.

[13] Y. Bao and T. Wierzbicki. On fracture locus in the equivalent strain and stress triaxiality space. *International Journal of Mechanical Sciences*, 46:81–98, 2004.

[14] I. Barsoum and J. Faleskog. Rupture mechanisms in combined tension and shear—-Experiments. *International Journal of Solids and Structures*, 44:1768–1786, 2007.

[15] S.S. Haltom, S. Kyriakides, and K. Ravi-Chandar. Ductile failure under combined shear and tension. *International Journal of Solids and Structures*, 50:1507–1522, 2013.

[16] V. Tvergaard. On localization in ductile materials containing spherical voids. *International Journal of Fracture*, 18:237–252, 1982.

[17] V. Tvergaard. Behaviour of voids in a shear field. *International Journal of Fracture*, 158:41–49, 2009.

[18] I. Barsoum and J. Faleskog. Micromechanical analysis on the influence of the Lode parameter on void growth and coalescence. *International Journal of Solids and Structures*, 48:925–938, 2011.

[19] K. L. Nielsen, J. Dahl, and V. Tvergaard. Collapse and coalescence of spherical voids subject to intense shearing: studied in full 3D. *International Journal of Fracture*, 177:97–108, 2012.

[20] C. Tekoğlu, J.-B. Leblond, and T. Pardoen. A criterion for the onset of void coalescence under combined tension and shear. *Journal of the Mechanics and Physics of Solids*, 60:1363–1381, 2012.

[21] M. Dunand and D. Mohr. Effect of Lode parameter on plastic flow localization after proportional loading at low stress triaxialities. *Journal of the Mechanics and Physics of Solids*, 66:133–153, 2014.

[22] C. Tekoglu. Void coalescence in ductile solids containing two populations of voids. *Engineering Fracture Mechanics*, 147:418–430, 2015.

[23] M. Gologanu, J.-B. Leblond, and J. Devaux. Approximate models for ductile metals containing non-spherical voids – case of axisymmetric prolate ellipsoidal cavities. *Journal of the Mechanics and Physics of Solids*, 41(11):1723–1754, 1993.

[24] M. Gologanu, J.-B. Leblond, G. Perrin, and J. Devaux. Recent extensions of Gurson's model for porous ductile metals. In P. Suquet, editor, *Continuum Micromechanics, CISM Lectures Series*, pages 61–130. Springer, New York, 1997.

[25] P. Ponte Castañeda and M. Zaidman. Constitutive models for porous materials with evolving microstructure. *Journal of the Mechanics and Physics of Solids*, 42:1459–1495, 1994.

[26] K. Danas and P. Ponte Castañeda. A finite-strain model for anisotropic viscoplastic porous media: I–Theory. *European Journal of Mechanics*, 28:387–401, 2009.

[27] S. M. Keralavarma and A. A. Benzerga. A constitutive model for plastically anisotropic solids with non-spherical voids. *Journal of the Mechanics and Physics of Solids*, 58:874–901, 2010.

[28] K. Madou and J.-B. Leblond. A Gurson-type criterion for porous ductile solids containing arbitrary ellipsoidal voids – I: Limit-analysis of some representative cell. *Journal of the Mechanics and Physics of Solids*, 60:1020–1036, 2012.

[29] K. Madou and J.-B. Leblond. A Gurson-type criterion for porous ductile solids containing arbitrary ellipsoidal voids – II: Determination of yield criterion parameters. *Journal of the Mechanics and Physics of Solids*, 60:1037–1058, 2012.

[30] A. A. Benzerga and J.-B. Leblond. Effective Yield Criterion Accounting for Microvoid Coalescence. *Journal of Applied Mechanics*, 81:031009, 2014.

[31] M. E. Torki, A. A. Benzerga, and J.-B. Leblond. On Void Coalescence under Combined Tension and Shear. *Journal of Applied Mechanics*, 82(7):071005, 2015.

[32] S. M. Keralavarma and S. Chockalingam. A Criterion for Void Coalescence in Anisotropic Ductile Materials. *International Journal of Plasticity*, 82:159–176, 2016.

[33] P. F. Thomason. Three–dimensional models for the plastic limit–loads at incipient failure of the inter-void matrix in ductile porous solids. *Acta Metallurgica*, 33:1079–1085, 1985.

[34] ME Torki, C. Tekoglu, J-B Leblond, and AA Benzerga. Theoretical and numerical analysis of void coalescence in porous ductile solids under arbitrary loadings. *International Journal of Plasticity*, 91:160–181, 2017.

[35] Jean-Baptiste Leblond and Mihai Gologanu. External estimate of the yield surface of an arbitrary ellipsoid containing a confocal void. *Comptes Rendus Mecanique*, 336:813–819, 2008.

[36] R. Hill. A theory of yielding and plastic flow of anisotropic solids. *Proceedings of the Royal Society of London A*, 193:281–297, 1948.

[37] A. A. Benzerga and J.-B. Leblond. Ductile fracture by void growth to coalescence. *Advances in Applied Mechanics*, 44:169–305, 2010.

[38] A. A. Benzerga. Micromechanics of Coalescence in Ductile Fracture. *Journal of the Mechanics and Physics of Solids*, 50:1331–1362, 2002.

[39] F. Scheyvaerts, P. R. Onck, C. Tekoğlu, and T. Pardoen. The growth and coalescence of ellipsoidal voids in plane strain under combined shear and tension. *Journal of the Mechanics and Physics of Solids*, 59:373–397, 2011.

[40] S. M. Keralavarma. A multi-surface plasticity model for ductile fracture simulations. *Journal of the Mechanics and Physics of Solids*, 103:100–120, 2017.

[41] M. Gologanu, J.-B. Leblond, and J. Devaux. Approximate Models for Ductile Metals Containing Non–spherical Voids — Case of Axisymmetric Oblate Ellipsoidal Cavities. *Journal of Engineering Materials and Technology*, 116:290–297, 1994.

[42] R. Hill. The essential structure of constitutive laws for metal composites and polycrystals. *Journal of the Mechanics and Physics of Solids*, 15:79–95, 1967.

[43] J. Mandel. Contribution théorique à l'étude de l'écrouissage et des lois d'écoulement plastique. In 11^{th} *International Congress on Applied Mechanics*, pages 502–509. Springer, Berlin, 1964.

[44] L. Morin, J.-B. Leblond, and A. A. Benzerga. Coalescence of voids by internal necking: theoretical estimates and numerical results. *Journal of the Mechanics and Physics of Solids*, 75:140–158, 2015.

[45] K. Kuna and D. Z. Sun. Three-dimensional cell model analyses of void growth in ductile materials. *International Journal of Fracture*, 81:235–258, 1996.

[46] T. Pardoen and J. W. Hutchinson. An extended model for void growth and coalescence. *Journal of the Mechanics and Physics of Solids*, 48:2467–2512, 2000.

[47] JW. Ju and LZ. Sun. Effective elastoplastic behavior of metal matrix composites containing randomly located aligned spheroidal inhomogeneities. part i: micromechanics-based formulation. *International Journal of Solids and Structures*, 38(2):183–201, 2001.

[48] LZ. Sun and JW. Ju. Effective elastoplastic behavior of metal matrix composites containing randomly located aligned spheroidal inhomogeneities. part ii: applications. *International Journal of Solids and Structures*, 38(2):203–225, 2001.

[49] M. Gologanu, J.-B. Leblond, G. Perrin, and J. Devaux. Theoretical models for void coalescence in porous ductile solids – II: Coalescence in "columns". *International Journal of Solids and Structures*, 38:5595–5604, 2001.

P5 A MECHANISM OF FAILURE IN SHEAR BANDS

A Mechanism of Failure in Shear Bands

M. E. Torki[1], A. A. Benzerga[1,2,3]

[1] *Department of Aerospace Engineering, Texas A&M University, College Station, TX 77843, USA*

[2] *Center for intelligent Multifunctional Materials and Structures, TEES, College Station, TX 77843, USA*

[3] *Department of Materials Science and Engineering, Texas A&M University, College Station, TX 77843, USA*

Abstract

We have carried out dilatant plasticity simulations to investigate the process of void-mediated failure inside a shear band. The constitutive model accounts for possibly inhomogeneous flow within the band, void rotation and void elongation. We found that the material in the band may soften with no increase in the void volume fraction. For a given matrix hardening capacity, the rate of softening was found to depend strongly on the ratio of shear band width to in-plane void spacing. The emergent softening led to complete loss of load bearing capacity thereby providing a physical mechanism of failure in shear bands. The mechanism is consistent with essential features of shear-fractured specimens in terms of surface roughness, porosity and dimple shape.

1 Introduction

Failure by shear banding is ubiquitous and occurs in complex fluids [1], granular materials [2, 3], rocks [4] polycrystals [5, 6], polymers [7] and metallic glasses [8, 9]. However, mechanisms of material separation inside shear bands have remained elusive. Elucidating a possible mechanism will not only potentially retard shear fractures, if desired, but also impact other applications where failure occurs under shear dominated loadings, as would arise metalworking, ballistic penetration, etc. The stress state in shear bands is generally complex depending on the loading path prior to the onset of strain localization [10]. Correspondingly, shear bands are generally dilational. While arbitrarily large tension-to-shear ratios may be encountered inside shear bands, here we focus on situations of vanishingly small tension-to-shear ratios and aim to present a physical model of complete material separation.

Voids are the main defects mediating ductile fracture [11, 12]. The plastic enlargement of these defects dominates at moderate to high ratios of tension-to-shear stress (tension-dominated loading), Fig. 1a. Voids are also believed to play an important role at low tension-to-shear ratios (shear-dominated loading), Fig. 1b. However, a specific mechanism by which failure occurs is still lacking. Void nucleation is material specific and will not be addressed here.

Well-established micromechanical models of void growth and coalescence [13, 14] predict infinite ductility under shear loading. This is due to two idealizations: (i) that the void volume fraction, f, is the sole internal parameter representing the defects; and (ii) that void coalescence occurs upon attainment of a critical value of f. Since the rate of growth of f is completely determined by the dilational part of the macroscopic plastic strain rate, which is nil in shear, no growth is predicted, hence no failure. An attempt to remedy this consists of amending the void growth law with a shear-dependent term [15]. This proposal is attractive but presents two shortcomings. Not only does it violate the principle of mass conservation underlying the void growth law but it also presumes that a void-growth-like behavior is required for failure in shear. On the other

hand, a much earlier mechanism-based model limited to isolated voids [16] did highlight the essential role of void rotation and possible linkage of neighboring voids by mere impingement.

More recent direct numerical simulations [17, 18, 19] revealed the existence of a maximum in the shear load response and exhibited three essential microscopic features: (i) void-induced strain localization at the sub-cell level; (ii) void rotation; and (iii) void elongation in the rotated state. However, such calculations are extremely challenging, and thus cannot be pursued much beyond the maximum load. Furthermore, they are not scalable so that a coarse-grained continuum model that mimics the behavior gleaned from these simulations is lacking [20].

Quite recently, Morin et al. [21] proposed mechanism-based modeling of failure under shear-dominated loadings. Their model accounts for void rotation and void shape change, but fails to account for the void-induced strain localization that may occur from the outset in shear. It also employs an *ad hoc* coalescence criterion, reminiscent of the critical void volume criterion used in conjunction with the Gurson model [14]. In this Letter, we present a parameter-free model of failure under shear-dominated loading, which accounts for sub-cell strain localization, void rotation and void shape change. We lay emphasis on qualitative aspects of the phenomenon and discuss the model's capabilities to simulate complete loss of stress carrying capacity in shear.

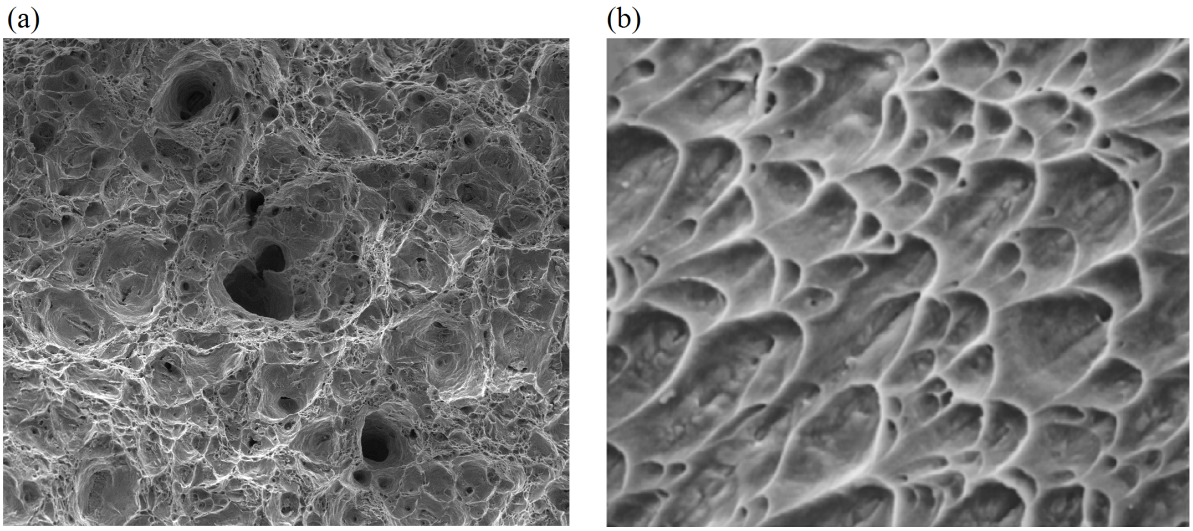

Figure 1: Typical fracture surfaces of metals failing in (a) tension, and (b) shear [12].

2 Formulation

When voids are at the micron scale and above, void-mediated fracture in the shear band may be described by continuum mechanics. The shear band is assumed to be acted upon by a shear stress, τ, and a normal tensile stress, σ, Fig. 2a. Voids are assumed to have nucleated, in some way, inside the band. A regular doubly-periodic array of voids is assumed for simplicity so that analysis of a single tetragonal cell, Fig. 2b, is sufficient. The aspect ratio of the cell, $\lambda \equiv H/L$, represents the current ratio of shear band thickness to in-plane void spacing. Other cell parameters include the void volume fraction, f, the void aspect ratio, $w \equiv a/R$, along with two unit vectors: $\mathbf{n}^{(3)}$ for the orientation of the void, modeled as a spheroid when it deforms, Fig. 2c, and $\mathbf{n}$ for the orientation of the localization plane, Fig. 3. Multiple possibilities for $\mathbf{n}$ may be chosen depending on the underlying spatial arrangement of voids. Here, only one such orientation

is considered, which is normal to the shear band. Initial values of all internal parameters are indicated with subscript 0.

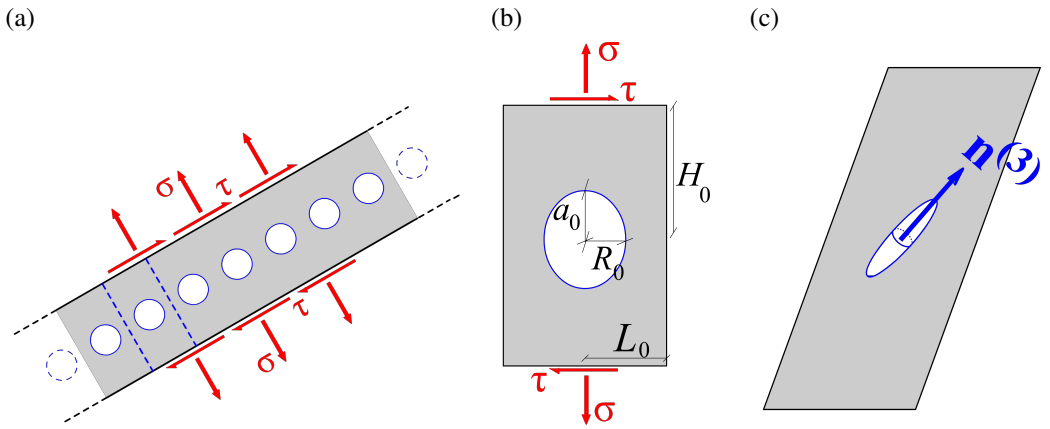

Figure 2: Problem formulation: (a) doubly periodic row of voids inside the shear band; (b) geometry of undeformed elementary cell; (c) homogeneous deformation of the cell involving void rotation.

To investigate failure in shear, we carried out numerical simulations using a continuum micromechanics framework for dilatant plasticity that captures the essential features of sub-cell deformation sketched in Fig. 3. Contrary to the direct numerical simulations in [17, 18, 19], we do not model the void explicitly,

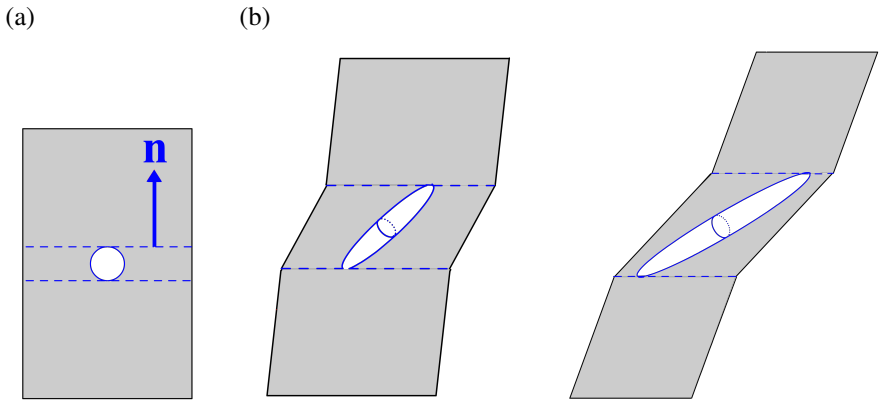

Figure 3: Essential features captured by the coarse-grained model: (a) void-induced strain localization; (b) void rotation; (c) void elongation.

but through the coarse-grained model. The effective elasticity domain is represented by the intersection of two convex domains. Its boundary is therefore determined by the intersection of two surfaces in stress space $\Phi^{\mathrm{H}}(\boldsymbol{\sigma}; f, w, \mathbf{n}^{(3)}) = 0$ and $\Phi^{\mathrm{I}}(\boldsymbol{\sigma}; f, w, \lambda, \mathbf{n}^{(3)}, \mathbf{n}) = 0$ where yield functions Φ^{H} and Φ^{I} correspond to homogeneous (Fig. 2c) and inhomogeneous (Fig. 3b) deformation of the cell, respectively. The plastic portion of the symmetric part of the velocity gradient, $\nabla\mathbf{v} \equiv \mathbf{L}$, is obtained by normality to the effective yield surface. For generally tensile stress states $\boldsymbol{\sigma}$, there is competition between the two yielding mechanisms [22, 23] with $\Phi^{\mathrm{H}} = 0$ prevailing in the early stages of any triaxial stressing process. For combined tension and shear, as in Fig. 2b, it is the σ/τ ratio that determines which yielding mechanism would dominate. Yield functions derived from first principles of micromechanics are used for Φ^{H} [24] and Φ^{I} [25, 26]. Evolution equations for the internal parameters in Φ^{H} were derived in [24]; also see [27] for computational details.

For sufficiently low σ/τ (shear-dominated loading) inhomogeneous yielding dominates from the outset so that all subsequent deformation history is governed by Φ^{I}. Details about the two-surface formulation may be found as Supplemental Material. Here, it suffices to exhibit the governing equations for inhomogeneous yielding:

$$\Phi^{\mathrm{I}} = \begin{cases} \left(\dfrac{|\sigma| - \mathcal{S}(\bar{\chi},\bar{w})}{\mathcal{V}(\bar{\chi})}\right)^2 + \dfrac{\tau^2}{(1-\bar{\chi}^2)\bar{\tau}^2} - 1 & \text{for } |\sigma| \geq \mathcal{S} \\ \dfrac{\tau^2}{(1-\bar{\chi}^2)\bar{\tau}^2} - 1 & \text{for } |\sigma| \leq \mathcal{S} \end{cases} \tag{1}$$

with

$$\mathcal{V}/\bar{\tau} = 2 - \sqrt{1+3\bar{\chi}^4} + \ln\frac{1+\sqrt{1+3\bar{\chi}^4}}{3\bar{\chi}^2} \tag{2}$$

$$\mathcal{S}/\bar{\tau} = \frac{\bar{\chi}^3 - 3\bar{\chi} + 2}{3\bar{\chi}\bar{w}} \tag{3}$$

where the effective ligament parameter, $\bar{\chi}$, and effective void aspect ratio, $\bar{w}$, correspond to an equivalent cylindrical void with axis $\mathbf{n}$, obtained by a volume-preserving projection of the rotating spheroidal void onto the localization plane. The exact shape, spheroidal versus cylindrical, has little incidence on yielding [28]. However, since equations (1) were derived for cylindrical voids [26], this choice is made here (see Supplemental Material). Also, $\bar{\tau}$ is the flow stress in shear of the material without voids, taken as a power law in the effective plastic strain $\bar{\tau} = \tau_0(1 + E\bar{\gamma}/3\tau_0)^N$ with τ_0 the initial yield strength, E Young's modulus, and N the hardening exponent. Implicit dependence upon the void axis $\mathbf{n}^{(3)}$ in (1) is through w and dependence upon the localization plane normal is through $\bar{\chi}$, $\bar{w}$ as well as $\sigma = \mathbf{n}\cdot\boldsymbol{\sigma}\mathbf{n}$ and $\tau = \mathbf{m}\cdot\boldsymbol{\sigma}\mathbf{n}$ with $\mathbf{m}$ a unit vector along the applied shear.

Upon continued plastic loading, the structure evolves according to (with $C = \mathbf{n}^{(3)}\cdot\mathbf{n}$, $S = \mathbf{n}^{(3)}\cdot\mathbf{m}$ and $c^3 = C^3(fw^2)/\lambda^2$):

$$\dot{f} = (1-f)D^{\mathrm{p}}_{kk} = (1-f)\Lambda\frac{\partial\Phi^{\mathrm{I}}}{\partial\sigma} \tag{4}$$

$$\frac{\dot{w}}{w} = \frac{1}{2}\left(\frac{3C^2}{c} - \frac{1}{f}\right)\mathbf{n}\cdot\mathbf{D}^{\mathrm{p}}\mathbf{n} + \frac{3CS}{c}\mathbf{m}\cdot\mathbf{D}^{\mathrm{p}}\mathbf{n} \tag{5}$$

$$\dot{\mathbf{n}}^{(3)} = (\boldsymbol{\Omega}^v + \boldsymbol{\Omega}^l)\mathbf{n}^{(3)} \tag{6}$$

$$\boldsymbol{\Omega}^l = \left(\frac{\dot{c}}{c} - \frac{1}{3}\left[\frac{\dot{f}}{f} + 2\left(\frac{\dot{w}}{w} - \frac{\dot{\lambda}}{\lambda}\right)\right]\right) \left(\mathbf{n}\otimes\mathbf{n} - \frac{C^2}{S^2}\mathbf{m}\otimes\mathbf{m}\right) \tag{7}$$

$$\dot{c} = (1-c)D_{33} \tag{8}$$

$$\frac{\lambda}{\lambda_0} = \frac{1}{\sqrt{\mathcal{J}}}\left(\mathbf{n}\cdot\mathbf{F}\mathbf{F}^T\mathbf{n}\right)^{\frac{3}{4}} \tag{9}$$

$$\mathbf{n} = \frac{\mathbf{F}^{-\mathrm{T}}\mathbf{n}_{(0)}}{|\mathbf{F}^{-\mathrm{T}}\mathbf{n}_{(0)}|} \tag{10}$$

Eqn. (4) expresses plastic incompressibility of the matrix [13] and Eqns. (5) and (6) are for the constrained motion of the top and bottom void boundaries due to elastic unloading above and below the void (see Supplemental Material for derivations.) Also, Λ in (4) is the plastic multiplier, $\mathbf{D}^{\mathrm{p}} \equiv \mathrm{sym}\mathbf{L}^{\mathrm{p}}$, $\mathbf{\Omega}^{v}$ in (6) represents the deviation from the continuum spin due to the eigen-rotation of the void, calculated using Eshelby concentration tensors [29] after [30, 27], $\mathbf{\Omega}^{l}$ is the shear-induced rotation that comes from mere distortion of void boundaries (dominant here), and $\mathbf{F}$ is the deformation gradient used to update the band orientation $\mathbf{n}$. Relations (5)–(8) are straightfroward generalizations of the evolution equations of Benzerga [22] in the absence of shear, whereas (9) is taken from [31]. The effective plastic strain is evolved using Gurson's identity:

$$\boldsymbol{\sigma} : \mathbf{L}^{\mathrm{p}} = (1 - f)\bar{\tau}\dot{\bar{\gamma}} \tag{11}$$

The above plastic relations were augmented with hypoelasticity within an objective co-rotational finite deformation framework. The nonlinear constitutive relations were integrated using an implicit time integration scheme similar to [27].

3 Results

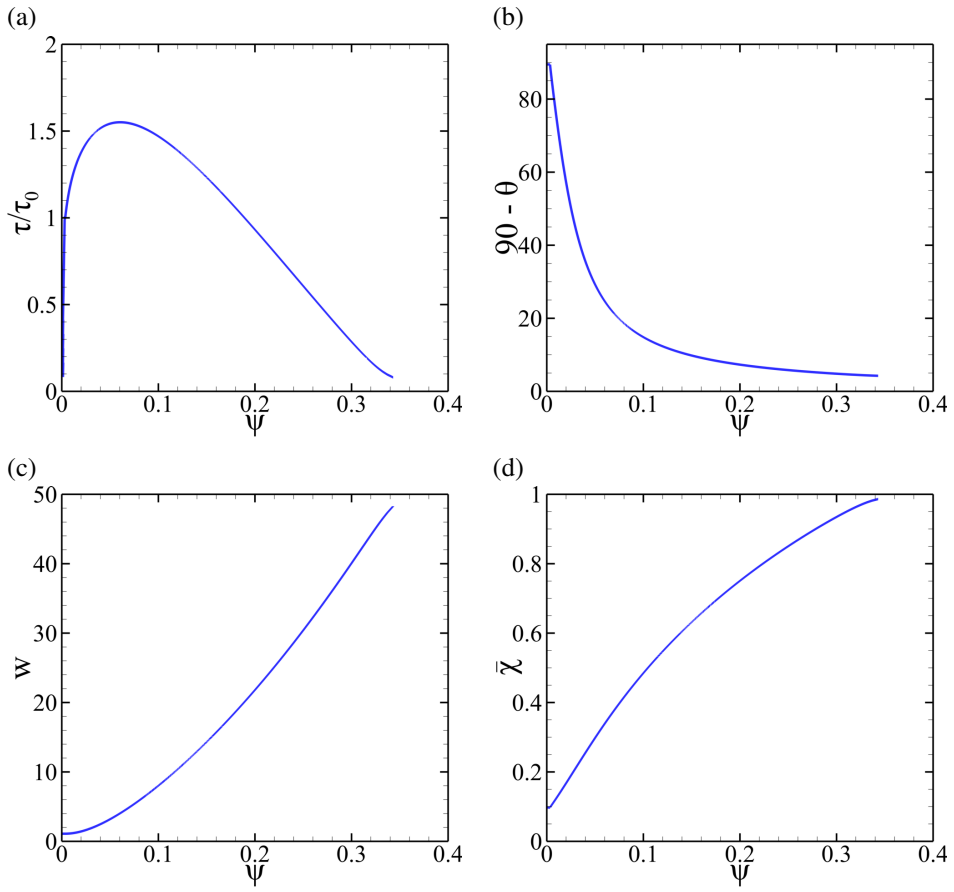

Figure 4: Typical results for vanishingly small tension-to-shear ratio, σ/τ. Against the shear angle, ψ, are plotted the (a) shear stress, τ, in units of τ_0; (b) void orientation, $\frac{\pi}{2} - \theta$ (°), measured from $\mathbf{n}$; (c) void aspect ratio, w; and (d) effective ligament parameter, $\bar{\chi}$. Simulation parameters are: $f_0 = 0.0005$, $w_0 = 1.1$, $\lambda_0 = 2$, $N = 0.2$, $\sqrt{3}\tau_0/E = 0.002$.

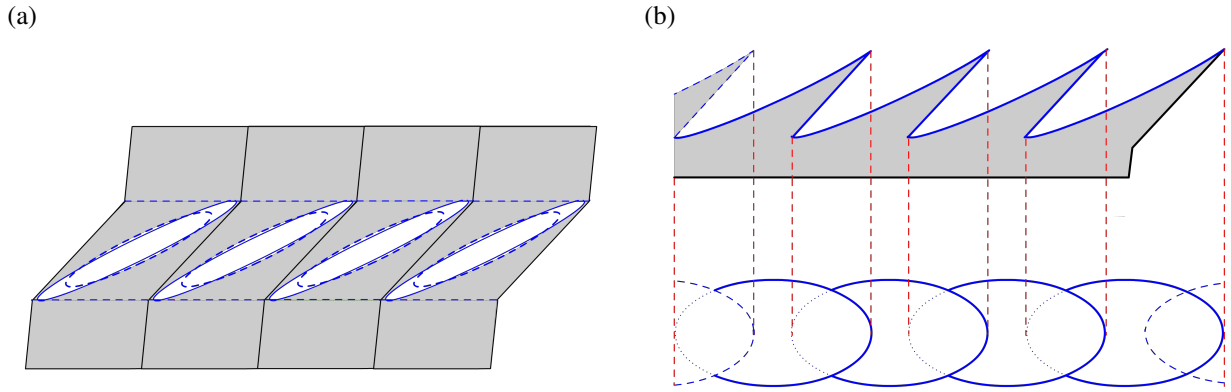

Figure 5: Predicted failure mechanism in shear and its connection to the fracture surface of Fig. 1b: (a) few neighboring cells near the ultimate state $\bar{\chi} = 1$; (b) side and top views of cut-out from (a) after material separation.

When failure is predicted, the typical shear stress versus shear angle response, Fig. 4a, results from competing effects of matrix hardening (set by N) and microstructural softening induced by void rotation, Fig. 4b, and elongation in the rotated state, Fig. 4c. The angle θ is such that $\cos\theta = \mathbf{n}^{(3)} \cdot \mathbf{n}$. As a result, the area of the void projected onto the plane of localization increases monotonically, as captured through the effective ligament parameter, $\bar{\chi}$, Fig. 4d. When $\bar{\chi}$ approaches unity all stress carrying capacity vanishes by virtue of (1). This occurs while the void volume fraction f remains constant (not shown). In actuality, some decrease in f is expected. To capture this detail would require a three-dimensional void model [21] and would have little effect on essential behavior (see Supplemental Material for further details).

To link the above findings with salient features of sheared fracture surfaces, Fig. 1b, consider few neighboring cells at about the ultimate state $\bar{\chi} = 1$ (dashed in Fig. 5a). We assume that final linkup would occur by some finer-scale microshear process, Fig. 5b. Alternatively, one may invoke that actual void distributions are not periodic so that it is likely that when the elongated void reaches the lateral boundaries, it will link up with a neighboring void. Details aside, a top view of the so-simulated fracture surface, Fig. 5c, provides a rationale for three key experimental observations: (i) parabolic dimples; (ii) low surface roughness; and (iii) low local porosity, relative to tensile fracture surfaces, Fig. 1a. Both roughness and porosity are related to the dimple height, which is set by the amount of rotation prior to failure. In the example shown (Fig. 4b) the rotation is actually much more than depicted in Fig. 5.

At fixed hardening capacity of the matrix material and fixed void volume fraction f_0, the strain to failure is dependent upon the ratio λ_0 of initial band thickness to in-plane void spacing, Fig. 6a. The rotation of the void, Fig. 6b, and its aspect ratio (Fig. 6c) are also sensitive to λ_0. For fixed porosity of initially spherical voids ($w_0 \approx 1$), varying λ_0 amounts to varying $\bar{\chi}_0 = R_0/L_0$ (Fig. 6d), which has a direct effect on the strain to failure.

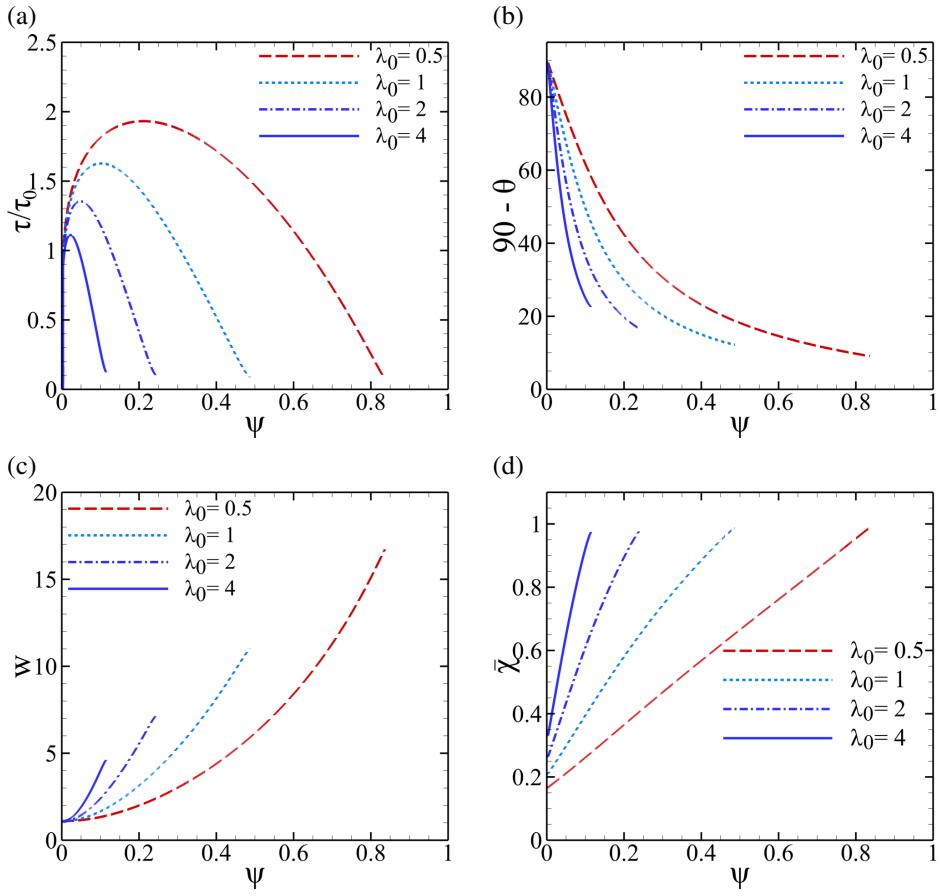

Figure 6: Effect of the ratio, λ_0, of shear-band width to in-plane void spacing for $f_0 = 0.01$, $w_0 = 1.1$, $N = 0.2$, $\sqrt{3}\tau_0/E = 0.002$.

To investigate this effect further, the initial ligament parameter $\bar{\chi}_0$ was varied over four decades, Fig. 7. The results illustrate three possible scenarios: (i) failure is predicted; (ii) weakening is predicted without

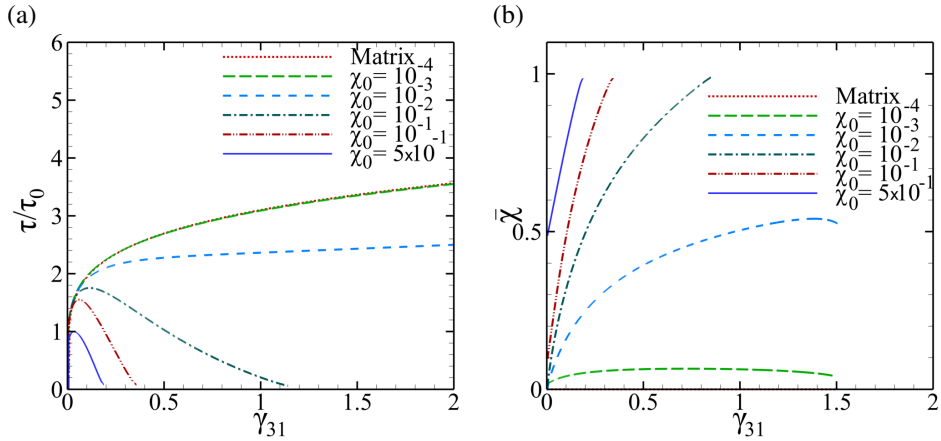

Figure 7: (a) Shear response and (b) evolution of ligament parameter for various values of the initial ligament parameter $\bar{\chi}_0 \equiv R_0/L_0$ using $w_0 = 1.1$, $\lambda_0 = 2$, $N = 0.2$, and $\sqrt{3}\tau_0/E = 0.002$.

failure; (iii) neither weakening nor failure are predicted.

Failure is predicted if the rotating void touches the cell boundaries (i.e. $\bar{\chi} \to 1$). This occurs for sufficiently large values of $\bar{\chi}_0$. Recall that $\bar{\chi}_0$ represents the initial size of voids that nucleate inside the shear band, relative to their in-plane spacing.

On the other hand, if the void is sufficiently small (the $\bar{\chi}_0 = 10^{-4}$ case in Fig. 7) the evolution of $\bar{\chi}$ exhibits a maximum after which it decreases, Fig. 7b. Physically, this situation corresponds to void closure in an asymptotic sense. Indeed, as the void takes on extremely elongated shapes (see e.g. Fig. 6c) the aspect ratio of the surrogate void vanishes ($\bar{w} \to 0$) as shown in Supplemental Material. We take this extreme "flattening" as an indication of void closure. The closed void, which is in the limit a microcrack, deforms as a material line so that if closure has occured before the void touches the cell boundaries, failure is not predicted. In this case, the effective flow stress of the material cannot be distinguished from that of the matrix, also shown in Fig. 7a, because $\bar{\chi} \ll 1$ at all stages.

An intermediate situation is when the void closes before it touches the boundaries, but now has a relatively large value of current effective void size to spacing ratio, i.e. $\bar{\chi} \sim 1$. For the set of simulation parameters used in Fig. 7, this scenario arises for $\bar{\chi}_0 = 10^{-3}$. In this case $\bar{\chi}$ reaches a maximum slightly above 0.5 (Fig. 7b) at a shear strain in excess of 2. Because the effective yield stress in shear scales with $1 - \bar{\chi}^2$ (see Eq. (1)) there is a noticeable reduction in the flow stress, hence weakening of the material, although failure is not predicted ($\bar{\chi}$ may not reach unity). The weakening effect predicted for $\bar{\chi}_0 = 10^{-3}$ is probably exaggerated and may be due to the idealization of the void shape used in deriving the post-localization evolution equations. It is, however, physically consistent with the $1 - \bar{\chi}^2$ scaling of the flow stress provided some evolution of the effective ligament parameter occurs in simple shear; see Supplemental Material for further elaboration.

4 Concluding remarks

The paper set out to elucidate one possible mechanism of failure under shear dominant-loading, as would prevail inside shear bands. The mechanism involves strain localization at the scale of individual voids, extreme void rotation and elongation. It provides a rationale for observed fracture surfaces in sheared specimens. When failure is predicted for sufficiently large initial void sizes relative to their spacing, a wide range of strains to complete loss of load bearing capacity emerge. The predicted wide range of values is consistent with experimental reports in thin-walled torsion tubes for various materials [32, 33].

Our results suggest that materials in which small voids are able to nucleate inside the shear band, such as metallic glasses [34], would have a lower fracture surface roughness. This is due to the vanishingly small dimple height, as the voids would have almost completely rotated.

Our results illustrate for the first time a possible mechanism of failure inside shear bands. They also show that a micromechanical dilatant plasticity framework can provide new insights into aspects of material behavior heretofore not explained using either continuum or atomistic approaches. The predictions connect macroscopic behavior with detailed microscopic information about observables (the voids) and measurable attributes thereof. Once the model is implemented to solve boundary-value problems, further contact with experiments can be made.

Acknowledgments

We gratefully acknowledge financial support from the National Science Foundation under grant CMMI-1405226.

References

[1] P. Schall and M. van Hecke. Shear Bands in Matter with Granularity. *Annual Review of Fluid Mechanics*, 42:67–88, 2010.

[2] K. A. Alshibli and S. Sture. Shear band formation in plane strain experiments of sand. *J. Geotech. Geoenviron. Eng.*, 126:495–503, 2000.

[3] C. M. Gourlay and A. K. Dahle. Dilatant shear bands in solidifying metals. *Nature*, 445:70–73, 2007.

[4] E. Gomez-Rivas and A. Griera. Shear fractures in anisotropic ductile materials: An experimental approach. *J. Struct. Geol.*, 34:61–76, 2012.

[5] Q. Wei, D. Jia, K. T. Ramesh, and E. Ma. Evolution and microstructure of shear bands in nanostructured Fe. *Applied Physics Letters*, 81:1240–1242, 2002.

[6] T. F. Morgeneyer and J. Besson. Flat to slant ductile fracture transition: Tomography examination and simulations using shear-controlled void nucleation. *Scripta Materialia*, 65:1002–1005, 2011.

[7] K. Friedrich. Crazes and shear bands in semi-crystalline thermoplastics. *Adv. Pol. Sci.*, 52-3:225–274, 1983.

[8] A. L. Greer, Y. Q. Cheng, and E. Ma. Shear bands in metallic glasses. 74:71–132, 2013.

[9] D. C. Hofmann, J.-Y. Suh, A. Wiest, G. Duan, M.-L. Lind, M. D. Demetriou, and W. L. Johnson. Designing metallic glass matrix composites with high toughness and tensile ductility. *Nature*, 451:1085–1090, 2008.

[10] T. F. Morgeneyer, T. Taillandier-Thomas, A. Buljac, L. Helfen, and F. Hild. On strain and damage interactions during tearing: 3D in situ measurements and simulations for a ductile alloy (AA2139-T3). *Journal of the Mechanics and Physics of Solids*, 96:550–571, 2016.

[11] A. A. Benzerga and J.-B. Leblond. Ductile fracture by void growth to coalescence. *Advances in Applied Mechanics*, 44:169–305, 2010.

[12] A. Pineau, A. A. Benzerga, and T. Pardoen. Failure of metals I. Brittle and Ductile Fracture. *Acta Materialia*, 107:424–483, 2016.

[13] A. L. Gurson. Continuum Theory of Ductile Rupture by Void Nucleation and Growth: Part I– Yield Criteria and Flow Rules for Porous Ductile Media. *Journal of Engineering Materials and Technology*, 99:2–15, 1977.

[14] V. Tvergaard and A. Needleman. Analysis of the cup–cone fracture in a round tensile bar. *Acta Metallurgica*, 32:157–169, 1984.

[15] K. Nahshon and J. W. Hutchinson. Modification of the Gurson Model for shear failure. *European Journal of Mechanics*, 27:1–17, 2008.

[16] F. A McClintock, S. M. Kaplan, and C. A. Berg. Ductile fracture by hole growth in shear bands. *International Journal of Fracture*, 2(4):614–627, 1966.

[17] V. Tvergaard. Shear deformation of voids with contact modeled by internal pressure. *International Journal of Mechanical Sciences*, 50:1459–1465, 2008.

[18] V. Tvergaard. Behaviour of voids in a shear field. *International Journal of Fracture*, 158:41–49, 2009.

[19] K. L. Nielsen, J. Dahl, and V. Tvergaard. Collapse and coalescence of spherical voids subject to intense shearing: studied in full 3D. *International Journal of Fracture*, 177:97–108, 2012.

[20] A. A. Benzerga, J.-B. Leblond, A. Needleman, and V. Tvergaard. Ductile Failure Modeling. *International Journal of Fracture*, 201:29–80, 2016.

[21] L. Morin, J.-B. Leblond, and V. Tvergaard. Application of a model of plastic porous materials including void shape effects to the prediction of ductile failure under shear-dominated loadings. *Journal of the Mechanics and Physics of Solids*, 94:148–166, 2016.

[22] A. A. Benzerga. Micromechanics of Coalescence in Ductile Fracture. *Journal of the Mechanics and Physics of Solids*, 50:1331–1362, 2002.

[23] A. A. Benzerga, J. Besson, and A. Pineau. Anisotropic ductile fracture. Part II: theory. *Acta Materialia*, 52:4639–4650, 2004.

[24] S. M. Keralavarma and A. A. Benzerga. A constitutive model for plastically anisotropic solids with non-spherical voids. *Journal of the Mechanics and Physics of Solids*, 58:874–901, 2010.

[25] A. A. Benzerga and J.-B. Leblond. Effective Yield Criterion Accounting for Microvoid Coalescence. *Journal of Applied Mechanics*, 81:031009, 2014.

[26] M. E. Torki, A. A. Benzerga, and J.-B. Leblond. On Void Coalescence under Combined Tension and Shear. *Journal of Applied Mechanics*, 82(7):071005, 2015.

[27] S. Kweon, B. Sagsoy, and A. A. Benzerga. Constitutive relations and their time integration for anisotropic elasto-plastic porous materials. *Computer Methods in Applied Mechanics and Engineering*, 310:495–534, 2016.

[28] L. Morin, J.-B. Leblond, and A. A. Benzerga. Coalescence of voids by internal necking: theoretical estimates and numerical results. *Journal of the Mechanics and Physics of Solids*, 75:140–158, 2015.

[29] J.D. Eshelby. The determination of the elastic field of an ellipsoidal inclusion, and related problems. *Proc. Roy. Soc*, A241:357–396, 1957.

[30] M. Kailasam and P. Ponte Castaneda. A general constitutive theory for linear and nonlinear particulate media with microstructure evolution. *Journal of the Mechanics and Physics of Solids*, 46(3):427–465, 1998.

[31] J.-B. Leblond and G. Mottet. A theoretical approach of strain localization within thin planar bands in porous ductile materials. *Comptes Rendus Mecanique*, 336:176–189, 2008.

[32] G. R. Johnson, J. M. Hoegfeldt, U. S. Lindholm, and A. Nagy. Response of various metals to large torsional strains over a large range of strain rates – Part 1: Ductile metals. *Journal of Engineering Materials and Technology*, 105:42–47, 1983.

[33] G.R. Johnson, J.M. Hoegfeldt, U.S. Lindholm, and A. Nagy. Response of various metals to large torsional strains over a large range of strain rates – Part 2: Less ductile metals. *Journal of Engineering Materials and Technology*, 105:48–53, 1983.

[34] Y. Shao, G-N Yang, K-F Yao, and X. Liu. Direct experimental evidence of nano-voids formation and coalescence within shear bands. *Applied Physics Letters*, 105(18):181909, 2014.

P6 MICROMECHANICS-BASED CONSTITUTIVE RELATIONS FOR POST-LOCALIZATION ANALYSIS

A Mechanism of Failure in Shear Bands
Supplemental Material for MethodsX:
Micromechanics-based Constitutive Relations for Post-Localization Analysis

M. Torki[1] and A. A. Benzerga[1,2]

[1] *Department of Aerospace Engineering, Texas A&M University*
College Station, TX 77843-3141, United States

[2] *Department of Materials Science and Engineering, Texas A&M University*
College Station, TX 77843-3141, United States

Abstract

Micromechanics-based constitutive relations for post-localization analysis are obtained to be used in a multi-surface representation of porous metal plasticity. Each yield surface involves a number of internal parameters. Hence, the constitutive relations must be closed with evolution equations for the internal parameters. The latter are essential to describing the gradual loss of load bearing capacity in shear. We also briefly discuss potential void closure due to void rotation and elongation in shear and show additional details regarding the simulations reported in the Letter.

1 Two-surface formulation

The natural framework to describe elastic deformation is lagrangian. On the other hand, the natural framework to describe plastic flow is eulerian. Formulations of elasto-plastic constitutive relations commonly adopt an additive decomposition of the total velocity gradient within an eulerian setting [1, 2]:

$$\boldsymbol{L} = \boldsymbol{L}^{\mathrm{e}} + \boldsymbol{L}^{\mathrm{p}} \tag{1}$$

so that a weak form of elasticity (hypoelasticity) is employed for $\boldsymbol{L}^{\mathrm{e}}$. In this Supplemental Material, we describe how we formulate $\boldsymbol{L}^{\mathrm{p}}$ in the context of a two-surface representation of dilatant plasticity. Background on the two-surface formulation may be found in [3, 4]; also see [5, 6] for recent perspectives. The effective yield surface is the intersection of two surfaces. The first, expressed in the form $\Phi^{\mathrm{H}}(\boldsymbol{\sigma}; f, w, \mathbf{n}^{(3)}) = 0$, represents homogeneous plastic flow, at an appropriate scale of description, and involves three internal parameters: void volume fraction, f, void aspect ratio, w, and void orientation, $\mathbf{n}^{(3)}$. It is used to describe void growth, and encompasses the famous Gurson model [7] for spherical voids under the constraint of no shape change. In our implementation, we used the model developed in [8]. The second yield surface, written as $\Phi^{\mathrm{I}}(\boldsymbol{\sigma}; f, w, \lambda, \mathbf{n}^{(3)}, \mathbf{n}) = 0$, corresponds to inhomogeneous plastic flow and involves two additional internal parameters: the orientation of the localized band, $\mathbf{n}$, and the relative void spacing[1], λ, associated with $\mathbf{n}$. It

[1] In the Letter, λ physically represents the ratio of shear band thickness to the in-plane void spacing.

is used to describe void coalescence, and encompasses the recently developed models of void coalescence in tension [9] and under combined tension and shear [10].

The two-surface formulation, also known as the hybrid model, was discussed in a recent review [6]. Since the plastic portion of the velocity gradient, $\boldsymbol{L}^{\mathrm{p}}$, is obtained by normality to the effective yield surface, the hybrid model presents the disadvantage of an ill-defined direction of plastic flow if the current loading point lies on a vertex of the yield surface. This problem arises because yield functions Φ^{H} and Φ^{I} were actually obtained independently for two elementary cells using micromechanics. To remedy this problem, a unified model has recently been developed [11]. The resulting yield surface exhibits regions of extreme curvature near the vertices of the hybrid model, but is fully smooth. This shortcoming of the hyrbid model has no consequences on the results presented in this Letter for a simple reason: under near simple shear, plastic flow is inhomogeneous from the outset. In other words, the current loading point is too far from any vertex.

2 Surrogate microstructure

The surrogate microstructure defined in the main text involves replacing the rotating void with an upright cylinder of axis $\mathbf{n}$, having the same volume and porosity, Fig. 1. This identification is needed for applicability

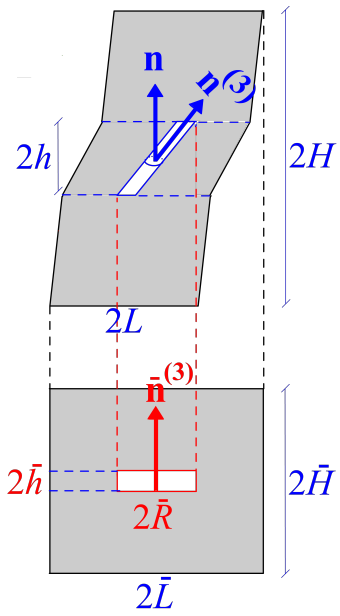

Figure 1: Concept of surrogate or intermediate configuration.

of yield function Φ^{I}; see Eqn (1) in the Letter. It implies introducing an effective void aspect ratio, $\bar{w} \equiv \bar{h}/\bar{R}$, and an effective ligament parameter, $\bar{\chi} \equiv \bar{R}/\bar{L}$, related to the internal parameters of the actual microstructure through:

$$\bar{w} = w\left(wS + \frac{1}{C}\right)^{-3} \tag{2}$$

and

$$\bar{\chi} = \left(\frac{f\bar{\lambda}}{\bar{w}}\right)^{\frac{1}{3}} \tag{3}$$

where use has been separately made of equality in void volumes and cell volumes. Here, C and S are shorthand notation for $C = \mathbf{n}^{(3)} \cdot \mathbf{n} \equiv \cos\theta$ and $S = \mathbf{n}^{(3)} \cdot \mathbf{m}$. Also, $\bar{\lambda}$ denotes the aspect ratio of the surrogate cell and is obtained from:

$$\bar{\lambda} = \frac{\lambda}{(1+\gamma_{\mathrm{mn}})^3} \tag{4}$$

where $\gamma_{\mathrm{mn}} = 2\mathbf{m} \cdot \boldsymbol{E}\mathbf{n}$ and $\boldsymbol{E} = \int \boldsymbol{D} dt$.

The concept of a surrogate microstructure is key to the predictions discussed in the Letter. In simple shear, the void rotates "faster" than the material so that $\bar{\chi}$ would evolve, unlike the actual ligament parameter $\chi \equiv R/L$. It is worth noting that an elementary estimation of the limit load in simple shear for the inclined cylinder of Fig. 1a delivers $\tau = (1-\chi^2)\bar{\tau}$ irrespective of the void inclination, with χ, not $\bar{\chi}$, appearing in the equation. This simple estimate is contrary to the projection-guided estimate of Eqn. (1) in the Letter. One cannot emphasize enough, however, that the elementary estimate is obtained using Gurson's shear field, also used in [10]. Presumably, this field becomes increasingly poor for inclined voids and large values of χ. An indication of that may be inferred from three-dimensional calculations for elongated voids reported in [12]. A qualitative theoretical argument supporting this is as follows. Let $\mathbf{n}^{(1)}$ be the unit vector perpendicular to $\mathbf{n}^{(3)}$ lying in the shearing plane, i.e. $\mathbf{n}$–$\mathbf{m}$ plane (Fig. 2). The lateral void boundaries (having $\mathbf{n}^{(1)}$ as a normal) are traction free, hence:

$$\mathbf{n}^{(1)} \cdot \boldsymbol{\sigma}\mathbf{n}^{(1)} = \mathbf{n}^{(3)} \cdot \boldsymbol{\sigma}\mathbf{n}^{(1)} = 0. \tag{5}$$

The latter equation implies no shear plastic strain accumulation on those surfaces

$$\mathbf{n}^{(3)} \cdot \boldsymbol{D}^{\mathrm{p}}\mathbf{n}^{(1)} = 0, \tag{6}$$

where use has been made of the flow rule associated with the von Mises yield criterion tacitly assumed in deriving the overall response. However, for large inclinations of the void, vectors $\mathbf{n}^{(1)}$ and $\mathbf{n}^{(3)}$ nearly coincide with $-\mathbf{n}$ and $\mathbf{m}$. It follows that the no-shearing condition above becomes

$$\mathbf{n} \cdot \boldsymbol{D}^{\mathrm{p}}\mathbf{m} \approx 0, \tag{7}$$

This condition is obviously violated by Gurson's shear velocity field, which leads to a uniform deviatoric strain rate and in particular to a uniform and *non-zero* value of $\mathbf{n} \cdot \boldsymbol{D}^{\mathrm{p}}\mathbf{m}$.

The above argument means that Gurson's shear field becomes increasingldy inadequate in those parts of the intervoid ligament that are close to the boundary of the inclined void. Furthermore, for inclined voids, this ligament is wide (in the direction of vector $\mathbf{n}^{(3)}$) and thin (in the direction of vector $\mathbf{n}^{(1)}$), see Fig. 5a of the Letter. Therefore, most of the intervoid ligament lies close to the boundary of the void, making the inadequacy of Gurson's field more pronounced. In summary, the proposed heuristics is based on the so-justified assumption that for an inclined cylinder, the limit load in shear would depend not only on χ but also on the void orientation relative to the cell's. This is precisely what surrogate parameter $\bar{\chi}$ captures, albeit approximately.

3 Evolution equations

Differential equations describing the evolution of internal variables in Φ^{H} were part of the developments in Ref. [8]. However, those associated with Φ^{I} were not developed in Ref. [10]. They were listed in the main text as equations (4)–(10). In particular, those pertaining to void shape and orientation, equations (5)–(8), are original and thus require special attention.

Consistent with the void geometry considered in deriving Φ^{I} in [10], we consider a deformed configuration under shear deformation, Fig. 2. Only the ligament region, of height $2h$, is shown for clarity. Recall that elastically unloaded zones lie above and below the void, as sketched in Fig. 3b of the Letter. For simplicity, these zones are modeled as rigid in what follows.

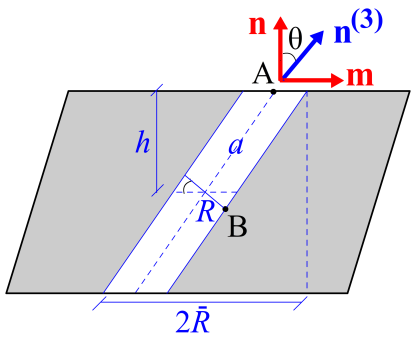

Figure 2: Inclined cylindrical void inside a deformed ligament under the effect of shear τ along $\mathbf{m}$ and normal stress σ along $\mathbf{n}$.

3.1 Evolution of void shape

To obtain the differential equation for void aspect ratio w, we first express that the top and bottom void boundaries are attached to the rigid zones. Due to symmetry, we focus on motion of the top boundary. Thus, the tangential and normal velocities of point A (Fig. 2) are given by:

$$v_1^{(\mathrm{A})} = 2h\frac{D_{31}}{c} = 2HD_{31} \quad , \quad v_3^{(\mathrm{A})} = h\frac{D_{33}}{c} = HD_{33} \tag{8}$$

where the x_1 and x_3 axes are identified with the directions of shear, $\mathbf{m}$, and normal to the band, $\mathbf{n}$, respectively. Accordingly, D_{31} and D_{33} are the relevant (non-zero) components of the plastic strain rate (superscript "p" dropped for convenience and elastic strain rates neglected). Also, $c \equiv h/H$ denotes the current ligament volume fraction.

Denoting the length of the inclined cylinder and its radius by $2a$ and $2R$, respectively (see Fig. 2), the time rate of a is obtained at fixed void orientation θ as:

$$\dot{a} = v_1^{(\mathrm{A})}S + v_3^{(\mathrm{A})}C = H(2D_{31}S + D_{33}C) \tag{9}$$

Hence, using the identity $H/a = C/c$ one gets

$$\frac{\dot{a}}{a} = \frac{C}{c}(2D_{31}S + D_{33}C) \tag{10}$$

The ligament volume fraction, c, is given by:

$$c^3 = C^3\frac{fw^2}{\lambda^2} \tag{11}$$

Next, the rate of change of R may be obtained (in terms of that of a) from plastic incompressibility of the matrix material as

$$\frac{\dot{R}}{R} = \frac{1}{2}\left[\left(\frac{L}{R}\right)^2\frac{H}{a}D_{33} - \frac{\dot{a}}{a}\right] = \frac{1}{2}\left(\frac{D_{33}}{f} - \frac{\dot{a}}{a}\right) \tag{12}$$

Combining (10) and (12) leads to the following evolution equation for the void aspect ratio:

$$\frac{\dot{w}}{w} = \frac{\dot{a}}{a} - \frac{\dot{R}}{R} = \frac{1}{2}\left(\frac{3C^2}{c} - \frac{1}{f}\right)\mathbf{n}\cdot\boldsymbol{D}^{\mathrm{p}}\mathbf{n} + \frac{3CS}{c}\mathbf{m}\cdot\boldsymbol{D}^{\mathrm{p}}\mathbf{n} \tag{13}$$

3.2 Evolution of void orientation

In general, the rate of rotation of the (immaterial) principal axes of the void may be directly obtained from the (material) rotation and strain rates of the void [13, 14], denoted by $\boldsymbol{\Omega}^v$ and $\boldsymbol{D}^v$, respectively. Here, we obtain $\boldsymbol{\Omega}^v$ as in [13,14] but specialized to the ligaments only. However, the contribution to the rotation rate of the axes that comes from mere void distortion (i.e. that tied to $\boldsymbol{D}^v$) is rederived from first principles. Madou and Leblond [14] have shown that the general form initiated in [13, 15] requires significant amendments due to strong nonlinear effects. They did so by introducing heuristic coefficients calibrated using a large number of finite-element based limit analyses. Here we obtain simpler, parameter-free and probably more accurate equations by considering the constrained kinematics pertaining to post-localization. Namely, this involves plastic incompressibility of the intervoid ligament and the fact that the top and bottom boundaries of the void move rigidly with the above and bottom material layers. Such equations are obviously valid only for post-localization. Thus, the rate of change of the void axis is given by equation (6) of the main text, rewritten here for completeness:

$$\dot{\mathbf{n}}^{(3)} = \boldsymbol{\omega}\mathbf{n}^{(3)}, \qquad \boldsymbol{\omega} = \boldsymbol{\Omega}^v + \boldsymbol{\Omega}^l \tag{14}$$

where the rotation tensor $\boldsymbol{\omega}$ accounts for the void spin, $\boldsymbol{\Omega}^v$, which is determined as in [13]. It is related to the continuum spin tensor $\boldsymbol{\Omega}$ via:

$$\boldsymbol{\Omega}^v = \boldsymbol{\Omega} - \frac{1}{c}\mathbb{C} : \boldsymbol{D}^{\mathrm{p}} \tag{15}$$

where $\mathbb{C}$ is the fourth order spin concentration tensor given by

$$\mathbb{C} = -(1-f)\mathbb{P} : \mathbb{A}, \qquad \mathbb{A} = [\mathbb{I} - (1-f)\mathbb{S}]^{-1} \tag{16}$$

with $\mathbb{A}$ the strain concentration tensor and $\mathbb{P}$ and $\mathbb{S}$ the Eshelby tensors [16] for a spheroidal inclusion of zero stiffness in an incompressible linear viscous matrix. Note that a $1/c$ term appears in (15) to represent the plastic rate of deformation inside the ligament.

Also, in (14) $\boldsymbol{\Omega}^l$ is an additional contribution to the effective void rotation that comes from mere distortion of void boundaries under the combined effect of tension and shear. With reference to (11), the time rate of c reads

$$3\frac{\dot{c}}{c} = 3\frac{\dot{C}}{C} + \frac{\dot{f}}{f} + 2\left(\frac{\dot{w}}{w} - \frac{\dot{\lambda}}{\lambda}\right) \tag{17}$$

The rates of internal parameters entering the right-hand side of this equation are all known, except the void orientation, which enters through C. The left-hand side can be determined by neglecting the volume change of the elastically unloaded zones. Thus,

$$\frac{\dot{c}}{c} = \frac{\dot{h}}{h} - \frac{\dot{H}}{H} = \frac{D_{33}}{c} - D_{33} = \frac{1-c}{c}\mathbf{n}\cdot\boldsymbol{D}^{\mathrm{p}}\mathbf{n} \tag{18}$$

Also,

$$\frac{\dot{\lambda}}{\lambda} = \frac{\dot{H}}{H} - \frac{\dot{L}}{L} = \mathbf{n}\cdot\boldsymbol{D}^{\mathrm{p}}\mathbf{n} - \frac{1}{2}\left(\mathbf{m}\cdot\boldsymbol{D}^{\mathrm{p}}\mathbf{m} + \mathbf{p}\cdot\boldsymbol{D}^{\mathrm{p}}\mathbf{p}\right) \tag{19}$$

where $\mathbf{p} = \mathbf{n}\times\mathbf{m}$ completes the triad of local base vectors. Therefore, equation (17) may be used to determine $\dot{C}/C$.

Furthermore, in the corotational formulation, where the material is taken stationary and thus $\mathbf{n}$ delivers no time rate, one simply has

$$\dot{C} = \dot{\mathbf{n}}^{(3)}\cdot\mathbf{n} \tag{20}$$

The component of $\dot{\mathbf{n}}^{(3)}$ along $\mathbf{m}$ can be derived considering that $\mathbf{n}^{(3)}$ is a unit vector, which entails

$$\left(\mathbf{n}^{(3)}\cdot\mathbf{m}\right)^2+\left(\mathbf{n}^{(3)}\cdot\mathbf{p}\right)^2+\left(\mathbf{n}^{(3)}\cdot\mathbf{n}\right)^2=1 \quad\Longrightarrow\quad \dot{\mathbf{n}}^{(3)}\cdot\mathbf{m}=-\frac{C}{S}\dot{\mathbf{n}}^{(3)}\cdot\mathbf{n} \tag{21}$$

Note that component $\mathbf{n}^{(3)}\cdot\mathbf{p}$ does not deliver a time rate since no shear is exerted along $\mathbf{p}$. Then, the identity $\dot{\mathbf{n}}^{(3)}=\boldsymbol{\Omega}^l\mathbf{n}^{(3)}$ requires that $\boldsymbol{\Omega}^l$ be expressed in the following format:

$$\boldsymbol{\Omega}^l=\frac{\dot{\mathbf{n}}^{(3)}\cdot\mathbf{m}}{S}\mathbf{m}\otimes\mathbf{m}+\frac{\dot{\mathbf{n}}^{(3)}\cdot\mathbf{n}}{C}\mathbf{n}\otimes\mathbf{n} \tag{22}$$

which, along with (17), leads to the following equivalent form:

$$\boldsymbol{\Omega}^l=\left(\frac{\dot{c}}{c}-\frac{1}{3}\left[\frac{\dot{f}}{f}+2\left(\frac{\dot{w}}{w}-\frac{\dot{\lambda}}{\lambda}\right)\right]\right)\left(\mathbf{n}\otimes\mathbf{n}-\frac{C^2}{S^2}\mathbf{m}\otimes\mathbf{m}\right) \tag{23}$$

where all terms and rates have been defined. Note that in the case of simple shear, treated in the Letter, this equation simplifies considerably since:

$$\dot{c}=0\quad,\quad \dot{f}=0\quad,\quad \dot{\lambda}=0$$

In summary, evolution equations (13) and (14) with due account of (23) are those labeled (5), (6) and (7) in the Letter. They were here derived for a rotating cylindrical void whose motion is constrained by the elastically unloaded zones above and below it. In the Letter, we heuristically use them for spheroidal voids. Similar equations can also be developed for rotating spheroidal voids. However, the geometry leads to more complex equations that would take away from the simplicity of the present treatment. Furthermore, when dealing with the special case of initially spherical voids ($w_0=1$) the void axis is arbitrarily defined. Under such circumstances, the principal stretch is used to resolve any indeterminacy upon deformation, as explained elsewhere [2]. In order to avoid this unnecessary complication, in the Letter we have used a void with a slight initial eccentricity ($w_0=1.1$) so that its axis $\mathbf{n}^{(3)}$ is well defined from the outset.

4 Void closure

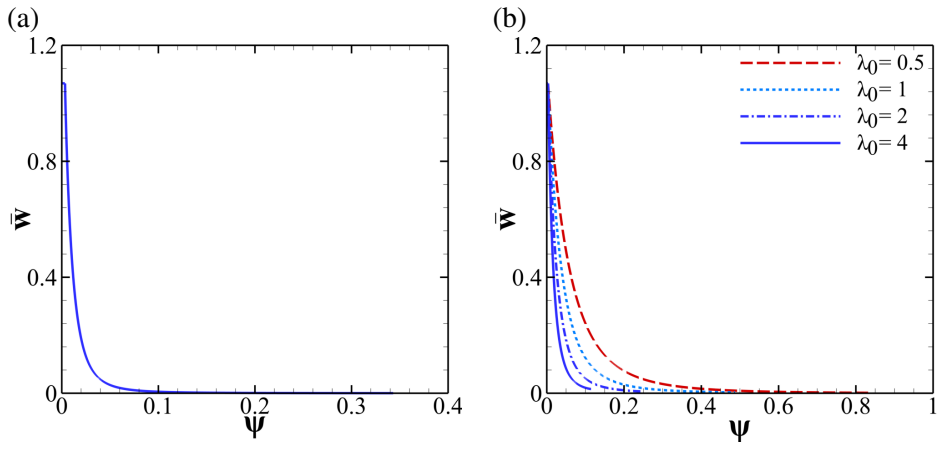

Figure 3: Void flattening in the surrogate microstructure by evolution of the effective void aspect ratio, $\bar{w}$ in (a) the case shown in Fig. 4 of the Letter using $\sigma/\tau=0.01$, $f_0=0.0005$, $w_0=1.1$, $\lambda_0=2$, $N=0.2$, $\sqrt{3}\tau_0/E=0.002$; and (b) the cases shown in Fig. 6 of the Letter using $\sigma/\tau=0.01$, $f_0=0.01$, $w_0=1.1$, $N=0.2$, $\sqrt{3}\tau_0/E=0.002$.

In exact finite element simulations of void growth in a shear field [17–19], the void volume fraction may slowly decrease if the tension-to-shear ratio is sufficiently low. By way of consequence, the void closes into a crack. Various ways of avoiding details pertaining to handling contact were explored by Tvergaard [17–19]. In our simulations, the void volume fraction f remains constant. As mentioned in the text, this is an approximation with no consequence on essential behavior, because f is not an essential internal state variable in simple shear. Since f is predicted to remain constant, void closure never occurs per se. However, it does in an asymptotic sense. To illustrate this, Fig. 3 shows the evolution of the effective void aspect ratio, $\bar{w}$, introduced in equation (2) for various cases reported in the Letter. As the void rotates, its projected length onto the localization plane increases. Thus, to maintain equality of volumes between the actual void and the surrogate void, the latter must go increasingly flat, i.e. $\bar{w} \to 0$. This is illustrated in the surrogate microstrutcure of Fig. 1. The faster the rotation the more severe the flattening in the surrogate cell.

References

[1] V. Tvergaard and A. Needleman. Analysis of the cup–cone fracture in a round tensile bar. *Acta Metallurgica*, 32:157–169, 1984.

[2] S. Kweon, B. Sagsoy, and A. A. Benzerga. Constitutive relations and their time integration for anisotropic elasto-plastic porous materials. *Computer Methods in Applied Mechanics and Engineering*, 310:495–534, 2016.

[3] A. A. Benzerga. Micromechanics of Coalescence in Ductile Fracture. *Journal of the Mechanics and Physics of Solids*, 50:1331–1362, 2002.

[4] A. A. Benzerga, J. Besson, and A. Pineau. Anisotropic ductile fracture. Part II: theory. *Acta Materialia*, 52:4639–4650, 2004.

[5] A. A. Benzerga and J.-B. Leblond. Ductile fracture by void growth to coalescence. *Advances in Applied Mechanics*, 44:169–305, 2010.

[6] A. A. Benzerga, J.-B. Leblond, A. Needleman, and V. Tvergaard. Ductile Failure Modeling. *International Journal of Fracture*, 201:29–80, 2016.

[7] A. L. Gurson. Continuum Theory of Ductile Rupture by Void Nucleation and Growth: Part I– Yield Criteria and Flow Rules for Porous Ductile Media. *Journal of Engineering Materials and Technology*, 99:2–15, 1977.

[8] S. M. Keralavarma and A. A. Benzerga. A constitutive model for plastically anisotropic solids with non-spherical voids. *Journal of the Mechanics and Physics of Solids*, 58:874–901, 2010.

[9] A. A. Benzerga and J.-B. Leblond. Effective Yield Criterion Accounting for Microvoid Coalescence. *Journal of Applied Mechanics*, 81:031009, 2014.

[10] M. E. Torki, A. A. Benzerga, and J.-B. Leblond. On Void Coalescence under Combined Tension and Shear. *Journal of Applied Mechanics*, 82(7):071005, 2015.

[11] L. Morin, J.-B. Leblond, A. A. Benzerga, and D. Kondo. A unified criterion for the growth and coalescence of microvoids. *Journal of the Mechanics and Physics of Solids*, 97:19–36, 2016.

[12] ME Torki. A unified criterion for void growth and coalescence under combined tension and shear. *International Journal of Plasticity*.

[13] M. Kailasam and P. Ponte Castaneda. A general constitutive theory for linear and nonlinear particulate media with microstructure evolution. *Journal of the Mechanics and Physics of Solids*, 46(3):427–465, 1998.

[14] K. Madou, J.-B. Leblond, and L. Morin. Numerical studies of porous ductile materials containing arbitrary ellipsoidal voids —II: Evolution of the length and orientation of the void axes. *European Journal of Mechanics*, 42:490–507, 2013.

[15] P. Ponte Castañeda and M. Zaidman. Constitutive models for porous materials with evolving microstructure. *Journal of the Mechanics and Physics of Solids*, 42:1459–1495, 1994.

[16] J.D. Eshelby. The determination of the elastic field of an ellipsoidal inclusion, and related problems. *Proc. Roy. Soc*, A241:357–396, 1957.

[17] V. Tvergaard. Shear deformation of voids with contact modeled by internal pressure. *International Journal of Mechanical Sciences*, 50:1459–1465, 2008.

[18] V. Tvergaard. Behaviour of voids in a shear field. *International Journal of Fracture*, 158:41–49, 2009.

[19] K. L. Nielsen, J. Dahl, and V. Tvergaard. Collapse and coalescence of spherical voids subject to intense shearing: studied in full 3D. *International Journal of Fracture*, 177:97–108, 2012.

P7 ON DUCTILE FRACTURE UNDER COMBINED TENSION AND SHEAR

On Ductile Fracture under Combined Tension and Shear

M. E. Torki[1], A. A. Benzerga[1,2,3]

[1] *Department of Aerospace Engineering, Texas A&M University, College Station, TX 77843, USA*

[2] *Center for intelligent Multifunctional Materials and Structures, TEES, College Station, TX 77843, USA*

[3] *Department of Materials Science and Engineering, Texas A&M University, College Station, TX 77843, USA*

Abstract

A hybrid micromechanics-based model is developed and numerically implemented to simulate ductile failure under combined shear and tension. The constitutive framework accounts for homogeneous and localized deformation processes. Earlier outcomes indicate that the shear-dominated deformation process is an intermediate state between a fully homogeneous and an ideally localized one with plasticity confined within intervoid ligaments. The deformation mechanism is closer to being homogeneous at early stages and would approach the ideal localized state towards the end. Existing evolution equations of void elongation and rotation are invoked during nearly-homogeneous yielding, and are derived for post-localized deformation under combined loading. While nearly-homogeneous yielding is governed by the current void configuration, the localized yield criterion acts upon a surrogate microstructure aligned with the normal to a possible plane of localization. The original form of the hybrid model predicts premature failure under shear-dominated loading notwithstanding the failure mechanism fully conforms to physics. Both the nearly-homogeneous and localized yield functions are, therefore, modified in accordance with existing numerical results with simple adjustable parameters. As opposed to failure under triaxial loading governed by evolution of porosity, failure under combined tension and shear is driven by the effective parameter dictated by the initial relative void spacing and evolved until its maximum value is achieved. The study was further specified to a state of *near-simple* shearing with a vanishingly small normal stress. The effects of initial porosity, those of the void and cell aspect ratios, and that of void misalignment with the principal loading directions were accounted for. Furthermore, the strain to failure was evaluated in terms of stress triaxiality for a complete scope of stress triaxialities upon the loading path constituted by combined normal and shear stresses. Finally, the same framework was utilized to simulate an example state of *near-pure* shearing under the plane-strain condition.

Key Words: Ductile fracture; Void coalescence; Combined tension and shear; Failure in shear; Porous plasticity.

1 Introduction

Ductile failure under combined tension and shear can be witnessed in abundant undesirable and desirable failure processes such as crack propagation under ductile-to-brittle transition (DBT), *e.g.* in welded structures [1], ballistic penetration [2], *etc* as well as engineering processes such as cutting and trimming [3], *etc*. Experimental observation of ductile fracture has been conveyed in the literature by such works as that of Johnson *et al.* [4, 5], who measured the torsional ductility in varieties of engineering metal alloys. Therein, one could observe up to 3 orders of magnitude of difference in γ_f from the lower to the upper limit. A compelling explanation regarding these remarkable differences in the measured ductilities still remains elusive.

Later on, Barsoum and Faleskog [6] conducted similar experiments by the introduction of notches to hollow tubes for illustrating the effect of triaxiality. They characterized the stress state in terms of stress triaxiality T and the *Lode* parameter L [7]. Haltom *et al.* [8] have recently conducted torsion experiments with the test specimen revisited. Unlike earlier torsion experiments on aluminum alloys and steels [9, 10], Haltom *et al.*'s experiments showed increasing ductility under stress states near simple shearing [8]. Altogether, experiments, though being revealing, are hard to conduct, especially in presence of shear, and may lead to conflicting results.

The present work tacitly assumes the preexistence of voids inside a material regardless of the mechanism that underlies the nucleation of voids. Nevertheless, micromechanical void nucleation analyses of the kind pioneered by Needleman [11] are still not available for such loadings. Except when mediated by limited void growth in presence of penny-shaped cracks, the indispensable stages to ductile fracture under triaxial loadings are void growth and void coalescence, which is conducive to ultimate fracture. The two stages are distinguishable from plastic deformation being homogeneous and inhomogeneous at the cell level, respectively. To date, the failure mechanism subsequent to void coalescence that is best understood is by *internal necking* (see [7] and references therein) has been motivated by the pioneering computational work of Koplik and Needleman [12]. On the other hand, microscale localization by so–called *internal shearing* has also been noticed on the basis of cell model calculations [6, 13–15]. As such, plastic deformation under shear at the micro scale is inhomogeneous from the outset. In particular, both void growth and coalescence under shear are accommodated by plastic deformation confined to the vicinity of inter-void ligaments. The inhomogeneous identity of deformation under such conditions has been witnessed from early ages [16]. In a weakly rate–sensitive material, void coalescence by internal necking or shearing manifests by the onset of elastic unloading in layers above and below the void [12, 15, 17]. Another prominent indication of failure in shear is *shear failure*, *i.e.* failure by shear banding as an instability phenomenon [18]. However, the mechanism of material separation under shear–dominated loadings as well as inside shear bands has remained elusive by far.

A tentative understanding on the effect of loading condition on ductile fracture is carried through macroscopic nondimensional descriptors expressed in terms of stress invariants or some equivalent invariant of the stress deviator at the cell level. The Lode parameter L is particularly used to *apparently* reflect the effect of shear. The latter is function of the Lode angle or, equivalently, the third invariant of the stress deviator, J_3 [19, 20]. However, *isotropic* scalar–valued parameters cannot reveal the essential features of shearing effects at the micro scale. Meanwhile, there has been remarkable attempt exerted on modeling ductile fracture under shearing effects at the cell level. Some researchers, including Tvergaard and coworkers [14, 21] have simulated this phenomenon by high–throughput FEM–based cell–model calculations under various conditions including near-simple shearing with plane strain or 3D cells [14, 21] as well as near-pure shearing [22]. In a sense, these sets of calculations can serve as benchmark for model assessment purposes. The technical challenges, however, clearly demonstrate that numerical cell–model studies, let alone structural calculations, of porous plasticity under combined loading are not only cumbersome, but also unfeasible at times, *e.g.* in the case of extreme shearing over 3D unit cells [14]. Micromechanics–based modeling would, in effect, eliminate the need for lengthy cell–model calculations. Deformation–induced anisotropies, however, constitute the essence of the damage mechanics of shear–dominated ductile fracture. This anisotropy is of two types: that related to the voids themselves (changes in void shape and orientation as well as their spatial arrangement) [21], and that related to the matrix, normally known as *plastic anisotropy* [23]. Thus, analyses of ductile fracture under shear–dominated loading and interpretation of currently available experiments rely, to a large extent, on accounting for the induced, and eventually initial anisotropies. In actual fact, the constitutive framework demands a paradigm shift in approaching ductile fracture in combined shear and tension, particularly at low stress triaxialities even if the anisotropy of the material is disregarded. More importantly, the post-localized constitutive behavior of porous materials is still at premature stage. Rather than merely on heuristics, plasticity models predicting void growth and coalescence under combined tension

and shear should be derived with a deeper insight into the physics of this process. Apropos of void coalescence, analytical physics–based models accounting for void coalescence under combined loading have been recently developed from first principles by the present author [24, 25]. Yet, the predictive capacity of these models in evolution-based simulation of ductile fracture remains to be evaluated. Moreover, a set of equations accounting for the evolution of effective parameters governing the post–coalescence microstructure is far from established. The only way to explore this problem without the present controversies is by adopting a *mechanism–based* approach. The present work is thus a step forward to the development of a more comprehensive constitutive theory for modeling ductile fracture under combined tension and shear, with particular focus on shear–dominated loadings. Without this step forward, the link between the real failure mechanism and the simulated process would still be missing. The micromechanical basis for an understanding of low–triaxiality fracture has been available since the early nineties [26,27] and has been used to model fracture in engineering materials, *e.g.* [28, 29]. Yet, the use of such equations has been restricted mostly to triaxial loading. The constitutive model expanded in the present context will be in part supplemented with the same models regarding void rotation and elongation prior to void coalescence. The counterparts of these equations, however, are lacking for the post-localized regime. Torki and Benzerga [30] derived evolution equations governing post-localized void elongation and rotation for cylindrical voids. The time integration of those equations, along with the associated flow rule based on the localized yield criterion in [24], was reflected through the results in [31], which elucidated a physics-based failure mechanism under shear dominant-loading, as would provide a rationale for observed fracture surfaces in sheared specimens. Failure under shear was proven to involve strain localization within inter-void ligaments, and was mediated by extreme void rotation and elongation. The framework provided therein was entitled to its own limitations. Firstly, it would deliver overconstrained responses due to the employed void idealization in that a cylindrical void should be pinned to the ligament ends throughout its bases. To move away from the resulting premature failure, added to better consistency with real microvoids, we were motivated to consider voids as spheroidal. To this end, post–localized evolution equations accounting for the rotation and elongation of voids under combined tension and shear will be derived from first principles for spheroidal voids, and the corresponding evolution of state will be compared to that emanating from its simpler counterpart for cylindrical voids [31]. The equations for pheroidal voids bare more complexity than their counterparts for cylindrical voids. Yet, the resulting framework can capture the salient features of shear–induced failure for the complete range of void shapes, *viz.* for *elongated*, *flat*, and nearly-spherical voids as well as for a complete range of initial void orientations. The outcomes are suggestive of different conducts for flat and elongated voids, as well as for voids variously oriented initially, under the same shear field whereas a cylindrical void under a shear field behaves all alike regardless of its shape and initial orientation. The elongation and rotation of spherical voids had earlier attracted McClintock *et al.* [32], who developed much simpler such equations for linearly viscous materials by considering the shear deformation as homogeneous rather than localized. Interestingly, the derived evolution equations for rotating voids can conveniently retrieve their simpler precursors developed by Benzerga [33] in absence of shear.

Alongside, the localized yield function developed from first principles by Torki *et al.* [24] will be invoked in competition to the homogeneous model after Keralavarma and Benzerga [34]. In this case, the two yield criteria are derived on the basis of different cell geometries, and thus the resulting two–surface model is termed *hybrid*. Contrary to the direct numerical simulations in [14, 21, 35], the void is not modeled explicitly, but through a the notion of an elementary cell. However, the latter numerical analyses can be considered as benchmark to assess the present hybrid model at the material cell level. The comparison between the complete model predictions with their cell-model counterparts from Ref's [14, 21] warrants some simple calibration to the model in both homogeneous and inhomogeneous yield criteria. Without a constitutive framework developed in terms of measurable and observable parameters, no such clear and simple calibration functions could have been introduced.

With the calibrated model at hand, the parametric studies will extend into the states of near–simple and

near–pure shearing. The effect of initial porosity will be conveyed through the initial ligament parameter χ_0. Further, the effect of void and cell sizes will be expressed in terms of the void and cell aspect ratios, w_0 and λ_0, respectively. A significant potential impact of the present work is the strain to failure evaluated in terms of stress triaxiality for a complete scope of stress triaxialities, especially for $T < 1/3$, upon imparting combined normal and shear stresses.

2 Evolution of State

This section addresses the body of requisite equations for the evolution of the material state in explicit or rate form. The first set of forthcoming equations are generic, and the evolution of void aspect ratio w and orientation $\mathbf{n}^{(3)}$ are intrinsic to the mechanism. Differential equations describing the evolution of w and $\mathbf{n}^{(3)}$ associated with Φ^{H} are part of the developments in Ref. [27, 34, 36]. Those associated with Φ^{I}, however, have not been developed except for triaxial stress states [33]. In a recent work by the authors [30], evolution equations have been proposed for the localized deformation mode mainly for cylindrical voids. In the present work, the counterparts of equations in [30] are propounded for spheroidal voids in the sequel. They key feature to take into account in this respect is the rigid-like behavior of the matrix above and below the void induced by elastic unloading [12]. So too has been corroborated for combined tension and shear via cell-model calculations [25].

2.1 Base vectors and plane normals

Let the principal loading directions be denoted by a global basis such as $(\mathbf{e}_1, \mathbf{e}_2, \mathbf{e}_3)$. The initial state of this basis, as well as the void lattice directors $(\mathbf{d}_1, \mathbf{d}_2, \mathbf{d}_3)$, are taken to rotate with the material. That is

$$\begin{aligned} &\mathbf{e}_m = \mathbf{R}\mathbf{e}_m^{(0)} \ , \ \mathbf{d}_n = \mathbf{R}\mathbf{d}_n^{(0)} \\ &\mathbf{F} = \mathbf{R}\mathbf{U} \end{aligned} \tag{1}$$

where $\mathbf{R}$ and $\mathbf{U}$ emanate from the polar decomposition of the deformation gradient tensor $\mathbf{F}$ at every step of the process, with $\mathbf{R}$ being the rotation part. $m =$ (L,T,S) stands for the principal orthotropy axes, and $n = 1, 2, 3$ constitutes the void lattice directors. The current deformation gradient can be derived on the basis of its incremental value at every time step, that is [37]

$$\mathbf{F}^{(i)} = \prod_{j=0}^{i} \mathbf{F}^{(j)} \tag{2}$$

where $\mathbf{F}^{(j)}$ is the deformation gradient between the $j-1$'st and j'th time steps constituted by the incremental displacements at the j'th step, where $j = 1, 2, ..., i$. Note that many commercial codes, such as ABAQUS, calculate $\mathbf{F}$ internally, and it thus need not be programmed when the constitutive model is coded in conjunction with those commercial software.

Upon invoking underlying microstructure, one can identify a discrete set of initial planes which could configure the post-localized inter-void ligaments. Each plane set is uniquely defined by a normal $\mathbf{n}$. Unless stated otherwise, a normal is convected through the transformation law for a directed area with unit magnitude. Therefore:

$$\mathbf{n} = \frac{\mathbf{F}^{-T}\mathbf{n}^{(0)}}{\left|\mathbf{F}^{-T}\mathbf{n}^{(0)}\right|} \tag{3}$$

with $|.|$ denoting a vector magnitude.

Within a plane with normal $\mathbf{n}$, two additional base vectors $\mathbf{m}$ and $\mathbf{p}$ can be defined in the interest of well-defined directions along and perpendicular to in-plane shear tractions. The latter two can be determined, at

every current step, directly from the resolved shear traction on the current plane with normal $\mathbf{n}$ and a cross product carried out on $\mathbf{n}$ and $\mathbf{m}$, respectively. That is

$$\begin{aligned} \mathbf{m} &= \frac{\tau_{\mathrm{n}}}{|\tau_{\mathrm{n}}|} \\ \mathbf{p} &= \mathbf{n} \times \mathbf{m} \end{aligned} \tag{4}$$

where the shear traction τ_{n} will be used in Eq. (33). In case, however, the shear traction vanishes, Eq. (4) would be ill-defined. In this case, $\mathbf{m}$ and $\mathbf{p}$ would stay constant, equal to their previous values (or to their initial values in case the loading is shearless throughout).

For the single cell undergoing normal and lateral as well as shear displacement, $\mathbf{F}^{(j)}$ reads:

$$\mathbf{F}^{(j)} = \left(1 + \frac{\delta u_m^{(j)}}{L}\right) \mathbf{m} \otimes \mathbf{m} + \left(1 + \frac{\delta u_p^{(j)}}{L}\right) \mathbf{p} \otimes \mathbf{p} + \left(1 + \frac{\delta u_n^{(j)}}{H}\right) \mathbf{n} \otimes \mathbf{n} + \frac{\delta u_t^{(j)}}{H} \mathbf{m} \otimes \mathbf{n} \tag{5}$$

where the constituents $\left(\delta u_m^{(j)}, \delta u_p^{(j)}, \delta u_n^{(j)}, \delta u_t^{(j)}\right)$ are the incremental displacements at the j'th step, where $j = 1, 2, ..., i$. Here, $\delta u_m^{(j)}$, $\delta u_p^{(j)}$, and $\delta u_n^{(j)}$ are the tensile displacement increments along directions $\mathbf{m}$, $\mathbf{p}$, and $\mathbf{n}$, respectively, and $\delta u_t^{(j)}$ is the tangential displacement increment over the top chord of the cell. Note that all these displacement increments are modified as to preserve the ratios among the stresses. Moreover,

$$L = L_0 \exp\left(\frac{\epsilon_{mm} + \epsilon_{pp}}{2}\right) \quad , \quad H = H_0 \exp \epsilon_{nn} \tag{6}$$

with ϵ_{mm}, ϵ_{pp}, and ϵ_{nn} are the normal strains resolved along the $\mathbf{m}$, $\mathbf{p}$ and $\mathbf{n}$ directions, respectively. Upon consideration of the single cell, $\mathbf{n}$ (denoting normal to the invoked localization plane) initially directed along $\mathbf{e}_3$ would stay constant thanks to the imposed deformation gradient $\mathbf{F}$. Accordingly, $\mathbf{m}$, $\mathbf{p}$ and $\mathbf{n}$ coincide with the global base vectors $\mathbf{e}_1$, $\mathbf{e}_2$ and $\mathbf{e}_3$, respectively.

Remark: The present solution framework is expanded based on a co-rotational formulation, *i.e.* the equations are expanded within the rotated material configuration. Therefore, Eq. (1) is implicit in the formulation.

2.2 Ligament volume fraction

$c \equiv h/H$ denotes the current ligament volume fraction, which can be expressed in correlation with (f, w, λ, θ) by writing

$$c = \frac{\ell \cos\beta}{H} = \frac{\ell}{b} \frac{\cos\beta}{w} \frac{a}{H} \tag{7}$$

But f can be expressed in the following form

$$f = \frac{1}{3\gamma w^2} \left(\frac{a}{L}\right)^2 \frac{a}{H} = \frac{1}{3\gamma w^2 \lambda} \left(\frac{a}{L}\right)^3 \;\; \therefore \;\; \frac{a}{H} = \frac{1}{\lambda} \frac{a}{L} = \left(\frac{3\gamma w^2 f}{\lambda^2}\right)^3 \tag{8}$$

where γ denotes the void shape factor, equaling 1/2 for a spheroid.

Therefore, (7), in combination with (8) and (A-12), gives

$$c = \left(\frac{3\gamma f}{w\lambda^2}\right)^{1/3} \sqrt{\frac{\mathscr{T}^2 + w^2}{\mathscr{T}^2 + 1}} \tag{9}$$

where $\mathscr{T} = S/C$, with S and C denoting, respectively, $\sin\theta$ and $\cos\theta$, with θ being a directional angle originated along $\mathbf{n}$ and ending at $\mathbf{n}^{(3)}$ with the sign convention as shown in Fig. 1.

Remark: The ligament volume fraction, according to (9), for the special case of an upright void with respect to normal $\mathbf{n}$ ($\mathscr{T} = 0$) simplifies into

$$c = \left(\frac{3\gamma f w^2}{\lambda^2}\right)^{1/3} = \frac{\chi w}{\lambda} \equiv \frac{a}{H}$$

noting that $f = c\chi^2/3\gamma$. By the same token, for a void after extreme shearing in a shear-dominated field ($\mathscr{T} \longrightarrow \infty$), it delivers

$$c \approx \left(\frac{3\gamma f}{w\lambda^2}\right)^{1/3} = \frac{\chi}{\lambda} \equiv \frac{b}{H}$$

2.3 Void aspect ratio

The evolving void aspect ratio can be more concisely and conveniently expressed in the form of its natural logarithm $s \equiv \ln w$, thus its rate $\dot{s}$ as follows.

– During nearly-homogeneous deformation:
The evolution equation for the void aspect ratio during nearly-homogeneous deformation is that proposed by Gologanu *et al.* [36], also adopted in [29]:

$$\dot{S} = \mathbf{Q} : \mathbf{D}^v \tag{10}$$

where

$$\mathbf{D}^v = k\mathbf{D}^{\mathrm{p}} + 3\left(\frac{1}{f}\mathbf{X}^v - \mathbf{X}\right) D^{\mathrm{p}}_{\mathrm{m}} \tag{11}$$

and $\mathbf{Q}$, $\mathbf{X}^v$ and $\mathbf{X}$ obey (32). The heuristic function k (following [36]) writes

$$\begin{aligned} &k = 1 + k_w k_f k_T \\ &k_w(w) = \frac{9}{2}\frac{\alpha_1 - \alpha_1^{\mathrm{Gar}}}{1 - 3\alpha_1} \\ &k_f(f) = (1 - \sqrt{f})^2 \\ &k_T(T,\epsilon) = \begin{cases} 1 - \dfrac{T^2 + T^4}{9} & \text{for} \quad \epsilon = +1 \\ 1 - \dfrac{T^2 + T^4}{18} & \text{for} \quad \epsilon = -1 \end{cases}, \qquad \epsilon \equiv \mathrm{sgn}(\sigma_{\mathrm{m}}\sigma'_{33}) \end{aligned} \tag{12}$$

and

$$T = \frac{\sigma_{kk}/3}{\sqrt{\frac{3}{2}\sigma' : \sigma'}} \tag{13}$$

where T is the stress triaxiality and ϵ is related to the third stress invariant; see [23].

– During localized deformation:

The challenge to the post-localized evolution of void aspect ratio and orientation resides in the kinematic cell boundary conditions during localized yielding. In particular, it amounts to intercepting the rigid-like zones (see Fig. 1b) with specific tangential points that depart from the void poles with the void being rotated. See Fig. 1.

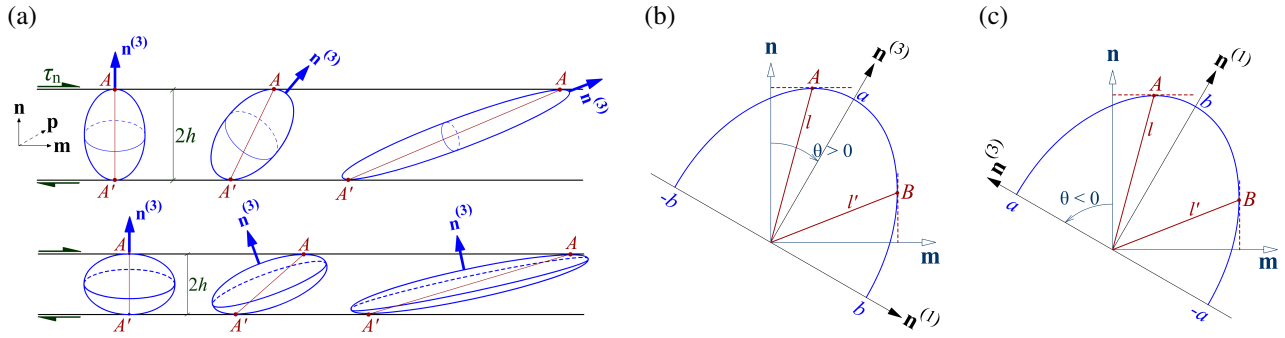

Figure 1: (a) Schematized post–localized deformation mechanism, and (b,c) the angles driving the evolved geometry for a spheroidal void under a shear field: (b) a prolate void ($w > 1$), (c) an oblate void ($w < 1$).

To obtain the post-localized differential equation for void aspect ratio w, the time rate of ℓ (shown in Fig. 1) should be developed on the account that the top and bottom void boundaries are attached to the rigid zones. The reader can refer to Eq's (A-10)–(A-15) as basics and Appendix C for derivation details. In essence, one can write:

$$\dot{s} = \frac{(w^2+\mathscr{T}^2)^2}{(w^4+\mathscr{T}^2)(1+\mathscr{T}^2)\left[2-3\frac{\mathscr{T}^2(2w^2-w^4+\mathscr{T}^2)}{(w^4+\mathscr{T}^2)(w^2+\mathscr{T}^2)}\right]}\left[\left(\frac{3}{c}-\frac{(w^4+\mathscr{T}^2)(1+\mathscr{T}^2)}{f(w^2+\mathscr{T}^2)^2}\right)D_{\mathrm{nn}}+\frac{6}{c}\frac{(w^2-1)\mathscr{T}}{w^2+\mathscr{T}^2}D_{\mathrm{nm}}\right] \tag{14}$$

for prolate voids ($w > 1$), and

$$\dot{s} = \frac{(w^2+\mathscr{T}^2)^2}{(w^4+\mathscr{T}^2)(1+\mathscr{T}^2)\left[1-\frac{\mathscr{T}^2(-2w^2+w^4-\mathscr{T}^2)}{(w^4+\mathscr{T}^2)(w^2+\mathscr{T}^2)}\right]}\left[\left(-\frac{3}{c}+\frac{(w^4+\mathscr{T}^2)(1+\mathscr{T}^2)}{f(w^2+\mathscr{T}^2)^2}\right)D_{\mathrm{nn}}-\frac{6}{c}\frac{(w^2-1)\mathscr{T}}{w^2+\mathscr{T}^2}D_{\mathrm{nm}}\right] \tag{15}$$

for oblate voids ($w < 1$). Here,

$$D_{\mathrm{nn}} = \mathbf{n}\cdot\mathbf{D}^{\mathrm{p}}\mathbf{n}$$
$$D_{\mathrm{mn}} = \mathbf{m}\cdot\mathbf{D}^{\mathrm{p}}\mathbf{n}$$

with the elastic strains neglected.

Note, for the special case of an upright void, that Eq. (14) simplifies into Eq. (12) of [33]. See Appendix C for more details and special cases.

2.4 Cell aspect ratio

A judicious method that enables to update the cell aspect ratio as function of the normal to the ligament $\mathbf{n}$ is that proposed by Leblond and Mottet [38], originally derived for a cubic initial unit cell. This method delivers the following relation for an initially orthorhombic cell:

$$\lambda(\mathbf{n}) = \frac{\lambda_0(\mathbf{n})}{\sqrt{\mathcal{J}}}\left(\mathbf{n}\cdot(\mathbf{F}\mathbf{F}^{\mathrm{T}})\mathbf{n}\right)^{\frac{3}{4}} \tag{16}$$

where $\mathbf{F}$ is the total deformation gradient, with its associated determinant $\mathcal{J} := \det\mathbf{F}$. See Appendix D for justification.

Remark 1: Under combined tensile and shear loadings, λ should never fall below its initial value λ_0. Hence, λ is replaced with λ_0 in case $\lambda \leq \lambda_0$.

Remark 2: The gauge functions Φ^{H} and Φ^{I} operate with spheroidally and cylindrically idealized voids, respectively, which cannot distinguish between the void and cell aspect ratios within the m–n and p–n planes. Yet, it is possible to evaluate the separate values of void and cell aspect ratios as well as the void axes within the two planes, as post-processed parameters. See Appendix F for more details. A recent work by Morin *et al.* reports internal state variables predicted from numerical implementation of the model proposed by Madou and Leblond [39], developed for an *ellipsoidal* void which directly operates as function of the separate void aspect ratios [40]. Nevertheless, the post-localized process therein is modeled heuristically with the aid of an accelerated porosity, which is not the aim of the present work.

2.5 Porosity

Throughout the plastic deformation process, f is governed by the plastic incompressibility law such that:

$$\dot{f} = (1-f)D^{\mathrm{p}}_{kk} = (1-f)\,\dot{\Lambda}\frac{\partial \Phi}{\partial \sigma_{\mathrm{m}}} \tag{17}$$

with $\dot{\Lambda}$ being the plastic multiplier in rate form.

2.6 Void orientation

In general, the rate of rotation of the (immaterial) principal axes of the void may be directly obtained from the (material) rotation and strain rates of the void [41, 42], denoted by $\mathbf{\Omega}^v$ and $\mathbf{D}^v$, respectively. Thus, the rate of change of the void axis is given by the following

$$\dot{\mathbf{n}}^{(3)} = \omega \mathbf{n}^{(3)}, \qquad \omega = \mathbf{\Omega}^v + \mathbf{\Omega}^l \tag{18}$$

where the rotation tensor ω is the total spin tensor that consists of the void spin, $\mathbf{\Omega}^v$, superposed by the void rotation with respect to the material, $\mathbf{\Omega}^l$. Here, we exploit $\mathbf{\Omega}^v$ as derived in [41, 42] during the nearly-homogeneous deformation process, and confine it to the plastic ligament at the post-localized deformation. Namely:

– During nearly-homogeneous deformation:

$$\mathbf{\Omega}^v = \mathbf{\Omega} - \mathbb{C} : \mathbf{D}^{\mathrm{p}} \tag{19}$$

– During the post-localized deformation:

$$\mathbf{\Omega}^v = \mathbf{\Omega} - \frac{1}{c}\mathbb{C} : \mathbf{D}^{\mathrm{p}} \tag{20}$$

where $\mathbb{C}$ is the fourth order spin concentration tensor given by

$$\mathbb{C} = -(1-f)\mathbb{P} : \mathbb{A}, \qquad \mathbb{A} = [\mathbb{I} - (1-f)\mathbb{S}]^{-1} \tag{21}$$

with $\mathbb{A}$ the strain concentration tensor and $\mathbb{P}$ and $\mathbb{S}$ the Eshelby tensors [43] for a spheroidal inclusion of zero stiffness in an incompressible linear viscous matrix. Note that a $1/c$ term appears in (20) to represent the plastic rate of deformation inside the ligament.

Also, in (18) $\mathbf{\Omega}^l$ is an additional contribution to the effective void rotation that comes from mere distortion of void boundaries under the combined effect of tension and shear.

– During nearly-homogeneous deformation:
By defining the plastic spin tensor as $\mathbf{\Omega}^{\mathrm{p}} = \mathbf{\Omega} - \omega$, one can write, during the nearly-homogeneous deformation:

$$\mathbf{\Omega}^{\mathrm{l}} = \frac{1}{2} \sum_{i \neq j,\, w_i \neq w_j} \frac{w_i^2 + w_j^2}{w_i^2 - w_j^2} \left[(\mathbf{n}_i \otimes \mathbf{n}_j + \mathbf{n}_j \otimes \mathbf{n}_i) : \mathbb{A} : \mathbf{D}^{\mathrm{p}} \right] \mathbf{n}_i \otimes \mathbf{n}_j \tag{22}$$

Then, by combining Eq's (19), (22), and (18), and by adopting the notation $w_1 = w_2 = w$ and $w_3 = 1$, one can evaluate the components of ω with respect to a laboratory frame. The case $w = 1$, however, requires a careful treatment; see [34].

– During localized deformation:
The post-localized $\mathbf{\Omega}^l$ should be rederived from first principles. Madou and Leblond [42] have shown that the general form initiated in [27, 41] requires significant amendments due to strong nonlinear effects. They did so by introducing heuristic coefficients calibrated using a large number of finite-element based limit analyses. Here we obtain simpler, parameter-free and probably more accurate equations by considering the constrained kinematics pertaining to post-localization. Namely, this involves plastic incompressibility of the intervoid ligament and the fact that the top and bottom boundaries of the void move rigidly with the above and bottom material layers. Upon the steps clarified in Appendix E, the post-localized $\mathbf{\Omega}^l$ reads:

$$\mathbf{\Omega}^l = \frac{\dot{S}}{S} \mathbf{m} \otimes \mathbf{m} + \frac{\dot{C}}{C} \mathbf{n} \otimes \mathbf{n} = \frac{\dot{\mathscr{T}}}{\mathscr{T}} \left(C^2 \mathbf{m} \otimes \mathbf{m} - S^2 \mathbf{n} \otimes \mathbf{n} \right) \tag{23}$$

where $\dot{\mathscr{T}}$ obeys the following equation

$$\dot{\mathscr{T}} = \frac{(\mathscr{T}^2 + w^2)(1 + \mathscr{T}^2)}{\mathscr{T}(1 - w^2)} \left[\frac{\dot{c}}{c} - \frac{1}{3} \left(\frac{\dot{f}}{f} - 2 \frac{\dot{\lambda}}{\lambda} \right) + \left(\frac{1}{3} - \frac{w^2}{\mathscr{T}^2 + w^2} \right) \dot{s} \right] \tag{24}$$

where

$$\begin{aligned} \frac{\dot{c}}{c} &= \frac{1 - c}{c} \mathbf{n} \cdot \mathbf{D}^{\mathrm{p}} \mathbf{n} \\ \frac{\dot{f}}{f} &= \left(\frac{1}{f} - 1 \right) D^{\mathrm{p}}_{kk} \\ \frac{\dot{\lambda}}{\lambda} &= D_{\mathrm{nn}} - \frac{1}{2} \left(D_{\mathrm{mm}} + D_{\mathrm{pp}} \right) \end{aligned} \tag{25}$$

with

$$D_{\mathrm{nn}} = \mathbf{n} \cdot \mathbf{D}^{\mathrm{p}} \mathbf{n} \quad , \quad D_{\mathrm{mm}} = \mathbf{m} \cdot \mathbf{D}^{\mathrm{p}} \mathbf{m} \quad , \quad D_{\mathrm{pp}} = \mathbf{p} \cdot \mathbf{D}^{\mathrm{p}} \mathbf{p}$$

and $\mathbf{p} = \mathbf{n} \times \mathbf{m}$ completes the triad of local base vectors.

Remark: $\dot{\mathscr{T}}$, according to (A-33), for the special case of an upright void with respect to normal $\mathbf{n}$ ($\mathscr{T} = 0$) simplifies into

$$\dot{\mathscr{T}} = -\frac{2}{3} \frac{w^2}{\mathscr{T}(1 - w^2)} \dot{s}$$

which, considering $\dot{s} > 0$ for a prolate void (see Eq. (A-23)) and $\dot{s} < 0$ for an oblate void (see Eq. (A-27)), delivers $\dot{\mathscr{T}} > 0$ for a prolate void and $\dot{\mathscr{T}} < 0$ for an oblate void under a positively directed

(rightward) shear field. By the same token, for a void after extreme shearing in a shear-dominated field ($\mathscr{T} \longrightarrow \infty$), it delivers

$$\dot{\mathscr{T}} \approx -\frac{1+\mathscr{T}^2}{\mathscr{T}}\left(\frac{1}{3}-w\right)\dot{s}$$

for a prolate void (at the $w \longrightarrow \infty$ limit), and

$$\dot{\mathscr{T}} \approx \frac{\mathscr{T}}{3}(1+\mathscr{T}^2)\dot{s}$$

for an oblate void (at the $w \longrightarrow 0$ limit), which are both positive limits. Therefore, it can be realized that, as schematized in Fig. 1, both prolate and oblate voids under a positively directed shear field reach a steady state rightward orientation. The transient rate of orientation, however, differs in the sense that a prolate void rotates rightward throughout the process whereas an oblate void rotates leftward transiently until it starts rotating rightward and continues until failure.

2.7 Equivalent plastic strain

The evolution of equivalent plastic strain $\bar{\epsilon}$ is obtained through the formation of plastic work equivalence between the macroscopic material and the sole matrix, written as

$$\sigma : \mathbf{D}^{\mathrm{p}} = (1-f)\bar{\sigma}\dot{\bar{\epsilon}} \tag{26}$$

where $\bar{\sigma}$ correlates with $\bar{\epsilon}$ through (28). Within the adopted solution scheme, Eq. (26 is utilized for calculating the residual associated with $\bar{\epsilon}$, as pointed out in Sec. 4. It is noteworthy that, at the post-localized regime, Eq. (26) can be exploited to update the plastic multiplier $\dot{\Lambda}$ explicitly by rearranging in the following format:

$$\dot{\Lambda} = (1-f)\frac{\bar{\sigma}\dot{\bar{\epsilon}}}{\sigma : \mathbf{N}} \quad , \quad \mathbf{N} = \frac{\partial \Phi^{\mathrm{I}}}{\partial \sigma} \tag{27}$$

3 Hybrid Model of Ductile Fracture

Preparatory to the definition of a hybrid fracture model, we shall conceptualize homogeneous vs. inhomogeneous yielding. The distinction between homogeneous and inhomogeneous yielding pertains to plastic deformation at the unit cell level. If a unit cell of arbitrary geometry deforms uniformly inside, and thus over its boundary, the plastic deformation is here named "homogeneous", otherwise termed "inhomogeneous". A popular case of inhomogeneous yielding arises from elastic unloading [12], whereafter strain rates become localized inside an inner-void ligament with *finite* thickness. This must, however, be clearly dissociated from Rice's theory of plastic localization [18], whereby strain rates can localize inside a band with *vanishing* thickness. This distinction is of utmost importance in porous material plasticity particularly where voids can act as initial heterogeneity. Among the featured homogeneous and inhomogeneous yielding processes are void growth and void coalescence, respectively. Nevertheless, the present-invoked terminology is more inclusive than the given examples. Consequent to tension superposed with shear, for instance, voids may grow or shrink down to *void closure* while plastic deformation is homogeneous at the cell level (depending on the ratio between normal and shear stresses). By the same token, yielding is inhomogeneous (almost) from the outset (see [31] for clear illustration) in that plasticity is majorly confined to a close vicinity of the void. Yet, void coalescence and failure might never be realized when the void volume fraction approaches zero (the limit to a dilute matrix). Example cases will be observed in the sequel.

The initial state in the numerical simulation of ductile fracture can be typically characterized with an underlying microstructure. A typical underlying microstructure with periodic or clustered arrays of voids is schematically shown in Fig. 2.

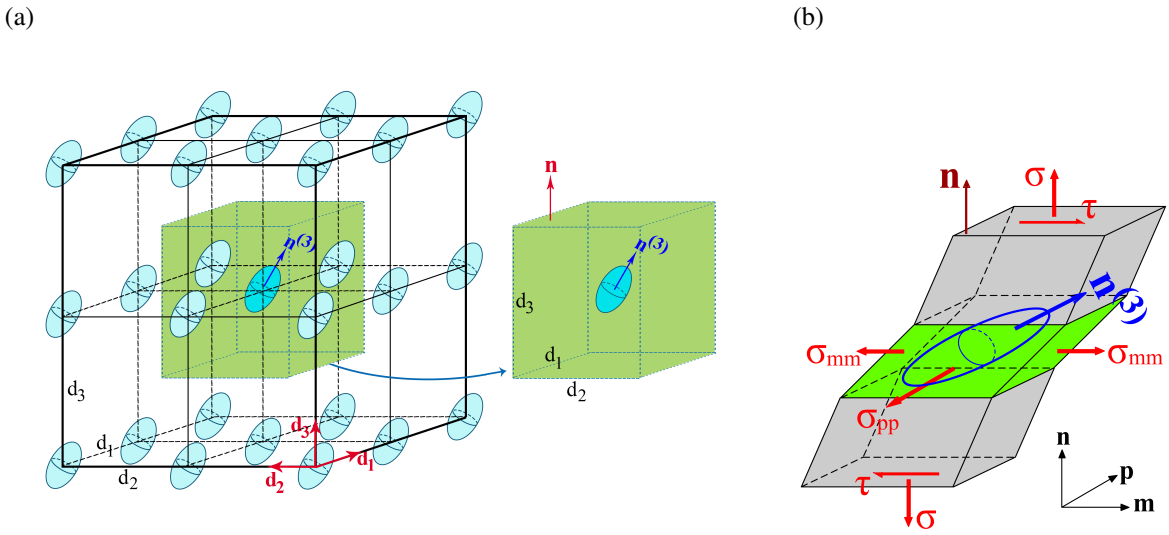

Figure 2: (a) Relative positioning of voids in a latticed distribution, accompanied by its equivalent orthorhombic unit cell (RVE) associated with normal $\mathbf{n}$ with geometric properties averaged over the tributary volume around the central void. (b) unit cell deformed under the effect of combined tension and shear.

The microstrucrural geometry can then be described with the aid of a representative volume element (RVE) constituted from the tributary volume surrounding the central void, as schematized in Fig. 2a. The same underlying microstructure can accommodate localized deformation inside several possible planes. These planes would give rise to the notion of "localization systems" describing the manner by which voids lying within a plane can interconnect. Each adopted plane of localization and, accordingly, the resulting RVE would then be identified with a normal vector $\mathbf{n}$ corresponding to the tributary plane. In the simplest case, the cell can be regarded initially orthorhombic which, after shearing, transforms (approximately) into monoclinic, as shown in Fig. 2b. Even upon this simplification, the macroscopic response of this cell is not solvable, be the yielding mechanism homogeneous or inhomogeneous. Rather, it is attainable through idealized elementary cells that can be utilized in the derivation of both the yield function and its corresponding evolution equations.

By definition, a *hybrid* model is founded on the microstructural state as idealized via different representative volume elements (RVE's) during various yielding mechanisms, here exemplified by homogeneous and inhomogeneous processes. The building blocks of the present hybrid model are two yield surfaces in the stress space expressed basically as $\Phi^{\mathrm{H}}(\sigma; f, w, \mathbf{n}^{(3)}) = 0$ and $\Phi^{\mathrm{I}}(\sigma; f, w, \lambda, \mathbf{n}^{(3)}, \mathbf{n}) = 0$, where the yield functions Φ^{H} and Φ^{I} correspond to homogeneous and inhomogeneous deformation of the cell, respectively. f is defined as the void volume fraction (porosity), w is the void aspect ratio, $\mathbf{n}^{(3)}$ is the void orientation determined by its main axis direction, and $\mathbf{n}$ is the plane in which plastic strains can localize and voids can impinge.

In the present context, Φ^{H} follows the model derived by Keralavarma and Benzerga [34], and Φ^{I} is the model after Torki *et al.* [24]. The assumptions underlying the mathematical modeling of homogeneous yielding allow for arbitrary orientation of voids whereas inhomogeneous yielding is only warranted within localization planes. For the sake of simplicity, the presently derived inhomogeneous yield conditions have been developed with the void being codirectional with the normal to the localization plane $\mathbf{n}$. To remedy this constraint, the real microstructure is mapped into a *surrogate* one, identified with a surrogate void aligned with $\mathbf{n}$. Upon reliance on an underlying microstructure, inhomogeneous deformation can be realized over more than one possible localization plane $\mathbf{n}$. Considering the notion of a multi-surface model, the

effective flow rule is normally expressed as a linear combination of all potentially involved flow potentials that include, herein, Φ^{H} and several feasible Φ^{I}'s in a concurrent manner. Rather, the model at the present stage accounts for a consecutive advancement of mechanisms. That is, the most favorable mechanism is triggered at every time step by considering the $\Phi = 0$ that is met first. The prime objective within this paper is to predict the constitutive behavior of a porous material at a single cell level regarded as a single point in space. Only one localization mode, out of all, has therefore been involved in the formulation. Yet, the normal to the only localization plane $\mathbf{n}$ is generally subjected to change as function of the deformation gradient tensor $\mathbf{F}$, which will be reflected in Eq. (3). It is worthy of note that the Kuhn-Tucker condition [44] is trivially satisfied in the present context owing to the lack of elastic unloading at the macro scale.

Both yield functions are expressed in terms of the stress space normalized by the matrix effective stress $\bar{\sigma}$. The latter is normally taken to depend on some effective plastic strain $\bar{\epsilon}$ as its conjugate strain. Here, the two are related through a power law of the form:

$$\bar{\sigma} = \sigma_0 \left(1 + \frac{\bar{\epsilon}}{\epsilon_0}\right)^N \tag{28}$$

with σ_0 the initial yield strength and N the hardening exponent.

Remark: As schematized in Fig. 3 and suggested by direct FEM modeling [21, 35], the de facto mechanism within the RVE under combined tension and shear as well as under shear dominance (Fig. 3c) is an intermediate mechanism between the fully homogeneous (Fig. 3a) and fully localized (Fig. 3b) extremes. As such, it is closer to the former at early stages and it approaches the latter end with further advancement of shearing. Therefore, both Φ^{H} and Φ^{I} are subject to some modification in order for the hybrid model be accountable for a thoroughly reliable simulation.

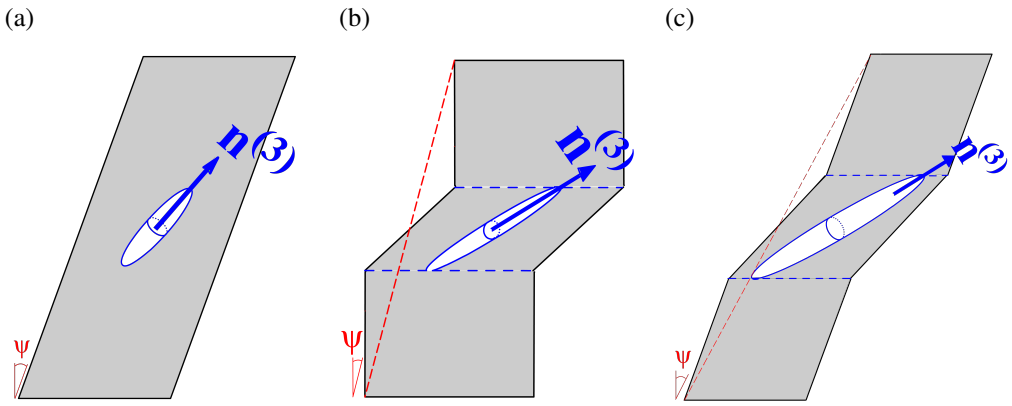

Figure 3: Predicted deformation mechanisms under near-simple shearing: (a) totally homogeneous extreme, (b) totally localized extreme (a) de facto inhomogeneous mechanism.

The following subsections thus present both models in modified form.

3.1 Nearly-homogeneous yielding

The geometric framework associated with nearly-homogeneous yielding, is that for a porous plastic solid composed of a plastically anisotropic matrix containing aligned spheroidal voids with arbitrary initial orientations [34]. Within this framework, the voids are taken as spheroidal, with two equal lateral radii (denoted with b) and a third mismatching radius (known as a) considered as the main semiaxis, as schematized in Fig.

1a. Correspondingly, $\mathbf{n}^{(3)}$ denotes the void axis along the main radius a, and $\mathbf{n}^{(1)}$ and $\mathbf{n}^{(2)}$ are orthogonal base vectors arbitrarily chosen in the transverse plane. This model incorporates the combined effects due to void shape and interaction, as well as that of matrix anisotropy, as being disregarded in this context. With matrix anisotropy disregarded, however, this criterion almost reduces to the GLD model [26] with minimal difference lying in the incorporation of void shape effects. The model can be generally expressed in the following form:

$$\Phi^{\mathrm{H}}(\sigma; f, w, \mathbf{n}^{(3)}) = C\frac{\sigma_{\mathrm{eq}}^2}{\bar{\sigma}^2} + 2(g+1)(g+qf)\cosh\left(\kappa\frac{\sigma:\mathbf{X}}{\bar{\sigma}}\right) - (g+1)^2 - (g+qf)^2 \tag{29}$$

with $f = \omega/\Omega$ and $w = a/b$ denoting void volume fraction (porosity) and aspect ratio, respectively. Here, a and b denote, respectively, the spheroidal void's major and minor semi-axes. Every spheroid can be uniquely identified by a main radius a that defines the void orientation $\mathbf{n}^{(3)}$ and two equal radii $b_1 = b_2 = b$ arbitrarily defined along perpendicular directions in the plane normal to $\mathbf{n}^{(3)}$, identified with $\mathbf{n}^{(1)}$ and $\mathbf{n}^{(2)}$. $w > 1$, $w < 1$ and $w = 1$ would then signify, respectively, a prolate, an oblate, and a spherical void. The porosity f within Φ^{H} is multiplied by a q factor which enables Φ^{H} to capture stress states near simple shearing, which should be above 4/3 [45, 46]. In the present context, the value proposed by Perrin and Leblond [47], $q = 4/e \approx 1.47$ is used. Also, σ_{eq} is the von-Mises equivalent stress as function of a Hill-type anisotropy tensor [48] which, for an isotropic matrix material, can be stated as

$$\sigma_{\mathrm{eq}}^2 = \frac{3}{2}\sigma : \mathbb{K} : \sigma \tag{30}$$

where $\mathbb{K}$ is related to Hill's tensor $\mathbb{p}$, reducing to $\mathbb{J}$ for an isotropic matrix, through

$$\mathbb{K} \equiv \mathbb{J} + \eta(\mathbf{X}\otimes\mathbf{Q} + \mathbf{Q}\otimes\mathbf{X}), \;\; \mathbb{J} \equiv \mathbb{I} - \frac{1}{3}\mathbf{I}\otimes\mathbf{I} \tag{31}$$

with $\mathbf{Q}$ and $\mathbf{X}$ written as

$$\begin{aligned}
\mathbf{Q} =& -\frac{1}{2}(\mathbf{n}^{(1)}\otimes\mathbf{n}^{(1)} + \mathbf{n}^{(2)}\otimes\mathbf{n}^{(2)}) + \mathbf{n}^{(3)}\otimes\mathbf{n}^{(3)} \\
\mathbf{X}^v =& \alpha_1(\mathbf{n}^{(1)}\otimes\mathbf{n}^{(1)} + \mathbf{n}^{(2)}\otimes\mathbf{n}^{(2)}) + (1-2\alpha_1)\mathbf{n}^{(3)}\otimes\mathbf{n}^{(3)} \quad , \quad \alpha_1 = \hat{\alpha}_1(w) \\
\mathbf{X} =& \alpha_2(\mathbf{n}^{(1)}\otimes\mathbf{n}^{(1)} + \mathbf{n}^{(2)}\otimes\mathbf{n}^{(2)}) + (1-2\alpha_2)\mathbf{n}^{(3)}\otimes\mathbf{n}^{(3)} \quad , \quad \alpha_2 = \hat{\alpha}_2(f)
\end{aligned} \tag{32}$$

and, as formerly stated, $\mathbf{n}^{(3)}$ is the void axis and $\mathbf{n}^{(1)}$ and $\mathbf{n}^{(2)}$ are orthogonal base vectors arbitrarily chosen in the transverse (perpendicular) plane. $\mathbf{X}^v$ is a counterpart of $\mathbf{X}$ that will be later utilized in the evolution equations for w and $\mathbf{n}^{(3)}$, in Eq. (10) for instance. $\bar{\sigma}$ is the isotropic matrix yield strength. Moreover, the expressions of C, g and κ in (29) as well as η in (31) and α_2, as functions of f, w, and/or $\mathbb{K}$ are provided in Appendix A. $\mathbb{J}$ denotes the deviatoric projection operator, $J_{ijkl} = \frac{1}{2}(\delta_{ik}\delta_{jl} + \delta_{il}\delta_{jk}) - \frac{1}{3}\delta_{ij}\delta_{kl}$ componentwise.

3.2 Inhomogeneous yielding

The yield function accounting for inhomongeneous yielding (including void coalescence) is the resultant of a localized homogenization of plastic dissipation over a cylindrical matrix embedding a coaxial cylindrical void. With full appreciation of all well-motivated models (examples of which could be found in [24, 25, 33, 49]), this model, in its base form, is the first analytical model describing void coalescence under a combination of internal necking and shearing, which has been proposed by Torki *et al.* [24]. Known as the

T–B–L model, it can be written in the form below:

$$\Phi^{\mathrm{I}}(\sigma; f, w, \lambda, \mathbf{n}^{(3)}, \mathbf{n}) = \begin{cases} \left(\dfrac{|\sigma_{\mathrm{n}}| - t(\bar{\chi}, \bar{w})\mathcal{S}}{b\mathcal{V}}\right)^2 + \left(\dfrac{\tau_{\mathrm{n}}}{\mathcal{T}}\right)^2 - 1 & \text{for } |\sigma_{\mathrm{n}}| \geq t\mathcal{S} \\ \left(\dfrac{\tau_{\mathrm{n}}}{\mathcal{T}}\right)^2 - 1 & \text{for } |\sigma_{\mathrm{n}}| \leq t\mathcal{S} \end{cases} \tag{33}$$

where $\sigma_{\mathrm{n}} = \mathbf{n}.\sigma\mathbf{n}$, $\tau_{\mathrm{n}} = |\sigma\mathbf{n} - \sigma_{\mathrm{n}}\mathbf{n}|$ are, respectively, the normal and shear tractions on the selected plane of localization (see Sec. 2.1 for further details), and

$$\begin{aligned} \frac{\mathcal{V}}{\bar{\tau}} &= 2 - \sqrt{1 + 3\bar{\chi}^4} + \ln \frac{1 + \sqrt{1 + 3\bar{\chi}^4}}{3\bar{\chi}^2} \\ \frac{\mathcal{S}}{\bar{\tau}} &= \frac{1}{3}\frac{\bar{\chi}^3 - 3\bar{\chi} + 2}{\bar{\chi}\bar{w}} \\ \frac{\mathcal{T}}{\bar{\tau}} &= 1 - (q_\chi \bar{\chi})^2 \end{aligned} \tag{34}$$

with $q_\chi = 1$ in its basic form. The effective ligament parameter, $\bar{\chi}$, and effective void aspect ratio, $\bar{w}$, correspond to a surrogate cylindrical void with axis $\mathbf{n}$. The exact shape, spheroidal versus cylindrical, has been seen to have minimal incidence on yielding [50]. However, equations (33) were derived for cylindrical voids [24], thus the choice made here.

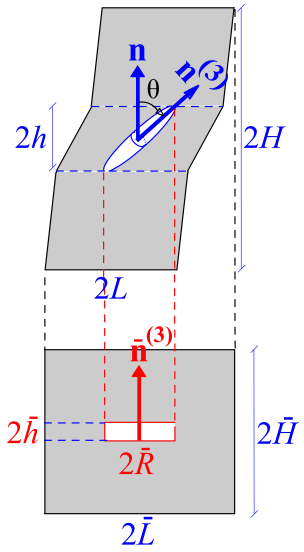

Figure 4: Surrogate configuration of a cell under combined tension and shear.

With reference to the surrogate RVE shown in Fig. 4, the surrogate parameters read

$$\begin{aligned} \bar{\chi}(\mathbf{n}) &= \frac{\bar{R}(\mathbf{n})}{\bar{L}(\mathbf{n})} \\ \bar{w}(\mathbf{n}) &= \frac{h(\mathbf{n})}{\bar{R}(\mathbf{n})} \\ \bar{\lambda}(\mathbf{n}) &= \frac{H(\mathbf{n})}{\bar{L}(\mathbf{n})} \end{aligned} \tag{35}$$

where the third parameter does not enter into Φ^{I} though being indirectly influential.

The modification factors (t, b) are chosen so as to extend the capability of the model into the limits of penny-shaped cracks ($w \longrightarrow 0$). With reference to [24], they read:

$$\begin{aligned} t(\bar{\chi}, \bar{w}) &= \frac{(t_0 + t_1\sqrt{\bar{\chi}})\bar{w}}{1 + (t_0 + t_1\sqrt{\bar{\chi}})\bar{w}} \\ b &= b_0 \\ l(\bar{\chi}, \bar{w}) &= 1 + \left(l_0 + l_1\sqrt{\bar{\chi}}\right)\bar{w} \end{aligned} \tag{36}$$

where t_0 and t_1 are adjustable parameters to be determined in conformity with numerical data, which could be taken as $(t_0, t_1, b_0, l_0, l_1) = (-0.84, 12.9, 0.9, -0.15, 0.035)$ for the time being [24]. Note $(l_0, l_1) = (0, 0)$ for $\bar{\chi} \leq 0.2$.

The q_χ factor does not exist in [24] but is hereby introduced since the shear stress response based on the present Φ^{I} is overconstrained despite being physically descriptive (see Appendix I). This overconstraint is partly due to plasticity ideally confined to the inter-void ligament and partly to the notion of $\bar{\chi}$ via the surrogate cell. The latter is revealed by recent cell-level calculations [21] where, at a state of shear domination, plastic deformation is inhomogeneous throughout, yet initially more diffuse than being confined inside the ligament, though it being more significant within a cubic cell region around the void (see Fig. 5c). The latter is also revealed by Appendix I. This overconstraint is strongly suggestive of a calibration to Φ^{I} whereby the effect of $\bar{\chi}$ in the shear term $\mathcal{T}$ or the corresponding evolution of void orientation is retarded based on physics. The following simple form is proposed for q_χ in the present context:

$$q_\chi = \left(q_0 + \frac{q_\infty - q_0}{q_0/\kappa^2 + 1}\right)(1 + \psi) \tag{37}$$

with $q_\infty = 1$ (pertaining to the absence of shear) and q_0 being function of boundary conditions and void geometry. To the best of the authors' knowledge, $q_0 = 1/3$ and $q_0 = 1/4$ can deliver the most reasonable conformity with FEM values, respectively, for spheroidal and cylindrical voids under axisymmetric and plane stress conditions. The above values increase to $q_0 = 1/2$ and $q_0 = 1/3$ in plane strain. Focus in the present context, however, is placed on spheroidal voids in plane stress. Also, $\kappa \equiv \sigma_{\mathrm{n}}/\tau_{\mathrm{n}}$ is the ratio between the normal and shear tractions on the plane of localization, and $\psi = \tan^{-1}\gamma_{\mathrm{mn}}$ is the shear angle in the $\mathbf{m}$–$\mathbf{n}$ plane.

The concept of a surrogate microstructure is key to the prediction of the onset of inhomogeneous deformation and the microstrucrural evolution thereof. It involves replacing the rotating void with an upright cylinder of axis $\mathbf{n}$, having the same volume and porosity, Fig. 4. This identification is needed for applicability of yield function Φ^{I}. It implies introducing an effective void aspect ratio, $\bar{w} \equiv \bar{h}/\bar{R}$, and an effective ligament parameter, $\bar{\chi} \equiv \bar{R}/\bar{L}$, related to the internal parameters of the actual microstructure through the following steps. The effective void aspect ratio, $\bar{w}$, can be obtained according to Eq. (A-13), considering $\bar{R} = \ell' \cos\beta'$, by writing

$$\cos^2\beta' = \frac{1}{1 + \tan^2\beta'} = \frac{(1 + \mathscr{T}^2 w^2)^2}{(1 + \mathscr{T}^2)(1 + \mathscr{T}^2 w^4)} \tag{38}$$

Also, volume preservation between the main and surrogate microstructures requires

$$\frac{2\pi}{3\gamma} b^2 a = 2\pi \bar{R}^2 \bar{h} \;\therefore\; \bar{h} = \frac{1}{3\gamma}\left(\frac{b}{\bar{R}}\right)^2 a \implies \bar{w} = \frac{1}{3\gamma w^2}\left(\frac{a}{\bar{R}}\right)^3 \tag{39}$$

However, since

$$\frac{a}{\bar{R}} = \frac{1}{\frac{\ell'}{a}\cos\beta'}$$

then, (A-15) and (39) deliver

$$\bar{w} = \frac{w}{3\gamma}\left(\frac{1+\mathscr{T}^2}{1+\mathscr{T}^2 w^2}\right)^{\frac{3}{2}} \tag{40}$$

Remark: $\bar{w}$, according to (40), for the special case of an upright void with respect to normal $\mathbf{n}$ ($\mathscr{T}=0$) simplifies into

$$\bar{w} = \frac{w}{3\gamma} = \frac{2}{3}w$$

All the same, for an elongated void ($w \longrightarrow \infty$), even when shearing is not extreme:

$$\bar{w} \approx \frac{1}{3\gamma \mathscr{T}^3 w^2} \approx 0$$

which is obviously also zero after extreme shearing ($\mathscr{T} \longrightarrow \infty$). By the same token, for a disk-like void ($w \longrightarrow 0$), even when shearing is not extreme:

$$\bar{w} \approx \frac{w}{3\gamma}(1+\mathscr{T}^2)^{\frac{3}{2}} \approx 0$$

which is obviously also zero after extreme shearing ($\mathscr{T} \longrightarrow 0$).

Indeed, thanks to the volume-preserving mapping between the main and surrogate microstructures, porosity f is common to all localization systems. The ligament parameter $\bar{\chi}$ can then correlate with f, $\bar{w}$, and $\bar{\lambda}$. It can be easily verified, from separate equality in void volumes and cell volumes, that

$$\bar{\chi} = \left(\frac{f\bar{\lambda}}{\bar{w}}\right)^{\frac{1}{3}} \tag{41}$$

where $\bar{\lambda}$ denotes the aspect ratio of the surrogate cell (as shown in Fig. 4) and is obtained from:

$$\bar{\lambda} = \frac{\lambda}{(1+\gamma_{\mathrm{mn}})^3} \tag{42}$$

where $\gamma_{\mathrm{mn}} = 2\mathbf{m}\cdot\mathbf{En}$, $\mathbf{E} = \int \mathbf{D}\,\mathrm{d}t$, and λ is evolved using (A-32).

Remark 1: Since, for a spheroidal void, the void poles can never reach the cell corners, the following counterpart of (42) is recommended to avoid computational errors at extreme shearing:

$$\bar{\lambda} = \frac{\lambda}{(1+\eta\gamma_{\mathrm{mn}})^3} \tag{43}$$

with $0.9 \leq \eta < 1$. In the present context, η has been considered 0.9 throughout.

Remark 2: In simple shear, the void rotates *faster* than the material so that $\bar{\chi}$ would increase, unlike the actual ligament parameter $\chi \equiv R/L$ that decreases with shearing. It is worth noting that an elementary estimation of the limit load in simple shear for the inclined void shown in Fig. 4a delivers $\tau = (1-\chi^2)\bar{\tau}$ irrespective of the void inclination, with χ, not $\bar{\chi}$, appearing in the equation. This simple estimate is contrary to the projection-guided estimate of Eq. (33), and would trigger a monotonically increasing stress response that can never exhibit failure. Admittedly, this simplistic Gurson-like shear field performs poorly for inclined voids, especially at large values of χ. An indication of that may be inferred from three-dimensional calculations for elongated voids reported in [25].

4 Time Integration of Constitutive Equations

4.1 Constitutive framework

Following the additivity premise, the total rate of deformation tensor $\mathbf{D}$ is decomposed in the following format [44]:

$$\mathbf{D} = \mathbf{D}^{\mathrm{e}} + \mathbf{D}^{\mathrm{p}}, \tag{44}$$

where the elastic part is given by:

$$\mathbf{D}^{\mathrm{e}} = \mathbb{L}^{-1} : \overset{\triangledown}{\sigma} \tag{45}$$

with $\mathbb{L}$ the isotropic tensor of elastic moduli which can be expressed, for an isotropic material, as

$$\mathbb{L} = 2\mu\mathbb{J} + K\mathbf{I} \otimes \mathbf{I} \tag{46}$$

where $K = E/3(1-2\nu)$ and $\mu = E/2(1+\nu)$ are, respectively, the shear and bulk moduli, $\mathbf{I}$ is the second-order identity tensor, and $\mathbb{J}$ has been defined in advance.

Further, $\overset{\triangledown}{\sigma}$ denotes the Jaumann objective stress rate defined by:

$$\overset{\triangledown}{\sigma} = \dot{\sigma} + \sigma\mathbf{\Omega} - \mathbf{\Omega}\sigma, \tag{47}$$

where $\mathbf{\Omega}$ is the skew symmetric part of the velocity gradient.

All the same, the plastic part of $\mathbf{D}$ originates from normality to a yield surface represented by a flow potential $\Phi = 0$ via the following relation:

$$\mathbf{D}^{\mathrm{p}} = \dot{\Lambda}\frac{\partial \Phi^{\mathrm{eff}}}{\partial \sigma} \tag{48}$$

where Λ is the plastic multiplier associated with the plastic strain tensor, and Φ^{eff} is the effective yield function, emanating from the innermost surface between those corresponding to Φ^{H} and Φ^{I} in the adopted consecutive approach.

The hybrid model presented in the foregoing sections is formulated within a corotational framework. That is, the constitutive relations are expressed in an intermediate configuration, which is rotated from the current one by the instantaneous rotation tensor $\mathbf{R}$ that results from the polar decomposition of the incremental deformation gradient as:

$$\mathbf{\Delta F} = \mathbf{RU} \tag{49}$$

Constitutive laws, therefore, need be written in the rotated configuration, with quantities indicated by the tilde ($\sim$) symbol. The so-derived equations relate merely with the stretch part of deformations, and the rotation part is admitted by rotating quantities to the intermediate configuration. The objective rate of stress $\overset{\triangledown}{\sigma}$ in (47) will be then replaced with $\dot{\sigma}$, and the spin tensor $\mathbf{\Omega}$ will vanish from the void orientation evolution (see Sec. 2.6), all thanks to the corotational formulation. Further details can be observed in [29].

Due to the existence of high geometric nonlinearity within the problems of porous plasticity, the implicit method of plasticity has been adopted to solve for state variables. Accordingly, the following state variables will be updated via the implicit method during nearly-homogeneous and post-localized deformation processes:

– During nearly-homogeneous deformation:

$$\mathbf{V} = \left[\sigma', \sigma_m, f, \bar{\epsilon}, \mathrm{d}\Lambda, S\right]^T \tag{50}$$

– During inhomogeneous deformation:

$$\mathbf{V} = \begin{cases} \left[\sigma', \sigma_m, f, \bar{\epsilon}, s\right]^T & \text{for } |\sigma_{\rm n}| \geq \mathcal{S} \\ \left[\sigma', \bar{\epsilon}, s\right]^T & \text{for } |\sigma_{\rm n}| \leq \mathcal{S} \end{cases} \tag{51}$$

with $\mathcal{S}$ defined after Eq. (33).

$\mathrm{d}\Lambda$ is the increment in plastic multiplier, and the rest of variables have been defined in the context. In the singular portion of the yield surface associated with $|\sigma_{\rm n}| \leq t\mathcal{S}$, $\mathbf{D}^p$ and $\mathbf{N} \equiv \partial\Phi/\partial\sigma$ will be traceless, and thus (σ_m, f) would stay constant. Note that Eq. (46) has been so expressed for the sake of better congruence with the separate consideration of σ' and $\sigma_{\rm m}$, as witnessed in Eq's (50) and (51).

The main portion within the flow rule (48) to derive the evolution equations of porosity f, void aspect ratio w, and equivalent plastic strain $\bar{\epsilon}$, is the first derivative of the flow potential Φ. Its relation corresponding to nearly-homogeneous and localized processes, following Eqs. (29,33), can be written as

$$\tilde{\mathbf{N}}^{\rm H} \equiv \frac{\partial \Phi^{\rm H}}{\partial \tilde{\sigma}} = 3C\frac{\tilde{\mathbb{H}} : \tilde{\sigma}}{\bar{\sigma}^2} + 2(g+1)(g+f)\kappa \sinh\left(\kappa \frac{\tilde{\sigma} : \tilde{\mathbf{X}}}{\bar{\sigma}}\right)\frac{\tilde{\mathbf{X}}}{\bar{\sigma}} \tag{52}$$

and

$$\tilde{\mathbf{N}}^{\rm I} \equiv \frac{\partial \Phi^{\rm I}}{\partial \tilde{\sigma}} = \frac{2}{\mathcal{V}^2}\left(\sigma_n - t\mathrm{sgn}(\sigma_n)\mathcal{S}\right)\tilde{\mathbf{n}} \otimes \tilde{\mathbf{n}}\, \mathcal{H}(|\sigma_n| - t\mathcal{S}) + 2\frac{\tilde{\tau}_{\mathbf{n}} \otimes \tilde{\mathbf{n}}}{\mathcal{T}^2} \tag{53}$$

with $\mathcal{H}(x)$ being the Heaviside step function, defined as 1 for $x > 0$ and zero otherwise. Accordingly:

$$\begin{aligned} &\frac{\partial \Phi}{\partial \tilde{\sigma}'} = \mathbb{J} : \frac{\partial \Phi}{\partial \tilde{\sigma}} \quad \therefore \quad \frac{\partial \Phi}{\partial \sigma_{kk}} \equiv \frac{1}{3}\frac{\partial \Phi}{\partial \sigma_{\rm m}} = \mathbf{I} : \frac{\partial \Phi}{\partial \tilde{\sigma}} \\ &\tilde{\mathbf{D}}^{\rm p} = \dot{\Lambda}\frac{\partial \Phi}{\partial \tilde{\sigma}} \quad \therefore \quad D^{\rm p}_{kk} \equiv 3D^{\rm p}_m = \dot{\Lambda}\frac{\partial \Phi}{\partial \sigma_{kk}} \end{aligned} \tag{54}$$

With the above foreword, the following steps towards the time integration of constitutive equations will be elaborated on below. Note that, within the confines of this article, the algebraic details of derivations are only given for the post-localization regime. The reader will be well-advised to follow [29] for steps to implementation of the K–B model in (29).

4.2 Newton-Raphson method

With similar procedure as that described in [29], a semi-implicit integration algorithm was employed to integrate the post-localized constitutive equations, with the state variables as assembled in (51). By the nonlinear nature of the problem, there is normally a nonzero difference between the left and right-hand terms in the evolution equations, e.g. in (48), (10), and (26). Therefore, one could define the residual with respect to every state variable, for instance, at the post-localized process, as

$$[\mathbf{R}] = \left[\mathbf{R}_{\tilde{\sigma}'},\ R_{\tilde{\sigma}_{\rm m}},\ R_f,\ R_{\bar{\epsilon}},\ R_s\right]^T \tag{55}$$

with their expressions written, in expanded form, as follows:

$$\begin{aligned}
\mathbf{R}_{\tilde{\sigma}'} &= \frac{1}{2\mu}\left(\frac{\tilde{\sigma}' - \tilde{\sigma}'_0}{\Delta t}\right) + \dot{\Lambda}\frac{\partial \Phi}{\partial \tilde{\sigma}'} - \tilde{\mathbf{D}}' \\
R_{\tilde{\sigma}_{\mathrm{m}}} &= \frac{1}{K\Delta t}\left(\sigma_{\mathrm{m}} - \sigma_{\mathrm{m}\,(0)}\right) + \dot{\Lambda}\frac{1}{3}\frac{\partial \Phi}{\partial \sigma_{\mathrm{m}}} - \tilde{D}_{kk} \\
R_f &= \frac{f - f_0}{\Delta t} - (1-f)\dot{\Lambda}\frac{\partial \Phi}{\partial \sigma_{kk}} \\
R_{\bar{\epsilon}} &= \frac{\bar{\epsilon} - \bar{\epsilon}_0}{\Delta t} - \frac{\dot{\Lambda}}{(1-f)}\left(\frac{\sigma}{\bar{\sigma}} : \frac{\partial \Phi}{\partial \tilde{\sigma}}\right)
\end{aligned} \tag{56}$$

where K and μ are the shear and bulk moduli, respectively. The derivatives of the post-localization flow potential Φ^{I} refer to (53). $\mathbf{V}_0$ and $\mathbf{V}$, respectively, denote the state variables at the beginning and the end of the time increment. The residual associated with $s \equiv \ln w$ is explicated distinctively in that it demands original derivation at the post-localized process.

– During nearly-homogeneous deformation:
Following [36], the time rate of the logarithmic void aspect ratio reads:

$$R_s = \frac{s - s_0}{\Delta t} - \dot{\Lambda}\tilde{\mathbf{Q}} : \left[k\mathbf{N}^{\mathrm{H}} + \left(\frac{1}{f}\tilde{\mathbf{X}}^v - \tilde{\mathbf{X}}\right)\frac{\partial \Phi^{\mathrm{H}}}{\partial \sigma_{\mathrm{m}}}\right] \tag{57}$$

with the parameters identified in (11) and (12).

– During inhomogeneous deformation:
We can firstly define intermediate parameters q_1 and q_2, following Eq's (14) and (15), secluding the normal and shear parts of $\dot{s}$. Namely:

$$q_1 = \begin{cases} \dfrac{\frac{6}{c}\frac{\mathscr{T}(w^2-1)(\mathscr{T}^2+w^2)}{(\mathscr{T}^2+w^4)(\mathscr{T}^2+1)}}{2 - 3\frac{\mathscr{T}^2(2w^2-w^4+\mathscr{T}^2)}{(\mathscr{T}^2+w^4)(\mathscr{T}^2+w^2)}} & \text{for } w \geq 1 \\ \dfrac{-\frac{6}{c}\frac{\mathscr{T}(w^2-1)(\mathscr{T}^2+w^2)}{(\mathscr{T}^2+w^4)(\mathscr{T}^2+1)}}{1 - \frac{\mathscr{T}^2(-2w^2+w^4-\mathscr{T}^2)}{(\mathscr{T}^2+w^4)(\mathscr{T}^2+w^2)}} & \text{for } w < 1 \end{cases} \tag{58}$$

and

$$q_2 = \begin{cases} \dfrac{\frac{(\mathscr{T}^2+w^2)^2}{(\mathscr{T}^2+w^4)(\mathscr{T}^2+1)}\left[\frac{3}{c} - \frac{(\mathscr{T}^2+w^4)(\mathscr{T}^2+1)}{f(\mathscr{T}^2+w^2)^2}\right]}{2 - 3\frac{\mathscr{T}^2(2w^2-w^4+\mathscr{T}^2)}{(\mathscr{T}^2+w^4)(\mathscr{T}^2+w^2)}} & \text{for } w \geq 1 \\ \dfrac{\frac{(\mathscr{T}^2+w^2)^2}{(\mathscr{T}^2+w^4)(\mathscr{T}^2+1)}\left[-\frac{3}{c} + \frac{(\mathscr{T}^2+w^4)(\mathscr{T}^2+1)}{f(\mathscr{T}^2+w^2)^2}\right]}{1 - \frac{\mathscr{T}^2(-2w^2+w^4-\mathscr{T}^2)}{(\mathscr{T}^2+w^4)(\mathscr{T}^2+w^2)}} & \text{for } w < 1 \end{cases} \tag{59}$$

, one can further define

$$\begin{aligned}
\mathbf{q} &= q_1\mathbf{m} + q_2\mathbf{n} \\
\mathcal{M} &= \mathbf{n} \otimes \mathbf{q}
\end{aligned} \tag{60}$$

which can supply the residual associated with s as follows:

$$R_s = \frac{s - s_0}{\Delta t} - \dot{\Lambda}\mathcal{M} : \mathbf{N}^{\mathrm{I}} \tag{61}$$

The Newton-Raphson procedure is then employed iteratively to solve the $[\mathbf{R}]^T = \mathbf{0}$ equation system at every time step:

$$[\mathbf{V}]_{i+1} = [\mathbf{V}]_i - \left[\frac{\partial[\mathbf{R}]}{\partial[\mathbf{V}]_i}\right]^{-1}[\mathbf{R}] \tag{62}$$

where the Jacobian matrix $\partial[\mathbf{R}]/\partial[\mathbf{V}]$ can be evaluated at every iteration within the time step or kept equal to the value at the beginning of the time step, and subscript i denotes the iteration number. Since, however, the number of iterations to convergence is more or less the same whether the initial or updated Jacobian is utilized. Therefore, $\partial[\mathbf{R}]/\partial[\mathbf{V}]_{(0)}$, i.e. the Jacobian at the beginning of every time step, has been used throughout the iteration process due to the fact that convergence is better guaranteed with the initial Jacobian unless the latter is singular[1].

Finally, the consistent tangent matrix (mainly developed for global equilibrium, as in a finite element-based analysis), denoted by $\mathbb{L}^{\tan}$ (*e.g.* DDSDDE in ABAQUS) is written as

$$\mathbb{L}^{\tan} = \frac{1}{\Delta t}\left(\frac{\partial\tilde{\sigma}'}{\partial\tilde{\mathbf{D}}} + \mathbf{I}\otimes\frac{\partial\tilde{\sigma}_{\mathrm{m}}}{\partial\tilde{\mathbf{D}}}\right) \tag{63}$$

which involves the following constituents:

$$\left[\frac{\partial\mathbf{V}}{\partial\tilde{\mathbf{D}}}\right] = -\left[\frac{\partial[\mathbf{R}]}{\partial[\mathbf{V}]}\right]^{-1}\left[\frac{\partial\mathbf{R}}{\partial\tilde{\mathbf{D}}}\right] \tag{64}$$

where use has been made of the same Jacobian as introduced in (62), and

$$\begin{aligned}\left[\frac{\partial\mathbf{V}}{\partial\tilde{\mathbf{D}}}\right] &= \left[\frac{\partial\tilde{\sigma}'}{\partial\tilde{\mathbf{D}}}, \frac{\partial\tilde{\sigma}_{\mathrm{m}}}{\partial\tilde{\mathbf{D}}}, \frac{\partial f}{\partial\tilde{\mathbf{D}}}, \frac{\partial\bar{\epsilon}}{\partial\tilde{\mathbf{D}}}, \frac{\partial s}{\partial\tilde{\mathbf{D}}}\right]^T \\ \left[\frac{\partial\mathbf{R}}{\partial\tilde{\mathbf{D}}}\right] &= \left[\frac{\partial\mathbf{R}_{\tilde{\sigma}'}}{\partial\tilde{\mathbf{D}}}, \frac{\partial R_{\tilde{\sigma}_{\mathrm{m}}}}{\partial\tilde{\mathbf{D}}}, \frac{\partial R_f}{\partial\tilde{\mathbf{D}}}, \frac{\partial R_{\bar{\epsilon}}}{\partial\tilde{\mathbf{D}}}, \frac{\partial R_s}{\partial\tilde{\mathbf{D}}}\right]^T\end{aligned} \tag{65}$$

To the reader's insight, the Jacobian components corresponding to the post-localized deformation process have been provided in Appendix G. For the nearly-homogeneous deformation regime, the reader can consult [29] regarding the Jacobian components.

5 Results

This section comprises the calculated results of microstructural variables from integration of constitutive laws for one single unit cell. Correspondingly, there exists only one localization plane with the normal being $\mathbf{e}_3$ throughout whereas the void is allowed to rotate under the effect of combined tension and shear. The voids' lattice is colinear with the global coordinate system, and the void, except stated otherwise, initially directs along $\mathbf{e}_3$. Due to it being neglected in the localized yield criterion, matrix anisotropy has been neglected throughout. Each set of results is extended into further subsets to demonstrate the evolution of various microstructural variables throughout the process. The ratios among the remote normal, lateral, and shear stresses remain constant throughout. Accordingly, stress triaxiality T and the Lode parameter L are constant.

The model is firstly assessed under triaxial loading, i.e. in absence of shear, in Appendix H for fixed stress triaxialities and prescribed initial void aspect ratios. The main set of results presented in the sequel represent combined tension and shear, with specific focus on shear-dominated loading. For the sake of

[1] In a single-variable problem, the initial slope in the Newton-Raphson method guarantees convergence unless the initial slope is infinite.

simplicity, lateral stresses are eliminated, and the axial-to-shear stress ratio $\kappa = \sigma/\tau$ varies from zero (representing simple shear) to infinity (signifying uniaxial loading).

Note that, in some plots comprising several sets of curves, only one line color has been itemized in the line legend to represent the line type rather than the depicted color.

5.1 Model assessment

This section presents the hybrid model predictions in comparison against the existing FEM-based cell-model calculations under combined tension and shear on the same RVE. To this end, the analyses carried out by Tvergaard and coworkers for plane-strain [21, 35] and 3D cells [14] under near-simple shear loading, with $\kappa = \sigma/\tau$ fixed at every analysis and varied from case to case, are considered as comparator. Within their observations, plastic deformation was viewed as initially scattered throughout the cell up to a prescribed maximum void aspect ratio, and then confined to a zone containing the inter-void ligament. From this point onward, the loading was applied onto the void interior. It is worthy of note that a FEM-based state of absolute simple shear, with $\kappa = 0$, is too computationally expensive for 3D cells and is, thus, not available in the literature except under the plane-strain condition. The cell sketches and a deformed configuration of the plane-strain cell are shown in Fig. 5.

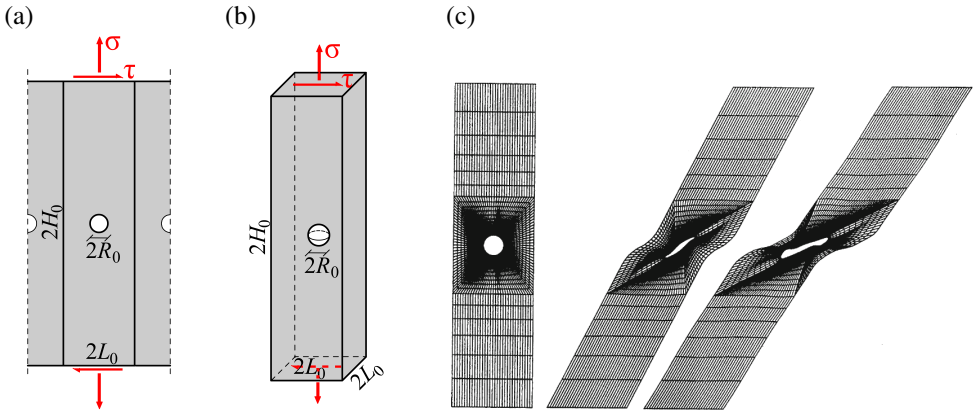

Figure 5: Schematic outline of periodic cells under combined tension and shear considered by Tvergaard and coworkers: (a) plane–strain [21], (b) 3D [14], (c) staged deformed configurations of the plane-strain cell in [21] under simple shear, *i.e.* $\kappa = 0$.

The initial microstructure in all references [14, 21, 35] is introduced based on the ($\chi_0 = R_0/L_0, w_0 = h_0/R_0, \lambda_0 = H_0/L_0$) triad (see Fig. 5), with χ_0 varying between 0.15 and 0.5, and $(w_0, \lambda_0) = (1, 4)$ remaining fixed. In the plane–strain cell, the out–of–plane dimension in both the void and the cell is considered unit and, hence, χ_0, w_0, λ_0 are all defined within the x_1–x_3 plane. In the 3D cell, however, the lateral dimensions are considered equal. Correspondingly, the initial porosity reads

$$f_0 = \frac{\pi}{4}\frac{w_0\chi_0^2}{\lambda_0}$$

in the plane-strain cell, and

$$f_0 = \frac{\pi}{6}\frac{w_0\chi_0^3}{\lambda_0}$$

in the 3D cell. For the sake of better coincidence between analytical and numerical results, model predictions are compared to FEM counterparts for the same initial porosity [40], with the initial microstructure and

hardening identified by $(\chi_0, w_0, \lambda_0) = (0.25, 1, 4)$. Note that the material constants are defined as

$$\frac{\sigma_0}{E} = 0.002 \quad , \quad E = 200\ GPa \quad , \quad \epsilon_0 = 0.002 \tag{66}$$

Furthermore, the hardening exponent is taken as $N = 0.1$ for the plane-strain and $N = 0.2$ for the 3D cell. In all FEM-based studies, the analyses have been carried out by considering a maximum void aspect ratio, beyond which the loading is applied onto the void faces rather than onto the cell upper and lower boundaries. Herein, the results pertaining to a maximum void aspect ratio of $w_{\max} = 10$ are considered as comparator.

Figure 6a shows the present hybrid model predicted normalized shear stress vs. shear angle in comparison to FEM outcomes from [35] and [21] for $\kappa = 0.6$ and $\kappa = 0$, respectively [1].

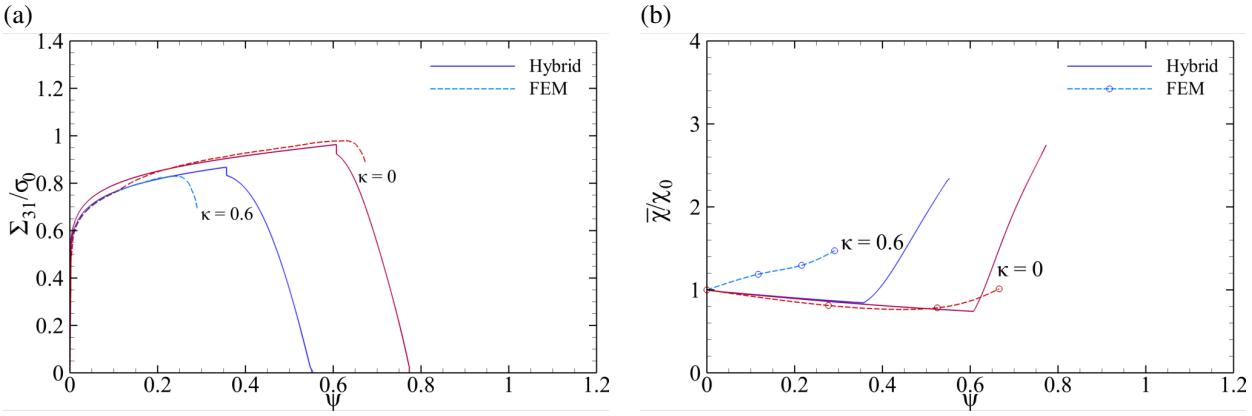

Figure 6: Comparison between the present model predictions vs. cell overall shear angle ψ with FEM cell-model outcomes of Tvergaard [21, 35] for an initially circular void inside a plane-strain unit cell under simple shear ($\kappa = 0$): (a) normalized shear stress, (b) normalized effective ligament parameter.

The normalized effective ligament parameter $\bar{\chi}/\chi_0$ for FEM-based results stems from the graphical deformed configurations showcased in [35] and [21] for selective shear angles. Note that $\bar{\chi}$ is normalized in the interest of a sound comparison inasmuch as χ_0 differs for a cylindrical and a spherical void with an identical porosity.

Figure 6b demonstrates that the effective ligament parameter $\bar{\chi}$ within the FEM framework reduces until the point of transition into inhomogeneous deformation whence it starts increasing. The former is characteristic of the void moving towards closure, which can be realized by virtue of Φ^{H} according to (29). This further corroborates that the cell behavior under simple shearing is initially closer to being nearly-homogeneous than localized.

Other comparisons are shown in Fig's 7 for a 3D cell with initial ligament parameters $\chi_0 = \{0.3, 0.5\}$ and $N = 0.2$.

One can envisage, in Fig. 7a that, for rather large porosity levels, when there is significant normal stress portion (for $\kappa = 1.25$ herein), the stress (spuriously) goes slightly up after the onset of inhomogeneous deformation due to the effect of normality slightly taking over before the stress continues to reduce steeply until failure. Further, Fig. 7d demonstrates that the overall trend of porosity evolution, inclining or declining, is common between analytical and numerical results with the difference lying in the dilatancy level in FEM values reflected by the more remarkable slope of evolution, especially at larger normal stress portions, *i.e.*

[1] The case of simple shear is represented by $\kappa = 0.02$ in the present analyses. This lies in the adopted displacement-controlled algorithm wherein the incremental strain ratios $\delta E_{\mathrm{mn}}/\delta E_{\mathrm{nn}}$ and $\delta E_{\mathrm{mm}}/\delta E_{\mathrm{nn}}$ are manipulated in terms of a prescribed axial displacement increment δu_n so as to control the remote stress ratios

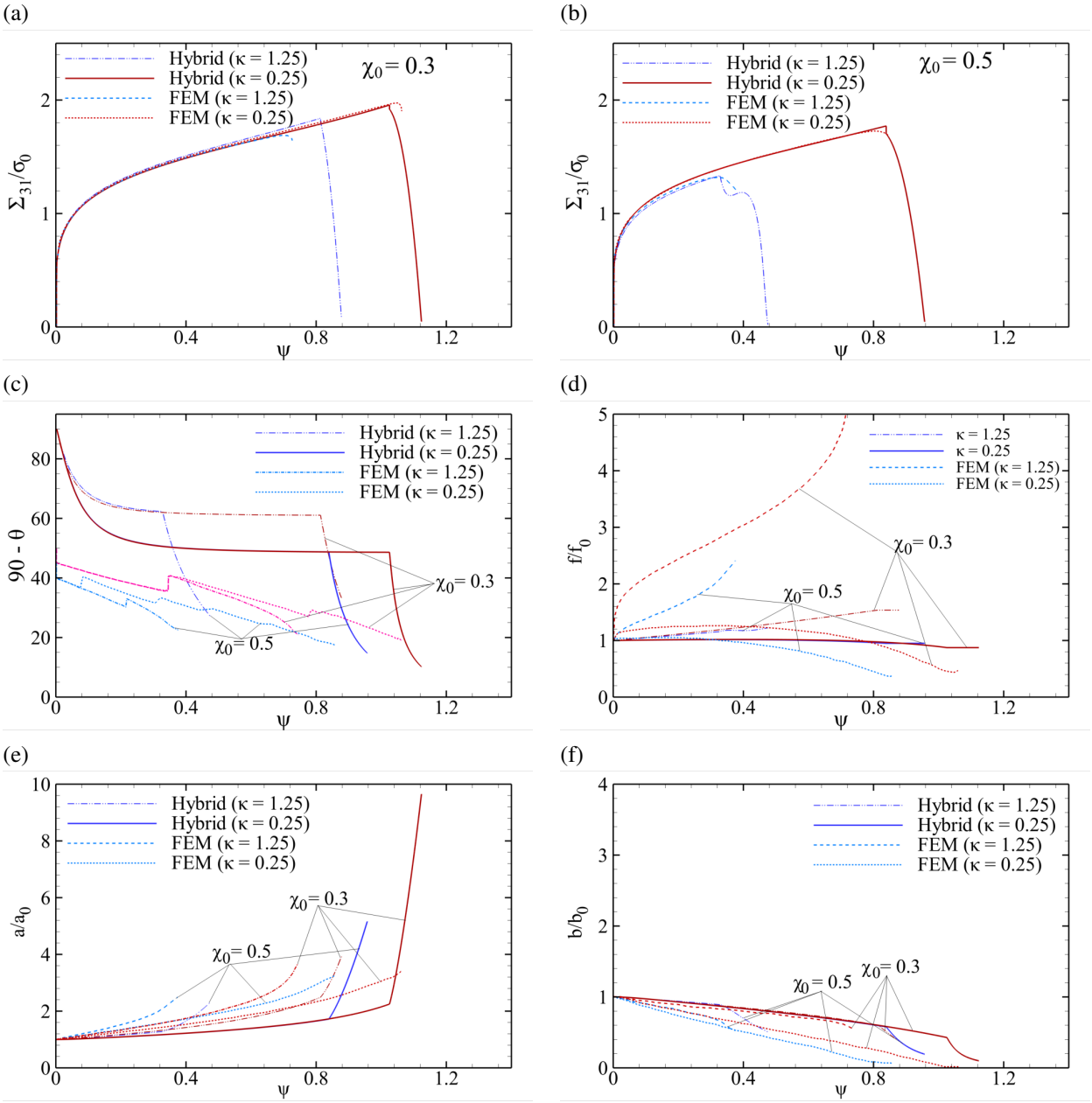

Figure 7: Comparison between the present model predicted variables with FEM outcomes of Nielsen *et al.* [14] for an initially spherical void inside a square-prismatic cell under combined axial and shear loading (with the ratio denoted with κ) and $\chi_0 = \{0.3, 0.5\}$: (a,b) normalized shear stress, (c) void angle with respect to the horizontal direction, (d) normalized porosity, (e,f) normalized major and minor void semi-axes.

larger κ's. Yet, the observed clear distinction between the FEM and analytical porosity values does not bare significant changes in the stress response (as shown in Fig. 7a) inasmuch as the failure mechanism is mainly influenced by $\bar{\chi}$ rather than porosity. For large shear stress portions ($\kappa = 0.25$), the analytical porosity ceases to evolve further at the inhomogeneous deformation process since yielding is governed by the shear part of Φ^{I} which conveys a traceless plastic rate of deformation, *i.e.* $D^{\mathrm{p}}_{kk} = 0$.

Note that the analytical evolution of $90 - \theta$ is founded on the initial void orientation directed towards $\mathbf{e}_3$ since $w_0 = 1.1$ has been taken slightly above unity to forestall the singular behavior of void orientation laws at the limit of a spherical void, and therefore, the initial orientation is well-defined. Within the numerical model, however, the orientation of a strictly spherical void is ill-defined. Upon convention, the void orientation in this case is considered along the principal stretch, which is close to that considered in [14, 21]. Accordingly, the jumps in the numerical evolution of orientation is an artifact employed to extract the major void axis. There is also merit in recognizing that there may exist a stagnation in the void orientation with $\theta_0 = 0$ especially at small time increments. To forestall this, $\mathbf{n}_0^{(3)}$ was slightly perturbed from $\mathbf{n} = \mathbf{e}_3$ such that $\theta_0 \longrightarrow 0^+$. A clearer elaboration on this issue will be provided in Section 5.5.

Finally, as depicted in Fig's 7(e) and (f), with an initial state associated with $w_0 \geq 1$, the major void semi-axis a elongates for all combinations of *axial* and *shear* stresses (devoid of lateral stresses), whereas the minor semi-axis b is shortened. In order for the latter also to elongate, sufficient lateral stresses should be applied.

A more extensive investigation on the various state variables under combined axial and shear stresses, upon the calibrated hybrid model, is presented next.

5.2 Effect of loading

This section addresses, through Fig. 8, the effect of loading, quantified via the $\kappa \equiv \sigma_{\mathrm{n}}/\tau_{\mathrm{n}}$ ratio, on the microstructural state variables with the same cell as considered in Sec. 5.1 and $\chi_0 = 0.3$. A complete scope of κ ranging from infinity (uniaxial loading) down to (near) zero (simple shearing) can best be exhibited in terms of $\bar{\epsilon}$ as the axial so as the shear strain each becomes vanishingly small at either of the two extremes.

It can be seen, through Fig's 8(a,b), that strain to the onset of localized deformation ϵ_c, as well as strain to failure ϵ_f, from infinity at $\kappa \longrightarrow \infty$ (corresponding to $T = 1/3$), decreases and then increases again with decreasing κ (increasing shear). As further investigated in Sec. 5.7, the minimum strain to failure occurs approximately at $\kappa = \mathcal{S}/\mathcal{T}$, which is nothing but the point of transition between the curved and planar parts of Φ^{I} (see [24] for more details). Furthermore, the difference between ϵ_c and ϵ_f becomes smaller with larger κ's since a larger portion of the normal stress superposed by shear accelerates rotation, as revealed by Fig. 8d, and thus hastens the increase of $\bar{\chi}$, as demonstrated by Fig. 8b. The latter also shows that, for sufficiently large κ's (*i.e.* $\kappa >> \mathcal{S}/\mathcal{T}$), $\bar{\chi}$ increases during both nearly-homogeneous and inhomogeneous processes whereas, for smaller κ's, it decreases during the nearly-homogeneous process. This alludes to the fact that, with larger normal stress portions, the void can rotate faster than the cell during the nearly-homogeneous process whilst, at shear-dominated processes, the cell moves faster during this process. During the inhomogeneous process, however, the void always rotates faster since plastic deformation is (ideally) confined to the ligament intercepted by void poles.

Moreover, one can assert, from Fig. 8c, that porosity increases, with its increase accelerated after the onset of localization, for $\kappa > \mathcal{S}/\mathcal{T}$, *i.e.* normally-dominated fields. All the same, for $\kappa < \mathcal{S}/\mathcal{T}$, *i.e.* shear-dominated fields, porosity decreases during the nearly-homogeneous process and stays constant after localized deformation begins. This lies in the traceless nature of $\mathbf{D}^{\mathrm{p}}$ according to Φ^{I} for this range of κ. The s_1 and s_2 void aspect ratios shown in Fig. 8e denote, respectively, a/b_1 and a/b_2. Under all combinations of (tensile) axial and shear stresses, in absence of sufficient lateral loads, s as well as s_1 and s_2 increase, with their increase accelerated after localization begins. Throughout the process, $s_1 > s_2$ and the difference between the two increases with deformation advancement. At the end of the inhomogeneous process, the

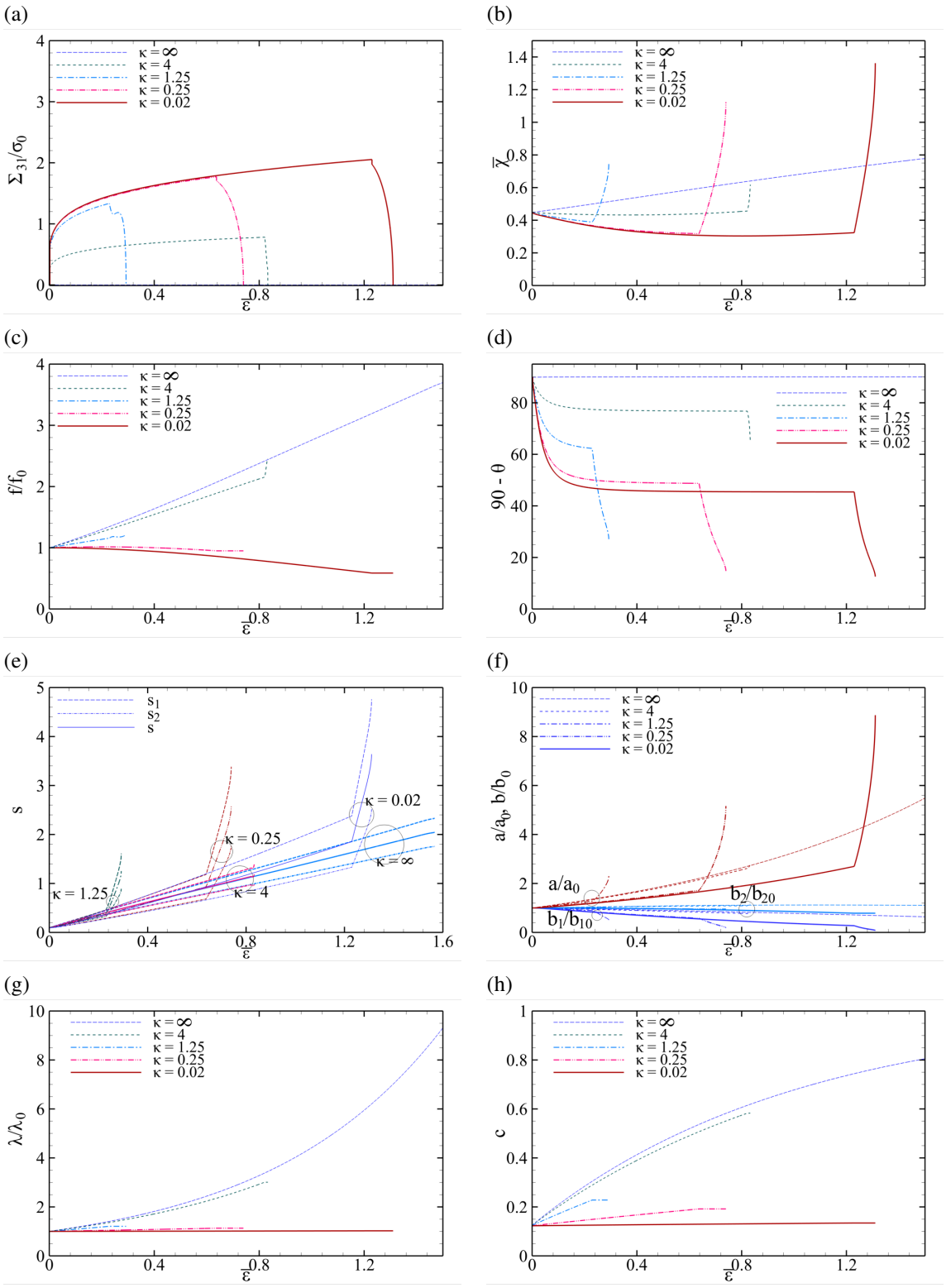

Figure 8: Predicted microstructural parameters upon the calibrated hybrid model, plotted against equivalent plastic strain $\bar{\epsilon}$ for the same initial microstructure as considered in Sec. 5.1 and $\chi_0 = 0.3$, under a full range of κ: (a) shear response, (b) effective ligament parameter, (c) normalized porosity, (d) void angle with the horizontal direction, (e) logarithmic void aspect ratio, (f) void semi-axes, (g) normalized cell aspect ratio, (h) ligament volume fraction.

void aspect ratio increases with its slope approaching infinity. This stage signifies the vertical movement of void poles after extreme shearing, as shown in Fig. 5c. Correspondingly, as depicted in Fig. 8f, the major and minor void semi-axes increase and decrease, respectively, with shearing, and the trend slope accelerates after the onset of localization. The out-of-plane axis also decreases slightly but stays almost constant throughout the process due to the loading being devoid of lateral stresses. The cell aspect ratio, as shown in Fig. 5g, increases only when there is a nonzero portion of axial stress, and it stays constant under simple shear ($\kappa \longrightarrow 0$). Similar to that of the void, λ_1 and λ_2 denote, respectively, H/L_1 and H/L_2, with the former evolving clearly faster under the effect of axial loading. The increasing trend of λ, as well as that of λ_1 and λ_2, retards at the post-localized regime due to axial deformation confined within the ligament. The ligament volume fraction c, as plotted in Fig. 5h, behaves somewhat similar to λ, increasing only when there is some normal stress present, and a retarded increasing trend after localization begins. The trend of increasing c is convex at normally-dominated loads ($\kappa > \mathcal{S}/\mathcal{T}$) that points to a slower increasing trend in the ligament volume fraction towards failure. Under shear-dominant fields, however ($\kappa < \mathcal{S}/\mathcal{T}$), the trend is concave, meaning the ligament enlarges faster at the beginning of plasticity but reaches its maximum soon afterwards. Under simple shearing, the ligament stays at its height.

In the forthcoming subsections, the results are limited to near-simple shearing (here denoted with $\kappa = 0.02$).

5.3 Effect of void spacing

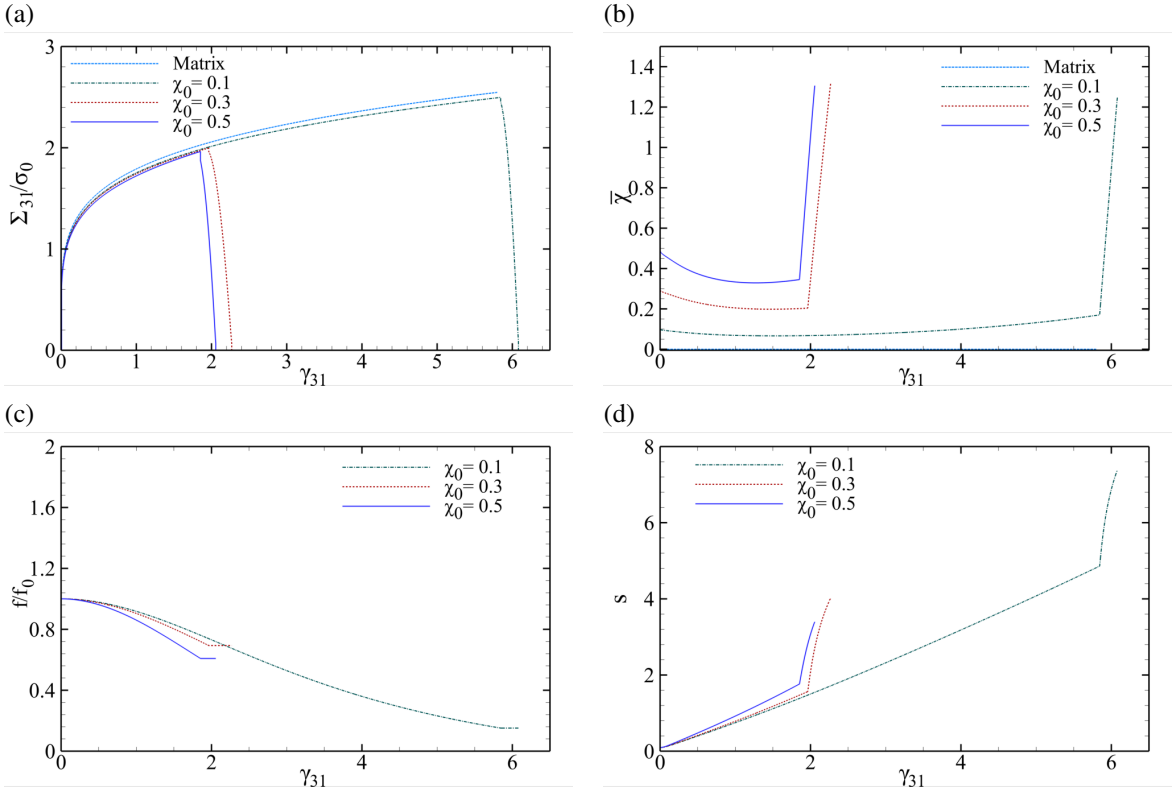

Figure 9: Predicted microstructural parameters for the same cell subjected to $\kappa = 0.02$ for various values of χ_0.

The effect of void spacing can be reflected through the notion of initial ligament parameter χ_0. Figure 9 presents selective state variables under near-simple shearing ($\kappa = 0.02$) with various values of χ_0, ranging from zero (pertaining to the limit of a dilute matrix) up to rather large values, *e.g.* 0.5. Figure 9a reveals that the stress curve (and the tangential stiffness accordingly) up to the point of transition (ϵ_c) is almost insensitive to void spacing provided the other (initial) microstructural parameters stay constant. However, ϵ_c and ϵ_f are closely related to χ_0. In particular, for very small values of χ_0, towards the limit of a dilute material, the onset of localized deformation, as well as failure, gets significantly delayed. At this limit, according to Fig. 9c, void closure (associated with porosity approaching zero) could be envisaged sooner than failure could occur. This mechanism corroborates that predicted solely from Φ^{I} as discussed in Fig. 7 of Ref. [30]. During nearly-homogeneous yielding, as shown in Fig. 9b, $\bar{\chi}$ decreases at the early stages of deformation, but it admits a minimum which sets the precursor for the onset of localized deformation. Namely, the cell rotates faster than the void at early stages of deformation while, at some point, the void rotation outpaces that of the cell. The localized deformation process begins after the minimum point in the $\bar{\chi}$ evolution curve. The void aspect ratio also, according to Fig. 9d, increases with a decreasing inclination slope. The largest slope of increasing s corresponds to the onset of localization, and void elongation slows down further towards failure.

5.4 Effect of cell aspect ratio

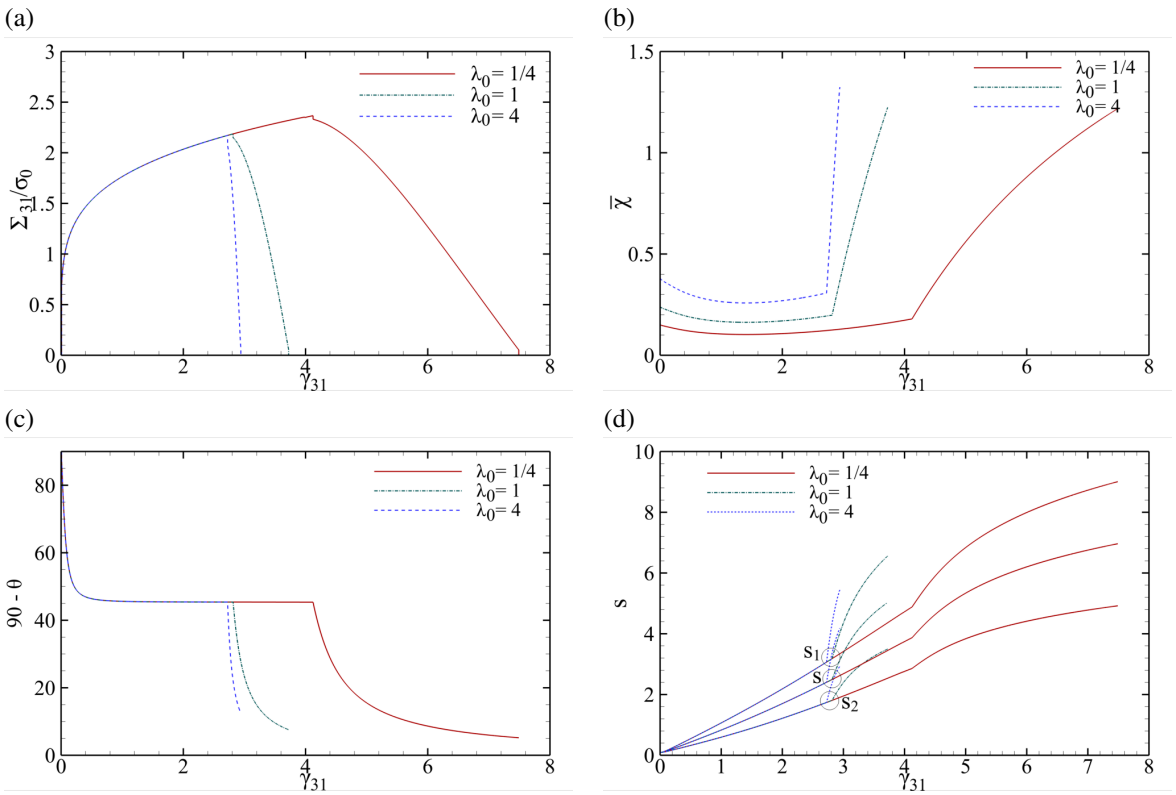

Figure 10: Predicted microstructural parameters for the same cell with $(f_0, w_0) = (0.01, 1.1)$ subjected to $\kappa = 0.02$ for various values of λ_0: (a) normalized shear response, (b) effective ligament parameter, (c) void angle with the horizontal direction, (d) logarithmic void aspect ratio.

The effect of initial cell aspect ratio is considered for investigation next. Other parameters, including initial porosity f_0 and void aspect ratio w_0, as well as the hardening exponent $N = 0.2$, are taken as fixed, upon selective values of $(f_0, w_0) = (0.01, 1.1)$. Figure 10 illustrates this effect. Due to the load representing simple shear ($\kappa = 0.02$), λ remains almost constant throughout, and thus is not shown.

At a fixed porosity level, the void spacing χ_0 is smaller in a shorter cell, and thus the void, even after deformation is localized, has to elongate and rotate more to reach the cell boundaries. The strains to localization and failure are hence larger with shorter cells, as seen in Fig. 10a. Correspondingly, the projection of a rotating-elongating void on a shorter intervoid distance (at a larger λ) evolves faster than that on a longer distance (at a smaller λ). The slope of $\bar{\chi}$ evolution, therefore, is smaller for a shorter cell, and vice versa (see Fig. 10b). The void would, accordingly, rotate (Fig. 10c) and elongate (Fig. 10d) more slowly at the post-localized deformation process, in a shorter cell and vice versa.

5.5 Effect of void shape

The effect of void shape is studied under two circumstances. The first set of figures show the effect of void aspect ratio, ranging from 1/4 to 4, on the microstructural behavior under simple shear, at fixed porosity level $f_0 = 0.01$ and cell aspect ratio $\lambda_0 = 4$, with the same hardening exponent $N = 0.2$.

Remark: In order to avert the rotation locking at the limit of $\theta \longrightarrow 0$, we must perturb the initial orientation from $\theta = 0$. The perturbation direction, however, differs for prolate and oblate voids. For a prolate void, θ_0 is slightly posited and, for an oblate void, it is slightly negated with respect to the positive counterclockwise orientation of θ. Figure 11 illustrates the effect of initial void aspect ratio w_0.

Figure 11f substantiates the mechanism shown in Fig. A-4b and schematized in Fig. 1b. Prolate and oblate voids rotate in opposite directions so that the larger axis moves towards aligning with the direction of the principal stretch, here initially lying close to 45° from the vertical direction and lying further down during the deformation process. Therefore, a prolate void rotates along with the shearing and an oblate rotates opposite thereto. There is, however, a maximum point within the angle curve pertaining to the oblate void which corresponds to a back-turn in rotation. The latter was also observed earlier with the difference being that, within the modified hybrid model, this instant takes place at the onset of localized deformation. This point further corresponds to the instant when the void closes, *i.e.* $a \longrightarrow 0$, $w \longrightarrow 0$ and $f \longrightarrow 0$ as indicated by Fig's 11 (b–d). At this point, deformation abruptly turns localized where, immediately afterwards, $\bar{\chi}$ starts ascending precipitously until failure. More appealingly, the third void semi-axis b_2 remains constant after this point, main axis a approaches zero (entailing void closure), and the in-plane minor semi-axis b_1 abruptly elongates. This observation signifies crack propagation for flat voids under limited void growth. Further, Fig. 11a shows the highest ductility as well as limit load for an initially spherical void. Meanwhile, an oblate void with $w = 1/x$ is more ductile than its prolate counterpart with $w = x$ ($x > 1$ implied) under a shear field.

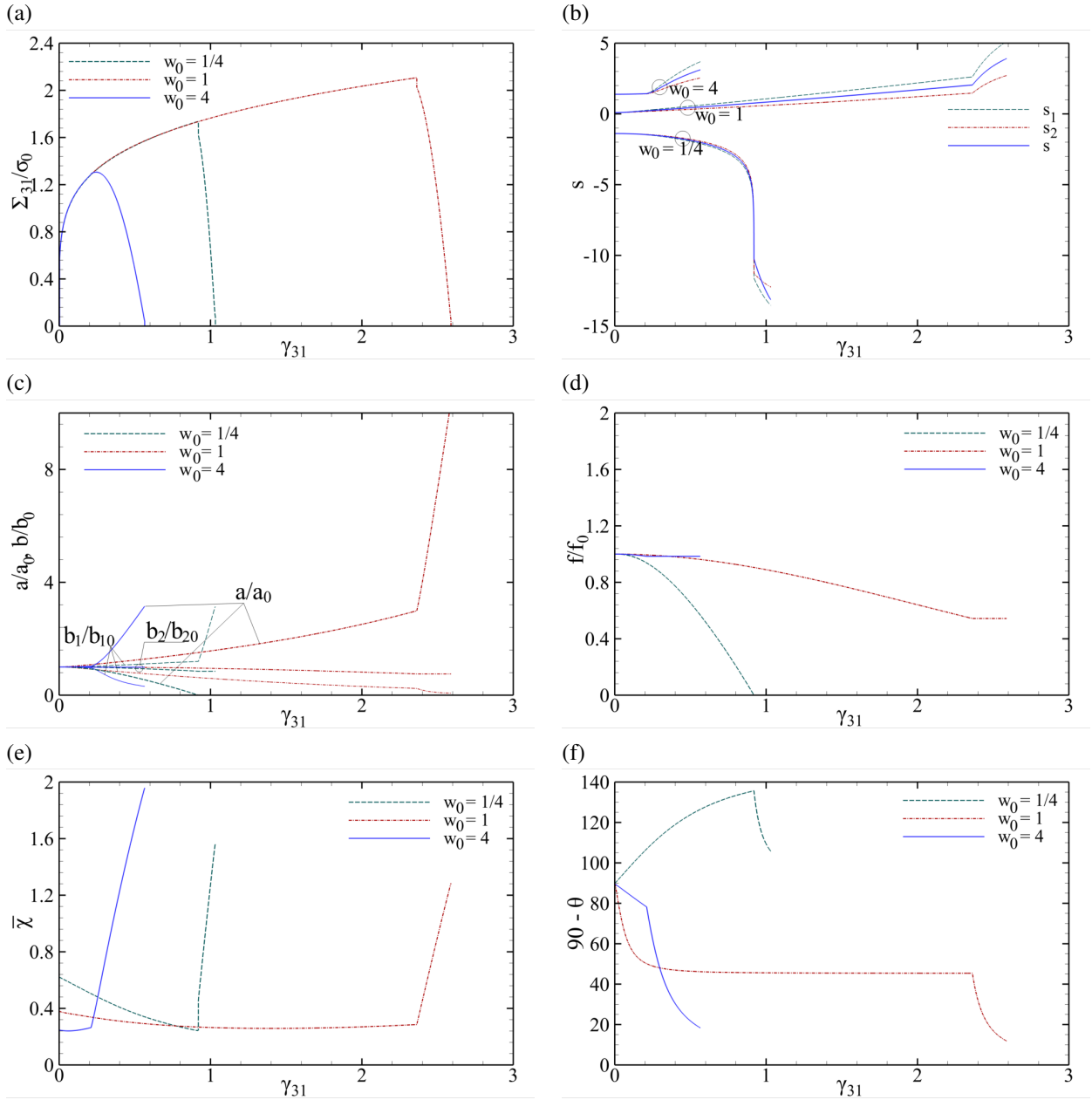

Figure 11: Predicted microstructural parameters for the same cell geometry with $(f_0, \lambda_0) = (0.01, 4)$ subjected to near-simple shearing ($\kappa = 0.02$) for various initially upright voids ($\theta_0 = 0$) with aspect ratios w_0 ranging from 1/4 to 4: (a) normalized shear response, (b) logarithmic void aspect ratio, (c) major and minor void semiaxes, (d) normalized porosity, (e) effective ligament parameter, (f) void angle with the horizontal direction.

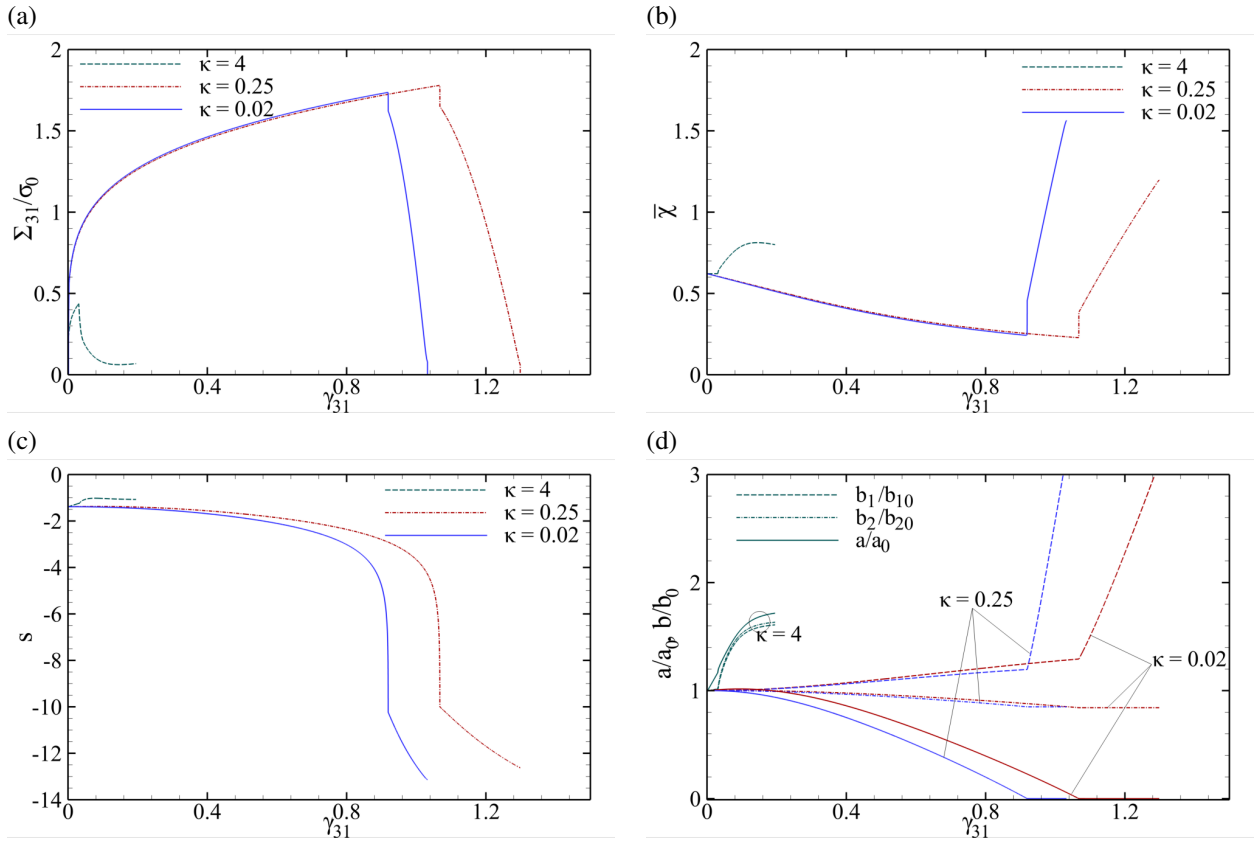

Figure 12: Predicted microstructural parameters for the same cell with $(f_0, \lambda_0) = (0.01, 4)$ and an initially upright oblate void (with $w_0 = 1/4$) under various combinations of axial and shear loading, identified with κ ranging from 4 to 0.02.

More insight into the behavior of oblate voids in shear fields can be acquired by considering the behavior of an oblate void under various load combinations (denoted with different κ's ranging from normally-dominated to shear-dominated loads). Figure 12 illustrates this effect. Figure 12a shows that no failure can be predicted for an initially upright oblate void under combined tension and shear with a dominant normal stress. This lies in the faster rotation of the cell with respect to the void towards the end of the deformation process shown in Fig. 12b, which comes effective after the maximum point in the $\bar{\chi}$ curve. Up to this point, as observed in Fig. 12c, the void tends towards a sphere and, thereafter, it starts flattening again, though at a slower rate. Under such a condition, the void axes evolve (more or less) in harmony as shown in Fig. 12d. For a shear-dominant loading, however, in conformity with Fig. 11, the void evolves towards closure, and its axes evolve with opposite trends, as clearly witnessed in Fig. 12d.

At fixed void shape, voids oriented along different directions with respect to the principal loading directions can bare significantly different shear responses. See Section 5.6 for elaboration.

5.6 Misaligned voids under simple shearing

In this section, the evolution of microstructural parameters is specified to prolate and oblate voids with various initial void orientations (with θ_0 ranging from $-30°$ to $30°$) under almost simple shearing, *i.e.* $\kappa = 0.02$. Figures 13 and 14 present, respectively, the effect of initial orientation on a prolate ($w_0 = 4$) and an oblate void ($w_0 = 1/4$).

It may appeal to the reader that, in this class of results, there is a numerical propensity of void stagnation when θ changes from negative to positive (see Section 5.5 for reasoning). The latter can be bypassed by stopping and restarting the analysis at the limit of $\theta \longrightarrow 0^-$ for a prolate void and $\theta \longrightarrow 0^+$ for an oblate void.

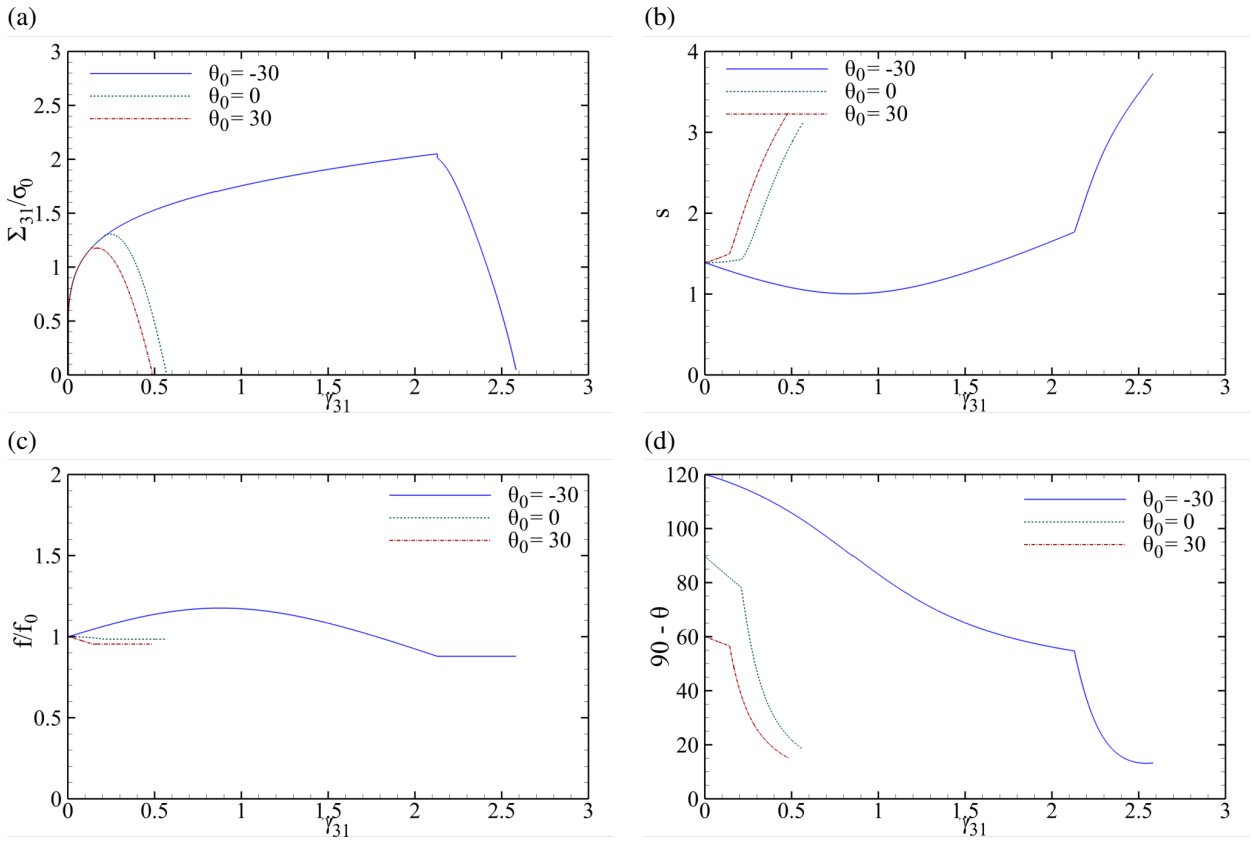

Figure 13: Predicted microstructural parameters for the same cell geometry with $(f_0, \lambda_0) = (0.01, 4)$ subjected to near-simple shearing ($\kappa = 0.02$) for a prolate void ($w_0 = 4$) initially placed at various orientations.

One can envisage, for a prolate void, the remarkable difference in strains to failure ranging from about 2.6 at $\theta_0 = -30^\circ$ to the range of 0.5 at $\theta_0 > 0$, as shown in Fig. 13a. This significant difference lies in antithetical trends in $s = \ln w$ when θ_0 is below or above zero, as depicted in Fig. 13b. In the former, the void is suppressed towards a sphere whereas, in the latter, it further elongates until failure. In the former, the cell rotates much faster than the void and makes the ligament volume shrink, and thus porosity increases unlike the case of $\theta_0 \geq 0$, as seen in Fig. 13c. Further, the void begins to rotate along with the cell (as seen in Fig. 13d) after it closes, with porosity becoming nil. From this point onward, the closed void elongates fast within the ligament (as shown in Fig. 13b) until ultimate failure to occur.

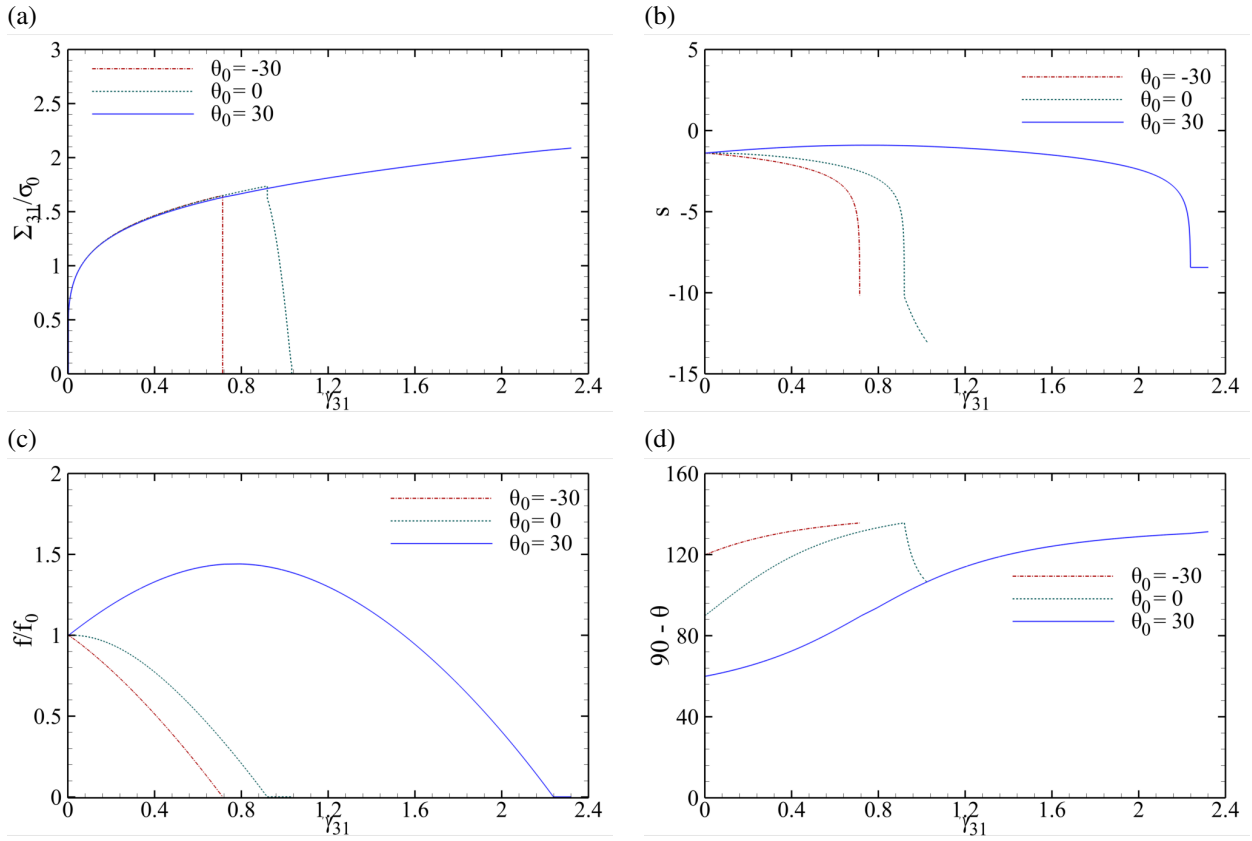

Figure 14: Predicted microstructural parameters for the same cell geometry with $(f_0, \lambda_0) = (0.01, 4)$ subjected to near-simple shearing ($\kappa = 0.02$) for an oblate void ($w_0 = 1/4$) initially placed at various orientations.

All the same, as revealed by Fig. 14b, an oblate void initially oriented colinear to the shear direction ($\theta_0 > 0$) is slightly suppressed towards a sphere until the moment when it aligns with the vertical direction $\theta = 0$, whereafter its aspect ratio starts decreasing again. This sets an inflection point in the orientation curve, Fig. 14d, whence the void rotates in the same direction but rather more slowly until its orientation reaches a plateau after void closure occurs $f \longrightarrow 0$, and thus failure would never happen due to void stagnation. For initial orientations opposite to the shear direction ($\theta_0 < 0$), however, the void behaves similar to an oblate void initially oriented vertical to shear ($\theta_0 = 0$). That is, the void reaches a state of closure with an (almost) abrupt loss of stress-bearing capacity.

Moreover, a state of near-pure shearing has been simulated with the same constitutive framework employed. The latter is distinguishable from near-simple shearing by its loading path and thus boundary conditions. See Appendix J for illustration.

5.7 Strain to failure vs. triaxiality

The last section presents the effective plastic strain at the onset of localized deformation ϵ_c as well as strain to failure ϵ_f in terms of stress triaxiality. ϵ_f, in particular, is an efficacious measure of intrinsic failure under combined normal and shear stresses on an arbitrary plane with normal $\mathbf{n}$. In some references, including [51], ϵ_c is normally regarded as the *strain to failure* for the material since the plastic deformation prior to this point is considerably larger than that after this onset. This section, however, reports both strains as function of triaxiality. The benchmark for this evolution is the same unit cell as shown in Fig. 5a,

with $(w_0, \lambda_0) = (1.1, 4)$, hardening exponent $N = 0.2$ and various initial ligament parameters χ_0, under combined normal and shear stresses. The two parameters of interest are consequences of Runge-Kutta integration of the following equations stating the time rate of $(f, w, \mathbf{n}^{(3)})$ as function of $\bar{\epsilon}$. To this end, Eq. (1) can be coupled with Eq's (17), (10) or (14) (for $w \geq 1$) or (15) (for $w < 1$), and (18). Therefore, with the "H" and "I" superscripts denoting nearly-homogeneous and inhomogeneous deformation processes, one can write:

$$\begin{aligned}
&\frac{\partial f}{\partial \bar{\epsilon}} = (1-f)^2 \frac{N_{\mathrm{kk}}}{\frac{\sigma}{\bar{\sigma}} : \mathbf{N}} \\
&\frac{\partial s^{\mathrm{H}}}{\partial \bar{\epsilon}} = (1-f)\frac{\mathbf{Q} : \mathbf{N}^{\mathrm{v}}}{\frac{\sigma}{\bar{\sigma}} : \mathbf{N}^{\mathrm{H}}} \quad , \quad \frac{\partial s^{\mathrm{I}}}{\partial \bar{\epsilon}} = (1-f)\frac{\mathcal{M} : \mathbf{N}^{\mathrm{I}}}{\frac{\sigma}{\bar{\sigma}} : \mathbf{N}^{\mathrm{I}}} \\
&\frac{\partial \mathbf{n}^{(3)}}{\partial \bar{\epsilon}} = (1-f)\frac{(\omega^{\mathrm{v}} + \omega^{\mathrm{l}})\mathbf{n}^{(3)}}{\frac{\sigma}{\bar{\sigma}} : \mathbf{N}}
\end{aligned} \tag{67}$$

where

$$\mathbf{N}^{\mathrm{v}} = \frac{1}{\dot{\Lambda}}\mathbf{D}^{\mathrm{v}}$$

$$\omega^{\mathrm{v}} = \frac{1}{\dot{\Lambda}}\mathbf{\Omega}^{\mathrm{v}} = \begin{cases} -\mathbb{C} : \mathbf{N}^{\mathrm{H}} & \text{for } \Phi = \Phi^{\mathrm{H}} \\ -\frac{1}{c}\mathbb{C} : \mathbf{N}^{\mathrm{I}} & \text{for } \Phi = \Phi^{\mathrm{I}} \end{cases}$$

$$\omega^{\mathrm{l}} = \frac{1}{\dot{\Lambda}}\mathbf{\Omega}^{\mathrm{l}} = \begin{cases} \mathbb{C} : \mathbf{N}^{\mathrm{H}} - \frac{1}{2}\sum\limits_{i\neq j,\, w_i \neq w_j} \frac{w_i^2 + w_j^2}{w_i^2 - w_j^2}\left[(\mathbf{n}_i \otimes \mathbf{n}_j + \mathbf{n}_j \otimes \mathbf{n}_i) : \mathbb{A} : \mathbf{N}^{\mathrm{H}}\right]\mathbf{n}_i \otimes \mathbf{n}_j & \text{for } \Phi = \Phi^{\mathrm{H}} \\ \frac{1}{\mathscr{T}}\left[\frac{1-c}{c}\mathbf{n}\cdot N^{\mathrm{I}}\mathbf{n} - \frac{1}{3}\left((\frac{1}{f}-1)N^{\mathrm{I}}_{\mathrm{kk}} - 2N^{\mathrm{I}}_{\mathrm{nn}}\right) + \left(\frac{1}{3} - \frac{w^2}{\mathscr{T}^2 + w^2}\right)\mathcal{M} : \mathbf{N}^{\mathrm{I}}\right]\left(C^2\mathbf{m}\otimes\mathbf{m} - S^2\mathbf{n}\otimes\mathbf{n}\right) & \text{for } \Phi = \Phi^{\mathrm{I}} \end{cases} \tag{68}$$

with reference to Eq's (11), (19) and (20), (22) and (A-38), as well as (A-33) and (A-35). One can exploit the single-step Runge-Kutta scheme in the integration process. Note that the effect of $\mathbf{n}$ has been disregarded in the above equation set because, at the current cell level, it remains constantly vertical.

One can notice, through Fig. 15, that ϵ_c is close to ϵ_f at the shear-dominant range of triaxialities. Yet, the difference therein cannot be neglected in a significant range of triaxial loads, *especially* in an interval of $0.5 < T < 2$ where void coalescence is accelerated due to the existence of lateral loads but significant stress-bearing capacity still remains after coalescence, before $\bar{\chi}$ can reach its critical value where the stresses vanish.

More importantly, in the shear-dominated region ($0 < T < 1/3$), both ϵ_c and ϵ_f admit their minimum values not at the simple-shear limit but somewhere between the two limits. Within a reasonable accuracy, it can be deduced that the minimum to ϵ_c and ϵ_f occurs almost at $\kappa = \mathcal{S}/\mathcal{T}$, which corresponds to

$$T(\epsilon_{f\min}) = \frac{1}{3}\frac{\mathcal{S}}{\sqrt{\mathcal{S}^2 + 3\mathcal{T}^2}} \tag{69}$$

for a combined normal-shear loading, with $\mathcal{S}$ and $\mathcal{T}$ defined in (33).

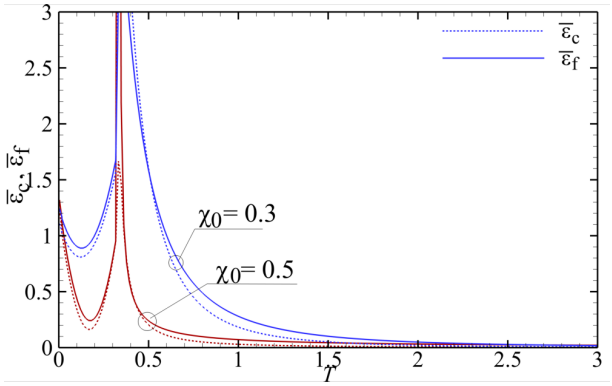

Figure 15: Predicted strain to onset of localization ϵ_c as well as strain to failure ϵ_f as function of stress triaxiality T for the same cell as shown in Fig. 5a, with $(w_0, \lambda_0) = (1.1, 4)$, hardening exponent $N = 0.2$ and various initial ligament parameters χ_0, upon a wide range of axial and shear loading combinations, identified with T ranging from 0 to 1/3, denoting combined normal and shear loading, and 1/3 to 3, representing triaxial loading.

6 Discussion

The constitutive framework developed in the present context provides a scheme for the simulation of ductile fracture in porous materials under arbitrary stress states, with specific capability of failure prediction under shear-dominated loading. The predicted failure process is characterized by the evolution of measurable and/or observable microstrucrural parameters including the relative void spacing, void aspect ratio, and void orientation. The first and foremost virtue within such a physics-based framework is clarity in the predicted mechanism. That is, whether or not this predicted mechanism can capture the essential features of failure under combined loading can be subjected to examination based on established circumstances whereby the model lends itself credibility or exposes its own shortcomings. Secondly, any modification or calibration that comes inevitable can be exerted on the most effective parameters and can be expressed in terms of the existing measurable and/or observable parameters. The present constitutive framework can then predict the fracture process under variegated initial conditions following a simple modification. In particular, the predicted process is well-behaved and progressive up to the failure instant (if any) whereas existing numerical analyses [14, 21, 22] have terminated soon after the onset of localized deformation let alone the lack of sufficient tools for resembling analyses for general 3D cells under extreme shearing. It can further provide grounds to vindicate the wide range of observable ductilities under shear loading for various metals [4, 5]. The enormous change in the failure strain reflected through Fig. 9 reveals the reason being the effect of initial relative void spacing χ_0 carried through by the effective ligament parameter $\bar{\chi}$ until ultimate failure.

Furthermore, the differences lying in the observed microscopic fracture surfaces can be rationalized by virtue of the evolving physical parameters affecting the simulated response. Fracture in ductile materials is always mediated by the existence of voids [52, 53]. However, fracture may be triggered by different mechanisms under different load combinations. The distinction between failure mechanisms can best be envisaged through fractography. Notably, fracture surfaces in ductile materials exhibit dimples under triaxial and shear-dominated stress states. The former, however, comprises deep elliptic-like dimples whereas the latter reveal parabolic dimples [53]. A graphically illustrative explanation on the correlation between observed and predicted fracture surfaces with the corresponding effective microstrucrure has been provided in [31].

As formerly pointed out in the introduction, the present work simulates ductile fracture with preexisting

void. Nevertheless, void nucleation under predominant shearing involves complex void–particle interactions [54] per se. This line of work has been investigated primarily by Needleman [11], and later work considered particle locking effects [55, 56]. Micromechanical void nucleation analyses of this caliber are still not available for shear-dominated loading. Whether or not these nucleation conditions fundamentally differ from those under tension remains to be investigated.

Void enlargement at medium to high triaxialities, as well as void shrinking at the limit of low triaxialities, are usually accompanied with void shape changes and distortion. Yet, the latter is more prominent at remarkable shear stresses characteristic of low stress triaxialities. In this regime, void distortion is a key origin to failure. Void distortion can be influenced by several factors, including the presence of shear stresses and void–particle interactions [55, 57]. Void locking and formation of penny–shaped cracks under limited void growth are among the clear examples [56,58,59]. Notwithstanding the existence of sophisticated cell-model numerical work [1, 14, 21], a major drawback within the established caliber of work on the effects induced by shear is a missing constitutive framework that takes into account the effective internal state variables that are both measurable and observable. These variables pertain mainly to the rotation and distortion of the microstructure under the effect of shear. Therefore, the major challenges to this task are primarily related to the void–mediated microstructural evolution mainly associated with void rotation and distortion under the effect of combined tension and shear.

A pivotal feature of ductile failure under shear is a void that moves faster than the cell, which is only characteristic of inhomogeneous deformation by plastic deformation localized within the inter-void ligament or a neighborhood thereof. Unless such a mechanism is incorporated into the constitutive model, failure under shear cannot be predicted. With the notion of a critical parameter, *e.g.* $(f+g)_c$, as adopted in [40], can prove efficacious in modeling procedures, yet cannot rationalize the physical process that accounts for the differences in void rotation and elongation rates.

Note that a state of *simple shear* is normally characterized by shear strains (shearing) with normal strains vanishing whereas *pure shear* is categorized by vanishing shear stresses. Within a dilute material, with no voids present, normal stresses are indispensable in the realization of simple shear, and normal strains are essential to pure shear [60]. For a porous material, however, the two can approximately coincide, even at low porosity levels, but upon similar *loading paths*. Namely, the normal strain can become vanishingly small at the limit of $\kappa \equiv \sigma/\tau \longrightarrow 0$, which can be revealed by λ and c remaining almost constant at this limit (see Fig. 8). If, however, the loading path changes, the responses can bare utmost differences even at equivalent stress states. The clear distinction between the results presented in Section 5.2 and Appendix J testifies this difference albeit the stress states being equivalent at $\kappa = 0$ in the cell shown in Fig. 5b and $\rho \equiv \sigma_1/\sigma_3 = -1$ in Fig. A-5. See Appendix J for more details.

Another prominent finding in failure under shear is void closure, mainly observed in oblate voids with $w < 1$ even though the possibility of it happening in prolate voids ($w > 1$) cannot be excluded at the limit of dilute material ($\chi_0 \longrightarrow 0$). It should be highlighted that when an oblate void closes, the void has turned so flat that it can trigger failure by impinging its neighboring voids under limited void growth, which is indicative of penny-shaped crack propagation. All the same, a prolate closing void turns into a needle-like figure that simply acts like a material line. No failure can thus be expected under such a condition.

It is also noteworthy that, at the limit of *isotropic* yielding, which occurs by virtue of a random distribution of voids, the ϵ_f vs. T curve is absolutely declining even for the $T < 1/3$ range. This distinction lies in the equivalence between a state of pure shear with a biaxial tension-compression loading with equal load magnitudes, which corresponds to infinite ϵ_c as well as ϵ_f. In other terms, the isotropic limit of a porous material at an arbitrary material point is independent of the loading path inasmuch as the material response is the same in all directions. The reader can consult Ref. [51] in regards to isotropic failure in ductile porous media. A recent work by the authors also presents the counterpart of this curve by incorporating the void shape effect for the isotropic limit of failure.

7 Conclusions

A micromechanics-based hybrid model describing a ductile fracture process under combined tension and shear up to ultimate failure was implemented with a bipartite yield criterion comprising nearly-homogeneous and inhomogeneous deformation processes. Upon a triaxial loading condition, nearly-homogeneous and inhomogeneous processes can best be represented by void growth and void coalescence, respectively. Under combined tension and shear with intermediate or extreme shearing, however, voids may grow or shrink at the nearly-homogeneous process (depending on the ratio between normal and shear stresses) and the inhomogeneous process can represent, in general, failure in shear by internal necking combined with internal shearing [14, 31]. Alongside, evolution equations were utilized for nearly-homogeneous deformation, and originally derived for inhomogeneous deformation under combined tension and shear. The microstructural state was described by a set of internal state variables, part of which were evolved implicitly using the Newton-Raphson iterative scheme, and the rest were evolved explicitly in terms of the independent (implicitly evolved) parameters. The post-localized evolution equations were derived for spheroidal voids both to relax the overconstraint induced by the cylindrical idealization and to capture the salient features of shear-induced deformation for elongated (needle-like) and flat (disk-like) as well as for spherical voids. The inhomogeneous yield criterion accounting for post-localized deformation appears as function of a surrogate microstructure aligned with the normal to a possible plane of localization.

With the hybrid model employed in its original form, the inhomogeneous yield criterion prevails under shear-dominated loading and, with the derived constitutive framework, can mimic the physics of failure in shear. Nonetheless, it cannot capture the quantitative aspect of the process in conformity with numerical findings. Both the nearly-homogeneous and inhomogeneous yield criteria were modified with simple adjustable parameters such that the failure mechanism was quantitatively retrieved for all combinations of normal and shear stresses. Some of featured outcomes are listed as follows:

- The implementation was assessed in reference to existing numerical results presented by Pardoen and Hutchinson [17] for triaxial loading as well as Tvergaard and coworkers [14,21] for combined tension and shear as well as a state of near-simple shearing. The latter was ground for the simple adjustment of the model. Stress triaxiality T, initial void aspect ratio w_0, and the normal-to-shear remote stress ratio κ were considered as comparator.

- Effects induced by the loading combination (represented by the normal-to-shear stress ratio) were investigated for an initially spherical void by examining various state variables under effect including, but not limited to, effective ligament parameter, porosity, void aspect ratio, and void orientation. The effective ligament parameter $\bar{\chi}$ defined over the above-mentioned surrogate cell is the main factor of influence that accounts for failure under combined tension and shear. It is itself a function in direct proportion to the current porosity as well as the cell aspect ratio, and scales inversely with the surrogate void aspect ratio. The latter starts with a finite value and evolves towards zero until failure.

- The effect of initial porosity, reflected through the initial ligament parameter χ_0 for an initially spherical void, was investigated under near-simple shearing. The onset of localized deformation as well as ultimate failure were delayed with a smaller χ_0. The limit of a dilute material ($\chi_0 \longrightarrow 0$) would exhibit no failure under shear.

- A shorter cell, characterized by a smaller cell aspect ratio λ, would have a larger strain to the onset of localization ϵ_c, as well as a larger strain to failure ϵ_f under near-simple shearing. The latter is rooted in the fact that unlike a larger-than-cubic cell (with $\lambda > 1$), a shorter-than-cubic cell ($\lambda < 1$) initially rotates faster than the void does. Besides, at a fixed porosity, a void within a shorter cell is more distant from the cell boundaries than its counterpart in a taller cell.

- Under near-simple shearing ($\kappa \approx 0$), an oblate void ($w < 1$), contrary to a prolate void ($w > 1$), rotates transiently opposite to the shearing direction. Yet, there is a turning point in the middle of the process, which normally occurs at the point of transition into the localized deformation mode, where the void starts moving back towards the shearing direction. Failure for an oblate void occurs in the form of penny-shaped crack propagation that is realized after void closure (characterized by the porosity f approaching zero). Altogether, for both prolate and oblate voids, the larger void axis tends to align with the direction of the principal stretch.

- The strain to the onset of localization ϵ_c, as well as strain to failure ϵ_f was plotted in terms of stress triaxiality for the whole scope of stress triaxialities ranging from zero to 1/3 (shear-dominated interval) and from 1/3 to 3 (normal-dominated interval) by numerical integration of the differential equations expressing porosity, void aspect ratio, and void orientation in terms of the equivalent plastic strain $\bar{\epsilon}$. Within the shear-dominant interval, ϵ_f admits a minimum that can be roughly expressed in terms of the microstructural parameters within the inhomogeneous yield criterion.

Appendix A K–B Model Parameters

The parameters embedded in (29) are functions of porosity f, void aspect ratio w and the Hill tensor $\mathbb{K}$. g, known as *secondary porosity* is defined as:

$$g = 0 \quad (\text{p}); \qquad g = \frac{e_2^3}{\sqrt{1-e_2^2}} = f\frac{e_1^3}{\sqrt{1-e_1^2}} = f\frac{(1-w^2)^{\frac{3}{2}}}{w} \quad (\text{o}) \tag{A-1}$$

where (p) and (o) stand for "prolate" ($w > 1$) and "oblate" ($w < 1$), respectively. By definition, g is non-zero for oblate voids only. e_1 and e_2 are, respectively, the eccentricities of the void and the outer boundary of the spheroidal RVE (shown in Fig. 2). The latter is an implicit function of f and w.

$$e_1^2 = \begin{cases} 1-\dfrac{1}{w^2} & (\text{p}) \\ 1-w^2 & (\text{o}) \end{cases}, \qquad \frac{(1-e_2^2)^n}{e_2^3} = \frac{1}{f}\frac{(1-e_1^2)^n}{e_1^3}, \qquad n = \begin{cases} 1 & (\text{p}) \\ 1/2 & (\text{o}) \end{cases} \tag{A-2}$$

Also,

$$\kappa = \begin{cases} 3\left\{1-\dfrac{2}{\ln f}\ln\dfrac{1-e_2^2}{1-e_1^2}\right\}^{-1/2} & (\text{p}) \\ 3\left\{1+\dfrac{(g_f-g_1)+\frac{4}{5}(g_f^{5/2}-g_1^{5/2})-\frac{3}{5}(g_f^5-g_1^5)}{\ln\frac{g_f}{g_1}}\right\}^{-1} & (\text{o}) \end{cases} \tag{A-3}$$

where

$$g_f \equiv \frac{g}{g+f}, \quad g_1 \equiv \frac{g}{g+1} \tag{A-4}$$

Next,

$$\alpha_2 = \begin{cases} \dfrac{(1+e_2^2)}{(1+e_2^2)^2+2(1-e_2^2)} & (\text{p}) \\ \dfrac{(1-e_2^2)(1-2e_2^2)}{(1-2e_2^2)^2+2(1-e_2^2)} & (\text{o}) \end{cases} \tag{A-5}$$

$$\begin{aligned} \eta &= -\frac{2}{3}\frac{\kappa(1-f)(g+1)(g+f)\text{sh}}{(g+1)^2+(g+f)^2+(g+1)(g+f)[\kappa K^*\text{sh}-2\text{ch}]}, \\ C &= -\frac{2}{3}\frac{\kappa(g+1)(g+f)\text{sh}}{(1-f+\frac{3}{2}\eta K^*)\eta}, \quad \text{sh} \equiv \sinh(\kappa K^*), \quad \text{ch} \equiv \cosh(\kappa K^*) \end{aligned} \tag{A-6}$$

where $K^* \equiv 2(\alpha_1 - \alpha_2)$.

α_2 and α_1 are identical to those introduced in [36] for isotropic materials, that read

$$\alpha_1 = \begin{cases} \left[e_1-(1-e_1^2)\tanh^{-1}e_1\right]/(2e_1^3) & (\text{p}) \\ \left[-e_1(1-e_1^2)+\sqrt{1-e_1^2}\sin^{-1}e_1\right]/(2e_1^3) & (\text{o}) \end{cases} \tag{A-7}$$

Finally:

$$\alpha_1^{\text{Gar}} = \begin{cases} \dfrac{1}{3-e_1^2} & (\text{p}) \\ \dfrac{1-e_1^2}{3-2e_1^2} & (\text{o}) \end{cases} \tag{A-8}$$

Appendix B Basic Equations governing post-localized state evolution

The tangency between the void poles and the rigid-like matrix is key to these derivations. For cylindrical voids, the void poles are connected to the matrix over the entire upper and lower circular cross sections, as depicted in Fig. 1a. Therefore, the distortion of voids under the effect of shearing will be all alike. The inhomogeneous microstructural evolution would then admit simple geometric relations. See [30] for details. All the same, a spheroidal void intercepts with the matrix at two single points of tangency, denoted with A and A' in Fig. 1. Correspondingly, prolate ($w > 1$) and oblate ($w < 1$) voids would deform in different manners. That is, prolate voids rotate along with shearing while oblate voids rotate backwards. Both voids, however, deform such that their larger axes incline towards the direction of principal stretch, which proves close to 45° under near–simple shearing. Both deformation modes were schematized in Fig. 1a. Altogether, the inhomogeneous microstructural evolution in presence of spheroidal voids can be described by means of the normal and tangential motions of the generatrix AA', as separately schematized for prolate and oblate voids in Fig. A-1 with more details on some intermediately defined angles. The angles identified according to Fig. A-1 are directional as stipulated by the figure, with the origin taken as the starting point.

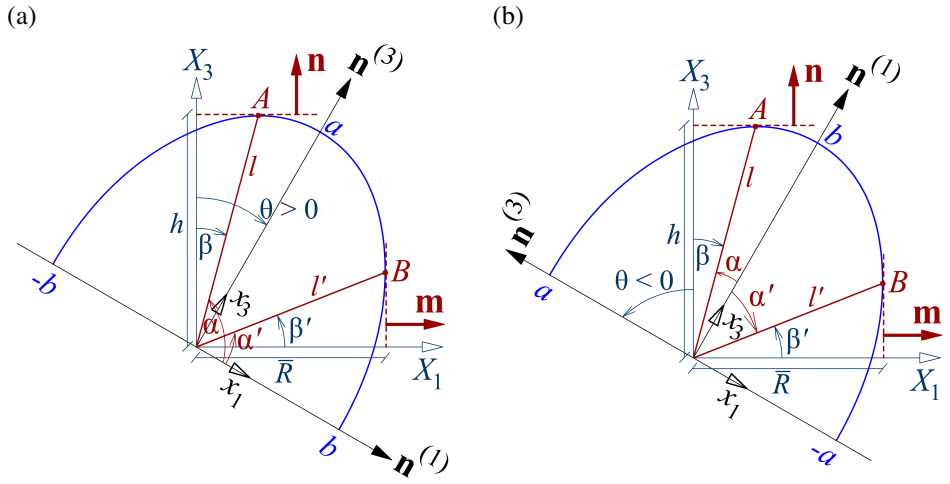

Figure A-1: Schematic outline of a spheroidal void under combined tension and shear: (a) a prolate void ($w > 1$), (b) an oblate void ($w < 1$).

θ is formed between the normal $\mathbf{n}$ (taken as origin) and the void axis $\mathbf{n}^{(3)}$. β forms between the same origin and line l passing through the tangency point A while β' originates at $\mathbf{m}$ towards line l' passing through the vertical tangency point B. Moreover, α and α' extends from the minor semiaxis $\mathbf{n}^{(1)}$ (taken as origin) to lines l and l', respectively. Nevertheless, not all of these angles are independent. In fact, all angles can be expressed in terms of θ as seen in the sequel. The genetratrices (ℓ, ℓ') have a key role in the geometric description of the post-localized microstructure. To begin with, one can recourse to the ellipse equation in the $X_1 - X_3$ coordinate system:

$$\mathcal{F} = \left(\frac{CX_1 - SX_3}{b}\right)^2 + \left(\frac{SX_1 + CX_3}{a}\right)^2 - 1 = 0 \tag{A-9}$$

Here, C and S are short-hand notation for $C = \mathbf{n}^{(3)} \cdot \mathbf{n} \equiv \cos\theta$ and $S = \mathbf{n}^{(3)} \cdot \mathbf{m}$.

At point A:

$$\frac{\mathrm{d}X_3}{\mathrm{d}X_1}=-\frac{\mathcal{F}_{,X_1}}{\mathcal{F}_{,X_3}}=0 \quad \therefore \quad \left(C+\frac{\mathscr{T}}{w^2}S\right)X_1=\left(S-\frac{\mathscr{T}}{w^2}C\right)X_3 \quad \therefore \quad \tan\beta=\frac{(w^2-1)\mathscr{T}}{w^2+\mathscr{T}^2} \tag{A-10}$$

where $\mathscr{T}=S/C=\tan\theta$. On the other hand, one can write

$$\tan\beta=\frac{X_{1A}}{X_{3A}}=\frac{x_{1A}+x_{3A}\mathscr{T}}{-x_{1A}\mathscr{T}+x_{3A}} \quad \therefore \quad \tan\alpha=\frac{1+\mathscr{T}\tan\beta}{\tan\beta-\mathscr{T}}=-\frac{w^2}{\mathscr{T}} \tag{A-11}$$

Moreover, the ellipse equation delivers the following expression for the tangential length ℓ:

$$x_{1A}^2=\frac{b^2}{1+\frac{\tan\alpha^2}{w^2}} \quad \therefore \quad \ell^2=x_{1A}^2+x_{3A}^2=(1+\tan\alpha^2)x_{1A}^2=\frac{\mathscr{T}^2+w^4}{w^2(\mathscr{T}^2+w^2)}a^2=\frac{\mathscr{T}^2+w^4}{\mathscr{T}^2+w^2}b^2 \tag{A-12}$$

All the same, at point B:

$$\frac{\mathrm{d}X_1}{\mathrm{d}X_3}=-\frac{\mathcal{F}_{,X_3}}{\mathcal{F}_{,X_1}}=0 \quad \therefore \quad \left(\mathscr{T}C-\frac{S}{w^2}\right)X_1=\left(\mathscr{T}S+\frac{C}{w^2}\right)X_3 \quad \therefore \quad \tan\beta'=\frac{(w^2-1)\mathscr{T}}{1+w^2\mathscr{T}^2} \tag{A-13}$$

On the other hand, one can write

$$\tan\beta'=\frac{X_{3B}}{X_{1B}}=\frac{-x_{1B}\mathscr{T}+x_{3B}}{x_{1B}+x_{3B}\mathscr{T}} \quad \therefore \quad \tan\alpha'=\frac{\mathscr{T}+\tan\beta'}{1-\mathscr{T}\tan\beta'}=\mathscr{T}w^2 \tag{A-14}$$

Finally, similar to (A-12), the ellipse equation delivers the following expression for the tangential length ℓ':

$$(\ell')^2=x_{1B}^2+x_{3B}^2=\frac{1+\mathscr{T}^2w^4}{w^2(1+\mathscr{T}^2w^2)}a^2=\frac{1+\mathscr{T}^2w^4}{1+\mathscr{T}^2w^2}b^2 \tag{A-15}$$

With the set of equations (A-10 – A-15) at hand, one has enough tools to calculate some pre and post-localized parameters of interest (as in Eq. (9)) plus the post-localized surrogate microstructural parameters in Sec. 3.2. The post-localization evolution equations as well as the surrogate microstructure for usage in Φ^{I} can be conveniently derived based on Eq's (A-10)–(A-15).

Appendix C Derivation of Post-localized $\dot{w}$

The time rate of ℓ, as schematized in Fig. A-1, governs the post-localized evolution of the void aspect ratio.

Due to symmetry, we focus on motion of the top boundary. Thus, the tangential and normal velocities of point A are given by:

$$\begin{aligned} v_1^{(\mathrm{A})}&=2h\frac{D_{\mathrm{mn}}}{c}=2HD_{\mathrm{mn}}\\ v_3^{(\mathrm{A})}&=h\frac{D_{\mathrm{nn}}}{c}=HD_{\mathrm{nn}} \end{aligned} \tag{A-16}$$

where the x_1 and x_3 axes are identified with the directions of shear, $\mathbf{m}$, and normal to the band, $\mathbf{n}$, respectively. Accordingly,

$$\begin{aligned} D_{\mathrm{nn}}&=\mathbf{n}\cdot\mathbf{D}^{\mathrm{p}}\mathbf{n}\\ D_{\mathrm{mn}}&=\mathbf{m}\cdot\mathbf{D}^{\mathrm{p}}\mathbf{n} \end{aligned}$$

with elastic strain rates neglected. Referring back to Eq. (A-16), one can write

$$\frac{\dot{\ell}}{\ell} = \frac{1}{\ell}(v_1^{(\mathrm{A})} S + v_3^{(\mathrm{A})} C) = \frac{C}{c}(2SD_{\mathrm{mn}} + CD_{\mathrm{nn}}) \tag{A-17}$$

exploiting the $H/\ell = C/c$ identity. The time rate of $s \equiv \ln w$ can be developed based on a relationship established among $\dot{a}$, $\dot{b}$, and $\dot{\ell}$ according to the following steps.

- Prolate voids ($w \geq 1$): From Eq. (A-12):

$$\frac{\dot{a}}{a} = \frac{\dot{\ell}}{\ell} + \frac{\mathscr{T}^2(2w^2 - w^4 + \mathscr{T}^2)}{(w^4 + \mathscr{T}^2)(w^2 + \mathscr{T}^2)}\dot{s} \tag{A-18}$$

Also, from incompressibility within the ligament:

$$\frac{\mathrm{d}}{\mathrm{d}t}\left(\pi L^2(2h) - \frac{2\pi}{3\gamma}b^2 a\right) = 0 \implies L^2\dot{h} = \frac{ab^2}{3\gamma}\left(2\frac{\dot{b}}{b} + \frac{\dot{a}}{a}\right) \therefore \frac{\dot{b}}{b} = \frac{1}{2}\left[3\gamma\left(\frac{L}{b}\right)^2 \frac{H}{a} D_{\mathrm{nn}} - \frac{\dot{a}}{a}\right] \tag{A-19}$$

noting that $\dot{L} = 0$ and $\dot{h} = \dot{H}$ after the onset of coalescence, and γ is the void shape factor, equaling 1/3 for a spheroidal and 1/2 for a cylindrical void. The porosity, however, can be expressed as

$$f = \frac{\frac{2\pi}{3\gamma}b^2 a}{\pi L^2(2h)} = \frac{1}{3\gamma}\left(\frac{b}{L}\right)^2 \frac{a}{H}$$

Therefore,

$$\frac{\dot{b}}{b} = \frac{1}{2}\left(\frac{D_{\mathrm{nn}}}{f} - \frac{\dot{a}}{a}\right) \tag{A-20}$$

which, together with (A-19), gives:

$$\dot{s} = \frac{\dot{a}}{a} - \frac{\dot{b}}{b} = \frac{3}{2}\frac{\dot{a}}{a} - \frac{1}{2}\frac{D_{\mathrm{nn}}}{f} \tag{A-21}$$

The combination of (A-21) and (A-18), exploiting the following identities:

$$\cos^2\beta = \frac{1}{1 + \tan^2\beta}$$
$$\sin 2\beta = \frac{2\tan\beta}{1 + \tan^2\beta}$$

delivers, with reference to (A-10):

$$\left[2 - 3\frac{\mathscr{T}^2(2w^2 - w^4 + \mathscr{T}^2)}{(w^4 + \mathscr{T}^2)(w^2 + \mathscr{T}^2)}\right]\dot{s} = \left(3\frac{\cos^2\beta}{c} - \frac{1}{f}\right)D_{\mathrm{nn}} + 3\frac{\sin 2\beta}{c}D_{\mathrm{nm}}$$
$$\therefore \dot{s} = \frac{(w^2 + \mathscr{T}^2)^2}{(w^4 + \mathscr{T}^2)(1 + \mathscr{T}^2)\left[2 - 3\frac{\mathscr{T}^2(2w^2 - w^4 + \mathscr{T}^2)}{(w^4 + \mathscr{T}^2)(w^2 + \mathscr{T}^2)}\right]}\left[\left(\frac{3}{c} - \frac{(w^4 + \mathscr{T}^2)(1 + \mathscr{T}^2)}{f(w^2 + \mathscr{T}^2)^2}\right)D_{\mathrm{nn}} + \frac{6}{c}\frac{(w^2 - 1)\mathscr{T}}{w^2 + \mathscr{T}^2}D_{\mathrm{nm}}\right] \tag{A-22}$$

For the special case of an upright void, where $\mathscr{T} = 0$:

$$\dot{s} = \frac{3}{2}\left(\frac{1}{c} - \frac{1}{3f}\right)D_{\mathrm{nn}} = \frac{9}{4c}\left(1 - \frac{\gamma}{\chi^2}\right)D_{\mathrm{eq}} \tag{A-23}$$

where use has been made of the expressions $f = c\chi^2/3\gamma$ and $D_{\rm eq} = 2/3D_{\rm nn}$. Note that (A-23) retrieves Eq. (12) of [33], which yields $\dot{s} \geq 0$ as long as $\chi \leq \sqrt{\gamma}$, and vice versa.

All the same, in the special case of a void after extreme shearing ($\mathscr{T} \longrightarrow \infty$ and $w \longrightarrow \infty$) under (near-) simple shear ($D_{\rm nn} \approx 0$):

$$\dot{s} = \frac{6}{c} \frac{w^2 + \mathscr{T}^2}{w^2 \mathscr{T} \left(2 + 3\frac{\mathscr{T}^2}{w^2+\mathscr{T}^2}\right)} D_{\rm nm} \tag{A-24}$$

which is positive upon $D_{\rm nm}$ being positive.

- Oblate voids ($w < 1$): From Eq. (A-12):

$$\frac{\dot{b}}{b} = \frac{\dot{\ell}}{\ell} - \left(\frac{2w^4}{\mathscr{T}^2 + w^4} - \frac{w^2}{\mathscr{T}^2 + w^2}\right) \dot{s} \tag{A-25}$$

Also, (A-21) can be recast as function of $\dot{b}/b$ as follows

$$\dot{s} = -3\frac{\dot{b}}{b} + \frac{D_{\rm nn}}{f}$$

which, together with (A-25), delivers the following rate of void shape for an oblate void:

$$\left[1 - \frac{\mathscr{T}^2(-2w^2 + w^4 - \mathscr{T}^2)}{(w^4 + \mathscr{T}^2)(w^2 + \mathscr{T}^2)}\right] \dot{s} = \left(-3\frac{\cos^2\beta}{c} + \frac{1}{f}\right) D_{\rm nn} - 3\frac{\sin 2\beta}{c} D_{\rm nm}$$
$$\therefore \dot{s} = \frac{(w^2 + \mathscr{T}^2)^2}{(w^4 + \mathscr{T}^2)(1 + \mathscr{T}^2)\left[1 - \frac{\mathscr{T}^2(-2w^2+w^4-\mathscr{T}^2)}{(w^4+\mathscr{T}^2)(w^2+\mathscr{T}^2)}\right]} \left[\left(-\frac{3}{c} + \frac{(w^4 + \mathscr{T}^2)(1 + \mathscr{T}^2)}{f(w^2 + \mathscr{T}^2)^2}\right) D_{\rm nn} - \frac{6}{c}\frac{(w^2 - 1)\mathscr{T}}{w^2 + \mathscr{T}^2} D_{\rm nm}\right] \tag{A-26}$$

For the special case of an upright void, where $\mathscr{T} = 0$:

$$\dot{s} = \left(-\frac{3}{c} + \frac{1}{f}\right) D_{\rm nn} = \frac{9}{2c}\left(-1 + \frac{\gamma}{\chi^2}\right) D_{\rm eq} \tag{A-27}$$

which has been simplified resembling (A-23). Note that (A-27) yields $\dot{s} \leq 0$ as long as $\chi \leq \sqrt{\gamma}$, and vice versa.

All the same, in the special case of a void after extreme shearing ($\mathscr{T} \longrightarrow 0^-$ and $w \longrightarrow 0$) under (near-)simple shear ($D_{\rm nn} \approx 0$), one can conveniently verify that $\dot{s} < 0$ upon $D_{\rm nm}$ being positive.

Appendix D Current Cell Aspect Ratio

The algebraic steps to the derivation of Eq. (16) are addressed in extension to Eq. (21) of Ref. [38] for initially cubic cells. To this end, one could firstly write:

$$\lambda(\mathbf{n}) = \frac{H(\mathbf{n})}{L(\mathbf{n})} = \frac{H_0(\mathbf{n})}{L_0(\mathbf{n})} \frac{H(\mathbf{n})/H_0(\mathbf{n})}{L(\mathbf{n})/L_0(\mathbf{n})} \tag{A-28}$$

where the 0 subscripts denote the initial state, and

$$\frac{H_0(\mathbf{n})}{L_0(\mathbf{n})} = \lambda_0(\mathbf{n})$$

Moreover, V_0 and V (initial and current cell volumes) are related via

$$V = \mathcal{J} V_0$$

which implies

$$\frac{H(\mathbf{n})}{H_0(\mathbf{n})} = \mathcal{J} \frac{A_0(\mathbf{n})}{A(\mathbf{n})} \tag{A-29}$$

The average cell length L and ligament area A correlate through

$$\frac{L(\mathbf{n})}{L_0(\mathbf{n})} = \sqrt{\frac{A(\mathbf{n})}{A_0(\mathbf{n})}} \tag{A-30}$$

On the other hand, a continuum relationship between A_0 and A reads

$$A\mathbf{n} = \mathcal{J}\mathbf{F}^{-T} A_0 \mathbf{n}_0$$

which can be recast, by exploiting a dot product, into the following

$$(A_0\mathbf{n}_0)\cdot(A_0\mathbf{n}_0) = \frac{1}{\mathcal{J}^2}(\mathbf{F}^T A\mathbf{n})\cdot(\mathbf{F}^T A\mathbf{n}) = \frac{1}{\mathcal{J}^2} A^2 \mathbf{n}\cdot\mathbf{F}\mathbf{F}^T\mathbf{n} \;\therefore\; \frac{A_0}{A} = \frac{1}{\mathcal{J}}\sqrt{\mathbf{n}\cdot\mathbf{F}\mathbf{F}^T\mathbf{n}} \tag{A-31}$$

Finally, the combination of (A-29 – A-31) yields

$$\lambda(\mathbf{n}) = \lambda_0(\mathbf{n})\mathcal{J}\left(\frac{A_0(\mathbf{n})}{A(\mathbf{n})}\right)^{\frac{3}{2}} = \frac{\lambda_0(\mathbf{n})}{\sqrt{\mathcal{J}}}\left(\mathbf{n}.(\mathbf{F}\mathbf{F}^{\mathrm{T}}).\mathbf{n}\right)^{\frac{3}{4}} \tag{A-32}$$

Appendix E Derivation of Post-localized Ω^l

With reference to (9), the time rate of c reads

$$\begin{aligned} 3\frac{\dot{c}}{c} &= \frac{\dot{f}}{f} - \left(\frac{\dot{w}}{w} + 2\frac{\dot{\lambda}}{\lambda}\right) + 3\left(\frac{\mathscr{T}\dot{\mathscr{T}} + w\dot{w}}{\mathscr{T}^2 + w^2} - \frac{\mathscr{T}\dot{\mathscr{T}}}{1+\mathscr{T}^2}\right) \\ \dot{\mathscr{T}} &= \frac{(\mathscr{T}^2 + w^2)(1+\mathscr{T}^2)}{\mathscr{T}(1-w^2)}\left[\frac{\dot{c}}{c} - \frac{1}{3}\left(\frac{\dot{f}}{f} - 2\frac{\dot{\lambda}}{\lambda}\right) + \left(\frac{1}{3} - \frac{w^2}{\mathscr{T}^2 + w^2}\right)\dot{s}\right] \end{aligned} \tag{A-33}$$

The rates of internal parameters entering the right-hand side of this equation are all known, except the void orientation, which enters through $\dot{\mathscr{T}}$. $\dot{c}/c$ can be determined by neglecting the volume change of the elastically unloaded zones. Thus,

$$\frac{\dot{c}}{c} = \frac{\dot{h}}{h} - \frac{\dot{H}}{H} = \frac{D_{33}}{c} - D_{33} = \frac{1-c}{c}\mathbf{n}\cdot\mathbf{D}^{\mathrm{p}}\mathbf{n} \tag{A-34}$$

Also,

$$\begin{aligned} \frac{\dot{f}}{f} &= \left(\frac{1}{f} - 1\right) D^{\mathrm{p}}_{kk} \\ \frac{\dot{\lambda}}{\lambda} &= \frac{\dot{H}}{H} - \frac{\dot{L}}{L} = D_{\mathrm{nn}} - \frac{1}{2}\left(D_{\mathrm{mm}} + D_{\mathrm{pp}}\right) \end{aligned} \tag{A-35}$$

where

$$D_{\rm nn} = \mathbf{n}\cdot\mathbf{D}^{\rm p}\mathbf{n} \quad , \quad D_{\rm mm} = \mathbf{m}\cdot\mathbf{D}^{\rm p}\mathbf{m} \quad , \quad D_{\rm pp} = \mathbf{p}\cdot\mathbf{D}^{\rm p}\mathbf{p}$$

and $\mathbf{p} = \mathbf{n}\times\mathbf{m}$ completes the triad of local base vectors. Since, however, $\Phi^{\rm I}$ does not deliver lateral strain rates, (A-35)$_2$ can be simplified through

$$\frac{\dot\lambda}{\lambda} = D_{\rm nn}$$

at the post-localization regime.

Furthermore, in the corotational formulation, where the material is taken stationary and thus $\mathbf{n}$ delivers no time rate, one simply has

$$\mathscr{T} = \frac{S}{C} = \frac{\mathbf{n}^{(3)}\cdot\mathbf{m}}{\mathbf{n}^{(3)}\cdot\mathbf{n}} \;\therefore\; \frac{\dot{\mathscr{T}}}{\mathscr{T}} = \frac{\dot S}{S} - \frac{\dot C}{C} \tag{A-36}$$

where

$$\dot S = \dot{\mathbf{n}}^{(3)}\cdot\mathbf{m} \quad , \quad \dot C = \dot{\mathbf{n}}^{(3)}\cdot\mathbf{n}$$

The component of $\dot{\mathbf{n}}^{(3)}$ along $\mathbf{m}$ can be derived considering that $\mathbf{n}^{(3)}$ is a unit vector, which entails

$$\left(\mathbf{n}^{(3)}\cdot\mathbf{m}\right)^2 + \left(\mathbf{n}^{(3)}\cdot\mathbf{p}\right)^2 + \left(\mathbf{n}^{(3)}\cdot\mathbf{n}\right)^2 = 1 \implies \dot{\mathbf{n}}^{(3)}\cdot\mathbf{n} = -\mathscr{T}\dot{\mathbf{n}}^{(3)}\cdot\mathbf{m} \;\therefore\; \frac{\dot S}{S} = \frac{1}{1+\mathscr{T}^2}\frac{\dot{\mathscr{T}}}{\mathscr{T}} \tag{A-37}$$

Note that component $\mathbf{n}^{(3)}\cdot\mathbf{p}$ does not deliver a time rate since no shear is exerted along $\mathbf{p}$. Finally, Ω^l can be recast in the following form:

$$\Omega^l = \frac{\dot S}{S}\mathbf{m}\otimes\mathbf{m} + \frac{\dot C}{C}\mathbf{n}\otimes\mathbf{n} = \frac{\dot{\mathscr{T}}}{\mathscr{T}}\left(C^2\mathbf{m}\otimes\mathbf{m} - S^2\mathbf{n}\otimes\mathbf{n}\right) \tag{A-38}$$

where $\dot{\mathscr{T}}$ is taken from (A-33).

Appendix F Separate Void Axes, Void and Cell Aspect Ratios

Under combined tension and shear, the void and cell deform unequally along the sheared direction $\mathbf{m}$ and the perpendicular one $\mathbf{p}$. The sequel provides details to obtain separate void and cell aspect ratios as well as void axes normalized by their initial values. Upon convention, the subscripts 1 and 2 pertain to the quantities within the n–m and n–p planes, respectively.

- During nearly-homogeneous deformation:
  Due to $\mathbf{D}^{\rm v}$, from Eq. (11), signifying the rate of deformation within the void:

$$\begin{aligned}
\frac{\dot{b_1}}{b_1} &= \mathbf{n}^{(1)}\cdot\mathbf{D}^{\rm v}\mathbf{n}^{(1)} \\
\frac{\dot{b_2}}{b_2} &= \mathbf{n}^{(2)}\cdot\mathbf{D}^{\rm v}\mathbf{n}^{(2)} \\
\frac{\dot a}{a} &= \mathbf{n}^{(3)}\cdot\mathbf{D}^{\rm v}\mathbf{n}^{(3)}
\end{aligned} \tag{A-39}$$

  Equations (A-39) can be integrated with respect to time so that the values of a/a_0, b_1/b_{10} and b_2/b_{20} are updated at every time step.

- During inhomogeneous deformation:
The time rate of normalized major semi-axis a/a_0 is a superposition of the values influenced by $D_{\rm nn}$ and $D_{\rm nm}$, declared with superscripts (n) and (sh), respectively. To this end, one can first refer to (A-18), (A-17), and (A-22) or (A-26) which deliver, respectively:

$$\begin{aligned}\left(\frac{\dot{a}}{a}\right)^{(\rm n)}&=\left(\frac{\dot{\ell}}{\ell}\right)^{(\rm n)}+\frac{\mathscr{T}^2(2w^2-w^4+\mathscr{T}^2)}{(\mathscr{T}^2+w^4)(\mathscr{T}^2+w^2)}\dot{s}^{(\rm n)}\\ \left(\frac{\dot{\ell}}{\ell}\right)^{(\rm n)}&=\frac{\cos^2\beta}{c}D_{\rm nn}=\frac{(\mathscr{T}^2+w^2)^2}{c(\mathscr{T}^2+w^4)(\mathscr{T}^2+1)}D_{\rm nn}\end{aligned}\tag{A-40}$$

where

$$\dot{s}^{(\rm n)}=\begin{cases}\dfrac{\frac{(\mathscr{T}^2+w^2)^2}{(\mathscr{T}^2+w^4)(\mathscr{T}^2+1)}\left[\frac{3}{c}-\frac{(\mathscr{T}^2+w^4)(\mathscr{T}^2+1)}{f(\mathscr{T}^2+w^2)^2}\right]}{2-3\frac{\mathscr{T}^2(2w^2-w^4+\mathscr{T}^2)}{(\mathscr{T}^2+w^4)(\mathscr{T}^2+w^2)}}D_{\rm nn} & \text{for } w\geq 1\\[2ex] \dfrac{\frac{(\mathscr{T}^2+w^2)^2}{(\mathscr{T}^2+w^4)(\mathscr{T}^2+1)}\left[-\frac{3}{c}+\frac{(\mathscr{T}^2+w^4)(\mathscr{T}^2+1)}{f(\mathscr{T}^2+w^2)^2}\right]}{1-\frac{\mathscr{T}^2(-2w^2+w^4-\mathscr{T}^2)}{(\mathscr{T}^2+w^4)(\mathscr{T}^2+w^2)}}D_{\rm nn} & \text{for } w<1\end{cases}\tag{A-41}$$

And, all the same

$$\begin{aligned}\left(\frac{\dot{a}}{a}\right)^{(\rm sh)}&=\left(\frac{\dot{\ell}}{\ell}\right)^{(\rm sh)}+\frac{\mathscr{T}^2(2w^2-w^4+\mathscr{T}^2)}{(\mathscr{T}^2+w^4)(\mathscr{T}^2+w^2)}\dot{s}^{(\rm sh)}\\ \left(\frac{\dot{\ell}}{\ell}\right)^{(\rm sh)}&=\frac{\sin 2\beta}{c}D_{\rm nm}=\frac{2\mathscr{T}(w^2-1)(\mathscr{T}^2+w^2)}{c(\mathscr{T}^2+w^4)(\mathscr{T}^2+1)}D_{\rm nm}\end{aligned}\tag{A-42}$$

where

$$\dot{s}^{(\rm sh)}=\begin{cases}\dfrac{\frac{6}{c}\frac{\mathscr{T}(w^2-1)(\mathscr{T}^2+w^2)}{(\mathscr{T}^2+w^4)(\mathscr{T}^2+1)}}{2-3\frac{\mathscr{T}^2(2w^2-w^4+\mathscr{T}^2)}{(\mathscr{T}^2+w^4)(\mathscr{T}^2+w^2)}}D_{\rm nm} & \text{for } w\geq 1\\[2ex] \dfrac{-\frac{6}{c}\frac{\mathscr{T}(w^2-1)(\mathscr{T}^2+w^2)}{(\mathscr{T}^2+w^4)(\mathscr{T}^2+1)}}{1-\frac{\mathscr{T}^2(-2w^2+w^4-\mathscr{T}^2)}{(\mathscr{T}^2+w^4)(\mathscr{T}^2+w^2)}}D_{\rm nm} & \text{for } w<1\end{cases}\tag{A-43}$$

In other terms, one could simply write

$$\dot{s}^{(\rm sh)}=q_1 D_{\rm nm}\quad,\quad \dot{s}^{(\rm n)}=q_2 D_{\rm nn}\tag{A-44}$$

with q_1 and q_2 defined in (58) and (59), respectively.

The normalized minor semi-axes b_1/b_{10} and b_2/b_{20} correlate through incompressibility within the ligament stated with distinct b_1 and b_2 as

$$\frac{\rm d}{{\rm d}t}\left(\pi L^2(2h)-\frac{2\pi}{3\gamma}b_1b_2a\right)=0\implies L^2\dot{h}=\frac{ab^2}{3\gamma}\left(\frac{\dot{b_1}}{b_1}+\frac{\dot{b_2}}{b_2}+\frac{\dot{a}}{a}\right)\ \therefore\ \frac{\dot{b_1}}{b_1}+\frac{\dot{b_2}}{b_2}=\frac{D_{\rm nn}}{f}-\frac{\dot{a}}{a}\tag{A-45}$$

where (A-20) has been utilized, and implicit is $b^2 = b_1 b_2$. The effect induced by $D_{\rm nn}$ on the minor semi-axes is equal time rate in the two, and that of $D_{\rm nm}$ is zero time rate on b_2. Accordingly, with reference to (A-45):

$$\begin{aligned}
&\left(\frac{\dot{b_1}}{b_1}\right)^{(\rm n)} = \left(\frac{\dot{b_2}}{b_2}\right)^{(\rm n)} = \frac{1}{2}\left[\frac{D_{\rm nn}}{f} - \left(\frac{\dot{a}}{a}\right)^{(\rm n)}\right] \\
&\left(\frac{\dot{b_2}}{b_2}\right)^{(\rm sh)} = 0 \quad , \quad \left(\frac{\dot{b_1}}{b_1}\right)^{(\rm sh)} = -\left(\frac{\dot{a}}{a}\right)^{(\rm sh)} \\
&\frac{\dot{b_1}}{b_1} = \left(\frac{\dot{b_1}}{b_1}\right)^{(\rm n)} + \left(\frac{\dot{b_1}}{b_1}\right)^{(\rm sh)} \quad , \quad \frac{\dot{b_2}}{b_2} = \left(\frac{\dot{b_2}}{b_2}\right)^{(\rm n)} + \left(\frac{\dot{b_2}}{b_2}\right)^{(\rm sh)}
\end{aligned} \tag{A-46}$$

and

$$\frac{\dot{a}}{a} = \left(\frac{\dot{a}}{a}\right)^{(\rm n)} + \left(\frac{\dot{a}}{a}\right)^{(\rm sh)} \tag{A-47}$$

with the constituents $\left(\dot{a}/a\right)^{(\rm n)}, \left(\dot{a}/a\right)^{(\rm sh)}$ are obtained, respectively, from (A-40) and (A-42), and $\left(\dot{b_1}/b_1\right)^{(\rm n)}, \left(\dot{b_2}/b_2\right)^{(\rm n)}$ originate from (A-46). Equations (A-46) and (A-47) are then integrated with respect to time steps so that the values of a/a_0, b_1/b_{10} and b_2/b_{20} are updated at every time step.

Once the above values are calculated, one can express the separate void aspect ratios in the following format:

$$\begin{aligned}
w_1 &= \frac{a}{b_1} = \frac{a}{a_0}\frac{a_0}{b_{01}}\frac{b_{01}}{b_1} = w_{10}\frac{a/a_0}{b_1/b_{01}} \\
w_2 &= \frac{a}{b_2} = \frac{a}{a_0}\frac{a_0}{b_{02}}\frac{b_{02}}{b_2} = w_{20}\frac{a/a_0}{b_2/b_{02}}
\end{aligned} \tag{A-48}$$

And, finally, the separate cell aspect ratios, in rate form, read

$$\begin{aligned}
\lambda_1 = \frac{H}{L_1} \;\therefore\; \frac{\dot{\lambda_1}}{\lambda_1} &= \frac{\dot{H}}{H} - \frac{\dot{L_1}}{L_1} = D_{\rm nn} - D_{\rm mm} \\
\lambda_2 = \frac{H}{L_2} \;\therefore\; \frac{\dot{\lambda_2}}{\lambda_2} &= \frac{\dot{H}}{H} - \frac{\dot{L_2}}{L_2} = D_{\rm nn} - D_{\rm pp}
\end{aligned} \tag{A-49}$$

Appendix G Post-localized Jacobian Components

The Jacobian matrix components are provided here for more clarity, with $R_{A,B} \equiv \frac{\partial R_A}{\partial B}$ and $\mathbf{0}$ being the second-order zero tensor. The major constituents of Jacobians are the second derivative of the flow potential with respect to the stress tensor, and the derivatives of $\mathbf{N}^{\rm I}$, as expanded in (53), with respect to the microstructural variables.

In general, the following identities will be used in the sequel:

$$\frac{\partial^2 \Phi^{\rm I}}{\partial\tilde{\sigma}'\partial\tilde{\sigma}'} = \mathbb{J} : \frac{\partial^2 \Phi^{\rm I}}{\partial\tilde{\sigma}\partial\tilde{\sigma}} : \mathbb{J} \quad , \quad \frac{\partial}{\partial\sigma_{kk}}\left(\frac{\partial \Phi^{\rm I}}{\partial\tilde{\sigma}'}\right) = \mathbb{J} : \frac{\partial^2 \Phi^{\rm I}}{\partial\tilde{\sigma}\partial\tilde{\sigma}} : \mathbf{I} \quad , \quad \frac{\partial^2 \Phi^{\rm I}}{\partial\sigma_{kk}\partial\sigma_{kk}} = \mathbf{I} : \frac{\partial^2 \Phi^{\rm I}}{\partial\tilde{\sigma}\partial\tilde{\sigma}} : \mathbf{I} \tag{A-50}$$

where, at the post-localization regime:

$$\frac{\partial^2 \Phi^{\rm I}}{\partial\tilde{\sigma}\partial\tilde{\sigma}} = \frac{2}{(\mathcal{V})^2}\left(\tilde{\mathbf{n}}\otimes\tilde{\mathbf{n}}\right)\otimes\left(\tilde{\mathbf{n}}\otimes\tilde{\mathbf{n}}\right)\;\mathcal{H}(|\sigma_n| - t\mathcal{S}) + \frac{2}{\mathcal{T}^2}\left[\mathbb{B} - \left(\tilde{\mathbf{n}}\otimes\tilde{\mathbf{n}}\right)\otimes\left(\tilde{\mathbf{n}}\otimes\tilde{\mathbf{n}}\right)\right] \tag{A-51}$$

where, in the reduced 9×9 notation, with σ reduced to $[\sigma_{11},\sigma_{12},\sigma_{13},\sigma_{21},\sigma_{22},\sigma_{23},\sigma_{31},\sigma_{32},\sigma_{33}]^T$, $\mathbb{B}$ writes:

$$\mathbb{B}^T=\begin{bmatrix} n_1^2 & n_1n_2 & n_1n_3 & n_1n_2 & 0 & 0 & n_1n_3 & 0 & 0\\ n_1n_2 & n_2^2 & n_2n_3 & n_2^2 & 0 & 0 & n_2n_3 & 0 & 0\\ n_1n_3 & n_2n_3 & n_3^2 & n_2n_3 & 0 & 0 & n_3^2 & 0 & 0\\ 0 & n_1^2 & 0 & n_1^2 & n_1n_2 & n_1n_3 & 0 & n_1n_3 & 0\\ 0 & n_1n_2 & 0 & n_1n_2 & n_2^2 & n_2n_3 & 0 & n_2n_3 & 0\\ 0 & n_1n_3 & 0 & n_1n_3 & n_2n_3 & n_3^2 & 0 & n_3^2 & 0\\ 0 & 0 & n_1^2 & 0 & 0 & n_1n_2 & n_1^2 & n_1n_2 & n_1n_3\\ 0 & 0 & n_1n_2 & 0 & 0 & n_2^2 & n_1n_2 & n_2^2 & n_2n_3\\ 0 & 0 & n_1n_3 & 0 & 0 & n_2n_3 & n_1n_3 & n_2n_3 & n_3^2 \end{bmatrix} \tag{A-52}$$

Also,

$$\begin{aligned}
\frac{\partial\Phi^{\mathrm{I}}}{\partial f}&=-2\frac{\partial\bar{\chi}}{\partial f}\left[\frac{1}{(b\mathcal{V})^3}\left(\sigma_n-\mathrm{sgn}(\sigma_n)t\mathcal{S}\right)\left[b\mathcal{V}\mathrm{sgn}(\sigma_n)(t\mathcal{S})_{,\bar{\chi}}+\left(\sigma_n-\mathrm{sgn}(\sigma_n)t\mathcal{S}\right)b\mathcal{V}_{,\bar{\chi}}\right]\mathcal{H}(\langle\sigma_n|-t\mathcal{S})+\frac{\tau_n^2}{(l\mathcal{T})^3}\mathcal{T}_{,\bar{\chi}}\right]\\
\frac{\partial\mathbf{N}^{\mathrm{I}}}{\partial f}&=-4\frac{\partial\bar{\chi}}{\partial f}\left[\frac{1}{(b\mathcal{V})^3}\left[\frac{1}{2}b\mathcal{V}\mathrm{sgn}(\sigma_n)(t\mathcal{S})_{,\bar{\chi}}+\left(\sigma_n-\mathrm{sgn}(\sigma_n)t\mathcal{S}\right)b\mathcal{V}_{,\bar{\chi}}\right](\tilde{\mathbf{n}}\otimes\tilde{\mathbf{n}})\,\mathcal{H}(\langle\sigma_n|-t\mathcal{S})+\frac{\tau_{\mathbf{n}}\otimes\mathbf{n}}{\mathcal{T}^3}\mathcal{T}_{,\bar{\chi}}\right]\\
\frac{\partial\Phi^{\mathrm{I}}}{\partial\bar{\sigma}}&=\frac{-2}{\bar{\sigma}}\left[\frac{\sigma_n\left(\sigma_n-\mathrm{sgn}(\sigma_n)t\mathcal{S}\right)}{(b\mathcal{V})^2}\mathcal{H}(\langle\sigma_n|-t\mathcal{S})+\left(\frac{\tau_n}{l\mathcal{T}}\right)^2\right]\\
\frac{\partial\mathbf{N}^{\mathrm{I}}}{\partial\bar{\sigma}}&=-4\left[\frac{1}{(b\mathcal{V})^2}\left(\frac{\sigma_n}{\bar{\sigma}}-\frac{1}{2}\mathrm{sgn}(\sigma_n)\frac{t\mathcal{S}}{\bar{\sigma}}\right)(\tilde{\mathbf{n}}\otimes\tilde{\mathbf{n}})\,\mathcal{H}(\langle\sigma_n|-t\mathcal{S})+\frac{\frac{\tau_n}{\bar{\sigma}}\otimes\mathbf{n}}{\mathcal{T}^2}\right]\\
\frac{\partial\Phi^{\mathrm{I}}}{\partial s}&=\frac{-2}{(b\mathcal{V})^3}\left(\sigma_n-\mathrm{sgn}(\sigma_n)t\mathcal{S}\right)\left[b\mathcal{V}\mathrm{sgn}(\sigma_n)(t\mathcal{S})_{,s}+\left(\sigma_n-\mathrm{sgn}(\sigma_n)t\mathcal{S}\right)b\mathcal{V}_{,s}\right]\mathcal{H}(\langle\sigma_n|-t\mathcal{S})-2\frac{\tau_n^2}{\mathcal{T}^3}\mathcal{T}_{,s}\\
\frac{\partial\mathbf{N}^{\mathrm{I}}}{\partial s}&=-4w\bar{w}_{,w}\left(\frac{1}{(b\mathcal{V})^3}\left[\frac{1}{2}b\mathcal{V}\mathrm{sgn}(\sigma_n)(t\mathcal{S})_{,s}+\left(\sigma_n-\mathrm{sgn}(\sigma_n)t\mathcal{S}\right)(b\mathcal{V})_{,s}\right](\tilde{\mathbf{n}}\otimes\tilde{\mathbf{n}})\,\mathcal{H}(\langle\sigma_n|-t\mathcal{S})+\frac{\tau_{\mathbf{n}}\otimes\mathbf{n}}{\mathcal{T}^3}\mathcal{T}_{,s}\right)
\end{aligned} \tag{A-53}$$

where the calibrated derivatives with respect to $\bar{\chi}$ and $\bar{w}$ are, respectively, as follows:

$$\begin{cases} (b\mathcal{V})_{,\bar{\chi}}=-b\dfrac{\bar{\sigma}}{\bar{\chi}}\sqrt{\bar{\chi}^2+\dfrac{1}{3}}\\ (t\mathcal{S})_{,\bar{\chi}}=-\dfrac{t_0}{2\bar{\chi}[\bar{w}(t_0+t_1\sqrt{\bar{\chi}})+1]^2}\mathcal{S}+t\dfrac{\bar{\sigma}}{2\sqrt{3}\bar{\chi}}\dfrac{\bar{\chi}-1}{\bar{w}}\\ \mathcal{T}_{,\bar{\chi}}=-l\dfrac{\bar{\sigma}}{\sqrt{3}} \end{cases} \quad \begin{cases} (t\mathcal{S})_{,\bar{w}}=\dfrac{-t^2\mathcal{S}}{\bar{w}}\\ \mathcal{T}_{,\bar{w}}=0\\ \bar{w}_{,w}=\frac{1-2\mathscr{T}^2w^2}{1+\mathscr{T}^2w^2}\frac{\bar{w}}{w} \end{cases} \tag{A-54}$$

Then:

$$\begin{cases} \mathbf{R}_{\tilde{\sigma}',\tilde{\sigma}'} = \frac{1}{2\mu}\frac{1}{\Delta t}\mathbb{J} + \dot{\Lambda}\dfrac{\partial^2\Phi^{\mathrm{I}}}{\partial\tilde{\sigma}'\partial\tilde{\sigma}'} \\ \mathbf{R}_{\tilde{\sigma}',\sigma_{\mathrm{m}}} = \dot{\Lambda}\dfrac{\partial}{\partial\sigma_{kk}}\left(\frac{\partial\Phi^{\mathrm{I}}}{\partial\tilde{\sigma}'}\right) \\ \mathbf{R}_{\tilde{\sigma}',f} = \dot{\Lambda}\mathbb{J} : \frac{\partial\mathbf{N}^{\mathrm{I}}}{\partial f} \\ \mathbf{R}_{\tilde{\sigma}',\bar{\epsilon}} = \dot{\Lambda}\frac{\partial\bar{\sigma}}{\partial\bar{\epsilon}}\mathbb{J} : \frac{\partial\mathbf{N}^{\mathrm{I}}}{\partial\bar{\sigma}} \\ \mathbf{R}_{\tilde{\sigma}',s} = \dot{\Lambda}\mathbb{J} : \frac{\partial\mathbf{N}^{\mathrm{I}}}{\partial s} \\ \text{where } \frac{\partial\sigma}{\partial\bar{\epsilon}} = \frac{\sigma_{\mathrm{S}}N}{\epsilon_0}\left(1+\frac{\bar{\epsilon}}{\epsilon_0}\right)^{N-1} \end{cases} \qquad \begin{cases} R_{\sigma_{\mathrm{m}},\tilde{\sigma}'} = \dot{\Lambda}\left[\dfrac{\partial^2\Phi^{\mathrm{I}}}{\partial\tilde{\sigma}'\partial\tilde{\sigma}'}\right]^T \\ R_{\sigma_{\mathrm{m}},\sigma_{\mathrm{m}}} = \frac{1}{K\Delta t} + \dot{\Lambda}\dfrac{\partial^2\Phi^{\mathrm{I}}}{\partial\sigma_{kk}\partial\sigma_{kk}} \\ R_{\sigma_{\mathrm{m}},f} = \dot{\Lambda}\,\mathbf{I} : \frac{\partial\mathbf{N}^{\mathrm{I}}}{\partial f} \\ R_{\sigma_{\mathrm{m}},\bar{\epsilon}} = \dot{\Lambda}\,\frac{\partial\bar{\sigma}}{\partial\bar{\epsilon}}\,\mathbf{I} : \frac{\partial\mathbf{N}^{\mathrm{I}}}{\partial\bar{\sigma}} \\ R_{\sigma_{\mathrm{m}},s} = \dot{\Lambda}\,\mathbf{I} : \frac{\partial\mathbf{N}^{\mathrm{I}}}{\partial s} \end{cases}$$

$$\begin{cases} R_{f,\tilde{\sigma}'} = -\dot{\Lambda}(1-f)\left[\frac{\partial\mathbf{N}^{\mathrm{I}}}{\partial\sigma_{\mathrm{kk}}}\right]^T \\ R_{f,\sigma_{\mathrm{m}}} = -\dot{\Lambda}(1-f)\dfrac{\partial^2\Phi^{\mathrm{I}}}{\partial\sigma_{kk}\partial\sigma_{kk}} \\ R_{f,f} = \dfrac{1}{\Delta t} + \dot{\Lambda}\,\mathbf{I} : \left[\frac{\partial\Phi^{\mathrm{I}}}{\partial\tilde{\sigma}} - (1-f)\frac{\partial\mathbf{N}^{\mathrm{I}}}{\partial f}\right] \\ R_{f,\bar{\epsilon}} = -\dot{\Lambda}(1-f)\,\frac{\partial\bar{\sigma}}{\partial\bar{\epsilon}}\,\mathbf{I} : \frac{\partial\mathbf{N}^{\mathrm{I}}}{\partial\bar{\sigma}} \\ R_{f,s} = -\dot{\Lambda}(1-f)\mathbf{I} : \frac{\partial\mathbf{N}^{\mathrm{I}}}{\partial s} \end{cases} \qquad \begin{cases} R_{\bar{\epsilon},\tilde{\sigma}'} = -\dfrac{\dot{\Lambda}}{\bar{\sigma}(1-f)}\left(\mathbf{N}^{\mathrm{I}} + \tilde{\sigma} : \dfrac{\partial^2\Phi^{\mathrm{I}}}{\partial\tilde{\sigma}\partial\tilde{\sigma}}\right) : \mathbb{J} \\ R_{\bar{\epsilon},\sigma_{\mathrm{m}}} = -\dfrac{\dot{\Lambda}}{\bar{\sigma}(1-f)}\left(\mathbf{N}^{\mathrm{I}} + \tilde{\sigma} : \dfrac{\partial^2\Phi^{\mathrm{I}}}{\partial\tilde{\sigma}\partial\tilde{\sigma}}\right) : \mathbf{I} \\ R_{\bar{\epsilon},f} = -\dfrac{\dot{\Lambda}}{\bar{\sigma}(1-f)^2}\,\tilde{\sigma} : \left[\mathbf{N}^{\mathrm{I}} + (1-f)\frac{\partial\mathbf{N}^{\mathrm{I}}}{\partial f}\right] \\ R_{\bar{\epsilon},\bar{\epsilon}} = \dfrac{1}{\Delta t} - \frac{\partial\bar{\sigma}}{\partial\bar{\epsilon}}\dfrac{\dot{\Lambda}}{\bar{\sigma}^2(1-f)}\,\tilde{\sigma} : \left[-\mathbf{N}^{\mathrm{I}} + \bar{\sigma}\frac{\partial\mathbf{N}^{\mathrm{I}}}{\partial\bar{\sigma}}\right] \\ R_{\bar{\epsilon},s} = -\dfrac{\dot{\Lambda}}{\bar{\sigma}(1-f)}\tilde{\sigma} : \frac{\partial\mathbf{N}^{\mathrm{I}}}{\partial s} \end{cases}$$

$$\begin{cases} R_{s,\tilde{\sigma}'} = -\dot{\Lambda}\mathcal{M} : \left(\dfrac{\partial^2\Phi^{\mathrm{I}}}{\partial\tilde{\sigma}\partial\tilde{\sigma}} : \mathbb{J}\right) \\ R_{s,\sigma_{\mathrm{m}}} = -\dot{\Lambda}\mathcal{M} : \dfrac{\partial^2\Phi^{\mathrm{I}}}{\partial\tilde{\sigma}\partial\tilde{\sigma}} : \mathbf{I} \\ R_{s,f} = -\dot{\Lambda}\left(\mathcal{M}_{,f} : \mathbf{N}^{\mathrm{I}} + \mathcal{M} : \mathbf{N}^{\mathrm{I}}_{,f}\right) \approx -\dot{\Lambda}\mathcal{M} : \mathbf{N}^{\mathrm{I}}_{,f} \\ R_{s,\bar{\epsilon}} = -\dot{\Lambda}\mathcal{M} : \mathbf{N}^{\mathrm{I}}_{,\bar{\epsilon}} \\ R_{s,s} \approx \dfrac{1}{\Delta t} \end{cases} \tag{A-55}$$

Appendix H Results under Triaxial loading

The authenticity of the hybrid model with respect to triaxial loading is assessed upon comparison with the results of Pardoen and Hutchinson [17]. The results herein are compared to those extracted from their microstructural model and those obtained from cell-model calculations. The following constants are common among all results:

$$f_0 = 10^{-2} \quad , \quad \lambda_0 = 1 \quad , \quad N = 0.1 \quad , \quad \frac{\sigma_0}{E} = 0.002 \quad , \quad E = 210\,GPa \quad , \quad \epsilon_0 = 0.002 \tag{A-56}$$

where σ_0 is the initial matrix yield strength and ϵ_0 is the conjugate strain thereof. E is the Young modulus, and the rest of parameters have been defined in due course. The values of initial void aspect ratio w_0 and stress triaxiality T, however, are varied. The comparison among the stress-strain results, corresponding to the unit cell schematized in Fig. A-2a, is shown in Fig. A-2.

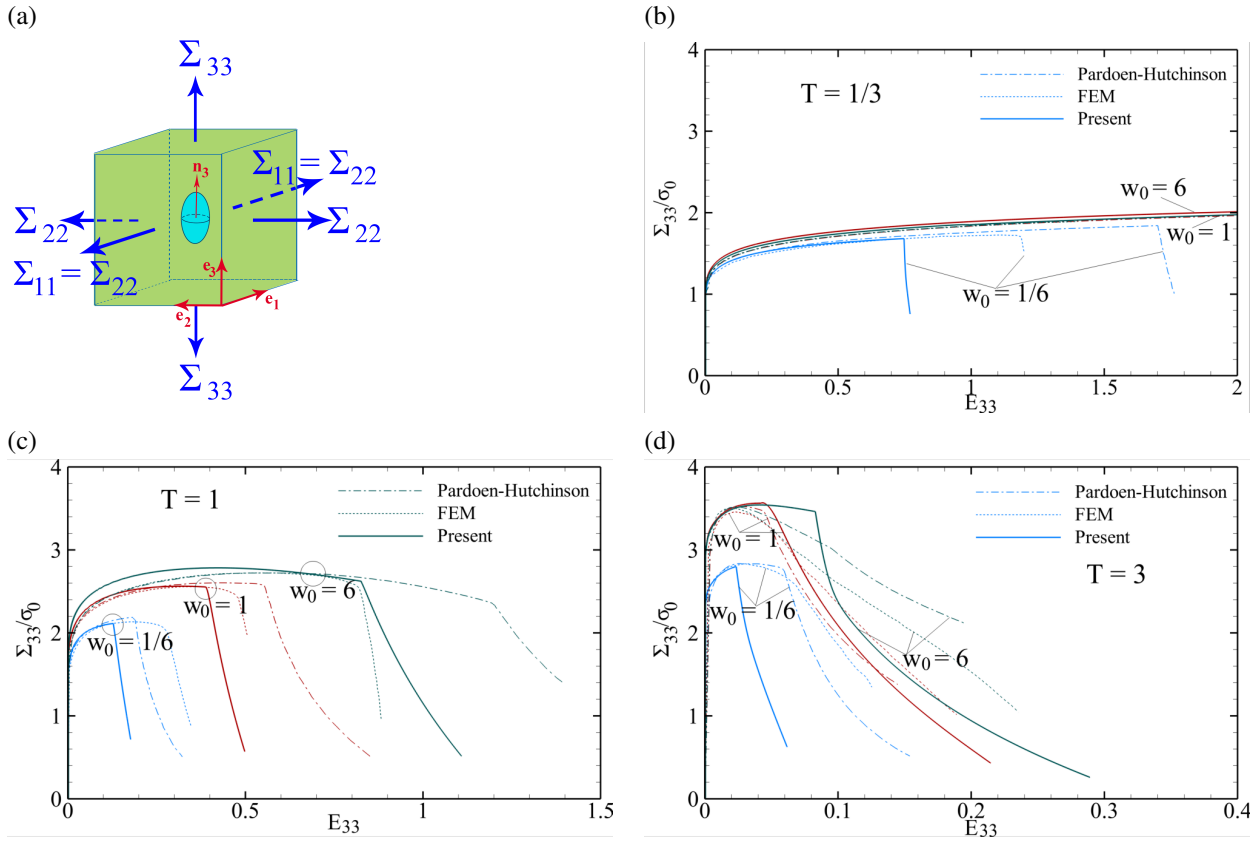

Figure A-2: Comparison of the present model predictions in absence of shear (solid curves), with the results extracted from Pardoen and Hutchinson's extended model (dashed curves), as well with those obtained from cell-model calculations (dotted curves) in [17] for several values of stress triaxiality and initial void aspect ratio.

It can be observed that the difference between present predictions and numerical and/or micromechanical results is more pronounced for $w_0 = 6$. This can be attributed to the rather exaggerated porosity growth predicted from the K–B model (as shown in Fig. A-3b) as well as the decreasing trend within $s = \ln w$, which would increase the stress level but reduce the strain to coalescence and strain to failure.

The evolution of the rest of microstructural variables for the specific case of $T = 1$ and different values of w_0 is shown in the next set of subfigures. The zero lateral strain rate at the post-coalescence process is corroborated by Fig. A-3f.

The predicted logarithmic void aspect ratio s is closely tied to its FEM counterpart during void growth except for large w_0's, where both analytical and numerical curves tend towards level but the former predicts a decreasing w. Moreover, the numerical curve declines after the onset of coalescence for a broader range of w_0's while the analytical s levels off at the post-coalescence process. Fig. A-3e, however, reveals that both major and minor void semiaxes a and b increase even after the onset of coalescence notwithstanding their ratio w decreases after this onset. Next, Fig. A-3c shows that the slope of increasing $\bar{\chi}$ ranges from convex to concave from an initially oblate to an initially prolate void. Accordingly, an initially flat void at a very low porosity level would be likely to never experience coalescence since $\bar{\chi}$ could reach a maximum before coalescence could occur. Moreover, the slope of variation in λ is almost equal for all w_0 values during void growth. After void coalescence, however, a cell with a larger w elongates faster than the same cell with smaller w's.

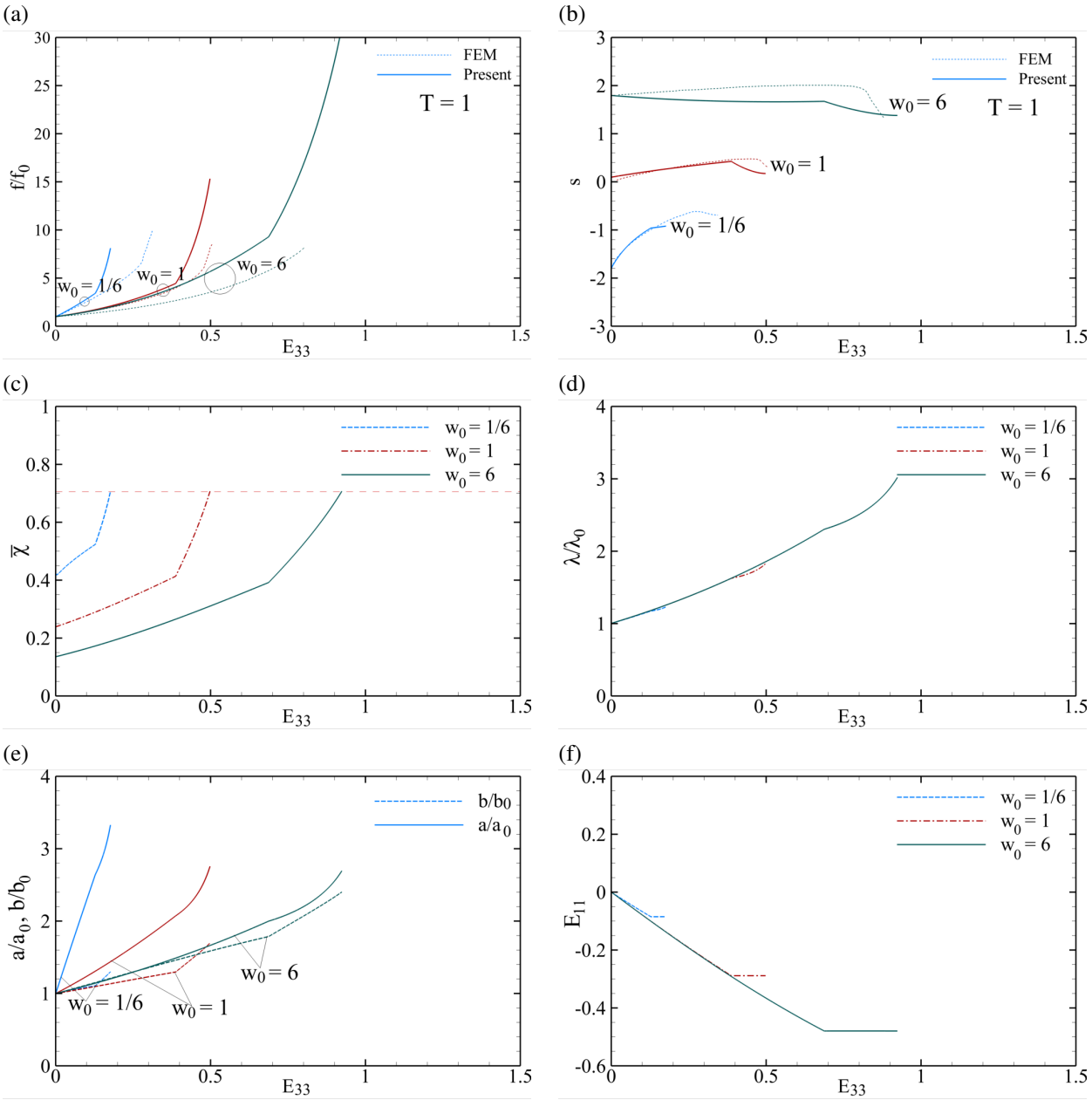

Figure A-3: Present model predictions under triaxial loading with a $T = 1$ stress triaxiality: (a,b) normalized porosity and logarithmic void aspect ratio, compared to FEM results in [17], (c,d) effective ligament parameter and normalized cell aspect ratio, (e,f) normalized void major and minor semiaxes, and lateral strains, respectively.

Appendix I Shear Failure Mechanism

The first set of results is aimed at realization of the *mechanism* by which failure occurs under combined tension and shear. For sufficiently low κ's, which signify shear-dominated loadings, the inhomogeneous yield criterion computationally overcomes from the outset, and all the subsequent deformation mechanism can be described by Φ^{I} along with the evolution equations tied to it. Nevertheless, as seen in the sequel, this deformation mechanism, though being fully commensurate with the physics of deformation, is quantitatively erroneous. This error can be attributed to the underlying premises within Φ^{I} which ideally confines plastic deformation within the ligament intercepting void poles [24].

The results are hereby presented for spheroidal voids, in comparison with their counterparts for cylindrical voids for a unit cell under $\kappa = 0.02$ with the initial simulation parameters given in the caption [1]. It should be remarked that, since a cylindrical void is tied to the upper and lower matrix materials over a whole surface rather than a single point, the whole range of void aspect ratios (below or above 1) behave similarly as far as void rotation is concerned. Nevertheless, a spheroidal void under the effect of shear behaves in different fashions when it is prolate ($w \geq 1$) or oblate ($w < 1$). Figure A-4 shows the comparison between microstructural parameters for spheroidal and cylindrical voids embedded in the same cell. All parameters are presented against the shear strain γ_{31}.

Figure A-4 is, by all means, indicative of premature failure rooted in the overconstrained nature of the inhomogeneous constitutive framework. This overconstraint can be ascribed, in part, to plasticity being neglected outside the inter-void ligament and, in part, to the notion of a surrogate cell where $\bar{\chi}$ dramatically accelerates rotation, elongation, and hence failure. This feature is suggestive of the $q_\chi \bar{\chi}$ calibration imparted to Φ^{I} in Section 3.2.

The largest distinction between the results pertaining to spheroidal and cylindrical voids can be envisaged for $w_0 < 1$ due to an opposite orientation evolution as plotted in Fig. A-4 b, and the smallest difference occurs for $w_0 > 1$ for the synergistic behavior of elongated cylindrical and spheroidal voids. The orientation evolution schematized in Fig. 1 can be realized for both prolate and oblate voids by examining Fig. A-4 b. It can be clearly seen that, soon after the beginning of the deformation process, the oblate void would stop rotating opposite to the shearing direction and begins to rotate along with shearing. Altogether, the overall rotation of an oblate void under shear is small in comparison to its prolate counterpart of the same porosity level.

Moreover, Fig's A-4 (e,f) reveal that, in both spheroidal void types, prolate and oblate, the larger of the two semi-axes enlarges under the effect of shear. Correspondingly, a in a prolate void and b in an oblate void enlarge while the other semi-axis acts in reverse manner. Accordingly, the void aspect ratio w, as plotted in Fig. A-4d, would decrease in an oblate void under shear and it increases for its prolate counterpart. For a cylindrical void, however, w increases regardless of its being below or above 1.

In all cases, failure is triggered by $\bar{\chi}$ reaching 1. Yet, $\bar{\chi}$ exhibits different evolution trends in different void shapes or aspect ratios before it reaches 1. With a cylindrical void, the trend for $\bar{\chi}$ is convex, and thus, the material may not encounter failure if the initial void volume fraction is smaller than a certain value (see [30] for details). For a spheroidal void, however, a convex trend (admitting the possibility that the material may not fail) can be envisaged only with a void being oblate. Otherwise, $\bar{\chi}$ increases with a concave evolution, and failure under shear is thus guaranteed.

Appendix J Near-pure Shearing Simulation

A pure shearing state is normally differentiated from simple shearing by its differing boundary condition, and thus its different deformation gradient. In a sense, pure shearing is regarded as shear loading with

[1] Details about the shear-dominated failure mechanism based on cylindrical voids may be found in [30].

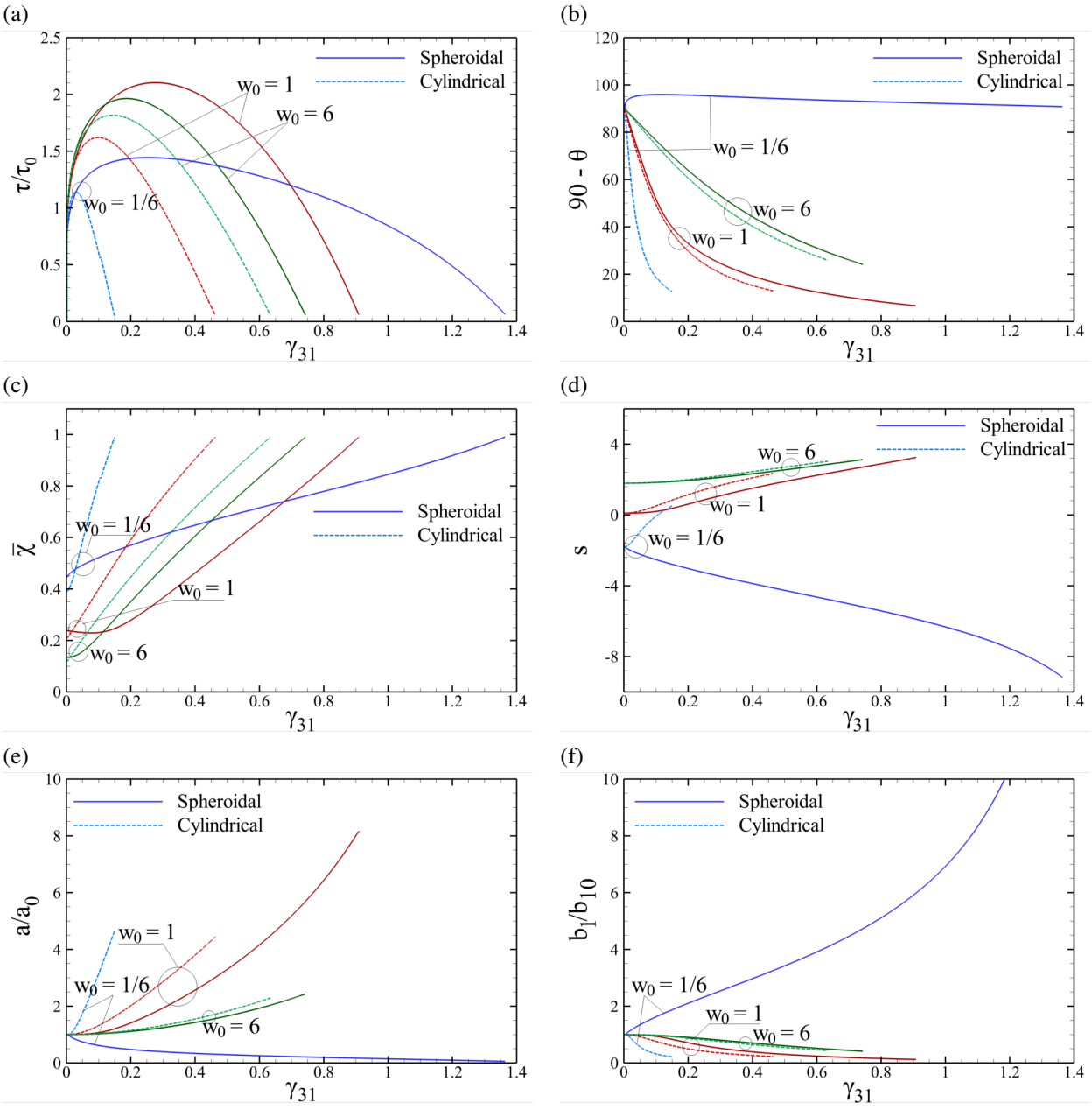

Figure A-4: Comparison of the predicted failure mechanisms based on the T–B–L criterion, for a cell under $\kappa = 0.02$, between a spheroidal and a cylindrical void of the same porosity with the simulation parameters identified as $f_0 = 0.0005$, $w_0 = 1.1$, $\lambda_0 = 2$, $N = 0.2$, $\sqrt{3}\tau_0/E = 0.002$: (a) normalized shear stress, (b) void angle with the vertical direction, (c) effective ligament parameter, (d) logarithmic void aspect ratio $s = \ln w$, (e,f) void major and along-shear minor semi-axes.

vanishing normal stresses. This notion overlaps with simple shearing as examined in the spirit of Sections 5.2–5.5 for a porous ductile solid. In another sense, however, pure shearing admits an equivalent biaxial stress state with equal and opposite normal stresses. Yet, the ductile material exhibits clearly different responses under the two equivalent stress states: the one with a predominant shear stress and that under equivalent biaxial loading. In the former, failure is observable by plastic flow localization at the vicinity of inter-void ligaments. In the latter, however, no failure is predicted, and the void undergoes limited or no rotation [22].

Tvergaard [22] was the first to propose an elementary voided cell to realize pure shearing equivalent to biaxial loading. He deduced that a parallelepiped RVE, as shown in Fig. A-5a, could capture the salient features of a ductile material deforming under this loading condition.

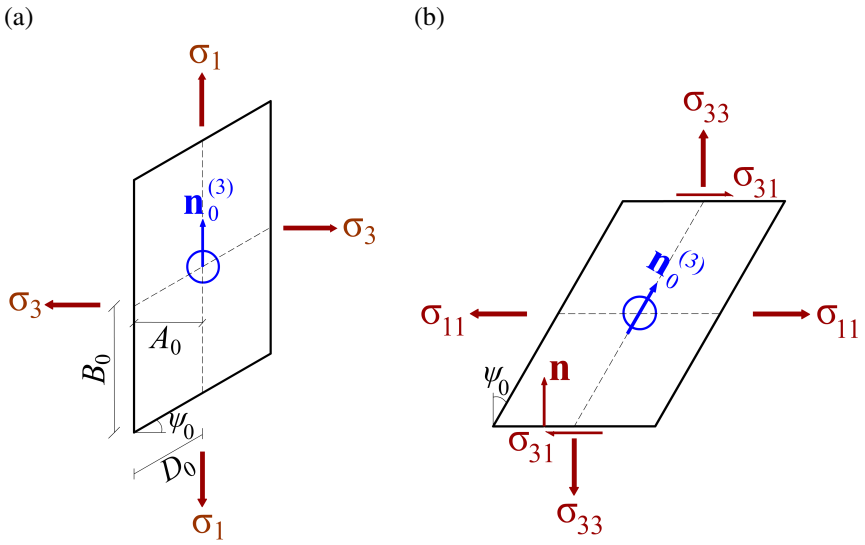

Figure A-5: (a) Elementary cell proposed by Tvergaard [22] to analyze a periodic array of voids under a state of near-pure shearing equivalent to biaxial loading under principal remote loads σ_1 and σ_3, (b) equivalent cell presently considered for simulation, under an equivalent state of combined tension and shear resulting from the resolution of σ_1 and σ_3 along the horizontal and vertical directions.

To this end, the unit cell in Fig. A-5a was subjected to a combination of two remote normal stresses σ_1 and σ_3 by Tvergaard [22] under a plane-strain boundary condition. The results mainly center around different load combinations identified by the ratio $\rho = \sigma_1/\sigma_3$ which should obviously be nonpositive in order that a near-pure shearing stress state is realized. Accordingly, $\rho = -1$ signifies pure shearing. The cell inclination angle $\psi_0 = 30^\circ$ and the $B_0/A_0 = 0.5$ ratio are the common geometric features among the analyses carried out by Tvergaard [22]. The former was chosen with reference to the outcomes in [61] to be near the most critical angle for shear-band formation along the voids' row.

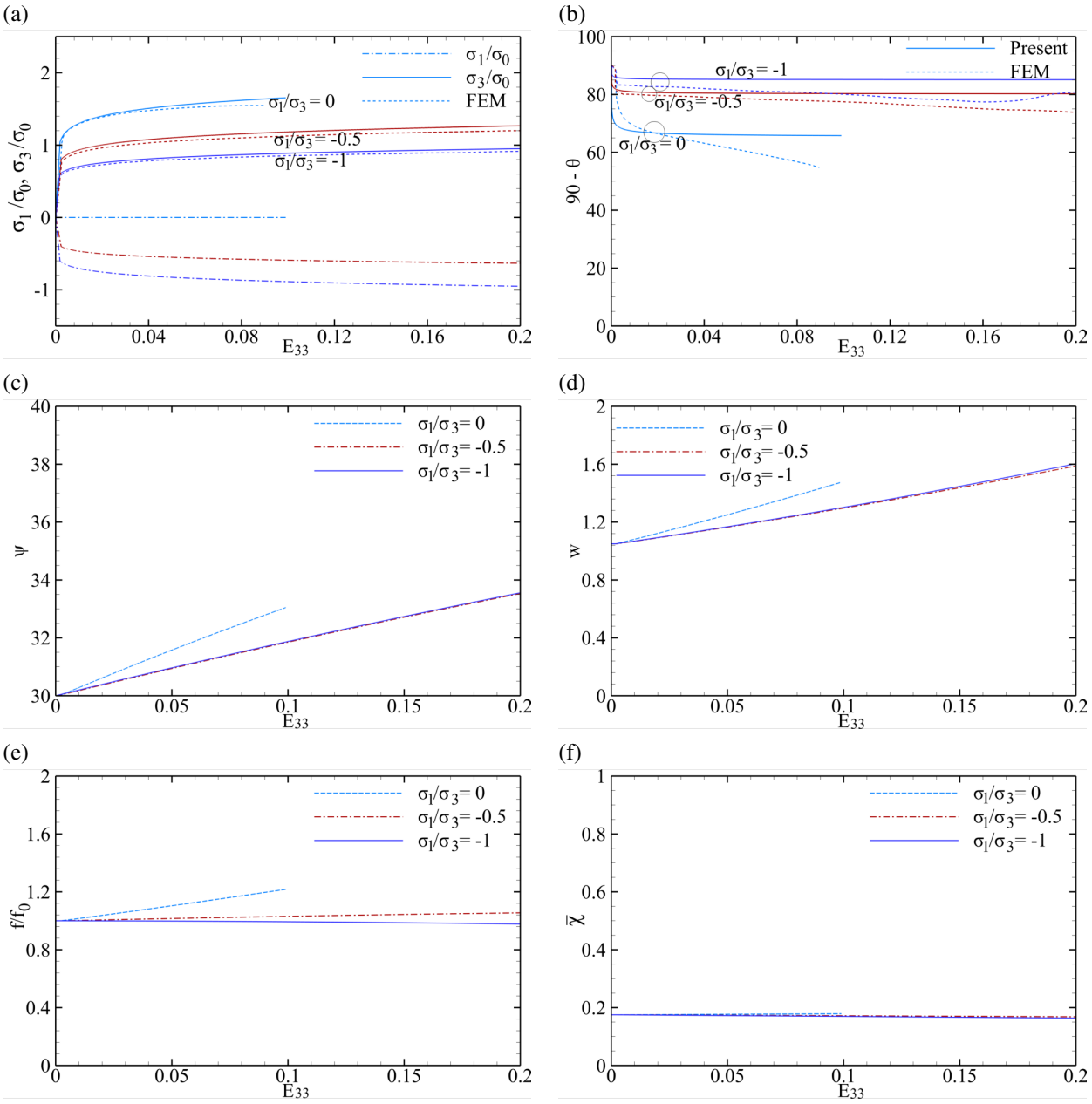

Figure A-6: Predicted stress response and microstructural state variables vs. normal strain for the unit cell schematized in Fig. A-5b under principal remote loads σ_1 and σ_3 with various values of the σ_1/σ_3 ratio and the initial microstructure denoted with $\psi_0 = 30°$, $B_0/A_0 = 0.5$ and $R_0/D_0 = 0.175$: (a,b) normalized principal stresses (with solid and dashed lines representing σ_1 and σ_3, respectively), and void angle with the x_1–x_2 plane, in comparison to the result counterparts from Tvergaard [22] on account of the unit cell in Fig. A-5a, (c) cell base angle with the the x_1–x_2 plane in Fig. A-5a, (d) void aspect ratio, (e) normalized porosity, (f) surrogate ligament parameter.

Figure A-6 showcases the stress response and selected microstrucrural parameters for several ρ values and $R_0/D_0 = 0.175$. The material constants are identical to those prescribed in Eq. (66). Results are

plotted against the average normal strain defined below, with the lower cell end held stationary [22]:

$$E_2^{\text{av}} = \ln\left(1 + \frac{u_3}{2B_0}\right) \tag{A-57}$$

, which is almost equal to E_{33} in the equivalent cell in Fig. A-5b.

Figure A-6a reaffirms the observable lack of failure under the allocated load combinations, alluding to the yielding mechanism as being nearly-homogeneous throughout, admitting $\Phi = \Phi^{\text{H}}$. To be more specific, one can envisage through Fig. A-6b that the void remains stationary past a transient rotation stage since the increasing effect of the resolved shear τ_n will be neutralized by the decreasing effect of the resolved normal stress σ_n in Fig. A-5b. Moreover, as indicated by Fig. A-6f, the relative inter-void distance only slightly declines due to the void being stagnant and the cell angle increasing rather linearly with the normal strain (Fig. A-6c) in such a way that the decrease in the void minor axis almost equals the decrease in the lateral cell dimension. An analogous effect can be envisaged in the evolution of porosity (Fig. A-6e) so that porosity exhibits some increase under uniaxial loading ($\rho = 0$) while it remains almost constant with a comparable lateral pressure (σ_3) superposed. Nevertheless, the void elongates under the collective effects of a positive σ_1 and a negative σ_3, as shown in Fig. (Fig. A-6d. Yet, void elongation is seen larger under uniaxial loading ($\rho = 0$) under the same strain level, not because of the void further elongating, rather because of the normal strain E_{33} being larger at the same level of void elongation due to the Poisson effect. Namely, the cell elongates faster than the void in presence of a biaxial stress state with lateral pressure.

References

[1] K. L. Nielsen. 3d modelling of plug failure in resistance spot welded shear-lab specimens (dp600-steel). *International Journal of Fracture*, 153(2):125–139, 2008.

[2] T Børvik, OS Hopperstad, T Berstad, and M Langseth. Numerical simulation of plugging failure in ballistic penetration. *International Journal of Solids and Structures*, 38(34-35):6241–6264, 2001.

[3] J. Mediavilla, R. H. J. Peerlings, and M. G. D. Geers. Discrete crack modelling of ductile fracture driven by non-local softening plasticity. *Int J Numer Meth Engr*, 66:661–688, 2006.

[4] G. R. Johnson, J. M. Hoegfeldt, U. S. Lindholm, and A. Nagy. Response of various metals to large torsional strains over a large range of strain rates – Part 1: Ductile metals. *Journal of Engineering Materials and Technology*, 105:42–47, 1983.

[5] G.R. Johnson, J.M. Hoegfeldt, U.S. Lindholm, and A. Nagy. Response of various metals to large torsional strains over a large range of strain rates – Part 2: Less ductile metals. *Journal of Engineering Materials and Technology*, 105:48–53, 1983.

[6] I. Barsoum and J. Faleskog. Rupture mechanisms in combined tension and shear—-Micromechanics. *International Journal of Solids and Structures*, 44:5481–5498, 2007.

[7] A. A. Benzerga and J.-B. Leblond. Effective Yield Criterion Accounting for Microvoid Coalescence. *Journal of Applied Mechanics*, 81:031009, 2014.

[8] S.S. Haltom, S. Kyriakides, and K. Ravi-Chandar. Ductile failure under combined shear and tension. *International Journal of Solids and Structures*, 50:1507–1522, 2013.

[9] Y. Bao and T. Wierzbicki. On fracture locus in the equivalent strain and stress triaxiality space. *International Journal of Mechanical Sciences*, 46:81–98, 2004.

[10] I. Barsoum and J. Faleskog. Rupture mechanisms in combined tension and shear—-Experiments. *International Journal of Solids and Structures*, 44:1768–1786, 2007.

[11] A. Needleman. A continuum model for void nucleation by inclusion debonding. *Journal of Applied Mechanics*, 54:525, 1987.

[12] J. Koplik and A. Needleman. Void growth and coalescence in porous plastic solids. *International Journal of Solids and Structures*, 24(8):835–853, 1988.

[13] F. Scheyvaerts, P. R. Onck, C. Tekoğlu, and T. Pardoen. The growth and coalescence of ellipsoidal voids in plane strain under combined shear and tension. *Journal of the Mechanics and Physics of Solids*, 59:373–397, 2011.

[14] K. L. Nielsen, J. Dahl, and V. Tvergaard. Collapse and coalescence of spherical voids subject to intense shearing: studied in full 3D. *International Journal of Fracture*, 177:97–108, 2012.

[15] M. Dunand and D. Mohr. Effect of Lode parameter on plastic flow localization after proportional loading at low stress triaxialities. *Journal of the Mechanics and Physics of Solids*, 66:133–153, 2014.

[16] D. C. Drucker. Continuum theory of plasticity on macroscale and microscale. *Journal of Materials*, 1(4):873, 1966.

[17] T. Pardoen and J. W. Hutchinson. An extended model for void growth and coalescence. *Journal of the Mechanics and Physics of Solids*, 48:2467–2512, 2000.

[18] J.R. Rice. The localization of plastic deformation. In W.T. Koiter, editor, *14th int. cong. Theoretical and Applied Mechanics*, pages 207–220. North–Holland, Amsterdam, 1976.

[19] Y. Bai and T. Wierzbicki. A new model of metal plasticity and fracture with pressure and Lode dependence. *International Journal of Plasticity*, 24:1071–1096, 2008.

[20] K. Nahshon and J. W. Hutchinson. Modification of the Gurson Model for shear failure. *European Journal of Mechanics*, 27:1–17, 2008.

[21] V. Tvergaard. Behaviour of voids in a shear field. *International Journal of Fracture*, 158:41–49, 2009.

[22] V. Tvergaard. Study of localization in a void-sheet under stress states near pure shear. *International Journal of Solids and Structures*, 75:134–142, 2015.

[23] A. A. Benzerga, J. Besson, and A. Pineau. Anisotropic ductile fracture. Part II: theory. *Acta Materialia*, 52:4639–4650, 2004.

[24] M. E. Torki, A. A. Benzerga, and J.-B. Leblond. On Void Coalescence under Combined Tension and Shear. *Journal of Applied Mechanics*, 82(7):071005, 2015.

[25] ME Torki, C. Tekoglu, J-B Leblond, and AA Benzerga. Theoretical and numerical analysis of void coalescence in porous ductile solids under arbitrary loadings. *International Journal of Plasticity*, 91:160–181, 2017.

[26] M. Gologanu, J.-B. Leblond, and J. Devaux. Approximate models for ductile metals containing non-spherical voids – case of axisymmetric prolate ellipsoidal cavities. *Journal of the Mechanics and Physics of Solids*, 41(11):1723–1754, 1993.

[27] P. Ponte Castañeda and M. Zaidman. Constitutive models for porous materials with evolving microstructure. *Journal of the Mechanics and Physics of Solids*, 42:1459–1495, 1994.

[28] A. A. Benzerga, J. Besson, and A. Pineau. Coalescence–Controlled Anisotropic Ductile Fracture. *Journal of Engineering Materials and Technology*, 121:221–229, 1999.

[29] S. Kweon, B. Sagsoy, and A. A. Benzerga. Constitutive relations and their time integration for anisotropic elasto-plastic porous materials. *Computer Methods in Applied Mechanics and Engineering*, 310:495–534, 2016.

[30] M. E. Torki and A. A. Benzerga. Micromechanics-based constitutive relations for post-localization analysis. *MethodsX*, 2018.

[31] M. E. Torki and A. A. Benzerga. A mechanism of failure in shear bands. *Extreme Mechanics Letters*, 23:67–71, 2018.

[32] F. A McClintock, S. M. Kaplan, and C. A. Berg. Ductile fracture by hole growth in shear bands. *International Journal of Fracture*, 2(4):614–627, 1966.

[33] A. A. Benzerga. Micromechanics of Coalescence in Ductile Fracture. *Journal of the Mechanics and Physics of Solids*, 50:1331–1362, 2002.

[34] S. M. Keralavarma and A. A. Benzerga. A constitutive model for plastically anisotropic solids with non-spherical voids. *Journal of the Mechanics and Physics of Solids*, 58:874–901, 2010.

[35] V. Tvergaard. Shear deformation of voids with contact modeled by internal pressure. *International Journal of Mechanical Sciences*, 50:1459–1465, 2008.

[36] M. Gologanu, J.-B. Leblond, G. Perrin, and J. Devaux. Recent extensions of Gurson's model for porous ductile metals. In P. Suquet, editor, *Continuum Micromechanics, CISM Lectures Series*, pages 61–130. Springer, New York, 1997.

[37] M. E. Gurtin, E. Fried, and L. Anand. *The mechanics and thermodynamics of continua*. Cambridge University Press, 2010.

[38] J.-B. Leblond and G. Mottet. A theoretical approach of strain localization within thin planar bands in porous ductile materials. *Comptes Rendus Mecanique*, 336:176–189, 2008.

[39] K. Madou and J.-B. Leblond. A Gurson-type criterion for porous ductile solids containing arbitrary ellipsoidal voids – II: Determination of yield criterion parameters. *Journal of the Mechanics and Physics of Solids*, 60:1037–1058, 2012.

[40] L. Morin, J.-B. Leblond, and V. Tvergaard. Application of a model of plastic porous materials including void shape effects to the prediction of ductile failure under shear-dominated loadings. *Journal of the Mechanics and Physics of Solids*, 94:148–166, 2016.

[41] M. Kailasam and P. Ponte Castaneda. A general constitutive theory for linear and nonlinear particulate media with microstructure evolution. *Journal of the Mechanics and Physics of Solids*, 46(3):427–465, 1998.

[42] K. Madou, J.-B. Leblond, and L. Morin. Numerical studies of porous ductile materials containing arbitrary ellipsoidal voids —II: Evolution of the length and orientation of the void axes. *European Journal of Mechanics*, 42:490–507, 2013.

[43] J.D. Eshelby. The determination of the elastic field of an ellipsoidal inclusion, and related problems. *Proc. Roy. Soc*, A241:357–396, 1957.

[44] J. C. Simo and T. JR. Hughes. *Computational inelasticity*, volume 7. Springer Science & Business Media, 2006.

[45] P. Ponte Castaneda. The effective mechanical properties of nonlinear composites. *Journal of the Mechanics and Physics of Solids*, 39:45–71, 1991.

[46] J.-B. Leblond, G. Perrin, and P. Suquet. Exact results and approximate models for porous viscoplastic solids. *International Journal of Plasticity*, 10:213–225, 1994.

[47] G. Perrin and J.-B. Leblond. Analytical study of a hollow sphere made of plastic porous material and subjected to hydrostatic tension— application to some problems in ductile fracture of metals. *Int. J. Plasticity*, 6(6):677–699, 1990.

[48] R. Hill. A theory of yielding and plastic flow of anisotropic solids. *Proceedings of the Royal Society of London A*, 193:281–297, 1948.

[49] C. Tekoğlu, J.-B. Leblond, and T. Pardoen. A criterion for the onset of void coalescence under combined tension and shear. *Journal of the Mechanics and Physics of Solids*, 60:1363–1381, 2012.

[50] L. Morin, J.-B. Leblond, and A. A. Benzerga. Coalescence of voids by internal necking: theoretical estimates and numerical results. *Journal of the Mechanics and Physics of Solids*, 75:140–158, 2015.

[51] S. M. Keralavarma. A multi-surface plasticity model for ductile fracture simulations. *Journal of the Mechanics and Physics of Solids*, 103:100–120, 2017.

[52] A. A. Benzerga and J.-B. Leblond. Ductile fracture by void growth to coalescence. *Advances in Applied Mechanics*, 44:169–305, 2010.

[53] A. Pineau, A. A. Benzerga, and T. Pardoen. Failure of metals I. Brittle and Ductile Fracture. *Acta Materialia*, 107:424–483, 2016.

[54] M. Achouri, G. Germain, P. Dal Santo, and D. Saidane. Experimental characterization and numerical modeling of micromechanical damage under different stress states. *Materials & Design*, 50:207–222, 2013.

[55] N. A. Fleck, J. W. Hutchinson, and V. Tvergaard. Softening by void nucleation and growth in tension and shear. *Journal of the Mechanics and Physics of Solids*, 37:515–540, 1989.

[56] K. Siruguet and J.-B. Leblond. Effect of void locking by inclusions upon the plastic behavior of porous ductile solids—I: theoretical modeling and numerical study of void growth. *International Journal of Plasticity*, 20:225–254, 2004.

[57] N. A. Fleck and J. W. Hutchinson. Void growth in shear. *Proceedings of the Royal Society of London A*, 407:435–458, 1986.

[58] L. Babout, Y. Bréchet, E. Maire, and R. Fougères. On the competition between particle fracture and particle decohesion in metal matrix composites. *Acta Materialia*, 52:4517–4525, 2004.

[59] L. Babout, E. Maire, and R. Fougeres. Damage initiation in model metallic materials: X-ray tomography and modelling. *Acta Materialia*, 52(8):2475–2487, 2004.

[60] M. Destrade, J. G. Murphy, and G. Saccomandi. Simple shear is not so simple. *International Journal of Non-Linear Mechanics*, 47(2):210–214, 2012.

[61] V. Tvergaard. Numerical study of localization in a void-sheet. *International Journal of Solids and Structures*, 25(10):1143–1156, 1989.

P8 DUCTILE FRACTURE IN ANISOTROPIC SOLIDS UNDER COMBINED TENSION AND SHEAR

Ductile Fracture in Anisotropic Solids under Combined Tension and Shear

M. E. Torki[1], A. A. Benzerga[1,2,3]

[1] *Department of Aerospace Engineering, Texas A&M University, College Station, TX 77843, USA*

[2] *Center for intelligent Multifunctional Materials and Structures, TEES, College Station, TX 77843, USA*

[3] *Department of Materials Science and Engineering, Texas A&M University, College Station, TX 77843, USA*

Abstract

A hybrid micromechanics-based model is developed and numerically implemented to simulate ductile fracture until failure under combined tension and shear considering Hill-type matrix anisotropy. The shear-dominated deformation process is an intermediate state between a completely homogeneous and an ideally localized one with plasticity fully confined within intervoid ligaments. The deformation mechanism is closer to being homogeneous at early stages and would approach the ideal localized state towards the end. Existing evolution equations of void elongation and rotation are invoked from earlier models during nearly-homogeneous yielding, and from a recent work by the authors for post-localized deformation under combined loading. By the very nature of its model, localized yielding acts upon a surrogate microstructure aligned with the normal to a possible plane of localization. The original form of the hybrid model predicts premature failure under shear-dominated loading notwithstanding the failure mechanism fully conforms to physics. Both the nearly-homogeneous and localized yield functions are, accordingly, modified in reference to existing numerical results with simple adjustable parameters. Rather than by the evolution of porosity, failure under combined tension and shear is driven by the effective parameter dictated by the initial relative void spacing and evolved until a maximum value is achieved. The study is further specified to a state of *near-simple* shearing with a vanishingly small normal stress in proportion to a significant shear. The parametric studies account for the effects due to varying normal and shear anisotropy parameters within the orthotropy local coordinate system. In particular, the material with weak planes in shear is subjected to combined tension and shear as well as near-simple shearing with the plane of weakness being variously oriented with respect to the principal loading frame. Results are reflected through measurable and/or observable parameters including but not limited to porosity, effective relative void spacing, void aspect ratio and orientation, as well as the material stress response in terms of the normal or shear strain.

Key Words: Ductile fracture; Void coalescence; Combined tension and shear; Matrix anisotropy; Hill-type anisotropy.

1 Introduction

Ductile fracture is inherently amenable to various heterogeneities at the macro scale regardless of the underlying microscopic process. Apart from those emanating from material gradients [1, 2], deformation-induced anisotropies can constitute an essential part of damage mechanics in porous materials, particularly in ductile fracture under combined loading. To the best of reported observations, this anisotropy can be professed as two types: that related to the voids themselves (changes in void shape and orientation as well as their

spatial arrangement) [3], and that related to the matrix, known as *plastic anisotropy* [4]. Thus, analyses of ductile fracture under combined tensile and shear loading, and the interpretation of currently available experiments rely, to a large extent, on accounting for the induced, and eventually initial anisotropies. At this stage, the material response is strictly sensitive towards the loading path, initial microstructure, and void distribution [5].

Experimental observation of shear-dominated fracture has been conveyed in the literature by the landmark work of Johnson *et al.* [6, 7], who measured the torsional ductility in varieties of engineering metal alloys. Therein, one could observe significant difference, up to 3 orders of magnitude, in the shear strain to failure γ_f. A compelling explanation regarding these remarkable differences in the measured ductilities has remained elusive until a recent work by the present authors [8]. Barsoum and Faleskog [9] also conducted similar experiments by the introduction of notches to hollow tubes for illustrating the effect of triaxiality. They characterized the stress state in terms of stress triaxiality T and the *Lode* parameter L [10]. Haltom *et al.* [11] have recently conducted torsion experiments with the test specimen revisited. Unlike earlier torsion experiments on aluminum alloys and steels [12, 13], their experiments showed increasing ductility under stress states near simple shearing [11]. Altogether, experiments, though being revealing, are hard to conduct, especially in presence of shear, and may lead to conflicting results. Yet, they can serve as benchmark for verification purposes within computational simulations.

A special line of work tends to set forth a tentative interpretation of the loading effects by means of macroscopic nondimensional descriptors expressed in terms of stress invariants or some equivalent invariant of the stress deviator. As such, stress triaxiality T, defined as the ratio between the hydrostatic stress and the von Mises equivalent stress, is the most widely used parameter in absence of shear [14–18], and the Lode parameter L is particularly utilized to reflect the *apparent* effect of shear. The latter is function of the Lode angle or, equivalently, the third invariant of the stress deviator, J_3 [9, 19–21]. These isotropic scalar-valued parameters may be revealing in some sense. Yet, they cannot portray the salient features of fracture at the micro scale. To this end, fracture processes can, at best, be rationalized at the cell level, *i.e.* at the limit of a representative volume element (RVE). Thereupon, the microstructural effects can be described by parameters that are measurable and/or observable. Provided this RVE is chosen judiciously (see [22] for methodology), plastic deformation can be well regarded as homogeneous or localized at the cell level. In the former, plasticity is diffuse throughout the cell. In a weakly rate–sensitive material, the latter manifests by the onset of elastic unloading in layers above and below the void [23–25] or by occasional concentration of plasticity within columns [26]. The former is known in the literature as *coalescence in layers* and the former has been termed *coalescence in columns* (necklace coalescence) [27]. While homogeneous yielding can drive the process at early stages, localized deformation is indispensable for failure to occur [3, 23]. In other terms, localized plasticity is the necessary condition for failure to occur. Nevertheless, it may not be sufficient therefor, especially under shearing effects [28].

Micromechanics-based modeling of ductile fracture can be traced back to the early work reported by McClintock [14], Rice and Tracey [15], Fleck and Hutchinson [29] (the latter accounting for the effect of shear) and the like. Intrinsic limitations, including consideration of isolated voids and parametric rather than closed form expression, prompted more advanced work. The first closed-form analytical gauge function in this respect is known after Gurson [16], which sets a yield criterion for a porous material containing spherical or cylindrical voids at the macro scale, and correlates with an evolution law for a single microstructural variable, the void volume fraction (porosity) f. Within the deformation process, however, anisotropies associated with matrix deformation and void shape would emerge as earlier noticed. Several extensions of the Gurson model have been developed over the past decades to account for these anisotropies. Assuming homogeneous yielding, Gurson's model and its extensions have set the caliber for decades. The Gurson–Tvergaard–Needleman (GTN) model, for instance, follows Tvergaard's and Needleman's modifications to Gurson's model to encompass the effects due to void interaction and void nucleation [30–32]. In passing, the Gologanu–Leblond–Devaux (GLD) model [33] extended Gurson's for non-spherical voids. This line of

models was further extended into incorporation of plastic anisotropy in [34, 35]. In the meantime, ductile damage models have been proposed, partly based on continuum thermomechanics [17, 18, 36] and partly based on homogenization [37–40], which have bee further implemented in simulations of damage evolution and forming processes in metals [41, 42].

A considerable fraction of work on shear-dominated ductile failure prediction in porous materials addresses supplementing existing Gurson-type yield criteria with damage models. Nahshon and Hutchinson [20], for instance, proposed a modified damage parameter (denoting porosity in absence of shear) through the addition of a heuristic function of J_3. This damage parameter, while remaining of a heuristic nature, could not preserve the identity of a physical parameter such as porosity. Morgeneyer and Besson [43] introduced a modified strain rate as function of the Lode parameter based on a Gurson-type yield criterion in order to simulate the transition from flat to shear-induced crack propagation. The work of the like rely, to a large extent, on heuristic modifications with the physical processes behind failure remaining elusive. Meanwhile, there has been remarkable attempt exerted on direct modeling of ductile fracture under shearing effects at the cell level. The pioneering work of Tvergaard and coworkers [3, 44–46] by high–throughput FEM–based cell–model calculations has set the standard for the past decade. They have analyzed FEM cells under various boundary conditions including near-simple shearing over plane-strain [3, 44] or 3D cells [45] as well as near-pure shearing [46] over plane-strain cells. These outcomes have provided a valuable cache for model assessment purposes. The technical challenges, however, clearly demonstrate that numerical cell–model studies, let alone structural calculations, under combined loading are not only cumbersome, but also unfeasible at times [45]. Micromechanics–based modeling would, in effect, eliminate the need for such lengthy calculations.

Any physics-based simulation of shear-induced failure would be mainly perceptible by the microstructural effects that trigger failure in shear that are, themselves, directly influenced by localized deformation. Work in this respect is meager in regards to both modeling and numerical implementation. A model accounting for localized deformation under combined tension and shear was recently developed by Keralavarma and Chockalingam for plastically anisotropic materials with Hill-type plastic anisotropy [47]. Preparatory to this model being developed, Kweon *et al.* [48] had simulated the ductile fracture process from the implicit numerical integration of a complete constitutive framework in rate form. They accounted for a complete range of void shape and orientation effects as well as Hill-type matrix plastic anisotropy in accordance with the homogeneous yield criterion proposed by Keralavarma and Benzerga [35]. Due to the lack of an equivalent inhomogeneous yield criterion admitting localized plasticity, they had clearly disregarded the localized regime at the time, and thus no failure was predicted therein. Yet another recent work by the present authors on the numerical implementation of the entire fracture process under combined tension and shear [8], though well-motivated and extensive, does not account for the effect of plastic anisotropy. This warrants the impending need to a more comprehensive investigation on the effect of matrix plastic anisotropy on ductile fracture under combined tension and shear. To this challenge, the yield criterion derived by Keralavarma and Benzerga [35], here denoted with the "K–B" model, is supplemented with that introduced by Keralavarma and Chockalingam [47], here briefly termed the "K–C" model. On account of the two yield surfaces being modeled by different RVE's, the resulting two-surface model is termed *hybrid*.

In actual fact, plastic deformation under shear domination at the micro scale is inhomogeneous from the outset [3, 44, 49]. However, the pristine forms of the two models are each one of the two extremes. As such, the exact shear deformation process is close to a modified version of K–B at early stages until K–C becomes dominant. In order to capture the quantitative aspect of the de facto shearing process, the K–B model should be utilized in modified form according to the simple modification proposed for stress states close to simple shearing [50, 51]. Besides, the surrogate microstructure exploited in the K–B model bares clear overconstraints in the response, which calls for another modification with a simple adjustable parameter. The benchmark results from [3, 44, 45] are considered as comparator for this purpose.

Moreover, the numerical simulation framework would not be complete unless the yield criteria are sup-

plemented to appropriate evolution laws. Accordingly, a set of equations accounting for the evolution of effective parameters governing the pre- and post–localized microstructural state are needed. More specifically, the main body of equations for the evolution of void shape and orientation incorporated with the K–B line of models has been available since the early nineties [33, 52] and has been used to model fracture in engineering materials [48, 53]. The counterparts to these equations have been recently developed by the present authors for cylindrical [54] and spheroidal voids [8]. The latter will be invoked in the present context both for the sake of better consistency with their former counterparts and capturing the essential features of shear–induced failure for a complete range of void shapes (elongated, flattened, and nearly-spherical voids). The utilized evolution equations for rotating voids can conveniently retrieve their simpler precursors developed by Benzerga [55] in absence of shear.

With the established model at hand, the parametric studies will begin under triaxial loading and would further extend into the states of combined normal and shear as well as near–simple shearing. The combined effects induced by matrix anisotropy will be assessed in a complete range of normal-to-shear stress ratios.

2 Hybrid Model of Ductile Fracture

The notion of homogeneous vs. inhomogeneous yielding was earlier conceptualized in Section 1. The distinction between homogeneous and inhomogeneous yielding pertains to plastic deformation at the elementary cell level. If a cell of arbitrary geometry deforms uniformly inside, and thus over its boundary, plastic deformation is known as homogeneous, otherwise inhomogeneous. In porous plasticity, inhomogeneous yielding is mainly characterized by localized plasticity [1]. To the best of the reported knowledge, plastic strains in porous metals can localize more prevalently at the vicinity of the inter-void ligaments (which arises from elastic unloading [23]) and more sporadically along inter-void columns. Provided the voids can impinge at either case, localized plasticity is associated with *void coalescence*. Correspondingly, void coalescence of the former and latter types is known as *coalescence in layers* and *coalescence in columns* (necklace coalescence), respectively. Except within plump cells or for very long voids, the former proves more ubiquitous, and is thus taken as the driving failure mechanism in the present context.

With reference to an underlying microstructure, as schematized in Fig. 1a, the mictostructural geometry can be locally described with the aid of a representative volume element (RVE), Fig. 1b (see [8] for more illustration). Note that, in general, the underlying microstructure can accommodate localized deformation along several possible planes. Only one possible plane has been shown in Fig. 1b which is truly the governing plane upon consideration of one single cell regarded as a single point in space.

[1] Strain localization in this case occurs inside an inner-void ligament with *finite* thickness. This must be clearly dissociated from Rice's theory of plastic localization [56], whereby strain rates can localize inside a band with *vanishing* thickness. This distinction is of utmost importance in porous material plasticity particularly where voids can act as initial heterogeneity.

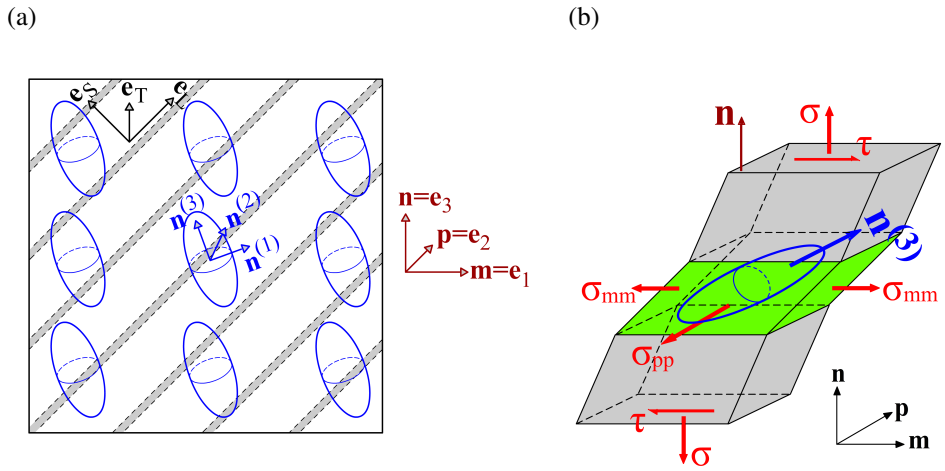

Figure 1: (a) Relative positioning of voids with local periodic distribution inside a plastically anisotropic matrix with orthotropy directors $(\mathbf{e}_L, \mathbf{e}_T, \mathbf{e}_S)$; (b) equivalent RVE after deformation under combined tension and shear.

Even with the use of such a simplified cell in Fig. 1b, the macroscopic response of this cell is not solvable, be the yielding mechanism homogeneous or inhomogeneous. Rather, it is attainable through idealized elementary cells that have been utilized in the derivation the yield criteria pointed out in the following subsections. The two yield surfaces are expressed basically as $\Phi^{\mathrm{H}}(\mathbb{p}; \sigma; f, w, \mathbf{n}^{(3)}) = 0$ and $\Phi^{\mathrm{I}}(\mathbb{p}; \sigma; f, w, \lambda, \mathbf{n}^{(3)}, \mathbf{n}) = 0$, where the yield functions Φ^{H} and Φ^{I} correspond to homogeneous and inhomogeneous deformation of the cell, respectively. f is defined as the void volume fraction (porosity), w is the void aspect ratio, $\mathbf{n}^{(3)}$ is the void orientation determined by its main axis direction, and $\mathbf{n}$ is the plane in which plastic strains can localize and voids can impinge. Moreover, $\mathbb{p}$ is Hill's tensor defined in Section 2.1. Rather than considering a concurrent effect of the two surfaces (through a linear combination), the model at the present stage accounts for a consecutive advancement of the two mechanisms. Namely, the most favorable mechanism is triggered at every time step by considering the $\Phi = 0$ that is met first.

Both yield functions are expressed in terms of the stress space normalized by the matrix effective stress $\bar{\sigma}$. The latter is normally taken to depend on some effective plastic strain $\bar{\epsilon}$ as its conjugate strain. Here, the two are related through a power law of the form:

$$\bar{\sigma} = \sigma_0 \left(1 + \frac{\bar{\epsilon}}{\epsilon_0}\right)^N \tag{1}$$

with σ_0 the initial yield strength and N the hardening exponent.

Remark: Upon observation [3, 44], the de facto mechanism within the RVE under combined tension and shear as well as under shear dominance is an intermediate mechanism between the fully homogeneous and fully localized extremes. As such, it is closer to the former at early stages and it approaches the latter end with further advancement of shearing. Therefore, both Φ^{H} and Φ^{I} are subject to some modification in order for the hybrid model be accountable for a thoroughly reliable simulation. The following subsections present both models in modified form.

2.1 Nearly-homogeneous yielding

The geometric framework associated with nearly-homogeneous yielding, is that for a porous plastic solid composed of a plastically anisotropic matrix containing aligned spheroidal voids with arbitrary initial orientations [35]. Within this framework, the voids are taken as spheroidal, with two equal lateral radii (denoted

with b) and a third mismatching radius (known as a) considered as the main semiaxis. Correspondingly, $\mathbf{n}^{(3)}$ denotes the void axis along the main radius a, and $\mathbf{n}^{(1)}$ and $\mathbf{n}^{(2)}$ are orthogonal base vectors arbitrarily chosen in the transverse plane. Following the work of Keralavarma and Benzerga [35], Φ^{I} can be expressed in the following form:

$$\Phi^{\mathrm{H}}(\mathbb{p};\sigma;f,w,\mathbf{n}^{(3)}) = C\frac{\sigma_{\mathrm{eq}}^2}{\bar{\sigma}^2} + 2(g+1)(g+qf)\cosh\left(\kappa\frac{\sigma:\mathbf{X}}{\bar{\sigma}}\right) - (g+1)^2 - (g+qf)^2 \tag{2}$$

with $f=\omega/\Omega$ and $w=a/b$ denoting void volume fraction (porosity) and aspect ratio, respectively. Here, a and b denote, respectively, the spheroidal void's major and minor semi-axes. Every spheroid can be uniquely identified by a main radius a that defines the void orientation $\mathbf{n}^{(3)}$ and two equal radii $b_1=b_2=b$ arbitrarily defined along perpendicular directions in the plane normal to $\mathbf{n}^{(3)}$, identified with $\mathbf{n}^{(1)}$ and $\mathbf{n}^{(2)}$. Correspondingly, $w>1$, $w<1$ and $w=1$ signify, respectively, a prolate, an oblate, and a spherical void. The q factor enables Φ^{H} to capture stress states near simple shearing, which should be above 4/3 [50,57]. In the present context, the value proposed by Perrin and Leblond [51], $q=4/e\approx 1.47$ is utilized. Also, σ_{eq} is the von-Mises equivalent stress as function of a Hill-type anisotropy tensor [58] which can be stated as

$$\sigma_{\mathrm{eq}}^2 = \frac{3}{2}\sigma:\mathbb{H}:\sigma \tag{3}$$

where $\mathbb{H}$ is related to Hill's tensor $\mathbb{p}$ (that reduces to the deviatoric projection operator $\mathbb{J}$ for an isotropic matrix defined below) through

$$\mathbb{H}\equiv\mathbb{p}+\eta(\mathbf{X}\otimes\mathbf{Q}+\mathbf{Q}\otimes\mathbf{X}),\quad \mathbb{p}\equiv\mathbb{J}:\mathbb{h}:\mathbb{J},\quad \mathbb{J}\equiv\mathbb{I}-\frac{1}{3}\mathbf{I}\otimes\mathbf{I} \tag{4}$$

with $\mathbf{Q}$ and $\mathbf{X}$ written as

$$\begin{aligned}
\mathbf{Q} =& -\frac{1}{2}(\mathbf{n}^{(1)}\otimes\mathbf{n}^{(1)}+\mathbf{n}^{(2)}\otimes\mathbf{n}^{(2)})+\mathbf{n}^{(3)}\otimes\mathbf{n}^{(3)} \\
\mathbf{X}^v =& \alpha_1(\mathbf{n}^{(1)}\otimes\mathbf{n}^{(1)}+\mathbf{n}^{(2)}\otimes\mathbf{n}^{(2)})+(1-2\alpha_1)\mathbf{n}^{(3)}\otimes\mathbf{n}^{(3)} \quad , \quad \alpha_1=\hat{\alpha}_1(w) \\
\mathbf{X} =& \alpha_2(\mathbf{n}^{(1)}\otimes\mathbf{n}^{(1)}+\mathbf{n}^{(2)}\otimes\mathbf{n}^{(2)})+(1-2\alpha_2)\mathbf{n}^{(3)}\otimes\mathbf{n}^{(3)} \quad , \quad \alpha_2=\hat{\alpha}_2(f)
\end{aligned} \tag{5}$$

$\mathbf{X}^v$ is a counterpart of $\mathbf{X}$ that will be later utilized in the evolution equations for w and $\mathbf{n}^{(3)}$, in Eq. (20) for instance. $\bar{\sigma}$ is the isotropic matrix yield strength. Upon convention, $\bar{\sigma}$ is adopted the yield strength in one principal direction of orthotropy, and the components of the anisotropy tensor $\mathbb{p}$ are scaled accordingly. Moreover, the expressions of C, g and κ in (2) as well as η in (4) and α_2, as functions of f, w, and/or $\mathbb{H}$ are provided in Appendix A. $\mathbb{h}$ is defined as the anisotropy tensor in the deviatoric stress sub-space.

In the $(\mathbf{e}_{\mathrm{L}},\mathbf{e}_{\mathrm{T}},\mathbf{e}_{\mathrm{S}})$ frame (Fig. 1a), the six Hill coefficients are termed h_{L}, h_{T}, h_{S}, h_{TS}, h_{SL} and h_{LT} which, for an isotropic matrix would all simplify to unity, *i.e.* $h_{\mathrm{L}}=h_{\mathrm{T}}=h_{\mathrm{S}}=h_{\mathrm{TS}}=h_{\mathrm{SL}}=h_{\mathrm{LT}}=1$. In general, the principal loading directions, here denoted with $(\mathbf{m},\mathbf{p},\mathbf{n})$, are not aligned with either the principal axes of orthotropy $(\mathbf{e}_L,\mathbf{e}_T,\mathbf{e}_S)$ or the void-tied basis $(\mathbf{n}^{(1)},\mathbf{n}^{(2)},\mathbf{n}^{(3)})$. Further details can be found in [35,48].

2.2 Localized yielding

For the sake of simplicity, Φ^{I} has been developed with the void being codirectional with the normal to the localization plane $\mathbf{n}$, as shown in Fig. 1b. To remedy this constraint, the real microstructure is mapped into a *surrogate* one, identified with a surrogate void aligned with $\mathbf{n}$, with the void and cell volumes being preserved as the key feature. See Fig. 2.

With reference to the surrogate RVE shown in Fig. 2, the surrogate parameters read

$$\begin{aligned}\bar{\chi}(\mathbf{n}) &= \frac{\bar{R}(\mathbf{n})}{\bar{L}(\mathbf{n})}\\ \bar{w}(\mathbf{n}) &= \frac{h(\mathbf{n})}{\bar{R}(\mathbf{n})}\\ \bar{\lambda}(\mathbf{n}) &= \frac{H(\mathbf{n})}{\bar{L}(\mathbf{n})}\end{aligned} \tag{6}$$

where the third parameter does not enter into Φ^{I} though being indirectly influential. Note that the entire surrogate mictostructure is fortunately expressible in terms of the main microstructure. See Sec. 3.1.

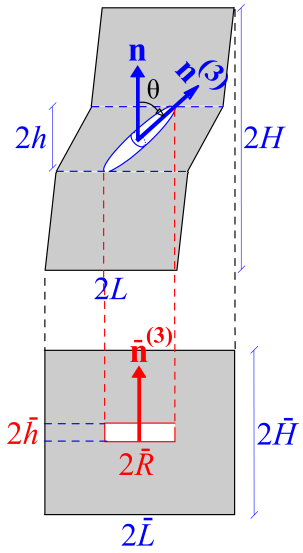

Figure 2: Surrogate configuration of a cell under combined tension and shear.

After Keralavarma and Chockalingam [47], Φ^{I} reads

$$\Phi^{\mathrm{I}} = \frac{1}{2}\frac{\sigma_{\mathrm{sh}} : \mathbb{P} : \sigma_{\mathrm{sh}}}{\bar{\tau}^2} + 2q_\chi f_{\mathrm{b}} \cosh\left(\frac{\sigma}{\sigma_{\mathrm{c}}} \ln \frac{1}{q_\chi f_{\mathrm{b}}}\right) - \left[1 + (q_\chi f_{\mathrm{b}})^2\right] \tag{7}$$

where $\sigma_{\mathrm{sh}} = \tau(\mathbf{n} \otimes \mathbf{m} + \mathbf{m} \otimes \mathbf{n})$ is the auxiliary shear stress tensor, and

$$\begin{aligned}\frac{\sigma_{\mathrm{c}}}{\bar{\tau}} &= 3b\sqrt{\frac{2}{5}\hat{h}_q}\left[\ln bu\left(1 + \sqrt{1 + \frac{1}{(bu)^2}}\right) - \sqrt{1 + \frac{1}{(bu)^2}}\right]_{u=1}^{1/f_{\mathrm{b}}}\\ 3b^2 &= \frac{\hat{h}_t}{\hat{h}_q} + \frac{5\alpha}{8\mathcal{W}^2}\frac{\hat{h}_a}{3\hat{h}_q} \quad , \quad \alpha = \frac{1}{12}\left[1 + q_\chi f_{\mathrm{b}} - 5(q_\chi f_{\mathrm{b}})^2 + 3(q_\chi f_{\mathrm{b}})^3\right]\end{aligned} \tag{8}$$

with $q_\chi = 1$ in the basic form, and the parameters $\hat{h}_q$, $\hat{h}_t$, and $\hat{h}_a$ being scalar anisotropy factors defined

in [35,47], expressed as

$$\begin{aligned}\hat{h}_q &= \frac{1}{6}\left[\hat{h}_{11}+\hat{h}_{22}+2\hat{h}_{12}+4(\hat{h}_{33}-\hat{h}_{23}-\hat{h}_{31})\right]\\ \hat{h}_t &= \frac{1}{4}\left[\hat{h}_{11}+\hat{h}_{22}+2(\hat{h}_{66}-\hat{h}_{12})\right]\\ \hat{h}_a &= \frac{\hat{h}_{44}+\hat{h}_{55}}{2}\end{aligned} \tag{9}$$

where $\hat{h}_{ij}$ denotes the ij-th component of tensor $\hat{\mathbb{h}}$, as the formal inverse of $\mathbb{h}$ (such that $\hat{\mathbb{h}} : \mathbb{h} = \mathbb{h} : \hat{\mathbb{h}} = \mathbb{J}$), expressed in Voigt–Mandel reduced form. Note that the special case of an isotropic J_2 matrix corresponds to $\hat{h}_{ij} = \delta_{ij}$ (with δ denoting the Kronecker delta) such that $\hat{h}_q = \hat{h}_t = \hat{h}_a = 1$. It is also worthy of note that $\mathbb{p}$ is to be calculated within the principal loading frame, that is initially taken coincident with the global coordinate system herein. Note also that, unlike those associated with Φ^{H} (where $\hat{h}_{ij}$ components are expressed in the void-tied basis), $\hat{h}_{ij}$'s corresponding to Φ^{I} are expressed in the basis tied to the *surrogate* void.

The concept of introducing q_χ into (8) follows the same rationale as set forth in [8], to capture the quantitative aspect of combined tension and shear as well as simple shearing. Interestingly, q_χ can be taken identical to that introduced in Eq. (37) in [8], with slight difference in the adjustable parameters. As such, one can write

$$q_\chi = \left(q_0 + \frac{q_\infty - q_0}{q_0/\kappa^2 + 1}\right)(1+\psi) \tag{10}$$

with $q_\infty = 1$ (pertaining to the absence of shear) and q_0 suggested as $q_0 = 1/3$.

Finally, $\mathcal{W}$ is a function of $f_b = \bar{\chi}^2$ and $\bar{w}$ that is calibrated modulo numerical results, that reads

$$\mathcal{W} = \begin{cases} \dfrac{q_\chi f_b \bar{w}^2}{4\mathcal{W}_0} + \mathcal{W}_0 & \text{for } \sqrt{q_\chi f_b}\bar{w} < 2\mathcal{W}_0 \\ \bar{\chi}\bar{w} & \text{for } \sqrt{q_\chi f_b}\bar{w} \geq \mathcal{W}_0 \end{cases} \tag{11}$$

where $\mathcal{W}_0$ is an adjustable parameter with the preferable value of 0.1 (see [47]).

Remark: The close interaction between voids and matrix anisotropy can be witnessed in the appearance of porosity f and void aspect ratio w during nearly-homogeneous deformation and their counterparts f_{b} and $\bar{w}$ during localized deformation. More specifically, this correlation is taken into account by the κ and $\mathbf{Q}$ parameters during nearly-homogeneous deformation, and its counterpart at inhomogeneous yielding is envisaged through the notion of σ_{c} in Eq. (8).

3 Evolution of State Variables

This section addresses the body of requisite equations for the evolution of the material state in explicit or rate form. Except for the void aspect ratio w and orientation $\mathbf{n}^{(3)}$, the evolution of which are intrinsic to the mechanism, the rest of the equations are generic. The equations describing the evolution of w and $\mathbf{n}^{(3)}$ associated with Φ^{H} are part of the developments in [35,52,59], and those associated with Φ^{I} are borrowed from the recent work by the authors [8]. They key feature to take into account in the latter respect is the rigid-like behavior of the matrix above and below the void induced by elastic unloading [60] above and below the void.

3.1 Surrogate parameters

The concept of a surrogate microstructure is key to the prediction of the onset of localized deformation and the microstrucrural evolution thereof. It involves replacing the rotating void with an upright cylinder of axis $\mathbf{n}$, having the same volume and porosity, Fig. 2. Figure 3 shows a closer schematic view of the post-localized deformation process under remote shearing as well as the geometric parametrization for surrogate and post-localized microstructural evolution. With regards to the surrogate microstrucrures, the vertical tangent at A', and appropos of the post-localized evolution of void shape and orientation, the horizontal tangent at point A should be accounted for.

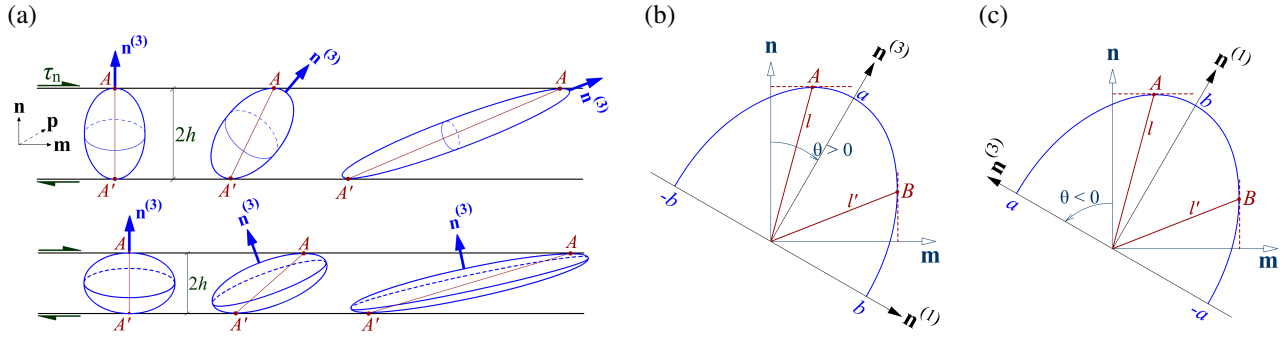

Figure 3: (a) Schematized post–localized deformation mechanism, and (b,c) the angles driving the evolved geometry for a spheroidal void under a shear field: (b) a prolate void ($w > 1$), (c) an oblate void ($w < 1$).

With reference to the algebraic details provided in [8], one can express the surrogate parameters in terms of the main microstructural state variables as follows:

$$\begin{aligned} \bar{w} &= \frac{w}{3\gamma}\left(\frac{1+\mathscr{T}^2}{1+\mathscr{T}^2 w^2}\right)^{\frac{3}{2}} \\ \bar{\lambda} &= \frac{\lambda}{(1+\eta\gamma_{\mathrm{mn}})^3} \\ \bar{\chi} &= \left(\frac{f\bar{\lambda}}{\bar{w}}\right)^{\frac{1}{3}} \end{aligned} \tag{12}$$

where $\mathscr{T} = S/C$, with S and C denoting, respectively, $\sin\theta$ and $\cos\theta$, with θ being a directional angle originated along $\mathbf{n}$ and ending at $\mathbf{n}^{(3)}$ with the sign convention as shown in Fig. 2. Also, $\gamma_{\mathrm{mn}} = 2\mathbf{m}\cdot\mathbf{En}$, $\mathbf{E} = \int \mathbf{D}\,\mathrm{d}t$, and λ is the main cell aspect ratio, that is evolved using (26). γ denotes the void shape factor, equaling 1/2 for a spheroid. Finally, η is originally 1, but heuristically recommended to avoid computational errors at extreme shearing, with $0.9 \leq \eta < 1$. In the present context, $\eta = 0.9$ has been granted throughout.

3.2 Base vectors and plane normals

The principal laboratory frame denoted by a global basis such as $(\mathbf{e}_1, \mathbf{e}_2, \mathbf{e}_3)$ as well as the principal orthotropy directors $(\mathbf{e}_L, \mathbf{e}_T, \mathbf{e}_S)$ are taken to rotate with the material. That is

$$\mathbf{e}_m = \mathbf{R}\mathbf{e}_m^{(0)}\ ,\ \mathbf{F} = \mathbf{RU} \tag{13}$$

where $\mathbf{e}_m$ denotes both laboratory and orthotropy base vectors (m = (L,T,S) stands for the principal orthotropy axes, and $n = 1, 2, 3$ constitutes the void lattice directors). Also, $\mathbf{R}$ and $\mathbf{U}$ emanate from the polar

decomposition of the deformation gradient tensor $\mathbf{F}$ at every step of the process, with $\mathbf{R}$ being the rotation part. The current deformation gradient can be derived on the basis of its incremental value at every time step, that is [61]

$$\mathbf{F}^{(i)} = \prod_{j=0}^{i} \mathbf{F}^{(j)} \tag{14}$$

where $\mathbf{F}^{(j)}$ is the deformation gradient between the $j-1$'st and j'th time steps constituted by the incremental displacements at the j'th step, where $j = 1, 2, ..., i$. Note that many commercial codes, such as ABAQUS, calculate $\mathbf{F}$ internally, and it thus need not be programmed when the constitutive model is coded in conjunction with those commercial software.

Upon invoking underlying microstructure, one can identify a discrete set of initial planes which could configure the post-localized inter-void ligaments. Each plane set is uniquely defined by a normal $\mathbf{n}$. Unless stated otherwise, a normal is convected through the transformation law for a directed area with unit magnitude. Therefore:

$$\mathbf{n} = \frac{\mathbf{F}^{-T}\mathbf{n}^{(0)}}{\left|\mathbf{F}^{-T}\mathbf{n}^{(0)}\right|} \tag{15}$$

with $|.|$ denoting a vector magnitude.

Within a plane with normal $\mathbf{n}$, two additional base vectors $\mathbf{m}$ and $\mathbf{p}$ can be defined in the interest of well-defined directions along and perpendicular to in-plane shear tractions. The latter two can be determined, at every current step, directly from the resolved shear traction on the current plane with normal $\mathbf{n}$ and a cross product carried out on $\mathbf{n}$ and $\mathbf{m}$, respectively. That is

$$\begin{aligned} \mathbf{m} &= \frac{\tau_{\mathrm{n}}}{|\tau_{\mathrm{n}}|} \\ \mathbf{p} &= \mathbf{n} \times \mathbf{m} \end{aligned} \tag{16}$$

where the shear traction τ_{n} will be used in Eq. (7). In case, however, the shear traction vanishes, Eq. (16) would be ill-defined. In this case, $\mathbf{m}$ and $\mathbf{p}$ would stay constant, equal to their previous values (or to their initial values in case the loading is shearless throughout).

For the single cell undergoing normal and lateral as well as shear displacement (see Fig. 1b), $\mathbf{F}^{(j)}$ reads:

$$\mathbf{F}^{(j)} = \left(1 + \frac{\delta u_m^{(j)}}{L}\right) \mathbf{m} \otimes \mathbf{m} + \left(1 + \frac{\delta u_p^{(j)}}{L}\right) \mathbf{p} \otimes \mathbf{p} + \left(1 + \frac{\delta u_n^{(j)}}{H}\right) \mathbf{n} \otimes \mathbf{n} + \frac{\delta u_t^{(j)}}{H} \mathbf{m} \otimes \mathbf{n} \tag{17}$$

where the constituents $\left(\delta u_m^{(j)}, \delta u_p^{(j)}, \delta u_n^{(j)}, \delta u_t^{(j)}\right)$ are the incremental displacements at the j'th step, where $j = 1, 2, ..., i$. Here, $\delta u_m^{(j)}$, $\delta u_p^{(j)}$, and $\delta u_n^{(j)}$ are the tensile displacement increments along directions $\mathbf{m}$, $\mathbf{p}$, and $\mathbf{n}$, respectively, and $\delta u_t^{(j)}$ is the tangential displacement increment over the top chord of the cell. Note that all these displacement increments are modified as to preserve the ratios among the stresses. Moreover,

$$L = L_0 \exp\left(\frac{\epsilon_{mm} + \epsilon_{pp}}{2}\right) \quad , \quad H = H_0 \exp \epsilon_{nn} \tag{18}$$

with ϵ_{mm}, ϵ_{pp}, and ϵ_{nn} are the normal strains resolved along the $\mathbf{m}$, $\mathbf{p}$ and $\mathbf{n}$ directions, respectively. Upon consideration of the single cell, $\mathbf{n}$ (denoting normal to the invoked localization plane) initially directed along $\mathbf{e}_3$ would stay constant thanks to the imposed deformation gradient $\mathbf{F}$. Accordingly, $\mathbf{m}$, $\mathbf{p}$ and $\mathbf{n}$ coincide with the global base vectors $\mathbf{e}_1$, $\mathbf{e}_2$ and $\mathbf{e}_3$, respectively. Note that the present solution framework is expanded based on a co-rotational formulation, *i.e.* the equations are expanded within the rotated material configuration. Therefore, Eq. (13) is tacitly assumed in the formulation.

3.3 Ligament volume fraction

$c \equiv h/H$ (see Fig's 2 and 3 for geometric details) denotes the current ligament volume fraction, which can be expressed in correlation with (f, w, λ, θ) as

$$c = \left(\frac{3\gamma f}{w\lambda^2}\right)^{1/3} \sqrt{\frac{\mathscr{T}^2 + w^2}{\mathscr{T}^2 + 1}} \tag{19}$$

with $\mathscr{T}$ defined in advance.

3.4 Void aspect ratio

The evolving void aspect ratio can be more concisely and conveniently expressed in the form of its natural logarithm $s \equiv \ln w$, thus its rate $\dot{s}$ as follows.

– During nearly-homogeneous deformation:
The evolution equation for the void aspect ratio during nearly-homogeneous deformation is that proposed by Gologanu *et al.* [59], also adopted in [48]:

$$\dot{s} = \mathbf{Q} : \mathbf{D}^v \tag{20}$$

where

$$\mathbf{D}^v \ = k\mathbf{D}^{\mathrm{p}} + 3\left(\frac{1}{f}\mathbf{X}^v - \mathbf{X}\right) D_{\mathrm{m}}^{\mathrm{p}} \tag{21}$$

and $\mathbf{Q}$, $\mathbf{X}^v$ and $\mathbf{X}$ obey (5). The heuristic function k (following [59]) writes

$$\begin{aligned} &k = 1 + k_w k_f k_T \\ &k_w(w) = \frac{9}{2}\frac{\alpha_1 - \alpha_1^{\mathrm{Gar}}}{1 - 3\alpha_1} \\ &k_f(f) = (1 - \sqrt{f})^2 \\ &k_T(T, \epsilon) = \begin{cases} 1 - \dfrac{T^2 + T^4}{9} & \text{for} \quad \epsilon = +1 \\ 1 - \dfrac{T^2 + T^4}{18} & \text{for} \quad \epsilon = -1 \end{cases}, \qquad \epsilon \equiv \mathrm{sgn}(\sigma_{\mathrm{m}}\sigma'_{33}) \end{aligned} \tag{22}$$

and

$$T = \frac{\sigma_{kk}/3}{\sqrt{\frac{3}{2}\sigma' : \sigma'}} \tag{23}$$

where T is the stress triaxiality and ϵ is related to the third stress invariant; see [4].

– During localized deformation:

In view of the horizontal tangent at point A in Fig. 3 and, with reference to the algebraic details provided in [8], one can write

$$\dot{s} = \frac{(w^2+\mathscr{T}^2)^2}{(w^4+\mathscr{T}^2)(1+\mathscr{T}^2)\left[2-3\frac{\mathscr{T}^2(2w^2-w^4+\mathscr{T}^2)}{(w^4+\mathscr{T}^2)(w^2+\mathscr{T}^2)}\right]} \left[\left(\frac{3}{c} - \frac{(w^4+\mathscr{T}^2)(1+\mathscr{T}^2)}{f(w^2+\mathscr{T}^2)^2}\right) D_{\mathrm{nn}} + \frac{6}{c}\frac{(w^2-1)\mathscr{T}}{w^2+\mathscr{T}^2} D_{\mathrm{nm}}\right] \tag{24}$$

for prolate voids ($w > 1$), and

$$\dot{s} = \frac{(w^2+\mathscr{T}^2)^2}{(w^4+\mathscr{T}^2)(1+\mathscr{T}^2)\left[1-\frac{\mathscr{T}^2(-2w^2+w^4-\mathscr{T}^2)}{(w^4+\mathscr{T}^2)(w^2+\mathscr{T}^2)}\right]}\left[\left(-\frac{3}{c}+\frac{(w^4+\mathscr{T}^2)(1+\mathscr{T}^2)}{f(w^2+\mathscr{T}^2)^2}\right)D_{\rm nn}-\frac{6}{c}\frac{(w^2-1)\mathscr{T}}{w^2+\mathscr{T}^2}D_{\rm nm}\right] \tag{25}$$

for oblate voids ($w < 1$). Here,

$$D_{\rm nn} = \mathbf{n}\cdot\mathbf{D}^{\rm p}\mathbf{n}$$
$$D_{\rm mn} = \mathbf{m}\cdot\mathbf{D}^{\rm p}\mathbf{n}$$

with the elastic strains neglected.

Note, for the special case of an upright void, that Eq. (24) simplifies into Eq. (12) of [55]. See [8] for more details and special cases.

3.5 Cell aspect ratio

A judicious method that enables to update the cell aspect ratio as function of the normal to the ligament $\mathbf{n}$ is that proposed by Leblond and Mottet [62], originally derived for an initially cubic unit cell. This method was extended into the more general case of an initially orthorhombic cell in [8], which delivers the following relation:

$$\lambda(\mathbf{n}) = \frac{\lambda_0(\mathbf{n})}{\sqrt{\mathcal{J}}}\left(\mathbf{n}\cdot(\mathbf{F}\mathbf{F}^{\rm T})\mathbf{n}\right)^{\frac{3}{4}} \tag{26}$$

where $\mathbf{F}$ is the total deformation gradient, with its associated determinant $\mathcal{J} := \det\mathbf{F}$. See [8] for justification. It should be noted, however, that, under combined tensile and shear loadings, λ should never fall below its initial value λ_0. Hence, λ is replaced with λ_0 in case $\lambda \leq \lambda_0$ [62].

3.6 Porosity

Generically throughout the plastic process, f is governed by plastic incompressibility such that:

$$\dot{f} = (1-f)D^{\rm p}_{kk} = (1-f)\,\dot{\Lambda}\frac{\partial\Phi}{\partial\sigma_{\rm m}} \tag{27}$$

with $\dot{\Lambda}$ being the plastic multiplier in rate form.

3.7 Void orientation

In general, the rate of orientation of the (immaterial) principal axes of the void may be directly obtained from the (material) rotation and strain rates of the void [63, 64], denoted by $\mathbf{\Omega}^v$ and $\mathbf{D}^v$, respectively. Thus, the rate of change of the void axis is given by the following

$$\dot{\mathbf{n}}^{(3)} = \omega\mathbf{n}^{(3)}, \qquad \omega = \mathbf{\Omega}^v + \mathbf{\Omega}^l \tag{28}$$

where the rotation tensor ω is the total spin tensor that consists of the void spin, $\mathbf{\Omega}^v$, superposed by the void rotation with respect to the material, $\mathbf{\Omega}^l$. Here, we exploit $\mathbf{\Omega}^v$ as derived in [63, 64] during the nearly nearly-homogeneous part of deformation, and confine it to the plastic ligament at the post-localized regime. Hence:

– During nearly-homogeneous deformation:

$$\mathbf{\Omega}^v = \mathbf{\Omega} - \mathbb{C}:\mathbf{D}^{\rm p} \tag{29}$$

– During the post-localized deformation:

$$\mathbf{\Omega}^{v} = \mathbf{\Omega} - \frac{1}{c}\mathbb{C} : \mathbf{D}^{\mathrm{p}} \tag{30}$$

where $\mathbb{C}$ is the fourth order spin concentration tensor given by

$$\mathbb{C} = -(1-f)\mathbb{P} : \mathbb{A}, \qquad \mathbb{A} = [\mathbb{I} - (1-f)\mathbb{S}]^{-1} \tag{31}$$

with $\mathbb{A}$ the strain concentration tensor and $\mathbb{P}$ and $\mathbb{S}$ the Eshelby tensors [65] for a spheroidal inclusion of zero stiffness in an incompressible linear viscous matrix. Note that a $1/c$ term appears in (30) to represent the plastic rate of deformation inside the ligament.

Also, in (28) $\mathbf{\Omega}^{l}$ is an additional contribution to the effective void rotation that comes from mere distortion of void boundaries under the combined effect of tension and shear.

– During nearly-homogeneous deformation:
By defining the plastic spin tensor as $\mathbf{\Omega}^{\mathrm{p}} = \mathbf{\Omega} - \omega$, one can write, during the nearly-homogeneous deformation:

$$\mathbf{\Omega}^{\mathrm{l}} = \frac{1}{2}\sum_{i\neq j,\, w_i \neq w_j} \frac{w_i^2 + w_j^2}{w_i^2 - w_j^2}\left[(\mathbf{n}_i \otimes \mathbf{n}_j + \mathbf{n}_j \otimes \mathbf{n}_i) : \mathbb{A} : \mathbf{D}^{\mathrm{p}}\right] \mathbf{n}_i \otimes \mathbf{n}_j \tag{32}$$

Then, by combining Eq's (29), (32), and (28), and by adopting the notation $w_1 = w_2 = w$ and $w_3 = 1$, one can evaluate the components of ω with respect to a laboratory frame. The case $w = 1$, however, requires a careful treatment; see [35].

– During localized deformation:
The post-localized $\mathbf{\Omega}^{l}$ was derived from first principles in [8]. Upon the steps clarified therein, the post-localized $\mathbf{\Omega}^{l}$ reads:

$$\mathbf{\Omega}^{l} = \frac{\dot{S}}{S}\mathbf{m}\otimes\mathbf{m} + \frac{\dot{C}}{C}\mathbf{n}\otimes\mathbf{n} = \frac{\dot{\mathscr{T}}}{\mathscr{T}}\left(C^2\mathbf{m}\otimes\mathbf{m} - S^2\mathbf{n}\otimes\mathbf{n}\right) \tag{33}$$

where $\dot{\mathscr{T}}$ obeys the following equation

$$\dot{\mathscr{T}} = \frac{(\mathscr{T}^2 + w^2)(1+\mathscr{T}^2)}{\mathscr{T}(1-w^2)}\left[\frac{\dot{c}}{c} - \frac{1}{3}\left(\frac{\dot{f}}{f} - 2\frac{\dot{\lambda}}{\lambda}\right) + \left(\frac{1}{3} - \frac{w^2}{\mathscr{T}^2 + w^2}\right)\dot{s}\right] \tag{34}$$

where

$$\begin{aligned}
\frac{\dot{c}}{c} &= \frac{1-c}{c}\mathbf{n}\cdot\mathbf{D}^{\mathrm{p}}\mathbf{n} \\
\frac{\dot{f}}{f} &= \left(\frac{1}{f} - 1\right) D^{\mathrm{p}}_{kk} \\
\frac{\dot{\lambda}}{\lambda} &= D_{\mathrm{nn}} - \frac{1}{2}\left(D_{\mathrm{mm}} + D_{\mathrm{pp}}\right)
\end{aligned} \tag{35}$$

with

$$D_{\mathrm{nn}} = \mathbf{n}\cdot\mathbf{D}^{\mathrm{p}}\mathbf{n} \quad , \quad D_{\mathrm{mm}} = \mathbf{m}\cdot\mathbf{D}^{\mathrm{p}}\mathbf{m} \quad , \quad D_{\mathrm{pp}} = \mathbf{p}\cdot\mathbf{D}^{\mathrm{p}}\mathbf{p}$$

and $\mathbf{p} = \mathbf{n}\times\mathbf{m}$ completes the triad of local base vectors.

Remark: Thanks to the involvement of $\dot{s}$ according to (24) and (25), prolate and oblate voids exhibit different rotation conducts under shearing, as schematized in Fig. 3a. As such, both prolate and oblate voids under a positively directed shear field reach a steady state rightward orientation. The transient rate of orientation, however, differs in the sense that a prolate void rotates rightward throughout the process whereas an oblate void rotates leftward transiently until it starts rotating rightward and continues until failure. See [8] for further details.

3.8 Equivalent plastic strain

The evolution of equivalent plastic strain $\bar{\epsilon}$ is obtained through the formation of plastic work equivalence between the macroscopic material and the excluded matrix, written as

$$\sigma : \mathbf{D}^{\mathrm{p}} = (1-f)\bar{\sigma}\dot{\bar{\epsilon}} \tag{36}$$

where $\bar{\sigma}$ correlates with $\bar{\epsilon}$ through (1). Within the adopted solution scheme, Eq. (36 can utilized for calculating the residual associated with $\bar{\epsilon}$, as declared in Section 4. Alternatively, it can be exploited to update the plastic multiplier $\dot{\Lambda}$ explicitly by rearranging in the following format:

$$\dot{\Lambda} = (1-f)\frac{\bar{\sigma}\dot{\bar{\epsilon}}}{\sigma : \mathbf{N}} \quad , \quad \mathbf{N} = \frac{\partial \Phi}{\partial \sigma} \tag{37}$$

Note that $\dot{\Lambda}$ has been taken to evolve, in [48], in accordance with the implicit evolution of $\mathrm{d}\Lambda$ using the instantaneous value of Φ at the beginning of every time step.

4 Time Integration of Constitutive Equations

The elements of time integration follow an implicit integration scheme expounded in detail in [8, 48]. The quintessential points will be outlined herein.

Following the additivity premise, the total rate of deformation tensor $\mathbf{D}$ is decomposed in the following format [66]:

$$\mathbf{D} = \mathbf{D}^{\mathrm{e}} + \mathbf{D}^{\mathrm{p}} \tag{38}$$

where the elastic part is given by:

$$\mathbf{D}^{\mathrm{e}} = \mathbb{L}^{-1} : \overset{\triangledown}{\sigma} \tag{39}$$

with $\mathbb{L}$ the isotropic tensor of elastic moduli, and $\overset{\triangledown}{\sigma}$ denotes the Jaumann objective stress rate defined by:

$$\overset{\triangledown}{\sigma} = \dot{\sigma} + \sigma\mathbf{\Omega} - \mathbf{\Omega}\sigma \tag{40}$$

where $\mathbf{\Omega}$ is the skew symmetric part of the velocity gradient.

All the same, the plastic part of $\mathbf{D}$ originates from normality to a yield surface represented by a flow potential $\Phi = 0$ via the following relation:

$$\mathbf{D}^{\mathrm{p}} = \dot{\Lambda}\frac{\partial \Phi^{\mathrm{eff}}}{\partial \sigma} \tag{41}$$

where Λ is the plastic multiplier associated with the plastic strain tensor, and Φ^{eff} is the effective yield function, emanating from the innermost surface between those corresponding to Φ^{H} and Φ^{I} in the adopted consecutive approach.

The hybrid model presented in the foregoing sections is formulated within a corotational framework. That is, the constitutive relations are expressed in an intermediate configuration, which is rotated from

the current one by the instantaneous rotation tensor $\mathbf{R}$ that results from the polar decomposition of the incremental deformation gradient [48]. Constitutive laws, therefore, need be written accordingly in the rotated configuration, with quantities indicated by the tilde ($\sim$) symbol. The so-derived equations relate merely with the stretch part of deformations, and the rotation part is admitted by rotating quantities to the intermediate configuration. The objective rate of stress $\overset{\triangledown}{\sigma}$ in (40) will be thus replaced with $\dot{\sigma}$, and the spin tensor $\mathbf{\Omega}$ will vanish from the void orientation evolution (see Sec. 3.7), all thanks to the corotational formulation. Further details can be observed in [48].

Due to the existence of high geometric nonlinearity within the problems of porous plasticity, the implicit method of plasticity has been adopted to solve for current state variables. Accordingly, the following independent state variables will be updated via the implicit method:

$$\mathbf{V} = \left[\sigma', \sigma_m, f, \bar{\epsilon}, s\right]^T \tag{42}$$

while the rest, including $\mathrm{d}\Lambda, \bar{\sigma}, \lambda$ as well as the surrogate parameters in (12) are explicitly evolved as function of the above independent variables with reference to Section 3. The main portion within the flow rule (41) to derive the evolution of the independent state variables is the first derivative of the flow potential Φ with respect to the stress tensor, here denoted with $\mathbf{N}$. Within the implicit time integration invoking the Newton-Raphson solution scheme, $\mathbf{N}$ is primarily used in the calculation of *residuals* (denoted with $[\mathbf{R}]$), and $\partial\mathbf{N}/\partial\sigma$ is mainly utilized in the *Jacobian* components ($\partial[\mathbf{R}]/\partial[\mathbf{V}]$) associated with the state variables in (42).

Following Eqs. (2) and (7), one can write

$$\tilde{\mathbf{N}}^{\mathrm{H}} \equiv \frac{\partial \Phi^{\mathrm{H}}}{\partial \tilde{\sigma}} = 3C\frac{\tilde{\mathbb{H}} : \tilde{\sigma}}{\bar{\sigma}^2} + 2(g+1)(g+f)\kappa \sinh\left(\kappa\frac{\tilde{\sigma} : \tilde{\mathbf{X}}}{\bar{\sigma}}\right)\frac{\tilde{\mathbf{X}}}{\bar{\sigma}} \tag{43}$$

and

$$\tilde{\mathbf{N}}^{\mathrm{I}} \equiv \frac{\partial \Phi^{\mathrm{I}}}{\partial \tilde{\sigma}} = 3\frac{\partial \sigma_{\mathrm{sh}}}{\partial \sigma} : \mathbb{p} : \frac{\sigma_{\mathrm{sh}}}{\bar{\sigma}^2} + 2\frac{f_{\mathrm{b}}}{\sigma_{\mathrm{c}}}\ln\frac{1}{f_{\mathrm{b}}}\sinh\left(\frac{\sigma_{\mathrm{n}}}{\sigma_{\mathrm{c}}}\ln\frac{1}{f_{\mathrm{b}}}\right)\mathbf{n}\otimes\mathbf{n} \tag{44}$$

where use has been made of the following derivatives

$$\begin{aligned} &\tau_{\mathrm{n}} = \sigma\mathbf{n} - \sigma_{\mathrm{n}}\mathbf{n} \;\; \therefore \;\; \frac{\partial \tau_{\mathrm{n}i}}{\partial \sigma_{kl}} = (\delta_{ik} - n_i n_k)n_l \\ &\therefore \;\; \left[\frac{\partial \sigma_{\mathrm{sh}}}{\partial \sigma}\right]_{ijkl} \equiv \frac{\partial [\sigma_{\mathrm{sh}}]_{ij}}{\partial \sigma_{kl}} = (\delta_{ik} - n_i n_k)n_j n_l + (\delta_{jl} - n_j n_l)n_i n_k \end{aligned} \tag{45}$$

where use has been made of the basic formulation of (7). For computation purposes, f_{b} obviously should be replaced by $q_\chi f_{\mathrm{b}}$.

With the above derivations at hand, the Newton-Raphson procedure is employed iteratively to solve the $[\mathbf{R}]^T = \mathbf{0}$ equation system at every time step:

$$[\mathbf{V}]_{i+1} = [\mathbf{V}]_i - \left[\frac{\partial [\mathbf{R}]}{\partial [\mathbf{V}]_i}\right]^{-1}[\mathbf{R}] \tag{46}$$

where the Jacobian matrix $\partial[\mathbf{R}]/\partial[\mathbf{V}]$ can be evaluated at every iteration within the time step or kept equal to the value at the beginning of the time step, and subscript i denotes the iteration number. Appendix B provides the Jacobian components pertaining to Φ^{I}, and those associated with Φ^{H} have been provided in [48].

5 Results

This section presents the calculated results of internal state variables from integration of the afore-mentioned constitutive framework for one single unit cell. Correspondingly, there exists only one localization plane with the normal being $\mathbf{e}_3$ throughout whereas the void is allowed to rotate under combined loading. The stress state is represented by a normal, two perpendicular lateral and a shear traction exerted on the upper and lower faces of the cell. Matrix anisotropy has been neglected throughout. Each set of results is extended into further subsets to demonstrate the evolution of various microstructural variables on the material response. The ratios among the remote normal, lateral, and shear stresses remain constant throughout. Accordingly, stress triaxiality T and the Lode parameter L are constant.

The model is firstly assessed against existing results under triaxial loading, *i.e.* in absence of shear, for fixed stress triaxialities and prescribed initial void aspect ratios. The next set of results presented in the sequel represent combined tension and shear, with specific focus on shear-dominated loading. To this end, the predicted results are first compared to cell-model calculations under combined normal and shear as well as near-simple shearing states. In the latter case, lateral stresses are eliminated for the sake of simplicity, and the axial-to-shear stress ratio $\kappa = \sigma/\tau$ varies from zero (representing simple shear) to infinity (signifying uniaxial loading).

Note that, in some plots comprising several sets of curves, only one line color has been itemized in the line legend to represent the line type rather than the depicted color.

5.1 Results under triaxial loading

5.1.1 Model assessment

This section presents the hybrid model predictions in comparison against the existing FEM-based cell-model calculations under triaxial loading. To this end, the analyses carried out by Pardoen and Hutchinson [24] (for isotropic matrices) and those calculated by Legarth and Tvergaard [67] (for Hill-type orthotropic matrices) are considered as comparator. The results herein are compared to their FEM outcomes obtained from cell-model calculations. The following constants are common among all results:

$$f_0 = 10^{-2} \quad , \quad \lambda_0 = 1 \quad , \quad N = 0.1 \quad , \quad \frac{\sigma_0}{E} = 0.002 \tag{47}$$

and the remaining ones are intrinsic to the material. In the isotropic matrix material [24],

$$E = 210 \text{ GPa} \tag{48}$$

and in the orthotropic matrix [67],

$$E = 70 \text{ GPa} \tag{49}$$

where σ_0 is the initial matrix yield strength and ϵ_0 is its conjugate strain. E is the Young modulus, and the rest of parameters have been defined in due course.

In the isotropic-matrix study [24], the values of initial void aspect ratio w_0 and stress triaxiality T are varied from case to case. Within the anisotropic case [67], however, the fixed values of initial void aspect ratio $w_0 = 1$ and stress triaxiality $T = 2$ have been utilized for comparison.

In the case of a Hill-type matrix, the FEM results were parametrized directly based on the basic Hill coefficients according to the primitive form of the Hill criterion [58] for the matrix material, reading as the following normalized form:

$$F(\sigma_{\mathrm{TT}} - \sigma_{\mathrm{SS}})^2 + G(\sigma_{\mathrm{LL}} - \sigma_{\mathrm{SS}})^2 + H(\sigma_{\mathrm{LL}} - \sigma_{\mathrm{TT}})^2 + 2\left(L\sigma_{\mathrm{TS}}^2 + M\sigma_{\mathrm{SL}}^2 + N\sigma_{\mathrm{LT}}^2\right) = \bar{\sigma}^2 \tag{50}$$

where the stress components are written in the material orthotropy frame, and $\bar{\sigma}$ is the matrix yield stress in one arbitrary direction, whereby the Hill coefficients must be scaled accordingly. In [67], $\bar{\sigma}$ was taken along the "L" direction. The present-invoked Hill coefficients are then expressible in terms of their primitive counterparts according to the following identities [68]:

$$\begin{cases} h_1 = -F + 2(H+G) \\ h_2 = -G + 2(H+F) \\ h_3 = -H + 2(F+G) \end{cases} \qquad \begin{cases} h_4 = L \\ h_5 = M \\ h_6 = N \end{cases} \tag{51}$$

Correspondingly, the $\mathbb{p}$ tensor expressed in reduced form can be written as

$$\mathbf{p} = \begin{bmatrix} G+H & -H & -G & 0 & 0 & 0 \\ -H & H+F & -F & 0 & 0 & 0 \\ -G & -F & F+G & 0 & 0 & 0 \\ 0 & 0 & 0 & L & 0 & 0 \\ 0 & 0 & 0 & 0 & M & 0 \\ 0 & 0 & 0 & 0 & 0 & N \end{bmatrix} \tag{52}$$

in the material orthotropy frame so long as the stress space is recast in the form $\sigma = [\sigma_{11}\ \sigma_{22}\ \sigma_{33}\ \sigma_{23}\ \sigma_{31}\ \sigma_{12}]^{\mathrm{T}}$. Legarth and Tvergaard had considered the following anisotropy cases [67]:

$$\text{Aniso (II):} \quad \begin{cases} F = 0.4 \\ G = 7.33 \\ H = 1 \end{cases} \qquad \text{Aniso (IV):} \quad \begin{cases} F = 2.5 \\ G = 0.3 \\ H = 1 \end{cases} \tag{53}$$

with $L = M = N = 9.6$.

It is noteworthy that, unlike from Eq. (37), the plastic multiplier follows a power representation as function of the yield function as well as the material yield stress:

$$\dot{\Lambda} = \dot{\bar{\epsilon}} \left(\frac{\Phi + 1}{\bar{\sigma}} \right)^{1/m} \tag{54}$$

which affects the evolution of $\bar{\epsilon}$ accordingly. Here, $\bar{\sigma}$ follows the power law in (1), and use has been made of the present Φ^{H} and Φ^{I} in lieu of the Hill potential in (50). Moreover, $m = 0.01$ has been used in reference to [67].

Figures 4 and 5 compare selective state variables with the results from Pardoen and Hutchinson (P-H) [24] and Legarth and Tvergaard (L-T) [67], respectively.

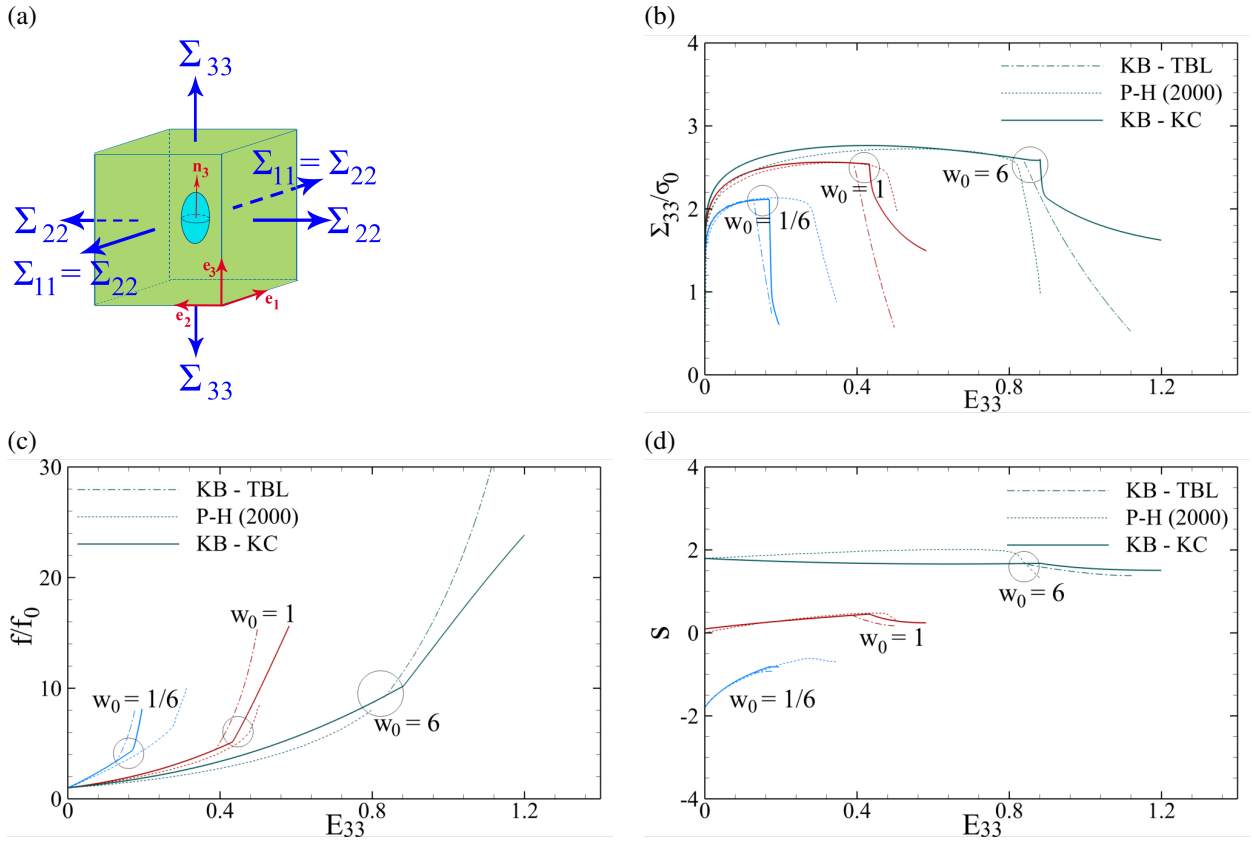

Figure 4: Comparison of the present model predictions in absence of shear (solid curves) with the results extracted from Pardoen and Hutchinson's cell-model calculations (dotted curves) [24] as well as those obtained from the hybrid model in [8] for $T = 1$ and various values of w_0: (a) schematic unit cell, (b) normal stress response, (c) normalized porosity, (d) logarithmic void aspect ratio $s \equiv \ln w$.

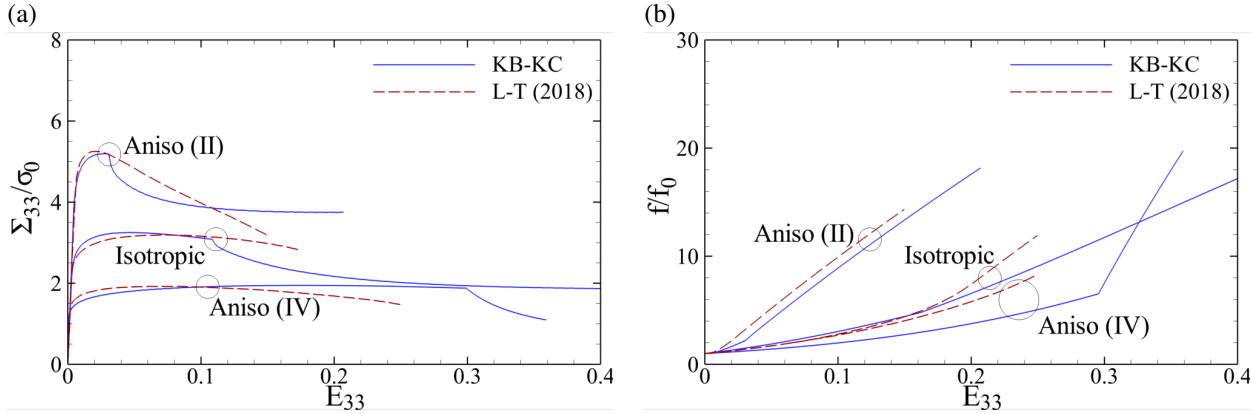

Figure 5: Comparison of the present model predictions in absence of shear (solid curves) with the cell-model calculations from Legarth and Tvergaard (dashed curves) [67] for the triaxiality of $T = 2$ and initial void aspect ratio of $w_0 = 1$ and various matrix anisotropy occurrences including the isotropic matrix as well as anisotropy (II) and (IV): (a) normal stress response, (b) normalized porosity.

The comparison among the stress-strain results, corresponding to the unit cell schematized in Fig. 4a, is shown in Fig. 4 for the typical triaxiality of $T = 1$. To gain better insight into the distinctive behaviors of different models, the present results are further compared to those from the alternative hybrid model devised by the present authors in [8] for plastically isotropic materials. The model therein consisted of the same K–B model as Φ^{H} (simplified for isotropic matrices) but a piecewise-continuous Φ^{I} known as T–B–L after Torki *et al.* [69]. The calculations are terminated when $\bar{\chi}$ exceeds $\sqrt{2}/2 \approx 0.707$ [55].

Figure 4a shows that the the KB–KC hybrid model predicts the onset of void coalescence later than the KB–TBL and mostly sooner than FEM analysis (except for highly elongated voids $w_0 >> 1$). The former is due to the coalescence stress being slightly above that from TBL as demonstrated by comparisons [47]. Note also that, with increasing w_0, the predicted post-localized ductility (and strain to failure ϵ_f accordingly) is higher from KC than from TBL due to the coalescence-induced stress being higher in the former.

Further, Fig. 4c reveals a convex evolution of porosity at larger values of w_0. Indeed, the slow stress-bearing decrease at this limit changes the predicted concavity of f such that, for $w_0 >> 1$, there is an apparent asymptotic limit thereto, which retards failure by void coalescence in layers. A similar retardation can be envisaged within FEM and TBL curves by the reducing porosity slopes with increasing w_0 whereas the observed slope decrease is more exaggerative by the KC model. More extensive investigation has is that the de facto yield mechanism for such long voids is closer to coalescence in columns (necklace coalescence) [27].

Moreover, the slope of the $s = \ln w$ curve during void growth declines with increasing void aspect ratios until it changes from a positive into a negative slope signifying a moderately decreasing w for $w_0 = 6$ whereas the FEM-based w still increases, though moderately so, for this case. This calls for further modification in the evolution law for s by (20). Furthermore, the decreasing post-localized slope within s is seen as the largest for nearly spherical initial voids ($w_0 \approx 1$), and it decreases for both prolate and oblate voids.

Last but not least, in view of Fig. 5, the difference between the onset of homogeneous softening for the isotropic and Aniso (IV) cases lies in the difference in the evolution curves for porosity f. That is, the sharper slope of f evolution according to the KB-KC hybrid model for the isotropic material gives rise to the maximum stress response reached sooner (*i.e.* at a smaller cumulative strain), and vice versa for Aniso (IV). This may warrant some modification to the $\dot{f}$ formulation that accounts for the effect of plastic anisotropy.

The results are hereby extended as to incorporate plastic anisotropy next for several stress triaxialities in combination with materials with various anisotropy (Hill) coefficients. Among all, there are three extensional and three shear orthotropy coefficients. In view of Fig. 1a, $\mathbf{e}_{\mathrm{S}}$ is conventionally directed along the axis of transverse isotropy, which presently coincides with the direction of principal normal loading Σ_{33}, and the other two are oriented according to the right-hand convention. Accordingly, the studies are subject to variation of $h_{\mathrm{L}} = h_{\mathrm{T}}$ and h_{S}. The h_{ij} components above and below unity represent materials that are, respectively, weaker and stronger than an isotropic material in response to Σ_{ij}. The varying scenarios are schematized in Fig. 6.

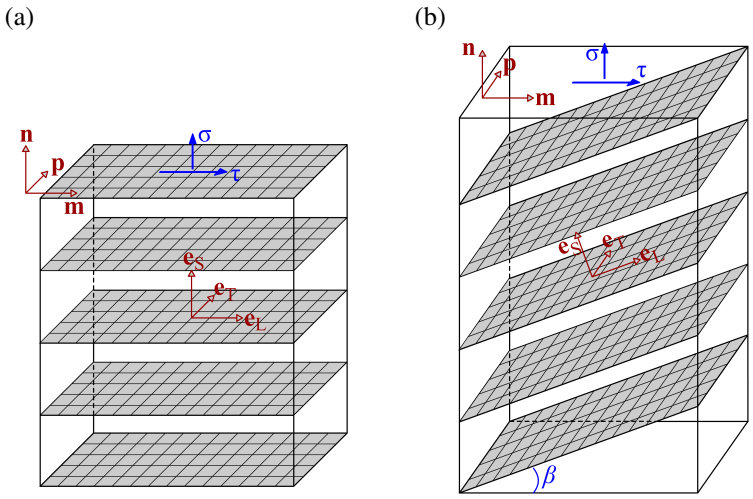

Figure 6: Coincident and rotated planes of transverse isotropy with respect to the principal loading directions: (a) $\mathbf{e}_{\mathrm{S}} = \mathbf{n}$, (b) $\mathbf{e}_{\mathrm{S}} = \sin\beta\mathbf{m} + \cos\beta\mathbf{n}$.

5.1.2 Effect of translational Hill coefficients

Figure 7 shows the variation of stress response under various triaxialities for materials with various $h_{\mathrm{L}} = h_{\mathrm{T}}$ values. The effect of varying h_{S} bares similar influence.

Note that, notwithstanding zero lateral loading at $T = 1/3$, there exist lateral strains due to the Poisson effect, and thus $h_{\mathrm{L}} = h_{\mathrm{T}}$ is significantly effective in the normal stress response. In this regard, a weak L–T plane generates a smaller normal limit load along $\mathbf{e}_{\mathrm{S}}$, and vice versa. Further, the effect of extensional Hill coefficients intensifies with increasing lateral loads or, equivalently, increasing triaxiality. Thereupon, smaller Hill coefficients bare a confining effect reflected through a higher limit load concurrent with a lower strain to coalescence as well as strain to failure, and vice versa. However, the strain to coalescence and failure are more significantly driven by triaxiality than the Poisson effect so that the latter two are almost equal for various Hill coefficients whereas the limit load is still remarkably affected by them.

The evolution of stress response and the rest of microstructural variables for the specific case of $T = 1$ and various values of $h_{\mathrm{L}} = h_{\mathrm{T}}$ and h_{S} is shown in the next set of subfigures.

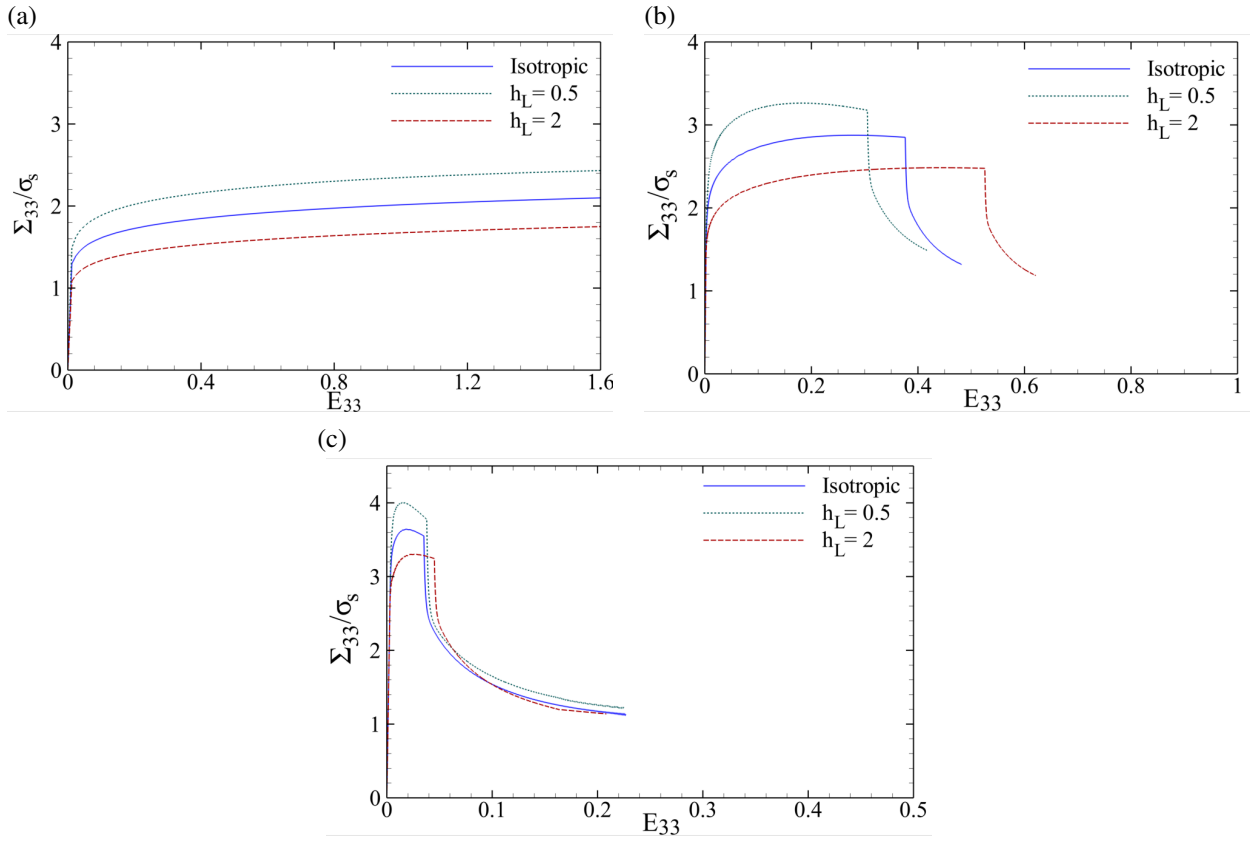

Figure 7: Present model predictions under triaxial loading with various stress triaxiality values and varying h_{L} Hill coefficients, based on the initial microstructure denoted with Eq. (47): (a) $T = 1/3$, (b) $T = 1$, (c) $T = 3$.

One can clearly observe similar effects induced by varying $h_{\mathrm{L}} = h_{\mathrm{T}}$ and h_{S} coefficients. With the same values of coefficients, the limit load, strain to coalescence and failure are very close for an intermediate triaxiality level. There is only slight softening associated with stronger matrices in the L–S plane ($h_{\mathrm{L}} = 0.5$) after the maximum stress response occurring at a lower strain level. One could expect more significant effects induced by h_{L} and h_{T} with large triaxialities ($T > 2$) and, all the same, more remarkable effects of h_{S} at lower triaxialities.

Moreover, the convexity of $\bar{\chi}$ during the post-localized deformation process is larger than that of porosity due to the smaller bounds thereto ($\chi_0 \leq \bar{\chi} < 1$) whereas porosity reaches at least one order of magnitude as much as its initial value f_0. Note that the post-localized lateral growth of the void, reflected by the decrease in $s = \ln w$, is more remarkable for a lower h_{S}, *i.e.* for a material stronger along the loading direction, being perpendicular to the transverse isotropy plane. Namely, the porosity increase level being almost equal, a void grows faster laterally past the coalescence limit when the material is stronger along the principal (normal) loading.

5.1.3 Effect of transverse isotropy plane misalignment

The next set of figures demonstrate the effect of misalignment within the transverse isotropy plane with respect to the principal loading direction $\mathbf{n} = \mathbf{e}_3$ for the material with $h_{\mathrm{L}} = h_{\mathrm{T}} = 2$, representative of a material with weaker bonds within the $\mathbf{m}$–$\mathbf{p}$ plane. The comparator among the cases is taken as the initial transverse isotropy plane misalignment angle denoted with β_0, as schematized in Fig. 6b.

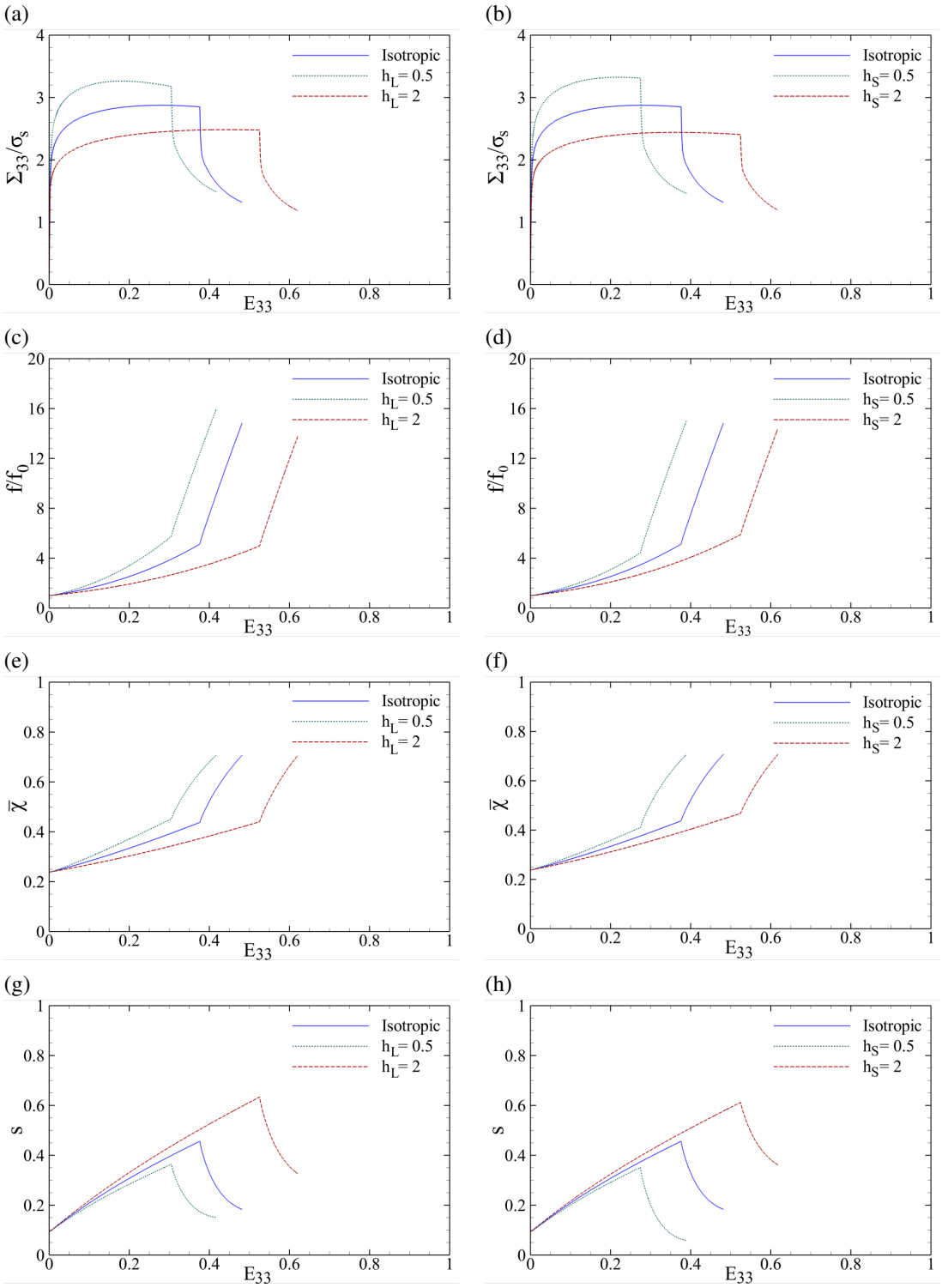

Figure 8: Present model predictions under triaxial loading with a $T = 1$ stress triaxiality and various values of $h_{\mathrm{L}} = h_{\mathrm{T}}$ and h_{S}, based on the initial microstructure denoted with Eq. (47): (a,b) normal stress response, (c,d) normalized porosity, (e,f) effective ligament parameter, (g,h) logarithmic void aspect ratio.

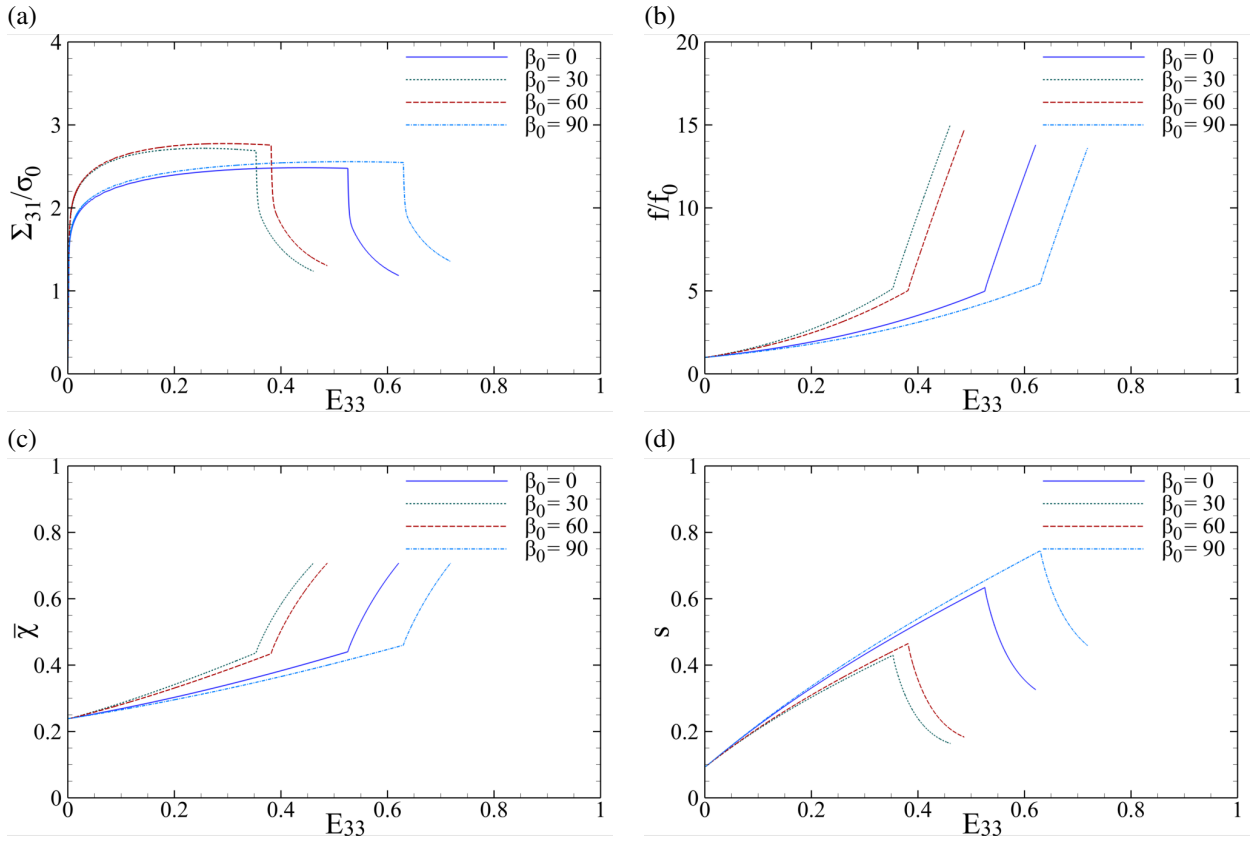

Figure 9: Present model predictions under triaxial loading with a $T = 1$ stress triaxiality, $h_S = 2$ axial Hill coefficient, and transverse isotropy planes with varying misalignment angles denoted with β_0, based on the initial microstructure denoted with Eq. (47): (a) normal stress response, (b) normalized porosity, (c) effective ligament parameter, (d) logarithmic void aspect ratio.

It can be observed, from Fig. 9, that a rotated plane of weakness against extension induces a higher limit load and less ductility since the microscopic bonds are mainly weak against the normal loading inside the plane, which proves smaller by virtue of projection. $\beta_0 = 0$ and $\beta_0 = 90$, however, bare close stress responses and ductilities (reflected by strain to failure ϵ_f) since, at nonzero lateral portion of loading, the Poisson effect would significantly affect the normal response which is, yet, less effective than the case when the plane of weakness is directed towards the principal normal loading Σ_{33}. In the latter case, corresponding to $\beta_0 = 90$, ductility is rather larger than for $\beta_0 = 0$ mainly on account of the smaller Poisson effect. In fact, a plane of weakness oriented at $^\circ 90$ virtually cuts the cell by smaller parallel cross sections with the subcell heights remaining equal, which reduces the lateral deformation at the resultant assembly. The resulting normal stress response would then be slightly higher, and the reduced lateral deformation mitigates the increase rates of porosity and $\bar{\chi}$ that would, itself, delay the onset of void coalescence.

5.2 Results under combined loading

5.2.1 Model assessment

The model ought to be further appraised under combined loading. To this end, model predictions are hereby compared against existing FEM-based cell-model calculations carried out by Nielsen and Tvergaard [45] for 3D cells under combined normal and shear loading. The loading effect is quantified by the $\kappa = \sigma/\tau$ ratio.

It is worthy of note that a FEM-based state of absolute simple shear, with $\kappa = 0$, is too computationally expensive for 3D cells and is, thus, not available in the literature except under the plane-strain condition. The cell sketches and a deformed configuration of the plane-strain cell are shown in Fig. 10.

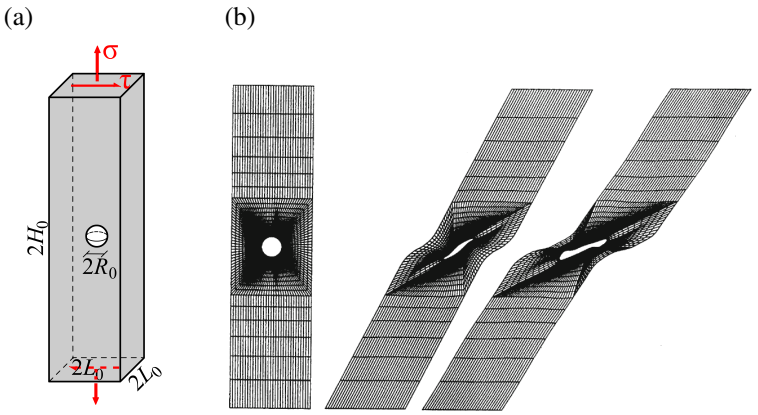

Figure 10: Schematic outline of periodic cells under combined tension and shear considered by Nielsen *et al.* [45], (b) staged deformed configurations of an example plane-strain cell (after Tvergaard [3]) under simple shear, *i.e.* $\kappa = 0$.

The initial microstructure in [45] is introduced based on the $(\chi_0 = R_0/L_0, w_0 = h_0/R_0, \lambda_0 = H_0/L_0)$ triad (see Fig. 10a), with χ_0 varying between 0.3 and 0.5, and $(w_0, \lambda_0) = (1, 4)$ remaining fixed. The lateral dimensions are also considered equal. For the sake of better coincidence between analytical and numerical results, model predictions are compared to FEM counterparts for the *same initial porosity* [70], which reads

$$f_0 = \frac{\pi}{6}\frac{w_0\chi_0^3}{\lambda_0}$$

with the initial microstructure and hardening identified by $(w_0, \lambda_0) = (1, 4)$ and $\chi_0 = \{0.3, 0.5\}$. Further, the material constants are defined as

$$\frac{\sigma_0}{E} = 0.002 \quad , \quad E = 200\,GPa \quad , \quad \epsilon_0 = 0.002 \tag{55}$$

and the hardening exponent is taken as $N = 0.2$. Note that a maximum void aspect ratio is a key consideration in Nielsen *et al.*'s analyses (see [3] for further clarification). Herein, the results pertaining to $w_{\max} = 10$ are considered as comparator.

Figure 11 shows the comparison between selected state variable predicted from the present model and FEM values. Note that the analytical evolution of $90 - \theta$ is founded on the initial void orientation directed towards $\mathbf{e}_3$ since $w_0 = 1.1$ has been taken slightly above unity to forestall the singular behavior of void orientation laws at the limit of a spherical void, and therefore, the initial orientation is well-defined. Within the numerical model, however, the orientation of a strictly spherical void is ill-defined. Upon convention, the void orientation in this case is considered along the principal stretch, which is close to that considered in [3,45]. Accordingly, the jumps in the numerical evolution of orientation is an artifact employed to extract the major void axis. There is also merit in recognizing that there exists a stagnation in the void orientation with $\theta_0 = 0$ especially at small time increments. To forestall this, $\mathbf{n}_0^{(3)}$ was slightly perturbed from $\mathbf{n} = \mathbf{e}_3$ such that $\theta_0 \longrightarrow 0^+$. The reader can consult [8] for more details.

The points of analysis termination in Fig. 11 (a,b) pertain to the vanishing of stress-bearing capacity (realized when $q_\chi f_\mathrm{b} \longrightarrow 1$) or the void rotating by $^\circ 90$ (*i.e.* $\theta \longrightarrow 90$). whichever happens sooner. For the selected microstructure, the former occurs sooner for intermediate shearing ($\kappa = 1.25$) and the latter prevails

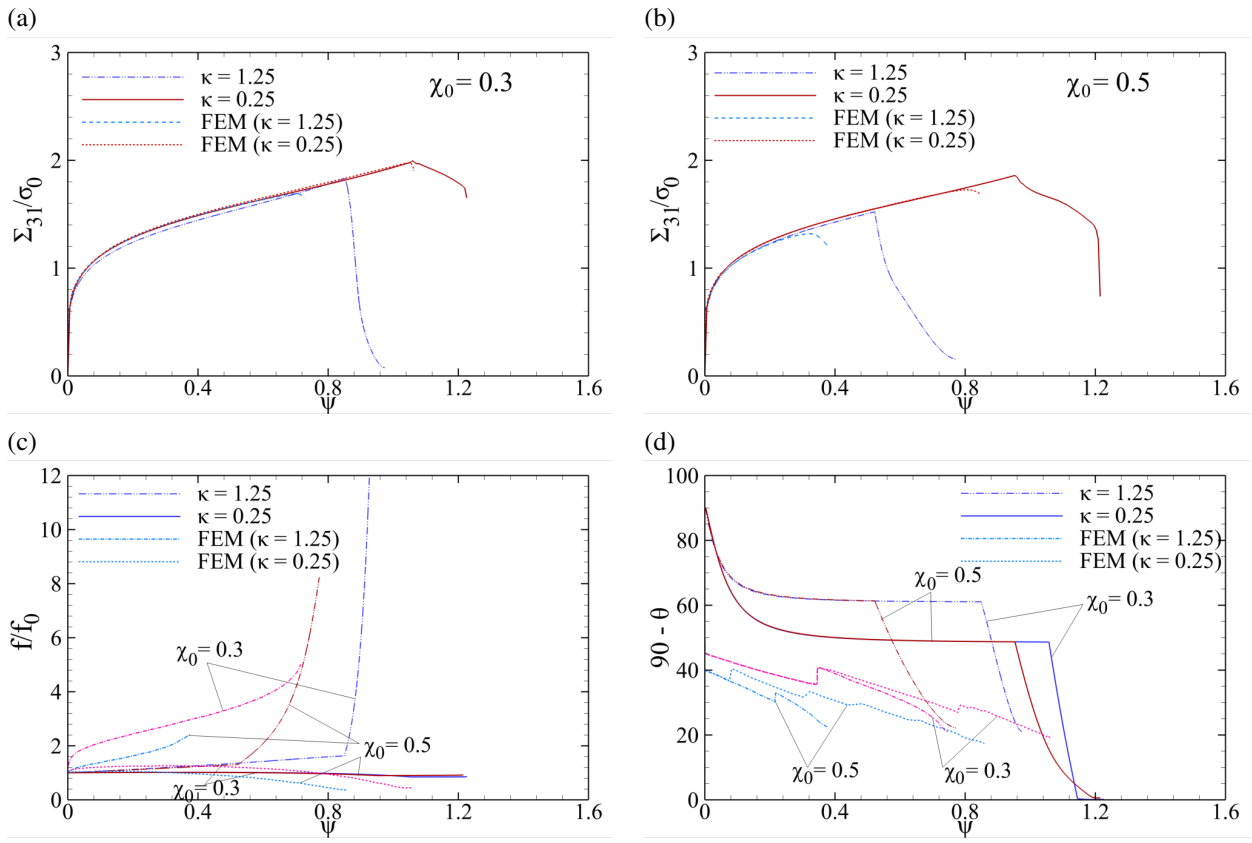

Figure 11: Comparison between the present model predicted variables with FEM outcomes of Nielsen *et al.* [45] for an initially spherical void inside a square-prismatic cell under combined axial and shear loading (with the ratio denoted with κ) and $\chi_0 = \{0.3, 0.5\}$: (a,b) normalized shear stress, (c) normalized porosity, (d) void angle with respect to the vertical direction.

at intense shearing ($\kappa = 0.25$). In case the void rotates by $^{\circ}90$, the void ceases to rotate any further, and thus the predicted stress response would not fall below the minimum stress at this point. Note that, thanks to the involvement of both normal and shear tractions in (7), the post-localized dropping of the stress response occurs rather gradually except under significant normal loading (at $\kappa = 1.25$), which accelerates void rotation past the localization onset. By way of contrast, the T–B–L model [69] is independent of the normal traction at intense shearing, thereby predicting more abrupt stress drop. The stress dropping slopes would, however, be rather sharp via both K–C and T–B–L at the limit of near-simple shearing, *i.e.* under $\kappa \longrightarrow 0$. See [8] for illustrations. Moreover, the modified Φ^{H} would still underestimate dilatation in presence of remarkable normal loading, as revealed by the FEM-based evolution of porosity being significantly larger at $\kappa = 1.25$. This calls for a more advanced model that can better capture the quantitative aspect of dilatation under combined tension and shear.

The following subsection extends the range of κ into near-simple shearing following the same hybrid model.

5.2.2 Effect of loading

Figure 12 demonstrates the effect of tensile-shear load combination represented by the value of κ from infinity (uniaxial loading) down to near zero (simple shearing). The predicted state, here plotted against shear strain γ_{31}, is compared to that resulting from the KB–TBL hybrid model introduced in [8].

The TBL model exploits the q_χ coefficient only in the range of shear predominance whereas the KC model invokes it everywhere as multiplied by $f_{\mathrm{b}} \equiv \bar{\chi}^2$ (rather than by $\bar{\chi}$ within TBL; see [8]) as the latter Φ^{I} is a single-piece function devoid of separate terms regarding the effect of shear. Therefore, the transition from the nearly-homogeneous to the localized mode is observed rather later in the KB-KC model in presence of significant normal loading, and is rather sooner in near-simple shearing due to q_χ being multiplied by $\bar{\chi}^2$ rather than by $\bar{\chi}$. Nevertheless, the two models, the former with q_χ being multiple of $\bar{\chi}$ and the latter with it being multiplied by $\bar{\chi}^2$, predict close points of transition. Nevertheless, failure points are further apart, especially at shear-dominant stress states well beyond simple shearing, here exemplified by $\kappa = 0.25$. The latter lies in slower evolution of $\bar{\chi}$ (Fig. 12c), itself triggered by slower variation of the void aspect ratio, as indicated by Fig. 12d. As further denoted in Fig's 12 (e,f), the in-plane void minor semi-axis b_1 saturates at $\kappa = 0.25$ while the major semi-axis a keeps increasing. There is, however, little physical evidence that can corroborate γ_f proving significantly larger for this range of κ. This warrants further endeavor in more advanced deformation-based yield functions under shear dominance. Moreover, the post-localized void dilatation, as shown in Fig. 12b, is remarkably higher with the use of the present Φ^{I} (KC) in comparison to that according to the TBL Φ^{I}. The reason is larger derivative values in presence of the hyperbolic cosine in relation to parabolic terms in TBL. The KC-induced porosity evolution is, however, better commensurate with numerical findings, as indicated by Fig. 11c. Yet, porosity remains almost constant according to KC at the limit of near-simple shearing just as it does according to TBL (with the only difference being that the latter admits absolutely zero porosity evolution).

The following subsections demonstrate the various effects germane to plastic anisotropy at the limit of near-simple shearing represented by $\kappa = 0.02$.

5.2.3 Effect of shear Hill coefficients

The effect of matrix plastic anisotropy is hereby studied under near-simple shearing with an initially spherical void embedded in the same cell as considered in Section 5.2.2, with $(w_0, \chi_0, \lambda_0) = (1.1, 0.5, 4)$ with a hardening exponent of $N = 0.2$. Focus is placed on shear Hill coefficients in the local coordinate system tied to the orthotropy directors, as tabulated in Table 1, with the material notation taken from [35].

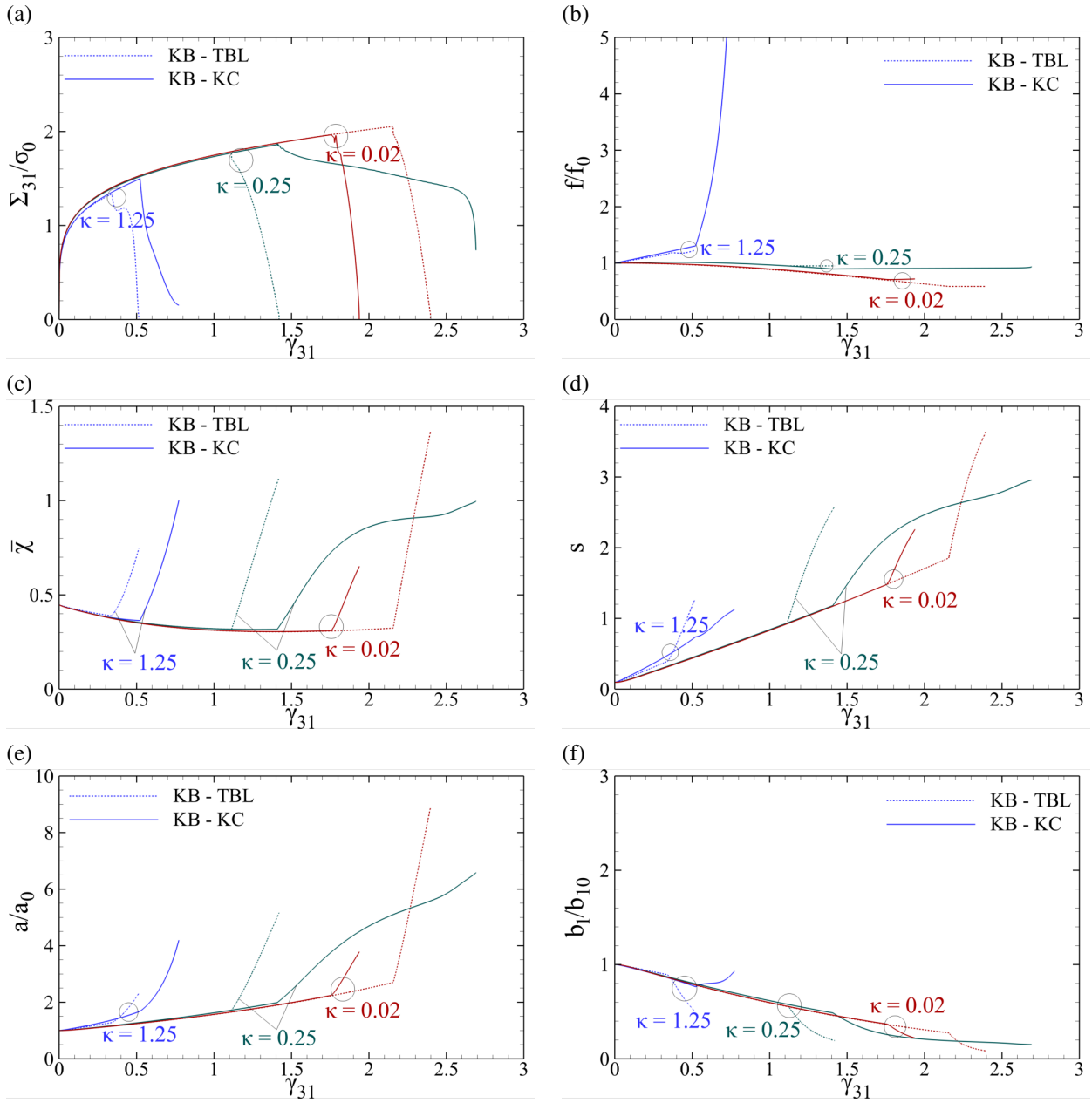

Figure 12: Predicted state variable evolution for the same microstructure considered in Section 5.2.1 under varieties of normal-shear loading combinations represented by the κ ratio: (a) normalized shear stress, (b) normalized porosity, (c) effective ligament parameter, (d) logarithmic void aspect ratio, (e,f) void major and along-shear minor semi-axes.

Table 1: Matrix anisotropy coefficients, h_i expressed in the basis of material orthotropy $(\mathbf{e}_\mathrm{L}, \mathbf{e}_\mathrm{T}, \mathbf{e}_\mathrm{S})$.

Matrix	h_L	h_T	h_S	h_TS	h_SL	h_LT
Isotropic	1.000	1.000	1.000	1.000	1.000	1.000
MAT1	1.000	1.000	1.000	2.333	2.333	1.000
MAT2	1.000	1.000	1.000	0.500	0.500	1.000

All the three materials have the same Hill coefficients along the three principal directions, *i.e.* h_L, h_T and h_S. Note once again that a large Hill coefficient in a given direction signifies the weakness/softness of the material in that direction. MAT1 and MAT2 are, therefore, softer and stiffer under shear in comparison to the isotropic material, respectively.

Figure 13 illustrates the effect of material variation on the internal state for the selected materials in Table 1 under near–simple shearing characterized by $\kappa = 0.02$.

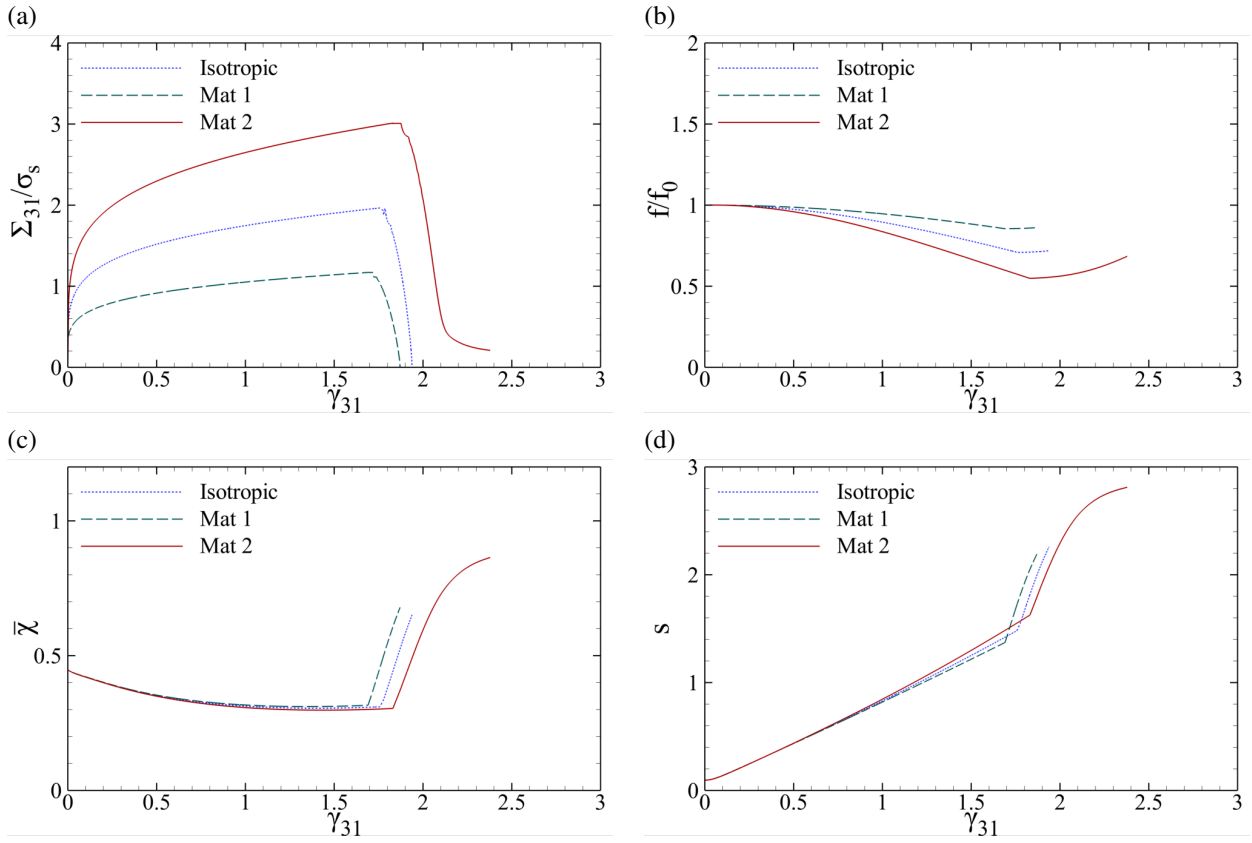

Figure 13: Predicted state variable evolution for the same microstructure considered in Section 5.2.1 with matrix materials according to Table 1 under near-simple shearing (characterized by $\kappa = 0.02$): (a) normalized shear stress, (b) normalized porosity, (c) effective ligament parameter, (d) logarithmic void aspect ratio.

Figure 13a reaffirms the stronger and weaker nature of MAT2 and MAT1 in comparison to the isotropic material, respectively. More appealingly, MAT2 is more ductile against shearing in addition to being stiffer. Accordingly, ductility and strength can coincide upon regular orthotropy against shear while the same feature

cannot be acquired under triaxial loading. It can also be observed, through Fig's 13 (c,d), that the *rates* of void elongation and effective ligament parameter are only slightly affected by matrix anisotropy when the material orthotropy directors are aligned with the main loading directions. Nevertheless, the *values* of these parameters become more distinctively apart with matrix shear anisotropy during localized deformation. A similar feature can be observed for void orientation, that has not been depicted for the sake of brevity.

The increased stress level for MAT2 can be ascribed to the sharper decrease in porosity f during nearly-homogeneous yielding, Fig. 13b which, itself, may be attributed to the faster void elongation depicted in Fig.13d. The latter takes place on account of faster squeezing of the rotating void by the stronger matrix owing to its stronger shear strength (h_{TS} and h_{SL}), that withstands material slippage along the shearing direction. That is, for the same shearing (γ_{31}) level, the void ought to distort more and close sooner for the stronger matrix against shear. A similar comparison has earlier been observed under triaxial loading [48]. In general, porosity evolution, be the void growing or shrinking, is faster for the material stronger in shear [48].

As seen farther, transformation of the $(\mathbf{e}_{\mathrm{L}}, \mathbf{e}_{\mathrm{T}}, \mathbf{e}_{\mathrm{S}})$ basis with respect to $(\mathbf{e}_1, \mathbf{e}_2, \mathbf{e}_3)$ for the same anisotropic material with respect to shear can induce minimal to significant changes in the elongation (and rotation) rate(s).

5.2.4 Effect of orthotropy basis change

This subsection addresses the internal state variation with a flip or rotation over the material orthotropy directors with respect to the principal loading plane identified by the $(\mathbf{e}_1, \mathbf{e}_2, \mathbf{e}_3)$ basis. To this end, the plane of transverse isotropy (normal to $\mathbf{e}_{\mathrm{S}}$) is subjected to flip or rotation, as sketched schematically in Fig. 14, with the latter planes denoted with grated lattices.

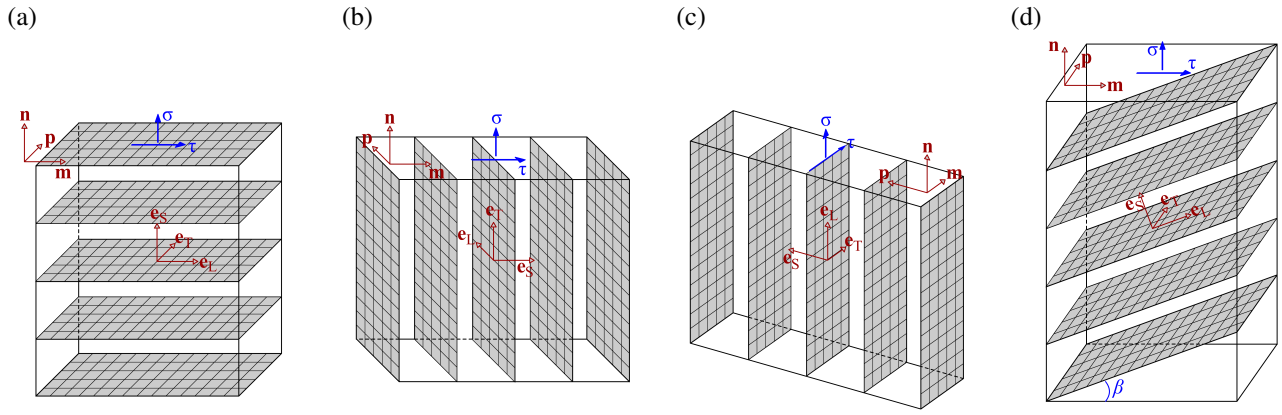

Figure 14: Flipped and rotated planes of transverse isotropy at the cell level, with the shear and normal tractions applied along $\mathbf{m}$ and $\mathbf{n}$, respectively: (a) $\mathbf{e}_{\mathrm{L}} = \mathbf{m}$, *i.e.* $L = 1$, (b) $\mathbf{e}_{\mathrm{L}} = \mathbf{p}$, *i.e.* $L = 2$, (c) $\mathbf{e}_{\mathrm{L}} = \mathbf{n}$, *i.e.* $L = 3$, (d) $\mathbf{e}_{\mathrm{L}} = \cos\beta\mathbf{m} + \sin\beta\mathbf{n}$.

Note that the right-permutation rule holds for all transformation scenarios. For the case of $L = 2$, for instance, $\mathbf{e}_{\mathrm{T}} = \mathbf{n}$ and $\mathbf{e}_{\mathrm{S}} = \mathbf{m}$, *i.e.* $(T, S) = (3, 1)$. The corresponding transformation tensor between the Cartesian and orthotropy frames, $\mathbf{R}^*$, obeys the following forms, as tabulated in Table 2, for the above–mentioned cases:

Table 2: $\mathbf{R}^*$ transformation tensors for the transverse isotropy planes schematized in Fig. 14.

Case	$\mathbf{e}_\mathrm{L} = \mathbf{m}$	$\mathbf{e}_\mathrm{L} = \mathbf{p}$	$\mathbf{e}_\mathrm{L} = \mathbf{n}$	$\mathbf{e}_\mathrm{L} = \cos\beta\mathbf{m} + \sin\beta\mathbf{n}$
$\mathbf{R}^*$	$\begin{bmatrix} 1 & 0 & 0 \\ 0 & 1 & 0 \\ 0 & 0 & 1 \end{bmatrix}$	$\begin{bmatrix} 0 & 0 & 1 \\ 1 & 0 & 0 \\ 0 & 1 & 0 \end{bmatrix}$	$\begin{bmatrix} 0 & 1 & 0 \\ 0 & 0 & 1 \\ 1 & 0 & 0 \end{bmatrix}$	$\begin{bmatrix} \cos\beta & 0 & -\sin\beta \\ 0 & 1 & 0 \\ \sin\beta & 0 & \cos\beta \end{bmatrix}$

$\mathbf{R}^*$ is exploited in the calculation of $\mathbb{h}$ and $\mathbb{p}$ in the global coordinate system. To this end, the global Cartesian Hill tensor, here named $\mathbb{h}^\mathrm{G}$, should be first evaluated following

$$\mathbb{h}^\mathrm{G} = (\mathbf{R}^{*\mathrm{T}} \otimes \mathbf{R}^{*\mathrm{T}}) : \mathbb{h}^\mathrm{LTS} : (\mathbf{R}^* \otimes \mathbf{R}^*) \tag{56}$$

with $\mathbb{h}^\mathrm{LTS}$ denoting the anisotropy tensor expressed in the orthotropy frame which, in reduced (*e.g.* Voigt) form, only comprises diagonal terms.

With (56) at hand, $\mathbb{p}$ in the global frame reads

$$\mathbb{p}^\mathrm{G} = \mathbb{J} : \mathbb{h}^\mathrm{G} : \mathbb{J} \tag{57}$$

which, after rotation invoking the instantaneous rotation tensor $\mathbf{R}$, is expressed as

$$\mathbb{p} = (\mathbf{R}^\mathrm{T} \otimes \mathbf{R}^\mathrm{T}) : \mathbb{p}^\mathrm{G} : (\mathbf{R} \otimes \mathbf{R}) \tag{58}$$

where $\mathbf{R}$ turns out as identity if the constitutive laws are integrated for a single point in space. Hence, $\mathbb{p} = \mathbb{p}^\mathrm{G}$ in this case.

Figure 15 shows the shear stress evolution for MAT1 and MAT2 with $\mathbf{e}_\mathrm{L}$ directed along $\mathbf{e}_1$, $\mathbf{e}_2$, and $\mathbf{e}_3$, briefly noted with the "L" index taking on values of 1, 2, and 3, respectively. See Fig. 1a.

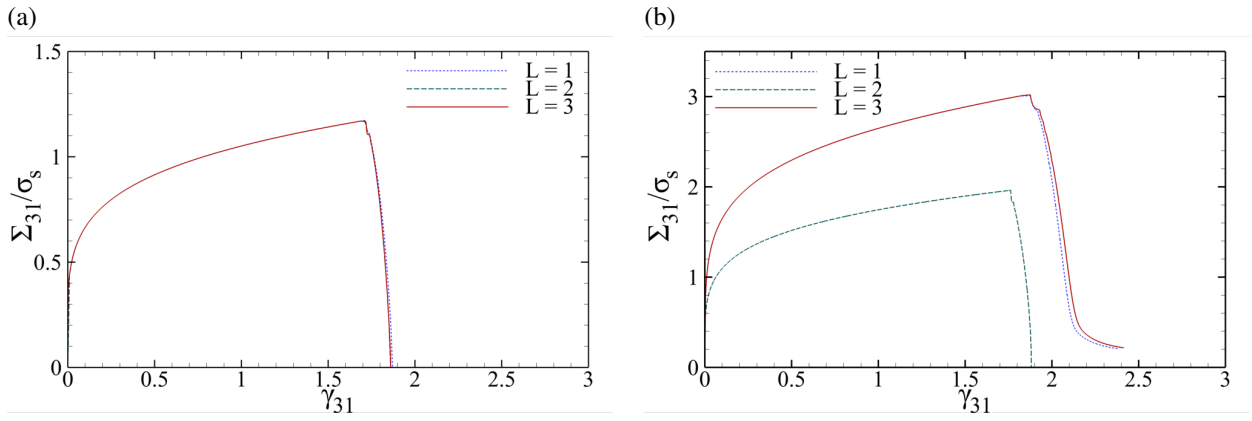

Figure 15: Normalized shear stress evolution: (a) for MAT1 and (b) for MAT2 (upon properties given in Table 1) under near–simple shearing characterized with $\kappa = 0.02$ for the same cell considered in Section 5.2.1 with $(w_0, \chi_0, \lambda_0) = (1.1, 0.5, 4)$, with $\mathrm{L} = 1, 2, 3$, denoting $\mathbf{e}_\mathrm{L}$ directed along $\mathbf{e}_1$, $\mathbf{e}_2$, and $\mathbf{e}_3$, respectively.

Figure 15a implies negligible difference in the softer material response under shear with flipping the weak macro-scale slip planes horizontally or vertically, with the ductility slightly higher for $\mathbf{e}_\mathrm{L} = \mathbf{e}_1$.

This happens due to the perspicuous coupling between shearing in the $x_1 - x_3$ and $x_2 - x_3$ by which one weak/strong plane enfeebles/stiffens the other response vs. shear and vice versa, thereby $\mathbf{e}_{\mathrm{L}} = \mathbf{e}_1$ and $\mathbf{e}_{\mathrm{L}} = \mathbf{e}_3$ exhibit close behaviors.

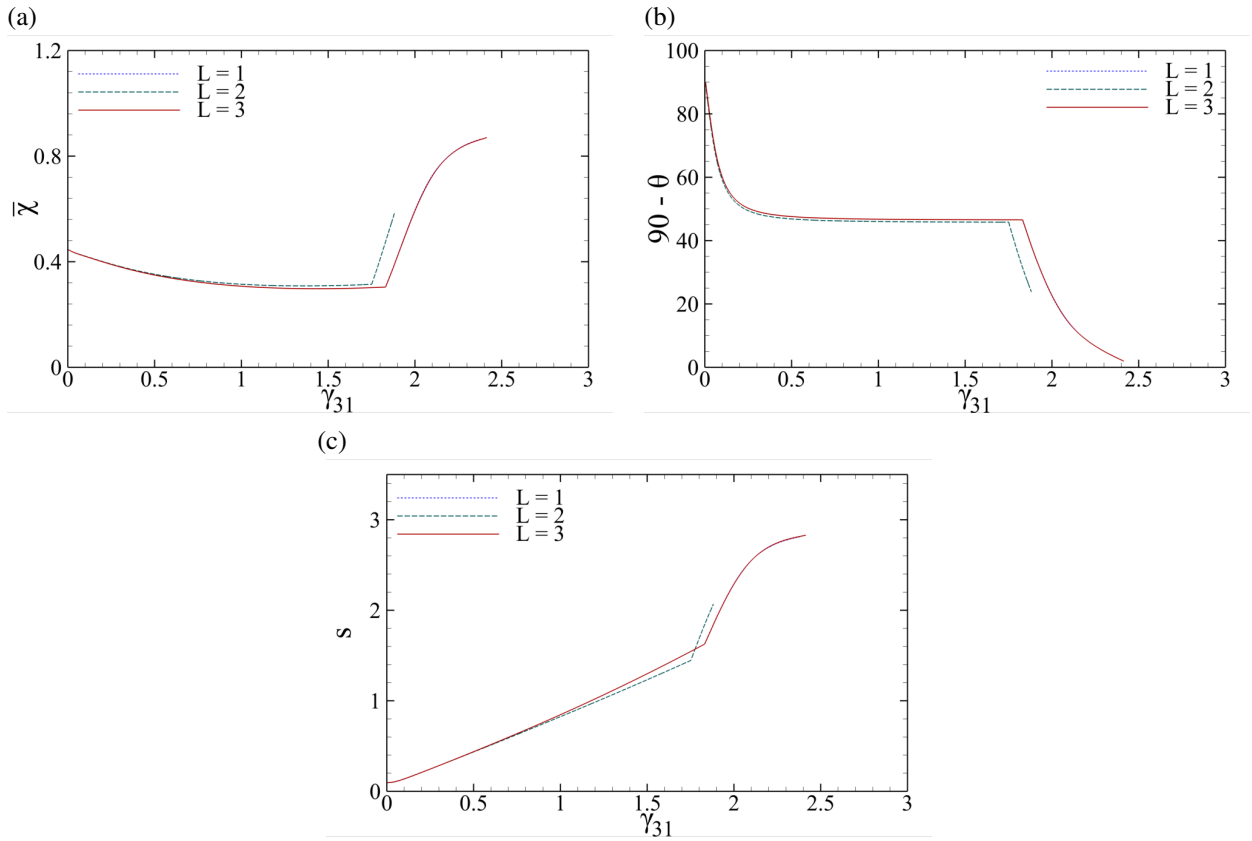

Figure 16: Additional selective state variables provided for MAT2 with the stress response shown in Fig. 15b: (a) effective ligament parameter, (b) void angle with respect to the horizontal axis, and (c) natural logarithmic void aspect ratio.

Note that, for both materials with varying shear Hill coefficients, the responses for $L = 1$ and $L = 3$ lie close to one other. This can be vindicated by the negligible Poisson effect under near-simple shearing such that both material configurations would constitute smaller parallel cross sections with the effective subcell heights remaining equal. In both scenarios, reflected by Fig's 14 (a) and (c), parallel planes operate almost independently under shearing for the weak material MAT1, and they would both act parallel plus an additional constraint caused by the strong orthotropy planes in MAT2. Meanwhile, the shear stresses act effectively equivalent in the $x_1 - x_3$ and $x_2 - x_3$ as earlier declared. This observation is antithetical to that under triaxial loading, where there is clear distinction between the outcomes upon variation of $\mathbf{e}_{\mathrm{L}}$ (see [48] for details). Nevertheless, within the $L = 2$ case, reflected by Fig. 14b, subcells function almost consecutively, *i.e.* in series, as being subjected to the shown shear traction τ. On this further occasion, the weak material MAT1 responds close to the other two cases due to being almost devoid of additional inter-planar shear constraints whereby the shear stress is distributed over smaller subcell cross sections. For the stronger material MAT2, however, $L = 1$ and $L = 3$ exhibit clear difference from $L = 2$. A closer examination of Fig. 14 can be indicative of this difference. That is, in the (a) and (c) subfigures, the inter-planar shear constraint is induced by the entire orthotropy planes being sheared whereas, in subfigure (b),

this constraint is caused by mere rotation of these planes against shear deformation. The former would clearly bare higher stress-bearing capacity and ductility, as demonstrated by Fig. 15b.

In order to gain more insight into this effect, other influential state variables are collected in Fig. 16 for MAT2. Note that the shear constraint within the rotating orthotropy planes, characterized by the $L = 2$ case and as schematized in Fig. 15b, fairly impedes void elongation, thus the corresponding void aspect ratio being smaller at the same shear strain level (Fig. 16c). Higher stresses are, however, demanded for the same strain level at the $L = 1$ and $L = 3$ cases considering the foregoing discussion.

The effect of rotating the plane of orthotropy on the state evolution under simple shearing comes next. The results will be presented for the weaker material in shear, MAT1 due to the targeted effect being more significant therefor. Fig. 17 illustrates the effect of rotating the plane of transverse isotropy around the $\mathbf{e}_{\mathrm{T}}$ axis on the internal state evolution for MAT1 upon properties provided in Table 1. The corresponding initial rotation angle β_0 (as shown in Fig. 14d) assumes negative, zero, and positive values.

A remarkable difference happens to the material conduct with β_0 changing sign. This large difference can be accredited to the equivalent stress state in the orthotropy frame. That is, $\beta_0 < 0$ imparts a pressure on the void, and thus delays failure in shear whereas $\beta_0 > 0$ increases tension which, in conjunction with shear, accelerates rotation and elongation, as demonstrated in Fig's 17 (b,e,f), respectively. As such, the porosity increase, indicated by Fig. 17c, would further expedite failure. Accordingly, the effective ligament parameter $\bar{\chi}$ would fast get to increase (Fig. 17d) and the void would dramatically elongate (Fig's 17 (e,f)), thereby failure being soon triggered by the void touching the cell boundaries. There being, as seen in Fig. 17a, failure triggered soon after the elastic limit, a weak plane of transverse isotropy (with respect to shear), rotated positively relative to the plane of loading, is reminiscent of a crack. Note that the predicted stress response is based on the heuristic modification employed in accordance with Eq. (10), and is thus amenable to further modification in prospect. More precise results may exhibit larger ductility for the $\beta_0 > 0$ case.

All the same, as formerly pointed out above, a negatively rotated transverse isotropy plane would induce confinement on the void axis, and suppresses the void against both rotation, as seen in Fig. 17b. Yet, due to the large lateral confinement induced onto the void, void elongation proves faster in this case, as demonstrated by Fig's 17 (e,f). Namely, the void would sooner squeeze and tend towards a needle when embedded in a negatively rotated plane of transverse isotropy.

6 Discussion

The hybrid model introduced in the present context exploits modified forms of the KB and KC models, according to (2) and (7), so as to accommodate a quantitatively sound sequence of deformation mechanisms that can mimic the entirely inhomogeneous damage process under combined tension and shear. The main terms subject to modification factors comprise porosity f and the surrogate ligament porosity f_{b} within KB and KC, respectively, constituting qf and $q_\chi f_{\mathrm{b}}$, respectively. The q factor, taken equal to that after Perrin and Leblond [51], was deemed essential by Ponte Castaneda [50, 57] such that this line of models (KB and the like) can mimic near-simple shearing stress states. All the same, q_χ was introduced by Torki and Benzerga [8] to cater for the point of transition from the process being closer to homogeneous into a localized one approaching that with plasticity confined to the intervoid ligaments and the rest behaving rigid-like. Note also that the evolution equations for internal state variables are invoked in their originally-derived forms (with the only exception being the k factor in (22), which has been proposed in terms of the microstructure and macroscopic stress state, regardless of the mechanism which plays a more remarkable rule in failure under shear). Notwithstanding the model at hand can capture the salient features of ductile fracture under combined loading, the heuristic nature of q and q_χ, albeit simple, is suggestive of more sophisticated models with regards to both the yield function Φ and the evolution equations. With respect to the former, the key feature to note is the existence of a yield criterion based on a more realistic mechanism-

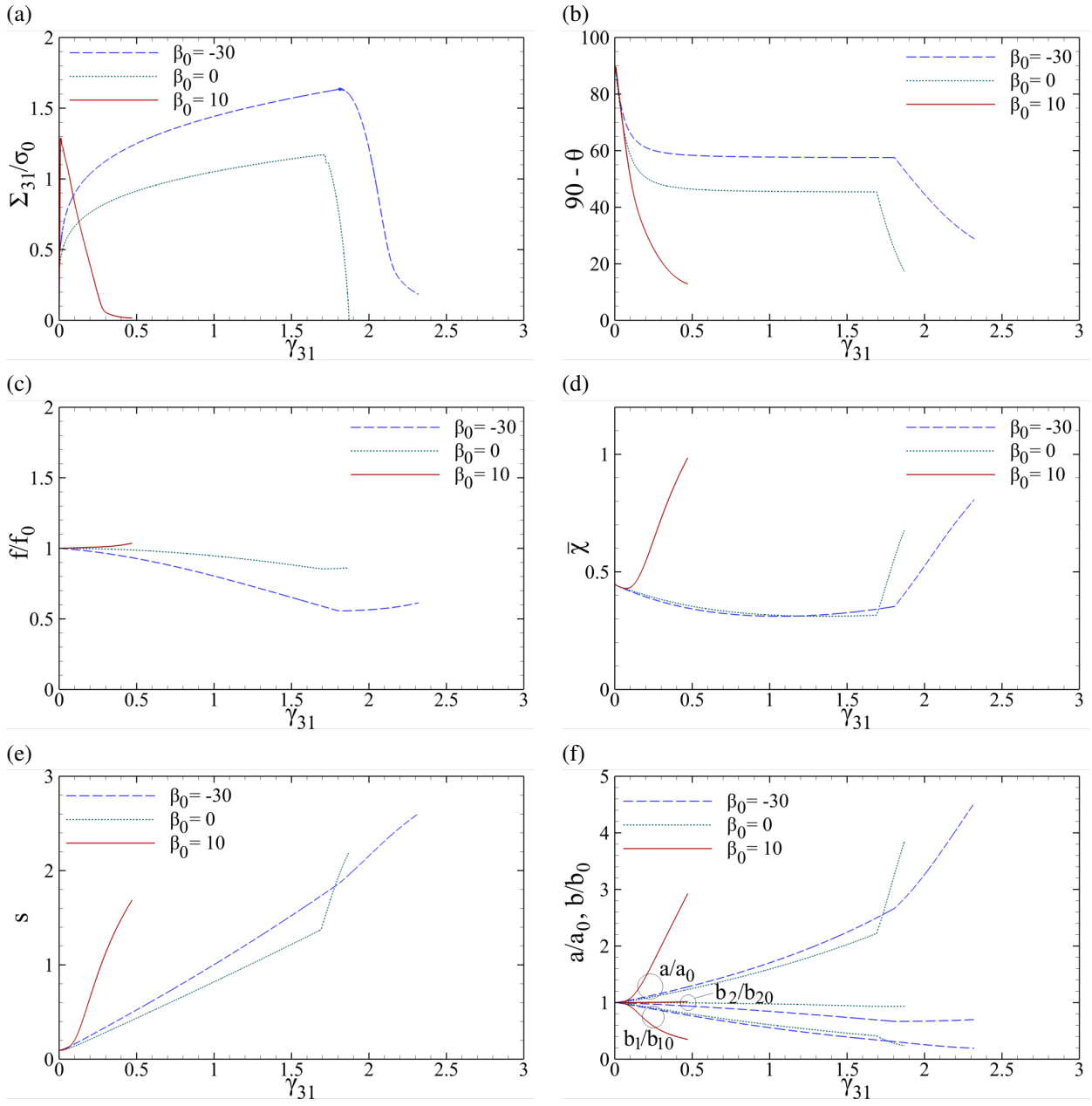

Figure 17: Selective internal state variables subjected to a rotated plane of transverse isotropy around the $\mathbf{e}_T$ axis for MAT1 (upon properties given in Table 1) under near–simple shearing characterized by $\kappa = 0.02$ for the same cell considered in Section 5.2.1 with $(w_0, \chi_0, \lambda_0) = (1.1, 0.5, 4)$: (a) normalized shear stress, (b) void angle with respect to the horizontal axis, (c) normalized porosity, (d) effective ligament parameter, (e) natural logarithmic void aspect ratio, (f) major and minor void semiaxes.

based shear velocity field that departs well from the simplistic Gurson-like field utilized in TBL and KC models. In the same respect, the general distinction between void and cell orientations should be accounted for. Except for the work of Madou and Leblond [71], no outstanding attempt has been made in this regard. Yet, the latter relies on FEM-based heurism, and is not indicative of mechanism-induced effects, especially those under shearing effects.

Apropos of evolution equations, the evolution equations for void aspect ratio and orientation play a pivotal role. For the state of nearly-homogeneous yielding, efforts have been made to make $\dot{s}$ and $\dot{\mathbf{n}}^{(3)}$ accountable for a wider range of loading conditions. Examples include the k factor in (22), after Gologanu *et al.* [59] and the modifications applied to $\dot{s}$ and $\dot{\mathbf{n}}^{(3)}$ under various triaxialities by Madou *et al.* [64]. Both endeavors, though well-motivated, have proposed their calibrations based on macroscopic loading descriptors, thereby being negligent of mechanisms true to the spirit of deformation, including that under shear. In particular, the post-localized $\dot{\mathbf{n}}^{(3)}$, which itself directly affects $\dot{s}$, calls for further sophistication. An alternatively simple method to capture the quantitative aspects of fracture under combined loading would then be to equip the post-localized $\mathbf{\Omega}^l$, according to (33), with some simple modification in terms of the $\kappa = \sigma/\tau$ ratio, which remains to be investigated.

As far as the numerical calculation cost is concerned, the TBL model is more cost-effective under shear-dominated loading, *i.e.* under $\kappa \longrightarrow 0$, thanks to Φ^{I} being merely a quadratic function of the shear traction τ. This would further create zero time rates for f and σ_{m}, and thus reduces the number of involved internal state variables within the iterative solution scheme (see [8] for details). Therefore, TBL would be computationally advantageous over KC in absence of plastic anisotropy, particularly at the limit of simple shear. On the other hand, the predicted ϵ_f upon KC appears to be spuriously high under medium shearing, *i.e.* under κ centering around 1, while it sounds to be nearly minimum at this limit (see [8]). Therefore, the transition strain (*i.e.* the strain to the onset of localization) can be considered as a crude measure of ϵ_f in this range of κ's.

Among the most notable implications of plastic anisotropy, in correlation with the induced anisotropies stemming from void elongation and/or rotation, is the manageable nature of the material response, with focus here placed on shear response. In other terms, ductility against combined loading can be engineered just as under triaxial loading by manipulating proper Hill coefficients or the placement of orthotropy planes, and examining the predictable response from the developed numerical framework such as that of the present model. The Hill coefficients mainly influence the portion of the response driven by hardening which, due to its interaction with the microstructure, affects the whole state evolution. Under triaxial loading, macroscopic ductility can be engineered by manipulating the translational Hill coefficients h_{L}, h_{T}, and h_{S}. Due to the Poisson effect, varying h_{L} and h_{T} would impart a similar effect to that observed from variation in h_{S}. Yet, higher ductility (here denoted with strain to failure ϵ_f) and larger strength (here denoted with the maximum stress response) cannot be attained simultaneously in absence of shear (here denoted with triaxial loading). By way of contrast, the two can coexist under shear-dominated loading, even for a material with weak planes of orthotropy against shear. One instance upon the presently-observed results is to place the plane of transverse isotropy either parallel to the plane of localization or normal thereto such that the shear traction is parallel to the plane. Alternatively, the plane of transverse isotropy can be rotated clockwise with respect to shearing, with the rotation axis being parallel to the in-plane base vector $\mathbf{p}$ (see Fig. 14d).

Moreover, according to the post-localized shear responses belonging to the various materials with different shear Hill coefficients (here represented by the isotropic matrix, MAT1 and MAT2) in Fig. 13, the effective ligament parameter $\bar{\chi}$ evolves towards saturation at lower values of $h_{\mathrm{SL}} = h_{\mathrm{TS}}$ such that, below a certain limit, failure is never predicted under simple shearing. Accordingly, shear Hill coefficients can be engineered such that, at a specific initial porosity level, failure under shear never occurs. A similar trend can be witnessed upon rotation within planes of transverse isotropy with fixed $h_{\mathrm{SL}} = h_{\mathrm{TS}}$ coefficients, Fig. 17. A negatively (clockwise) rotated plane of transverse isotropy can engender a $\bar{\chi}$ that saturates to a value below $1/\sqrt{q_\chi}$ (corresponding to the void touching the cell boundaries). At frozen shear Hill coefficients, the rotation angle of the plane of transverse isotropy can thus be engineered so as to obtain a material with

infinite strain to failure under near-simple shearing.

7 Concluding Remarks

A hybrid micromechanics-based model was introduced and numerically implemented for Hill-type anisotropic materials so as to simulate the entire ductile fracture process associated with void elongation and rotation under combined tension and shear. The combined deformation process was envisaged as an intermediate state between a completely homogeneous and an ideally localized one with plasticity fully confined within intervoid ligaments and the rest acting rigid-like. In its essence, the hybrid model was a two-surface one with its constitutive framework constructed by two modified yield criteria supplemented to a system of evolution equations for the effective microstructural state variables. The yield criterion was driven by the intersection of two yield surfaces upon their functions developed by Keralavarma and coworkers [35, 47], employed with simple adjustable parameters to account for combined stress states. The two-surface model was supplemented to existing equations accounting for the time rate of porosity and equivalent plastic strain as well as those pertaining to void elongation and rotation. The latter two were borrowed from [59] and a recent work by the present authors [8] for the nearly-homogeneous and localized parts of the deformation process, respectively.

The microstructural evolution during the nearly-homogeneous part of deformation is governed by porosity f, void aspect ratio w, and void orientation $\mathbf{n}^{(3)}$. All the same, localized deformation acts upon a surrogate microstructure aligned with the normal to a possible plane of localization (denoted with $\mathbf{n}$), thereby being driven by an effective ligament parameter $\bar{\chi}$ and an effective void aspect ratio $\bar{w}$. The latter two are functions of the main state variables including f, w, and the angle between $\mathbf{n}$ and $\mathbf{n}^{(3)}$. The internal state constitutive framework was numerically integrated using the Newton-Raphson solution scheme, and the results were parametrized based on various load combinations (through $\kappa = \sigma/\tau$ denoting the ratio between the remote normal and shear tractions) as well as various Hill coefficients. The predictive capability of the model was primarily assessed by comparison to their existing numerical counterparts from the work of Pardoen and Hutchinson [24] and Nielsen *et al.* [45] under triaxial and combined loading conditions, respectively. The combined effects of plastic anisotropy and stress state were evaluated by variation of translational Hill coefficients ($h_{\mathrm{L}} = h_{\mathrm{T}}$ and h_{S}) in absence of shear and variation of shear Hill coefficients ($h_{\mathrm{SL}} = h_{\mathrm{TS}}$) under the near-simple shearing state (here denoted with $\kappa \longrightarrow 0$). The axis of transverse isotropy $\mathbf{e}_{\mathrm{S}}$ was taken initially parallel to the principal normal loading, and the remaining orthotropy directors $\mathbf{e}_{\mathrm{L}}$ and $\mathbf{e}_{\mathrm{T}}$ obey the right-hand law. The results were further extended by mere rotation of the plane of transverse isotropy with fixed Hill coefficients. The key outcomes can be itemized as follows:

- Thanks to the Poisson effect, changing the in-plane translational Hill coefficients h_{L} and h_{T} would impart an effect on the response close to that by changing the out-of-plane coefficient h_{S}.

- The effect of extensional Hill coefficients intensifies with increasing the lateral portion of loading or, equivalently, increasing triaxiality. Smaller Hill coefficients bare a confining effect that would give rise to a higher limit load accompanied by a lower strain to coalescence as well as strain to failure, and vice versa.

- A void is distorted, *i.e.* squeezes (via f decrease), elongates (via w increase), and rotates faster inside a stronger matrix against shear (with $h_{\mathrm{SL}} < 1$ and $h_{\mathrm{TS}} < 1$). Such a matrix withstands material slippage along the shearing direction. Hence, the void ought to distort more and close sooner at the same shear strain level.

- Higher ductility cannot be accompanied by larger strength in absence of shear (here denoted with triaxial loading). Yet, the two can coexist under shear-dominated loading. To this end, the plane

of transverse isotropy can be placed either parallel or perpendicular to the plane of possible strain localization or normal, the latter such that the shear traction is parallel to the plane. The plane of transverse isotropy can alternatively be rotated clockwise with respect to shearing.

- Below a certain limit of h_{SL} or h_{TS}, or beyond a certain rotation angle within the plane of transverse isotropy, failure is never predicted under near-simple shearing. Thereupon, shear Hill coefficients, or the placement of orthotropy planes, can be engineered such that, at a specific initial porosity level, failure under shear never occurs.

Appendix A KB Model Parameters

The parameters embedded in (2) are functions of porosity f, void aspect ratio w and the Hill tensor $\mathbb{H}$. g, known as *secondary porosity* is defined as:

$$g = 0 \quad (\text{p}); \qquad g = \frac{e_2^3}{\sqrt{1-e_2^2}} = f\frac{e_1^3}{\sqrt{1-e_1^2}} = f\frac{(1-w^2)^{\frac{3}{2}}}{w} \quad (\text{o}) \tag{A-1}$$

where (p) and (o) stand for *prolate* $(w > 1)$ and *oblate* $(w < 1)$, respectively. By definition, g is non-zero for oblate voids only. e_1 and e_2 are, respectively, the eccentricities of the spheroidal void and the spheroidal RVE. The latter is an implicit function of f and w.

$$e_1^2 = \begin{cases} 1-\dfrac{1}{w^2} & (\text{p}) \\ 1-w^2 & (\text{o}) \end{cases}, \qquad \frac{(1-e_2^2)^n}{e_2^3} = \frac{1}{f}\frac{(1-e_1^2)^n}{e_1^3}, \qquad n = \begin{cases} 1 & (\text{p}) \\ 1/2 & (\text{o}) \end{cases} \tag{A-2}$$

Also,

$$\kappa = \begin{cases} 3\left\{1-\dfrac{2}{\ln f}\ln\dfrac{1-e_2^2}{1-e_1^2}\right\}^{-1/2} & (\text{p}) \\ 3\left\{1+\dfrac{(g_f-g_1)+\frac{4}{5}(g_f^{5/2}-g_1^{5/2})-\frac{3}{5}(g_f^5-g_1^5)}{\ln\frac{g_f}{g_1}}\right\}^{-1} & (\text{o}) \end{cases} \tag{A-3}$$

where

$$g_f \equiv \frac{g}{g+f}, \quad g_1 \equiv \frac{g}{g+1} \tag{A-4}$$

Next,

$$\alpha_2 = \begin{cases} \dfrac{(1+e_2^2)}{(1+e_2^2)^2+2(1-e_2^2)} & (\text{p}) \\ \dfrac{(1-e_2^2)(1-2e_2^2)}{(1-2e_2^2)^2+2(1-e_2^2)} & (\text{o}) \end{cases} \tag{A-5}$$

$$\begin{aligned} \eta &= -\frac{2}{3}\frac{\kappa(1-f)(g+1)(g+f)\text{sh}}{(g+1)^2+(g+f)^2+(g+1)(g+f)[\kappa K^*\text{sh}-2\text{ch}]}, \\ C &= -\frac{2}{3}\frac{\kappa(g+1)(g+f)\text{sh}}{(1-f+\frac{3}{2}\eta K^*)\eta}, \quad \text{sh} \equiv \sinh(\kappa K^*), \quad \text{ch} \equiv \cosh(\kappa K^*) \end{aligned} \tag{A-6}$$

where $K^* \equiv 2(\alpha_1 - \alpha_2)$.

α_2 and α_1 are identical to those introduced in [59] for isotropic materials, that read

$$\alpha_1 = \begin{cases} \left[e_1-(1-e_1^2)\tanh^{-1}e_1\right]/(2e_1^3) & (\text{p}) \\ \left[-e_1(1-e_1^2)+\sqrt{1-e_1^2}\sin^{-1}e_1\right]/(2e_1^3) & (\text{o}) \end{cases} \tag{A-7}$$

Finally:

$$\alpha_1^{\text{Gar}} = \begin{cases} \dfrac{1}{3-e_1^2} & (\text{p}) \\ \dfrac{1-e_1^2}{3-2e_1^2} & (\text{o}) \end{cases} \tag{A-8}$$

Appendix B Jacobian Components for Φ^{I}

The Jacobian components for Φ^{I} according to (7) are hereby addressed for use in the Newton-Raphson scheme declared in Eq. (46). Upon convention, $R_{A,B} \equiv \frac{\partial R_A}{\partial B}$ and $\mathbf{0}$ denotes the second-order zero tensor. The major Jacobians constituents are constructed from the second-order derivative of the yield function with respect to the stress tensor, and the derivatives of $\mathbf{N}^{\mathrm{I}}$, as expanded in (44), with respect to the microstructural variables.

In general, the following identities will be used in the sequel:

$$\frac{\partial^2\Phi^{\mathrm{I}}}{\partial\tilde{\sigma}'\partial\tilde{\sigma}'} = \mathbb{J} : \frac{\partial^2\Phi^{\mathrm{I}}}{\partial\tilde{\sigma}\partial\tilde{\sigma}} : \mathbb{J} \quad , \quad \frac{\partial}{\partial\sigma_{kk}}\left(\frac{\partial\Phi^{\mathrm{I}}}{\partial\tilde{\sigma}'}\right) = \mathbb{J} : \frac{\partial^2\Phi^{\mathrm{I}}}{\partial\tilde{\sigma}\partial\tilde{\sigma}} : \mathbf{I} \quad , \quad \frac{\partial^2\Phi^{\mathrm{I}}}{\partial\sigma_{kk}\partial\sigma_{kk}} = \mathbf{I} : \frac{\partial^2\Phi^{\mathrm{I}}}{\partial\tilde{\sigma}\partial\tilde{\sigma}} : \mathbf{I} \tag{A-9}$$

where, at the post-localization regime:

$$\frac{\partial^2\Phi^{\mathrm{I}}}{\partial\tilde{\sigma}\partial\tilde{\sigma}} = \frac{3}{\bar{\sigma}^2}\frac{\partial\sigma_{\mathrm{sh}}}{\partial\sigma} : \mathbb{p} : \frac{\partial\sigma_{\mathrm{sh}}}{\partial\sigma} + 2f_{\mathrm{b}}\left(\frac{\ln 1/f_{\mathrm{b}}}{\sigma_{\mathrm{c}}}\right)^2 \cosh\left(\frac{\sigma_{\mathrm{n}}}{\sigma_{\mathrm{c}}}\ln 1/f_{\mathrm{b}}\right)(\mathbf{n}\otimes\mathbf{n})\otimes(\mathbf{n}\otimes\mathbf{n}) \tag{A-10}$$

with $\partial\sigma_{\mathrm{sh}}/\partial\sigma$ following Eq. (45).

Also,

$$\begin{aligned}
\frac{\partial\mathbf{N}^{\mathrm{I}}}{\partial f} &= \frac{2}{\sigma_{\mathrm{c}}^2}f_{\mathrm{b},f}\left[\left((\sigma_{\mathrm{c}} - \sigma_{\mathrm{c},f_{\mathrm{b}}}f_{\mathrm{b}}\ln\frac{1}{f_{\mathrm{b}}} - \sigma_{\mathrm{c}})\right)\sinh\frac{\sigma_{\mathrm{n}}}{\sigma_{\mathrm{c}}}\ln\frac{1}{f_{\mathrm{b}}} - \sigma_{\mathrm{n}}\ln\frac{1}{f_{\mathrm{b}}}\cosh\frac{\sigma_{\mathrm{n}}}{\sigma_{\mathrm{c}}}\ln\frac{1}{f_{\mathrm{b}}}\right]\mathbf{n}\otimes\mathbf{n} \\
\frac{\partial\mathbf{N}^{\mathrm{I}}}{\partial\bar{\sigma}} &= \frac{-2}{\bar{\sigma}}\left(3\frac{\partial\sigma_{\mathrm{sh}}}{\partial\sigma} : \mathbb{p} : \frac{\sigma_{\mathrm{sh}}}{\bar{\sigma}^2} + \frac{f_{\mathrm{b}}}{\sigma_{\mathrm{c}}}\ln\frac{1}{f_{\mathrm{b}}}\left[\sinh\left(\frac{\sigma_{\mathrm{n}}}{\sigma_{\mathrm{c}}}\ln 1/f_{\mathrm{b}}\right) + \frac{1}{\sigma_{\mathrm{c}}}\ln\frac{1}{f_{\mathrm{b}}}\cosh\left(\frac{\sigma_{\mathrm{n}}}{\sigma_{\mathrm{c}}}\ln 1/f_{\mathrm{b}}\right)\right]\mathbf{n}\otimes\mathbf{n}\right) \\
\frac{\partial\mathbf{N}^{\mathrm{I}}}{\partial s} &= -2\frac{f_{\mathrm{b}}}{\sigma_{\mathrm{c}}^3}\ln\frac{1}{f_{\mathrm{b}}}\left[\sigma_{\mathrm{n}}\ln\frac{1}{f_{\mathrm{b}}}\cosh\left(\frac{\sigma_{\mathrm{n}}}{\sigma_{\mathrm{c}}}\ln 1/f_{\mathrm{b}}\right) + \sigma_{\mathrm{c}}\sinh\left(\frac{\sigma_{\mathrm{n}}}{\sigma_{\mathrm{c}}}\ln 1/f_{\mathrm{b}}\right)\right]\sigma_{\mathrm{c},\bar{w}}\bar{w}_{,w}w\mathbf{n}\otimes\mathbf{n}
\end{aligned} \tag{A-11}$$

where

$$f_{\mathrm{b},f} = \frac{2}{3}\frac{\bar{\lambda}}{\bar{\chi}\bar{w}}$$

$$\sigma_{\mathrm{c},f_{\mathrm{b}}} = \bar{\sigma}\sqrt{\frac{6}{5}\hat{h}_q}\left[b_{,f_{\mathrm{b}}}\left(\ln\frac{1}{f_{\mathrm{b}}} + b\left[\frac{1}{\sqrt{b^2+1}} - \frac{1}{\sqrt{b^2+f_{\mathrm{b}}^2}}\right] + \ln\mathcal{U}\right) - \left(\frac{b}{f_{\mathrm{b}}} + \frac{f_{\mathrm{b}}}{\sqrt{b^2+f_{\mathrm{b}}^2}}\right) + b\frac{\mathcal{U}_{,f_{\mathrm{b}}}}{\mathcal{U}}\right]$$

$$\mathcal{U} = \frac{b+\sqrt{b^2+f_{\mathrm{b}}^2}}{b+\sqrt{b^2+1}} \;\therefore\; \frac{\mathcal{U}_{,f_{\mathrm{b}}}}{\mathcal{U}} = \frac{1+\frac{bb_{,f_{\mathrm{b}}}+f_{\mathrm{b}}}{\sqrt{b^2+f_{\mathrm{b}}^2}}}{b+\sqrt{b^2+f_{\mathrm{b}}^2}} - \frac{1+\frac{bb_{,f_{\mathrm{b}}}}{\sqrt{b^2+1}}}{b+\sqrt{b^2+1}}$$

$$b_{,f_{\mathrm{b}}} = \frac{5}{24}\frac{\hat{h}_a}{\hat{h}_q\bar{w}^2 b}\left(\frac{\alpha_{,f_{\mathrm{b}}}}{2} - \alpha\frac{\bar{\mathcal{W}}_{,f_{\mathrm{b}}}}{\bar{\mathcal{W}}}\right)\;,\; \alpha_{,f_{\mathrm{b}}} = \frac{1}{12}\left(1 - 10f_{\mathrm{b}} + 9f_{\mathrm{b}}^2\right)\;,\; \bar{\mathcal{W}}_{,f_{\mathrm{b}}} = \begin{cases}\dfrac{\mathcal{W}}{2\mathcal{W}_0}\mathcal{W}_{,f_{\mathrm{b}}} & \text{for } \sqrt{q_\chi f_b}\bar{w} < 2\mathcal{W}_0 \\ \mathcal{W}_{,f_{\mathrm{b}}} & \text{for } \sqrt{q_\chi f_b}\bar{w} \geq \mathcal{W}_0\end{cases}\;,\; \mathcal{W}_{,f_{\mathrm{b}}} = \frac{\bar{w}}{2\bar{\chi}}$$

$$\sigma_{\mathrm{c},\bar{w}} = \bar{\sigma}\bar{\sigma}\sqrt{\frac{6}{5}\hat{h}_q}\left[b_{,\bar{w}}\ln\frac{1}{f_{\mathrm{b}}} - \frac{b}{f_{\mathrm{b}}}f_{\mathrm{b},\bar{w}} + \frac{bb_{,\bar{w}}}{\sqrt{b^2+1}} - \frac{bb_{,\bar{w}}+f_{\mathrm{b}}f_{\mathrm{b},\bar{w}}}{\sqrt{b^2+f_{\mathrm{b}}^2}} + b_{,\bar{w}}\ln\mathcal{U} + b\frac{\mathcal{U}_{,\bar{w}}}{\mathcal{U}}\right]$$

$$b_{,\bar{w}} = -\frac{5}{24}\frac{\alpha}{b}\frac{\hat{h}_a}{\hat{h}_q}\frac{\bar{\mathcal{W}}_{,\bar{w}}}{\bar{\mathcal{W}}^3}\;,\; \bar{\mathcal{W}}_{,\bar{w}} = \begin{cases}\dfrac{\mathcal{W}}{2\mathcal{W}_0}\mathcal{W}_{,\bar{w}} & \text{for } \sqrt{q_\chi f_b}\bar{w} < 2\mathcal{W}_0 \\ \mathcal{W}_{,\bar{w}} & \text{for } \sqrt{q_\chi f_b}\bar{w} \geq \mathcal{W}_0\end{cases}\;,\; \mathcal{W}_{,\bar{w}} = \frac{2}{3}\bar{\chi}\;,\; \frac{\mathcal{U}_{,\bar{w}}}{\mathcal{U}} = \frac{b_{,\bar{w}} + \frac{bb_{,\bar{w}}+f_{\mathrm{b}}f_{\mathrm{b}\bar{w}}}{\sqrt{b^2+f_{\mathrm{b}}^2}}}{b+\sqrt{b^2+f_{\mathrm{b}}^2}} - \frac{b_{,\bar{w}} + \frac{bb_{,\bar{w}}}{\sqrt{b^2+1}}}{b+\sqrt{b^2+1}}$$

where use has been made of the basic formulation of (7) for the sake of brevity. For computation purposes, $f_{\rm b}$ obviously should be replaced by $q_\chi f_{\rm b}$.

Then:

$$\left\{\begin{array}{l}
\mathbf{R}_{\tilde{\sigma}',\tilde{\sigma}'} = \frac{1}{2\mu}\frac{1}{\Delta t}\mathbb{J} + \dot{\Lambda}\dfrac{\partial^2\Phi^{\rm I}}{\partial\tilde{\sigma}'\partial\tilde{\sigma}'} \\
\mathbf{R}_{\tilde{\sigma}',\sigma_{\rm m}} = \dot{\Lambda}\dfrac{\partial}{\partial\sigma_{kk}}\left(\frac{\partial\Phi^{\rm I}}{\partial\tilde{\sigma}'}\right) \\
\mathbf{R}_{\tilde{\sigma}',f} = \dot{\Lambda}\mathbb{J} : \frac{\partial\mathbf{N}^{\rm I}}{\partial f} \\
\mathbf{R}_{\tilde{\sigma}',\bar{\epsilon}} = \dot{\Lambda}\frac{\partial\bar{\sigma}}{\partial\bar{\epsilon}}\mathbb{J} : \frac{\partial\mathbf{N}^{\rm I}}{\partial\bar{\sigma}} \\
\mathbf{R}_{\tilde{\sigma}',s} = \dot{\Lambda}\mathbb{J} : \frac{\partial\mathbf{N}^{\rm I}}{\partial s} \\
\text{where } \frac{\partial\sigma}{\partial\bar{\epsilon}} = \frac{\sigma_{\rm S}N}{\epsilon_0}\left(1+\frac{\bar{\epsilon}}{\epsilon_0}\right)^{N-1}
\end{array}\right.
\qquad
\left\{\begin{array}{l}
R_{\sigma_{\rm m},\tilde{\sigma}'} = \dot{\Lambda}\left[\dfrac{\partial^2\Phi^{\rm I}}{\partial\tilde{\sigma}'\partial\tilde{\sigma}'}\right]^T \\
R_{\sigma_{\rm m},\sigma_{\rm m}} = \frac{1}{K\Delta t} + \dot{\Lambda}\dfrac{\partial^2\Phi^{\rm I}}{\partial\sigma_{kk}\partial\sigma_{kk}} \\
R_{\sigma_{\rm m},f} = \dot{\Lambda}\,\mathbf{I} : \frac{\partial\mathbf{N}^{\rm I}}{\partial f} \\
R_{\sigma_{\rm m},\bar{\epsilon}} = \dot{\Lambda}\,\frac{\partial\bar{\sigma}}{\partial\bar{\epsilon}}\,\mathbf{I} : \frac{\partial\mathbf{N}^{\rm I}}{\partial\bar{\sigma}} \\
R_{\sigma_{\rm m},s} = \dot{\Lambda}\,\mathbf{I} : \frac{\partial\mathbf{N}^{\rm I}}{\partial s}
\end{array}\right.$$

$$\left\{\begin{array}{l}
R_{f,\tilde{\sigma}'} = -\dot{\Lambda}(1-f)\left[\frac{\partial\mathbf{N}^{\rm I}}{\partial\sigma_{\rm kk}}\right]^T \\
R_{f,\sigma_{\rm m}} = -\dot{\Lambda}(1-f)\dfrac{\partial^2\Phi^{\rm I}}{\partial\sigma_{kk}\partial\sigma_{kk}} \\
R_{f,f} = \dfrac{1}{\Delta t} + \dot{\Lambda}\,\mathbf{I} : \left[\frac{\partial\Phi^{\rm I}}{\partial\tilde{\sigma}} - (1-f)\frac{\partial\mathbf{N}^{\rm I}}{\partial f}\right] \\
R_{f,\bar{\epsilon}} = -\dot{\Lambda}(1-f)\,\frac{\partial\bar{\sigma}}{\partial\bar{\epsilon}}\,\mathbf{I} : \frac{\partial\mathbf{N}^{\rm I}}{\partial\bar{\sigma}} \\
R_{f,s} = -\dot{\Lambda}(1-f)\mathbf{I} : \frac{\partial\mathbf{N}^{\rm I}}{\partial s}
\end{array}\right.
\qquad
\left\{\begin{array}{l}
R_{\bar{\epsilon},\tilde{\sigma}'} = -\dfrac{\dot{\Lambda}}{\bar{\sigma}(1-f)}\left(\mathbf{N}^{\rm I} + \tilde{\sigma} : \dfrac{\partial^2\Phi^{\rm I}}{\partial\tilde{\sigma}\partial\tilde{\sigma}}\right) : \mathbb{J} \\
R_{\bar{\epsilon},\sigma_{\rm m}} = -\dfrac{\dot{\Lambda}}{\bar{\sigma}(1-f)}\left(\mathbf{N}^{\rm I} + \tilde{\sigma} : \dfrac{\partial^2\Phi^{\rm I}}{\partial\tilde{\sigma}\partial\tilde{\sigma}}\right) : \mathbf{I} \\
R_{\bar{\epsilon},f} = -\dfrac{\dot{\Lambda}}{\bar{\sigma}(1-f)^2}\,\tilde{\sigma} : \left[\mathbf{N}^{\rm I} + (1-f)\frac{\partial\mathbf{N}^{\rm I}}{\partial f}\right] \\
R_{\bar{\epsilon},\bar{\epsilon}} = \dfrac{1}{\Delta t} - \frac{\partial\bar{\sigma}}{\partial\bar{\epsilon}}\dfrac{\dot{\Lambda}}{\bar{\sigma}^2(1-f)}\,\tilde{\sigma} : \left[-\mathbf{N}^{\rm I} + \bar{\sigma}\frac{\partial\mathbf{N}^{\rm I}}{\partial\bar{\sigma}}\right] \\
R_{\bar{\epsilon},s} = -\dfrac{\dot{\Lambda}}{\bar{\sigma}(1-f)}\tilde{\sigma} : \frac{\partial\mathbf{N}^{\rm I}}{\partial s}
\end{array}\right.$$

$$\left\{\begin{array}{l}
R_{s,\tilde{\sigma}'} = -\dot{\Lambda}\mathcal{M} : \left(\dfrac{\partial^2\Phi^{\rm I}}{\partial\tilde{\sigma}\partial\tilde{\sigma}} : \mathbb{J}\right) \\
R_{s,\sigma_{\rm m}} = -\dot{\Lambda}\mathcal{M} : \dfrac{\partial^2\Phi^{\rm I}}{\partial\tilde{\sigma}\partial\tilde{\sigma}} : \mathbf{I} \\
R_{s,f} = -\dot{\Lambda}\left(\mathcal{M}_{,f} : \mathbf{N}^{\rm I} + \mathcal{M} : \mathbf{N}^{\rm I}_{,f}\right) \approx -\dot{\Lambda}\mathcal{M} : \mathbf{N}^{\rm I}_{,f} \\
R_{s,\bar{\epsilon}} = -\dot{\Lambda}\mathcal{M} : \mathbf{N}^{\rm I}_{,\bar{\epsilon}} \\
R_{s,s} \approx \dfrac{1}{\Delta t}
\end{array}\right. \tag{A-12}$$

References

[1] A. Pineau and T. Pardoen. Failure of Metals. *Comprehensive Structural Integrity*, 2:684–797, 2007. Chapter 2.06.

[2] A. Mortensen and S. Suresh. Functionally graded metals and metal-ceramic composites: Part 1 processing. *International materials reviews*, 40(6):239–265, 1995.

[3] V. Tvergaard. Behaviour of voids in a shear field. *International Journal of Fracture*, 158:41–49, 2009.

[4] A. A. Benzerga, J. Besson, and A. Pineau. Anisotropic ductile fracture. Part II: theory. *Acta Materialia*, 52:4639–4650, 2004.

[5] N. Thomas and A. A. Benzerga. On fracture loci of ductile materials under nonproportional loading. *International Journal of Mechanical Sciences*, 2013. . In preparation.

[6] G. R. Johnson, J. M. Hoegfeldt, U. S. Lindholm, and A. Nagy. Response of various metals to large torsional strains over a large range of strain rates – Part 1: Ductile metals. *Journal of Engineering Materials and Technology*, 105:42–47, 1983.

[7] G.R. Johnson, J.M. Hoegfeldt, U.S. Lindholm, and A. Nagy. Response of various metals to large torsional strains over a large range of strain rates – Part 2: Less ductile metals. *Journal of Engineering Materials and Technology*, 105:48–53, 1983.

[8] M. E. Torki and A. A. Benzerga. On ductile fracture under combined tension and shear. *Journal of the Mechanics and Physics of Solids*, page (under review), 2019.

[9] I. Barsoum and J. Faleskog. Rupture mechanisms in combined tension and shear—-Micromechanics. *International Journal of Solids and Structures*, 44:5481–5498, 2007.

[10] A. A. Benzerga and J.-B. Leblond. Effective Yield Criterion Accounting for Microvoid Coalescence. *Journal of Applied Mechanics*, 81:031009, 2014.

[11] S.S. Haltom, S. Kyriakides, and K. Ravi-Chandar. Ductile failure under combined shear and tension. *International Journal of Solids and Structures*, 50:1507–1522, 2013.

[12] Y. Bao and T. Wierzbicki. On fracture locus in the equivalent strain and stress triaxiality space. *International Journal of Mechanical Sciences*, 46:81–98, 2004.

[13] I. Barsoum and J. Faleskog. Rupture mechanisms in combined tension and shear—-Experiments. *International Journal of Solids and Structures*, 44:1768–1786, 2007.

[14] F. A. McClintock. A criterion for ductile fracture by the growth of holes. *Journal of Applied Mechanics*, 35:363–371, 1968.

[15] J. R. Rice and D. M. Tracey. On the enlargement of voids in triaxial stress fields. *Journal of the Mechanics and Physics of Solids*, 17:201–217, 1969.

[16] A. L. Gurson. Continuum Theory of Ductile Rupture by Void Nucleation and Growth: Part I– Yield Criteria and Flow Rules for Porous Ductile Media. *Journal of Engineering Materials and Technology*, 99:2–15, 1977.

[17] G. Rousselier. Ductile fracture models and their potential in local approach of fracture. *Nucl. Eng. Design*, 105:97–111, 1987.

[18] J. Lemaitre. A Continuous Damage Mechanics Model for Ductile Fracture. *Journal of Engineering Materials and Technology*, 107:83–89, 1985.

[19] Y. Bai and T. Wierzbicki. A new model of metal plasticity and fracture with pressure and Lode dependence. *International Journal of Plasticity*, 24:1071–1096, 2008.

[20] K. Nahshon and J. W. Hutchinson. Modification of the Gurson Model for shear failure. *European Journal of Mechanics*, 27:1–17, 2008.

[21] Viggo Tvergaard and Kim Lau Nielsen. Relations between a micro-mechanical model and a damage model for ductile failure in shear. *Journal of the Mechanics and Physics of Solids*, 58:1243–1252, 2010.

[22] A. A. Benzerga, J. Besson, and A. Pineau. Anisotropic ductile fracture. Part I: experiments. *Acta Materialia*, 52:4623–4638, 2004.

[23] J. Koplik and A. Needleman. Void growth and coalescence in porous plastic solids. *International Journal of Solids and Structures*, 24(8):835–853, 1988.

[24] T. Pardoen and J. W. Hutchinson. An extended model for void growth and coalescence. *Journal of the Mechanics and Physics of Solids*, 48:2467–2512, 2000.

[25] M. Dunand and D. Mohr. Effect of Lode parameter on plastic flow localization after proportional loading at low stress triaxialities. *Journal of the Mechanics and Physics of Solids*, 66:133–153, 2014.

[26] M. Gologanu, J.-B. Leblond, G. Perrin, and J. Devaux. Theoretical models for void coalescence in porous ductile solids – II: Coalescence in "columns". *International Journal of Solids and Structures*, 38:5595–5604, 2001.

[27] A. A. Benzerga and J.-B. Leblond. Ductile fracture by void growth to coalescence. *Advances in Applied Mechanics*, 44:169–305, 2010.

[28] M. E. Torki and A. A. Benzerga. A mechanism of failure in shear bands. *Extreme Mechanics Letters*, 23:67–71, 2018.

[29] N. A. Fleck and J. W. Hutchinson. Void growth in shear. *Proceedings of the Royal Society of London A*, 407:435–458, 1986.

[30] V. Tvergaard, A. Needleman, and K. K. Lo. Flow localization in the plane strain tensile test. *Journal of the Mechanics and Physics of Solids*, 29:115–142, 1981.

[31] V. Tvergaard. On localization in ductile materials containing spherical voids. *International Journal of Fracture*, 18:237–252, 1982.

[32] V. Tvergaard and A. Needleman. Analysis of the cup–cone fracture in a round tensile bar. *Acta Metallurgica*, 32:157–169, 1984.

[33] M. Gologanu, J.-B. Leblond, and J. Devaux. Approximate models for ductile metals containing non-spherical voids – case of axisymmetric prolate ellipsoidal cavities. *Journal of the Mechanics and Physics of Solids*, 41(11):1723–1754, 1993.

[34] A. A. Benzerga and J. Besson. Plastic potentials for anisotropic porous solids. *European Journal of Mechanics*, 20A:397–434, 2001.

[35] S. M. Keralavarma and A. A. Benzerga. A constitutive model for plastically anisotropic solids with non-spherical voids. *Journal of the Mechanics and Physics of Solids*, 58:874–901, 2010.

[36] R. K. Abu Al-Rub and G. Z. Voyiadjis. On the coupling of anisotropic damage and plasticity models for ductile materials. *International Journal of Solids and Structures*, 40(11):2611 – 2643, 2003.

[37] M. Gărăjeu, JC. Michel, and P. Suquet. A micromechanical approach of damage in viscoplastic materials by evolution in size, shape and distribution of voids. *Computer Methods in Applied Mechanics and Engineering*, 183(3-4):223–246, 2000.

[38] S. Hao, W. K. Liu, and C. T. Chang. Computer implementation of damage models by finite element and meshfree methods. *Computer Methods in Applied Mechanics and Engineering*, 187(3-4):401–440, 2000.

[39] K. Danas and P. Ponte Castañeda. A finite-strain model for anisotropic viscoplastic porous media: I–Theory. *European Journal of Mechanics*, 28:387–401, 2009.

[40] S. Ghosh, J. Bai, and D. Paquet. Homogenization-based continuum plasticity-damage model for ductile failure of materials containing heterogeneities. *Journal of the Mechanics and Physics of Solids*, 57:1017–1044, 2009.

[41] S. Ganapathysubramanian and N. Zabaras. Computational design of deformation processes for materials with ductile damage. *Computer Methods in Applied Mechanics and Engineering*, 192(1-2):147–183, 2003.

[42] K. Danas and N. Aravas. Numerical modeling of elasto-plastic porous materials with void shape effects at finite deformations. *Composites Part B: Engineering*, 43:2544–2559, 2012.

[43] T. F. Morgeneyer and J. Besson. Flat to slant ductile fracture transition: Tomography examination and simulations using shear-controlled void nucleation. *Scripta Materialia*, 65:1002–1005, 2011.

[44] V. Tvergaard. Shear deformation of voids with contact modeled by internal pressure. *International Journal of Mechanical Sciences*, 50:1459–1465, 2008.

[45] K. L. Nielsen, J. Dahl, and V. Tvergaard. Collapse and coalescence of spherical voids subject to intense shearing: studied in full 3D. *International Journal of Fracture*, 177:97–108, 2012.

[46] V. Tvergaard. Study of localization in a void-sheet under stress states near pure shear. *International Journal of Solids and Structures*, 75:134–142, 2015.

[47] S. M. Keralavarma and S. Chockalingam. A Criterion for Void Coalescence in Anisotropic Ductile Materials. *International Journal of Plasticity*, 82:159–176, 2016.

[48] S. Kweon, B. Sagsoy, and A. A. Benzerga. Constitutive relations and their time integration for anisotropic elasto-plastic porous materials. *Computer Methods in Applied Mechanics and Engineering*, 310:495–534, 2016.

[49] D. C. Drucker. Continuum theory of plasticity on macroscale and microscale. *Journal of Materials*, 1(4):873, 1966.

[50] P. Ponte Castaneda. The effective mechanical properties of nonlinear composites. *Journal of the Mechanics and Physics of Solids*, 39:45–71, 1991.

[51] G. Perrin and J.-B. Leblond. Analytical study of a hollow sphere made of plastic porous material and subjected to hydrostatic tension— application to some problems in ductile fracture of metals. *Int. J. Plasticity*, 6(6):677–699, 1990.

[52] P. Ponte Castañeda and M. Zaidman. Constitutive models for porous materials with evolving microstructure. *Journal of the Mechanics and Physics of Solids*, 42:1459–1495, 1994.

[53] A. A. Benzerga, J. Besson, and A. Pineau. Coalescence–Controlled Anisotropic Ductile Fracture. *Journal of Engineering Materials and Technology*, 121:221–229, 1999.

[54] M. E. Torki and A. A. Benzerga. Micromechanics-based constitutive relations for post-localization analysis. *MethodsX*, 2018.

[55] A. A. Benzerga. Micromechanics of Coalescence in Ductile Fracture. *Journal of the Mechanics and Physics of Solids*, 50:1331–1362, 2002.

[56] J.R. Rice. The localization of plastic deformation. In W.T. Koiter, editor, *14th int. cong. Theoretical and Applied Mechanics*, pages 207–220. North–Holland, Amsterdam, 1976.

[57] J.-B. Leblond, G. Perrin, and P. Suquet. Exact results and approximate models for porous viscoplastic solids. *International Journal of Plasticity*, 10:213–225, 1994.

[58] R. Hill. A theory of yielding and plastic flow of anisotropic solids. *Proceedings of the Royal Society of London A*, 193:281–297, 1948.

[59] M. Gologanu, J.-B. Leblond, G. Perrin, and J. Devaux. Recent extensions of Gurson's model for porous ductile metals. In P. Suquet, editor, *Continuum Micromechanics, CISM Lectures Series*, pages 61–130. Springer, New York, 1997.

[60] ME Torki, C. Tekoglu, J-B Leblond, and AA Benzerga. Theoretical and numerical analysis of void coalescence in porous ductile solids under arbitrary loadings. *International Journal of Plasticity*, 91:160–181, 2017.

[61] M. E. Gurtin, E. Fried, and L. Anand. *The mechanics and thermodynamics of continua*. Cambridge University Press, 2010.

[62] J.-B. Leblond and G. Mottet. A theoretical approach of strain localization within thin planar bands in porous ductile materials. *Comptes Rendus Mecanique*, 336:176–189, 2008.

[63] M. Kailasam and P. Ponte Castaneda. A general constitutive theory for linear and nonlinear particulate media with microstructure evolution. *Journal of the Mechanics and Physics of Solids*, 46(3):427–465, 1998.

[64] K. Madou, J.-B. Leblond, and L. Morin. Numerical studies of porous ductile materials containing arbitrary ellipsoidal voids —II: Evolution of the length and orientation of the void axes. *European Journal of Mechanics*, 42:490–507, 2013.

[65] J.D. Eshelby. The determination of the elastic field of an ellipsoidal inclusion, and related problems. *Proc. Roy. Soc*, A241:357–396, 1957.

[66] J. C. Simo and T. JR. Hughes. *Computational inelasticity*, volume 7. Springer Science & Business Media, 2006.

[67] B. N. Legarth and V. Tvergaard. Effects of plastic anisotropy and void shape on full three-dimensional void growth. *Journal of Applied Mechanics*, 85(5):051007, 2018.

[68] A. A. Benzerga. *Rupture ductile des tôles anisotropes*. PhD thesis, Ecole Nationale Supérieure des Mines de Paris, 2000.

[69] M. E. Torki, A. A. Benzerga, and J.-B. Leblond. On Void Coalescence under Combined Tension and Shear. *Journal of Applied Mechanics*, 82(7):071005, 2015.

[70] L. Morin, J.-B. Leblond, and V. Tvergaard. Application of a model of plastic porous materials including void shape effects to the prediction of ductile failure under shear-dominated loadings. *Journal of the Mechanics and Physics of Solids*, 94:148–166, 2016.

[71] K. Madou and J.-B. Leblond. Numerical studies of porous ductile materials containing arbitrary ellipsoidal voids — I: Yield surfaces of representative cells. *European Journal of Mechanics*, 42:480–489, 2013.

P9 ON COALESCENCE OF 3D VOIDS UNDER COMBINED TENSION AND SHEAR

On Coalescence of 3D Voids under Combined Tension and Shear

M. E. Torki[1], F. A. Medrano[1], A. A. Benzerga[1,2], J.-B. Leblond[3]

[1] *Department of Aerospace Engineering, Texas A&M University, College Station, TX 77843, USA*

[2] *Department of Materials Science and Engineering, Texas A&M University, College Station, TX 77843, USA*

[3] *Sorbonne Universites, UPMC Univ Paris 06, CNRS, UMR 7190*

Institut Jean Le Rond d'Alembert, F-75005, Paris, France

Abstract

A micromechanics-based yield criterion is developed capable of modeling plastic damage by internal necking and/or internal shearing in solids with highly distorted microstructures with relatively high levels of porosity. The microstructure is represented with a 3D cylindrical elementary cell with an elliptical cross section and a coaxial cylindrical void representing a 3D (ellipsoidal) cavity. The model is derived from limit analysis on the cell subjected to combined tension and shear with plastic flow ideally confined to the ligaments. With the feasible approximations employed, the model emerges as extension to an existing model accounting for similar loading but for a cylindrical cell with a circular cross section. The model is first derived for *homothetic* cells, characterized by equal normalized void spacing along the major and minor axis directions, and is then generalized as to incorporate independent void spacing ratios. The model predictions were assessed against finite-element based outcomes obtained for various cell geometries estimating limit loads on the same cylindrical unit cell exploiting quasi-periodic boundary conditions. Effects induced by void spacing ratios along the major and minor axes, void shape along either axis, and a cell distortion parameter are investigated.

Key Words: Ductile fracture; Void coalescence; Low triaxiality; Internal necking; Combined tension and shear.

1 Introduction

Ductile fracture in porous materials under combined loading conditions, esp. tensile and shear interactions, is among the most desirable, yet controversial, subjects within the community of solid mechanics. Apart from being computationally demanding, esp. in near-simple shearing processes, there are challenges associated with it being analytically modeled. One major challenge is with regards to damage evolution under shear-dominated loading. Within the body of existing models, damage is commonly identified by virtue of the trace of the rate-of-deformation tensor, which either vanishes or is vanishingly small under intense shear fields. Therefore, the majority of existing models, including Gurson [11] and all extensions thereof [33, 14, 8, 9, 10, 13, 17, 20] predict no damage at the limit of simple shear. Even more recent advances, such as that of Nahshon and Hutchinson [21] based on heuristic modification of the damage parameter f as function of the third invariant of the stress deviator J_3, the modified damage parameter loses its physical denotation. Besides, the de facto physical process that triggers failure remains elusive.

On the other hand, the independent state variables that govern the equations after the onset of coalescence differ from the parameters affecting void growth. This distinction encompasses both loading components and geometric parameters. Void growth can be expressed in terms of the mean and von-Mises equivalent stresses whereas void coalescence is mainly governed by the normal and shear resolved tractions on a specific plane, termed *localization plane* [12]. Moreover, the parameters uniquely affecting void growth are void volume fraction (also known as *porosity*), void aspect ratio, and void orientation [9, 13]. Void coalescence, however, is mainly influenced by normalized void spacing and void aspect ratio. A second charge in simulating ductile failure is then the difference in the *constitutive* frameworks prior to and after void coalescence in the time integration process, as a consequence of fundamental differences in the boundary conditions. This charge involves development of constitutive relations at a coalescence state to be further supplemented to the pre-coalescence framework.

The context of reported work regarding ductile fracture under combined loading states can be categorized into micromechanics-based and numerical works. A fraction of micro-mechanics-based models tend to improve constitutive equations. Morgeneyer and Besson [19], for instance, introduced a modified strain rate through a shear void nucleation term in terms of the Lode parameter in to simulate the transition from flat to shear-induced slanted crack propagation based on a Gurson-type yield criterion. In another effort, Cao *et al.* [6] have introduced an ad-hoc modification of an existing constitutive model to deliver better accuracy for void growth at both low and high stress triaxialities with the basic form of the Gurson model. Another subset of micromechanics-based work develop gauge functions as yield criteria. The mathematical procedure is carried out through limit analysis, with the distinguishing character as plasticity being diffuse (in void growth modeling) or localized (in void coalescence modeling). In this regard, models accounting for void growth are well-established and sophisticated. Yet, the body of void coalescence models is still nascent. Following the pioneering work of Thomason [27], Benzerga [2] remedied the singularity within Thomason's model with respect to penny-shaped cracks. This area of work had remained dormant before Pardoen and Hutchinson [24] could propose a more advanced heuristic micro-mechanics-based void coalescence model for triaxial loading. Over the past decade, Tekoglu *et al.* [26] extended the applicability of Thomason's and Benzerga's models into combined tension and shear founded on a semi-analytical method utilizing a simple shear-induced velocity profile. It further remained for Benzerga and Leblond [4], Torki *et al.* [30, 31], and also Morin *et al.* to develop void coalescence models from first principles until [20] introduced a model for void growth accompanied by void coalescence in a unified perspective. A recent extension of this work has been carried out by Torki [28].

Another class of work, including [16, 25], examine failure mechanisms founded on finite-element-based cell-model evolution problems. This class of work can be considered as comparator, yet are not well suited for comprehensive parametric studies due to their high computational demand. Micro-mechanics-based models are hence preferable in this respect.

There are multiple considerations that motivate the present work. One possible significance of the work is to relax simplifying assumptions in the analysis of microstructures with initial 3D voids which may have to undergo significant deformation before the voids can transform into spheroids that could be idealized with cylindrical voids [30, 31]. Among the existing models, the model introduced by Madou and Leblond [17] accounts for the growth of 3D voids represented with ellipsoids. A most proper counterpart thereof for void coalescence is an extension to those of [30, 31], that were best suited to spheroidal voids, to idealize 3D voids using elliptical cross sections. One simple and prevalent example of this phenomenon is a plane strain condition, where the material, being constrained from one direction, accommodates a larger void dilatation in the other direction [20]. Within the context of existing models, except for the Madou-Leblond model for void growth, the constitutive framework operates based on the effective void shape and spacing coming from the geometric average of those in the two directions which may lead to off-hand results at extreme cases. This warrants the endeavor to develop yield criteria capable of describing independent void shapes and spacing along the main directions perpendicular to the dominant loading.

Another remarkable application is with regards to the effect of loading. Under combined tension and shear and, in particular, under intense shear fields, a microstructure with voids even initially spheroidal will soon evolve into a distorted one with voids turning into spheroids. Recent investigations with an effort to simulate this phenomenon, though well-motivated, either rely on heuristic critical parameters [38, 36, 20], without the physical grounds being known, or on high-throughput computations [34, 35, 23, 22, 22, 37, 15]. The present model, at best, can be supplemented with the Madou-Leblond model [17], altogether constituting a hybrid model capable of simulating ductile fracture in its entirety, from void growth to coalescence, ensued by ultimate failure.

2 Model in Absence of Shear

2.1 Geometry and Loading

The outline of a porous microstructure under remotely applied loading is schematized in Fig. 1a. The exact treatment of such a problem is complex if not impossible. The least level of complexity can be ascribed to the coalescence limit load not being worked out analytically for an orthorhombic cell containing an ellipsoidal void. Therefore, a surrogate cell is considered, as shown in Fig. 1b, which may not be space filling but is amenable to mathematical treatment. This was the cornerstone behind the introduction of this sort of cell (with a circular base) by Benzerga and Leblond [4].

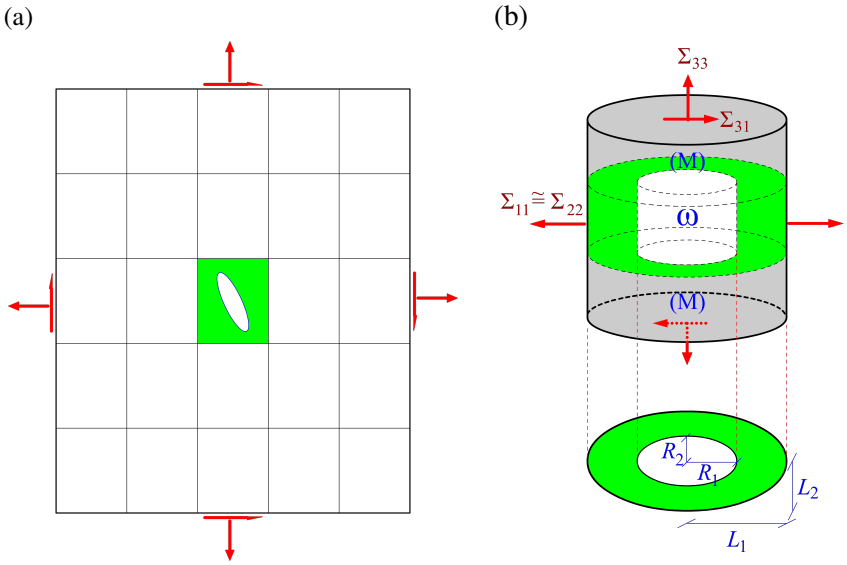

Figure 1: (a) Schematic outline of a porous microstructure under remotely applied loading; (b) geometry of a representative cylindrical cell with elliptical base and void under combined tension and shear.

The elementary volume Ω is a cylindrical cell of height $2H$ and an elliptical base with major and minor lengths L_1 and L_2, respectively, containing a coaxial cylindrical void ω of height $2h$ and major and minor radii, R_1 and R_2, Fig. 1a. The local cylindrical basis $(\mathbf{e}_r, \mathbf{e}_\theta, \mathbf{e}_z)$ and its global Cartesian counterpart $(\mathbf{e}_1, \mathbf{e}_2, \mathbf{e}_3)$ are utilized in the derivations that follow. The imposed displacement boundary conditions, as shown in Fig. 1b, give rise to a macroscopic stress state with a dominant axial stress, $\Sigma_{33} > \Sigma_{11}$, $\Sigma_{33} > \Sigma_{22}$, as well as shear stresses, Σ_{31} and Σ_{32}. While the analyzed geometric framework is not space filling, it sets a reasonable approximation of a periodic framework containing distorted unit cells. In absence of shear, $\Sigma_{11} = \Sigma_{22}$ identically if the prescribed boundary displacement are applied

with axial symmetry. In presence of shear, however, the $\Sigma_{11} = \Sigma_{22}$ assumption is an approximation. In either case, however, both lateral stresses Σ_{11} and Σ_{22} are ineffective on void coalescence [4]. Upon the same method expounded in [4, 30, 31], the cell is further subdivided into a central porous layer identifying a ligament domain, $\Omega_{\rm lig}$, attached to two dense matrices above and below. The height of the central region, ideally set by the void height $2h$ [30], can represent the thickness of a shear band inside which failure is induced by a combined state of tensile and shear loads, termed *shear failure* [29]. The matrix layers admit dilatant plasticity during void growth (or any equivalent diffuse plastic deformation) [20] whereas they behave rigidly after the onset of void coalescence (or any equivalent localized plastic deformation) [14, 1, 7] due to the unloading above and below the cavity. Upon the same convention as used in [4, 30, 31], the interfaces between the ligament and matrices are denoted with $S_{\rm top}$ and $S_{\rm bot}$, with $S_{\rm int}$ being the union thereof. The microstructural geometry can be uniquely identified by means of the following dimensionless parameters, only five of which are independent.

$$\begin{aligned} \alpha_{\rm v} &= \frac{R_1}{R_2} \quad , \quad \alpha_{\rm c} = \frac{L_1}{L_2} \\ \chi_1 &= \frac{R_1}{L_1} \quad , \quad \chi_2 = \frac{R_2}{L_2} \\ w_1 &= \frac{h}{R_1} \quad , \quad w_2 = \frac{h}{R_2} \\ \lambda_1 &= \frac{H}{L_1} \quad , \quad \lambda_2 = \frac{H}{L_2} \end{aligned} \tag{1}$$

where $\alpha_{\rm v}$ and $\alpha_{\rm c}$ are, respectively, the void and cell in-plane aspect ratios. χ_i is the ligament parameters along the cell axis x_i (with $i = 1, 2$), and w_1 and w_2 are, respectively, the out-of-plane void aspect ratios in the $x_1 - x_3$ and $x_2 - x_3$ planes. Finally, λ_1 and λ_2 are the cell aspect ratios in the corresponding planes. Note that, in principle, $\alpha_{\rm v}$ and $\alpha_{\rm c}$ can take any positive value below or above 1. Without loss of generality, however, one can consider the cell major axis along x_1, *i.e.* $\alpha_{\rm c} \geq 1$ while $0 < \alpha_{\rm v} < \infty$. For the sake of convenience, the parameters adopted for presenting results are $\alpha_{\rm c}, \chi_1, \chi_2, w_1, \lambda_1$. λ_1 and λ_2 are ineffective in the yield condition for void coalescence while they can influence the onset of coalescence through the notion of porosity f [20].

2.2 Constitutive relations

The plastically-deformable ligament material is taken, at the micro scale, to obey the von-Mises yield criterion with the associated flow rule (see [4] for more details). The rigid matrices would only affect the displacement boundary conditions, as seen in the sequel. At the macro scale, however, the effective yield criterion can be derived from a variational definition emanating from the fundamental inequality of limit analysis that writes

$$\forall\, \mathbf{D}, \quad \boldsymbol{\Sigma} : \mathbf{D} \leq \Pi(\mathbf{D}), \qquad \Pi(\mathbf{D}) = \inf_{\mathbf{v} \in \mathcal{K}(\mathbf{D})} \langle \sup_{\boldsymbol{\sigma}^* \in \mathcal{C}} \sigma^*_{ij}\, d_{ij} \rangle_\Omega; \tag{2}$$

where $\Pi(\mathbf{D})$ is the effective plastic dissipation which, in the case of a discontinuous velocity field across the interface S, should be added by an extra term

$$\frac{1}{\Omega} \int_S \sup_{\boldsymbol{\sigma}^* \in \mathcal{C}} t^*_i\, [\![v_i]\!]\, {\rm d}S \tag{3}$$

$\langle \cdot \rangle$ stands for averaging over what comes in its subscript (be it a volume, surface or line), $\mathcal{K}(\mathbf{D})$ is the set of kinematically admissible velocity fields $\mathbf{v}$ compatible with $\mathbf{D}$, and $\inf$ and $\sup$ are short-hand notation for, respectively, the infimum and supremum over a set. $\mathcal{C}$ is the microscopic reversibility domain bounded by

the matrix yield surface (see [4] for more details), and $\mathbf{t}^*$ denotes the traction acting on the interface with the associated velocity jump $[\![\mathbf{v}]\!]$.

Upon the same methodology described in [4, 30, 31], the complete yield surface comprises two subsets wherein the effective dissipation Π is differentiable and non-differentiable, that are manifested by curved and planar parts, respectively. The former is synonymous to the parametric representation of the yield surface written as

$$\Sigma_{ij} = \frac{\partial \Pi}{\partial D_{ij}}(\mathbf{D}) \tag{4}$$

where $\mathbf{D}$ is no longer arbitrary (despite that in $(2)_1$) but a conjugate to $\mathbf{\Sigma}$ through the macroscopic flow rule. The planar parts, however, can be derived only with reference to the primitive inequality stated in (2). [30, 31] include sufficient details in this respect.

2.3 Reference velocity field

Even though the exact velocity field governing the cell motion is not analytically obtainable even under triaxial loading, the choice of a trial field leads to an upper bound of the yield surface [3] evidently if it is compatible with the boundary conditions. The presence of rigid blocks above and below the void, considering equality between the lateral strain rates of different layers, entails $D_{11} = D_{22} = 0$ (also $D_{12} = 0$ in presence of shearing in the $x_1 - -x_2$ plane). By the same token, the velocity jump across S_{int} must be purely tangential. Following [4], the velocity field for a *reference* cylindrical cell with circular bases ought to be consistent with the following constraints:

$$\begin{cases} V_r(L,\theta,z) = 0 \quad , \quad V_\theta(L,\theta,z) = 0 & (-h \le z \le h; 0 \le \theta \le 2\pi) \\ V_z(r,\theta,\pm h) = \pm D_{33} H & (0 \le r \le L; 0 \le \theta \le 2\pi) \\ [\![\mathbf{V}]\!].\mathbf{n} = 0 & \forall \mathbf{x} \in S_{\text{int}} \end{cases} \tag{5}$$

with D_{33} and $\mathbf{n}$ being the prescribed axial strain rate and normal vector to the interface, ideally taken equal to the normal to the localization plane denoted by $\mathbf{e}_3$. The capital notation for $\mathbf{V}$ alludes to the reference cell. It goes without saying that the rigid zones ($h \le |z| \le H$) should admit a constant velocity. Following Tracey [32], the conditions in (5) are satisfied with the following simplest field within the plastic ligament, along with the incompressibility condition (tr $\mathbf{d}$ = div $\mathbf{v} = 0$):

$$\mathbf{V}(\mathbf{x}) = \left(\frac{A}{r} - B\frac{r}{2}\right)\mathbf{e}_r + Bz\mathbf{e}_z \tag{6}$$

with A and B determined by boundary conditions as

$$A = \frac{D_{33}L^2}{2c} \quad , \quad B = \frac{D_{33}}{c}$$

where $c = h/H$ is the ligament volume fraction.

2.4 Elliptical velocity field

The velocity field for the cell with an elliptical cross section can be deduced from a contravariant coordinate transformation [5]. In order that the extended velocity field can deliver a closed-form solution, the cell cross section should be *homothetic* with the void, *i.e.* $\chi_1 = \chi_2$, as shown in Fig. 2. This renders the values of α constant throughout the cell domain. The cell with arbitrary χ_1 and χ_2 will be discussed in Sec. 2.4.2.

Let the contravariant and covariant coordinates for an ellipse be denoted via superscripts and subscripts, respectively. Then, one can write

$$\left(x^1, x^2, x^3\right) = (r, \theta, z) \quad , \quad (x_1, x_2, x_3) = (x, y, z) \tag{7}$$

Provided the area is kept common between the reference (circular) and current (elliptical) cross sections, one can easily verify that $R = \sqrt{R_1 R_2}$ and $L = \sqrt{L_1 L_2}$. Correspondingly

$$\chi = \sqrt{\chi_1 \chi_2} \quad , \quad w = \sqrt{w_1 w_2} \tag{8}$$

The dual representation of the velocity field $\mathbf{v}$ is expressible as

$$\mathbf{v} = v^i \mathbf{g}_i = v_i \mathbf{g}^i \tag{9}$$

where the first expression shows a contravariant and the second denotes a covariant representation. The local basis denoted by $\mathbf{g}_i$ is arbitrary and $\mathbf{g}^i$ is its *reciprocal* basis. It can be easily verified that the Cartesian coordinates in $(7)_2$ can be expressed using the following format:

$$\begin{aligned} x &= \sqrt{\alpha(r)} r \cos\theta \\ y &= \frac{1}{\sqrt{\alpha(r)}} r \sin\theta \end{aligned} \tag{10}$$

where

$$\begin{aligned} &\alpha(r) = \frac{r_1(r)}{r_2(r)} \\ &R_1 \leq r_1 \leq L_1 \quad , \quad R_2 \leq r_2 \leq L_2 \quad \therefore \quad \alpha_{\mathrm{v}} \leq \alpha(r) \leq \alpha_{\mathrm{c}} \end{aligned}$$

where α_{v} and α_{c} follow (1), and $r = \sqrt{r_1 r_2}$ is implied. Equation (10) obviously admits an elliptical relation through the elimination of θ from the first two rows. The transformation between cylindrical and Cartesian coordinates could then be realized through the mapping function $(x, y, z) = \hat{\mathbf{z}}(r, \theta, z)$ with the following definition:

$$\hat{\mathbf{z}}(\mathbf{x}) = \sqrt{\alpha}\, r \cos\theta \mathbf{e}_1 + \frac{r}{\sqrt{\alpha}} \sin\theta \mathbf{e}_2 + z\mathbf{e}_3 \tag{11}$$

Broadly, an infinite number of ellipses can pass through any point inside the cell domain. The values of r_1 and r_2 are, therefore, indeterminate while their product $r_1 r_2 = r^2$ is determined. To forestall this ambiguity, we first derive the yield criterion for the case $\alpha_{\mathrm{v}} = \alpha(r) = \alpha_{\mathrm{c}}$, where the void is homothetic with the cell, here termed the *homothetic cell*. The r_1/r_2 ratio is then well-defined, and can be named α throughout the cell. Secondly, as further clarified in Section 2.4.2, $\alpha(r)$ for non-homothetic coaxial cells can be arbitrated by means of an approximation based on volumetric averages of the parameters defined in Eq. (20).

2.4.1 Homothetic cells

In case the outer ellipse is taken homothetic with the inner (void) one, then $\chi_1 = \chi_2 = \chi$. This idealized case is associated with $\alpha(r) = \alpha$. A homothetic cell cross section is schematized in Fig. 2.

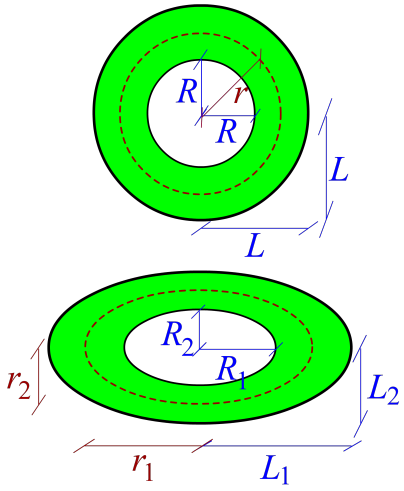

Figure 2: Reference circular cross section and its homothetic elliptical counterpart.

The local basis associated with (11) reads

$$\begin{aligned} & \mathbf{g}_k = \partial_{x^k}\hat{\mathbf{z}}(\mathbf{x}) = \partial_{x^k}(\sqrt{\alpha}\, r\cos\theta)\mathbf{e}_1 + \partial_{x^k}(\frac{r}{\sqrt{\alpha}}\sin\theta)\mathbf{e}_2 + \mathbf{e}_3 \\ \therefore \quad & \mathbf{g}_1 = \sqrt{\alpha}\,\cos\theta\mathbf{e}_1 + \frac{1}{\sqrt{\alpha}}\,\sin\theta\mathbf{e}_2 \\ & \mathbf{g}_2 = -\sqrt{\alpha}\, r\sin\theta\mathbf{e}_1 + \frac{r}{\sqrt{\alpha}}\cos\theta\mathbf{e}_2 \\ & \mathbf{g}_3 = \mathbf{e}_3 \end{aligned} \tag{12}$$

The reciprocal of $\mathbf{g}_k$ is derived from the reciprocity condition expressed as $\mathbf{g}_k \cdot \mathbf{g}^l = \delta_k^l$, with δ denoting the Kronecker delta (where $\delta_k^l \equiv \delta_{kl}$, so expressed for better harmony with the dot product):

$$\begin{aligned} \mathbf{g}^k = \nabla_{\hat{z}} x^k(\hat{z}) \quad \therefore \quad & \mathbf{g}^1 = \frac{1}{\sqrt{\alpha}}\cos\theta\mathbf{e}_1 + \sqrt{\alpha}\sin\theta\mathbf{e}_2 \\ & \mathbf{g}^2 = \frac{1}{r}\left(-\frac{1}{\sqrt{\alpha}}\sin\theta\mathbf{e}_1 + \sqrt{\alpha}\cos\theta\mathbf{e}_2\right) \\ & \mathbf{g}^3 = \mathbf{e}_3 \end{aligned} \tag{13}$$

The gradient operator is defined over the contravariant coordinates as follows:

$$\nabla = \mathbf{g}^i\partial_{x^i} \quad \therefore \quad \nabla\mathbf{g}_k(\mathbf{x}) = \frac{\partial\mathbf{g}_k}{\partial x^m} \otimes \mathbf{g}^m(\mathbf{x}) \tag{14}$$

where summation is implied over i and m ranging form 1 to 3. With a few steps aside, the following gradients are induced:

$$\begin{aligned} \nabla\mathbf{g}_1 &= \frac{1}{r}\mathbf{g}_2 \otimes \mathbf{g}^2 \\ \nabla\mathbf{g}_2 &= \frac{1}{r}\left(\mathbf{g}_2 \otimes \mathbf{g}^1 - \mathbf{g}_1 \otimes \mathbf{g}^2\right) \\ \nabla\mathbf{g}_3 &= \mathbf{0} \end{aligned} \tag{15}$$

where $\mathbf{0}$ stands for a null tensor. Following the contravariant representation of $\mathbf{v}$ in (9), the gradient thereof can be written in the following form:

$$\begin{aligned}\nabla\mathbf{v} &= v^i\nabla\mathbf{g}_i + \mathbf{g}_i\otimes\nabla\mathbf{v}^i \\ &= v^i\frac{\partial\mathbf{g}_i}{\partial x^m}\otimes\mathbf{g}^m + \mathbf{g}_i\otimes\left(\frac{\partial v^i}{\partial x^m}\mathbf{g}^m\right) \\ &= \frac{1}{r}\left[v^1\mathbf{g}_2\otimes\mathbf{g}^2 + v^2\left(\mathbf{g}_2\otimes\mathbf{g}^1 - \mathbf{g}_1\otimes\mathbf{g}^2\right)\right] + v^i_{,m}\mathbf{g}_i\otimes\mathbf{g}^m\end{aligned} \tag{16}$$

where the chain rule has been exploited, and $v^i_{,m}$ is short-hand notation for $\partial v^i/\partial x^m$. Hence, the divergence of the velocity field, identified as the trace of its gradient, will be obtained by transforming the tensor products into dot products in (16). That is

$$\text{div}\mathbf{v} = \text{tr}\left(\nabla\mathbf{v}\right) = \frac{1}{r}\frac{\partial}{\partial r}(rv_r) + \frac{\partial v_\theta}{\partial\theta} + \frac{\partial v_z}{\partial z} \tag{17}$$

which asserts that, with the given geometry, the divergence in the cylindrical cell with a homothetic elliptical base is surprisingly identical to that in its reference (circular base) counterpart. Therefore, the same volume-preserving velocity field for the reference cell in (6) can be utilized to construct that for the current cell. That is, following (9):

$$\mathbf{v} = v_r\mathbf{g}_1 + v_\theta\mathbf{g}_2 + v_z\mathbf{g}_3 \tag{18}$$

where $\mathbf{v}$ is distinguished from $\mathbf{V}$ to illustrate the distinction between the elliptical and the reference cell. The local basis denoted with $\mathbf{g}_i$ can be represented in polar coordinates using the rotation tensor:

$$\begin{aligned}\begin{bmatrix}\mathbf{g}_1\\ \mathbf{g}_2\\ \mathbf{g}_3\end{bmatrix} &= \begin{bmatrix}\sqrt{\alpha}\cos\theta & \frac{1}{\sqrt{\alpha}}\sin\theta & 0\\ -\sqrt{\alpha}r\sin\theta & \frac{1}{\sqrt{\alpha}}r\cos\theta & 0\\ 0 & 0 & 1\end{bmatrix}\begin{bmatrix}\cos\theta & -\sin\theta & 0\\ \sin\theta & \cos\theta & 0\\ 0 & 0 & 1\end{bmatrix}\begin{bmatrix}\mathbf{e}_r\\ \mathbf{e}_\theta\\ \mathbf{e}_z\end{bmatrix} \\ &= \frac{1}{2}\begin{bmatrix}(\sqrt{\alpha}+\frac{1}{\sqrt{\alpha}}) + (\sqrt{\alpha}-\frac{1}{\sqrt{\alpha}})\cos 2\theta & -(\sqrt{\alpha}-\frac{1}{\sqrt{\alpha}})\sin 2\theta & 0\\ -(\sqrt{\alpha}-\frac{1}{\sqrt{\alpha}})\sin 2\theta & r\left((\sqrt{\alpha}+\frac{1}{\sqrt{\alpha}}) - (\sqrt{\alpha}-\frac{1}{\sqrt{\alpha}})\cos 2\theta\right) & 0\\ 0 & 0 & 1\end{bmatrix}\begin{bmatrix}\mathbf{e}_r\\ \mathbf{e}_\theta\\ \mathbf{e}_z\end{bmatrix}\end{aligned} \tag{19}$$

Therefore, the extended velocity field, subsequent to (6), is written as

$$\mathbf{v}(\mathbf{x}) = \frac{D_{33}}{c}\left[\frac{1}{4}\left(\frac{L^2}{r} - r\right)\left[(\mathcal{A}+\mathcal{B}\cos 2\theta)\mathbf{e}_r - \mathcal{B}\sin 2\theta\mathbf{e}_\theta\right] + z\mathbf{e}_z\right] \tag{20}$$

where $\mathcal{A} = \sqrt{\alpha}+1/\sqrt{\alpha}$ and $\mathcal{B} = \sqrt{\alpha}-1/\sqrt{\alpha}$ on account of $\alpha \geq 1$. Unlike the velocity field corresponding to a circular cylindrical cell, the velocity field at the present context is dependent upon θ in addition to r. The plastic dissipation would then appear in the form of a coupled integral, which is too complicated to calculate analytically. This warrants the use of some approximation that will be described in the following subsection.

2.4.2 Arbitrary coaxial cells

A cylindrical cell with an arbitrary elliptical cross section can have a coaxial void with a R_1/R_2 ration differing from L_1/L_2, as schematically shown in Fig. 3.

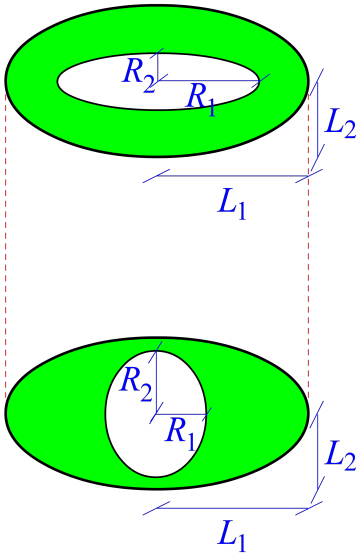

Figure 3: Schematic cross sections of a cylindrical cell with arbitrary inner (void) ellipses coaxial with the same outer (boundary) ellipse.

The steps to derive the coalescence criterion for coaxial cylindrical cells having elliptical bases with arbitrary χ_1 and χ_2 are similar to those for homothetic cells, except for α varying with r which renders the volumetric integral not analytically calculable. Out of the infinite number of ellipses passing through every point lying in the cell domain, one can pick that emanating from a known $\mathcal{A}$ and $\mathcal{B}$ profile. As later demonstrated in the results, an upper bound to the dissipation for this case can be evaluated by neglecting the r–derivative of α and considering a simplified linear profile for the variation of $\mathcal{A}$ and $\mathcal{B}$ with r. To this end, let the subscripts 'v' and 'c' pertain to the inner ellipse (void boundary) and the outer ellipse (cell boundary), respectively. Correspondingly, the outer ellipse can be identified with $\alpha_{\rm c}$, which can be prescribed by the user and is generally different from that of the void ellipse $\alpha_{\rm v}$, the latter uniquely determined from known values of χ_1 and χ_2. It can be easily verified that

$$\alpha_{\rm v} = \frac{\chi_1}{\chi_2}\alpha_{\rm c} \tag{21}$$

Therefore, the corresponding values of $\mathcal{A}$ and $\mathcal{B}$ obey the following relations:

$$\begin{aligned} \mathcal{A}_{\rm v} &= \sqrt{\frac{\alpha_{\rm v}\chi_1}{\chi_2}} + \sqrt{\frac{\chi_2}{\alpha_{\rm v}\chi_1}} \quad , \quad \mathcal{B}_{\rm v} = \left| \sqrt{\frac{\alpha_{\rm v}\chi_1}{\chi_2}} - \sqrt{\frac{\chi_2}{\alpha_{\rm v}\chi_1}} \right| \\ \mathcal{A}_{\rm c} &= \sqrt{\alpha_{\rm c}} + \frac{1}{\sqrt{\alpha_{\rm c}}} \quad , \quad \mathcal{B}_{\rm c} = \sqrt{\alpha_{\rm c}} - \frac{1}{\sqrt{\alpha_{\rm c}}} \end{aligned} \tag{22}$$

where $\alpha_{\rm c} \geq 1$ is implied in the definition of $\mathcal{B}_{\rm c}$.

Remark: The yield load corresponding to the coalescence limit is majorly affected by the minimum void spacing and minorly affected by its maximum value. Hence, as henceforth seen in Sec. 5, the yield load in a non-homothetic cell proves smaller in comparison to its homothetic counterpart. Correspondingly, an upper bound to the yield load will be obtained from $\chi_{\rm max}$ taken as the effective ligament parameter, and a lower bound thereof will be a function of $\chi_{\rm min}$ involved in the equations. However, a more rigorous upper bound to the yield load can be estimated via the following relation

$$\alpha_{\rm v} = \frac{\chi_{\rm min}}{\chi_{\rm max}}\alpha_{\rm c}$$

which gives rise to the following modified counterpart of (22):

$$\begin{aligned}
\mathcal{A}_{\mathrm{v}} &= \sqrt{\frac{\alpha_{\mathrm{v}}\chi_{\min}}{\chi_{\max}}} + \sqrt{\frac{\chi_{\max}}{\alpha_{\mathrm{v}}\chi_{\min}}} \quad , \quad \mathcal{B}_{\mathrm{v}} = \left| \sqrt{\frac{\alpha_{\mathrm{v}}\chi_{\min}}{\chi_{\max}}} - \sqrt{\frac{\chi_{\max}}{\alpha_{\mathrm{v}}\chi_{\min}}} \right| \\
\mathcal{A}_{\mathrm{c}} &= \sqrt{\alpha_{\mathrm{c}}} + \frac{1}{\sqrt{\alpha_{\mathrm{c}}}} \quad , \quad \mathcal{B}_{\mathrm{c}} = \sqrt{\alpha_{\mathrm{c}}} - \frac{1}{\sqrt{\alpha_{\mathrm{c}}}}
\end{aligned} \tag{23}$$

where $\alpha_{\mathrm{c}} \geq 1$ is implied. The simplest profile that can be conceived is a linear function of dimensionless variable r/L, which preserves the upper-bound character. Let

$$\begin{aligned}
\mathcal{A}(r) &= \mathcal{A}_{\mathrm{v}} + (\mathcal{A}_{\mathrm{c}} - \mathcal{A}_{\mathrm{v}}) \frac{\frac{r}{L} - \chi}{1 - \chi} \\
\mathcal{B}(r) &= \mathcal{B}_{\mathrm{v}} + (\mathcal{B}_{\mathrm{c}} - \mathcal{B}_{\mathrm{v}}) \frac{\frac{r}{L} - \chi}{1 - \chi}
\end{aligned} \tag{24}$$

which can be alternatively expressed in terms of $u = (L/r)^2$ formerly defined. No matter how simple the linear functions are, the effective dissipation integral in (29) cannot be determined analytically. However, the $\mathcal{A}$ and $\mathcal{B}$ therein can be replaced with their volumetric averages, here denoted with $\bar{\mathcal{A}}$ and $\bar{\mathcal{B}}$. To this end, the integral has been expanded below only for one case, and the other will be obtained likewise.

$$\bar{\mathcal{A}} = \frac{1}{1/\chi^2 - 1} \int_1^{1/\chi^2} \mathcal{A}(u) du = \frac{\chi^2}{1 - \chi^2} \left[\left(\mathcal{A}_{\mathrm{v}} - (\mathcal{A}_{\mathrm{c}} - \mathcal{A}_{\mathrm{v}}) \frac{\chi}{1 - \chi} \right) u + 2(\mathcal{A}_{\mathrm{c}} - \mathcal{A}_{\mathrm{v}}) \frac{\sqrt{u}}{1 - \chi} \right]_1^{1/\chi^2}$$

Therefore

$$\begin{aligned}
\bar{\mathcal{A}} &= \frac{\mathcal{A}_{\mathrm{v}} + \chi \mathcal{A}_{\mathrm{c}}}{1 + \chi} \\
\bar{\mathcal{B}} &= \frac{\mathcal{B}_{\mathrm{v}} + \chi \mathcal{B}_{\mathrm{c}}}{1 + \chi}
\end{aligned} \tag{25}$$

which clearly simplifies into $\bar{\mathcal{A}} = \mathcal{A}$ and $\bar{\mathcal{B}} = \mathcal{B}$ in the case of a homothetic cell, identified by $\mathcal{A}_{\mathrm{v}} = \mathcal{A}_{\mathrm{c}} = \mathcal{A}$ and $\mathcal{B}_{\mathrm{v}} = \mathcal{B}_{\mathrm{c}} = \mathcal{B}$. Once again, it should be highlighted that $\chi = \sqrt{\chi_1 \chi_2}$ is the geometric average of the major and minor ligament parameters.

2.5 Effective yield criterion

With the velocity field at hand, one can calculate the effective plastic dissipation, whereby the stress subspace at the yield limit can be derived. To this end, the equivalent microscopic strain rate should be evaluated. The criterion will be firstly derived for homothetic cells, and it will then be extended into non-homothetic ones. With reference to (20), one can write:

$$\begin{aligned}
d_{rr} &= v_{r,r} = -\frac{D_{33}}{4c} \left(\frac{L^2}{r^2} + 1 \right) (\mathcal{A} + \mathcal{B} \cos 2\theta) \\
d_{r\theta} &= d_{\theta r} = \frac{1}{2} \left(\frac{v_{r,\theta} - v_\theta}{r} + v_{\theta,r} \right) = \frac{D_{33}}{4c} \mathcal{B} \sin 2\theta \\
d_{\theta\theta} &= \frac{v_r + v_{\theta,\theta}}{r} = \frac{D_{33}}{4c} \left(\frac{L^2}{r^2} - 1 \right) (\mathcal{A} - \mathcal{B} \cos 2\theta) \\
d_{zz} &= v_{z,z} = \frac{D_{33}}{c}
\end{aligned} \tag{26}$$

with the commas representing partial derivatives. The rest of $\mathbf{d}$ components equal zero. Therefore:

$$\begin{aligned}\mathbf{d}:\mathbf{d} &= d_{rr}^2 + d_{\theta\theta}^2 + d_{zz}^2 + 2d_{r\theta}^2 \\ \therefore d_{\mathrm{eq}}^2 &= \frac{2}{3}\mathbf{d}:\mathbf{d} = \frac{1}{12}\left(\frac{D_{33}}{c}\right)^2\left[(\mathcal{A}^2+\mathcal{B}^2\cos^2 2\theta)\,u^2 - 4(\mathcal{A}\mathcal{B}\cos 2\theta)\,u + (\mathcal{A}^2+\mathcal{B}^2+8)\right]\end{aligned} \tag{27}$$

where $u = (L/r)^2$ and c has been defined in advance. With reference to the details stated in [4], the volumetric effective plastic dissipation reduces to the following expression:

$$\Pi^{\mathrm{vol}} = \bar{\sigma}c(1-f_{\mathrm{b}})\langle\, d_{\mathrm{eq}}\,\rangle_{\Omega_{\mathrm{lig}}} \tag{28}$$

with $f_b = \chi^2$ being the porosity within the ligament. Note that, thanks to the cross section being homothetic, $\chi_1 = \chi_2 = \chi$. Due to d_{eq} being independent of z, Eq. (28) can be recast in the following form:

$$\frac{\Pi^{\mathrm{vol}}}{\bar{\sigma}} = \frac{c}{\pi L^2}\int_R^L\int_0^{2\pi} d_{\mathrm{eq}} r\,dr\,d\theta \;=\; \frac{c}{2\pi}\int_1^{1/\chi^2}\int_0^{2\pi}\frac{d_{\mathrm{eq}}}{u^2}\,du\,d\theta \tag{29}$$

The exact integral will be too complex. However, following [30], the following approximation can be exploited, which violates the upper-bound character but simplifies the expression significantly:

$$\frac{1}{2\pi}\int_0^{2\pi} d_{\mathrm{eq}}\,d\theta \approx \sqrt{\frac{\int_0^{2\pi} d_{\mathrm{eq}}^2\,d\theta}{2\pi}} \quad\therefore\quad \frac{\Pi^{\mathrm{vol}}}{\bar{\sigma}} \approx c\int_1^{1/\chi^2}\sqrt{\frac{1}{2\pi}\int_0^{2\pi}\frac{d_{\mathrm{eq}}^2}{u^2}d\theta}\;du \tag{30}$$

where the integral inside the square root should be evaluated term by term, following $(27)_2$, which amounts to

$$\begin{aligned}\frac{\Pi^{\mathrm{vol}}}{\bar{\sigma}} &\approx \frac{|D_{33}|}{2\sqrt{3}}\int_1^{1/\chi^2}\sqrt{\left[\frac{1}{2\pi}\int_0^{2\pi}(\mathcal{A}^2+\mathcal{B}^2\cos^2 2\theta)d\theta\right]u^{-2} - 4\left[\frac{1}{2\pi}\int_0^{2\pi}(\mathcal{A}\mathcal{B}\cos 2\theta)d\theta\right]u^{-3} + \left[\frac{1}{2\pi}\int_0^{2\pi}(\mathcal{A}^2+\mathcal{B}^2+8)d\theta\right]u^{-4}}\;du \\ &= \frac{|D_{33}|}{2\sqrt{3}}\int_1^{1/\chi^2}\sqrt{\frac{\mathcal{A}^2+\frac{\mathcal{B}^2}{2}}{u^2}+\frac{\mathcal{A}^2+\mathcal{B}^2+8}{u^4}}\;du \\ &= \frac{|D_{33}|}{2\sqrt{3}}\left[\sqrt{2\mathcal{A}^2+\mathcal{B}^2}\ln\left(2u\left[(2\mathcal{A}^2+\mathcal{B}^2)+\sqrt{(2\mathcal{A}^2+\mathcal{B}^2)\left(\frac{2(\mathcal{A}^2+\mathcal{B}^2+8)}{u^2}+2\mathcal{A}^2+\mathcal{B}^2\right)}\right]\right) - \sqrt{\frac{2(\mathcal{A}^2+\mathcal{B}^2+8)}{u^2}+2\mathcal{A}^2+\mathcal{B}^2}\right]_1^{1/\chi^2}\end{aligned} \tag{31}$$

All the same, the surface dissipation stemming from the velocity jump, reading

$$[\![v_r]\!] = -v_r \tag{32}$$

(with the remaining components all being zero) simplifies to the following form (see [4] for further details):

$$\begin{aligned}\Pi^{\mathrm{surf}} &= \bar{\sigma}c(1-f_{\mathrm{b}})\langle\,\frac{\left|[\![\mathbf{v}]\!]\right|}{\sqrt{3}}\,\rangle_{\Omega_{\mathrm{lig}}} = \frac{c\bar{\sigma}}{4\pi L^2 h}\int_R^L\int_0^{2\pi}\frac{|v_r|}{\sqrt{3}}r\,dr\,d\theta \\ \therefore\;\frac{\Pi^{\mathrm{surf}}}{\bar{\sigma}} &= \frac{|D_{33}|}{4\pi L^2 h\sqrt{3}}\int_R^L\int_0^{2\pi}(L^2-r^2)(\mathcal{A}+\mathcal{B}\cos 2\theta)dr\,d\theta = \frac{|D_{33}|\,\mathcal{A}}{6\sqrt{3}}\left[2\frac{L}{h}+\frac{R}{h}\left(\frac{R^2}{L^2}-3\right)\right] \\ &= \frac{|D_{33}|\,\mathcal{A}}{6\sqrt{3}}\,\frac{\chi^3-3\chi+2}{\chi w}\end{aligned} \tag{33}$$

where w is the effective void aspect ratio. To obtain w, for a specific w_1 (see (1) for definitions), one can write

$$\frac{w_2}{w_1} = \frac{R_1}{R_2} = \frac{R_1}{L_1}\frac{L_1}{L_2}\frac{L_2}{R_2} = \frac{\chi_1}{\chi_2}\alpha \quad\therefore\quad w^2 = w_1 w_2 = \frac{\chi_1}{\chi_2}\alpha w_1^2 \tag{34}$$

Both the primitive inequality of limit analysis in (2) and the parametric representation of the yield function in (4) lead to the following effective yield criterion:

$$|\Sigma_{33}| = \Sigma^{\mathrm{vol}} + \Sigma^{\mathrm{surf}} \tag{35}$$

where use has been made of the $\mathrm{sgn}(D_{33}) = \mathrm{sgn}(\Sigma_{33})$ identity (see [30] for proof), and

$$\begin{aligned}
\frac{\Sigma^{\mathrm{vol}}}{\bar{\sigma}} &= \frac{1}{2\sqrt{3}} \left[\sqrt{\mathcal{C}_1} \ln \left(4u\sqrt{\mathcal{C}_1} \left[\sqrt{\mathcal{C}_1} + \sqrt{\mathcal{C}_1 + \frac{\mathcal{C}_2}{u^2}} \right] \right) - \sqrt{\mathcal{C}_1 + \frac{\mathcal{C}_2}{u^2}} \right]_1^{1/\chi^2} \\
\frac{\Sigma^{\mathrm{surf}}}{\bar{\sigma}} &= \frac{\mathcal{A}}{6\sqrt{3}} \frac{\chi^3 - 3\chi + 2}{\chi w}
\end{aligned} \tag{36}$$

where

$$\mathcal{C}_1 = \mathcal{A}^2 + \frac{\mathcal{B}^2}{2} \quad , \quad \mathcal{C}_2 = \mathcal{A}^2 + \mathcal{B}^2 + 8$$

Remark: Equation (35) retrieves Eq's (23) and (26) of [4] for the special case of a cylindrical cell with a circular cross section. Thereupon, it can be easily verified that

$$\begin{aligned}
\frac{\Sigma^{\mathrm{vol}}}{\bar{\sigma}} &= \frac{1}{\sqrt{3}} \left(2 - \sqrt{1 + 3\chi^4} + \ln \frac{1 + \sqrt{1 + 3\chi^4}}{3\chi^2} \right) \\
\frac{\Sigma^{\mathrm{surf}}}{\bar{\sigma}} &= \frac{1}{3\sqrt{3}} \frac{\chi^3 - 3\chi + 2}{\chi w}
\end{aligned} \tag{37}$$

With the approximation employed in Sec. 2.4.2, Σ^{vol} for a non-homothetic cell would have the same expression as stated in $(36)_1$ except for introducing $\bar{\mathcal{A}}$ and $\bar{\mathcal{B}}$ into the equation in lieu of $\mathcal{A}$ and $\mathcal{B}$, respectively. The surface dissipation, however, can be calculated analytically. With reference to Eq. (24):

$$\begin{aligned}
\frac{\Pi^{\mathrm{surf}}}{\bar{\sigma}} &= \frac{|D_{33}|}{4\pi L^2 h\sqrt{3}} \int_R^L \int_0^{2\pi} (L^2 - r^2)(\mathcal{A}(r) + \mathcal{B}(r)\cos 2\theta) dr d\theta \\
&= \frac{|D_{33}|}{24\sqrt{3}\,\chi(1-\chi)w} \left[3(1 + \chi - 2\chi^2)(\mathcal{A}_{\mathrm{c}} - \mathcal{A}_{\mathrm{v}}) + 4(\chi^3 - 3\chi + 2)(\mathcal{A}_{\mathrm{v}} - \mathcal{A}_{\mathrm{c}}\chi) \right] \\
\Sigma^{\mathrm{surf}} &= \frac{\Pi^{\mathrm{surf}}}{|D_{33}|}
\end{aligned} \tag{38}$$

which clearly simplifies into $(36)_2$ in the case of a homothetic cell.

3 Model under Combined Tension and Shear

Following [30, 31], the velocity field in the reference cell corresponding to combined triaxial and shear loadings should satisfy the following constraints:

$$\begin{cases}
v_r(L,\theta,z)\mathbf{e}_r + v_\theta(L,\theta,z)\mathbf{e}_\theta &= \frac{2z}{c}\left(D_{31}\mathbf{e}_1 + D_{32}\mathbf{e}_2\right) & (-h \le z \le h; 0 \le \theta \le 2\pi) \\
v_z(r,\theta,\pm h) &= \pm D_{33} H & (0 \le r \le L; 0 \le \theta \le 2\pi) \\
[\![\mathbf{v}]\!].\mathbf{n} &= 0 & \forall \mathbf{x} \in S_{\mathrm{int}}
\end{cases} \tag{39}$$

which, in its simplest form, along with the incompressibility condition (div $\mathbf{v} = 0$), is fulfilled by the following Gurson-like velocity only emanating from the shear field (in the ligaments only):

$$\mathbf{V}^{\mathrm{sh}}(\mathbf{x}) = \frac{2z}{c}\left(D_{31}\mathbf{e}_1 + D_{32}\mathbf{e}_2\right) \tag{40}$$

which should be supplemented to the expansion field in (6), and c has been defined in advance. The capital notation in $\mathbf{V}$ denotes the reference cell. Since, however, (40) is directly expressed in terms of the covariant (here Cartesian) coordinates (see $(7)_2$), the same field can be employed in the cell with an elliptical cross section. That is

$$\mathbf{v}^{\mathrm{sh}} = \mathbf{V}^{\mathrm{sh}}$$

which can further be transformed into contravariant (cylindrical) coordinates as

$$\begin{aligned} v_r^{\mathrm{sh}} &= \frac{2z}{c}\left(D_{31}\cos\theta + D_{32}\sin\theta\right) \\ v_\theta^{\mathrm{sh}} &= \frac{2z}{c}\left(-D_{31}\sin\theta + D_{32}\cos\theta\right) \end{aligned} \tag{41}$$

which corresponds to the following strain-rate components, the rest proving zero:

$$\begin{aligned} d_{rz}^{\mathrm{sh}} = d_{zr}^{\mathrm{sh}} &= \frac{1}{c}\left(D_{31}\cos\theta + D_{32}\sin\theta\right) \\ d_{z\theta}^{\mathrm{sh}} = d_{\theta z}^{\mathrm{sh}} &= \frac{1}{c}\left(-D_{31}\sin\theta + D_{32}\cos\theta\right) \end{aligned} \tag{42}$$

The corresponding equivalent strain rate can be derived from the combined effect of expansion and shear fields in the double contraction, expressed as follows:

$$\mathbf{d} : \mathbf{d} = \mathbf{d}^{\mathrm{e}} : \mathbf{d}^{\mathrm{e}} + 2\mathbf{d}^{\mathrm{e}} : \mathbf{d}^{\mathrm{sh}} + \mathbf{d}^{\mathrm{sh}} : \mathbf{d}^{\mathrm{sh}} = \mathbf{d}^{\mathrm{e}} : \mathbf{d}^{\mathrm{e}} + \mathbf{d}^{\mathrm{sh}} : \mathbf{d}^{\mathrm{sh}} \tag{43}$$

since the nonzero terms in $\mathbf{d}^{\mathrm{sh}}$ are only off-diagonal. Therefore, the steps to solve this problem are identical to those in [30, 31], which lead to the following piecewise function

$$\left(\frac{|\Sigma_{33}| - \Sigma^{\mathrm{surf}}}{\Sigma^{\mathrm{vol}}}\right)^2 \mathcal{H}(|\Sigma_{33}| - \Sigma^{\mathrm{surf}}) + \frac{\Sigma_{31}^2 + \Sigma_{32}^2}{\mathcal{T}^2} - 1 = 0 \tag{44}$$

where $\mathcal{H}(x)$ is the Heaviside function, admitting a unit value when $x > 0$ and zero otherwise. $\mathcal{T}$ is the shear stress at zero axial stress (*i.e.* the maximum shear stress), which obeys the following expression

$$\mathcal{T} = (1 - \chi_1\chi_2)\bar{\tau} \equiv \frac{S_{\mathrm{lig}}}{S}\bar{\tau} \tag{45}$$

where $\bar{\tau} = \bar{\sigma}/\sqrt{3}$ is the matrix shear strength, and S_{lig} and S denote the cross sectional areas pertaining to the ligament and the whole cross section, respectively. Noting that $\chi_1\chi_2 = f_{\mathrm{b}}$ sets the porosity in the band, Eq. (45) follows a simple linear rule of mixture between the yield stresses of the matrix and the void. The shear field employed herein delivers sensible stresses at intermediate shear stresses. At intense shear fields, however, it proves inadequate esp. for closer-by voids along the shear field, as later showcased in Sec. 6.2.

4 Model Synopsis

The yield criterion accounting for void coalescence under combined tension and shear in a microstructure represented by a cylindrical unit cell with elliptical void and cell is hereby repeated for ease of reference:

$$\Phi(\boldsymbol{\Sigma}, \chi_1, \chi_2, w_1, w_2, \alpha_{\rm v}, \alpha_{\rm c}) = \left(\frac{|\Sigma_{33}| - \Sigma^{\rm surf}}{\Sigma^{\rm vol}}\right)^2 \mathcal{H}(|\Sigma_{33}| - \Sigma^{\rm surf}) + \frac{\Sigma_{31}^2 + \Sigma_{32}^2}{\mathcal{T}^2} - 1 \qquad (46)$$

with $\mathcal{H}(x)$ being the Heaviside step function (with $\mathcal{H}(x) = 1$ for $x > 1$, $\mathcal{H}(x) = 0$ for $x < 0$, and $\mathcal{H}(0) = 1/2$), and

$$\chi_i = \frac{R_i}{L_i} \quad , \quad w_i = \frac{h}{R_i}$$
$$\alpha_{\rm v} = \frac{R_1}{R_2} \quad , \quad \alpha_{\rm c} = \frac{L_1}{L_2}$$

with i taking in the values of 1 and 2. Among the geometric arguments, only four of them are independent and need be prescribed. They are adopted to be $(\chi_1, \chi_2, w_1, \alpha_{\rm c})$ in the present context. The rest follow from these independent parameters as

$$w_2 = \frac{\chi_1}{\chi_2}\alpha_{\rm c} w_1$$
$$\alpha_{\rm v} = \frac{\chi_{\rm min}}{\chi_{\rm max}}\alpha_{\rm c}$$

and

$$w^2 = \frac{\chi_1}{\chi_2}\alpha_{\rm c} w_1^2$$
$$\chi^2 = \chi_1\chi_2$$

are the geometric average values that are inserted into the following microstructural functions:

$$\frac{\Sigma^{\rm vol}}{\bar{\sigma}} = \frac{1}{2\sqrt{3}}\left[\sqrt{\mathcal{C}_1}\ln\left(4u\sqrt{\mathcal{C}_1}\left[\sqrt{\mathcal{C}_1} + \sqrt{\mathcal{C}_1 + \frac{\mathcal{C}_2}{u^2}}\right]\right) - \sqrt{\mathcal{C}_1 + \frac{\mathcal{C}_2}{u^2}}\right]_1^{1/\chi^2}$$
$$\frac{\Sigma^{\rm surf}}{\bar{\sigma}} = \frac{1}{24\sqrt{3}\,\chi(1-\chi)w}\left[3(1+\chi-2\chi^2)(\mathcal{A}_{\rm c} - \mathcal{A}_{\rm v}) + 4(\chi^3 - 3\chi + 2)(\mathcal{A}_{\rm v} - \mathcal{A}_{\rm c}\chi)\right]$$
$$\frac{\mathcal{T}}{\bar{\sigma}} = \frac{1-\chi^2}{\sqrt{3}}$$

where

$$\mathcal{A}_{\rm v} = \sqrt{\frac{\alpha_{\rm v}\chi_{\rm min}}{\chi_{\rm max}}} + \sqrt{\frac{\chi_{\rm max}}{\alpha_{\rm v}\chi_{\rm min}}} \quad , \quad \mathcal{B}_{\rm v} = \left|\sqrt{\frac{\alpha_{\rm v}\chi_{\rm min}}{\chi_{\rm max}}} - \sqrt{\frac{\chi_{\rm max}}{\alpha_{\rm v}\chi_{\rm min}}}\right|$$
$$\mathcal{A}_{\rm c} = \sqrt{\alpha_{\rm c}} + \frac{1}{\sqrt{\alpha_{\rm c}}} \quad , \quad \mathcal{B}_{\rm c} = \sqrt{\alpha_{\rm c}} - \frac{1}{\sqrt{\alpha_{\rm c}}}$$
$$\bar{\mathcal{A}} = \frac{\mathcal{A}_{\rm v} + \chi\mathcal{A}_{\rm c}}{1+\chi} \quad , \quad \bar{\mathcal{B}} = \frac{\mathcal{B}_{\rm v} + \chi\mathcal{B}_{\rm c}}{1+\chi}$$
$$\mathcal{C}_1 = \bar{\mathcal{A}}^2 + \frac{\bar{\mathcal{B}}^2}{2} \quad , \quad \mathcal{C}_2 = \bar{\mathcal{A}}^2 + \bar{\mathcal{B}}^2 + 8$$

and, upon convention, $\chi_{\rm min} = \min(\chi_1, \chi_2)$ and $\chi_{\rm max} = \max(\chi_1, \chi_2)$. The $\alpha_{\rm c} \geq 1$ is implied in the definition of $\mathcal{B}_{\rm c}$.

5 Cell-Model Calculations

The FEM analysis framework in this section is an extension to that introduced in [31] for a quarter cylindrical cell with a circular cross section, here taken as reference. The current cell with an elliptical cross section is then generated from a function that maps the reference mesh into a new mesh with inner and outer boundaries being elliptical. Similar to [31], the analysis framework is of a single-step small-strain finite-element identity [18]. The *elastic* strain rates would then vanish at the limit load instant. This would make the results disassociated with elastic moduli, which could be chosen arbitrarily. Correspondingly, an incompressible velocity field would be induced by plastic deformation. To this end, a high value of Poisson's ratio should be enforced (here $\nu = 0.49$), which renders the matrix material nearly isochoric elastic-perfectly-plastic. The ratio between the yield strength to Young's modulus is taken $\bar{\sigma}/E = 0.0002$. ABAQUS (Version 6.17) was employed to carry out analyses, with the geometric nonlinearity (NLGEOM) switched off.

Note that periodicity equations cannot be directly applied to pairs of points in a cylindrical cell for it being not space-filling, and thus such pairs that can obey periodicity do not exist. However, similar conditions can be imposed that mimic periodic conditions, thus its name "quasi-periodic". For any two points admitting periodic correspondence:

$$\Delta\mathbf{u} = (\mathbf{E} + \mathbf{\Omega}).\Delta\mathbf{x} \tag{47}$$

where $\Delta\mathbf{u}$ is the difference in displacement between the points separated by the vector $\Delta\mathbf{x}$. The remote stresses that correspond to the cell yield point are not known from the outset. Therefore, a macroscopic strain $\mathbf{E}$ (representing a strain rate) should be enforced on the cell represented with

$$\mathbf{E} = E_{11}(\mathbf{e}_1 \otimes \mathbf{e}_1 + \mathbf{e}_2 \otimes \mathbf{e}_2) + E_{33}\mathbf{e}_3 \otimes \mathbf{e}_3 + E_{31}(\mathbf{e}_1 \otimes \mathbf{e}_3 + \mathbf{e}_3 \otimes \mathbf{e}_1) + E_{32}(\mathbf{e}_2 \otimes \mathbf{e}_3 + \mathbf{e}_3 \otimes \mathbf{e}_2) \tag{48}$$

or in matrix form

$$\mathbf{E} = \begin{bmatrix} E_{11} & 0 & E_{31} \\ 0 & E_{22} & E_{32} \\ E_{31} & E_{32} & E_{33} \end{bmatrix}$$

where

$$\begin{aligned} E_{11} &= \ln\left(\frac{L_1}{L_{10}}\right) \approx \frac{U_1}{L_{10}} \\ E_{22} &= \ln\left(\frac{L_2}{L_{20}}\right) \approx \frac{U_2}{L_{20}} \\ E_{33} &\equiv \ln\left(\frac{H}{H_0}\right) \approx \frac{U_3}{H_0} \\ E_{31} &\equiv \frac{U_{t1}}{2H_0} \\ E_{32} &\equiv \frac{U_{t2}}{2H_0} \end{aligned} \tag{49}$$

Here, U_1 and U_2 denote prescribed displacements (representing velocities) on the lateral vertical lines passing through all points standing on $(x_1, x_2) = (L_1, 0)$ and $(x_1, x_2) = (0, L_2)$, respectively (see Appendix B for details). The displacements for interlain points should be distributed in conformity with the ellipse equation. See Eq. (11).

Moreover, U_3 as well as U_{t1} and U_{t2} are, respectively, the normal and tangential displacements (along x_1 and x_2) prescribed on the top surface. The stress components emanating from the imposed strains are calculated from volumetric averaging over the entire cell (see [31] for details).

On the other hand, the macroscopic rotation tensor must be of the form:

$$\mathbf{\Omega} = \Omega_{31}(\mathbf{e}_3 \otimes \mathbf{e}_1 - \mathbf{e}_1 \otimes \mathbf{e}_3) + \Omega_{32}(\mathbf{e}_3 \otimes \mathbf{e}_2 - \mathbf{e}_2 \otimes \mathbf{e}_3) \tag{50}$$

which, in simplest sense, can be taken $\mathbf{\Omega} = \mathbf{0}$. However, this would trigger a vertical displacement on the lateral surface, which can be averted by considering $\Omega_{13} = -\Omega_{31} = E_{31}$ and $\Omega_{23} = -\Omega_{32} = E_{32}$.

The periodic boundary conditions (47) can then be expressed as

$$\begin{Bmatrix} \Delta u_1 \\ \Delta u_2 \\ \Delta u_3 \end{Bmatrix} = \begin{bmatrix} E_{11} & 0 & 2E_{31} \\ 0 & E_{11} & 2E_{32} \\ 0 & 0 & E_{33} \end{bmatrix} \begin{Bmatrix} \Delta x_1 \\ \Delta x_2 \\ \Delta x_3 \end{Bmatrix} \tag{51}$$

which are further replaced by the quasi-periodic conditions as follows

- On the top surface, $\Delta\mathbf{u} = \mathbf{u}(x_1, x_2, H) - \mathbf{u}(x_1, x_2, -H)$ and $\Delta\mathbf{x}^T = \{0, 0, 2H\}$ so that:

$$\begin{cases} \Delta u_1 = 4E_{31}H \\ \Delta u_2 = 4E_{32}H \\ \Delta u_3 = 2E_{33}H \end{cases} \tag{52}$$

- On the plane Ox_1x_3,

$$u_2(x_1, 0, x_3) = 0 \tag{53}$$

- On the plane Ox_2x_3,

$$u_1(0, x_2, x_3) = 0 \tag{54}$$

- On the lateral surface ($x_1^2/L_1^2 + x_2^2/L_2^2 = 1$, $-H \leq x_3 \leq H$) multi-point constraints are imposed so that the nodes lying on a semi-ellipse remain on a similar semi-ellipse with major and minor radii consistent with the prescribed values of E_{11} and E_{22}. That is

$$\begin{aligned} &\mathbf{u}_1^{\text{ref}}(x_1, x_2, x_3) = U_1 \cos\theta \quad , \quad \mathbf{u}_2^{\text{ref}}(x_1, x_2, x_3) = U_2 \sin\theta \\ &\left(\frac{x_1}{L_1}\right)^2 + \left(\frac{x_2}{L_2}\right)^2 = 1 \end{aligned} \tag{55}$$

  where $\mathbf{u}_i^{\text{ref}}$ are the displacements of some reference node on the semi-circle at some height x_3. Then, at $\mathbf{x}^T = \{L_1, 0, x_3\}$ noting $\Delta\mathbf{u} = \mathbf{u}(x_1, x_2, x_3) - \mathbf{u}^{\text{ref}}$, one can write:

$$\begin{cases} \Delta u_1 = E_{11}(x_1 - L_1) \\ \Delta u_2 = E_{22}x_2 \\ \Delta u_3 = 0 \end{cases} \tag{56}$$

  Correspondingly, at $\mathbf{x}^T = \{0, L_2, x_3\}$:

$$\begin{cases} \Delta u_1 = E_{11}x_1 \\ \Delta u_2 = E_{22}(x_2 - L_2) \\ \Delta u_3 = 0 \end{cases} \tag{57}$$

Remark: To simulate coalescence states, lateral strain rates, here represented with lateral strains, should be prevented, *i.e.* $E_{11} = E_{22} = 0$, hence $U_1 = U_2 = 0$.

The mesh for every unit cell is generated through a mapping correspondence from the reference cell with circular cross sections. The method is hereby explained for two types of cells: homothetic and non-homothetic, the latter entailing a two-step mapping. In all configurations, L_1 and H were kept equal to 1, and the remaining dimensions were dictated by the prescribed values of $\chi_1, \chi_2, w_1, \alpha_c$, as defined in Sec. 2.1. An example mesh for a non-homothetic cell, with $(\chi_1, \chi_2, w_1, \alpha_c) = (0.6, 0.267, 1, 4)$, is shown in Fig. 4.

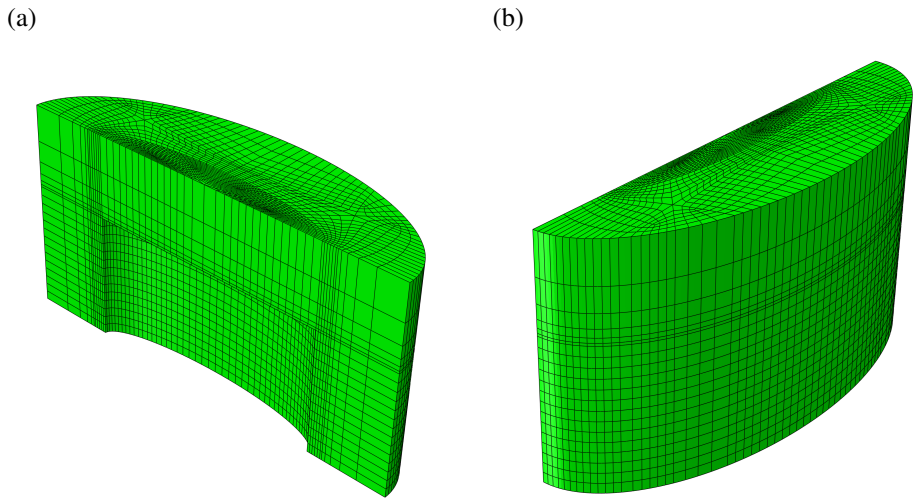

Figure 4: Example mesh for a non-homothetic cell with its geometry identified by $(\chi_1, \chi_2, w_1, \alpha_c) = (0.6, 0.267, 1, 4)$: (a) frontward inclined view; (b) backward inclined view.

5.1 Cells under triaxial loading

5.1.1 Homothetic cells

The meshes for homothetic cells were created originally for a reference cylindrical cell with circular cross sections, a unit outer radius $L = 1$, and specific values of void height h emanating from w_1. Denoting small and capital alphabets for the current and reference cells, respectively, with reference to Eq. (11):

$$x_1 = rL_1 \cos\theta \quad , \quad x_2 = rL_2 \sin\theta \tag{58}$$

where $r = \sqrt{X_1^2 + X_2^2}$ and $\tan\theta = X_2/X_1$ are the radius and angle (with respect to the X_1 positive direction) of every node in the reference configuration.

The plastic strain contours for example geometries with varying α_c, various $\chi_1 = \chi_2$, and several w_1's are shown in the subsequent figures. Figure 5 shows different contours under triaxial loading for varying values of α_c and fixed values of other parameters given as $\chi_1 = \chi_2 = 0.4$ and $w_1 = 1$.

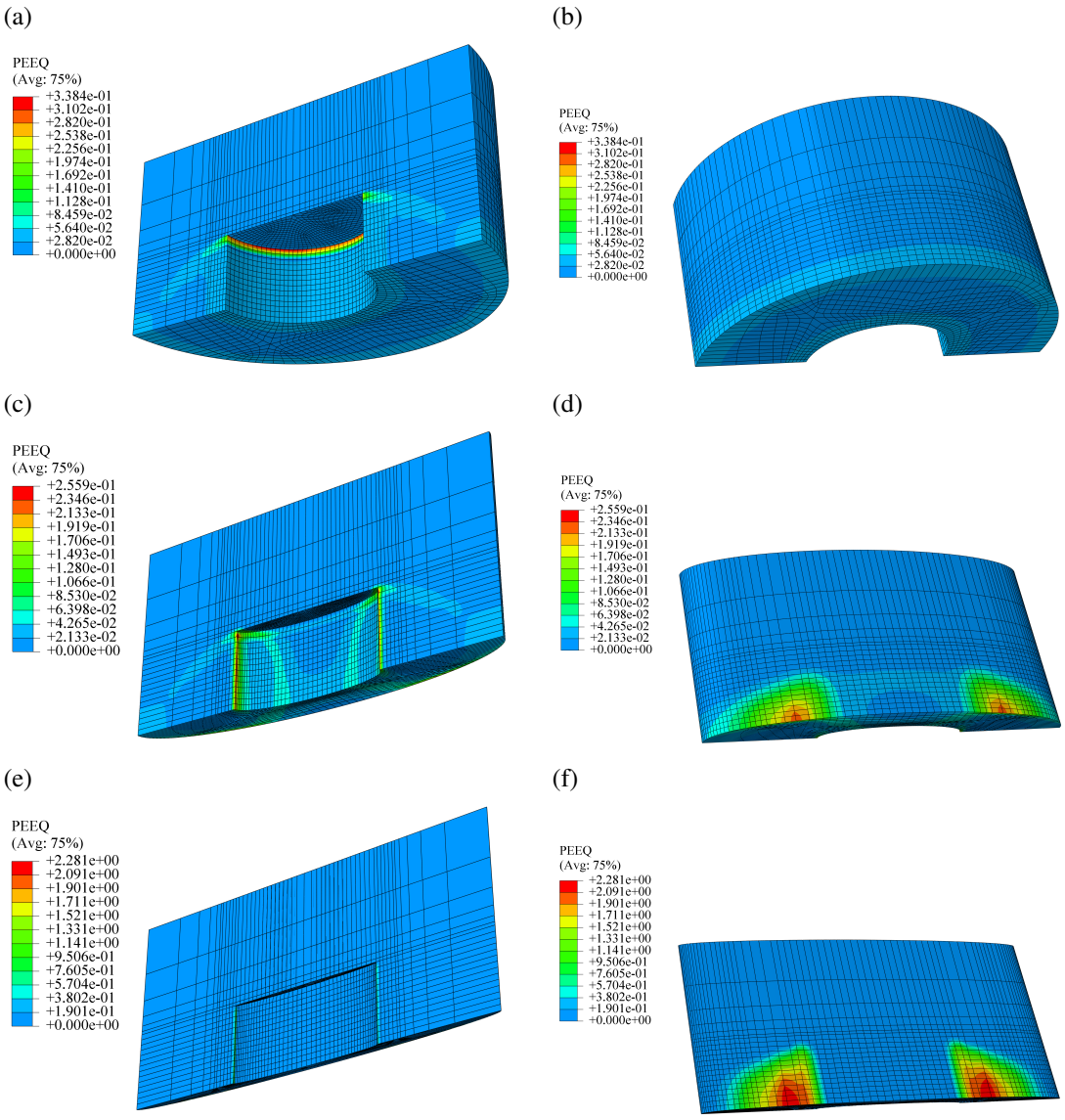

Figure 5: PEEQ (equivalent plastic strain) contours on cell quarters for varying values of α_c and fixed values of other parameters specified as $\chi_1 = \chi_2 = 0.4$ and $w_1 = 1$: (a,c,e) frontward inclined views, with α taken as 1, 4, and 16; (b,d,f) backward inclined views.

Figure 6 shows different contours under triaxial loading for varying values of $\chi_1 = \chi_2$ chosen to be 0.25, 0.4, and 0.6 (left-hand subfigures, with $w_1 = 1$) or various values of w_1 taken 0.5, 1, and 2 (right-hand subfigures, with $\chi_1 = \chi_2 = 0.4$) and $\alpha_c = 2$ kept fixed.

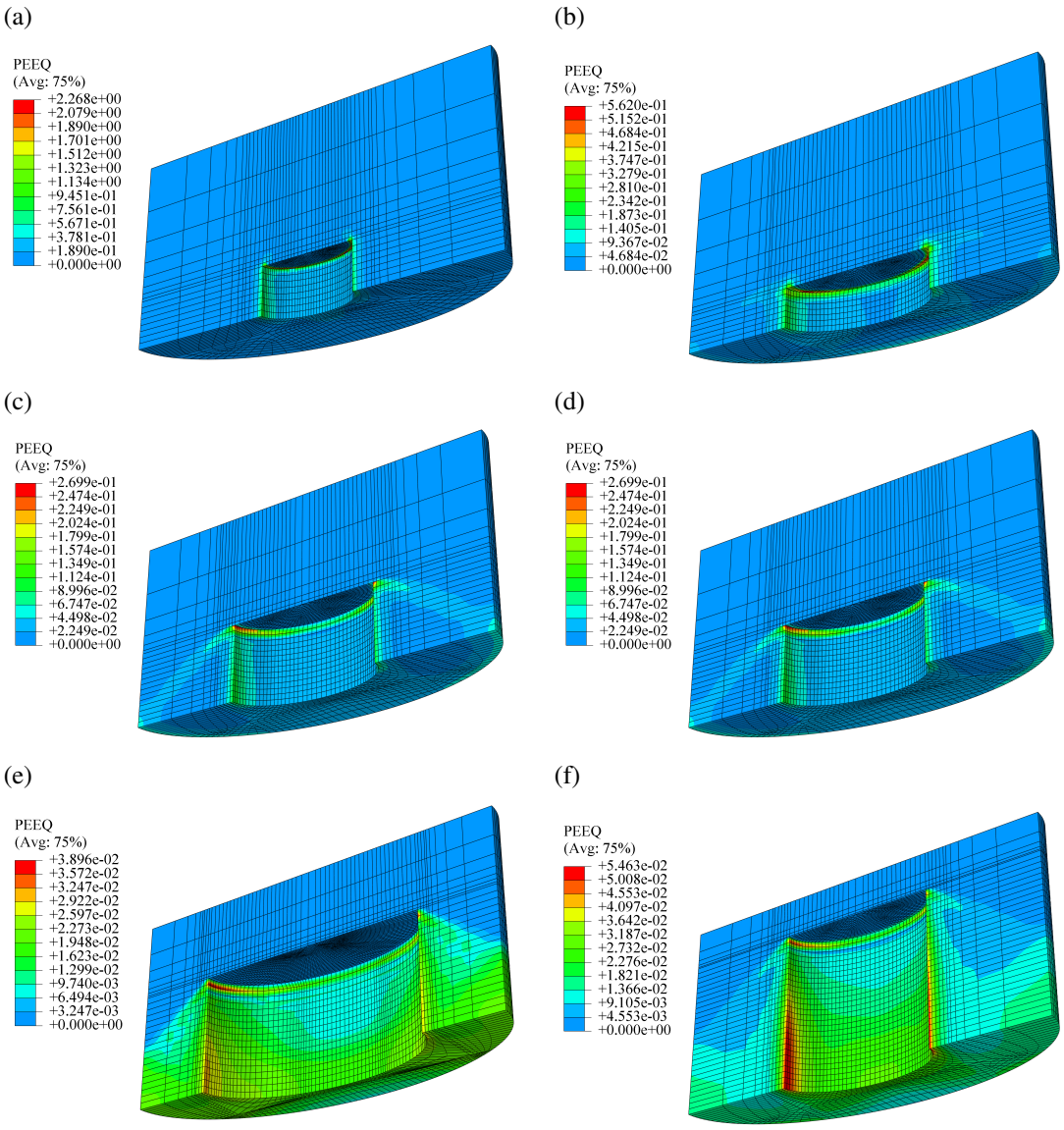

Figure 6: PEEQ (equivalent plastic strain) contours on cell quarters for $\alpha_c = 2$ kept fixed and: (a,c,e) varying values of $\chi_1 = \chi_2$, with $w_1 = 1$; (b,d,f) various values of w_1, with $\chi_1 = \chi_2 = 0.4$.

5.1.2 Non-homothetic cells

Extra care should be taken in meshing a non-homothetic cell based on a reference cell. To this end, the cell can be subdivided into sub-regions with different mapping conditions. Appendix A illustrates details about this multi-regional mapping. Figure 7 shows different contours under triaxial loading for varying values of χ_1, with $\chi_1\chi_2 = \chi^2$ staying constant to 0.16, and fixed values of other parameters given as $w_1 = 1$ and α_c taken as 1 or 2.

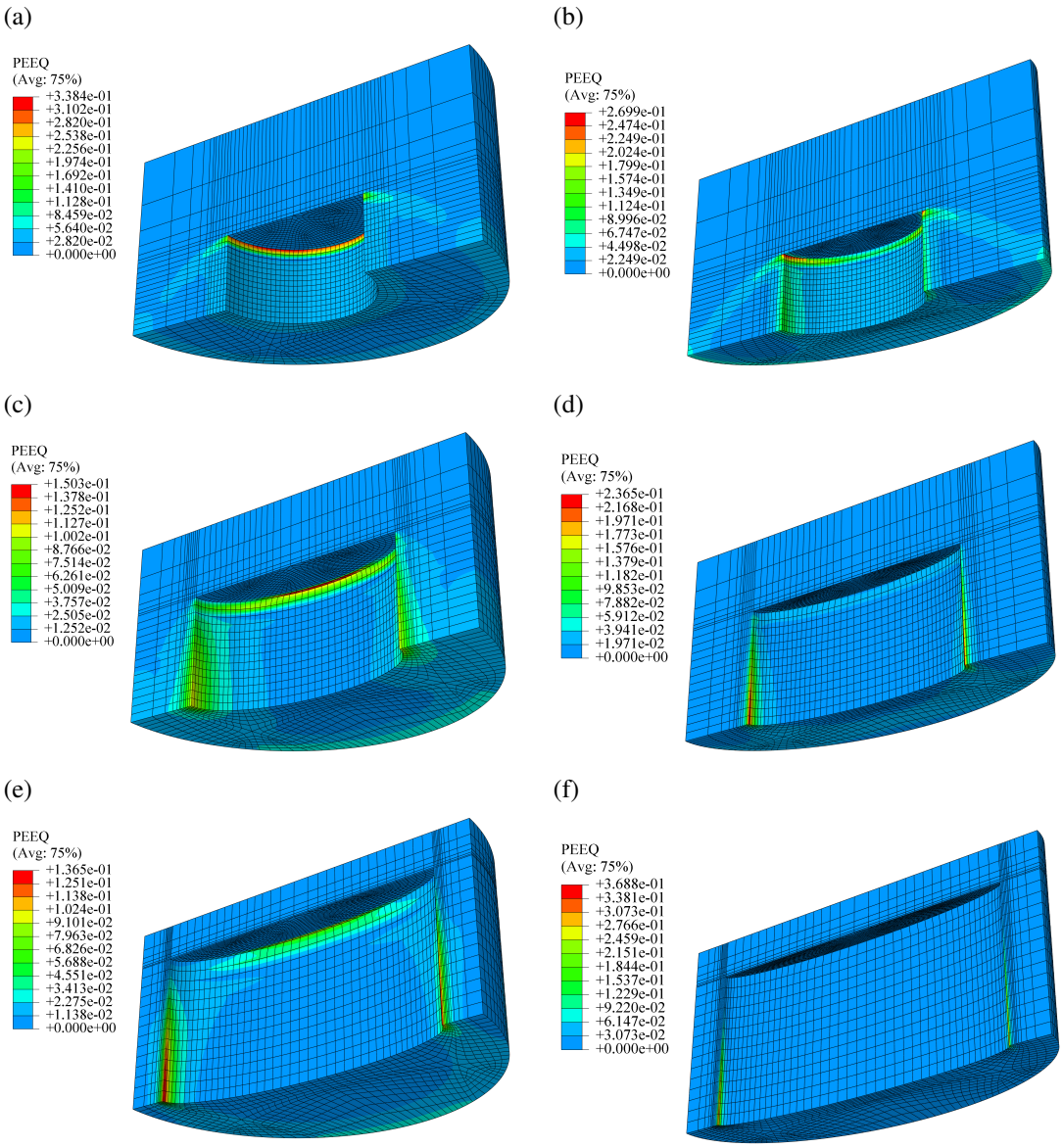

Figure 7: PEEQ (equivalent plastic strain) contours on cell quarters for varying values of χ_1, taken as 0.4, 0.6, and 0.8 with $\chi_1\chi_2 = 0.16$ fixed, and specified values of other parameters given as $w_1 = 1$ and α_c taken as 1 or 2: (a,c,e) $\alpha_c = 1$; (b,d,f) $\alpha_c = 2$.

5.2 Cells under combined loading

This section exhibits velocity contour plots under combined tension and shear in the interest of better clarity. The contours are shown with a cut-off in plastic strains so as to highlight the most intense plastic zones only. Figure shows the velocity fields for values of α_c being below unity (1/4), unity, and above unity (16) for tensile, combined tensile and shear, and intense shear loading conditions.

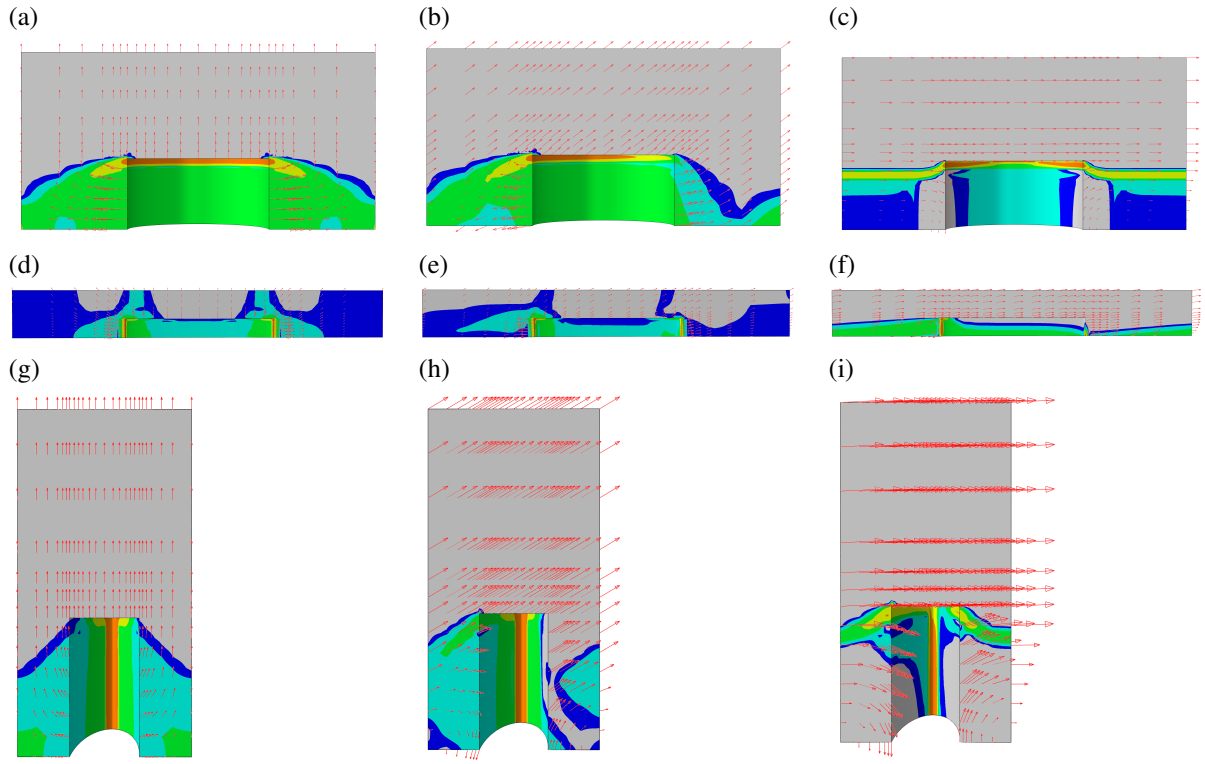

Figure 8: Velocity vectors, accompanied by PEEQ showcasing highly-plastic zones on cell quarters for $\chi_1 = \chi_2 = 0.4, w_1 = 1$ and various values of α_c values under tensile, combined tensile and shear, and intense shear loading conditions: (a-c) $\alpha_c = 1$ (reference cell); (d-f) $\alpha_c = 16$ with shearing along x_1; (g-i) $\alpha_c = 4$ with shearing along x_2.

6 Results

The results are presented for prescribed values of $(\chi_1, \chi_2, w_1, \alpha_c)$ as formerly defined. For homothetic cells, $\chi_1 = \chi_2 = \chi$ and $\alpha_v = \alpha_c = \alpha$ are prescribed in addition to w_1, and w_2 as well as χ and w will come as geometric averages as stated in (46). All results are presented with $\lambda_1 = 1$, though being directly ineffective.

6.1 Results in absence of shear

Figure 9 depicts the variation of the axial yield load vs. the α ratio for a homothetic cell, in comparison to its numerical counterparts for selective α's. Subfigures (a) and (b) show evolutions with several values of $\chi_1 = \chi_2 = \chi$ and w_1, respectively.

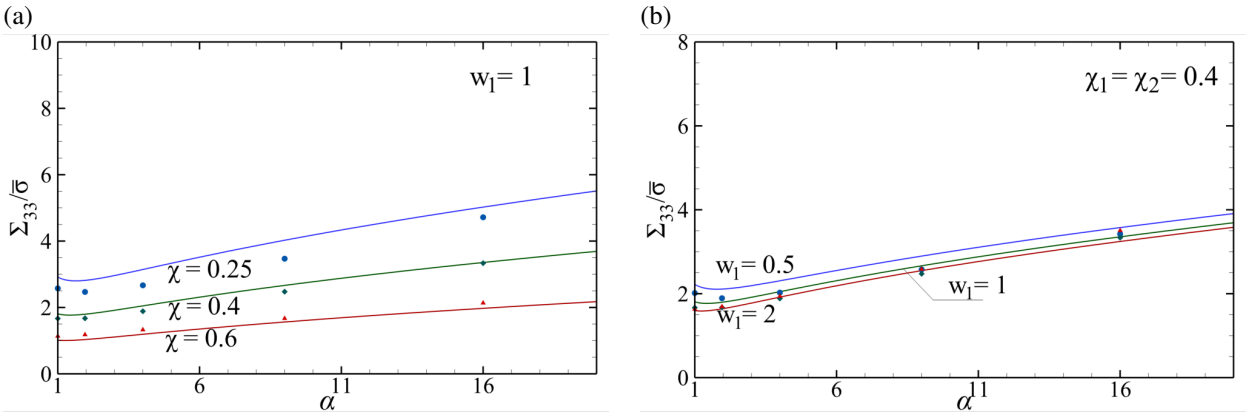

Figure 9: Evolution of axial yield load vs. the α ratio for a homothetic cell, in comparison to its numerical counterparts and (a) several $\chi_1 = \chi_2 = \chi$'s with $w_1 = 1$; (b) several w_1's with $\chi = 0.4$. The solid lines stand for analytical values, and the dots show numerical ones from cell-model calculations.

Alternatively, the variation of the yield load as function of the void spacing and void aspect ratio, *i.e.* against the values of $\chi_1 = \chi_2 = \chi$ and w_1 (with effective w obtained from (34)), for several values of the α ratio, is shown in Fig. 10 for a homothetic cell. The curves for a circular cross section stand below those for $\alpha > 1$ (and, correspondingly, for $\alpha < 1$).

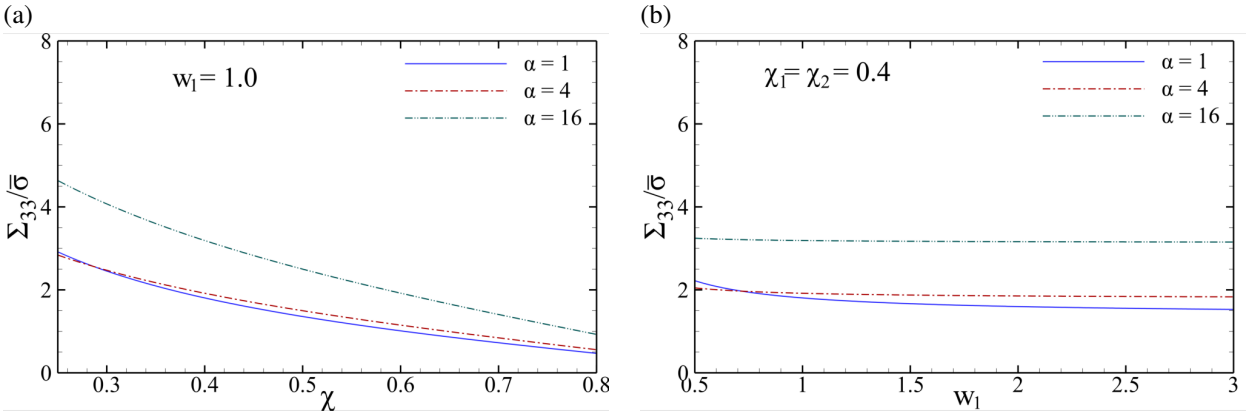

Figure 10: (a) Effect of $\chi_1 = \chi_2 = \chi$, (b) effect of w_1 on the axial yield load for a homothetic cell with $\chi = 0.4$ and several values of the α ratio.

All the same, similar results can be presented for non-homothetic cells, with arbitrary values of χ_1 and χ_2 and, correspondingly, arbitrary α_v and α_c. For convenience, χ_1 and χ_2 are chosen such that the effective spacing χ, according to (8), stays constant, equaling 0.4 in the present context. Figure 11 demonstrates the effect of χ_1, ranging from 0.4 to 0.8, on the evolution of the yield load against the α_c ratio.

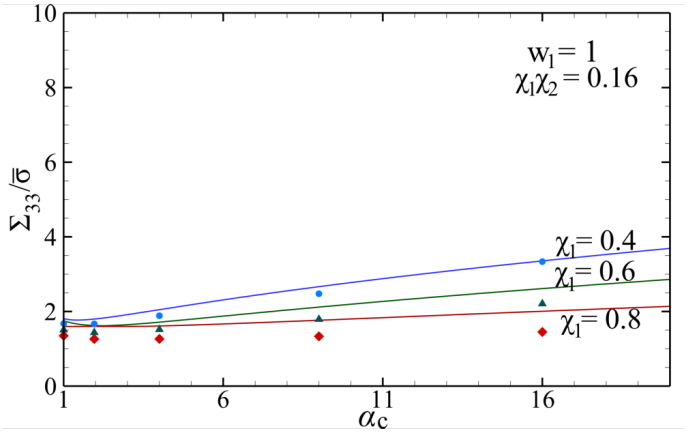

Figure 11: (a) Effect of different χ_1 values, ranging from 0.4 to 0.8, while $\chi = 0.4$ and $w_1 = 1$, on the evolution of the yield load against the α_c ratio. The solid lines stand for analytical values, and the dots show numerical ones from cell-model calculations.

6.2 Results under combined tension and shear

For the state of combined tension and shear, the results are presented for homothetic cells (for arbitrary cells, they will be similar). The shear stress is once applied along x_1 and once along x_2, one being the semi-major and the other being the semi-minor axis. Figure 12 shows the correlation of normal and shear stresses for the aforesaid conditions and several values of the α ratio.

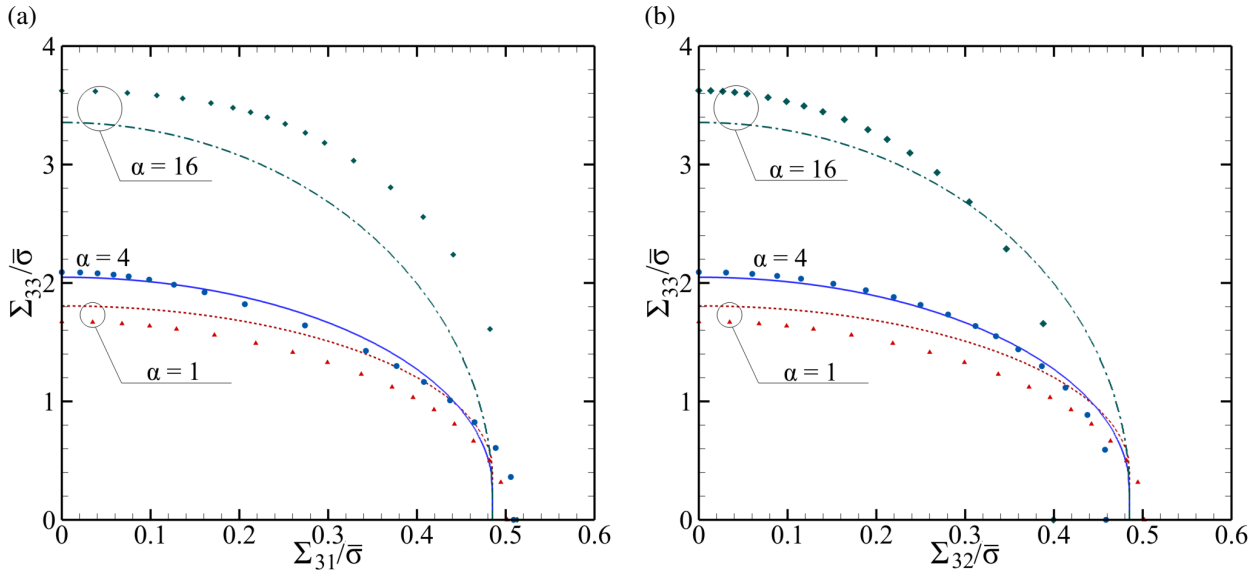

Figure 12: Correlation between normal and shear stresses for a homothetic cell with $\chi = 0.4$ and $w_1 = 1$ with several values of α: (a) under shearing applied along x_1 (major axis); (b) under shearing applied along x_2 (major axis). The solid lines stand for analytical values, and the dots show numerical ones from cell-model calculations.

In order to have a better insight into the yield surface, the yield surface can be presented in the Σ_{33}–Σ_{31}–Σ_{32} stress space, as shown in Fig. 13 for the homothetic cell with frozen microstructure denoted with $\chi = 0.4$ and $w_1 = 1$ and several values of α. Symmetry with respect to the Σ_{31} and Σ_{32} is envisaged.

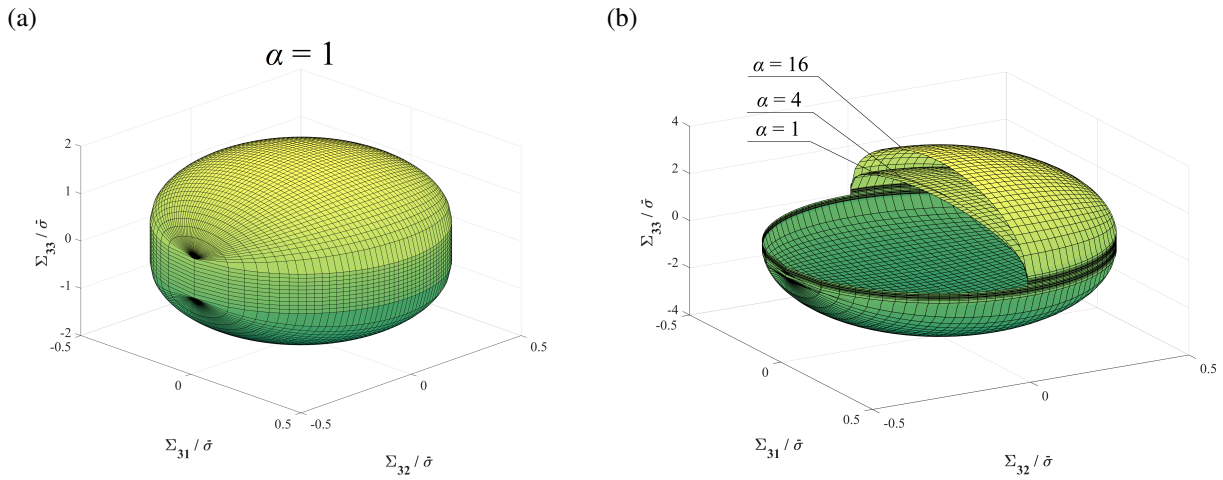

Figure 13: Correlation among Σ_{33}, Σ_{31}, and Σ_{32} for a homothetic cell with $\chi = 0.4$ and $w_1 = 1$: (a) reference cell with a circular cross section; (b) effect of the α ratio selected below, equal, and above 1. The latter surfaces are shown partially for better clarity of the effect.

7 Discussion

In accordance with both analytical and numerical results, the minimum limit load, in almost all geometric configurations, corresponds to $\alpha_c = 2$ rather than the circular cross section denoted by $\alpha_c = 1$. Beyond this point, for $\alpha_c \geq 2$, the axial limit load increases with increasing α_c which increases the overall stiffness of the cross section and makes void impingement harder. Figure 5 exhibits the reason for this as being the increasing lateral constraint on the central part of the cell, which renders the ligament stiffer and harder to yield. The higher stiffness can further be witnessed along with decreasing $\chi_1 = \chi_2$ as well as decreasing w_1, in Fig. 6. This corroborates the increase in the limit load with both decreasing trends. Figure 7 demonstrates that, even at fixed effective ligament parameter χ, increasing χ_1 decreases the *net* spacing between two adjacent voids, and thus impingement would be accelerated altogether. Figure 11 authenticates this observation.

Comparing subfigures 9a and 9b reveals that the predicted analytical limit loads are in sensible agreement with their exact counterparts, being mindful of the fact that the model does not incorporate any adjustable parameters. However, differences may become more notable in some cases. Due to the use of the approximation introduced in (31), the model loses its upper-bound nature at large values of χ. Yet, the coincidence between the values is better in this case in that the analytical and numerical values get closer.

Regarding the effects induced by the microstructural geometry, the effect of void spacing χ at fixed w_1, reflected through the notion of porosity, is more pronounced in the yield load compared to the effect of the void aspect ratio along one of the two axes, here w_1. The reason is the former affects the yield condition in the whole ligament domain whereas the latter only influences the surface dissipation. Nevertheless, for very small void aspect ratios, though not shown here, when the effective aspect ratio w falls below 0.5 (approaching the limit of a penny-shape crack), the model erroneously overpredicts the yield limit since coalescence by *internal necking* is certainly questionable. See [30] for further discussion on the singular behavior of the model in this limit.

A closer scrutiny of the model demonstrates that, through the introduction of $\bar{\mathcal{A}}$ and $\bar{\mathcal{B}}$, Σ^{vol} is symmetric modulo α_c being smaller or greater than 1. The difference between the limit loads pertaining to $\alpha_c < 1$ and $\alpha_c > 1$ is then attributed to Σ^{surf} through the notion of w which, according to (34), scales with α_c at fixed

w_1. A larger value of α_c would then increase the limit load via increasing Σ^{surf}, as seen in Fig. 10a. Figure 10b, ratifies this finding through the effect of w_1 on the coalescence load at a fixed χ. This observation is physically intuitive in the sense that the larger the value of α_c, the sooner the two adjacent voids can impinge in the direction where w is fixed (here w_1) since less strain energy has to be dissipated from velocity jumps between the ligament and matrix.

Figure 11 demonstrates that, at fixed effective void spacing χ and w in one direction (here w_1), the closest upper bound to numerical limit loads pertains to a homothetic cell. Yet, the difference between analytical and numerical values remains reasonable even at intense differences between χ_1 and χ_2. At the limit of $(\chi_1, \chi_2) \longrightarrow (1, \chi^2)$, ellipticity of the cell (through the notion of α_c) would not remarkably affect the limit load after the value of 1, the reason being the only normalized intervoid distance influencing the yield point is $\chi_2 = \chi^2$ which stays almost constant regardless of the α_c ratio (this observation is corroborated by numerical findings). At this limit, the voids have to impinge along both directions, and thus, the limit load value is finite rather than zero. See Fig. 14a.

For α_c values below 1, the cell can be be represented with an equivalent geometry with $\alpha_c > 1$ but flipping χ_1 and χ_2. This would deliver a larger limit load since the impingement of voids along x_2 is obviously a lot more demanding, as shown in Fig. 14b.

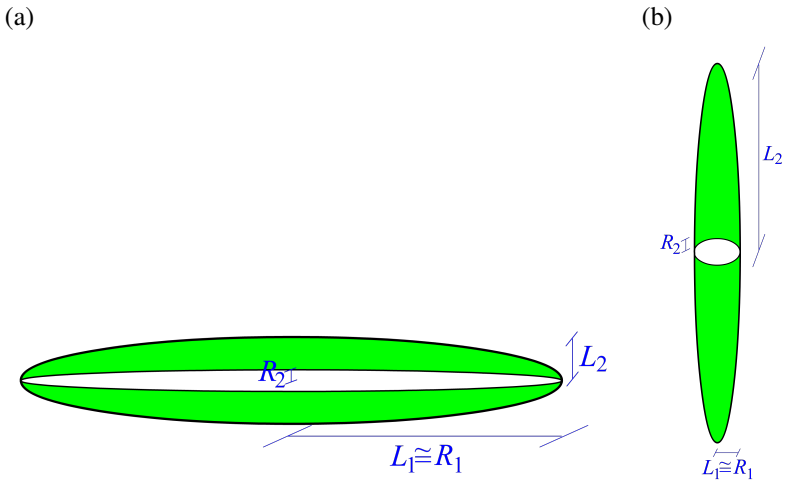

Figure 14: Schematic outline of extremely non-homothetic cells when the void boundaries reach out to the cell boundaries along x_1: (a) $\alpha_c >> 1$; (b) $\alpha_c << 1$.

Apropos of the combined effect of tension and shear, one can envisage, in Fig. 12, that the numerical yield surface for $\alpha_c >> 1$ lies (mostly) exterior to its analytical counterpart, yet with a reasonable difference. For smaller values of α_c, however, the analytical yield surface is (mostly) an upper bound to its numerical counterpart, still with reasonable difference.

Moreover, Fig. 8 demonstrates that, for a shear stress applied along the major axis, the maximum shear stress $\mathcal{T}$, *i.e.* the shear limit load at zero axial stress, stays almost constant considering the rather even distribution of shear strains/velocities. For shearing along the minor axis, however, some normal strain (and stress) is developed in the form of local vortices around the void. As a consequence, $\mathcal{T}$, especially for larger values of α_c, decreases with increasing α_c. Nevertheless, $\mathcal{T}$ in the analytical model is agnostic to the shearing direction. This reveals the limitation of the simplistic Gurson-like shear field developed based on a linear shear velocity profile along the vertical direction in both directions. The constraint warrants a more realistic shear velocity profile that can take into account the effects induced by the cell shape (considering the present discussion) as well as the void shape (considering the limitation elucidated in [31]).

8 Concluding Remarks

This article presents the steps to introduction of an analytical yield criterion endowed with normalized geometric parameters to describe void coalescence under arbitrary loading conditions (represented with combined tension and shear loads) in ductile solids with arbitrary microstructures (represented with 3D voids embedded in 3D matrix cells). The only stress components affecting void coalescence by internal necking and/or internal shearing over a given localization plane are the axial and shear resolved tractions [30]. The microstructure was approximately represented with a 3D cylindrical elementary cell with an elliptical cross section and a coaxial cylindrical void. The model was derived from limit analysis on the cell subjected to combined tension and shear with a J_2 plasticity confined to inter-void ligaments. The model was derived in three stages: (*i*) model for a homothetic cell, characterized with equal void normalized spacing along the major and minor cell axes, under triaxial loading; (*ii*) model for a non-homothetic cell, characterized with independent void normalized spacing along the axes, under triaxial loading; (*iii*) model for a non-homothetic cell under combined tension and shear. Upon a similar approximation employed in the derivations to that introduced in [30], the model appears as an extended counterpart of that introduced in the same reference, and thus retrieves the same model at the limit of cells with circular cross sections.

The predictive capability of the model was assessed by comparing the analytical limit loads with their numerical counterparts for selective geometric cases resulting from single-step limit analysis FEM calculations over the same cells under quasi-periodic boundary conditions. The generic microstructure was uniquely identified with four dimensionless parameters termed $(\chi_1, \chi_2, w_1, \alpha_c)$, signifying the normalized void spacing along the two main cell axes, void aspect ratio along one main axis, and the ratio between the main cell semi-axes, respectively. The results were presented under tensile as well as combined tensile and shear loading conditions. The former set of results then comprised the axial limit load examining the separate or combined effects of each and every microstructural parameter. All the same, the combined state of tensile and shear loads was introduced with a yield locus displaying the correlation between axial and shear stresses. Following a simple linear velocity profile, the maximum shear stress (in absence of axial loading) was predicted as being agnostic to the shearing direction. The exact numerical values, however, did exhibit some difference mainly for the case of shearing applied along the minor axis of the cell.

Acknowledgments

The theoretical part of the present work has been, in part, directed by Prof. J. Walton, a professor of Mathematics at Texas A&M University. The authors would like to acknowledge his smart contribution.

Appendix A Mapping for Non-homothetic Cell Meshing

In order to reproduce the mesh for a non-homothetic cell from a reference cell with circular cross sections, the cell can be subdivided into the sub-regions shown in Fig. A-1.

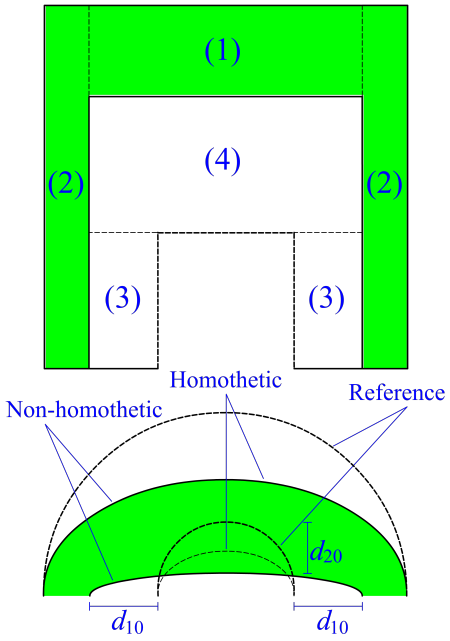

Figure A-1: Various zones with different mapping functions for mesh generation of non-homothetic cells, and the cross section for each region.

The nodes are firstly mapped into a homothetic cell from the reference cylindrical cell (with circular cross sections), and are then mapped from the homothetic cell into a non-homothetic one with a secondary mapping. The initial mapping produces regions (1) and (2), and the secondary mapping generates regions (3) and (4). Upon a similar procedure leading to (58), the mapping functions for each and every region will be written as follows:

– Zone (1)

$$\begin{aligned} x_1^{(1)} &= \frac{R_1}{R} r\cos\theta = \sqrt{\alpha_{\rm v}}\, r\cos\theta \\ x_2^{(1)} &= \frac{R_2}{R} r\sin\theta = \frac{1}{\sqrt{\alpha_{\rm v}}} r\sin\theta \end{aligned} \tag{A-1}$$

where $r = \sqrt{X_1^2 + X_2^2}$ and $\tan\theta = X_2/X_1$ with capital notations defined in advance, and $\alpha_{\rm v}$ is obtained from (21).

– Zone (2)

With a linear transformation between the reference and non-homothetic voids, the void boundary still remains elliptical. The distance between the nodes on reference and non-homothetic void surfaces

can be expanded as a linear function of the known distances d_{10} and d_{20} which can be stated in the following equivalent form:

$$d_1 = (\chi - \chi_1)\left(-1 + \frac{\frac{r}{L} - \chi}{1 - \chi}\right) L_1 \cos\theta$$
$$d_2 = (\chi - \chi_2)\left(-1 + \frac{\frac{r}{L} - \chi}{1 - \chi}\right) L_2 \sin\theta$$

which delivers the coordinates of the non-homothetic nodes as

$$\begin{aligned} x_1^{(2)} &= \left[(\chi - \chi_1)\left(-1 + \frac{\frac{r}{L} - \chi}{1 - \chi}\right) + \frac{r}{L}\right] L_1 \cos\theta \\ x_2^{(2)} &= \left[(\chi - \chi_2)\left(-1 + \frac{\frac{r}{L} - \chi}{1 - \chi}\right) + \frac{r}{L}\right] L_2 \sin\theta \end{aligned} \tag{A-2}$$

– Zone (3)

This zone only differs in the vertical coordinates from zone (2). In fact, from the homothetic to the non-homothetic cell, w_1 has to stay constant, and thus, the void height should be adjusted with respect to the reference cell. To this end, one can write

$$x_3^{(3)} = \frac{x_3^{(\mathrm{v})}}{X_3^{(\mathrm{v})}} X_3$$

where the subscript (v) stands for the void boundary. Moreover

$$x_3^{(\mathrm{v})} = w_1 R_1 = w_1 \chi_1 L_1$$
$$X_3^{(\mathrm{v})} = wR = w\chi L$$

Since, however, L_1 has been considered equal to L in the mapping, the above derivations, together with (34), write

$$\begin{aligned} x_1^{(3)} &= x_1^{(2)} \quad , \quad x_2^{(3)} = x_2^{(2)} \\ x_3^{(3)} &= \frac{1}{\chi\sqrt{\alpha_{\mathrm{c}}}} X_3 \end{aligned} \tag{A-3}$$

– Zone (4)

Zone (4) is similar to zone (3) in differing in the vertical component with respect to zone (2). For this zone:

$$\begin{aligned} x_1^{(4)} &= x_1^{(2)} \quad , \quad x_2^{(4)} = x_2^{(2)} \\ x_3^{(4)} &= (\chi - \chi_1)\left(-1 + \frac{X_3 - \chi}{H - \chi}\right) + X_3 \end{aligned} \tag{A-4}$$

Since $L_1 = L = H = 1$ has been considered in the configurations, some of the above equations simplify.

Appendix B Quasi-Periodic Boundary Conditions on the Unit Cell

This section expounds the boundary conditions imposed on a quarter of the unit cell in more specific equations. The independent degrees of freedom, appearing as prescribed displacements, are reflected by an axial U_3 and a tangential U_{t2} displacement at each center-line. It should be noted that U_{t2} is the only possible tangential displacement that can preserve the quasi-periodicity boundary conditions provided only one quarter of the cell is modeled, or else symmetry with respect to the $x_2 - x_3$ plane will be broken. Therefore, in the case that shearing along x_1 is desired, the modeled configuration should rotate by 90 degrees such that the modeled x_2 represents the desired x_1. The various surfaces and edges of the computational domain are schematized in Fig. A-2.

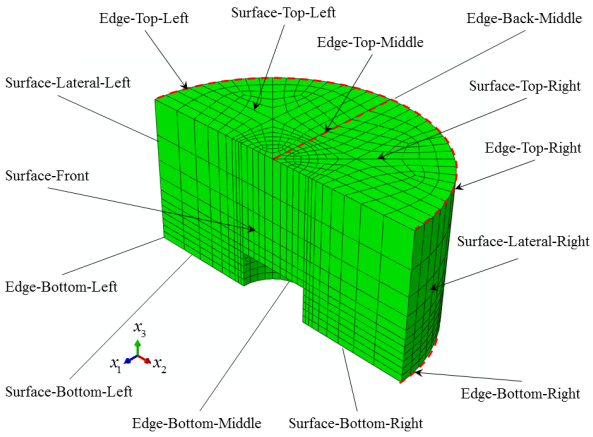

Figure A-2: Various surfaces and edges over a finite-element mesh for one quarter of an example unit cell with its geometry denoted with microstructural parameters given as $(\chi_1, \chi_2, w_1) = (0.6, 0.267, 1.0)$, with the coordinate origin standing at the void center in the undeformed configuration.

Edge-Top-Middle

$$\begin{aligned} u_2(x_1, 0, H) &= \frac{1}{2} U_{t2}, \\ u_3(x_1, 0, H) &= \frac{1}{2} U_3. \end{aligned} \tag{A-5}$$

Surface-Top-Left/Surface-Top-Right

$$\begin{aligned} u_1(x_1, -x_2, H) - u_1(x_1, x_2, H) &= 0, \\ u_2(x_1, -x_2, H) + u_2(x_1, x_2, H) &= U_{t2}, \\ u_3(x_1, -x_2, H) + u_3(x_1, x_2, H) &= U_3. \end{aligned} \tag{A-6}$$

Edge-Top-Left/Edge-Top-Right

$$\begin{aligned} u_1(x_1, -\sqrt{L_2^2 - (\frac{x_1}{\alpha_c})^2}, H) &= u_1(x_1, \sqrt{L_2^2 - (\frac{x_1}{\alpha_c})^2}, H) = \frac{x_1}{2L_1} U_1, \\ u_2(x_1, \pm\sqrt{L_2^2 - (\frac{x_1}{\alpha_c})^2}, H) &= \frac{1}{2}\left(U_{t2} \pm \sqrt{1 - (\frac{x_1}{L_1})^2}\, U_2\right), \\ u_3(x_1, \pm\sqrt{L_2^2 - (\frac{x_1}{\alpha_c})^2}, H) &= \frac{1}{2} U_3. \end{aligned} \tag{A-7}$$

Surface-Lateral-Left/Surface-Lateral-Right

$$\begin{aligned} u_1(x_1, -\sqrt{L_2^2 - (\frac{x_1}{\alpha_c})^2}, x_3) = u_1(x_1, \sqrt{L_2^2 - (\frac{x_1}{\alpha_c})^2}, x_3) &= \frac{x_1}{2L_1} U_1, \\ u_2(x_1, -\sqrt{L_2^2 - (\frac{x_1}{\alpha_c})^2}, x_3) - u_2(x_1, \sqrt{L_2^2 - (\frac{x_1}{\alpha_c})^2}, x_3) &= -\sqrt{1 - (\frac{x_1}{L_1})^2}\, U_2, \\ u_3(x_1, -\sqrt{L_2^2 - (\frac{x_1}{\alpha_c})^2}, x_3) - u_3(x_1, \sqrt{L_2^2 - (\frac{x_1}{\alpha_c})^2}, x_3) &= 0. \end{aligned} \tag{A-8}$$

Edge-Bottom-Left/Edge-Bottom-Right

$$\begin{aligned} u_1(x_1, -\sqrt{L_2^2 - (\frac{x_1}{\alpha_c})^2}, 0) &= u_1(x_1, \sqrt{L_2^2 - (\frac{x_1}{\alpha_c})^2}, 0) = \frac{x_1}{2L_1} U_1, \\ u_2(x_1, \pm\sqrt{L_2^2 - (\frac{x_1}{\alpha_c})^2}, 0) &= \pm\frac{1}{2}\sqrt{1 - (\frac{x_1}{L_1})^2}\, U_2, \\ u_3(x_1, \pm\sqrt{L_2^2 - (\frac{x_1}{\alpha_c})^2}, 0) &= 0. \end{aligned} \tag{A-9}$$

Edge-Bottom-Middle

$$\begin{aligned} u_2(x_1, 0, 0) &= 0, \\ u_3(x_1, 0, 0) &= 0. \end{aligned} \tag{A-10}$$

Surface-Bottom-Left/Surface-Bottom-Right

$$\begin{aligned} u_1(x_1, -x_2, 0) - u_1(x_1, x_2, 0) &= 0, \\ u_2(x_1, -x_2, 0) + u_2(x_1, x_2, 0) &= 0, \\ u_3(x_1, -x_2, 0) + u_3(x_1, x_2, 0) &= 0. \end{aligned} \tag{A-11}$$

Edge-Back-Middle

$$u_1(-L_1, 0, x_3) = -\frac{1}{2} U_1. \tag{A-12}$$

Surface-Front

$$u_1(0, x_2, x_3) = 0. \tag{A-13}$$

where $\alpha_c = L_1/L_2$.

References

[1] I. Barsoum and J. Faleskog. Rupture mechanisms in combined tension and shear—-Micromechanics. *International Journal of Solids and Structures*, 44:5481–5498, 2007.

[2] A. A. Benzerga. Micromechanics of Coalescence in Ductile Fracture. *Journal of the Mechanics and Physics of Solids*, 50:1331–1362, 2002.

[3] A. A. Benzerga and J.-B. Leblond. Ductile fracture by void growth to coalescence. *Advances in Applied Mechanics*, 44:169–305, 2010.

[4] A. A. Benzerga and J.-B. Leblond. Effective Yield Criterion Accounting for Microvoid Coalescence. *Journal of Applied Mechanics*, 81:031009, 2014.

[5] R. M. Bowen and C. Wang. *Introduction to vectors and tensors*, volume 2. Courier Corporation, 2008.

[6] T-S. Cao, M. Mazière, K. Danas, and J. Besson. A model for ductile damage prediction at low stress triaxialities incorporating void shape change and void rotation. *International Journal of Solids and Structures*, 63:240–263, 2015.

[7] M. Dunand and D. Mohr. Effect of Lode parameter on plastic flow localization after proportional loading at low stress triaxialities. *Journal of the Mechanics and Physics of Solids*, 66:133–153, 2014.

[8] X. Gao, J. Faleskog, and C. F. Shih. Cell model for nonlinear fracture analysis - II. Fracture-process calibration and verification. *International Journal of Fracture*, 89:375–398, 1998.

[9] M. Gologanu, J.-B. Leblond, and J. Devaux. Approximate models for ductile metals containing non-spherical voids – case of axisymmetric prolate ellipsoidal cavities. *Journal of the Mechanics and Physics of Solids*, 41(11):1723–1754, 1993.

[10] M. Gologanu, J.-B. Leblond, G. Perrin, and J. Devaux. Recent extensions of Gurson's model for porous ductile metals. Part II: A Gurson-like model including the effect of strong gradients of macroscopic fields. In P. Suquet, editor, *Continuum Micromechanics*, pages 97–130. Springer–Verlag, 1995.

[11] A. L. Gurson. Continuum Theory of Ductile Rupture by Void Nucleation and Growth: Part I– Yield Criteria and Flow Rules for Porous Ductile Media. *Journal of Engineering Materials and Technology*, 99:2–15, 1977.

[12] S. M. Keralavarma. A multi-surface plasticity model for ductile fracture simulations. *Journal of the Mechanics and Physics of Solids*, 103:100–120, 2017.

[13] S. M. Keralavarma and A. A. Benzerga. A constitutive model for plastically anisotropic solids with non-spherical voids. *Journal of the Mechanics and Physics of Solids*, 58:874–901, 2010.

[14] J. Koplik and A. Needleman. Void growth and coalescence in porous plastic solids. *International Journal of Solids and Structures*, 24(8):835–853, 1988.

[15] Z. G. Liu, W. H. Wong, and T. F. Guo. Void behaviors from low to high triaxialities: Transition from void collapse to void coalescence. *International Journal of Plasticity*, 84:183–202, 2016.

[16] T. Luo and X. Gao. On the prediction of ductile fracture by void coalescence and strain localization. *Journal of the Mechanics and Physics of Solids*, 113:82–104, 2018.

[17] K. Madou and J.-B. Leblond. A Gurson-type criterion for porous ductile solids containing arbitrary ellipsoidal voids – II: Determination of yield criterion parameters. *Journal of the Mechanics and Physics of Solids*, 60:1037–1058, 2012.

[18] K. Madou and J.-B. Leblond. Numerical studies of porous ductile materials containing arbitrary ellipsoidal voids — I: Yield surfaces of representative cells. *European Journal of Mechanics*, 42:480–489, 2013.

[19] T. F. Morgeneyer and J. Besson. Flat to slant ductile fracture transition: Tomography examination and simulations using shear-controlled void nucleation. *Scripta Materialia*, 65:1002–1005, 2011.

[20] L. Morin, J.-B. Leblond, A. A. Benzerga, and D. Kondo. A unified criterion for the growth and coalescence of microvoids. *Journal of the Mechanics and Physics of Solids*, 97:19–36, 2016.

[21] K. Nahshon and J. W. Hutchinson. Modification of the Gurson Model for shear failure. *European Journal of Mechanics*, 27:1–17, 2008.

[22] K. L. Nielsen, J. Dahl, and V. Tvergaard. Collapse and coalescence of spherical voids subject to intense shearing: studied in full 3D. *International Journal of Fracture*, 177:97–108, 2012.

[23] K. L. Nielsen and V. Tvergaard. Ductile shear failure or plug failure of spot welds modelled by modified gurson model. *Engineering Fracture Mechanics*, 77(7):1031–1047, 2010.

[24] T. Pardoen and J. W. Hutchinson. An extended model for void growth and coalescence. *Journal of the Mechanics and Physics of Solids*, 48:2467–2512, 2000.

[25] C. Tekoğlu. Representative volume element calculations under constant stress triaxiality, lode parameter, and shear ratio. *International Journal of Solids and Structures*, 51:4544–4553, 2014.

[26] C. Tekoğlu, J.-B. Leblond, and T. Pardoen. A criterion for the onset of void coalescence under combined tension and shear. *Journal of the Mechanics and Physics of Solids*, 60:1363–1381, 2012.

[27] P. F. Thomason. Three–dimensional models for the plastic limit–loads at incipient failure of the intervoid matrix in ductile porous solids. *Acta Metallurgica*, 33:1079–1085, 1985.

[28] M. E. Torki. A unified criterion for void growth and coalescence under combined tension and shear. *International Journal of Plasticity*.

[29] M. E. Torki and A. Benzerga. A mechanism of failure in shear bands. *Extreme Mechanics Letters*.

[30] M. E. Torki, A. A. Benzerga, and J.-B. Leblond. On Void Coalescence under Combined Tension and Shear. *Journal of Applied Mechanics*, 82(7):071005, 2015.

[31] ME Torki, C. Tekoglu, J-B Leblond, and AA Benzerga. Theoretical and numerical analysis of void coalescence in porous ductile solids under arbitrary loadings. *International Journal of Plasticity*, 91:160–181, 2017.

[32] D. M. Tracey. Strain hardening and interaction effects on the growth of voids in ductile fracture. *Engineering Fracture Mechanics*, 3:301–315, 1971.

[33] V. Tvergaard. Influence of void nucleation on ductile shear fracture at a free surface. *Journal of the Mechanics and Physics of Solids*, 30:399–425, 1982.

[34] V. Tvergaard. Behaviour of voids in a shear field. *International Journal of Fracture*, 158:41–49, 2009.

[35] Viggo Tvergaard and Kim Lau Nielsen. Relations between a micro-mechanical model and a damage model for ductile failure in shear. *Journal of the Mechanics and Physics of Solids*, 58:1243–1252, 2010.

[36] F. J. Vernerey, W. K. Liu, B. Moran, , and G. B. Olson. A micromorphic model for the multiple scale failure of heterogeneous materials. *Journal of the Mechanics and Physics of Solids*, 56:1320–1347, 2008.

[37] W. H. Wong and T. F. Guo. On the energetics of tensile and shear void coalescences. *Journal of the Mechanics and Physics of Solids*, 82:259–286, 2015.

[38] L. Xue. Constitutive modeling of void shearing effect in ductile fracture of porous materials. *Engineering Fracture Mechanics*, 75:3343–3366, 2008.

P10 ON VOID COALESCENCE IN COLUMNS IN COMPETITION WITH COALESCENCE IN LAYERS

On Void Coalescence in Columns in Competition with Coalescence in Layers

M. E. Torki[1], F. A. Medrano[1], A. A. Benzerga[1,2], J.-B. Leblond[3]

[1] *Department of Aerospace Engineering, Texas A&M University, College Station, TX 77843, USA*

[2] *Department of Materials Science and Engineering, Texas A&M University, College Station, TX 77843, USA*

[3] *Sorbonne Universites, UPMC Univ Paris 06, CNRS, UMR 7190*

Institut Jean Le Rond d'Alembert, F-75005, Paris, France

Abstract

Void coalescence in columns (*necklace* coalescence) is a newly uncovered ductile fracture mechanism that has not been exhaustively investigated in the literature. An in-depth study into micromechanics-based modeling of necklace coalescence, per se and in competition to coalescence in layers, is addressed. The model is developed from homogenization on the same microstructure employed to predict void growth followed by coalescence in layers through a unified perspective [1]. Yet, the plastic deformation was rearranged so as to mimic plasticity localized within plastic plugs embedding the void. The model is formed as a yield function endowed with the effects induced by loading as well as void shape, cell shape, and relative intervoid distance. The predictive capability of the model is authenticated from successful comparison to reported results as well as to FEM values resulting from single-step cell-model calculations with a nearly-isochoric plastic process controlled by remotely prescribed normal and lateral strains. Yield surfaces accounting for void growth ensued by coalescence in columns and layers are plotted to probe the effects of the ligament parameter, void and cell aspect ratios. The innermost surface denoting the driving yielding mechanism is found to be fully determined by the microstructure. Besides, special plasticity mechanisms exist during the process prior to localized deformation. Amongst them are void growth associated with stagnation in the radial velocity, and vertically-localized plasticity with stagnation within the vertical velocity that could lead to so-called *void collapse* in certain microstructural states.

Key Words: Ductile fracture; Porous plasticity; Strain localization; Coalescence in layers; Coalescence in columns.

1 Introduction

During every ductile fracture process, localized plastic deformation is the most vivid indication of failure characteristics. This instant mostly correlates with the onset of drop in the stress bearing vs. equivalent plastic strain [2]. Except for quasi-brittle modes of failure (like that triggered by particle cracking, especially in aluminum composites consisting of soft matrices and hard particles [3]), there is significant plastic deformation at the post-localized deformation regime. Apart from being significant, plastic deformation demonstrates significant paradigm change in the damage mechanism after this onset, that can depend on various extrinsic factors such as the specimen geometry and matrix texture [4].

In exception for shear-dominated fields imparted on materials with vanishingly small porosities, whereby the voids elongate and rotate but may never link up [5] (except in case a shear band forms), strain localization is associated with incipient deformation-induced concentration of voids within thin planar layers or along beads (plugs) within thin cylindrical regions [2, 3]. The former is named *coalescence in layers* and the latter was termed *coalescence in columns* by Benzerga [3], and we will adhere to the same terminology throughout the present work. Void coalescence in layers, as most ambivalently observed in the form of *internal necking*, potentially combined with *internal shearing* [6], has been investigated extensively in the literature, starting from the pioneering work of Koplik and Needleman [7] that uncovered the constitutive properties of internal necking in accordance with evolution analyses of stress and strain, porosity, and void aspect ratio founded on cell-model calculations. In particular, the lateral strains cease to evolve, *i.e.* the lateral strain rates vanish throughout internal necking. The onset of internal necking has been predicted by virtue of the heuristic introduction of a porosity acceleration factor q to the Gurson model by Tvergaard and Needleman [8], later noted as the *Tvergaard parameter*. Thomason [9] carried out the first attempt to introduce a descriptive model for the onset of internal necking through the assessment of some plastic limit load in the intervoid ligament in a square-prismatic RVE containing a prismatic void with a square basis. His RVE consisted of rigid zones above and below the void with plastic flow confined in between. Depending on the microstructure evolution scheme, Benzerga *et al.* [10] evaluated the performance of the various versions of Thomason's model. Later on, the void shape effect was investigated by Pardoen and Hutchinson [11] through the heuristic introduction of the void aspect ratio w as to extend Thomason's model to spheroidal voids. It remained for Benzerga and Leblond [12], Torki *et al.* [6, 13], and Keralavarma *et al.* [14] to deliver the first completely analytical line of models accounting, respectively, for internal necking, combined internal necking and shearing, with isotropic and anisotropic matrix materials. The first and foremost feature underlying the analytical nature of the aforementioned models is the use of a cylindrical RVE containing a coaxial cylindrical void. The same RVE was employed by Morin *et al.* [15] to relax the condition of zero lateral boundary strain rates to allow for void growth with seamless transition into coalescence by internal necking.

The distinction between coalescence in layers and columns is partly dictated by the loading condition, especially the prevalence of the axial-to-lateral stress or vice versa [2], and partly by the microstructure [16]. In a triaxial stress state, every value of stress triaxiality (defined as the ratio between the mean normal stress to the Mises equivalent stress) can be attributed to two loading conditions, one with a prevailing normal stress and one with the lateral stress being dominant. Therefore, stress triaxiality is not a revealing descriptor regarding this effect. Rather, the more distinctive macroscopic parameter is the Lode parameter, that mainly involves the third invariant of the stress tensor J_3. It is defined as $L = \sqrt{3}\tan\theta$, where θ is the well-known Lode angle utilized in the Haigh-Westergaard nondimensional stress space, admitting the relation $\cos 3\theta = (27/2)\det(\mathbf{\Sigma}'/\Sigma_e)$, with Σ_e being the Mises equivalent stress and uppercase letters used to denote remote macroscopic stresses [2]. Accordingly, coalescence in columns is known to prevail for a Lode parameter $L = +1$ (which represents predominant lateral stress) as well as for $L = -1$ (which implies the converse) and elongated voids. The latter was explored by Benzerga [3] in the peculiar distribution of voids in laminated plates, where the extremely prolate (elongated) voids were generated through decohesion of the metallic matrix circumscribing inclusions elongated by the rolling process. Yet, macroscopic load descriptors cannot capture the salient features of the fracture process at the microstructural level. This warrants the consideration of *mechanism-based* models that predict the limit load at the cell level in terms of the current microstructural state.

Gologanu *et al.* were the first and only ones who strove to develop a micromechanics-based model that could describe coalescence in columns [16, 17]. Their model was derived on the sole basis of re-homogenization on the homogenized plastic plugs surrounded by a solid torus. More specifically, they could not originate a closed-form yield condition that could describe a state of plasticity localized along the plugs. Rather, the model was left implicit with one independent arbitrary parameter (see Sec. 4.1 and [16]

for more details), any prescribed value of which clarified one pair of lateral and axial stress values at a specific porosity. Moreover, the only microstructural parameter they inserted in the model was porosity. As no other work of consequence is reported in this respect, the present work includes, yet is not limited to, two significant objectives: first to suggest a first-ever closed-form mathematical model capable of describing a state of coalescence in columns, in solo and in competition with an existing model predicting coalescence in layers; secondly to incorporate the effects induced by the microstructural geometry in addition to that of the stress state. The latter will be expressed in terms of the effects of the intervoid distance as well as by void and cell shapes on each yielding mechanism, which helps demonstrate the driving yielding mechanism exclusive to every microstructural state in a periodic medium.

2 Problem Statement

2.1 Microstructural geometry

Every micromechanical problem can be described through the definition of a reference volume element (RVE). The virtue of a proper choice of RVE is two-fold: describing the microstructural geometry of the problem as well as simulating the load and displacement boundary conditions. The RVE at hand, originally proposed by Benzerga and Leblond [12], had supplied the first analytical model accounting for coalescence in layers. The same RVE then proved efficacious in extending the model to incorporation of shear stresses [6, 13]. More extensively, the same RVE was utilized in interconnecting between void growth and coalescence under triaxial loading, alone [1] or superposed by shear (in a recent work by the first author). It can be shown, through the course of the present work, that the same RVE can be exploited in the derivation of an analytical model describing void coalescence in columns.

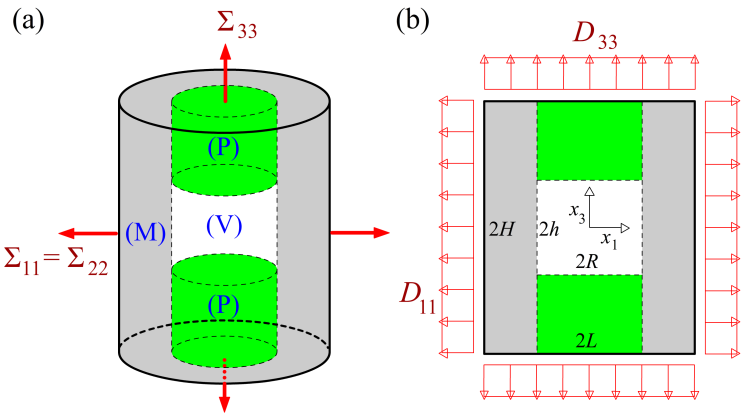

Figure 1: (a) Geometry of a cylindrical RVE representing column-like coalescence under a triaxial loading scheme; (b) lateral projection of the RVE with the induced geometry and macroscopic rate-of-deformation components belonging to each subpart.

The elementary volume Ω is a cylindrical cell embedding a coaxial cylindrical void ω, acted upon by macroscopic axial and lateral stresses as outlined in Fig. 1a [1]. Consider the RVE subdivision as shown in Fig. 1a. The overall volume can be then decomposed into the following constituents:

$$\Omega = V(\Omega) = \Omega^{(\mathrm{P})} + \Omega^{(\mathrm{V})} + \Omega^{(\mathrm{M})} \tag{1}$$

[1] Despite its being not space filling, the given RVE stands as a reasonable approximation of more complex geometries in periodic media, *e.g.* a circumscribing hexagonal-prismatic or a square-prismatic cell.

where the subparts (V), (P), and (M) stand for the void, the porous part (excluding the void), and the matrix tori, respectively.

The overall geometry of the RVE is then determined by the independent dimensionless parameters defined as follows:

$$\chi = \frac{R}{L} \quad , \quad w = \frac{h}{R} \quad , \quad \lambda = \frac{H}{L} \quad \therefore \quad c = \frac{h}{H} = \frac{\chi w}{\lambda} \tag{2}$$

where χ is the ligament parameter, w and λ are the void and cell aspect ratios, respectively, and the auxiliary parameter c serves as a control parameter whose value below unity ensures that the void stays within the confines of the cell.

2.2 Kinematic relations

The continuity from the macroscopic perspective entails that the following relationships hold among the macroscopic rates of deformation:

$$D_{33}^{(\mathrm{P+V})} = D_{33}^{(\mathrm{M})} = D_{33} \tag{3}$$

Moreover, with regards to tr$(\mathbf{D})$ one can write:

$$\begin{aligned} &D_{kk} = \frac{1}{\Omega}\int_{\Omega} d_{kk}\,\mathrm{d}\Omega = \frac{1}{\Omega}\left[\int_{\Omega} d_{kk}^{(\mathrm{P+V})}\,\mathrm{d}\Omega + \int_{\Omega} d_{kk}^{(\mathrm{M})}\,\mathrm{d}\Omega\right] \\ &\int_{\Omega} d_{kk}^{(\mathrm{M})}\,\mathrm{d}\Omega = \Omega^{(\mathrm{M})} D_{kk}^{(\mathrm{M})} = 0 \quad \therefore \quad D_{kk} = \chi^2 \int_{\Omega^{(\mathrm{P+V})}} d_{kk}^{(\mathrm{P+V})}\,\mathrm{d}\Omega = \chi^2 D_{kk}^{(\mathrm{P+V})} \end{aligned} \tag{4}$$

where $\Omega^{(\mathrm{P+V})}/\Omega = \chi^2$. Hence, exploiting (3), one could write:

$$D_{11}^{(\mathrm{P+V})} = \frac{D_{11}}{\chi^2} + \frac{1}{2}\left(\frac{1}{\chi^2} - 1\right) D_{33} \tag{5}$$

Due to the isochoric nature of every plastic process within a solid material, *i.e.* the (P) and (M) zones, $\mathbf{D}^{(\mathrm{P})}$ and $\mathbf{D}^{(\mathrm{M})}$ are traceless, whereas $\mathbf{D}^{(\mathrm{P+V})}$ does not lie in this category since it encloses a void. Therefore,

$$D_{kk}^{(\mathrm{M})} = 0 \quad \therefore \quad D_{11}^{(\mathrm{M})} = -\frac{D_{33}}{2} \tag{6}$$

2.3 Tentative velocity field

The isochoric nature of plasticity entails that $\Omega^{(\mathrm{P})}$ and $\Omega^{(\mathrm{M})}$ stay constant, and the following equation sets are analogous:

$$\Omega^{(\mathrm{P})} = \text{cte} \quad , \quad \Omega^{(\mathrm{M})} = \text{cte} \quad \therefore \quad d_{kk}^{(\mathrm{P})} = \mathrm{div}\mathbf{v}^{(\mathrm{P})} = 0 \quad , \quad d_{kk}^{(\mathrm{M})} = \mathrm{div}\mathbf{v}^{(\mathrm{M})} = 0 \tag{7}$$

The tori obey a Gurson-like velocity field, which reads:

$$\begin{aligned} &v_r^{(\mathrm{M})} = \frac{A}{r} - \frac{B}{2} r \quad , \quad v_z^{(\mathrm{M})} = Bz \\ &v_z^{(\mathrm{M})}(H) = BD_{33} \;\therefore\; B = D_{33} \quad , \quad v_r^{(\mathrm{M})}(L) = D_{11}L \;\therefore\; A = \frac{D_{kk}L^2}{2} \end{aligned} \tag{8}$$

The plugs, in the simplest-case scenario, admit the following form of v_r:

$$v_r^{(\mathrm{P})} = D_{11}^{(\mathrm{P+V})} r = \frac{1}{2\chi^2}\left(D_{kk} - \chi^2 D_{33}\right) r \tag{9}$$

Therefore, satisfying $v_r^{(\mathrm{P})}(R) = v_r^{(\mathrm{M})}(R)$ reassures a C^0-order continuity along the r direction. The z-wise velocity function should then be derived from a zero-divergence condition. Hence,

$$\mathrm{div}^{(\mathrm{P})} \equiv v_{r,r}^{(\mathrm{P})} + \frac{v_r^{(\mathrm{P})}}{r} + v_{z,z}^{(\mathrm{P})} = 0 \quad \therefore \quad v_z^{(\mathrm{P})} = -2D_{11}^{(\mathrm{P})} z + C(r) \tag{10}$$

Whilst there exist infinite solutions to $C(r)$, the highest-order solution that can give rise to a closed-form yield function is a constant parameter: $C(r) = C_0$. To find this constant parameter:

$$v_z^{(\mathrm{P})}(H) = D_{33}H \ \therefore \ C_0 = D_{kk}^{(\mathrm{P+V})}H \Longrightarrow v_z^{(\mathrm{P})} = \frac{1}{\chi^2}[D_{kk}(H-z) + \chi^2 D_{33} z] \tag{11}$$

One can easily observe that the derived $v_z^{(\mathrm{P})}$ is discontinuous with respect to z. While this distribution is contrary to reality, it proves feasible in the macroscopic scale provided the macroscopic dissipation induced by this discontinuity is affixed to the total dissipation function. This will be further clarified in Sec. 2.4.

A more realistic velocity field is created upon higher continuity induced by a higher-order choice of $v_z^{(\mathrm{P})}$. To this end, one can arbitrate the following field for $v_z^{(\mathrm{P})}$:

$$v_z^{(\mathrm{P})} = D_{33} z + 2\frac{D_{kk}}{\chi^2}(H-z)\left[1 - \left(\frac{r}{R}\right)^2\right] \tag{12}$$

which, upon satisfaction of $\mathrm{div}\mathbf{v} = 0$, delivers the following r component:

$$v_r^{(\mathrm{P})} = \frac{-r}{2}\left(D_{33} + \frac{D_{kk}}{\chi^2}\left[-2 + \left(\frac{r}{R}\right)^2\right]\right) \tag{13}$$

2.4 Effective dissipation

$\Pi(\mathbf{D})$, being the effective plastic dissipation, is the upper bound to the plastic power (*i.e.* work flow) through the fundamental inequality of limit analysis written as:

$$\forall\, \mathbf{D}, \quad \boldsymbol{\Sigma} : \mathbf{D} \leq \Pi(\mathbf{D}), \qquad \Pi(\mathbf{D}) = \inf_{\mathbf{v}\in\mathcal{K}(\mathbf{D})} \langle \sup_{\boldsymbol{\sigma}^*\in\mathcal{C}} \sigma_{ij}^* \, d_{ij} \, \rangle_\Omega + \frac{1}{\Omega}\int_S \sup_{\boldsymbol{\sigma}^*\in\mathcal{C}} t_i^* \, [\![v_i]\!] \, \mathrm{d}S \tag{14}$$

which sets a variational definition of the effective yield criterion for a porous material if the velocity field is discontinuous across an arbitrary interface S. $\langle\cdot\rangle_\Omega$ stands for averaging over Ω, $\mathcal{K}(\mathbf{D})$ is the set of kinematically admissible velocity fields that are compatible with $\mathbf{D}$, $\inf$ and $\sup$, respectively, represent the infimum and supremum over a set, and $\mathcal{C}$ is the microscopic reversibility domain with its boundary being the matrix yield surface $\bar{\sigma}$. Finally, $\mathbf{t}^*$ denotes the traction acting on its corresponding interface, and $[\![\mathbf{v}]\!]$ is the velocity discontinuity (*i.e.* jump) across the same interface.

On account of a J_2 flow theory, Π can be simplified into the following:

$$\Pi = \frac{1}{\Omega}\int_\Omega \bar{\sigma} d_{\mathrm{eq}} \, \mathrm{d}\Omega \quad , \quad d_{\mathrm{eq}} = \sqrt{\frac{2}{3}\mathbf{d} : \mathbf{d}} \tag{15}$$

where d_{eq} is a consequence of the velocity field associated with the infimum to the set of all kinematically admissible volumetric averages. The simplest admissible velocity field is, indeed, close to the minimum of

interest though it may not be the minimum itself. As such, it can be granted an infimum. With reference to the derivations in Sec. 2.3, d_{eq} can be obtained from the following components of $\mathbf{d}$:

$$\begin{aligned} d_{rr}^{(\mathrm{P})} &= v_{r,r}^{(\mathrm{P})} = D_{11}^{(\mathrm{P+V})} \\ d_{\theta\theta}^{(\mathrm{P})} &= \frac{v_r^{(\mathrm{P})}}{r} = d_{rr}^{(\mathrm{P})} \\ d_{zz}^{(\mathrm{P})} &= v_{z,z}^{(\mathrm{P})} = -2D_{11}^{(\mathrm{P+V})} \\ \therefore \quad d_{\mathrm{eq}}^{(\mathrm{P})} &= 2\left|D_{11}^{(\mathrm{P+V})}\right| \end{aligned} \tag{16}$$

in the minimum-continuity field and, by the same token,

$$d_{\mathrm{eq}}^{(\mathrm{P})} = \sqrt{\mathcal{R}}|D_{33}| \tag{17}$$

upon higher continuity, where

$$\mathcal{R} = \mathcal{U}_0 + 2\mathcal{U}_1 u + \mathcal{U}_2 u^2 \tag{18}$$

with $u = (r/L)^2$, and

$$\begin{aligned} \mathcal{U}_0 &= (\xi_1 - 1)^2 \\ \mathcal{U}_1 &= \xi_1 + \xi_1^2(\delta - 1) \\ \mathcal{U}_2 &= \frac{13}{12}\xi_1^2 \\ \xi &= \frac{D_{kk}}{D_{33}} \quad , \quad \xi_1 = 2\frac{\xi}{\chi^2} \\ \delta &= \frac{2}{3}\left(\frac{\lambda(1-v)}{\chi}\right)^2 \end{aligned} \tag{19}$$

Moreover,

$$\begin{aligned} d_{rr}^{(\mathrm{M})} &= v_{r,r}^{(\mathrm{M})} = -\frac{1}{2}\left(\frac{D_{kk}}{u} + D_{33}\right) \\ d_{\theta\theta}^{(\mathrm{M})} &= \frac{v_r^{(\mathrm{M})}}{r} = \frac{1}{2}\left(\frac{D_{kk}}{u} - D_{33}\right) \\ d_{zz}^{(\mathrm{M})} &= v_{z,z}^{(\mathrm{M})} = D_{33} \\ \therefore \quad d_{\mathrm{eq}}^{(\mathrm{M})} &= \sqrt{\frac{1}{3}\left(\frac{D_{kk}}{u}\right)^2 + D_{33}^2} \end{aligned} \tag{20}$$

Therefore, the layer-wise effective dissipations will turn out as

– Minimum continuity:

$$\Pi^{(\mathrm{P})} = \frac{1}{\Omega^{(\mathrm{P})}} \int_{\Omega^{(\mathrm{P})}} d_{\mathrm{eq}}^{(\mathrm{P})} \, \mathrm{d}\Omega = 2\left|D_{11}^{(\mathrm{P+V})}\right| \bar{\sigma} \tag{21}$$

Besides, the discontinuity between $v_z^{(\mathrm{P})}$ and $v_z^{(\mathrm{M})}$ promotes an additional term as stated parametrically in (14), rewritten herein as follows:

$$\Pi^{\mathrm{surf}} = \frac{1}{\Omega^{(\mathrm{P})}} \int_{S_{\mathrm{int}}} \bar{\tau} [\![\mathbf{v}]\!] \, \mathrm{d}S \tag{22}$$

where $\bar{\tau} = \bar{\sigma}/\sqrt{3}$ is the matrix shear strength in terms of the uniaxial yield strength, and $S_{\rm int}$ is the area of the interface connecting (P) and (M) at $r = R$. Then

$$\begin{aligned} [\![\mathbf{v}]\!]_{r=R} &= \left| v_z^{(\mathrm{P})} - v_z^{(\mathrm{M})} \right|_{r=R} = \frac{|D_{kk}|}{\chi^2}(H-z) \\ \therefore \quad \Pi^{\rm surf} &= \frac{1}{\pi R^2 (H-h)} \int_h^H \bar{\tau} [\![\mathbf{v}]\!] (2\pi R \, \mathrm{d}z) = \frac{w}{\chi^2} \frac{1-c}{c} |D_{kk}| \, \bar{\tau} \end{aligned} \tag{23}$$

– Higher continuity:

$$\Pi^{(\mathrm{P})} = \frac{|D_{33}| \, \bar{\sigma}}{1-c} \int_{v=c}^1 \mathcal{I} \, \mathrm{d}v \quad , \quad \mathcal{I} = \int_{u=0}^1 \sqrt{\mathcal{R}(u)} \, \mathrm{d}u \tag{24}$$

where $\mathcal{I}$ is fortunately calculable analytically. Since $\mathcal{U}_2 \geq 0$, the following integral will be admitted provided the following discriminant is positive [18]:

$$\Delta = \mathcal{U}_0 \mathcal{U}_2 - \mathcal{U}_1^2 > 0 \tag{25}$$

Then, the integral is expressible as follows:

$$\mathcal{I} = \frac{1}{2} \left[(u + \mathcal{B}) \sqrt{\mathcal{R}(u)} + \mathcal{P} \ln |\mathcal{L}| \right]_{u=0}^1 \tag{26}$$

where

$$\begin{aligned} \mathcal{B} &= \frac{\mathcal{U}_1}{\mathcal{U}_2} = \frac{12}{13} \left(\frac{1}{\xi_1} + \delta - 1 \right) \\ \mathcal{P} &= \frac{\mathcal{U}_0 - \frac{\mathcal{U}_1^2}{\mathcal{U}_2}}{\sqrt{\mathcal{U}_2}} = \sqrt{\frac{12}{13}} \frac{1}{|\xi_1|} \left[(\xi_1 - 1)^2 - \frac{12}{13} \left(1 + \xi_1 (\delta - 1) \right)^2 \right] \\ \mathcal{L} &= \sqrt{\mathcal{U}_2 \mathcal{R}(u)} + \mathcal{U}_2 u + \mathcal{U}_1 \end{aligned} \tag{27}$$

Note that the discriminant in (25) is absolutely positive on account of $u > 0$.

The overall integral in (24), however, is not solvable analytically. With the existing mathematical tools, one can numerically estimate the integral. Alternatively, one can approximate the integral by expressing $\mathcal{I}$ in terms of the average value $(\langle \sqrt{\delta} \rangle_{\Omega^{(\mathrm{P})}})^2$. See Appendix A. Note that continuity between $v_z^{(\mathrm{P})}$ and $v_z^{(\mathrm{M})}$ is satisfied, thereby eliminating the additional surface dissipation.

Moreover,

$$\Pi^{(\mathrm{M})} = \frac{1}{\Omega^{(\mathrm{M})}} \int_{\Omega^{(\mathrm{M})}} d_{\rm eq}^{(\mathrm{M})} \, \mathrm{d}\Omega \equiv \frac{1}{1-\chi^2} \int_{v=0}^1 \int_{u=\chi^2}^1 \bar{\sigma} d_{\rm eq}^{*(\mathrm{M})}(u,v) \, \mathrm{d}u \, \mathrm{d}v = \frac{\bar{\sigma}}{1-\chi^2} \int_{\chi^2}^1 d_{\rm eq}^{*(\mathrm{M})} \, \mathrm{d}u \tag{28}$$

The integral in $\Pi^{(\mathrm{M})}$ can be evaluated in exact or approximate form. The exact form is presented herein, and its approximate counterpart will be reported in Appendix A.

Using (20), one can recast and evaluate the integral in (28) in the following form:

$$\begin{aligned} \Pi^{(\mathrm{M})} = \frac{\bar{\sigma}|D_{33}|}{1-\chi^2} \int_{\chi^2}^1 \sqrt{\left(\frac{\xi_2}{u}\right)^2 + 1} \; \mathrm{d}u &= |\xi_2| \left[\sqrt{1 + \left(\frac{u}{\xi_2}\right)^2} - \sinh^{-1}\left(\frac{|\xi_2|}{u}\right) \right]_{u=\chi^2}^1 \\ &= \frac{|D_{kk}|}{\sqrt{3}(1-\chi^2)} \left[\sinh^{-1}\left(\mathcal{Y}|\xi_2|\right) - \sqrt{1 + \frac{1}{(\mathcal{Y}\xi_2)^2}} \right]_{\mathcal{Y}=1}^{1/\chi^2} \end{aligned} \tag{29}$$

where $\xi_2 = \xi/\sqrt{3}$, with ξ defined in (19).

Altogether, the total dissipation is the volumetric average of Π functions over the whole volume. With c_P and c_T denoting the volume fractions of the (P) and (M) subvolumes, the following can be written:

$$\Pi = c_P \left(\Pi^{(\mathrm{P})} + \Pi^{\mathrm{surf}} \right) + c_T \Pi^{(\mathrm{M})} \quad , \quad c_P = \chi^2 (1 - c) \; , \; c_T = 1 - \chi^2 \tag{30}$$

where Π^{surf} obeys (23) in the minimum continuity and $\Pi^{\mathrm{surf}} = 0$ in the higher continuity fields.

2.5 Yield criterion

The nondimensional counterpart of (14), normalized with respect to $\bar{\sigma} D_{33}$, gives rise to the functions f and g defined as follows:

$$\forall \xi \qquad f(\xi) \leq g(\xi)$$

where

$$\begin{aligned} f(\xi) &= \frac{\frac{\Sigma}{\bar{\sigma}} : \mathbf{D}}{D_{33}} = (\xi - 1) \frac{\Sigma_{11}}{\bar{\sigma}} + \frac{\Sigma_{33}}{\bar{\sigma}} \\ g(\xi) &= \frac{1}{D_{33}} \frac{\Pi}{\bar{\sigma}} \end{aligned} \tag{31}$$

where ξ has been defined in (19). Owing to the existence of absolute functions within $g(\xi)$, there are, respectively, three and two zones associated with the outcoming yield surface corresponding to the minimum and higher-continuity fields at a frozen microstructure. In the former, there exist two straight and one curved subsurface, which are connected through a C^0 continuity level. The algebraic features of g in the minimum and higher-continuity fields resemble other functions normalized with the same logic in [1] and [6, 13], respectively.

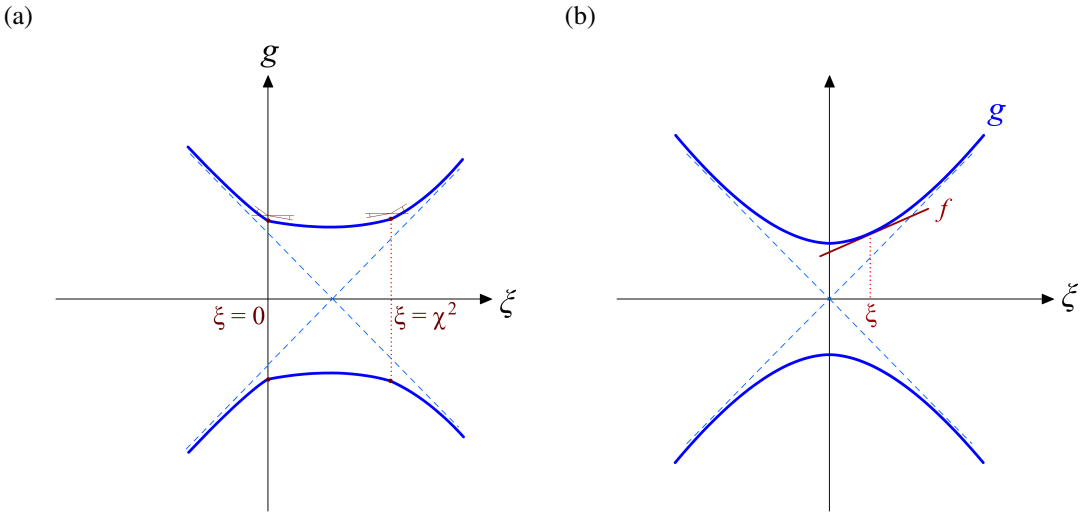

Figure 2: Schematized outline of the g normalized function upon the definition of $(31)_2$, with its asymptotic behavior at $\xi \longrightarrow \infty$: (a) upon minimum continuity, (b) upon higher continuity.

The items below describe the various subsections of the yield criterion, accompanied by figures schematizing the corresponding zones on the yield locus. The schematic outline of the present g function is shown

in Fig. 2. Note that there exists a singularity within Π and g in the higher-continuity field at $\xi = 0$. The latter two functions should thus be evaluated in limit form at this point.

2.5.1 Minimum continuity

The $g(\xi)$ function in this case is decomposed into the following terms:

$$\frac{g(\xi)}{\text{sgn}\,(D_{33})} = (1-c)\left(\left|\xi-\chi^2\right| + \frac{w}{\sqrt{3}}\frac{1-c}{c}|\xi|\right) + |\xi_2|\left[\sinh^{-1}\left(\mathcal{Y}|\xi_2|\right) - \sqrt{1+\frac{1}{(\mathcal{Y}\xi_2)^2}}\right]_{\mathcal{Y}=1}^{1/\chi^2} \tag{32}$$

which delivers the following first derivative with respect to ξ:

$$g'(\xi) = (1-c)\text{sgn}\left(\xi-\chi^2\right) + \frac{\text{sgn}\,(\xi)}{\sqrt{3}}\left(w\frac{(1-c)^2}{c} + \left[\sinh^{-1}\left(\mathcal{Y}|\xi_2|\right)\right]_{\mathcal{Y}=1}^{1/\chi^2}\right) \tag{33}$$

The Π, and in consequence, the g function are non-differentiable at the points that renders the absolute functions zero. There are two points with this property that are itemized below.

1. *Singular (straight) zones*

   At the yield point (*i.e.* at the boundary of $\mathcal{C}$), f and g should meet, but f is not allowed to cross g. Therefore:

   – At $\xi = 0$:

   $$\begin{aligned} f^{'}(\xi) &= \frac{\Sigma_{11}}{\bar{\sigma}} \\ \frac{g^{'}(\xi)}{\text{sgn}\,(D_{33})} &= -(1-c) + \frac{w}{\sqrt{3}}\frac{(1-c)^2}{c}\text{sgn}\,(\xi) \end{aligned} \tag{34}$$

   Then, at the yield point, one can write:

   $$\begin{aligned} &f^{'}(\xi) \leq g^{'}(\xi) \;\therefore\; \left|\frac{\Sigma_{11}}{\bar{\sigma}}\text{sgn}\,(D_{33}) + (1-c)\right| \leq \frac{w}{\sqrt{3}}\frac{(1-c)^2}{c} \\ &f(\xi) = g(\xi) \;\therefore\; \frac{\Sigma_{33}}{\bar{\sigma}} = \frac{\Sigma_{11}}{\bar{\sigma}} + \text{sgn}\,(D_{33})\,(1-c\xi^2) \end{aligned} \tag{35}$$

   – At $\xi = \chi^2$:

   $$\begin{aligned} f^{'}(\xi) &= \frac{\Sigma_{11}}{\bar{\sigma}} \\ \frac{g^{'}(\xi)}{\text{sgn}\,(D_{33})} &= (1-c)\text{sgn}\left(\xi-\chi^2\right) + \frac{w}{\sqrt{3}}\frac{(1-c)^2}{c} + \frac{1}{\sqrt{3}}\left[\sinh^{-1}\left(\mathcal{Y}\frac{\chi^2}{\sqrt{3}}\right)\right]_{\mathcal{Y}=1}^{1/\chi^2} \end{aligned} \tag{36}$$

Then, at the yield point, we have:

$$f^{'}(\xi) \leq g^{'}(\xi) \;\therefore\; \left| \frac{\Sigma_{11}}{\bar{\sigma}} \mathrm{sgn}\,(D_{33}) - \frac{1}{\sqrt{3}} \left[\left[\sinh^{-1}\left(\mathcal{Y}\frac{\chi^2}{\sqrt{3}}\right) \right]_{\mathcal{Y}=1}^{1/\chi^2} + w\frac{(1-c)^2}{c} \right] \right| \leq 1 - c$$

$$f(\xi) = g(\xi) \;\therefore\; \frac{\Sigma_{33}}{\bar{\sigma}} = \frac{\Sigma_{11}}{\bar{\sigma}}(1-\chi^2) + \mathrm{sgn}\,(D_{33})\,\frac{\chi^2}{\sqrt{3}} \left[\frac{(1-c)^2}{c} + \left[\sinh^{-1}\left(\mathcal{Y}\frac{\chi^2}{\sqrt{3}}\right) - \sqrt{1 + \frac{3}{(\mathcal{Y}\chi^2)^2}} \right]_{\mathcal{Y}=1}^{1/\chi^2} \right] \tag{37}$$

The corresponding f and g curves as well as the zone associated with this $\xi = 0$ and $\xi = \chi^2$ are schematized in Fig. 3.

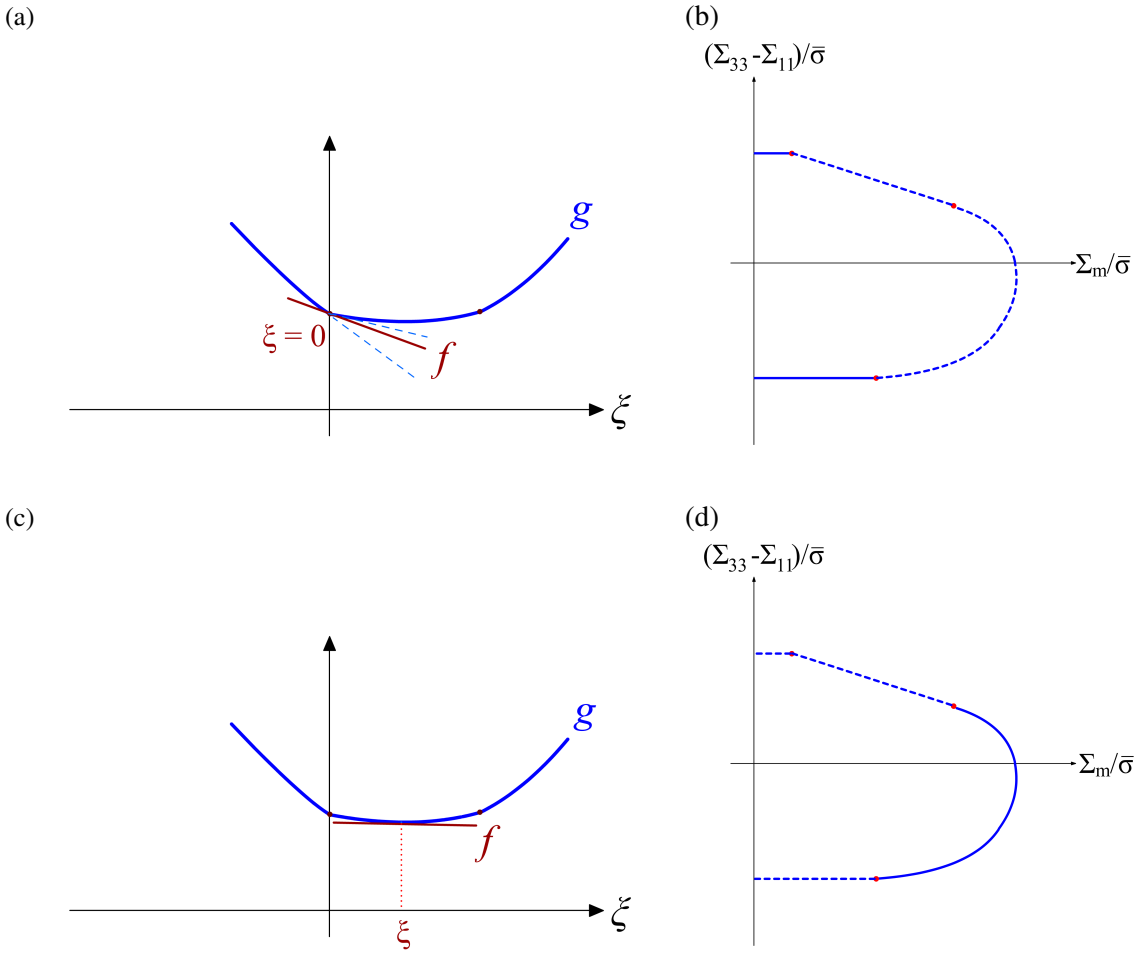

Figure 3: (a,b) Schematized f and g functions, with its corresponding zone on a representative yield surface at the vicinity of $\xi = 0$; (c,d) schematized f and g functions, with its corresponding zone on a representative yield surface at the vicinity of $\xi = \chi^2$.

2. *Regular (curved) zones* $\left(\xi \in \mathbb{R} - \{0, \chi^2\}\right)$

At any point ξ besides 0 and χ^2, the dissipation function Π and, by consequence, the g function are differentiable. The corresponding f and g curves as well as the regular zone associated with $\xi \in \mathbb{R} - \{0, \chi^2\}$ are schematized in Fig. 4.

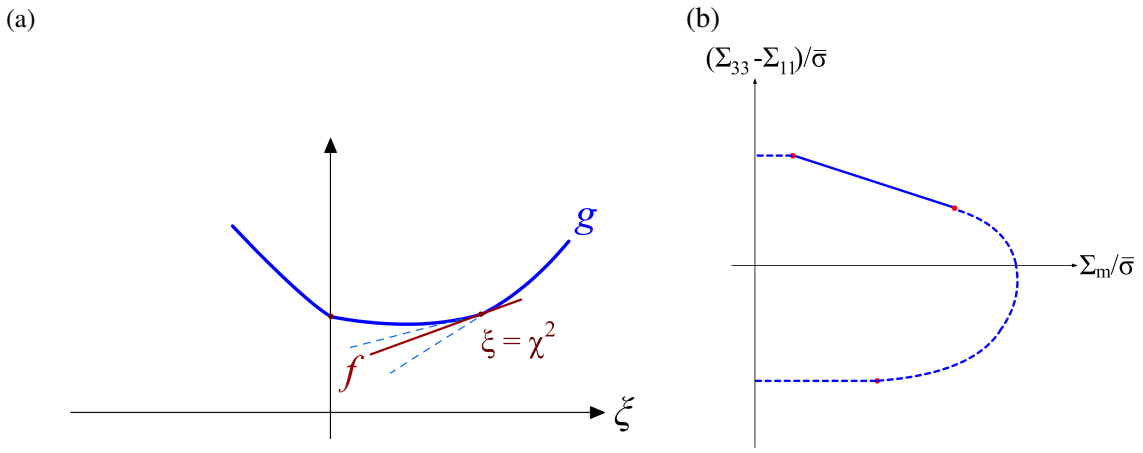

Figure 4: Schematized f and g functions, with its corresponding zone on a representative yield surface at any real value of $\xi \in \mathbb{R} - \{0, \chi^2\}$.

At the yield point, the variational definition of the effective yield criterion is equivalent to the following relation that expresses the macroscopic stress tensor as the first derivative of the dissipation function.

$$\forall \mathbf{D} \quad \mathbf{\Sigma} = \frac{\partial \Pi}{\partial \mathbf{D}} \iff \forall \xi \quad f^{'}(\xi) = g^{'}(\xi)\ ,\ f(\xi) = g(\xi) \tag{38}$$

Note that the total dissipation has been calculated only for the upper cell half. Accordingly, the lateral stress quotient will be half the total lateral stress. Therefore:

$$\begin{aligned}
\Sigma_{11} = \frac{\partial \Pi}{\partial D_{11}} \ \therefore\ \frac{\Sigma_{11}}{\bar{\sigma}} \text{sgn}\left(D_{33}\right) &= (1-c)\text{sgn}\left(\xi - \chi^2\right) + \frac{\text{sgn}\left(\xi\right)}{\sqrt{3}}\left(w\frac{(1-c)^2}{c} + \left[\sinh^{-1}\left(\mathcal{Y}|\xi_2|\right)\right]_{\mathcal{Y}=1}^{1/\chi^2}\right) \\
\Sigma_{33} = \frac{\partial \Pi}{\partial D_{33}} \ \therefore\ \frac{\Sigma_{33}}{\bar{\sigma}} \text{sgn}\left(D_{33}\right) &= (1-c)(1-\chi^2)\text{sgn}\left(\xi - \chi^2\right) + \text{sgn}\left(\xi\right)\left[\frac{w}{\sqrt{3}}\frac{(1-c)^2}{c} + (\alpha_1 - \alpha_2) + (\beta_1 - \beta_2)\right]
\end{aligned} \tag{39}$$

where

$$\begin{aligned}
\sqrt{3}\alpha_1 &= \sinh^{-1}|\xi_2| \quad , \quad \sqrt{3}\alpha_2 = \sinh^{-1}\frac{|\xi_2|}{\chi^2} \\
\sqrt{3}\beta_1 &= \sqrt{1+\xi_2^2} \quad , \quad \sqrt{3}\beta_2 = \sqrt{\xi_2^2+\chi^4}
\end{aligned} \tag{40}$$

The elimination of ξ is not a straight-forward process, and has thus been relegated to Appendix B.

In essence, the regular portion of the yield surface can be expressed as follows:

$$\left[\tfrac{\Sigma_{33}-\Sigma_{11}}{\bar{\sigma}} + (1-c)\chi^2\text{sgn}\left(D_{kk}\right)\right]^2 + 2\chi^2\cosh\left(\sqrt{3}\left[\tfrac{\Sigma_{11}}{\bar{\sigma}} - (1-c)\left(1 + \tfrac{w}{\sqrt{3}}\tfrac{1-c}{c}\right)\text{sgn}\left(D_{kk}\right)\right]\right) - (1+\chi^2) = 0 \tag{41}$$

See Appendix A for justification.

Remark: A complete form of the $\operatorname{sgn}(D_{33}), \operatorname{sgn}(D_{kk}) = \operatorname{sgn}(\xi)\operatorname{sgn}(D_{33}), \operatorname{sgn}\left(D_{kk}-\chi^2 D_{33}\right) = \operatorname{sgn}\left(\xi-\chi^2\right)\operatorname{sgn}(D_{33})$ set is a complicated piecewise function that is derived from the normality rule. However, each sign value can be simplified in the whole $\mathbb{R}$ or, at least, in the interval of interest. A trace through the parametric curve of any arbitrary surface with the subparts itemized above entails that the above set of signs, each sign considered *in its own interval of interest*, can be written in terms of the stress components as follows:

$$\operatorname{sgn}(D_{33}) = \operatorname{sgn}(\Sigma_{33}) \quad , \quad \operatorname{sgn}(D_{kk}) = \operatorname{sgn}(\Sigma_{11}) \quad , \quad \operatorname{sgn}\left(D_{kk}-\chi^2 D_{33}\right) = \operatorname{sgn}(\Sigma_{11}) \tag{42}$$

The complete yield criterion based on the minimum-continuity velocity field can thus be expressed as a piecewise-continuous function $\mathcal{F}^{\text{col}} = 0$ as follows

$$\mathcal{F}^{\text{col}} = \begin{cases} \dfrac{\Sigma_{33}-\Sigma_{11}}{\bar{\sigma}} - (1-c\chi^2)\operatorname{sgn}(\Sigma_{33}) \text{ for } \left|\dfrac{\Sigma_{11}}{\bar{\sigma}}\operatorname{sgn}(\Sigma_{33}) + (1-c)\right| \leq \dfrac{w}{\sqrt{3}}\dfrac{(1-c)^2}{c} \\ \dfrac{\Sigma_{33}-(1-\chi^2)\Sigma_{11}}{\bar{\sigma}} - \dfrac{\chi^2}{\sqrt{3}}\operatorname{sgn}(\Sigma_{33}) \left(\dfrac{(1-c)^2}{c} + \left[\sinh^{-1}\left(\mathcal{Y}\dfrac{\chi^2}{3}\right) - \sqrt{1+\dfrac{1}{\left(\mathcal{Y}\frac{\chi^2}{3}\right)^2}} \right]_{\mathcal{Y}=1}^{1/\chi^2} \right) \\ \text{for } \left| \dfrac{\Sigma_{11}}{\bar{\sigma}}\operatorname{sgn}(\Sigma_{33}) - \frac{1}{\sqrt{3}} \left(w\frac{(1-c)^2}{c} + \left[\sinh^{-1}\left(\mathcal{Y}\frac{\chi^2}{3}\right) \right]_{\mathcal{Y}=1}^{1/\chi^2} \right) \right| \leq 1-c \\ \left[\dfrac{\Sigma_{33}-\Sigma_{11}}{\bar{\sigma}} + (1-c)\chi^2\operatorname{sgn}(\Sigma_{11}) \right]^2 + 2\chi^2\cosh\left(\sqrt{3}\left[\dfrac{\Sigma_{11}}{\bar{\sigma}} - (1-c)\left(1+\dfrac{w}{\sqrt{3}}\dfrac{1-c}{c}\right)\operatorname{sgn}(\Sigma_{11}) \right] \right) - (1+\chi^2) \quad \text{Otherwise} \end{cases} \tag{43}$$

The counterpart to this equation will be provided in Appendix A.

2.5.2 Higher continuity

Inasmuch as Π is differentiable (see Fig. 2b), thereby the whole yield surface being smooth, the yield function will be expressible in derivative form. To this end, the following fundamental derivative must be determined first:

$$\mathcal{I}_{,\xi_1} = \frac{1}{2}\left[\mathcal{B}'\sqrt{\mathcal{R}} + (u+\mathcal{B})\mathcal{R}^* + \mathcal{P}'\ln|\mathcal{L}| + \mathcal{P}\frac{\mathcal{L}'}{\mathcal{L}} \right]_{u=0}^{1} \tag{44}$$

where, with reference to the definitions in (27) and ξ_1 from (19), we have:

$$\begin{aligned} \mathcal{B}' &= \frac{\partial\mathcal{B}}{\partial\xi_1} = \frac{-12}{13\xi_1^2} \\ \mathcal{P}' &= \frac{\partial\mathcal{P}}{\partial\xi_1} = \frac{\sqrt{12}}{13^{3/2}}\operatorname{sgn}(\xi_1)\left[-2(\delta-1)^2 + 3 - \frac{1}{\xi_1^2} \right] \\ \mathcal{R}^* &= \frac{1}{2\sqrt{\mathcal{R}}}\frac{\partial\mathcal{R}}{\partial\xi_1} = \frac{\frac{13}{12}\xi_1 u^2 + [1+2(\delta-1)\xi_1]u + (\xi_1-1)}{\sqrt{\frac{13}{12}\xi_1^2 u^2 + 2\xi_1[1+(\delta-1)\xi_1]u + (\xi_1-1)^2}} \\ \mathcal{L}' &= \frac{\partial\mathcal{L}}{\partial\xi_1} = \sqrt{\frac{13}{12}}|\xi_1|\,\mathcal{R}^* + \frac{13}{6}\xi_1 u + [1+2(\delta-1)\xi_1] \end{aligned} \tag{45}$$

which is utilized in the following relations that constitute the stress field within the plastic plugs:

$$\begin{aligned}
\frac{\Sigma_{11}^{(\mathrm{P})}}{\bar{\sigma}}\mathrm{sgn}\left(D_{33}\right) &= \frac{2}{\chi^2(1-c)}\int_{v=c}^{1}\mathcal{I}_{,\xi_1}\,\mathrm{d}v \\
\frac{\Sigma_{33}^{(\mathrm{P})}}{\bar{\sigma}}\mathrm{sgn}\left(D_{33}\right) &= \frac{1}{1-c}\left[-\left(\xi_1-\frac{2}{\chi^2}\right)\int_{v=c}^{1}\mathcal{I}_{,\xi_1}\,\mathrm{d}v+\int_{v=c}^{1}\mathcal{I}\,\mathrm{d}v\right]
\end{aligned} \tag{46}$$

Then, according to (30), the total stress field can be expressed as

$$\begin{aligned}
\frac{\Sigma_{11}}{\bar{\sigma}} &= \frac{\Sigma_{11}^{(1)}}{\bar{\sigma}}+\frac{\Sigma_{11}^{(2)}}{\bar{\sigma}} \\
\frac{\Sigma_{33}}{\bar{\sigma}} &= \frac{\Sigma_{33}^{(1)}}{\bar{\sigma}}+\frac{\Sigma_{33}^{(2)}}{\bar{\sigma}}
\end{aligned} \tag{47}$$

where

$$\begin{aligned}
\frac{\Sigma_{11}^{(1)}}{\bar{\sigma}}\mathrm{sgn}\left(D_{33}\right) &= 2\int_{v=c}^{1}\mathcal{I}\,\mathrm{d}v \\
\frac{\Sigma_{33}^{(1)}}{\bar{\sigma}}\mathrm{sgn}\left(D_{33}\right) &= -2(\xi-1)\int_{v=c}^{1}\mathcal{I}_{,\xi_1}\,\mathrm{d}v+\chi^2\int_{v=c}^{1}\mathcal{I}\,\mathrm{d}v \\
\frac{\Sigma_{11}^{(2)}}{\bar{\sigma}}\mathrm{sgn}\left(D_{kk}\right) &= \alpha_1-\alpha_2 \\
\frac{\Sigma_{33}^{(2)}}{\bar{\sigma}}\mathrm{sgn}\left(D_{kk}\right) &= \beta_1-\beta_2
\end{aligned} \tag{48}$$

with the (1) and (2) superscripts pertaining to $\Pi^{(\mathrm{P})}$ from (24) and $\Pi^{(\mathrm{M})}$ from (29), respectively. Also, α_1, ..., and β_2 have been defined in (40). Note further that $\mathrm{sgn}\left(D_{33}\right)$ and $\mathrm{sgn}\left(D_{kk}\right)$ can be expressed in terms of the stress field from (42).

Figure 5 shows the schematic comparison between the two models derived from minimum and higher-continuity fields. Section 4.2 elaborates on the difference between the two surfaces.

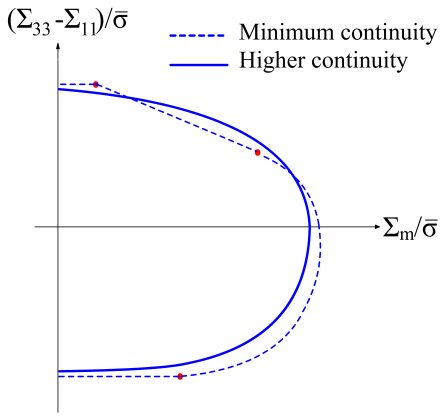

Figure 5: Schematic comparison between the yield loci accounting for necklace void coalescence based on minimum and higher continuity fields.

3 Cell-Model Calculations

There is a rather large cache of cell-model calculations on porous cells with the purpose of assessing the predictive capabilities of the semi-analytical [9, 19, 20] or completely analytical flow potentials accounting for void growth [21–23] or void coalescence [6, 7, 12, 13, 24] . The cell geometries were carried out for either tetragonal or cylindrical cells containing either spheroidal or cylindrical voids. The calculations in the present study are for the very same unit cell used in the development of the model, Fig. 1. The strategy for authenticating the FEM calculations for the purpose of validating micromechanical models is the application of a finite displacement under a small-strain finite element framework (with geometric nonlinearity deactivated), which has proven the numerical equivalent of the limit analysis theory (see [25]). As the elastic solution almost vanishes in the limit-analysis theory, the elastic constants may be chosen arbitrarily, and the Poisson ratio is taken close to 0.5 ($\nu = 0.49$) to mimic an isochoric dynamic process in the plastic regime. The typical yield strength to Young's modulus ratio of $\bar{\sigma}/E = 0.0002$ has also been adopted. It is noteworthy that the FEM results tend to mimic the yield point at a fixed geometric state. Correspondingly, the analyses, in spite of being evolutionary, are single-step calculations where the velocity field $\mathbf{v}$ is described with the aid of a displacement field $\mathbf{u}$, and thus the rate of deformation tensor $\mathbf{D}$ is represented by an imposed strain tensor $\mathbf{E}$.

Unlike in previous studies, since the loading and cell geometry admit an axisymmetric condition, an axisymmetric element type is utilized in the present study, and thus the lateral projected section of the main RVE is modeled. This scheme induces multi-fold increase in the calculation speed. More importantly, the elaborate equations as for the imposition of quasi-periodic boundary conditions will end up being remarkably simpler by virtue of replacing circles with lines [2]. Considering the upper half of the cell with symmetry conditions imposed on the lateral plane, the displacement $\mathbf{u}$ at field point $\mathbf{x}$ writes

$$\mathbf{u}(\mathbf{x}) = (\mathbf{E} + \mathbf{\Omega}).\mathbf{x} + \tilde{\mathbf{u}}(\mathbf{x}) \tag{49}$$

where $\mathbf{E}$ is the macroscopic strain tensor, $\mathbf{\Omega}$ is the (skew-symmetric) macroscopic rotation tensor and $\tilde{\mathbf{u}}$ is a periodic displacement field being the so-called *periodicity vector*. For any two points in periodic correspondence:

$$\Delta\mathbf{u} = (\mathbf{E} + \mathbf{\Omega}).\Delta\mathbf{x} \tag{50}$$

where $\Delta\mathbf{u}$ is the difference in displacement between the points separated by the vector $\Delta\mathbf{x}$. As such, the macroscopic strain enforced on the cell is represented by the following tensor:

$$\mathbf{E} = E_{11}\mathbf{e}_1 \otimes \mathbf{e}_1 + E_{33}\mathbf{e}_3 \otimes \mathbf{e}_3 = \begin{bmatrix} E_{11} & 0 \\ 0 & E_{33} \end{bmatrix} \tag{51}$$

where, in terms of the imposed displacements (U_1, U_3), we have

$$\begin{aligned} E_{11} &\equiv \ln\left(\frac{L}{L_0}\right) \approx \frac{U_1}{L_0} \\ E_{33} &\equiv \ln\left(\frac{H}{H_0}\right) \approx \frac{U_3}{H_0} \end{aligned} \tag{52}$$

And, in absence of shear distortion, $\mathbf{\Omega} = \mathbf{0}$. The periodic boundary conditions (50) now read:

$$\begin{Bmatrix} \Delta u_1 \\ \Delta u_3 \end{Bmatrix} = \begin{bmatrix} E_{11} & 0 \\ 0 & E_{33} \end{bmatrix} \begin{Bmatrix} \Delta x_1 \\ \Delta x_3 \end{Bmatrix} \tag{53}$$

More specifically, the displacement functions simplify to the following values for the various subparts:

[2] The prefix *quasi-* alluding to the non-space-filling nature of a cylindrical geometry. See more details in [6].

- On the top surface, $\Delta\mathbf{u} = \mathbf{u}(x_1, H) - \mathbf{u}(x_1, -H)$ and $\Delta\mathbf{x}^T = \{0, 2H\}$ so that:

$$\begin{cases} \Delta u_1 = 0 \\ \Delta u_3 = 2E_{33}H \end{cases} \tag{54}$$

- On the plane Ox_2x_3,

$$u_1(0, x_3) = 0 \tag{55}$$

- On the lateral surface ($x_1 = \pm L$, $-H \leq x_3 \leq H$), the nodes lying on a projected horizontal line should remain within a distance consistent with the prescribed value of E_{11}. Let $\mathbf{u}^{\text{ref}}$ be the displacement of some reference node on the line at some height x_3, say $\mathbf{x}^T = \{L, x_3\}$ and $\Delta\mathbf{u} = \mathbf{u}(x_1, x_3) - \mathbf{u}^{\text{ref}}$, then:

$$\begin{cases} \Delta u_1 = E_{11}(x_1 - L) \\ \Delta u_3 = 0 \end{cases} \tag{56}$$

The ratio between the lateral and axial stresses is governed by the U_1/U_3 ratio. The input time step needs to be large enough to ensure that the limit load is reached. Average remote stresses over the cell are calculated from summation over the average stresses on all elements. Namely,

$$\Sigma_{ij} = \sum_{n=1}^{N} \sum_{m=1}^{M} (\sigma_{ij})_n^m v_n^m \tag{57}$$

where N is the total number of elements, M the number of Gauss points per element (here $M = 8$), and $v_n^m = V_n^m/\Omega$ the volume fraction assigned to integration point m within element n. The components of interest are Σ_{33} and Σ_{11}.

A comprehensive explanation on the periodicity equations expressed mathematically has been reported in Appendix B of [6]. Therein, E_{11} was enforced zero (after the whole set of equations were presented) to mimic coalescence by internal necking and/or shearing. Similar calculations have been worked out by Morin *et al.* [1] under triaxial loading (and by the first author of the present work under combined triaxial and shear loading) that incorporated both void growth and coalescence by internal necking, where the microstructure was to be chosen in such a way that internal necking be realized as the governing mechanism for strain localization. In the present context, however, no restriction will be enacted on the microstructural parameters nor on the U_1/U_3 ratio. Therefore, the localization mechanism will be governed by both the microstructural state and the U_1/U_3 ratio. The only constraint exerted on the geometry is then to assure that, with the adopted (χ, w, λ) set, the void fully fits into the unit cell. That is, the condition $c < 1$ should be satisfied, where c has been defined in Sec. 2.1.

4 Results

4.1 Comparison to Gologanu et al. [16]

The model developed by Gologanu *et al.* [16] is an earlier-developed model considered as reference to evaluate the predicted yield surfaces based on the present model. Unlike the present model, the former mainly involves porosity f as a microstructural parameter. The present model based on minimum continuity is hereby compared to its counterpart in [16], where porosity is dictated by χ through the following relation:

$$f = \frac{w}{\lambda}\chi^3 \tag{58}$$

Figure 6 shows the comparison between the latter and the present model based on the minimum-continuity field for various values of porosity. The results are presented for a rather small cell aspect ratio $\lambda = 1/3$ whose effective yielding mechanism is coalescence in columns rather than in layers at larger hydrostatic portions of the loading. The effect of microstructure on the effective yielding mechanism will be more clearly elaborated on in Section 5.

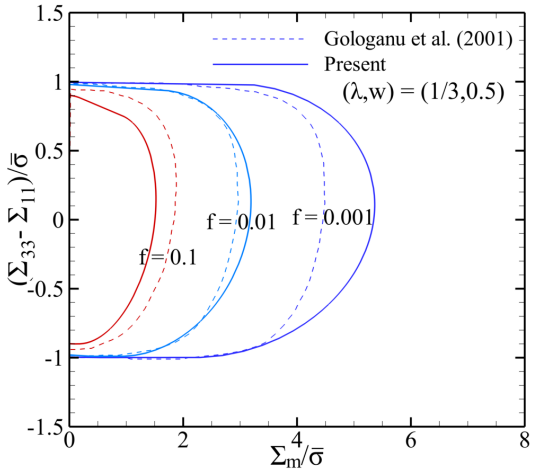

Figure 6: Comparison between the present model predictions with those of Gologanu *et al.* [16] for various porosity values and the other parameters as given.

The difference between the present and the reference models lies in the fact that the model proposed by Gologanu *et al.* [16] relies on macroscopic kinematic boundary conditions regardless of the microscopic cell-level kinematics, that are affected by microstructural geometry per se. At lower porosity levels, the present model predicts a larger limit load at higher hydrostatic stresses characteristics of larger lateral stresses since larger lateral loads would induce a negative axial velocity in the plugs, which demands a larger axial limit load.

All the same, the presently predicted limit load at higher porosities is smaller than that from Gologanu *et al.* [16] in that the latter considers the plug as homogeneous throughout the cell height whereas the present model accounts for the large void spacing which gives rise to rather large porosity levels. Consequently, the evaluated limit load would be smaller.

4.2 Effect of velocity continuity

The present section elaborates on the comparison between the models based on different continuity levels: minimum and higher continuity fields. Figure 7 exhibits the difference between the models for various void aspect ratios, ligament parameters, and cell aspect ratios.

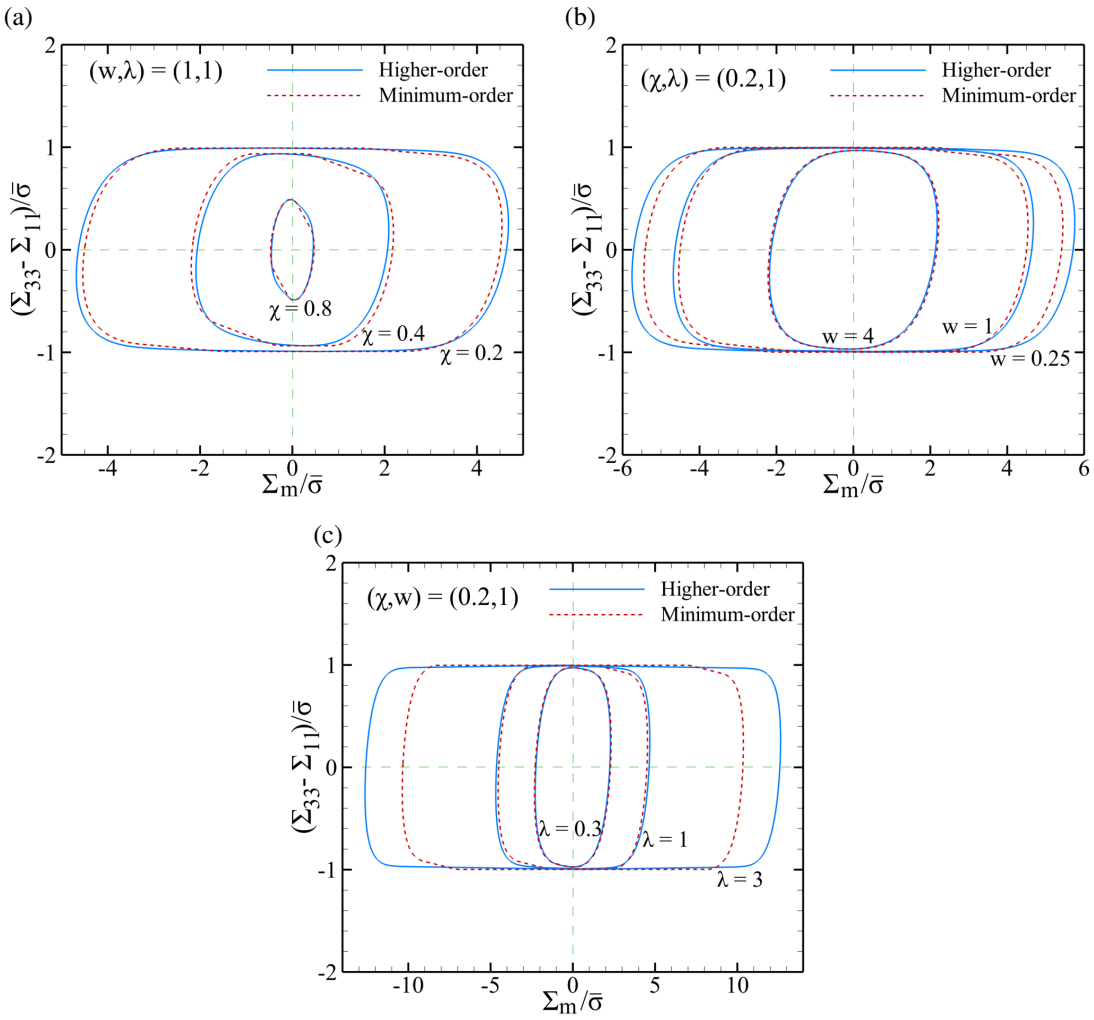

Figure 7: Comparison between yield surfaces based on minimum and higher-continuity fields: (a) for fixed (w, λ) and various ligament parameters χ, (b) for fixed (χ, λ) and various void aspect ratios w, (c) for fixed (χ, w) and various cell aspect ratios λ.

At low hydrostatic stresses, characteristic of mainly deviatoric loads, the predicted limit load is the least sensitive to the velocity profile. This limit corresponds to minimal relative axial velocity between the plugs and the torus, with the whole cell admitting minimal, albeit nonzero, expansion. All the same, higher continuity within the axial velocity would trigger a higher limit load at larger hydrostatic stresses representative of higher lateral stresses superposed by axial loading. This entails a larger Poisson effect when the torus and plugs are clamped than when they act in parallel modulo minimum continuity. By the same token, the difference between the two surfaces proves inconsequential at large χ's and w's as well as small λ's due to the Poisson effect being limited. Accordingly, the higher-continuity yield surface is a tight lower bound to its minimum-continuity counterpart at large χ's and w's as well as small λ's, and is an upper bound thereof at smaller χ's and w's as well as higher λ's. This upper bound becomes rather spuriously large with increasingly large hydrostatic stresses in that the higher-continuity field exerts overconstraint on the point-wise velocity gradients. As explored in the sequel, the minimum-continuity model stands closer to numerical values, and will be thus favored over the other for assessment purposes.

Note also that the spuriously large hydrostatic stresses pertaining to $\chi = 0.2$, $w = 0.25$, and $\lambda = 3$

is indicative of coalescence in columns as an erroneous yielding mechanism. The effective mechanism corresponding to these parameters is coalescence in layers. Section 5 further illustrates this matter.

5 Effective Yield Surface

The yield surface devised by Eq's (43) and (47) has a large portion in proximity with the surface accounting for void growth by way of homogeneous plasticity which are, more specifically, the planar subsurfaces of (43) and the zones with nearly horizontal slopes in (47). However, the highly-curved subsurface is the main matter of difference. In the minimum-continuity model, $(43)_3$ is counterpart to the planar part signifying coalescence in layers, *i.e.* with internal necking. The coalescence mechanism involves a zero increase in the lateral strain, *i.e.* a zero lateral rate of deformation $D_{11} = 0$, which prompts a rigid behavior in the matrix (M) subparts. A recent work by Morin *et al.* [1] expresses yielding by void growth seamlessly ensued by coalescence in layers through a unified perspective. This model is built upon the same RVE as shown in Fig. 1 but with different kinematic boundary conditions admitted, as depicted in Fig. 8.

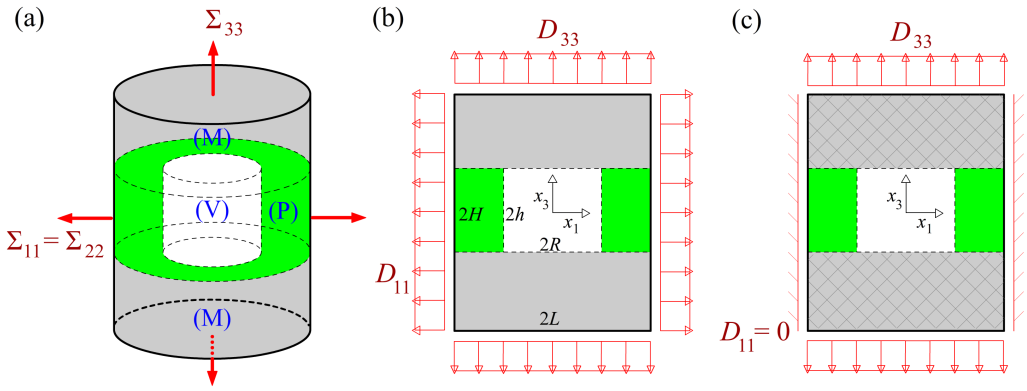

Figure 8: Reference volume element corresponding to the unified model, incorporating void growth via homogeneous plasticity ensued by coalescence by way of internal necking.

This model, also termed *unified*, should be compared to its counterparts derived herein, (43) or (47). An upper bound to the net yield surface for a specified microstructure will be then close to the interior surface between the two surfaces.

Details aside (see [1] for the whole path to this model), the comparison between the two models is well-posed through the development of the unified model upon the same ξ ratio. By letting

$$\zeta = \frac{1}{\sqrt{3}} \frac{\xi}{(1-c)\xi + c}$$

, the derivations in [1] prove the following:

$$\begin{aligned}
\Pi^{\text{uni}} &= c\Pi^{(\text{P+V})} + (1-c)\Pi^{(\text{M})} + \Pi^{\text{surf}} \\
\Pi^{(\text{P+V})} &= \bar{\sigma}\left|(\frac{1}{c}-1)D_{kk} + D_{33}\right| \left[\zeta \sinh^{-1}(\zeta u) - \sqrt{\frac{1}{u^2}+\zeta^2}\right]_1^{1/f_b} \\
\Pi^{(\text{M})} &= \bar{\sigma}|D_{kk} - D_{33}| \\
\Pi^{\text{surf}} &= \bar{\sigma}|D_{kk}|\,\Sigma^{\text{surf}} \quad , \quad \Sigma^{\text{surf}} = \frac{\bar{\sigma}}{3\sqrt{3}} \frac{\chi^3 - 3\chi + 2}{\chi w}
\end{aligned} \tag{59}$$

where $c = \chi w/\lambda$ is the porous volume fraction, and $f_b = \chi^2$ is the porosity within the intervoid ligament. The porous, void, and matrix subparts are represented as depicted in Fig. 8a.

After the elimination of ξ and rearranging the unified yield surface, the following piecewise function can be written, following the derivations carried out in [1]:

$$\mathcal{F}^{\text{uni}} = \begin{cases} \mathscr{T} - (1 - f_b) \\ \text{if} \left| \frac{\Sigma_{11}}{\bar{\sigma}} + (1-c) \left[(1-f_b) + \text{sgn}\left(-(1-c) + c\mathscr{T}^{\text{coal}} - \frac{\Sigma_{33}-\Sigma_{11}}{\bar{\sigma}} \right) \right] \right| \leq \frac{t\Sigma^{\text{surf}}}{\bar{\sigma}} \\ \\ \mathscr{T}^2 + 2f_{\text{b}} \cosh \sqrt{3} \left(\dfrac{\Sigma_{33} - \text{sgn}\left(\Sigma_{33}\right) t\Sigma^{\text{surf}}}{\bar{\sigma}} - \mathscr{T} \right) - (1 + f_{\text{b}}^2) \qquad \text{if } |\mathscr{T}| \geq \mathscr{T}^{\text{coal}} \\ \\ (\mathscr{T}^{\text{coal}})^2 + 2f_{\text{b}} \cosh \sqrt{3} \left(\dfrac{\Sigma_{33} - \text{sgn}\left(\Sigma_{33}\right) t\Sigma^{\text{surf}}}{\bar{\sigma}} - \mathscr{T}^{\text{coal}} \right) - (1 + f_{\text{b}}^2) \qquad \text{Otherwise} \end{cases} \tag{60}$$

where

$$\mathscr{T} = \frac{1}{c} \left[\frac{\Sigma_{33} - \Sigma_{11}}{\bar{\sigma}} + (1-c)\text{sgn}\left(-(1-c) + c\mathscr{T}^{\text{coal}} - \frac{\Sigma_{33} - \Sigma_{11}}{\bar{\sigma}} \right) \right]$$

$$(\mathscr{T}^{\text{coal}})^2 = \frac{5}{3} + f_{\text{b}}^2 - \frac{4}{3}\sqrt{1 + 3f_{\text{b}}^2}$$

Further, $t\Sigma^{\text{surf}}$ was proposed in [6] to overcome the limitation of the unified model, at the coalescence level, to flattened voids. The recommended calibration function t reads:

$$t(\chi, w) = \frac{(t_0 + t_1\chi)w}{1 + (t_0 + t_1\chi)w} \tag{61}$$

where t_0 and t_1 are parameters to be determined from numerical results (the choice of $t_0 = -0.84$, $t_1 = 20.6$ recommended in [13] is a proper one).

Since Eq's (43) and (60) are piecewise with overlapping intervals, one proper method to evaluate the net surface, denoting the driving failure mechanism at a microstructure, is to calculate the radius of the yield locus within the $\Sigma_{11} - \Sigma_{33}$ space at every value of Σ_{11}. The innermost surface will then be that corresponding to the minimum radius. That is:

$$\mathscr{R}^2_{\text{min}} = \min\{\Sigma_{11}^2 + \Sigma_{33}^2\} \quad \forall\, \Sigma_{11} \tag{62}$$

Figure 9 shows the column-coalescence and unified surfaces accompanied by the net surface for example microstructural states. The surfaces denoting coalescence in columns are named "column" surfaces henceforth. homogeneous plasticity is more or less common to the two models, *i.e.* almost equally predicted by the two criteria. The distinction between the two yielding mechanisms can therefore be mainly observed through the portion at the vicinity of the hydrostatic stress axis. Details aside, one can deduce that coalescence in layers is the driving yielding mechanism except for very slim plugs (for values of $\chi \leq 0.2$), flat voids (for values of $w \leq 0.5$), and long cells (for values of $\lambda > 1$) whereas coalescence in columns is the prevalent mechanism for thick plugs (for $\chi \geq 0.3$), elongated voids (for $w > 1$), and stumpy cells (for $\lambda \leq 0.5$). Section 6 embodies a clearer distinction between the two mechanisms at various microstructural formations.

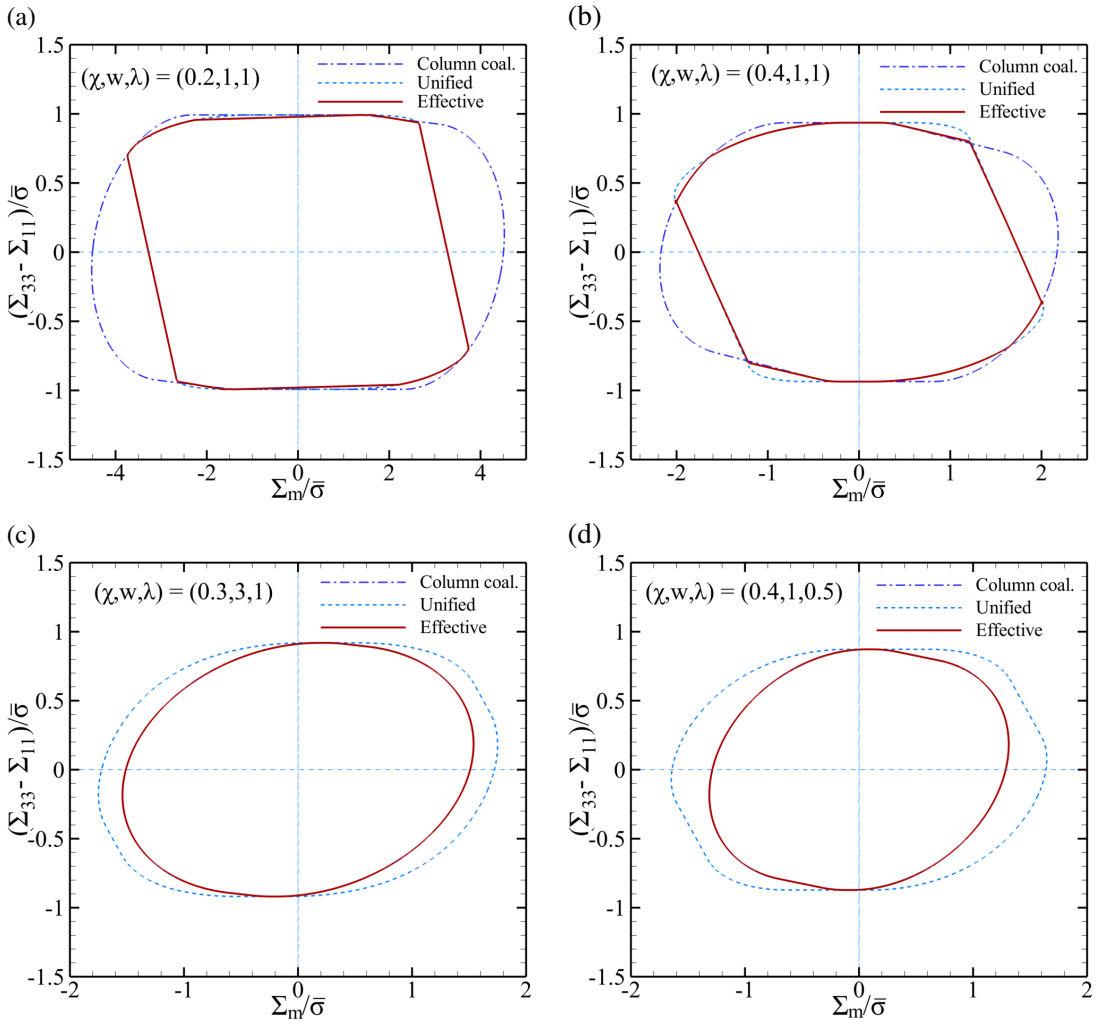

Figure 9: Comparison between column and unified surfaces for representative microstructural configurations, and exhibition of the net surface for each microstructure. (a,b) demonstrate the effect of increasing porosity, mainly signified by the χ parameter. (c,d) illustrate the effect of elongated voids and shortened cells. Note that shortened voids and elongated cells have similar effects as exhibited in (a,b).

6 Representative Yield Loci

This section comprises a comprehensive investigation on the effects induced by each microstructural parameter (with the other two constants kept constant) on the effective yielding mechanism. Each figure compares the yield loci corresponding to void growth as well as void coalescence in layers anc columns, the innermost of which is the predicted effective mechanism. All curves are compared to their FEM counterparts calculated in accordance with Section 3. To this end, the portion with large Σ_m values is the main distinctive zone which exhibits the main difference between various localization schemes: in columns or in layers, whichever occurs sooner. Homogeneous plasticity ensued by plastic localization in layers is accounted for by the *unified* model, whereas that signifying plasticity localized in columns is represented by Eq. (43). The latter loses the upper-bound character at limited ranges of microstructural parameters but is generally closer than its higher-order peer in (47) to numerical values. Figure 10 demonstrates the effects induced by every

microstructural parameter on the effective yield surface.

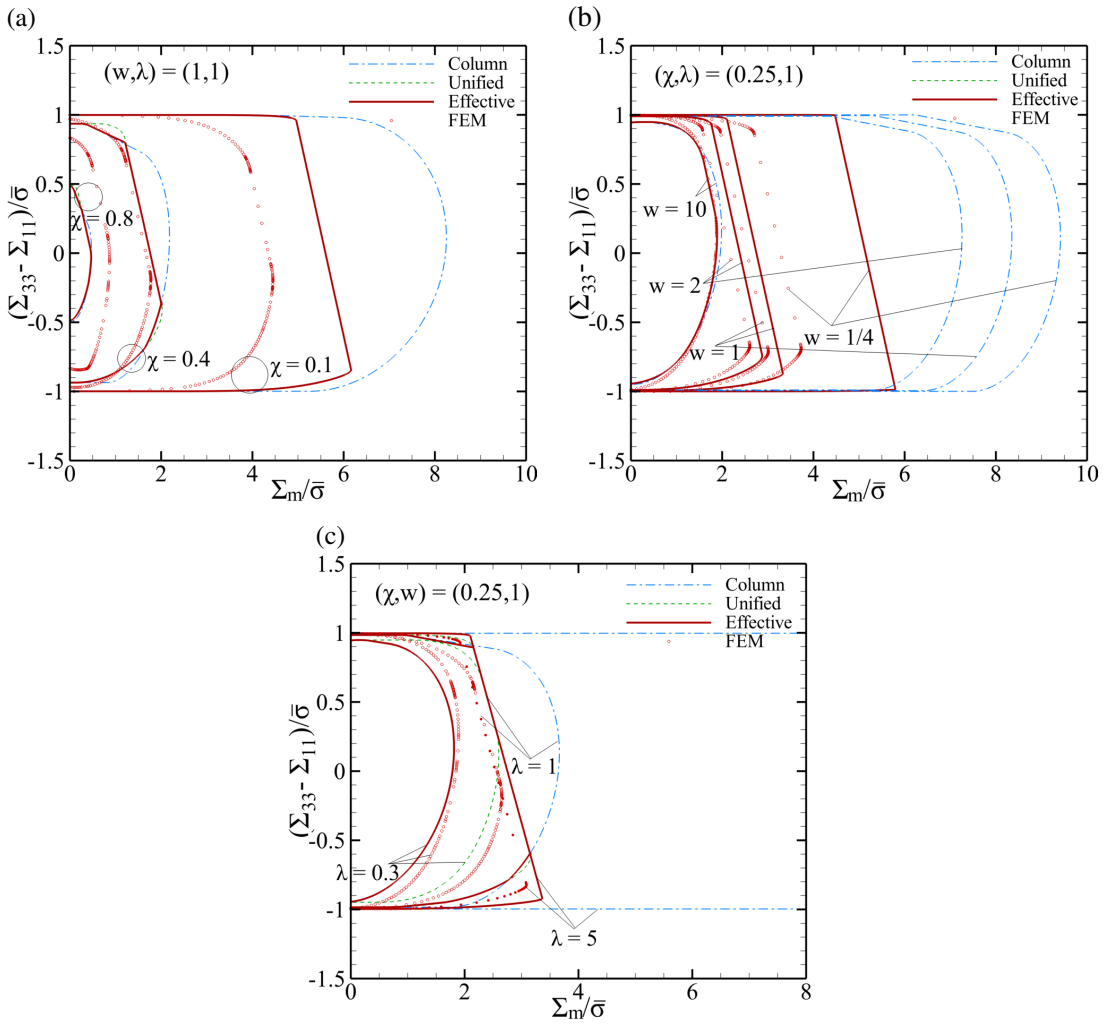

Figure 10: Effects induced by variation of microstructural parameters on the yield loci representing homogeneous plasticity ensued by coalescence in layers (denoted with the *unified* model) as well as plasticity localized in columns (denoted with the *column* model): (a) effect of ligament parameter χ; (b) effect of void aspect ratio w; (c) effect of cell aspect ratio λ. Note that the choice of a large λ in (b) lies in the ability to pick a wider range of w without the ligament aspect ratio exceeding unity, *i.e.* $c < 1$.

While the figures entail attentive examination, it can be conveniently observed that changing the χ or w variable from small to large values (while the rest are kept fixed) would transfer the driving yielding mechanism from layered into column coalescence. Incidentally, for large values of χ and w, the two yielding mechanisms occur almost synonymously while coalescence in layers is triggered slightly sooner, and vice versa. For cell aspect ratios well below unity ($\lambda < 1$), however, coalescence in columns is clearly preferred with significant distance between the two predicted mechanisms.

Moreover, the present model accounting for column coalescence violates the upper-bound character [2] at very large values of χ and w as well as for small values of λ. In particular, with χ approaching unity, both (43) and (60) violate this character. This is rooted in the idealized choice of velocity fields that predict yielding at lower stress states. However, the predicted driving mechanism is both qualitatively and

quantitatively (except for $\chi \longrightarrow 1$) well commensurate with the FEM outcomes.

Above all, λ induces an opposite effect on the driving yielding mechanism compared to χ and w being varied. That is, changing λ from small to large values (while the rest are constant) would transfer the driving yielding mechanism from column into layered coalescence. Further, the effect of the cell aspect ratio λ is more remarkable when plasticity is localized in columns whereas it bares almost no effect on void coalescence occurring in layers. Thereupon, the points exhibiting FEM results for $\lambda = 5$ have been identified with solid circles in order to be more easily distinguishable from those pertaining to $\lambda = 1$ since they stand on the same slanted line denoting coalescence in layers.

A deeper insight into the driving yielding mechanism can be acquired through the following velocity vector plots for each microstructural state exemplified in Fig. 10. These vector plots exclusively belong to the distinctive portion of the loci at the vicinity of the Σ_m axis. Note that, for the sake of better clarity in the localization of deformations, the plastic strains are highly cut off with respect to the elastic lower bound such that the highly plastic regions are mainly visible. Moreover, a logarithmic scale has been employed in the contours to better showcase the spatial variation of plastic strains. This allows for better distinguishing of the driving yielding mechanism.

Remark: As revealed by Fig. 11(c,f,i), the plugs enclosing the voids need not undergo significant plastic deformation for the mechanism to be accounted column-like coalescence. Rather, what dictates the driving yielding mechanism it is the major direction along which the strains become localized, notwithstanding there may exist larger plasticity zones within the unit cell. Meanwhile, a complete examination of FEM results at fixed microstructural states reveals some additional yielding mechanisms that emerge from a full trace of the stress state on the yield surface. The reader is well-advised to see Appendix C in this regard.

7 Concluding Remarks

An all-inclusive investigation was probed into micromechanical modeling of ductile fracture by void coalescence in columns, *i.e. necklace* coalescence in competition to coalescence in layers by internal necking. The model accounting for coalescence in columns was developed based on homogenization on the same unit cell employed to predict void growth succeeded by coalescence in layers, termed the *unified* model as advanced in a recently-reported work [15]. Yet, the plastic deformation was structured according to a different framework so as to mimic the true material behavior under plasticity mainly localized within the plastic plugs circumscribing the void, thus its name *column-like* coalescence. The model is endowed with the involvement of geometrically unique microstructural descriptors, and was successfully compared to previously predicted values from Gologanu [17] as well as to their FEM counterparts from the present study. The FEM outcomes were results to single-step cell-model calculations with a nearly-isochoric plastic process controlled by remotely prescribed normal and lateral strains. Various yield surfaces were plotted demonstrating the effects of variation in the ligament parameter χ as well as void and cell aspect ratios, w and λ, respectively. At each case, the two yield surfaces ensued by coalescence in layers and columns, as well as the effective surface (the innermost of the two) were compared to one another and to their FEM counterparts. The driving mechanism was observed to be fully determined by the microstructural state. That is, the effective yielding mechanism is void growth followed by coalescence in layers for smaller χ's and w's as well as for larger λ's. It would tend towards coalescence in columns when χ approaches 1, w is well above 1, and also when λ is well below 1. Among all, the effect of λ is more remarkable in the distinction between coalescence in layers and columns.

Aside from that, special plasticity mechanisms were visualized through the course of plastic deformation prior to void coalescence in layers or columns. These comprise void growth associated with stagnation in the radial velocity between the radial bounds of the void, as well as vertically-localized plasticity associated with stagnation in the vertical velocity. The latter could lead to a particular phenomenon here termed *void*

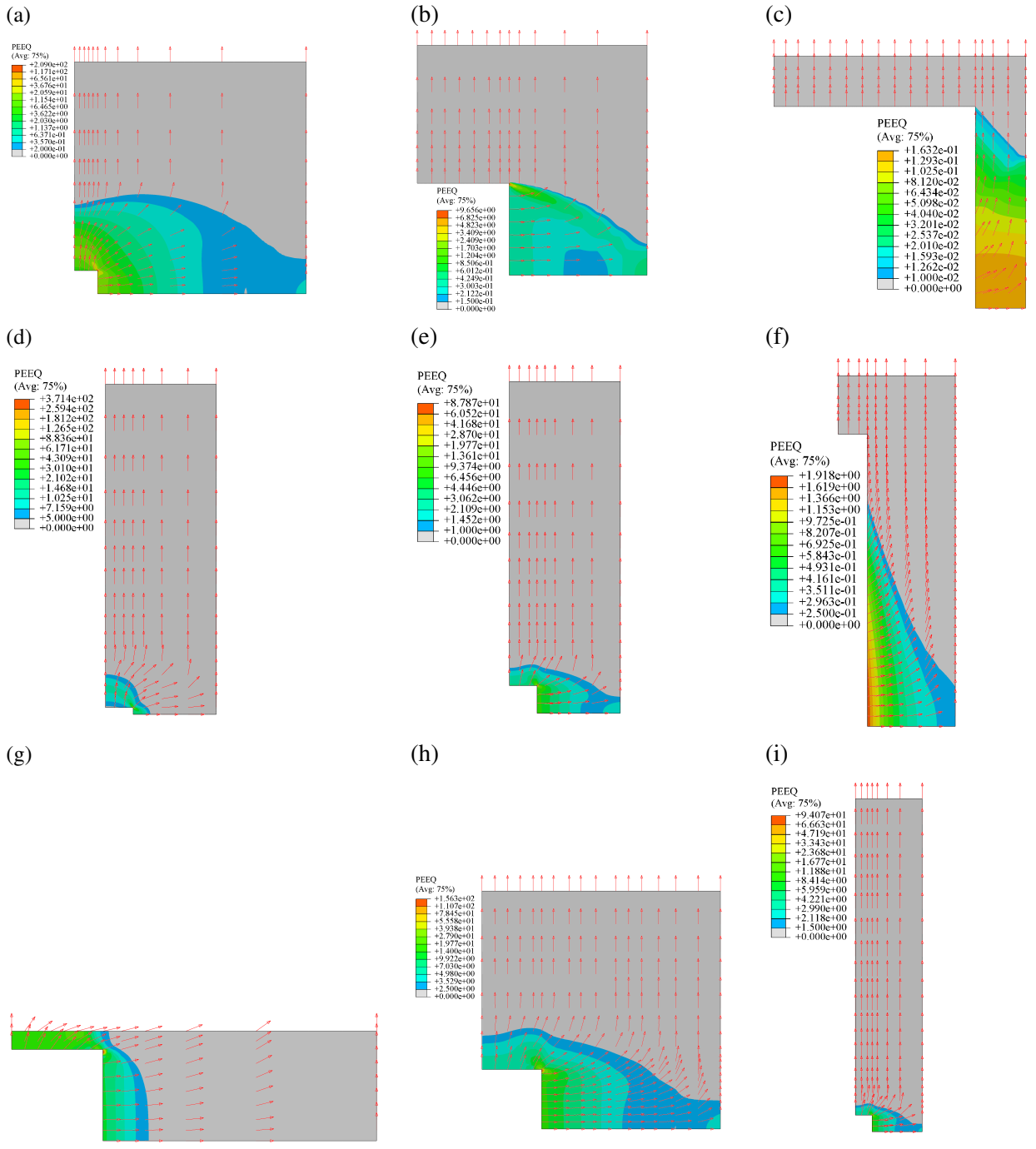

Figure 11: Velocity vector plots for the microstructural parameters exemplified in the Fig. 10 plots: (a–c) varying values of χ from small to large, admitting coalescence ranging from layered to column-like (occurring in approximate simultaneity with the layered scheme); (d–f) varying values of w from small to large, inducing a similar effect to that of χ; (g–i) varying values of λ from small to large, admitting coalescence ranging from column-like (almost simultaneous with layered) to purely layered.

collapse if the stagnation point approaches a zero height.

Acknowledgment

The authors affectionately acknowledge support from the National Science Foundation under Grant Number CMMI-1405226. JBL acknowledges financial support from Institut Universitaire de France (IUF).

Appendix A Approximate Yield Criterion

A.1 Minimum continuity

Following the scheme suggested in [20], also utilized in [6, 13], one can write:

$$\Pi^{(\mathrm{M})} \approx \bar{\sigma}\sqrt{\frac{1}{3}\left(\frac{1}{1-\chi^2}\int_1^{1/\chi^2}\frac{D_{kk}}{u}\,\mathrm{d}u\right)^2 + D_{33}^2} = \bar{\sigma}\sqrt{\frac{1}{3}\left(\frac{\ln\left(1/\chi^2\right)}{1-\chi^2}\right)^2 D_{kk}^2 + D_{33}^2} \tag{A-1}$$

which loses the upper-bound character and yet stays close to the rigorous upper-bound of the function. Correspondingly, the $g(\xi)$ function, as defined in (31), is decomposed into the following terms:

$$g(\xi) = \mathrm{sgn}\left(D_{33}\right)\left[(1-c)\left(\left|\xi-\chi^2\right| + \frac{w}{\sqrt{3}}\frac{1-c}{c}|\xi|\right) + \sqrt{\frac{1}{3}\left(\ln\frac{1}{\chi^2}\right)^2\xi^2 + (1-\chi^2)^2}\right] \tag{A-2}$$

Following the same rationale expounded in Section 2.5, the subsurfaces of the yield surface can be derived as follows:

1. *Singular (straight) zones*

   – At $\xi = 0$:

$$\begin{aligned} f^{'}(\xi) &= \frac{\Sigma_{11}}{\bar{\sigma}} \\ \frac{g^{'}(\xi)}{\mathrm{sgn}\left(D_{33}\right)} &= -(1-c) + \frac{w}{\sqrt{3}}\frac{(1-c)^2}{c}\mathrm{sgn}\left(\xi\right) \end{aligned} \tag{A-3}$$

   which is identical to (34). Then, at the yield point, one can write:

$$\begin{aligned} f^{'}(\xi) \le g^{'}(\xi) \;\therefore\; \left|\frac{\Sigma_{11}}{\bar{\sigma}}\mathrm{sgn}\left(D_{33}\right) + (1-c)\right| &\le \frac{w}{\sqrt{3}}\frac{(1-c)^2}{c} \\ f(\xi) = g(\xi) \;\therefore\; \frac{\Sigma_{33}}{\bar{\sigma}} &= \frac{\Sigma_{11}}{\bar{\sigma}} + \mathrm{sgn}\left(D_{33}\right)\left(1-c\xi^2\right) \end{aligned} \tag{A-4}$$

   which is identical to (35).

   – At $\xi = \chi^2$:

$$\begin{aligned} f^{'}(\xi) &= \frac{\Sigma_{11}}{\bar{\sigma}} \\ \frac{g^{'}(\xi)}{\mathrm{sgn}\left(D_{33}\right)} &= (1-c)\mathrm{sgn}\left(\xi-\chi^2\right) + \frac{w}{\sqrt{3}}\frac{(1-c)^2}{c} + \frac{\frac{1}{3}\left(\ln\frac{1}{\chi^2}\right)^2\xi^2}{\mathcal{Q}} \end{aligned} \tag{A-5}$$

   where $\mathcal{Q} = \sqrt{\frac{1}{3}\left(\ln\frac{1}{\chi^2}\right)^2\xi^2 + (1-\chi^2)^2}$. Then, at the yield point, we have:

$$\begin{aligned} f^{'}(\xi) \le g^{'}(\xi) \;\therefore\; \left|\frac{\Sigma_{11}}{\bar{\sigma}}\mathrm{sgn}\left(D_{33}\right) - \left[\frac{\frac{1}{3}\left(\ln\frac{1}{\chi^2}\right)^2\chi^2}{\mathcal{R}_1} + \frac{w}{\sqrt{3}}\frac{(1-c)^2}{c}\right]\right| &\le 1-c \\ f(\xi) = g(\xi) \;\therefore\; \frac{\Sigma_{33}}{\bar{\sigma}} = \frac{\Sigma_{11}}{\bar{\sigma}}(1-\chi^2) + \mathrm{sgn}\left(D_{33}\right)\left[\mathcal{Q} + \frac{w\chi^2}{\sqrt{3}}\frac{(1-c)^2}{c}\right] & \end{aligned} \tag{A-6}$$

2. *Regular (curved) zones* $\left(\xi \in \mathbb{R} - \{0, \chi^2\}\right)$

According to the parametric representation of the yield surface:

$$\begin{aligned}
\frac{\Sigma_{11}}{\bar{\sigma}}\text{sgn}\left(D_{33}\right) &= (1-c)\text{sgn}\left(\xi-\chi^2\right) + \frac{w}{\sqrt{3}}\frac{(1-c)^2}{c}\text{sgn}\left(\xi\right) + \frac{\frac{1}{3}\left(\ln\frac{1}{\chi^2}\right)^2\xi}{\mathcal{Q}} \\
\frac{\Sigma_{33}}{\bar{\sigma}}\text{sgn}\left(D_{33}\right) &= (1-c)(1-\chi^2)\text{sgn}\left(\xi-\chi^2\right) + \frac{w}{\sqrt{3}}\frac{(1-c)^2}{c}\text{sgn}\left(\xi\right) + \frac{\frac{1}{3}\left(\ln\frac{1}{\chi^2}\right)^2\xi + (1-\chi^2)^2}{\mathcal{Q}}
\end{aligned} \tag{A-7}$$

where $\mathcal{Q}(\xi) = \sqrt{\frac{1}{3}\left(\ln\frac{1}{\chi^2}\right)^2\xi^2 + (1-\chi^2)^2}$.

In the interest of eliminating ξ from (A-7), let

$$\mathcal{X}_1 = \frac{\xi}{\mathcal{R}} \quad , \quad \mathcal{X}_2 = \frac{1}{\mathcal{R}} \quad \therefore \quad \xi = \frac{\mathcal{X}_1}{\mathcal{X}_2}$$

Then, (A-7) can be recast by the following form:

$$\begin{aligned}
&\begin{bmatrix} \frac{1}{3}\left(\ln\frac{1}{\chi^2}\right)^2 & 0 \\ \frac{1}{3}\left(\ln\frac{1}{\chi^2}\right)^2 & (1-\chi^2)^2 \end{bmatrix}\begin{bmatrix}\mathcal{X}_1 \\ \mathcal{X}_2\end{bmatrix} = \begin{bmatrix}\frac{\bar{\Sigma}_1}{\bar{\sigma}} \\ \frac{\bar{\Sigma}_2}{\bar{\sigma}}\end{bmatrix} \\
\therefore \quad &\begin{bmatrix}\mathcal{X}_1 \\ \mathcal{X}_2\end{bmatrix} = \begin{bmatrix} \frac{3}{\left(\ln\frac{1}{\chi^2}\right)^2} & 0 \\ \frac{-1}{(1-\chi^2)^2} & \frac{1}{(1-\chi^2)^2} \end{bmatrix}\begin{bmatrix}\frac{\bar{\Sigma}_1}{\bar{\sigma}} \\ \frac{\bar{\Sigma}_2}{\bar{\sigma}}\end{bmatrix}
\end{aligned} \tag{A-8}$$

On the other hand, from (39), with ξ and $\mathcal{R}$ inserted in terms of $(\mathcal{X}_1, \mathcal{X}_2)$, one can write:

$$\left(\frac{\mathcal{X}_1}{\mathcal{X}_2}\right)^2 = \frac{3}{\left(\ln\frac{1}{\chi^2}\right)^2}\left[\frac{1}{\mathcal{X}_2^2} - (1-\chi^2)^2\right] \quad \therefore \quad \frac{1}{3}\left(\ln\frac{1}{\chi^2}\right)^2\mathcal{X}_1^2 + (1-\chi^2)^2\mathcal{X}_2^2 = 1 \tag{A-9}$$

which, in combination with (A-8), leads to the following expression pertaining to the regular portion:

$$3\left(\frac{\bar{\Sigma}_1/\bar{\sigma}}{\ln\frac{1}{\chi^2}}\right)^2 + \left(\frac{\bar{\Sigma}_2 - \bar{\Sigma}_1}{\bar{\sigma}}\right)^2 - 1 = 0 \tag{A-10}$$

where

$$\begin{aligned}
\frac{\bar{\Sigma}_1}{\bar{\sigma}} &= \frac{\Sigma_{11}}{\bar{\sigma}}\text{sgn}\left(D_{33}\right) - (1-c)\left[\text{sgn}\left(\xi-\chi^2\right) + \frac{w}{\sqrt{3}}\frac{(1-c)}{c}\text{sgn}\left(\xi\right)\right] \\
\frac{\bar{\Sigma}_2}{\bar{\sigma}} &= \frac{\Sigma_{33}}{\bar{\sigma}}\text{sgn}\left(D_{33}\right) - (1-c)\left[(1-\chi^2)\text{sgn}\left(\xi-\chi^2\right) + \frac{w}{\sqrt{3}}\frac{(1-c)}{c}\text{sgn}\left(\xi\right)\right]
\end{aligned}$$

The complete approximate yield function based on the minimum-continuity field can thus be expanded as the following piecewise-continuous function:

$$\mathcal{F}^{\text{col}} = \begin{cases} \dfrac{\Sigma_{33} - \Sigma_{11}}{\bar{\sigma}} - (1 - c\chi^2)\text{sgn}\left(\Sigma_{33}\right) \text{ for } \left| \dfrac{\Sigma_{11}}{\bar{\sigma}}\text{sgn}\left(\Sigma_{33}\right) + (1-c) \right| \leq \dfrac{w}{\sqrt{3}} \dfrac{(1-c)^2}{c} \\ \dfrac{\Sigma_{33} - (1-\chi^2)\Sigma_{11}}{\bar{\sigma}} - \left[\mathcal{Q}_0 + \dfrac{w\chi^2}{\sqrt{3}} \dfrac{(1-c)^2}{c} \right] \text{sgn}\left(\Sigma_{33}\right) \\ \text{for} \left| \dfrac{\Sigma_{11}}{\bar{\sigma}}\text{sgn}\left(\Sigma_{33}\right) - \left[\dfrac{\frac{1}{3}\left(\ln \frac{1}{\chi^2}\right)^2 \chi^2}{\mathcal{Q}_0} + \frac{w}{\sqrt{3}} \frac{(1-c)^2}{c} \right] \right| \leq 1 - c \\ 3\left(\dfrac{\bar{\Sigma}_1/\bar{\sigma}}{\ln \frac{1}{\chi^2}} \right)^2 + \left(\dfrac{\bar{\Sigma}_2 - \bar{\Sigma}_1}{\bar{\sigma}} \right)^2 - 1 \qquad \text{Otherwise} \end{cases} \tag{A-11}$$

where

$$\mathcal{Q}_0 = \sqrt{\frac{1}{3}\left(\ln \frac{1}{\chi^2}\right)^2 \chi^4 + (1-\chi^2)^2}$$

$$\frac{\bar{\Sigma}_1}{\bar{\sigma}}\text{sgn}\left(\Sigma_{33}\right) = \frac{\Sigma_{11}}{\bar{\sigma}} - (1-c)\text{sgn}\left(\Sigma_{11}\right)\left[1 + \frac{w}{\sqrt{3}}\frac{(1-c)}{c}\right]$$

$$\frac{\bar{\Sigma}_2}{\bar{\sigma}}\text{sgn}\left(\Sigma_{33}\right) = \frac{\Sigma_{33}}{\bar{\sigma}} - (1-c)\text{sgn}\left(\Sigma_{11}\right)\left[(1-\chi^2) + \frac{w}{\sqrt{3}}\frac{(1-c)}{c}\right]$$

Figure A-1 shows the comparison between the two surfaces various void aspect ratios, ligament parameters, and cell aspect ratios.

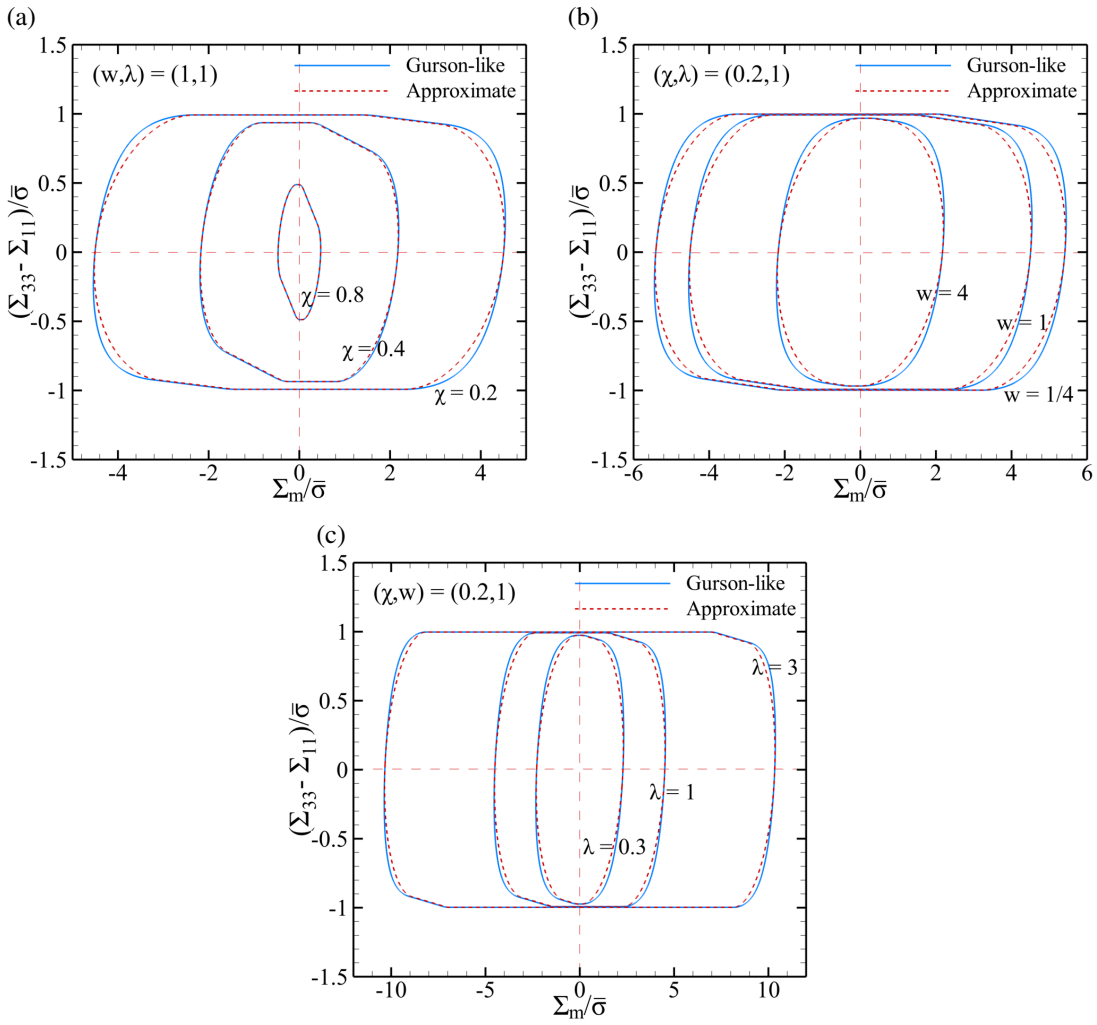

Figure A-1: Comparison between minimum-continuity yield surfaces based on exact and approximate integrations: (a) for fixed (w, λ) and various ligament parameters χ, (b) for fixed (χ, λ) and various void aspect ratios w, (c) for fixed (χ, w) and various cell aspect ratios λ.

A.2 Higher continuity

Following the scheme suggested in [20], one can approximate $\Pi^{(\mathrm{P})}$ in (24) by replacing $\mathcal{I}$ with $\bar{\mathcal{I}}$ constituted by $(\langle\sqrt{\delta}\rangle_{\Omega^{(\mathrm{P})}})^2$. That is

$$\Pi^{(\mathrm{P})} \approx |D_{33}|\,\bar{\sigma}\bar{\mathcal{I}} \tag{A-12}$$

with the terms identical to those in (27) except for $\mathcal{U}_1$, which is replaced by $\bar{\mathcal{U}}_1$ equaling

$$\bar{\mathcal{U}}_1 = \xi_1 + \xi_1^2\left[\left(\langle\sqrt{\delta}\rangle_{\Omega^{(\mathrm{P})}}\right)^2 - 1\right] = \xi_1 + \xi_1^2\left[\frac{1}{6}\left(\frac{\lambda(1-c)}{\chi}\right)^2 - 1\right] \tag{A-13}$$

where use has been made of $\langle\sqrt{\delta}\rangle_{\Omega^{(\mathrm{P})}}$ reading

$$\langle\sqrt{\delta}\rangle_{\Omega^{(\mathrm{P})}} = \sqrt{\frac{2}{3}}\frac{\lambda}{\chi}\left(\frac{1}{1-c}\int_c^1 v\,\mathrm{d}v\right) = \frac{\lambda}{\chi}\frac{1-c}{\sqrt{6}}$$

Correspondingly, the counterpart to (46) becomes:

$$\begin{aligned}\frac{\Sigma_{11}^{(\mathrm{P})}}{\bar{\sigma}}\mathrm{sgn}\left(D_{33}\right) &= \frac{2}{\chi^2}\bar{\mathcal{I}}_{,\xi_1}\\ \frac{\Sigma_{33}^{(\mathrm{P})}}{\bar{\sigma}}\mathrm{sgn}\left(D_{33}\right) &= \left[-\left(\xi_1-\frac{2}{\chi^2}\right)\bar{\mathcal{I}}_{,\xi_1}+\bar{\mathcal{I}}\right]\end{aligned} \tag{A-14}$$

Then, according to (30), the total stress field can be expressed identically to that in (47), with the following components:

$$\begin{aligned}\frac{\Sigma_{11}^{(1)}}{\bar{\sigma}}\mathrm{sgn}\left(D_{33}\right) &= 2\bar{\mathcal{I}}\\ \frac{\Sigma_{33}^{(1)}}{\bar{\sigma}}\mathrm{sgn}\left(D_{33}\right) &= -2(\xi-1)\bar{\mathcal{I}}_{,\xi_1}+\chi^2\bar{\mathcal{I}}\end{aligned} \tag{A-15}$$

with $\Sigma_{11}^{(2)}$ and $\Sigma_{33}^{(2)}$ identical to those in (48).

Appendix B Elimination of ξ from (39)

In the $\xi\in\mathbb{R}-\{0,\chi^2\}$ region where Π is differentiable, the latter can be recast in terms of D_{33} and D_{kk}, here termed $\Pi^*(D_{kk},D_{33})$, which delivers the following auxiliary stresses:

$$\begin{aligned}\Sigma_1^* &= \frac{\partial\Pi}{\partial D_{kk}} = \mathrm{sgn}\left(D_{33}\right)\mathrm{sgn}\left(\xi\right)\left(\alpha_1-\alpha_2\right)\\ \Sigma_2^* &= \frac{\partial\Pi}{\partial D_{33}} = \mathrm{sgn}\left(D_{33}\right)\left(\beta_1-\beta_2\right)\end{aligned} \tag{A-16}$$

where $\partial\Pi^*/\partial D_{kk}$ is carried out on the condition of D_{33} remaining fixed, and vice versa. Moreover, one can write, by exploiting the $\cosh$ of a subtraction in (A-16)$_1$:

$$\cosh\left(\sqrt{3}\mathrm{sgn}\left(D_{kk}\right)\frac{\Sigma_1^*}{\bar{\sigma}}\right)=\frac{\beta_1\beta_2-\xi_2^2}{\chi^2}\ \therefore\ \chi^2\cosh\left(\sqrt{3}\mathrm{sgn}\left(D_{kk}\right)\frac{\Sigma_1^*}{\bar{\sigma}}\right)=1-\mathrm{sgn}\left(D_{33}\right)\beta_1\frac{\Sigma_2^*}{\bar{\sigma}} \tag{A-17}$$

where use has been made of Eq's (40) and that $\mathrm{sgn}\left(D_{33}\right)\mathrm{sgn}\left(\xi\right)=\mathrm{sgn}\left(D_{kk}\right)$. Therefore, ξ_2 can be eliminated from (A-17) and (40) combined:

$$\xi_2^2=\left[\frac{1-\chi^2\cosh\left(\sqrt{3}\mathrm{sgn}\left(D_{kk}\right)\frac{\Sigma_1^*}{\bar{\sigma}}\right)}{\frac{\Sigma_2^*}{\bar{\sigma}}}\right]^2-1 \tag{A-18}$$

Moreover, exploiting $\sinh$ of a subtraction in (A-16)$_1$, together with (40), gives:

$$\sinh\left(\sqrt{3}\mathrm{sgn}\left(D_{kk}\right)\frac{\Sigma_1^*}{\bar{\sigma}}\right)=\frac{|\xi_2|}{\chi^2}\mathrm{sgn}\left(D_{33}\right)\frac{\Sigma_2^*}{\bar{\sigma}} \tag{A-19}$$

Finally, the following identity, combined with Eq's (A-17) and (A-19), together with (40), supplies the following Gurson-like relation between Σ_1^* and Σ_2^*:

$$\begin{aligned}&\cosh^2\left(\sqrt{3}\mathrm{sgn}\left(D_{kk}\right)\frac{\Sigma_1^*}{\bar{\sigma}}\right)-\sinh^2\left(\sqrt{3}\mathrm{sgn}\left(D_{kk}\right)\frac{\Sigma_1^*}{\bar{\sigma}}\right)=1\ \therefore\ (\beta_1\beta_2-\xi_2^2)^2-\xi_2^2(\beta_2-\beta_1)^2=\chi^2\\ &\therefore\ \left(\frac{\Sigma_2^*}{\bar{\sigma}}\right)^2+2\chi^2\cosh\left(\sqrt{3}\mathrm{sgn}\left(D_{kk}\right)\frac{\Sigma_1^*}{\bar{\sigma}}\right)-(1+\chi^2)=0\end{aligned} \tag{A-20}$$

where the sgn (D_{kk}) inside the $\cosh$ term can be removed for being ineffective.

It now suffices to express Σ_1^* and Σ_2^* in terms of Σ_{11} and Σ_{33} so as for Eq. (A-20) to relate the latter two stresses. To this end, one can refer to (A-16) and (39) simultaneously, so that

$$\begin{aligned}\frac{\Sigma_1^*}{\bar{\sigma}} &= \frac{\Sigma_{11}}{\bar{\sigma}} - (1-c)\left(1 + \frac{w}{\sqrt{3}}\frac{1-c}{c}\right)\text{sgn}\,(D_{kk}) \\ \frac{\Sigma_2^*}{\bar{\sigma}} &= \frac{\Sigma_{33}-\Sigma_{11}}{\bar{\sigma}} + (1-c)\chi^2\text{sgn}\,(D_{kk})\end{aligned} \tag{A-21}$$

Appendix C Special Mechanisms

While the yield locus around the $\Sigma_{33} - \Sigma_{11}$ intercept conveys the way strains localize at the failure instant, there exist particularly appealing plasticity mechanisms within the dynamic process during the pre-localization regime. This section tends to probe into these mechanisms through depicting the velocity vector plots at the bottom and top portions of each yield locus examined in Sec. 2.5. The bottom portion of a locus denotes when the lateral stress is either the major one ($\Sigma_{11} > \Sigma_{33}$) or has limited difference with the axial stress. The top portion, however, represents the converse. Altogether, the special mechanisms of plastic flow during the pre-localization phase can be categorized as follows:

– *During void growth ensued by coalescence in layers*:

In the top half of the surface, there exists a zone associated with a stagnation within the radial velocity component v_r. At the stagnation radius, the deformation is mainly elastic with limited plasticity. This would reduce the plastic region mainly up to the radius of stagnation, and hence the effective RVE will have the same height with but a smaller radius than the whole cell. At the limit of coalescence in layers, the stagnation radius turns into the radius of the cell.

– *During void growth ensued by coalescence in columns*:

All the same, in the bottom half of the surface, there exists a zone associated with a stagnation within the vertical velocity component v_z. At the stagnation height, the deformation is mainly elastic with limited plasticity. This would reduce the plastic region mainly up to the height of stagnation, and hence the effective RVE will have the same radius with but a smaller height than the whole cell. At the zone of coalescence in columns, the stagnation height reduces to zero, and a highly-sheared zone forms between the plugs and the torus. This phenomenon can be termed *void collapse*. The condition upon which void collapse can occur is set forth by the following relationship between the lateral and axial stresses:

$$\begin{aligned}&\Sigma_{33} - \Sigma_{11} < 0 \quad , \quad \Sigma_m > 0 \\ \Longrightarrow\ &2\Sigma_{11} > -\Sigma_{33} \equiv |\Sigma_{33}| \quad \therefore \quad |\Sigma_{33}| < 2|\Sigma_{11}|\end{aligned} \tag{A-22}$$

The various conditions stated above are schematized in Fig. A-2.

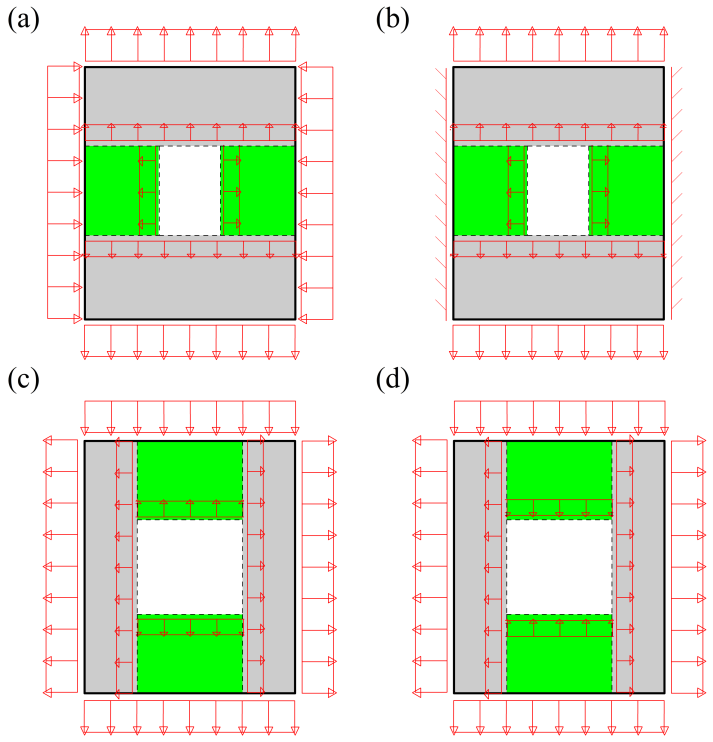

Figure A-2: Schematic special flow mechanisms with their corresponding velocity vectors: (a,b) radial stagnation during void growth ensued by layered coalescence in the top portion of the yield surface (with the axial stress being the major one); (c,d) vertical stagnation during void growth ensued by column coalescence (void collapse) in the bottom portion of the yield surface (with the lateral stress being the major one).

The trend of realizing the above special mechanisms through variation of each microstructural parameter can be described according to the following trends:

C.1 Variation of χ

Let's focus on small to medium values of χ first. Within a very slight variation in Σ_m in the bottom portion of the yield surface, the vertical velocity slope will shift from continuous (denoting homogeneous plasticity) to discontinuous, and a stagnation point will appear in v_z. This can be attributed as void collapse when the height of stagnation shrinks to zero, that can be envisaged at higher χs. On the top portion, however, the stagnation will be triggered in v_r, characterized by homogeneous plasticity (void growth) which is ensued by coalescence in layers. At large values of χ, void collapse occurs at significantly lower values of Σ_m, and plasticity will proceed in homogeneous manner for larger mean stresses. The top portion of the yield surface will behave similarly to that of small to medium χs. Since, with slight decrease in Σ_m, the height of stagnation in v_z drops towards zero in thin plugs, void collapse has more inclination to occur with larger voids, *i.e.* at greater χs, and nonetheless, less likely to happen in smaller cells (with less χs) due to the opposite reason. Figure A-3 demonstrates that via velocity vector plots.

C.2 Variation of w

Evolution of the void aspect ratio w is entitled to the same special mechanisms. However, the transition from a continuous v_z into that with stagnation occurs at a wider range of Σ_m from larger to smaller Σ_m

values, especially at larger values of λ. Moreover, void collapse at larger ws is not as intense as that in larger values of χ due to the plastic torus being more bulky. Moreover, on the top portion, the stagnation triggered in v_r (characterized by homogeneous plasticity ensued by coalescence in layers) occurs in larger ws but not likely to be realized at very large ws, e.g. $w = 10$. Figure A-4 demonstrates that via velocity vector plots.

C.3 Variation of λ

Variation of the cell aspect ratio λ correlates with the same special mechanisms. Resembling that in small to medium ws, the transition from a continuous v_z into that with stagnation occurs at a rather wide range of Σ_m from larger to smaller Σ_m values. It sounds more appealing that vertical velocity stagnation takes place even in very thin plugs, ***i.e.*** at long voids and short cells (see Fig. A-5b). Since, with limited decrease in Σ_m, the height of stagnation in v_z drops towards zero in thin plugs, void collapse is more propensive to occur in short cells, ***i.e.*** at small λs, and all the same, less prone to happen in long cells due to the converse reason. Figure A-5 depicts special flow mechanisms at various λs via velocity vector plots.

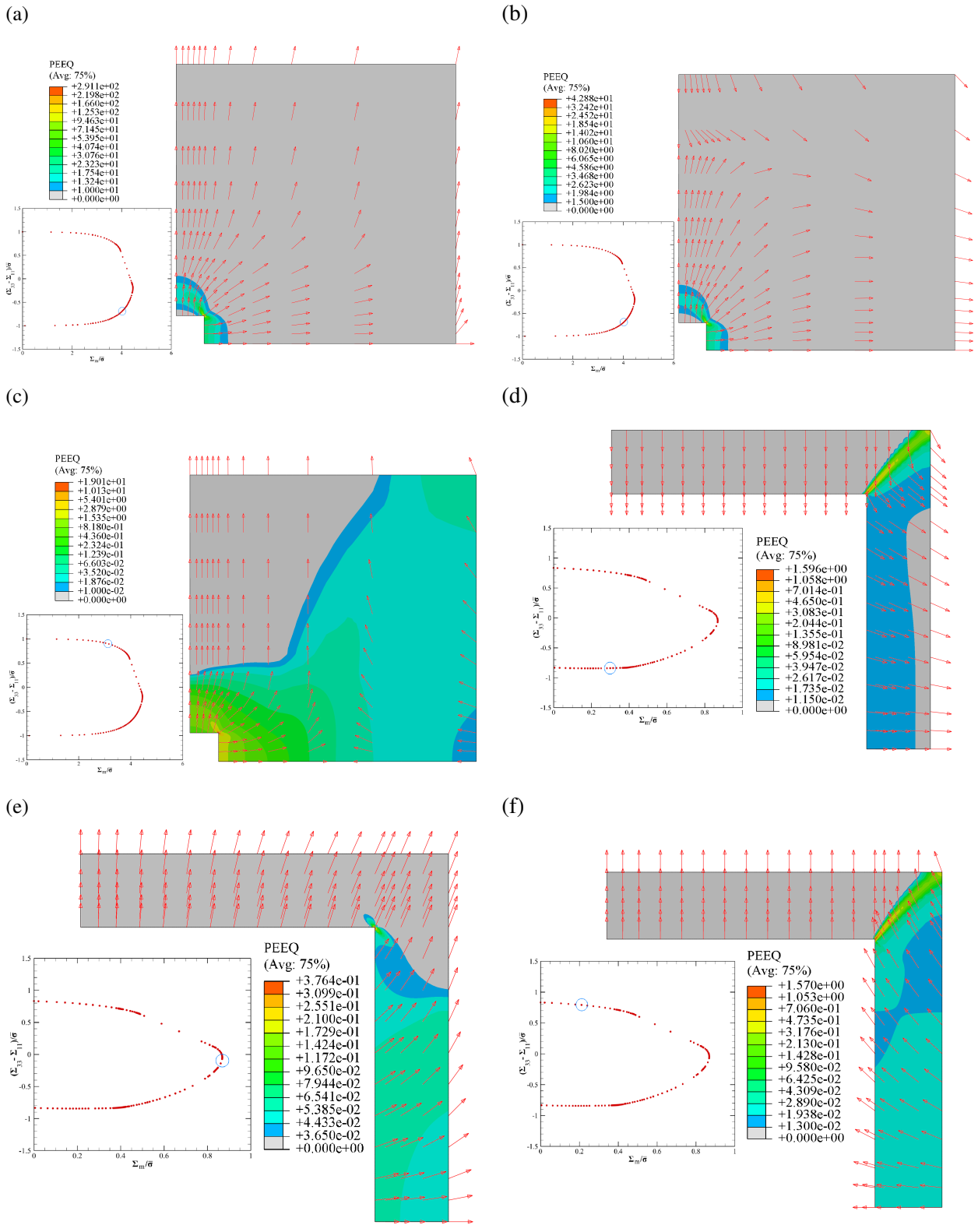

Figure A-3: Velocity vector plots signifying special flow mechanisms at small-to-medium and large ligament parameters, accompanied by their corresponding neighborhoods on the yield surfaces: (a,b) and (d,e) bottom portions of the yield surface for small and large χs with continuous and discontinuous vertical velocity gradients, the latter denoting column coalescence; (c) and (f) top portions of the yield surface for small and large χs with discontinuous radial velocity gradients. Void collapse is observed at (d) when the stagnation height approaches zero.

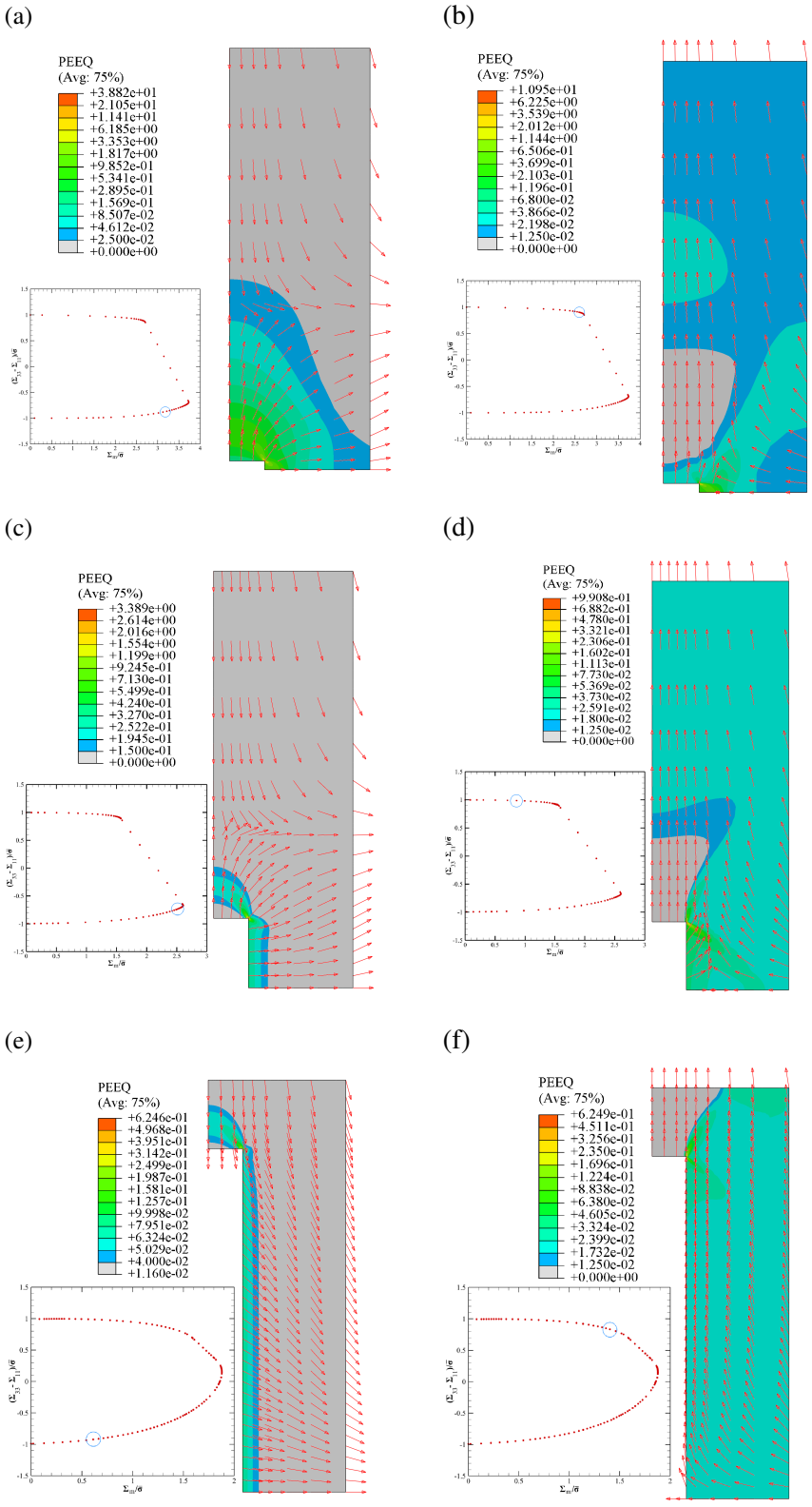

Figure A-4: Velocity vector plots, accompanied by their corresponding neighborhoods on the yield surfaces, showing special flow mechanisms at various void aspect ratios: (a,b) bottom and top yield surface portions for small and medium ws; (c,d) bottom and top portions of the yield surface for large ws; (e,f) bottom and top portions of the yield surface for very large ws, void collapse being observed in the former.

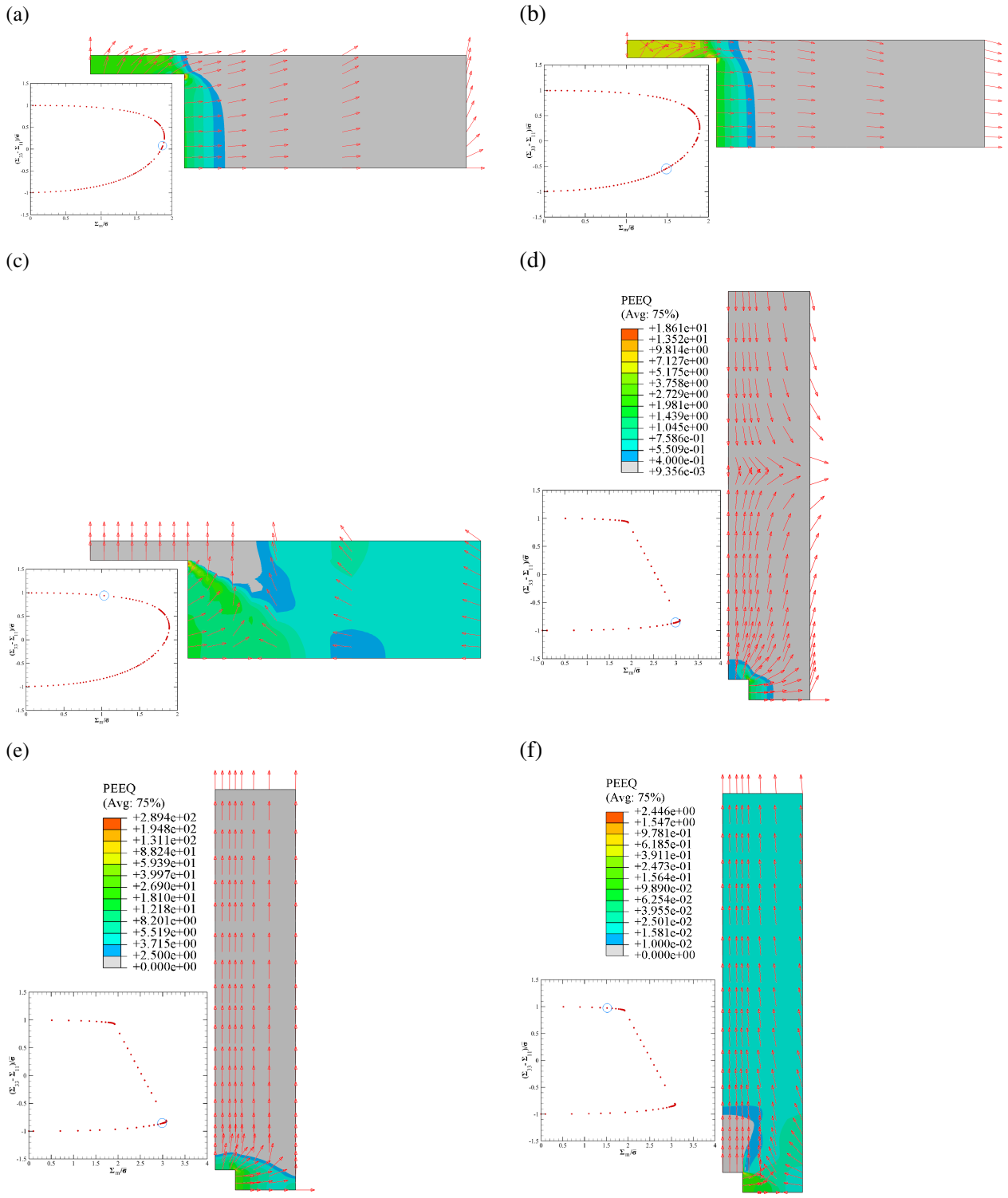

Figure A-5: Velocity vector plots signifying special flow mechanisms at small-to-medium and large cell aspect ratios, accompanied by their corresponding neighborhoods on the yield surfaces: (a,b) and (d,e) bottom portions of the yield surface for small and large λs with continuous and discontinuous vertical velocity gradients, the latter denoting column coalescence; (c) and (f) top portions of the yield surface for small and large λs with discontinuous radial velocity gradients. Void collapse is observed at (d) when the stagnation height approaches zero.

References

[1] L. Morin, J.-B. Leblond, A. A. Benzerga, and D. Kondo. A unified criterion for the growth and coalescence of microvoids. *Journal of the Mechanics and Physics of Solids*, 97:19–36, 2016.

[2] A. A. Benzerga and J.-B. Leblond. Ductile fracture by void growth to coalescence. *Advances in Applied Mechanics*, 44:169–305, 2010.

[3] A. A. Benzerga. *Rupture ductile des tôles anisotropes*. PhD thesis, Ecole Nationale Supérieure des Mines de Paris, 2000.

[4] A. Pineau, A. A. Benzerga, and T. Pardoen. Failure of metals I. Brittle and Ductile Fracture. *Acta Materialia*, 107:424–483, 2016.

[5] M. E. Torki and A. A. Benzerga. A mechanism of failure in shear bands. 23:67–71, 2018.

[6] ME Torki, C. Tekoglu, J-B Leblond, and AA Benzerga. Theoretical and numerical analysis of void coalescence in porous ductile solids under arbitrary loadings. *International Journal of Plasticity*, 91:160–181, 2017.

[7] J. Koplik and A. Needleman. Void growth and coalescence in porous plastic solids. *International Journal of Solids and Structures*, 24(8):835–853, 1988.

[8] V. Tvergaard and A. Needleman. Analysis of the cup–cone fracture in a round tensile bar. *Acta Metallurgica*, 32:157–169, 1984.

[9] P. F. Thomason. A three–dimensional model for ductile fracture by the growth and coalescence of microvoids. *Acta Metallurgica*, 33(6):1087–1095, 1985.

[10] A. A. Benzerga, J. Besson, and A. Pineau. Coalescence–Controlled Anisotropic Ductile Fracture. *Journal of Engineering Materials and Technology*, 121:221–229, 1999.

[11] T. Pardoen and J. W. Hutchinson. An extended model for void growth and coalescence. *Journal of the Mechanics and Physics of Solids*, 48:2467–2512, 2000.

[12] A. A. Benzerga and J.-B. Leblond. Effective Yield Criterion Accounting for Microvoid Coalescence. *Journal of Applied Mechanics*, 81:031009, 2014.

[13] M. E. Torki, A. A. Benzerga, and J.-B. Leblond. On Void Coalescence under Combined Tension and Shear. *Journal of Applied Mechanics*, 82(7):071005, 2015.

[14] S. M. Keralavarma and S. Chockalingam. A Criterion for Void Coalescence in Anisotropic Ductile Materials. *International Journal of Plasticity*, 82:159–176, 2016.

[15] L. Morin, J.-B. Leblond, and A. A. Benzerga. Coalescence of voids by internal necking: theoretical estimates and numerical results. *Journal of the Mechanics and Physics of Solids*, 75:140–158, 2015.

[16] M. Gologanu, J.-B. Leblond, G. Perrin, and J. Devaux. Theoretical models for void coalescence in porous ductile solids – II: Coalescence in "columns". *International Journal of Solids and Structures*, 38:5595–5604, 2001.

[17] M. Gologanu. *Etude de quelques problèmes de rupture ductile des métaux*. PhD thesis, Université Paris 6, 1997.

[18] I. S. Gradshtein and I. M. Ryzhik. Tables of integrals, sums, series and products, 1971.

[19] P. F. Thomason. Three–dimensional models for the plastic limit–loads at incipient failure of the inter-void matrix in ductile porous solids. *Acta Metallurgica*, 33:1079–1085, 1985.

[20] C. Tekoğlu, J.-B. Leblond, and T. Pardoen. A criterion for the onset of void coalescence under combined tension and shear. *Journal of the Mechanics and Physics of Solids*, 60:1363–1381, 2012.

[21] A. Needleman. A numerical study of necking in circular cylindrical bars. *Journal of the Mechanics and Physics of Solids*, 20:111–127, 1972.

[22] V. Tvergaard. Influence of voids on shear band instabilities under plane strain conditions. *International Journal of Fracture*, 17:389–407, 1981.

[23] V. Tvergaard. On localization in ductile materials containing spherical voids. *International Journal of Fracture*, 18:237–252, 1982.

[24] S. M. Keralavarma. A multi-surface plasticity model for ductile fracture simulations. *Journal of the Mechanics and Physics of Solids*, 103:100–120, 2017.

[25] K. Madou and J.-B. Leblond. Numerical studies of porous ductile materials containing arbitrary ellipsoidal voids — I: Yield surfaces of representative cells. *European Journal of Mechanics*, 42:480–489, 2013.